NATIONAL AERONAUTICS AND SPACE ADMINISTRATION

Technical Report 32-1550

Volume IV

Mariner Mars 19 1 Project Final Report

Science Results

Prepared by
Mariner Mars 1971 Science Experimenter Teams

Technical Report 32-1550

Volume IV

Mariner Mars 1971 Project Final Report

Science Results

Prepared by
Mariner Mars 1971 Science Experimenter Teams

JET PROPULSION LABORATORY
CALIFORNIA INSTITUTE OF TECHNOLOGY
PASADENA, CALIFORNIA

July 15, 1973

Preface

The work described in this Report was performed under the cog. ance of the Mariner Mars 1971 Project.

This five-volume document constitutes the Mariner Mars 1971 Project Final Report. Volume I consists of Project development through launch and trajectory-correction maneuver. Volume II presents the preliminary science results derived from data evaluation to December 14, 1971. (The information contained in Volume II has appeared in *Science*, Vol. 175, January 1972.) Volume III describes the Mission Operations System and covers flight operations after trajectory-correction maneuver through the standard orbital mission up to the onset of solar occultations in April 1972. Volume IV consists of the science results derived from the standard orbital mission and some preliminary interpretations of the data obtained from the extended mission. Volume V is an evaluation of mission success based upon comparisons of science results with the experiment objectives.

Detailed information on Project organization, Project policies and requirements, subsystem development, and other technical subjects has been excluded from the Project Final Report volumes. Where appropriate, reference is made to the JPL informal documentation containing this information. The development of most *Mariner 9* subsystems is documented in JPL Technical Memorandums.

Contents

Contents (contd)

Contents (contd)

Contents (contd)

Contents (contd)

Contents (contd)

Contents (contd)

Contents (contd)

Contents (contd)

Contents (contd)

Contents (contd)

Contents (contd)

Contents (contd)

Contents (contd)

Abstract

This Technical Report contains science results from the mission of *Mariner 9*, the first planetary orbiting spacecraft. *Mariner 9* was inserted into Mars orbit on November 14, 1971, and expired on October 27, 1972. A summary of significant mission events is also included.

Mariner 9 observed the impact-cratered surface of Mars, discovered volcanic mountains, rift valleys, tectonic faults, and various types of terrain showing evidence of fluvial and wind erosion. It recorded an atmosphere with a complex meteorology of clouds, storms, and weather fronts; and photographed Phobos and Deimos, the two satellites of Mars. The results of analyses derived from these observations are presented in this Report. They have been written by individual experimenters or by members of the experiment teams and represent analysis efforts through November 1972.

Note to Data Users

National Aeronautics and Space Administration (NASA) policy requires that experimental data acquired from NASA-sponsored missions be deposited in the National Space Science Data Center[1] (NSSDC). These data are then available to the general science user at distribution costs determined by NSSDC. The content of the filed data is negotiated with each experiment's Principal Investigator and is dependent on the instrumentation used. Generally, the attempt is to store the received experimental data, after processing to remove instrumental distortions and effects. Results of analysis are not maintained at NSSDC. Inquiries regarding the specific nature of the *Mariner 9* data available should be made to NSSDC.

More explicit guidance can be given for the *Mariner 9* television pictures, especially with respect to the material used in this Report. The pictures are derived from five processing sources:

(1) Real time during operations (MTVS, JPL).

(2) Reduced Data Record (RDR: Image Processing Laboratory, JPL).

(3) Rectified and Scaled (R&S: Image Processing Laboratory, JPL).

(4) Experimenter Analysis Support (EAS: Image Processing Laboratory, JPL).

(5) Special Processing (AIL: Artificial Intelligence Laboratory, Stanford University).

The first two listed items (MTVS, RDR) for *Mariner 9* pictures are available from NSSDC with supporting data primarily describing the location of the pictures. The R&S products were made only for "Mapping A frames" (wide-angle camera pictures) and selected "B frames" (narrow-angle camera pictures). These are also available from NSSDC. EAS and AIL processing, by their nature, are specialized to assist analysis. For general distribution each picture would require an extensive description to clarify the processing, its intent, and cautions for interpretation. Therefore, EAS and AIL processed pictures are not stored at NSSDC. Users wishing copies of such material should communicate directly with the responsible author.

Finally, some remarks about identification. Because of the large number of pictures and the many processed versions, a specific identification method was devised for ordering copies from NSSDC and for references. The picture identification must include (a) and either (b) or (c) including the designation MTVS or RDR or EAS, etc.

(a) DAS Time, an 8 digit number between 1,491,192 and 13,511,828. This number is derived from a spacecraft clock and is common to all versions of the same picture. It is also used to identify the supporting data and to correlate with data from other *Mariner 9* instruments.

---

[1]National Space Science Data Center
National Aeronautics and Space Administration
Goddard Space Flight Center
Greenbelt, Maryland 20771

(b) MTVS Roll and File Number, of the form xxxx-xx. The first four digits are the MTVS roll number and are normally unique for each orbit. The numbers were controlled by the acquisition sequence of the spacecraft operation. The remaining digits are the file number or sequential position in the roll where a particular version of a picture can be found.

(c) RDR, P&S, EAS, and AIL products are identified by an Image Processing Laboratory (IPL) roll and process time of the form "roll number given," numerical month, day, year and time of day (hours, minutes, seconds in 24-hour time). Similar to the MTVS identifier, the IPL roll number identifies the picture roll, and the process time indicates the sequential position within the roll. However, the ordering of pictures and the numbering are controlled by the processing sequence requested and have no formal relation to the MTVS or spacecraft acquisition sequence.

More detailed information describing the *Mariner 9* mission, data acquisition, and data processing, especially for the television imagery, can be found in Volumes I, II, and Volume II Addendum, of the *Mariner Mars 1971 Television Picture Catalog*, JPL Technical Memorandum 33-585. Questions regarding the availability and distribution of this Catalog should be addressed to NSSDC.

I. An Overview of Geologic Results From *Mariner 9*[1]

Harold Masursky

U. S. Geological Survey, Flagstaff, Arizona 86001

A. Introduction and Mission Summary

This section provides a summary of *Mariner 9* mission operations insofar as they affected acquisition of geologic data. Selected results with a minimum of supporting evidence are presented to give, as briefly as possible, the geologic highlights of the mission. More detailed discussions of various regional and topical problems are given in other sections by various members of the Television Team.[2] Also included are hypotheses inferred from preliminary evidence, but which will have to await the test of later geologic mapping and detailed topical studies. These hypotheses are included to call attention to areas in which potentially valuable work can be performed. It should be emphasized that many of the observations and hypotheses given have developed during discussions with many of the members of the Television Team. My purpose here is to attempt a first distillation from the enormous body of facts and theory generated by the mission as a guide to the other sections in this Report and to present the most salient geologic results that distinguish Mars as a planet both from Earth and the Moon.

Mariner 9 was launched from Cape Kennedy on May 30, 1971, and was inserted into Mars orbit on November 13 (UT); the spacecraft continued to take pictures

and to make measurements until October 27, 1972. More than 54 billion bits of information were transmitted to Earth. More than 7300 pictures were taken of Mars and its satellites, about 1500 pictures of the planet were obtained by the 50-mm focal-length, wide-angle television camera, which has a resolution of 1 to 3 km (Ref. I-1). These pictures have been mosaicked into a preliminary map of the entire surface of Mars at a scale of 1:25,000,000; a preliminary shaded relief map, the first detailed complete map of Mars, has been published at the same scale (Ref. I-2).

The narrow-angle camera (500-mm focal length) acquired high-resolution pictures (100 to 300 m) of between 1 and 2% of the surface. Geodesy pictures taken by the wide-angle camera from higher altitudes cover most of the southern hemisphere. These low-resolution pictures (4 to 9 km) were taken to provide control points for maps to be made from the high-resolution pictures. Thirty photomosaic maps at a scale of 1:5,000,000 also have been made for preliminary analysis and plotting of various types of data; later editions, based on improved control and use of enhanced pictures, have been made (Ref. I-3; also see Section XXXXIII of this Report); final maps will be made over the next several years.

Many pictures were taken to show time variations in cloud cover, polar cap frost, and light and dark surface markings (Ref. I-4; also see Section XIII of this Report) on the planet. The infrared interferometer spectrometer (Ref. I-5) and ultraviolet spectrometer (Refs. I-6 and I-7), in addition to acquiring the atmospheric data, made pressure measurements from which the

---

cartographers will attempt to compare integrated contour maps tied to occultation measurements (Refs. I-8 and I-9, also see Section XXXVII of this Report) and Earth-based radar (Refs. I-10 and I-11). Systematic geologic mapping will be performed on the final cartographic products. Rectification, scaling, and additional enhancement of pictures and their integration with numerical results from the other experiments, such as gravity measurements provided by the celestial mechanics experimenters (Ref. I-12), will allow more sophisticated analysis, particularly about the thickness and density of the crust.

Because Mars is a low-contrast object, the pictures must be extensively computer-enhanced to bring out surface detail. Suppression of electronic noise in the television subsystem and upgrading of enhancement techniques, especially early in the mission when dust obscured the surface, allowed the image detail to be made visible (Ref. I-13).

With the loss of Mariner 8, extensively pre-planned different, but complementary, objectives established for both spacecraft had to be integrated into a new mission plan for Mariner 9. On the arrival of Mariner 9 at Mars, the planet-wide dust storm that had been observed in late September was still raging (Ref. I-14) so that this complex post-launch mission plan also had to be abandoned. Reconnaissance pictures were taken until January 1 when the dust storm subsided sufficiently to begin mapping sequences along with selected pictures taken for geodesy, variable features, atmosphere, and satellite studies. This mode continued with numerous successive modifications brought on by operational constraints until 70% of the planet had been mapped.

After a period of 2 months, when pictures could not be taken because of solar occultation, the mapping mission was resumed. During this period the northern spring season progressed, and the north polar hood had disappeared. Two new stars (Arcturus and Vega) were used for the first time in any space program to orient the spacecraft in more favorable picture-taking attitudes, thus allowing the remaining 30% of the planet in the northern hemisphere to be mapped. Some candidate landing sites for the Viking Program (Ref. I-15) also were photographed. After another interruption of 6 weeks during superior conjunction (Mars and the spacecraft passed behind the Sun), the final extended mission picture sequences were taken to fill gaps in the photographic coverage, to photograph areas of special interest,

to monitor the retreat of the north polar cap (Ref. I-16), and to study cloud formation over the volcanic constructs such as Nix Olympia (Ref. I-17).

B. Volcanic Features

The first features that emerged through the dust pall that blanketed the planet were four dark spots visible in high-altitude reconnaissance pictures, these spots later proved to be the four highest peaks on the planet, each of which is surmounted by a summit crater or complex of craters (Ref. I-18; Figure 1 of Ref. I-19). Gradual atmospheric clearing revealed first the full extent of the great volcanic pile of Nix Olympica, which rises high above the Amazonis basin floor (Figure 10 of Ref. I-20; Ref. I-21). (Estimates of its height by various methods of altimetry vary from 8 to 27 km.) This single volcanic edifice is about twice as wide as the largest of the Hawaiian volcanic pile and is about equal in volume to the total extrusive mass of the Hawaiian Islands chain. The form of the flank flows and of the lava channels with natural levees is strikingly similar to those of Hawaii and the Galapagos, suggesting that the flows may be basaltic in composition as on these comparable terrestrial structures (Refs. I-19 and I-22).

The three other volcanoes, also of surprisingly large size, lie along the Tharsis ridge. The summit of South Spot, from current altimetry data, lies more than 17 km above the floor of the Amazonis basin to the west. This estimated elevation difference almost equals the maximum relief on Earth, which amounts to about 20 km. The lava flows that radiate from the summit caldera of South Spot are not long and thin as are those of Nix Olympica, but rather are short and stubby (Refs. I-19 and I-21; also see Section II of this Report). This difference in form suggests probable differences in the composition of the flank flows. Those of South Spot are clearly less fluid than those of Nix Olympica and may be more silicic, possibly andesitic in composition. Short stubby flows of similar appearance are common in the upper parts of some continental volcanoes such as Mt. Hood and Mt. Rainier.

It is possible that variation in temperature and gas content could account for these differences in flow morphology, rather than a difference in original composition. The lack of craters and the morphologic crispness of the lava flows indicate that the upper layers of these large volcanoes are relatively young geologically, whatever their composition. The discovery of geologically youthful, large volcanic structures indicates that Mars

has been internally active. These features also provide a plausible source for much of the carbon dioxide and water in the atmosphere.

The Amazonis basin floor is covered in many places by a succession of lobate-fronted flows (Fig. I-1a) that resemble terrestrial basalt flows and the basalt flows that fill the mare basins on the Moon (Figs. I-1b and I-1c).
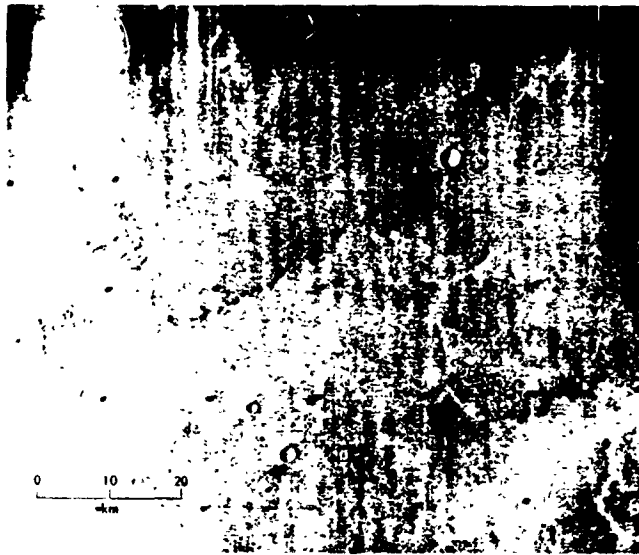
Fig. I-1a. Lobate lava flow front on basin floor similar to basaltic flows on Earth and the Moon. (MTVS 4179-30, DAS 06966613)
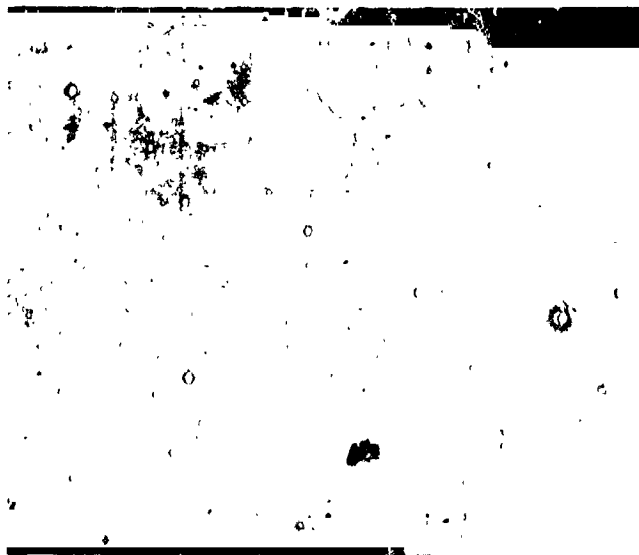
Fig. I-1b. *Lunar Orbiter V photograph showing lobate flow front on the Moon in the central part of the Imbrium basin. Similar flows collected at the Apollo landing site are basaltic in composition.*

Fig. I-1c. Elongate lava flows in northern Oceanus Procellarum photographed by the metric camera on *Apollo 15.*

Low mare-type domes with summit craters resemble basaltic shield volcanoes common on both Earth and the Moon. Domes of this type are scattered over the basin floors in the Amazonis and Elysium regions (Refs. I-20 and I-21; also see Section II of this Report).

In some areas the plains are slightly uplifted and transsected by faults. Some of these closely spaced horsts and graben are modified, often assuming a streamlined appearance attributed to the long-term effects of eolian erosion (Figs. 2a, 2b of Ref. I-23; also see Figs. X-2a and X-2b of this Report). Craters are more abundant in these structured terrains than on unfaulted plains; the most obvious of these faulted areas forms a large aureole around Nix Olympica. These rocks may represent an earlier generation of lava flows related to ancestral Nix Olympica volcanism (Ref. I-21; also see Section II of this Report).

Another type of volcanic feature is exemplified in the Hesperia region (22°S, 253°W; see Ref. I-19). This feature is characterized by a line of calderas in the center of a pattern of circular and radiating faults and channels with irregularly distributed volcanic blankets. This unusual feature lies within an area of plains, and no large volcanic pile or constructional edifice is evident (Ref. I-24; also see Section IV of this Report). The channels closely resemble terrestrial and lunar lava channels.

Fig. I-2a. Mosaic of wide-angle pictures showing complex of faults surrounding the volcanic structure in the Alba region. It resembles terrestrial volcanic complexes with central cauldrons. (MTVS 4224-63, DAS 08443019; MTVS 4222-69, DAS 08371134; MTVS 4222-57, DAS 08370854)

Another example of a volcanic feature lies in the Alba region (40°N, 110°W; Fig. I-2a). Here an array of faults encircles a large depression in the central part of a very low prominence. This depression resembles a cauldron rather than a caldera. The morphology of these deposits and their relation to the tectonic features resemble those of terrestrial intracontinental volcanic centers such as those of Scotland (Refs. I-25 through I-27); Norway (Ref. I-28); New England (Ref. I-29); and Africa (Ref. I-30) that contain more differentiated rocks of more variable composition than flood basalts and shield volcanoes. These terrestrial volcanic centers, when deeply eroded, commonly display ring and radial dikes, cone sheets, and evidence of cauldron subsidence.

Three other types of volcanic features are well developed. The first is typified by lines of craters 2 to 10 km in diameter along structural breaks parallel to major graben (Figs. 25 and 26 of Ref. I-20). Lines of volcanic

Fig. I-2b. Polygonally broken filling of crater cut by fault; inferred to be volcanic filling. Resembles terrestrial lava lakes that have solidified. (MTVS 4174-27, DAS 06822588)

vents such as the craters along the southwest rift zone of Mauna Loa, Hawaii (Ref. I-31) are common in terrestrial areas with a similar structural pattern. The second type, which occurs in the floors of some Martian craters (Fig. I-2b) along fault zones, consists of polygonal blocks segmenting what appear to be frozen lava lakes in pit craters like those near the summit of Kilauea, Hawaii. Craters of this type also occur on the Moon, where they have been called "turtleback" craters (Fig. I-2c). The third type of volcanic feature consists of complex ridges that are commonly steeper on one side (Figs. I-3a and I-3b). They occur in areas where lobate flow fronts and broad low domes imply basaltic volcanism. They resemble the lunar mare ridges that are interpreted as faults along which basaltic lava has squeezed upward. Similar squeezeups are common on terrestrial basalt flows, but on a much smaller scale.

C. Tectonic Features

Sloping eastward from the Tharsis ridge crest is a large equatorial plateau or tableland. This plateau is broken by three sets of fractures trending east–west, northwest, and northeast. The paucity of craters indicates that the rocks underlying the plateau are geologically young. East of the mosaic of fault blocks, the graben between blocks coalesce into the great equatorial canyon or rift valley system (Fig. I-4), 6 km deep in places, that
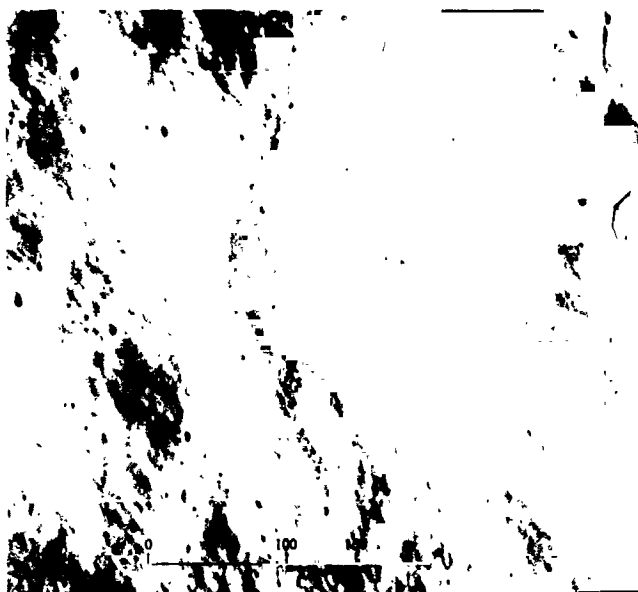
Fig. I-2c. "Turtleback" lunar crater near crater Tycho photographed by *Lunar Orbiter V*; inferred to be volcanic filling of crater.

Fig. I-3b. Narrow-angle view of Midd'e Spot showing radiating fracture with accompanying extrusives similar to lunar mare ridges. (MTVS 4096-81, DAS 04402170)
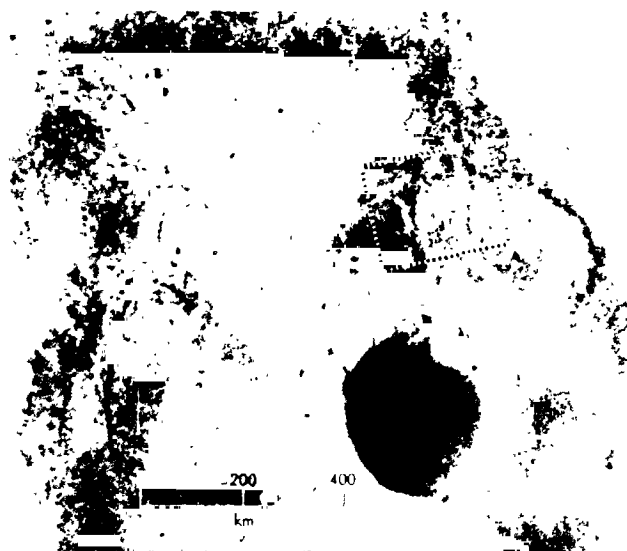
Fig. I-3a. Wide-angle view of Middle Spot caldera.
(MTVS 4081-3, DAS 03930239)

Fig. I-3c. Complex fracture with extrusives on floor of the Amazonis basin. (MTVS 4287-15, DAS 11443439)

extends almost 5000 km to the east (Fig. I-5a). Some volcanism associated with the inferred faulting that initiated these unanticipat·d Martian structures is suggested by the previously mentioned lines of craters along fractures parallel to the main rift valley system. These chain craters, however, lack obvious rim deposits and alternatively could be the product of collapse of surficial ma-

terials into subsurface fissures. The steep lateral valleys in places appear to be debris channels for mass wasted material. In other channels there are closed depressions that may be degraded volcanic vents. The upper reaches of the shallow sinuous valleys along the southern margin of the rift valley system appear to require formational processes other than mass wasting (Ref. I-32).
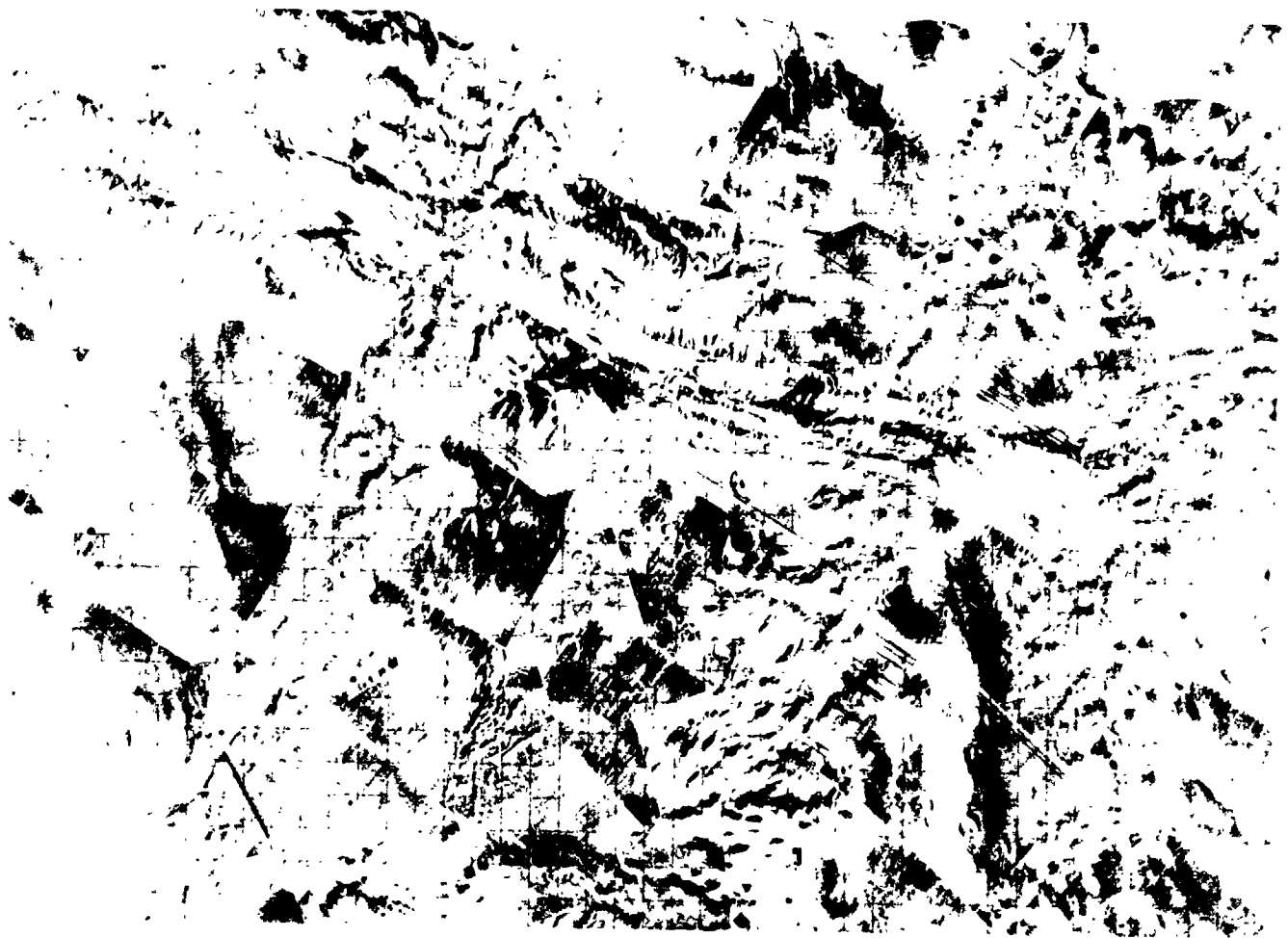
Fig. I-4. Mosaic of *Mariner 9* wide-angle pictures of rift valley system showing termination in the fault complex at the west end where the area stands highest.

Along the cliffs bounding the high plateau, layers and deposits are exposed which average about 100 m in thickness. The uppermost layer usually seems to be the most resistant and forms a rocky rim. The rocks may be volcanic, as they lie adjacent to the lines of craters that could be feeder vents. In places, markedly eroded layers are visible within the canyon floors, and many layers of light and dark rocks are exposed (Fig. I-5b). The layers within these presumed valley fill deposits do not seem to match the more obscure and massive layering in the canyon walls; thus, these more finely layered deposits could represent earlier generations of valley fill now being stripped out by erosion. In many areas the cliffs are bordered by masses of debris that apparently have slid into the adjacent lowlands. In other areas the material retains its coherence and descends in a series of terraces that are similar in appearance to the chaotic terrain described in pictures taken by *Mariners 6* and 7 (Refs. I-33 and I-34; also see Section VI of this Report).

D. Channels

Emerging from the northern plateau lands, a complex array of broad, sinuous channels descends into a regionally depressed area (Figs. I-6a and I-6b). As the channels merge on the border of the flat, low Chryse area, the channel floors show multiple braided channels and streamlined islands (Fig. I-6c) that confirm the northward direction of flow consistent with the regional slope of the surface determined from infrared and ultraviolet spectral data.

Lying on the level, high plateau surface are other channels; these are sinuous and have many tributaries (Refs. I-35 through I-37; also see Section III of this Report). These channels descend to the east and north, becoming broader and more clearly defined. The tributaries and the form of the braided channels are unlike those of terrestrial and lunar volcanic sinuous rilles, and

6
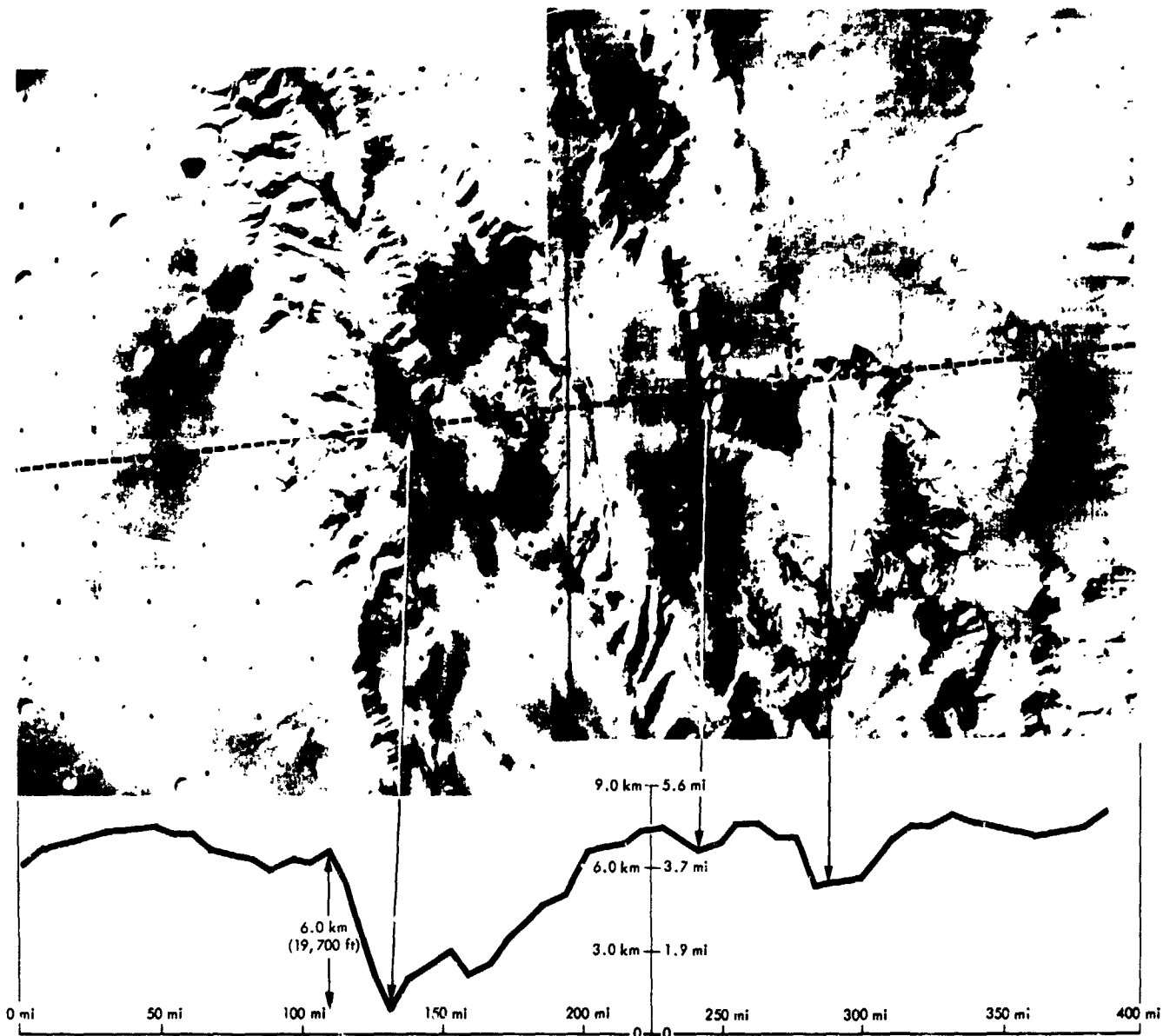
Fig. I-5a. Inferred elevation profile across rift valley system using pressure measurements made by the ultraviolet spectrometer.

closely resemble terrestrial intermittent stream channels. Their form and degree of freshness strongly suggest flow of liquid water in the recent geologic past of Mars (Fig. I-7).

Some channels originate in great masses of hummocky to broken, slabby material at the base of cliffs, and may be related in origin to this chaotic terrain as proposed by McCauley et al. (Ref. I-20) and Masursky et al. (Ref. I-19). Sharp et al. (Ref. I-33) proposed, from the *Mariner 6* and 7 pictures, that the collapse of these rocks

and formation of large-scale landslides may be caused by melting of permafrost. The more extensive photographic coverage leads to the logical extension of the permafrost proposal; that is, water derived from the melting of the permafrost seeped out from under the slides, formed the broad sinuous channels, and flowed into the northern lowlands. The only terrestrial analogs to these enormous channels, which are 30 to 60 km wide, are the Channeled Scablands of the Columbia plateau in the United States and the sandur plains (glacial outwash) of Iceland, which fringe the large glaciers (Ref.
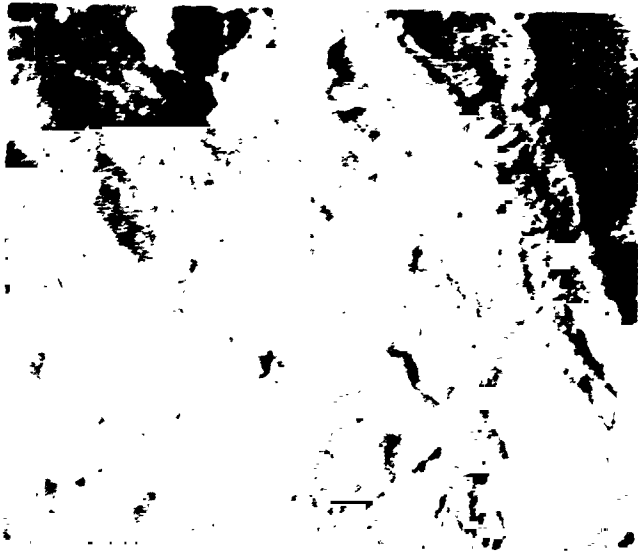
Fig. I-5h. Light and dark layers in equatorial zone; layers do not match layers in adjacent walls of canyon and may be later fill now being stripped by erosion. (MTVS 4182-11, DAS 10492589)

Fig. I-6b. Wide-angle picture showing channel and landslide debris. (MTVS 4201-60, DAS 07586808)
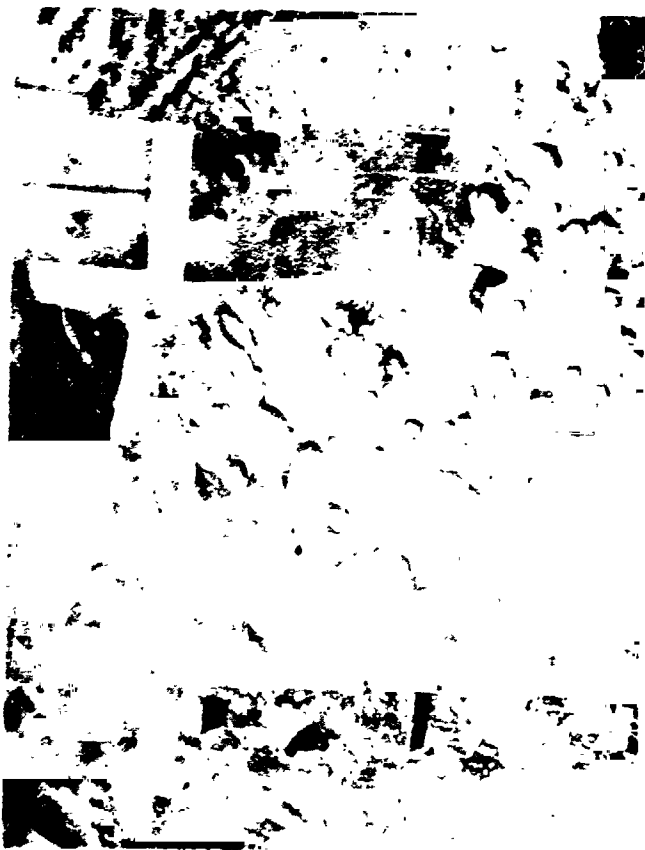
Fig. I-6a. Mosaic of wide-angle pictures showing broad, sinuous channels emerging from base of landslide debris and flowing north into the lowland.
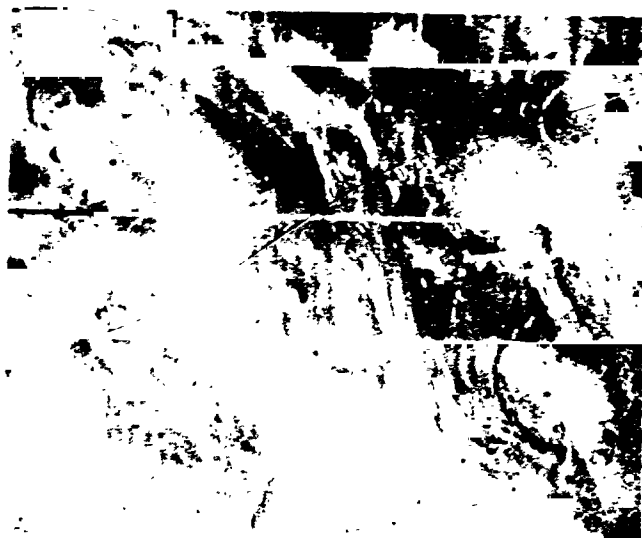
Fig. I-6c. Braided channel with its source near the toe of a hummocky debris landslide. (MTVS 4206-63, DAS 07830588)

I-37; also see Section III of this Report). In both areas, great volumes of glacial meltwater result in torrential floods with accompanying fluvial erosion and deposition.

Two proposals have been made to account for the melting of permafrost over large areas. The first hypothesis is that local heating by volcanic activity would mobilize the fluids; the second proposes planet-wide

BROAD CHANNELS

SINUOUS CHANNELS

CHANNEL NETWORKS
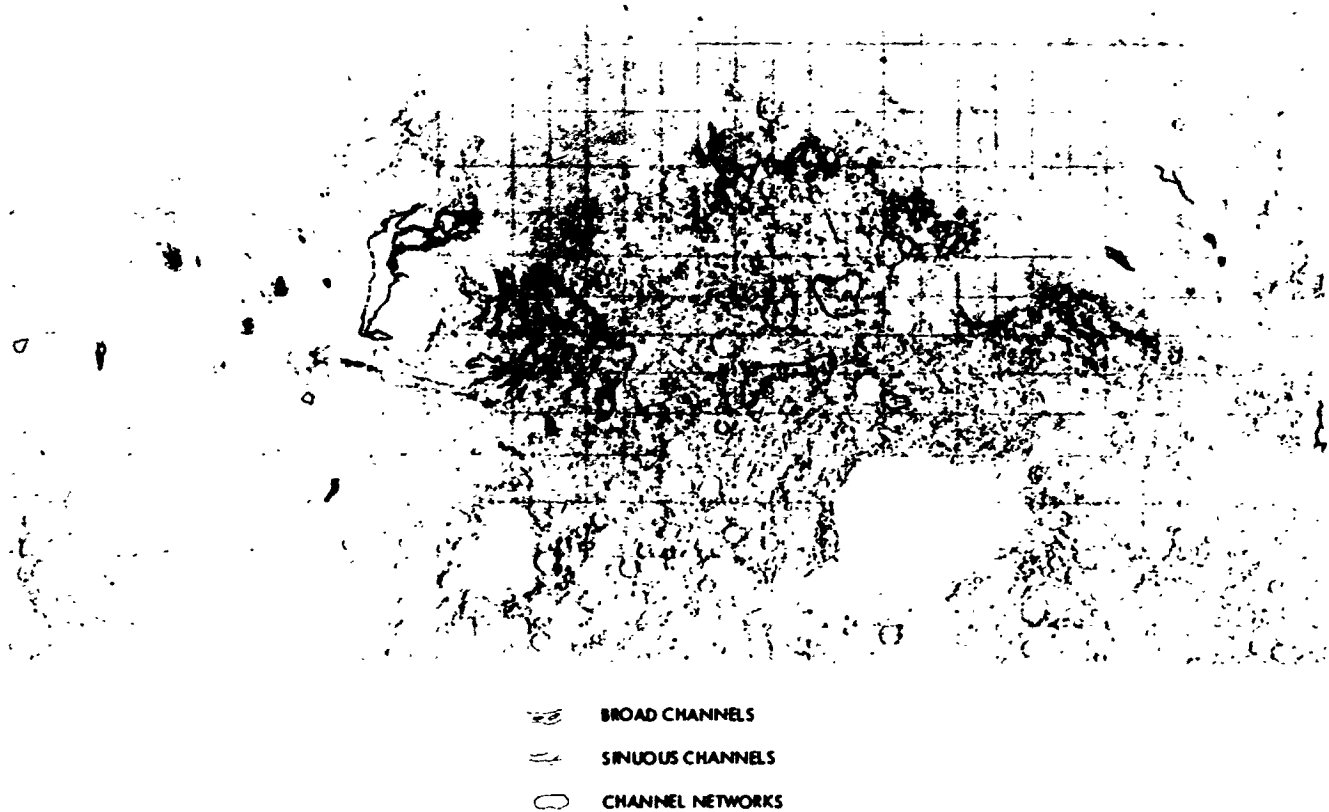
Fig. I-7. Map showing distribution of three fluvial-type channels on Mars.

heating as a result of secular or cyclical changes in climate. A climate interglacial episode conceivably could melt the permafrost in the large equatorial region and thus be the cause not only of the chaotic terrain, but also of the channels.

Somewhat different, very sinuous valleys with many tributaries lie on the high-level plateau surface in the Rasena, Mare Erythraeum, and Memnonia regions. The channels with braided floors descend to the east and north, becoming broader and more clearly defined (Ref. I-32). They apparently are formed by a different process than the broad, chaos-related channels. Their primary and secondary tributaries, dendritic patterns, and lack of apparent source areas seem to require rainfall collected into integrated channels along with both surface erosion and deposition in alluvial basins.

Another type of channel is widespread in the ancient cratered terrain as near Sinus Sabaeus (8°S, 334°W). Complex networks of tiny coalescent channels run down

the sides of many craters. Their origin is not unequivocal, but they also resemble fluvial channels and imply formation of precipitation collection. If this origin is correct, widespread rainfall is necessary to feed the channels. The occurrence of the channels in the equatorial zone suggests that only a slight temperature rise would be necessary to produce liquid water there if the water partial pressure were to be raised at the same time. An "interglacial" episode that melted the polar caps and planet-wide permafrost should be adequate to allow flowing water to exist in the equatorial zone on the surface of Mars.

Another type of channel is associated with volcanic centers (Fig. I-8a). The channels start on the flanks of volcanic craters and are less well defined downstream. This relationship is the opposite of that generally observed in fluvial channels. These features closely resemble lunar sinuous rilles such as the Hadley and Prinz rilles (Fig. I-8b) and are now generally thought to be collapsed lava channels in basaltic rocks, as is
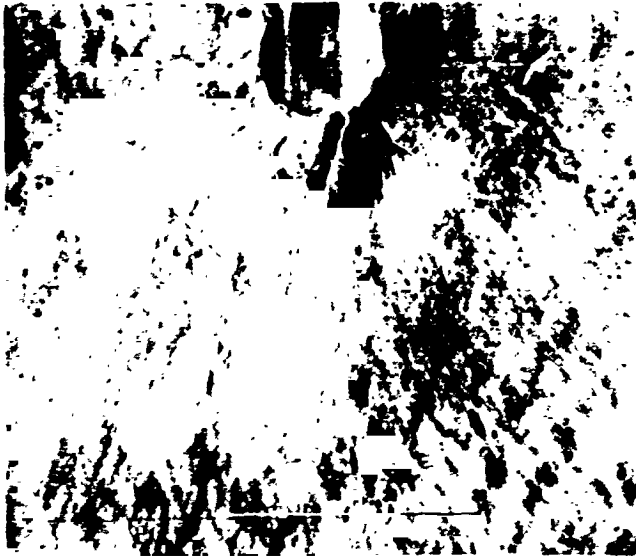
Fig. I-8a. Lava channel on flank of crater, starts in crater and descends, becoming smaller in contrast to the fluvial-type channels that grow downstream. (MTVS 4298-39, DAS 13496088)
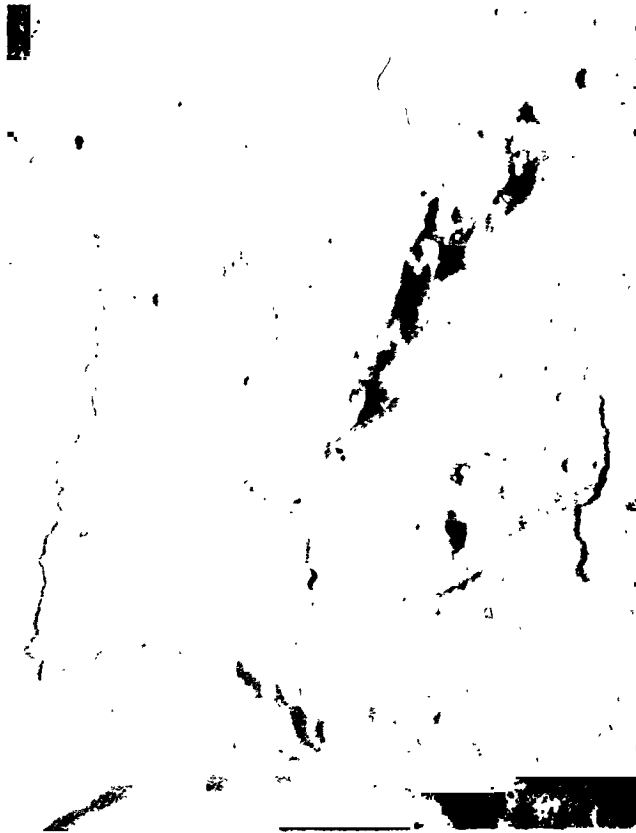
Fig. I-8b. Prinz Rilles in northwest part of Moon photographed by *Lunar Orbiter V*. Crater at head of the rille is the size of the crater Prinz. The rille descends to the north, becoming narrower and more shallow in contrast to the fluvial channels on Mars.

inferred from the samples and photographs returned as a result of the *Apollo 15* mission.

In summary, channels can be divided into four groups: the three varieties discussed with characteristics that imply a fluvial origin in which water must be the transport medium (broad and sinuous, narrow with braided floors and tributaries, and small and closely spaced), and a fourth variety with characteristics that imply a volcanic origin involving molten lava flows.

E. Polar Features

Monitoring of the polar regions allowed observation of the rapid retreat of the frost cover from its maximum extent of more than 50° across when photographed in 1969 to a minimum of less than 10° across in 1972 (Refs. I-16, I-19, and I-38). Ancient cratered terrain extends from north of the equator southward to the south polar region, where it is overlapped by two younger units. The older of these overlying units is moderately cratered and has many closed depressions that appear to be deflation hollows (Fig. I-9a). This "etch-pitted" unit is composed of alternating resistant and non-resistant rock layers which produce numerous topographic benches and slopes along exposed edges. The exposures of etch-pitted terrain surrounding the polar region indicate a zone of high wind velocity which

Fig. I-9a. Etch-pitted terrain in south polar region which overlies the ancient cratered terrain and is overlain by the laminated terrain. The closed depressions probably were made by the deflation. The winds are particularly strong adjacent to the polar ice, as they are on Earth in Antarctica and Greenland. (MTVS 4132-21, DAS 05453843)

is stripping the surface and forming deflation hollows. The etch-pitted unit is overlain by layered rocks originally termed the "laminated terrain" (Fig. I-9b). The two units of young layered deposits do not overlie the ancient terrain in a plate-like fashion. Although they total 6 km in thickness, they occur at a lower elevation than the surrounding ancient cratered terrain and are covered by ice at the pole (Ref. I-7). Thus, these layered rocks occupy a saucer-shaped depression that defines a discrete basin in both polar regions. It may be that the polar rocks have been depressed by formerly thicker polar ice. A quantitative measure of the degree of this deformation could be an indicator of the mobility of the Martian subcrust.

The uniformly bedded layers best observed in the laminated terrain are estimated to range from 10 to 30 m in thickness. There are about 20 layers in each cuesta-like ridge, of which there are 6 to 12 encircling the pole. The individual thin layers appear to be cyclical deposits, as may be the groups of layers that form the ridges that showed in the Mariner 6 and 7 pictures (Ref. I-39). The ledges are being eroded; they are smoothly rounded, unlike the sharp-edge ridges in the etch-pitted and central plateau regions. Subjacent craters are partially covered in many places, apparently being re-exhumed after burial. The upper surfaces of these deposits on

0   500   1000
km

Fig. I-10. Mosaic of wide-angle pictures of south polar region showing the terrain units and residual cap. The polar deposits stand higher and overlie the ancient "continental" cratered terrain. The laminated deposits dip inward and are topographically lower than the surrounding cratered terrain forming the polar basin.

Fig. I-9b. Laminated terrain in the south polar region overlain by residual ice. It eroded with rounded edges and was deposited cyclically. The short cycles comprise eight to ten layers which make up ledges that form the circumpolar features. (MTVS 4213-21, DAS 08080243)

which the remnant polar ice cap lies are grooved radial to the pole (Ref. I-32). These grooves may have been formed by wind erosion or perhaps even glacial scour.

The south and north polar regions are similar (Figs. I-10 and I-11) and apparently have acted as sediment traps throughout much of the history of Mars. Sedimentation in these areas must have started when the planet cooled enough to initiate frost accumulation in the polar region. Pervasive wind erosion in the equatorial regions took place; these sediments then were transported, principally in suspension, and deposited into the polar regions. The polar deposits may be thought of as glacio-eolian, formed when the dust particles, acting as nuclei around which the snow crystals form, are laid down as horizontal layers. A similar process takes place on Earth where rain, wind, and snow sweep the atmosphere clean of dust particles. Alternatively descending air currents in the polar high-pressure zone may abet the entrapment of dust particles on the surface ice, much in the same way as dust is entrapped in terrestrial ice fields and in glaciers.

Fig. I-11. Mosaic of wide-angle pictures of the north polar region showing the terrain and residual cap. The region lies 3 km lower than the south pole. The polar deposits lie on plains deposits of "ocean basin" type. The topography is not well enough known to determine whether the deposits are in a basin.

F. Eolian Features

The planet-wide dust storm appears to have blanketed much of the surface with bright silt and clay-size particles, obscuring most of the dark markings normally observed telescopically. Since the end of the storm, bright material has been locally scoured from the surface revealing the darker, presumably coarse-grained, underlying surface. During the mission, a local dust storm was observed, and after its passage a dark track was visible (Ref. I-7). As the mission progressed, the classic dark surface markings began to re-emerge as the fine-grained and brighter surficial materials were scoured and redeposited (Ref. I-4).

Uniformly distributed deposits that fringe the polar regions and blanket the plains correspond to terrestrial loess, widespread deposits of silt and clay-size particles. Their redistribution reveals dark, irregular markings and light and dark tails emanating from craters and other topographic obstacles. The light tails appear to be wind-deposited material; the dark tails appear to be mostly wind-scoured zones in the lee of various topographic

obstacles. In other cases some dark streaks appear to be dark deposits.

In some areas dark markings in wide-angle pictures have been resolved into sand dune fields in the narrow-angle pictures (Ref. I-40; see Section XI of this Report). This dune field, about 50 km across, lies in the bottom of a crater. The spacing of the crests of individual dunes is on the order of 1 to 2 km. In size and shape this feature is similar to many dune fields and sand sheets in terrestrial deserts such as the Mojave Desert in southern California, within which the Kelso dune field is a good analog (Ref. I-41). Adjacent to the etch-pitted south polar terrain is an area of "riffles" that resemble longitudinal or seif dunes. Equatorward, in addition to the dune fields; the mottled cratered plains and smooth plains are areas of irregular to uniform, eolian loess-like deposits that indicate even lower wind velocities. The identification of dunes is significant because dunes indicate that saltation is operative on the surface despite the tenuous atmosphere. With saltation occurring, numerous eolian erosion and depositional features should be expected at larger scales; some of these features are described in Ref. I-23 (see Section X of this Report) and are compared with pure erosion forms in the coastal desert of Peru.

G. Impact Craters

Although impact craters are common on about one-half of the planet's surface, fresh craters with well developed ejecta blankets are rare (Ref. I-36). A few small craters show hummocky continuous ejecta blankets and well developed rays. Most small craters, however, exhibit degraded ejecta blankets and no ray patterns.

Interpretation of lunar craters indicates that the first crater-related feature that disappears by erosion is the ray material, which originally extended outward for many crater diameters. The continuous ejecta blankets, up to two crater diameters in width, are more resistant to wind erosion. However, these deposits eventually lose their hummocky character, but the outer irregular edges remain as low ridges. The very slow degradation of craters on the Moon is largely by impact gardening; on Mars the erosion is probably dominantly eolian. Most of the ray material of lunar craters and terrestrial experimental craters is fine-grained; such material on Mars would be subject to degradation and transportation by winds. Thus, the paucity of ray craters is an indicator of the effectiveness of the eolian erosional and depositional processes on Mars.

Prominent in the southern hemisphere of the planet are craters ranging from the limit of resolution (200 to 300 m) up to the Hellas and Argyre basins. (Hellas is 2000 km in diameter and one-half again the size of the Imbrium basin on the Moon.) The cratering in this hemisphere is similar to that in the southern highlands of the near side and much of the far side of the Moon (Refs. I-19 and I-42; also see Section VII of this Report). The abundance of craters here is such that this terrain must be very old geologically. The crater frequency is less, however, than on Phobos, the satellite of Mars, and in the most heavily cratered of the lunar uplands (Ref. I-43, also see Section VIII of this Report). This lower crater frequency probably indicates destruction of some craters by various processes that include all previously mentioned, i.e., volcanism, tectonism, channel generation, and eolian erosion and deposition.

The Argyre basin is ringed by radially and concentrically textured mountainous terrain that indicates its similarity to the lunar multi-ringed impact basins such as Imbrium and Orientale (Refs. I-44 and I-45). However, the deposits are altered by subsequent events, including eolian modification, so they do not display the structural and depositional textures still preserved in the drastically less dynamic lunar environment (Ref. I-46). Rough textured, externally and internally terraced, generally circular craters with central peaks are thought, as on the Moon, to be of impact origin if not so degraded as to have these diagnostic characteristics obliterated.

Craters of impact type are clearly distinct from the smooth-rimmed volcanic craters with their commonly attendant radiating lava channels and flows. Secondary crater arrays are visible in several areas and are distinct from the linear arrays of volcanic craters along structural lineaments. They are, however, far less abundant than on the Moon and generally cannot be identified as to source.

H. Planet-Wide Distribution of Geologic Units

The cratered terrain apparently is the most ancient on Mars, and probably records, as on the Moon, the impact of cosmic debris on the early differentiated planet (Refs. I-47 and Fig. 1 of I-21; also see Fig. II-1 of this Report). Preliminary correlation of gravity mapping achieved by tracking the *Mariner 9* spacecraft with topography from several sources indicates that the rocks in the lowlands and plateau regions previously described are largely isostatically compensated. This result is in agreement with the distribution of rocks on the Moon, where the highlands are underlain by low density crustal rocks with high Al/Si ratios, and the lowlands are underlain by basalts that probably rest directly on mantle rocks. For Mars, the cratered terrain that occupies most of the southern hemisphere may represent the more siliceous "continental" crustal rocks. The Amazonis and adjacent Elysium basin and the northern lowlands may be underlain by basalts resting on the mantle and may be the gross equivalents to the terrestrial ocean basins and Oceanus Procellarum on the Moon. Within the primitive cratered terrain are areas filled by smoother, younger material with lower, but still substantial, crater populations These "cratered plains" are overlain by smooth deposits which form the smooth plains that comprise several different units. The smooth plains locally exhibit lobate lava flow fronts and broad low shield volcanoes, attesting to the probable basaltic nature of the smooth deposits.

Mantling the smooth lava plains are possible alluvial deposits at the mouths of the channels in the Chryse and Lunae Palus regions. These deposits probably form piedmont alluvial and possibly playa sequences near where the channels debouch into the lowlands, so that some of the smooth plains may consist of sedimentary deposits. Pediplanation may have taken place in a few areas along channel margins and where plateau edges and isolated hills and mesas seem to be retreating (Ref. I-37; also see Section III of this Report).

Eolian deposits derived from the polar-eolian sediment traps may have been spread equatorward (Ref. I-48; also see Section IX of this Report). The thickness of these loess and dune deposits on the northern lava plains can be estimated from their apparent thickness in the south polar region. Here the mantling eolian material cannot exceed tens to hundreds of meters in thickness, for it partially masks but does not fill in the south polar cratered terrain. Thinner deposits of eolian sediments (possibly silt and sand) cover the central part of the planet in places. Apparently these deposits in the central part of the planet are mobile, as the continually changing light and dark patterns monitored after the great dust storm attest. They must be only a few meters in thickness, as they do not obscure textural detail in the cratered and faulted terrain. Thicker loess deposits probably lie within Hellas and other similar large circular basins and craters, but their thickness cannot be determined; such regions do appear, however, to be the source areas for many Martian dust storms including that of 1971 (Ref. I-14).

The south polar glacio-eolian rocks overlie the cratered terrain, the north polar deposits overlie smooth and cratered plains. The north polar region is about 3 km lower than the southern region. This observation is consistent with the morphology of the terrain, which suggests that the south polar region is part of the continental mass; the north polar region is part of the "ocean" basin floor.

The margins of the central continental block are different. At 100 to 130°W, the margin is abrupt and the slopes are steep; the crest of the Tharsis ridge is marked by the three aligned volcanic structures. Perhaps this continental margin is the site of incipient plate tectonic movement; alternatively, the volcanoes may lie along a zone of vertical movement bounding the continental block. The northern margin is irregular with gentler slopes. The contact between the cratered plains and the low-lying smooth plains is gradational, and has many irregularly disposed hills and mesas. The central canyon or troughed zone may mark a rift zone developed by the highland rocks sliding into the northern lowlands; again alternatively, the canyons may mark complex vertical faulting with the most complex faulting in the area of greatest uplift and adjacent to the thickest young volcanic rocks that overlie the continental crust.

I. Geologic History

The various topical studies presented in this Report and the regional geologic mapping accomplished to date permit an expansion and refinement of the earlier preliminary geologic histories presented for the equatorial belt (Refs. I-20 and I-21; also see Section II of this Report). The principal data used are overlap relations between geologic units and differences in their crater populations. These relations show that Mars has a decipherable history that dates far back in time. This history may place some boundary conditions on theories about the evolution of its atmosphere and development of an ice regime. The heavily cratered generally high-standing rocks that lie predominantly in the mid- and southern latitudes are the most ancient on the planet, as has been recognized since *Mariners 6* and 7 (Ref. I-49).

Large lunar basins such as Imbrium formed after the initial differentiation of the entire Moon. Ejecta from these basins contain norites, anorthositic gabbros, and anorthosites that form the crustal rocks which stand high because of their lesser density. A similar process prob-

ably took place on Mars so that the high-standing, heavily cratered rocks are part of the early differentiated "continental" crust.

During the time of rapidly decreasing flux of impacting bodies, the many large, flat-floored craters formed as well as the large impact basins, Hellas, Argyre, and Libya. Hellas appears to be the oldest as its rim has been almost completely destroyed, and the number of superimposed craters around its edge is comparable to the rest of the heavily cratered terrain. Argyre and Libya are more rugged than Hellas and have fewer superimposed craters. They probably formed later.

Impact presumably continued at a decreasing rate, but volcanism started early in this episode. The oldest volcanic feature recognized is a shield volcano on the northeast rim of the Hellas basin. This heavily cratered (it has twice as many craters as the oldest of the plains units) and eroded feature at first was difficult to recognize; other features may be found as systematic geologic analysis continues. The ancient volcano is particularly significant because it indicates that volcanism of the type observed in the Amazonis region began very early in Mars history and within the ancient cratered terrain. Old plains units mantle parts of the ancient cratered terrain and are marked by lower crater frequencies. They are difficult to delineate because erosion and deposition have obscured the contacts. The oldest plains unit that can be mapped satisfactorily occurs in the Lunae Palus area and overlies part of the volcanic structures in the Hesperia region. It has a crater density greater than most of the lunar maria. Its absolute age, like that of other Martian units, is difficult to assess because the relative contributions to the flux of cometary and asteroidal impacts are not known.

Next younger in age are the heavily faulted plains around Nix Olympica, in Arcadia, and in Alba. They appear to be basalt flows similar to those in the surrounding smooth plains, which have been slightly uplifted, faulted, heavily modified by eolian erosion, and moderately cratered. Mottled cratered terrain underlies large areas in the northern regions. It is moderately cratered and partially covered by eolian deposits. Volcanism probably started in the Nix Olympica area about the same time that these plains formed. The erosional scarp at the base of Nix Olympica suggests that these layers were being eroded while the upper part of the mountain was still being constructed. The next youngest plains unit

14

occurs in the Phoenicis Lacus and Elysium areas. It is moderately cratered and faulted; the number of craters is comparable to that on most lunar maria. It embays knobby terrain, indicating that the process forming the latter unit began before deposition of the moderately cratered plains.

Upwarping or epirorogeny then took place in the Tharsis region, resulting in mosaic-like fault patterns as well as the extensive rifting to the east in the main part of the Coprates canyon system. The upper part of the Nix Olympica, as well as the Tharsis, shield volcanoes then formed. Contemporaneously the young lava plains with their abundant flow fronts and lava domes were extruded. Chaotic terrain developed later along the margins of the equatorial plateau. Broad channels then formed, apparently over a considerable time, as some of their floors are moderately cratered and others are little cratered. Their development may have paralleled the construction of the large volcanoes.

Eolian deposition and erosion extended over a considerable time up to the present; in the polar regions, deposits of the laminated terrains were being deposited and eroded and redeposited in great mantles of loess-like deposits that thin equatorward. Etch-pitted plains surrounding the poles attest to the intensity of eolian erosion of earlier deposits in the vicinity of the polar caps. This erosion raises the possibility that earlier generations of laminated terrain have been redistributed. The present polar deposits may record only the latest such episode of deposition of layered materials.

The possible fluvial channels may record episodes when water was much more abundant in the atmosphere than at present. Planet-wide warmer "interglacial" periods would release not only the water locked in the polar caps, but also that frozen in the subsurface as permafrost. Similar warmer and colder periods also are characteristic of terrestrial history. Still continuing is the erosional modification of landforms and deposition of widespread silt and clay "loess" deposits and local sand dunes.

References

I-1. Masursky, H., Batson, R., Borgeson, W., Carr, M., McCauley, J., Milton, D., Wildey, R., Wilhelms, D., Murray, B., Horowitz, N., Leighton, R., Sharp, R., Thompson, W., Briggs, G., Chandeysson, P., Shipley, E., Sagan, C., Pollack, J., Lederberg, J., Levinthal, E., Hartmann, W., McCord, T., Smith, B., Davies, M., de Vaucouleurs, G., and Leovy, C., "Television Experiment for Mariner Mars 1971," *Icarus*, Vol. 12, p. 10, 1970.

I-2. U. S. Geological Survey, Shaded Relief Map of Mars, Atlas of Mars, MM 25M IR 1:25,000,000 Cartographic Series, I-810, 1972.

I-3. Batson, R. M., "Cartographic Products from the Mariner 9 Mission," *J. Geophys. Res.*, Vol. 78, 1973.

I-4. Sagan, C., Veverka, J., Fox, P., Dubisch, R., French, R. Gierasch, P., Quam, L., Lederberg, J., Levinthal, E., Tucker, R., Eross, B., and Pollack, J. B., "Variable Features on Mars II: Mariner 9 Global Results," *J. Geophys. Res.*, Vol. 78, 1973.

I-5. Hanel, R. A., Conrath, B., Hovis, W., Kunde, V., Lowman, P., Maguire, W., Pearl, J., Pirraglia, J., Prabhakara, C., Schlachman, B., Levine, G., Straat, P., and Burke, T., "Investigation of the Martian Environment by Infrared Spectroscopy on Mariner 9," *Icarus*, Vol. 17, p. 423, 1972.

References (contd)

I-6. Barth, C. A., Stewart, A. I., Hord, C. W., and Lane, A. L., "Mariner 9 Ultraviolet Spectrometer Experiment: Mars Airglow Spectroscopy and Variations in Lyman Alpha," *Icarus*, Vol. 17, p. 457, 1972.

I-7. Hord, C. W., Barth, C. A., Stewart, A. I., and Lane, A. L., "Mariner 9 Ultraviolet Spectrometer Experiment: Photometry and Topography of Mars," *Icarus*, Vol. 17, p. 443, 1972.

I-8. Kliore, A. J., Cain, D. L., Fjeldbo, G., Seidel, B. L., Sykes, M. J., and Rasool, S. I., "The Atmosphere of Mars From Mariner 9 Radio Occultation Measurements," *Icarus*, Vol. 17, p. 484, 1972.

I-9. Cain, D. L., Kliore, A. J., Seidel, B. L., Sykes, M. J., and Woiceshyn, P. M., "Approximations to the Mean Surface of Mars and Mars Atmosphere Using Mariner 9 Occultations," *J. Geophys. Res.*, Vol. 78, 1973.

I-10. Downs, G., Goldstein, R. M., Green, R. R., and Morris, G. A., "Mars Radar Observations: A Preliminary Report," *Science*, Vol. 174, p. 1324, 1971.

I-11. Pettengill, G. H., Rogers, A. E. E., and Shapiro, I. I., "Martian Craters and a Scarp as Seen by Radar," *Science*, Vol. 174, p. 1321, 1971.

I-12. Lorell, J., Born, G., Christensen, E., Esposito, P., Jordan, J. F., Laing, P., Sjogren, W., Wong, S., Reasenberg, R., Shapiro, I., and Slater, G., "Gravity Field of Mars From Mariner 9 Tracking Data," *Icarus*, Vol. 18, No. 2, 1973.

I-13. Levinthal, E. C., Green, W. B., Cutts, J. A., Jahelka, E. D., Johansen, R. A., Sander, M. J., Seidman, J. B., Young, A. T., and Soderblom, L. A., "Mariner 9 Image Processing Products," *Icarus*, Vol. 18, p. 75, 1973.

I-14. Capen, C. F., and Martin, L. J., *The Developing Stages of the Martian Yellow Storms of 1971*, Lowell Observatory Bulletin No. 157, 211, 1971.

I-15. Soffen, G. A., and Young, A. T., "The Viking Mission to Mars," *Icarus*, Vol. 16, p. 1, 1972.

I-16. Soderblom, L. A., Malin, M. C., Cutts, J. A., and Murray, B. C., "Mariner 9 Observations of the Surface of Mars in the North Polar Region," *J. Geophys. Res.*, Vol. 78, 1973.

I-17. Leovy, C. B., Briggs, G. A., and Smith, B. A., "Mars Atmosphere During the Mariner 9 Extended Mission: Television Results," *J. Geophys. Res.*, Vol. 78, 1973.

I-18. Masursky, H., in Driscoll, Everly, "Mariner Views a Dynamic Volcanic Mars," *Science News*, Vol. 101, No. 7, p. 106, 1972.

I-19. Masursky, H., Batson, R. M., McCauley, J. F., Soderblom, L. A., Wildey, R. L., Carr, M. H., Milton, D. J., Wilhelms, D. E., Smith, B. A., Kirby, T. B., Robinson, J. C., Leovy, C. B., Briggs, G. A., Young, A. T., Duxbury, T. C., Acton, C. H., Murray, B. C., Cutts, J. A., Sharp, R. P., Smith, S., Leighton, R. B., Sagan, C., Veverka, J., Noland, M., Lederberg, J., Levinthal, E., Pollack, J. B., Moore, J. T., Jr., Hartmann, W. K., Shipley, E. N., de Vaucouleurs, G., and Davies, M. E., "Mariner 9 Television Reconnaissance of Mars and Its Satellites: Preliminary Results," *Science*, Vol. 175, p 395, 1972.

References (contd)

1-20. McCauley, J. F., Carr, M. H., Cutts, J. A., Hartmann, W. K., Masursky, H., Milton, D. J., Sharp, R. P., and Wilhelms, D. E., "Preliminary Mariner 9 Report on the Geology of Mars," *Icarus*, Vol. 17, p. 289, 1972.

1-21. Carr, M. H., Masursky, H., and Saunders, R. S., "A Generalized Geologic Map of Mars," *J. Geophys. Res.*, Vol. 78, 1973.

1-22. Simkin, T., and Howard, K. A., "Caldera Collapse in the Galapagos Islands," *Science*, Vol. 169, p. 429, 1970.

1-23. McCauley, J. F., "Mariner 9 Evidence for Wind Erosion in the Equatorial and Mid-Latitude Regions of Mars," *J. Geophys. Res.*, Vol. 78, 1973.

1-24. Carr, M. H., "Volcanism on Mars," *J. Geophys. Res.*, Vol. 78, 1973.

1-25. Bailey, E. B., Clough, C. T., Wright, W. B., Richey, J. E., Wilson, C. V., "Tertiary and Post-Tertiary Geology of Mull, Loch Aline, and Oban," 455 pp., *Mem. Geol. Surv. Scotland*, 1924.

1-26. Anderson, E. M., "Cone-Sheets and Ring Dykes: The Dynamical Explanation," *Bull. Volcanol.*, Vol. 1, p. 35, 1937.

1-27. Richey, J. E., *Scotland: The Tertiary Volcanic Districts*, 3rd ed., revised by MacGregor, A. G. and Anderson, F. W., 119 pp., Dept. Sci. Ind. Res., Geol. Survey and Museum, Edinburgh, 1961.

1-28. Oftedahl, C., *Permian Igneous Rocks of the Oslo Graben*, Norway, 23 pp., Intern. Geol. Congr., 21st Copenhagen, 1960, Guide to Excursions, Nos. A11 and C7, 1960.

1-29. Kingsley, L., "Cauldron Subsidence of the Ossipee Mountains," *Am. J. Sci.*, Vol. 22, 5th Series, p. 139, 1931.

1-30. Korn, H., and Martin, H., "The Messum Igneous Complex in South-West Africa," *Trans. Geol. Soc. Africa*, Vol. 57, p. 83, 1954.

1-31. McDonald, G. A., and Hubbard, D. H., *Volcanoes of the National Parks in Hawaii*, 5th edition, Hawaii National Historical Association, Hawaii National Park, 56 pp., 1970.

1-32. Masursky, H., Arthur, D. W. G., Batson, R. M., Borgeson, W. T., Briggs, G. A., Carr, M. H., Cutts, J. A., Davies, M. E., de Vaucouleurs, G., Hartmann, W. K., Lederberg, J., Leighton, R. B., Leovy, C. B., Levinthal, E., McCauley, J. F., Milton, D. J., Murray, B. C., Pollack, J. B., Sagan, C., Sharp, R. P., Shipley, E. N., Smith, B. A., Soderblom, L. A., Veverka, J., Wildey, R. L., Wilhelms, D. E., and Young, A. T., "A Planet-Wide View of the Geology of Mars," *Geol. So. Am., Abstracts with Programs*, Vol. 4, p. 584, 1972.

1-33. Sharp, R. P., Soderblom, L. A., Murray, B. C., and Cutts, J. A., "The Surface of Mars: 2. Uncratered Terrains," *J. Geophys. Res.*, Vol. 76, p. 331, 1971.

References (contd)

I-34. Sharp, R. P., "Mars: Fretted and Chaotic Terrain," *J. Geophys. Res.*, Vol. 78, 1973.

I-35. Masursky, H., Batson, R. M., Carr, M. H., McCauley, J. F., Milton, D. J., Soderblom, L. A., Wildey, R. L., Wilhelms, D. E., Lederberg, J., Levinthal, E., de Vaucouleurs, G., Briggs, G. A., Young, A. T., Smith, B. A., Cutts, J. A., Leighton, R. B., Murray, B. C., Sharp, R. P., Hartmann, W. K., Leovy, C. B., Davies, M. E., Sagan, C., Veverka, J., Shipley, E. N., and Pollack, J. B., "Mariner 9 Mars Television Experiment" (abstract), *Bull. Am. Astronom. Soc.*, Vol. 4, Part II, p. 356, 1972.

I-36. Masursky, H., Batson, R. M., Carr, M. H., McCauley, J. F., Milton, D. J., Soderblom, L. A., Wildey, R. L., Wilhelms, D. E., Lederberg, J., Levinthal, E., de Vaucouleurs, G., Briggs, G. A., Young, A. T., Smith, B. A., Cutts, J. A., Leighton, R. B., Murray, B. C., Sharp, R. P., Hartmann, W. K., Leovy, C. B., Davies, M. E., Sagan, C., Veverka, J., Shipley, E. N., and Pollack, J. B., *A Planet-Wide View of the Geology of Mars as Observed from Mariner 9* (Abstract), COSPAR, 15th Plenary Meeting, May 10-24, 1972, Madrid, Spain, Program/Abstracts, 1972.

I-37. Milton, D. J., "Water and Processes of Degradation in the Martian Landscape," *J. Geophys. Res.*, Vol. 78, 1973.

I-38. Murray, B. C., Soderblom, L. A., Sharp, R. P., and Cutts, J. A., "The Surface of Mars: 1. Cratered Terrains," *J. Geophys. Res.*, Vol. 76, p. 313, 1971.

I-39. Sharp, R. P., Murray, B. C., Leighton, R. B., Soderblom, L. A., and Cutts, J. A., "The Surface of Mars: 4. South Polar Cap," *J. Geophys. Res.*, Vol. 76, p. 357, 1971.

I-40. Cutts, J. A., and Smith, R. S. U., "Eolian Deposits and Dunes on Mars," *J. Geophys. Res.*, Vol. 4, 1973.

I-41. Sharp, R. P., "Wind Ripples," *J. Geology*, Vol. 71, p. 617, 1963.

I-42. Wilhelms, D. E., "Comparison of Martian and Lunar Multi-Ringed Circular Basins," *J. Geophys. Res.*, Vol. 78, 1973.

I-43. Hartmann, W. K., "Martian Cratering IV: Mariner 9 Initial Analysis of Cratering Chronology," *J. Geophys. Res.*, Vol. 78, 1973.

I-44. Hartmann, W. K., and Kuiper, G. P., "Concentric Structures Surrounding Lunar Basins," *Arizona University Lunar and Planetary Lab Communications*, Vol .1, p. 51, 1962.

I-45. Hartmann, W. K., and Wood, C. A., "Moon: Origin and Evolution of Multi-Ringed Basins," *The Moon*, Vol. 3, p. 4, 1971.

I-46. Wilhelms, D. E., and McCauley, J. F., "Geologic Map of the Nearside of the Moon," *U. S. Geological Survey Geologic Atlas of the Moon, I-703*, 1971.

I-47. Masursky, H., "An Apollo View of Lunar Geology," in *Lunar Science IV*, Chamberlain, J. W., and Watkins, Carolyn, Lunar Science Institute, 511, 1973.

References (contd)

1-48. Soderblom, L. A., Kreidler, T. J., and Masursky, H., "The Latitudinal Distribution of a Debris Mantle on the Martian Surface," *J. Geophys. Res.*, Vol. 78, 1973.

1-49. Leighton, R. B., and Murray, B. C., "One Year's Processing and Interpretation—An Overview," *J. Geophys. Res.*, Vol. 76, p. 293, 1971.

Acknowledgments

PRECEDING PAGE BLANK NOT FILMED

II. A Generalized Geologic Map of Mars[1]

M. H. Carr

U. S. Geological Survey, Menlo Park, California 94025

Harold Masursky

U. S. Geological Survey, Flagstaff, Arizona 86001

R. S. Saunders

Jet Propulsion Laboratory/California Institute of Technology, Pasadena, California 91103

A generalized geologic map of Mars has been constructed largely on the basis of differences in the topography of the surface. The success by which the geology can be deduced from surface topography depends on how distinctively the originai topography of a feature reflects its mode of origin and the extent to which subsequent modification can be recognized and assessed. We are fortunate in having a number of topographic features on Mars whose form is highly diagnostic of their origin. Of particular note are the shield volcanoes and lava plains. In some areas, the original features have been considerably modified by subsequent erosional and tectonic processes. These have not, however, resulted in homogenization of the planet's surface, but rather have emphasized its variegated character by leaving a characteristic imprint in specific areas. The topography of the planet, therefore, lends itself well to remote geologic interpretation.

The map (Fig. II-1) is an outgrowth of an earlier version of the equatorial belt (Ref. II-1). The techniques

and conventions used are similar to those used for the Moon and have been fully described elsewhere (Ref. II-2). The surface has been divided into several units, each of which has a specific range of topographic characteristics. In the map explanation (Fig. II-2), the units are arranged according to their age as inferred from superposition and transection relations, crater counts, etc. The map also provides a generalized indication of tectonic deformation. Most of the units represent materials of a specific origin deposited within a restricted period of time. Other units, such as the chaotic and knobby materials, are not strictly geologic deposits, but are modifications of pre-existing materials. The modifications, however, have been so drastic as to, in effect, create new geologic units, and they are mapped as such.

For this early version of the map, data from the various spectral instruments have been largely ignored because of the difficulty in obtaining the data in a form readily correlatable with the visual image. However, we would not expect that, at the scale at which the map is depicted here, the spectral data would significantly affect delineation of the various units. The scale was dictated by
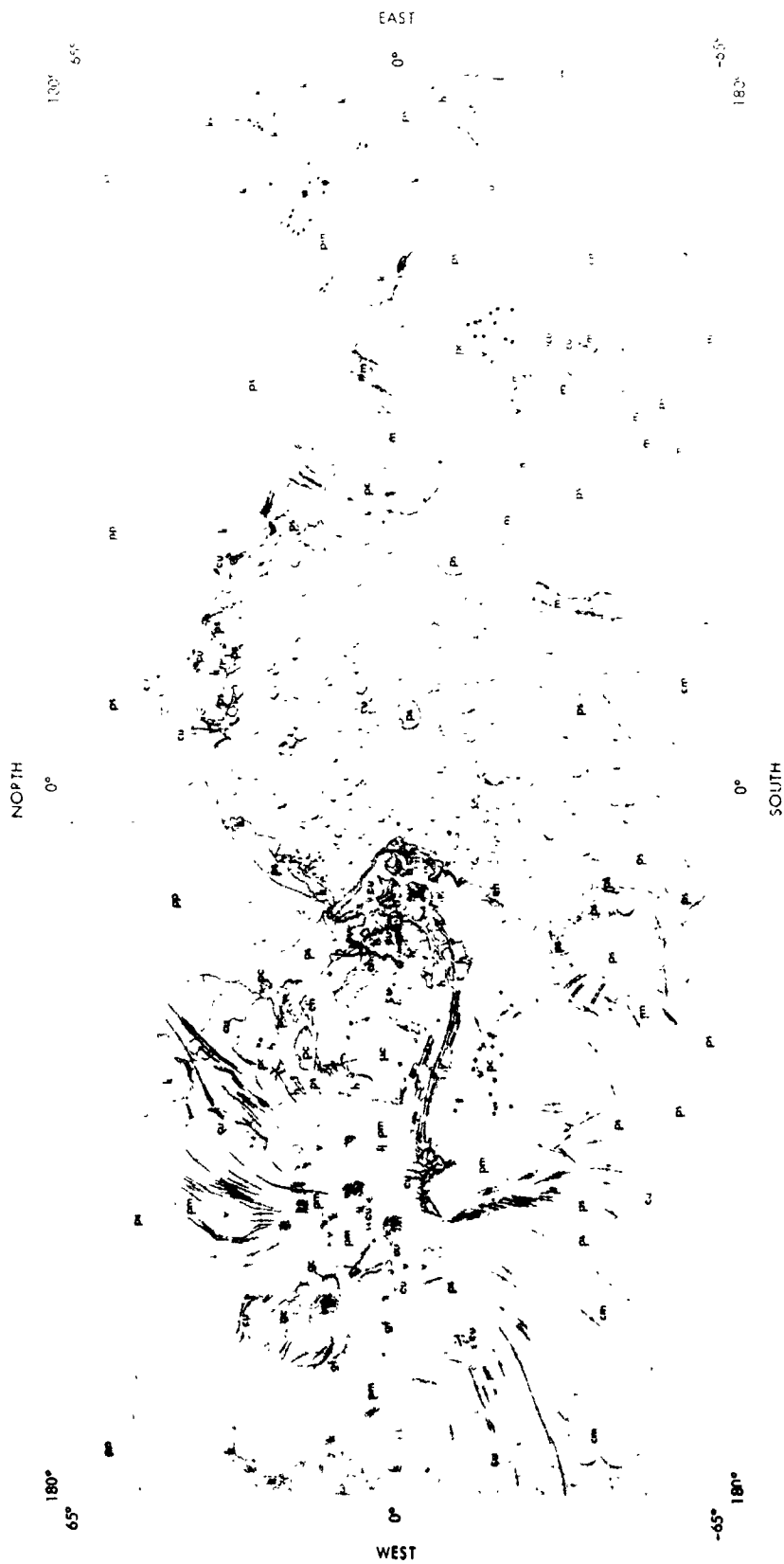
Fig. II-1. Generalized geologic map of the region of Mars between 65°N and 65°S latitude.

STRUCTURAL SYMBOLS

FAULTS, BAR AND BALL ON DOWNTHROWN SIDE.

GRABEN, WHERE FAULTS MAPPED SEPARATELY, BALL ON DOWNTHROWN BLOCK. WHERE GRABEN IS NARROW, SHOWN BY SINGLE LINE AND BALL.

ROUNDED ESCARPMENT, CARET POINTS DOWNHILL.

LOW RIDGE, RESEMBLING THOSE ON LUNAR MARIA

LINEAMENT

LIST OF UNITS

ch	CHANNEL DEPOSITS	ss	SPARSELY CRATERED PLAINS
c	CANYON DEPOSITS	sm	MODERATELY CRATERED PLAINS
s	CHAOTIC DEPOSITS	pc	HEAVILY CRATERED PLAINS
k	KNOBBY DEPOSITS	pp	MOTTLED CRATERED PLAINS
g	GROOVED TERRAIN MATERIAL, COARSE	m	MOUNTAINOUS DEPOSITS
gf	GROOVED TERRAIN MATERIAL, FINE	cm	CRATERED DEPOSITS, MANTLED
v	VOLCANIC DEPOSITS	cu	CRATERED DEPOSITS, UNDIVIDED

Fig. II-2. Age relations and explanations of map symbols.

publication format and should not be taken as indicative of a present level of knowledge. The map is a very coarse generalization of the information available. A more detailed map that will do justice to the wealth of information in the *Mariner* 9 photography will be published in the not too distant future.

A. Description of Units

1. Densely Cratered Units

Densely cratered terrain covers approximately one-half of the planet's surface, including most of the central and southern portions of the map and the south polar regions. The cratered area was photographed by *Mariners* 4, 6, and 7 in 1964 and 1969 and has been described in detail by Murray et al. (Ref. II-3). The surface is almost saturated with large (>20 km), flat-floored craters; the density of smaller craters, which are mostly bowl-shaped, falls short of saturation by a factor of 10. Several large ring structures resembling lunar basins occur within the densely cratered terrain (Ref. II-4; also see Section VII

of this Report). The character of the cratered terrain varies both locally and on a regional scale. Around the large impact basins, positive relief features are more common than elsewhere, providing the basis for discriminating a mountainous unit (m). In other areas, the cratered terrain appears to be partly mantled, so that fewer intermediate and small (<20 km) craters are present, and the larger craters appear subdued. A unit termed "cratered deposits, mantled" (cm) has therefore been designated; the rest of the densely cratered deposits is left undivided (cu).

a. **Cratered deposits, undivided (cu).** Forms the primitive accretionary surface of the planet. Occurs primarily in the southern mid-latitudes, but extends to 40°N around the 330°W meridian. Isolated areas occur in the volcanic province. Saturated with large, flat-floored, commonly rimless, craters. Intercrater areas flat and featureless except for scattered small, bowl-shaped craters. Locally may be partly covered by younger deposits, so that the topography has a muted appearance. Ridges, resembling those on the lunar maria, occur in some of the muted areas. Probably consists mostly of reworked impact breccias, but locally includes younger volcanic and eolian deposits.

b. **Cratered deposits, mantled (cm).** Mapped only where extensive areas appear mantled. Fewer intermediate and small-size craters (<20 km) than unit cu. Occurs primarily in high southern latitudes. Interpreted as cratered deposits mantled by various thicknesses of younger material. Lobate flow fronts indicate volcanic materials in some areas, but the mantling material almost certainly includes significant portions of eolian debris.

c. **Mountainous deposits (m).** Forms the rugged parts of the rims of the three largest recognized impact basins, Argyre, Libya, and Hellas. Argyre (50°S, 43°W) is surrounded by rugged terrain that is cut by graben. The Libya basin (15°N, 270°W) rim is preserved as a distinct mountainous unit only at the south side of the basin. The Hellas (45°S, 295°W) rim is subdued. Mountainous terrain with relief comparable to Argyre is preserved only in isolated areas, particularly to the east where there is a complex array of isolated mountains. The mountainous unit is interpreted as remnants of parts of the primitive crust uplifted during the formation of the impact basins. Remnants of basin ejecta are also included.

2. Plains-Forming Materials

Plains, showing various degrees of cratering, occur over most of the planet not covered by the densely cratered

units. The plains-forming materials are thought to be largely volcanic and eolian in origin. They have been divided into three units on the basis of the number and character of the superimposed craters.

a. Heavily cratered plains materials (pc). The most heavily cratered of the plains units, but has fewer large craters than the densely cratered units described. Equivalent to unit mc of McCauley et al. (Ref. II-1). Occurs mainly in the areas north and south of Lunae Palus and in Hesperia. Ridges resembling those on the lunar maria are common. Interpreted as old lava plains similar to the lunar maria. (Small areas of material similar to this are present widely throughout the densely cratered area; they are not mapped because of scale limitations.)

b. Moderately cratered plains materials (pm). Has fewer craters in the size range of 2 to 20 km than unit pc, but more than unit ps (Ref. II-5; see Section IV of this Report). Occurs in Elysium around the major shield volcanoes, in the Arcadia–Tharsis region, where it is exposed mainly as islands surrounded by unit ps, and in the region of Phoenicus Lacus. In the Arcadia–Tharsis region, the unit is almost everywhere intensely fractured. It is interpreted as volcanic lava plains intermediate in age between units ps and pc.

c. Sparsely cratered plains materials (ps). Occurs mainly in the Amazonis–Tharsis region and in the large impact basins in the densely cratered province. Unit ps is the least cratered and presumably the youngest of the plains units. At wide-angle resolution, it is relatively featureless, except in places close to its contact with the densely cratered terrain where indistinct ridges and low rounded hills are common. At narrow-angle resolution, irregular lobate scarps suggestive of flow fronts are common, especially in the Tharsis region. Low hills, islands of highly fractured terrain, sinuous channels, and polygonal fractures occur in other areas. More rarely, the narrow-angle pictures are featureless. In the Tharsis region, the plains appear to be composed mainly of volcanic flows, as lobate flows are detectable on nearly all narrow-angle pictures. In the Amazonis region and in the large impact basins, Argyre, Hellas, and Libya, volcanic features are rare and the eolian component probably dominates. The unit embays all other units, confirming the young age inferred from the crater counts.

d. Mottled cratered plains materials (pp). Occurs only at high northern latitudes where it forms an annulus around the pole. The density of large (>20 km) craters is comparable to that of unit pc, but the density of smaller craters is substantially lower. Large craters are subdued and apparent mainly because of an albedo contrast between the light crater floors and the dark surrounding materials. The local albedo contrasts give the unit a mottled appearance. The albedo of the unit as a whole is lower than that of unit ps with which it is generally in contact to the south. It is interpreted as cratered plains material (pc) overlain by a mantle of eolian debris.

3. Volcanic Units

Included under this heading are all volcanic units associated with roughly circular volcanic structures, as distinct from the extensive plains units. Because of limitations of scale, only two categories are depicted: a general unit (v) and another unit, consisting of two facies (gc and gf), which form some very distinctive terrain around Nix Olympica.

a. Volcanic materials (v). Includes materials associated with shield volcanoes, volcanic domes, and volcanic craters (units vs, vd, and vc of Ref. II-1). Most of these features are circular, radially symmetric, have a central crater and gently sloping flanks. They occur primarily outside the densely cratered region, although two features within the densely cratered province are indicated on the map. The volcanic deposits have a wide range of ages. Those associated with Nix Olympica are relatively young (Ref. II-6; also see Section VIII of this Report); those within the cratered province are relatively old (Ref. II-5; see Section IV of this Report).

b. Grooved terrain materials (gf and gc). Two facies of grooved terrain are recognized: a unit gc with a coarse surface topography which occurs close to Nix Olympica, and a unit gf with a finer surface texture which occurs farther away. The coarse unit gc is characterized by linear mountains 1 to 5 km wide and typically 100 km long. The mountains are commonly separated by valleys that have flat floors with a fine striation parallel to the length of the valleys. The unit appears to be broken into blocks along arcuate faults that tilt the blocks gently inward toward Nix Olympica. The fine textured unit gf is characterized by closely spaced equidimensional mountains whose horizontal and vertical dimensions decrease outward from Nix Olympica until the mountains merge with the surrounding plains. Both units are complexly embayed by the surrounding plains deposits.

The grooved terrain deposits may represent old volcanic materials derived from the Nix Olympica center and since complexly fractured by the continual tectonic activity associated with the formation of the central shield. An alternative hypothesis is that the grooved ter-

rain represents the outer remnants of a once much larger Nix Olympica that has been reduced in size by whatever process has formed the bounding scarp.

4. Other Units

In several areas, erosional and tectonic processes have resulted in the formation of distinctive geologic units. Four categories have been identified:

(1) *Channel deposits* (ch). These have all the characteristics of terrestrial stream deposits. They occur in long, linear, sometimes sinuous channels that commonly have well developed tributaries. Narrow-angle pictures show terraces, bars, finely braided networks of channels, and superimposed meanders. The most prominent channels head in the area of chaotic terrain around $2°$N, $30°$W, and run northwest to the Chryse basin. Most, but not all, other channels occur in the densely cratered terrain near its contact with the plains The unit is interpreted as materials deposited by a fluid, presumably water (Ref. II-7; also see Section III of this Report).

(2) *Canyon deposits* (y). This unit includes materials that are exposed on the floor of the major rift system that extends 4000 km across the surface close to the equator between $30°$ and $100°$W. The talus on the canyon walls is excluded. In most places the floor appears smooth, but locally jumbled blocks are present. At the eastern end of the canyon, the unit merges with the chaotic terrain. At the western end, the unit is pinched out as the canyon grades into a zone of branching troughs.

(3) *Chaotic deposits* (h). Chaotic deposits have been described in detail previously (Ref. II-8). The surface of the unit is crossed by numerous intersecting cracks that break the surface into blocks with a wide range of sizes and which may be tilted slightly in different directions. The chaotic deposits normally occur in locally low areas, occasionally in completely closed basins. The outcrop areas are usually surrounded by an inward-facing scarp. The main area of occurrence is a broad region around $5°$S latitude, $35°$W longitude. The origin of the unit is obscure. Some process of sapping from below and subsequent collapse is required.

(4) *Knobby dep.* (k). The unit is characterized by irregular rounded hills and intervening plains. The hills are all sizes, from several hundred kilometers down to the limit of resolution (<1 km). The unit occurs mostly in a zone up to 500 km wide between the cratered terrain and the plains units. In general, the individual hills are larger, have more rectilinear outlines and flatter tops closer to the cratered terrain. Farther from the cratered terrain, they become rounded and smaller in both horizontal and vertical dimensions until they merge with the surrounding plain. The unit includes the unit kt of McCauley et al. (Ref. II-1), and the fretted terrain of Sharp (Ref. II-9; also see Section VI of this Report).

B. Structural Features

Mars is characterized by an abundance, if not a great variety, of structural features. The most common are graben, typically 1 to 5 km wide. They may occur as closely spaced, parallel arrays as in the Arcadia region, or as isolated fractures several thousand kilometers long as in the Mare Sirenum region. The distribution of graben is markedly nonuniform. Most are part of a system of faults approximately radial to the Tharsis ridge. The western part of the Coprates canyon also appears to be part of this set. The focal point of this vast system of fractures is the Phoenicis Lacus area, which is also the highest part of the ridge. The pattern appears to have formed as a result of the extension associated with the broad domical uplift of the Tharsis region.

Elsewhere fractures occur concentric and radial to the large impact basin of the densely cratered province (Ref. II-4; see Section VII of this Report) Fractures also occur locally around the large shield volcanoes (Ref. II-5; see Section IV of this Report) and at, and parallel to, the margin of the densely cratered terrain to form the knobby and fretted terrains (Ref. II-9; also see Section VI of this Report).

Mare ridges are the other common structural feature. They occur primarily on the most heavily cratered plains unit (pc). West of the Tharsis ridge, they are aligned along directions concentric with the center of the Tharsis ridge.

References

II-1. McCauley, J. F., Carr, M. H., Cutts, J. A., Hartmann, W. K., Masursky, H., Milton, D. J., Sharp, R. P., and Wilhelms, D. E., "Preliminary Mariner 9 Report on the Geology of Mars," *Icarus,* Vol. 17, p. 289 1972.

II-2. Wilhelms, D. E., *Geologic Mapping of the Second Planet,* U. S. Geological Survey Interagency Report: Astrogeology 55, 1972.

II-3. Murray, B. C., Soderblom, L. A., Sharp, R. P., and Cutts, J. A., "The Surface of Mars: 1. Cratered Terrains, *J. Geophys. Res.,* Vol. 76, p. 313, 1971.

II-4. Wilhelms, D. E., "Comparison of Lunar and Martian Multi-Ringed Circular Basins," *J. Geophys. Res.,* Vol. 78, 1973.

II-5. Carr, M. H., "Volcanism on Mars," *J. Geophys. Res.,* Vol. 78, 1973.

II-6. Hartmann, W. K., "Martian Cratering IV: Mariner 9 Initial Analysis of Cratering Chronology," *J. Geophys. Res.,* Vol. 78, 1973.

II-7. Milton, D. J., "Water and Processes of Degradation in the Martian Landscape," *J. Geophys. Res.,* Vol. 78, 1973.

II-8. Sharp, R. P., Soderblom, L. A., Murray, B. C., and Cutts, J. A., "The Surface of Mars: 2. Uncratered Terrains, *J. Geophys. Res.,* Vol. 76, p. 331, 1971.

II-9. Sharp, R. P., "Mars: Fretted and Chaotic Terrains," *J. Geophys. Res.,* Vol. 78, 1973.

III. Water and Processes of Degradation in the Martian Landscape[1]

Daniel J. Milton

U. S. Geological Survey, Menlo Park, California 94025

Since at least the *Mariner* encounters in 1969, Mars, despite its own individuality, has been regarded as a planet in a state of development intermediate between that of the Moon and Earth. The histories of impact, volcanism, and tectonic disturbance on three bodies are to a first approximation similar, despite such differences as the horizontal mobility of crustal segments on Earth and their apparent stability on the other two bodies. On the Moon we see constructional landforms such as impact craters, volcanoes, and volcanic plains, most persisting from the early epochs of lunar history. Most landscapes on Earth, however, owe their appearance to erosion, principally the work of running water, as much as to constructional processes. Features of the primeval epoch have long since been destroyed, and any area has passed through so many cycles of erosion and rejuvenation that there is some time in the past beyond which its history is indecipherable.

It is the thesis of this section that erosion has been active on Mars so that, unlike the Moon, many of the surface landforms are products of degradation. Unlike Earth, erosion has not been a universal process, but one areally restricted and intermittently active, so that we see a landscape that is the product of one or two cycles of erosion and large areas of essentially undisturbed primitive terrain.

It is a second thesis that, as on the continents of Earth, running water has been the principal agent of degradation. At the present time, the surface temperature and the pressure and water content of the atmosphere make bodies of liquid water at the surface impossible or at least confined to a few small areas at certain seasons. Many features on Mars, however, are most easily explained by assuming running surface water at some time in the past. For a few features, running water is not merely the easiest explanation within the range of our imagination, but the only possible explanation. If these cases, which involve water courses as large as the largest rivers or torrential floods on Earth, can be established, then an hypothesis of aqueous origin should have a favorable hearing for the much wider spread of features for which the evidence is less conclusive.

A. Channels Shaped by Flowing Water

The first great Martian controversy began almost a century ago with Schiaparelli's announcement that he had discovered channels (canali) on Mars. *Mariner 9* has revealed that channels are indeed a prominent feature of the Martian surface (although very different from those envisioned by Schiaparelli and Lowell) and introduced a second controversy on Martian channels, although this time on a higher level of their nature rather than their reality. A preliminary description and maps of

Fig. III-1a. Channel between Memnonia and Amazonis near 5°S latitude, 150°W longitude, apparently eroded by running water. Wide-angle view with direction of flow from top to bottom (south to north). The width of the area is about 260 km. Lighting is from the right. (MTVS 4174-45, DAS 06822798; MTVS 4258-31, DAS 09628614)

Fig. III-1b. Middle section of Amazonis channel. The individual narrow-angle frames cover an area of about 30 by 40 km. Figure III-1b is reoriented so that lighting is from the top. (MTVS 4294-12, DAS 12477650; MTVS 4294-16, DAS 12499720; MTVS 4294-20, DAS 12499790)

their distribution within the equatorial region are given by McCauley et al. (Ref. III-1). Carr et al. (Ref. III-2; see Section II of this Report) also map the location of major channels. The most convincing evidence for an aqueous origin, in the available photography, is found in the broad channels in Chryse, the two long channels in Lunae Palus, and especially a smaller channel between Memnonia and Amazonis.

The Amazonis channel (Fig. III-1a) is about 350 km long, and the widest of a complex of channels spread over a zone almost 100 km wide. Positive indication of the direction of flow is difficult, but flow from south to north is suggested by bars in the wake of islands and the pattern of truncation at the base of bars. Establishing the direction of flow is never a problem terrestrially, and it is surprising how symmetrical are the up- and down-stream directions of single channels without tributaries. Flow from south to north is consistent with a regional gradient of about 1 km over the length of the channel, as indicated by Mariner 9 infrared spectroscopy (Ref. III-3, also see Section XX of this Report) although regional warping of the surface may have occurred since the formation of the channels.

Segments of the Amazonis channel differ in character. The upstream section (right-hand frame of Fig. III-1b) lies within the somewhat diffuse outlines of a crater. Here the channel consists of many broad branches, one of which is smooth-floored; the others are marked by ridges and troughs parallel to its length. The middle section has a slightly sinuous, smooth-floored main channel of even width. This broadens downstream into a complexly braided reach (Fig. III-1c), which, beyond

these narrow-angle pictures, gathers again into a single channel that crosses a crater and debouches onto a featureless plain

If a single feature is to be chosen on which to base an argument for running water on Mars, it is this braided reach of the Amazonis channel. The similarity to the braided type of terrestrial river channel (Fig. III-2) is so great that were it not for the craters, it would be easy to envision these as pictures of Earth. Analogy, however, is an insufficient argument, unless it is shown that the features reflect phenomena unique to flowing water. It is hardly believable that this pattern could have arisen by any means not involving horizontal flow, for example by faulting or vertical collapse. Water, however, is not the only substance that can flow. On Earth the wind blows, ice moves as glaciers, lava pours forth from volcanoes, and flows of volcanic ash and perhaps some avalanches and landslides are dense, turbulent, fluidized suspensions of solid particles entrained in gas. Each of these produces characteristic landforms quite different from that in question. Some consideration of why they differ may help to clarify the unique nature of water as a morphologic agent.

Both erosional and depositional landforms produced by wind are seen in the Mariner 9 pictures, as discussed by McCauley (Ref. III-4; see Section X of this Report) and Cutts and Smith (Ref. III-5; see Section XI of this Report). The power of wind in transporting material depends on the exchange of momentum between the boundary layer and a large mass extending far above the zone of interaction with the ground surface. On an almost smooth surface, wind erosion produces parallel

Fig. III-1c. Braided section in lower part of Amazonis channel. This narrow-angle mosaic, like Fig. III-1b, contains frames covering 30 by 40 km. (MTVS 4258-35, DAS 09628649; MTVS 4258-39, DAS 09628729)

linear scours and ridges. Dunes, the ordinary depositional feature, may have complex forms individually, but dune fields as a whole show a symmetry with respect to the direction of prevailing winds. The lateral sinuosities which characterize the braided reach of the Amazonis channel indicate a fluid uncoupled from a larger moving mass and hence a fluid that, unlike wind, is confined or almost confined to the channels themselves.

The sinuosities also rule out glacier ice, although for somewhat different physical reasons. The curvature of the channels and subchannels indicates a fluid with considerable momentum, eliminating any fluid moving as slowly as ice. Erosive glacial features are simple; arcuate features may be deposited at the ice margin, but these are transverse to flow direction. Any features at all resembling those of the braided Amazonis channel associated with terrestrial glacial deposits are attributed to the action of meltwater rather than to ice itself.

The impression on the observer implied by the term "river of lava" conceals some fundamental differences between lava and water. The eroding and transporting capacity of water results from the turbulent nature of its flow. Lava, however, generally flows laminarly and has little or no erosive capacity. Lava channels on Earth and

Fig. III-2. Braided section of Sagavanirtok River, Alaska. Compare obliquely truncated downstream end of bars (toward bottom of frame) with those in Fig. III-1c. Width of frame about 2 km. (U. S. Navy Photograph BAR 283-055)

the apparently identical features photographed on the flanks of Nix Olympica (Ref. III-6; also see Section IV of this Report) form as liquid lava withdraws from the already solidified portions of the flow. The truncation of older subchannels at the bottom end of bars in the Amazonis channel indicates active erosion of material, which would not be accomplished by lava.

Fluidized suspensions of volcanic ash in volcanic gas (nuées ardentes) have been proposed by Cameron (Ref. III-7) as the erosive agent responsible for sinuous rilles on the Moon. The terrestrial examples cited by Cameron to indicate that nuées ardentes have significant erosive power appear, however, to involve a misreading of her sources. Nuées ardentes at Mt. Pelée characteristically deposit rather than erode; troughs apparently are formed only on steep slopes after the quantity of gas is diminished to a point at which the flow is essentially a debris slide rather than a gas-charged flow (Ref. III-8). The 1783 flow at Asama Volcano eroded only below the point at which the ash flow encountered and engulfed a pond, transforming it into a mud flow (Ref. III-9). The weak erosive capacity of ash flows probably reflects a low margin of energy above that necessary to maintain the suspension itself; that is, any expenditure of energy for erosion would result in the collapse of the flow.

Only a high-density, low-viscosity true liquid moving over a particulate bed could form channels like those in Amazonis. Water would be available with less violent change from the present Martian regimen than such conceivable alternatives as ammonia or hydrocarbons or, if the atmospheric pressure exceeded 5 bars, carbon dioxide itself.

Terrestrial stream channels exhibit systematic relationships between their various dimensional characteristics and the conditions of flow, and these have been extensively quantified. Few of these involve planimetric data alone, which is nearly all that *Mariner 9* provides. For example, the ratios of meander length and radius of curvature to the channel width for the northern channel in Lunae Palus (Fig. III-3) lie close to an extrapolation of the lines of empirical fit for terrestrial aqueous channels (Ref. III-10). It is tempting to apply more complex relationships to the Martian channels, for example to use the Manning equation to compute discharge, but the error involved in estimating small differences in elevation such as bank heights and slopes is so large that the procedure seems futile. Qualitative description and inferences seem sufficient for the present.

In terrestrial braided streams, the bars reflect deposition and erosion of sediment in a quasi-steady state. Once material is deposited in the channel, flow is concentrated in the flanking channels, scouring their beds and eroding the banks until the bar emerges as an island. In order for braiding to develop, sediment transport is essential; in addition, the outer banks of the channel must be erodible, so that they, rather than the incipient bars, are attacked. Highly braided streams tend to have greatly and rapidly fluctuating volumes of flow. Bars generally build up during the high stage until they are awash. The relief of the Martian channels is not measurable to an accuracy that would allow calculation of the cross section, but the volume of flow of the Amazonis channel, which is far from the largest on Mars, must have been at least the proportions of its terrestrial namesake.

The straight or slightly sinuous single channel upstream reflects greater confinement of the developing channel. There appears to be a raised embankment along the west bank. If this is not an illusion of albedo, it may be the edge of a tilted fault block (faults parallel to this occur in the region) along which the stream was confined, and which provided a notch that allowed it to break through the rim of the crater just upstream. Within the crater there is another complex reach. It does not appear to be in a state of equilibrium as does the braided reach, but to have developed in discrete stages. The smooth-surfaced high remnant could be a lake deposit formed when the crater was a closed basin, and the channels of different character may have developed successively when local baselevel changed as the crater was breached. The lineated channels here and on the margins of the middle section downstream suggest scouring of the bed without deposition.

Altogether, the Amazonis channel and the entire set of narrower, more or less parallel channels form a very immature drainage system, clearly discordant to the cratered terrain which it traverses. It resembles terrestrial catastrophic flood channels more than evolved river systems. The most violent flood recognized in the terrestrial geologic record, the discharge of the ice-dammed glacial Lake Missoula, which produced the Channeled Scablands of Washington (Ref. III-11), yielded 40 km³/hr (Ref. III-12) or 70 times the average discharge of the Amazon. The erosional landforms produced resemble those in the upper part of the channel. While depositional bars occur in the Channeled Scablands, they do not have the complexity or perfection of those of the lower reach of the Amazonis channel. The history of the Amazonis and other

Fig. III-3. Large channels in Lunae Palus near 22°N, 65°W. North is at the top. Direction of flow in the two large channels is to the east. Width of frame about 600 km. The area west of the bend in the southern channel (partly concealed by a dark circle produced in the *Mariner* television subsystem) is shown in Fig. III-6. (MTVS 4193-90, DAS 07399738)

Martian channels may have involved a succession of catastrophic floods punctuating periods of more steady flow.

Other channels on Mars appear similar to those in Amazonis, but their nature is obscured either by the lack of good narrow-angle camera coverage or by actual modification. (Some features resemble, perhaps more than accidentally, dry desert watercourses choked by windblown sand.) Teardrop-shaped bars are seen at the mouths of the two long channels in Lunae Palus, which show bends that appear to correspond to the free meanders of terrestrial rivers (Fig. III-2). The broadest channels, those in Chryse, show scoured channel forms and depositional bars.

The Chryse channels are the only ones for which a potential source of water is apparent. They head in chaotic terrain and have tributaries more or less proportional in size to the area of chaotic terrain which they drain (Ref. III-1). Sharp et al. (Ref. III-13) suggested that chaotic terrain, as seen in the *Mariner 6* pictures, is a

region of decayed ground ice. The relation to the Chryse channels revealed by *Mariner 9* suggests that decay involved not merely evaporation but rapid melting of large volumes of ground ice. In contrast, there is no obvious source of water near the heads of the Amazonis or Lunae Palus channels.

B. Channels Probably Shaped by Running Water

A pattern entirely different from that of the channels discussed above is shown by a channel in Mare Erythraeum (Fig. III-4). The downstream half of the channel shows the interlocking tight bends with high, sharp-pointed inner cusps, irregular widenings, and the (apparently) large depth-width ratio which are features characteristic of lunar sinuous rilles rather than meandering terrestrial rivers. Lunar sinuous rilles are now generally regarded as unroofed lava tubes (Refs. III-14 and III-15). The dendritic pattern of tributaries in the upper part of the channel is not found in lunar rilles, but resembles that of
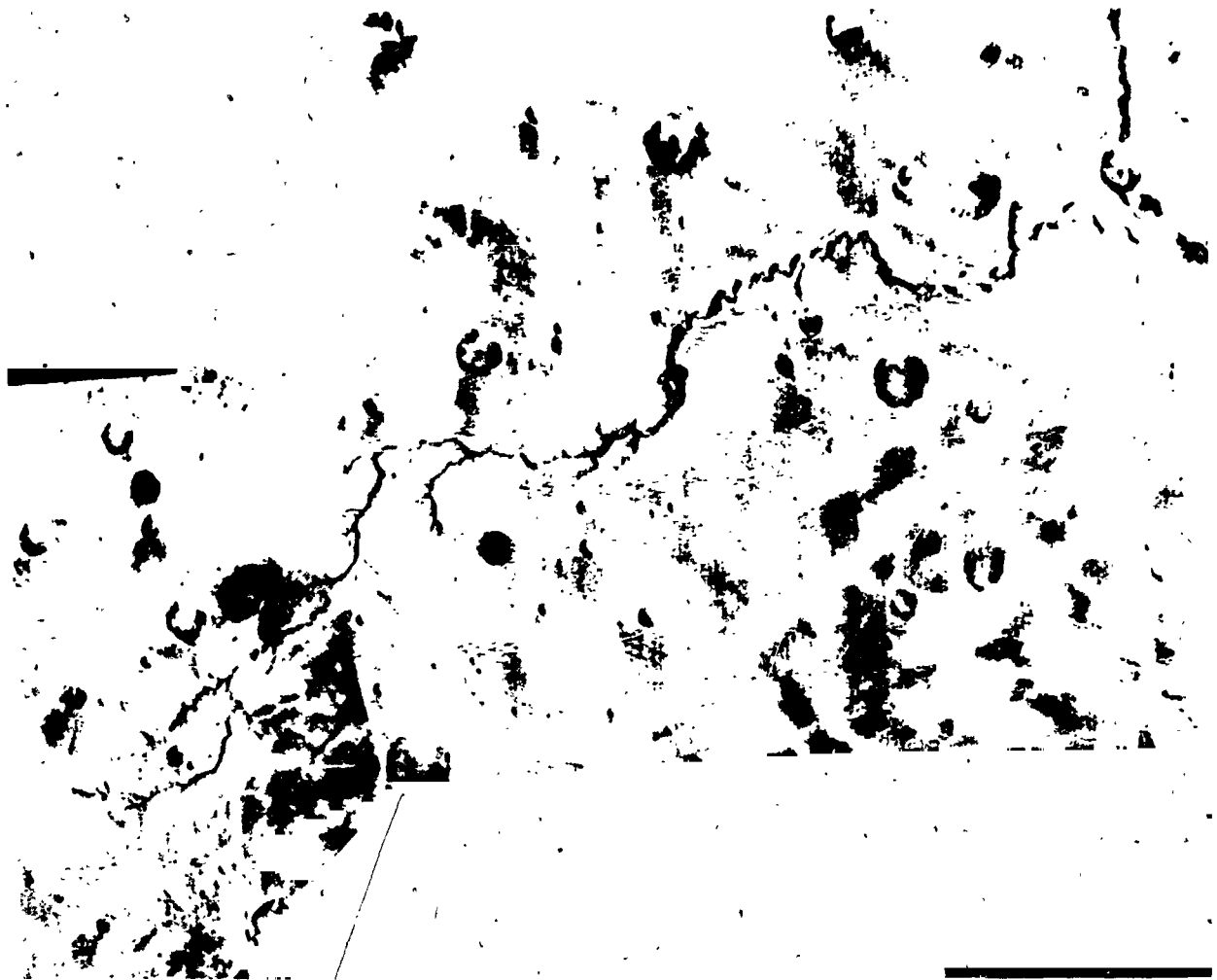
Fig. III-4. Channel in Mare Erythraeum, approximately 400 km in length. Center of frame near 29°S, 40°W. Lower section resembles sinuous rilles on the Moon; upper section resembles entrenched arroyos of deserts on Earth. (MTVS 4160-78, DAS 06354848; MTVS 4245-27, DAS 09160804; MTVS 4158-87, DAS 06283028)

entrenched arroyo systems on Earth. Nevertheless, the entire channel system seems to exhibit an internal coherence that makes any twofold hypothesis of origin unappealing, for example a lava tube extended headward by subsequent aqueous erosion. A larger channel (Fig. III-5) in Rasena with the same high apparent depth-width ratio but lower sinuosity again resembles lunar rilles. In this case its course through heavily cratered terrain makes a lava tube seem especially unlikely.

The characteristic features of sinuous rilles on the Moon remain unexplained. Hadley Rille is clearly not the core of a narrow flow (as are the channels on the flanks of Nix Olympica), but is thought to have formed during the drainage of a semiconsolidated lava lake (Ref.

III-15). Its difference from terrestrial rivers may depend less on the different rheologic properties of lava and water than on the fact that its boundaries are determined by thermal processes rather than mechanical erosion and sedimentation. The speculation may be hazarded that sinuous rille-like channels on Mars may have formed by the partial melting of a permafrost zone.

The smaller deep valleys on the margins of wide depressions, notably the great equatorial chasm of Mars, markedly resemble terrestrial canyon systems (Fig. 4a of Ref. III-16; also see Fig. V-4a of this Report). In fact, the larger systems on the south side of the chasm are a good match in size and in plan for the Grand Canyon of the Colorado. In both, the side canyons end at steep head-

Fig. III-5. Channel in Rasena. Center of frame near 20°S, 182°W. Length of channel about 700 km. The apparently high depth-to-width ratio is more suggestive of lunar rilles than terrestrial river channels. (MTVS 4167-18, DAS 06606778)
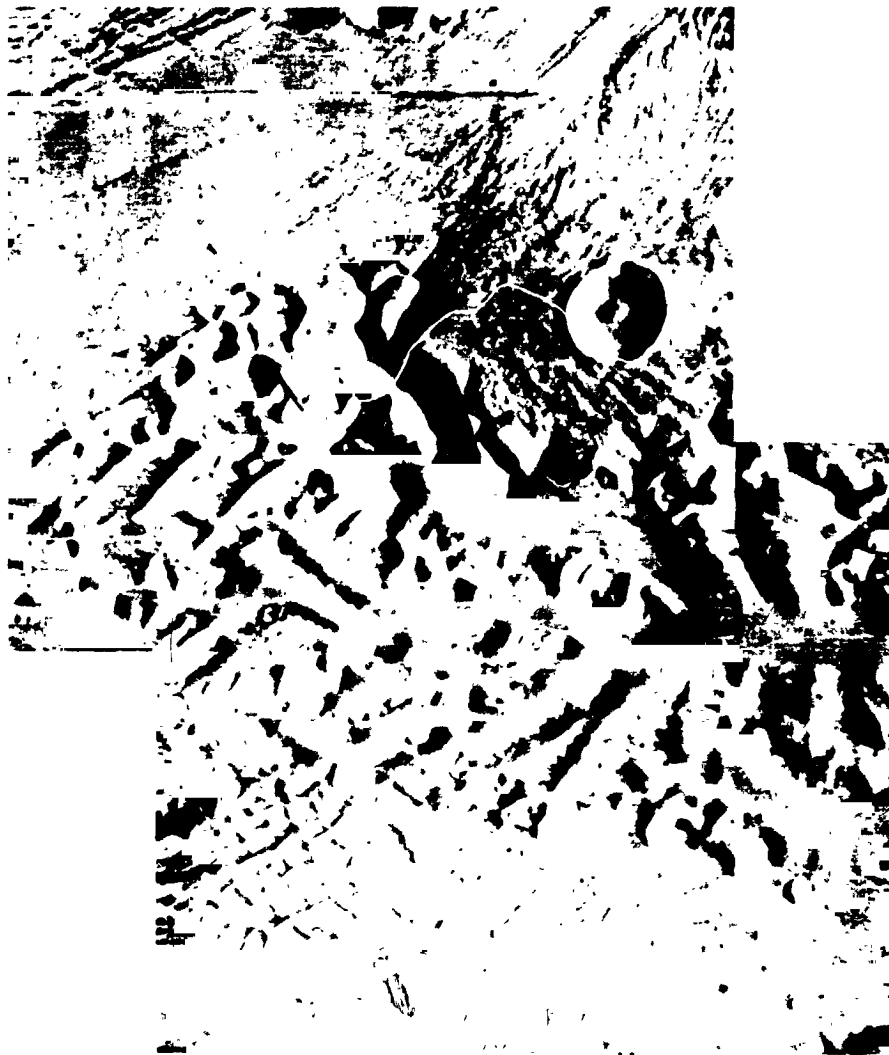
Fig. III-6. Two-picture mosaic showing dendritic canyon system developed from an angular fracture set. Wind scour has modified the upper plateau level. Note that the ejecta from the large crater has been more resistant to erosion. The area shown is about 50 km wide, located at 22°N and 73.5°W. Sunlight is from the right. (MTVS 4297-8, DAS 13313735; MTVS 4297-12, DAS 13313806)

walls, most of which appear to have been etched out along joints and faults. The transformation by erosion of an angular fracture pattern to a system of curving canyons can be clearly seen at the bend of the southern Lunae Palus channel (see Fig. III-6). A controlling factor ι the excavation of the side canyons of the Grand Canyon is artesian sapping, undermining of the head walls by springs. The distance from the Colorado River to which these canyons have reached is roughly proportional to the volume of ground water flow. Artesian sapping could be responsible for Martian canyons as well.

Sharp (Ref. III-16; see Section V of this Report) proposes that erosion of Martian canyons takes place by hypothetical dry sapping in which the cliffs are undermined by evaporation of ground ice without production of liquid water. One would expect such a process to act uniformly on all exposed walls, and thus reduce rather than increase anfractuosities. Narrow relicts such as those in the left-hand picture of the narrow-angle mosaic (Fig. III-7b) suggest that retreat diminishes when the hinterland is reduced, which would be the case if ground water flow toward the scarp were important. Nevertheless, some

mechanism of cliff recession on a broad front seems nec...sary to explain the many wide, flat-floored valleys, for example those in Ismenius Lacus (Fig. III-7a). Broad valleys on Earth are generally caused by lateral corrasion by a stream meandering from side to side eroding wherever the outside of a bend impinges on the valley wall. A different mechanism is probable for at least some valleys on Mars. The exhumation of craters as the cliff retreats (see the middle picture in Fig. III-7b) points to some form of sapping rather than lateral corrasion. The inner and outer walls of the bend of the narrower canyons, which show a broad curve on the outside and a cuspate point on the inside, are approximately equidistant from a simple curve in the center of the channel, suggesting parallel retreat.

In the same valley system, a large mass tilts down into the valley (Fig. III-7b, bottom left). This is not the usual pattern of slump, in which blocks slip downward so that their upper surface slopes back from the valley (which commonly is seen on Mars, as well as Earth), but one that suggests removal of a considerable amount of material from the lower part of the slump block, not just at its outer edge. An analogous configuration in Tennessee, und by an analysis of topographic data, has been explained as a result of ground water sapping (Ref. III-17).

In summary, the pattern of cliffs, canyons, and flat-floored valleys indicates sapping of some type. Certain features specifically indicate localized ground water sapping; others possibly can be explained by dry sapping or a more unlocalized ground water flow. Removal of debris remains a problem. Either water was sufficient for transport, even in valleys and on plains in which *Mariner 9* pictures do not reveal the marks of running water, or the residue after decay of ground ice was so minor, or finely comminuted, that it could be removed by the wind. Either hypothesis is tenable, and both may be true; some arguments for the first are given below.

The erosional features discussed above have been explained by the action of water largely of subterranean origin. Melting of ground ice is indicated in the case of the Chryse channels, which emanate from chaotic terrain, and is probable elsewhere. A separate question is whether it has rained (or snowed and melted at the surface) on Mars. If the Martian surface has a high infiltration capacity, water would sink underground before it would gather into streams large enough for detectable erosion. There are many areas on Mars, however, which have

small channels that suggest a surface source of water (Figs. III-8 and III-9). The pattern of closely spaced, slightly sinuous channels joining and redividing to form a reticulate rather than dendritic system, but with a preponderance of junctions in the downslope direction, resembles that which develops on steep pediments and alluvial slopes in arid regions of Earth. On Mars these channels generally occur on moderately steep but smooth slopes, particularly on the outer rims of craters. In general, narrow-angle pictures of these channels are disappointingly uninformative, in part because viewing conditions happened to be unfavorable, but perhaps also because the channels are ancient and have been subsequently modified by other processes. Excellent narrow-angle pictures, however, have been taken of a set of gullies on the slopes of Alba (Fig. III-9). Although here a case could be made for an origin as lava channels, channels of this type occur commonly on the slopes of apparent impact craters (Fig. III-8). An atmospheric source for the water is suggested by the fact that the channels head very close to the ridge crests, and by the presence of channels on both the inside and outside walls of the same craters. Such channel nets occur abundantly in certain areas of Mars. Their distribution may have a climatic basis, although it may in part represent areas relict from a wider distribution, where they have not been destroyed by subsequent geologic events.

C. Planation as a General Process on Mars

The product of scarp retreat is a plain at the foot of the scarp. If, as suggested above, scarp retreat is the result of the action of running water, a plain so produced may be regarded, in a broad sense, as a fluvial landform to which the channels are merely headward extensions. Whether water in any significant amount ever flowed over the surfaces, except near the head scarp and in the channels, is difficult to determine. Certainly the detail observed in many narrow-angle pictures of such surfaces points to wind as the active morphologic agent (Ref. III-4; see Section X of this Report), but this reflects the regime in the present and recent past rather than at the time of formation of the surface.

It has been established as a basic principle of terrestrial geomorphology that regional erosion normally does not involve a general lowering of ground level, but takes place by recession of a scarp that maintains a characteristic angle of slope, leaving a planation surface, or pediplain, to mark its retreat. A history of development

Fig. III-7a. Broad, flat-floored valley in Ismenius Lacus, debouching into fretted terrain. Center of frame near 41°N, 342°W. Width of frame approximately 550 km. (MTVS 4251-47, DAS 09378149; MTVS 4251-55, DAS 09378289)

Fig. III-7b. This narrow-angle mosaic shows the detail in the area outlined in Fig. III-7a. Scrap retreat by artesian sapping would explain most of the features. (MTVS 4285-48, DAS 10650904; MTVS 4251-51, DAS 09378189; MTVS 4210-66, DAS 07975343)
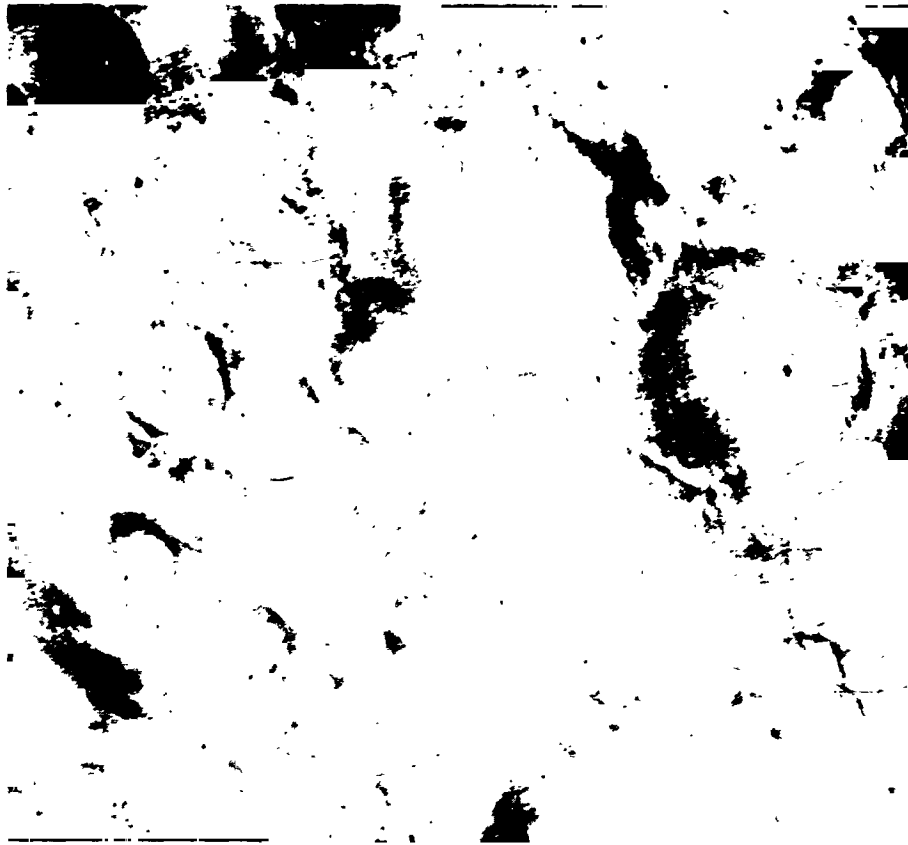
Fig. III-8. Gullies on rim of old impact craters in Sinus Sabaeus, near 9°S, 327°W. Width of frame about 300 km. The patterns in this figure and in Fig. III-9 resemble gully systems on moderate slopes in terrestrial deserts, and may have formed by runoff of precipitation. (MTVS 4261-36, DAS 09736554)

of successive surfaces, or denudation chronology, can be worked out. In the geologically less complex continents, notably those of the southern hemisphere, attempts to integrate morphologic history with stratigraphic and tectonic histories have met with considerable success (Ref. III-18).

Analysis of landscape development on Mars in terms of planation surfaces introduces a perspective to Martian history that is valuable in supplementing the approach based on methods used on the essentially erosion-free Moon. Although analogies to Earth may be misleading, they also can be useful. As a trivial example, it was suggested in early press reports on the *Mariner 9* mission that the cliffs at the base of Nix Olympica could be sea cliffs. The corollary was not considered, that the surfaces at the base would then be surfaces of marine planation. The ineffectiveness of marine erosion in producing broad, level surfaces was established in the nineteenth century as the outcome of long controversy.

The same arguments could be applied to Mars, even if the former presence of oceans is not excluded a priori.

More significantly, the level surfaces are the key to dating in Martian history. Relative and eventually absolute dating must rely on crater statistics. As on the Moon, either crater frequency or crater morphology can be used as an index of age; both depend on the mechanism of erosion. The assertion by McGill and Wise (Ref. III-19) that crater degradation has been a continuous process is assuredly premature. There are indications that some plains on Mars are stripped surfaces where erosion has removed a weaker upper layer and stopped at a more resistant layer. Craters on these surfaces may have formed during the earlier period of exposure. In addition, some level-rimmed craters appear to be collapse features developed on younger deposits over the site of buried impact craters so that their frequency dates, if anything, a surface that is not even exposed.

Fig. III-9. Gullies on slope of volcano Alba near 45°N, 116°W. Width of frame about 60 km. (MTVS 4182-96, DAS 07039903)

If there is no marked layering, planation commonly works back from a base level so as to maintain a slope at a grade on which it is just possible for debris to be transported. Such graded surfaces appear to exist on Mars, and would be additional evidence for a gravity-controlled, presumably fluvial, erosion system, but more accurate elevations than currently available are necessary to distinguish them with certainty. The problem of the control of erosion levels on Mars, whether of graded or stripped surfaces, is an important one. If artesian sapping is a major factor in scarp retreat, stripped surfaces could mark the base of a permeable (or potentially permeable. if melting is of importance) layer. The presence of multiple stepped surfaces, how-

ever, suggests that there is no single planet-wide control on erosion levels.

Although they may show features relict from an earlier stage of cratering and a later stage of eolian erosion, the broad plains may be regarded as the most extensive of the landforms produced during a fluvial stage of Martian history. When this age occurred and whether there was more than one are problems that seem answerable with further analysis of the data. Questions beginning "Why" are of a different order. If a century of speculation has not produced a convincing cause for glacial ages on Earth, the explanation for a fluvial age on Mars may not be soon forthcoming.

References

III-1. McCauley, J. F., Carr, M. H., Cutts, J. A., Hartmann W. K., Masursky, H., Milton, D. J., Sharp, R. P., and Wilhelms, D. E., "Preliminary Mariner 9 Report on the Geology of Mars," *Icarus*, Vol. 17, p. 289, 1972.

III-2. Carr, M. H., Masursky, H., and Saunders, R. S., "A Generalized Geologic Map of Mars," *J. Geophys. Res.*, Vol. 78, 1973.

III-3. Conrath, B., Curran, R., Hanel, R., Kunde, V., Maguire, W., Pearl, J., Pirraglia, J., Welker, J., and Burke, T., "Atmospheric and Surface Properties of Mars Obtained by Infrared Spectroscopy on Mariner 9," *J. Geophys. Res.*, Vol. 78, 1973.

III-4. McCauley, J. F., "Mariner 9 Evidence for Wind Erosion in the Equatorial and Mid-Latitude Regions of Mars," *J. Geophys. Res.*, Vol. 78, 1973.

III-5. Cutts, J. A., and Smith, R. S. U., "Eolian Deposits and Dunes on Mars," *J. Geophys. Res.*, Vol. 78, 1973.

III-6. Carr, M. H., "Volcanism on Mars," *J. Geophys. Res.*, Vol. 78, 1973.

III-7. Cameron, W. S., "An Interpretation of Schroter's Valley and Other Lunar Sinuous Rilles," *J. Geophys. Res.*, Vol. 69, p. 2423, 1964.

III-8. Perret, F. A., *The Eruption of Mont Pelee, 1929, 1932*, Carnegie Inst. Wash. Publ. 458, 1973.

III-9. Aramaki, S., "The 1783 Activity of Asama Volcano, 1," *Japan, J. Geol. Geography. Trans.*, Vol. 27, p. 216, 1956.

III-10. Leopold, L. B., Wolman, M. G., and Miller, J. P., *Fluvial Processes in Geomorphology*, 522 pp., William Freeman and Co., San Francisco, 1964.

III-11. Bretz, J H., Smith, H. T. U., and Neff, G. E., "Channeled Scabland of Washington: New Data and Interpretations," *Bull. Geol. Soc. Am.*, Vol. 67, 1956.

III-12. Malde, H. E., *The Catastrophic Late Pleistocene Bonneville Flood in the Snake River Plain, Idaho*, U. S. Geological Survey Professional Paper 596, 52 pp., 1968.

III-13. Sharp, R. P., Soderblom, L. A., Murray, B. C., and Cutts, J. A., "The Surface of Mars: 2. Uncratered Terrains," *J. Geophys. Res.*, Vol. 76, p 331, 1971.

III-14. Greeley, R., "Lunar Hadley Rille: Consideration of Its Origin," *Science*, Vol. 172, p. 722, 1971.

III-15. Howard, K. A., Head, J. W., and Swann, G. A., "Geology of Hadley Rille," *Proceedings of the Third Lunar Science Conference*, 1-14, M.I.T. Press, 1972.

III-16. Sharp, R. P., "Mars: Troughed Terrain," *J. Geophys. Res.*, Vol. 78, 1973.

III-17. Stearns, R. G., "Warping of the Western Highland Rim Peneplain in Tennessee by Ground-Water Sapping," *Bull. Geol. Soc. Am.*, Vol. 78, p. 1111, 1967.

References (contd)

III-18. King, L. C., *The Morphology of the Earth*, 2nd ed., 726 pp., Hafner Publishing Co., New York, 1967.

III-19. McGill, G. E., and Wise, D. U., "Regional Variations in Degradation and Density of Martian Craters," *J. Geophys. Res.*, Vol. 77, p. 2433 1972.

Acknowledgments

IV. Volcanism on Mars[1]

Michael H. Carr

U. S. Geological Survey, Menlo Park, California 94025

One of the earliest and most significant of the *Mariner 9* results was the recognition of prominent volcanic features on Mars. At the height of the dust storm, which occurred at the beginning of the orbital phase of the mission, the only surface features clearly visible outside the polar areas were four dark spots in the Amazonis–Tharsis region. Each was soon seen to include, at its center, a complex summit pit. The morphology of the craters, and their position atop mountains high enough to be above much of the obscuring dust in the atmosphere, strongly suggested a volcanic origin. As the atmosphere cleared, the four spots were revealed to be centered on four enormous shield volcanoes with summit calderas (Refs. IV-1 and IV-2). Subsequent photography of the remainder of the planet has revealed a wide variety of volcanic features, indicating that volcanism has played a major role in the evolution of the planet.

The volcanic features have a markedly asymmetric distribution (Fig. IV-1). The planet can be roughly divided into two hemispheres. One includes nearly all the central volcanic features and the sparsely cratered plains; the other, for the most part, is densely cratered terrain, superficially resembling the lunar highlands.

---

[1]Publication authorized by the Director, U.S. Geological Survey.

The volcanic areas are generally high. The three shield volcanoes in Tharsis appear to lie on a broad northeast–southwest trending ridge, approximately 3 to 5 km above the mean Mars level (Ref. IV-3; also see Section XXXVI of this Report); the largest of all the shields, Nix Olympica, lies on the western flank of this ridge. The volcanic features of Elysium are similarly in a region of high elevation.

Volcanic and tectonic features appear to be closely related. Fractures radiate in nearly all directions from the Tharsis region (Ref. IV-4; also see Section II of this Report), especially to the northeast where one of the most intensely fractured regions of Mars occurs. Here numerous fractures trend northeast–southwest, the same direction along which the three Tharsis shield volcanoes are aligned. Additional highly fractured terrain occurs just south of Tharsis in the Phoenicis Lacus area, and the Coprates canyon ("Grand Canyon of Mars") begins on the eastern flank of the Tharsis ridge.

Because the *Mariner 4, 6,* and *7* photography was largely confined to the densely cratered terrain, the spectacular volcanic constructs of the Amazonis, Tharsis, and Elysium regions were unsuspected. On the basis of *Mariner 6* and *7* pictures, several authors (Refs. IV-5 and IV-6), employing arguments similar to those applied to
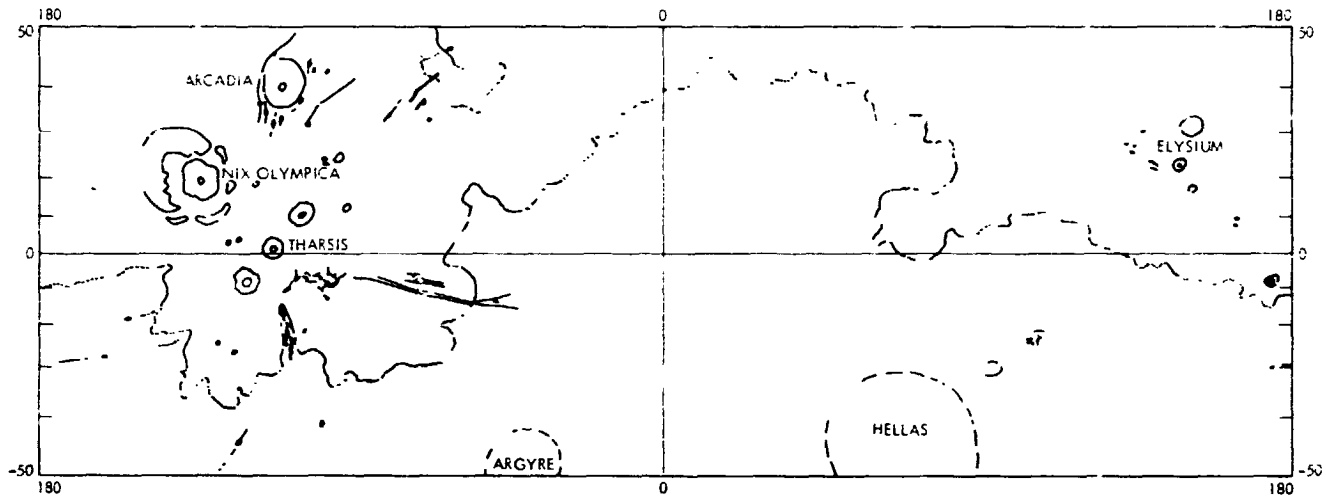
Fig. IV-1. Index map showing the location of the main volcanic features patterned. Most lie in the Tharsis–Arcadia and Elysium regions, but isolated features occur elsewhere. The shaded line marks the boundary between the densely cratered province and the sparsely cratered plains. Major structures are also shown.

the lunar highlands. suggested that volcanic processes had been significant on Mars and were responsible for the formation of many of the craters in the densely cratered terrain. The problem of the origin of the densely cratered terrain is not, however, addressed in this section. The concern here is with the obvious volcanic constructs which lie largely, but not exclusively, outside the cratered terrain. It is assumed that the densely cratered terrain is a very primitive part of the Martian crust. If volcanic features are widely present there, they bear very little genetic relation to the younger, less ambiguous, volcanic features that abound elsewhere.

A. Volcanic Features

1. Shield Volcanoes

The largest volcanic features on Mars are shield volcanoes. The term "shield" is applied to terrestrial volcanoes that are built by successive outpourings of mainly basaltic lavas into broad, gently sloping structures. Mauna Loa in Hawaii is the classic example and the largest active volcanic feature on Earth. It is approximately 200 km across at its base and stands approximately 9 km above the sea floor. The main mode of eruption is relatively quiet effusion of lavas either along fissures on the flanks of the structure or from the summit caldera (Ref. IV-7).

By analogy with terrestrial examples, the term shield has been applied to several features on Mars which appear to be broad volcanic constructs with central calderas.

The most prominent are Nix Olympica (18°N, 134°W), North Spot (11°N, 104°W), South Spot (9°S, 120°W), and Middle Spot (1°N, 113°W), all in the Amazonis–Tharsis region, and an unnamed feature at 24°N, 212°W, in Elysium. The Martian shields are substantially larger than their terrestrial counterparts. The Nix Olympica shield is 600 km across, and there is some evidence that its size has been reduced significantly by erosion. North, South, and Middle Spot are each approximately 400 km across. The heights are still uncertain, but present indications are that the summit of Nix Olympica stands 23 km above the surrounding terrain (Ref. IV-8; also see Section XXXI of this Report), and that the other shields have similar, but slightly smaller, vertical dimensions.

Although they differ in detail, the shields all have the same general characteristics. Each is roughly circular in outline and has a central summit depression. The central pit may be simple or complex. South Spot (Fig. IV-2), Middle Spot, and the Elysium shield all have simple summit craters. Nix Olympica (Fig. IV-3) and North Spot have complex summit calderas in which successive collapse pits have formed about different centers. At the scale of the wide-angle camera, the flanks of the shields have a fine radial pattern that either feathers out into the surrounding terrain or terminates abruptly at a scarp marking the edge of the shield. The radial pattern at the outer edge of the South Spot shield is unusually coarse and results from numerous radially elongate lobes, superimposed on one another, and more rarely from short, sinuous, rille-like radial depressions (Fig. IV-2). Narrow-angle detail of the flanks of Nix Olympica (Fig. IV-4) also

Fig. IV-2. West flank of the shield volcano at Nodus Gordii (9°S, 120°W), informally called South Spot. The smooth-floored central caldera is approximately 140 km across and surrounded by a smooth zone with concentric graben. Beyond the smooth zone, the surface has a marked radial pattern made up largely of numerous mutually intersecting, radially elongate, lobes. The surrounding plains appear to cover part of the shield to the southwest. (MTVS 4182-45, DAS 07038748)

reveals long, radially elongate lobes and a narrow channel-like feature, interpreted as a lava channel or collapsed lava tube, running along the crest of a low radial ridge. On all the shields a much coarser, crudely concentric, pattern is superimposed on the radial pattern. The concentric pattern appears to result from slight breaks in slope which divide the shield flanks into a series of indistinct, rounded, sometimes mutually inte. ting terraces.

The Tharsis shields have, in addition to the subtle slope changes, a well developed concentric fracture pattern. South Spot has a prominent set of graben immediately outside the central crater and several less distinct circular fractures as far out as two crater diameters from the center of the shield. Along parts of some of the fractures are lines of craters.

North Spot and the Elysium shield (Fig. IV-5) both have concentric fractures as far as 300 km from the central crater. Middle Spot has numerous concentric graben

on its flanks (Fig. IV-6) in addition to concentric lines of craters (MTVS 4267-52, DAS 09917609).[2] Some concentric structures occur outside the shield itself, and very prominent concentric cracks occur just to the north. Near the central crater is a different type of circular structure, part scarp, part ridge; its center is farther north than the center of the central crater (Fig. IV-7). The origin of the structure is uncertain. It may have formed by movement along a circular fault or by ring-dike intrusion, or both.

The three Tharsis shields appear to have undergone modification that is in some way related to the major northeast–southwest structure along which the three shields are aligned. The northeast and southwest edges of the Tharsis shields are embayed, and the shields are
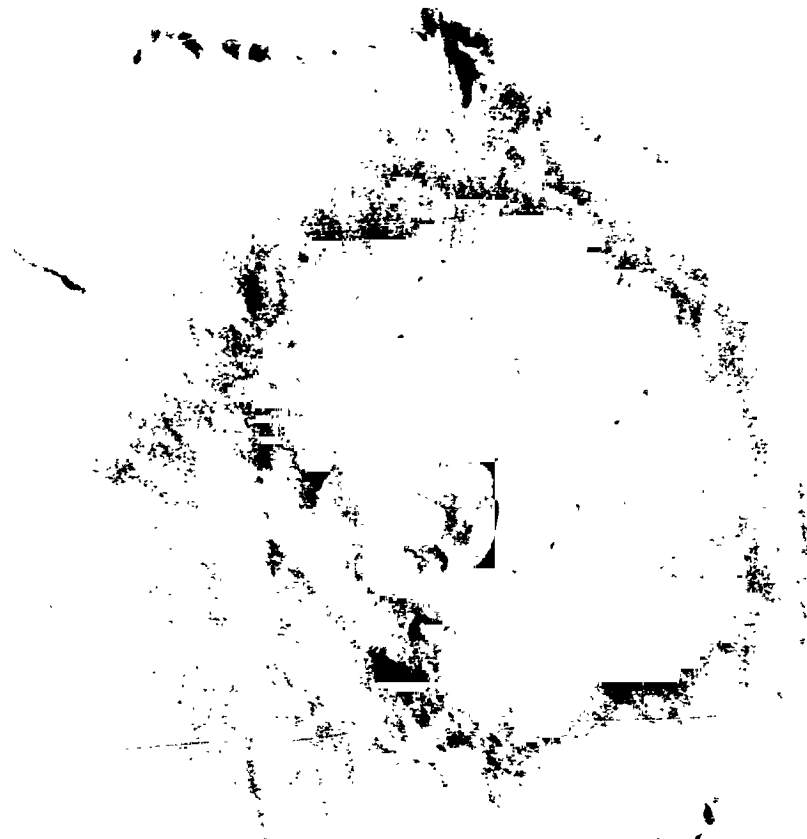
Fig. IV-3. Computer-processed picture of Nix Olympica (18°N, 134°W), the largest of the Martian shield volcanoes. The structure is approximately 600 km across. The summit caldera is 65 km in diameter and stands 23 km across the surrounding plains. The edge of the structure is marked by an escarpment approximately 2 km high. (IPL Roll 1288, 160226)

cut by numerous closely spaced, linear, almost crevasse-like, depressions aligned along the northeast–southwest direction. The embayment in the edge of South Spot almost reaches the central crater. Sparsely cratered terrain surrounds each of the shields, and contacts take various forms. The edge of the Nix Olympica shield is almost everywhere a steep escarpment against which the surrounding plains abut. In contrast, plains materials appear to cover the edges of the three Tharsis shields so that the radial and concentric structures of the shields are truncated as they dip beneath the plains (Fig. IX-6). Scarps occur only to the northeast and southwest of the shields, around the embayments. Here plains materials appear to have encroached at the expense of the shield to form

steep escarpments. The most prominent of the Elysium shields grades imperceptibly into the surrounding plains in such a way that its edge cannot be precisely determined.

Nix Olympica is unique among the Martian shield volcanoes in being surrounded by an aureole of what appears to be highly fractured terrain (Ref. IV-4). This distinctive unit extends from the edge of the shield to as far as 1400 to 1500 km from the shield center. It is not continuous, but complexly embayed by the plains. The terrain is made up of closely spaced, elongate, sub-parallel ridges and troughs such that the tops of the ridges form accordant summits at a somewhat higher elevation than the surrounding plains. The individual
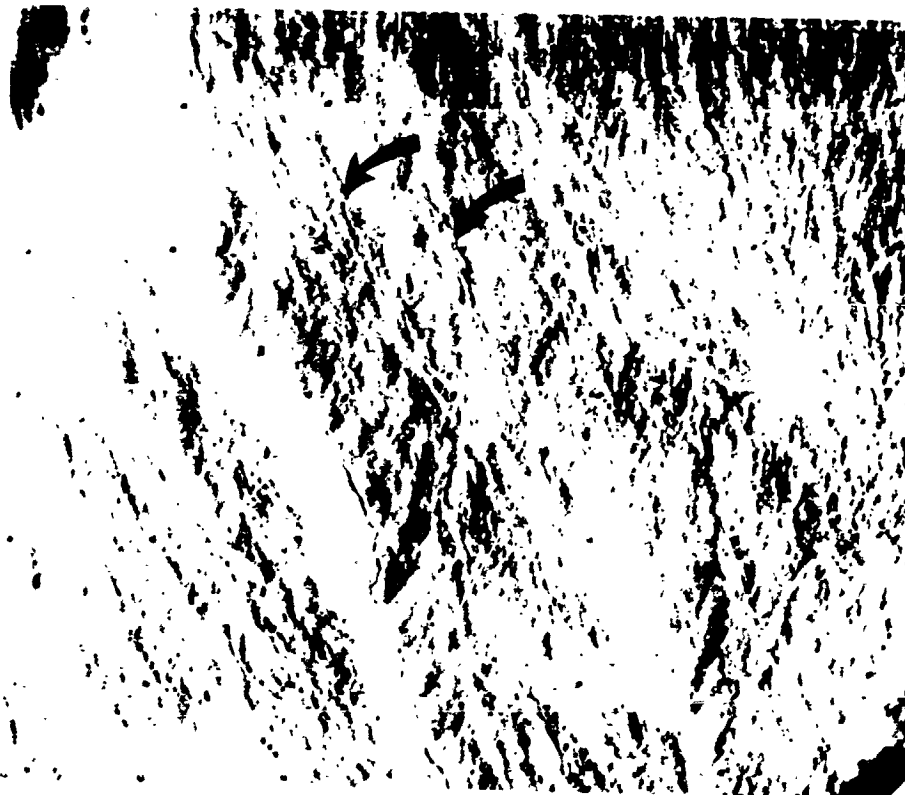
Fig. IV-4. Narrow-angle picture of the northwest flanks of Nix Olympica showing the fine surface detail. The arrows indicate radially elongate lobes. In the west half of the picture, on top of a low ridge, is a 250-m-wide channel, interpreted as a lava channel or collapsed lava tube. (MTVS 4133-96, DAS 05492413)

troughs are for the most part embayed by the plains materials. Movement appears to have occurred along arcuate faults, which, west of Nix Olympica, divide the fractured terrain into a series of blocks that dip gently northeast.

The origin of the aureole is unclear. One possibility is that it is a pediment that formed as the escarpment around Nix Olympica advanced toward the center of the shield. Another possibility is that the aureole is all that remains of one or more ancient shield volcanoes. The pediment hypothesis implies that the Nix Olympica shield was once two to three times its present size and that it has been reduced to its present size by erosion. There are several difficulties with this interpretation. The surface of the Nix Olympica shield appears to be relatively young (Ref. IV-9; also see Section VIII of this Report); a very fine surface texture is preserved on the flanks, and very few impact craters are present. Thus, if the aureole is a pediment, then either it had to form in a relatively short time during which there was little modification to the surface of the shield itself, or renewed eruptions

created a relatively fresh surface on the shield. There is a strong contrast between the structure of the aureole and the structure of the shield. No traces of the large arcuate faults that cut the aureole can be found on the shield. The finer-scale fracturing of the aureole is also absent. The major structures of the aureole are so large that a considerable thickness of younger deposits would be required to achieve their complete burial. The implication is that the aureole is older than much of the upper-most portions of the shield, supporting the hypothesis that it represents the remnants of one or more old shield volcanoes similar to Nix Olympica but long since destroyed.

2. Domes

In the Tharsis region are several volcanic constructs that differ from the shields by being smaller and having steeply sloping sides. Their genetic significance is uncertain. They may be the form that a shield takes with only a small volume of lava. On the other hand, they may
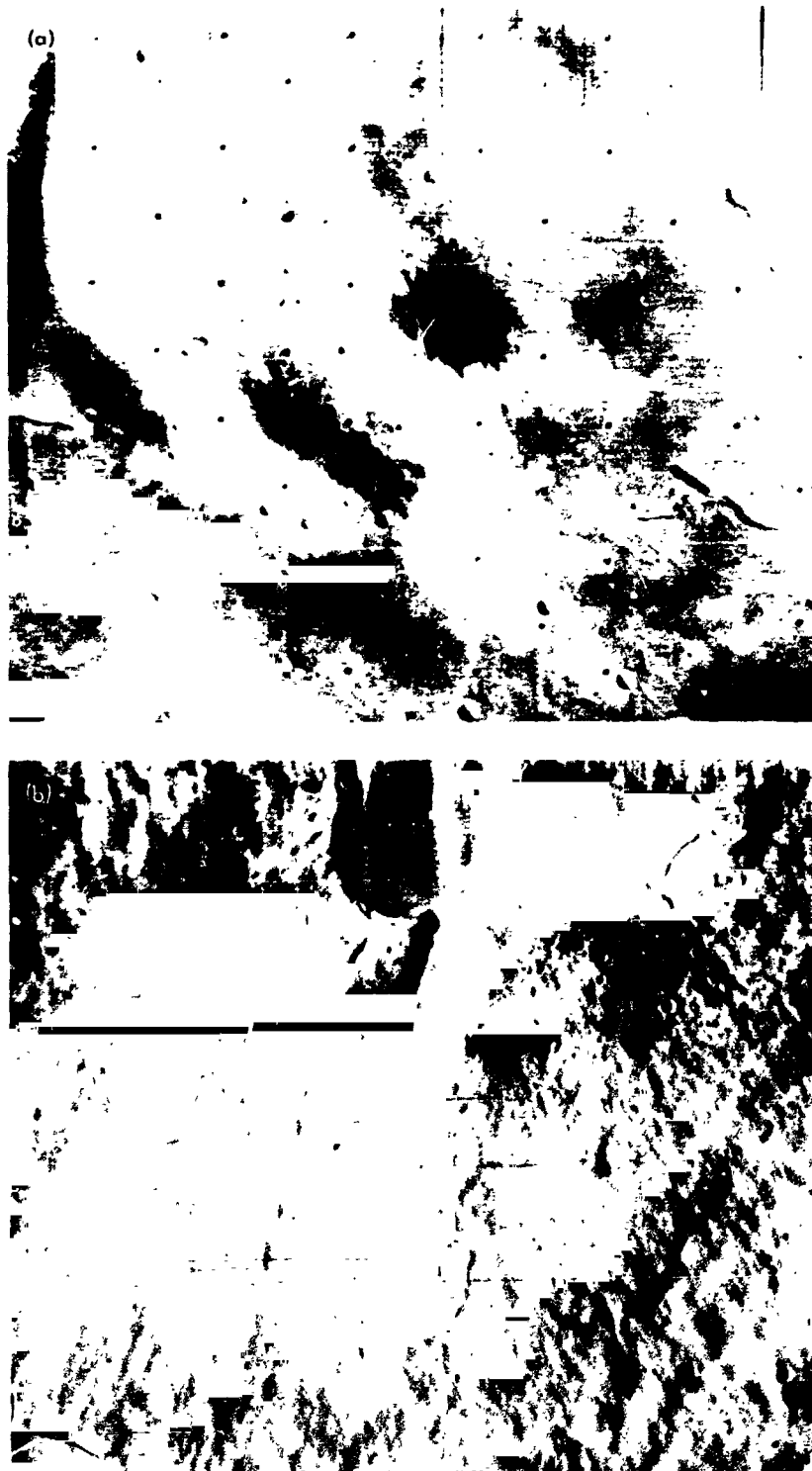
Fig. IV-5. (a) The Elysium shield at 24°N, 212°W. The structure is approximately 200 to 250 km across and markedly symmetrical. Concentric fractures occur as far as 300 km from the central crater. The surrounding plains are more heavily cratered than in the Tharsis region. (MTVS 4298-43, DAS 13496123) (b) Narrow-angle detail showing the central crater and the fine radial structure on the flanks. (MTVS 4298-39, DAS 13496088)

Fig. IV-6. Two-picture mosaic of the shield volcano at Pavonis Lacus (1°N, 113°W), informally named Middle Spot. The entire structure is approximately 400 km across. The central crater is 40 km in diameter and intersects a ring structure to the north. Concentric graben occur both on the flanks of the shield and in the surrounding plains. To the northwest are embayments in the edge of the shield. (MTVS 4184-54, DAS 07111128; MTVS 4184-60, DAS 07111198)
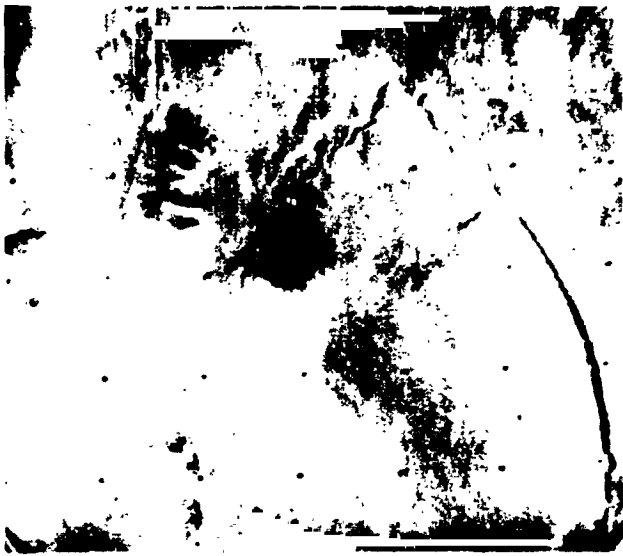
Fig. IV-7. Oblique narrow-angle view of the central pit and ring structure of Middle Spot. The smooth crater-free floor and talus on the walls of the summit pit are clearly visible. Radial ridges similar to lunar mare ridges connect the central pit to the ring. The dark patches formed during the mission and are almost certainly eolian in origin. (MTVS 4267-44, DAS 09917329)

indicate a different lava chemistry. They are sufficiently distinctive morphologically to be separated from shield volcanoes and are here termed "domes." At 13°N latitude, 91° longitude, is a dome approximately 180 km across with a central summit pit 60 km across (MTVS 4189-72, DAS 07255398). The flanks are smooth, convex upward, and form a sharp contact with the surrounding plains (Ref. IV-2). The central pit is complex, consisting of several nested craters, each with steep walls and level, sparsely cratered floors (MTVS 4231-39, DAS 08657889). Some larger, more subdued, circular depressions occur on the flanks on either side of the central pit. Another 150-km-diameter dome at 24°N, 97°W, differs markedly from the one just described (Fig. IV-8). Numerous clo ely spaced, fine channels run from the central pit down the flanks of the dome and disappear under the surrounding plains (MTVS 4271-52, DAS 10061459). A larger channel, 2 km across, begins in the central crater and ends in an irregular depression in the plains just beyond the edge of the dome. Several other more subdued domes also occur in this same north Tharsis region.

A different type of dome occurs in Elysium at 32°N, 209°W. It is approximately 200 km across, has a flat top, but steep sides that terminate abruptly against the surrounding plains (Fig. IV-9). At the resolution of the wide-angle camera, the top of the dome appears rough

in contrast to the smooth appearance of the two domes previously described. The feature lacks a prominent central pit, but there are numerous small craters (< 15 km) on the surface, the largest appears to be a caldera that has undergone several episodes of collapse (Fig. IV-16a). Radiating from the crater are several narrow channels, chains of craters, and numerous fine striae. A narrow sinuous channel occurs at the eastern edge of the dome at its junction with the surrounding plains. The surface features of the dome appear to dip under the surrounding plains, except to the west, where an escarpment cuts into the dome (Fig. IV-10b).

3. Craters

Several craters, morphologically distinct from typical impact craters, occur in the Tharsis and Elysium regions. These craters are presumed to be volcanic. Particularly distinctive because of their scalloped outlines are multiple craters at 40°N, 110°W (Fig. IV-11), 36°N, 93°W (Fig. IV-8a), and 11°N, 185°W. Crater rims, where present, have a smooth surface that terminates against the surrounding terrain with a sharp break in slope, giving the features very distinct circular outlines. These circular outlines contrast markedly with the irregular stellate outlines that characterize the rims of large, fresh impact craters. Other probable volcanic craters to the west of Middle Spot have a simple outline, but they also have smooth, regularly shaped, well demarcated rims.

The craters at 40°N, 110°W, are at the center of a much larger circular structure. The regional northeast–southwest fracture patterns are deflected around the structure, so that the fractures form an almost complete ring approximately 700 km in diameter (Fig. IV-11). At the center of the ring is a complex of several intersecting craters. Faint radial ridges connect the craters to the fracture ring; otherwise, the terrain within the ring is relatively featureless. Outside the ring is a faint radial pattern similar to that at the edges of the large Tharsis shield volcanoes. Narrow-angle television pictures show the radial pattern to result partly from numerous fine channels with well developed tributaries (MTVS 4182-96, DAS 07039903). Several impact craters occur both on and within the fracture ring. In the discussion below, a case will be made for this feature being an old, partly collapsed, shield volcano.

4. Other Central Volcanic Structures

Throughout the cratered province are many craters with morphologies difficult to reconcile with a simple impact origin. Many may have been changed so
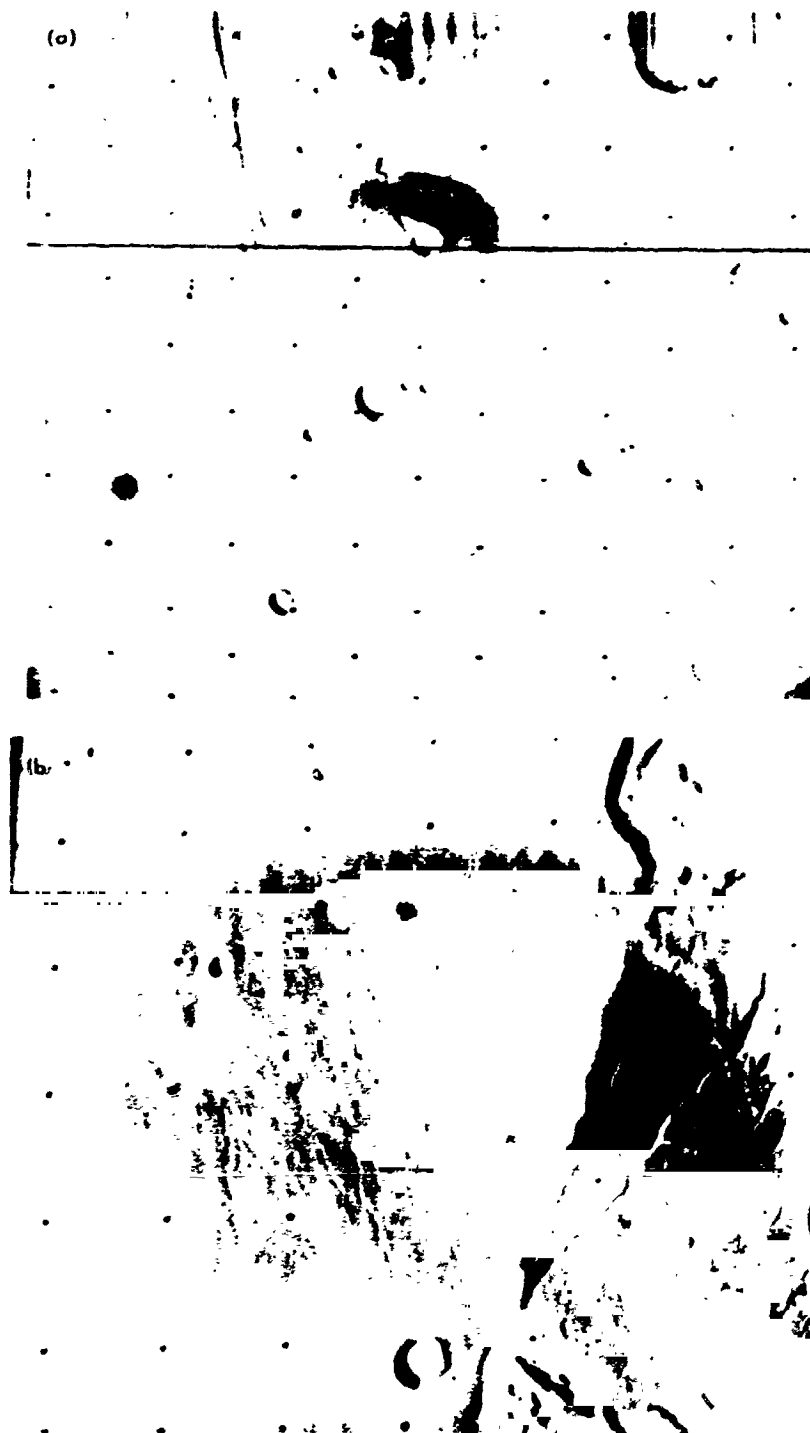
Fig. IV-8. (a) Dome, 150 km in diameter, at 24°N, 97°W. To the northeast corner of the picture is a large volcanic crater with a scalloped outline and smooth, well defined rim. (MTVS 4187-90, DAS 07183788) (b) Narrow-angle picture showing the channels on the flanks of the dome. A 2-km-wide channel begins in the central pit and ends in a shallow depression in the surrounding plains. Numerous other narrower channels extend down the flanks of the dome and are cut off at the base by the surrounding plains. (MTVS 4271-52, DAS 10061459)
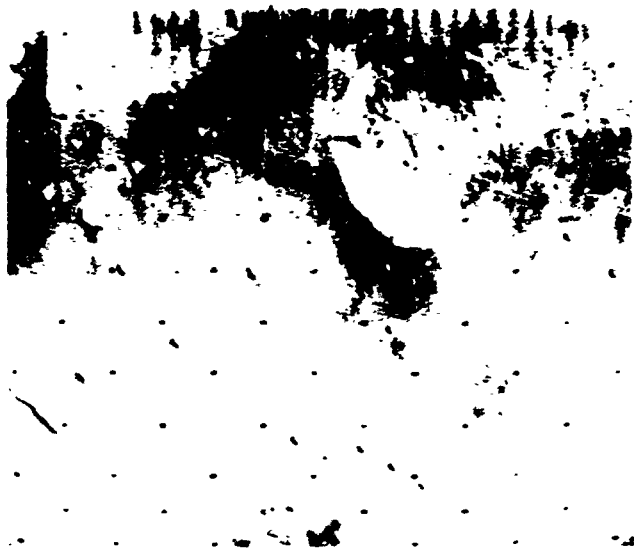
Fig. IV-9. Flat-topped dome at 32°N, 209°W, in Elysium. The structure is approximately 200 km across, has a very sharp outline and no large central summit pit. A channel runs along the northeast edge of the structure. To the west is an embayment around which an escarpment has developed. (MTVS 4242-56, DAS 09054544)

thoroughly by eolian processes that the characteristics of impact have been almost completely obliterated. Others, however, are so unlike typical impact craters that some form of volcanism must be invoked to explain their origin There are widespread areas formed by volcanic plains in the cratered province (see below), so that the presence of volcanic craters in the region is not surprising. Two particularly striking examples are described here.

In the cratered terrain at 23°S, 253°W, is a probable volcanic feature unusual both in its location outside the main volcanic regions, and in its peculiar morphology (Fig. IV-12). The feature lies well within the cratered terrain, but in an area where there appears to be a relatively young, sparsely cratered unit, which resembles the lunar maria. At the center of the structure is a circular depression, approximately 15 km across, connected by a channel to an elliptical depression of similar dimensions, 35 km to the southwest. Around the central depression is a fracture ring approximately 45 km in diameter. Numerous ridges and depressions extend outward from the ring as far as 200 km. A 4-km-wide, flat-floored channel extends to the southwest of the ring; a narrower, more sharply defined channel occurs to the northwest; several oth.. channels may be seen to the west. The eastern part of the structure appears to be buried by material resembling that of the lunar maria.

The structure has been given the informal name of "dandelion" because of its flower-like appearance.

About 350 km southwest of the "dandelion" is another probable volcanic construct (Fig. IV-13). An indistinct depression, 70 km in diameter, occurs in the center of a structure approximately 350 km across. The flanks have a pronounced radial pattern that terminates abruptly against the surrounding plains. Several irregular depressions suggestive of collapse occur in the plains beyond the edge of the central structure. The number of impact craters on the feature suggests that it is much older than the volcanic features of the Tharsis and Elysium regions.

5. Volcanic Plains

While the radially symmetric volcanic structures such as the shields and domes present the most spectacular evidence of volcanism on Mars, the materials that form the sparsely cratered plains may be volumetrically more significant. The plains, which surround the central structures, are relatively featureless at the resolution of the wide-angle camera. Narrow-angle pictures, however, commonly show long, low, lobate scarps (Fig. IV-10b) that strongly resemble features in Mare Imbrium on the Moon. The lunar scarps, which have been widely interpreted as lava flow fronts, are difficult to discern, and relatively few have been documented. In contrast, lobate flow fronts are visible on many, if not most, of the narrow-angle pictures of the plains in the volcanic regions of Mars. Ridges similar to lunar mare ridges are also common, particularly on some of the more heavily cratered plains. By analogy with the lunar maria, then, the plains are probably largely volcanic in origin. Eolian deposits may be present locally, and are particularly likely in those areas where little surface detail is apparent. It is clear, from the different extent to which the plains have been cratered, that they are not everywhere the same age.

In many areas of the densely cratered province, the cratered surface appears to be partly or wholly covered by plains-forming materials. In some places, as around the volcanic feature at 23°S, 253°W, the cratered terrain appears to be completely buried; in other areas, only a subdued impression of the largest craters is apparent. In yet other areas, only the smaller craters are buried. Such effects could result from eolian deposition and this almost certainly has occurred. However, volcanic activity also appears to have been widespread, as indicated by lobate scarps (as at 5°S, 343°W), lunar-nare-like ridges, and irregular depressions, and products of this activity
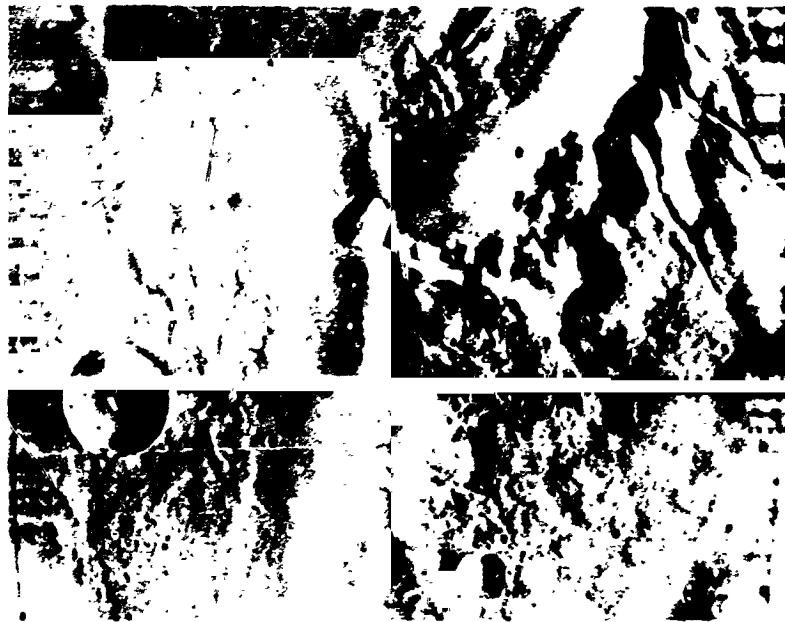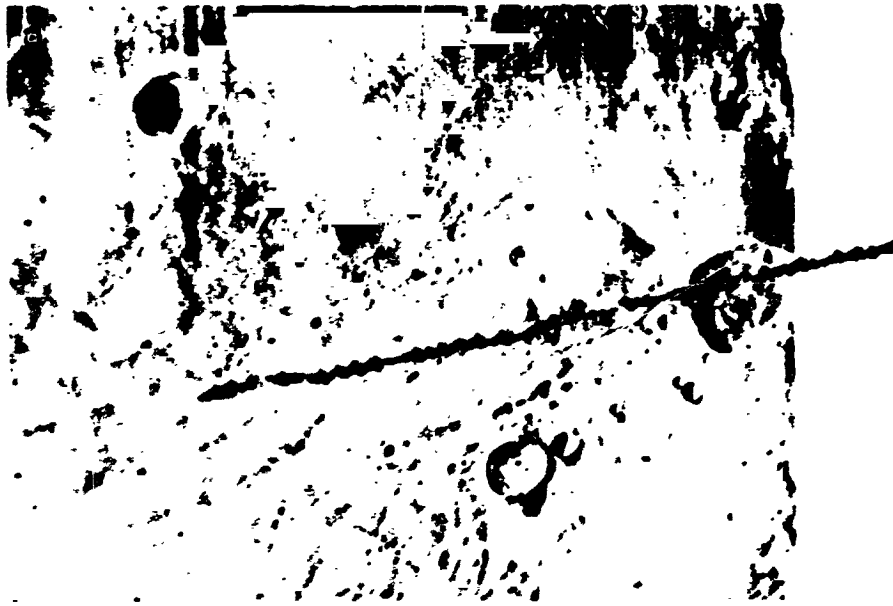
Fig. IV-10. (a) Narrow-angle detail picture of the Elysium dome shown in Fig. IV-9. Lines of craters and fine channels radiate from a 9-km-wide pit that has undergone multiple collapse. The fine channels disappear under the surrounding plains in the extreme southwest corner of the picture. (MTVS 4242-59, DAS 09054379) (b) More narrow-angle detail of the Elysium dome showing the escarpment at the west edge and the radial channels buried by the surrounding plains. Lobate structures on the plains are strongly suggestive of lava flows. (MTVS 4298-51, DAS 13496368)

Fig. IV-11. Arcadia ring at 40°N, 110°W. A northeast–southwest trending set of fractures is deflected around a circular structure to form a fracture ring 600 km across. At the center of the ring just below the dark band are some shallow depressions with scalloped walls. Radial ridges connect the depression and the fracture ring. Outside the fracture ring, the terrain has a radial pattern similar to that on the flanks of the Tharsis shields. The white patch to the northeast is a cloud. (MTVS 4222-69, DAS 08371134)

may cover much of the cratered surface. Thus, although the most spectacular volcanic features occur in the sparsely cratered regions, both volcanic plains and circular constructs are found within the densely cratered province indicating that volcanism has been in effect all over the planet.

B. Discussion

In this discussion, it will be argued that the crust of Mars, in contrast to that of Earth, is stationary with respect to the rest of the planet. There are no apparent Martian equivalents of terrestrial subduction zones and mid-oceanic ridges that accompany crustal plate motions. The volcanic features typically associated with these zones on Earth are similarly absent on Mars. On the other hand, Martian equivalents of intra-plate volcanic features, such as shield volcanoes and flood basalts, do occur, albeit in a somewhat different form because of

the lack of plate movement. It will be further argued that volcanism has been an active proce   nce very early in Mars history.

One of the most striking characteristics of the volcanic features on Mars is their distribution. Mars can be divided into two hemispheres by a plane dipping 50° to the equator such that on one hemisphere are nearly all the volcanic features and sparsely cratered plains, and on the other is nearly all the densely cratered terrain. The division is not exact, as some cratered terrain occurs in the volcanic hemisphere and vice versa; nevertheless, the difference between the two hemispheres is striking. By analogy with Earth, one can invoke a simple convection cell within the mantle of Mars such that upwelling occurs in the volcanic province and downwelling occurs in the cratered province. Some support for this model is derived from the fracture pattern around the Tharsis region. Fractures extend several thousand kilometers out in different directions from Tharsis to

Fig. IV-12. Volcanic complex in Mare Tyrrhenum (23°S, 253°W). Numerous channels and low ridges radiate from a 15-km-diameter central depression surrounded by a fracture ring 45 km across. The eastern part of the structure is partially buried by the adjacent plains materials, which resemble lunar maria. (MTVS 4238-56, DAS 08909224)

form a pattern similar to that which occurs, on a much smaller scale, around terrestrial diapirs such as salt domes. The fractures are what one would expect from a broad domical uplift around Tharsis as might be caused by upwelling of the underlying mantle.

Even if such convection has occurred in the Martian mantle, it does not appear to have caused different parts of the crust to move laterally with respect to one another. It is tempting to look upon the Coprates canyon as a rift zone, away from which the crust has moved, and to interpret the Phoenicis Lacus rift zone as a transform fault. This interpretation does not, however, survive close scrutiny, as the complementary transform fault at the east end of the canyon is missing and there is no evidence of linear subduction zones anywhere on Mars. Terrestrial subduction zones, with their intensely folded arcuate mountain belts, are evident even on very poor satellite pictures, and on Mars any subduction zone should be similarly visible. The almost complete lack of other compressional features or strike-slip structures also argues forcibly for a crust free of lateral movement. This conclusion is strengthened by the types of volcanic features on Mars, their distribution, and their size.

1. Factors Contributing to Incidence of Volcanism

The incidence and type of most terrestrial volcanoes are closely controlled by movement of the crustal plates with respect to one another (see, for example, Refs. IV-10 through IV-12). Most, but not all, volcanism is concentrated along the plate junctions, the type of volcanism depending on the type of junction. Along mid-oceanic ridges, where new crust is being formed, volcanic activity is mainly tholeiitic, accompanied by minor amounts of alkaline and olivine basalt (Ref. IV-13). At subduction zones, where the plates are consumed, volcanism is more varied. In the case of a continental plate over-riding a downgoing oceanic plate, the volcanic belt may be zoned, either with tholeiites near the junction and high-alumina basalts and alkali basalts in succession inland, or with andesites near the junction and more potassic rocks inland (Ref. IV-14). At the junction of two oceanic plates, magmas are mainly andesitic; at continent-to-continent junctions, very little volcanism occurs (Ref. IV-12). Several types of terrestrial volcanic activity are difficult to relate to plate margins and subduction zones, although they may have been affected by plate movement. Conspicuous among these are the
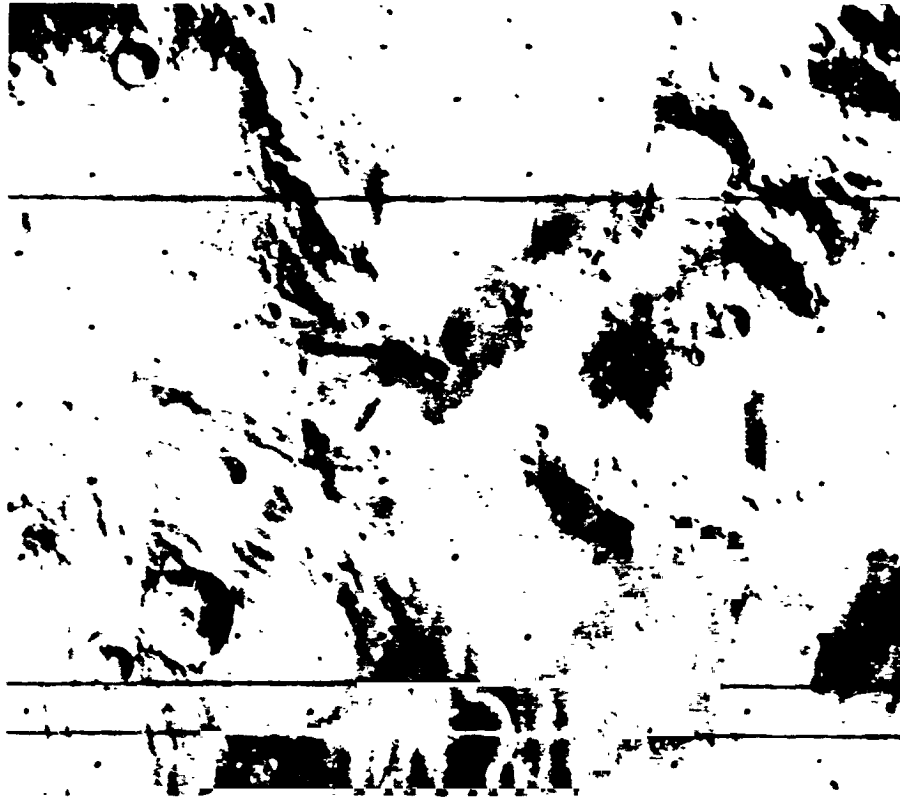
Fig. IV-13. Volcanic dome at 29°S, 264°W, at the northeast edge of the Hellas basin. The central depression, at the western edge of the picture, is indistinct, but a strong radial pattern on the flanks is clearly visible. Superimposed craters suggest a relatively old age. (MTVS 4290-04, DAS 11974069)

volcanics of mid-oceanic islands such as Hawaii, the subaerial flood basalts such as those of the Columbia River plateau (Ref. IV-15) and Greenland, and the confocal volcano-tectonic complexes such as those of the Mogollon plateau (Ref. IV-6).

It is only these last three types of features that appear to have equivalents on Mars. There are certainly many resemblances between Hawaiian and Martian shield volcanoes, and between the Columbia River basalts and the Martian plains. A less convincing case can be made for resemblance between some of the large ring structures on Mars and terrestrial ring complexes. Features resembling stratovolcanoes and breached structures that might be indicative of explosive activity are notable for their absence on Mars. Terrestrially, these types of volcanoes (pyroclastic and explosive) are most common inland of subduction zones in areas of andesitic or alkalic volcanism.

2. Comparison of Nix Olympica With Hawaiian Shield Volcanoes

Comparison of the terrestrial and Martian shield volcanoes will be explored in some detail, as each feature may contribute to the understanding of the other. The Martian shield volcanoes appear to be much larger than their terrestrial counterparts. The large size of the shields on Mars may result from being stationary over a magma source for a long period of time; in contrast, terrestrial shield volcanoes are almost certainly moving with respect to their magma source in the mantle, and become extinct before achieving a comparable size.

The largest and best known terrestrial shield volcanoes occur in Hawaii. Active shields lie at the southeast end of the Hawaiian Emperor chain, a line of extinct volcanoes that stretches several thousand kilometers across the Pacific Ocean (Ref. IV-16). The presently active Hawaiian

volcanoes, Kilauea, Mauna Loa, and Hualalai are at the southeastern end of the Hawaiian Archipelago; the other Hawaiian volcanoes become progressively older to the northwest (Ref. IV-17). Similarly, the submarine volcanoes that make up the Hawaiian Emperor chain become progressively older to the northwest such that Koko Seamount about 500 km from Hawaii, is 46 million years old (Ref. IV-18). Each individual volcano of the chain appears to go through a similar evolutionary cycle, an initially rapid stage of building by the quiet effusion of tholeiitic lavas is followed by a less copious, more pyroclastic stage with eruption of more alkalic basalts, hawaiites, and mugearites. In the final stages, nephelinitic and related rocks may be erupted, after which the volcano becomes inactive (Ref. IV-19)

According to Swanson (Ref. IV-20), the rate of magma supply to Kilauea and Mauna Loa since 1952 averages 0.1 km /yr, which could build the present Mauna Loa structure within 0.3 million years (Ref. IV-7). This figure is consistent with K–Ar dates (Ref. IV-17) and paleomagnetic data (Ref. IV-21). There is, however, some evidence that the eruption is episodic and that the very recent rates may be a maximum for the Hawaiian Emperor chain as a whole (Ref. IV-22). The source of the magma is problematical, but Earthquake tremors as deep as 50 to 60 km directly beneath Kilauea (Ref. IV-23) and exotic xenoliths in some of the lavas (Ref. IV-24) have been interpreted as indicating origin from depths of at least 60 km.

Wilson (Ref. IV-25) suggested that the Hawaiian Islands formed as the crust and the rigid part of the upper mantle moved northwest over a fixed "hot spot" in the mantle. Morgan (Ref. IV-26) extended the concept to include the entire Hawaiian Emperor chain as well as several other chains within the Pacific Basin. He also introduced the concept of "convection plumes" in the lower mantle. According to Morgan, thermal instabilities near the core–mantle boundary caused upward convection of a plume of hot mantle rocks. Where the plume comes in contact with the rigid lithosphere, its constituent materials spread out over a large area to migrate slowly back down to the lower mantle. Shield volcanoes form over the plumes and become extinct as the plate on which the shield sits moves away from the site of the plume. Protracted movement of the Pacific plate over the stationary plume presently under Hawaii has resulted in the Hawaiian Emperor chain.

If we assume that in the Martian mantle, beneath Nix Olympica, a plume exists that is similar to the one pro-

posed beneath the Hawaiian Emperor chain, we can calculate how long it would take to build Nix Olympica. Recent photogrammetric data indicate that the summit of Nix Olympica is 23 km above the surrounding plains, which is in good agreement with the ultraviolet spectrometer value of 25 km. Taking 90 km as the diameter of the summit pit, and 600 km as the diameter of the entire structure, then the volume of Nix Olympica is 2.6 × 10⁵ km . Shaw (Ref IV-22) estimates that, in about the last 45 million years, 8.5 × 10⁵ km of lava have erupted to form the Hawaiian segment of the Hawaiian Emperor chain. This gives a rate of accumulation of about 2 × 10⁻² km /yr over the last 45 million years. If we assume the same rate for Nix Olympica, it would take 130 million years to construct the entire shield. Clearly this number has value only for comparative purposes, as we have no idea what the accumulation rates actually are on Mars. One hundred and thirty million years may be a minimum accumulation age because, for comparison, we have chosen the Hawaiian Emperor chain, which is the most active volcanic feature on Earth. The choice was based partly on analogy and partly on the fact that more is known about Hawaii than any other active volcanic feature. A more valid comparison might be made with some of the less active mid-oceanic islands such as Reunion and the Galapagos but accurate data on eruption rates are not available. It appears likely, however, that Nix Olympica would take a few hundred million years to build at the lower eruption rates that are more typical of mid-oceanic islands.

Almost certainly we are not seeing all of Nix Olympica that once existed. Part has been destroyed by whatever mechanism is called on to form the escarpment around the structure; part must be hidden because of subsidence of the crust under the weight of the huge volcanic pile. Considering these probable hidden and destroyed parts of the shield, it is not inconceivable that Nix Olympica could have been accumulating for as long as a billion years. Furthermore, if the interpretation of the aureole of grooved terrain around Nix Olympica as remnants of ancient shields or extensions of the main structure is correct, then volcanic activity may have been taking place at the site for considerably longer than this. The alternative to this reasoning is a high rate of eruption compared with the most typical terrestrial analogs.

The probable long accumulation time implies that the Martian crust was stationary with respect to the mantle for long periods of time. Astonishing rates of volcanism would be required to build Nix Olympica if Martian crustal plates were moving with respect to the magma

source. Other features of Martian volcanoes reflect this lateral stability. Their radial symmetry and lack of contiguous chains contrast with the Hawaiian shields, which almost certainly form in chains as a result of relative shifts between terrestrial lithosphere and mantle. The apparent lack of Martian volcanic constructs indicative of pyroclastic activity is also worth noting. In the case of the Hawaiian shields, the late pyroclastic, alkalic stage has been attributed to differentiation in a lithospheric magma chamber that has been isolated from the magma source deep in the mantle as a result of plate movement (Ref. IV-25). If a stable Mars crust is assumed, a magma chamber in the lithosphere beneath the volcano could not be cut off from the magma source to fractionate in isolation and produce alkalic differentiates. The late pyroclastic stage, therefore, would not be expected to occur. [It should be noted, however, that Jackson and Wright (Ref. IV-24) do not agree with Wilson that the alkali lavas are differentiates that form as a result of phase movement. They believe that copious eruption of tholeiitic basalts leads to chemical heterogeneities in the mantle. Fractional melting of different variants leads to eruption of alkali lava.]

The conclusion that plate movement does not occur on Mars and that Nix Olympica was stationary over its magma source has important implications for the origin of terrestrial shield volcanoes. Some hypotheses of origin invoke localized convection in the mantle to create the melting zone over which the volcano develops. In these hypotheses, plate motion is incidental and not necessary for the volcano to originate. In other theories, melting is caused by interaction between the moving lithospheric plate and the mantle beneath. Here plate motion is a prerequisite. Shield volcanoes appear to have developed on Mars without the help of plate tectonics, which lends credence to the hypothesis in which plate motion is not required.

The height of Nix Olympica has implications regarding the depth of origin of the magma. Eaton and Murata (Ref. IV-27) suggested that differences in density between the lava in its conduit and the surrounding rocks creates a hydrostatic head. They calculated that, for delivery of magma to the summit of Mauna Loa, a depth of origin of 57 km is required, which is consistent with the Earthquake data. A similar calculation cannot be made for Mars because the densities are so uncertain. If the density differences were, however, the same as for Mauna Loa, then a 130-km depth of origin would be required. Whatever the actual value, a rigid crust substantially thicker than that of Earth is indicated. This

conclusion is consistent with the gravity anomalies that occur in the Tharsis volcanic region (Ref. IV-25).

3. Comparison of Nix Olympica With Other Martian Shield Volcanoes

Nix Olympica has the freshest appearance of all Martian shield volcanoes. Several lines of evidence suggest that the Tharsis volcanoes are older and in various stages of collapse. The surfaces lack the fine texture that occurs on the flanks of Nix Olympica, suggesting an older age for their surfaces. All of the Tharsis shields have arcuate faults on their flanks and in the plains just beyond the edge of the shields. These are lacking at Nix Olympica. The structures are interpreted as faults along which the central part of the structure has subsided. Of the three Tharsis shields, South Spot appears to be in the most advanced stage of collapse, and North Spot appears to be the freshest. The large size of the summit pit of South Spot compared with the other shields suggests that it has been enlarged by collapse along arcuate faults similar to the ones that presently bound the central crater. An older age for South Spot is also indicated by the lack of definition of the central crater in the northwest. Of the three Tharsis shields, South Spot also appears to be in the most advanced state of destruction by erosion. The lobate structures at the outer margin are very coarse, embayment by the plains is extensive, and the embayments to the northeast and southwest are the most well developed. All of these factors, while not proof, are suggestive of an inactive structure, certainly older than Nix Olympica, and probably older than North and Middle Spots.

The large circular structure in Arcadia (Fig. IV-11) may represent a yet more advanced state of collapse of a shield volcano. The structure consists of a fracture ring, 600 km in diameter, in the center of which are the remnants of some caldera-like pits. Outside the fracture ring, the terrain has a radial texture very similar to the Tharsis shields. It is suggested that this is a very old extinct shield, the center of which has collapsed along arcuate fractures. An alternative interpretation of the feature is that it is analogous to terrestrial confocal volcano–tectonic ring complexes (Ref. IV-6).

The oldest central volcanic features occur within the cratered province. The features are too small to have a sufficient number of craters for satisfactory statistics; nevertheless, the superimposed craters do provide some measure of relative age. For the shield volcano to the northeast of Hellas, the number of superimposed craters

up to 40 km in diameter is indistinguishable from the rest of the densely cratered province. At 40 km, the curve for the densely cratered terrain crosses the 3-billion-year isochron (see Ref. IV-9, also see Section VIII of this Report)—indicating a very old age for the feature. A similar shield at 9°S, 155 W, has a crater density intermediate between the Tharsis shields and the Hellas shield.

4. Volcanic Plains

Most of the plains have been divided into three broad units on the basis of the number of superimposed craters; a fourth plains unit, which occurs only in the high northern latitudes, appears to be mantled by younger material (Ref. IV-4; also see Section II of this Report). The crater frequencies on the three non-mantled units are shown in Fig. IV-14. Meaningful counts are not possible for the mantled units because of the overlying materials. The most heavily cratered plains unit has a crater density that approaches that of the densely cratered province. The crater distribution suggests an age of 1 to 2 billion years if the age estimates of Hartmann (Ref. IV-9; see Section VIII of this Report) are correct. The less densely cratered units indicate ages of several hundred million years.

Caution should be exercised in interpreting these ages. Hartmann's isochrons are calculated on the assumption that most of the impacting bodies are asteroidal. He determines the flux history of Earth and the Moon, then makes estimates of the cratering history of Mars by taking into account the distribution of asteroids between Earth and Mars and the different cratering effects on Earth, Moon, and Mars. He estimates his error as a factor of 3, but the error could be much larger than this if the large impact craters on Earth and the Moon are primarily cometary in origin and not asteroidal. A high cometary component would result in older ages for Mars because of the smaller difference in the number of cometary impacts between Earth and Mars as compared with asteroidal impacts. Whatever the actual age, the point to be emphasized is that some of the volcanic plains appear to be old and may well be in the range of 1 to 4 billion years, suggesting an early beginning to Martian volcanism. This is consistent with the long accumulation age suggested for Nix Olympica and the apparently old age of the volcanic feature at the edge of Hellas.
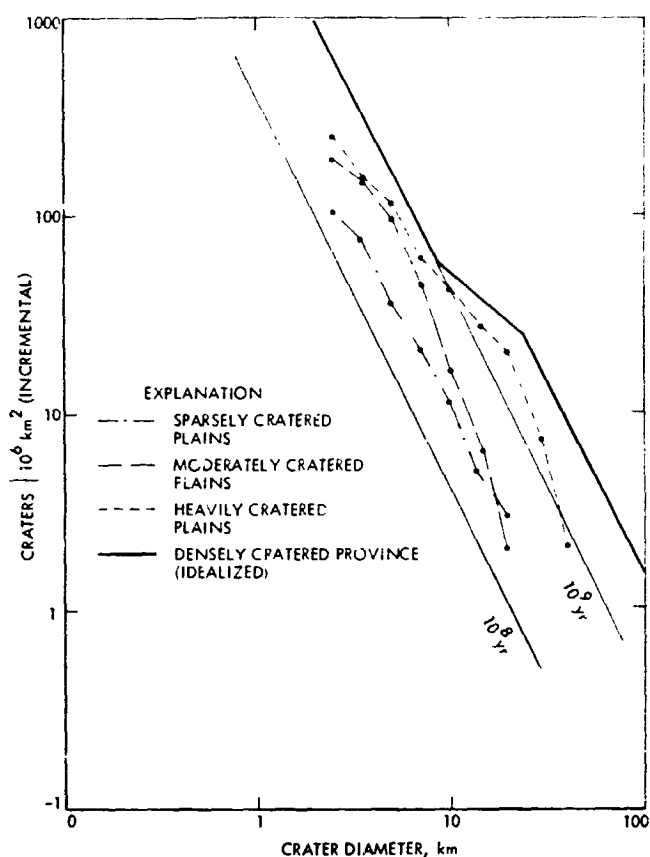
Fig. IV-14. Crater counts on different plains units are compared with the crater frequencies for the densely cratered province. Isochrons showing possible ages are from Hartmann (Ref. IV-9; also see Section VIII of this Report).

References

IV-1. Masursky, H., Batson, R. M., McCauley, J. F., Soderblom, L. A., Wildey, R. L., Carr, M. H., Milton, D. J., Wilhelms, D. E., Smith, B. A., Kirby, T. B., Robinson, J. C., Leovy, C. B., Briggs, G. A., Young, A. T., Duxbury, T. C., Acton, C. H., Jr., Murray, B. C., Cutts, J. A., Sharp, R. P., Smith, S., Leighton, R. B., Sagan, C., Veverka, J., Noland, M., Lederberg, J., Levinthal, E., Pollack, J. B., Moore, J. T., Jr., Hartmann, W. K., Shipley, E. N., de Vaucouleurs, G., and Davies, M. E., "Mariner 9 Television Reconnaissance of Mars and Its Satellites: Preliminary Results," *Science*, Vol. 175, p. 294, 1972.

IV-2. McCauley, J. F., Carr, M. H., Cutts, J. A., Hartmann, W. K., Masursky, H., Milton, D. J., Sharp, R. P., and Wilhelms, D. E., "Preliminary Mariner 9 Report on the Geology of Mars," *Icarus*, Vol. 17, p. 289, 1972.

IV-3. Kliore, A. J., Fjeldbo, G., Seidel, B. L., Sykes, M. J., Woiceshyn, P. M., "S-Band Radio Occultation Measurements of the Atmosphere and Topography of Mars with Mariner 9: Extended Mission Coverage of Polar and Intermediate Latitudes," *J. Geophys. Res.*, Vol. 78, 1973.

IV-4. Carr, M. H., Masursky, H., and Saunders, R. S., "A Generalized Geologic Map of Mars," *J. Geophys. Res.*, Vol. 78, 1973.

IV-5. McGill, C. E., and Wise, D. V., "Regional Variations in Degradation and Density of Martian Craters," *J. Geophys. Res.*, Vol. 77, p. 2433, 1972.

IV-6. Elston, W. E., "Evidence for Lunar Volcano-Tectonic Features," *J. Geophys. Res.*, Vol. 76, p. 5690, 1971.

IV-7. Macdonald, G. A., and Abbott, A. T., *Volcanoes in the Sea: The Geology of Hawaii*, University of Hawaii Press, Honolulu, 1970.

IV-8. Wu, S. S. C., Shafer, F. J., Nakata, G. M., Jordan, R., and Blasius, K. R., "Photogrammetric Evaluation of Mariner 9 Photography," *J. Geophys. Res.*, Vol. 78, 1973.

IV-9. Hartmann, W. K., "Martian Cratering IV: Mariner 9 Initial Analysis of Cratering Chronology," *J. Geophys. Res.*, Vol. 78, 1973.

IV-10. Martin, R. F., and Piwinskii, A. J., "Magmatism and Tectonic Settings," *J. Geophys. Res.*, Vol. 77, p. 4966, 1972.

IV-11. Dickinson, W. R., "Relations of Andesites, Granites and Derivative Sandstones to Arc Trench Tectonics," *Rev. Geophys. Space Phys.*, Vol. 8, p. 813, 1970.

IV-12. Gilluly, J., "Plate Tectonics and Magmatic Evolution," *Geol. Soc. Amer. Bull.*, Vol. 82, p. 2382, 1971.

IV-13. Engel, A. E. J., and Engel, C. E., "Composition of Basalts From the Mid-Atlantic Ridge," *Science*, Vol. 144, p. 1330, 1964.

IV-14. Dickinson, W. R., and Hatherton, T., "Andesitic Volcanism and Seismicity Around the Pacific, *Science*, Vol. 157, p. 801, 1967.

IV-15. Waters, A. C., "Basaltic Magma Types and Their Tectonic Associations—Pacific Northwest of the United States," in "The Crust of the Pacific Basin," *Am. Geophys. Monogr.*, Vol. 6, p. 158, 1962.

References (contd)

IV-16. Jackson, E. D., Silver, E. A., Dalrymple, G. B., "Hawaiian-Emperor Chain and Its Relation to Cenozoic Circumpacific Tectonics," *Geol. Soc. Amer. Bull.*, Vol. 83, p. 601, 1972.

IV-17. McDougall, I., "Potassium-Argon Ages From Lavas of the Hawaiian Islands," *Geol. Soc. Amer. Bull.*, Vol. 75, p. 107, 1964.

IV-18. Claque, D. A., and Dalrymple, G. B., "Age of Koko Seamount Chain, *Earth Planet. Sci. Lett.* (in press).

IV-19. Powers, H. A., "Composition and Origin of Basaltic Magma of the Hawaii Islands," *Geochim. et Cosmochim. Acta*, Vol. 7, p. 77, 1955.

IV-20. Swanson, D. A., "Magma Supply Rate at Kilauea Volcano, 1952–1971," *Science*, Vol. 177, p. 169, 1972.

IV-21. Doell, R. R., and Cox, A., "Paleomagnetism of Hawaiian Lava Flows," *J. Geophys. Res.*, Vol. 70, p. 3377, 1965.

IV-22. Shaw, H. R., "Mantle Convection and Volcanic Periodicity in the Pacific: Evidence from Hawaii," *Geol. Soc. Amer. Bull.* (in press).

IV-23. Eaton, J. P., "Evidence of the Source of Magma in Hawaii From Earthquakes, Volcanic Tremors and Ground Deformation (abs)," *Am. Geophys. Union Trans.*, Vol. 48, p. 254, 1967.

IV-24. Jackson, E. D., and Wright, T. L., "Zenoliths in the Honolulu Volcanic Series, Hawaii" *J. Petrology*, Vol. 11, p. 405, 1970.

IV-25. Wilson, J. T., "A Possible Origin of the Hawaiian Islands," *Canadian J. Phys.*, Vol. 41, p. 863, 1963.

IV-26. Morgan, W. J., "Convection Plumes in the Lower Mantle," *Nature*, Vol. 230, p. 42, 1971.

IV-27. Eaton, J. P., and Murata, K. J., "How Volcanoes Grow," *Science*, Vol. 132, p. 925, 1960.

IV-28. Lorell, J., Born, G., Christensen, E., Esposito, P., Jordan, J., Laing, P., Sjogren, W., Wong, S., Reasenberg, R., and Shapiro, I., "Gravity Field of Mars from Mariner 9 Tracking Data," *Icarus*, Vol. 18, No. 2, 1973.

PRECEDING PAGE BLANK NOT FILMED

V. Mars: Troughed Terrain[1]

Robert P. Sharp

Division of Geological and Planetary Sciences
California Institute of Technology, Pasadena, California 91109

One of the spectacular revelations of the *Mariner 9* pictures was the assemblage of huge troughs in the Tithonius Lacus–Coprates region of equatorial Mars. These features represent a significant phase in the planet's evolution, and their interpretation although necessarily highly speculative is justified by the potential for indicating something of the nature of surficial and internal conditions and processes of Mars.

Although the terms "canyons" (Ref. V-1) and "canyonlands" have been widely used for these features and this terrain, presumably because of a similarity to the deeply dissected high plateaus of western United States, these designations do not appear particularly appropriate. Some of the "canyons" are actually closed depressions (Fig. V-1a), and others, although joined together, do not compose a normally integrated trunk and tributary system, and their floors are not smoothly graded. The term "canyon" also implies a genesis by running water (Ref. V-2). For these reasons, the individual features are herein termed "troughs," and the area they inhabit is called "troughed terrain," terms designed to be purely descriptive without genetic implications. This is a brief and preliminary report on these features, which will undoubtedly be a subject of more detailed future treatment.

A. Salient Facts Concerning Troughed Terrain

1. Geographic Location

Troughed terrain occupies an equatorial belt extending from about 0° to 16°S latitude between longitudes 45° to 90°. This is largely within the classical Martian dark areas of Tithonius Lacus, Coprates, and the westernmost part of Aurorae Sinus. It is now clear that individual dark markings on Mars earlier recognized by Earth-based telescopic observations, as for example Coprates and Agathodaemon, lie within this belt of troughs. Some expression of these features has thus been seen from Earth, but too dimly to perceive their true nature.

2. Dimensions

Individual troughs range up to 200 km wide and several hundred kilometers long. Cumulatively, the troughs compose a belt with a maximum width of 500 km and a length of 2700 km. Simple calculations, assuming conservative average wall slopes of 10°, indicate maximum depths of at least 3 km; photogrammetrical data yield a similar value (Ref. V-3; also see Section XXXXII of this Report); Earth-based radar measurements suggest 4.5 km (Ref. V-4); and ultraviolet spectrometer data have been interpreted as indicating 6 km.

Fig. V-1. (a) Closed trough 350 km long and estimated more than 3 km deep; located 0.2°S latitude, 76.5° longitude. (MTVS 4193-54, DAS 07399108) (b) Blunt-ended trough with small troughs presumably developed from pit chains continuing beyond. Swirl-like markings on floor may indicate dissection of a layered floor deposit; located 4.9°S latitude, 77° longitude. Overlaps south edge of Fig. V-1a. (MTVS 4193-45, DAS 07398758)

3. Planimetric Geometry

The trend of most troughs, as well as the belt they compose, is parallel on a bearing E15°S. In detail, trough walls are highly irregular with projecting points, sharp indentations, arcuate scallops, and large open embayments. Some trough ends are acute, but most are blunt, and a few are almost rectangular (Fig. V-1b). Some troughs are wholly closed depressions (Fig. V-1a), with a vertical closure estimated in excess of 3 km, assuming a conservative wall slope of 10°. The floors of adjoining troughs do not appear to be graded along a continuous profile.

4. Trough Floors

Large parts of trough floors look topographically featureless at a resolution of 1 to 2 km. However, narrow-angle pictures with much greater resolution show that they are mostly a chaotic jumble of angular forms (Figs. V-2b and V-2c), irregularly knobby, or marked by rounded rolls and hummocks (Fig. V-3b). Albedo markings on trough floors are stronger, more numerous, and geometrically more complex than on the adjoining upland. Complex swirl patterns are locally visible (Fig. V-1b). Only a small number of bowl-shaped craters (0.5 to 1 km) are seen on trough floors in addition to a few larger (to 30 km), indistinct circular forms. The possibility that the troughs may be fossil features, albeit young fossils, with respect to the current Martian environment needs to be kept in mind. If this were so, the present irregular topography of the trough floors may not represent the conditions at the time the troughs were formed.

Rising as much as 3 km (Ref. V-3) above the floors of several troughs are narrow, spinelike, intra-trough ridges, with widths up to 20 km and lengths to 300 km (Figs. V-3b and V-4b). In one place, a flat-top tableland, 90 km long and 35 km wide, rises more than 2 km above a trough floor (Fig. V-5a). The topography and markings on its flanks, revealed by narrow-angle pictures, suggest near-horizontal layered materials (Fig. V-5b). The lower slopes, starting at a uniform level, are intimately rilled and slide scarred. Irregular, but conformable, albedo patterns elsewhere on trough floors (Fig. V-1b) may indicate similar deposits. Such deposits and their dissected condition indicate a complex history of trough-floor evolution.

5. Trough Walls

A sharp brink separates trough walls from the upland surface, and below this rim the walls are usually steepest (Figs. V-2b, V-2c, and V-6b). The upper parts of many walls are scarred by U-shaped chutes that descend fully developed from the brink (Figs. V-2b, V-2c, and V-4b). These chutes give way below either to smooth slopes or to an anastomosing complex of sharp ridges separated by broad open swales or gullies, somewhat resembling but not wholly comparable in detail to badland topography (Fig. V-6b). The flanks of intra-trough ridges are similarly sculptured (Fig. V-4b). Some long slopes display all three characteristics: U-shape chutes, smoothness, and anastomosing ridges.

Aside from a greater coherence possibly suggested by the steepness below the rim, layering is not generally seen in materials composing most trough walls. This may be partly a matter of resolution, as faint suggestions of near-horizontal layering are seen in one specially treated picture of an intra-trough ridge (Fig. V-4b). Knobs, spurs, and other irregularities on the walls suggest that other types of inhomogeneity exist within the wall materials. One prominent spur, projecting 75 km outward from the wall, may mark the location of a dike (Fig. V-3a), and the shape and arrangement of some narrow spurs and adjacent re-entrants suggest local structural control, probably fractures.

Impressive among wall features are the numerous large, arc-shaped re-entrants cutting back into the upland with a minimum headwall height of 1.5 to 2 km (Figs. V-2b and V-2c). At their feet are accumulations of jumbled blocky debris. Arc-shaped rotated blocks are also seen on the face of some trough walls.

6. Extra-Marginal Features and Relationships

Although not one of the most heavily cratered parts of Mars, the upland surrounding the troughs has a moderate density of craters up to 50 km in diameter. Some larger craters appear to have served as a site for initiation of some small troughs which are generally geometrically discordant with the prevailing trend. Other discordant troughs, up to 100 km long and an estimated 0.5 to 1 km deep, have also formed within the upland seemingly without crater association.

Aside from two cones, with central craters, adjacent to a trough near 10°S latitude and 55° longitude, features obviously of volcanic origin are not scattered through the belt of troughs. However, the eastern edge of the largest volcanic field on Mars lies but a short distance northwest of the troughed terrain.
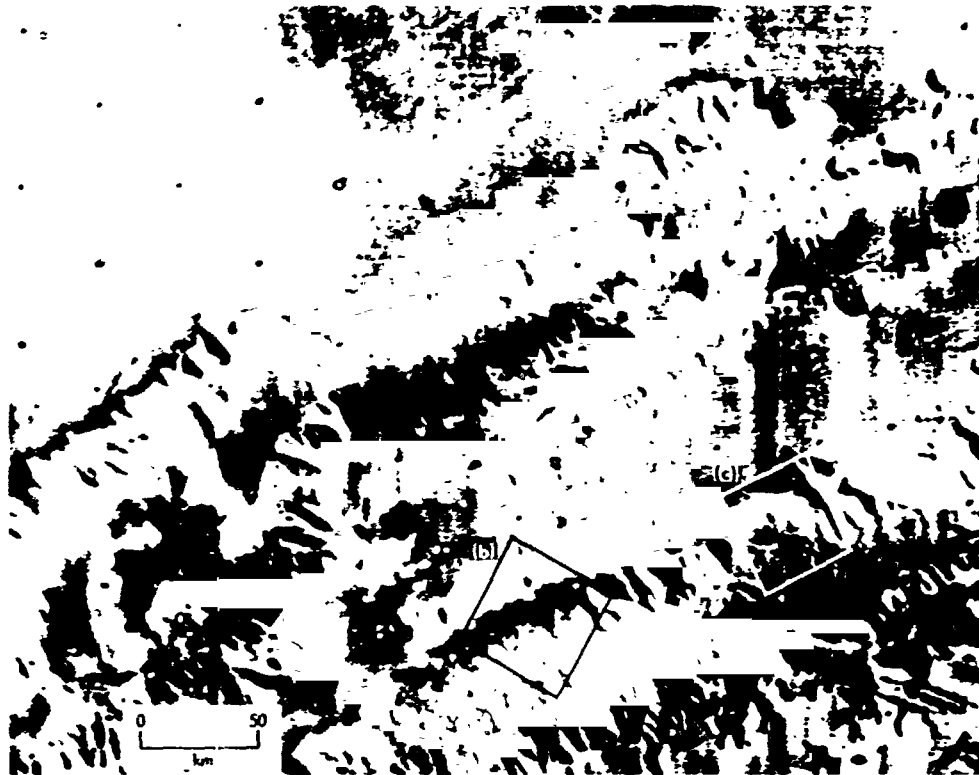
Fig. V-2. (a) Adjacent troughs showing variations in wall sculpture and an intervening parallel pit chain. (MTVS 4191-45, DAS 07326798) (b) Close-up view of part of large slide area on north wall of lower trough. (MTVS 4273-16, DAS 10132999) (c) Another slide mass and scarp on north wall of the same trough. Irregular terrain on floor below is typical landslide topography. Height of scarp is at least 1.5 to 2.3 km (MTVS 4275-24, DAS 10204679)
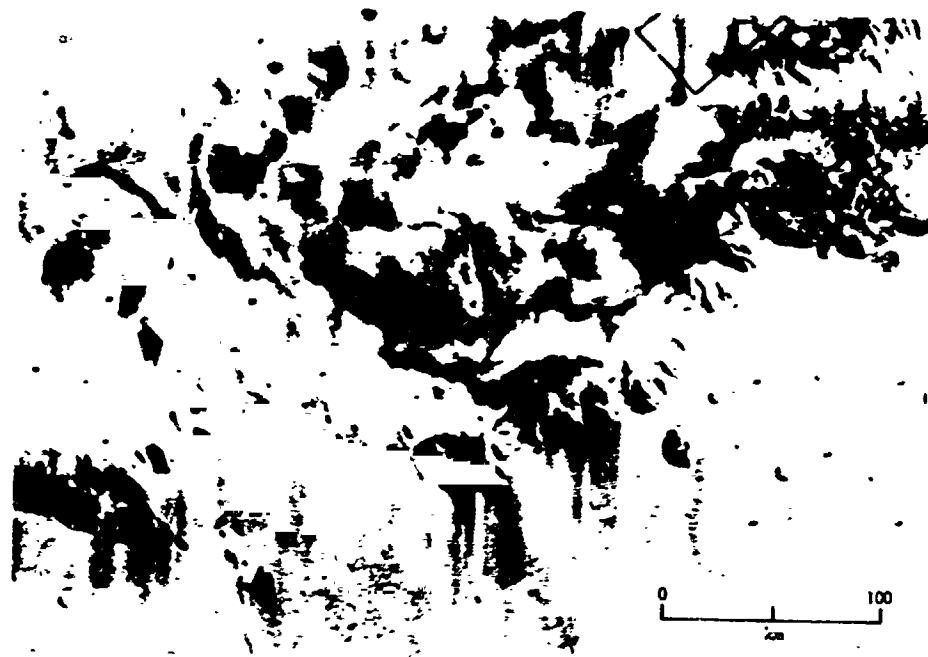
Fig. V-3. (a) Projecting spur (arrow marked) may represent a resistant dike left in relief by wall recession. Continuation on upland indicated by low ridge. (MTVS 4195-33, DAS 07470578) (b) Details of floor morphology of above trough within area marked near upper right. Rough terrain at lower left is part of intra-trough ridge. Unusual number of small, bowl-shaped craters suggests some antiquity, and sinuous, linear, rounded ridges are suggestive of mass movement. (MTVS 4295-36, DAS 12865578)

Fig. V-4. (a) Segment of a trough, at 7.75°S latitude, 84.3° longitude, showing parallel
pit chain (upper edge), intra-trough ridge (middle right), and dendritic tributaries (lower
half). (MTVS 4144-87, DAS 0585,968) (b) Specially processed narrow-angle view of intra-
trough ridge showing irregular slide topography at top, anastomosing pattern of sharp
ridges on far flank, remnant of cratered upland surface and curving fault graben on top,
and U-shaped avalanche chutes below rim on near (south) side. (MTVS 4191-42, DAS
07326762)
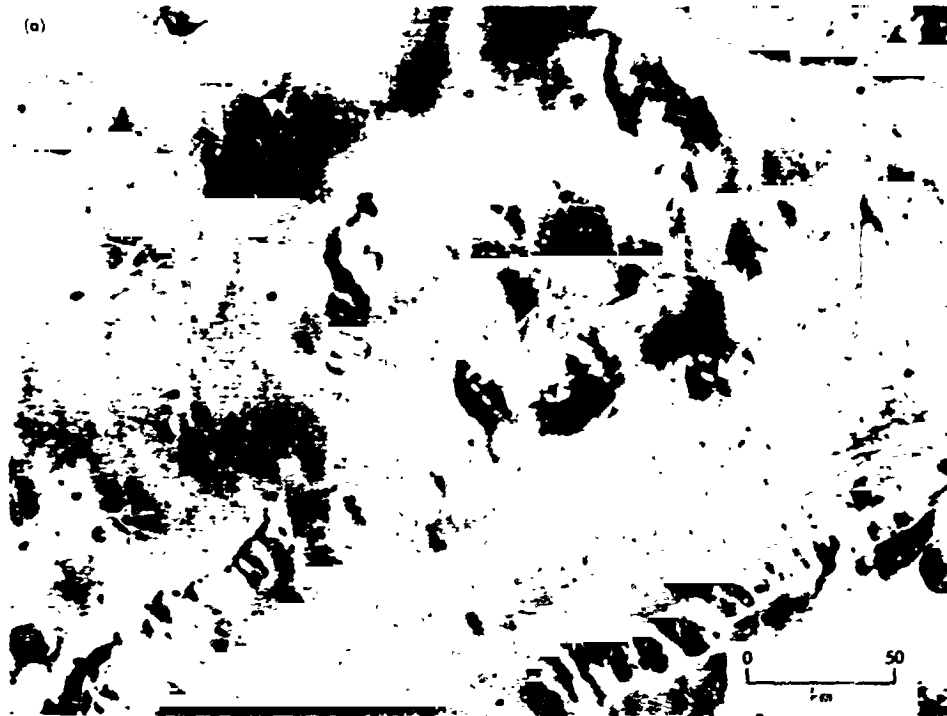
Fig. V-5. (a) Trough with swirl pattern on floor, located 6.2°S latitude, 49.5° longitude. (MTVS 4199-45, DAS 07614498) (b) Close up view showing that swirl pattern is a dissected tableland of layered deposits. Rill-like dissection of lower slopes starts at a specific layer and strongly resembles erosion by fluid seepage. Height of tableland may be 2 km. (MTVS 4241-59, DAS 09017619)
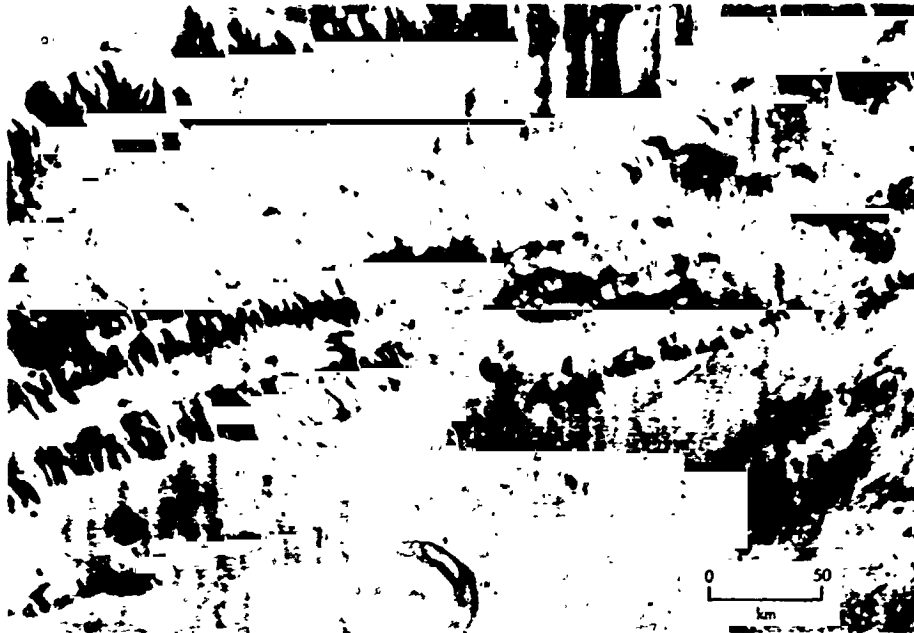
Fig. V-6. (a) Large trough with smaller parallel troughs and prominant pit chain, located 14.8°S latitude, 62.7° longitude. (MTVS 4197-33, DAS 07542468); (b) Close-up view of far (north) wall of above trough showing badland-like pattern of anastomosing ridges of a type possibly produced by dry mass movements, but more commonly attributed, on Earth, to fluvial erosion. (MTVS 4197-36, DAS 07542503)

On the upland in the vicinity of troughs, linear chains of pits (Figs. V-4a and V-6a) parallel the troughs or extend beyond their blunt ends (Fig. V-4b). The pits are of circular to irregular outline, smooth-walled, narrow-bottomed, and seemingly rimless. Individual pits, 1 to 15 km across, are estimated to be up to 0.5 km deep, and pit chains attain lengths up to 350 km. As the pits grow, they develop elongation and become integrated along the chain, eventually producing a small trough with strongly scalloped walls (Fig. V-6a). Pit chains are not unique to the troughed area; excellent examples are abundantly seen in the volcanic area to the northwest.

A complex of shallow graben 1 to 5 km wide and up to 100 km long, locally accompanied by low horsts of similar dimension, traverse the upland adjacent to some troughs. In places, these features parallel the troughs, but elsewhere they are discordantly truncated by trough walls. At least some of the graben are old enough to be cut by craters up to 10 km in diameter. Curiously, within the troughed area, fractures bounding graben and horsts have not developed pits, and this is true elsewhere on Mars as at 35 N, 105 W.

In the sector between 77 and 57° W, principally but not exclusively on the south side of a trough, are a number of steep-walled, angular, dendritic tributaries extending up to 150 km back from the rim (Fig. V-4a). These tributaries decrease in size headward from a maximum width of 10 km and a depth of perhaps 1 km at the trough edge. The trunk tributaries and their secondary and tertiary branches display a strong angular pattern, presumably reflecting control by fractures, essentially none of which is parallel to the trend of the troughs. Small-scale pitting is seen at the heads of some tributaries.

The troughed terrain passes westward directly into a festoon-like complex of linear, U-shaped hollows and, by transition, eastward into the principal area of chaotic terrain and into large areas of smooth lowlands bounded by abrupt cliffs, known as fretted terrain (Ref. V-5; also see Section VI of this Report).

B. Inferences

The parallelism of individual troughs and their walls, of associated pit chains, and of horsts and graben, all bearing about E15°S, implies strong control by structures in the Martian crust, presumably fractures.

Widening and extension of troughs by some mechanism of wall recession, rather than solely by pulling apart, is strongly suggested by blunt trough ends. Acute ends would be anticipated if the troughs had formed only by spreading unless transform faulting has occurred, for which there is no independent evidence. Spurs projecting as much as 75 km inward from trough walls also indicate extensive wall recession.

The scalloped and embayed configuration of the trough rim, its sharpness, U-shaped chutes, arc-shaped blocks on trough walls, and local piles of jumbled debris on trough floors below deep wall embayments indicate that mass movements in the form of slides, slumps, and probably debris avalanches have been a major agent of wall sculpturing and presumably of wall recession. The dendritic tributaries extending up to 150 km into the upland imply the action of a sapping process working headward along different sets of fractures. This same sapping process may be a principal cause of mass movements on trough walls and, therefore, of wall recession.

Chains of unrimmed pits appear to develop by collapse along fractures owing to removal of underlying support. Continuing collapse causes growth, and once the pits attain a moderate size and depth the sapping process may become effective, causing them to enlarge more irregularly and to merge longitudinally to create a small trough with strongly scalloped walls.

The occurrence of 2-km thick accumulation of layered materials on a trough floor (Fig. V-5b) suggests that other troughs may be partly filled with similar material. The layering is much too strong for this to be simply a slumped wall block. The agent of dissection of the deposits is not known, but the potential for dissection could be created by subsidence of a nearby floor segment or the integration of two trough floors lying at different levels.

The small number of craters on trough floors implies either a youthful age or an activity that destroys craters. The troughs cannot be very old or they would show greater signs of modification. They appear to be among the younger features of the Martian surface, even though they may be fossil or relict with respect to the present surface environment.

C. Genesis of Troughs

The following is a speculative scenario as to how the troughs may have been initiated and how they subsequently grew to their present form and size.

The initial event appears to have been the formation of parallel fractures trending about E15 S. Two types of fractures or two sets of different age seem to have formed. One set, seemingly older and possibly shallow, experienced movements creating shallow graben and low horsts. The second set, possibly of greater depth, experienced removal of underlying support which created chains of pits by collapse. Downward movement of debris could have been facilitated by a highly fragmented condition resulting from antecedent impacting. The pits grew larger, partly by further collapse, possibly aided by wall recession through sapping, until they merged longitudinally along the fracture to create a small trough with highly scalloped walls (Figs. V-1b and V-6a). Continued subsidence, sapping, and wall recession by mass movements widened these troughs until they merged laterally creating still larger troughs. The evidence for such lateral mergers is provided by spinelike intra-trough ridges which represent remnants of the septa originally separating adjacent troughs. The troughs also grew longitudinally by wall recession, and blunt trough ends were thereby created.

The sapping process postulated to cause wall recession and to create the dendritic tributaries may have occurred through the deterioration of exposed ground ice either by evaporation or melting. Evaporation is more likely, under present environmental conditions, but melting could have taken place under radically different conditions, if such existed, sometime in the past. Thus, the process if current is best described as ground-ice sapping, but if older it may have involved ground-water sapping (Ref. V-6; also see Section III of this Report).

U-shaped chutes high on trough walls look like features created on steep terrestrial slopes by dry debris avalanches. The fact that the chutes start fully developed at trough rims supports an origin through some mass-movement process rather than fluvial erosion. The anastomosing pattern of ridges on wall slopes and on the flanks of intra-trough ridges might also be the product of dry mass movements because similar patterns, of much smaller scale to be sure, are created on steep slopes on Earth underlain by fine-grained unconsolidated materials, such as dune sand or loose soil, by removal of material through dry flowage. However, the resemblance of these anastomosing ridges to fluvially dissected terrestrial bad-land features suggests that running water also merits consideration as a possible genetic agent. If that is their origin, then they are fossil forms.

Trough enlargement by wall recession has consumed large areas of the old cratered upland and may have continued for tens of millions to hundreds of millions of years. The freshness of some of the large slide scars on trough walls and of the piles of jumbled debris at their feet (Fig. V-2c) suggests an activity continuing essentially to the present.

Wall recession must have dumped huge quantities of rock debris on the trough floors. What has been the disposition of this material? The answer is constrained by the large volume involved and by a vertical closure exceeding 3 km in at least one trough. Methods of moving the missing material up, down, or laterally need to be considered.

The geometrical configuration of troughs and the lack of visible ejecta around their margins speak strongly against explosion as the disposal agent. Eolian deflation, the other obvious means of moving material up and out, is so constrained by the huge size and geometry of the troughs and by the need to reduce all materials to a fine grain size, including lag concentrates armoring the surface, that deflation has probably played but a minor role at best. Furthermore, products of eolian activity such as dunes or characteristic wind-scoured forms are not seen on trough floors.

Surface transport by some flowing medium, for example water, cannot create closed troughs of the type shown in Fig. V-1a and could have occurred only eastward from the belt of integrated troughs into an area of chaotic and fretted terrain. Burial of chaotic terrain by debris from the troughs would then be expected, unless the chaotic terrain is younger. In that case, water probably would not have been able to flow eastward because that area, not having yet collapsed to form chaotic terrain, would be higher than the trough floors. Some other route, which is not apparent, would thus have to be found. For these reasons, it seems unlikely that water has had a major hand in carrying any significant amount of debris away from the area of troughed terrain. However running water derived from melting ground ice, under climatic conditions vastly different from those now prevailing, might have played a role in removing material from the dendritic tributaries (Fig. V-4a), carving the badland topography of bounding slopes (Figs. V-4a and V-6b), and redistributing materials on the trough floors.

The most satisfactory disposition of the material missing from the troughs appears to be downward, by subsidence caused through removal of underlying sup-

port The dissolution of rock materials is not an attractive possibility because of the probable lack of easily soluble substances and the need for a solvent The melting of segregated ground ice is more attractive, but suffers from quantitative qualifications The planimetrically measured area of troughed terrain is $6 \cdot 10$ km². If a mean trough depth of 3 km is assumed, the troughs represent a volume of $1.8 \cdot 10$ km. If the troughs were formed solely by subsidence caused by melting of segregated ground ice, some $1.6 \cdot 10$ km of water would have resulted If all of Mars had a subsurface ice layer of a thickness equal to that required to form the troughs, it would represent $5.9 \cdot 10$ km of water Bubey (Ref. V-7) estimates that the total supply of water on Earth, in all forms, is $1.67 \cdot 10$ km, which is roughly 3.8 times that calculated above for Martian ground ice alone. As Earth is volumetrically 7 times larger than Mars, the above figure would require that Mars has experienced a several times greater proportionate degassing than Earth, which is difficult to believe. Abnormal developments of ground ice peripheral to the Nix Olympica volcanic field, a greater volatile content in Martian than in terrestrial materials (Ref. V-8), or the possibility that the Martian ice is not water substance might afford ways of getting around this argument. Other arguments against ground-ice deterioration as the principal mechanism of trough development are based on the need to develop segregated bodies of ice and the great depth of freezing required, as summarized earlier (Ref. V-5)

Proximity of troughed terrain to the largest volcanic field on Mars suggests the possibility of magma withdrawal as a cause of subsidence. Volumetric relationships are favorable, for a single volcano such as Nix Olympica,

if it is 23 km high as now thought, represents a greater volume of material than is missing from the troughs. Why the magma should move hundreds of kilometers laterally before being extruded is a more troubling question.

Another quantitatively adequate mechanism for creating the troughs would be lateral spreading of crustal plates. The character and configuration of the troughs cannot be explained satisfactorily by spreading alone, but in combination with wall recession through some sapping process, an acceptable picture emerges. The spreading mechanism would provide an ever deepening and widening sump into which materials from the receding walls could be dumped by mass-movement processes. Unless subduction zones exist on Mars, and signs of them have not yet been recognized, the lateral spreading hypothesis carries an interesting implication of planetary expansion

Spreading is an exciting hypothesis and has major implications concerning the internal constitution and behavior of Mars. However, Carr (Ref. V-9; also see Section IV of this Report) argues against plate tectonics on Mars from volcanic relationships, and spreading is not a particularly satisfying explanation for the festoons of hollows west of the troughed terrain or of the chaotic and fretted terrains to the east and north. Nonetheless, in our present state of ignorance concerning Mars, it is wise to keep all reasonable options open, and ground-ice deterioration by evaporation or melting, magma withdrawal, and lateral spreading all appear capable of having played some role in creating the troughed terrain and its accompanying features.

References

V-1. McCauley, J. F., Carr, M. H., Cutts, J. A., Hartmann, W. K., Masursky, H., Milton, D. J., Sharp, R. P., and Wilhelms, D. E., "Preliminary Mariner 9 Report on the Geology of Mars," *Icarus*, Vol. 17, p. 289, 1972.

V-2. Howell, J. V. (ed), *Glossary of Geology and Related Earth Sciences*, Amer. Geol. Inst., 1957.

V-3. Blasius, K. B., "A Study of Martian Topography by Analytical Photogrammetry," *J. Geophys. Res.*, Vol. 78, 1973.

V-4. Pettengill, G. H., Rogers, A. E. E., and Shapiro, I. I., "Martian Craters and a Scarp as Seen by Radar," *Science*, Vol. 174, p. 1321, 1971.

V-5. Sharp, R. P., "Mars: Fretted and Chaotic Terrains," *J. Geophys Res.*, Vol. 78, 1973.

V-6. Milton, D. J., "Water and Processes of Degradation in the Martian Landscape," *J. Geophys. Res.*, Vol. 73, 1973.

V-7. Rubey, W. W., "Geologic History of Sea Water," *Geol. Soc. Amer. Bull.*, Vol. 62, p. 1111, 1951.

V-8. Fanale, F. P., "History of Martian Volatiles: Implications for Organic Synthesis," *Icarus*, Vol. 15, p. 279, 1971.

V-9. Carr, M. H., "Volcanism on Mars," *J. Geophys. Res.*, Vol. 78, 1973.

Acknowledgments

VI. Mars: Fretted and Chaotic Terrains[1]

Robert P. Sharp

Division of Geological and Planetary Sciences
California Institute of Technology, Pasadena, California 91109

Fretted terrain is but one of a variety of lowland terrains on the Martian surface which, like members of an isomorphous series, have some characteristics in common and are shaped by some of the same genetic processes. They are artificially separated to facilitate handling (Table VI-1). At one extremity are the south polar pits described elsewhere (Ref. VI-1; also see Section XVI of this Report); at the other are the huge equatorial troughs.

Fretted terrain is characterized by smooth, flat, lowland areas separated from a cratered upland by abrupt escarpments of complex planimetric configuration and a maximum estimated height approaching 1 to 2 km (Fig. VI-1). It is the product of some unusual erosive or abstractive process that has created steep escarpments and caused them to recede into a complex planimetric configuration leaving behind a smooth, flat lowland surface. Although a relatively late development on the Martian surface, fretted terrain has formed over a significant span of time, and in places it may be older than some phases of the extensive northern hemisphere volcanism (Ref. VI-2; also see Section IV of this Report).

Chaotic terrain differs from fretted terrain, with which it is geographically associated, in having a rough floor

topography featuring a haphazard jumble of large angular blocks, and by arc-shaped slump blocks on its bounding escarpments, often with arc-shaped fractures extending into the adjoining upland (Fig. VI-2). Chaotic terrain was initially recognized and described from features incompletely shown on *Mariner 6* frames (Ref. VI-3). Its existence has now been confirmed by *Mariner 9* pictures, and the characteristics, location, and areal extent of chaotic terrain have been more accurately and completely defined.

Like fretted terrain, chaotic terrain occupies lowland settings within an older, cratered upland surface. It has clearly developed at the expense of this cratered upland, and its relatively youthful age is further demonstrated by a paucity of recognizable craters.

This is a preliminary report on the nature and possible genesis of these two terrain types. More will undoubtedly be written about them as the *Mariner 9* pictures and data are more thoroughly analyzed.

A. Geographic Relationships

Fretted terrain is recognized principally in five separate areas within the northern hemisphere, with only a minor extension south of the equator. Other areas of fretted

terrain may exist, but they are obscured or modified beyond certain recognition. The largest area and most typical development is along and for 5° and 10° on either side of 40° N latitude between longitudes 280° and 350°. This region of fretted terrain debouches northward into an extensive lowland plain which occultation measurements show to be one of the topographically lowest parts of the northern hemisphere (Ref. VI-4; also see Section XXXVI of this Report). The fretted terrain so far recognized covers a total of about 4.75 × 10⁶ km², or 3% of the Martian surface.

Chaotic terrain is geographically associated on the west with the huge equatorial troughs and on the east and north with fretted terrain. It is, perhaps, genetically related to both, but in setting and characteristics it is more closely allied to fretted terrain into which it grades in many places (Fig. VI-3). Chaotic terrain is concentrated principally into an equatorial region from about 3°N to 12°S between longitudes 15° and 40° where it is the dominant feature. Small patches of chaotic terrain are more widely scattered, ranging as far west as 75° longitude and north to 15° latitude. Some of these are associated with areas of fretted terrain, but others are isolated and look as though they might have developed upon the sites of relatively large craters. The total area of chaotic terrain is about 5.5 × 10⁵ km². This is about one-third the area estimated in 1969 from *Mariner 6* pictures. It is now clear that areas of indistinctly recorded troughed and fretted terrains were included in the 1969 value. Chaotic terrain makes up only about 0.4% of the total Martian surface.

B. Description of Fretted Terrain

1. Planimetric Configuration

A striking characteristic of fretted terrain is its irregular planimetric pattern (Figs. VI-1 and VI-4). The steep escarpment separating lowlands from uplands typically traces a ragged course with deep embayments, projecting headlands, and smaller arc-shaped indentations. Only where strongly controlled by older structures, such as linear fractures or crater scars, are the escarpments broadly linear and curvilinear. Even there, association with other forms yields a complex pattern.

Especially noteworthy are the steep-walled, flat-floored chasms or channels, some linear and some irregularly winding (Fig. VI-1), which deeply penetrate the surrounding upland and debouch in tributary fashion into areas of smooth lowland. The larger and principal channels increase in width northward, but terminate at the edge of the fretted terrain region where it borders on the area of lowland plain to the north. Also characteristic are numerous island-like outliers, resembling the mesas, buttes, and towers of Monument Valley, rising above the

Table VI-1. Some types of Martian lowland terrains

Terrain type	Description	Type area
Pitted terrain	Abundant, flat, smooth-floored, steep-walled pits, tens of kilometers across, an estimated 100 to 400 m deep, developed in sedimentary blankets	South polar region
Etched terrain	Exhumed, rough-floored, lowland areas of highly irregular planimetric outline produced by integration of pits developed in sedimentary blankets	South polar region at 65° to 70°S
Fretted terrain	Smooth-floored lowland bounded by abrupt escarpments of uniform height and highly irregular planimetric configuration, tributary flat-floored chasms, developed into an old cratered surface 1 to 2 km higher	40°N between 280° and 350°
Hollowed terrain	A complex of elongate U-shaped hollows, an estimated 2 to 3 km deep, strongly controlled by intersecting sets of linear fractures	5° to 10°S between 90° and 110°
Chaotic terrain	Jumbled chaos of slump and collapse blocks in lowland depressions bounded by steep walls with arcuate fractures	3° to 12°S between 15° to 35°
Troughed terrain	Huge, steep-walled troughs, up to several hundred kilometers long and possibly 5 km deep, integrated into a belt 2700 km long by 500 km wide, wall-side slumps, intra-trough ridges, orthogonal and dendritic wall scars	0° to 16°S between 45° and 90°
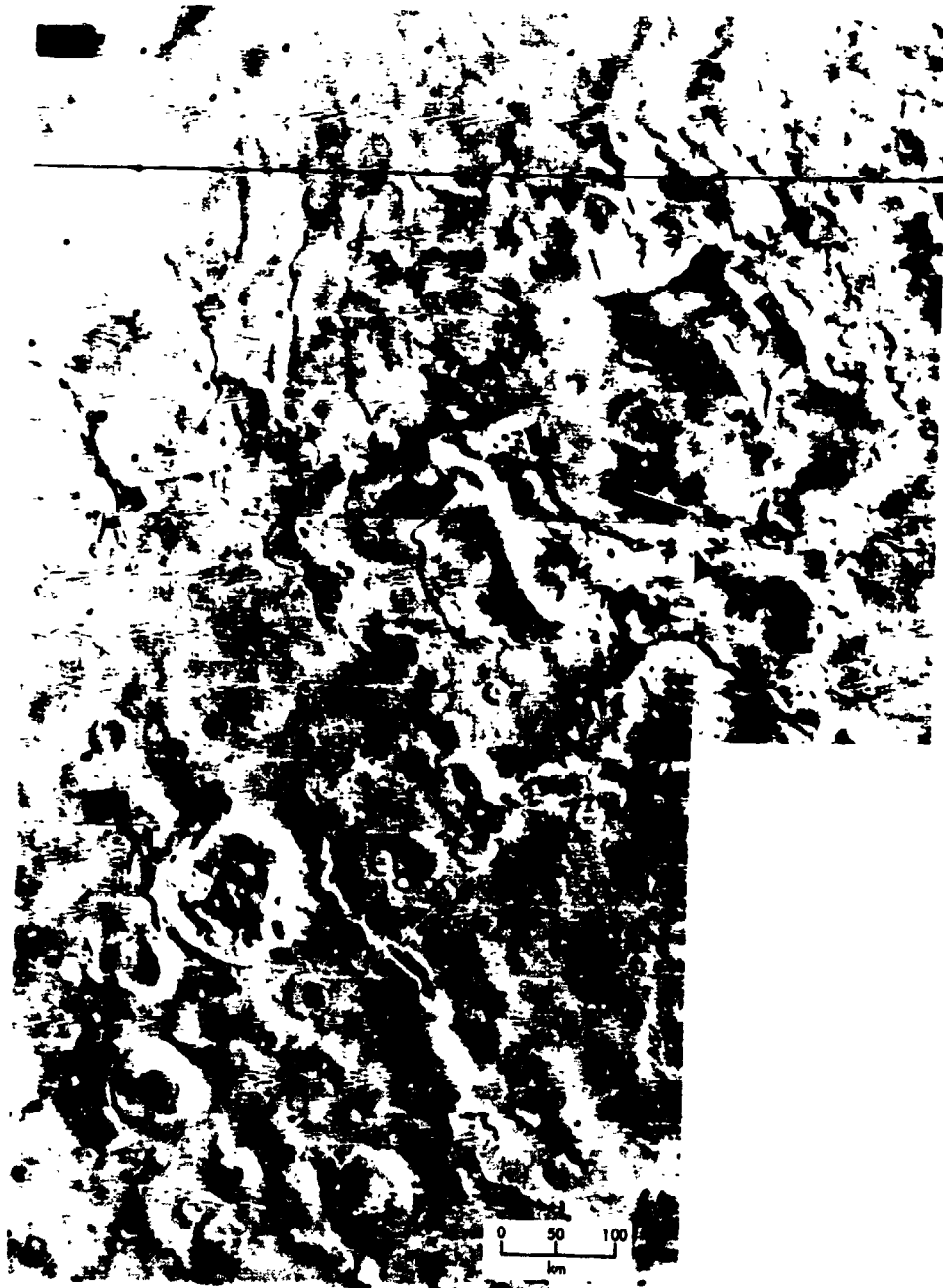
Fig. VI-1. Area of fretted terrain centered at 40.1°N latitude, 337.4° longitude, display-
ing typical complex planimetric patterns, smooth floor, abrupt escarpments, separated
outliers, and sinuous flat-floored tributary chasms. (MTVS 4251-47, DAS 09378154; MTVS
4251-56, DAS 09378294)
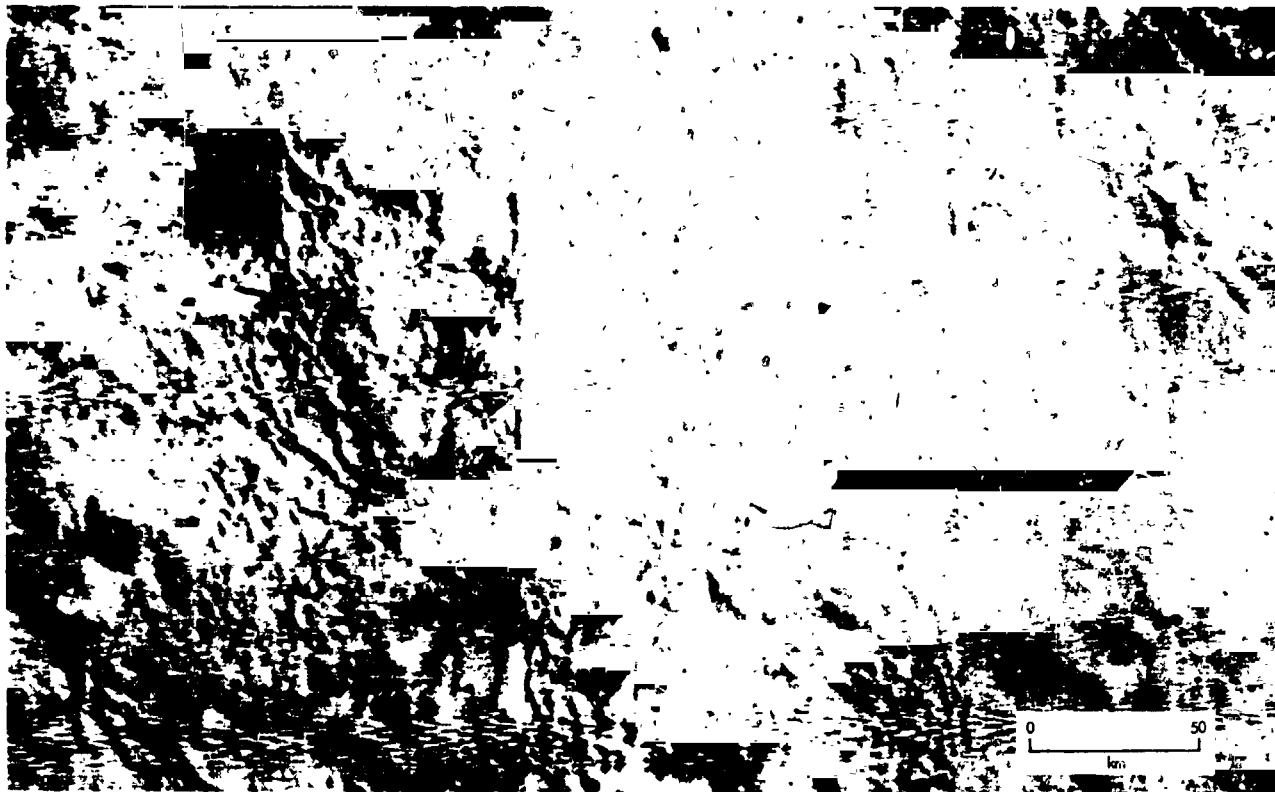
Fig. VI-2. Representative area of chaotic ter--'n at **6.5°S** latitude, **26.3°** longitude, with crescent-shaped blocks and arcuate fractures strongly ⏤ggestive of collapse. (N 'VS 4247-44, D~⏤ 09232974)

smooth-floored lowland (Fig. VI-5). These outliers become generally smaller, more widely spaced, and less numerous outward from the bounding escarpment.

2. Floor Characteristics

The lowland floors of fretted terrain appear smooth at a wide-angle resolution of 1 km. Narrow-angle pictures (Fig. VI-5), with resolutions of 200 to 300 m, confirm this general smoothness, although they show some low undulations and a few local areas of rough topography that may represent complex structures within the Martian crust, possibly the residual roots of old, deeply penetrating craters. Most floors display only an occasional small, fresh, bowl-shaped crater, but a few scattered craters up to 25 km in diameter are seen Irregular mottling by albedo markings is somewhat more prominent than on adjacent lands, and some of these markings mimic the configuration of a nearby escarpment.

Extensive reaches of the lowland floor appear to lie at an impressively uniform altitude, as though reduced to a common base level. This holds true even for the long penetrating fingers of tributary chasms and for the floors of larger craters integrated into the lowland. The uniform height of long reaches of the bounding escarpment is another manifestation of this relationship.

3. Wall Characteristics

Escarpments enclosing the lowlands usually break off from the uplands with a sharp, well defined brink. Escarpment slopes appear to be mostly straight and smooth without marked concavity. Orthogonal or dendritic scarring is largely absent, and slump blocks so characteristic of chaotic terrain, are lacking. No layering or structure is identifiable in the wall materials; they appear homogeneous and massive.

Escarpment height is largely a matter of estimation. If a conservative 10° slope is assumed, heights of 0.5 to 1 km are common. Some escarpments are lower; few, if any, appear to exceed 2 km. Ultraviolet spectrometer profiles confirm heights of this general magnitude.

Fig. VI-3. Chaotic terrain associated with smooth-floored areas of fretted terrain, crescent-shaped slump blocks at left margin of lower area. (MTVS 4201-60, DAS 07686808)
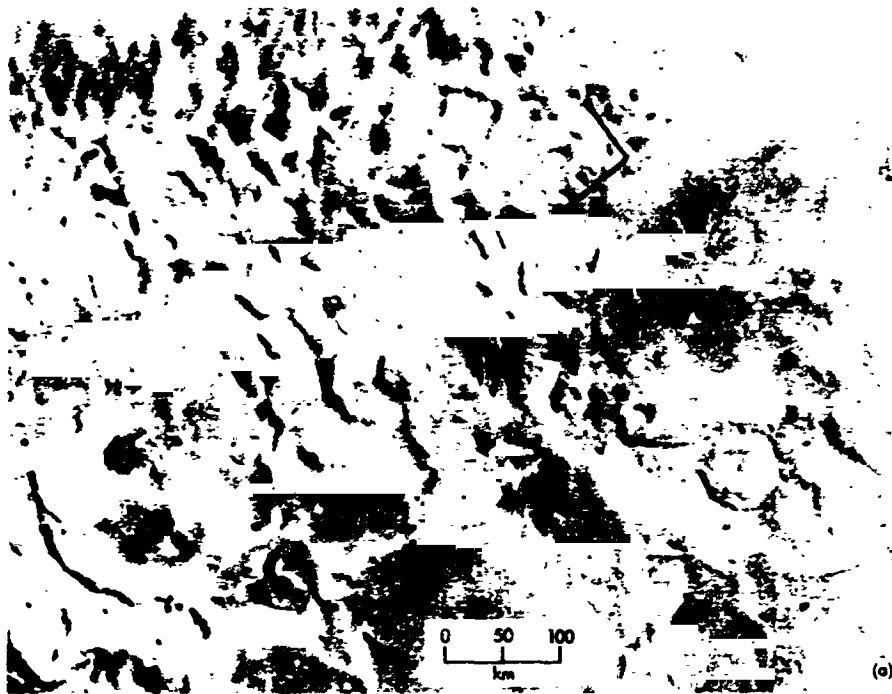
Fig. VI-5. Wide- and narrow-angle pictures of fretted terrain to illustrate angularity of outlines, smoothness of floor, abruptness of escarpments, and nature of outliers. (MTVS 4212-69, DAS 08047308; MTVS 4212-72, DAS 08047343)

4. Upland Surface

The upland surface enclosing areas of fretted terrain is mostly well cratered, but otherwise it is relatively smooth. Upland craters are locally embayed by the escarpments of fretted terrain, and in such instances the crater floors are integrated into the lowlands.

C. Description of Chaotic Terrain

1. Floor Characteristics

The most distinctive feature of chaotic terrain is its rough floor topography, most typically an irregular jumble of angular blocks of various sizes, many preserving remnants of the relatively smooth upland surface (Fig. VI-6a). The largest blocks are several kilometers across and tens of kilometers long. At some sites, the angular shape and equant dimensions of blocks may reflect control by two or more sets of linear fractures. Once formed, these blocks seem to suffer further breakup and reduction in size, and the equant blocks ultimately become pyramidal. Eventually, they may be entirely destroyed, leaving a smooth floor like that of fretted terrain.

2. Bounding Escarpments

Some areas of chaotic terrain involve a transition from slightly fractured upland through a highly fractured zone to a jumble of irregular blocks (Fig. VI-2). Other areas are sharply bounded by an abrupt escarpment of irregular planimetric configuration (Fig. VI-3). The vertical relief of this escarpment is a matter of estimation, but most escarpments seem to range from something less than 1 km to a little more than 2 km, with a maximum approaching 3 km. They are, in places, higher than the escarpments bounding most areas of fretted terrain. Locally, chaotic-terrain escarpments display a succession of crescent-shaped indentations, and on their faces are crescent-shaped slump blocks up to several kilometers wide and tens of kilometers long. Some of these blocks bear remnants of the upland surface, now rotated backward into the escarpment face. Locally, arcuate markings, presumably fractures, extend back into the surrounding upland with similar scale and configuration. Most escarpments have a sharp, well defined brink, and a few of the highest display orthogonal scarring like that seen on the walls of the large equatorial troughs.

D. Age Relationships

Fretted terrain appears to be among the younger landform developments of the Martian surface, but not all areas of fretted terrain are of a single age. Fretted terrain

has clearly developed at the expense of the old cratered surface of Mars which constitutes the adjacent upland. The smooth floor of most areas of fretted terrain is only weakly cratered, primarily by small, fresh, bowl-shaped craters. This suggests relative youth, although accumulation and erosion on such floors may obscure some craters, making the floors look younger than they really are.

At least some fretted terrain must have a modest antiquity for it appears to be partly buried along the western edge of an extensive volcanic field between latitudes 5 and 15° north near longitude 75°. The date of volcanism is not rigorously known, but crater frequencies and other considerations suggest an age on the order of hundreds of millions of years (Refs. VI-2 and VI-5; also see Sections IV and VIII of this Report).

At least one area of fretted terrain has subdued outlines suggestive of mantling by a blanket of younger material (Fig. VI-7). This impression of greater age is substantiated by a much larger-than-normal crater population. Other areas of irregular topography elsewhere on Mars have characteristics suggesting that they may represent fretted terrain, now so modified as to be virtually unrecognizable. Thus, the fretting process may have embraced a considerable span of time, and not all of the recognizable areas of fretted terrain have the same age.

Chaotic terrain is also judged to be youthful on essentially the same bases. However, the seeming paucity of craters, even of the small bowl-shaped variety, within areas of chaotic terrain may be due in part to the difficulty of recognizing such features within the chaos of jumbled blocks. Furthermore, craters could be rather quickly obscured on the steep sides of the blocks. Associated areas of fretted and chaotic terrain, of which there are a number, cannot be too different in age, and the generally sharp outlines of their features strongly suggest relative youth.

E. Genesis of Fretted and Chaotic Terrains

The following statements on genesis are necessarily highly speculative. The development of fretted terrain is thought to be initiated by some structural or topographic break in the old cratered Martian surface. The wall of a large crater, a linear crack, or a winding channel may have, in different instances, served as the initiating locus.

Once a steep escarpment is created, in areas favorable to the formation of fretted terrain, it recedes by an
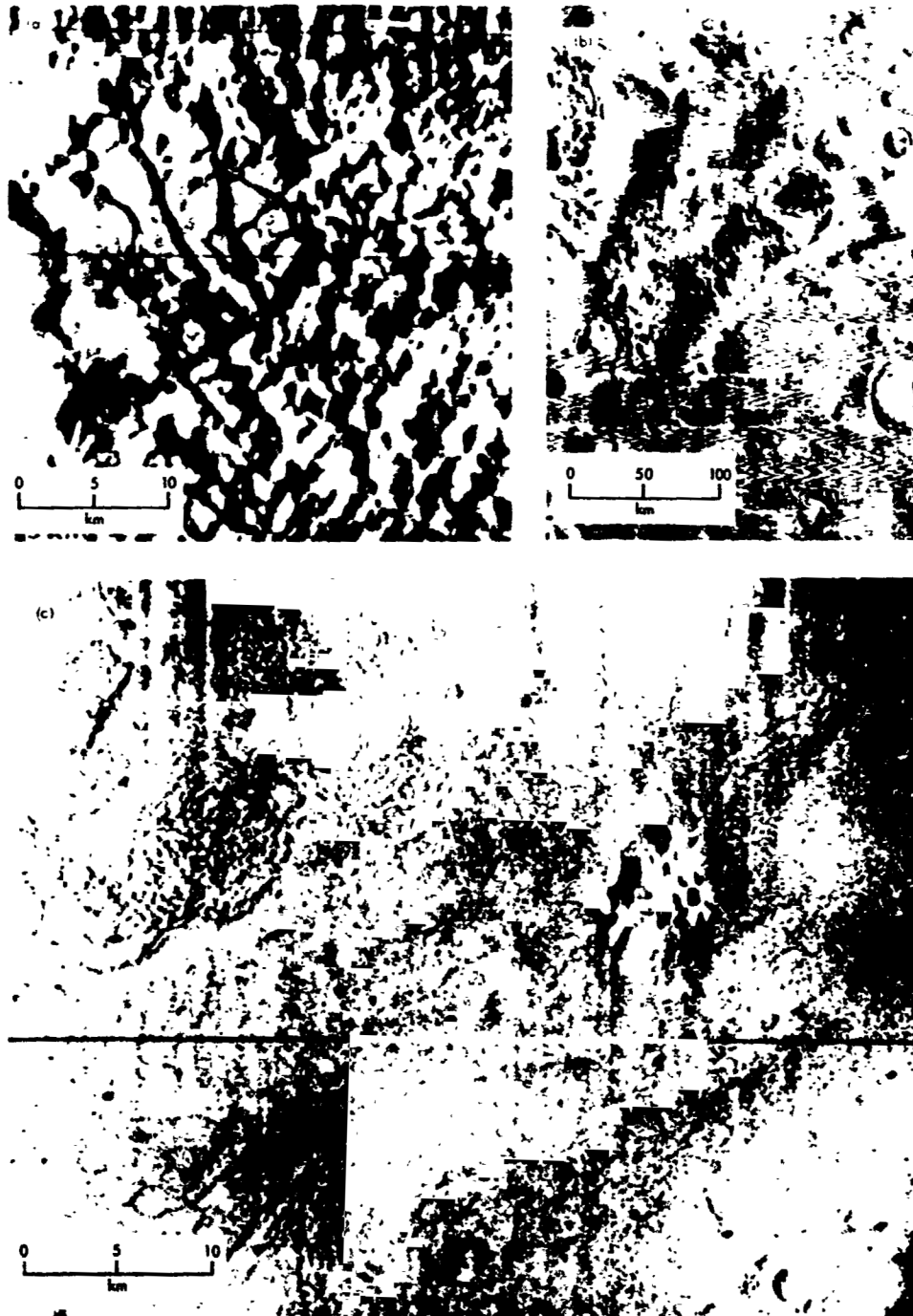
Fig. VI-6. A composite of one wide-angle and two narrow-angle pictures of chaotic terrain. (a) Details of angular blocks (MTVS 4201-30, DAS 07686213). (b) Small isolated area of chaotic terrain (MTVS 4247-40, DAS 09232904). (c) Arcuate fracturing suggestive of collapse leading to development of chaotic terrain at 1.9°S latitude, 186.5° longitude. (MTVS 4209-75, DAS 07938353)

Fig. VI-7. An area of older blanketed and more abundantly cratered fretted terrain at 44°N latitude, 61.5° longitude. (MTVS 4233-92, DAS 08731179)

undermining or sapping mechanism, maintaining its steepness but developing a complex planimetric configuration. This is the fretting process. Scarp recession leaves a smooth, flat floor and isolates outlying island-like buttes, mesas, and towers. The bounding slopes of these outliers also recede, reducing them in size and eventually in number.

On Earth, scarp recession occurs most readily where there is some structural or stratigraphic inhomogeneity near the scarp base to facilitate undermining. Horizontal strata with a massive member overlying weak incompetent layers, as occurs in the plateau region of the southwestern United States, provide nearly ideal conditions. The undermining on Earth is produced largely by differential weathering and ground-water sapping.

Layering within the materials of the upper 1 to 2 km of the Martian crust is not out of the question, and it might involve a volcanic sequence or a thick deposit of eolian detritus. However, such materials would have to be relatively old, as the surface they underlie is scarred by many large craters. An attractive alternative is the possibility that otherwise relatively homogeneous near-surface Martian material has a sharp, planar, physical discontinuity at a depth of 1 to 2 km. Such a discontinuity

might have formed in relation to frozen ground developed to that depth.

An evaluation of the possibilities of perennially frozen ground (permafrost) and ground ice under the surface of Mars is thus in order. Direct observations of Martian surface temperatures, both Earth-based and from spacecraft, indicate that a model formulated by Leighton and Murray (Ref. VI-6) permits calculation of seemingly reasonable mean annual surface temperatures for various latitudes. From this it appears that the surface thermal regimen of Mars is favorable to the development of frozen ground everywhere, including the equatorial region where the mean annual temperature is in the neighborhood of −60 C. The important questions are: How thick might the frozen layer be, and could it contain significant quantities of ground ice, particularly in a segregated state?

Nothing is known for certain about the internal geothermal flux of Mars, and the insulating properties of its surface materials are a subject of estimation. However, a working assumption that the Martian geothermal flux is perhaps one-half that of Earth and that insulation factors such as vegetation and snow cover on Earth are two or three times as effective as the presumably fragmented debris on the barren Martian surface, along with the much lower Martian surface temperatures, suggest that frozen ground could extend to depths 2 to 4 times greater on Mars than on Earth.

On Earth, the most representative maximum depths of frozen ground are 600 to 650 m (Ref. VI-7), although an anomalous 1500 m has been reported. Mean annual surface temperatures at these sites are currently −10° to −15°C. However, this deep frozen ground may be a product of Pleistocene chilling when surface temperatures were probably distinctly lower. These figures suggest that the ground beneath the Martian surface could be frozen to depths conservatively estimated at 1 to 3 km.

More important than depth of freezing is whether the postulated Martian frozen ground contains any significant quantity of frozen volatiles. Only in the extreme polar regions are temperatures low enough to permit formation of solid CO_2. Elsewhere the most likely frozen volatile is water. On Earth, the ice in frozen ground represents water of meteoric origin. The amount of water vapor currently in the Martian atmosphere is too small to form more than a small amount of ice dispersed through a few tens of meters of ground, and that would be poleward of 40° to 50° latitude (Ref. VI-6). If signif-

icant masses of H_2O ground ice derived from meteoric sources exist under the Martian surface, they must be fossil, reflecting major secular or periodic climatic variations in the past.

An interesting alternative is that ground ice on Mars represents water substance that never reached the surface, but was captured by freezing within the crust owing to the extremely low temperature conditions. This is a speculation worth entertaining, and it could help account for the relative abundance of CO_2 and paucity of H_2O in the present Martian atmosphere, although other explanations for the CO_2/H_2O relationship have been proposed (Ref. VI-8). The degassing associated with the recent northern hemisphere volcanism may have contributed significantly to Martian ground ice, particularly in areas surrounding the volcanic field. Ground ice of this origin would represent a rather recent development within Martian history, since this volcanism is relatively young (Refs. VI-2 and VI-5; also see Sections IV and VIII of this Report).

On Earth, ground ice exists within the interstices of frozen crustal materials and as segregated bodies in the form of layers, lenses, and dikes. It is the deterioration of these segregated bodies that causes differential sinking and collapse of the land surface. We have no way of knowing whether ground ice on Mars would occur in segregated bodies or not, but the speculation that it does is permissible.

The possibility that the surface beneath Mars in areas of fretted terrain has been frozen to a depth of about 1 to 2 km thus seems reasonable. This could be the discontinuity, or the base level, which is expressed in the remarkable uniformity of cliff height and the concordance of the smooth floors of fretted terrain, a concept developed in greater detail by Soderblom and Wenner (Ref. VI-9).

On Earth, a common cause of cliff recession is undermining by ground water. On Mars, a comparable function may currently be performed by ground ice. Undermining could occur when ground ice, either in segregated bodies or in rock interstices, is exposed on the scarp face and melts or evaporates, the latter being more likely under present climatic conditions. This could allow the rock materials to crumble, undermining the escarpments and causing recession while maintaining steepness. Inhomogeneities in the amount and distribution of ground ice and in the nature and structure of materials

could result in differential recession producing the highly irregular escarpment seen on *Mariner 9* pictures

The recessional process would soon come to a halt, if the debris shed by the escarpment were not removed. Under current conditions, wind is generally regarded as a likely agent of debris removal. For wind to be effective in any significant degree, *all* of the rock detritus must be relatively fine grained. If that is not the initial condition of the detritus shed from the escarpments, then it must be reduced to that state by weathering. On Mars this is not an easy task; thermal fracturing seems an inadequate mechanism (Ref. VI-10) for particle reduction but perhaps it should not be wholly ignored, and Malin (Ref. VI-11) is evaluating the matter of salt weathering.

The alternative possibility that the undermining is effected by ground water, as urged by Milton (Ref. VI-12, also see Section III of this Report), has the virtue that the water, if plentiful enough, could carry the resulting debris northward into the lower area of relatively featureless plain lying north of fretted terrain. The problem involved in postulating ground-water action and fluvial transport is the requirement of a wholly different climatic and atmospheric environment on Mars that would permit the existence of liquid water on the Martian surface. Such conditions would have had to exist for a considerable time judging by the amount of debris that was removed to create the extensive area of fretted terrain and the probability that the process worked slowly; it was not a catastrophic procedure. If of fluvial origin, fretted terrain is fossil, and the implication of major and enduring climatic change is highly significant.

Why fretted terrain is not more widely developed on the Martian surface is a moot question. It may be that proximity to the large-scale volcanism of the northern hemisphere has been a factor in terms of larger than normal quantities of degassed volatiles to form ground ice or ground water and in deformation of the surface to initiate receding scarps. The low-lying plain area farther north may also be a consideration.

Another hypothesis, perhaps worthy of consideration, is that frozen ground and significant quantities of ground ice developed under these now fretted parts of the Martian surface to a depth of 10 km rather than 1 or 2 km. If 10% of this frozen mass were in the form of segregated ice bodies that distended the ground, then a 10% decrease in volume would occur if the ice were removed by melting or evaporation. This would produce about 1 km of sinking of the ground level. However, 10 km seems an extreme thickness for frozen ground and fretted terrain does not look at all like surfaces on Earth which have collapsed because of ground-ice thawing.

That subsidence, fracturing, and slumping have played a part in the development of chaotic terrain was inferred from the *Mariner 6* pictures of 1969 and now seems established by *Mariner 9*. Subsidence, of a type possibly leading to the formation of chaotic terrain, is strongly suggested by the fracture pattern evident in a narrow-angle picture (Fig. VI-6c). As subsidence and slumping are usually initiated by removal of subsurface material, the crux of the origin of chaotic terrain becomes—what process or processes could perform that task? The dissolution of rock materials, the deterioration of ground ice, or the evacuation of magma by volcanism are three possible mechanisms meriting consideration.

The solution hypothesis suffers from the need for soluble rocks and a suitable solvent. If Mars were rich in carbonatites and its volatiles were acidic, solution might occur. This seems a modest possibility at best.

Ground-ice deterioration is attractive but suffers some qualifications. The ground ice would have to occur in segregated bodies, some means of causing its deterioration must be postulated, and the question of quantitative adequacy is all important. Woronow (Ref. VI-13), using McElroy's (Ref. VI-8) analysis of Martian atmospheric evolution, gives reasons for thinking that the amount of water outgassed during the lifetime of Mars is wholly inadequate to produce the 2- to 3-km subsidence suggested by chaotic terrain, even if all the water were concentrated as ground ice solely under the chaotic terrain areas. The more generous estimates of Sagan and Mullen (Ref. VI-14) also appear insufficient.

Another troubling problem is the depth of freezing required unless the ice were concentrated in a single layer just below the surface. If Martian frozen ground is postulated to have a generous 20% segregated ice content, then freezing to a depth of 10 km would be required to yield 2 km of subsidence upon deterioration of the ground ice. This may not be an impossible depth, but it strains the limit of seemingly reasonable assumptions.

Even though the creation of large areas of chaotic terrain, inset 2 to 3 km below the upland, solely through ground-ice deterioration may be questioned on quantitative grounds, ground ice may still have played a significant role in the recession of bounding escarpments, in the development of wall-side slump blocks, and in the further

breakup of the chaotic blocks created by collapse. There are also areas of chaotic terrain which do not look as though they had experienced much subsidence, perhaps just enough to initiate cracks which were then widened into chasms by ground-ice deterioration (Fig. VI-3). The thought that small scattered patches of chaotic terrain (Fig. VI-6b) might be created by the local destruction of ground ice is also appealing.

Another argument has been advanced by McCauley et al. (Ref. VI-15) regarding the possible role of ground ice in chaotic terrain formation. In places, large seemingly scoured channels emerge full-born from areas of chaotic terrain. These authors suggested that the channels were occupied by huge floods of water, resulting

from melting of ground ice, which burst forth upon the Martian surface like a Spokane-type flood (Ref. VI-16). The vacated areas presumably collapsed into chaotic terrain

If deterioration of ground ice is not the only or even the principal cause of chaotic terrain, then the subsurface movement of magma in association with volcanism seems the other most likely agent. This thought is supported by the general proximity of the principal areas of chaotic terrain to the major recent volcanic fields in the northern hemisphere of Mars. It may be that volcanic subsidence owing to withdrawal of magma has initiated the development of chaotic terrain, which was then furthered by ground-ice deterioration.

References

VI-1. Sharp, R. P., "Mars: South Polar Pits and Etched Terrain, *J. Geophys. Res.*, Vol. 78, 1973.

VI-2. Carr, M. H., "Volcanism on Mars," *J. Geophys. Res.*, Vol. 78, 1973.

VI-3. Sharp, R. P., Soderblom, L. A., Murray, B. C., and Cutts, J. A., "The Surface of Mars: 2. Uncratered Terrains," *J. Geophys. Res.*, Vol 76, p. 331, 1971.

VI-4. Kliore, A. J., Fjeldbo, G., Seidel, B. L., Sykes, M. J., and Woiceshyn, P. M., "S-Band Radio Occultation Measurements of the Atmosphere and Topography of Mars with Mariner 9: Extended Mission Coverage of Polar and Intermediate Latitudes," *J. Geophys. Res.*, Vol. 78, 1973.

VI-5. Hartmann, W. K., "Martian Cratering IV: Mariner 9 Initial Analysis of Cratering Chronology," *J. Geophys. Res.*, Vol. 78, 1973.

VI-6. Leighton, R. B., and Murray, B. C., "Behavior of Carbon Dioxide and Other Volatiles on Mars, *Science*, Vol. 163, p. 136, 1966.

VI-7. Price, L. W., *The Periglacial Environment, Permafrost, and Man*, Asso. Amer. Geographers, Com. on College Geog., Resource Paper 14, 88 pp., 1972.

VI-8. McElroy, M. B., "Mars: An Evolving Atmosphere," *Science*, Vol. 175, p. 443, 1972.

VI-9. Soderblom, L. A., and Wenner, D. B., "A Fossil Water Table on Mars" (in preparation).

VI-10. Ryan, J. A., "The Case Against Thermal Fracturing on the Lunar Surface," *J. Geophys. Res.*, Vol. 67, p. 2549, 1962.

References (contd)

VI-11. Malin, M. C., "Salt Weathering on Mars?" (in preparation).

VI-12. Milton, D. J., "Water and Processes of Degradation in the Martian Land-scape," *J. Geophys. Res.*, Vol. 78, 1973.

VI-13. Woronow, A., "Origin of the Martian Chaotic Terrains," *Science*, Vol. 178, p. 649, 1972.

VI-14. Sagan, C., and Mullen, G., "Earth and Mars: Evolution of Atmospheres and Surface Temperatures, *Science*, Vol. 177, p. 52, 1972.

VI-15. McCauley, J. F., Carr, M. H., Cutts, J. A., Hartmann, W. K., Masursky, H., Milton, D. J., Sharp, R. P. and Wilhelms, D. E., "Preliminary Mariner 9 Report on the Geology of Mars," *Icarus*, Vol. 17, p. 289, 1972.

VI-16. Bretz, J H., "The Lake Missoula Floods and the Channeled Scabland," *J. Geol.*, Vol. 77, p. 505, 1969.

Acknowledgments

VII. Comparison of Martian and Lunar Multi-Ringed Circular Basins[1]

Don E. Wilhelms

U. S. Geological Survey, Menlo Park, California 94025

Six Martian multi-ringed circular basins are described here. Argyre, Hellas, Libya, "Martian Schrödinger," Edom, and Iapygia. The term "multi-ringed circular basin," or simply "basin," is derived from lunar studies (Refs. VII-1 and VII-2) and refers to large crater-like features that have more than one raised ring. On the Moon, there is a size continuum between craters and basins; the transition occurs between 150 and 300 km (Ref. VII-3, p. 445). The larger the feature, the more rings it has and the wider their spacing.

On both the Moon and Mars, the basins are genetically distinct from the material that fills them (cited works; Ref. VII-4). The fill, which on the Moon is largely mare basalt, was emplaced a considerable time after formation of the basin (Ref. VII-5, pp. 309–311, and Ref. VII-4). Thus, the terms "basin," for the containing structure, and "mare," the fill, are in no way synonymous. The depth to which the basin is filled, and the specific ring that forms the "coastline" of the fill, varies from basin to basin and is controlled by endogenous factors not directly related to the basin-forming process. This discussion concentrates on the basins and only in passing mentions the fill, which on Mars is usually a light-colored plains-forming material.

---

[1]Publication authorized by the Director, U. S. Geological Survey.

A. Lunar Basins

At the present stage in Martian studies, the basins are best investigated by comparison with the better photographed and long studied lunar basins. The youngest and best preserved large lunar basin, Orientale, is a necessary reference object for all lunar and Martian basin studies because it displays with minimum modification the features of a newly formed basin (Fig. VII-1). The basin proper consists of three concentric, prominent, rugged mountain rings. The inner two are together called the Rook Mountains (Montes Rook); the third, Montes Cordillera. All three rings contain topographic elements that are concentric and radial to the basin. Degree of organization increases outward: The inner ring is the least complete and has the most randomly oriented elements; the Cordillera ring is the most continuous and has the most radial and concentric elements. The Cordillera ring is probably highest as a whole, but parts of the second Rook ring equal or exceed it in height. The spacing between rings increases outward by a regular ratio that seems to be common to all lunar basins (Ref. VII-1, pp. 64–65). The depressions between the rings and inside the inner ring are occupied by less rugged, rather chaotic, materials (and by the later flat mare fill).

Outside the third (Cordillera) ring, which encloses the basin proper, most topographic elements are oriented approximately radially to the basin. There are rugged

Fig. VII-1. Orientale basin of the Moon. North at the top; dark mare-filled crater Grimaldi east–northeast of basin. Three rings of mountains are the dominant features of the basin proper. The discontinuous innermost ring and the higher, nearly complete, second ring are together called Montes Rook (Rook Mountains). Outside Montes Rook and separated from them by a ring depression containing hummocky terrain is the third and main ring, Montes Cordillera, 950 km in diameter. Outside this are radially lineated basin ejecta and radial valleys; the conspicuous valley south–southeast of the basin is Vallis Bouvard. (*Lunar Orbiter 4*, frame 187-M)

in diameter), is exposed only as a ring of islands 675 km in diameter. The second ring, under our preferred interpretation (Refs. VII-1 and VII-4) is exposed mainly as Montes Alpes and the rugged terrain near Archimedes. The third and main basin ring is best developed in Montes Carpatus, Montes Apenninus, and Montes Caucasus. This is the most continuous and largest conspicuous ring (1500 km in diameter), and corresponds to Montes Cordillera of Orientale (950 km).

At both basins, this third ring approximately bounds the basin proper and marks the beginning of the deposits of ejecta. At the larger Imbrium basin, most ejecta near the basin is hummocky, and is mixed with rock fractured during basin formation; the lineated ejecta blanket (the

radial valleys such as Vallis Bouvard, and finer, braided ridges. At the distal margins of this lineated terrain are clusters of craters having subequal size and morphology. For reasons extensively discussed in the lunar literature (cited works), the Orientale basin is believed to have been produced by an impact. The raised rings were probably uplifted by shock waves and modified by faulting; the lineated peripheral material is the ejecta; the satellitic craters are the secondary impact craters. The exact origin of radial valleys like Bouvard (and Vallis Rheita of the Nectaris basin) is less well understood; they may be formed by secondary fragments ejected along low trajectories (Ref. VII-5, pp. 317–318).

Another lunar basin that is a useful analog for the Martian basins is Imbrium (Fig. VII-2), the largest lunar basin. It is much more deeply flooded by mare material than is Orientale. The innermost ring, which probably corresponds to the inner Rook ring of Orientale (450 km

Fig. VII-2. North-central part of the Moon including the Imbrium basin. North at the top. Archimedes is 80 km in diameter. Generalized crests of four rings are shown (see Refs. VII-1 and VII-2). Montes Carpatus, Apenninus, and Caucasus together compose the main Imbrium basin ring. The two inner rings shown correspond to the two Rook rings of the Orientale basin (see Fig. VII-1). A fourth ring, emphasized by the edge of Sinus Medii, lies outside the main ring here. Note the structure radial to the basin (Mount Wilson Observatory photograph, unpublished).

Fra Mauro Formation) begins beyond this rugged material. At a considerable distance from Montes Apenninus is still another ring. Part of it bounds Sinus Medii or the south and continues northeast into the terra. This ring consists mostly of a low swell locally bounded by a basin-facing scarp and has far fewer rugged peaks than do the mountainous chains that compose the three inner rings.

The majority of known and suspected Martian basins are smaller and more degraded than Orientale and Imbrium, and are best compared with a lunar farside basin such as Korolev (Fig. VII-3). This degraded basin has lost most of the radially lineated ejecta and other morphologic detail that it, like Orientale, Imbrium, and most craters, once undoubtedly had.

B. Argyre

The Argyre basin (named for an approximately coterminous, bright telescopic feature) has the most complete rugged rim of all large Martian basins. The plains fill

Fig. VII-3. The Korolev basin on the far side of the Moon, centered at 4°S latitude, 157° longitude. North at the top. There are two conspicuous rings and a faint possible additional innermost ring. The main ring, averaging 430 km in diameter, is divided into two parts in the west. Radial lineations southwest (below and left) of the main ring may be basin ejecta. (*Lunar Orbiter I*, 38-M).

measures about 800 km across except where a promontory juts into it. Argyre has many of the features of the Orientale and Imbrium basins, but differs in some respects. These concentric inner rings and two or three partial outer rings have been identified (Fig. VII-4). The inner, most speculative ring is marked by isolated islands (Figs. VII-5a and VII-6) and the end of the promontory (Fig. VII-5c). This ring is like the inner Imbrium ring. The second and third rings are in the main part of the rugged rim (Figs. VII-5 and VII-6). They probably correspond to the second and third rings of Orientale and Imbrium. The component rugged peaks of the second ring have mostly irregular outlines and subordinate concentric and radial elements. The third ring, approximately 1200 km in diameter, resembles the third (Cordillera) ring of Orientale, although it is less continuous. It is bounded on the basin side by a steep scarp and on the outside by a plateau (Fig. VII-6). In this ring and the plateau are numerous coarse and fine radial structures; large structures like Vallis Bouvard occur in all but the northeast sector. The spacing increases outward from each of these three rings to the next by a ratio like that observed in lunar basins. Between the rings, in some places, are subsidiary concentric rings (Fig. VII-5a).

An additional partial ring is marked by discontinuous ridges with smooth convex-upward profiles that are somewhat like lunar mare ridges, but unlike lunar *basin* ridges (Fig. VII-5c). Finally, there are two long inward-facing low scarps backed by a featureless plateau (Figs. VII-5b, VII-5c, and VII-6). These scarps, which may be connected into a single structure, are like the fourth ring of Imbrium and are tentatively considered the fourth principal ring of Argyre.

In a lunar basin, the lineated basin ejecta is deposited on the plateau outside the third ring. At Argyre, the radial lineations that are clearly visible outside the third ring could be scours or faults in bedrock and not depositional texture of ejecta, but some finely lineated terrain could represent the Argyre ejecta blanket (MTVS 4162-66, DAS 06426598).[2] No secondary impact craters have been discovered unless the widenings along the Bouvard-like valleys are of this origin. Systematic mapping probably will be required to locate the Martian basin secondaries, as it was on the Moon except for the obvious ones of Orientale.

---

[2]Numbers in parentheses that appear in the text refer to *Mariner 9* television pictures not included in this section, but which provide additional pertinent explanatory material. All *Mariner 9* pictures may be ordered from the National Space Science Data Center, Code 601, Greenbelt, Maryland 20771.
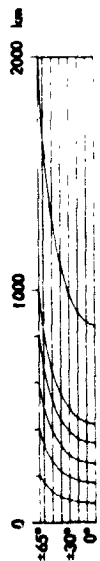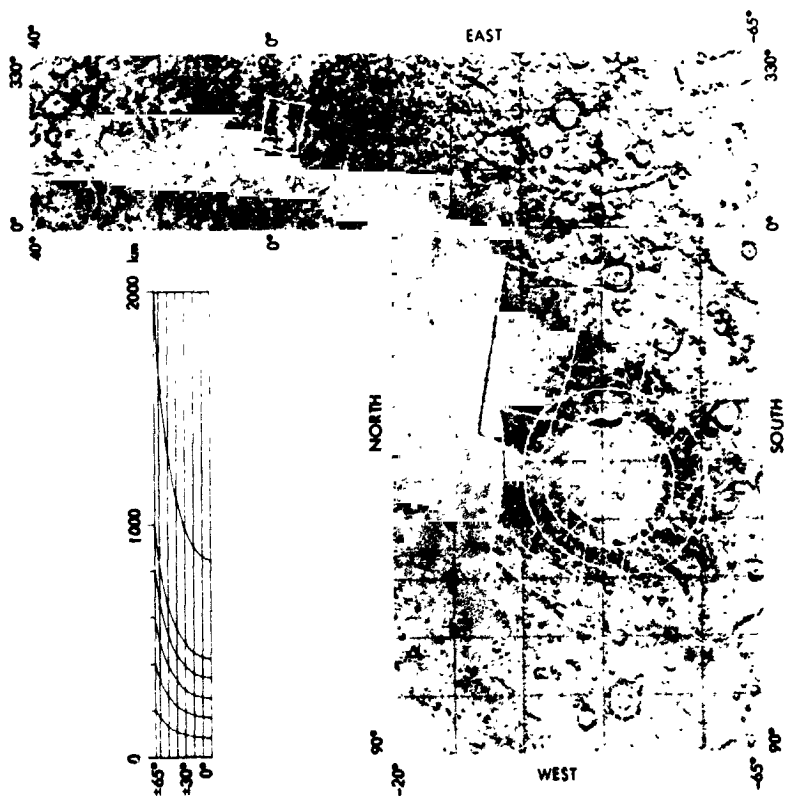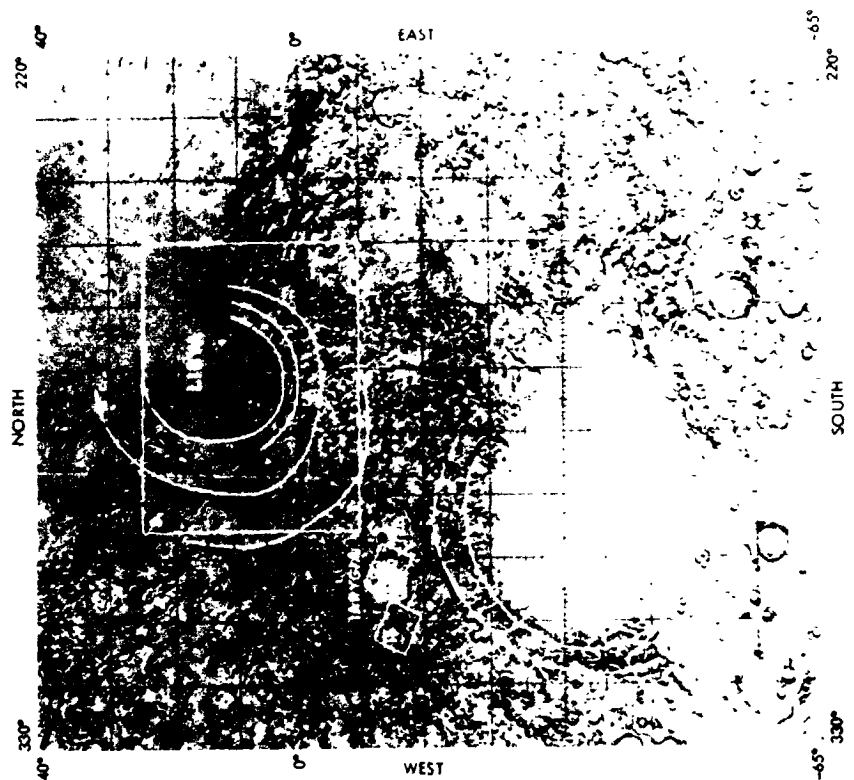
Fig. VII-4. Shaded relief map of part of Mars showing generalized crests of rings of the larger basins discussed in text, and outlines of photographic figures. Figure outlines are plotted by comparison of features, not by corner coordinates except where identifiable features are lacking. Map was prepared by the U. S. Geological Survey under the direction of R. M. Batson; airbrush relief portrayal by P. M. Bridges and J. L. Inge. Mercator projection (causing great increase in scale toward high latitudes).
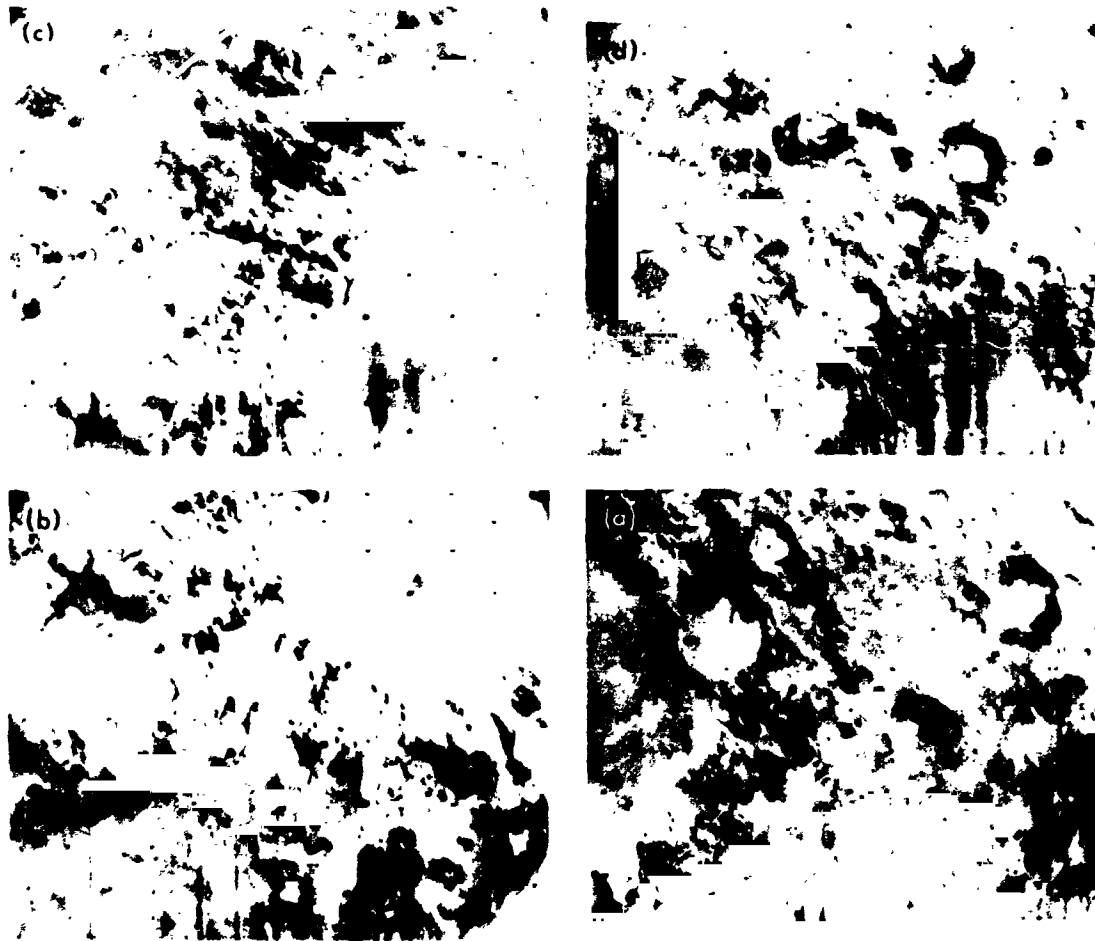
Fig. VII-5. Overall views of the Argyre basin (*Mariner* 9 "geodesy" frames; see Fig. VII-4 for location and orientation). (a) Southeast sector. The rugged basin rim has a predominantly concentric structure. A radial valley (containing a much younger channel) extends outside the rugged rim. Several small islands, probably marking a buried innermost ring, protrude through the plains fill. Large crater 200 km in diameter. (MTVS 4143-06, DAS 05812550) (b) Southwest sector. The rugged rim is divided roughly into two concentric ring belts. The inner of these (the "second" basin ring) has a random structure, and the outer one a radial structure. Part of a low basin-concentric scarp is at the left (west). (MTVS 4134-06, DAS 05524578) (c) Northwest sector. The rugged promontory near the center of the picture may contain parts of two rings, the inner one of which (the innermost basin ring) is mostly buried by plains material elsewhere. A conspicuous arcuate trough divides this promontory and other, less conspicuous, peaks of the second basin ring from the third ring. The outer part of the rugged rim (third ring) is radially structured in the north half of the picture. A short ridge-like ring and a long, outer basin-facing scarp like that of (b), or its continuation, are left (west) of the rugged rings (see Fig. VII-4 for guide to locations). (MTVS 4137-09, DAS 05596608) (d) Northeast sector. The rugged part of the rim, composed of two indistinct rings, is embayed by plains material north of the large (200-km) crater. (MTVS 4143-09, DAS 05812628)

Fig. VII-8. Strip across southwest flank of Argyre basin. The plains fill and some small islands possibly marking the first ring are at the top (northeast). Next is a rugged ring of mountain peaks (the second ring) mostly having irregular outlines and random orientation. Next outward is an apparently higher rugged ring (third ring) with a steep, jagged, basin-facing scarp and a more gentle southern flank. A conspicuous valley radial to the basin begins at the scarp and continues into the plateau-like flank. At the bottom of the mosaic is a low scarp facing the basin, an outer (fourth) basin ring. Note the rugged crater-like forms amidst the ring structures; these may be heavily damaged ore-basin craters. (Mosaic of MTVS 4164-45, DAS 06497928; MTVS 4162-45, DAS 06426038; MTVS 4164-33, DAS 06497788, top to bottom)

C. Hellas

Hellas, whose main rim is about 2000 km across (between crests), is the largest circular basin so far discovered (Fig. VII-4). The main rim is probably analogous to the 1500-km ring of the Moon's largest basin, Imbrium. This correspondence is uncertain, however, because Hellas is harder to describe in lunar terms and to visualize as a whole than is Argyre. Hellas may be basically different or the difference may be only apparent and may result from concealment of its inner rings by the plains fill or by blowing dust, or merely from the inferior photographic coverage.

The northern and eastern rims are composed of rugged peaks that resemble those of Argyre and of the large lunar basins, but are more degraded and more widely spaced (Fig. VII-7). Most are irregularly oriented, but there are some radial and concentric elements. Indistinct, irregular troughs may divide the peaks here into two broad rings, but the rings are less continuously traceable than in lunar basins and in Argyre. No attempt is made to draw them east of the basin, where peaks occur over a very large area (Fig. VII-7). The northeast rim is heavily embayed and flooded by plains material so that the rim breaks up into numerous isolated islands surrounded by plains.

The western rim (Fig. VII-8) consists of two rings. A rugged, partly sharp-crested and partly broad ring, rather like the third ring of Argyre, is bounded by an inward-facing scarp and a smaller outward-facing scarp. Quite near this ring is another consisting of a series of smooth concentric ridges. These ridges resemble certain degraded rings of lunar basins, but are more numerous and more closely spaced; in spacing they resemble subrings southeast of Argyre (Fig. VII-5a). A terrestrial tectonic analog has been suggested for them (Ref. VII-6, p. 54). Other vague ring structures whose relation to Hellas is best seen on the shaded relief map (Fig. VII-4), occur west of the basin. They resemble the short ridge-like ring of Argyre (Fig. VII-5c) and are not very lunar in morphology or spacing; they are, however, poorly photographed. The reason for the difference between the east rim (wide expanses of separated peaks) and west rim (discrete concentric ridges) is not known.

Fig. VII-7. Eastern borderland of Hellas basin. North is at top. Area covers about 1500 km east to west. (MTVS 4133-09, DAS 05489596)
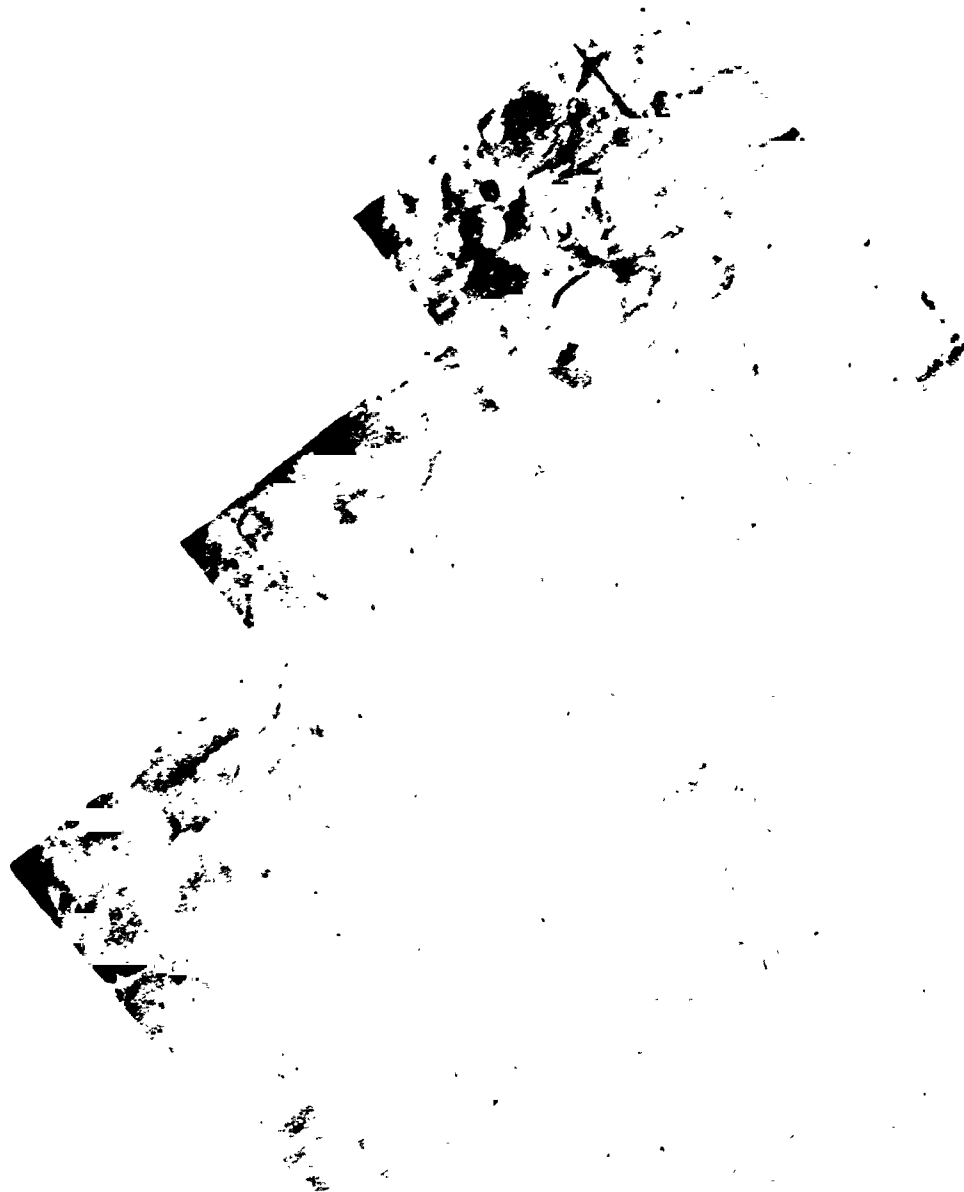
Fig. VII-8. Western rim of Hellas basin. The broadly rugged main rim of the basin is succeeded outward (left) by smoother parallel ridges concentric with the rim. (Mosaic of MTVS 4139-72, DAS 05671158; MTVS 4139-66, DAS 05671088; MTVS 4139-60, DAS 05671018; MTVS 41408-54, DAS 05743118, top to bottom)

The southwest rim is quite indistinct and is covered by finely braided material that resembles lineated basin ejecta (MTVS 4145-45, DAS 05886688). This appearance may be coincidental, however, for the lineations in the eastern part of this region are not closely radial to the basin. This southwestern sector might be depressed because of the presence of a basin older than Hellas, as suggested by some vague ring structures (Fig VII-4; MTVS 4159-06, DAS 06316138). Another pre-Hellas basin may cause the depression that allowed the flooding in the northeast. Similar relations are common on the Moon, as around the Imbrium basin (Fig. VII-2) where the pre-Imbrian basins Serenitatis, Vaporum, and Aestuum were low points for the deposition of the Imbrium ejecta and are now flooded by mare material.

Hellas is most likely an impact feature; however, the incompleteness and unusual spacing of its ring structures forces the question of origin to remain open. Possibly the main circular part of Hellas is a normal impact basin and the irregularities are due to pre-Hellas basins or modifications by internal processes. Systematic mapping or better photographs will be required to resolve these possibilities.

D. Libya

The Libya basin (named in Ref. VII-7) is a less obvious basin than Argyre and Hellas because it is less complete, much of its rim being buried by plains deposits (Figs. VII-4 and VII-9). Its identity as a multi-ringed circular
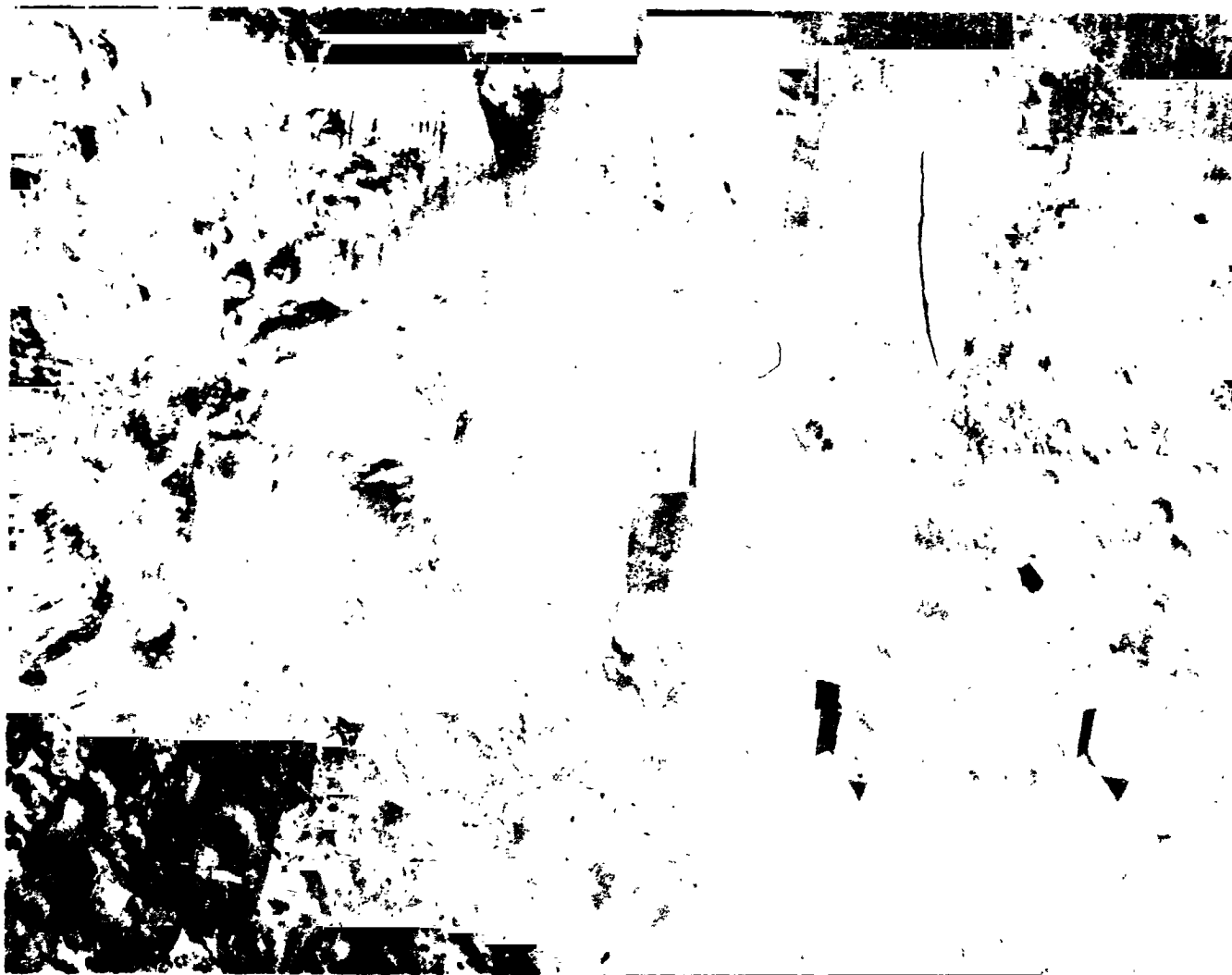
Fig. VII-9. Libya basin. Arc of mountains concave northward toward main plains fill is best exposed part of basin rim. Arrow marks outer basin-concentric scarp. Post-basin graben concentric with the basin occur northwest and southeast of the basin. Photomosaic by U. S. Geological Survey.

basin is well established. however, by an arcuate belt of rugged peaks that border the plains on the south; this belt re-emerges in more subdued form northwest of the plains fill. The inner edge of this rugged basin rim makes a circle about 1100 km in diameter. In addition, there is a long concentric scarp in the terra south of the basin (Fig. VII-9, arrow).

The peaks of the main arc south of the plains fill have a rough basin-concentric arrangement that is here tentatively interpreted to be threefold (Fig. VII-4); the threefold ch racter is most apparent southeast of the plains fill (Fig. VII-9). Peaks of all three rings have some concentric and radial edges; the outer (third) ring has the most radial elements. Moreover, the plateau southeast of this ring has basin-radial structure in places (Fig. VII-4, centered about 0˚ latitude, 248° longitude; "lineated terrain" of Ref. VII-7, Fig. 17b). This threefold structure suggests analogy with the three inner rings of Argyre, Orientale, and Imbrium. Alternatively, the two inner rings together may be the equivalent of the second Rook ring of Orientale, in which case the Libya equivalent of the inner Rook ring is buried by fill. Post-basin graben occur inside the third ring, where they also occur in lunar basins (faintly visible at Imbrium in Fig. VII-2; more complete analogy at Humorum). The outer scarp (Fig. VII-9, arrow), the fourth Libya ring, is analogous in position and length to the Imbrium scarp south of Sinus Medii (Fig. VII-2), but is higher and steeper.

Ejecta of Libya have not been identified; the radial features to the southeast are probably structural. Extensive tracts of knobby terrain east of the basin fill were previously suggested to be ejecta of Libya or bedrock shattered during its formation (Ref. VII-7), but this hypothesis has been rendered unlikely by systematic mapping, which shows that the knobby terrain is not confined to basin peripheries but borders most of the contact between the densely cratered and sparsely cratered parts of Mars (Ref. VII-8; also see Section II of this Report).

The extensive modification of Libya results from its position athwart the contact between the Moon-like densely cratered province and the sparsely cratered plains. Plains deposits have buried the northeast basin rim and embayed the southwestern rim. The circular outline of this embayment suggests that it is localized by a pre-Libya basin, which (as at Hellas) has caused the Libya rim in this sector to be depressed. The peripheral concentric graben indicate radial tension after basin formation, perhaps long after. Sharp scarps in the plains fill over the first and third basin rings indicate even later adjustment (e.g., MTVS 4186-75, DAS 07147423).

E. "Martian Schrödinger"

The multi-ringed basins that remain to be discussed are smaller than Argyre, Hellas, and Libya. By far the freshest is a double-ringed basin, 200 km in diameter, centered at 52˚S latitude, 81˚ longitude; it does not coincide with a well defined telescopic albedo feature, so it is here referred to by the name of the lunar feature (325-km diameter) which it most closely resembles. ("Martian Schrödinger," like other small features that are here called basins, will doubtless receive a specific crater name from the IAU.) Two rings are very well defined (Fig. VII-10). The outer one is concentrically structured like a typical crater rim, and the inner one is a ring of rugged peaks much like that of the lunar Schrödinger ("peak ring" of Ref. VII-2, pp. 13, 63). The extensive ejecta blanket of "Martian Schrödinger" is fine-textured and may be superposed on fairly sharp rilles that cut the adjacent plains. This basin is obviously very young by Martian standards and shows how other features of similar size once may have looked. For lunar features, 200 km is within the size range in which a second ring appears.

F. Edom

A somewhat larger, more degraded, basin is Edom (named in Ref. VII-7). Its 450-km rimcrest-to-rimcrest diameter is comparable to the lunar nearside basins Crisium and Humorum (500 and 425 km, respectively) and to the farside Korolev basin (430 km; Fig. VII-3). The main Edom ring (Fig. VII-11) everywhere faces the plains in a (usually jagged) scarp. In some places, it is rugged and elevated above the plateau behind it; in other places, it is level with the plateau. An inner ring, surrounded by the plains fill, looks, on the available pictures, partly like "terra" islands and partly like a lunar mare ridge. The inner rings of several lunar basins, including Imbrium and Crisium, are also made up of islands of the basin ring plus ridges caused either by intrusions along fractures following the buried ring, or by differential compaction over the buried ring. A scarp southwest of the main Edom ring and parallel to it may be a third Edom ring.

Radial structures south of the main ring (MTVS 4170-36, DAS 06714788) look like lunar basin-related structures, ejecta or gouge. Elsewhere around Edom such structures presumably are buried, eroded, or poorly photographed.

Fig. VII-10. "Martian Schrödinger." (a) The outer ring is 200 km in diameter. The northern (upper) part of the ejecta blanket, including some faint secondary crater chains, seems to bury part of the narrow rilles. (Mosaic of MTVS 4154-54, DAS 06138898; MTVS 4156-51, DAS 06210438, top to bottom.) (b) Detail of (a) 10× the scale. (MTVS 4245-19, DAS 09159719)

G. Iapygia

The main ring of the Iapygia basi:. (named in Ref. VII-7) resembles that of Edom in size and morphology. The two other rings are probably present, but are indistinct. The existence of an inner one is indicated by a circular albedo pattern (Fig. VII-12) that probably is caused by topographic control of dust deposition. The existence of an outer ring is suggested by subtle variations in topography. Both these rings would probably show up better in pictures taken at lower-angle Sun illumination (about 45° in Fig. VII-12).

In contrast, radial structures are more extensive around Iapygia, at least to the west, than around Edom (Fig. VII-13). Cratered rims are grooved and squared off like many lunar rims near basins. Also there are grooves in

the intercrater plateau. The apparent differences between Iapygia and Edom are probably due to differences in local geologic factors such as post-basin deposition and erosion, not to differences in age. The western interior of Iapygia, like the western periphery, seems to be less thickly mantled than the interior of Edom.

H. Other Basins

At least two other circular features between Edom/ Iapygia and "Martian Schrödinger" in size have faint traces of inner second rings (23°N latitude, 327° longitude; 21°N latitude, 298° longitude). Systematic search on low-Sun photography may reveal (or has revealed) others. Considering how many have been found, one suspects that most or all circular structures on Mars
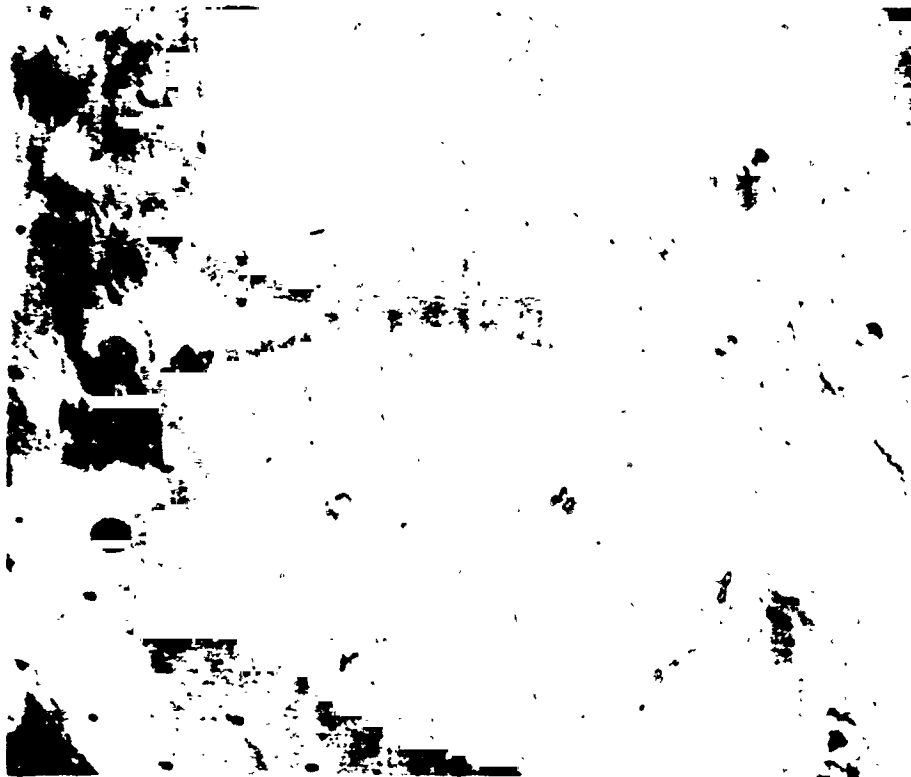
Fig. VII-11. Edom basin, main ring (450-km diameter) and partial inner ring.
(MTVS 4170-51, DAS 06715208)

Fig. VII-12. Eastern rim and interior of Iapygia basin. (a) The presence of an inner ring concentric with the rim (main ring) is suggested by the albedo pattern. Area covered is about 400 km long. (MTVS 4183-33, DAS 07074658) (b) Detail of rim at 10× the scale of Fig. VII-12a. The rugged texture may be mostly erosional, not primary. (MTVS 4183-36, DAS 07074693)

Fig. VII-13. Southwestern periphery of Iapygia basin, showing extensive structure radial to basin (to upper right: east–northeast). (MTVS 4181-33, DAS 07002628)

above 200 or 300 km in diameter have a second (or more) ring that is obscured by younger deposits. Thus, the formation of rings may well follow the same laws as on the Moon.

An additional probable large basin is centered at 83° S latitude, 262° longitude, near the south pole [*Mariner 7* frame 7N19; Ref. VII-9, pp. 707–708]. It consists of a semi-circular arc, about 900 km in diameter, that looks much like the main ring of large lunar and Martian basins. It is about the size of Montes Cordillera of Orientale. The south pole lies just inside the ring. Other rings are not obvious, although an inner, probably second, ring is suggested by a few peaks at 79° to 80°S latitude, 270° to 280° longitude. Other rings, if present, are buried by post-basin deposits, including polar ice.

I. Summary and Conclusions

This preliminary study has shown many similiarities between Martian and lunar multi-ringed basins. There is a similar relation between basin size and number of rings (Table VII-1). The second ring seems to appear in the crater-basin continuum in roughly the same diameter range, judging from the one large Martian feature

Table VII-1. Principal Martian and lunar multi-ringed circular basins discussed in this section

Basin	Number of conspicuous rings	Diameter of ring believed to bound basin proper (measured between crests), km
Hellas (Mars)	?	2000
Libya (Mars)	4	1900
Imbrium (Moon)	4	1300
Argyre (Mars)	4	1200
Orientale (Moon)	3	950
Edom (Mars)	3	450
Iapygia (Mars)	2	450
Korolev (Moon)	2	430
"Schrodinger" (Mars)	2	200

so far discovered that is fresh enough to have the second ring preserved ("Martian Schrödinger," 200 km).[3] The large basins Argyre and Libya resemble large lunar basins

[3]Hartmann (Refs. VII-9 and VII-10; see also Section VIII of this Report) also recognizes the basic similarity between Martian and lunar basins, but believes that multiple rings may appear at a smaller feature size on Mars than on the Moon (and at a still smaller size on Earth).

quite closely in ring morphology, ring spacing, apparent number of rings (four), and morphology of radial structures outside the main basin. However, the largest basin of all, Hellas, does not appear to completely fit the pattern, for reasons not yet known. The smaller basins Edom and Iapygia are much like their degraded lunar equivalents. Ejecta and secondary impact craters have not been identified with certainty around any Martian basins except "Martian Schrödinger."

The similarities are tentatively considered great enough to indicate that Martian and lunar basins were formed by the same process. Morphological and statistical studies of lunar basins have strongly indicated this process to be impact.

All but one of the basins described here are ancient features that are part of the impact-dominated hemisphere of Mars, and would be lost to view if present in the young, predominantly volcanic hemisphere. "Martian Schrödinger," coincidentally also in the cratered hemisphere, is young enough to be still visible even if in the volcanic hemisphere.

Systematic mapping, which will be forthcoming from the planned program of quadrangle mapping at the 1:5,000,000 scale, should be directed at elucidating the problem of Hellas, checking the positive preliminary results presented here, and surveying all large Martian circular features for similarities and dissimilarities to the continuum of Martian and lunar craters and basins.

References

VII-1. Hartmann, W. K., and Kuiper, G. P., "Concentric Structures Surrounding Lunar Basins," *Arizona Univ. Lunar and Planetary Lab. Commun.*, Vol. 1, pp. 51–66, 1962.

VII-2. Hartmann, W. K., and Wood, C. A., "Moon: Origin and Evolution of Multi-Ring Basins," *The Moon*, Vol 3, p. 4, 1971.

VII-3. Stuart-Alexander, D. E., and Howard, K, A., "Lunar Maria and Circular Basins—A Review," *Icarus*, Vol. 12, p. 440, 1970.

VII-4. Wilhelms, D. E., and McCauley, J. F., *Geologic Map of the Near Side of the Moon*, U. S. Geol. Survey Misc. Geol. Inv. Map I-703, 1971.

VII-5. Baldwin, R. B., *The Measure of the Moon*, 488 pp., University of Chicago, 1963.

VII-6. Lowman, P. D., *The Third Planet*, 170 pp., Weltflugbild Rheinhold Müller, Feldmeilen/Zürich, Switzerland, 1972.

VII-7. McCauley, J. F., Carr, M. H., Cutts, J. A., Hartmann, W. K., Masursky, H., Milton, D. J., Sharp, R. P., and Wilhelms, D. E., "Preliminary Mariner 9 Report on the Geology of Mars," *Icarus*, Vol. 17, p. 289, 1972.

VII-8. Carr, M. H., Masursky, H., and Saunders, R. S., "A Generalized Geologic Map of Mars," *J. Geophys. Res.*, Vol. 78, 1973.

VII-9. Hartmann, W. K., "Interplanet Variations in Scale of Crater Morphology— Earth, Mars, Moon," *Icarus*, Vol. 17, p. 707, 1972.

VII-10. Hartmann, W. K., "Martian Cratering IV: Mariner 9 Initial Analysis of Cratering Chronology," *J. Geophys. Res.*, Vol. 78, 1973.

VIII. Martian Cratering IV: *Mariner 9* Initial Analysis of Cratering Chronology

William K. Hartmann

Planetary Science Institute, Tucson, Arizona 85704

A. Review of Martian Cratering Analyses

Öpik (Ref. VIII-1) and Tombaugh in *American Astronomer's Report* (Ref. VIII-2) surmised that craters might be abundant on Mars. Craters on Mars were proven to exist through photography by *Mariner 4* in mid-1965. In the first analysis of these pictures by Leighton et al. (Ref. VIII-3), it was pointed out that the crater density of the Martian terrain photographed resembled "remarkably closely the lunar uplands." On this basis, Leighton et al. concluded that the age of the surface was 2 to 5 aeons. Immediately following this, Witting et al. (Ref. VIII-4), Anders and ·nold (Ref. VIII-5), and Baldwin (Ref. VIII-6) pointed out that the Martian cratering rate must be higher than the lunar rate and that the age should be appropriately reduced. The three papers gave ratios of Martian to lunar cratering rates of 15, 25, and 5 to 10, respectively, and all derived ages of the Martian craters in the range 0.3 to 0.8 aeon, about one-tenth the initial estimate.

The next generation of crater studies, still based on *Mariner 4* results, revised the age upward to the original estimate. This resulted primarily from utilizing new crater counts on improved *Mariner 4* pictures, from correcting the lunar crater counts which were being used as a reference, and from correcting the erroneous assumption that surface age could be scaled linearly in proportion to the crater density on Mars expressed as a fraction of the crater density on the ancient lunar uplands. The latter assumption is incorrect because the pre-mare lunar cratering rate was much higher than the post-mare lunar cratering rate, which has been more uniform and thus allows better age scaling. Binder (Ref. VIII-7), Hartmann (Ref. VIII-8), and Öpik (Ref. VIII-9) referenced their counts to assumed lunar mare ages of 4.5, 4, and 4.5 aeons (later radiogenic dates from *Apollo* and *Luna* samples: 3 to 4 aeons) and derived ages for the largest Martian craters of 2.2 to 3, 3.6, and >3 aeons, respectively. Hartmann and Öpik pointed out that impact velocity on Mars was different from that on the Moon and applied a correction factor.

With the publication of these papers, agreement appeared to be reached on the essentials of age estimation based on craters and on the result that the large craters

were several aeons old and not post-Cambrian in age. Discussion in the literature at this point turned to effects of erosion and the state of crater preservation. Hartmann (Ref. VIII-8) had pointed out that the mean or maximum age of a group of craters of a given size was strongly size dependent, using the term "crater retention age" for the age of the oldest crater of any given size in the given geologic province. He concluded that many craters smaller than diameter $D = 50$ km had been obliterated by erosion or filling, but that larger craters gave a crater retention age, indicating the late stages of planet accretion Öpik (Ref. VIII-9) similarly concluded that the largest craters had survived from the end of a primeval period of intense cratering, but that many smaller craters had been erased by eolian erosion acting at one-thirtieth the rate found in terrestrial deserts. Binder (Ref. VIII-7) also called for "large-scale subaerial erosion" in the early history of Mars, to account for depletion of craters smaller than $D = 40$ km, and related this result to spectrometric evidence for weathered, oxidized iron minerals that imply a denser atmosphere in the past.

Marcus (Ref. VIII-10) also analyzing *Mariner 4* data, found depletion of craters smaller than about 20 to 30 km, and concluded that the surface was nearly saturated with larger craters. Chapman et al. (Refs. VIII-11 and VIII-12) found that the observed craters were degraded in form and made a comprehensive study of the effect of erosive processes on the morphologies of craters and their diameter distribution. These authors concluded that cratering of Mars had produced a cumulative total of 0.1 to several kilometers of dust, and that either extensive crater overlap or erosion transport processes were required to account for the observed morphologies and diameter distribution. In their more detailed paper, Chapman et al. (Ref. VIII-11) derived a dust-filling model for crater obliteration which predicted a series of crater morphologies close to that observed.

At this time, only 0.5% of the Martian surface had been photographed at high resolution, as pointed out most clearly by Öpik (Ref. VIII-9). Most authors implied that since cratering was an external process and the *Mariner 4* pictures cut a long swath across Mars, the cratering could be expected to be similar in most regions. Other cautions were sounded at this time. Binder (Ref. VIII-13) criticized the counts of Chapman et al. (Ref. VIII-11), Marcus (Ref. VIII-10), and Leighton et al. (Ref. VIII-14) for including many small craters which were not confirmed in comparison of their separate counts. Chapman et al. (Ref. VIII-12) pointed out in reply that these small craters had little effect on the crater density

analyses, which were based on the better determined large craters. Wells and Fielder (Ref. VIII-15) criticized Öpik's (Ref. VIII-9) assumption (and that of the other authors) that the craters being analyzed were principally astroblemes. In retrospect, we note that while recent *Mariner* results have disclosed large volcanic calderas, the *Mariner 4* pictures portrayed what is now known to be a heavily cratered part of Mars in which impact craters are believed to predominate. In summary, it appears that *Mariner 4* analyses yielded a valid and consistent picture of a geologically ancient surface with some erosion effects.

Russell and Mayo (Ref. VIII-16), pursuing an early suggestion by Öpik (Ref. VIII-1) and Tombaugh (Ref. VIII-2), measured the size distribution of Martian oases and concluded that they were impact sites. This has not been confirmed by recent data; Juventae Fons and Lunae Lacus, for example, are chaotic terrain collapse sites; Trivium Charontis is not marked by any usual structure; and other classical oases are of less certain nature. Some oases may be dark patches formed in crater floors.

In mid-1969, the second generation of close-up images of Mars became available with far-encounter and near-encounter picture sequences by *Mariners* 6 and 7. By chance, these two spacecraft took nearly all of their near-resolution images in the highly cratered portions of Mars, as did *Mariner 4*. Furthermore, the far-encounter pictures were taken at a low phase angle and considerably poorer resolution than the high-resolution views. For these reasons, the *Mariner 6* and 7 crater analyses were similar in result to those of *Mariner 4*; neither produced any radical change in the conception of Martian cratering, nor did more than hint at the remarkable heterogeneity later revealed by the *Mariner 9* mission. The principal new relevant results were additional support for the hypothesis of past erosion and suggestions that this erosion, evidence for collapse-induced "chaotic terrain," occurred not at a constant or smoothly changing rate, but in episodic events.

In the preliminary analysis of *Mariner 6* and 7 data, Leighton et al. (Ref. VIII-17) conclude that "several billion years" would be required "to produce the density of large craters . . . in the more heavily cratered areas." This is the first recognition of the differences in crater density from one province to another. Murray et al. (Ref. VIII-18), in the final *Mariner 6* and 7 report, studied not only crater numbers but also crater morphology, and reached a number of important conclusions:

(1) Little correlation exists between crater density and classical albedo markings.

(2) Small craters are morphologically different from big craters, being more bowl-shaped.

(3) Large craters date back to a very early period.

(4) Horizontal transport of material is much greater on Mars than on the Moon and affects the crater forms.

(5) Past erosion processes on Mars may have been episodic.

These conclusions are supported by the present *Mariner* 9 analysis. Conclusions reached by Murray et al. (Ref. VIII-18), which differ from those reached here, include.

(1) "Craters are the dominant landform on Mars."

(2) "The size-frequency distribution of impacting bodies that produced the present Martian bowl-shaped craters differs from that responsible from post-mare primary impacts on the Moon..."

Subsequent analyses of data from *Mariners* 6 and 7 focused on the implications of past erosion history on Mars. Hartmann (Ref. VIII-19) found that the diameter distribution of the craters and dynamics of orbital encounter were consistent with impacts by the asteroid population near Mars and required much greater cratering rates and erosion rates in early Martian history. Hartmann (Ref. VIII-20) suggested that a major agent obliterating craters was the deposition of windblown dust in crater floors. McGill and Wise (Ref. VIII-21) found localized differences in small-crater populations and proposed "general continuity of crater formation and degradation with locally sporadic formation and/or degradation of the smallest craters visible."

Oberbeck and Aoyagi (Ref. VIII-22) opened a new area of investigation by proposing that the incidence of doublet craters (nearly tangent to each other) was much higher than random. Such doublets were compared to the terrestrial examples of Clearwater Lake East and West, in Canada, and were attributed to the breakup of incoming meteoroids by tidal stresses set up during passage through the gravitational field of Mars. This hypothesis has not yet been widely studied.

At the beginning of the *Mariner* 9 mission then, there was consensus on the following points:

(1) In heavily cratered regions, the oldest large craters ($D \gtrsim 50$ km) date back 3 to 4.5 aeons.

(2) The earliest history of Mars (some 10^x years?) was marked by intense bombardment associated with accretion.

(3) More erosion and/or obliteration of craters occurred on Mars in the past than is occurring now, and this erosion may have either been concentrated in the earliest history, occurred in sporadic episodes, or both.

(4) Local variations in cratering from region to region exist, but were believed to be relatively minor.

B. Significance of Crater Morphology

At the outset of any discussion of cratering on Mars, it is crucial to determine the relation between the Martian craters and similar features on Earth and the Moon. Only if the features are related can we use them to understand the evolutionary state of the Martian crust vis-a-vis that of Earth and the Moon; i.e., only then can we capitalize on the *Mariner* 9 opportunity to practice comparative planetology. Therefore, it is the purpose here to demonstrate that Mars exhibits a sequence of crater forms which matches a sequence found on both Earth and the Moon.

A comparison of crater forms on the three planets is complicated by the undoubted presence on Mars of large volcanic craters. The most clearcut examples, such as those near Phoenicis Lacus and Nix Olympica, lie on the summits of volcanic mountains, large even by terrestrial standards. In these cases, identification of volcanic origin is simple because of characteristics such as summit location, scarps, coalescing rims, and other morphologic features. The largest of these volcanic summit calderas is that near Phoenicis Lacus, having a diameter of about 125 km. The diameter of the caldera on Nix Olympica is about 72 km. This raises a question whether similar sized calderas could appear in abundance in other parts of the planet and be mistaken for impact craters. However, the clear diagnostic characteristics of these volcanic craters, the fact that the Martian craters taken in toto match the diameter distribution predicted for impact of asteroid fragments (see later part of this section), and the frequent indications of ejecta blankets suggest that impact craters predominate and that volcanic craters on Mars, at least at the multi-kilometer size ranges considered here, do not constitute the majority of craters.

Figure VIII-1 shows a size comparison of craters of various morphologic types found on Earth, Mars, and
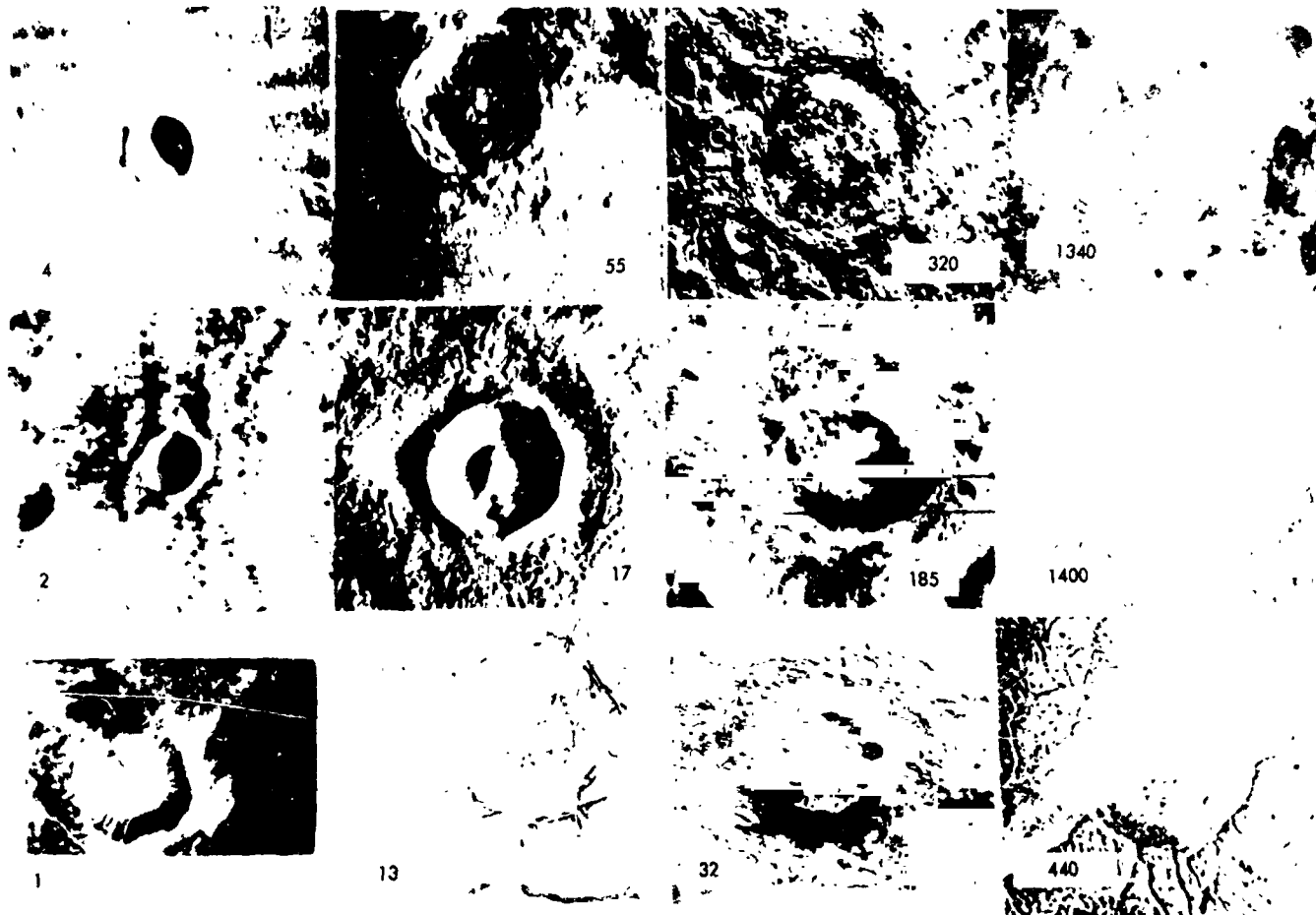
Fig. VIII-1. Comparison of crater types on Moon (top), Mars (middle), and Earth (bottom) showing four types of crater morphology. Diameter in kilometers is given in boldface numbers. Crater types from left to right are bowl-shaped, central peaks, interior ring of peaks, and large basin.

the Moon. If the extensive data on lunar craters are fitted together with field geologic data from studies of terrestrial craters (e.g., Dence et al. in Ref. VIII-23, p. 339), it is evident that a range in crater form exists starting at small diameters with simple bowl-shaped craters, proceeding through what Dence termed complex craters with central uplifts or peaks, and extending to lunar examples of craters with rings of peaks on the crater floor, an example being the crater Schrödinger. At still larger diameters, all manifestations of central mountains disappear and the crater rim is surrounded by a series of concentric ring faults. These concentric systems are not prominent on Mars or Earth, and on the Moon the older examples are severely eroded.

Figure VIII-2 compares the sizes of these crater types on three planets. On Earth, craters as small as 10 km

commonly have central uplifts; on the Moon, the central peak frequency is maximized nearer a diameter of 90 km. Similarly, there is an offset in mean size for other properties, as pointed out in an earlier paper by Hartmann (Ref. VIII-24) based on data from *Mariners 6* and 7. The *Mariner* 9 data confirm the basic observation of the earlier paper, namely that each crater type occurs at smaller physical dimension as the planet grows larger. In the earlier paper, this was attributed to the fact that as surface gravity increases, a smaller volume of rock suffices for gravitational adjustments to overcome the constant strength of rocky material.

It is concluded that similarities exist in basic crater morphology between Martian, lunar, and terrestrial examples, and that most of the larger craters can be compared on the basis of impact theory.
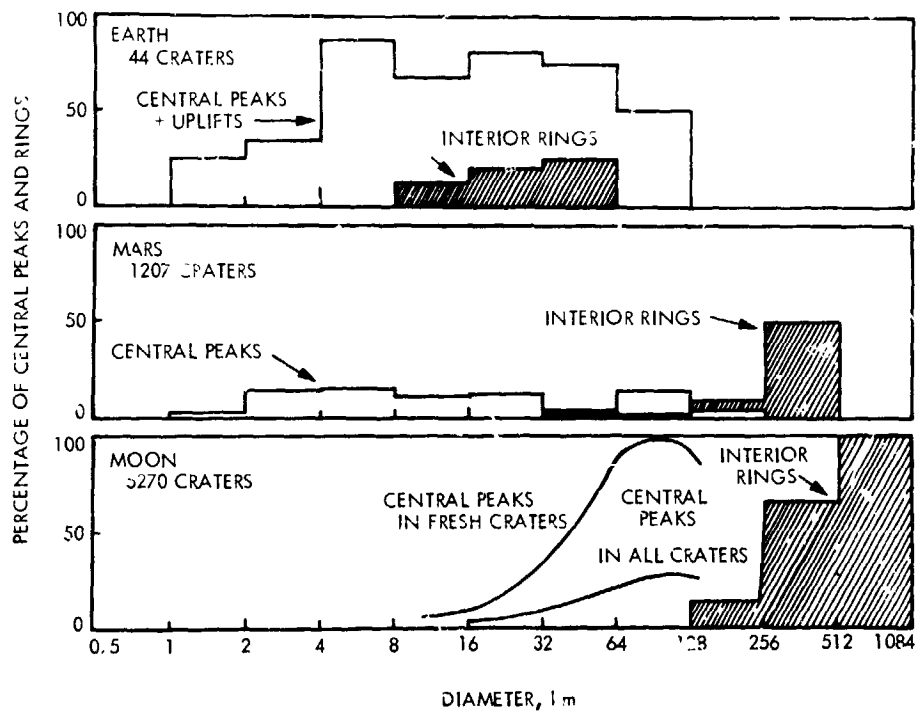
Fig. VIII-2. Histogram showing frequency of occurrence of central peaks and interior rings as a function of diameter for craters on Earth, Mars, and the Moon. Smaller surface gravity results in larger dimension for transition from central peaks to interior rings.

C. Undersaturation: Fossil Record of Asteroid Mass Distribution

The asteroids, which may be related to the population of objects impacting Mars, nearly fit a regular power-law distribution in mass or diameter, except at large sizes, as first pointed out by Kuiper et al. (Ref. VIII-25) and recently confirmed by Van Houten et al. (Ref. VIII-26). The irregularities in mass distribution of large asteroids should be transformed into irregularities in the distribution of large craters on Mars, if most of the Martian craters are caused by asteroidal impacts. The irregularity in question is a flattening of the asteroid size distribution between asteroid diameters of approximately 7 and 50 km.

By converting the asteroid mass distribution into the distribution of crater diameters that would be produced on Mars by asteroid impacts, Hartmann (Ref. VIII-19) predicted that "asteroidal impact craters, if they fall below the saturation line, would show a plateau or flat spot in the crater diameter distribution in approximately the interval $50 < D < 500$ km." The 1971 paper compared the predicted crater distribution with a small sample of craters from *Mariner 4, 6,* and *7* cratering data. Statistical scatter was large among the crater sizes considered, but it was concluded that "the Martian craters do show at

least marginal evidence of the fossil imprint of the asteroid mass distribution." *Mariner 9* data extend the cratering statistics to such a large sample that a much more meaningful comparison can be conducted.

The first problem that must be solved is that of saturation. If true saturation were approached, the diameter distribution of craters would be highly restricted because the diameter distribution would be determined by the maximum geometric packing of craters. Therefore, it is important to guarantee that the areas studied are free from this saturation effect. *Mariner 4, 6,* and *7* pictures all showed regions where the crater density was quite high. *Mariner 9* pictures have clearly shown that some provinces on Mars are sparsely cratered, undersaturated, and apparently young. Thus, it is possible to select regions where saturation 's not important and to test for saturation in other regions.

This has been done in the following way: A crater catalog of all craters down to 64 km has been prepared using *Mariner* pictures and preliminary USGS Mars photomosaic charts for latitudes south of +32° where the north polar haze is not an obscuring influence. The catalog was checked against the USGS airbrush structural map with the result that some 30 craters were

added, bringing the total to 550 craters. To define three provinces, the charts were divided into three groups, sparsely cratered, moderately cratered, and heavily cratered. Only the heavily cratered province approaches saturation. Therefore, we have at least two independent groups of data to determine the size distribution of craters in unsaturated regions, and a test for the asteroidal mass distribution can be attempted.

Figure VIII-5 shows the diameter distributions (in logarithmic increments) for craters in the three types of provinces mentioned. Data from the crater catalog for $D > 64$ km are fitted to counts from individual pictures for $D < 64$ km. The upper envelope for all curves is the saturation line, which is based on data from the most heavily cratered lunar uplands and from experiments. Below the three curves showing Martian provinces are predicted diameter distributions for arbitrary numbers of asteroid impacts based on the recent Palomar–Leiden asteroid survey (Ref. VIII-26) and other sources, discussed by Hartmann (Ref. VIII-19). Figure VIII-3 is thus an updated version of Figure 1 of Ref. VIII-19. The asteroid counts can be adjusted by vertical sliding according to the total density of craters considered.

On the basis of the earlier discussion, it had been hoped that *Mariner* 9 would produce a large enough sample of craters so that the fossil record of asteroid mass distribution could be detected or refuted. However, this would have required a large crater sample, i.e., that all of Mars be cratered to the same density as found in the *Mariner* 4, 6, and 7 regions. Instead, as indicated in Fig. VIII-3, large regions are sparsely cratered and the statistics are insufficient to settle the question. The numerals "2" in Fig. VIII-3 indicate, for each curve, where the number of craters in the logarithmic increment drops to two.

The conclusions reached on the basis of Fig. VIII-3 are:

(1) Even the heavily cratered regions of Mars are not saturated with craters.

(2) At $D \gtrsim 100$ km, the Martian craters are quite consistent with known asteroid statistics.

(3) Although the slope of the size distribution of craters flattens or becomes more positive with increasing size in the size range $D > 181$ km, as predicted from comparison with asteroid mass distributions, the absolute numbers of craters are too small to allow a definite conclusion as to correlation or noncorrelation with the asteroid mass distribution.

(4) No data are inconsistent with asteroid impacts.

Fig. VIII-3. Comparison of observed diameter distributions of craters on Mars (solid lines) with predicted diameter distributions caused by impacts of all Mars-crossing asteroids (upper dashed line) and "% of the "inner asteroids" in the Palomar–Leiden survey (lower dashed line). Uppermost curve is the empirical saturation limit. The observed Mars curves show some flattening at large diameters as would be predicted from the asteroids, but the statistics involve very small numbers. The level corresponding to two craters in a single logarithmic diameter increment is indicated by arrows on each curve.

D. Implication of Hemispheric Asymmetry in Crater Density

Figure VIII-4 shows a Mercator plot of large Martian craters based on the above-mentioned catalog of all craters of $D > 64$ km. The plot reveals a crustal asymmetry. The hemisphere centered south of Deucalionis Regio is heavily cratered, and contains the Hellas, South
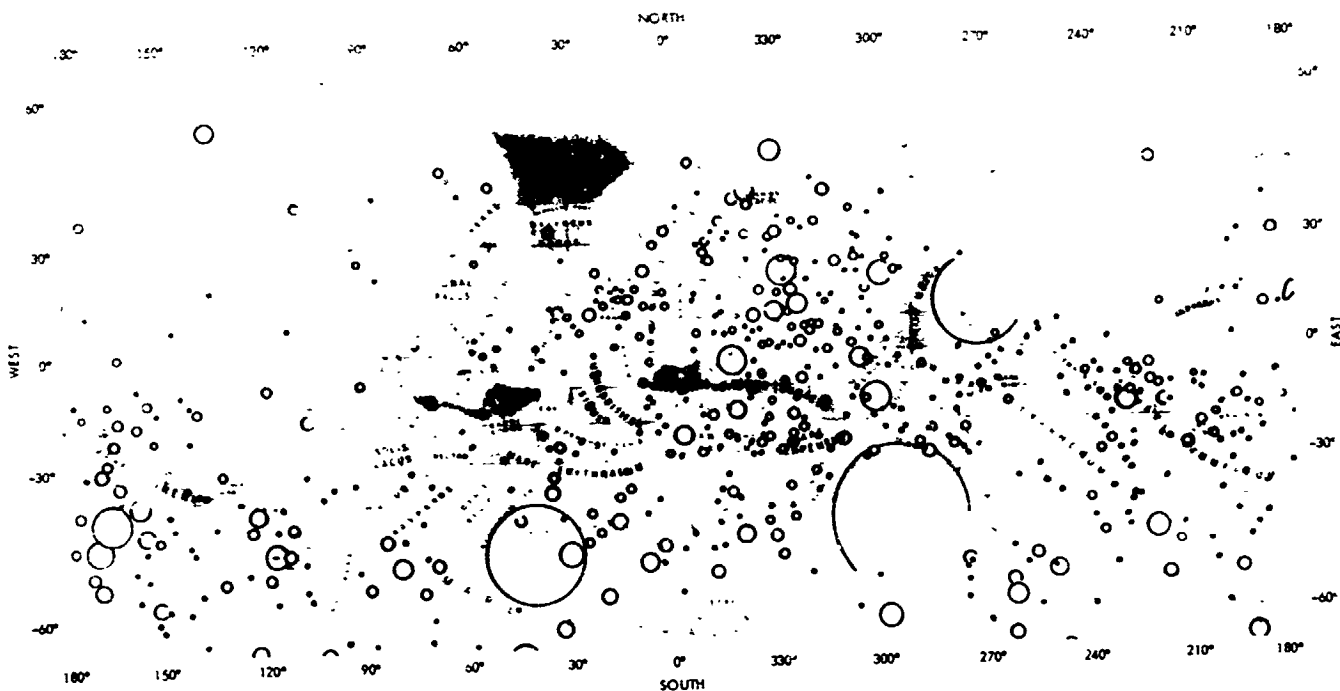
Fig. VIII-4. Distribution of all craters on Mars larger than 64 km in diameter. Solid dots show craters between 64 and 90 km in diameter; open circles show larger craters scaled to their approximate true size.

Polar, Argyre, and Moeris Lacus basins. The hemisphere centered among the volcanoes near Nix Olympica is sparsely cratered. The fact that the south polar region (except for the inner cap itself, latitude $> 80°$) is heavily cratered and that Mariner 9 pictures, after north polar haze clearing, revealed a sparsely cratered north polar region strengthens the hemispheric asymmetry seen in Fig. VIII-4.

The rough division of Mars into heavily and sparsely cratered hemispheres occurs along neither latitude medians nor longitude parallels. Rather the great circle best fitting the division is inclined from about 50°N to 50°S latitude. It is thus extremely difficult to relate such an asymmetry on a rotating planet to external influences, such as nonisotropic meteoroid bombardment. It appears that the crater deficiency in the volcanic region is due to depletion by internally generated processes.

These processes are indicated by the unique geology of the region. The whole bright, sparsely cratered region surrounding Nix Olympica and Tharsis is elevated several kilometers above the mean Martian radius and surrounded by a strong radial pattern of faults. The Coprates canyon lies radial to the domed region. Shield volcanoes reaching an additional few kilometers above this dome lie near its center. The "desert" between the

volcanic shields is characterized on high-resolution ($\frac{1}{2}$ to 1 km) pictures by lobate flow-like structures resembling lunar and terrestrial lava flows.

Clearly, strong volcanic and tectonic activity has obliterated the ancient cratered crust in the Tharsis volcanic dome, the Elysium volcanic dome. and nearby areas. The nature of such processes will be discussed elsewhere in a separate paper;[1] evidence points to crustal updoming of a type recognized on Earth and reflecting incipient convection, but falling short of full-fledged plate tectonics as developed on Earth. It is of interest to note that hemispheric asymmetries of crustal structure appear on the Moon (mare/terra), Mars, and Earth (oceanic/continental), probably indicating that primeval uniform surfaces become heterogeneous through the action of impact basin formation, sediment deposition, and mantle activity.

E. Relative Dating: Survey of Crater Densities

Figure VIII-5 shows the map of Mars contoured according to density of craters of $D \geq 64$ km. There is no correlation between the density of these large craters and

---

[1] Accepted for publication in Icarus.
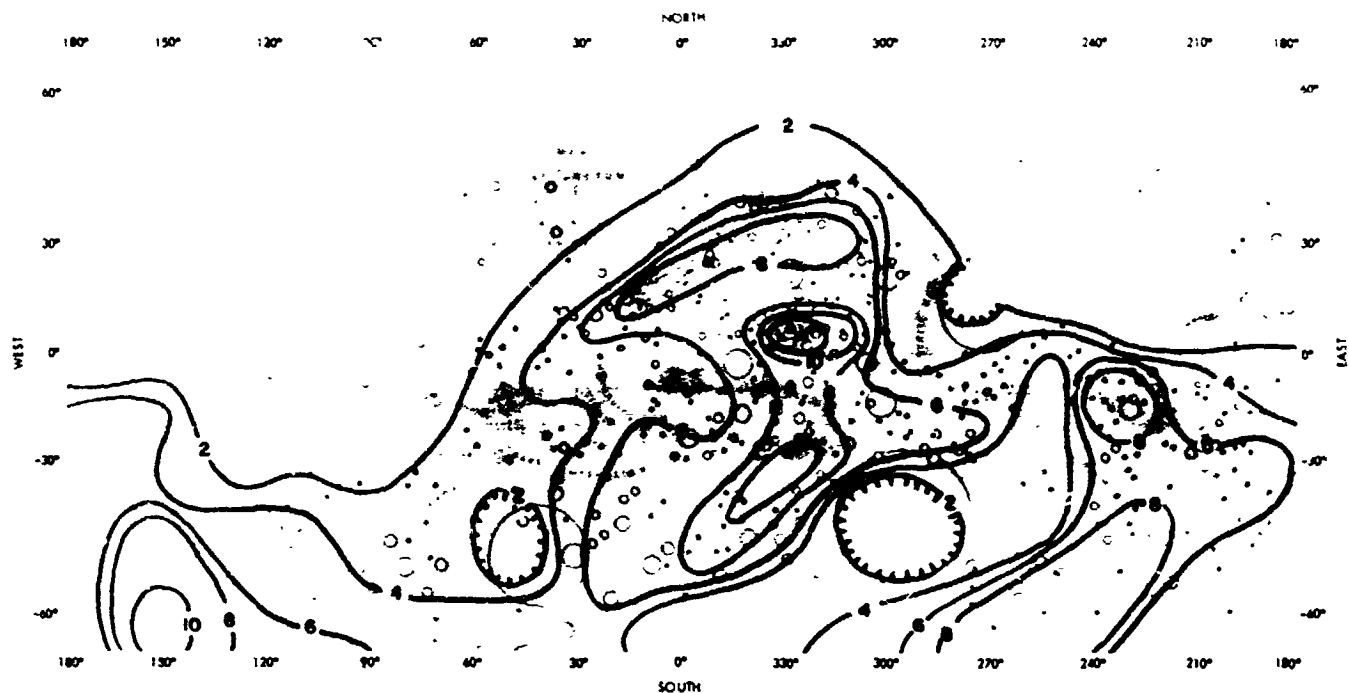
Fig. VIII-5. Contours of crater density on Mars for craters larger than 64 km in diameter. Units give the number of craters per equal-area block (block area $\approx 8.05 \times 10^5$ km^2).

the classical albedo markings seen from Earth. Although a number of bright "deserts," such as Tharsis, Elysium, Argyre, and Hellas, have much lower density than dark "maria," such as Mare Sirenum and Sinus Sabaeus, a simple correlation between darkness and high crater density is violated by the large, bright cratered regions of Moab and Arabia. Hence, craterform surface irregularities or crater ejecta patterns are not the direct cause of the classical markings.

The largest Martian basins, indicated on Fig. VIII-5, have bright featureless floors where crater density is anomalously low. This suggests either that the basins are being filled in by blowing dust, or that such dust (of light color) has formed a veneer over smooth, stratigraphically young lava deposits similar to those that filled the largest lunar basins.

An examination of Martian crater densities on the global scale, as revealed by Figs. VIII-4 and VIII-5, suffices to construct a generalized stratigraphic column, i.e., a relative chronology, which is shown in Table VIII-1. This part of this section describes this, and subsequent parts indicate the degree to which absolute dates can be determined, and how the varying shape of the crater diameter distribution can be used to interpret localized geologic history.

Figure VIII-6 is a summary of Martian cratering data and serves as a useful introduction to the discussion of erosion history. That the heavily cratered region falls below the saturation line found on the Moon is a sure indication that substantial erosive and depositional processes have destroyed the earliest traces of accretion. However, the high density of craters in regions such as Deucalionis Regio and neighboring areas photographed by *Mariners* 6 and 7 suggests that these areas are quite primitive and may date back to the end of the accretion process. This conclusion is in accord with the previous analyses of Martian cratering, as discussed in the first part of this section. The marked irregularity in slope of the cratering curve for heavily cratered areas at diameters about 5 to 50 km is a strong indication that many smaller craters have been obliterated, as lunar, cometary, and asteroid observational data indicate that the initial diameter distribution of craters smaller than about 64 km should be a power law forming a straight line with slope about -2 (Refs. VIII-11 and VIII-20).

A significant new feature revealed by *Mariner* 9 is the behavior of craters smaller than 4 km in diameter, as shown in Fig. VIII-6. In both the heavily and sparsely cratered regions, this curve displays the approximately -2 slope characteristics of uneroded terrain, where no craters have been removed from the initially produced

Table VIII-1. Preliminary relative chronology based on observed crater densities

Time	Event	Observational data
Recent	Minor erosion and obliteration at sub-hectometer scale (greater rate than lunar erosion)	Dust storms, variable deposits, but lack of severe crater obliteration among hectometer-scale craters ($D < 100$ m)
Episodic?	Flow channel formation (water flow?)	Sparsely cratered, dendritic, sinuous flow channels
Continuing process?	Cyclic deposition and destruction of pre-existing relief in polar caps	Sparsely cratered polar regions (latitude 75° with layered structure)
	Shield volcano formation	Sparsely cratered shields near Tharsis and elsewhere
	Subsidence and collapsing	Fractured and partly destroyed craters around rim of chaotic terrain
Relative chronology uncertain	Extensive volcanism	Flows and large shield volcanoes in sparsely cratered provinces in and around Tharsis
	Stressing and tectonic fracturing	Major lineament pattern radial to elevated Tharsis region
	Transport and partial infilling of major basins, e.g., Hellas	Sparsely cratered, bright floors in depressed basins
	Modest erosion transport, deposition, and crater obliteration	Evidence for partial obliteration (by filling?) of intermediate-size, old craters (10 km $< D < 60$ km); deficiency of kilometer-scale craters with respect to Phobos
	Extensive erosion	Even most heavily cratered provinces are not quite saturated with craters
	Formation of large basins, e.g., Hellas	Traces of ejecta blanket around Hellas
Very early	Heavy cratering, accretion	Most heavily cratered provinces nearly saturated

diameter distribution. Most of these craters are sharp and bowl-shaped, as first discussed in detail by Murray et al. (Ref. VIII-18). These facts. together with the evidence for heavy early erosion, indicate that the amount of erosion on Mars in the recent geologic past is less than in the distant past. While the average rate of erosion has shown a decline, we cannot be sure that the decline has been monotonic, as the existence of arroyo-like channels and stratified polar deposits strongly suggests episodic variations in erosive rates superimposed on the general decline. While these qualitative interpretations are summarized in Table VIII-1, we will next attempt a more quantitative interpretation.

F. Absolute Dating: Interplanetary Correlations in Cratering Chronology

In analyzing craters on the Martian surface, we are in the favorable situation of having already dated cratered comparison surfaces on two planets, and uneroded surfaces near Mars on Phobos and Deimos. All these surfaces, in different regions of the solar system, can be utilized as control surfaces. The question addressed here is how best to utilize these data in order to illuminate Martian chronology.

It is desirable to prepare a master diagram showing crater density versus age for all dated surfaces in the solar system. From this could be read the ages of Martian provinces on the basis of known crater densities. In principle, such a diagram could be purely empirical although, in the present stage of exploration, some assumptions must be made about the mass distribution of impacting bodies and about time behavior of cratering in the past, as indicated by the following discussion.

Let D = crater diameter, T = crater retention age of surface for specified D, F = crater frequency for the same specified D (also called crater density), and R = rate of formation of craters/km² for craters of the same specified D. If the cratering rate, R, were constant

$$T = F/R$$

But we know from *Apollo* and *Luna* analyses that R has not been constant. Therefore, we assume only that the time dependency of the cratering rate, $R(t)$, has been the same for all planets, i.e., normalizing to the Moon

$$R(t)_{planet}/R(t)_{Moon} = k_{planet} = \text{constant for all times } t$$
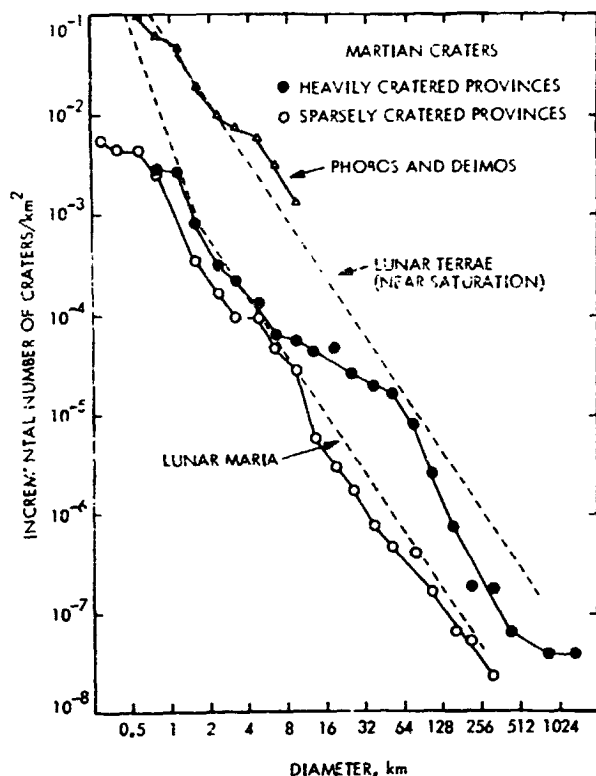
Fig. VIII-6. Diameter distributions of craters (averaged from many Mariner 9 pictures) in heavily and sparsely cratered Martian provinces (defined in text). For comparison, the uppermost curve (triangles) shows crater densities observed on Phobos and Deimos. Martian craters smaller than 8 km are deficient by one to two orders of magnitude relative to Phobos and Deimos, a fact indicating extensive Martian crater obliteration processes.

Thus, k varies from planet to planet, but for any planet is time-independent. In terms of accretionary theory of planet growth, this is equivalent to assuming that the solar nebula cleared uniformly, although the density of interplanetary debris depended on position.

The crater retention age of a surface on any planet should therefore be proportional to a quantity defined here as adjusted crater density, F/k; that is

$$T = F/R_{planet} = F/kR_{Moon} \propto F/k$$

The objective of this discussion is thus to construct an empirical plot of adjusted crater density, F_{planet}/k, against age for dated surfaces, so that data from all planets will fall on a single curve, which may then be used to date Martian surfaces.

Cratering rate is defined here as the rate of formation of craters of a specified D, or as the rate of impacts of

given energy, but not as the number of impacts by particles of a given mass. The difference arises because the impact velocity on different planets differs because of orbital and gravitational effects. Modal impact velocities for the Moon, Mars, and Earth are listed by various sources as 14, 10, and 18 km/sec, respectively (see summary by Hartmann in Refs. VIII-8 and VIII-19). According to energy scaling laws, crater diameter is approximately proportional to $(MV^2)^{1/3}$, where $M =$ meteorite mass and $V =$ velocity. Hence, to match a lunar crater of given size requires a terrestrial impact by a meteorite only 0.6× as massive as that striking the Moon and a Martian impact by a meteorite 2× as massive.

We will now attempt to define the relative Martian, terrestrial, and lunar cratering rates (i.e., k values) by normalizing to the Moon because the best crater statistics and related age data are lunar. Determination of k requires determination of the space density of meteoroids at the planetary orbit, determination of gravitational cross-section effects, and determination of impact velocity effects. In the case of Earth and the Moon, the main difference in k is caused by gravitational cross-section differences, as pointed out by Mutch (Ref. VIII-27), who derives a terrestrial impact rate 2.15× as great as the lunar rate for a given mass. Because terrestrial meteorites strike at higher velocity, bodies only 0.6× as massive are required to cause a crater of the same size as a crater formed on the Moon. Hence, because of the meteoritic mass distribution law for cumulative number, N, and mass, M, $N \propto M^{-0.7}$, this corresponds to an increase by 1.4 in cratering rate, giving 1.4 × 2.15, i.e., a rate 3.0× higher on Earth than on the Moon. However, this must be reduced by several factors, such as the focusing effect of the Earth on the front face of the Moon and the size-dependent atmosphere breakup of weak meteoritic and cometary material in Earth's atmosphere. These factors are discussed in more detail by Hartmann in Ref. VIII-8. It is thus concluded that the effective terrestrial crater formation rate is about 2× higher than that on the Moon for the crater sizes considered here (1 to 100 km).

To determine the cratering rate ratio, k, for Mars, we must first investigate the meteoritic environment at Mars. Four sources of data serve to estimate the Martian meteoritic environment: (1) The Mariner 4 dust detector measured a micrometeorite flux (impacts m⁻² sec⁻¹) increasing away from Earth to a value of 4.5× that at Earth, measured at the perihelion of Mars. Beyond perihelion, lower values were recorded, suggesting that Mars efficiently sweeps up material in orbits overlapped by its own. The mass distribution recorded for small

particles near Mars orbit was similar to that near Earth (Ref. VIII-28). (2) Dycus (Ref. VIII-29) has reviewed meteorite distribution in the solar system and concluded that the flux in undisturbed space at Mars averages 14× that at Earth's orbit, and at the top of the Martian atmosphere, 7× that at the top of Earth's atmosphere. (3) Data of Anders and Arnold (Ref. VIII-5), from a computer calculation of asteroid histories, give an asteroidal flux at Mars about 25× the meteorite flux at Earth. (4) Data on known Mars-crossing asteroids and their lifetimes have been utilized by the author, along with data of Öpik (Ref. VIII-30) and Dycus (Ref. VIII-29), to compute Martian environment fluxes for the largest impacting bodies. All these data taken together are relatively consistent in agreeing on the following statement: The particles in Mars' orbit have the same mass distribution as that measured near Earth and the Moon, but have about one order of magnitude higher number density, with an uncertainty of about a factor of 3. Because these particles impact Mars at 10/14 the speed that applied to impacts on the Moon, particles 1.96× larger are needed to form a crater of given size; hence, the cratering rate is diminished by $1.96^{-\text{?}}$, or 0.62. Hence, the Martian cratering rate is 6.2× the lunar rate.

The uncertainty of a factor of 3 in Martian flux immediately indicates that our absolute dates will have an uncertainty at least this large. However, our current total ignorance of absolute Martian chronology makes the ability to discriminate even 10^7 and 10^9 year old surfaces useful.

In order to plot the desired diagram of adjusted crater density, D/K versus age, it is necessary to summarize available data on dated cratered surfaces in the solar system. Lunar data through *Apollo 15*, including *Luna 16*, have been analyzed in detail by Hartmann (Ref. VIII-31). Astroblemes on the Canadian Shield, which has an exposure age of about 1.3 aeons and is younger than lunar surface, were analyzed by Hartmann (Ref. VIII-32) and Baldwin (Ref. VIII-33). Fifteen astroblemes larger than $D = 8$ km were cataloged in an area of 3.7×10^6 km². In order to extend our time scale, it is desirable to find a considerably younger area that is cratered and well studied; for this reason, certain eastern states in the United States, covered with Paleozoic and Cenozoic sediments of exposure age about 0.3 aeon, were studied. This updates an early analysis by Shoemaker et al. (Ref. VIII-34). Ten astroblemes or crypto-volcanic structures of $D > 4$ km were cataloged in a ten-state area of 1.72×10^6 km².

In the lunar areas cited, the diameter distribution of craters, and hence the crater density F, is well defined, and most of the relevant crater counts have been published. However, in the Canadian Shield and eastern United States, erosion effects are important, and a detailed discussion is in order.

Diameter distributions of craters in Canada and in the eastern United States are plotted in Fig. VIII-7. The distributions probably do not follow the normal -2 power law by craters on well preserved surfaces, as expected in view of the active erosion in the regions considered. The effective exposure ages of the two areas are estimated to be 1.1 and 0.3 aeons, respectively. In order to measure the crater density in these eroded terrestrial provinces, from the scanty statistical sample, we assume the basic premises of Hartmann (Ref. VIII-20), to which the reader is referred. The result of that discussion is that, at sufficiently large diameter, the original -2 power law will be followed, whereas below a certain diameter, erosion will have affected the distribution, and a more gentle (less negative) slope or a turnover will be observed. Under certain idealized circumstances of extended obliteration by deposition, a -1 power law is expected, but a sharp episode of deposition would produce a sharp cutoff. According to the 1971 discussion (Fig. VIII-2), the smallest diameter crater retained since province formation in the Canadian province (1.1 aeon) is about 128 km and in the U.S. province (0.3 aeon) is about 32 km. Therefore, in order to deduce the crater density from Fig. VIII-7, we have several useful boundary conditions:

(1) Slopes of about -2 are expected above the diameters mentioned.

(2) Immediately below the diameters mentioned, a more gentle slope is expected.

(3) Numbers of astroblemes known in the literature are sufficiently large to give some confidence that the intercepts (vertical positions) of these curves can be located in Fig. VIII-1.

(4) Crater density (intercept) in the Canadian Shield should be higher by a factor of 3.7 than that in the eastern United States because of its greater exposure age.

Figure VIII-7 includes dashed curves that show the interpreted North American crater densities based on the above considerations. The similarity of the data in the segments with -1 slopes indicates similar obliteration rates, i.e., similar extended erosion effects, in the Canadian and U.S. provinces.
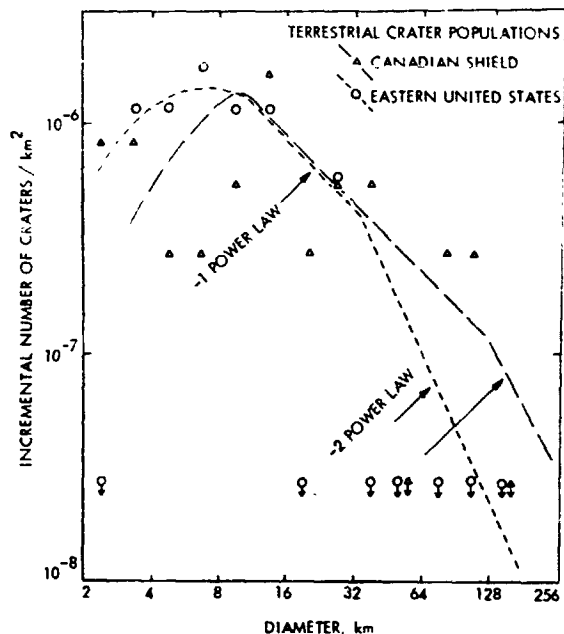
Fig. VIII-7. Attempts to derive crater densities on the Canadia·i Shield and in the eastern United States. Intervals containing no craters are shown by downward pointing arrows at the bottom. The dashed lines are fitted to the data following theoretical boundary conditions (described in text).

In order to compare crater densities on different planetary surfaces, we must now adopt a convention for expressing crater density. This could be done, for example, by using the cumulative number of craters/km² larger than a certain size; for example, 64 km or 1 km. But a difficulty arises because, at 1 km, erosive effects are large on Earth, and confusion with secondary craters and endogenic craters exists on the Moon. If we adopt a diameter cutoff as large as 64 km, which would avoid the terrestrial erosion problem, we are limited to large areas with consequent low resolution of specific dated geologic provinces. Clearly, some intermediate diameter is optimum and some extrapolation and interpretation of crater curves will be necessary, as was exemplified by the *extreme* case of interpretation required in Fig. VIII-1. I have previously adopted a convention that seems to remain useful here. Instead of defining crater density in terms of actual cumulative numbers per kilometer at a certain diameter cutoff, a relative crater density scale is used, the average overall front-side lunar maria defined as unity, as this provides the best combination of crater statistics and age determination of any solar system surface. The maria present, incidentally, a cumulative crater density of $F = 2.0 \times 10^{-4}$ craters larger than 4 km/km². Densities on other stratigraphic units are determined by comparing the entire diameter distribution, with emphasis given to the diameter range from 2 to 64 km (where statistics are good), with no weight given to diameter ranges where the slope seriously departs from values between -1.8 and -2.2 (a departure in all cases so far studied believed to result from erosion processes).

Table VIII-2 shows the data we have assembled and allows a plot correlating ages and crater densities on various planets. Figure VIII-8 shows this plot. The dashed line in Fig. VIII-8 shows that the data for the

Table VIII-2. Crater data for dated· surfaces

Surface	Age, aeons	Crater density, D, relative to lunar material	Applicable relative cratering rate, k	Adjusted crater density, D/k
Moon, Uplands	4.4?	>32 (saturated)	1	32
Phobos, Deimos	4.2?	>32 (saturated)	6	5.4
Apennine Front	4.1	2.9	1	2.9
Fra Mauro	3.9	2.5	1	2.5
Mare Tranquillitatis	3.6	1.6	1	1.6
Mare Fecunditatis	3.45	0.6	1	0.8
Palus Putredinis	3.3	0.35	1	0.35
Oceanus Procellarum	3.2	0.75	1	0.75
Canadian Shield	1.3	0.67	2	0.33
Eastern U. S.	0.3	0.13	2	0.065

·For saturated surfaces such as the lunar ·.·olands, Phobos, and Deimos, there are no radioisotopic dates, but the saturation with craters and independent calculations of cratering rates during early accretion history suggest ages near that of the solar system.
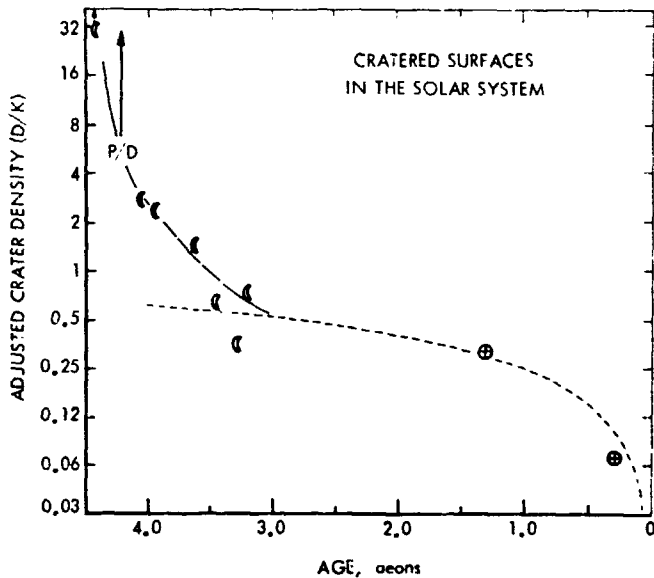
Fig. VIII-8. Synthesis of solar system data on age of cratered dated surfaces on Earth and the Moon. P/D marks assumed age and measured crater density on Phobos and Deimos. Age is plotted versus "adjusted crater density" as defined in text. Dashed line shows a fit assuming constant cratering rate; before 3 aeons, the cratering rate was much higher. Estimated ages of Martian surfaces are read as discussed in text.

last 3 aeons are compatible with a constant cratering rate, within a factor of 2; but before 3 aeons ago, the cratering rate was much higher. This result has been found previously by Öpik (Ref. VIII-9), Hartmann (Refs. VIII-19 and VIII-32), and Baldwin (Ref. VIII-33). The constancy of the cratering rate in the last 3 aeons gives added confidence that we can date young Martian features, such as Nix Olympica, by direct scaling to known cratering rates measured on Earth and the Moon, without much concern for our assumption that the time behavior of change in cratering rate was the same for Mars, Earth, and Moon.

G. Absolute Dating: Analysis of Erosion History

Figure VIII-9 shows an application of cratering theory to the raw data used in Fig. VIII-6. Several theoretical curves are given to indicate the predicted crater diameter distribution at various times in the past, under conditions hypothesized for Mars. These theoretical curves, to be discussed below, are based on the crater obliteration theory developed in various forms independently by Öpik (Ref. VIII-9), Hartmann (Refs. VIII-8 and VIII-20), and Chapman et al. (Ref. VIII-11). The specific theory applied here was first developed in essentially the pres-

ent form in an unpublished thesis by Chapman (Ref. VIII-35).

The theoretical curves in Fig. VIII-9 are developed as follows: From the previous paragraphs, we have a best estimate of the crater formation rate on Mars at present. This is 6.2× the lunar rate, or 3.54 (10⁴) craters larger than 4 km/km²/aeon. Thus, curves AA' and BB' in Fig. VIII-9 can obviously be constructed to represent the numbers of craters formed in 10⁷ years and 10⁸ years, respectively, at the *present* cratering rate. The number of craters formed in 4 × 10⁹ years (CC') is not so easily plotted, however, as the early cratering rate is believed to have been nonuniform. Curve CC', therefore, is based on the data in Fig. VIII-8 and lies at 9× curve BB' (≠ 4× curve BB'). Curves AA', BB', and CC' all reflect cratering with no erosion whatsoever.

Curve EE' represents the steady state of craters under a constant rate of deposition, about 10⁻⁴ cm/yr in crater
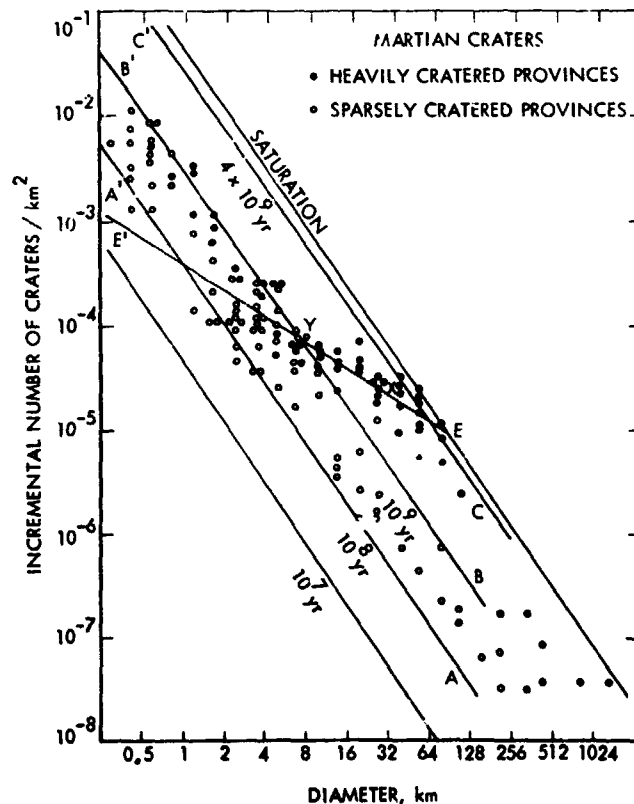
Fig. VIII-9. Raw crater counts for heavily cratered and sparsely cratered provinces on Mars (compare averaged results in Fig. VIII-6), with theoretical isochrons as derived in text. Solid lines marked 10⁷, 10⁸, 10⁹, and 4 × 10¹¹ years show crater densities expected with no erosion for surfaces of the indicated ages. The line EE' is a theoretical result based on erosion and deposition at a constant rate (see text).

floors. This deposition can be viewed as principally due to windblown dust, as discussed by Hartmann in Ref. VIII-20, or as a cumulative effect of various other erosion processes of constant effect averaged over long periods. (Deposition at other constant rates would have the same slopes, but different vertical intercepts. Deposition at non-constant rates would have different slopes. Sudden catastrophic deposition, e.g., by lava inundation, would produce a near-vertical cutoff in craters. See works cited above.)

If the heavily cratered regions filled curve CXE', the interpretation would be that these regions formed 4 aeons ago, have been cratered continually since, and have experienced a constant erosion and deposition rate with 10^{-4} cm/yr accumulating in crater floors. However, the heavily cratered regions do not fit the segment XE', but rather have the additional complexity of bending nearly along XYB'. The segment YB' falls on the curve of a surface cratered with no erosion for about the last aeon. It is concluded that:

(1) The oldest parts of Mars reveal a history that begins just after the accretion phase ceased.

(2) The original accreted surface was largely destroyed by early intense erosion (effects of an early dense atmosphere?), accounting for the fact that the surface is not now saturated.

(3) A long period ensued in which erosion occurred at a relatively constant, intermediate rate. (Episodic "fine structure" in this erosion cannot be excluded.)

(4) During roughly the last aeon, the erosion and deposition rate has been so much reduced from its former value that most kilometer-scale craters this young show negligible erosion effects.

In Ref. VIII-20, the bowl-like morphology of kilometer-scale craters, noted by Murray et al. (Ref. VIII-18), was treated as an unsolved puzzle. This is now accounted for by the lack of recent erosion. Indeed, it is now clear that the sharp, bowl-like morphology and the complete preservation of these craters reflected in the diameter distribution strongly *necessitate* the conclusion that erosion on Mars recently has been much reduced from its former values.

Figures VIII-10 and VIII-11 present the detailed curve fitting, based on the idealized, simple theory presented above, for the raw data applying to the heavily and sparsely cratered regions, respectively. The theoretical curve fitted to the heavily cratered provinces (Fig.
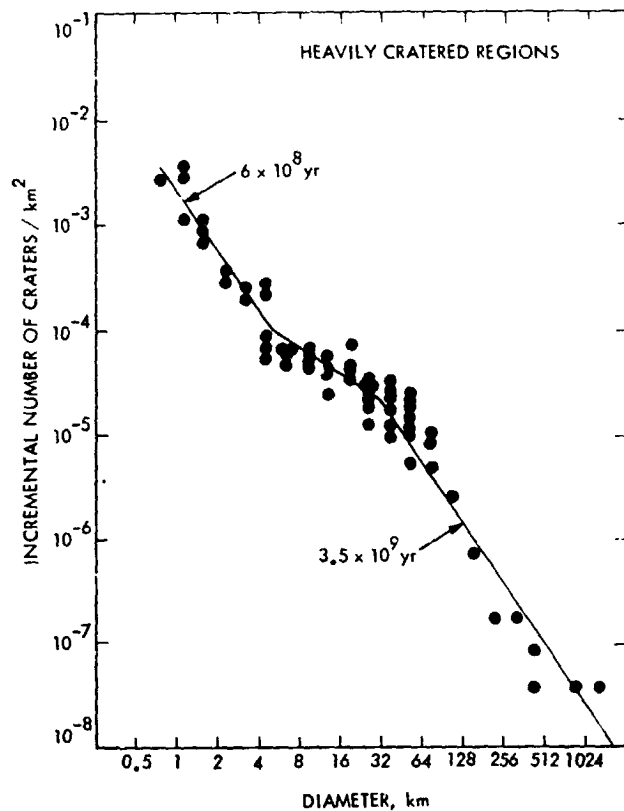
Fig. VIII-10. Crater diameter distribution in heavily cratered regions fitted to two isochrons (3.5 and 0.6 aeons) and showing a flattened segment characteristic of deposition before 6 aeons ago.

VIII-10) would fit a 3.5-aeon-old region in which deposition in craters occurred at a rate of 10^{-4} cm/yr until 0.6 aeon ago. The fitted curve assumes that erosion was negligible for the last 0.6 aeon. The curve fitted to the sparsely cratered region describes an area that formed (by volcanic inundation?) 0.3 aeon ago. A marginal "kink" in the curve between 2 and 4 km suggests some erosion (perhaps the end of the erosion indicated by Fig. VIII-10?) reduced to a negligible value by 0.25 aeon ago.

Figures VIII-10 and VIII-11 contain data summarizing the two dissimilar hemispheres of Mars. Their analysis, in the preceding paragraph, is believed to indicate in first-order terms the erosional history of Mars. In detail, the history may be more complex. The essence of the conclusion supports an inference by Binder and Cruikshank (Ref. VIII-36) that a much more extensive atmosphere was required in the past to create the limonite, or oxidized basalt, coloring Mars, and at the same time sheds light on the existence of arroyo-like channels. The implication is that a denser atmosphere and greater

116
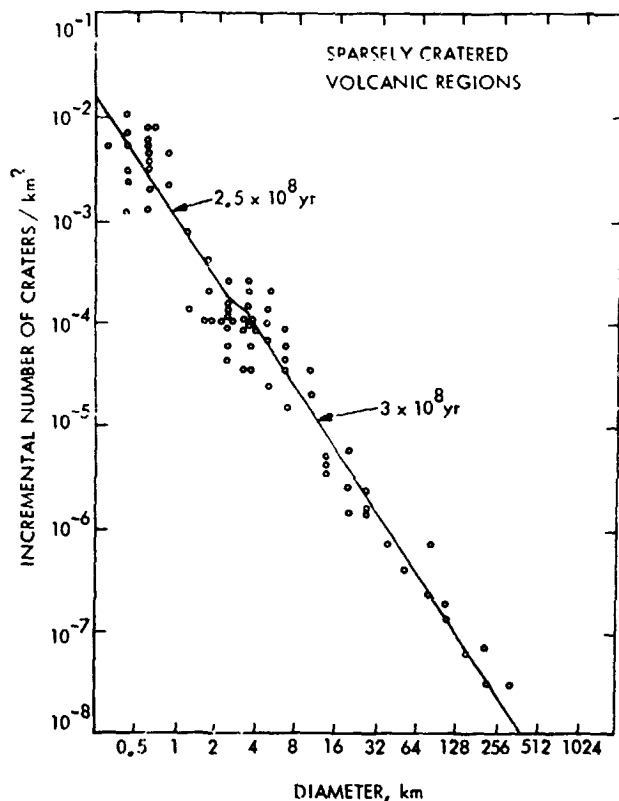
Fig. VIII-11. Crater diameter distribution in the sparsely cratered, volcanic regions fitted to isochrons from Fig. VIII-9. The flattened segment between 3 and 2.5 × 10⁵ years is of marginal significance, but serves to illustrate resolution in time scale.

Fig. VIII-12. Crater diameter distribution observed on slopes of Nix Olympica volcano with that from lunar maria for comparison. Craters larger than 8 km in diameter are primarily calderas near the summit. Solid line is an isochron corresponding to primary impact cratering for 1.3 × 10⁵ years.

humidity applied before 600 million years ago on Mars, and that only the volcanic provinces, such as Tharsis, exhibit surfaces contemporaneous with the post-Cambrian stratigraphic column on Earth.

H. Absolute Dating: Martian Shield Volcanoes

Figures VIII-12 through VIII-15 show attempts at detailed analysis of specific Martian features, namely four of the widely publicized volcanoes with summit calderas. These were chosen as probable representatives of the youngest constructional geologic features, whose dating would indicate the most recent volcanic activity of major extent on Mars.

The principal problem here is the abundance of volcanic pit and chain craters that lie on the flanks of the large volcanoes. By counting all discernible craters (as has been done in the preceding paragraphs, with the exception of the large obvious calderas such as Nix Olympica), one would count many endogenic craters along with impacts and determine only an upper limit

on age. In the case of Nix Olympica (Fig. VIII-12), clearcut calderas of $D > 16$ km cluster near the summit, but the craters of $D < 2$ km on the slopes define a fairly clear curve with slope equal to that expected for the impacts. Thus, the low-diameter end is used to fit an isochron as shown in Fig. VIII-9, and this curve is found to correspond to an age about 1×10^8 years. A different technique is used for the volcanoes near Nodus Gordii (Fig. VIII-13) and Ascraeus Lacus (Fig. VIII-14). All craters were counted, but then suspected impacts were separated out by rim and interior morphology and plotted with a different symbol. The isochrons fitted were weighted toward the data for impacts only. In Fig. VIII-14, the additional measure was taken of counting craters on the floor of the plain immediately in contact with the base of the Ascraeus Lacus shield. It was found that the sum of all craters outnumbers the craters on the plain, indicating once again that the shield has an admixture of endogenic craters, since the shield is assumed to have a constructional surface younger than the plain. The counts of probable impacts fit fairly well with the counts of craters on the plain, which is believed to
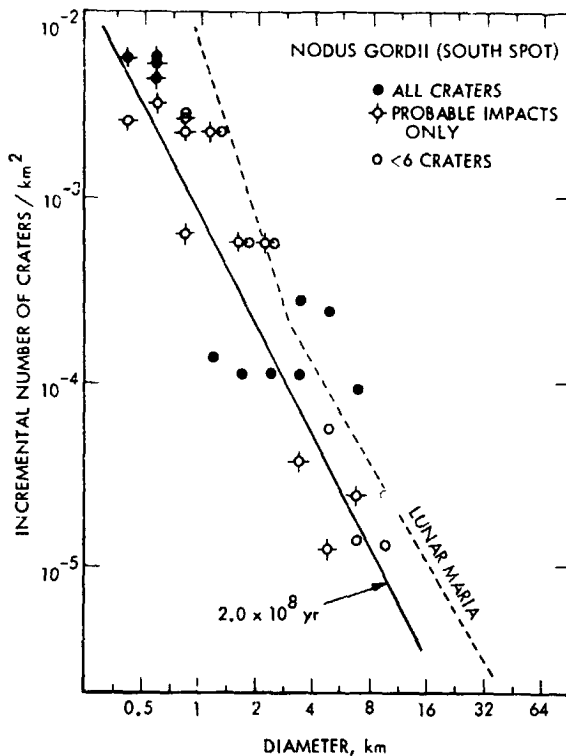
Fig. VIII-13. Crater diameter distribution for Nodus Gordii volcano, with comparison to lunar maria. Solid line is an isochron fitted to probable impact craters only and indicates primary impact cratering for 2×10^8 years.

Fig. VIII-14. Crater diameter distribution on Ascraeus Lacus volcano with comparison to lunar maria. Solid line is an isochron fitted to probable impact craters and indicates primary impact cratering for 1×10^8 years. Solid data points = 6 or more craters/diameter increment in each picture studied; open circles, less than 6.

be relatively free of endogenic craters. For Pavonis Lacus (Fig. VIII-15) the craters counted were, on most of the pictures, not readily distinguishable into impact and non-impact craters, but it was believed, on the basis of fault patterns, that some of the smaller craters may associate with chains and clusters of endogenic craters. Thus, the drawn isochron is weighted toward the less abundant larger craters ($D > 2$ km).

An upper limit of age can be based on isochrons drawn through the data for all craters, although it is believed that the isochrons in Figures VIII-12 through VIII-15 are closer to the actual caldera ages. It is concluded in this way that all four of the well known volcanoes have surfaces that formed less than 500 million years ago. Within the uncertainty of the method, they all appear to have formed about 100 million years ago.

I. Absolute Dating: South Pole

It is evident from *Mariner 9* pictures that, in the extreme polar zones, craters have been obliterated and replaced by topography composed of numerous stratified

layers. Original relief must have been destroyed, as there is no mechanism to prevent craters from forming at the poles. The fall-off in crater density is particularly sharp between 80° and 81°S latitude.

Mariner 6 and *7* results indicated a lower crater density near the south pole than elsewhere (Ref. VIII-20), but it remains of interest to estimate the age of the youngest regions as an indication of the youth of recent erosion and deposition processes on Mars. The following paragraphs present a preliminary analysis of the extreme south polar region south of 81° latitude, based on the data in Fig. VIII-16.

Because of the sparseness of cratering and the small size of the region considered, the statistics on craters are scanty. The few large craters present ($D > 8$ km) have been recorded on the USGS airbrush south polar map; in addition, counts have been made on several wide- and narrow-angle pictures of *Mariner 9* and two *Mariner 7* pictures. In view of the paucity of craters, it
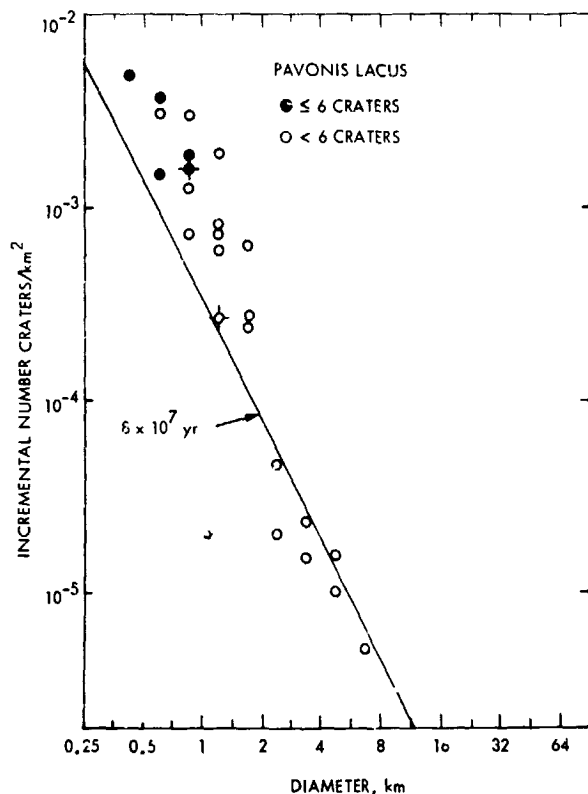
Fig. VIII-15. Diameter distribution of craters on Pavonis Lacus volcano. Solid line is an isochron indicating primary impact cratering for 8×10^7 years.

Fig. VIII-16. Diameter distribution of craters through extreme south polar region (south of −81°). Isochrons of 10^7 and 10^8 years are indicated, but these have steeper slopes than the dashed line which is fitted to the observed data. The data are interpreted to indicate deposition at a declining rate; 1-km craters in the south polar zone appear to be less than 10^8 years old. "Z" indicates diameter increments with no craters counted on each picture studied (see text for method of plotting).

was believed helpful to indicate diameter increments on Fig. VIII-16 where no craters were counted on some pictures. These instances are represented as Z points and are plotted in Fig. VIII-16 at a vertical position corresponding to one-half crater. This was done up to 2 diameter increments beyond the largest observed crater in a given picture and in "empty" diameter increments bracketed by increments with craters. Only one picture in this region yielded as many as six craters in a single diameter interval. The counts at $D > 1$ km are regarded as defining the upper limit of impact crater density in the polar zone, since I attempted to include all possible craters, including degraded examples, except for irregular depressions in the "pitted terrain" (deflation basins?). However, for $D < 1$ km, it is conceivable that incompleteness is more important than in Figs. VIII-12 through VIII-15, as the polar pictures were taken at ranges usually exceeding 3000 km, while the volcanoes were photographed frequently from less than 2000 km.

As seen in Fig. VIII-16, the data points from the sparsely cratered pole cluster around the isochron for about 1×10^8 years. However, it can be seen that the

dashed line, of slope −1.6, is a better fit than the isochron of −2 slope. A curve of −1.6 slope does not fit the model of obliteration by deposition at a constant rate (slope −1), which has been referred to and applied above (e.g., Figs. VIII-9 and VIII-10). However, as pointed out by Chapman (Ref. VIII-35), a curve of slope intermediate between −2 and −1 fits a situation with erosion/deposition *declining* at a constant rate. As it does not appear that incompleteness in counts of small craters can be sufficient to create the observed shallow slope, it is concluded that the slope is closer to −1.6 than to −2.

Considering the previous data on other regions of Mars, the most straightforward interpretation of the polar data is that erosion and/or deposition rates were much greater in the past at the pole and in other parts of Mars than they are now. While these processes terminated or declined abruptly in other parts of Mars about 6×10^8 years ago, they declined more slowly in

the polar zone. Deposition in stratified layers, possibly by trapping of dust in seasonal and perihelic dust storm cycles, continues at a decreasing rate today, and this rate is higher near the poles than on the volcanic shields studied here. Crater retention ages (lifetimes) at the south pole may be approximately 3×10^5 years for 32-km craters, and only 6×10^5 years for 1-km craters.

J. Summary and Conclusions

Early analyses of cratering and other Martian surface properties that indicated extensive ancient erosion have been strongly supported by *Mariner 9* data. Positive evidence of erosive loss of Martian craters comes from the much greater abundance of kilometer-scale craters on Phobos and Deimos than on the Martian surface (Fig. VIII-6). Craters of various classes of complexity are found on Mars as well as on Earth and the Moon. By their great variations in density, these craters indicate a history of Martian erosion and crustal development intermediate between Earth and the Moon. Approximately one hemisphere of Mars reveals an ancient cratered surface with craters in varying states of freshness. The diameter distribution does not match the initial production curve, but approximates that predicted by an idealized model of obliteration through deposition of material in craters at a constant rate. In both hemispheres, however, the small craters are sharp, bowl-shaped, and match the shape of the initial production curve. This indicates strongly that, in the recent past, the erosion and deposition declined markedly, so that recent craters have been preserved in nearly their original form.

The volcanic region around Tharsis was fractured and resurfaced by lava flows near the time of, or more recently than, the termination of the erosion. Craters in this region are generally well preserved, and the shield volcanoes near Nix Olympica, Nodus Gordii, Ascraeus Lacus, and Pavonis Lacus are among the youngest, large-scale constructional features. The sparsely cratered area within 9° of the south pole has an age similar to that of the shield volcanoes.

I have attempted to go beyond the relative chronology to establish absolute dates for some of the events mentioned. The major source of uncertainty is in the rate of impacts on Mars, resulting in an uncertainty of at least a factor of 3. Within these limits, it is believed that the oldest surfaces, such as that near Deucalionis Regio display craters dating back 3 to 4 aeons ago (Fig. VIII-10), but not back to planet formation, since the region is not saturated with large craters as is the lunar terrae. From that time until about 6×10^8 years ago, erosion and deposition were much more extensive than they are now, and an effective deposition rate in craters is estimated at 10^{-4} cm/yr applied during much of this period. It is surmised that much dust accumulated during this period in the now near-featureless basins of Hellas and Argyre. About 6×10^8 years ago, the erosion rate declined quite rapidly in most regions, but perhaps less rapidly in the polar regions (Fig. VIII-16). The sparsely cratered regions around Tharsis were resurfaced about 3×10^8 years ago by volcanic activity (Fig. VIII-11), which produced the four major shield volcanoes about 1×10^8 years ago (Figs. VIII-12 through VIII-15). Deposition declined more slowly at the poles, adding to the stratified deposits and causing the diameter distribution to have a diagnostic intermediate slope. Lifetimes of kilometer-scale craters near the pole may be as low as 6×10^5 years.

There is no strong evidence in the cratering data for episodic erosive events. Catastrophic episodes of erosion can be ruled out, since they would produce characteristic downward bends (positive slopes) or sharp cutoffs in the diameter distribution, and these are not observed. Minor erosion episodes such as discussed by McGill and Wise (Ref. VIII-21), possibly even associated with fluvial activity in the sinuous channels, are not precluded, as some channels appear to cut sparsely cratered areas. However, it is suggested that this activity may be a remnant of even more extensive erosion activity in the middle periods of Martian history. The cause and chronology of fluvial activity remains perhaps the most important problem in the Martian studies.

References

VIII-1. Öpik, E. J., "Mars and the Asteroids," *Irish Astron. J.*, Vol. 1, p. 22, 1950.

VIII-2. American Astronomers Report, reference to C. W. Tombaugh, *Sky and Telescope*, Vol. 9, p. 272, 1950.

VIII-3. Leighton, R., Murray, B., Sharp, R., Allen, J., and Sloan, R., "Mariner IV Photography of Mars: Initial Results," *Science*, Vol. 149, p. 627, 1965

VIII-4. Witting, J., Narin, F., and Stone, C., "Mars: Age of Its Craters," *Science* Vol. 149, p. 1496, 1965.

VIII-5. Anders, E., and Arnold, J. R., "Age of Craters on Mars," *Science*, Vol. 149, p. 1494, 1965.

VIII-6. Baldwin, R. B., "Mars: An Estimate of the Age of Its Surface," *Science* Vol. 149, p. 1496, 1965.

VIII-7. Binder, A. B., "Mariner IV: Analysis of Preliminary Photographs," *Science*, Vol. 152, p. 1053, 1966.

VIII-8. Hartmann, W. K., "Martian Cratering," *Icarus*, Vol. 5, p. 565, 1966.

VIII-9. Öpik, E. J., "The Martian Surface," *Science*, Vol. 153, p. 255, 1966.

VIII-10. Marcus, A. H., "Martian Craters: Number Density," *Science*, Vol. 160, p. 1333, 1968.

VIII-11. Chapman, C., Pollack, J., and Sagan, C., *An Analysis of the Mariner-4 Photography of Mars*, Smithsonian Astrophys. Obs. Special Report No. 268, 1968.

VIII-12. Chapman, C., Pollack, J., and Sagan, C. "An Analysis of the Mariner-4 Cratering Statistics," *Astron. J.*, Vol. 74, p. 1039, 1969.

VIII-13. Binder, A. B., "Martian Craters: Comparison of Statistical Counts," *Science*, Vol. 164, p. 297, 1969.

VIII-14. Leighton, R., Murray, B., Sharp, R., Allen, J., and Sloan, R., "Mariner IV Pictures of Mars," *Mariner Mars 1964 Project Report: Television Experiment Part 1: Investigator Reports*, Technical Report 32-884, Jet Propulsion Laboratory, Pasadena, 1967.

VIII-15. Wells, R. A., and Fielder, G., "Martian and Lunar Craters," *Science*, Vol. 155, p. 354, 1967.

VIII-16. Russell, J. A., and Mayo, M., "The Frequency-Size Distribution of Martian Oases," *Publ. Astron. Soc. Pacific*, Vol. 82, p. 138, 1970.

VIII-17. Leighton, R. B., Horowitz, N. H., Murray, B. C., Sharp, R. P., Herriman, A. H., Young, A. T., Smith, B. A., Davies, M. E., and Leovy, C. B., "Mariner 6 and 7 Television Pictures: Preliminary Analysis," *Science*, Vol. 166, p. 49, 1969.

VIII-18. Murray, B. C., Soderblom, L. A., Sharp, R. P., and Cutts, J. A., "The Surface of Mars: 1. Cratered Terrains," *J. Geophys. Res.*, Vol. 76, p. 313, 1971.

VIII-19. Hartmann, W. K., "Martian Cratering II: Asteroid Impact History," *Icarus*, Vol. 15, p. 396, 1971.

References (cont'd)

VIII-20. Hartmann, W. K., "Martian Cratering III: Theory of Crater Obliteration," *Icarus*, Vol. 15, p. 410, 1971.

VIII-21. McGill, G. E., and Wise, D. U., "Regional Variations in Degradation and Density of Martian Craters," *J. Geophys. Res.*, Vol. 77, p. 2433, 1972.

VIII-22. Oberbeck, V., and Aoyagi, M., "Martian Doublet Craters," *J. Geophys. Res.*, Vol. 77, p. 2419, 1972.

VIII-23. Dence, M., Innes, M., ard Robertson, P., "Recent Geological and Geophysical Studies of Canadian Craters," *Shock Metamorphism of Natural Meterials*, edited by B. French and N. Short, Mono Book Co. Baltimore, 1968.

VIII-24. Hartmann, W. K., "Interplanet Variations in Crater Morphology," *Icarus*, Vol. 18 (in press).

VIII-25. Kuiper, G. P., "Survey of Asteroids," *Ap. J. Suppl.*, Vol. 3, p. 289, 1958.

VIII-26. Van Houten, C. J., Van Houten-Groeneveld, I., Herget, P., and Gehrels, T., "The Palomar-Leiden Survey of Faint Minor Planets," *Astron. Astrophys. Suppl.*, Vol. 2, p. 339, 1970.

VIII-27. Mutch, T. A., *Geology of the Moon*, Princeton University Press, 1970.

VIII-28. Alexander, W., McCracken, C., and Bohn, J., "Zodiacal Dust: Measurements by Mariner IV," *Science*, Vol. 149, p. 1240, 1965.

VIII-29. Dycus, R. D., "The Meteorite Flux at the Surface of Mars," *Pubs. Astron. Soc. Pac.*, Vol. 81, p. 399, 1969.

VIII-30. Öpik, E. J., "The Stray Bodies in the Solar System, Part I: Survival of Cometary Nuclei and the Asteroids," *Adv. Astron. Astrophys.*, Vol. 2, p. 219, 1963.

VIII-31. Hartmann, W. K., "Paleocrate Ring on the Moon: Review of Post-Apollo Data," *Astrophys. and Space Sci.*, Vol. 17, p. 48, 1972.

VIII-32. Hartmann, W. K., "Terrestrial and Lunar Flux of Large Meteorites in the Last Two Billion Years," *Icarus*, Vol. 4, p. 157, 1965.

VIII-33. Baldwin, R. B., "On the History of Lunar Impact Cratering: The Absolute Time Scale and the Origin of Planetesimals," *Icarus*, Vol. 14, p. 36, 1971.

VIII-34. Shoemaker, E. M., Hackman, R., and Eggleton, R., "Interplanetary Correlation of Geologic Time," *Advances in Astronaut. Sci.*, Vol. 8, p. 70, 1961.

VIII-35. Chapman, C. R., *Topics Concerning the Surfaces of Mercury, Mars and the Moon*, Ph.D. thesis, unpublished, Harvard University, 1967.

VIII-36. Binder, A. B., and Cruikshank, D. P., "Lithological and Mineralogical Investigation of the Surface of Mars," *Icarus*, Vol. 5, p. 521, 1966.

Acknowledgments

Note Added in Proof

Ongoing research and several correspondents have illuminated certain areas of this initial analysis of *Mariner 9* cratering data. The most important area relates to the rate of crater formation on Mars. George Wetherill has pointed out to the author that available Mars-crossing asteroids are poor indicators of the present cratering rate because of the unlikelihood of their actually hitting Mars. Several workers are now assessing new mechanisms for bringing asteroidal fragments into orbits for potential Mars-collision, but no definite estimates of flux rate have yet come from this work. Verne Oberbeck points out that gravitational field differences between Earth, Mars, and the Moon affect crater sizes, introducing an additional small correction to the cratering rate estimated here. The result is that while the relative ages quoted here for Martian provinces and structure are believed to be correct, work now in progress may soon make it possible to improve the estimates of absolute age. There is some suggestion that absolute ages of young features such as the large volcanoes could increase by a factor of 2 or 3. The writer hopes to pursue these problems as new data emerge. He also thanks George McGill for additional comments which have resulted in a number of improvements to the manuscript.

PRECEDING PAGE BLANK NOT FILMED

IX. The Latitudinal Distribution of a Debris Mantle on the Martian Surface[1]

L. A. Soderblom, T. J. Kreidler, and Harold Masursky

U. S. Geological Survey, Flagstaff, Arizona 86001

The evidence of processes that erode and redistribute massive amounts of material on Mars has been well documented by pictures from *Mariners 4, 6, 7*, and *9*. Chaotic terrain, first recognized in *Mariner 6* pictures by Sharp et al. (Ref. IX-1), has been shown by *Mariner 9* to occupy a significant fraction of the central and north-central parts of the planet (Ref. IX-2; also see Section VI of this Report). Murray et al. (Ref. IX-3) noted the great "horizontal redistribution of material" implied by the severe degradation of the large flat-floored craters. McCauley (Ref. IX-4; also see Section X of this Report), Cutts and Smith (Ref. IX-5; see Section XI of this Report), Cutts (Ref. IX-6; see Section XV of this Report), and Sagan (Ref. IX-7; see Section XII of this Report) describe abundant evidence in the *Mariner 9* photography for eolian erosional and depositional forms which are found from the poles to the equator. Milton (Ref. IX-8; also see Section III of this Report) discusses mammoth Martian channels down which great volumes of material were transported, presumably by water. *Mariner 7* pictures of the south polar region discussed by Sharp et al. (Ref. IX-9) first showed a complex set of irregularly shaped, depressed areas near 70°S latitude. *Mariner 9* pictures have shown that these areas are the erosional remnants of a number of sedimentary blankets that have been deposited on older terrains at both poles (Refs. IX-10 and IX-11; also

see Section XIV of this Report). These sediments are currently being eroded as indicated by craters on subjacent terrains which are partially exposed along scarps. Thus, a variety of major erosional and depositional processes have been operative on Mars throughout the geologic past. This section presents results of a planet-wide survey of *Mariner 9* high-resolution pictures designed to determine the present distribution of erosional debris. The results indicate that deposition and erosion of the debris mantles at a given locale occurred in several stages. The present distribution of debris strongly correlates with latitude, being symmetrically disposed about both polar regions. The results provide some insight as to the sources and the nature of the processes involved in the deposition and erosion of these mantling deposits.

A. Observations

The existence of mantling debris blankets was first recognized in photography of the polar regions. Surrounding the sedimentary deposits in both polar regions, small craters (1 to 5 km), formed on older cratered terrain and plains, display a peculiar morphology (Refs. IX-10 and IX-11; also see Section XIV of this Report). Sharp crater rims are visible, but the crater floors appear elevated as if the interiors had been partly filled. Often the fill reaches the rim of the crater so that the crater

resembles a circular, raised pedestal with a nearly flat top. Based on these observations a survey of 1300 *Mariner 9* narrow-angle frames was made to establish the planet-wide distribution and variation of these blankets. During the search the following definitions of mantled terrain and unmantled terrain were established. Mantled terrain is characterized by the presence of small, sharp-rimmed craters (1 to 10 km in diameter) which have elevated floors. On unmantled terrain, the small craters have a fresh, bowl-shaped appearance. Figures IX-1 through IX-3 show examples of mantled and unmantled terrain at southern, equatorial, and northern latitudes. In the latitude zone between 40°N and the south pole, the study was conducted with narrow-angle pictures acquired during the standard mission after the dust storm had subsided (revolutions 100–262). The polar hood was present during that period north of 40°N latitude. For latitudes north of 40°N, narrow-angle pictures acquired during the extended mission (revolutions 416–529) were used. By that time the north polar hood had dissipated.

An obvious question arises as to whether variations in viewing conditions, slant range, transparency of the atmosphere, or low-lying hazes and fogs might have affected the appearance of the small craters. Figure IX-3a shows a northern mantled terrain in which both a sharp, fresh, unmantled crater and several sharp-rimmed craters with filled interiors can be seen. Based on pictures like these, the morphological differences are evidently real and are not created by poor atmospheric visibility, ground hazes, poor resolution, or illumination conditions.

Figure IX-4 is an example of the data acquired for one complete quadrangle in the survey. The distribution of mantled versus unmantled terrain is shown on the basis of examination of each narrow-angle picture within the quadrangle. The central part of the sample quadrangle shows a wide zone from about 40°S to 50°S latitude in which most (~two-thirds) of the identifications are uncertain. For all but about one-fourth of the frames above and below this band, certain identification of the presence or absence of the mapped unit can be made. The uncertainty between 40°S and 50°S probably arises from gradual thinning of the mantle northward. Figure IX-5 shows a planet-wide map of the mantling deposits. Because of the uncertainties just mentioned, the boundaries are gradational and their positions uncertain by several degrees.

Several important observations can be made from Fig. IX-5. First, the mantles are symmetrically dis-

posed about the north and south polar regions, extending toward the equator to about 30° or 40° north and south latitudes. Second, the mantle is not correlated with any specific regional geologic terrain type (Ref. IX-12; also see Section II of this Report) and generally lies outside the area of early reconnaissance described by McCauley et al. in Ref. IX-13. All varieties of Martian terrain,

Fig. IX-1. Mantled terrains in the Martian southern hemisphere. These Mariner 9 narrow-angle pictures cover areas 80 km (1a) and 60 km (1b) wide at Sun elevation angles of 21° and 45°, respectively. Locations are annotated in Fig. IX-5. (1a) MTVS 4157-17, DAS 06245543. (1b) MTVS 4202-15, DAS 07721003.

excluding the highly localized, large volcanic constructs, can be found both mantled and unmantled. Hence, the debris mantle is one of the most recent material units in the Martian geologic sequence.

B. Comparison With Other Data

Studies of the populations of small craters display similar latitudinal correlations which can be understood in light of the mantles discussed here. The density of craters in the size range of 600 to 1200 m falls off sharply away from the equator in crossing the southern mantled–unmantled boundary shown in Fig. IX-5 (Ref. IX-14). It was also noticed in that study that larger craters (4 to 10 km in diameter) and central peaks both gradually disappear southward of 30 S and are almost absent south of 60 S. This suggests that the mantles gradually thin out equatorward between 60 S and 30 S. The mantle depth apparently varies from the order of 100 m to 1 km. Figures IX-1 and IX-3 show that this depth may be highly variable locally, being deeper in natural traps such as small steep-walled craters.
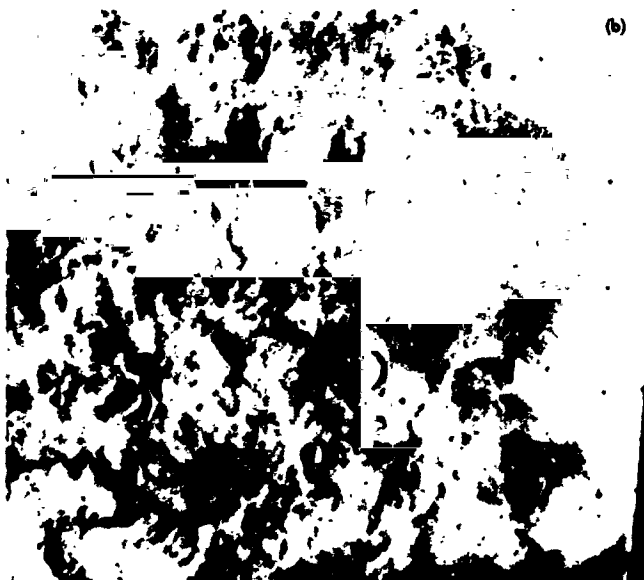
Fig. IX-2. Unmantled terrains in the Martian equatorial zone. These are wide-angle pictures covering areas about 45 km wide under solar elevation angles of about 40°. Locations are shown in Fig. IX-5. (2a) MTVS 4287-12, DAS 11443370. (2b) MTVS 4163-68, DAS 64622613.
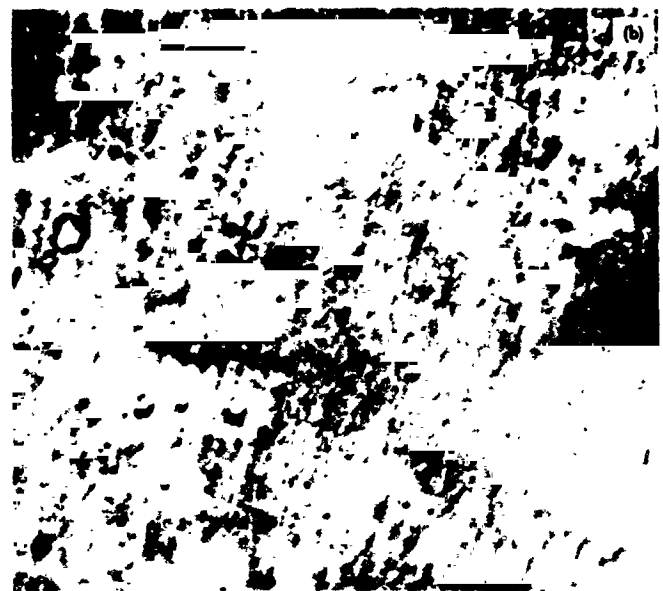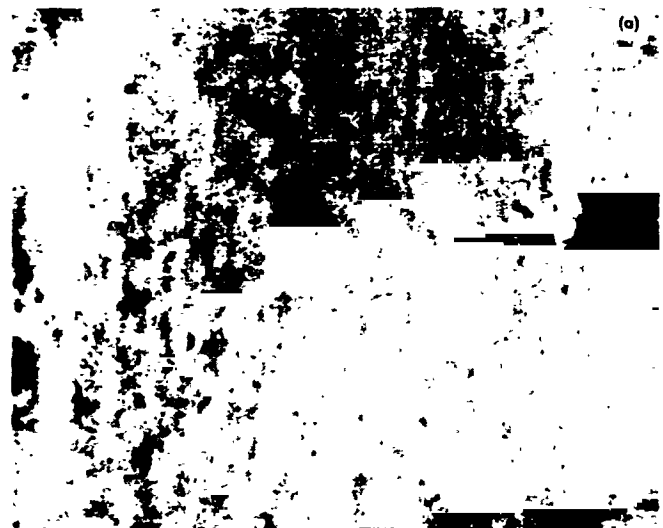
Fig. IX-3. Mantled terrains in the northern hemisphere. These frames cover areas about 170 km wide with 30° solar elevation angles. Locations are shown in Fig. IX-5. (3a) MTVS 4292-4, DAS 11482194. (3b) MTVS 4289-111, DAS 11836026.
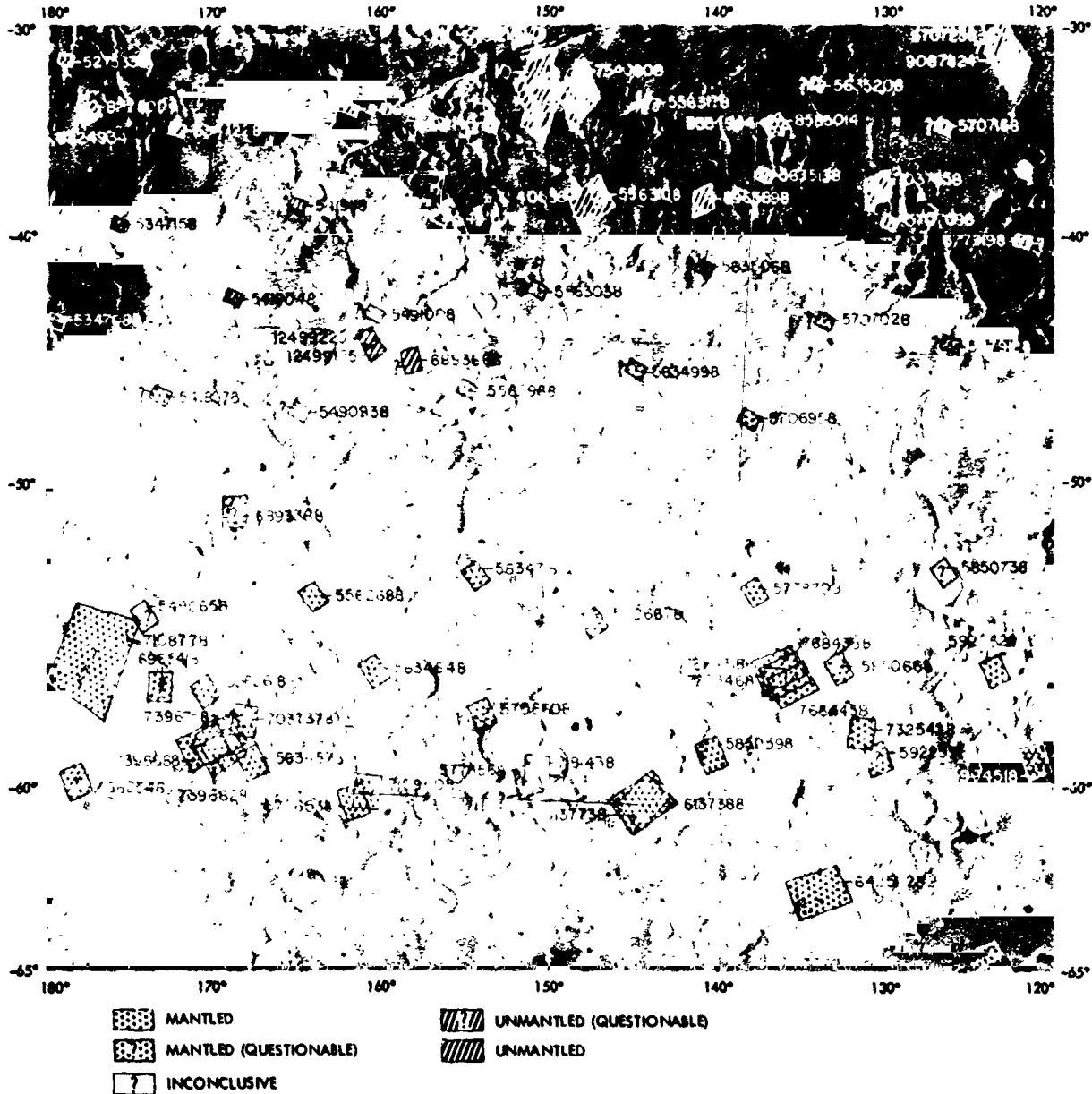
Fig. IX-4. Identification of mantled and unmantled terrains in single narrow-angle pictures. This quadrangle is an example showing the results of the survey for one area of Mars. The wide zone of questionable identifications between 40°S and 50°S is indicative of the irregular nature of the mantle as it thins northward.
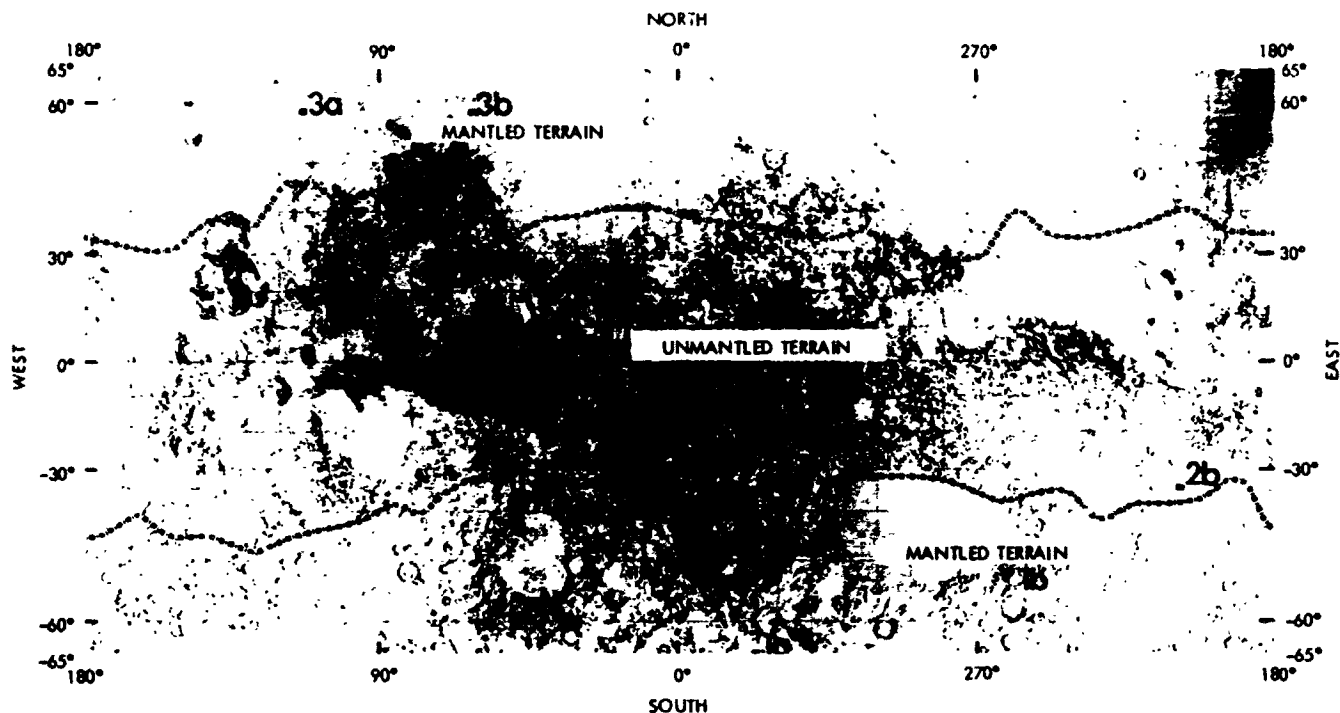
Fig. IX-5. Planet-wide distribution of mantled and unmantled terrains. Data such as shown in Fig. IX-4 have been generalized in the map shown here. The boundaries between mantled and unmantled areas are uncertain by about ±5°.

C. Discussion of Sources and Processes

As the mantling debris unit is symmetrically distributed around both poles and because these mantles apparently thin out toward the equator, the source areas for these debris blankets probably are within the polar regions. Two types of depositional or sedimentary deposits are found in both polar regions (Refs. IX-10 and IX-11; also see Section XIV of this Report). These include: (1) near polar layered deposits on which the permanent ice caps have formed, and (2) older smooth plains in which numerous pits and hollows have been eroded. Figures IX-6a and IX-6b are wide-angle pictures that show the eroded appearance of the two deposits near the south pole. Erosion of the deposits has partly exposed the underlying cratered terrains, a process thought to be continuing.

These complex polar terrains are substantially different in age, and separated by erosional unconformities. (Refs. IX-10 and IX-11; also see Section XIV of this Report). Thus, multiple stages are implied in the redistribution of material on Mars. Materials must have been transported to, deposited in, and eroded from the polar regions in several cycles. Figures IX-1a, IX-1b, IX-3a, and IX-3b further support this concept of cycles of erosion and

deposition. Craters with filled interiors appear as circular buttes with floors above the level of the surrounding terrain; in many cases no central depression is observable. It is difficult to imagine a simple process that would fill only the crater interiors. The entire region probably was at one time mantled with a blanket of debris thick enough to bury the craters entirely. Subsequently erosion has removed most of the debris, leaving the materials protected within crater interiors as relict outliers of the formerly continuous blanket.

The materials of the polar sediments must have been derived from elsewhere. Figure IX-6c shows an eroded terrain in the unmantled equatorial zone which may represent such a source. Cutts (Ref. IX-15; also see Section XVII of this Report) presents a similar conclusion. McCauley (Ref. IX-4; see Section X of this Report) considers much of the equatorial region as a zone of deflation and presents evidence for the lowering of many less resistant plains surfaces by wind action. In contrast to the polar units, which are sedimentary deposits, the equatorial units being eroded are the ancient cratered terrains and less densely cratered plains. Thus, the concept of multiple stages in material deposition and redistribution even applies to the oldest Martian terrains.
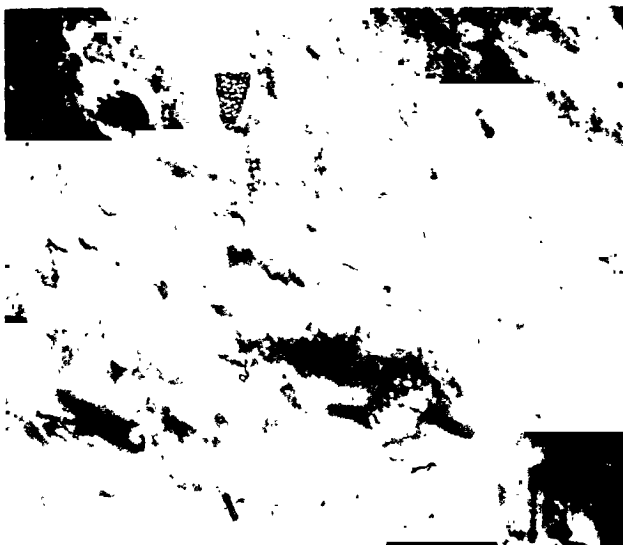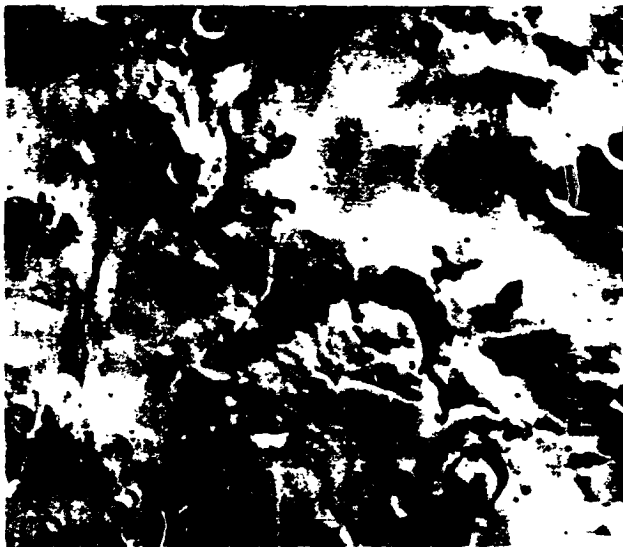
Fig. IX-6. Possible source areas of mantling debris on Mars. (Top) Etch-pitted plains of the south polar region shown here are being eroded along cliff-forming scarps. Area shown is located near 70°S latitude, 0° longitude, and covers an area about 800 km wide. (MTVS 4188-6, DAS 07216758) (Middle) Central polar layered deposits of the south polar region shown here are being eroded, exposing the underlying older cratered terrains. Area shown is about 800 km wide and is located near 75°S, 170°W. (MTVS 4222-9, DAS 08367844) (Bottom) Erosional scarps along cratered plains in the equatorial region of Mars. These enormous erosional systems may be the source areas for the polar deposits. Area shown is about 400 km wide, centered near 3°N latitude and 85° longitude. (MTVS 4190-90, DAS 07327778)

Because of the strong symmetry of the debris mantles around the poles and the patterns of erosion observed today in the polar regions, we suggest that eolian transportation has been the active agent both in originally depositing debris in the polar regions and in later transporting it toward the equator. A possible mechanism for originally depositing materials in the polar regions is the condensation of CO_2 ices on atmospheric dust particles which are brought to the surface during the annual periods of polar CO_2 frost deposition. During other seasons the polar deposits are probably being eroded by strong polar winds. Models of atmospheric circulation (Ref. IX-16) show that the most violent Martian surface winds occur along the periphery of the retreating CO_2 frost cover. Although the model winds have highly variable amplitude and direction, the net effect would be to diffuse material and transport it out of the polar regions. A recent study by Cutts (Ref. IX-6; also see Section XV of this Report) shows that erosional features, wind deposits, and scoured areas occur in radial patterns consistent with the transport of material out of the polar region.

D. Summary

A relatively young mantling deposit of debris surrounds both polar regions and extends toward the equator to latitudes 30° to 40° north and south. This mantle apparently has been derived by wind erosion of sedimentary deposits in the polar regions, a process that is probably continuing now. The distribution of the mantle is not correlated with any particular terrain type for it has masked the small crater populations on young and old terrains alike. The paucity of small fresh craters at high latitudes can be directly attributed to the presence of this debris blanket. It is clear that extreme care should be exercised in using the populations of small craters to establish the chronology of the evolution of geologic provinces on Mars.

References

IX-1. Sharp, R. P., Soderblom, L. A., Murray, B. C., and Cutts, J. A., "The Surface of Mars: 2. Uncratered Terrains," *J. Geophys Res.*, Vol. 76, p. 331, 1971.

IX-2. Sharp, R. P., "Mars: Fretted and Chaotic Terrains," *J. Geophys. Res.*, Vol. 78, 1973.

IX-3. Murray, B. C., Soderblom, L. A., Sharp, R. P., and Cutts, J. A., "The Surface of Mars: 1. Cratered Terrains," *J. Geophys. Res.*, Vol. 76, p. 313, 1971.

IX-4. McCauley, J. F., "Mariner 9 Evidence for Wind Erosion in the Equatorial and Mid-latitude Regions of Mars," *J. Geophys. Res.*, Vol. 78, 1973.

IX-5. Cutts, J. A., and Smith, R. S. U., "Eolian Deposits and Dunes on Mars," *J. Geophys. Res.*, Vol. 78, 1973.

IX-6. Cutts, J. A., "Wind Erosion in the Martian Polar Regions," *J. Geophys. Res.*, Vol. 78, 1973.

IX-7. Sagan, C., "Sandstorms and Eolian Erosion on Mars," *J. Geophys. Res.*, Vol. 78, 1973.

IX-8. Milton, D. J., "Water and Processes of Degradation in the Martian Landscape," *J. Geophys. Res.*, Vol. 78, 1973.

IX-9. Sharp, R. P., Murray, B. C., Leighton, R. B., Soderblom, L. A., and Cutts, J. A., "The Surface of Mars: 4. South Polar Cap," *J. Geophys. Res.*, Vol. 76, 357, 1971.

References (contd)

IX-10. Murray, B. C., Soderblom, L. A., Cutts, J. A., Sharp, R. P., Milton, D. J., and Leighton, R. B., "Geological Framework of the South Polar Region of Mars," *Icarus*, Vol. 17, p. 328, 1972.

IX-11. Soderblom, L. A., Malin, M. C., Cutts, J. A., and Murray, B. C., "Mariner 9 Observations of the Surface of Mars in the North Polar Region," *J. Geophys. Res.*, Vol. 78, 1973.

IX-12. Carr, M. H., Masursky, H., and Saunders, R. S., "A Generalized Geologic Map of Mars," *J. Geophys. Res.*, Vol. 78, 1973.

IX-13. McCauley, J. F., Carr, M. H., Cutts, J. A., Hartmann, W. K., Masursky, H., Milton, D. J., Sharp, R. P., and Wilhelms, D. E., "Preliminary Mariner 9 Report on the Geology of Mars," *Icarus*, Vol. 17, p. 289, 1972.

IX-14. Soderblom, L. A., West, R., Herman, B., Kreidler, T. J., and Murray, B. C., "Martian Crater Populations" (in preparation).

IX-15. Cutts, J. A., "Nature and Origin of Layered Deposits of the Martian Polar Regions," *J. Geophys. Res.*, Vol. 78, 1973.

IX-16. Leovy, C., and Mintz, Y., "Numerical Simulation of the Atmospheric Circulation and Climate of Mars," *J. Atmos. Sci.*, Vol. 26, p. 1167, 1969.

Acknowledgments

X. *Mariner* 9 Evidence for Wind Erosion in the Equatorial and Mid-Latitude Regions of Mars[1]

John F. McCauley

U.S. Geological Survey, Flagstaff, Arizona 86001

Mariner 9 revealed a wide variety of features that can be attributed to wind activity. Sagan et al. (Ref. X-1) deal with the problem of the light and dark markings which are interpreted as surficial wind streaks consisting of mobile sand. The role of the wind in producing lineations and other landforms in the polar regions was described by Cutts (Ref. X-2; see Section XV of this Report) and by Sharp (Ref. X-3; see Section VI of this Report). Depositional features produced by the wind, such as dunes, are the subject of a companion paper by Cutts and Smith (Ref. X-4; see Section XI of this Report).

Mariner 4 revealed that Martian craters are generally softer and shallower appearing than those on the Moon. These characteristics were ascribed with reservation by Sharp (Ref. X-5) to wind activity. *Mariners 6* and *7* showed that the floors of many craters and the large circular depressions such as Hellas were the probable sites of deposition of windblown material (Ref. X-6) and that some of the dark markings might be caused by wind scouring (Ref. X-7). Other wind-related landforms were not identified from these early flyby missions primarily because the resolution of the pictures was too low and

the coverage of the planet was too limited. Until *Mariner 9* the true scope of eolian regime on Mars was not known, and it was by no means certain that the wind was a truly significant surface-shaping process.

The main purpose of this section is to present the television evidence for extensive wind erosion principally in the equatorial and mid-latitude regions of Mars ($\pm 65°$ latitude), and to compare these presumed erosional features with selected erosional landforms from the coastal desert of Peru known to be of eolian origin. The evidence for widespread erosion on Mars prompted an examination of certain aspects of its wind regime that are thought to be significant geologically. The intent of this examination, given as a prelude to the pictorial data, is to assess the vigor and overall surface sculpturing capability of the Martian eolian regime.

A. The Martian Eolian Regime

The *Mariner 9* television data have confirmed indirectly, from the presence of a variety of wind-related features, that:

(1) An adequate source of loose, sand-sized material must be present over much of the surface.

(2) Winds of sufficient velocity must occur at least episodically in order to cause this sand to move by saltation so that it can abrade the surfaces over which it moves concomitant with attrition of the sand grains themselves.

(3) Fine-grained materials produced by sandblasting are exported in suspension from zones of active erosion and trapped at least temporarily as loess or windblown dust deposits in the polar regions and in local topographic depressions.

When considering the wind regime on Mars, one special factor that should be emphasized is the element of time. On Mars intense wind erosion may have been going on without significant interruption for aeons. On Earth the effects of wind erosion are often masked or intimately mixed with the effects of running water because of dramatically varying climatic conditions that date from the Pleistocene. Blackwelder (Ref. X-8) pointed out that although some writers previously had overestimated the effects of the wind in sculpturing the landforms of the southwestern United States, "it is difficult to avoid the conclusion that in a completely rainless desert, wind would be the only carving agency at work, and hence no matter how much time might be required, it would gradually whittle away the land surface."

Many writers have pointed to the impact process as the most copious probable source of fine fragmental material on Mars. Early in its history, a regolith like that on the Moon almost surely developed with a similar size-frequency distribution and percentage of glass and lithic fragments (Ref. X-9). With the development of an atmosphere and the onset of wind action, the initially high percentage of impact-generated glass droplets and spheres in the regolith should have diminished, and the percentage of more durable mineral and lithic fragments should have increased as a result of selective attrition of the glass. Thus, an adequate source of durable, wind-reworked, and fractionated loose material derived originally from an impact regolith surely must be present. *Mariner 9* discovered several other possible sources of sand such as the numerous fluvial channels described by Milton (Ref. X-10; see Section III of this Report). The mass wasting of the many unanticipated cliff faces as well as crater walls and the permafrost deterioration models proposed to account for the chaotic terrain (Refs. X-6 and X-11; also see Section VI of this Report) should also supply some fine fragmental debris. Extensive volcanic activity (Ref. X-12; see Section IV of this Report) also might have provided abundant volcaniclastic material, but flows are the only

volcanic deposits identified so far; ash deposits, possibly because of their intrinsically nondistinctive surface textures, have not yet been identified.

Various aspects of the eolian regime on Mars have been reviewed by Ryan (Ref. X-13) Sagan and Pollack (Ref X-14), and Arvidson (Refs. X-15 and X-16), but with emphasis on the problem of yellow clouds. Using methods devised by Bagnoid (Ref. X-17), each has calculated entrainment functions for different assumed conditions on the planet, the entrainment function being the relation between threshold drag velocity and particle size. For saltation to begin, the threshold drag velocity must be exceeded, after which some lower velocity (the impact velocity) is required to sustain movement within the saltation curtain Calculated Martian entrainment functions show that a wide range of threshold drag velocity values exists for various latitudes and altitudes. All curves are of the same general shape as that of Earth, indicating that it is progressively more difficult to entrain particles in both the coarser and finer size range. The minimum required velocity for Mars appears to lie at about 200 μm in contrast to about 100 μm for Earth (Fig. 9 of Ref. X-7; also see Fig. XI-9 of this Report). The trough about the minimum velocity is much sharper for Mars, suggesting a more pronounced immunity from saltation transport in those size ranges on either side of the minimum than is the case on Earth.

The many estimates given in the literature of the actual wind velocities needed to initiate saltation should be considered only as gross approximations because the boundary layer and fine-scale surface roughness conditions are poorly understood. These estimates are significant here only insofar as they are involved in this assessment of the overall power or effectiveness of wind erosion processes on Mars. Sagan and Pollack (Ref. X-14) estimate that wind velocities in excess of 300 km/hr above the boundary layer on Mars are required to initiate grain movement for a surface pressure of 10 mb. Lateral velocities of up to 100 km/hr have been reported from telescopic observations of dust storms, and *Mariner 9* television data indicate probable lateral movement of dust storms or clouds of up to 200 km/hr. Gust velocities of two or three times these transverse velocities then do not seem unreasonable. Kuenan (Ref. X-18) has shown experimentally that eolian erosion on Earth is from 100 to 1000 times more effective than erosion taking place over comparable distances within water, an effect that is in part a direct function of the greater kinetic energies involved in air transport. In comparing the energies involved in terrestrial and Martian saltation transport, we can

estimate from Sagan and Pollack (Ref. X-14) that the threshold drag velocity required for a 200-μm grain might be as much as 10 times greater on Mars, assuming the particles to be of the same density and shape. Saltating grains on Mars should then have 10 times greater momentum and 100 times more kinetic energy than saltating particles on Earth.

Because most wind abrasion takes place primarily by chipping and spalling, the brittleness of the saltating fragments becomes a factor of importance in comparing the two wind regimes. As also pointed out by Kuenen (Ref. X-18), the loss of fragment mass as a result of brittleness is not proportional to impact momentum, but increases at a high ratio of the increase in momentum. This observation leads to the conclusion that the rate of fragment attrition should be even faster on Mars than on Earth because:

(1) Relatively brittle mineral fragments such as feldspars and pyroxenes derived from the impact regolith are probably more numerous than on Earth.

(2) The momentum of saltating grains is about 10 times greater.

(3) The fluid density of the atmosphere of Mars is about 10⁻² that of Earth.

The fluid cushioning effect of the atmosphere on Earth is sufficient to produce a lower size limit of about 40 to 50 μm, below which sandblast action cannot occur. Particles of this size and smaller are cushioned from one another or diverted around obstacles without striking them. Thus, their capability to effect sandblasting is negligible. On Mars, atmospheric cushioning should be almost nonexistent, and thus should permit particles in the very small size ranges once in motion to act as instruments of abrasion. The lower size cutoff for saltation and consequent sandblasting on Mars, combined with the normally greater abundance of small particles for any comminution regime, should together profoundly influence Martian erosion rates.

Arvidson (Ref. X-16) has scaled the Bagnold relation that predicts the rate of sediment movement as a function of fluid densities, drag velocities, and the accelerations of gravity and finds that, given suitably sized material and sufficiently high wind velocities, the saltation flux on Mars might be on the order of 20 times greater than that on Earth. In addition, Ryan (Ref. X-13) estimated that the bulk of the grains in saltation on Mars might reach heights three to four times higher than

on Earth so that beveling and undercutting of cliffs or other prominences and the winnowing away of debris at their base could be a more extensive and efficient process than in terrestrial deserts. All of the above considerations suggest collectively that wind erosion on Mars is a far more intense geologic process than on Earth, and that it probably proceeds at substantially faster rates than observed even in the most arid, windswept terrestrial regions.

Little data are available on eolian planation rates in terrestrial deserts so that it is presently impossible to calculate meaningful rates for Mars. An attempt, which omits many important geologic considerations, has been made by Sagan (Ref. X-19, also see Section XII of this Report). The rate at which primary landforms are subdued, material exported, and the original surface lowered is highly variable and depends on a complex interplay of factors in addition to those discussed previously. These other factors include: intermittent running water, variations in bedrock competence, various non-eolian cliff-sapping processes, mass wasting in concert with eolian undercutting, chemical and mechanical weathering, the relative abundance of moving sand, and diurnal and seasonal variations in the wind regime. The effects of these factors vary from place to place within any desert and from one desert to another so that the influence of each cannot be evaluated even in a qualitative sense. Nevertheless, wind is capable of removing large volumes of material from deserts as well as flood plains and glaciated regions to form loess blankets in regions of calmer air. The most extensive of these are in the Yellow River basin of central China, where they cover tens of thousands of square kilometers and are reported to be as much as 300 m thick. Similar eolian deflation, transport, and deposition seem to have occurred throughout much of the equatorial and mid-latitude regions of Mars. The magnitude of this process appears to be highly variable, probably for the same reasons as on Earth.

Telescopic evidence has long attested to the capability of the atmosphere to transport dust-size fragments; the planet-wide dust storm that obscured the surface of Mars for the first 50 days of the *Mariner 9* mission was dramatic confirmation that suspension transport is operative. Arvidson (Ref. X-15) has shown that the settling velocities for suspended particles are about the same for Earth and Mars, so that fine material entrained in the atmosphere can be transported over comparably long distances. The early clearing of the dust storm of 1971 in the south polar region and the presence of

layered deposits of probable eolian origin in the north and south polar regions suggest that much of the dust derived from the equatorial zone preferentially settles and accumulates at least temporarily in these regions (Ref. X-20; also see Section IX of this Report). The separation of fragmental debris into deposits of fine-grained dust (loess) and coarser sand which remain behind to produce further erosion is probably a more significant geologic process on Mars than on Earth. If suspension transport, coupled with an export and temporary storage mechanism, were not operative, the entire surface would become choked and mantled by wind-blown debris, and the process of wind erosion would essentially cease.

B. *Mariner 9* Television Evidence for Wind Erosion

Wind erosion features on Mars are generally recognizable only in the narrow-angle pictures and then with difficulty, because each picture covers such a small area, thereby making it hard to establish the regional context of individual features. On pictures of comparable resolution on Earth (200 to 300 m for the smallest detectable object), windforms would be difficult to detect. Many of the narrow-angle pictures taken before about revolution 140 in the region from 65°S latitude up to about the equator are either featureless or streaked and hazy, suggesting that blowing sand or suspended dust obscured the surface. Evidence for wind erosion is nevertheless widespread, but only a very limited array of the more illustrative examples can be shown here. A full classification of the types of landforms produced by the wind and the extent of eolian modification of the various geologic units described by McCauley et al. (Ref. X-11) and Carr et al. (Ref. X-21; also see Section II of this Report) will have to await more detailed studies.

Landforms produced by confined channel flowage are generally characterized by sinuous patterns so that the pictorial signature of a water-eroded surface is almost unmistakable given sufficient photographic resolution. In semi-arid to arid regions on Earth, the episodic effects of running water in concert with mass wasting tend to produce rugged landforms characterized by many slopes near the angle of repose or steeper. In those few regions on Earth where running water has played a sufficiently subordinate role, and where wind has been the dominant agent of erosion for a sufficient length of time, eolian landforms are characterized by linear bedrock scouring, cliff fluting, and, in advanced states of erosion, by pronounced streamlining parallel to the direction of the

prevailing winds. Moving coarse to fine sand blankets, containing ripples or dunes of varied form, often smooth more rugged non-wind-related landforms rather than making them more rugged as is often erroneously assumed.

Seven general categories of probable wind erosion features are now recognized on Mars: (1) modified crater rims, (2) irregular pits and hollows, (3) streamlined ridges, (4) linear grooves, (5) fluted cliffs, (6) reticulate ridges, and (7) subdued and sand-mantled terrain. None of these landforms is primary in the sense that it is created solely by the wind. As with terrestrial eolian erosion features, they are modifications of earlier deposits resulting from other processes.

Craters are the most ubiquitous single landform on Mars and are generally more degraded than lunar craters of comparable size. Most of these round, randomly distributed craters are believed to be of impact origin, so that before modification they probably looked much like the freshest lunar craters such as Tycho or Aristarchus. Only a few Martian craters really appear fresh such as the one shown by Cutts and Smith (Ref. X-4; also see Fig. XI-6a of this Report) and the 2-km crater near 37.0°N and 344.2°W (MTVS 4210-66, DAS 07975423)[a] which also exhibits a well preserved ray system. Early in Mars history, crater modification by ballistic erosion accompanied by seismic shaking and local volcanic blanketing must have occurred much like on the Moon. Subsequent to the evolution of an atmosphere, wind became an additional and important factor in the crater modification process, thereby accounting in part for the distinctive appearance of most Martian craters.

At least three basic types of crater or crater rim modification can be attributed to wind erosion. Figure X-1a shows a 20-km assumed impact crater near 38°N, 261°W, with a sharp rim crest and a pronounced central peak, but encompassed by a rim unlike that around any crater on the Moon. This unusual rim is recognizable out to about one crater diameter and is bounded by a subdued scarp. A smooth depression zone, apparently a ring syncline, is present close to the rim crest beyond which sharp, straight radial fractures are present along with discontinuous roughly concentric lineaments that loosely resemble graben. This structural pattern is similar to that commonly observed in the bedrock beneath the ejecta

---

[a] Numbers in parentheses in text refer to *Mariner 9* pictures not included in this section, but which provide additional explanatory material. All *Mariner 9* pictures may be ordered from the National Space Science Data Center, Code 601, Greenbelt, Maryland 20771.
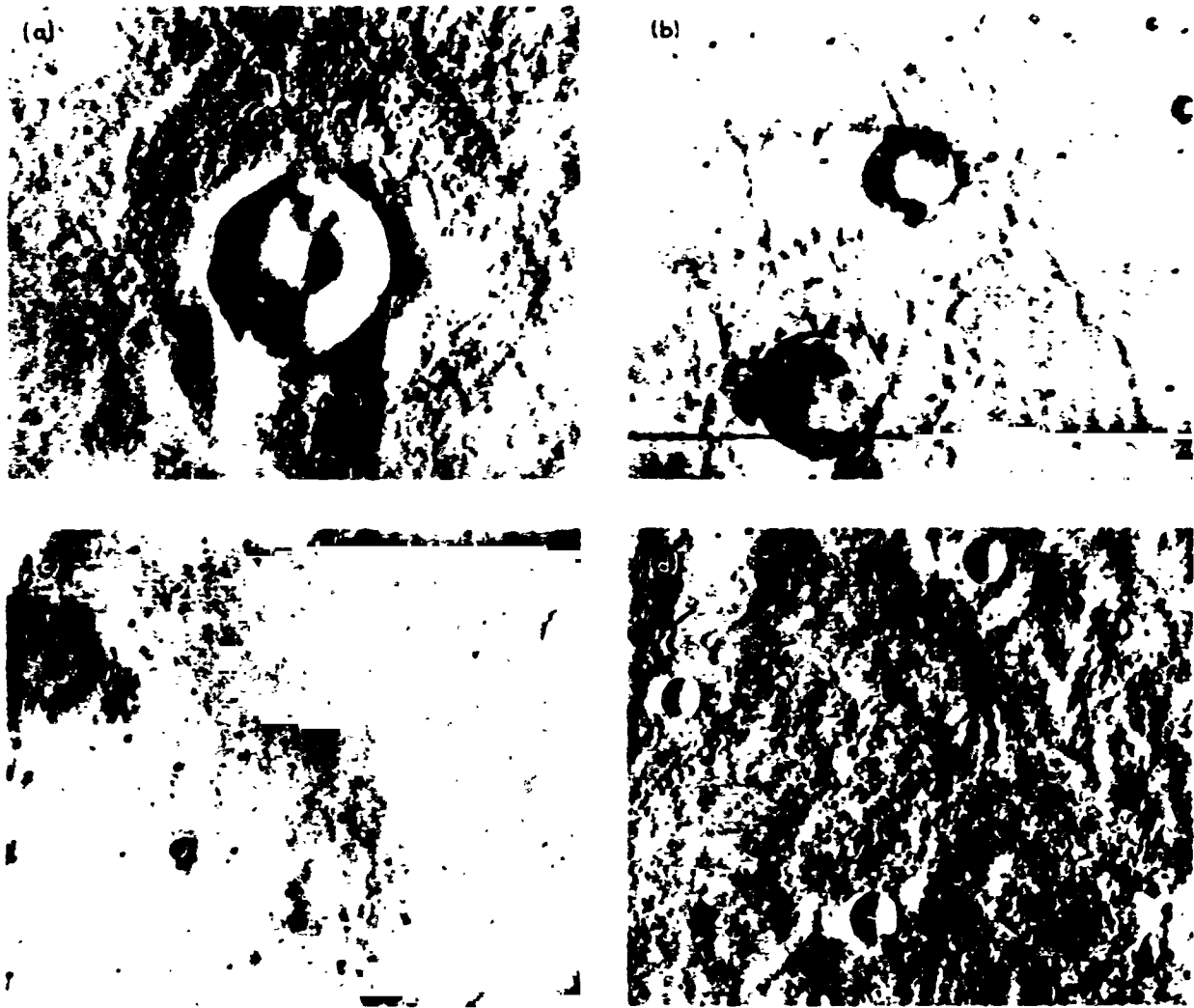
Fig. X-1. (a) Sharp-rimmed, 20-km crater encompassed by a radially and concentrically fractured rim. (MTVS 4230-66, DAS 06623029) (b) Multiple rampart craters; the largest is 8 km across. (MTVS 4186-63, DAS 07147283) (c) Pedestal craters 1 to 2 km across surrounded by sharp serrate ledges. (MTVS 4294-26, DAS 12500070) (d) Irregular pits and hollows on lunar-like plains material. (MTVS 5017-19, DAS 11797070)

blankets of some terrestrial impact craters such as Flynn Creek, Tennessee, as well as experimental explosion craters (Ref. X-22). Similar appearing structural patterns have not been described around volcanic craters. The fragmental ejecta blanket that is inferred to have originally surrounded this crater appears to be eroded to sufficient depth to partly or completely expose the sub-ejecta bedrock structures never visible around lunar craters. The presence of a sharp rim crest on this crater and succeeding examples is not inconsistent with extensive wind erosion, the sensitivity of the wind to slight resistance discontinuities being well established. The rim crest here is interpreted to represent the steeply upturned bedrock beneath the ejecta; this bedrock should be relatively

more resistant to erosion than the disaggregated, intensely fractured, ejecta of the original blanket. The surrounding plain is lower than the crater rim; conceivably the coarse rubble of the ejecta blanket could have acted as a deflation armor, thus temporarily protecting the pre-crater bedrock from erosion to the same level as the surrounding ejecta-free terrain.

Many Martian craters are surrounded by single or multiple crenulated ramparts at a distance of about one-half to one crater diameter. Figure X-1b shows two craters near 6.5°N, 285°W, the largest of which is about 8 km in diameter. Craters of this type are fairly common throughout the equatorial region, particularly on those

moderately cratered plains that exhibit sinuous lunar-like mare ridges (Ref. X-11). Craters of this type are rare in the more complex highly cratered terrain. If these are indeed impact craters, the unusual form of their rim deposits also might be explained by wind erosion. Two ejecta facies are generally recognized around fresh lunar impact craters: a rough inner rim facies, and an outer radial facies that grades at about one crater diameter into chains, loops, and clots of secondary craters (Ref. X-23). These facies and their contacts with the surrounding plain could represent wind resistance discontinuities, and thereby erode at different rates than their surroundings. They do not appear to be eroded to sufficient depth to expose the pre-crater bedrock as is assumed for the crater described in Fig. X-1a.

The craters shown in Fig. X-1c near 4.5°N, 152°W, represent yet another type of erosion and are also indicative of the extent of deflation and lowering of certain plains surfaces on Mars. Here many small craters about 1 km in diameter are located on raised pedestals that are encompassed by relatively steep, serrated scarps lying at a distance of about two crater diameters. The craters are too small to show discernible rim textures, but deposition of continuous to thin and discontinuous ejecta commonly occurs out to several diameters from a primary impact crater. As in the previous examples, the ejecta blankets appear to have acted as a surface armor or lag surface which has temporarily protected the underlying materials from deflation. The plains surrounding the ramparts at the edge of the assumed ejecta blankets are inferred to have been lowered by at least the height of the scarps since these craters formed. Preliminary wind tunnel experiments by Ronald Greeley at Ames Research Center have simulated this temporary armoring effect. Alternatively, these craters might be volcanic in origin and be surrounded by flows; in this case the same process would be operative, but with much of the relief on the serrated scarps primary rather than secondary. The degree of lowering of the surrounding plains would, therefore, be less than for impact craters.

Most craters on Mars are not surrounded by scarps and most also lack distinctive rim deposits, suggesting in these cases that erosion has proceeded at a uniform rate both on the plains and craters. Where elevation discontinuities are present, it can be inferred that the surrounding terrain is more susceptible to erosion than the encompassing ejecta blanket and consequently consists of weakly consolidated materials. Further, evidence that parts of the plains are composed of weakly cohesive materials is seen in the crescent-shaped hollows of a narrow-

angle camera picture (MTVS 4254-55, DAS 09484799) at 5.0 N and 151.5°W. These features are described in more detail by Cutts and Smith (Ref. X-4; see Fig. XI-8 of this Report) who compare them to similar recent depressions in the Coachella Valley, near Palm Springs, California.

Three prominent 5-km craters, without apparent rim deposits but with sharp rim crests, are seen in Fig. X-1d, located near 35°S, 302°W. Also shown are plains containing numerous flow fronts and linear ridges with lobate flanks. Plains of this type are generally interpreted to be of volcanic origin and probably consist of a sequence of flows and fissure eruptions as on the Moon. The surface of these flows, unlike their lunar counterparts, appears to be eroded into numerous irregular knobs or residual nubbins lying within larger, very irregular depressions. Numerous elongate gouge-like features occur in the upper right of the picture and appear to be secondary impact craters unrelated to the other depressions and knobs. The textural pattern observed on these lunar-like plains is dissimilar to the original surfaces of flows on either the Moon or Earth, and is interpreted as a secondary erosional imprint, possibly due to wind abrasion and selective winnowing of less resistant zones within the flows. If these are fine-grained volcanic rocks, Martian wind erosion must be sufficiently vigorous or the exposure time so long that rocks which terrestrially tend to be very resistant to aeolian erosion have been extensively degraded.

Parts of the aureole of structured terrain surrounding Nix Olympica (Ref. X-12; also see Section IV of this Report) show what appears to be wind-produced streamlining (Fig. X-2a). These elongated ridges are 10 to 15 km long and 3 to 5 km wide and exhibit a pronounced alignment that is parallel to numerous fine surface grooves. Irregular to elongate pits, on the order of 1 km or smaller in size, are present between the ridges and are interpreted as small deflation hollows. The crests of most of these ridges are sharp and keel-like in appearance, and the ends of the ridges are sharply tapered. Whatever the origin of this terrain, its present morphology is strongly suggestive of extensive wind modification. On Earth, similar-appearing streamlined residual knobs produced by wind erosion are called "yardangs" (Ref. X-8; for examples from the coastal desert of South America see Fig. X-4b). Another variant of streamlined terrain lies in a moderately cratered part of the Aeolis region (Fig. X-2b). Here the relief is more subdued, and the erosion effects are more subtle. This erosion surface is characterized by closely spaced, sharp-crested
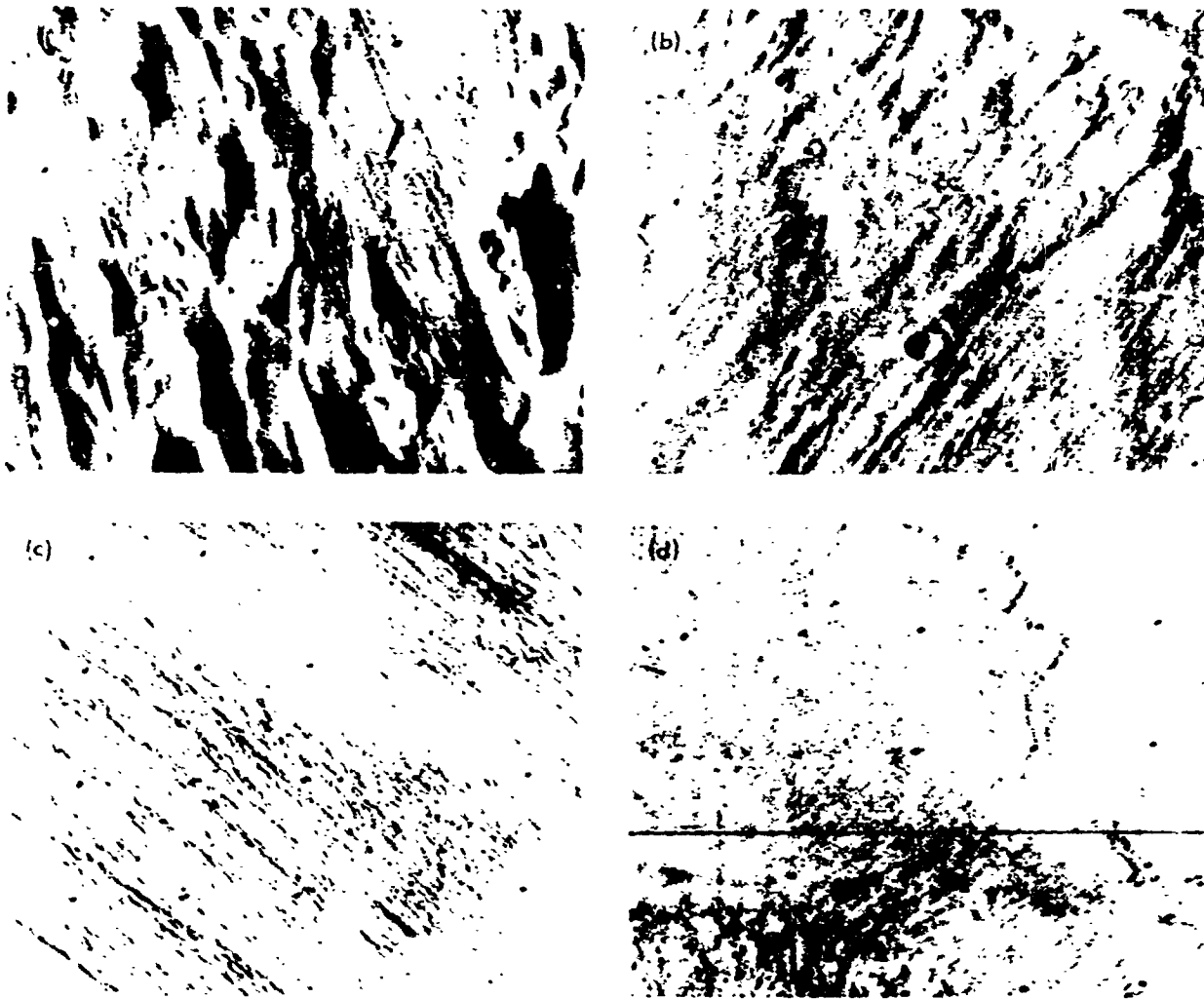
Fig. X-2. (a) Elongated ridges and troughs aligned with numerous small pits and fine grooves. (MTVS 4174-75, DAS 06823393) (b) Streamlined ridges and tapering mesas. (MTVS 4296-4, DAS 12985394) (c) Fine parallel grooves in relatively smooth uncratered plains. (MTVS 4174-63, DAS 06823253) (d) Fluted mesa and residual ridges.(MTVS 4205-54, DAS 07794575)

ridges separated by smooth troughs that grade into low, tapering, wedge-shaped mesas that appear to be relicts of originally more extensive strata. The 4-km crater with a sharp rim crest near the lower center shows a faint rampart like those described previously. This crater must be either more resistant to wind erosion than the scoured terrain around it or be younger than most of the inferred denudation. Parts of the plains of southern Amazonis exhibit what appear to be wind scour features. Figure X-2c, which is about 30 km across, shows an array of sub-parallel ridges and grooves that are interpreted to be selectively etched, closely spaced bedrock fractures. However, as will be seen later, some or most of the linearity in this picture could be due to the presence of trains of sub-resolution granule ripples of the type

found on some thoroughly deflated, coarsely fragmental terrestrial desert surfaces.

Wind erosion effects on a stratified plateau in southern Zephyria are illustrated in Fig. X-2d, which measures about 40 km in width. The front of the plateau to the east shows a complex fluted pattern that grades westward into a series of elongate residual knobs, probably yardangs but very much smaller than those in Fig. X-2a. This pattern is similar to that seen along the edges of some of the laminated terrain in the polar regions (Ref. X-2). Cliff retreat appears to be in a more advanced state here because of the deeper fluting of the edges of the scarps and the development of small yardangs and residual nubbins. Figure X-3A, although near 80°S, 64.5°W,
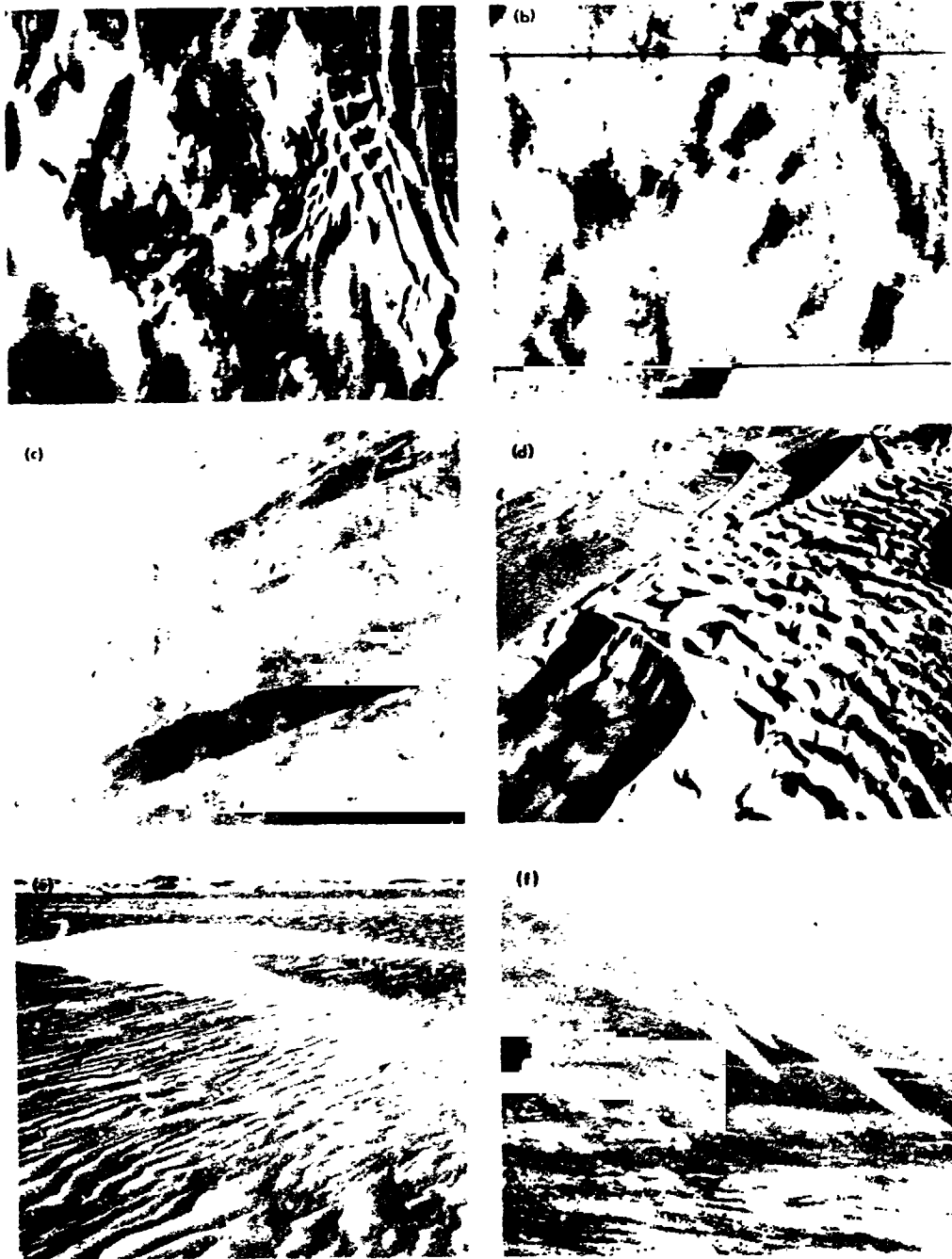
Fig. X-3. (a) Reticulate ridges in south polar region. (MTVS 4212-15, DAS 08044333) (b) North rim of Argyre basin. (MTVS 4162-63, DAS 06426563) (c) High-altitude photograph of sand streaks in the coastal desert of Peru. (d) Low-altitude oblique photograph of similar sheet in central Peru. (e) Ground photograph of detached barchan and rippled surface over which sheets move. (f) Thin sand sheets in northern Peru that do not obscure subjacent beach features.

and outside the area of main concern, is included because it illustrates yet another important effect of wind erosion. In the right center of the picture is an unusual and complex array of linear, interconnected reticulate ridges, approximately 15 by 50 km in extent. The ridges are continuous, show no breaching, and stand out among the surrounding plains and small hills like walls of an ancient ruin. The origin of the reticulate pattern is problematic; igneous or clastic dikes are a possibility, but not an exclusive explanation. Whatever the genesis of the pattern, the present morphology can best be explained by selective wind scouring. The materials of the reticulate ridges must be more competent than those between and beyond so that they have been etched out of the surrounding strata to now stand out in bold relief.

The previous four examples of wind erosion features are characterized mostly by linear patterns and are located, for the most part, within plains areas that appear almost featureless at wide-angle camera resolutions. The cratered terrain also exhibits the probable imprint of wind action, but of a different type. Figure X-3b shows softened, mantled terrain on the north flank of the Argyre basin. Much of the cratered terrain within the equatorial region of Mars is of similar appearance and is texturally far more subdued than lunar terrain of comparable geologic setting. Within the cratered terrain, an abundance of mobile sand winnowed from a thick impact regolith is to be expected. This sand may form, as in some terrestrial deserts, a slow-moving mobile blanket that partly or completely buries original topography to varying depths. Much of the softness and nonlunar appearance of the cratered regions can be explained by the presence of such a blanket produced by eolian interaction with the ancient impact regolith.

The foregoing examples are of necessity only a small sample of the array of wind erosion features recognized in the narrow-angle pictures. Preliminary screening of all available narrow-angle frames revealed at least 100 in which probable wind erosion forms are present. The overall abundance and regional distribution of the windforms described cannot be determined because of the paucity of narrow-angle camera coverage of the planet. Windforms seem to be more common, however, in the plains areas which, from preliminary heighting data, appear to be low. They are not evident on topographic highs such as the Tharsis ridge. This tentative observation is consistent with the calculations by Sagan and Pollack (Ref. X-14), which show that the entrainment function is quite sensitive to differences in pressure with

vation, although the relative competence of the rocks in the high and low regions must also be a factor.

The light and dark streaks described by Sagan et al. (Ref. X-24) indicate that wind erosion is still occurring on Mars. Many of the light streaks, particularly those of the Syrtis Major region, are similar in appearance to terrestrial sand sheets that are typically lighter than the deflated desert pavement over which they move. The large and slower-moving sand sheets, such as those in Peru, vary in magnitude from complex dune arrays up to 20 or 30 m thick, several hundred meters in width, and kilometers in length; their appearance in low-resolution vertical photography is shown in Fig. X-3c. They usually consist of a complex array of coalescing barchans, transverse and lee dunes that rise and fall over the local topography as seen in the oblique photograph in Fig. X-3d. The dark, granular, ripple-marked surface over which these sheets often move is shown, along with a small 3-m barchan detached from the main sheet, in Fig. X-3e. Some terrestrial sand sheets, on the other hand, produce strong local albedo contrast, but are so thin that they do not obscure underlying topography (Fig. X-3f). These sheets are faster moving and often change in shape on a diurnal basis.

Although both types are actually depositional features, they are an integral part of the eolian regime because they ablate the surfaces that they move over and around. Attrition of the saltating grains also occurs in concert with their aggregate movement until the grains reach a size small enough to be carried away in suspension, a factor essential for perpetuation of the eolian erosion process.

C. Selected Terrestrial Landforms Produced by Wind Erosion

Parts of the coastal desert of Peru, particularly the central region from the Paracas Peninsula to the mouth of the Rio Ica, have been free from the effects of running water since at least the late Pleistocene time. This part of the desert, like most of the coastal region of Peru, is undergoing rapid tectonic uplift. Many of the recently exposed beaches and marine abrasion platforms have never experienced significant fluvial erosion in contrast to the surface of most other terrestrial deserts that have undergone several climatic cycles since the Pleistocene or that experience spasmodic heavy rainfall. Winds of 20 to 30 km/hr blow each afternoon with great constancy of velocity and directional pattern. Vegetation is virtually

absent, and an ample supply of relatively immature sand locally containing an unusually high percentage of lithic and mineral fragments is present. The sand is derived from recently raised beaches and marine abrasion platforms, although exotic streams from the high Andes also contribute much quartz sand to the total supply. Numerous sea stacks in a wide size spectrum along with abundant fault scarps provide the first-order landforms that are undergoing attack by the wind. The almost unique character of this desert and its potential as a source of insights into Martian eolian processes led to a geomorphic reconnaissance of coastal Peru in October 1971, just before the *Mariner 9* encounter. The work was sponsored by NASA and carried out as a joint effort between the U.S. Geological Survey and the various Peruvian agencies listed in the Acknowledgments. A report summarizing the preliminary results of the study from which most of these data have been derived was recently prepared by Grolier et al. (Ref. X-25).

The most impressive products of wind erosion in Peru are the streamlined, wind-beveled hills or yardangs that range from tens of meters to several kilometers in length. Their appearance from the air is like that of a fleet of inverted ships of various sizes and shapes. In the background of Fig. X-4a an array of these unusual features, located just west of the Rio Ica near Cerros Las Tres Piramides, can be seen. They are formed in evenly bedded, loosely consolidated, Tertiary sediments that probably lie unconformably on the non-guillied, wind-stripped, gently deformed sediments in the background. The largest of the triple hills near the center background of the photograph is 1.0 km in length. Two steep-walled, flat-floored deflation hollows, the more circular of which is 0.5 km across, are present in the left foreground. Figure X-4b illustrates the same type feature in a more advanced stage of wind beveling and streamlining. These yardangs, located about 17 km north–northwest of the mouth of the Rio Ica, have been carved into the somewhat more massive siltstones of the Pisco Formation, also of Tertiary age. The largest of these ridges with the central groove along its crest is 0.5 km in length. Note their pronounced aerodynamic shape and the linear light and the dark, generally parallel streaks that surround each ridge. The transverse spacing of these streaks here is on the order of several meters. They are trains of granule ripples with aligned crests that contain coarser darker material on the gentle windward slope of each ripple (Ref. X-26). Eolian bedforms such as ripples and dunes can be distinguished on the basis of grain size and wavelength as described by Wilson (Ref. X-27). The sand that is the chief sculpturing agent of the yardangs is continuously being de-

rived by winnowing and eddying from these relatively coarse metastable deflation surfaces. Figure X-5a is a vertical view of the same region, 8 km in width, oriented with west at the top The yardangs seen in Fig. X-4b are at the extreme right of the photograph. The Rio Ica, an exotic stream with its source in the high Andes, flows from the upper right to lower left; the prevailing wind direction is from left to right across the photograph. The dark, complexly faulted crystalline rocks that here underlie the streamlined remnants of the light Pisco Formation can be seen in the upper part of the photograph. They have been smoothed, selectively etched along fractures, and partly blanketed by coarse sand, but not sculptured into yardangs because of their greater competence. The broad light and dark streaks in the lower right of the photograph are parallel to the prevailing winds; the light streaks probably are ephemeral thin blankets of loose sand derived from the yardangs upwind, and the dark streaks are ripple-marked pavement over which these sheets move.

The yardangs of coastal Peru are pure eolian features; no running water has been involved in their formation. Mechanical and chemical disintegration of the original sediments, sandblasting by saltation, and the consequent selective winnowing of zones of weakness within these rocks are sufficient to explain their development. They compare closely in form and approximately in scale to the probable Martian erosion features depicted in Figs. X-2a and X-2b, although those in Fig. X-2a appear to have much sharper crests and are generally larger.

Another of the many varied reactions of lithogically complex surfaces to essentially the same wind conditions is seen in Fig. X-5b, the width of which is about 4 km and is located in the Pampa Lechuza near the middle of the Paracas Peninsula, Peru. The soft-apping hills in the background are wind-modified and sand-blanketed sea stacks now about 200 m above sea level. They consist of faulted Paleozoic and pre-Cambrian crystalline rocks. In the foreground and upper right, a sequence of weak Tertiary sediments of the Paracas Formation dip gently to the left and have been beveled into a flat stack of tapering plates closely resembling those previously shown in Fig. X-2b, and the relicts of the so-called laminated terrain in the polar regions by Murray et al. (Fig. 7 of Ref. X-28). Note the prominent ripple trains on the flat parts of the Pampa that indicate the prevailing wind direction, which is from top to bottom in the photograph. The tapered edges of the beveled sediments are askew to this direction in contrast to the yardangs discussed earlier and the streamlined remnant at the extreme right

(a)

(b)

Fig. X-4. (a) Wind-beveled hills, stripped Tertiary sediments and deflation pits near the Rio Ica in central Peru. (b) Yardangs in the Pisco Formation, 17 km from the mouth of the Rio Ica, central Peru.

(b)
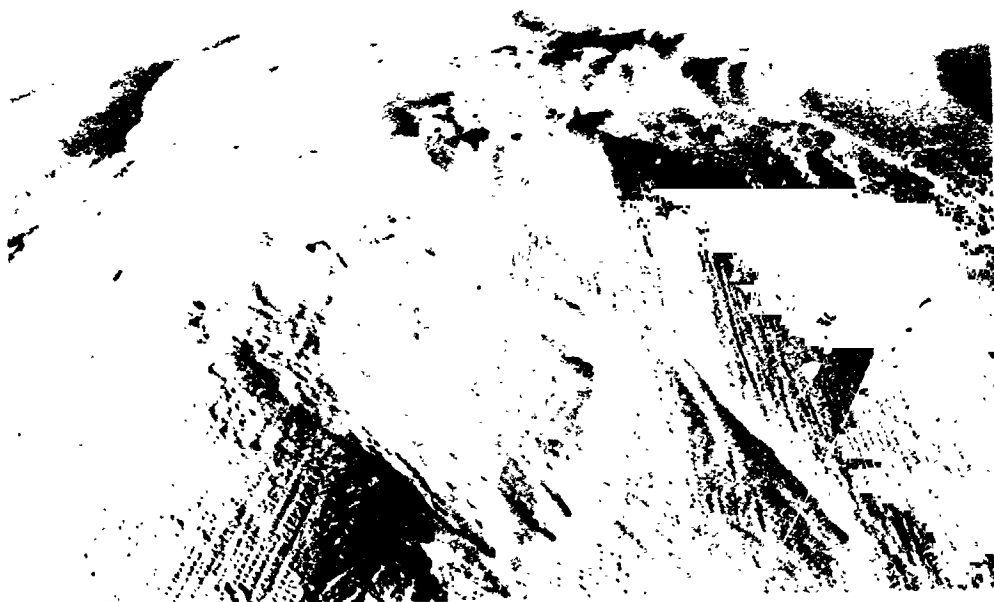
Fig. X-5. (a) High-altitude view of the same features seen in Fig. X-4b. (b) Wind-eroded mesa and ripple trains, Paracas Peninsula, central Peru.

of the picture. This discordance is probably the result of local tilt of these beds, with the tapered edges at the lower right of the stack parallel to the strike direction of the beds. The transverse spacing of the ripple trains is on the order of tens of meters, and their wavelengths are typically 3 to 5 m. If granule ripple trains are present on Mars, as they should be in the light of *Mariner 9* data, their presence just below the limit of identification resolution might produce some of the linear effects seen in Fig. X-2c.

Parallel cliff fluting of weakly consolidated sediments by sandblast action is another variant of the eolian regime in central Peru. Figures X-6a and X-6b illustrate this effect along the base of Cerro Lechuza, about 7 km south of the Pozo Santo Mission on the Carretera Panamericana. Figure X-6a is an oblique view of the fluted cliffs, which are 2.0 km in extent and from 20 to 30 m above the dark lag gravel and granule-rippled pampa to the right. The spacing between the notches is about 50 m. Figure X-6b is a vertical view of the same area oriented with northeast at the top. It clearly shows that fluting occurs only in the light beds in this part of the Tertiary sequence; the overlying darker beds have been stripped back by wind action but have not developed flutes, nor have they gone to the stage of small yardangs as seen in the left center of the photograph. These two illustrations contain features similar to those observed in Fig. X-2d.

Selective wind etching of complexly faulted Tertiary sediments can be observed about 5 km due south of the resort community of Paracas (Fig. X-7a). The distance across the bottom of this photograph is about 3 km. Two prominent resistant beds that stand like walls above the surrounding terrain crop out in the lower right. These same two beds can be traced discontinuously into the right background where they are offset by numerous small faults. The pattern seen here is strikingly similar to that described for Fig. X-3a in the south polar region of Mars. The origin of the resistant layers is almost surely different, but the same type of selective eolian etching must be operative.

Almost complete sand and granule blanketing of wind-smoothed sea stacks can be seen in Fig. X-7b, located in the Cerro Lechuza near the western edge of the Paracas Peninsula. Trains of chevron-shaped ripples occur on the surface of the blanket (lower left of photograph), and the tops of the steeper stacks show exposed bedrock such as the two hills with dark tops in the center. An ancient sand-choked gully without tributaries lies in the upper

center of the photograph, one of the few traces of erosion by running water in this entire region. This terrain resembles that shown in Fig. X-3b; although the primary landforms present in each formed by very different processes, the secondary effects of wind smoothing and partial to complete blanketing by coarse-moving sand is inferred to produce the same morphologic results.

D. Conclusions

(1) The wind regime on Mars is more powerful than that on Earth, and the processes of eolian saltation and suspension transport are more significant on a planet-wide scale than they are terrestrially.

(2) The ravages of wind erosion on Mars are pervasive; at least seven types of eolian erosion features can be recognized. Wind is considered to be the principal agent of surface sculpturing and transport. Its influence accounts for many of the differences between Martian and lunar features, particularly the distinctive morphology of many craters on Mars.

(3) The degree of erosion apparently varies with the type of rocks present and their relative competence or resistance to wind action, as is also true in terrestrial deserts. The clearest examples of wind erosion features are generally found in the plains regions, which tend to be topographically low.

(4) Some plains surfaces have been stripped and lowered on the order of tens of meters. The material removed from these surfaces within the equatorial regions has probably been trapped at least temporarily in the polar regions in the form of loess deposits.

(5) Running water has played a subordinate role in developing the Martian landforms described here. Most of the surface modification seen in these narrow-angle pictures can be explained by eolian erosion or deposition or both superimposed on primary forms generated by impact, volcanism, or tectonism.

(6) Detailed comparisons between the almost unique wind-produced landforms of the rainless desert of central Peru and those inferred to be of eolian origin on Mars reveal striking similarities of form. The conclusion that they originated by essentially similar processes seems inescapable.
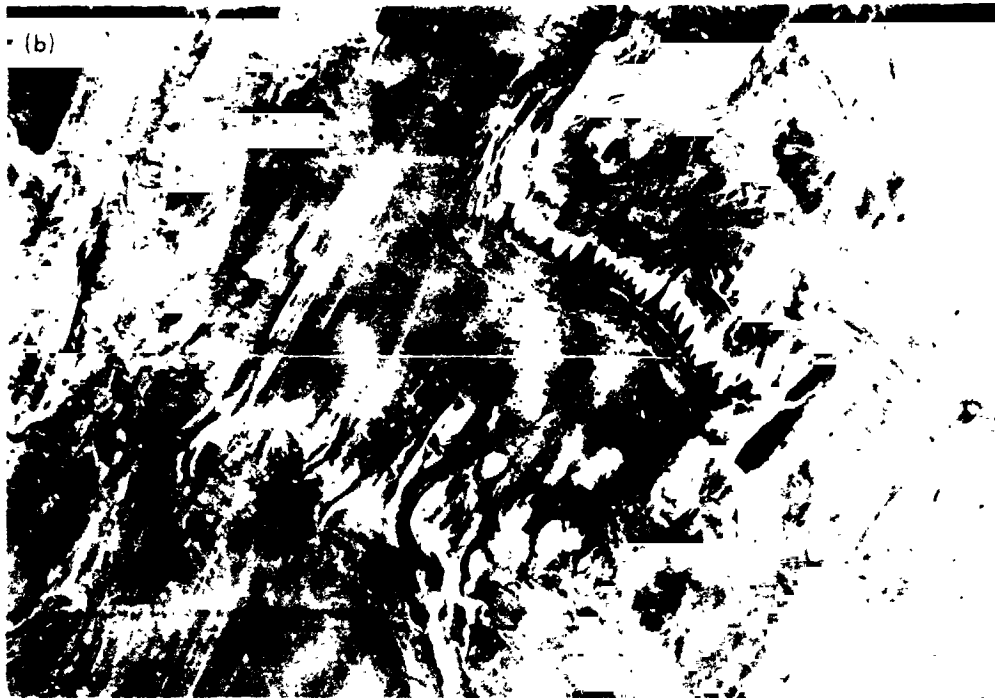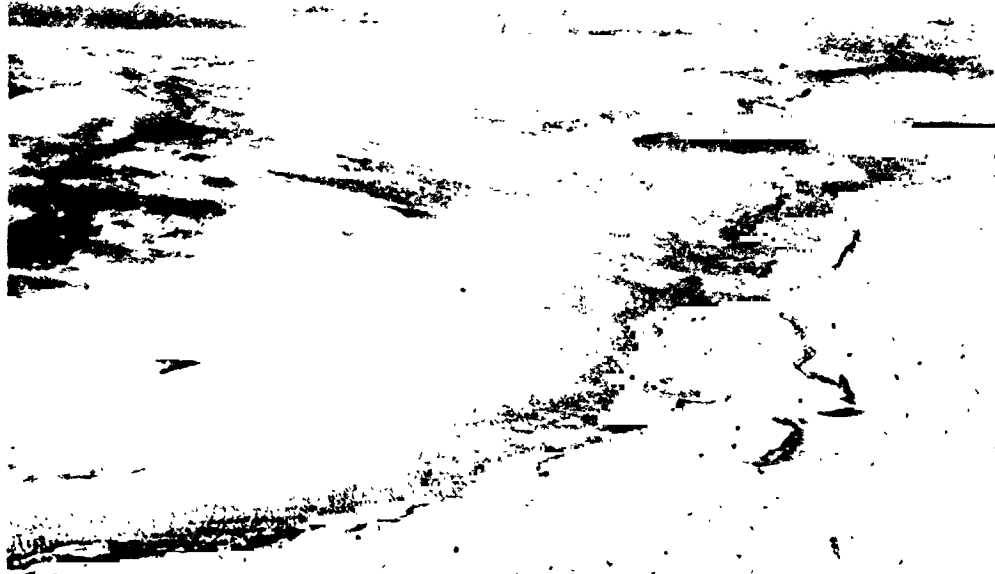
Fig. X-6. (a) Wind-fluted cliffs in soft Tertiary sediments, central Peru. (b) High-altitude view of the same features seen in Fig. X-6a.

Fig. X-7. (a) Reticulate ridges in faulted Tertiary sediments, 5 km south of Paracas, central Peru. (b) Sand- and granule-blanketed terrain near the west edge of the Paracas Peninsula, central Peru.

References

X-1. Sagan, C., Veverka, J., Fox, P., Dubisch, R., Lederberg, J., Levinthal, E., Quam, L., Tucker, R., Pollack, J. B., and Smith, B. A., "Variable Features on Mars: Preliminary Mariner 9 Television Results," *Icarus*, Vol. 17, p. 346, 1972.

X-2. Cutts, J. A., "Wind Erosion in the Martian Polar Regions," *J. Geophys. Res.*, Vol. 78, 1973.

X-3. Sharp, R. P., "Mars: Fretted and Chaotic Terrains," *J. Geophys. Res.*, Vol. 78, 1973.

X-4. Cutts, J. A., and Smith, R. S. U., "Eolian Deposits and Dunes on Mars," *J. Geophys. Res.*, Vol. 78, 1973.

X-5. Sharp, R. P., "Surface Processes Modifying Martian Craters," *Icarus*, Vol. 8, p. 472, 1968.

X-6. Murray, B. C., Soderblom, L. A., Sharp, R. P., and Cutts, J. A., "The Surface of Mars: 1. Cratered Terrains," *J. Geophys. Res.*, Vol. 76, p. 313, 1971.

X-7. Cutts, J. A., Soderblom, L. A., Sharp, R. P., Smith, B. A., and Murray, B. C., "The Surface of Mars: 3.Light and Dark Markings," *J. Geophys. Res.*, Vol. 76, p. 343, 1971.

X-8. Blackweider, E., "Yardangs," *Geological Society of American Bulletin*, Vol. 45, p. 159, 1934.

X-9. Mason, C. C., "The Nature of the Martian Surface as Inferred From the Particle-Size Distribution of Lunar Surface Material," *Geologic Society of America Bulletin*, Vol. 82, p. 2625, 1971.

X-10. Milton, D. J., "Water and Processes of Degradation in the Martian Landscape," *J. Geophys. Res.*, Vol. 78, 1973.

X-11. McCauley, J. F., Carr, M. H., Cutts, J. A., Hartmann, W. K., Masursky, H., Milton, D. J., Sharp, R. P., and Wilhelms, D. E., "Preliminary Mariner 9 Report on the Geology of Mars," *Icarus*, Vol. 17, p. 289, 1972.

X-12. Carr, M. H., "Volcanism on Mars," *J. Geophys. Res.*, Vol. 78, 1973.

X-13. Ryan, J. A., "Notes on the Martian Yellow Clouds, *J. Geophys, Res.*, Vol. 69, p. 3759, 1964.

X-14. Sagan, C., and Pollack, J. B., "Windblown Dust on Mars," *Nature*, Vol. 223, p. 791, 1969.

X-15. Arvidson, R. E., "Aeolian Processes on Mars: Erosive Velocities, Settling Velocities, and Yellow Clouds," *Geological Society of America Bulletin*, Vol. 83, p. 1503, 1972.

X-16. Arvidson, R. E., "Aeolian Processes on Mars: Erosive Velocities, Settling Velocities, and Yellow Clouds, A Reply," *Geological Society of America Bulletin*, Vol. 84, p. 349, 1973.

X-17. Bagnold, R. A., *The Physics of Blown Sand and Desert Dunes*, 265 pp., Chapman & Hall, London, 1941.

References (contd)

X-18. Kuenen, Ph. H., "Experimental Abrasion 4. Eolian Action," *Geology*, Vol. 68, p. 427, 1960.

X-19. Sagan, C., "Sandstorms and Eolian Erosion on Mars," *J. Geophys. Res.*, Vol. 78, 1973.

X-20. Soderblom, L. A., Kreidler, T. J., and Masursky, H., "Latitudinal Distributions of Erosional Debris on the Martian Surface," *J. Geophys. Res.*, Vol. 78, 1973.

X-21. Carr, M. H., Masursky, H., and Saunders, R. S., "A Generalized Geologic Map of Mars," *J. Geophys. Res.*, Vol. 78, 1973.

X-22. Roddy, D. J., "The Flynn Creek Crater, Tennessee," *Shock Metamorphism of Natural Materials*, p. 291, Mono Book Corporation, Baltimore, 1968.

X-23. Wilhelms, D. E., "Summary of Lunar Stratigraphy—Telescopic Observations," *U.S. Geological Survey Professional Paper*, 599-F, 47 pp., 1970.

X-24. Sagan, C., Veverka, J., Fox, P., Dubisch, R., French, R., Gierasch, P., Quam, L., Lederberg, J., Levinthal, E., Tucker, R., Eross, B. and Pollack, J. B., "Variable Features on Mars II: Mariner 9 Global Results," *J. Geophys. Res.*, Vol. 78, 1973.

X-25. Grolier, M. J., McCauley, J. F., Morris, E. C., and Erickson, G. E., *Desert Landforms of Peru, a Photographic Atlas of Morphologic Types*, U.S. Geological Survey Interagency Report: Astrogeology 57 (in press).

X-26. Simons, F. S., and Ericksen, G. E., "Some Desert Features of Northwest Central Peru," *Sociedad Geológica del Perú*, Vol. 26, p. 229, 1953.

X-27. Wilson, I. G., "Universal Discontinuities in Bedforms Produced by the Wind," *J. Sed. Petrology*, Vol. 42, p. 667, 1972.

X-28. Murray, B. C., Soderblom, L. A., Cutts, J. A., Sharp, R. P., Milton, D. J., and Leighton R. B., "Geological Framework of the South Polar Region of Mars," *Icarus*, Vol 17, p. 328, 1972.

Acknowledgments

PRECEDING PAGE BLANK NOT FILMED

XI. Eolian Deposits and Dunes on Mars[1]

J. A. Cutts
Jet Propulsion Laboratory/California Institute of Technology, Pasadena, California 91103

R. S. U. Smith
Division of Geological and Planetary Sciences
California Institute of Technology, Pasadena, California 91109

Eolian features on Earth are found primarily in arid regions where rainfall is sparse and vegetation has been unable to arrest the transport of surface materials by wind. When it became apparent that Mars was a dry world, although with a significant atmosphere, it was natural to infer wind would play an important, if not dominant, role in modifying the form and appearance of the surface. Global obscurations of the major continental-scale albedo features of the planet observed from Earth were first interpreted many years ago as massive dust storms (Ref. XI-1). The more subtle and gradual seasonal and secular changes in these features, interpreted at first as the growth of vegetation, in more recent years, also have been attributed to wind action (Ref. XI-2). High-resolution views of albedo markings from *Mariners 6* and 7 (Ref. XI-3) and from *Mariner 9* (Ref. XI-4) have left little doubt that wind transports Martian surface materials.

Most of these observations are relative to superficial effects. The dust storms and surface markings could be explained in terms of a thin veneer of material, perhaps

millimeters thick. Observations of changes on a diurnal or annual time scale required that this be the case, and the seeming reversibility of many changes seemed to indicate a cycle in which material was returned to its source.

More detailed analysis of the *Mariner 9* pictures reported in this section and in other sections in this Report now reveals that eolian activity is not only a superficial effect, but a surface process of profound importance in the geologic evolution of Mars.

Moderate- and large-scale topographic features that may be attributed to wind erosion have been described (Refs. XI-5 and XI-6; also see Sections X and XV of this Report), and latitudinal variations in crater morphology have been interpreted in terms of eolian deposition and erosion in the mid-latitudes of Mars (Ref. XI-7; also see Section IX of this Report). Eolian deposits also are believed to exist in equatorial and polar latitudes. Smooth plains interpreted as eolian materials embay volcanic terrains (Ref. XI-8; also see Section II of this Report); deeply eroded layered deposits mantle older cratered

terrains and underlie the residual frost caps (Ref. XI-9; also see Section XVII of this Report)

This section assesses the pictorial evidence for the existence of eolian dunes on Mars. The dune is the most familiar of terrestrial eolian features, and the occurrence of analogous features on Mars has important consequences for the geologic and meteorologic environment of the planet. We find our most convincing evidence for dune formation in the Hellespontus region of Mars, and the principal conclusions of this section are based on this identification of a dune mass in that location. However, possible dune features exhibiting a great variety of morphologies in other parts of Mars are also examined, and the progressive modification of cratered terrains by deposition of dune-forming materials is discussed. This section is a companion to the analysis of eolian erosion features given by McCauley in Section X of this Report (see Ref. XI-5).

A. Dune Characteristics

Dunes are constructional topographic forms that develop from assemblages of loose fragments of mineral or rock in certain size ranges under the action of a moving fluid such as wind. Bagnold (Ref. XI-10) first provided the insights that explained why grains of sand collect into dunes instead of scattering evenly over the land as do fine grains of dust. Bagnold recognized that particles forming dunes move predominantly by saltation, a bouncing motion initiated when a grain is picked up from the surface by a turbulent eddy, moves in a downwind trajectory on assuming the motion of the wind, and impacts the surface at a shallow angle. If this impact is on much larger particles or on solid, unbroken rock, the grain rebounds into the air, although it may impart some motion (traction) to the larger particles. If it encounters similar or smaller size particles and if the wind is strong enough, it will spray them into the air. At lower wind velocities, the motion can be sustained only on rock and pebble surfaces because the energy of impact with a surface of fine particles becomes dissipated. Thus, under these conditions, moving grains collect on patches of stable grains and the landscape is not uniformly mantled, but is comprised of segregated bodies of sand (Ref. XI-10). These bodies can assume fairly simple individual dune forms such as barchans or linear seif dunes. Depending on the availability of sand and the nature of the wind regime, these individuals can persist or coalesce into complex forms of diverse morphology.

Bagnold eloquently described, but did not adequately explain, the various shapes that dunes assume and maintain.

"In the great deserts, instead of finding chaos and disorder, the observer never ceases to be amazed at a simplicity of form, an exactitude of repetition and a geometric order unknown in nature on a scale larger than that of crystalline structure. In places vast accumulations of sand weighing millions of tons move inexorably, in regular formation, over the surface of the country, growing, retaining their shape, even breeding, in a manner which by its grotesque imitation of life, is vaguely disturbing to an imaginative mind. Elsewhere, the dunes are cut to another pattern—lined up in parallel ranges, peak following peak in regular succession like the teeth of a monstrous saw for scores, even hundreds of miles without a break and without a change of direction over a landscape so flat that their form cannot be influenced by any local geographical features."

Today an explanation of the complex variations in morphology seen in terrestrial dunes is still lacking, but the quotation encapsulates some of the characteristics of dunes that can help us to recognize them in orbital photography of another planet.

B. Observations of Dunes

1. Hellespontus Region

The single most convincing example of a dune field on Mars is found in a large, dark-floored crater at 47.5°S, 331°W, in the Hellespontus region of Mars. The complex of sinuous coalescing ridges and individual marginal forms corresponds almost exactly to the distribution of dark albedo materials in the crater floor. This section reviews the morphologic similarities with eolian forms on Earth that lead us to concur with an earlier report (Ref. XI-11) that the feature is indeed a dune mass.

Oval in ground plan and elongated in a northerly direction (Fig. XI-1a), the suspected Hellespontus dune mass measures about 60 by 30 km. Its morphology is dominated by a series of prominent, subparallel ridges 1 to 2 km apart and trending N15°W to N35°W; they are represented in Fig. XI-1b by the heavy lines. Viewed stereoscopically, many of these appear to have rounded crests, similar steepness of slope on either side of the ridge crest, and to be separated by flat surfaces about as wide as the ridges (Fig. XI-2c). Ridges of this system are crossed by narrower, apparently sharper-crested

ridges trend- ·t north to N30°E; these lack the continuity elevations at intersections with the NNW ridges (Figs. XI-2e and XI-2h).

The margins of the mass possess a diversity of morphology lacking over the interior. Variations occur both around the perimeter and across the marginal zone. On the northeast and northwest margins. narrow ridge features are oriented approximately NNW, meeting the perimeter of the dune mass at varying angles. These narrow ridge features appear to be transitional to individual crudely equant forms (Figs. XI-1a and XI-1b). which are not seen along the remainder of the perimeter of the dune mass. The morphology and transitional relationships are described in more detail in the subsequent paragraphs.

Parallel ridges of the north margin, 2 to 5 km long, trend N15°W to N25°W and are ¼ to ½ km apart (Fig. XI-2b). This zone of closely spaced ridges extends about 15 km south where it abuts the region of widely spaced ridges, but contains enclaves of topography which lack any discernible linearity (see Fig. XI-2b, lower-right corner). Southwest from the northern apex, the ridges are subparallel to branching, ½ km apart, 1 to 4 km long and trending north to N25°W (Fig. XI-2a). Along the margin are individual, crudely equant features ½ to 1 km across, the largest of these has a peaked, crescentic appearance opening northward when viewed stereoscopically. Southeastward from the northern tip of the mass, the closely spaced ridges are bordered by a zone of individual features with somewhat different characteristics. In Fig. XI-2c the ridges are 1 to 4 km long, ½ to 1 km apart, and trend N20°W to N35°W; on their borders, the triangular individual features are about 1 km across and are closely spaced in rows en echelon with their corners touching. Along the southeastern margin, the widely spaced ridges curve southwestward at their ends, and some large, crescent-shaped features are seen.

Near the crater in Fig. XI-2f is a series of 1-km crescentic features, each opening westward and heading at one of the arms of the next crescent east in an en echelon manner, strongly reminiscent of the arrangement of closely spaced terrestrial barchan dunes. At the top of Fig. XI-2h is a crescentric feature about 1 km across with a gentle, domed northeast side. Along its southwest side it has a straight, steep slope curving into blunt horns ½ km long; the northern horn merges into one of the widely spaced ridges. This feature strongly resembles a

barchan dune as do, to a lesser degree, some other ridge terminations.

Parallel to the western margin of the mass are ridges ½ to 1½ km apart trending N20°E to N30°E (Fig. XI-2g). These appear to be a coalescence of somewhat crescentic features opening northwestward; each individual is about ½ km across and has, on its north side, a ridge up to 1 km long oriented with the trend of the coalesced ridge. Northward from here, the ridges are less prominent, and individual features ½ to 1 km across are up to 3 km from the main mass (Fig. XI-2d). Some appear crescentic opening northward, with sharp, north-trending spurs on their northwest corners and bulbous protrusions on their northeast corners. They may be better developed forms of the crudely equant features seen in Fig. XI-2a and described in the preceding paragraphs.

The crater floor, which underlies the entire mass of ridges and individual forms, is locally crossed by southeasterly trending trenches (Fig. XI-1a). The southern part of the crater is covered by long dark filaments that branch irregularly and trend generally SSW except where they are locally crossed at high angle by similar short filaments. These filaments meet the main mass in a zone along the southern part of the margin which is characterized by ridges as opposed to assemblages of individual forms. At one location (Fig. XI-2h), the marginal ridges appear to splay out and locally merge with the dark filaments. The relationship of these dark filaments with the main mass and their general geometric anastomosing pattern is not unlike that seen in terrestrial seif dune complexes (e.g., Ref. XI-12). Alternatively they may represent fracture patterns or erosional scour features in the crater which have trapped dune-forming materials. They are not mapped in Fig. XI-1b.

2. Comparison With Terrestrial Features

We have not attempted to find exact terrestrial analogies of the ridge structures and individual forms described above. However, the pictures shown in Fig. XI-3 do show some characteristics of terrestrial dunes. They show the importance of resolution in their definition; they indicate the diversity of ridge structures and individual dunes found in nature; and they display an "ordered chaos" quite similar in style to that seen in the Hellespontus crater described above.

Figures XI-3a through XI-3d show various segments of the Algodones dunes, southeastern Imperial County, California, at scales increasing from that of Fig. XI-2 to about 30 times larger. These dunes have been described

Fig. XI-1a. Suspected dune mass in Hellespontus near 475°S, 331°W. As viewed by the *Mariner* 9 wide-angle camera, the general area is characterized by large subdued craters with irregular dark markings in their flat floors. The mosaic of high-resolution pictures shows the dark marking at the lower right of the wide-angle frame (inset) to be a complex of ridges with a diverse marginal topography comprised of ridges and individual features. Surrounding the suspected dune mass is a substrate displaying craters and some structural patterns. The filamentary dark markings which merge with the dune mass near the bottom of the mosaic also may be dunes. (Mosaic: MTVS 4264-20, DAS 09807499; MTVS 4264-16, DAS 09807429; MTVS 4228-15, DAS 08548829. Inset: IPL Roll 267, 220313.)
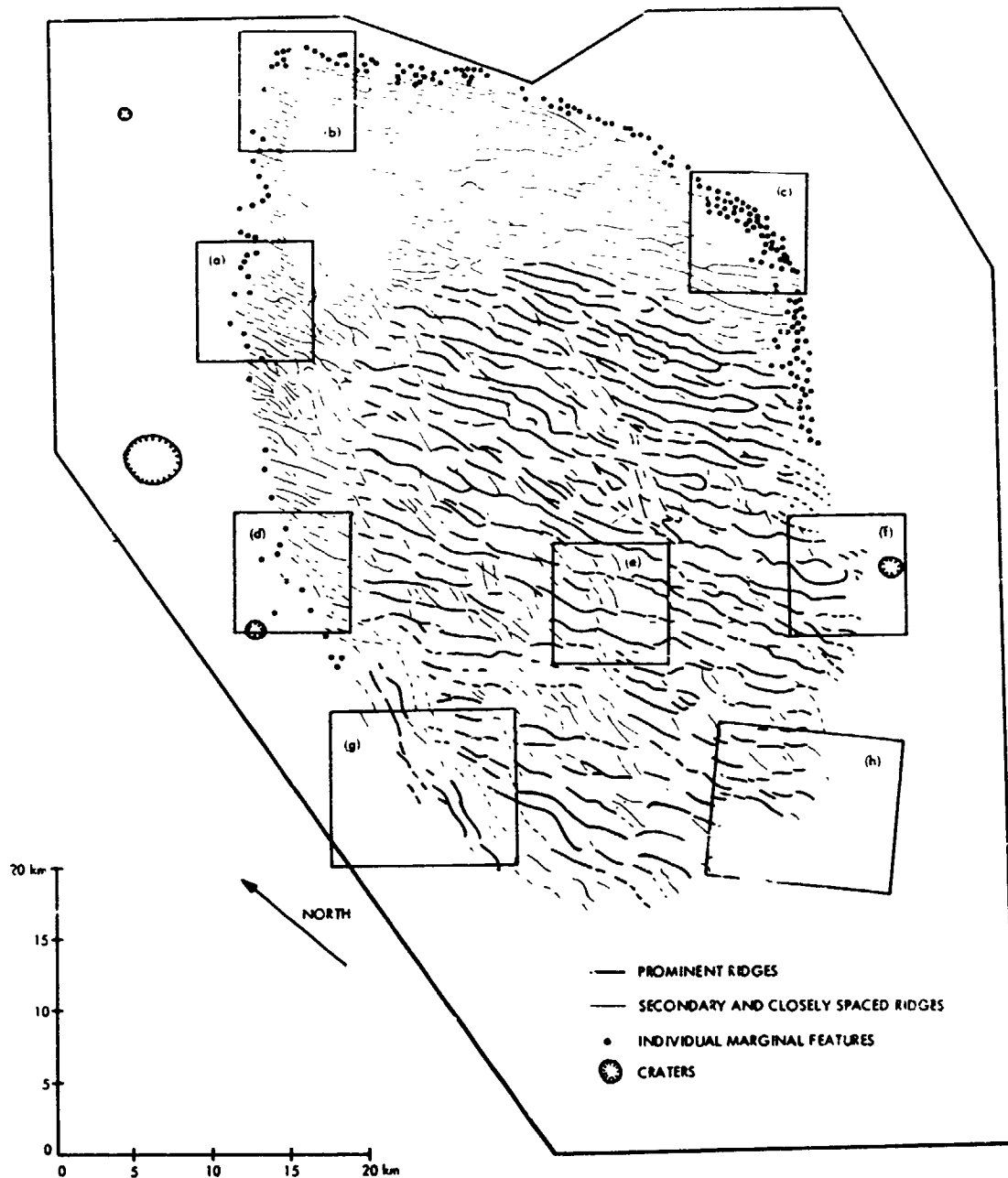
Fig. XI-1b. Map showing the principal features of the suspected Hellespontus dune mass (Fig. XI-1a) at the same scale. The most prominent subparallel ridges trending N115°W to N35°W are represented as heavy lines. Narrower, sharper-crested ridges crossing these in various parts of the mass are denoted by light lines. Dots indicate crescentic triangular or irregular forms that may be individual dunes. The dashed lines indicate ridge structures in which the continuation of individual ridges is uncertain. In areas in the submarginal zone, which has been left blank, the dune mass appears structureless. The rectangles identify areas that appear enlarged in Fig. XI-2.

Fig. XI-2. Features of the marginal zone of the suspected Hellespontus dune mass are compared with one another and with the ridge structure near the center of this feature.
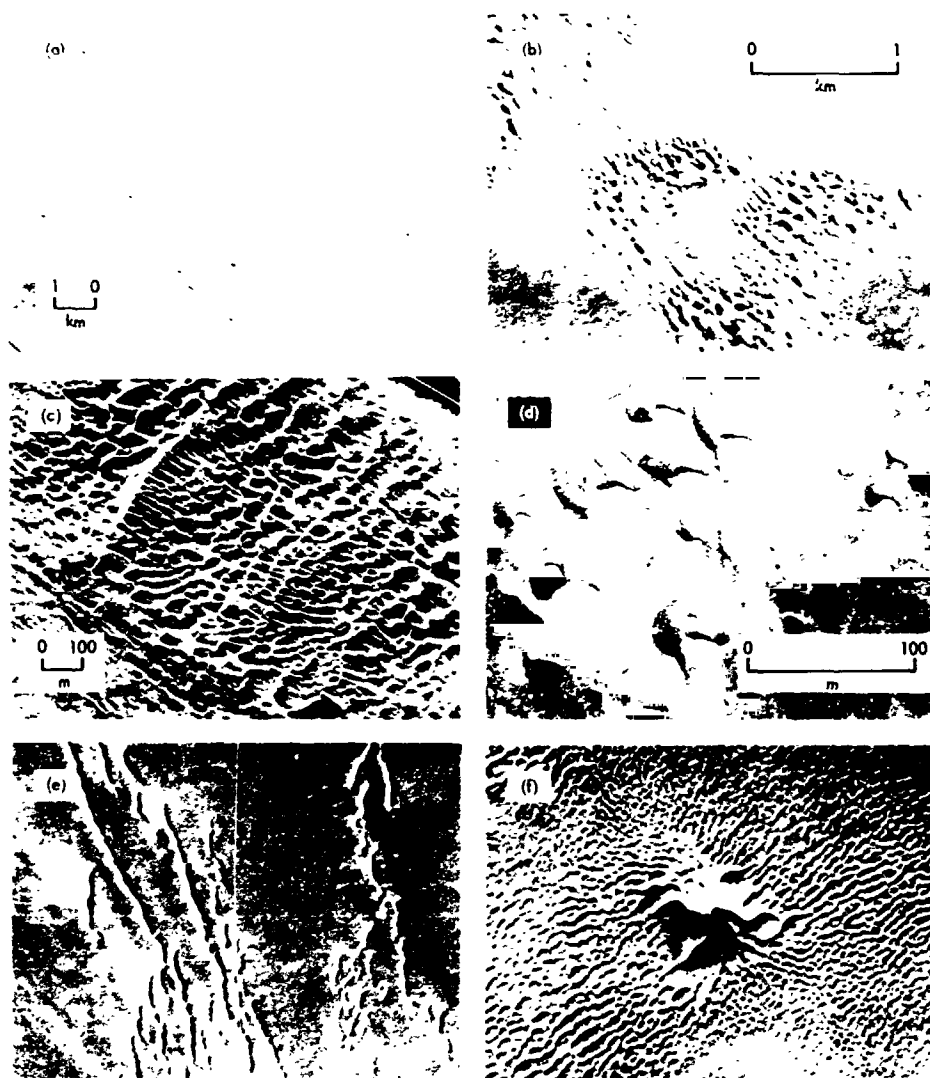
Fig. XI-3. Terrestrial photographs showing some of the characteristics of dune fields. No strict similarities with any of the Martian features is intended here. Figures XI-3a through XI-3d illustrate the importance of resolution in recognizing the topography in the Algodones dunes of Southern California. The low-resolution photograph (a) has several times the resolution of the *Mariner 9* narrow-angle camera. Thus, *Mariner 9* pictures of this area would show only a subtle wavelike pattern. The highest-resolution photograph (d) shows the barchan dune, a crescentic individual dune with its steep slip face on the concave side of the feature. Some of the individual forms on the periphery of the Hellespontus feature (Fig. XI-2) may be barchans several times the scale of those shown here. Although the barchan is the easiest dune to understand theoretically, it is not the only type of individual dune. The peaked or pyramidal forms found in the Sahara desert (f) may be closer in characteristics to the triangular dunes (Fig. XI-2c). The narrow ridge structures (e) also resemble other suspected Martian dune features. Figures XI-3a through XI-3d are Algodones dunes, southeastern California, at various scales. (a) USAF 665V048, 1967. (b) 61S7274A, 1961. (c) M29 137 SMCS (CAIP) 630, 1962. (d) Photographed by R. S. U. Smith, 1972. (e–f) From Ref. XI-17.

by Norris and Norris (Ref. XI-13), small crescentic dunes (barchans) within them have been described by Norris (Ref. XI-14) and R. S. U. Smith (Refs. XI-15 and XI-16). Figure XI-3a shows a northeastward orientation of large-scale features within the main dune mass and the marginal ridges oriented northwesterly along the elongation direction of the dune mass. Figure XI-3b, from farther southeast in the dunes, shows the "megabarchans" of Norris and the swarms of barchans on the intervening flats. Note that these swarms are apparently concentrated into discrete lanes controlled by sand flux from the low points on the southeast margin of the northwest dune mass. Figure XI-3c shows the characteristic surficial morphology of the dune mass. Note the sinuous, parallel ridge crests and lower crossing ridges. Figure XI-3d shows some of the small barchan dunes like those in the swarms of Fig. XI-3b; these move southeasterly, but were deformed by strong northerly winds shortly before the picture was taken. Note their characteristic crescentic shape and rough similarity to the "megabarchans" in Fig. XI-3b, despite their being more than an order of magnitude smaller.

In gross appearance the large-scale repetitive features of the Algodones dune mass (Fig. XI-3a) resemble the central portion of the suspected dune mass of Hellespontus (Fig. XI-2e). Although the scales in both figures are similar, the resolution of the terrestrial photograph is much greater, which may account for the greater abundance of fine structure. Structure at the 100-m scale and below is typical of large-scale terrestrial eolian ridges. H. T. U. Smith (Ref. XI-17) describes individual large ridges of this type as composite dunes; some other authors, notably Wilson (Refs. XI-18 and XI-19), believe that they represent distinct eolian features (draas) with a different mode of formation than simple smaller scale ridge dunes. These smaller-scale ridge dunes have been considered to fall into two classes. Transverse dunes form perpendicular to a prevailing wind and exhibit a shallow windward slope and a steep leeward slope or slip face upon which sand lies at the angle of repose (approximately 34°). Longitudinal dunes have steeply sloping and essentially symmetrical ridge structures which, in some cases, seem to be aligned with the vector sum of winds from quite different directions (Ref. XI-10). Stereoscopic examination indicates that the large-scale ridges of the suspected Hellespontus dune mass are morphologically different from simple transverse dunes; because of the scale difference alone, this is not surprising.

One notable difference between most terrestrial dunes and the individual features marginal to the suspected

Hellespontus dune mass is albedo. Terrestrial dunes usually appear light against a darker background or with very little contrast. This can be attributed to the fact that most terrestrial dune sands are predominantly quartz (Ref. XI-20). The crescentic, equant triangular, and filamentary forms seen in Hellespontus appear dark against a light background. Photographs of crescentic or barchan dunes in Peru (Refs. XI-21 and XI-22) also have this appearance, although it seems to be exceptional. In the Peruvian cases, the dunes are found to be primarily minerals and lithic fragments derived from andesite. Infrared interferometer spectrometer measurements from Mariner 9 indicate basic rock compositions (Ref. XI-23). Thus, the sands of Mars may consist, not of quartz, but of dark minerals deficient in silica.

Dune features of the Sahara desert reproduced from H. T. U. Smith (Ref. XI-17, pp. 38 and 44) appear in Figs. XI-3e and XI-3f; their scale is not given, but is roughly comparable to Fig. XI-3b. The peaked dunes in Fig. XI-3f illustrate that there are types of individual dune forms other than the barchan. The barchan with its crescentic form with horns trailing downward is the simplest dune geometrically and perhaps the easiest to understand theoretically. However, other types of individual dunes are found terrestrially (Ref. XI-17), and we would not be surprised if individual dunes on the margins of the Hellespontus feature have divergent morphologies.

In summary, the suspected Hellespontus dune mass has many features in common with terrestrial dune masses including the scale and diversity of its surface morphology. In the interior of the mass, these include: (1) consistent trend of the subparallel widely spaced ridges; (2) their irregular sinuosity; (3) local branching of ridges; (4) even ridge spacing; (5) ridge length far exceeding width; (6) presence of peaks and saddles along ridges; (7) irregular marginal topography of some ridges; (8) presence of flat terrain, possibly the crater floor, beneath some ridges; and (9) irregular crossing of the widely spaced ridges by a lower set of narrow, short ridges subparallel to each other, but oblique to the trend of the main ridges. Along the margins of the dune mass, these similarities include: (1) presence of low, closely spaced ridges parallel to the widely spaced interior ridges (Figs. XI-2a, XI-2b, and XI-2c); (2) their sinuosity, length versus width and local branching; (3) presence of individual forms (Figs. XI-2a, XI-2c, XI-2d, and XI-2f); (4) crescentic appearance of some individuals (Figs. XI-2d, XI-2f, and XI-2h); (5) en echelon arrangement of individuals (Figs. XI-2c and XI-2f); (6) presence of

oblique marginal ridges, which may be coalesced en echelon individuals (Fig. XI-2g); (7) bending of widely spaced ridges at their ends against the margin (Fig. XI-2h); and (8) irregular ground plan of the entire mass (Fig. XI-1a).

Structural and erosional forms show some of these characteristics but not all; we can, therefore, find no other reasonable explanation for the feature other than a dune mass.

3. Inferences About Wind Regime

The ridge mass we have been describing corresponds closely to an area of dark albedo on the crater floor. Dark albedo markings on crater floors are common on Mars, particularly in the Hellespontus region, and we suspect that, (1) these features are also dunes; and (2) crater floors are favored sites for the accumulation of dune-forming materials.

The mere existence of a large accumulation of dune-forming sand in a particular topographic setting tends to imply a balance between the effects of winds from several directions. Sharp (Ref. XI-24) described a dune mass in California where topography has modified a prevailing wind regime. He attributes the accumulation of sand in the Kelso dunes to strong storm winds channeled by mountain passes cancelling the effects of prevailing westerly winds. Comparable topographic modification of wind directions and intensities may cause sand to accumulate in crater floors on Mars.

Some preliminary ideas about the wind regime in the vicinity of the Hellespontus crater can be gained from studies of albedo markings. Albedo streaks emanating from craters are the most reliable indication of wind direction, but dark albedo markings biased to one side of the crater floor have also been used to infer wind patterns (Refs. XI-6 and XI-25; also see Sections XV and XIII of this Report). The mere existence of such a large accumulation of dune-forming materials in the Hellespontus crater tends to imply a balance between the effects of winds from several directions. However, dark albedo markings in craters in the vicinity (presumably also dune accumulations) lie in the northeastern parts of the crater floors, suggesting dominant winds from the southwest. It may be significant that the major ridge structures are perpendicular to this direction; small features resembling barchans (Fig. XI-2d) are bilaterally symmetrical with respect to it, and the dark filamentary forms are roughly aligned with it. We speculate that much of the dune material is accreting from the southwest.

C. Other Possible Dune Features

Many other features visible in the *Mariner 9* pictures may be either primary dune features or impact, fluvial, volcanic, or erosional features that have been highly modified in appearance by a mantle of dune sand. Some examples of such features are discussed below.

1. Diverse Patterns in Dark-Floored Craters

A mosaic of high-resolution pictures (Fig. XI-4) shows small-scale (20 to 30 km), dark-floored craters near 65°S. The dark floor of the crater with the more subdued rim (lower left) is comprised of long, curving sub-parallel dark streaks which divide and coalesce in a manner suggesting the ridge structures found in terrestrial dune fields (Fig. XI-3c). This pattern differs from that observed in the Hellespontus crater. The ridges are lower and more closely spaced and show much less branching and modification by cross-cutting ridge patterns. However, the contrast with the nearby dark-floored crater (Fig. XI-4, upper right) is even more marked. The rim of this crater is more prominent; although the dark markings within it have a similar shape and location, the fine structure within it is entirely different. On the left side, it comprises five concentric dark-toned arcs, indicating either concentrations of dark material or steep slopes facing toward the center of the crater. There is some suggestion of a radiating pattern transecting and modifying these arcs. To the right side, the arcs merge and develop into dendritic patterns branching into the northern parts of the crater floor and terminate at the sharp albedo contact, which is found about one-fourth of the crater diameter inside the rim.

The gross features of the pattern in the crater at the upper right are unlike those found in terrestrial dune fields. Yet if the pattern in the crater at the lower left is a dune field, the proximity, setting within a dark albedo feature, and the general tonal characteristics would seem to argue that eolian modification also is involved in this crater. Perhaps the pattern in the crater floor is polygenetic with radial and concentric structural features controlling the distribution of dune materials; volcanic flow fronts or impact melts also may be involved.

2. Dunes Formed by Topographic Obstructions

While the dune-forming process can give rise to primary topographic forms in the middle of a flat and featureless plain, pre-existing topography can, as we have seen with the Hellespontus dune mass, control the location of a dune mass. Pre-existing topographic features

Fig. XI-4. Dark-floored craters near 65°S. In the crater with the subdued rim (lower left), the series of curving features resembles ridge forms found in dune fields. The detail in the other crater (upper right) is more complex. The concentric circular features may be structural or volcanic, but the general similarity in setting and texture with its companion crater suggests eolian modification. (IPL Roll 1571, 131138; IPL Roll 1571, 130245)

can also have a much more direct influence on the location and morphology of dunes. Climbing dunes and lee dunes that are draped over mountain ridges are terrestrial examples. The features in Fig. XI-5 may also fit this classification. All of them lie south of 65°S. Figs. XI-5a and XI-5b are immediately peripheral to the layered deposits of laminated terrain which occupy the central polar regions in both hemispheres.

The extremely regular ridge pattern (Fig. XI-5a) is developed from south of the crater rim and splays out into the central part of the crater floor. In Fig. XI-5b a ridge pattern also is developed within a crater floor; however, in this case, the south part of the crater floor is mantled by several hundred meters of layered deposits. The ridges are developed perpendicular to the escarpment that represents the abrupt margin of these layered deposits and extends to the northwest away from the pole. Both the features of Figs. XI-5a and XI-5b contrast with those shown in Figs. XI-1, XI-2, and XI-4 in that the suspected dune features are light against the dark crater floor. The ridge patterns are also longer, straighter, and exhibit fewer coalescing and cross-cutting members.

The suspected dune features of Figs. XI-5c and XI-5d differ from those of Figs. XI-5a and XI-5b in that they are developed outside rather than inside craters. Curving away from the rim of a crater near 65°S, 365°W, is an assemblage of light and dark streaks extending toward the northwest. In this particular case, however, it is difficult to discriminate topographic relief within these features. The existence of discrete filamentary forms is strongly suggestive of terrestrial dunes. The features extending to the northwest of the crater shown in Fig. XI-5d are much less regular, but do exhibit topographic relief. They may be dunes; they may also be residual ridges which have survived the erosion of a thick blanket of materials which once mantled a broad area in this part of Mars.

3. Cratered Terrain Modification by Eolian Deposits

The observation of highly subdued, non-lunar-like cratered terrains by *Mariners* 6 and 7 led Murray et al. (Ref. XI-26) to conclude that a uniquely Martian process was modifying the surface. The complete planetary mapping coverage provided by *Mariner* 9 reveals an entire
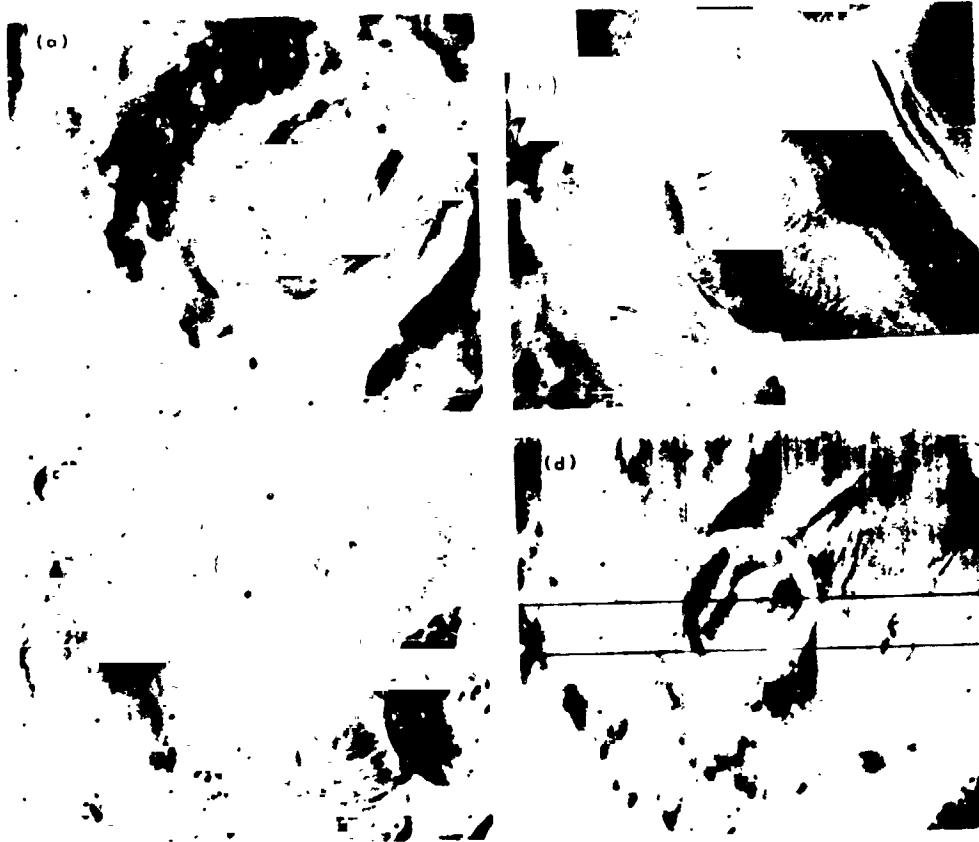
Fig. XI-5. Features resembling dunes which appear to be controlled by the topography of the craters with which they are associated. The features within the craters (Figs. XI-5a and XI-5b) are close to the margin of laminated terrain in the south polar region. The crater in Fig. XI-5b is partly mantled by laminated terrain, and the ridge features in the crater floor are aligned perpendicular to the marginal escarpments. Figures XI-5c and XI-5d show possible dune features outside craters contiguous with the crater rims. (a) MTVS 4269-19, DAS 09986839. (b) MTVS 4222-12, DAS 08367879; MTVS 4285-67, DAS 10654504. (c) MTVS 4196-8, DAS 07504633. (d) MTVS 4162-27, DAS 06425303.

spectrum in the modification of cratered terrain on Mars. McCauley (Ref. XI-5; also see Section X of this Report) recognized erosional stripping of cratered terrain in certain areas of Mars, evidenced by erosional pedestals of impact craters and etching of ejecta blankets. Impact, volcanism, mass movement, and possibly even water erosion are other processes that may modify cratered terrains. Here we attempt to isolate modification caused by deposits of dune-forming materials.

A pair of the most pristine impact craters so far recognized on Mars is shown in Fig. XI-6a. The craters exhibit the well preserved rim structures, central peaks, and bright-ray patterns that are typical of Copernican craters on the Moon. In Fig. XI-6b is a scene that is more typical of Mars at almost exactly the same range and con-

ditions of illumination and viewing. The crater rims are subdued, and the central peaks have disappeared; the bright ray pattern has vanished and has been replaced by a mottled albedo pattern. Such patterns are now regarded as surficial and time variable and attributable to eolian activity (Ref. XI-4). This is a sufficient explanation for the disappearance of the ray patterns; the loss of central peaks and the muting of topography may also be explained by eolian deposits, although other mechanisms may have contributed.

Figure XI-6c shows what may be another stage in the modification of cratered terrains by eolian materials. A wind-mobilized flux of material across the surface is indicated by the occurrence of light and dark streaks extending from craters and other topographic protuber-
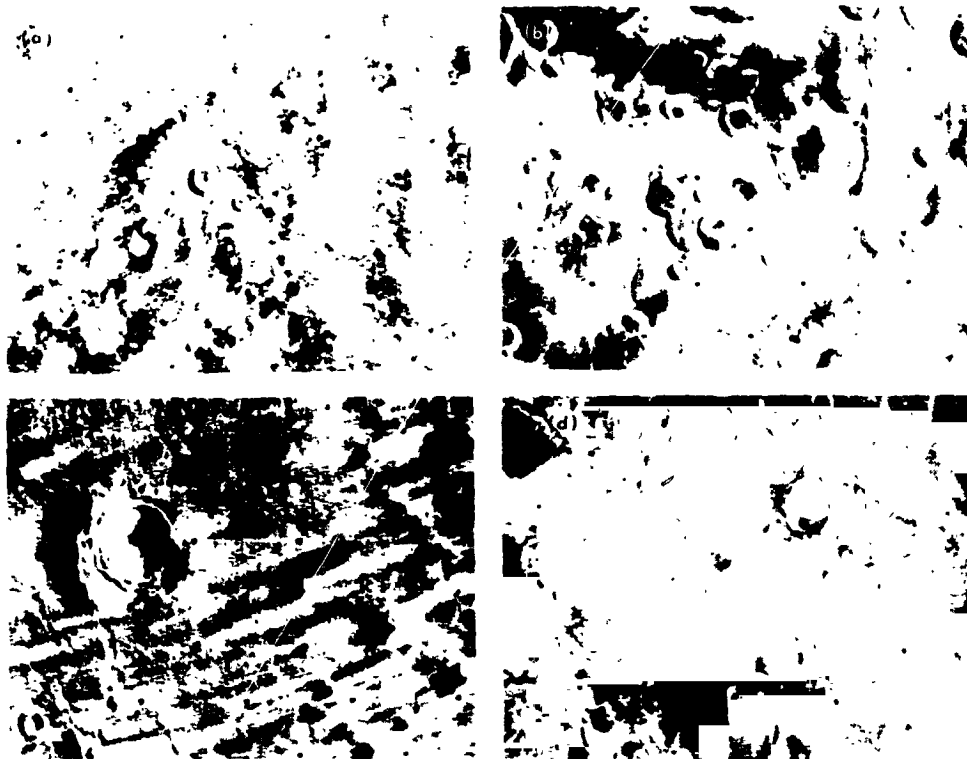
Fig. XI-6. Modification of cratered terrains by eolian processes. (a) Cratered terrain near 39°N, 30°W, in which ejecta patterns are preserved as albedo markings and the rims and central peaks of the two large impact craters are preserved. (MTVS 4298-120, DAS 13460623) (b) A typical scene in which the albedo markings are attributed to eolian activity; the subdued appearance of the surface at 63°S, 251°W, suggests eolian activity, and the subdued appearance of the surface suggests eoliar deposition. (MTVS 4174-6. DAS 06820768). (c) Eolian deposition may have reached a more advanced stage with the development of a complex topography on the crater rim near 25°S, 248°W. (MTVS 4240-32, DAS 08981114). (d) Still further eolian activity is suggested at 10°S, 330°W, where sinuous dune-like forms cover the inter-crater spaces. (MTVS 4288-27, DAS 11620533)

ances. However, the large 50-km crater does not exhibit a simple rim or even a terraced structure, but consists of a series of regular, or en echelon, ridges with roughly bilateral symmetry about the axis represented by the streak patterns. Some of this symmetry may be illusory, a consequence of the albedo of the surficial materials affecting the discrimination of topography. However, this crater and others like it are non-lunar-like and differ in appearance from those found on many Martian terrains. Dune accumulation may account for some of the features seen here.

This deposition may not be confined to the crater rims. The intercrater spaces also exhibit sinuous features (Fig. XI-6d) which, in some cases, originate at crater rims or are draped around them. Some of these features appear to be channels (Ref. XI-27; also see Section III

of this Report). They appear to have been modified in tonal relationships and subdued in topographic relief, perhaps by accumulations of dune materials. However, some of the dark sinuous features may actually be dunes extending across the light intercrater spaces.

4. Suspected Dunes on Polar Laminated Terrains

The central parts of the polar regions are occupied by layered deposits, developing thicknesses of up to several kilometers, and termed "laminated terrain" by Murray et al. (Ref. XI-28), who suggest that these deposits are comprised of dust mixed with volatiles. A model for the incorporation of dust derived from the equatorial and mid-latitudes into the deposits has been developed by Cutts (Ref. XI-9; also see Section XVII of this Report). Some disagreement exists on the nature of the present

surface of this deposit. Murray and Malin (Ref. XI-29) contend that massive constructional features in the form of plates account for its main characteristics. Cutts (Refs. XI-6 and XI-9; also see Sections XV and XVII of this Report) presents an alternative view that wind erosion of the layered deposits can account for the absence of impact centers and the pits, flutes, and grooves that are intimately associated with the terraced slopes developed within the layered deposits.

Pits, flutes, and grooves, however, are not the only small-scale features seen on the surface of the layered deposits. Figure XI-7 shows a series of distinctly different features and textures which may be dunes. The most convincing of these (Fig. XI-7d) is from the north polar region; it strongly resembles terrestrial swarms of barchan and transverse dunes, the former being marginal features merging into the latter in the congested central zone (compare with Fig. XI-3d). Figure XI-7c shows a feature in the south polar region which may be similar. Figures XI-7a and XI-7b show peaked topography near the limit of resolution along the crests of gentle slopes; these could be peaked dunes. Figure XI-7e show topography which is irregular in detail, but which has two persistent trends of sinuous and branching ridges oblique to each other. Figure XI-7f shows features in the laminated terrain, possibly similar to that of Fig. XI-7e, but more irregular.

Even if one were to assume that all features on the layered deposits are products of eolian action, he should question whether it is possible to distinguish erosional features from dune features when the scale of all of these features is only marginally above the resolution of the images. This objection is a valid one, but there is other evidence for distinguishing erosional from dune-mantled surfaces which is applicable to the layered deposits. Erosion of a layered deposit should produce a surface in which materials have either been etched away or lie in the configurations in which they were originally deposited Dunes formed on a layered surface will consist of loose mobile materials, derived perhaps from isturbance of the substrate, which mask and cover the surface layering. The features of Fig. XI-7 display this latter relationship. For example, in Figs. XI-7a and XI-7b, the assemblages of peaked topography embay and mask outcrops of layered strata. In Fig. XI-7c we recognize albedo differences that are not due to frost, that do not correspond to contacts between laminated layers such as those visible in Fig. XI-7b, but that could be explained in terms of a swarm of dunes overlying a dune-free surface.

5. Elongate Depressions of Amazonis–Memnonia

Large, elongate troughs of eolian erosion are the prominent landforms on two overlapping narrow-angle pictures (MTVS 4171-57, DAS 06751223; MTVS 4254-55, DAS 09484799)[2] at about 1.5°N, 157°W, and covering an area greater than 3000 km² in Amazonis–Memnonia (Fig. XI-8a). In the second frame mentioned, which shows them most clearly, they are northeasterly oriented elliptical streaks with steep slopes, possibly slip faces, along their southwest margins, extending in a semicircular arc of about 90° to the direction of elongation. Most of them are 1½ to 2 km wide by 2½ to 3 km long, but range up to 2½ by 7 km; some streaks extend 15 km. Some display a broad medial ridge, tapering to a point at the southwest end of the feature.

These features seem to have been developed in a featureless uncratered plain, probably a fairly thick blanket of unconsolidated sediment. Stereoscopic examination shows no noticeable slope leading to the sharp escarpments at the heads of the features. However, each of five similar features clustered in the upper left of Fig. XI-8a shows such slopes and is barchanoid in form, about 2 km long by 2 km wide.

Possible terrestrial analogs to these troughs have been found in a zone of intense eolian sand flux in Coachella Valley, California. On a sand plain, featureless except for scattered bushes, troughs about 200 m long by several meters deep have been excavated behind buildings. There appears to be some sand deposition upwind of the buildings, but a prominent crescentic slip face has not yet developed there. These troughs have probably been cut in less than 20 years. It is unknown what their eventual dimensions may reach or what size feature might form behind a larger obstacle.

Because the Coachella Valley features have formed in sand, their Martian analogs are inferred to have formed in noncohesive materials. For this reason we have included them in the class of dune-like phenomena rather than with the erosional pits formed in consolidated or cohesive materials (Refs. XI-5 and XI-6; also see Sections X and XV of this Report).

---

[2]Numbers in parentheses that appear in the text refer to *Mariner* 9 television pictures not included in this section, but which provide additional explanatory material. All *Mariner* 9 pictures may be ordered from the National Space Science Data Center, Code 601, Greenbelt, Maryland 20771.

Fig. XI-7. Unusual textures that may represent dune-forming processes on the laminated terrains of the polar regions of Mars. These terrains are believed to have fo. .ed originally as layers of dust, and so an eolian origin eems plausible. The principal problem here may be in distinguishing between constructional (dunes) and erosional forms. (a) MTVS 4240-16, DAS 08979679. (b) MTVS 4242-2, DAS 09051572. (c) MTVS 4229-8, DAS 08584179. (d) MTVS 4298-6, DAS 13463049. (e) MTVS 4295-106, DAS 12906668. (f) MTVS 4149-21, DAS 06029803.
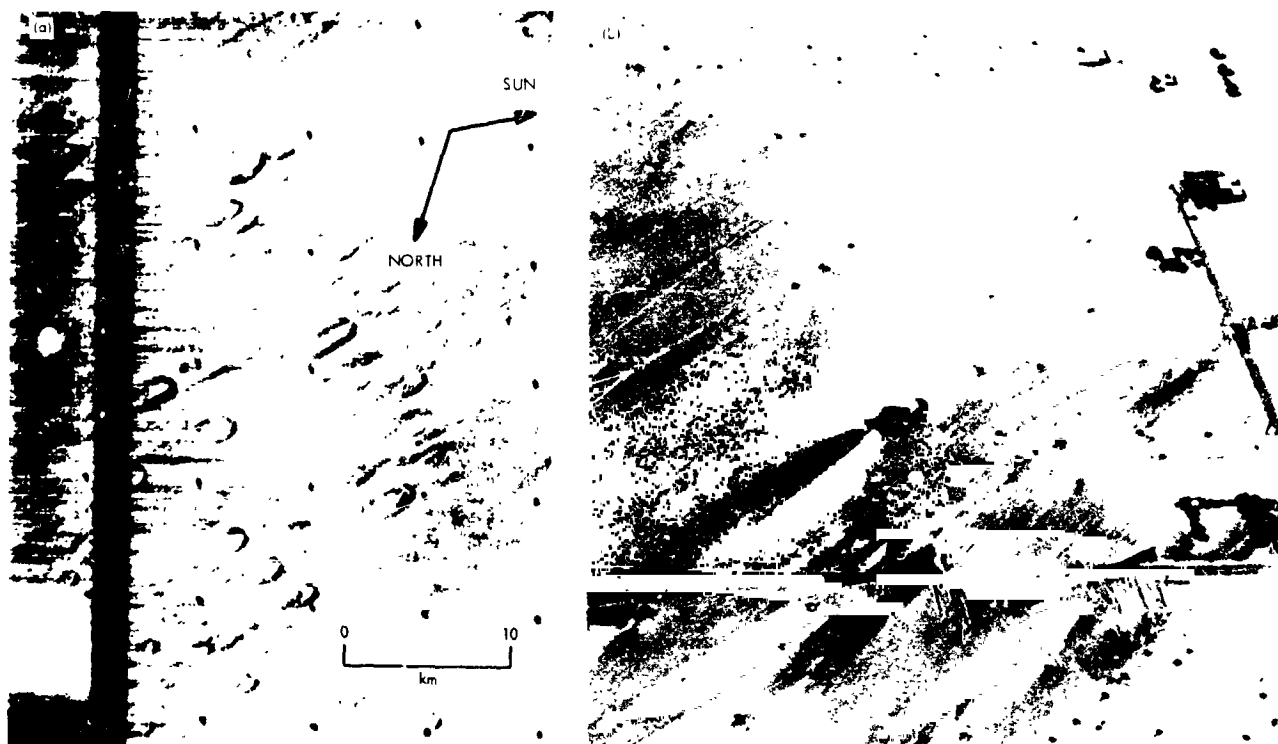
Fig. XI-8. (a) Elongate depressions in the Amazonis–Memnonia region of Mars. (MTVS 4254-55, DAS 09484799) (b) Depressions in an area of active sand flux in Coachella Valley, Southern California (photographed by J. F. McCauley, reversed in printing).

D. Implications

1. A Salta

The m   ng evidence of dunes on Mars is provided by the coalescing ridges and diverse marginal features seen in the Hellespontus region. The principal implication of dunes is a supply of noncohesive particles in the Martian surface environment and wind velocities sufficient for saltation transport. The existence of a saltation regime on Mars was inferred previously by Cutts et al. (Ref. XI-3) from the sharp boundaries of albedo features in *Mariner 6* and 7 pictures. Their conclusion was later questioned by Sagan et al. (Ref. XI-30), who agreed that the features were formed by wind action, but felt that the sharp boundaries could be explained in terms of abrupt changes in wind speed, causing suspended material to be dropped. Dunes are not amenable to an alternative explanation of this sort. Thus, we feel that we can now confidently assert the existence of a saltation regime on Mars. Many implications of a saltation regime such as wind abrasion, wind scour, and dust production are discussed in Ref. XI-5 (also see Section X of this Report)

2. Shapes and Variations of Albedo Features

The existence of saltation on the Martian surface may explain the morphology and temporal behavior of certain albedo features. Craters also are in many areas associated with light or dark streaks, which assume many morphologic forms (Refs. XI-4 and XI-11). One variant, shown for example in Fig. 1a of Ref. XI-6 (also see Fig. XV-1a of this Report) is a dark streak which originates within the floor of a crater. One plausible explanation of this phenomenon is that the floor of the crater has collected dark dune-forming materials and that a blowout has occurred under conditions of unusually strong winds. The subsequent behavior of dark streaks might be controlled by a variety of factors. If the substrate were bedrock or lag gravel, then it might tend to remain stable. If the substrate were mantled with dust, the newly introduced saltating particles might accelerate change by removing dust particles from the vicinity.

Observations of variable features suggest that certain types of albedo markings are stable. We might under-

stand this in two ways. These features might correspond to dust deposits in which the grain size is too small for motion to be directly initiated by the wind (Ref. XI-10). Furthermore, sources of larger particles capable of saltation and which could eject dust particles into the atmosphere might be a considerable distance from the dust deposit. An alternative explanation applies if the surface is a lag gravel. In these circumstances, finer material can become embedded between larger fragments and can change the albedo as it creates a reservoir of fines. The lag gravel might then protect the reservoir against crosswinds. R. S. U. Smith (Ref. XI-15) has invoked this reasoning to explain the persistence during crosswinds of high albedo streamers emanating from the horns of barchan dunes within the Algodones dune chain of southeastern California.

3. Interpretation of Non-Eolian Features

The existence of sand fluxes and sand accumulations is an important factor to be considered in the interpretation of non-eolian features. Eolian activity is evidently a process currently operating on Mars; therefore, even the youngest fluvial, volcanic, structural, or impact features are susceptible to some degree of modification. Eolian action can alter the original tonal relationships; the darkness of the furrows or channels in Fig. XI-6d is a possible example of his effect. It can also bury the original topography. The possibility that will most confuse interpretation, however, occurs when eolian constructional forms (dunes) actually resemble the modified forms of the primary fluvial or volcanic features being studied. This may be happening in Fig. XI-6d. The gradational character of eolian modification also makes highly ambiguous age dating based on crater abundances.

4. Age of Dunes

For crater-floor dunes such as those in Hellespontus, there are at least two "ages" of interest: the age of the dune topography and the residence time of eolian materials within the crater. One possibility is that dune materials have been continuously accumulating in the dune mass for a long period of time. Alternatively, there may be a continuous or episodic flux of materials into and out of the dune mass which is a temporary, although large, reservoir of sand. If our interpretation of dark streaks extending from craters as sand blowouts is correct, then the residence time of eolian materials in craters such as these must be rather short. The dune topography may be regenerated on a different and perhaps much shorter time scale.

The possibilities seem to be more limited for the suspected dune features of laminated terrain (Fig. XI-7). Here we suspect that dunes are actually migrating across broad open plains, and their distribution is not controlled so closely by pre-existing topography. The layered deposits are relatively young geologically (Refs. XI-9 and XI-28, also see Section XVII of this Report), and dune formation and development on these surfaces must be younger still.

5. Global Variations in the Martian Surface Environment

Several lines of evidence suggest that eolian activity is widespread if not ubiquitous on Mars. Pristine cratered surfaces are rare, and only elevated volcanic features such as the summit area of Nix Olympica display crisp non-eolian topography. Superficial eolian effects are indicated in many areas as characteristic albedo features. Suspension of dust has been observed directly by Mariner 9, and thick deposits are inferred to lie in the laminated terrains of both polar regions.

The existence of an eolian saltation regime is most directly demonstrated by the dune features of Hellespontus. It seems reasonable, however, that it is also a planet-wide process and that dunes should not be confined to this one area. Mariner 9 pictures suggest, but do not prove, that dune structures are to be found in locations as diverse as the equatorial cratered terrains and the polar laminated terrains with topographic structures close to the resolution limit (100 m) of the Mariner 9 cameras. The existence of saltation also implies transport and abrasion of materials. Possible erosional features formed by these processes, including deep stripping of craters, plains, and volcanic features, are discussed in Ref. XI-5 and in Section X of this Report.

The significance of these observations and inferences is perhaps dramatized by a comparison with the lunar surface environment. The Moon is mantled with an impact regolith which shows some selenographic variations in thickness and composition, but remarkably homogeneous morphologic and mechanical characteristics. Impact regolith formation on Mars has not been considered to be identical with that of the Moon; Mason (Ref. XI-31) has emphasized that the thin atmosphere of Mars will reduce the amount of glass formed because it screens out all impacting meteorites smaller than about 10 g. However, our conclusion from Mariner 9 observations is that there is no homogeneous impact regolith on Mars. On much of the surface it has been either mantled in

colian sand or dust or modified, perhaps beyond recognition, by colian erosion. In certain areas colian action may be less effective, and an impact regolith or pristine volcanic surface may exist. Yet, in most areas, colian action is competing effectively with other surface processes in forming the Martian surface. Thus, Mars no longer appears to be a Moon with an atmosphere, but a planet with diverse surface environments.

References

XI-1. de Vaucouleurs, G., *Physics of the Planet Mars* Faber and Faber, London, 1954.

XI-2. Sagan, C., and Pollack, J. B., "Windblown Dust on Mars," *Nature*, Vol. 223, p. 791, 1969.

XI-3. Cutts, J. A., Sharp, R. P., Smith, B. A., Murray, B. C., and Soderblom, L. A., "The Surface of Mars: 3. Light and Dark Markings," *J. Geophys. Res.*, Vol. 76, p. 343, 1971.

XI-4. Sagan, C., Veverka, J. Fox, P., and Dubisch, R., "Variable Features on Mars: Preliminary Mariner 9 Television Results," *Icarus*, Vol. 17, p. 346, 1972.

XI-5. McCauley, J. F., "Mariner 9 Evidence for Wind Erosion in the Equatorial and Mid-Latitude Regions of Mars," *J. Geophys. Res.*, Vol. 78, 1973.

XI-6. Cutts, J. A., "Wind Erosion in the Martian Polar Regions," *J. Geophys. Res.*, Vol. 78, 1973.

XI-7. Soderblom, L. A., Kreidler, T. J., and Masursky, H., "The Latitudinal Distribution of a Debris Mantle on the Martian Surface," *J. Geophys. Res.*, Vol. 78, 1973.

XI-8. Carr, M. H., Masursky, H., and Saunders, R. S., "A Generalized Geologic Map of Mars," *J. Geophys. Res.*, Vol. 78, 1973.

XI-9. Cutts, J. A., "Nature and Origin of Layered Deposits of the Martian Polar Regions," *J. Geophys Res.*, Vol. 78, 1973.

XI-10. Bagnold, R. A., *The Physics of Blown Sand and Desert Dunes*, 265 pp., Methuen, London, 1941.

XI-11. McCauley, J. F., Carr, M. H., Cutts, J. A., Hartmann, W. K., Masursky, H., Milton, D. J., Sharp, R. P., and Wilhelms, D. E., "Preliminary Mariner 9 Report on the Geology of Mars," *Icarus*, Vol. 17, p. 289, 1972.

XI-12. Warren, A. G., "Observations on Dunes and Bi-modal sands in the Ténéré Desert," *Sedimentology*, Vol. 19, p. 37, 1972.

XI-13. Norris, R. M., and Norris, K. S., "Algodones Dunes of Southeastern California," *Geol. Soc. America Bull.*, Vol. 72, p 605, 1961.

XI-14. Norris, R. M., "Barchan Dunes of Imperial County, California," *J. Geology*, Vol. 74, p. 292, 1966.

References (contd)

XI-15 Smith. R. S. U., *Migration and Wind Regime of Small Barchan Dunes Within the Algodones Dune Chain. Imperial County, California.* University of Arizona unpubl. MS. thesis. 125 pp.. 1970.

XI-16 . mith. R. S. U . "Barchan Dunes in a Seasonally-Reversing Wind Regime. Southeastern Imperial County, California (Abs)." *Geol. Soc. America. Abstracts with Programs.* Vol. 4, p. 340. 1972.

XI-17. Smith. H. T. U., *Eolian Geomorphology. Wind Direction, and Climatic Change in North Africa.* Air Force Cambridge Research Laboratories Rept. No. AFCRL-63-443, 48 pp.. 1963.

XI-18. Wilson, I. G., "Discontinuities in Eolian Bedforms." *Journal of Sedimentary Petrology.* Vol. 42, p. 667 1972.

XI-19. Wilson. I. G., "Sand Waves," *New Scientist*, p. 634. March 23, 1972.

XI-20. Smalley, I. J., "Formation of Quartz Sand." *Nature*, Vol. 211, p. 476. 1966.

XI-21. Hastenrath, S. L., "The Barchans of the Arequipa Region. Southern Peru." *Geomorphologie Zeitschrift*, Vc 11, p. 300, 1967.

XI-22. Finkel, H. J., "The Barchans of Southern Peru," *J. Geology*, Vol. 67, p. 614. 1959.

XI-23. Hanel, R., Conrath, B.. Hovis, W.. Kunde, V., Lowman, P., Maguire, W., Pearl, J.. Pirraglia, J., Prabhakara, C., Schlachman, B., Levin, G., Straat, P., and Burke, T., "Investigation of the Martian Environment by Infrared Spectroscopy on Mariner 9." *Icarus*, Vol. 17, p. 423, 1972.

XI-24. Sharp. R. P., "Kelso Dunes, Mojave Desert, California," *Geol. Soc. Am. Bull.*, Vol. 77, p. 1045, 1966.

XI-25. Sagan, C., Veverka, J., Fox, P., Dubisch, R., French, R. Gierasch, P., Quam, L., Lederberg, J., Levinthal, E., Tucker, R.. Eross, B., and Pollack, J. B., "Variable Features on Mars II: Mariner 9 Global Results," *J. Geophys. Res.*, Vol. 78, 1973.

XI-26. Murray, B. C., Soderblom, L. A., Sharp, R. P., and Cutts, J. A., "The Surface of Mars: 1. Cratered Terrains," *J. Geophys. Res.*, Vol. 76, p. 313, 1971.

XI-27. Milton, D. J., "Water and Processes of Degradation in the Martian Landscape," *J. Geophys. Res.*, Vol. 78, 1973.

XI-28. Murray. B. C., Soderblom, L. A., Cutts, J. A., Sharp, R. P., Milton, D. J., and Leighton, R. B., "Geological Framework of the South Polar Region of Mars," *Icarus*, Vol. 17, p. 328, 1972.

XI-29. Murray, B. C., and Malin, M. C., "Polar Wandering on Mars" (in preparation).

XI-30. Sagan, C., Veverka, J., and Gierasch, P., "Observational Consequences of Martian Wind Regimes," *Icarus*, Vol. 15, p. 253, 1971.

XI-31. Mason, C. C., "Nature of the Martian Surface as Inferred From the Particle-Size Distribution of Lunar Surface Material," *Geol. Soc. Am. Bull.*, Vol. 82, p. 2625, 1971.

Acknowledgments

XII. Sandstorms and Eolian Erosion on Mars

Carl Sagan
Laboratory for Planetary Studies
Cornell University, Ithaca, New York 14850

It is now apparent that windblown sand plays a major role in the Martian environment (Refs. XII-1 through XII-3; also see Section XIII of this Report). The existence of major particle transportation events such as the great sand and dust storm of 1971 implies the lateral transport of large quantities of material on Mars and provides a convenient mechanism for the filling of craters—an event directly implied both by the crater frequency-diameter statistics (Refs. XII-4 and XII-5), and by the appearance of Martian craters. In addition, *Mariner 9* has uncovered a range of probable major deflationary features (Refs. XII-6 and XII-7; also see Sections XV and XVI of this Report). But because the Martian atmosphere has a mean surface density more than two orders of magnitude less than the corresponding density for Earth's atmosphere, the wind velocity necessary to initiate grain motion will be much larger on Mars. Such fast-moving sand particles, saltating close to the Martian surface, can produce by collision and subsequent abrasion significant erosion of the Martian terrain. In addition, because of the higher velocities of such particles on Mars, secondary particles, produced by collisions with the pulverized surface, will have sufficiently high velocities to themselves produce abrasion. Because of the smaller atmospheric density on Mars drag is less, and smaller particles can abrade on Mars than on Earth.

Simple scaling analysis shows that the time for a particle undergoing saltation to reach the free-stream velocity is $\propto (\rho V)^{-1}$, which is a factor of 10 longer on Mars than on Earth. However, the particle remains aloft for a period $\propto g^{-1}$, which compensates by a factor of almost 3. The trajectories of saltating particles on Earth (Ref. XII-8) show them to rise rapidly (the time to achieve free-stream velocities) and then to fall slowly in a long straight trajectory tangential to the ground. The rise time is $\langle\langle$ one-third the fall time. Thus, in general, there is adequate time for saltating particles on Mars to reach free-stream velocities, and we will hereafter identify such particle and wind velocities.

We attempt here a calculation of the rate of eolian erosion (both abrasion and deflation) on Mars. The critical quantity is $V_{\bullet t}$, the threshold critical velocity necessary, at the surface, to initiate grain motion. On Earth, typical values of $V_{\bullet t}$ are ~ 20 cm sec^{-1} (Ref. XII-8; see also Ref. XII-9). With the usual logarithmic dependence of $V_{\bullet}$ through the velocity boundary layer, typical winds in a sandstorm at a few meters altitude are many meters per second. At $V_{\bullet t}$ particles about 100-μm radius are set into motion. Motion of smaller particles can be initiated by momentum exchange with 100-μm particles, but larger particles cannot be set into motion except at velocities

$V > V_*$. As the stress necessary to initiate grain motion is $\sim \rho_a V_*^2$ where ρ_a is the atmospheric density, to first order V_* for Mars should be a factor of 10 larger than for Earth. More detailed calculations confirm this view (Refs. XII-1 and XII-10 through XII-12), and we henceforth adopt for Mars $V_* \sim 2$ m sec^{-1}. Corresponding velocities above the velocity boundary layer on Mars are many tens of meters per second. Independent evidence of such velocities during a dust or sandstorm is provided by Mariner 9 observations (Refs. XII-3, XII-13, and XII-14; also see Sections XIII, XIX, and XX of this Report). The critical radius at which particle motion is first initiated is about 200 μm for Mars (Ref. XII-1).

In a typical terrestrial sandstorm, there is a clearly discerned upper boundary of the sand cloud at a height $z \sim 1$ m (see e.g. Ref. XII-8). The value of z depends on the rebounding surface. Abrasion is restricted to this lowermost meter. The bulk of the horizontal sand flow occurs, however, in the lowest centimeter. A crude estimate of z can be obtained from simple Newtonian physics, as saltating particles will be entrained by the horizontal wind component no higher than the apoapsis of their ballistic trajectories. Adopting the common approximation that the vertical component of the wind is about one-fifth the horizontal component, we find

$$z = 0.02 V_*^2/g \tag{1}$$

where V_* is a typical horizontal wind velocity within the sand cloud and g is the acceleration due to gravity. For Earth, a typical value of V_* in the lower boundary layer when V_* is just reached at the surface is ~ 6 m sec^{-1}, implying $z \sim 10$ cm. For a sandstorm, $V_* \sim 20$ sec^{-1} implies $z \sim 1$ m. Equation (1) should provide an upper limit on z within the uncertainties on the rebounding surface, but the trajectories of saltating particles (see, e.g., Ref. XII-8) show them to be entrained within a factor ~ 2 of their apoapses.

Equation (1) can therefore be used to make a crude estimate of the sandstorm heights on Mars. For $V_* \sim 30$ m sec^{-1}, $z \sim 5$ m; for $V_* \sim 100$ m sec^{-1}, $z \sim 50$ m. At the peak of a Martian sandstorm, $V_* \sim 150$ m sec^{-1} is probably not excessive, corresponding to a surface velocity only twice V_*, in some formulations. In this case, $z \sim 120$ m. Accordingly, we adopt for major Martian sandstorms $z \sim 100$ m. Under conditions described below, even higher values of z may prevail.

From values of z we can derive typical values of n, the number density of saltating grains in the sand cloud, by a consideration of sand fluxes. The transportation rate of saltating particles is known both from observation (Ref. XII-15) and from first principles (Ref. XII-8) to be

$$q_* = B(\rho_a/g)V_*^3 \tag{2}$$

where B is a dimensionless multiplier of order unity. Equation (2) gives the rate of sand transport in grams per second per unit width of lane. For erosion problems we are concerned with a flux of particles in grams per square centimeter per second. The corresponding expression is then

$$F \simeq (f\rho_a/gz)V_*^3 \tag{3}$$

where f is the fraction of the year characterized by sandstorms of velocity V_*. We can also write

$$F \simeq f n m V_*^3 \tag{4}$$

where $n = n(z)$, and m is the mass of the saltating particles.

We note for future reference that if τ is the normal incidence optical depth through an aerosol-filled atmosphere, $n \sim b\tau/\sigma z$, where b is the cross-section weighted fraction of aerosols in saltation rather than suspension, and σ is the geometrical cross section $\simeq \pi a^2$. Thus, alternatively,

$$F \simeq (fmb\tau/\sigma z)\, V_* \tag{5}$$

Combining Equations (3) and (4), we find

$$n = (\rho_a V_*^2/mgz) \tag{6}$$

For Earth, $V_* \sim 10$ m sec^{-1} and $z \sim 1$ m yield $n \sim 700$ cm^{-3}. This figure is consistent with the common description of visibility $s \lesssim 1$ m in an intense terrestrial sandstorm: $n \simeq (\tau/\sigma s) \sim 100$ cm^{-3}.

Likewise for Mars, $V_* \sim 50$ m sec^{-1} and $z \sim 100$ m yield $n \sim 3$ cm^{-3}. The larger sandstorm thickness and lower atmospheric density dominate the larger velocities and make Martian sandstorm densities less than terrestrial values. From the speed of fallout of the 1971 sand and dust storm, it is likely that $b > 10^{-2}$ and possible that $b > 10^{-1}$. During the storm $\tau \geq 2$. Thus, $n\sigma z > 2 \times 10^{-2}$ and possibly $> 2 \times 10^{-1}$, where $n > 2 \times 10^{-3}$ cm^{-3} and possibly $> 2 \times 10^{-2}$ cm^{-3}. Finally, Hertzler (Ref. XII-16), in wind tunnel experiments discussed below, generated sandstorms under simulated Martian conditions with mn

ranging from 10^{+} to 10^{-} g cm^{-}. For his 100-μm particles, this corresponds to n between 10^{-1} and 10^{-} g cm^{-}. Thus, the calculations and the observations imply roughly consistent values of n. We adopt for Martian sandstorms $n \sim 10^{-1}$ cm^{-}.

The two crude estimates of z embodied in Equations (1) and (6) imply

$$n \sim (2\rho_a/m) \qquad (7)$$

which yield, both for Earth and Mars, values of n (150 and 0.2 cm^{-}, respectively) consistent with the above estimates which involved explicit choices of V_*. Equation (7) expresses the condition that the energy density of the atmosphere, due to bulk motion, $\rho_a V_*^2$, equals the kinetic energy density, $\frac{1}{2} nmV_*^2$, of the saltating grains.

Because the eolian abrasion rate goes as a high power of V_*, information on the highest velocities available in a sandstorm is important. An absolute upper limit on V_* is $Ma = 1 \sim 200$ m sec^{-1}, only a factor of 2 larger than some anticipated sandstorm velocities. Saltating particles striking the surface eject into the atmosphere suspendable dust grains too small to be picked up directly by the wind. This momentum exchange results in a small fraction of the dust having velocities in excess of the saltating sand. This is one reason that the erosion rate may be weighted toward particles with $V > V_*$.

There is another, more entertaining, possibility. The Clausius mean free path for grain–grain collisions for all particles with the same velocity is

$$\lambda = (0.75/n\sigma) \qquad (8)$$

The number of particles with free paths shorter than x is $1 - \exp(-x/\lambda)$, so 10% of the grains have $x < 0.1\lambda$, etc. The horizontal displacement of a saltating particle is, from Equation (1) and $z \sim \frac{1}{2} gt^2$,

$$l \sim V_* t \sim 0.2 V_*^2/g \sim 10z \qquad (9)$$

which also corresponds to the observed trajectories. In the 1971 Martian sand and dust storm, $\lambda \sim 80$ m [for $n \sim 10^{-1}$ cm^{-3}] $\ll l$. One-tenth of the particles encounter more than 100 collisions in a single equivalent trajectory.

Thus, the circumstances of large numbers of grain–grain collision, uncommon on Earth except in the densest sandstorms always of limited areal extent, may not be uncommon on Mars. The net result is a tendency for the velocity distribution function of sand grains to approach Maxwell–Boltzmann statistics. Unlike a molecular gas, this sand grain gas is largely two-dimensional (in the prevailing wind direction), and the collisions are much less inelastic. The following brief discussion, assuming strict Maxwell–Boltzmann statistics, represents only a limiting case to the true Martian sandstorm. For $V_* \sim 100$ m sec^{-1}, the kinetic temperature of the sand grain gas is $\sim 10^{20}$ °K. Because of the logarithmic variation of velocity through the boundary layer and its slow variation above, the grain gas will be approximately isothermal with a scale height, H, just equal to the molecular gas scale height of the Martian atmosphere. $H > z$ now because of the high-velocity Maxwell tail of the distribution function. The partial pressure of the sandstorm particles at 100 m sec^{-1} is ~ 0.3 mb. Other properties of a 10^{20} °K two-dimensional grain gas in contact with its condensate at ~ 0°K will be described elsewhere. The primary conclusion is that grain–grain collisions produce a high-velocity tail to the velocity distribution function. For Maxwell–Boltzmann statistics $\sim 1\%$ of the grains for $V_* \sim 100$ m sec^{-1} will be transonic (between $Ma = 0.9$ and $Ma = 1.0$).

We have mentioned that the rapid decline of the 1971 storm implies, through the Stokes–Cunningham equation, saltating grains as an important source of opacity. The fact that only the tops of the volcanic peaks in Tharsis were visible by *Mariner 9* in September and October 1971 suggests that sand grains were then aloft at altitudes of about 10 km, consistent with the $z \sim H$ derived here.

The collision cross section, σ, of the grains is also approximately the absorption cross section for photons. Thus, the condition $\lambda < z$ for frequent collisions and a high-velocity tail also corresponds to the condition $b\tau \geq 1$ for a substantial optical depth in saltating particles. It is possible that the grain–grain collisions contribute to the self-sustaining nature of the sandstorm. During the storm, the energy densities of saltating particles and of atmospheric motions of gas are comparable [cf. Equation (7)]. For saltation over 10% of the area of the planet, a few weeks of solar insolation provide enough energy for V_* of a few tens of meters/second. This time scale is consistent with the observed time scale for generation of the 1971 Martian storm. We note in passing that Equation (7) for $\lambda = z$ and Equation (8) yield $z \sim (\rho_P/\rho_a)a \sim 100$ m, where ρ_P is the particle bulk density $\simeq 3$ g cm^{-3}.

I have been unable to find a published analytic expression for R, the rate of sandstorm eolian erosion near a planetary surface. R clearly depends on a high power

of the free-stream sandstorm velocity, V_*. A factor of V_* arises from the kinetic energy of impact. An additional factor of V_* arises from the representation of the flux as a number density of particles, n, times a velocity. Furthermore, n may increase with a power of V_*, depending on the vertical height of the sandstorm. The efficiency of abrasion also may increase with V_*. We anticipate $R \propto V_*^\nu$, where $\nu \geq 3$.

One cm³ of rock contains $\sim a^{-3}$ equivalent components, each the size of the saltating particles, assumed to be of uniform radius a. Therefore, each target of this size is collided with every $t \sim ma^2/F$ seconds, a quantity independent of a. Here m is the particle mass. Almost independent of the mineralogy, the bond spacing is on the order of 1 Å. Assume each bond has an effective energy $E \sim 3$ eV $\sim 5 \times 10^{-12}$ ergs. Therefore, in the equivalent cross-sectional area of an impacting particle, the eroding face has $\sim 10^{16} a^2$ bonds, and $\sim 10^{16} a^2 E$ ergs per face. As there are five faces connecting an exposed target volume to the rest of the rock of which it is a part, $\sim 5 \times 10^{16} a^2 E$ ergs are necessary for dislodgement. The number of impacts necessary for dislodgement is the ratio of this quantity to the kinetic energy per saltating particle. An efficiency factor η has been introduced to collect in one place the dependence of the abrasion on the target bonding, elasticity, and composition, and the composition and shape of the saltating particles. It represents the fraction of the impacting kinetic energy converted to abrasion. Thus,

$$R = 1.0 \times 10^{-17} a\eta(F/E)V_*^2 \tag{10}$$

Combining Equation (10) with Equation (4) yields

$$R = 1.0 \times 10^{-17} (a\eta fnm/E)V_*^2 \tag{11}$$

while Equations (10) and (3) yield

$$R = 1.0 \times 10^{-17} (a\eta f\rho_a/gzE)V_*^3 \tag{12}$$

Whether we consider $\nu = 3$ or $\nu = 5$ depends on whether we hold n or z constant. Because $z \propto g^{-1}$, R is independent of g. We now compare our results with observation.

Kuenen (Ref. XII-17) experimented on the production of ventifacts by sandblasting hard rock in a wind tunnel. Erosion was determined by weighing. In a typical experiment at Beaufort Force 6, a mass loss $\Delta m/m = -0.06$ was accomplished in 2700 experimental hours. This corresponds to $\Delta a/a = -0.02$, and, for an initial 300-g rock, to a loss of 9.2×10^{-2} cm. By adopting Kuenen's correc-

tion for the ratio between the quantity of sand set into motion in his wind tunnel and in nature, we find from ventifacts $R \sim 3.2 \times 10$ cm sec at $V_* \sim 11$ m sec. In the same experiment, using the same sand grains (1-mm diameter) at Beaufort Force 10 (~ 25 m sec), $R \sim 2.2 \times 10^2$ cm sec is found. This corresponds to $\nu \sim 5$ if z and n are imagined independent of V_*, confirming the ideas behind Equation (12). In another experiment in a circuit tunnel, summarized in Table 2 of Ref. XII-17, ν again varies between 3 and 5 over a modest range in V_*. Erosion rates in a third experiment, summarized in Figure 4 of Ref. XII-17, imply $R \sim 4 \times 10^2$ cm sec for $f \sim 1$ at $V_* \sim 13$ m sec. There is some variation among the results obtained in different ways by Kuenen, a variation easily understood in terms of the differences in his procedures. In some cases erosion of rock by sand is being measured; in others, of the sand itself. The results his Table 2 suggest that when the soft parts of sand grains were eroded away the efficiency of subsequent abrasion declined. Combining Kuenen's results with Equation (11) to derive η, we find

$$4 \times 10^{-1} \leq \eta \text{ (grains)} \leq 4 \times 10^{-2}$$
$$4 \times 10^{-3} \leq \eta \text{ (rocks)} \leq 4 \times 10^{-4} \tag{13}$$

Another test of this formulation is provided by wind tunnel experiments performed by Hertzler (Ref. XII-16) in the McDonnell Aircraft 14-foot environment simulator. Piles of silica flour in the size range of 1 to 100 μm and white sugar sand in the size range of 100 to 700 μm were subjected to typical Martian surface pressures and high flow velocities. The velocities measured refer to some constant level within the velocity boundary layer, but experiments also were performed on the threshold velocities under Earth ambient conditions. Because we know for the particle sizes in question that the critical threshold velocity is ~ 20 cm sec^{-1} (Ref. XII-8), it is possible to scale to first order Hertzler's reported velocities to Martian surface threshold velocities. The comparison is crude and differences between boundary layer physics of Mars and Earth will enter; but these effects are unlikely to significantly affect the first-order results. Hertzler finds, for particles within this size range, values of V_*, between 1.3 and 2.9 m sec. This range includes the extremes of the experimental uncertainties, and a mean value of about 2 m sec^{-1} in agreement with other theoretical results seems appropriate. Doubling the ambient pressure almost doubles V_{*t}, a pressure dependence slightly steeper than conventional theory implies (see, for example, Ref. XII-1). These wind tunnel experiments find that larger flow velocities are needed to saltate smaller particles, as conventional theory predicts.

Hertzler also performed experiments on abrasion, for instance of aluminum surfaces coated with zinc oxide. In one experiment particles were transported at $V_* \simeq 160$ m sec^{-1} with a number density $n \sim 10^{-2}$ cm^{-3} for 1600 sec. A 1-mil zinc oxide coating was completely eroded, and substantial abrasion of the underlying aluminum was observed. Corresponding figures apply to many other surface coatings. The overall erosion rate is about 10^{-5} cm sec^{-1}, or somewhat larger. Comparison with Equation (11) for Hertzler's n, a, and V_* gives $\eta \sim 10^{-3}$ to 10^{-4} not significantly different from the η (rock) values from Kuenen [Equation (13)].

What velocity is necessary for a single incident particle to dislodge its own mass? From the discussion leading to Equation (10), this critical velocity $V_{**} = (10^{17} \, aE/m\eta)^{1/2}$. For the numbers we have already employed, $V_{**} \simeq 14\eta^{-1/2}$ m sec^{-1}. For $\eta \sim 10^{-3}$, $V_{**} \simeq 440$ m sec$^{-1} \sim$ Mach 2. Also $V_{**} \propto a^{-1/2}$. Thus, no grain moves at V_{**} on Mars. The low values of η for both Earth and Mars may be related to the fact that cumulative impacts are necessary for dislodgement.

Inland winds of Beaufort Force 6 blow on Earth a fraction $f \sim 0.02$ of the year (Ref. XII-18). With $\eta = 4 \times 10^{-3}$ and $n \sim 100$ cm^{-3} we find that, if dense sandstorms are stirred by such winds, they produce an erosion rate ~ 3 Å sec^{-1} in the lowest meter. Such sandstorms are not frequent on Earth, and aqueous and other erosional processes dominate.

On Mars the astronomical evidence suggests that sandstorms are much more frequent. The 1971 planet-wide storm lasted for $f > 0.15$ a Martian year. There is evidence that such storms occur every perihelion, although generally with shorter duration. Because of collisional injection of high-velocity suspendable particles into the atmosphere, and collisional approaches to Maxwell-Boltzmann statistics, I take the effective V_* for abrasion as 50 to 100 m sec^{-1}. With $f \sim 0.1$, $\eta \sim 10^{-4}$, and $n \sim 10^{-1.5}$ cm^{-3}, we find for Mars

$$R \sim 10^{-6.5} \text{ cm sec}^{-1} \qquad (14)$$

This large number applies to present conditions. In other epochs aqueous erosion may have been more important, and eolian less. The chief uncertainty in Equation (14) is in n. As the sandstorm height ranges from 100 m to 8 km on Mars, abrasion there can play a major role in the erosion of major features, not excluding production of the cliffs at the bases of large Martian volcanoes, where n should be large.

We can also estimate crudely the eolian deflation flux, F_d, of saltating particles on Mars. From Equations (2) and (9),

$$F_d = (f\rho_a/g l)V_* \simeq 5f\rho_a V_* \qquad (15)$$

This leads to very high value for deflation. But saltation ensures, in the most general case, a near-equilibrium between deflation and deposition for saltating particles. The rate-limiting step then is not deflation, but avoidance of deposition. Topographic control of deflationary hollows thus seems to be of importance. The deflationary fluxes F_d are grams per second per unit surface area, and should be distinguished from the saltation fluxes, F, discussed earlier, which are grams/second per unit area normal to the saltation. From Equation (4), typical values of F for Earth are $\sim 10^5$ particles cm^{-2} sec^{-1}, and for Mars the same value for $n \sim 10^{-1}$ cm^{-3}.

Because of the V dependence, it is clear that places on Mars which tend to have unusually high prevailing winds may have significantly greater eolian abrasion and deflation rates than places otherwise comparable but with lower wind velocities. A factor of 2 in the prevailing peak winds is worth almost an order of magnitude in the erosion rates.

These erosion rates imply that small craters on Mars with diameters below a few tens of kilometers, especially those in highland areas, have ages much less than the age of the surface of Mars. This is consistent with the cratering statistics and the morphology work of many authors (see, e.g., Refs. XII-4 and XII-5). For example, Chapman et al. in Ref. XII-4 find, for craters 10 to 25 km in diameter and for some models of the distribution function of impacting objects and cratering physics, ages of tens to hundreds of millions of years, quite consistent with Equation (14). These results also imply that large volcanic piles found on Mars (Ref. XII-19) are probably no more than hundreds of millions of years old, especially in view of the high-velocity slope winds which should be generated in their vicinity (Refs. XII-20 and XII-21). This conclusion is in accord with the ages determined from the crater densities on the slopes of the volcanoes, normalized by the Phobos and Deimos cratering densities (Ref. XII-22).

For the erosion of very large objects, abrasion may produce slumping of, for example, crater ramparts or mountain bases, without entirely removing the relevant geometric forms. Our eolian abrasion rates are large compared with terrestrial eolian rates, but comparable

to or smaller than terrestrial aqueous erosion rates. Just as major tectonic features are not rapidly leveled by such erosion on Earth, they should survive eolian abrasion on Mars.

Nevertheless some crater-poor terrains may be produced entirely by eolian erosion, rather than by other processes which have been postulated to date. These erosion rates are sufficiently great that differential erosion of hard and soft rock parts should be marked. Numerous ventifacts of the sort described for eolian regimes in Antarctica by Morris et al. (Ref. XII-25) may be produced. Because, as Morris et al. stress, some of these ventifacts have a marked artificial appearance, there exist possibilities for misapprehension about the nature of Martian landforms as viewed from a lander camera or high-resolution orbiter camera.

In other regions the wind velocities may be much less, and in these regions we may see very old craters of modest size. The combined analyses of numerical circulation models from temperature field results from the infrared interferometer spectrometer and streak statistics imply that, for example, equatorial wind regimes may differ from high-latitude wind regimes on Mars, and that the winds may vary greatly from place to place on the surface (Ref. XII-3; also see Section XIII of this Report). Accordingly future cratering statistic studies directed toward determining erosional processes should not perform global cratering averages, but should be performed region by region.

Hartmann (Ref. XII-24) has derived, from his examination of Martian cratering statistics, the result that there was a discrete epoch of high erosion after the initial accretion of the planet but before later cratering events. This view is not operationally distinct from the implications of this section which are that significant erosion and filling of craters have occurred contemporaneously with their production and since the accretion of Mars.

Our results also apply to questions of the sterilization and survival of space vehicles intended for landing on Mars. With an erosion rate of about 1 cm yr⁻¹ an unsterilized spacecraft deposited on the surface of Mars would after some years be eroded to a depth of centimeters, thus releasing all unsterilized organisms within the surficial layer. On the other hand, about ½ erg is released per impact event, and some significant fraction of that should go into heating. It is therefore likely that, because of the high values of saltation velocity on Mars, erosion events are self-sterilizing. The abrasion rates also imply the entire removal of some varieties of spacecraft surface coatings during a nominal 90-day mission. This is another reason why times and places of low-velocity winds should be selected for spacecraft landings.

These high abrasion rates, combined with the high expected crater and negative relief filling rates, imply that we see back only part way into Martian history at scales of hundreds of kilometers or less. Thus, if very old small volcanoes on Mars were absent, this would not argue against ancient volcanism on the planet. The absence of old sinuous channels does not argue against channel production mechanisms in the early history of the planet, and so on (Ref. XII-4).

The amount of dust made available on Mars by this abrasion can be considerable and, depending on the rate of tectonic construction of new surfaces, may be not inconsiderable compared with other sources of dust generation such as micrometeoritic infall or fragmentation during crater formation.

If the Martian climate is unstable in the sense of having episodes of abundant liquid water, temperature gradients during each epoch should be much more moderated than today and wind velocities should be much less. However, aqueous erosion processes would then occur.

References

XII-1. Sagan, C., and Pollack, J. B., "Windblown Dust on Mars," *Nature*, Vol. 223, p. 791, 1969.

XII-2. Sagan, C., Veverka, J., Fox, P., Dubisch, R., Lederberg, J., Levinthal, E., Quam, L., Tucker, R., Pollack, J., and Smith, B., "Variable Features on Mars: Preliminary Mariner 9 Television Reconnaissance," *Icarus*, Vol. 17, p. 346, 1972.

XII-3. Sagan, C., Veverka, J., Fox, P., Dubisch, R., French, R., Gierasch, P., Quam, L., Lederberg, J., Levinthal, E., Tucker, R., Eross, B., and Pollack, J., "Variable Features on Mars II: Mariner 9 Global Results," *J. Geophys. Res.*, Vol. 78, 1973.

XII-4. Chapman, C. R., Pollack, J. B., and Sagan, C., "An Analysis of the Mariner 4 Cratering Statistics," *Astron. J.*, Vol. 74, p. 1039, 1969.

XII-5. Hartmann, W. K., "Martian Cratering II: Asteroid Impact History," *Icarus*, Vol. 15, p. 396, 1971.

XII-6. Cutts, J. A., "Wind Erosion in the Martian Polar Regions," *J. Geophys. Res.*, Vol. 78, 1973.

XII-7. Sharp, R. P., "Mars: South Polar Pits and Etched Terrain," *J. Geophys. Res.*, Vol. 78, 1973.

XII-8. Bagnold, R. A., *Physics of Blown Sand and Desert Dunes*, London. Methuen, 1964.

XII-9. Sindowski, K. H., "Korngröszn und Kornform-Auslese Beim Sandtransport Durch Wind," *Giol. Jahrb.*, Vol. 71, p. 517, 1956.

XII-10. Golitsyn, G. S., "On the Martian Dust Storms." *Icarus*, Vol. 13, p 113, 1973.

XII-11. Hess, S., *Martian Winds and Dust Clouds*, paper presented at NATO Advanced Study Institute on Planetary Atmospheres, Istanbul, 1972.

XII-12. Gierasch, P., and Goody, R "A Model of a Martian Great Dust Storm," *J. Atmos. Sci.*, Vol. 30 (in press).

XII-13. Leovy, C. B., Briggs, G. A., and Smith, B. A., "Mars Atmosphere During the Mariner 9 Extended Mission: Television Results," *J. Geophys. Res.*, Vol. 78, 1973.

XII-14. Conrath, B., Curran, R., Hanel, R., Kunde, V., Maguire, W., Pearl, J., Pirraglia, J., Welker, J., and Burke, T., "Atmospheric and Surface Properties of Mars Obtained by Infrared Spectroscopy on Mariner 9," *J. Geophys. Res.*, Vol. 78, 1973.

XII-15. Hsu, S. A "Wind Stress Criteria in Eolian Sand Transport," *J. Geophys. Res.*, Vol. 76 p. 8684, 1971.

XII-16. Hertzler, R. G., McDonnell Aircraft Corporation Report, E⁻ 1966.

XII-17. Kuenen, P. H., "Experimental Abrasion 4: Eolian Action," *J. Geol.*, Vol. 68, p. 427, 1960.

References (contd)

XII-18. Braak, C., *Het Klimaat van Nederland*, Publication 32, Royal Dutch Meteorological Institute, 1929.

XII-19. Masursky, H., Batson, R. M., McCauley, J. F., Soderblom, L. A., Wildey, R. L., Carr, M. H., Milton, D. J., Wilhelms, D. E., Smith, B. A, Kirby, T. B., Robinson, J. C., Leovy, C. B., Briggs, G. A., Young, A. T., Duxbury, T. C., Acton, G. H., Murray, B. C., Cutts, J. A., Sharp, R. P., Smith, S. A., Leighton, R. B. Sagan, C., Veverka, J., Noland, M., Lederberg, J., Levinthal, E., Pollack, J. B., Moore, J. T., Jr., Hartmann, W. K., Shipley, E. N., de Vaucouleurs, G., and Davies, M. E., "Mariner 9 Television Reconnaissance of Mars and Its Satellites: Preliminary Results," *Science*, Vol. 175, p. 294, 1972.

XII-20. Gierasch, P., and Sagan, C., "A Preliminary Assessment of Martian Wind Regimes, Icarus, Vol. 14, p. 312, 1971.

XII-21. Sagan, C., Veverka, J., and Gierasch, P., "Observational Consequences of Martian Wind Regimes," *Icarus*, Vol. 15, p. 253, 1971.

XII-22. Pollack, J. B., Veverka, J., Noland, M., Sagan, C., Duxbury, T. C., Acton, C. H., Born, G. H., Hartmann, W. K., Milton, D. J., and Smith, B. A., "Mariner 9 Television Observations of Phobos and Deimos," *Icarus*, Vol. 17, p. 394, 1972.

XII-23. Morris, E. C., Mutch, T. A., and Holt, H. E., *Atlas of Geologic Features in the Dry Valleys of South Victoria Land, Antarctica*, USGS Interagency Report: Astrogeology 52, 1972.

XII-24. Hartmann, W. K., "Martian Cratering III: Theory of Crater Obliteration," *Icarus*, Vol. 15, p. 410, 1971.

Acknowledgments

XIII. Variable Features on Mars II:
Mariner 9 Global Results

C. Sagan, J. Veverka, P. Fox, R. Dubisch, R. French, and P. Gierasch
Laboratory for Planetary Studies
Cornell University, Ithaca, New York 14850

L. Quam, Lederberg, E. Levintha!, R. Tucker, and B. Eross
Artificial Intelligence Laboratory; and Department of Genetics, Stanford Medical School
Stanford University, Stanford, California 94305

J. B. Pollack
NASA Ames Research Center, Moffett Field, California 94305

One of the principal objectives of the *Mariner 9* mission was to examine, at high resolution and extended time baseline, the long-observed surface albedo variations on Mars. The preliminary results of this investigation have been presented by Sagan et al. (Ref. XIII-1). The time-variable Martian dark areas and representative semi-tone areas were found commonly to be resolved into two kinds of fine structure: streaks and splotches. Most streaks emanate from craters, although some begin at positive relief features. Bright streaks tend to be long and narrow; dark streaks are shorter and broader. Typical streak lengths are ten of kilometers. Splotches are irregular markings that exhibit a significant tendency to be located inside craters, often asymmetrically against a crater wall. But larger splotches may wash over crater ramparts onto adjoining terrain.

Systematic observations have been made of a large variety of splotches and streaks during the mission. In many cases, all three photometric angles were held closely constant so that true variations in the albedo of these markings could be separated from changes in shadows and the effects of the surface scattering function. These observations were designed to detect relative albedo changes within the field of view. No conclusions are based on absolute photometry. Major variations in splotches and dark streaks were uncovered with a characteristic time scale for variation ≤ 2 weeks. In many cases, variations on a time scale of 1 day were sought; such rapid variations must be relatively uncommon, as none were discovered. No variations of bright streaks, either in production or dissipation, were found. In several locales, most notably Syrtis Major, the configuration

of dark and bright streaks corresponds remarkably well to the classical Earth-based configuration of the dark area which the streaks constitute. Observed time variations in the distribution of such streaks correspond to regions in which the albedo variations were previously observed from Earth. Sagan et al.(Ref. XIII-1) proposed that the distribution and time variation of streaks and splotches are the causes of the classical seasonal and secular variations of Martian albedo markings.

Two principal hypotheses were proposed in pre-Mariner 9 days to explain these variations: biology and windblown dust. While convincing evidence against biological explanations are not forthcoming, mainly because a wide range of properties can be proposed for hypothetical Martian organisms, the evidence of Ref. XIII-1 is strongly in favor of windblown dust producing streaks and splotches and their time variations. A range of explanations of the streaks and splotches was mentioned in Ref. XIII-1. For example, bright streaks might be produced by bright dust trapped in negative relief dust sinks (such as crater bottoms) in the waning stages of the dust storm, and subsequently deflated by strong gusts. Or fine dust, deposited uniformly by a dust storm, may subsequently be stirred up, suspended, and blown away because of collisions with saltating grains, everywhere but in the lee of crater walls where the wind velocities are low. Examples of both of these cases on a smaller scale are known in Antarctic dry valleys (Ref. XIII-2). Alternatively, dust darker than the mean albedo of a given area might be layered down by the wind from a prevailing direction everywhere but in the lee of crater ramparts. But in these cases, as with other explanations of the streaks, they will point in the direction of the wind flow. Thus, it was proposed in Ref. XIII-1 that the streaks may be natural wind vanes and, possibly, anemometers, placed down on the Martian surface.

In this section, we present global maps of the streaks, streak/splotch correlations, and a comparison of wind flow patterns deduced from these maps with results on the general circulation of the Martian atmosphere. We derive a new estimate of the wind velocities necessary to initiate dust movement on the Martian surface, exhibit detailed examples of variations in three regions of Mars, and present new conclusions on the mechanisms of wind-initiated albedo changes.

A. Global Streak Maps

The entire surface of Mars was mapped for streaks, both bright and dark. The primary data product on which the mapping was based were Ozalid mosaics of wide angle pictures prepared by the Astrogeology Branch, U.S. Geological Survey. In addition to being a convenient data source, for example, allowing easy mapping of streaks which traversed wide-angle picture boundaries, it also limited our effective maximum detectable streak length to about 10 km. There are many smaller streaks to be seen on narrow-angle pictures, but Mariner 9 has not provided adequate narrow-angle coverage of Mars to permit useful high-resolution streak mapping. The mosaics cover the time interval between revolutions 101 and 222, corresponding to $L_s = 320°$ to 353°, or late summer in the southern hemisphere. Our results apply only to this season.

Quite different results may apply to other seasons. This is indicated by the fact that only the appearance of dark streaks, never the removal of dark streaks nor the appearance of bright streaks was observed during this time interval. Such a situation cannot continue indefinitely if Mars is to maintain the general Earth-based appearance it has exhibited for more than a century. On the other hand, the frequency of alteration of streaks observed must represent some integration of streaks produced recently and streaks produced at some more remote times, perhaps on the order of 1 year into the past.

Streaks were mapped by four different co-authors of this section, with significant overlap among their counts to guarantee no major systematic errors caused by personal equation. The relative number of marginal streaks proved to be few, primarily cases on the borderline between short streaks and long splotches, spilling over crater walls. The final streak maps were carefully proofed against the original compilations. In the present study, we are concerned only with the weather vane, not with the hypothesized anemometer, aspect of the streaks. Accordingly, streak lengths are displayed on two scales: the short arrows correspond to streaks ≤ 60 km long; the long arrows correspond to streaks ≥ 60 km long. Dark streaks are represented by solid arrows, bright streaks by dashed arrows. The results are displayed in Figs. XIII-1 through XIII-7 in Lambert conformal and Mercator maps. There are some where the number of parallel streaks was so great in a given small area that representation of each streak on maps of this scale would have been impossible (Fig. 16 of Ref. XIII-1). In such cases, all regions of great arrow density, only a representative sampling of streaks is indicated. No loss in generality for streak direction results from this convention.
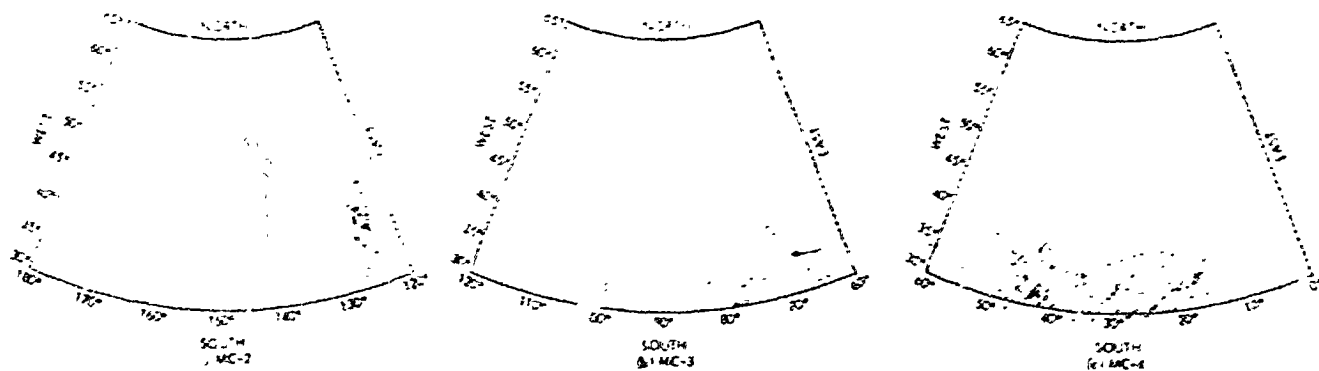
Fig. XIII-1. Streak maps of Mars. Solid arrows represent dark streaks; dashed arrows represent bright streaks. The arrow length is about four times the streak length, but is approximate. The shortest arrows shown (2° of latitude long) represent streaks ≃ 30 km in length. Regions of the planet north of 50°N would not be mapped for streaks because of obscuration by the polar hood. The absence of streaks in these regions, evident in Figs. XIII-1 and XIII-2, may not be real. (a) MC-2, (b) MC-3, and (c) MC-4.
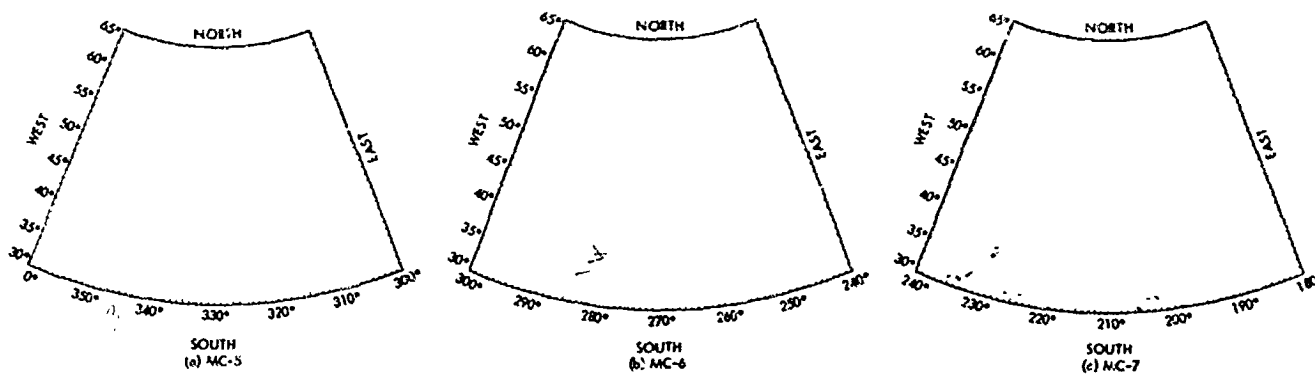
Fig. XIII-2. Streak maps of Mars: (a) MC-5, (b) MC-6, and (c) MC-7.
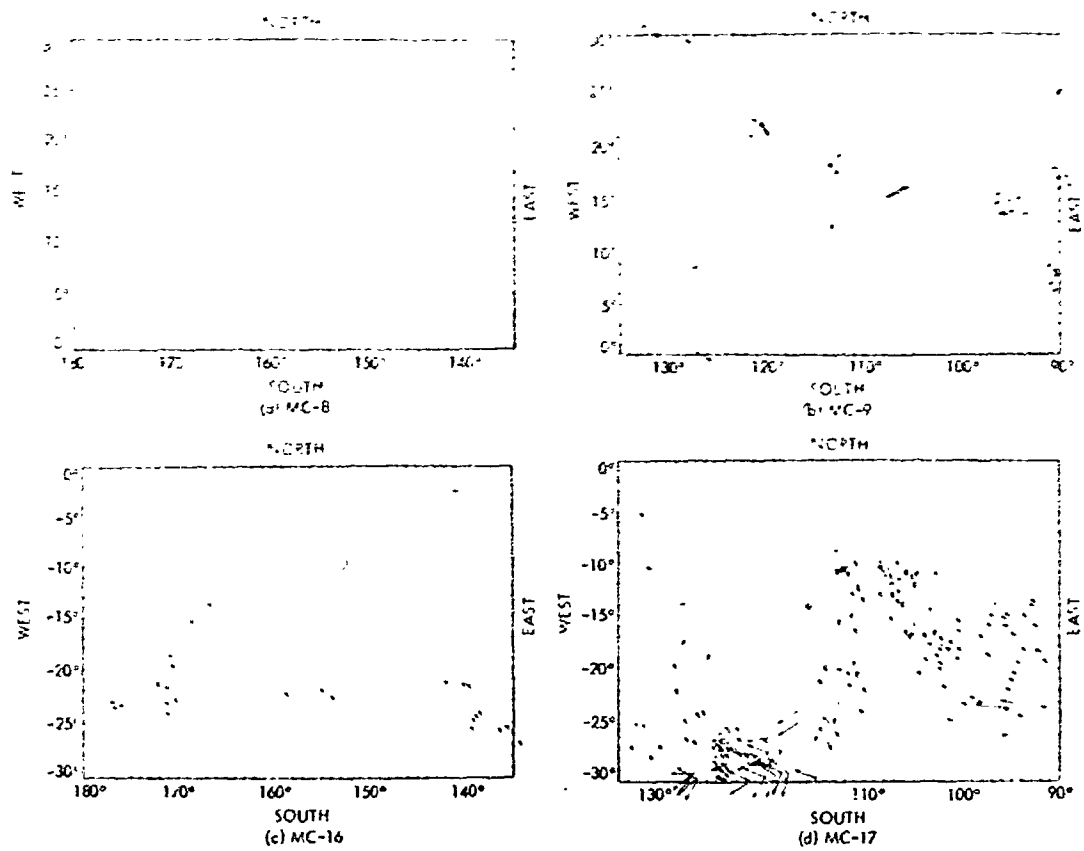
Fig. XIII-3. Streak maps of Mars: (a) MC-8, (b) MC-9, (c) MC-16, and (d) MC-17.
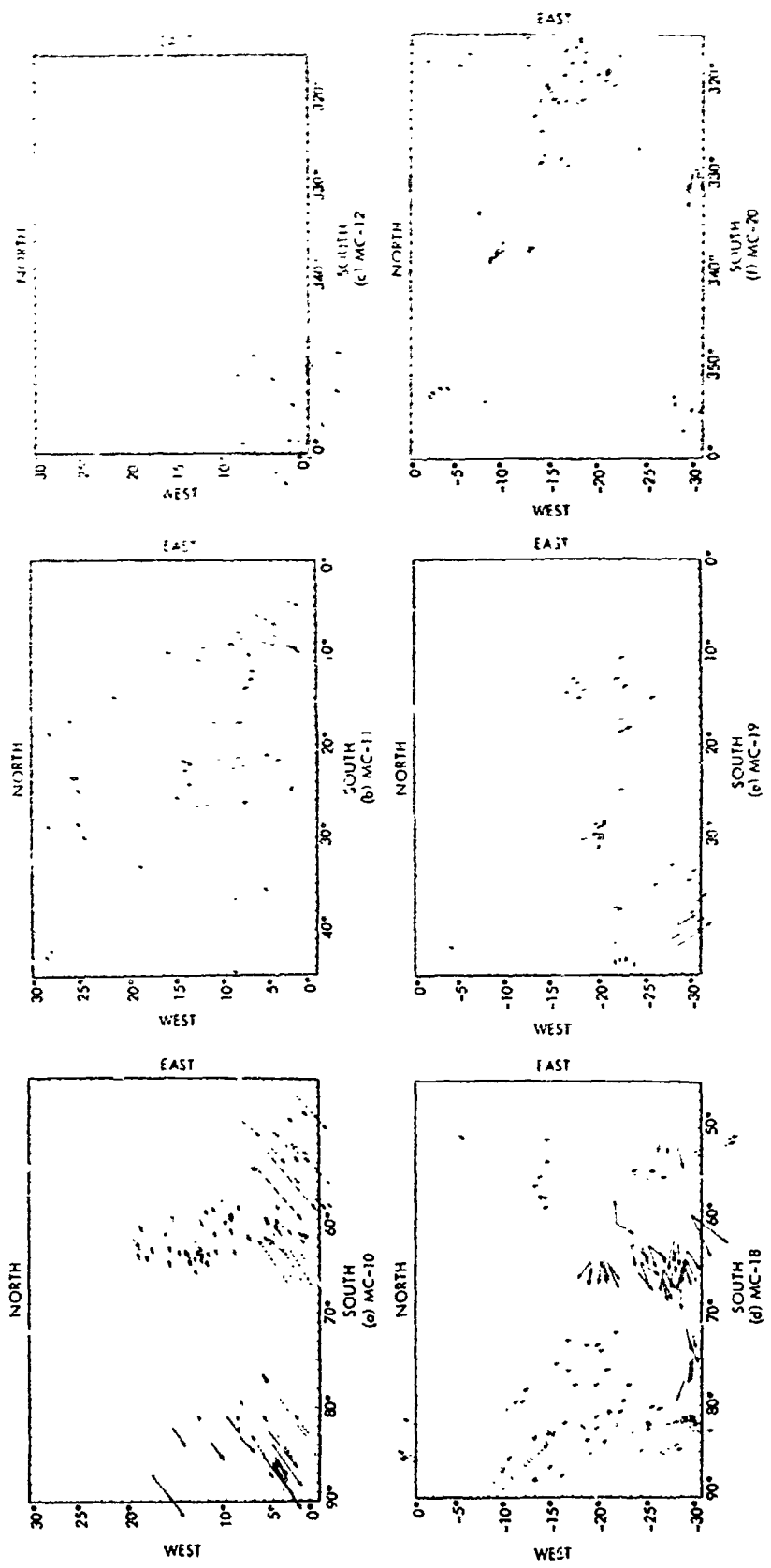
Fig. XIII-4. Streak maps of Mars: (a) MC-10, (b) MC-11, (c) MC-12, (d) MC-18, (e) MC-19, and (f) MC-20.
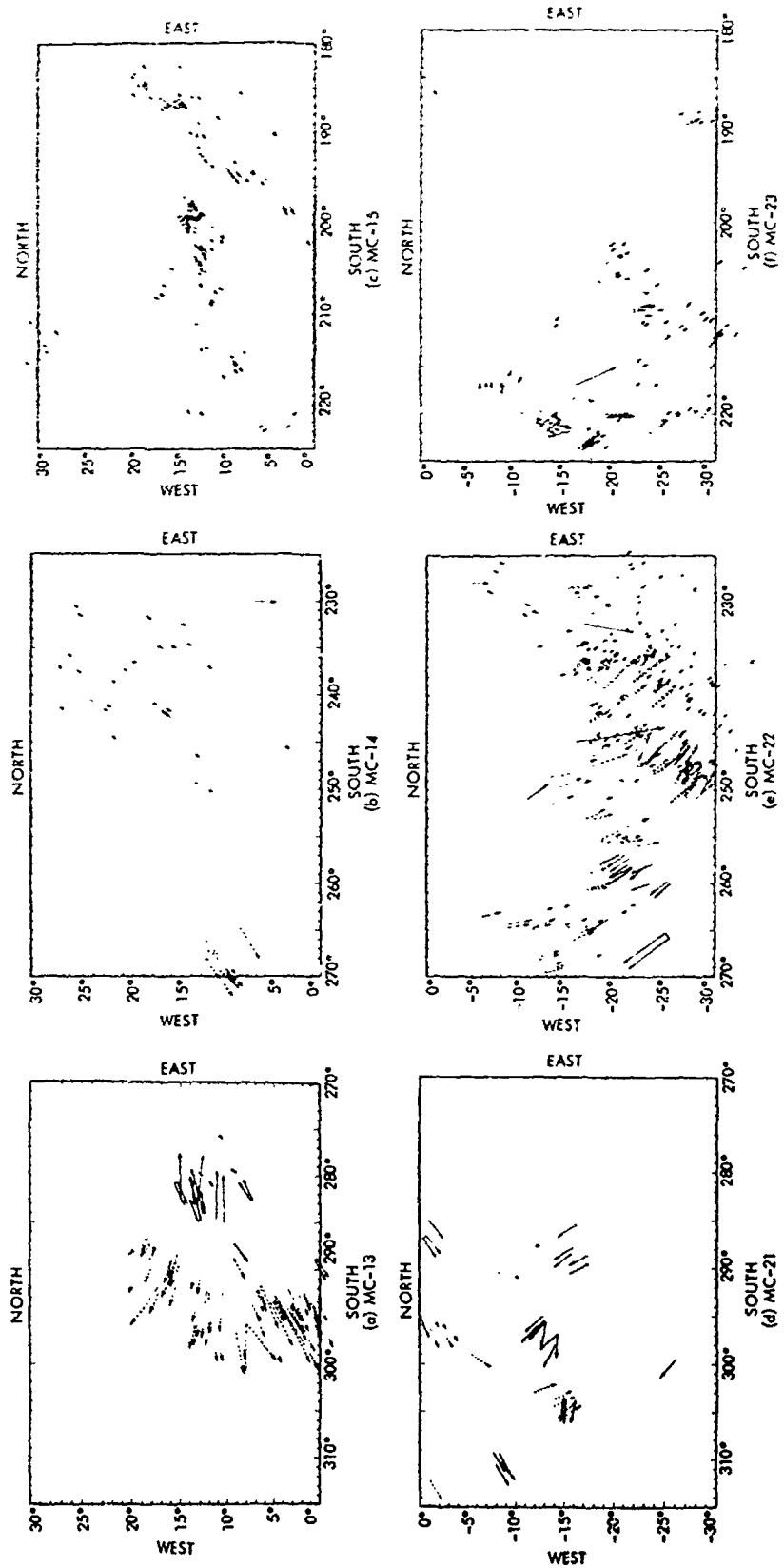
Fig. XIII-5. Streak maps of Mars: (a) MC-13, (b) MC-14, (c) MC-15, (d) MC-21, (e) MC-22, and (f) MC-23.
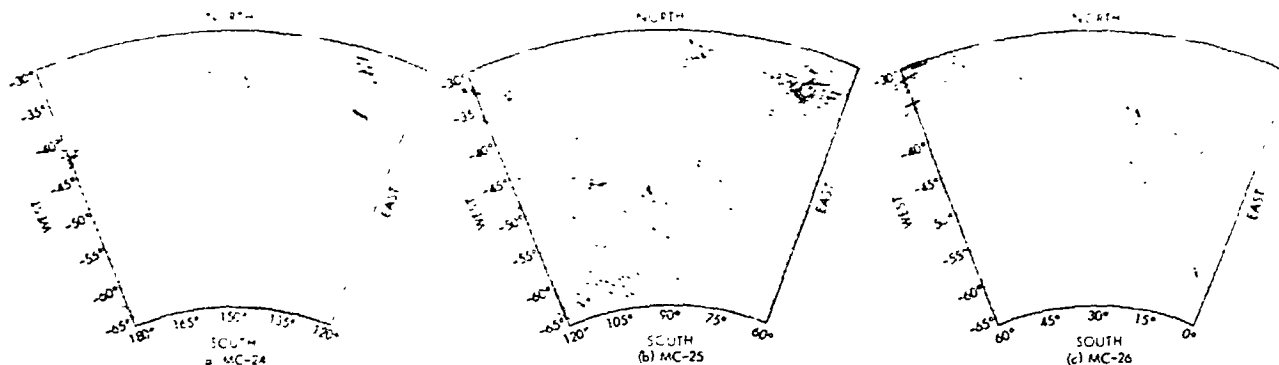
Fig. XIII-6. Streak maps of Mars: (a) MC-24, (b) MC-25, and (c) MC-26.
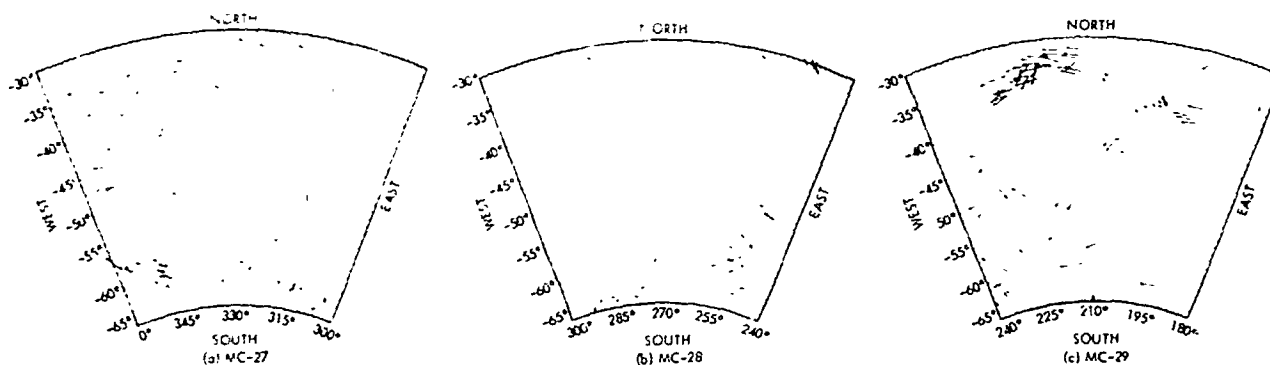
Fig. XIII-7. Streak maps of Mars: (a) MC-27, (b) MC-28, and (c) MC-29.

Figures XIII-8 and XIII-9 show the streaks in Mercator projection on Earth-based albedo and *Mariner 9* topographic maps, respectively. The existence of the north polar hood and an apparently real paucity of streaks in the south circumpolar region for the L_s of these observations is the reason for the blank areas in the north and the absence of streak maps for regions south of $-65°$. In Figs. XIII-8 and XIII-9, only the prevailing streak direction within each 10° by 10° grid square is shown. Where there are two prevailing directions, both are shown. As indicated in the rosette diagram for the Solis Lacus region (Fig. XIII-10), one or two prevailing directions are almost always a good approximation. Where there is a notably high density of streaks in a grid square, it is represented by a thick arrow. Wind directions have been plotted for both bright and dark streaks, which in some regions give concordant and in other regions discordant directions, probably because they have been produced at different times.

B. Implications of the Streak Maps

We have previously shown (Fig. 16 of Ref. XIII-1) that the configuration of Syrtis Major corresponds well

to the distribution of constituent dark streaks. In Fig. XIII-11, we similarly plot the distribution of streaks in the vicinity of Solis Lacus, a well known seasonal and secular variable. The Earth-based outline of Solis Lacus, circa 1969, after the Lowell Observatory cartography, also is shown. Considering the variability of this feature, the agreement between the classical configuration and the locus of streaks is excellent, consistent with our previous conclusions. We propose that marked secular changes in Solis Lacus [see, e.g., Ref. XIII-3, p. 140] are due to extraordinary wind regimes, redistributing fine dust in this area. Other factors being equal, small dark regions surrounded on all sides by bright areas should be more susceptible to eolian secular changes (Ref. XIII-4). Ultimately a reconstruction of several different wind regimes, a kind of eolian stratigraphy, should be possible from data such as exhibited in Fig. XIII-11. We return to this subject elsewhere.

In addition to specific cases, such as Syrtis Major and Solis Lacus, we see from Fig. XIII-8 that the global distribution of streaks corresponds well to the general configuration of dark areas as viewed from Earth. In these figures there are many cases where two different
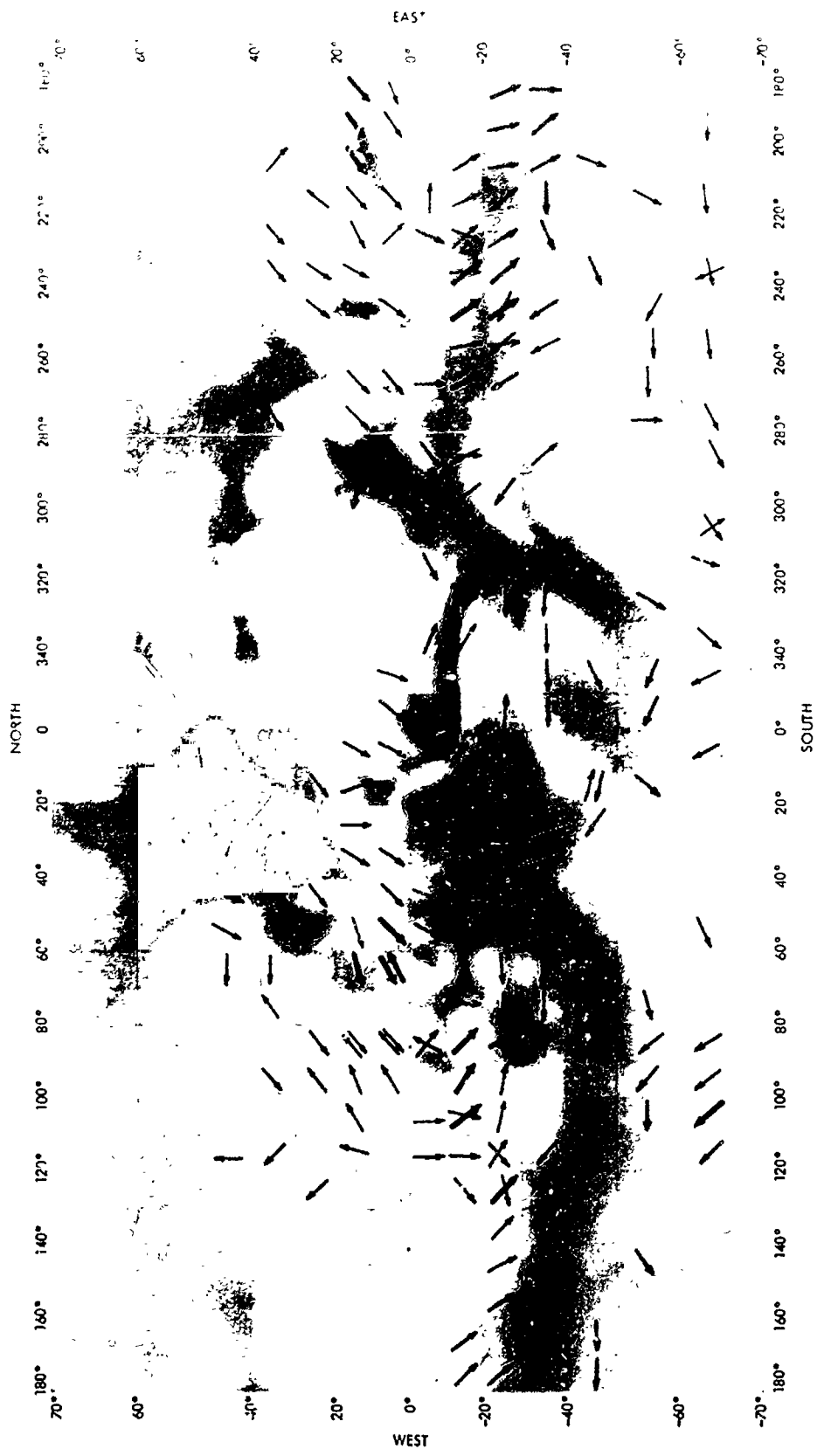
Fig. XIII-8. Prevailing streak directions (averaged over $10° \times 10°$ squares) superimposed on a Lowell Observatory Earth-based albedo map of Mars. Thick arrows indicate heavily streaked areas.
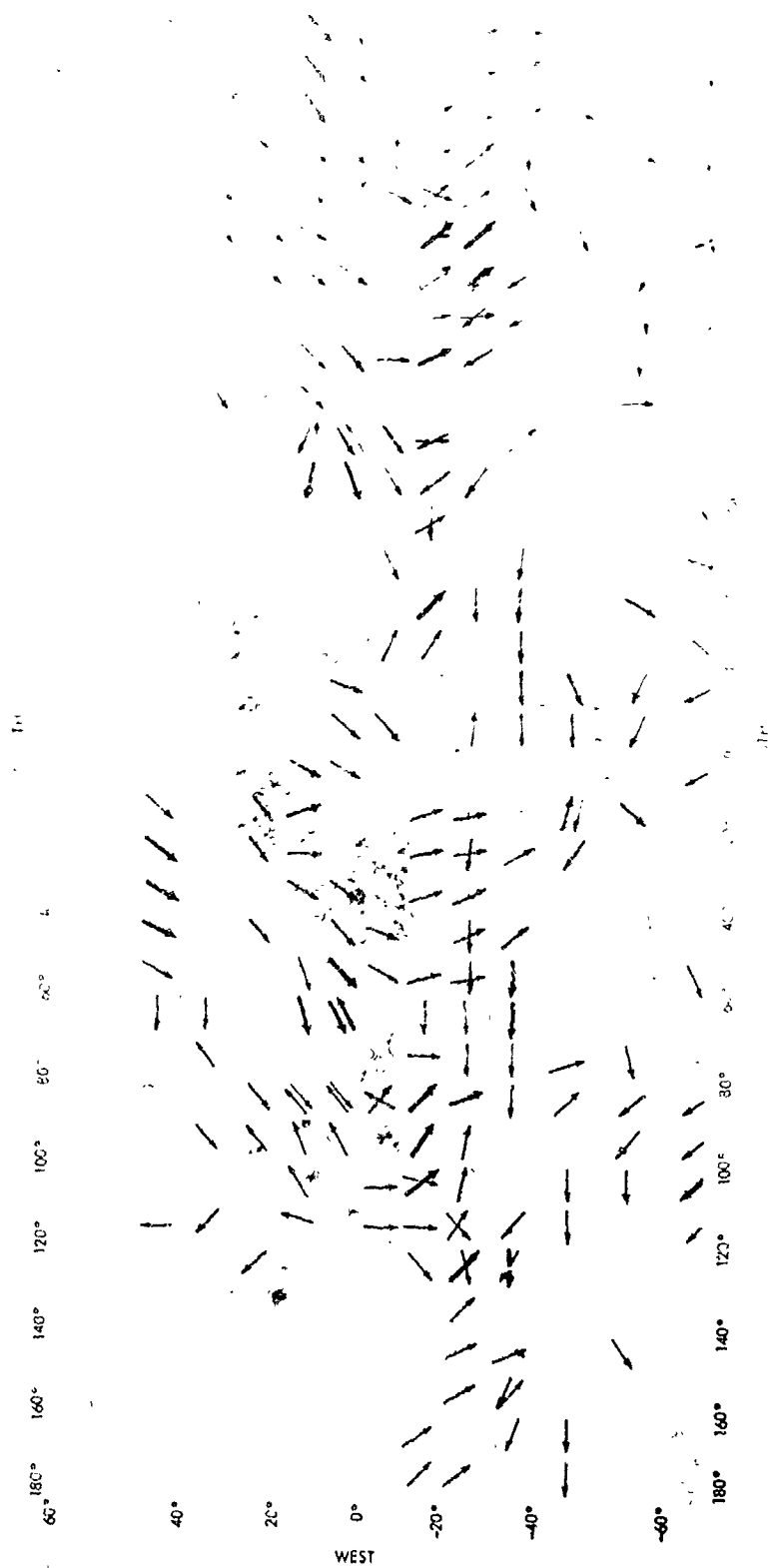
Fig. XIII-9. Prevailing streak directions (averaged over 10° × 10° squares) superimposed on the Mariner 9 topographic map of Mars
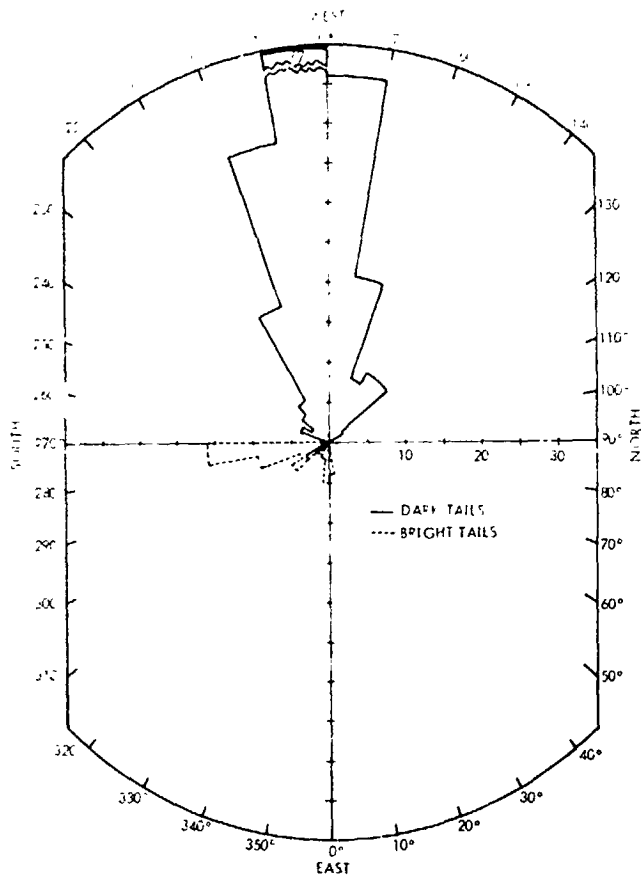
Fig. XIII-10. Rosette diagram of the wind streaks in the Solis Lacus region shown in Fig. XIII-11. Plotted is the number of dark and bright streaks as a function of azimuth.
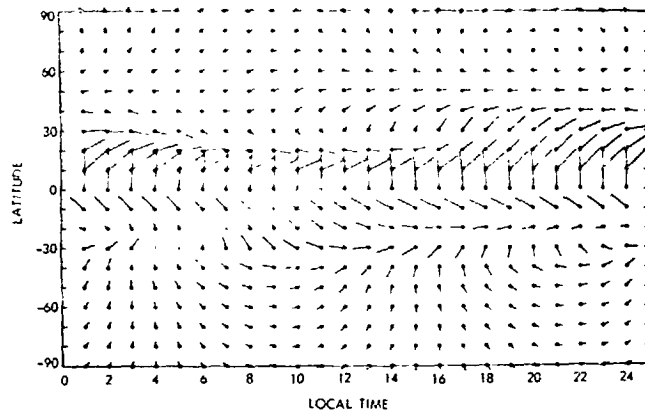
Fig. XIII-12. IRIS wind fields determined from pressure–temperature profiles of the Martian atmosphere. The season is summer in the southern hemisphere. The wind direction is into the grid points; a wind vector equal in length to one grid spacing corresponds to a velocity of 80 m sec^{-1} (courtesy of J. A. Pirraglia).
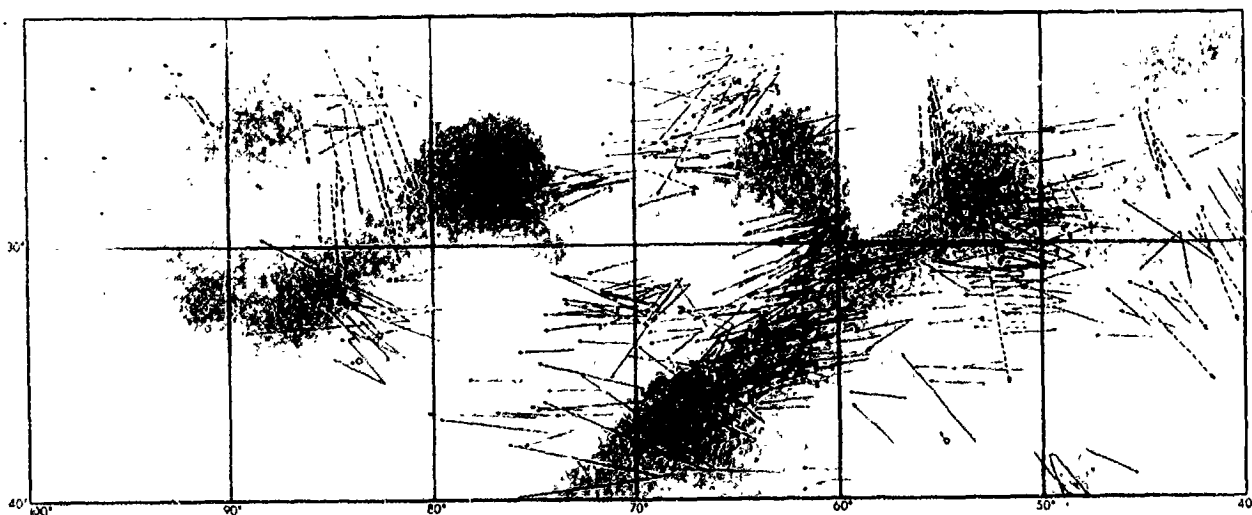
Fig. XIII-11. Streak map of the Solis Lacus region of Mars superimposed on an Earth-based albedo map of the area. Solid arrows represent dark streaks; dashed arrows represent bright streaks. The arrow length is approximately four times the length of the streak. Where many similar streaks occur close together, only one is shown with a number indicating the number of such streaks. Craters with short incipient dark streaks are mapped as circles with short arrows in the direction of the incipient tail.

flow directions are in evidence. We interpret this as the remnants of the flow regimes in the Martian atmosphere in two different epochs, probably two different seasons. It also is possible that a subset of flow directions belongs to the great 1971 dust storm and is not typical of wind patterns in the absence of global storm systems.

In the latitude band between 20°N and 20°S in Figs. XIII-3 and XIII-5, there is a clear tendency for the flow to be from the northeast north of the equator and from the northwest south of the equator. This pattern corresponds to the zonally averaged surface wind calculated by Leovy and Mintz (Ref. XIII-5) for southern hemisphere summer. It also appears in the wind field maps derived from the *Mariner 9* infrared interferometer spectrometer (IRIS) experiment (Fig. XIII-12). The IRIS wind fields are determined from the pressure–temperature profiles obtained by inversion of the infrared emission spectrum. The results above the surface boundary layer displayed in Fig. XIII-12 were derived by Dr. J. A. Pirraglia (cf. Refs. XIII-6 and XIII-7; also see Section XX of this Report) from temperatures during the dust storm. An approximate dynamical theory is used. It is especially important for our purposes that: (1) topography is neglected, and (2) the results are most uncertain close to the equator. Winds at the equator are probably overestimated. The general configuration of the flow pattern is probably correct, however, and the agreement between the calculated winds and the streak orientations in the latitude band ±20° is remarkably good.

At equatorial latitudes the calculated winds are strongest and are practically steady. At higher latitudes their magnitudes are less and the direction varies during a diurnal cycle. Pirraglia's calculation isolates the large-scale steady winds from the diurnally varying winds. We know that there is a range of other winds expected on Mars, including slope and obstacle winds driven by the large elevation differences (Refs. XIII-8 through XIII-10), and winds driven by the large temperature gradient between frosted and unfrosted polar ground (Ref. XIII-11). At higher latitudes, we might expect such winds to dominate, and the steady component that Pirraglia calculates to dominate at low latitudes.

The streak maps (Figs. XIII-1 through XIII-7) support this contention. The flow indicated at high latitudes does not correspond to that predicted either by Pirraglia or by Leovy and Mintz (Ref. XIII-5). An interesting regularity at higher latitude is the indication of a steady

easterly flow component at latitudes 20° to 40°S. This is the latitude range and initial direction of flow of the 1971 global dust storm, and it is not impossible that this flow component is a marker of that storm.

Other peculiarities may be connected with topography. There is the appearance of radial flow away from a region centered at 5°N, 110°W. This is the area of Tharsis, the highest region on Mars. The flow markers suggest wind transport downhill here, although this is not the predicted flow direction in the vicinity of such elevations in current theories during daytime. Such downhill flows are common on Earth at night, however, because of radiative cooling of the ground. A divergence or bifurcation of the flow patterns near 20°S, 110°W, seems to be connected with the presence of rough terrain there (Fig. XIII-3d); the winds appear to move to avoid the rough region.

The preceding results provide us with a new estimate of the threshold velocity necessary to initiate grain motion on the Martian surface. There is a modest variation among various recent estimates of the critical velocity, V above the surface boundary layer necessary to initiate grain motion on the surface. Sagan and Pollack (Refs. XIII-12 and XIII-13; also see Ref. XIII-1) estimated this velocity at about 65 m sec⁻¹ for a 15-mb surface pressure level, about 80 m sec⁻¹ for 10 mb, and about 110 m sec⁻¹ for 5 mb. Golitsyn (Ref. XIII-14) proposed that these values may be reduced by about 30% by introducing sharp roughness gradients. Hess (Ref. XIII-15), recalculating the problem, derives V for an 8-mb surface pressure to be between 38 and 60 m sec⁻¹, depending on the velocity distribution function through the boundary layer. Yet another independent estimate, by Gierasch and Goody (Ref. XIII-16), derives about 30 m sec⁻¹ for a surface pressure of 5 mb. The range among these models is about a factor of 2 for comparable surface pressures for the threshold velocity, V_{*t}, to initiate grain motion at the ground, but rises to a factor of almost 4 for the velocity above the boundary layer because of variations among models on the functional form of the velocity distribution function through the boundary layer. Distinguishing among these results is a matter of some importance for understanding the generation of dust storms and eolian transport on Mars. It also has a more practical importance: Lower velocities present no problem to a lander mission such as Viking, while the higher velocities pose grave hazards.

The existence of a 40° wide equatorial latitude band in which the streak patterns strikingly follow the mean

general circulation with significant deviations outside
this band indicates that the global wind velocities at the
borders of the band are approximately the velocities appropriate for initiating grain movement on the surface.
From the IRIS results (Fig. XIII-12), these velocities
range from V = 50 to 90 m sec^{-1} above the surface
boundary layer. Were topography introduced, somewhat
higher velocities would be implied (Ref. XIII-5). Because
grain transport typically occurs on timescales ~10 days
rather than ~1 day (this section), it is not the mean
wind of the general circulation, but the high-velocity tail
of the distribution function of the general circulation
winds which must be operative. These velocities lie in
the middle of the range for the 5-mb surface pressure
summarized above and derived from quite different considerations. Moreover, a recent revision of the wind
velocities at these altitudes and at the start of the dust

storm for the numerical circulation models of Ref.
XIII-5, raises these values to 40 to 50 m sec^{-1} at equatorial latitudes (Ref. XIII-11). Velocities derived from
the wavelengths of lee wave clouds (Ref. XIII-17) are
of this same order.

C. Polar Winds

As we have mentioned, few wind indicators are present
at very high latitudes, both because of obscuration and
possibly because of efficient scouring of fine particles from
the polar regions. The high splotch density in the south
circumpolar region in some sense compensates for the
low streak density there; there is a marked absence of
streaks in the most heavily splotched polar regions.
Nevertheless, there are a few locales both in the north

Fig. XIII-13. The north polar cap of Mars, showing the prominent dark polar collar. The
season is late spring in the northern hemisphere. (MTVS 5019-40, DAS 13317550)

Mare Acidalium Fig XIII-1 and in the south (Mare Australe Fig XIII-6) where many streaks are directed away from the poles This is hardly an invariable high-latitude phenomenon there is also a westerly circumpolar component as inspection of Figs. XIII-6 and XIII-7 clearly shows, but it nevertheless seems noteworthy. The most straightforward explanation would be in terms of the polar cap temperature gradient winds postulated by Leovy et al in Ref. XIII-11. The pole-fleeing streaks in Mare Acidalium (Fig. XIII-1) are interesting because this mare is one of the few dark areas at these latitudes for which seasonal changes are expected at the observed season. It is possible that seasonal albedo variations at high latitudes are driven by such polar winds. The most likely mechanism would be the eolian removal of bright overlying dust, revealing the darker material underneath, as postulated for several varieties of seasonal changes (Refs. XIII-1, XIII-9, XIII-12, and XIII-13).

A related phenomenon may be the north polar collar. This dark band, surrounding and following the northern ice cap in its summer retreat to the pole, has been reported by many visual observers (Refs. XIII-18 and XIII-19). Because of possible psychophysiological contrast effects, and especially because of the interpretation of the northern collar as moistened ground, the very existence of the collar has been called into question in recent years. Mariner 9 extended mission photography has demonstrated unambiguously (Fig. XIII-13) the existence of the north polar collar. Under the circumstances, the report by Earth-based visual observers that the collar follows the retreating polar cap toward the pole must now be taken seriously.

Both the existence of the collar and its retreat also can be understood in terms of polar winds, deflating a thin, bright surficial layer of dust in the immediate vicinity of the northern polar cap edge. But why did *Mariner 9* find no evidence for a south polar collar? If the south collar visibility indeed follows the curve of de Vaucouleurs (Fig. 31 of Ref. XIII-18), peak visibility corresponds to $L_s \simeq 210°$. *Mariner 9* did not observe Mars near this L_s, and the observations were made after the atmospheric dust settled.

Another curious circumstance is that the southern circumpolar streaks are, almost without exception, dark streaks; while the northern streaks, and especially the Mare Acidalium streaks, are largely bright during *Mariner 9* observations.

One possible explanation of some of these phenomena is the following: The steep temperature gradient between frosted and unfrosted terrains at the edge of the retreating polar ice cap produces strong winds. These winds deflate fine, bright surficial dust, uncovering the dark splotchy terrain which follows the waning periphery of the cap. The transported bright material is layered down somewhat equatorward, producing bright circumpolar streaks. High polar winds are also consistent with the probably eolian etch pits seen exclusively in polar region.

D. Correlations of Streaks and Splotches

We also have mapped the distribution of crater splotches over the entire Martian surface, using the techniques and cautions described above for the streak mapping program. Splotches spilling over crater ramparts and splotches unconnected with craters were not mapped. Streaks and splotches in five representative regions of Mars are displayed in Figs. XIII-14 through XIII-18. The convention for representing streaks is described above. Splotches are represented by sketches within crater boundaries showing the approximate configurations of the splotches. Only craters larger than about 50 km are shown. We see that splotches tend to be localized toward one face of the containing crater (Ref.
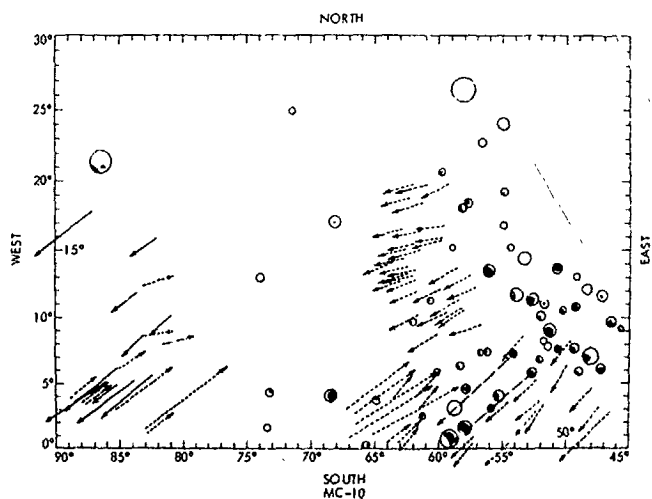
Fig. XIII-14. Splotch/streak map of the MC-10 region. This is the area surrounding Lunae Palus. Shown are all craters larger than about 50 km in diameter and all dark crater splotches. Solid arrows indicate the directions of dark crater tails, and dashed arrows those of bright crater tails. The arrow length is approximately four times the length of the tail. The shortest arrows shown are 2° (of latitude) and represent crater tails < 30 km in length.
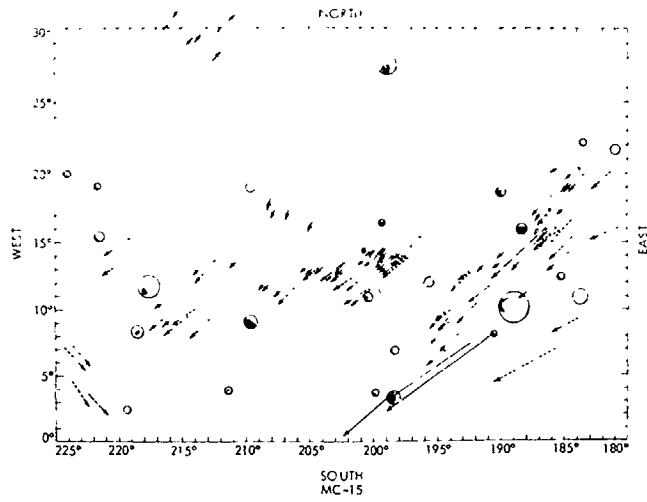
Fig. XIII-15. Splotch/streak map of the MC-15 region, Cerberus—Elysium.
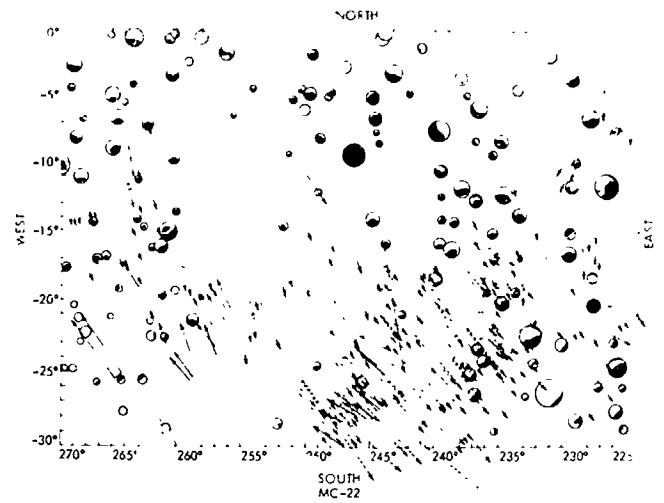
Fig. XIII-17. Splotch/streak map of the MC-22 region, Mare Tyrrhenum—Hesperia.
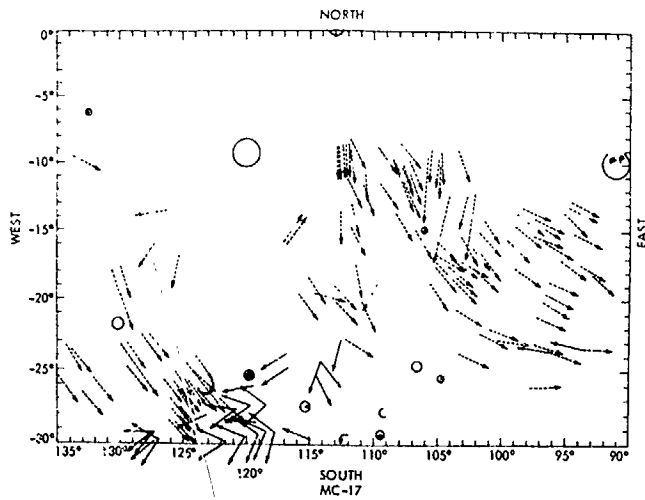
Fig. XIII-16. Splotch/streak map of the MC-17 region, Tharsis—Daedelia.
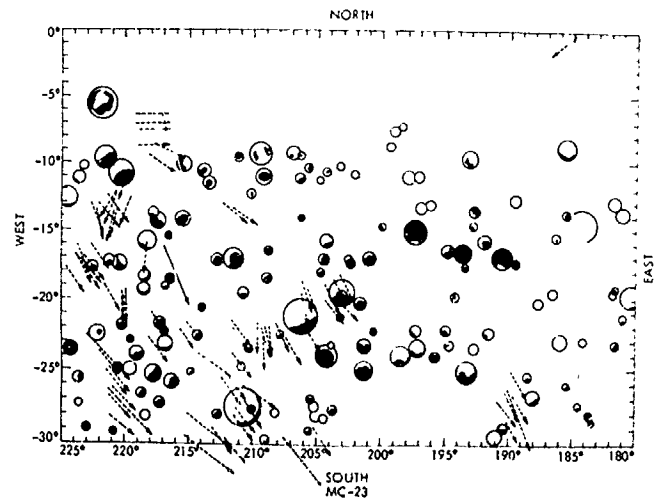
Fig. XIII-18. Splotch/streak map of the MC-23 region Mare Cimmerium—Zephyria.

XIII-1. There is at least in many cases, a tendency for splotches in adjacent craters to be localized in the same face of their respective craters. This face tends to be the direction toward which the wind has been blowing, according to the predominant nearby streak wind direction indicators.

As is usual in our present ignorance of Martian surface processes, there are two explanations of this correlation, each the obverse of the other. In the first view, the winds have blown dark material into the craters, where they have accumulated against the leeward ramparts. In the second view, the winds have preferentially deflated bright material off the leeward ramparts of the craters, exposing the underlying darker material, possibly basement rock. The resulting streaks would then bear a closer relationship to Saharan sand streamers, described by Smith (Ref. XIII-20) as "relatively thin, ribbon- or banner-like accumulations of sand downwind from localized source areas or from topographic constrictions. Where long, straight, parallel and separated by relatively sand-free strips, they serve to indicate consistency and direction of sand-moving winds."

Accordingly, we postulate some cases on Mars in which dark mobile material within crater floors is overlain with bright mobile material, perhaps as a consequence of local or global dust storms. Subsequent deflation of the crater produces long, bright downwind streaks emanating from the crater, and eventually exposes underlying dark material on the interior leeward side of the crater. Subsequent winds, possibly from another direction, then can deflate the exposed dark material, producing incipient dark tails. Dark splotches with associated dark tails are known, e.g., in Bosporos (Fig. 27 of Ref. XIII-1). The development of dark crater tails from craters with pre-existing bright tails is also known, e.g., in Hesperia (Fig. 23 of Ref. XIII-1). These views are consistent with the conclusions that we will draw from a detailed study of albedo variations in three selected regions, Syrtis Major, Lunae Palus, and Promethei Sinus. In other cases, the dark splotchy material may be bedrock, and the dark streaks may be produced by deflation of overlying bright material.

E. Syrtis Major

At the resolution of the *Mariner 9* cameras, the classical albedo feature Syrtis Major is outlined by a concentration of bright and dark streaks. The bright streaks dom-

inate near the western (stable) edge of Syrtis Major. The dark streaks outline the eastern, variable edge. Fig. XIII-19) of Syrtis Major (Ref. XIII-1). Telescopic evidence suggest that the eastern boundary of Syrtis Major varies seasonally (Ref. XIII-3). Syrtis Major has the steepest slope of any extensive dark area on Mars.

Since the end of the 1971 dust storm, *Mariner 9* pictures have revealed a gradual darkening of Syrtis Major at resolutions of the wide-angle camera (Figs. XIII-20 through XIII-22) and the narrow-angle camera (Figs. XIII-23 through XIII-26) This darkening resulted largely from the appearance, development, and merging of dark crater tails of the type seen in Fig. XIII-19, which are characteristic of Syrtis Major. In other areas, dark tails do not have the patchy, discontinuous appearance of the Syrtis Major tails. This nonuniform patchiness of the tails and their tendency to shed tangentially from topographic protuberances such as crater walls suggest that they are produced by eolian erosion of extensive, but very thin, deposits of bright material, resulting in the exposure of dark, wind-resistant, underlying material. Radar evidence suggests that the region of Fig. XIII-19 is a relatively smooth surface, sloping from west to east (left to right on Fig. XIII-19), making it a likely locale for eolian transport.

We assume that, after the 1971 dust storm, much of this slope was covered by a thin layer of bright dust. Subsequent winds, blowing predominantly downslope have scoured off this material, especially in regions where wind speeds are intensified by topography. A close examination of the high-resolution, narrow-angle pictures (Figs. XIII-22 through XIII-26) is especially instructive in this context. Many instances of dark tails, or sections of dark tails "shedding off" craters can be seen. This is especially evident in Fig. XIII-8.

We postulate efficient micro-traps for the dust scoured off in the above manner. Our model predicts that Syrtis Major will continue to darken until it is affected by either a local or global dust storm. The contrasts involved between the dark and bright portions of Syrtis Major are small, being typically about 10% (for the albedo markings in Fig. XIII-24).

As in other regions of Mars, white streaks exist in Syrtis Major, but have not been seen to change (Fig. XIII-27). Their nature (erosional or depositional) and time of origin (before, during, or after the dust storm) remain enigmatic.

Fig. XIII-19. General view of VF Region 8, Syrtis Major. This wide-angle picture, centered at 13°N, 283°W, is about 360 km across. (MTVS 4186-72, DAS 07147383)
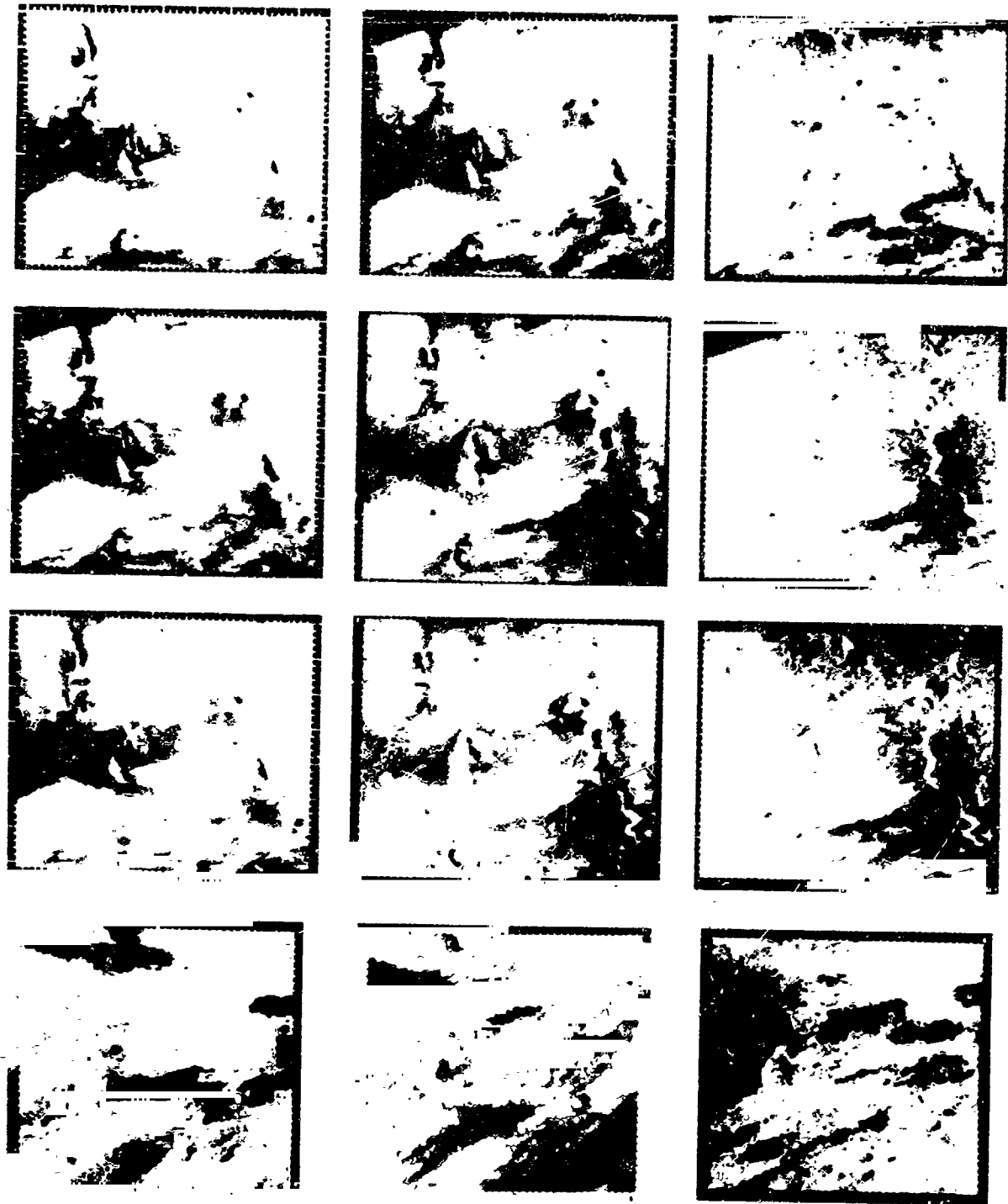
Fig. XIII-20. Darkening of Syrtis Major at wide-angle resolution. The area shown in the top three rows is about 270 km across and is centered at 15.°2N, 282.°8W. It corresponds approximately to the upper third of Fig. XIII-1. First row (left to right): revolution 155, revolution 223, revolutions 233 to 155. Second row (left to right): revolution 233, revolution 430, revolutions 430 to 233. Third row (left to right): revolution 155, revolution 430, revolutions 430 to 155. (Stanford AIL Picture Product STN 0191, 102105-6-7) The last row shows a closeup of the bottom sections of the window above. Left to right: revolution 155, revolution 233, revolutions 233 to 155. Center 13.°8N, 283.°9W; X = 140 km (Stanford AIL Picture Product STN 0164, 041505) Note that the photometric geometry is closely similar on revolutions 155 and 223, but significantly different on revolution 430.

Fig. XIII-21. Darkening of Syrtis Major at wide-angle camera resolution. The area shown is about 140 km across and is centered at 11.°7N. 284.°5W. It corresponds to the lower left of Fig. XIII-1. Left to right: revolution 155, revolution 233, revolutions 233 to 155. (Stanford AIL Picture Product STN 0164, 041506)
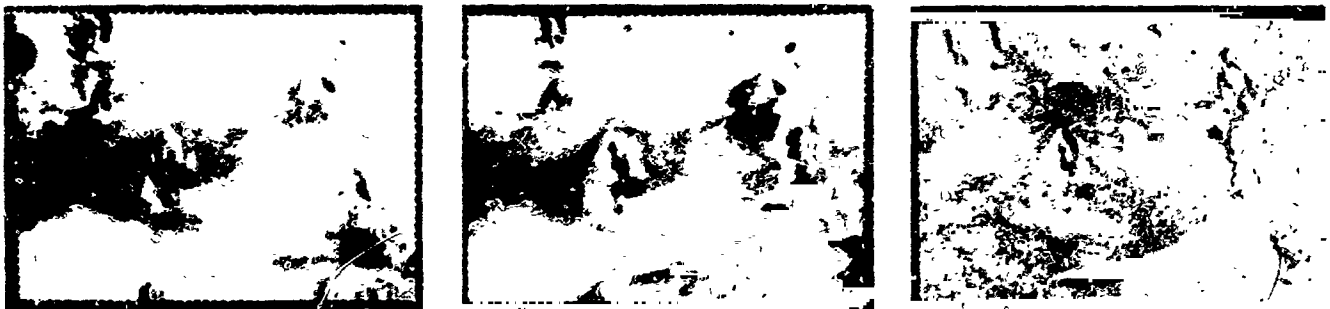
Fig. XIII-22. Darkening of Syrtis Major at wide-angle camera resolution. The area shown is about 250 km across and is centered at 14.°6N and 282.°8W. It corresponds to the upper third of Fig. XIII-1. Left to right: revolution 155, revolution 430, revolutions 430 to 155. As the photometric geometry differs appreciably between revolutions 155 and 430, topographic detail has not been cancelled successfully in the picture difference. (Stanford AIL Picture Product STN 0191, 102101)

Fig. XIII-23. Darkening of Syrtis Major at narrow-angle camera resolution. The area shown is about 50 km across and is centered at 13.°2N and 282.°9W. Left to right: revolution 233, revolution 430, revolutions 430 to 233. The photometric geometry differs considerably between the two views, and topographic detail remains in the picture difference (e.g., crater at lower right). (Stanford AIL Picture Product STN 0191, 102111)
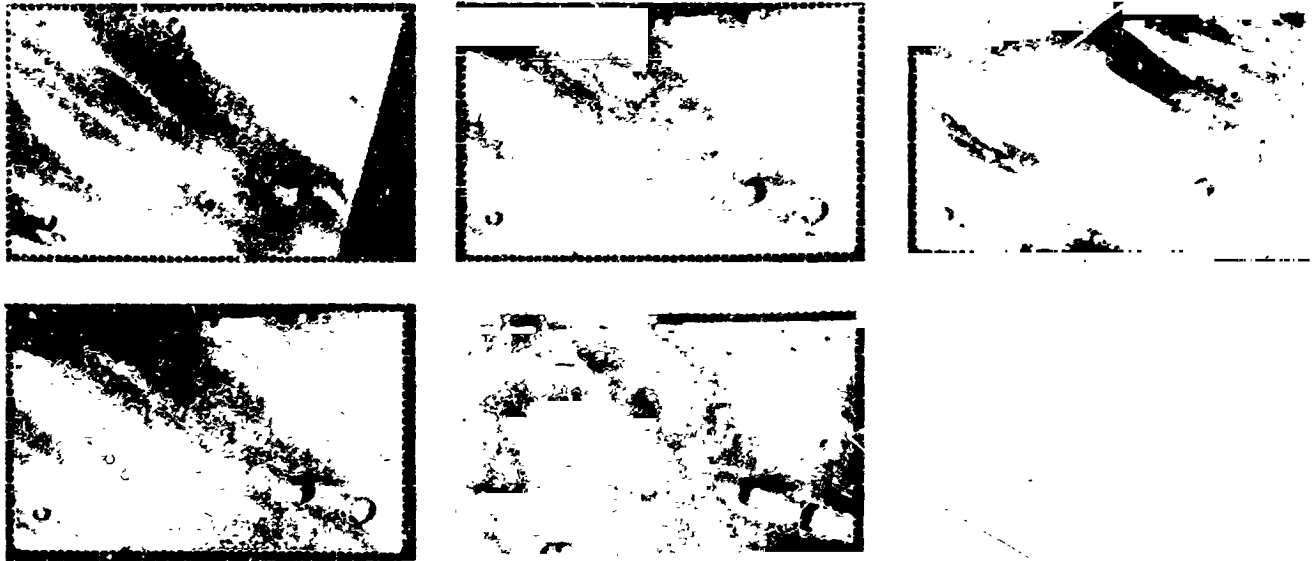
Fig. XIII-24. Another example of the darkening of Syrtis Major at narrow-angle camera resolution. The area shown is about 50 km across and is centered at 10.°8N and 283.°6W. Top row (left to right): revolution 155, revolution 233, revolutions 233 to 155. Bottom row (left to right): revolutions 233 and 430. These two pictures were not differenced because satisfactory alignment could not be obtained because of a significant change in the photometric geometry between the two pictures. (Stanford AIL Picture Product STN 0191, 102113)
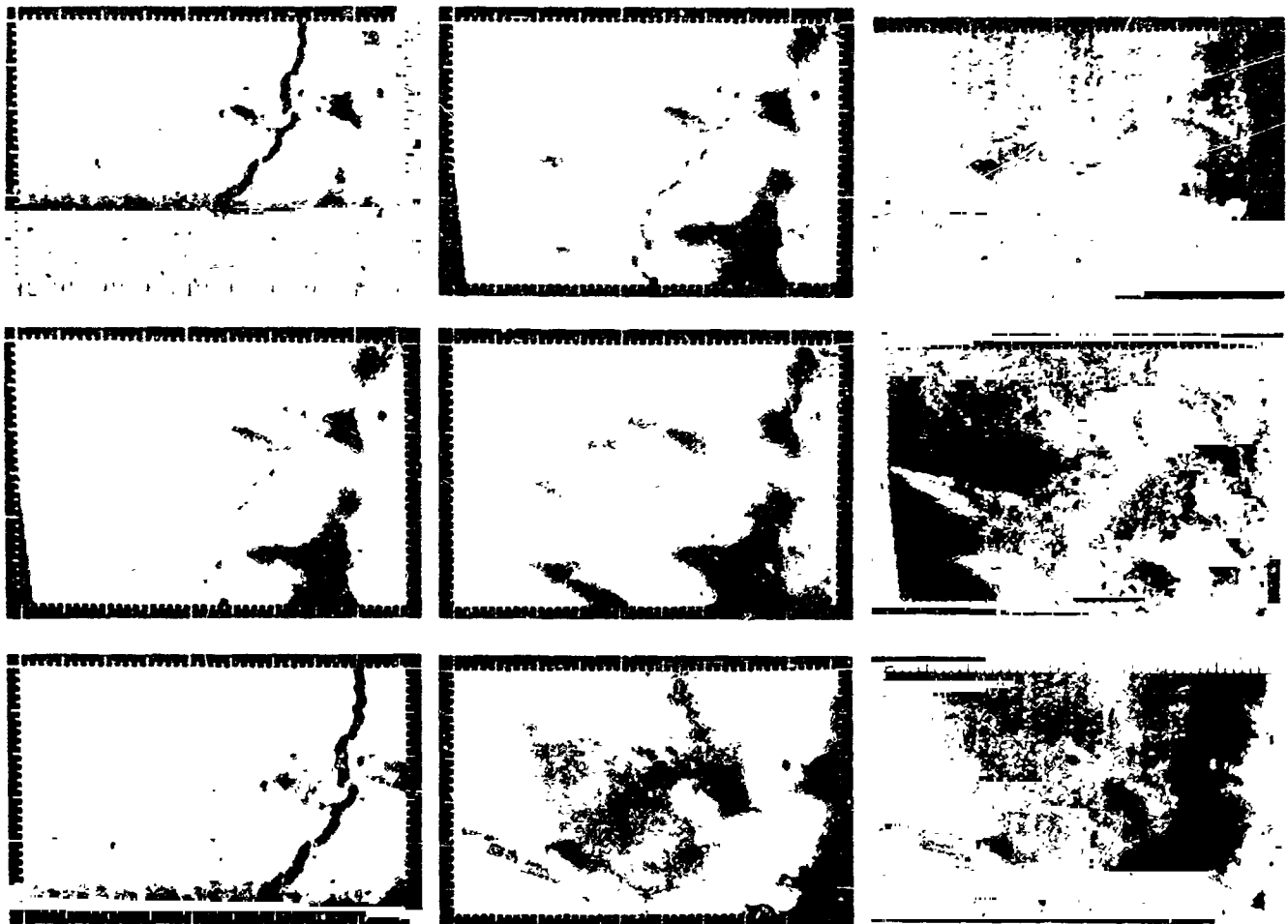
Fig. XIII-25. Appearance and development of dark tails in Syrtis Major at narrow-angle camera resolution. Top row shows an area about 44 km across centered at 14.°9N and 281.°6W. Left to right: revolution 155, revolution 237, revolutions 237 to 155. The photometric geometry is similar in the two views. (Stanford AIL Picture Product STN 0172, 040504) The middle row shows an enlargement of the center section of the above region (about 22 km across). Left to right: revolution 155, revolution 237, revolutions 237 to 155. The bottom row shows a corresponding enlargement of the lower-left corner of the original window. (Stanford AIL Picture Product STN 0172, 060656)
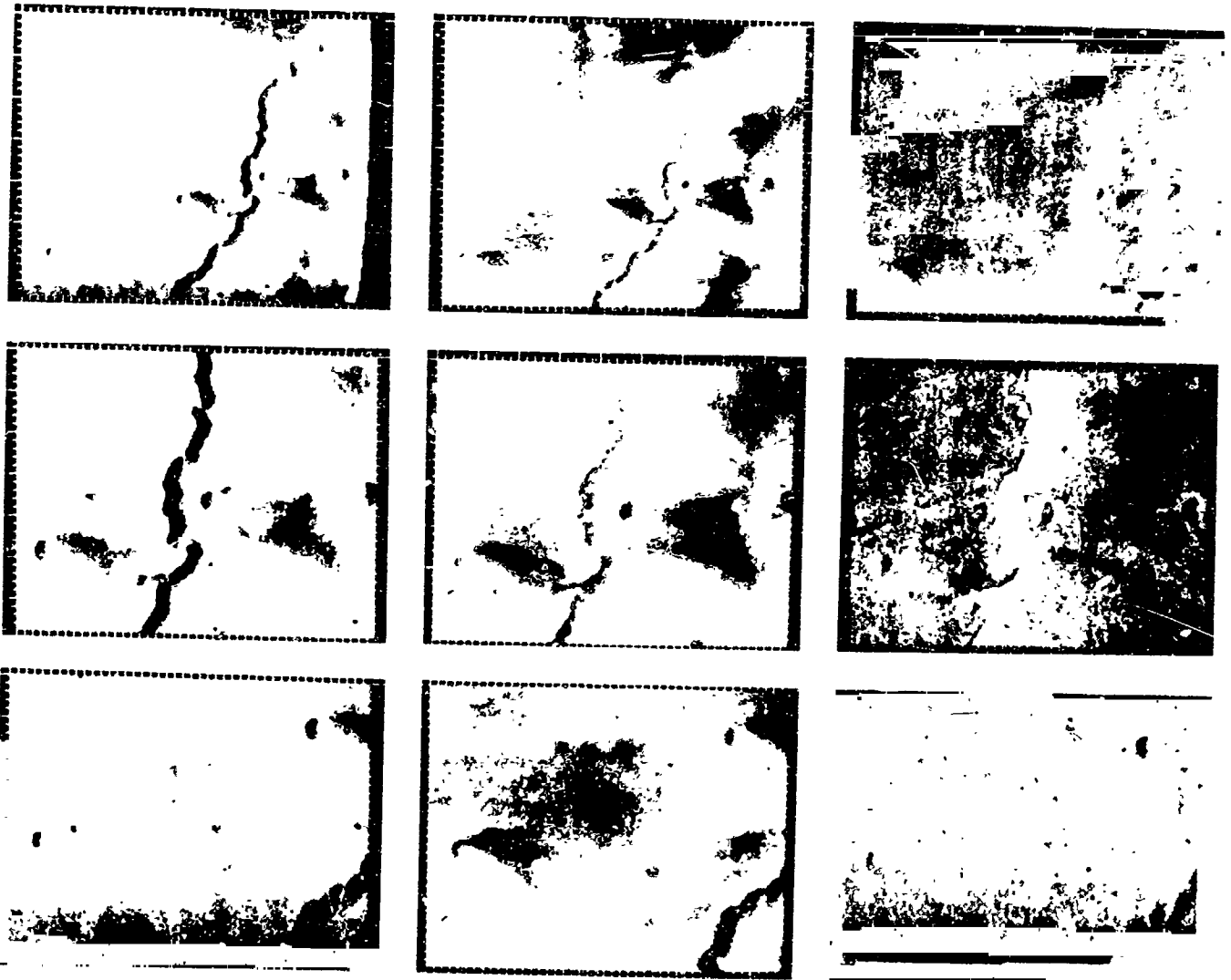
Fig. XIII-26. Development of dark tails at narrow-angle camera resolution in the region of Fig. XIII-25. Top row (left to right): revolution 155, revolution 233, revolutions 233 to 155. Middle row: revolution 237, revolution 430, revolutions 430 to 237. Bottom row: revolution 155, revolutions 430 to 155. The photometric geometry is similar for revolutions 155 and 233, but differs significantly for revolution 430. The area is about 50 km across and is centered at 14.°9N, 281.°9W. (Stanford AIL Picture Products STN 0191, 102114, 102115, 102116, 102117)
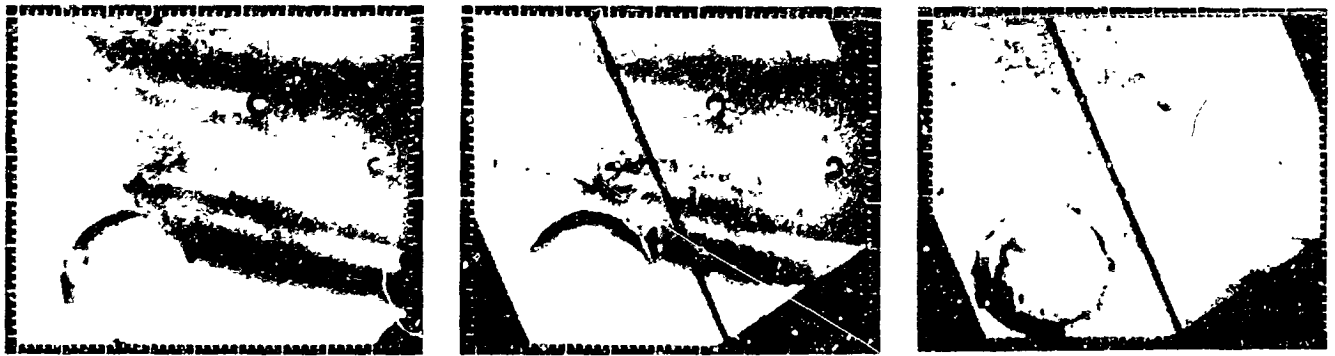
Fig. XIII-27. Permanence of white streaks in Syrtis Major at narrow-angle camera resolution. The area is about 35 km and is centered at 4.°6N, 294°W. Left to right: revolution 194, revolution 233, revolutions 233 to 194. The photometric geometry differs in the two views, making it impossible to cancel topographic features in the picture difference. (Stanford AIL Picture Product STN 0191, 102110)

F. Lunae Palus

The region studied (VF11) lies close to the classical albedo feature Lunae Palus, suspected of being both a seasonal and secular variable by telescopic observers (Ref. XIII-21). Mariner 9 photography resolves the region into a wide, deep channel dissecting relatively smooth surrounding plains (Fig. XIII-28).

Although no albedo changes in these plains have yet been detected in Mariner 9 pictures, strong localized albedo changes have been found within the channel itself (Fig. XIII-29). At least three separate areas were observed to darken during the mission. The largest of these is about 20 by 70 km in size. Only a slight change is evident at wide-angle camera resolution between revolutions 125 and 160, but a very pronounced darkening occurred sometime during the 39-day interval between revolutions 160 and 238 (Fig. XIII-29).

A high-resolution view of the floor of the channel, including a section of the largest of the three darkening areas, is shown in Fig. XIII-30. This area is outlined in Fig. XIII-28. At the resolution of the narrow-angle camera, it is clear that darkening occurred within the channel between revolutions 125 and 160 (Fig. XIII-31), although this is not evident at wide-angle camera resolution (Fig. XIII-29). The two views shown in Fig. XIII-31 do not overlap exactly and are not aligned with respect to each other. They are therefore difficult to compare directly. To facilitate the comparison, three arrows are shown in each view. The top two point to a pair of dark, round spots; the bottom arrow points to a characteristic bend in the small channel seen in the figure. The view on the left was obtained on revolution 125, that on the right 17

days later on revolution 160. The change that has occurred in this region is made evident in Fig. XIII-32, which shows rectified, scaled, similarly projected and aligned views of the region surrounding the three arrows in Fig. XIII-31. The two dark, round spots (about 1 km) can be seen just below the center of the window in the left (revolution 125) and middle (revolution 160) sections of Fig. XIII-32. Similarly the characteristic bend in the channel occurs at the bottom-left corner of both sections. The right section of Fig. XIII-32 shows a picture-element by picture-element difference of the two sections on the left. Notice that the two round spots cannot be seen in the difference as they have not changed. Similarly the channel is not evident. However, a significant amount of darkening is seen to have taken place in the immediate neighborhood of the two dark spots between revolutions 125 and 160. The lateral extent of the change may be inferred from the fact that the two spots are about 10 km apart.

The observed darkening of regions within the Lunae Palus channel can best be understood in terms of the gradual removal, by winds, of fine bright dust deposited during the 1971 dust storm over the albedo markings within the channel (Figs. XIII-30 through XIII-32); it is consistent with an eolian explanation for their variability. It is possible that a channeling and intensification of winds may be produced by the main Lunae Palus channel, thus leading to more effective eolian erosion within the channel than on the surrounding plains. This would result in a greater apparent variability (e.g., darkening) within the channel than on the plains following a major dust storm. Likewise, the great Coprates rift valley, so long that one end may be near noon when the other is before sunrise, may generate and channel very high winds.

Fig. XIII-28. Overall wide-angle camera view of VF Region 11, Lunae Palus, centered at about 21°N, 63°W. The picture is about 300 km across. The region outlined is shown at high resolution in Fig. XIII-3. (IPL Roll 1329, 181918)

Fig. XIII-29. Changes within the Lunae Palus channel at wide-angle camera resolution. Left to right: revolutions 125, 160, and 238. Note the pronounced darkening within the channel during the 39-day interval between revolutions 160 to 238. Center: 23°N, 66°W; X = 260 km. (Stanford AIL Picture Products STN 0166, 042911, 042912)

Fig. XIII-30. Narrow-angle camera view of the region outlined in Fig. XIII-28. Revolution 160. Center: 22°N, 65°W; X = 75 km. (IPL Roll 1329, 185802)

Fig. XIII-31. Right: Revolution 160. Same area as in Fig. XIII-30, but shown in orthographic projection. Left: Same region seen on revolution 125. These two views do not overlap exactly and are not aligned wth respect to each other. In each view, the upper two arrows point to a pair of dark spots, while the bottom arrow points to a characteristic bend in the small channel. (IPL Roll 1329, 124209)

Fig. XIII-32. Region of the two dark spots and the small channel shown in Fig. XIII-31. Left: revolution 125. Middle: revolution 160. The two views, similarly scaled and projected, were aligned relative to each other and differenced picture element by picture element to give the picture difference at right. Note the darkening in the vicinity of the two dark spots. Center: 22.°6N, 64.°5W; X = 30 km. (Stanford AIL Picture Product STN 0166, 042904)

G. Promethei Sinus

Figure XIII-33 is a wide-angle view of Promethei Sinus, an extensively splotched, cratered region near the south pole of Mars. According to Ref. XIII-3 Promethei Sinus is variable, but it is not known whether the variations are seasonal. For the study of variable features, the two regions outlined in Fig. XIII-33 are of special interest. The more important of the two is shown at high resolution in Fig. XIII-34. Two kinds of characteristic dark splotches are seen: (1) those inside craters, usually running up against the crater's inner walls, and (2) splotches lying outside of craters. The latter have a very characteristic morphology with one long edge rather amorphous in outline, while the other is scalloped and pointed.

As shown, dark splotches tend to lie on the downwind side of craters. On this basis, the prevalent wind direction in Fig. XIII-34 is from top to bottom. Scalloped edges are also characteristic of eolian phenomena, with the wind always blowing at right angles to the scalloped edge. Thus, one inference from the scallops is a wind direction from top to bottom in Fig. XIII-34, which would be consistent with that inferred from the location of splotches within the two craters. In this case, the dark scalloped splotches could be interpreted as underlying, wind-resistant dark material, exposed by scouring off bright overlying material. Other interpretations are discussed below. The contrast between the bright and dark splotches in this region is about 20%.

Several regions of special interest are designated by letters in Fig. XIII-34, their behavior during the *Mariner 9* mission is documented in Figs. XIII-35 through XIII-40. Figure XIII-35 shows the development in less than 13 days (i.e., sometime between revolutions 99 and 126) of a 10-km dark region. This region, resembling a leaf or a spearhead, remained unchanged subsequently, even though surrounding areas were undergoing variation.

Fig. XIII-33. Wide-angle camera view of VF Region 26, Promethei Sinus, centered at 71°S, 269°W, and about 750 km across. The solid outline shows the area of Fig. XIII-34. (MTVS 4211-9, DAS 08008038)

Fig. XIII-34. Narrow-angle camera view of the region outlined (solid) in Fig. XIII-1. The picture is about 80 km across, and is centered at 69.°6S, 253.°1W. Several regions of special interest, discussed in the text, are indicated by letters. (MTVS 4213-12, DAS 08079893)
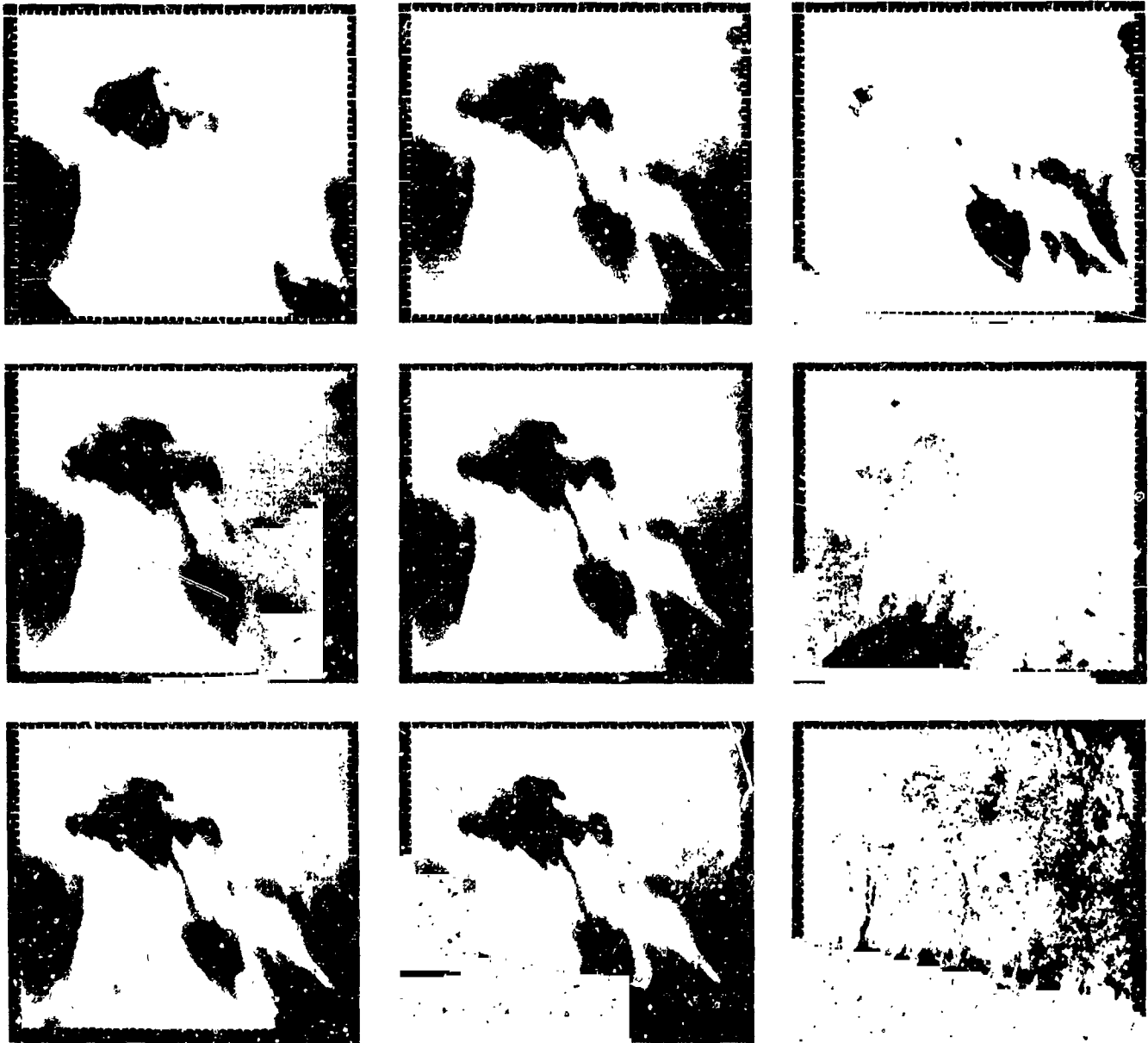
Fig. XIII-35. Changes in region A. Top row (left to right): revolution 99, revolution 126, revolutions 126 to 99. Middle row: revolution 126, revolution 179, revolutions 179 to 126. Bottom row: revolution 181, revolution 220, revolutions 220 to 181. The window is about 20 km across, and is centered at 70.°1S, 253.°3W. (Stanford AIL Picture Products STN 0167, 050609, 050610, 050611)
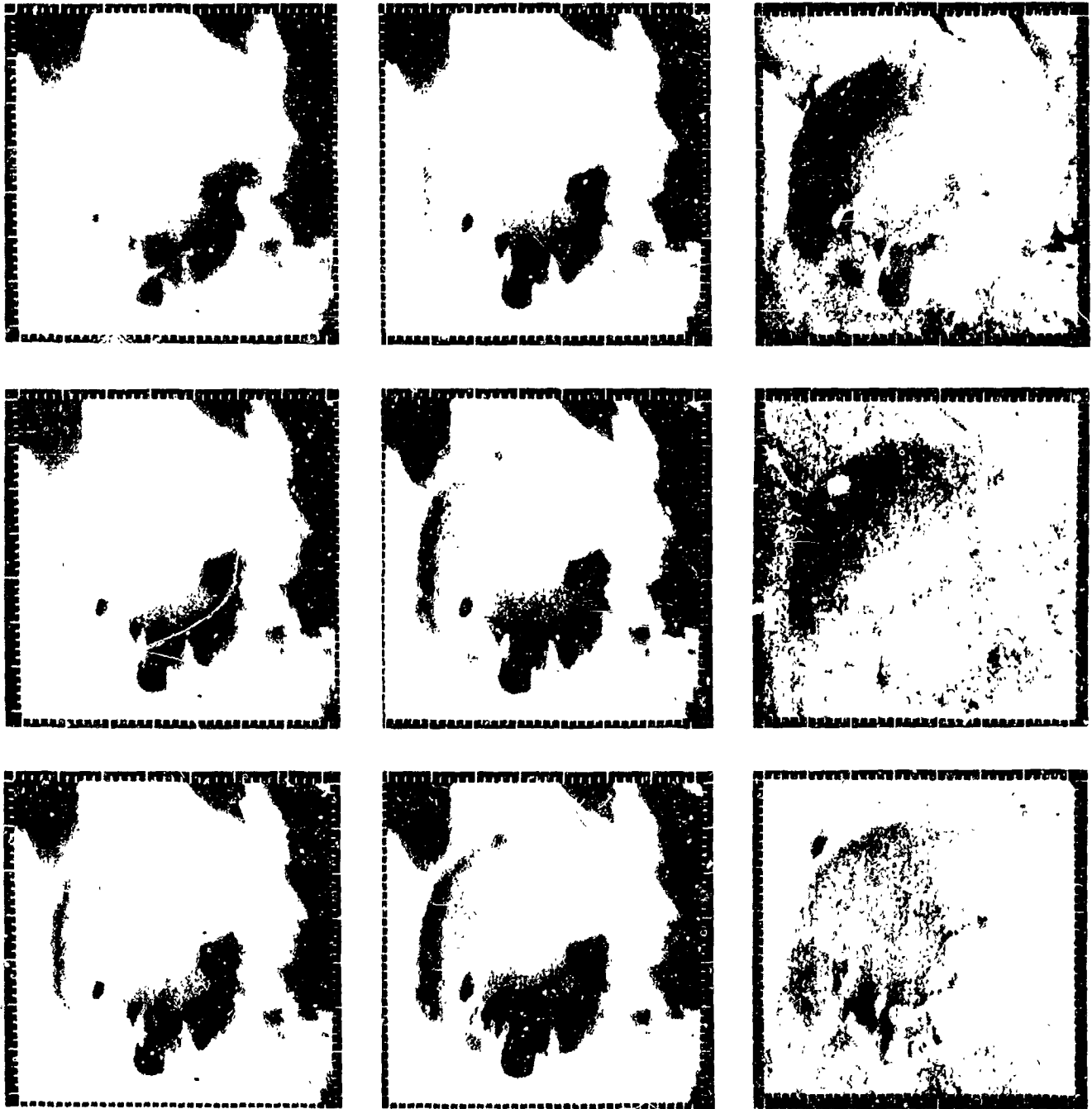
Fig. XII-36. Changes in region B. Top row (left to right): revolution 126, revolution 179, revolutions 179 to 126. Middle row: revolution 179, revolution 181, revolutions 181 to 179. Bottom row: revolution 181, revolution 220, revolutions 220 to 181. The window is about 20 km across and is centered at 69.°9S, 253.°7W. (Stanford AIL Picture Products STN 0173, 061109, 061110, 061111)
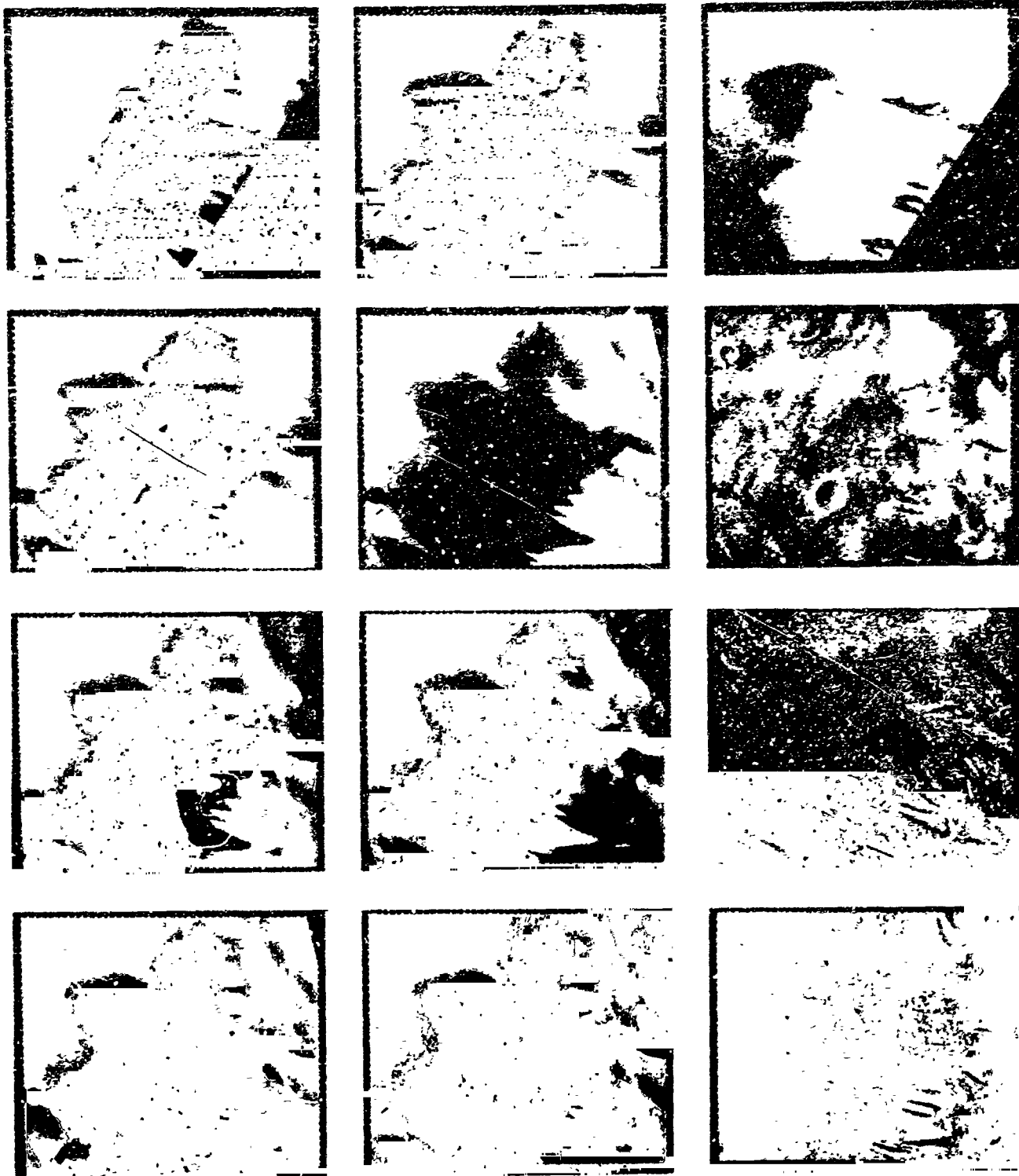
Fig. XIII-37. Changes in region C. First row (left to right): revolution 99, revolution 126, revolutions 126 to 99. Second row: revolution 126, revolution 179, revolutions 179 to 126. Third row: revolution 179, revolution 181, revolutions 181 to 179. Fourth row: revolution 181, revolution 220, revolutions 220 to 181. The window is about 45 km across and is centered at 70.°3S, 254.°2W. (Stanford AIL Picture Products STN 0173, 061105, 061106, 061107, 061108)
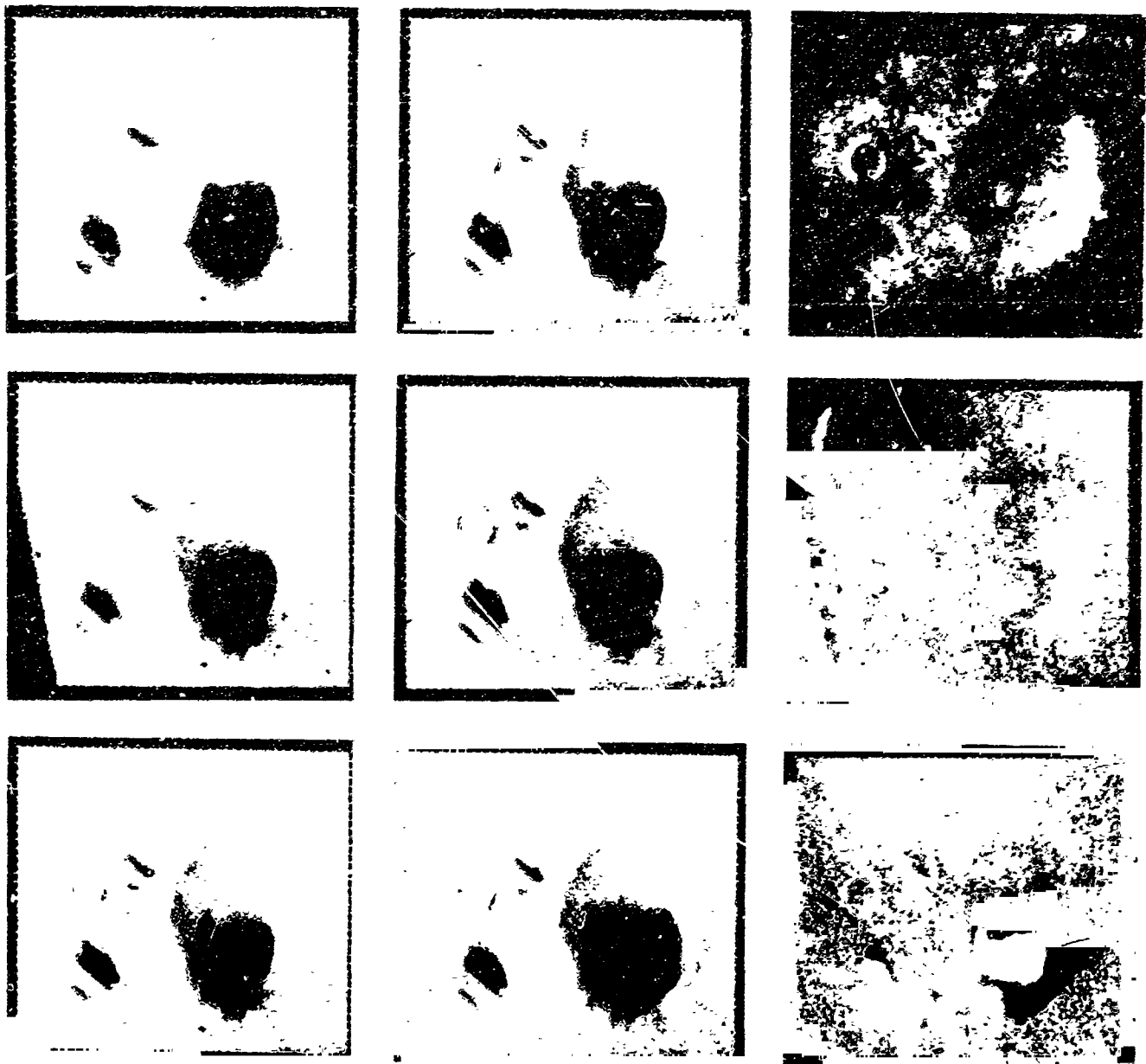
Fig. XIII-38. Changes in region D. Top row (left to right): revolution 126, revolution 181, revolutions 181 to 126. Middle row: revolution 179, revolution 181, revolutions 181 to 179. Bottom row: revolution 181, revolution 220, revolutions 220 to 181. The window is about 20 km across and is centered at 69.°3S, 252.°7W. (Stanford AIL Picture Products STN 0173, 061101, 061102, 061103)
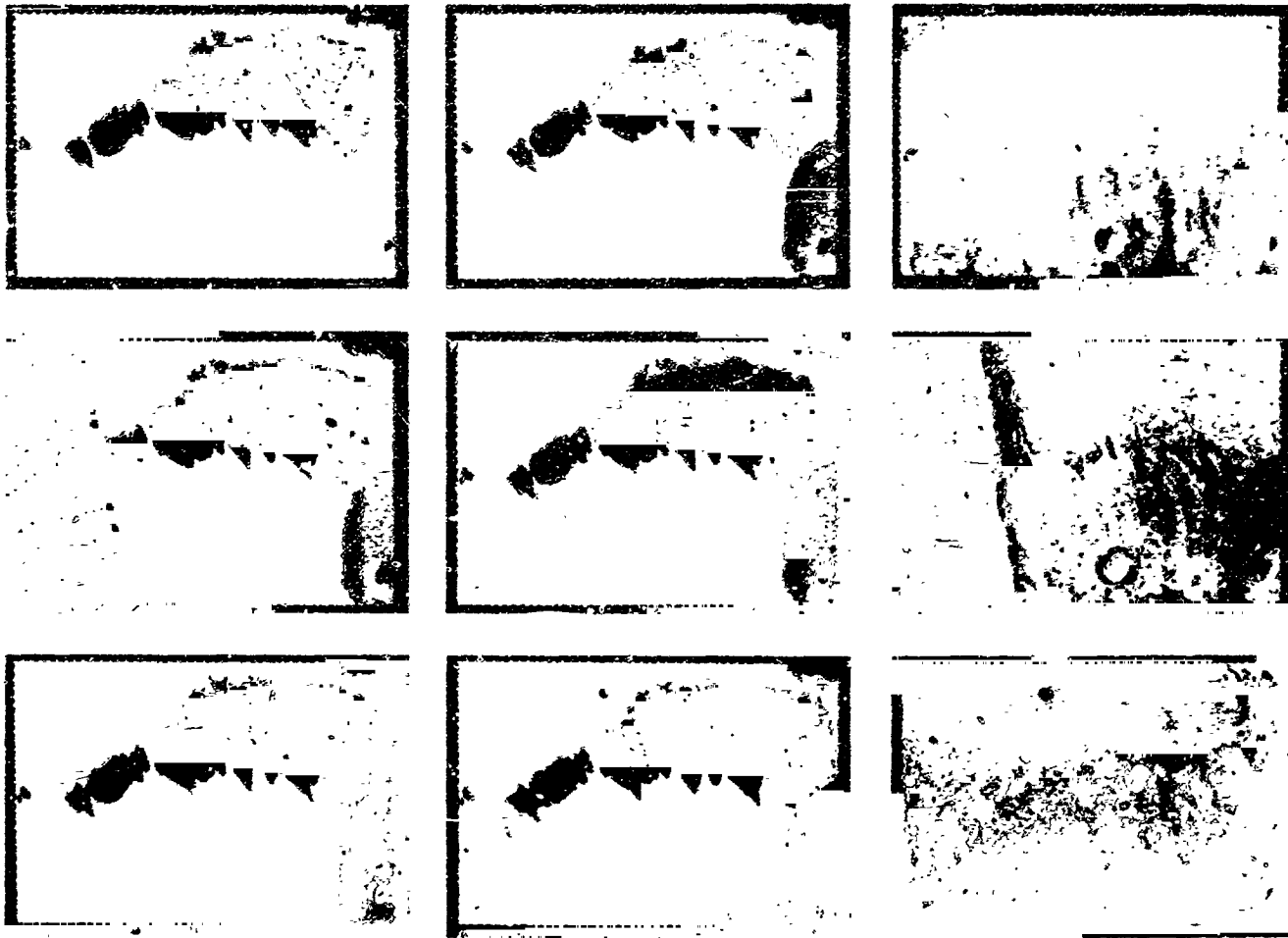
Fig. XIII-39. Changes in region E. Top row (left to right): revolution 126, revolution 181, revolutions 181 to 126. Middle row: revolution 179, revolution 181, revolutions 181 to 179. Bottom row: revolution 181, revolution 220, revolutions 220 to 181. The window is about 45 km across and is centered at 69.°8S, 252.°5W. (Stanford AIL Picture Products STN 0173, 061112, 061113, 061114)
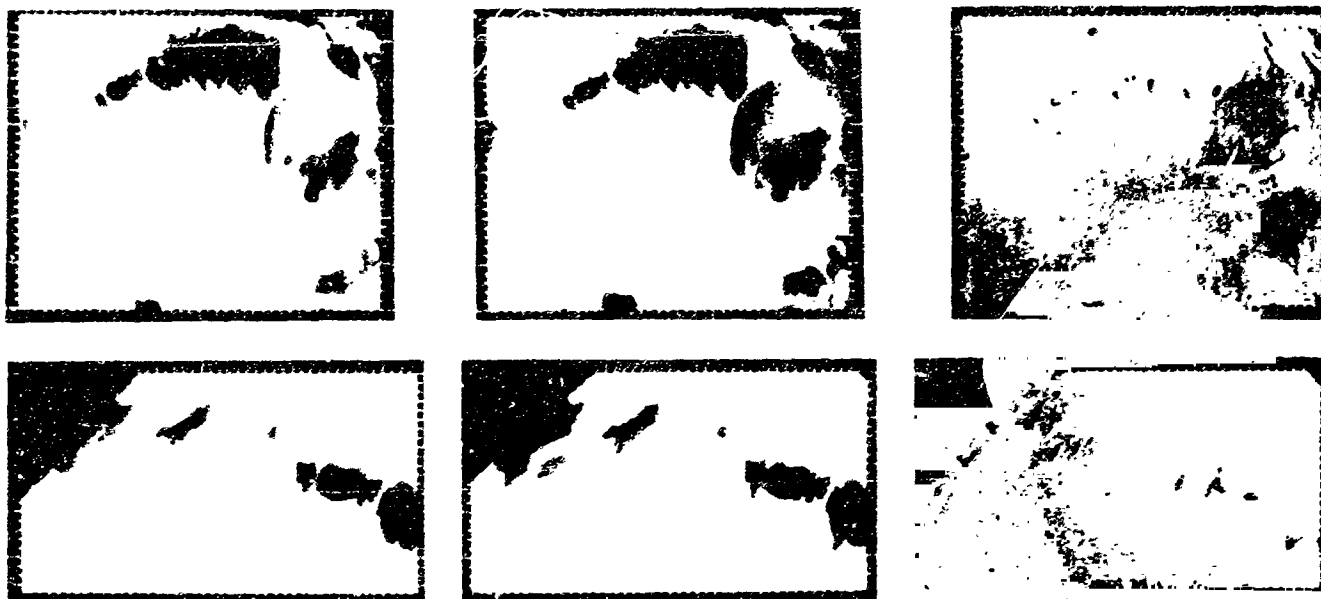
Fig. XIII-40. Changes in region F are shown in the bottom row. Left to right: revolution 181, revolution 220, revolutions 220 to 181. This window is about 40 km across, and is centered at 69.°6S, 251.°8W (Stanford AIL Picture Product STN 0173, 061104). The top row shows changes in regions B, D, E over the same time interval. Left to right: revolution 181, revolution 220, revolutions 270 to 181. The top window is about 60 km across, and is centered at 69.°6S, 253.°1W. (Stanford AIL Picture Product STN 0166, 042905)

Figure XIII-36 shows some of the significant changes that took place in region B, after revolution 126. (Unfortunately, this region was not observed on revolution 99.) In this region, the splotch within the crater changed slightly between revolutions 126 and 179, and significantly between revolutions 181 and 220. In region D, however, changes occurred only between revolutions 181 and 220 (Fig. XIII-38).

At the time of the formation of the leaf in region A, a strong change occurred in region C (top row of Fig. XIII-36). The change consisted of a general growth of the dark splotch by the extension of the points on the scalloped edge, as well as by the outward displacement of the amorphous edge. No subsequent changes were observed.

A sudden change in region E was observed between revolutions 181 and 220 (Fig. XIII-39), resulting in the extension of the points along the scalloped edge of the splotch. A similar change took place in region F at the same time (Fig. XIII-40).

A pattern of swift changes, interrupted by relatively long periods of quiescence, seems typical of Promethei Sinus. It is significant that regions A and C, which changed drastically between revolutions 99 and 126, did not participate in the major changes that affected the entire area between revolutions 181 and 220. A saturation effect seems to be involved. This major change affected surrounding areas, even at a scale detectable in low-resolution, wide-angle pictures (Fig. XIII-41).

H. Wind Tunnel Analogs of Martian Dust Transport

A set of experiments possibly relevant to Martian eolian dust patterns was conducted by Hertzler (Refs. XIII-22 and XIII-23) in the McDonnell Aircraft Corporation's 14-foot environmental simulator. Ambient conditions ranged from 5.35 to 26.7 mb and were at room temperature. Two specimens simulating Martian surface material were employed: a silica flour with particle diameters largely ranging between 1 and 100 μm, and a white sugar sand with particle diameters largely ranging from 100 to 700 μm. Piles of these powders, about 1 cm in thickness, were placed on smooth aluminum plates at the orifice of a wind tunnel. The velocities measured were at an altitude within the surface boundary layer and ranged up to 40 m sec^{-1}. The resulting morphology of windblown dust apparently depended much more on particle size and layer thickness than upon wind velocity.
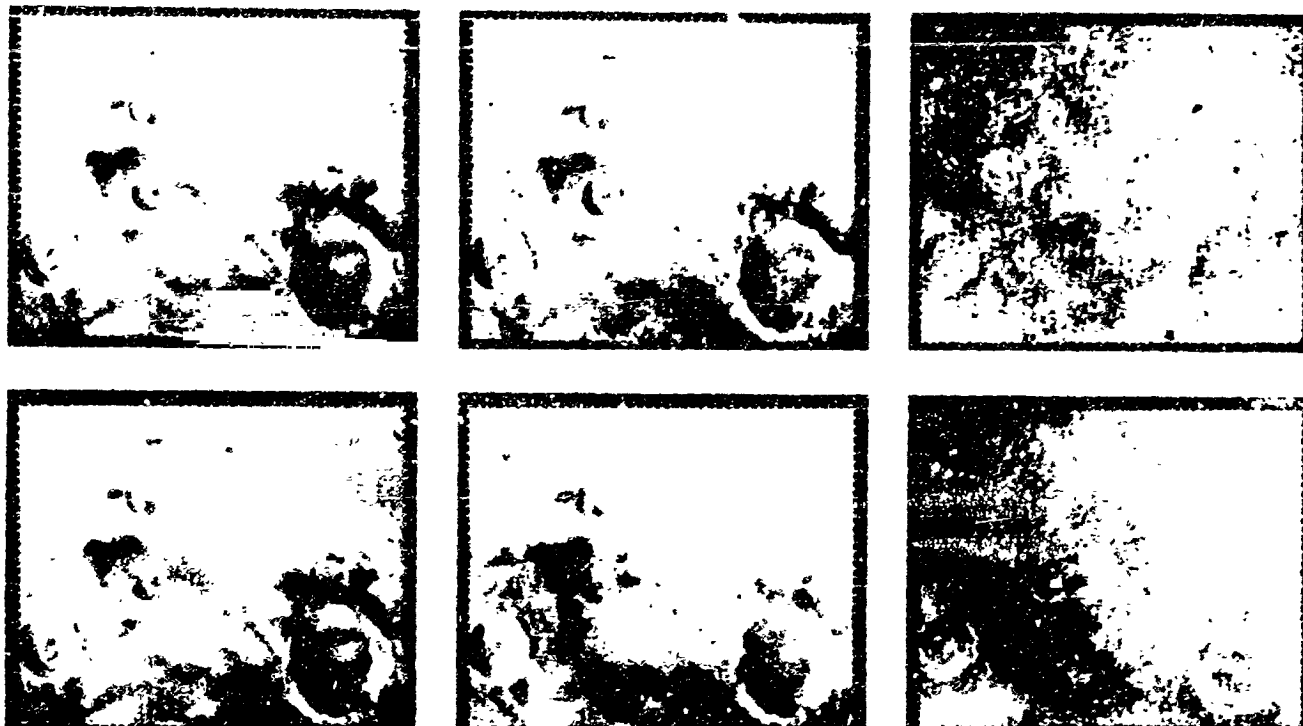
Fig. XIII-41. Changes at wide-angle resolution in adjoining regions. Top row (left to right): *revolution 179, revolution 181, revolutions 181 to 179. Bottom row: revolution 179, revolution 220, revolutions 220 to 179. The window is about 220 km across and is centered at 72.°4S, 267.°2W; its outline is shown dashed in Fig. XIII-1.* (Stanford AIL Picture Products STN 0174, 061305, 061307)

In Fig. III-42 are shown "before" and "after" photographs of a layer of sugar sand exposed to these winds for about 100 min. Here a marked embayment is produced by the removal of bright material, revealing underlying dark material; the wind direction is into the figure, and the extent of the remaining bright material has decreased due to removal. In Fig. XIII-43 is shown a nearly identical experiment with a layer of silica flour exposed to these winds for about 100 min, but with the baseplate inclined at an angle of 20°. Long streamers are produced opposite to the direction of wind flow, possibly because of the backward gravitational displacement of particles. The scalloped material in Promethei Sinus resembles Fig. XIII-42 much more than Fig. XIII-43.

Figure XIII-44 shows the results of an experiment performed on sugar sand for less than 10 min, but at velocities at the surface significantly above the threshold velocities for grain motion. The resulting pattern, like that in Fig. XIII-42 but unlike that in Fig. XIII-43, resembles Promethei Sinus.

The difference in scale is about 10^3, so the following comparison of wind tunnel and Martian eolian morphologies must be treated with some caution. From the optical depth of the great 1971 dust storm, the precipitated thickness of atmospheric particulates is easily estimated to be about 1 mm. Thus, the thin layers being removed in the wind tunnel experiments are not inappropriate to the Martian case.

As time passes in Fig. XIII-44 it seems likely that, as more and more sand is removed, the dark indentations will grow windward with time. If this is an appropriate analog of the growth of scallops in Promethei Sinus (Fig. XIII-39), however, it implies bright material being driven by winds in precisely the opposite sense to that indicated by the adjacent crater splotch (Fig. XIII-34). We therefore lean to the alternative view that the scallops are generated by winds blowing from the straight to the scalloped edge, consistent with the crater splotch reading. This requires dark rather than bright mobile material. Or it might be accomplished by the preferential
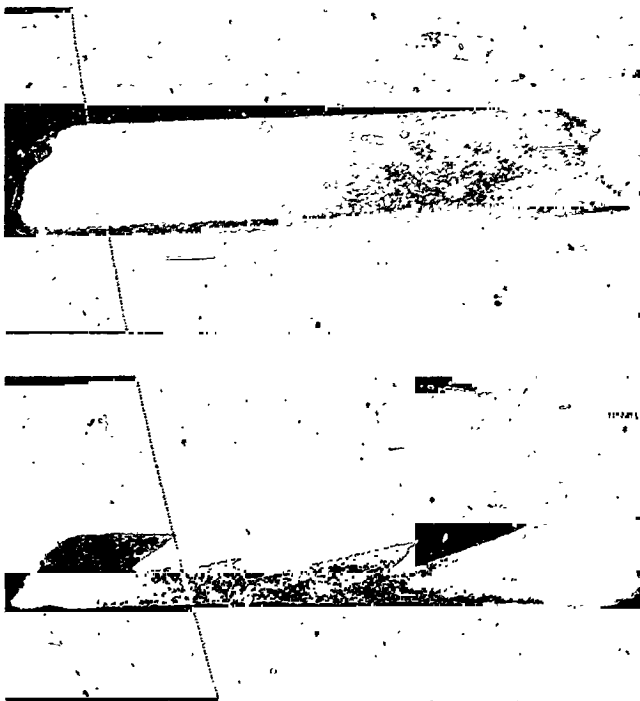
Fig. XIII-42. Photographs of a layer of sugar "sand" exposed to simulated Martian winds ($\lesssim$40 m sec⁻¹) for 100 min. Wind direction is into the picture. From Hertzier (Refs. XIII-26 and XIII-27). (a) Before and (b) After.
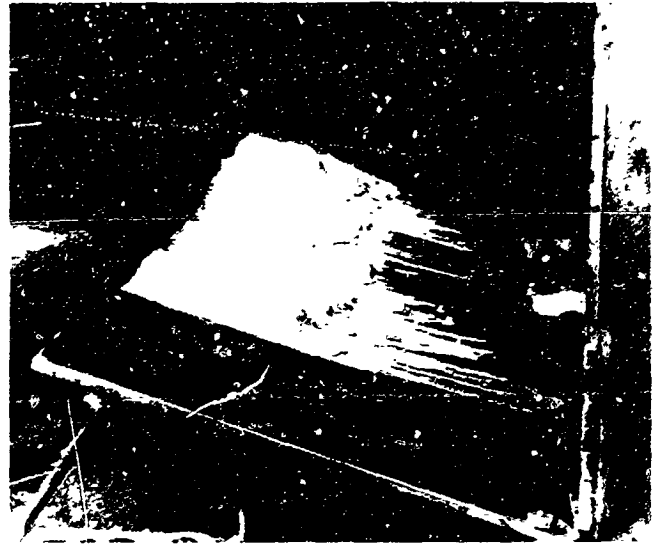
Fig. XIII-43. Results of a wind tunnel experiment similar to that described in Fig. XIii-42, but with the baseplate inclined at 20° to the wind. Wind direction is from right to left. From Hertzier (Refs. XIII-26 and XIII-27).

Fig. XIII-44. Results of a wind tunnel experiment similar to that described in Fig. XIII-42. Here the sugar sand was exposed for about 10 min to wind velocities significantly in excess of the threshold velocity needed to initiate grain movement. Wind direction is from right to left. From Hertzier (Refs. XIII-26 and XIII-27).

denudation of overlying bright material from the points of the scallops, perhaps because the underlying dark material is very smooth, as in a vitreous lava flow. The discontinuous appearance of the leaf in 13 days with no subsequent alteration is strongly suggestive of a saturation phenomenon of the sort specifically anticipated in windblown dust models (Ref. XIII-13) for cases of the removal of overlying bright material from underlying dark. This supports the last explanation. Nevertheless, it is unfortunate that, with information available both on the motion of the scallops and the direction of the prevailing winds, we are at this time unable to decide whether it is bright or dark mobile material that is primarily responsible for the phenomena observed in Promethei Sinus.

One additional implication of both Bagnold's and Hertzler's results is that such eolian transport tends to smooth and streamline the particle pile in such a way as to resist further transport. The existence of extensive dust and sand transport on Mars today must therefore be due to the rapid generation, either by eolian deposition as after a dust storm or by volcanism, of new piles of particulates.

I. Classical Variable Features From the *Mariner 9* Perspective

Certain secular changes can be correlated to Martian topography, while no convincing topographic connection can be found for certain others. In the first category is the darkening of Phasis in 1877–1879 (Ref. XIII-3) near Solis Lacus. The area affected corresponds closely to a wedge-like extension of rugged terrain into the otherwise smooth region of Solis Lacus (cf. Fig. XIII-9).

The smoothness and isolation of the Solis Lacus region explains its susceptibility to secular changes (Refs. XIII-3 and XIII-4), especially when it is realized that the dark streaks are responsible for the major albedo markings in the area (see Fig. XIII-11).

Generally speaking, albedo markings are not closely correlated with topography: albedo markings are quite superficial. There are, however, a few interesting trends. Large depressions such as the Coprates rift valley and the enclosed depression Juventae Fons tend to appear as dark albedo features from Earth. In the Coprates rift valley, one can invoke scouring of fines by channeled winds as in the Lunae Palus canyon, but what is the explanation for Juventae Fons?

Also, in general, strong secularly variable features tend to lie in smooth regions. Examples are the Solis Lacus region and Syrtis Major itself. The western stable edge of Syrtis Major is determined by topography. The eastern edge lies on a smooth sloping plane and is defined by dark, variable crater tails.

One of the most famous secular variations in the annals of Martian observations is the change in Hydaspes (Ref. XIII-3). This feature has lapsed into insignificance after being a prominent dark band joining Margaritifer Sinus to Niliacus Lacus from 1858 to 1871. Its trend corresponds closely to that of several channels running through the collapsed chaotic terrain into Chryse. This is a good example of a topographically controlled secular change.

On the other hand, no topographic control is evident in the strong darkening observed in Noachis in 1928 by Antoniadi (Ref. XIII-3). The region affected by this change is identical topographically to surrounding features which were not affected.

On the basis of recent Earth-based observations it has been claimed (Ref. XIII-24) that, contrary to the classical view, Martian seasonal changes involve variations in the bright rather than the dark areas. We find, for the *Mariner 9* season, no evidence to support this claim. Motion of dark splotches, development of dark streaks, and the filling in with dark material of bright intercrater regions have all been seen, while corresponding developments of bright features have not been observed. However, as pointed out in Ref. XIII-1, such a trend cannot continue indefinitely if Mars is to maintain its mean albedo. Comparison with *Mariner 6* and *7* results and Viking Orbiter observations may uncover development of bright material in the complementary seasons. We suspect that bright and dark materials are transported on Mars.

J. Rates of Dust Transport

From the foregoing data, we derive some simple results on the rates of lateral transport of dust on Mars at times other than during major dust storms. The material transport in the leaf region of Promethei Sinus amounts to about 2 km in time intervals ≤ 19 days. Taking a threshold velocity of about 2 m sec^{-1}, the prevailing winds transporting the mobile dust must blow for about 10^3 sec about 15 min in ≤ 19 days. Some of the streaks are several hundred kilometers long. If we assume that streak material is transported only at V_{*t}, this implies occasional

strong prevailing winds of this velocity, with no significant dissipative currents for about 1 day out of several hundred. If the dust is carried higher in the boundary layer, the timescale for a pronounced directionality of strong winds can be even less. The continuity of the streaks, unaffected by local topography, argues for non-local transport, possibly high in the boundary layer; the remarkable straightness of the streaks argues for high winds with a strong prevailing character for about 1 day, not an unlikely requirement.

On Earth, saltating particles can induce creep in surface grains many times their own diameter. For Mars the diameter ratio should be even larger. Thus, small bright particles can induce creep in large dark particles. On Earth, typical sandstorm creep velocities are about 1 cm/sec (Ref. XIII-25); on Mars they should be correspondingly larger. Thus, during 1 day on Mars, creep of about 1 km is possible. It is curious, therefore, that the same velocities for the same periods of time can account by saltation for the production of bright streaks and by creep for the motions of dark material in places like Promethei Sinus.

Hertzler (Ref. XIII-23) estimated eolian transport rates under typical Martian conditions when the threshold stress is exceeded. Typical values range from 3×10^{-3} g cm^{-1} sec^{-1} to 3×10^{-1} g cm^{-1} sec^{-1}. Thus, a layer of dust 1 cm thick could easily be removed in 1 Martian day, under conditions of moderately high winds, a result quite consistent with that just derived on the timescale for the generation of streaks. These numbers imply typical dust removal rates, for an area the size of the leaf in Promethei Sinus, of about 100 tons/sec, most of which, being in saltating particles, will be immediately redeposited.

Deflation of dust out of gravitational potential wells such as craters probably requires velocities $> V_{*t}$; in this case also transport times are reduced. The high values of V deduced here and elsewhere have important consequences for eolian erosion rates on Mars, as discussed in a separate publication.

The contrasts between adjacent bright and dark terrain $\simeq 20\%$ which we find may be due either to composition differences, to particle size differences, or to both. The two differences may indeed be connected through preferential weathering of small particles (Ref. XIII-9). It is easy to show that for typical Martian particle radii of about 100 μm, the contrasts can be explained by particle size differences $\simeq 30\%$. The absence of greater contrasts on Mars must be due to a wide range of particle sizes being transported in major meteorological events such as the great dust storm of 1971.

The apparent generation of bright streaks in some Martian areas only as a result of the global dust storm (Ref. XIII-1) suggests that bright streaks require exceptionally high velocities for their formation. Accordingly, typical bright streak particles would be significantly below the most easily saltated particle size; i.e., $\ll 100$ μm (Ref. XIII-1). This deduction explains the otherwise puzzling fact that many cases of the development of dark streaks and splotches have been uncovered since the settling of the great 1971 storm, but no cases of the development of bright material have been detected. The high stability of the bright streaks is expected for an array of particles with threshold velocities far above the minimum, V_{*t}. But the bright streak regions must be free of larger particles with threshold velocities near the minimum V_{*t}; saltation of such larger particles would, by momentum exchange, set the smaller particles of the bright streaks into suspension. Likewise, dark areas are darkened when larger saltating particles eject smaller bright fines which are then carried off in suspension.

References

XIII-1. Sagan, C., Veverka, J., Fox, P., Dubisch, R., Lederberg, J., Levinthal, E., Quam, L., Tucker, R., Pollack, J. B., and Smith, B. A., "Variable Features on Mars: Preliminary Mariner 9 Results," *Icarus*, Vol. 17, p. 346, 1972 (Paper I).

XIII-2. Morris, E. C., Mutch, T. A., and Holt, H. E., *Atlas of Geologic Features in the Dry Valleys of South Victoria Land, Antarctica*, USGS Interagency Report: Astrogeology 52, 1972.

XIII-3. Antoniadi, E. M., *La Planete Mars*, Hermann, Paris, 1930.

XIII-4. Pollack, J. B., and Sagan, C., "Secular Changes and Dark-Area Regeneration on Mars," *Icarus*, Vol. 6, p. 434, 1967.

XIII-5. Leovy, C., and Mintz, Y., "Numerical Simulation of the Atmospheric Circulation and Climate of Mars," *J. Atmos. Sci.*, Vol. 26, p. 1167, 1969.

XIII-6. Hanel, R., Conrath, B., Hovis, W., Kunde, V., Lowman, P., Maguire, W., Pearl, J., Pirraglia, J., Prabhakara, C., Schlachman, B., Levin, G., Straat, P., and Burke, T., "Investigation of the Martian Environment by Infrared Spectroscopy on Mariner 9," *Icarus*, Vol. 17, p. 423, 1972.

XIII-7. Conrath, B., Curran, R., Hanel, R., Kunde, V., Maguire, W., Pearl, J., Pirraglia, J., Welker, J., and Burke, T., "Atmospheric and Surface Properties of Mars Obtained by Infrared Spectroscopy on Mariner 9," *J. Geophys. Res.*, Vol. 78, 1973.

XIII-8. Gierasch, P., and Sagan, C., "A Preliminary Assessment of Martian Wind Regimes, *Icarus*, Vol. 14, p. 312, 1971.

XIII-9. Sagan, C., Veverka, J., and Gierasch, P., "Observational Consequences of Martian Wind Regimes," *Icarus*, Vol. 15, p. 253, 1971.

XIII-10. Blumsack, S. L., "On the Effects of Large Scale Temperature Advection in the Martian Atmosphere," *Icarus*, Vol. 15, p. 429, 1971.

XIII-11. Leovy, C., Zurek, R., and Pollack, J., "Mechanisms for Mars Dust Storms," *J. Atmos. Sci.*, Vol. 30 (in press).

XIII-12. Sagan, C., and Pollack, J. B., *A Windblown Dust Model of Martian Surface Features and Seasonal Changes*, Smithsonian Astrophysical Observatory Special Report 255, 1967.

XIII-13. Sagan, C., and Pollack, J. B., "Windblown Dust on Mars," *Nature*, Vol. 223, p. 791, 1969.

XIII-14. Golitsyn, G. S., "On the Martian Dust Storms," *Icarus*, Vol. 18, p. 113, 1973.

XIII-15. Hess, S., *Martian Winds and Dust Clouds*, paper presented at NATO Advanced Study Institute on Planetary Atmospheres, Istanbul, 1972.

XIII-16. Gierasch, P., and Goody, R., "A Model of a Martian Great Dust Storm," *J. Atmos, Sci.*, Vol. 30 (in press).

References (contd)

XIII-17. Leovy, C., Briggs, G., Young, A. T., Smith, B. A., Pollack, J., Shipley, E., and Wildey, R., "Mariner 9 Television Experiment: Progress Report on Studies of the Mars Atmosphere," *Icarus*, Vol. 17, p. 373, 1972.

XIII-18. de Vaucouleurs, G., *Physics of the Planet Mars*, Faber and Faber, London, 1954.

XIII-19. Dollfus, A., "New Optical Measurements of Planetary Diameters IV. Size of the North Polar Cap of Mars," *Icarus*, Vol. 18, p. 142, 1973.

XIII-20. Smith, H. T. U., *Eolian Geomorphology, Wind Direction, and Climatic Change in North Africa*, Final Report AF Contract 19 (628)-29S, 1963.

XIII-21. Focas, J. H., "Etude Photometrique et Polarimetrique des Phenomenes Saisonniers de la Planete Mars," *Ann. d'Astrophysique*, Vol. 24, p. 309, 1961.

XIII-22. Hertzler, R. G., *Particle Behavior in a Simulated Martian Environment*, McDonnell Aircraft Corporation Report E720, 1966.

XIII-23. Hertzler, R. G., *Behavior and Characteristics of Simulated Martian Sand and Dust Storms*, McDonnell Aircraft Corporation Report E720, 1966.

XIII-24. Boyce, P. B., and Thompson, D. T., "A New Look at the Martian Violet Haze Problem. I. Arabia-Syrtis Major," *Icarus*, Vol. 18, No. 2, 1973.

XIII-25. Bagnold, R. A., *The Physics of Blown Sand and Desert Dunes*, Methuen, London, 1954.

Acknowledgments

PRECEDING PAGE BLANK NOT FILMED

XIV. *Mariner* 9 Observations of the Surface of Mars in the North Polar Region[1,2]

L. A. Soderblom
U.S. Geological Survey, Flagstaff, Arizona 86001

M. C. Malin and B. C. Murray
Division of Geological and Planetary Sciences
California Institute of Technology, Pasadena, California 91109

J. A. Cutts
Jet Propulsion Laboratory/California Institute of Technology, Pasadena, California 91103

The *Mariner* 9 extended mission began in early June 1972 (revolution 416) following a period of multiple solar occultations of the spacecraft by Mars during which science operations ceased. During the extended mission, the north polar cap receded from about 85% of its maximum extent to nearly minimum size in late October 1972. This corresponded to the period from about 1 Martian month after vernal equinox until shortly after summer solstice.

Early in the mission, during November and December 1971, the recession of the south polar cap was also monitored. However, those observations showed only limited retreat because the spacecraft arrived at Mars shortly before the annual recession in the south ended (Ref. XIV-1). The north polar cap was in the darkness of northern winter throughout most of the standard mission. Even in the best observations, made during the last few revolu-

tions of the standard mission (revolutions 245 and 262), the surface was severely obscured by the north polar haze. Only the northern sinuous, circumpolar, bright forms were visible through the haze (Ref. XIV-1). The survival of *Mariner* 9 through the period of the extended mission represented an unprecedented opportunity to monitor the north polar cap through most of its recession.

Because of a shortage of attitude control gas on the spacecraft, the number of pictures returned during the extended mission was severely limited. Faced with this shortage of frames, the philosophy adopted for the north polar region was to first map the polar region with wide-angle frames of best possible resolution ($\sim$ 3 km) and, at several week intervals, to continue monitoring the recession of the cap from high altitude (resolution $\sim$ 6 km) in order to cover the entire cap in single frames. Based on study of the mapping coverage completed early (revolutions 416–451), many areas were targeted for high-resolution coverage during the July 10 and August 7 imaging sequences (revolutions 478 and 528). These areas

were selected to study the high-resolution appearance of the retreating frost margin and of a variety of terrain types and terrain boundaries, most of which were still covered with frost. These observations were halted by a period around solar conjunction during which the return of imaging data was impossible. In early October communications were resumed, and two more tape loads of data were transmitted to Earth on October 12 and 16, 1972. By this time, as anticipated, the polar ice cover had receded to nearly its minimum extent. Another 18 narrow-angle pictures were targeted for these playbacks in order to sample new terrains recognized in the August wide-angle coverage and to rephotograph interesting areas which were frost-covered in the pre-conjunction photography.

In all, only 36 narrow-angle frames could be devoted to the reconnaissance of the north polar region. Each frame was critically targeted to obtain as much information as possible about the terrain types and relations between the various geologic units. These frames therefore represent a highly biased sample of the region. Most of them contain areas where the topography or the albedo variations were complex; others show transition zones between various terrains. The north polar region is, in reality, composed of a far greater percentage of smooth areas than is indicated by this collection of high-resolution pictures.

Our purpose is to describe and to compare the various geologic units found in the polar regions, to present observations which pertain to the volatiles problem, and to discuss processes inferred to be operating in both polar regions. Studies of the south polar region (Ref. XIV-1) left a number of unanswered questions as to the uniqueness of certain deposits and morphologies to the polar environment. As north and south polar units rest on very different regional geologic units, the comparison of the two emphasizes uniquely polar units and processes.

A. Recession of the North Polar Cap

Figures XIV-1 through XIV-3 are polar mosaics that show the evolution of the north polar ice cap during the extended mission. Figure XIV-1 is a composite of 17 wide-angle frames acquired during the first 3 weeks in an effort to complete the mapping of the entire planet. As the mapping took 2½ weeks to complete, the images in this mosaic are not synchronous. The other two mosaics consist of two pictures each, which were acquired 12 hours apart.

A peculiar polygonal outline of the north polar cap was observed during most of its recession. This aspect was already weakly developed at the beginning of the extended mission (Fig. XIV-1 and more obviously Fig. XIV-9). This polygonal character was confirmed when a single global frame was acquired during the fifth week (Fig. XIV-4). By the ninth week the polygonal outline had become very pronounced (Fig. XIV-2) and had disappeared by the nineteenth week (Fig. XIV-3). The polygonal shape remained roughly the same but receded on all sides. It is, therefore, unlikely that the polygonal outline was controlled by local topography such as scarps and ridges. The polygonal outline could result from some form of regional topographic control, variation in surface textures, or atmospheric phenomena. Further, the only textural or atmospheric effects imagined here would themselves be controlled by regional topography. If the polygonality is atmospherically induced, for instance by a series of standing waves controlling frost deposition, the direction and stability of these waves would probably also be controlled by regional topography. Regional textural alignments would also most easily be induced by wind patterns fixed by regional topography.

Radio occultation data (Ref. XIV-2; also see Section XXXVI of this Report) have shown that the mottled cratered plains in the north polar region are about 4 km lower than the cratered terrains in the south polar region. The data show further that the upper surfaces of the layered deposits are at about the same altitude at both poles. This suggests that the sedimentary complex in the north polar region is substantially thicker than that in the south. The regional topography invoked to explain the polygonal cap may have resulted from tectonic adjustment of the crust to loading of the central north polar region by thick deposits.

Figure XIV-5 compares the Earth-based telescopic data of Fischbacher et al. (Ref. XIV-3) with the averaged position of the cap edge from *Mariner 9* pictures. It appears that the north polar recession, monitored during the *Mariner 9* observation period, followed its usual pattern and rate. Also shown in Fig. XIV-5 is the prediction of the position of the retreating cap edge from a CO_2 polar cap model (Ref. XIV-4). The recession of the north polar cap closely followed this model until the cap approached a diameter of about 10°. At that point retreat abruptly stopped. Based on a similar behavior of the south cap, Murray et al. (Ref. XIV-1) suggested that the residual permanent cap might be H_2O ice. A permanent, exposed CO_2 mass, although less stable, cannot be ruled out
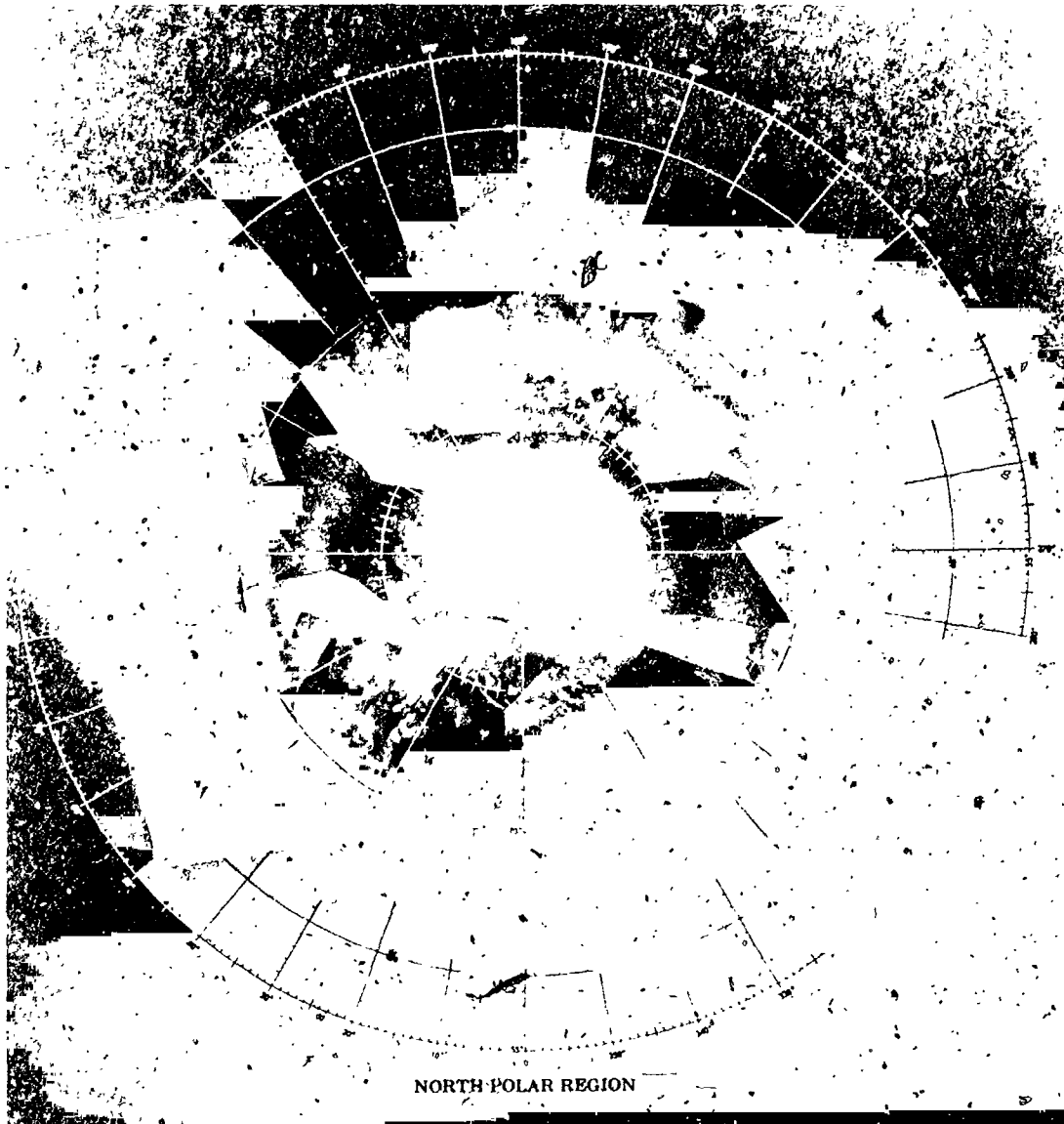
Fig. XIV-1. Distribution of retreating frost in the Martian north polar region 1 to 1½ Martian months after vernal equinox. These frames were acquired during revolutions 416 through 451 at the beginning of the extended mission as part of an effort to complete the systematic mapping of Mars. The frames have been stereographically rectified; variable solar illumination effects have been suppressed, and shades of gray have been adjusted to show detail in the frost. The "ground" thus appears black. The frames were acquired over a range of L_s (angular distance of Mars in its orbit from vernal equinox) between 35° and 45°. The frost cover shown is about 2700 km in diameter.
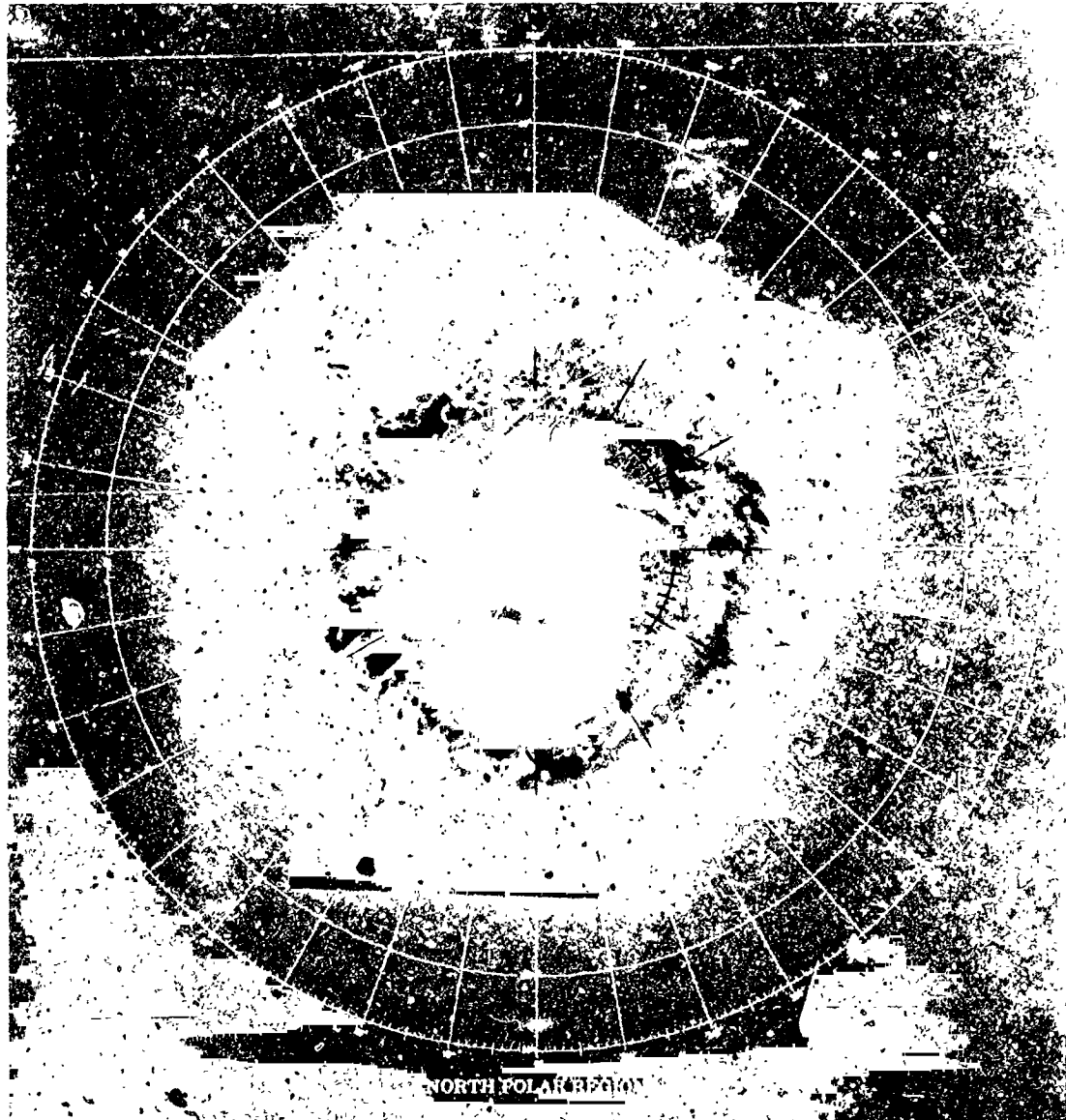
Fig. XIV-2. Distribution of retreating frost 2 Martian months after vernal equinox. The two frames used in the mosaic were acquired 12 hr apart on revolutions 528 and 529 ($L_s = 65°$). The image processing is as in Fig. XIV-1. Notice the intense polygonal outline of the frost boundary. (MTVS 4296-46, DAS 12994247; MTVS 4296-102, DAS 13028127)

As noted by Sharp et al. (Ref. XIV-5), the edge of the south polar cap displayed a very irregular outline during its initial stages of retreat photographed by *Mariner 7* in 1969. Numerous outlying patches of frost were preserved in crater floors and many dark, isolated defrosted patches, usually associated with crater rims, appeared within the frost cover. Thus, the south polar densely cratered terrain mapped by *Mariner 9* (Ref. XIV-1) strongly influenced the character of the retreating edge of the south polar cap. The edge of the northern cap, although diffuse

as it retreated through 65°N to 70°N, did not show marked irregularity, implying a general lack of local topographic control (Fig. XIV-1). A notable exception is the large crater at 65°N, 10°W. By the ninth week of the extended mission, the frost boundary had reached approximately 75°N latitude and the outline of the cap became irregular displaying numerous detached patches (Fig. XIV-2). As discussed below, this is a zone of irregular scarps and pits developed in circumpolar plains surrounding the central polar layered deposits (termed
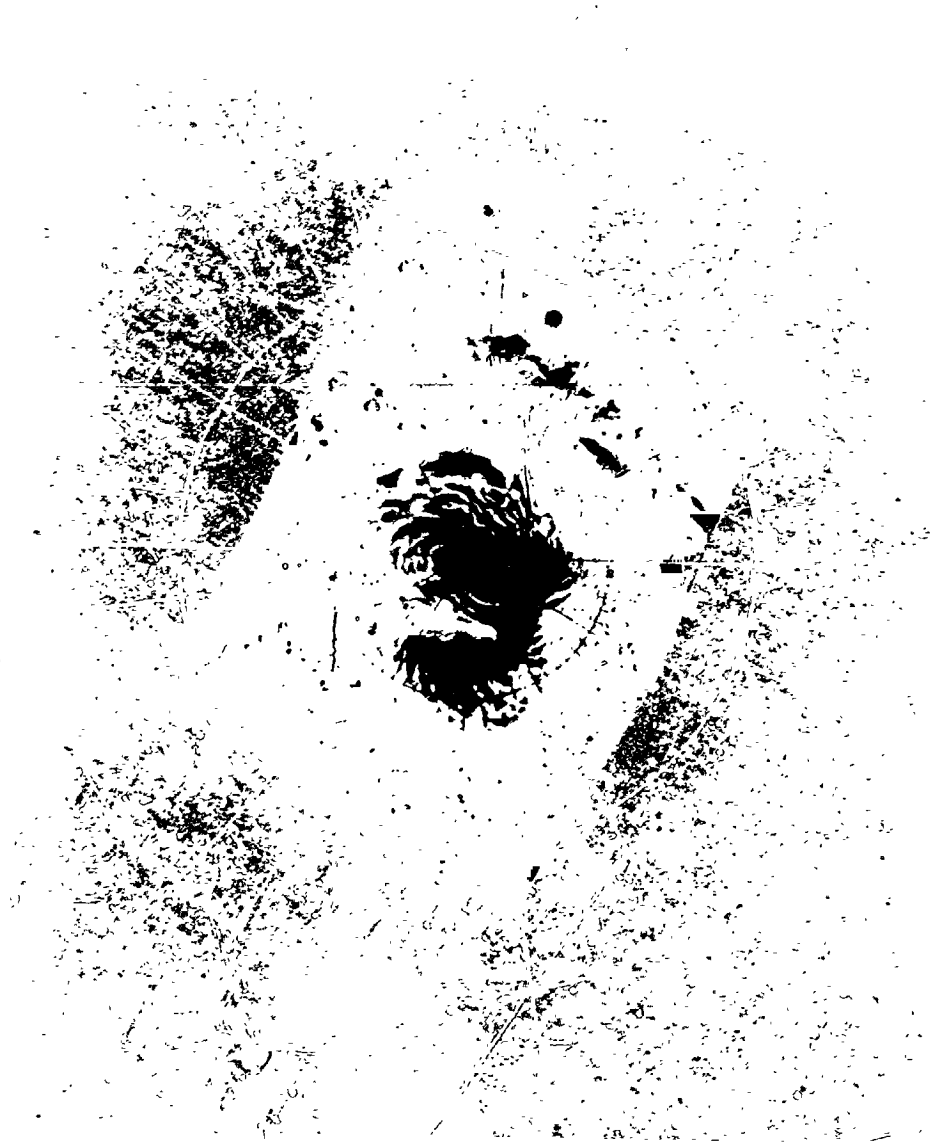
Fig. XIV-3. Martian north polar frost cap nearing its minimal extent about ½ Martian month after summer solstice. As in Fig. XIV-2, the two frames mosaicked here were acquired on successive revolutions (revolutions 667 and 668). The processing is as in Fig. XIV-1 except that the shades of gray have been adjusted to show some detail in both frosted and defrosted areas. (MTVS 4297-92, DAS 13317550; MTVS 4297-46, DAS 13353320)
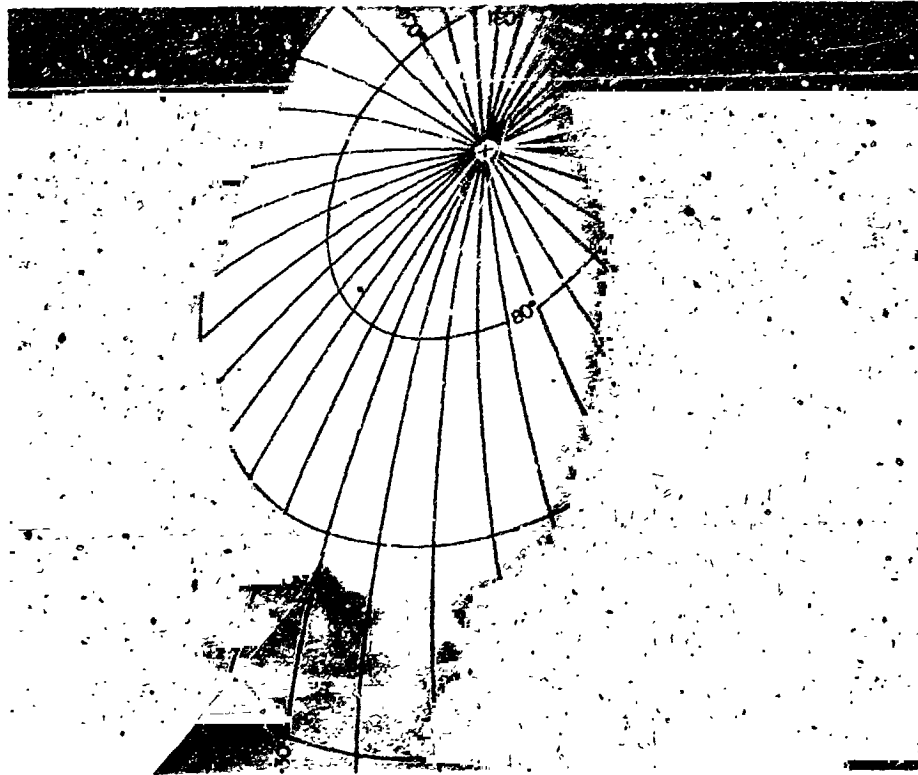
Fig. XIV-4. Global view of the north polar region as it appeared 1¾ months after vernal equinox. This frame was acquired at $L_s \cong 50°$ on revolution 478 and shows the frost distribution at a stage about halfway between Figs. XIV-1 and XIV-2. It has not been processed as were Figs. XIV-1 through XIV-3 as most of the cap was overexposed. It does, however, show the polygonal outline as it became increasingly pronounced. (MTVS 4295-72, DAS 12874573)

"laminated terrain" in Ref. XIV-1). As the frost continued to retreat between weeks 9 and 19, sinuous defrosted patterns began to develop in the central polar region (Fig. XIV-3). A similar phenomenon was noticed in the south polar region early in the standard mission. Two narrow-angle frames of the central polar sinuous features near the north pole are compared in Fig. XIV-6. The frames do not overlap, but are adjacent to one another (see Fig. XIV-9). The first (Fig. XIV-6a) was acquired before frost had dissipated; the second (Fig. XIV-6b) was obtained about 10 weeks later and shows the defrosted slopes facing southward. Thus, as is the case of the south polar region (Ref. XIV-1) the configuration of the receding frost is both strongly influenced by and highlights local subtle topography. Figure XIV-7 shows another area where retreating frost enhanced details in local topography. An unusual array of very fine, lineated dark and light markings is visible in the transition zone between the frosted and defrosted areas. The individual dark markings are 1 km or less in width and are 2 or

3 km apart. These patterns, which are probably eolian landforms, characterize one of the smooth plains units found in the north polar region.

Another distinctive characteristic of the north polar region is the circumpolar variation in albedo in the frost-covered areas (Figs. XIV-1 and XIV-2). Similar variations were noted by Sharp et al. (Ref. XIV-5) in the *Mariner 7* wide-angle photography of the south polar cap acquired during a southern season similar to that for Fig. XIV-1 in the north. In that study many frosted crater floors appeared very dark compared to the surrounding terrain, and many frosted ridges were very bright. From comparing Figs. XIV-1 and XIV-3, it is apparent that the dark circumpolar bands which appeared in the early extended mission coincide with the dark bands in the defrosted terrain seen in the last north polar regional coverage. It is therefore likely that these contrasts in albedo observed in the ice cap result from partial exposure of rock materials through an incomplete frost cover.
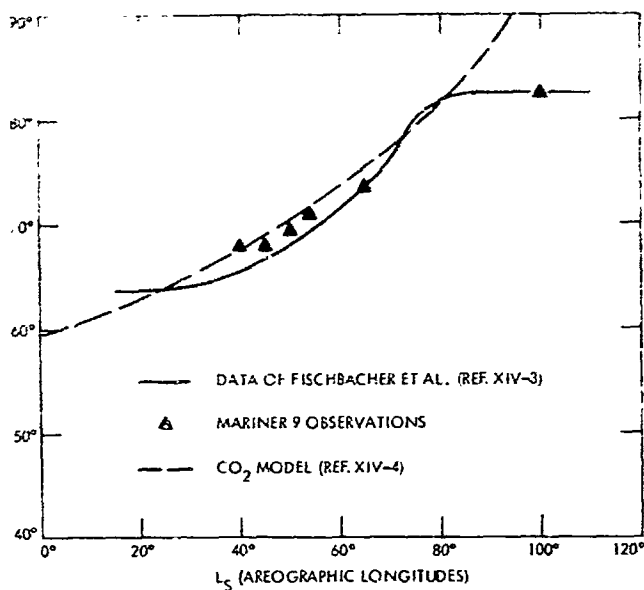
Fig. XIV-5. Observed and predicted recession rates of the north polar cap. *Mariner 9* observations of the extent of the north polar cap are compared with telescopic observations recorded by Fischbacher et al. (Ref. XIV-3) and with a CO₂ ice cap model presented by Leighton and Murray (Ref. XIV-4).

B. Comparisons of Geologic Units of the Polar Regions

Mariner 9 observations of the south polar region of Mars show that four principal geologic units are exposed (Ref. XIV-1). The oldest is an ancient, densely cratered unit that occupies most of the southern hemisphere and is overlain unconformably by three younger polar deposits. The oldest of these, a lightly cratered, massively bedded unit, has a flat upper surface which has been eroded in some areas into a complex of pits and hollows encompassed by steep, sharp-rimmed cliffs (Ref. XIV-4; also see Section XVI of this Report). The zone of pitting within this unit is confined approximately to the 70°S to 80°S latitude belt. Resting unconformably upon the pitted plains unit is the next youngest major south polar unit, termed "laminated terrain" in Ref. XIV-1. Referred to herein as *layered deposits*, this unit forms a vast sedimentary complex some 1500 km in diameter centered at the south pole. It is composed of horizontal strata of apparently very uniform thickness. The youngest south polar deposit is the residual ice cap which survives after the dissipation of the annual CO₂ frost cap. It rests on the flat upper surfaces of the central part of the layered deposits.

The north polar region contains a similar array of units, as shown in the preliminary geologic map in Fig. XIV-8.

As the south polar region, an older cratered unit is overlain unconformably by a series of younger deposits that are roughly concentric with the pole. Figure XIV-9 is a photomosaic processed to minimize albedo variation and to maximize local detail. Table XIV-1 compares the sequences of the geologic units found in the two polar regions. In contrast to the densely cratered terrain in the south polar region, the oldest unit in the north polar region is a moderately cratered plains unit. Like the south polar region, pitted plains, layered deposits, and a permanent ice cap are also found in the central north polar area. The purpose of the following discussion is to describe each of the north polar terrain units and to compare them with those recognized in the south polar region.

1. Mottled Cratered Plains Unit and Superimposed Debris Mantle

The oldest terrains in the north and south polar regions are compared in Fig. XIV-10. In the north the oldest unit is a moderately cratered plains unit situated in the 55°N to 70°N latitude band. Termed here "mottled cratered plains" (mcp), it is characterized at wide-angle resolution (~3 km) by an abundant population of small craters (10 to 20 m in diameter, or smaller) and a highly mottled appearance. This unit is distinctly different from the cratered terrain of the southern hemisphere because it lacks the characteristic massive ridges, hummocks, and a dense population of craters 50 to 300 km in diameter. The mottled pattern consists of a complex of streaks of bright material and concentrations of bright material highlighting the interior and exterior parts of crater rims. This unit has a lower average albedo than does most of Mars and is one of the few regional units that is intrinsically characterized by its albedo. McCauley et al. (Ref. XIV-7) and Carr et al. (Ref. XIV-8; also see Section II of this Report) describe another cratered plains unit which is also characterized by a low albedo.[3]

At higher resolution (~300 m), as shown in Fig. XIV-10d, the same mottling characteristic is observed in and around smaller craters (2 to 5 km in diameter). In addition this terrain has a mantled appearance similar to that recognized in high-resolution views of south polar cratered terrain (Ref. XIV-1). Small craters appear sharp and fresh, but often appear filled to their brims. It has been shown by Soderblom et al. (Ref. XIV-9; also see

---

[3]It is interesting to note that these dark cratered plains bear similar relationships to cratered terrain as do the lunar mare to lunar uplands, such as differences in albedo, crater populations, and elevation.
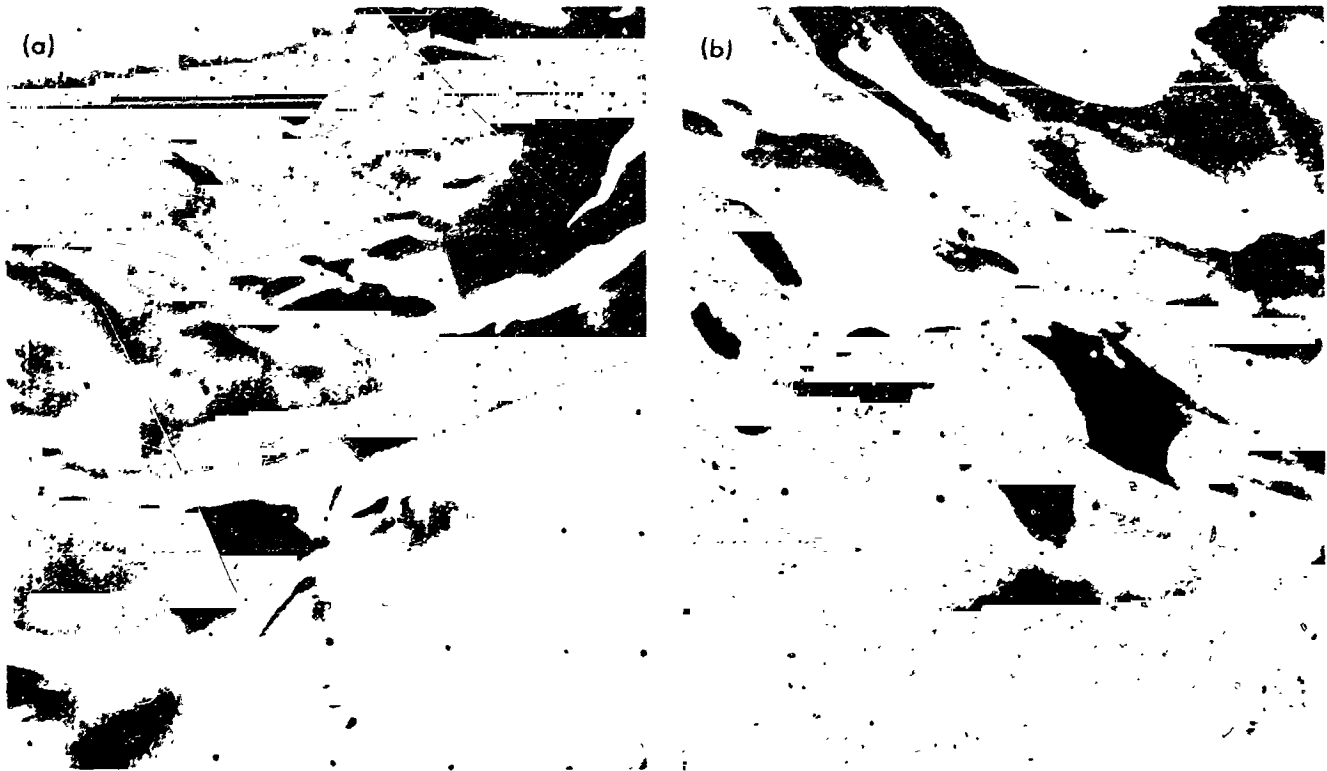
Fig. XIV-6. Disappearance of frost at resolution of the narrow-angle camera. (a) This high-resolution frame was acquired during the ninth week of the extended mission and shows the central polar deposits still frost-covered. The area shown is approximately 200 km wide, located at 85°N, 16°W. Notice the crater partially buried by the layered deposits. (MTVS 4295-59, DAS 12870618) (b) This frame was acquired during the nineteenth week of the extended mission as the frost cap was nearing its minimum size. The area shown is immediately adjacent to that covered in (a). The dark areas represent defrosted slopes in the layered deposits which face outward from the cap. These slopes receive the maximum of solar insolation and, as in the south polar deposits, defrost first. (MTVS 4297-71, DAS 13352795)

Section IX of this Report) that craters displaying this characteristic surround both polar regions in belts extending down to 55° latitudes. In the mottled cratered plains the rims and exteriors of the small craters usually display a high albedo similar to that of the inferred debris mantles described below. We suggest that the bright materials are remnants of the debris mantle which at one time buried the mottled cratered plains and which has since been removed, leaving patches of light materials trapped in the rugged and coarser textured parts of the craters such as their rims and ejecta blankets.

The mottled cratered plains are partially mantled by bright deposits in the 55°N to 70°N latitude bands. No such mantle was recognized as a discrete unit in the south polar region. This unit has a substantially greater crater population than do the central polar units described below. In addition, unlike those deposits, this unit displays a substantial population of 10- to 30-km craters that appear to be partially buried. It is distributed

in a broken ring near 65°N extending southward of 55° at some longitudes (see Fig. XIV-8). Figures XIV-10b and XIV-10c show the serrated pattern in the boundaries between this unit and the mottled cratered plains unit. These boundaries appear to be independent of local topographic relief and show a pronounced spiraling pattern between longitudes 240° and 300° (Figs. XIV-8 and XIV-9). Because the mottled streaks on the cratered plains grade into the serrated boundaries and because the small craters on the mottled cratered plains appear to be filled and mantled by bright material (material of albedo similar to the bright plains), it is concluded that these deposits are loose debris blankets which are being stripped away by eolian processes, exposing the underlying mottled cratered plains.

Cutts (Ref. XIV-10; also see Section XV of this Report) concludes that albedo markings and topographic details at an equivalent latitude belt in the south polar region indicate strong eolian modification. As described by

Fig. XIV-7. Possible eolian features highlighted by the frost. This frame was acquired on July 10, 1972, and shows a number of fine topographic details highlighted by the frost. The area shown is approximately 180 km wide, centered near 70°N, 180°W. Individual features are about 1 km in width and 10 km in length, separated by about 3 km. (MTVS 4295-107, DAS 12906668)

Table XIV-1. Comparison of stratigraphic sequences in the Martian polar regions

North polar region	South polar region
Youngest	
Permanent ice deposits (pi) _____	Permanent ice deposits
Layered deposits (ld) _____	Layered deposits
Unconformity	Unconformity
Smooth plains (sp$_1$); etch-pitted _____ plains (epp); rippled plains (rp); debris mantle (sp$_2$)	Pitted plains
Unconformity	Unconformity
Mottled cratered plains (mcp) _____	
_____	Cratered terrain
Oldest	
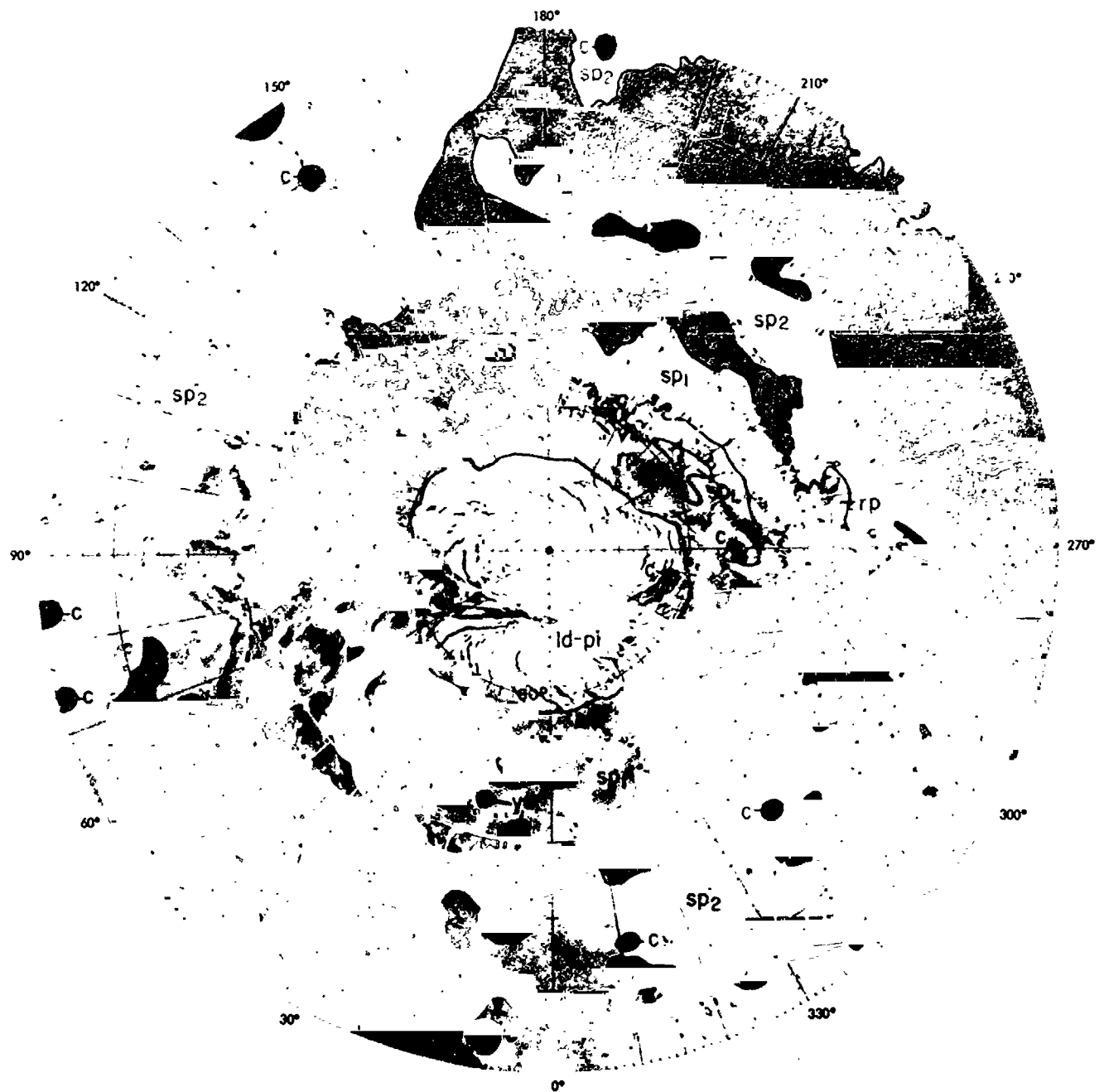
Fig. XIV-8. Preliminary geologic terrain map of the north polar region of Mars. (Refer to Table XIV-1.) The major terrains shown in order of increasing age are: (ld-pi—blue) layered deposits and permanent ice; (sp$_1$—orange, rp—flamingo, epp—purple) smooth plains, rippled plains, and etch-pitted plains; (sp$_2$—yellow) a light deposit which thinly mantles the underlying cratered plains; and (mcp—green) mottled cratered plains. Two lesser units are shown: (c—brown) craters and (vd—red) volcanic deposits.
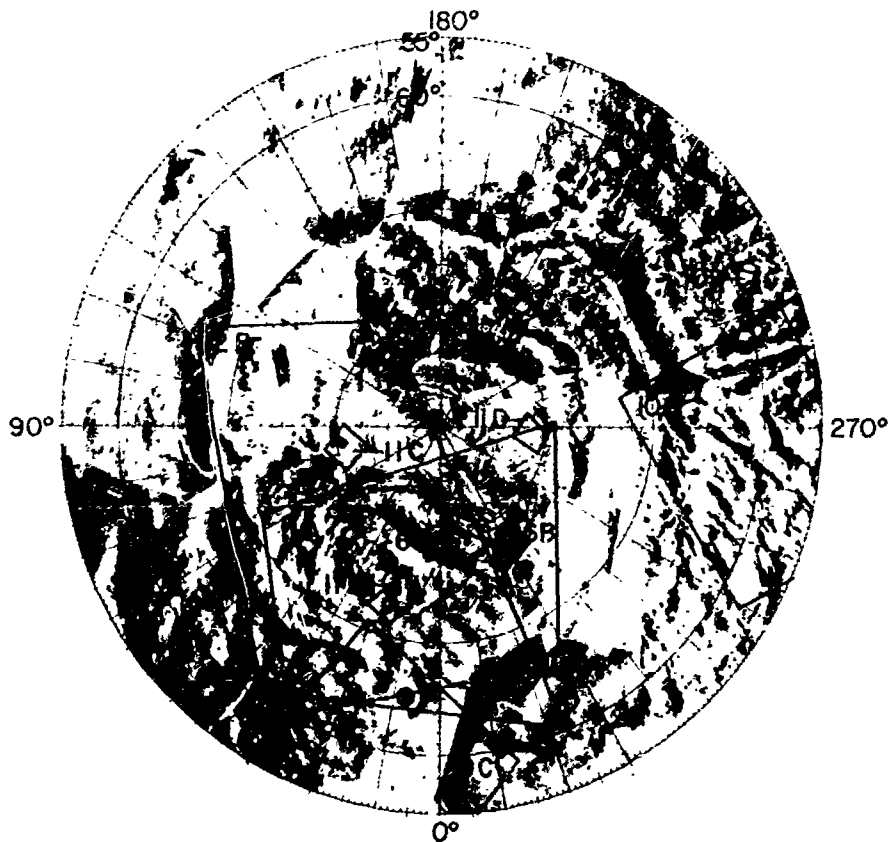
Fig. XIV-9. Photomosaic of north polar mapping frames with footprints of text figures. This is a mosaic of frames acquired during revolutions 416 through 451, some of which were used in Fig. XIV-1. The frames have been stereographically rectified and high-pass filtered to enhance local detail and suppress albedo variations. Thus, detail is visible both in the frost-covered area (inside ~ 70°N) and in the surrounding defrosted area. The edge of the frost is accentuated as a light/dark band between 65°N and 70°N. Notice the polygonal outline. Footprints of pictures used as figures are also shown.

Soderblom et al. (Ref. XIV-9; see Section IX of this Report), the symmetrical distribution of mantling debris surrounding the polar regions suggests general transport of debris out of both polar regions. It is therefore probable that the equivalent of this debris unit *does* exist in the south polar region and is simply not recognizable as it rests on a terrain of about the same albedo.

2. Circumpolar Smooth, Etch-Pitted, and Rippled Plains

The central polar layered deposits in the south polar region rest unconformably on a series of smooth and pitted plains. A similar set of units, with one additional variant, is recognized in the north polar region in an equivalent latitude band (70°N to the edge of the layered

deposits). Two of the units, etch-pitted plains (epp) and rippled plains (rp), are apparently erosional and depositional modifications of the smooth plains unit (sp_1).

A broad belt of the inner smooth plains unit is shown in Fig. XIV-11a. It has a lower crater abundance than does the light debris mantle (sp_2) and is probably substantially thicker because underlying craters protrude through the deposit in only a very few places. In one area (Fig. XIV-11a) several conical constructs (vd) with summit craters are visible. These features, inferred to be volcanic cones, are 50 to 100 km across at their bases. Unlike most of the features described by Carr et al. (Ref. XIV-8; also see Section II of this Report), the cones are very symmetrical and with no visible evidence of flows on their flanks or near their bases. Such "volcanic cones"
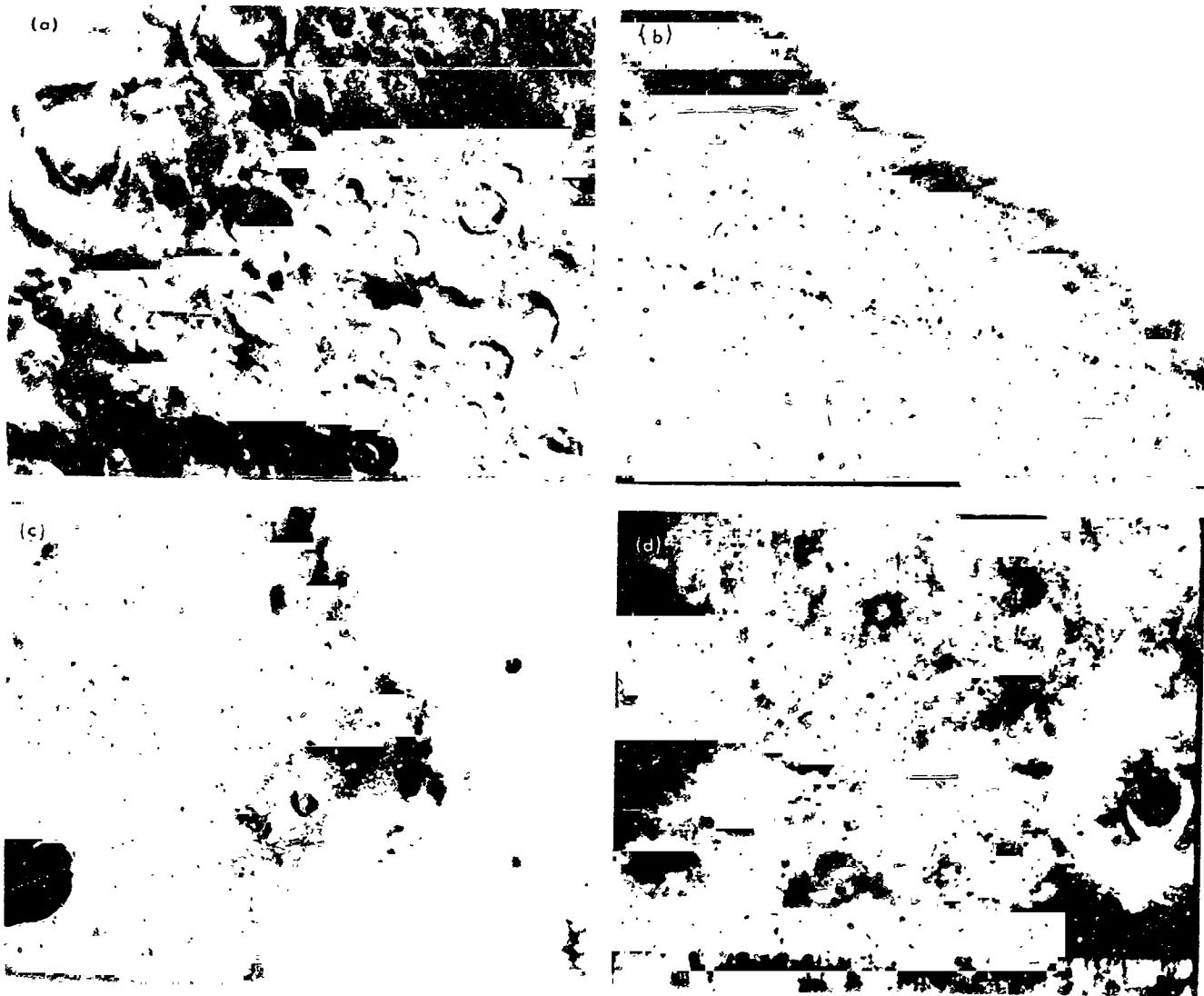
Fig. XIV-10. Mottled cratered plains (mcp) and light debris mantle (sp₂). (a) *Mariner 9* wide-angle picture of the densely cratered terrain of the south polar region is compared with two wide-angle frames (b and c) showing the mottled cratered plains and debris mantle of the north polar region. (d) Narrow-angle frame displaying the mantled appearance of the mottled cratered plains. The wide-angle frames cover approximately 1000 km in width, and the narrow-angle frame 100 km. (a) MTVS 4213-15, DAS 08079928. (b) MTVS 4288-55, DAS 11622910. (c) MTVS 4291-51, DAS 12152887. (d) MTVS 4289-65, DAS 11800046.

are not uniformly distributed throughout the unit and may not be fundamentally related to its overall genesis.

As in the south polar region, the smooth plains subjacent to the layered deposits have been intensely eroded into cliff-rimmed pits and hollows. In some areas these pits coalesce and become so deep that the underlying mottled cratered plains have been exposed. Etch-pitted plains (epp) shown in Fig. XIV-8 are mapped where the surface of the smooth plains (sp₁) has been eroded in such a manner. Figures XIV-11a, XIV-11b, and XIV-11c

show the nature of the pits and their relationship to the smooth plains unit. In both polar regions these cliff-faced etch pits are concentrated poleward of about the 70° latitudes.

The last morphological variant of the circumpolar smooth plains is shown in Fig. XIV-7. This unit, termed "rippled plains" (rp), occurs in close proximity to the central polar layered deposits. Like the smooth plains (sp₁) it has a paucity of small craters. A few larger craters on the subjacent terrain protrude through the unit.

At narrow-angle resolution it is characterized by an abundant, highly coherent pattern of waveforms which vary in wavelength from a few hundred meters to a few kilometers.

By comparing Figs XIV-3 and XIV-8, it can be seen that the low albedo band which surrounds the layered deposits between 70°N to 80°N is confined to the etch-pitted plains, rippled plains, and mottled cratered plains. If these units do represent various states of modification of the inner smooth plains in this area, the dark band could be interpreted as arising either from sorting phenomena caused by active winds in these areas or from a stratification of light and dark materials within the plains units.

As the etch pits are concentrated in the 70° to 80° latitudes around both poles and because they show a great similarity in the erosional morphology, we suggest that the process involved in developing etch pits is a process unique to the polar regions. The variations in resistance between the debris mantle and circumpolar smooth plains is possibly related to the presence or absence of volatiles.

3. Central Polar Layered Deposits and Permanent Ice Caps

As observed at the south pole, the youngest of the geologic units in the north is a sedimentary complex approximately centered at the pole (Figs. XIV-3, XIV-8, and XIV-9). The layered deposits in the north and south polar areas display dramatic symmetry. Both have a paucity of craters; both are located approximately between 70° latitude and the poles; and both consist of even layers of approximately uniform thickness. Finally, the uppermost stratum of each is the permanent ice deposit.

Murray et al. (Ref. XIV-1) concluded that the layered deposits in the south polar region rest unconformably on etch-pitted plains and densely cratered terrain. The north polar layered deposits also unconformably overlie older terrains. In Fig. XIV-11c the layered deposits rest on several benches eroded in the plains. In Fig. XIV-11d a large flat-floored crater can be seen protruding through the layered deposits, thus indicating that unconformable deposition has occurred in the north polar region as well as in the south.

At a regional scale the erosional patterns of both sedimentary complexes are similar. Both display large erosional channels spiraling radially outward (Fig. XIV-12). Both show sinuous and angular slopes in the eroded complex which appear very smooth as seen in narrow-angle photography. The north polar deposits appear to have a greater number of layers, suggesting greater total thickness (see Fig. XIV-12). This is substantiated by occultation data (Ref. XIV-2; also see Section XXXVI of this Report) which show that: (1) the basal terrains (mcp) in the north lie about 4 km lower than the cratered terrains in the south, whereas (2) the upper surfaces of the north and south central polar layered deposits are at about the same altitude. This may lend support to the theory by Murray et al. (Ref. XIV-11) that the distribution and thickness of the polar ice deposits are controlled at atmosphere-volatile equilibria.

C. Summary and Conclusions

Figures XIV-1 through XIV-5 demonstrate that the recession rate of the north polar cap, as monitored by *Mariner 9*, was not significantly different than has been observed from Earth in the past. Thus, the dynamic planet-wide dust storm does not seem to have had a noticeable effect on the thickness of the CO_2 deposit which developed during the standard mission.

The dominant role of local topography in controlling the configuration of the retreating cap is confirmed. At narrow-angle resolution the retreating frost has highlighted topographic detail that may represent Martian polar eolian deposits. At wide-angle resolution the topography of the smooth plains, rugged etch-pitted terrain, and complex central polar deposits is emphasized by the frost. Topographic control of the polar ice margin also appears effective on a regional scale. The polygonal boundary, which persisted at least through the ninth week of observation, might be controlled by regional topography possibly caused by a tectonic readjustment to thick accumulations of deposits at the pole.

In general the distributions of geologic units in the north and south polar regions are similar. The oldest units in each of the polar regions (densely cratered terrains and mottled cratered plains) are also the most dominant units of the north and south hemispheres (Ref. XIV-8; also see Section II of this Report). In both regions plains deposits of intermediate age rest stratigraphically on top of the oldest terrains. In the north a bright debris
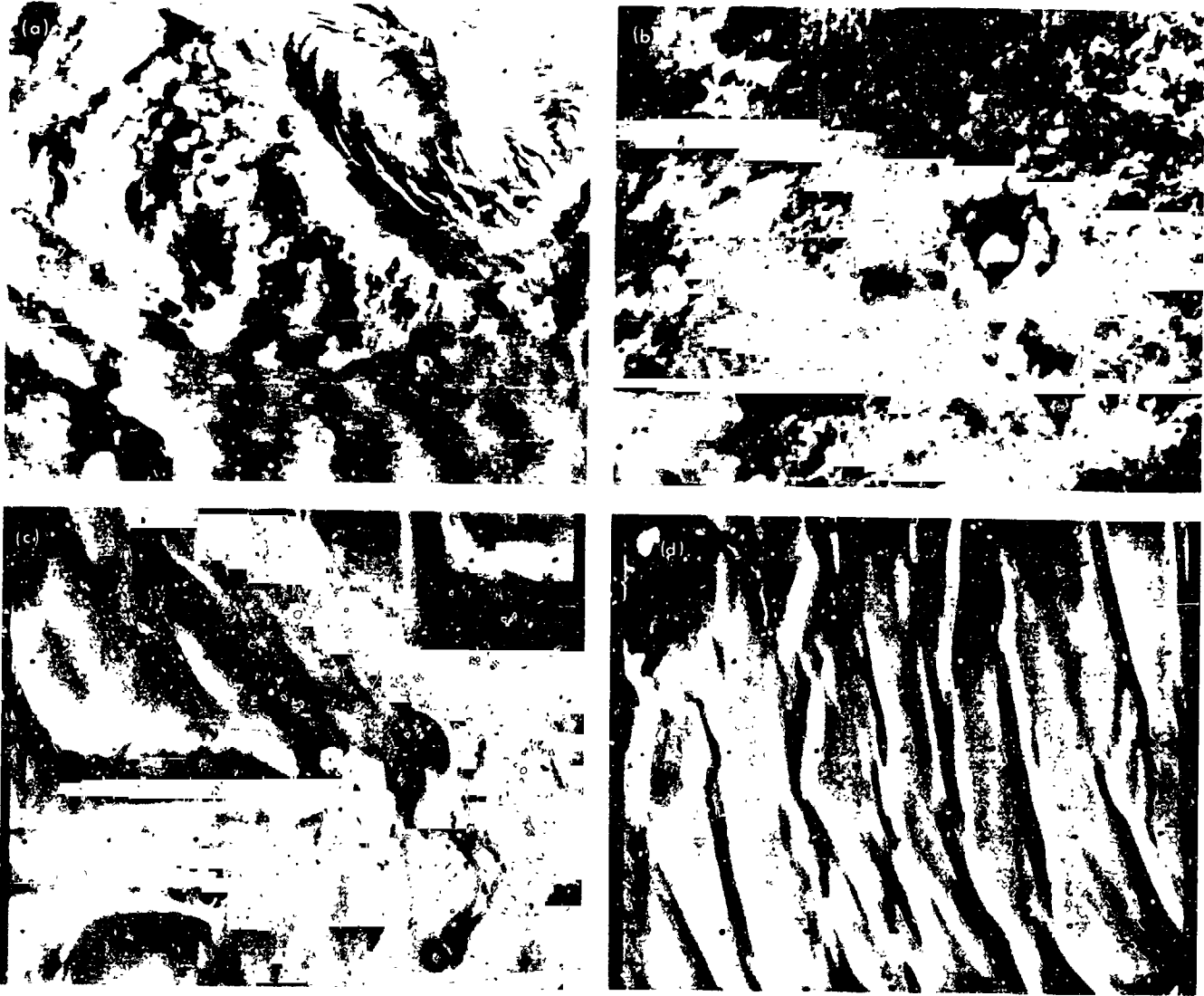
Fig. XIV-11. Etch-pitted plains, smooth plains, and layered deposits. (a) Shown in the upper left is a wide-angle view of the rough etch-pitted terrain developed in the inner smooth plains near the central polar layered deposits. (MTVS 4289-115, DAS 11836131) Two craters in the lower-right corner are situated on cones thought to be of volcanic origin. The area shown is about 1200 km wide. (MTVS 4289-115, DAS 11836131) (b) This high-resolution view shows etch pits developed in the smooth plains unit similar to those seen in the south polar region (width ~ 240 km). (MTVS 4295-63, DAS 12870688) (c) Here the central polar layered deposits can be seen resting unconformably on the inner smooth plains unit which has been eroded into cliffs (width 150 km). The escarpments have very similar appearance to those seen in the south polar region found in the same unconformable relationship to the layered deposits. (MTVS 4294-55, DAS 12502590) (d) In this high-resolution picture a crater can be seen emerging through the central polar laminated deposits (width 150 km). (MTVS 4294-111, DAS 12538500)

Fig. XIV-12. Comparison of erosional morphologies in the north and south central polar deposits. These two wide-angle frames show erosional channels of similar size and character developed in the layered deposits of the north and south polar regions. The south polar frame (a) was acquired on revolution 216, and the north polar view (b) on revolution 416. The areas covered are approximately 1500 km in width. (a) MTVS 4250-11, DAS 09339094. (b) MTVS 4287-111, DAS 1148197 $\therefore$.

deposit mantles the mottled cratered plains. The boundaries between the two are diffuse and serrated implying eolian erosion. Although it is not clear as to whether the etch-pitted units in the north and south are the same material, we conclude that the similarities in geographic location and morphological style of the etch pits at both polar regions indicate that etch pitting is a unique polar process. Finally the layered deposits of the north and south polar regions appear to be uniquely polar, eroded by uniquely polar processes.

References

XIV-1. Murray, B. C., Soderhlom, L. A., Cutts, J. A., Sharp, R. P., Milton, D. J., and Leighton, R. B.. "Geological Framework of the South Polar Region of Mars," *Icarus*, Vol. 17, p. 328, 1972.

XIV-2. Khore, A. I., Fieldbo, G., Seidel, B. L., Sykes, M. J., and Woiceshyn, P. M., "S-Band Radio Occultation Measurements of the Atmosphere and Topography of Mars with Mariner 9: Extended Mission Coverage of Polar and Intermediate Latitudes," *J. Geophys. Res.*, Vol. 78, 1973.

References (contd)

XIV-3. Fischbacher, G. E., Martin, L. J., and Baum, W. A., *Martian Polar Cap Boundaries*, Final Report, Part A, under contract No. 951547, to Jet Propulsion Laboratory, Pasadena, Calif., Planetary Research Center, Lowell Observatory, Flagstaff, Arizona, 1969.

XIV-4. Leighton, R. B., and Murray, B. C., "Behavior of Carbon Dioxide and Other Volatiles on Mars," *Science*, Vol. 153, p. 136, 1966.

XIV-5. Sharp, R. P., Murray, B. C., Leighton, R. B., Soderblom, L. A., and Cutts, J. A., "The Surface of Mars: 4. South Polar Cap," *J. Geophys. Res.*, Vol. 76, p. 357, 1971.

XIV-6. Sharp, R. P., "Mars: South Polar Pits and Etched Terrain," *J. Geophys. Res.*, Vol. 78, 197?.

XIV-7. McCauley, J. F., Carr, M. H., Cutts, J. A., Hartmann, W. K., Masursky, H., Milton, D. J., Sharp, R. P., and Wilhelms, D. E., "Preliminary Mariner 9 Report on the Geology of Mars," *Icarus*, Vol. 17, p. 289, 1972.

XIV-8. Carr, M. H., Masursky, H., and Saunders, R. S., "A Generalized Geologic Map of Mars," *J. Geophys. Res.*, Vol. 78, 1973.

XIV-9. Soderblom, L. A., Kreidler, T. J., and Masursky, H., "The Latitudinal Distribution of a Debris Mantle on the Martian Surface," *J. Geophys. Res.*, Vol. 78, 1973.

XIV-10. Cutts, J. A., "Wind Erosion in the Martian Polar Regions," *J. Geophys. Res.*, Vol. 78, 1973.

XIV-11. Murray, B. C., Malin, M. C., and Yeung, M., "Volatiles on Mars—Theory vs Observation" (in preparation).

Acknowledgments

XV. Wind Erosion in the Martian Polar Regions

James A. Cutts

Jet Propulsion Laboratory/California Institute of Technology, Pasadena, California 91103

The existence of global Martian dust storms provides one positive form of evidence that the atmosphere can transport surface materials on Mars. The observations by *Mariners* 6, 7, and 9 of surface markings associated with topographic obstacles (Refs. XV-1 and XV-2) also have been interpreted to mean that wind deposits, erodes, and redistributes materials on the surface. These features also have been observed to change with time (Ref. XV-2); their ephemeral character, as well as tending to confirm their eolian origin, also suggests that they involve a superficial mantle of materials. With the exception of a few conspicuous sand dune features (Ref. XV-3), there has been no well demonstrated case of topographic features attributable to wind action.

In this section, a plausible model of prevailing wind directions in the south polar region is developed, based on observations of surface albedo features. A demonstration is given that lineations, grooves, and elongated pits found in this part of Mars lie parallel to the wind directions given by the model. A natural inference is that these features, which on morphologic evidence alone might be considered structural, solution, or even glacial features, actually were formed by wind erosion. With this indication of the efficacy of wind action near the pole, the possibility is considered that wind has sculptured the present topography of laminated terrain in the interior parts of the north and south polar regions.

A. South Polar Wind Model Based on Albedo Features

Dominating many *Mariner* 9 pictures are conspicuous streaks or plumes that originate at a crater, ridge, or scarp and extend up to hundreds of kilometers across the surface of the planet. Some of these features are darker, others lighter than the surrounding terrain. Many dark plumes appear to develop from within the floor of a crater and extend outside it, thus providing an unambiguous indication of wind direction (Fig. XV-1a). In some cases, however, and particularly in the south polar region, the dark markings tend to be confined to the floors of craters (Fig. XV-1b). Although these markings seem biased to one side of the crater, and to exactly the same side in a group of neighboring craters, the directional indication is equivocal. The presence of nearby craters with plumes (Figs. XV-1c and XV-1d) shows that where dark markings are confined to the crater floor they occupy that same part of the floor from which the plume extends. Thus, an albedo marking in the southern part of the floor of a crater indicates a wind from the north. This simple relationship is of great value in constructing a model of the wind patterns around the south polar region.

Figure XV-2 shows wind directions inferred from the markings on crater floors and, in a few cases, shows the
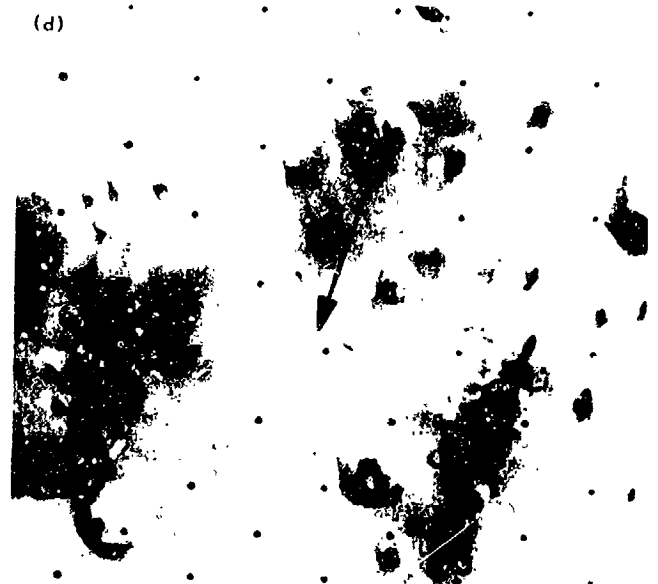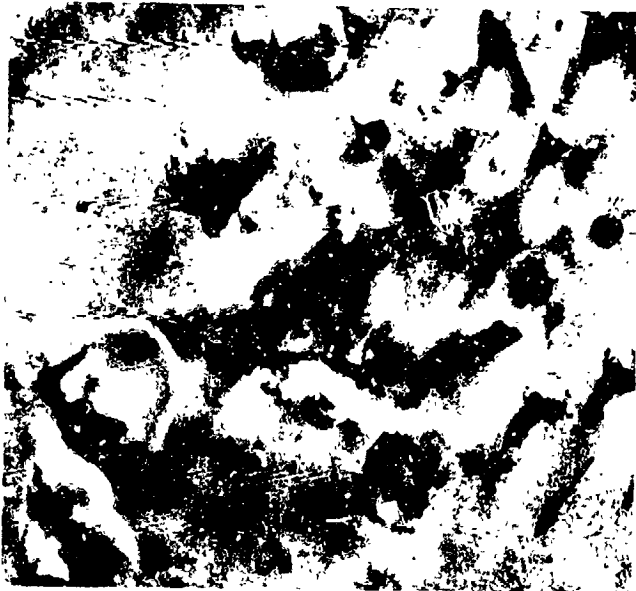
Fig. XV-1. Dark albedo features associated with craters attributable to wind. (a) Plume features extending from craters. Wind direction is clearly implied (see arrow). (IPL Roll 1934, 171026) (b) In this group of craters the dark markings are mostly confined to the same side of the crater floors. The directional indication is ambiguous. (IPL Roll 260, 222739) (c and d) Marking in crater floors and plumes. The ambiguity of crater floor markings is resolved. (IPL Roll 1622, 14061; IPL Roll 1936, 220916)

Fig. XV-2. Photomosaic of the south polar region of Mars. Arrows indicate wind directions inferred from dark albedo markings associated with craters (see text). This is also a location map for Figs. XV-3a through XV-3b, Fig. XV-4, and Fig. XV-5. The numbers and letter subscripts refer to the figure identifications used in the text. The upper-left-hand corner of each picture is denoted by a solid dot. Prepared by U. S. Geological Survey with rectified pictures by the Image Processing Laboratory (IPL).

fully developed plume features. These markings, found in the range of from 60° to 75°S latitude, occur in some of the pits and basins of pitted terrain as well as in association with craters. Closer to the pole the surface is predominantly mantled with layered deposits described as laminated terrain by Murray et al. (Ref. XV-4). Because few, if any, craters are present on this surface, this basic wind direction indicator is lost. Local or small-scale (1 to 50 km) albedo features are not conspicuous in this area except near Thyles Mons (77°S, 155°W).

A striking feature of the wind map (Fig. XV-2) is the strong symmetry about the polar rotation axis. Directions are predominantly southeasterly so that in polar projection one has the impression of a counterclockwise spiral circulation, with winds at the surface blowing away from the poles. Outflow winds, spiraling as a result of the coriolis force, are observed near the terrestrial ice caps of Greenland and Antarctica. The Martian surface markings may have been formed by similar circulation patterns which may develop when they lie just outside the margin of the receding polar cap. The regularity and symmetry of the markings suggest that strong winds with a consistent direction are a regular planetary phenomenon which may have been occurring since the formation of the atmosphere, and which may have produced more profound effects on the surface than superficial albedo markings.

High-resolution pictures of the three basic terrain types of the south polar region (cratered terrain, pitted terrain, and laminated terrain) reveal a variety of topographic features with strong directional patterns. Morphologic considerations alone suggest an eolian origin as only one of several possibilities. However, by comparing wind directions implied by albedo markings with directional trends of these topographic forms, we can test the eolian hypothesis. In some cases this comparison is straightforward because an albedo feature which we assumed to be eolian is associated with the topographic form we wish to test. In other cases the topographic form lies between two albedo features, and wind direction is inferred from an average of measurements on these two features. In the absence of nearby albedo features, a mean of directions found in the entire latitudinal belt is used.

This wind model based on surface albedo markings is an intermediate step in studying the effect of wind on polar terrains. It is applicable in an annular zone with an inner margin near 75°S latitude in which features have been recognized. The behavior of winds closer to

the pole is likely to be much more complex. As the perennial frost deposit is highly irregular (Fig. XV-2) and offset from the areographic pole, the outflow winds will not be symmetrical with respect to it.

B. Possible Wind Erosion Forms of the South Polar Region

Mariner 9 pictures show several types of topographic features, many with strong directional patterns suggestive of wind erosion. On the cratered terrains they are least pronounced, which may indicate that these surfaces are resistant to wind erosion. The pitted terrain however, displays a variety of depressed and etched features with a strong directional trend.

1. Pitted Terrain

Figure XV-3 shows several examples of possible wind erosional features that occur on the pitted terrain. The pictures were obtained by the Mariner 9 narrow-angle (high-resolution) camera, and all features are found in the 60° to 75°S latitude band where the inferences about wind direction based on albedo markings are thought to be most reliable (Fig. XV-2).

In the first example (Fig. XV-3a) the thin, sparsely cratered veneer visible in the upper right of the picture is marked with numerous parallel grooves. The jagged edge of this veneer, which has apparently been stripped from the underlying surface, shows several prominent indentations that are aligned with the grooves. The wind direction inferred from the albedo features is parallel with the grooves within the accuracy of the model (±10° at this location). The topographic features are therefore interpreted as wind erosion grooves that parallel the direction of a prevailing wind system. Yardangs, which form in loosely consolidated materials such as snow and silt (Ref. XV-5), are the nearest terrestrial analogy to these features. The pattern of the indentations at the margin of the depositional veneer is aligned with the grooves and may represent differences in response to erosion of the material along the margin.

The wind direction inferred from surface markings (arrow) is also parallel to the principal alignment of surface texture in the terrain appearing in Fig. XV-3b. A prominent feature is the ridge that is developed tangential to and in the "lee" of the large crater. Several small features with a finely etched appearance are seen at the lower left. One possible interpretation of the
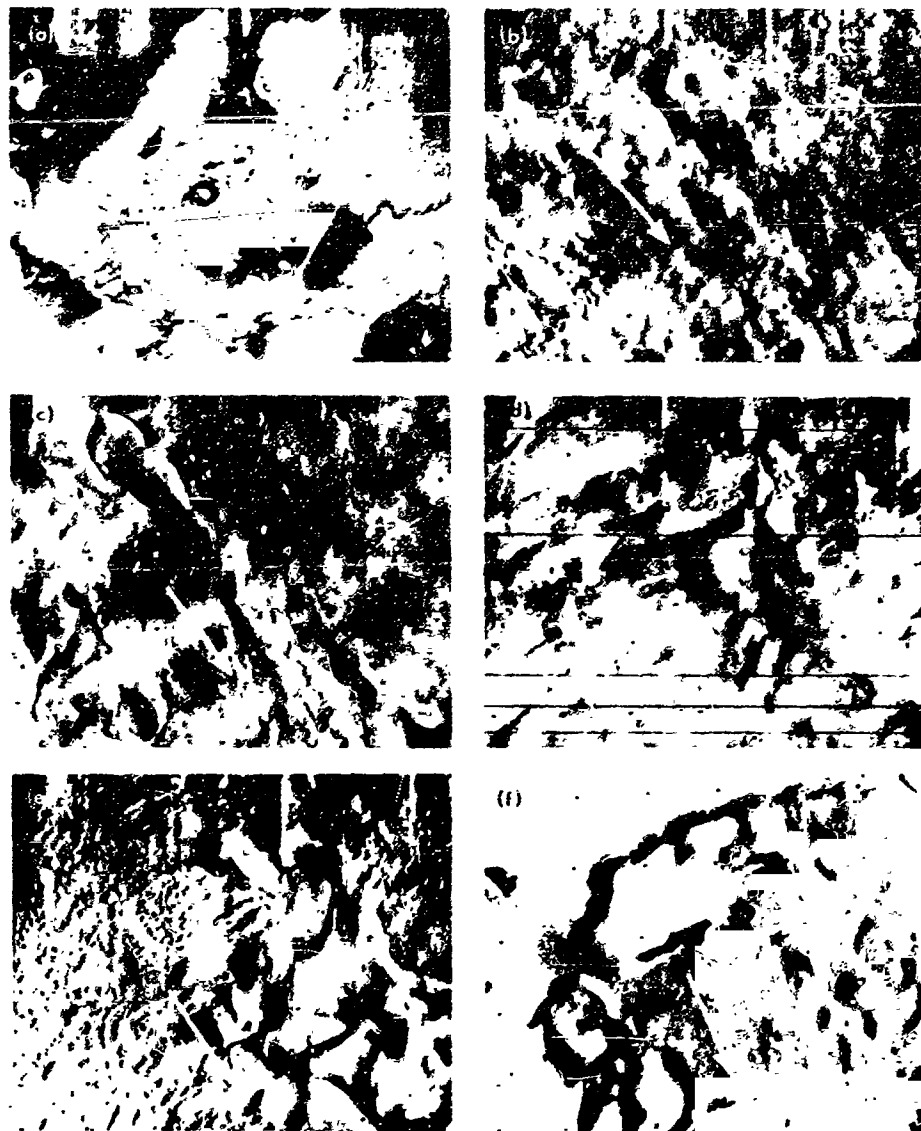
Fig. XV-3. Possible wind erosion features on the pitted terrain. Arrows show wind directions inferred from albedo markings in the vicinity of the features (see Fig. XV-2). (a) MTVS 4155-27, DAS 06173723. (b) MTVS 4232-3, DAS 08691911. (c) MTVS 4270-23, DAS 10023239. (d) MTVS 4203-12, DAS 07756353. (e) MTVS 4168-9, DAS 06640693. (f) MTVS 4234-14, DAS 08763869.

geology is that the large crater is in the process of exhumation from a depositional mantle. If this is valid, then the ridge tangential to the crater rim may be either a dune deposit or part of the original mantling deposit which is protected from erosion in this leeside location.

The shallow basins of Fig. XV-3c apparently have developed with a preferential elongation parallel to the wind direction. However, the edges of the basins are not straight but sinuous, although not as smooth, graceful,

and repetitive as forms found in the laminated terrains nearer the pole.

In the fourth example of erosional features on the pitted terrain (Fig. XV-3d), elongated depressions are developed perpendicular to the wind direction given by the albedo feature model. However, the ragged rims of the depressions, which in one case intersects the wall of an impact crater, are morphologically distinct from the straight and sinuous rims of those depressions that are

elongated parallel to the prevailing wind. A remarkable analogy for this is found in terrestrial snow deposits. Erosional basins are observed to elongate parallel to and perpendicular to a prevailing wind. The latter category exhibits ragged, irregular rims (Ref. XV-6).

Similar transverse depressions with jagged rims (Fig. XV-3e) are associated with irregular, smooth-floored depressions without pronounced directional properties. These depressions range in size from small 3- to 5-km pits to much larger basins up to 40 or 50 km in diameter. Irregular basins on Earth are sometimes attributable to deflation by wind, the great Qattara depression in the Egyptian Sahara being the most notable example.

A different type of irregular depression, with a hummocky floor and highly irregular margin, appears in Fig. XV-3f. A notable feature of this depression is the dark albedo occurring at what is inferred to be the downwind margins of the depression. Features on the opposite margin suggest slumping of the depression walls, which distinguishes these irregular basins from those of Fig. XV-3e.

Through the application of the wind model and the exercise of terrestrial analogy, the six terrain surfaces of Fig. XV-3 can be attributed to wind erosional modification. Variations in the surface materials, pre-existing topography, and wind regime may account for the conspicuous differences in the appearance of the surface at the different localities. There are other features in the same latitude zone where lineations are probably structurally controlled. An example is the intricate grid pattern known informally as the "Inca City," which Sharp (Ref. XV-7; also see Section XVI of this Report) discusses in context of a more complete descriptive treatment of south polar pits and etched terrains.

2. Laminated Terrain: Small-Scale Features

Layered deposits cover a large area of the central polar regions in both hemispheres. In the southern hemisphere many narrow-angle pictures have been obtained of the margin of the layered deposits where the older, underlying cratered terrain or pitted terrain surfaces emerge. This marginal area exhibits curving, sinuous and re-entrant escarpments, partially buried craters, dune forms, and small-scale fluting and grooving of the surface.

A lobe of laminated terrain extending almost to 72° longitude exhibits many of these features. Part of a wide-angle picture (Fig. XV-4a) displays the escarpment that is marginal to this feature and is used to locate three

narrow-angle pictures (Figs. XV-4b, XV-4c, and XV-4d). The elongate pits and grooves (Fig. XV-4b) are typical of the small-scale texture of laminated terrain. In some cases a preferred direction is obvious and individual pits are asymmetrical, wider at one end with almost a teardrop shape. In other cases (Fig. XV-4c) a texture is clearly apparent, but the direction is less pronounced. A series of dune-like ridges (Fig. XV-4b) lies adjacent to the escarpment that marks the margin of the layered deposits.

Pits and grooves have been identified on about one-quarter of the laminated terrain surface for which narrow-angle photography exists. However, much of the visible structure is at the limit of resolution of these pictures, and at a higher resolution it may be even more widespread. The pits and grooves are, in many cases, parallel to or inclined at a small angle with the trend of the escarpments. However, in Fig. XV-4c the fluting is essentially perpendicular to one escarpment, yet parallel to another one that embays the layered deposits. A major escarpment re-entrant that extends toward the pole displays a different kind of surface texture (Figs. XV-2 and XV-5). This texture has a prominent north–south grain that is roughly parallel to the axis of the re-entrant. The long bright streaks and the arrays of delicate bright features arranged at a high angle are morphologically distinct from the pits and grooves of Fig. XV-4.

Proving that the flutes and textures of laminated terrain are due to wind action is more difficult than for the features of the pitted terrain. Pits and grooves on the lobe of laminated terrain (Fig. XV-4) are in the latitude range where albedo features provide a consistent wind indicator for the pitted terrains. However, on the inter-scarp plains of laminated terrain (Fig. XV-4), the direction of the fluting is generally within 30° of north and south. It changes from west of north at 230° longitude to east of north at 215° longitude, whereas only values west of north are expected from examining the adjacent albedo features. If the flutes are wind features, a plausible explanation is that topographic relief of the marginal escarpments modifies the wind patterns from those that prevail on a planar surface. The bright streaks aligned with the major escarpment re-entrant, which occur much closer to the pole (Figs. XV-2 and XV-5), may even be an expression of topographic channeling of winds.

The morphology of the flutes and textures of laminated terrain are not inconsistent with an eolian origin. The flutes are very different from the pits of pitted terrain (Fig. XV-3), but material differences between the pitted
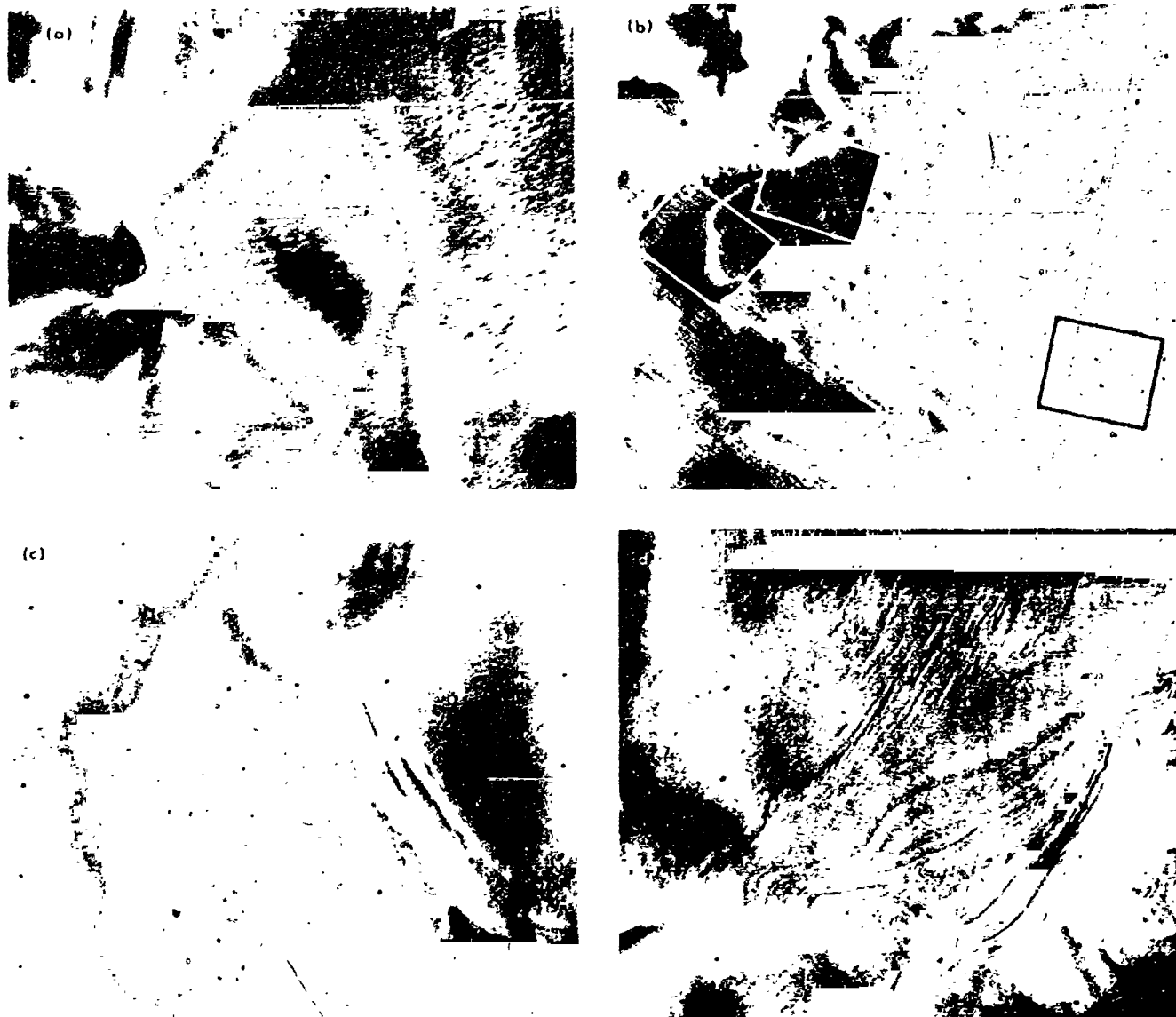
Fig. XV-4. Part of a wide-angle frame (a) is used to locate narrow-angle frames (b), (c), and (d) showing elongated pits, grooves, and dunes on and adjacent to the laminated terrains of the south polar region. (a) MTVS-4171-5, DAS 06748808. (b) MTVS 4213-21, DAS 08080243. (c) MTVS 4226-15, DAS 08152273. (d) MTVS 4285-66, DAS 10684504

terrain and the layered deposits, earlier suggested by Murray et al. (Ref. XV-4), could account for this. If wind features form on the pitted terrain, one would expect them also on the layered terrains. This evidence, together with the dune-like ridges (Fig. XV-4d) discussed in more detail by Sharp (Ref. XV-7; also see Section XVI of this Report) and Cutts and Smith (Ref. XV-8; also see Section XI of this Report) makes an eolian origin plausible for the small-scale features of laminated terrain. One might speculate that the pits of Figs. XV-4b and XV-4c indicate only the erosion of a layered deposit,

whereas bright streaks and other textures (Fig. XV-5b) express erosion and redeposition in the form of dunes.

3. Laminated Terrain: Large-Scale Features

In viewing images of both the north and south polar caps (Fig. XV-6) when they are close to their minimum size, one is struck by the similarity of the Martian frost patterns to cloud patterns induced by rotational motions in Earth's atmosphere. The frost distribution seems to reflect large-scale topographic features in the underlying laminated terrain. In this section we examine the pos-
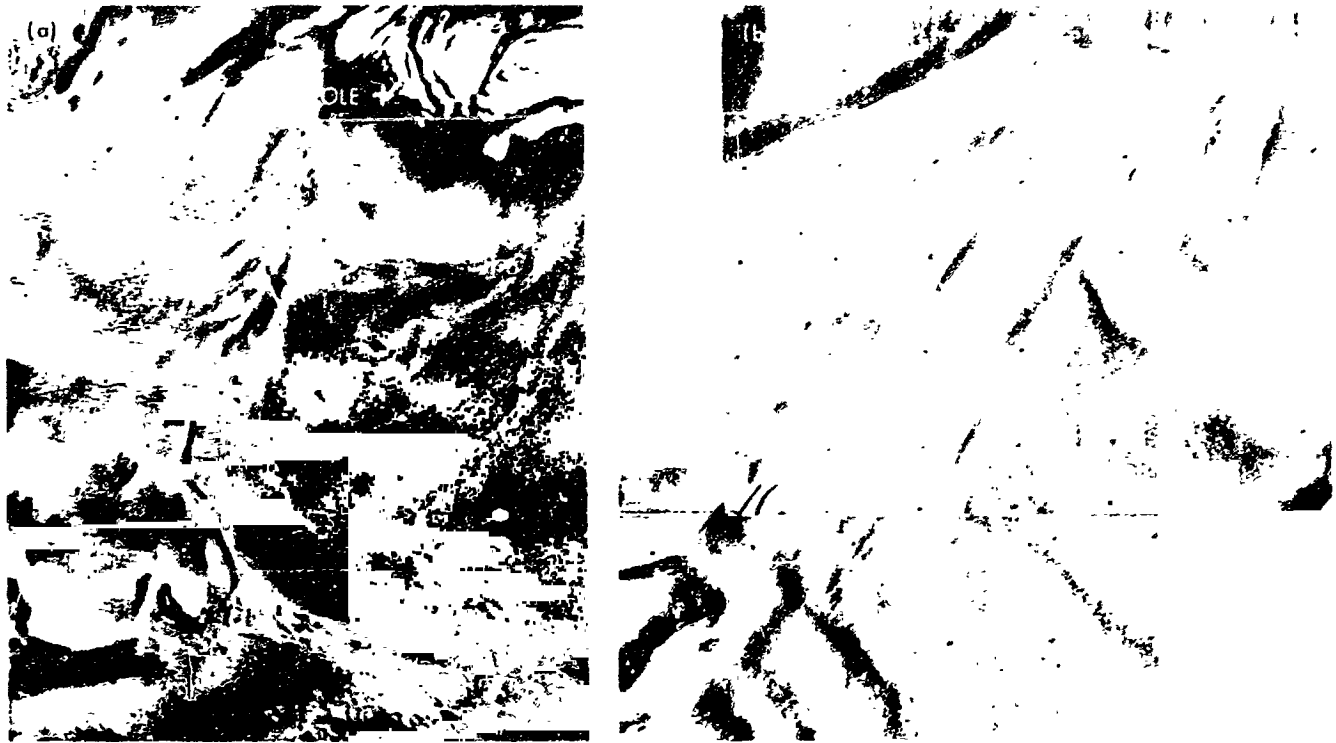
Fig. XV-5. (a) A major escarpment re-entrant extending toward the south pole is seen in part of a wide-angle picture. (IPL Roll 167, 142409) (b) A mosaic of narrow-angle views of the apex of this re-entrant displays a strongly directional texture aligned along the re-entrant axis. The topography in this area is attributed to wind erosion and deposition. Wind erosion may have etched out the entire re-entrant. (MTVS 4248-11, DAS 09267099; MTVS 4248-16, DAS 09267169)

sibility that these features have been sculptured by rotational or spiral motions in the atmosphere of Mars.

Albedo markings have been cited here as evidence of wind directions between 75°S and 60°S, but are of no direct help in defining wind directions in inner polar zones including the perennial polar cap. The geometry of albedo markings and erosional features in the south polar annular zone supports the idea that outflow winds from the polar cap spiral toward the west. A *Mariner 9* picture of atmospheric effects during the recession of the north polar cap (Fig. XV-7) shows a jet-like formation apparently spiraling clockwise away from the pole. There is no evidence that this particular formation is causing erosion, but this is certainly the kind of flow pattern that is envisaged for winds producing erosional effects between 60°S and 75°S in the south polar region. Descending masses of air near the cold polar regions and the outflow wind from the subliming polar caps moving under differential pressure, coriolis and centripetal forces apparently create the conditions for these types of atmospheric motions. However, the jet-like formation does not extend into the inner part of the polar cap and gives no indication of what the flow patterns are in that region.

Pseudo-circular features underlying the polar caps appear to be scarps or troughs developed in layered deposits which may consist of dust, volcanic ash, and water ices (Ref. XV-4). Some of these features resemble the escarpment outside the residual polar cap (Fig. XV-4), although fine-scale texture in the inner polar zone shows no strong preferred orientation. The escarpments form en echelon and in some places create either closed loops or gently expanding spirals which can give the impression of a stack of plates of decreasing size assembled at the pole (Ref. XV-4). In some areas, however, the escarpments diverge to form series of small jagged re-entrants (Fig. XV-8).

The laminated terrain underlying the residual north polar cap appears to consist of two circular patterns, one centered near the pole and one centered near 82°N, 0° (Fig. XV-6b; Fig. 2 of Ref. XV-9; also see Fig. XIV-2 of this Report). Separating these two patterns is a major escarpment re-entrant with similar geometry to that seen in the south polar region (Fig. XV-5). Only moderate-resolution pictures of this feature are available and they show no fine-scale texture, but the analogous feature in the south does show alignment of bright streaks and

other fine detail (Fig. XV-5b) which may be eolian in origin.

The planimetric complexity of the features underlying the perennial polar caps precludes a simple geometric argument for a wind erosional origin. However, complex wind patterns in the inner polar regions are not improb-

able, particularly during the summer seasons when the frost distribution is irregular. If wind erosion does operate elsewhere in the polar region it should also be effective in the vicinity of the residual caps, although the resulting features may also reflect material differences within the deposits and differential ablation of volatiles. One might speculate that the residual frost caps cause rotational flows to develop with almost closed flow patterns. The circular features underlying the two segments of the north polar cap (Fig. XV-6b) might have been developed by two such disturbances with different centers. The physics of atmospheric rotational motions does not require that they be centered on the rotational pole
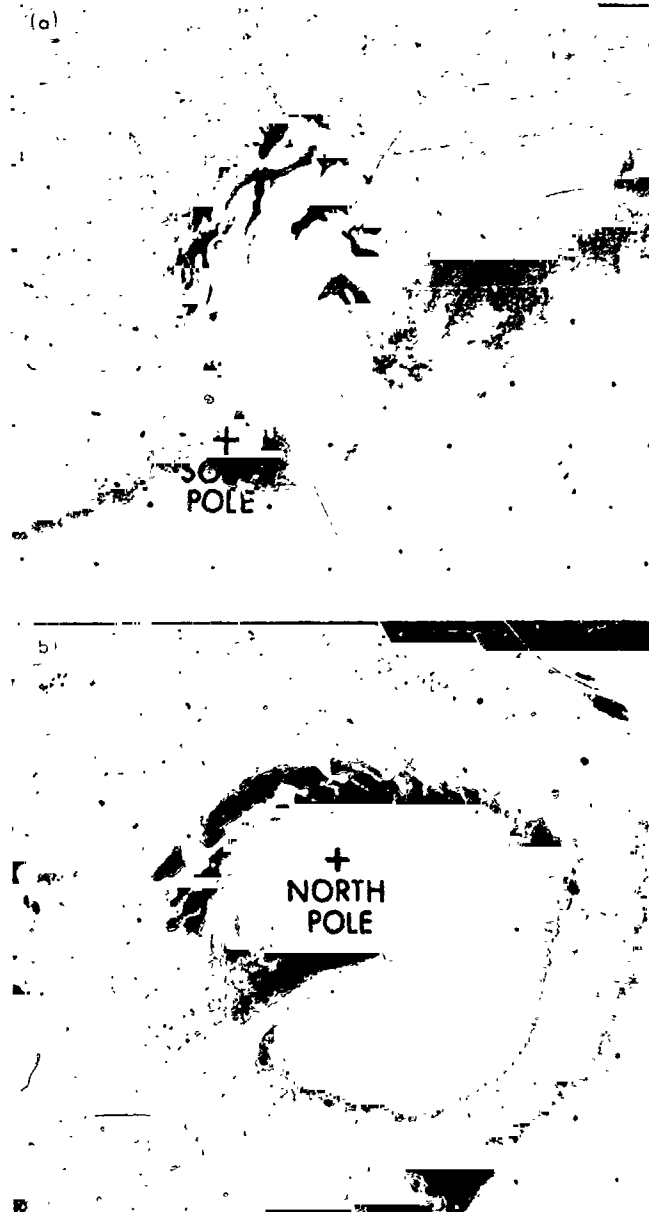
Fig. XV-6. (a) Wide-angle view of the south polar cap. The configuration of the frost strongly expresses the form of the underlying topography. The circular and spiral forms in this underlying "laminated terrain" are attributed to sculpture by wind. (MTVS 4190-8, DAS 07288788) (b) Wide-angle view of the north polar cap. (MTVS 4296-46, DAS 13317550)
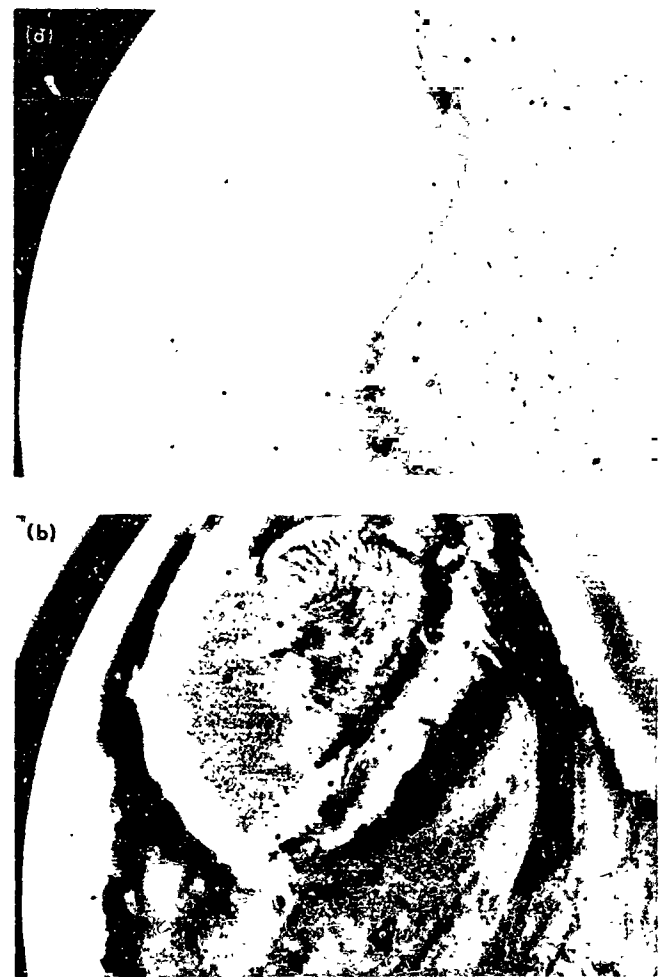
Fig. XV-7. Cloud motions confirming the existence of circular or spiral motions in the north polar atmosphere. (a) Shading-corrected picture in which the contrast of the polar cap region has been exaggerated and very little cloud structure can be seen. (MTVS 4295-70, DAS 12874573) (b) High-pass filtered version enhances fine detail at the expense of photometric fidelity and shows a jet-like formation extending from the cap edge. (MTVS 4295-72, DAS 12874573)

of the planet. Scarps and troughs underlying the residual polar caps could result from air motions both parallel to the slopes and also highly inclined to them. Possible examples of the former kind outside the polar cap appear in Fig. XV-4b and examples of the latter in Figs. XV-4c and XV-5b. However, wind erosion remains a highly speculative explanation of the features underlying the residual ice caps.

Fig. XV-8. V-shaped promontories and re-entrants at the margin of laminated terrains in the northern polar regions. (a) Part of a wide-angle picture. (MTVS 4290-114, DAS 12013129) (b) A higher-resolution view of part of the margin shows the topography in more detail, but was obtained from too great a range to show the layering. These features are attributed to wind action circling perpendicular to the escarpment edge. (MTVS 4295-58. DAS 12870618)

C. Discussion

Eolian erosion on Earth is most effective in fine, loosely consolidated deposits. In most materials the larger rock fragments that are left behind when finer materials are winnowed away armor the surface. Further deflation is restricted to creep of larger pebble-sized components under the impact of saltating sand-sized particles and the reduction of the pebble-sized components to a finer grain size by mechanical impact of the saltating particles and other weathering processes. Even though the protracted time scale of the Martian surface might allow even the slowest processes to achieve visible effects, armoring of the surface is a potential obstacle to erosion on Mars.

According to current ideas on the nature of laminated terrain (Ref. XV-4 and XV-10; also see Section XVII of this Report), these deposits consist of dust and ash possibly mixed with frozen volatiles. Fine-grained, loosely consolidated materials of this type should be easily deflated without the formation of a residual armor of larger particles. Thus, there seems to be no particular difficulty with an eolian explanation for the pits, fluting, and grooving that have been recognized on the laminated terrain surface.

It has been pointed out (Ref. XV-4) that the pitted terrain erodes in a different fashion than the laminated terrain. Slopes on the pitted terrain are characteristically concave in profile with a sharp upper edge. The laminated terrains, in contrast, are smooth, gracefully sculptured surfaces with gentle slopes; the upper edges of the slopes are not sharp, but rounded. Thus, the physical response of the pitted terrain seems quite different, and this might be attributable to a significant proportion of particles too large for saltation to be effective. This could explain why erosional features on the pitted terrain unit, which is older than the laminated terrain since it underlies it stratigraphically, are much less widespread and confined to a small part of the total area of the unit. Armoring could be confined to a relatively thin zone near the top of the unit, for where pits form they seem to have developed rapidly into deep basins with steep walls (Ref. XV-7; also see Section XVI of this Report). It is felt that the observational correlation between albedo features and erosional stripping and grooving is strong evidence that wind action has sculptured this part of Mars.

An alternative theory of formation of the quasi-circular topographic features of the polar regions has been ad-

vanced by Murray and Malin (Ref. XV-11). They interpret the features as a complex sequence of "fossil latitudinal circles related to ancient pole positions over the last 10⁶ years." According to this model, formation of both individual laminations and stacks of laminations develops in response to the mean insolation at the poles, which changes as a result of perturbations in Mars' ellipticity. The present topography of laminated terrain is not viewed as an erosional surface, but a series of constructional forms controlled by the changing heights at which solid and gaseous carbon dioxide reach equilibrium during deposition.

The most conspicuous failing of the polar wandering theory is that the circumpolar features at the two poles are not symmetric. The eolian theory suggested in this section has no such exact requirement. However, it can account for the fact that the pseudocircular topographic features are offset from the poles. There is no physical reason why rotational atmospheric flow would be exactly centered on the rotation axis of Mars.

Another failing of the polar wandering model is that it only predicts the formation of circular stacked plates. The features of laminated terrain cannot be so simply described. Many topographic forms are found which cannot be described as scarps facing equatorward. The sinous escarpments in the region of Thyles Mons (77°S, 155°W) clearly bear a genetic similarity to the circumpolar escarpments, but could never be described as "fossil latitudinal circles." Much of the laminated terrain in the north polar regions consists of curving troughs and not scarps (e.g., Fig. XV-8; MTVS 4296-39, DAS 12991412;

MTVS 4296-31, DAS 12991272)[1] and does not fit with this "polar wandering model." The polar wandering theory is so geometrically confining that it cannot possibly account for the great variety of topographic forms that occurs on laminated terrain. Wind action, which from terrestrial experience is known to create a great variety of topographic shapes, does not have this limitation.

D. Conclusions

Photographic evidence suggests that many topographic features of the polar regions of Mars may have been sculptured by wind action. In the case of the pitted terrain, this is established by relating the orientations of elongate basins and grooves to patterns of albedo markings that are generally accepted to be wind-formed. Small-scale flutes and other textures of laminated terrain recognized outside the perennial ice cap in the south polar region are also attributed to eolian action. Winds flowing off the polar cap and spiraling toward the west seem to be responsible. More speculatively the large-scale circumpolar features which underlie the residual polar caps may be related to wind erosion. Rotational motions localized on circular segments of the perennial frost deposits are proposed as a mechanism. Thus, both the formation and erosion of laminated terrain may be controlled by atmospheric motions and eolian processes.

[1]Picture identifications in text refer to *Mariner 9* pictures not included in this section, but which provide additional explanatory material. All *Mariner 9* pictures may be ordered from the National Space Science Data Center, Code 601, Greenbelt, Maryland 20771.

References

XV-1. Cutts, J. A., Soderblom, L. A., Sharp, R. P., Smith, B. A., and Murray, B. C., "The Surface of Mars: 3. Light and Dark Markings," *J. Geophys. Res.*, Vol. 76, p. 343, 1971.

XV-2. Sagan, C., Veverka, J., Fox, P., Dubisch, R., Lederberg, J., Levinthal, E., Quam, L., Tucker, R., Pollack, J. B., and Smith, B. A., "Variable Features on Mars: Preliminary Mariner 9 Television Results," *Icarus*, Vol. 17, p. 346, 1972.

XV-3. McCauley, J. F., Carr, M. H., Cutts, J. A., Hartmann, W. K., Masursky, H., Milton, D. J., Sharp, R. P., and Wilhelms, D. E., "Preliminary Mariner 9 Report on the Geology of Mars," *Icarus*, Vol. 17, p. 289, 1972.

XV-4. Murray, B. C., Soderblom, L. A., Cutts, J. A., Sharp, R. P., Milton, D. J., and Leighton, R. B., "Geological Framework of the South Polar Region of Mars," *Icarus*, Vol. 17, p. 328, 1972.

XV-5. Blackwelder, E., "Yardangs," *Bulletin of the Geological Society of America*, Vol. 45, p. 159, 1934.

XV-6. Seligman, G., *Snow Structure and Ski Fields*, 555 pp., Jos. Adam, Belgium, 1931, reprinted 1962.

XV-7. Sharp, R. P., "Mars: South Polar Pits and Etched Terrain," *J. Geophys. Res.*, Vol. 78, 1973.

XV-8. Cutts, J. A., and Smith, R. S. U., "Eolian Deposits and Dunes on Mars," *J. Geophys. Res.*, Vol. 78, 1973.

XV-9. Soderblom, L. A., Malin, M. C., Cutts, J. A., and Murray, B. C., "Mariner 9 Observations of the Surface of Mars in the North Polar Region," *J. Geophys. Res.*, Vol. 78, 1973.

XV-10. Cutts, J. A., "Nature and Origin of Layered Deposits in the Martian Polar Regions," *J. Geophys. Res.*, Vol. 78, 1973.

XV-11. Murray, B. C., and Malin, M. C., "Polar Wandering on Mars," *Science* (in press).

Acknowledgments

XVI. Mars: South Polar Pits and Etched Terrain[1]

Robert P. Sharp

Division of Geological and Planetary Sciences

California Institute of Technology, Pasadena, California 91109

In its 1969 flight past Mars, *Mariner 7* photographed some highly irregular closed depressions near the prime meridian at latitudes 70° to 74° south, within the area then covered by annual polar frost (Ref. XVI-1). These were unlike any features seen on *Mariner 6* and 7 pictures at lower latitudes. They were termed "etch pits" from a resemblance to forms etched by a corroding agent, but in 1969 it was uncertain whether these pits existed solely within the annual frost cover or were features of the underlying substrate.

The *Mariner 9* pictures of 1971–1972 clearly establish that the pits are features of the substrate. They are further shown to be extremely abundant in some areas poleward of 73° south (Figs. XVI-1 and XVI-2), and to occur in a wide variety of shapes, sizes, and arrangements (Fig. XVI-3).

The simple term "pit" is now used for these topographically closed depressions, and areas extensively in-

dented by such features are termed "pitted terrain." As pits enlarge they become integrated, eventually producing a terrain more properly described as etched. Etched terrain is seen within the south polar area at about 70° south (Fig. XVI-1).

Although pitted and etched terrains are unusual and interesting in themselves, their principal value lies in what they tell us concerning the history and evolution of the south polar area and of Mars. Particularly significant is the indication of alternating episodes of deposition and erosion within the south polar region. Considerations are limited to the region poleward of 65° south, although pictures from the north polar area also suggest the existence of pitted terrain there (Ref. XVI-2; also see Section IX of this Report).

A. South Polar Sedimentary Blankets

The *Mariner 7* flight of 1969 revealed that much of the polar area southward of 80° latitude was craterless and relatively smooth. This has been confirmed by *Mariner 9*

---

[1]Contribution 2266, Division of Geological and Planetary Sciences, California Institute of Technology, Pasadena.
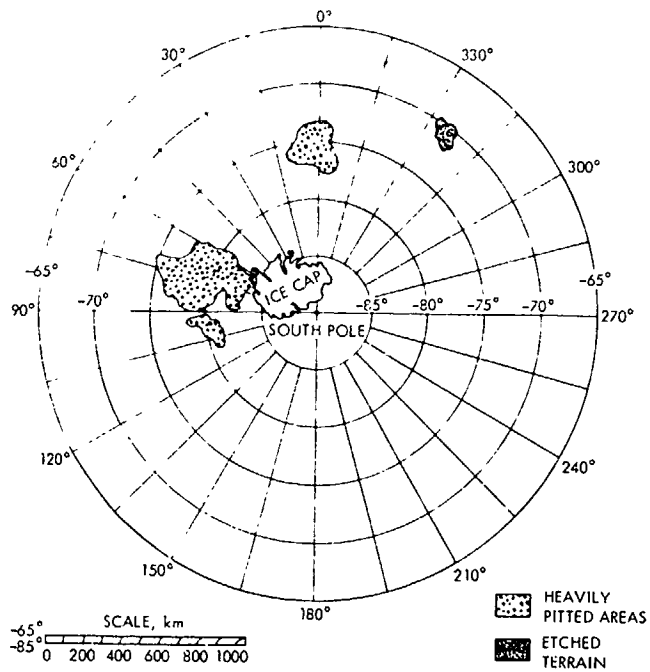
Fig. XVI-1. Map of south polar area showing location of the principal areas of pitted and etched terrain.

HEAVILY PITTED AREAS

ETCHED TERRAIN

SCALE, km
0 200 400 600 800 1000
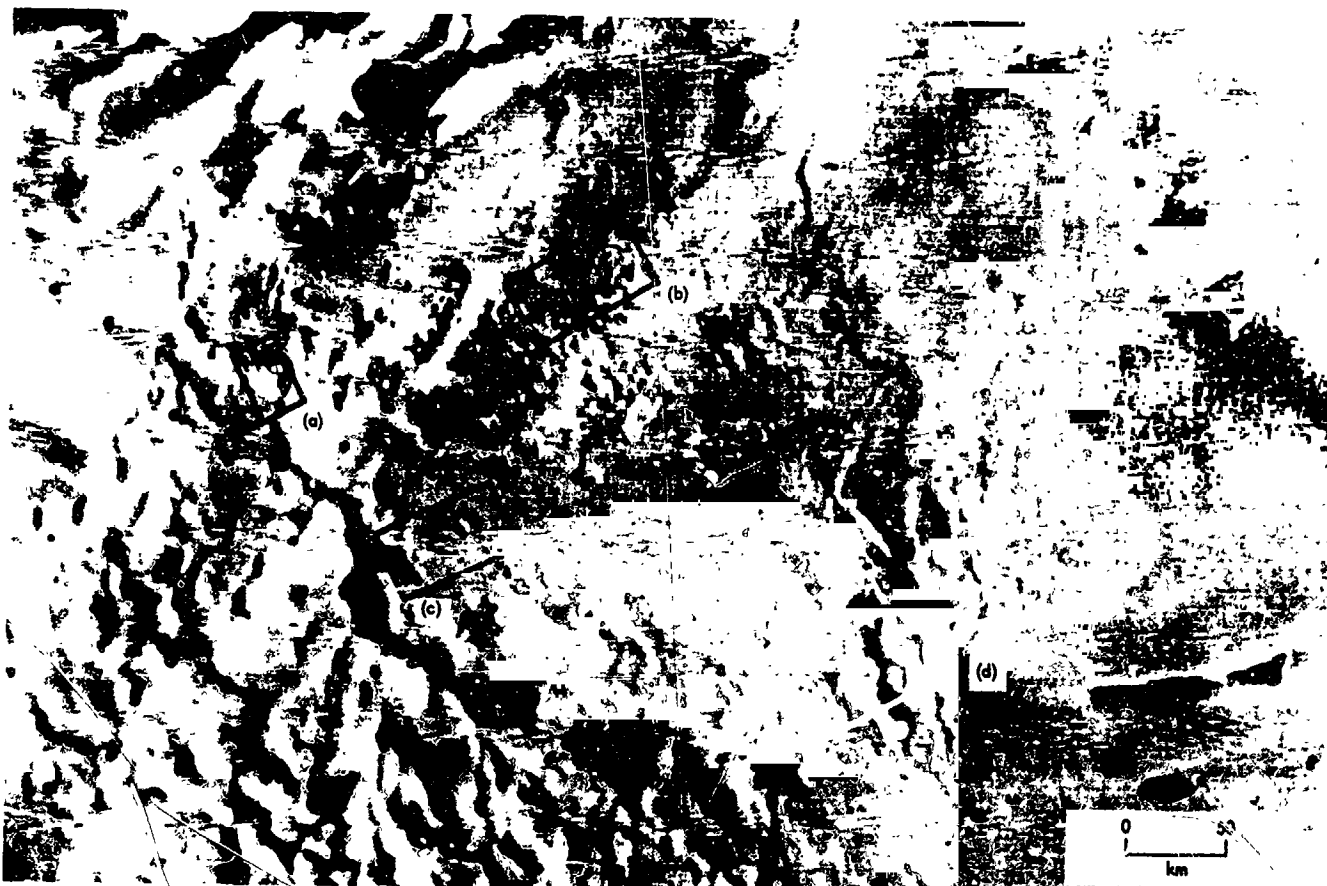
Fig. XVI-2. Pitted terrain peripheral to south polar residual ice sheet, upper left. (MTVS 4251-20, DAS 09375004) Details of pitting and related features are shown in close-up views in Fig. XVI-3.

pictures, which also show large areas of smooth terrain (at resolution of 1 to 2 km) extending north to at least 70 south latitude. About 60% of the area poleward of that latitude has very low relief. These featureless areas are now seen to be covered by mantles of material which bury the underlying cratered surface (Ref. XVI-3).

It is not a function of this article to provide a thorough description of these blankets, as they are being treated elsewhere (Ref. XVI-4; also see Section XVII of this Report). However, they are so intimately associated with pitting and etching that some knowledge of their salient characteristics is needed. The types of blankets identified are shown in Table XVI-1. The residual ice sheet and the annual frost cover are more ephemeral phenomena not treated here.

Part of the area covered by the layered blanket is a smooth featureless plain bearing the imprint of shallow linear grooves and only a few small, fresh, bowl-shaped craters. Elsewhere, this blanket has been extensively eroded, exposing a well developed internal layering (Fig. XVI-3b), which appears to be essentially horizontal. As many as 50 individual beds can be identified in single exposures. Total thickness of the layered blanket is estimated, with considerable uncertainty, at C to possibly several kilometers (Refs. XVI-2 and X .4 through

Table XVI-1. Types of Martian south polar blankets

Youngest	I Layered blanket (unpitted but highly sculptured)
	II Massive blankets
	A. Homogeneous and structureless (most extensively pitted and etched)
Oldest	B. Locally strongly structured (strongly eroded)
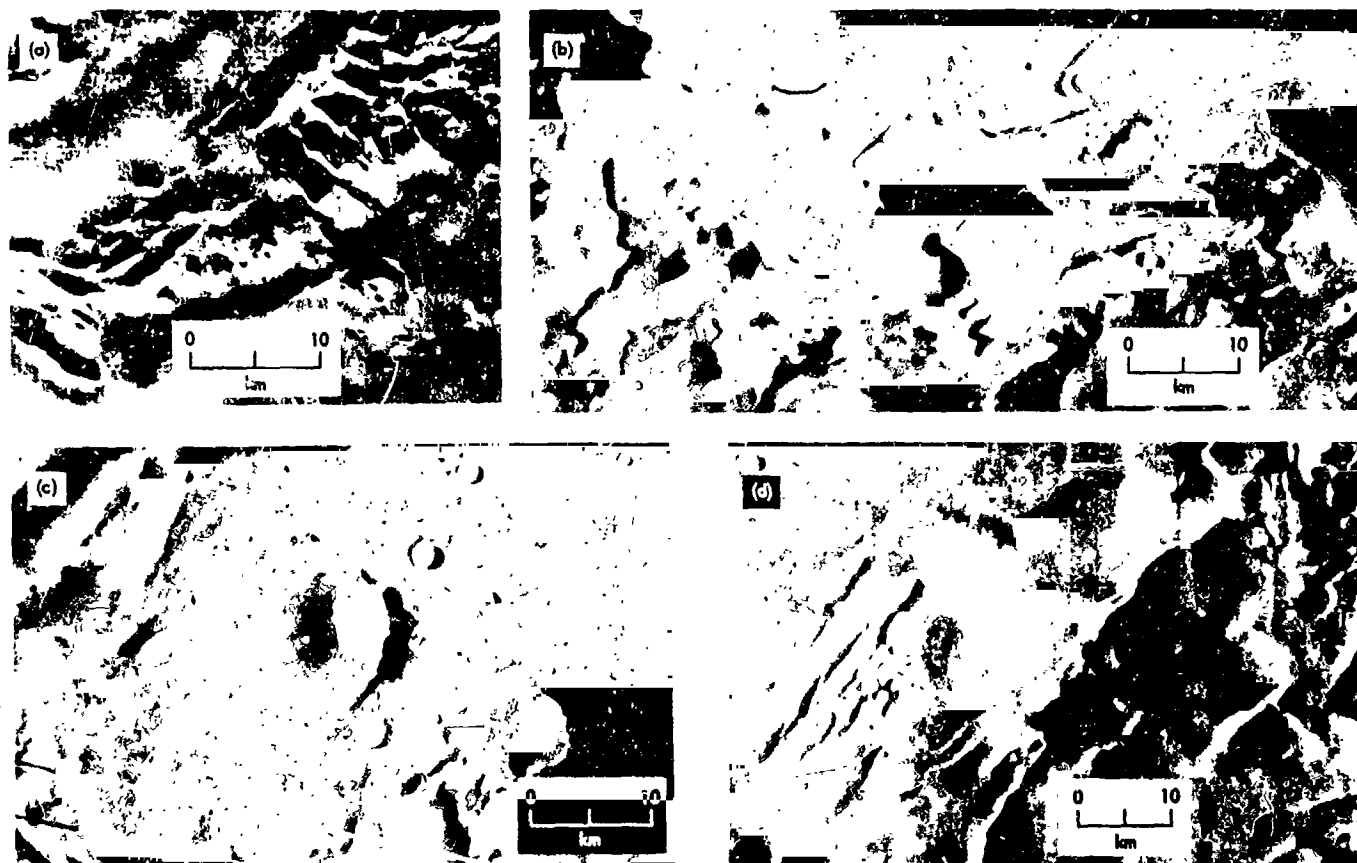
Fig. XVI-3. Details of areas of pitted terrain outlined in Fig XVI-2. (a) Structures in massive blanket etched out by wind to produce a quasi-"Inca City." (MTVS 4261-12, DAS 09734769) (b) Irregular pits in massive blanket and a remnant of the younger layered blanket. (MTVS 4247-7, DAS 09231189) (c) Pits in massive blanket with unusual abundance of young craters. (MTVS 4251-24, DAS 09375039) (d) Pit complex in massive blanket. (MTVS 4146-3, DAS 05918715)

XVI-7; also see Sections XIV, XVII, and XVIII of this Report).

The layered blanket appears to rest unconformably upon one or more massive blankets, and in some places directly upon the uneven bedrock surface. This stratigraphic relationship and the paucity of craters on its surface suggest that the layered sequence is the youngest of all the polar blankets, except the annual frost and the residual ice sheet. Although extensively eroded and locally pocked with smooth-sided, shallow hollows, the stratified blanket has not suffered pitting and etching of the type to be described.

Remnants of massive unlayered blankets mantle other parts of the south polar region. The youngest of these, seemingly homogeneous and structureless, is the most extensively pitted and etched unit (Figs. XVI-2 through XVI-5). Its thickness is conservatively estimated to range from about 400 m at 80° to 70°S to about 50 m at 65°S.

This structureless unit appears to rest unconformably on one or more still older massive blankets which locally, at least, have strongly developed near-vertical linear to gently curving structures. These structures locally consist of intersecting sets, which have been etched out by differential erosion to produce regular geometrical patterns, the most striking of which was christened "Inca City" (Fig. XVI-3a).

Constitution of both the layered and massive blankets is strictly a matter of speculation. One of the more appealing suggestions is that they are eolian accumulations consisting of fine particulate matter, some possibly of volcanic origin, which fell from the atmosphere along with, or alternating with, particles of frozen volatiles, largely H_2O and CO_2 (Refs. XVI-3, XVI-4, and XVI-8, also see Sections XV and XVII of this Report).

B. Pits

1. Geometry and Size

Pits of the south polar region are sharply outlined, closed depressions with abrupt walls (Fig. XVI-4). They range primarily from one-half to several tens of kilometers across and have a maximum depth of about 400 m, conservatively calculated from an assumed 10° wall slope. Large pits are deeper than small pits, and some compound pits, formed by integration, have stepped floor levels. Outlines range from simple and smoothly curving to cuspate, irregularly indented, and locally

angular where structural control is strong. Pits occur in groups, and the term "pitted terrain" is applied to areas where pits are especially numerous (Fig. XVI-4a). In some places, the shapes and patterns seemingly reflect control by structures in the pitted blanket or the influence of some directional property of the eroding agent. However, a lack of consistency in shape and arrangement is common elsewhere.

2. Pit Floors

Some floors are smooth and others are rough. Aside from local strong albedo markings, smooth floors display only gentle undulations or minor topographic irregularities at the foot of pit walls and a very few small (0.5 to 1 km), fresh, bowl-shaped craters.

Rough floors have knobs, ridges, and craters of two varieties: small, fresh, and bowl-shaped; and larger (to 10 km) deteriorated craters, many of which retain remnants of what looks like a central filling. It will be argued later that these rough floors have been exhumed from beneath the blanketing material. Smooth-floored pits, by contrast, have bottomed within the blanket.

3. Pit Walls

Pit walls break sharply from the surrounding upland, and most wall faces appear smooth at the limit of resolution (0.3 to 0.4 km). Only faint suggestions of orthogonal scourings are seen on some, and a few show small scallops just below the brink. Occasional slump blocks and slump cracks are associated with pits (Fig. XVI-4b). In profile, the walls appear largely straight of slope with a steepening just below the brink and a concave transition at the base. Their slope is not known, but for purposes of depth calculation it is conservatively estimated at 10°. With one possible exception, layering has not been seen in the wall materials. Outliers of the dissected blanket composing small buttes and mesas have bounding slopes with features like those of pit walls.

4. The Extra-Marginal Upland

The upland surface immediately bordering pits is mostly smooth and relatively featureless. It is but sparsely indented, to different degrees in different areas, by fresh, bowl-shaped, relatively small (<10 km) craters. The upland surface is also scarred by parallel grooves up to 0.5 km wide and several kilometers long, and it locally bears groups of irregular wavelike ridges. Additionally, upland
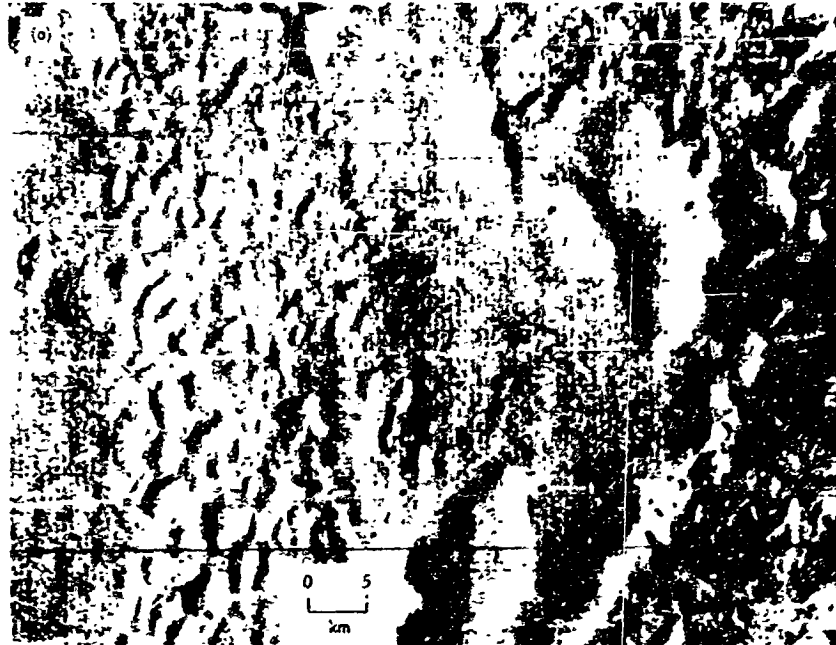
Fig. XVI-4. (a) Assemblage of pits within massive sedimentary blanket at 73.7°S, 66.8°W. (MTVS 4132-21, DAS 05453843) (b) A large complex pit at 71.1°S, 358.3°W, which exposes rough bedrock floor underlying the massive blanket. Steep, slump-marked walls, and local dark albedo markings on floor merit note. (MTVS 4234-15, DAS 08763869)

surfaces display parallel flutes, circular depressions (0.5 km across), and short irregular ridges in various configurations that produce a finely textured appearance.

C. Etched Terrain

Near its outer edge, removal of the blanketing sheet is so extensive that the terrain can no longer be characterized as pitted. It is better termed "etched" (Fig. XVI-5). Etched terrains develop where the massive blanketing material has an estimated thickness of only 50 to 100 m. As thinning occurs northward, the best etched terrain area is in the neighborhood of 70°S (Fig. XVI-1). In addition to the highly irregular planimetric arrangements of blanket remnants (Fig. XVI-5), the other striking characteristic of etched terrain is the exhumed bedrock floor.

D. Evidences of Wind Action in South Polar Area

Putting pits and etched terrain aside momentarily, attention is directed to other features on the south polar blankets which can reasonably be attributed to the work of wind. Several groups of transverse wave-like ridges are seen in narrow-angle pictures. In the best of these (Fig. XVI-6a), the ridges display shapes and patterns like those of transverse dunes on Earth, although the 0.5- to 1-km spacing of ridge crests is large by terrestrial standards. However, the resolution is about 0.5 km, so smaller features possibly present are simply not visible. A significant number of small, irregular clusters of little mounds and ridges observed in the south polar area may also be dunes, an interpretation favored by their setting within the surrounding terrain. On Earth, dunes are composed of sand, not of finer materials such as dust or clay, unless the latter are pelletized (Refs. XVI-9 and XVI-10). It seems a reasonable assumption that dunes on Mars are also composed of sand-sized particles.

Erosional features of possible eolian origin are currently more evident and more widely displayed than depositional forms on the south polar blankets. The topographic surface of the layered blanket has clearly been produced by some erosional process for the surface truncates the depositional layers. Although the topography reflects some control by the layering, it has an unusual overall appearance, lacking the integration and organization of normally dissected landscapes. The generally curving slopes, the streamlined hills and ridges, and the curiously shaped hollows and niches suggest it was formed by a

medium that flowed as a mass across the entire surface. Because the area is peripheral to the residual south polar ice cap, the possibility of glacial erosion has been entertained. Ice is a surprisingly facile agent of erosion; however, at the temperatures now prevailing in the south polar region the amount of slip occurring at the base of an ice sheet, and therefore the amount of basal erosion, would be nil. The ice would be firmly frozen to the substrate, unless one postulates a layer of liquid carbon dioxide à la Sagan (Ref. XVI-7; also see Section XVIII of this Report).

The other agent likely to produce a morphology of this type is wind, and the topographic surface looks more characteristic of wind scouring than ice scouring, especially in terms of hollows, niches, and re-entrants. The probability of wind scour is supported by the abundant quasi-parallel grooves, resembling large yardangs (Ref. XVI-9), which curve, fan out, or converge in delicate adjustment to larger topographic forms. Even more suggestive of wind action are short stubby flutes that mark the surface in some areas. Plots of groove and flute orientation (Ref. XVI-8; also see Section XV of this Report) suggest that the wind blew outward from the south pole in a counterclockwise spiral.

In summary, the features and relationships just described suggest that winds have strongly scoured the surface of the presumably fine-grained sedimentary blankets of the south polar region, a conclusion also reached by Cutts (Ref. XVI-8; also see Section XV).

E. Exhumation

The case for exhumation is based principally on geometrical patterns and the unusual appearance of knobs, ridges, and craters on exhumed bedrock surfaces compared with their appearance elsewhere on Mars. The following points are noted: (1) The complex planimetric pattern involving blanketed spots and intervening lowland areas would be difficult, or impossible, to create by any depositional mode. It is easily formed by selective erosion. (2) The highly irregular, frayed margin of the blanket and the outliers of blanket material forming small buttes and mesas suggest erosional removal. (3) Windows within the remnant blanket, which expose the underlying rough floor, have the configuration of erosional rather than depositional features. (4) The interior depression of many craters on the bedrock floor appears to be largely filled, creating what might be called a crater ring. (5) Bedrock knobs and ridges rising above the lowland have a peculiar appearance, possibly resulting from a residual
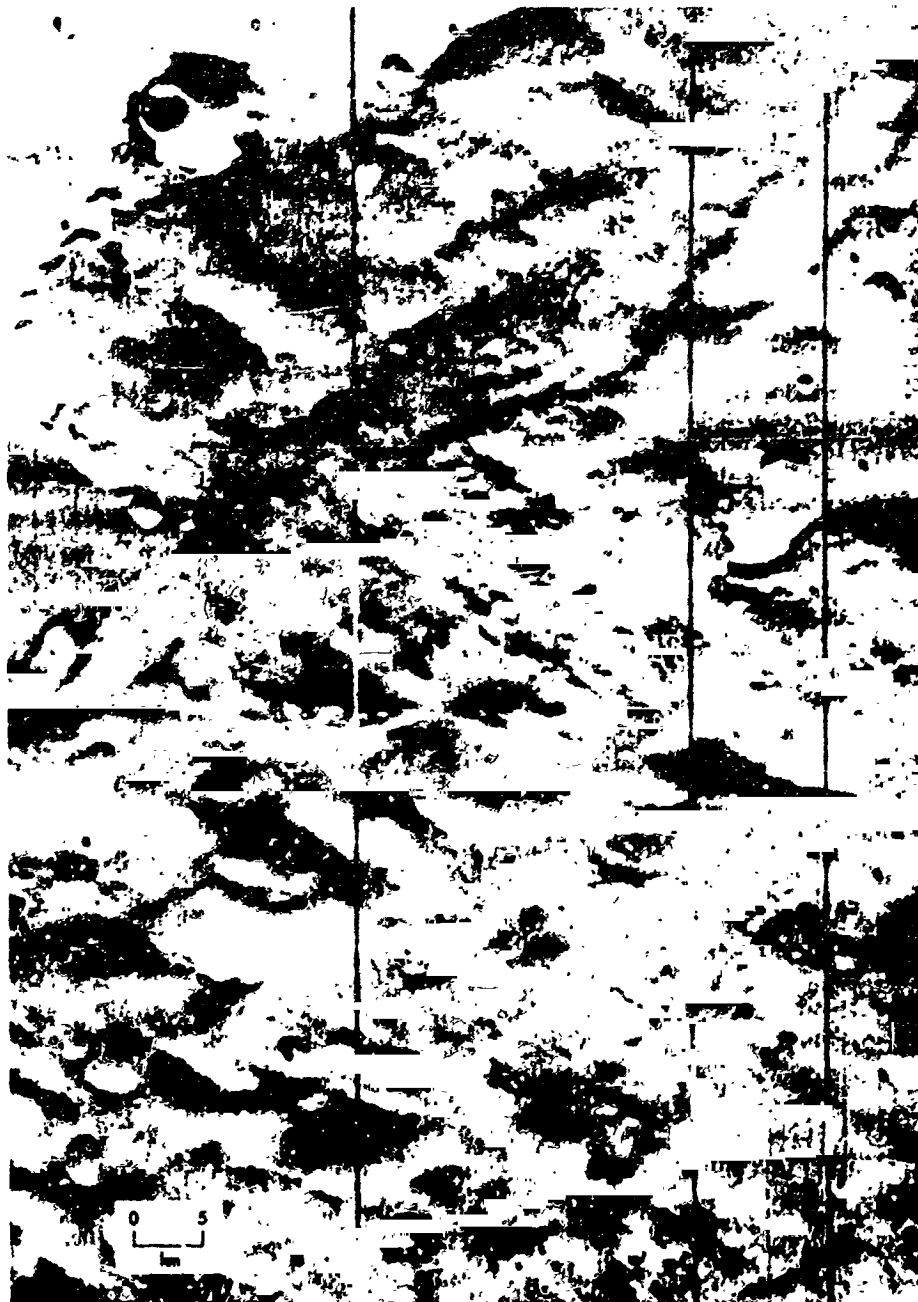
Fig. XVI-5. Representative etched terrain at 67.1°S, 326.1°W. Ragged edge of thin massive blanket, rough exhumed bedrock floor, outlier of blanket, and small fresh craters all notable. (MTVS 4200-105, DAS 07648203)

Fig. XVI-6. (a) Cluster of transverse dunes in a broad hollow on surface of layered blanket at 81.9°S, 48.7°W. (MTVS 4286-104, DAS 10684504) (b) Linear grooves and flutes attributed to wind cutting on surface of layered blanket at 86.7°S, 270°W. (MTVS 4248-12, DAS 09267099)

mantling of their flanks. (6) In some instances, a part of a crater may be almost wholly obscured by blanketing material, but the other part is clearly exposed. It is easier to produce this relationship by erosion rather than by deposition if the blanketing material has been laid down from a suspended state in the atmosphere. (7) The number and maximum size of fresh, bowl-shaped craters indenting the surface of the massive blanket remnants, although small, are significantly greater than on the rough lowland floor. Although the lowland surface is older in absolute terms, as shown by its population of larger degraded craters, it has been exposed to recent cratering for a shorter time. While the blanket was accumulating fresh craters, the underlying floor was still buried and protected.

Exhumation is probably not limited to the south polar region, because other areas on Mars also show the peculiar appearance of an exhumed topography (Ref. XVI-11; also see Section IX of this Report). However, exhumation is seemingly widespread in the south polar region and constitutes a significant chapter in its history.

F. Origin of Pits and Etched Terrain

Closed depressions can be created by localized removal of material upward, downward, or laterally. The fact that the bedrock surface, upon which the surficial blankets of the south polar region rest, appears intact in pit floors indicates that localized downward movement as a mass has not occurred. The configuration and arrangement of the pits further indicate that lateral spreading is an unlikely cause. This leaves upward movement as the most likely possibility, and explosion or deflation as the most probable mechanisms.

Explosions, whether of volcanic or impact origin, create predominantly circular depressions surrounded by a rim of ejected debris, neither of which characterizes the south polar pits. Thus, by elimination, deflation appears to be the most reasonable mechanism, and this possibility is supported by the evidence for extensive wind erosion just recounted. If the polar region blankets contain frozen volatiles, evaporation could also contribute significantly to pit formation, and the genetic process would then involve a combination of deflation and ablation. Restriction of the pits to the south polar blankets, which may be wholly of eolian origin (Refs. XVI-4 and XVI-8; also see Sections XV and XVII of this Report), also favors wind work. What the atmosphere brings, the atmosphere can presumably take away. A blanket of eolian origin will

necessarily be composed of well sorted, uniformly fine-grained debris, which means that armoring of the surface by concentrations of coarse, immobile, deflation-inhibiting particles would not develop. The presence of dunes in the polar area, presumably composed of mobile sand-sized particles, is further supportive of the eolian hypothesis. Few things are more effective than saltating sand grains for blasting finer particles into the air so they can be carried away in suspension.

The modest depth, an estimated 50 to 400 m, of polar pits is also a favorable factor. Although 400 m exceeds the depth of hollows on Earth attributed to deflation (Refs. XVI-12 through XVI-15), it is not inconsistent with the estimated strength (Ref. XVI-16; also see Section X of this Report), durations, and virtually unopposed action of winds on Mars. Deflation on Earth is almost always opposed by other processes tending to fill any hollows created by wind.

Walls of Martian polar depressions are sharp-brinked and more abrupt than walls of most terrestrial deflation hollows of large size. Slumps and orthogonal scars on some Martian pit walls suggest the possibility of wall recession caused by an undermining process. In this regard, frozen volatiles could be important, especially if they happen to be concentrated or enriched within specific zones or layers. Their evaporation could produce an undermining that would keep the walls steep and cause them to recede.

Etched terrain is regarded simply as an advanced stage of pit development that occurs primarily where the mantling blanket is thin (50 to 100 m). Expanded pits have coalesced, producing large bedrock areas denuded of the overlying mantle.

For these reasons and considerations, the pits and etched terrain of the south polar region are attributed to a combination of deflation and ablation.

G. Discussion

The south polar pits and etched terrain have interesting implication as to the history of the polar region and of the planet. They attest to alternating episodes of eolian deposition and erosion. Sometimes the south polar area has served as a sump for the accumulation of airborne debris and associated particles of frozen volatiles. At other times, the wind patterns or wind effectiveness

change, and the atmosphere begins to remove the blanket of material it has earlier spread over the south polar region.

Causes for the alternating episodes of erosion and deposition are speculative. They could be related to astrophysical variations involving precession of the planetary axis and other orbital perturbations (Ref. XVI-17) or possibly to episodes of volcanism, of which there is ample independent evidence, that periodically filled the Martian atmosphere with volatiles and fine volcanic dust, some of which ended up in the polar sumps because of considerations previously outlined by Leighton and Murray (Ref. XVI-18). During periods of volcanic quiescence, the prevailing polar winds could have partly removed the accumulated materials by deflation and ablation.

The surficial appearance of south polar blankets indicates that the present, or the immediate past, has been a period primarily of removal. Relationships between individual blankets further suggest that erosional removal has not always been completed before further accumulation occurred. The alternation between deposition and erosion has happened more than once, and possibly more often than the visible evidence indicates. The freshness, paucity, and small size of craters on the current surfaces of blanket remnants indicate that those particular surfaces are not old in terms of Martian history, and that different blankets are clearly of different ages. The fact that any craters are seen at all indicates some antiquity in view of the rather strong flux of erosional and depositional activity. The older blanket remnants may date back tens to hundreds of millions of years.

An additional indication of at least modest antiquity for the older massive blanket remnants is their internal structure of seemingly near-vertical fractures. Processes localized by these structures could have hardened adjacent materials, which were then etched into positive relief by subsequent erosion (Fig. XVI-3a). Volcanic fluids or gases moving surfaceward along fractures could result in such an alteration, a possibility that merits consideration because of the independent evidence of polar-region volcanism provided by features interpreted as cones, craters, and lava flows. However, the respective temporal relationship of local volcanism and blanket accumulation is not known.

A record of accumulation and erosion is preserved in the south polar region and presumably in the north polar area as well (Ref. XVI-2; also see Section XVI of this Report). These episodes must reflect changes that also affect non-polar areas of Mars, and such relationships are described by Soderblom et al. in Ref. XVI-11 (also see Section IX of this Report).

References

XVI-1. Sharp, R. P., Murray, B.C., Leighton, R. B., Soderblom, L. A., and Cutts, J. A., "The Surface of Mars: 4. South Polar Cap," *J. Geophys. Res*, Vol. 76, p. 357, 1971.

XVI-2. Soderblom, L. A., Malin, M. C., Cutts, J. A., and Murray, B. C., "Mariner 9 Observations of the Surface of Mars in the North Polar Region," *J. Geophys. Res.*, Vol. 78, 1973.

XVI-3. Murray, B. C., Soderblom, L. A., Cutts, J. A., Sharp, R. P., Milton, D. J., and Leighton, R. B., "Geological Framework of the South Polar Region of Mars," *Icarus*, Vol. 17, p. 328, 1972.

References (contd)

XVI-4. Cutts, J. A., "Nature and Origin of Layered Deposits of the Martian Polar Regions," *J. Geophys. Res.*, Vol. 78, 1973.

XVI-5. Murray, B. C., and Malin, M. C., "Volatiles on Mars—Theory vs Observation (submitted to *Science*).

XVI-6. Murray, B. C., and Malin, M. C., "Mars Atmosphere—A Late Arrival?" (in preparation).

XVI-7. Sagan, C., "Liquid Carbon Dioxide and the Martian Polar Laminae," *J. Geophys. Res.*, Vol. 78, 1973.

XVI-8. Cutts, J. A., "Wind Erosion in the Martian Polar Regions," *J. Geophys. Res.*, Vol. 78, 1973.

XVI-9. Blackwelder, E., "Yardangs," *Geol. Soc. Amer. Bull.*, Vol. 45, p. 159, 1934.

XVI-10. Blackwelder, E., "Evolution of Desert Playas," *Geol. Soc. Amer. Bull.*, Vol. 57, p. 1179, 1946.

XVI-11. Soderblom, L. A., Kreidler, T. J., and Masursky, H., "The Latitudinal Distribution of a Debris Mantle on the Martian Surface," *J. Geophys. Res.*, Vol. 78, 1973.

XVI-12. Ball, J., "Problems of the Libyan Desert," *Geogr. J.*, Vol. 70, p. 21, 1927.

XVI-13. Ball, J., "The Qattara Depression of the Libya Desert and the Possibility of Its Utilization for Power Production," *Geogr. J.*, Vol. 83, p. 289, 1933.

XVI-14. Berkey, C. P., and Morris, F. K., "Geology of Mongolia," *Amer. Mus. Nat. Hist.*, Vol. 2, *Natural History of Asia*, 475 pp., 1927.

XVI-15. Smith, H. T. U., *Photo-interpretation Studies of Desert Basins in Northern Africa*, Air Force Cambridge Res. Labs. Rept. 68-0590, 77 pp., 1969.

XVI-16. McCauley, J. F., "Mariner 9 Evidence for Wind Erosion in the Equatorial and Mid-Latitude Regions of Mars," *J. Geophys. Res.*, Vol. 78, 1973.

XVI-17. Murray, B. C., Ward W. R., and Yeung, S. C., "Periodic Insolation Variations on Mars," Vol. 180, p. 638, 1973.

XVI-18. Leighton, R. B., and Murray, B. C., "Behavior of Carbon Dioxide and Other Volatiles on Mars," *Science*, Vol. 153, p. 133, 1966.

Acknowledgments

PRECEDING PAGE BLANK NOT FILMED

XVII. Nature and Origin of Layered Deposits of the Martian Polar Regions

James A. Cutts

Jet Propulsion Laboratory/California Institute of Technology, Pasadena, California 91103

One of the most remarkable contributions of the *Mariner 9* television reconnaissance of Mars has been the discovery of complex sequences of layered deposits in the Martian polar regions. These deposits, termed "laminated terrain" by Murray et al. (Ref. XVII-1), were unanticipated before *Mariner 9*. Although the integration of photographic materials into maps of this part of Mars and the reduction of important data on topography are, as yet, incomplete, several basic characteristics that pertain directly to their nature and origin already have been recognized (Table XVII-1). The purpose of this article is to present pictorial evidence for these basic characteristics, to draw inferences about the nature of the deposits and the depositional process, and to express a particular set of ideas on the depositional and erosional history of Mars. The origin of the layered deposits is also discussed by Murray et al. (Ref. XVII-2) and Sagan (Ref. XVII-3; also see Section XVIII of this Report), who draw significantly different conclusions from the *Mariner 9* observations than those presented here.

A. Basic Characteristics of Layered Deposits

Layered deposits have been observed by the *Mariner 9* television cameras in both north and south polar regions (Refs. XVII-1 and XVII-4; also see Section XIV of this Report). In the northern hemisphere, the deposits cover

Table XVII-1. Nature and origin of laminated terrain

P1	Fine particles of rock powder (1 to 50 μm) are formed by mechanical means, principally impact interaction from the sand-sized debris produced by mass movements such as scarp recession in the depressed terrains and lowlands surrounding Nix Olympica
T1	They are carried away in suspension by winds which formed them
D1	They are deposited, preferentially, in the polar regions where the conditions of polar winter favor deposition
T2	A change in the polar environment, perhaps a reduction in the extent of the perennial frost cap, results in destabilization of the deposits and fine material is eroded and transported away from the pole
D2	Minor dune deposits form on and immediately peripheral to laminated terrain
D3	A major depositional belt forms between the 50° and 70° parallels

about 1.1×10^6 km² of the planetary surface; in the southern hemisphere they are somewhat more extensive and cover 1.5×10^6 km². Although they are not distributed symmetrically about the areographic poles (90° north and south), the layered deposits occupy most of the area poleward of the 80° parallels, appear to be confined to the area poleward of 70°, and underlie the remnant perennial frost caps (Fig. XVII-1).

(a) 180°

90° — 270°

0°

(b) 0°

90° 270°

180°
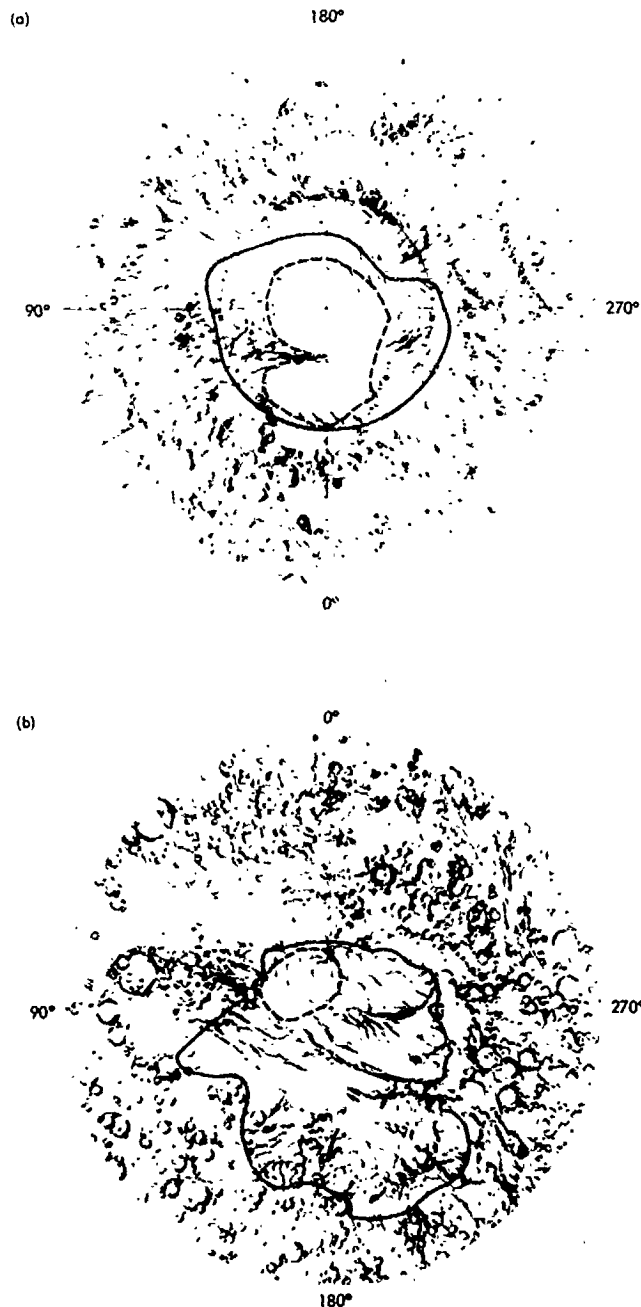
Fig. XVII-1. Distribution of layered deposits in the polar regions of Mars. Reproduced from maps published '(a) Murray et al. (Ref. XVII-1) and (b) Soderblom et al. (Ref. XVII-4; also see Section XIV of this report). The perennial polar caps underlie the layered deposits in both hemispheres.

Although layering is clearly evident in the deposits of both polar regions, a more detailed description of the stratigraphic characteristics and the surface morphology in general is possible in the south polar region because the photographic coverage is more extensive and of higher resolution. Figure XVII-2 shows one of the most striking examples of layering in the materials underlying the polar regions in which the relationship to topography is most explicit. Along the slope separating the fluted surface of the upland (upper left) from the mottled plains (lower right) can be seen parallel light and dark banding which converges near the top of the frame into an undifferentiated shaded slope. Where one of these bands changes direction near the bottom of the frame (arrow), it changes tone from dark to light. The relationship to the solar azimuth indicates that this particular band represents a sharp change of slope and suggests that the entire banded zone is a terraced slope. Lay.ring in the underlying materials is inferred from the continuity and conformal character of the terracing. Precise quantitative measurements of the altitude difference across the terraced slope, which could be used to determine the thickness of individual layers, are not available. However, if the terraces slope at between 10° and 20°, then the layers are probably between 10 and 50 m thick.

Banding is not confined to the relatively simple topography shown in Fig. XVII-2, but occurs in many different topographic settings. Eight different examples are seen in Figs. XVII-3 and XVII-4, which also display varying degrees of visibility of the layering. The bands appear to follow contours and are tentatively interpreted as the edges of near-horizontal strata outcropping on smooth slopes of varying inclinations. It seems clear that the strata are exposed because of erosion. Where erosion has produced steep slopes (upper part of Fig. XVII-2), the bands are narrow; where the slopes are shallow (lower part of Figs. XVII-2, XVII-3a, XVII-4a, and XVII-4d), the bands appear broader. In some cases, the bands may not correspond to changes of slope, but merely to material differences that appear as brightness contrasts (Figs. XVII-3a and XVII-3c). The variety in the visibility of the layering may indicate differences in the surface processes that have operated on the layered strata.

In all of these pictures there is a consistent impression of the continuity of the stratification and an absence of splitting and joining, or pinching and thickening of the layers. There are a few examples (Fig. XVII-2, center right; Fig. XVII-4d, lower right) where the layering seems irregular, but even these may be a consequence of exposure at a surface of anomalous local topographic relief. These features may also represent deviations from near-horizontal orientation of the layering, an implicit assumption in the interpretations of the previous paragraph. There are also some strange bumps within certain
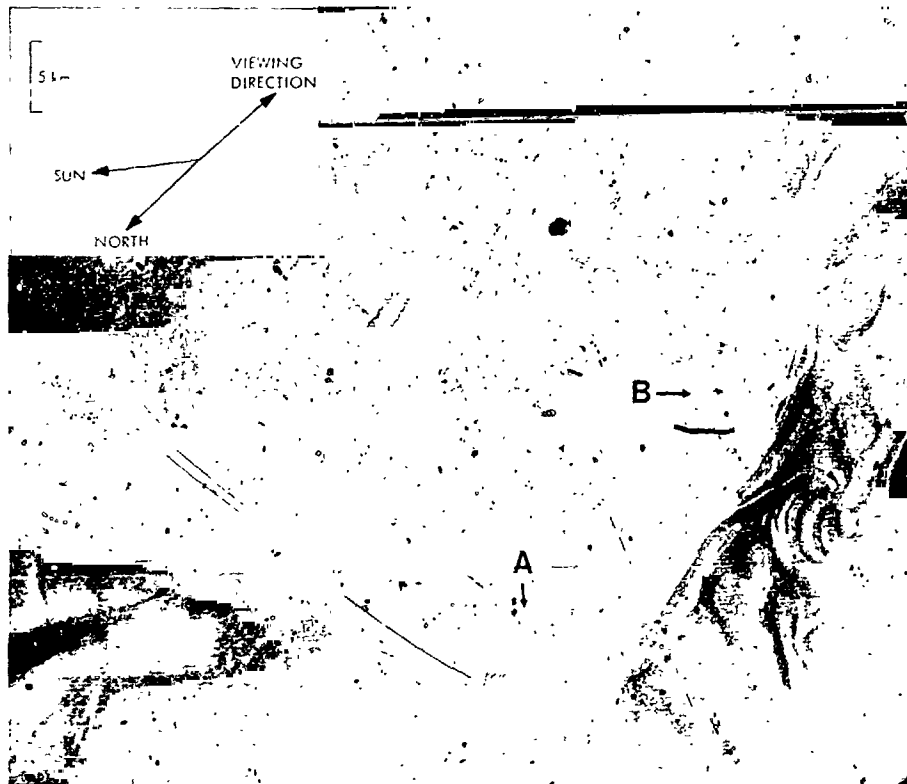
Fig. XVII-2. The unique characteristic of the laminated terrains is the layered nature of the deposits that underlie them. These layers are most apparent when exposed at the escarpments which extend for hundreds of kilometers across the polar region. At one of these escarpments, the conformal bands are interpreted as a terraced escarpment separating the fluted upland (top) from the complex sinuous features of the lowland (right). One of the broader bands changes tone from light to dark at A where it is parallel to the solar azimuthal direction, indicating that it is terraced and suggesting that the entire escarpment is terraced. Each visible terrace is interpreted as a single layer or in some cases multiple layers. As the slope gets steeper along the escarpment, a number of narrow terraces, which seem to be associated with thin layers (B), merge into a broader dark band similar in appearance to the much broader and deeper terrace which was first described (A). The terrace may therefore consist of a number of sublayers which erosion has not effectively separated. The very finest dark bands seen at B are thought to correspond to layers about 30 m thick. Scale and solar viewing and north azimuthal directions are identified in the figure. The viewing angle is 27°, and the solar zenith angle 70°. (MTVS 4213 21. DAS 08080243)

layers (Fig. XVII-2). However, for the most part, individual layers seem uniformly thick and conform with one another in the striking fashion which first prompted the descriptive term "laminated terrain."

It is much more difficult to evaluate variations in thickness between layers. An initial impression is that the widths of the outcrops where layers are exposed are rather similar. Two factors may tend to reinforce this view. First, there are no examples of extremely broad outcrops embedded between thinner ones. Second, we have no knowledge of finer layering beyond the resolution limit of the *Mariner 9* television cameras. However,

on closer scrutiny of the pictures, there are definite variations in the width of outcrops that emerge.

There may be much less variation in layer thickness than in outcrop or terrace width. Variations in the slope at which layers are exposed seem to account for much of the variation in outcrop width in Fig. XVII-2. Terraces also appear to be less well developed on some layers than others, giving the impression of composite thicker layers. Furthermore, it is only the shallow slopes where the layer outcrops are wide that the finer layers can be resolved. Accounting for these effects in Fig. XVII-2, the broader dark bands are interpreted to be composite
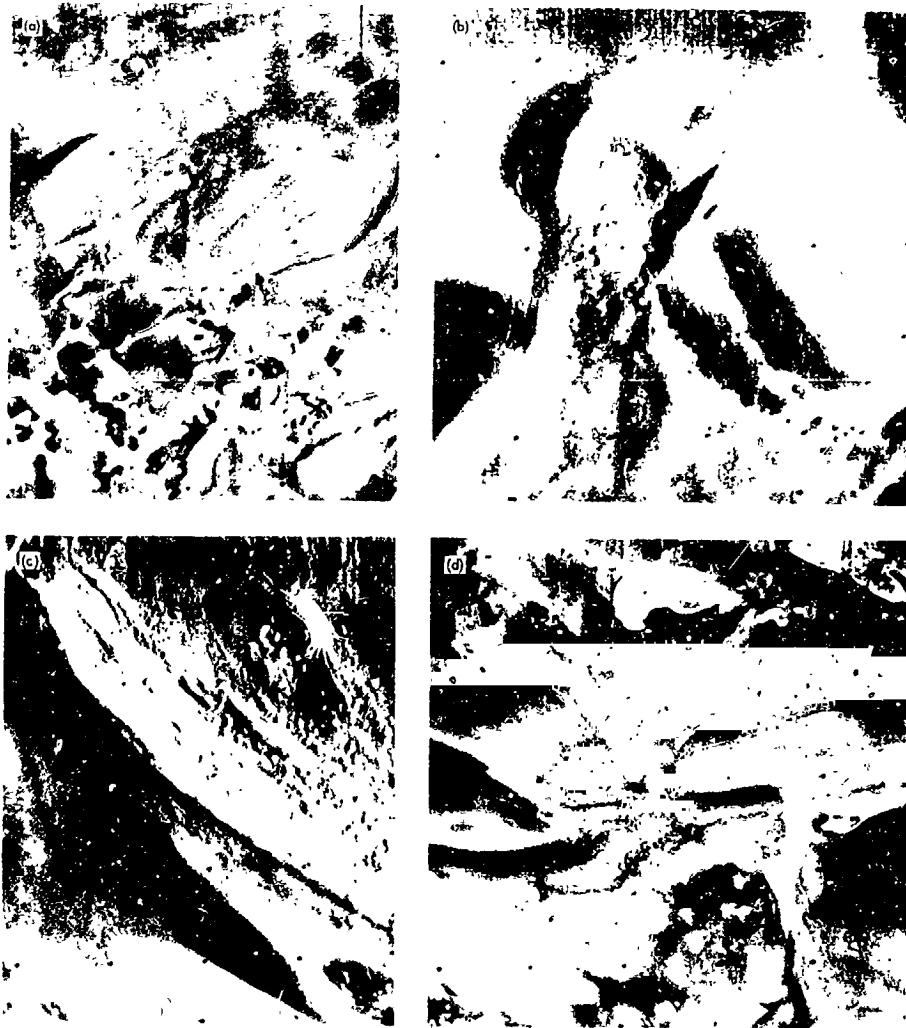
Fig. XVII-3. (a) The oval tableland of layered deposits partially covers the pitted terrain which emerges near the bottom of the frame. (MTVS 4247-7, DAS 09231189) (b) Cratered terrains also come into contact with the layered deposits; a crater is apparently being exhumed from beneath the deposits. (MTVS 4226-3, DAS 08151853) (c) The characteristics of the layered deposits are not the same everywhere. The more massive layering and the indentation seen in the escarpment could reflect a meteorite impact or some other form of post-depositional modification. (MTVS 4264-8, DAS 09806799) (d) The frost of the perennial south cap which lies on top of the layered deposits is not thick, at least in this area, relative to the escarpment height. (MTVS 4216-7, DAS 09734629)
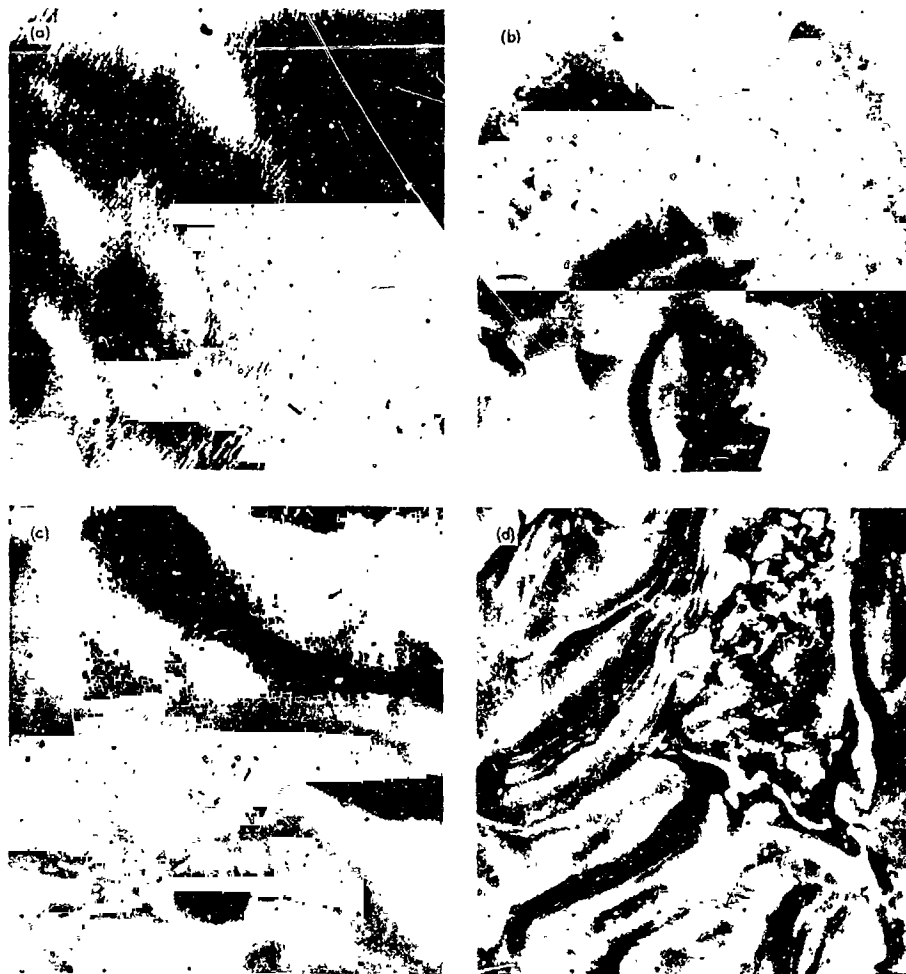
Fig. XVII-4. Areographic variations in the characteristics of the surface of the layered deposits. The regular patterns of pits seen in (a) are typical of the region of a lobe of terrain near 75°S. These features have been interpreted as wind erosional forms with terrestrial analogies (Paper I; also see Section XV of this report). The gross patterns of light and dark in this frame are real and may be related to the layering in the subsurface. The surface in this area is eroded to a plain that is almost parallel to the plain of the layers. (MTVS 4222-5, DAS 08367809) (b) Layered deposits mantle a cratered terrain surface, and most of the rim of a crater is still visible (see upper left). Layering is visible in the wall of the large flat-floored basin (bottom center). Dark markings in the floor of this basin and elsewhere are similar to features observed in the floors of craters in many parts of Mars. They have been attributed to saltation transport and sorting of materials (Ref. XVII-6; see Section XI of this report). (MTVS 4167-95, DAS 06604713) (c) Dark markings in Thyles Mons (lower left) are associated with fine-scale patterns quite different from those in Fig. XVII-4a. The dark markings and the muted character of the layering in this part of the layered deposits suggests horizontal redistribution of materials in this area also, and the fine patterns may be dunes. (MTVS 4233-11, DAS 08728169) (d) Although exposures of the layered deposits are very much in evidence, the most remarkable feature of this picture is the abundance of small bright spots in the segment that is partly frost covered. These spots may correspond to accumulations of ice in pits and other topographically shaded locations. If this is so, the surrounding terrain may be much rougher than it appears to be. (MTVS 4261-20, DAS 09734909)

layers, and the total number of layers is estimated to far exceed the number of dark bands that can be counted. The finer-scale outcrops which are resolved (B) seem to have similar widths, implying that the corresponding layers have similar thicknesses.

Although banding is perhaps the most distinctive feature of the terrain surface underlain by the layered deposits, this surface displays other significant characteristics; the most surprising is the absence of recognizable impact craters. This does not provide any direct information regarding the time the underlying layers were formed, contrary to the earlier report of Murray et al. (Ref. XVII-1). Impact craters could have formed after the layers were deposited, but before the erosion that exposed the layers.

Despite the absence of impact craters the layered terrain surface is not smooth, but displays a considerable amount of topographic relief at the smallest scales visible to the *Mariner 9* cameras. Much of the grooving and fluting is most readily attributed to erosion (Ref. XVII-5, hereafter called Paper I; also see Section XV of this Report). However, some of the features and textures are more suggestive of dunes (Ref. XVII-6; also see Section XI of this Report). Although some albedo differences (Figs. XVII-3a, XVII-3c, and XVII-4a) suggest differential erosion of the layers, others (the dark markings in Figs. XVII-4b and XVII-4c) show no close relationship to the

layering and seem more readily explained by surface reworking, redistribution, and sorting of materials.

Layered deposits also show distinctive topography at much larger scales. Characteristic of the deposits are continuous escarpments that display a variety of planimetric forms. The slope visible in Fig. XVII-2 is part of one escarpment that extends in a lobe almost to 70°S. It is shown in more detail in Figure 4 of Paper I (see Fig. XV-4 of this Report). More typical is the occurrence of en echelon forms. Near the poles, they are subcircular facing away from the poles, and provide the site of the perennial polar cap (Fig. XVII-5b). In another location, Thyles Mons (Fig. XVII-5a), they are sinuous; the exact nature of the topography is obscured by the dark albedo markings with which they are associated. The layered deposits also are characterized by large-scale curving channels and major escarpments re-entrants, which are described in more detail in Paper I.

The boundary relationships of the layered deposits (Fig. XVII-3) have considerable bearing on their age and physical properties. The layered deposits have clearly buried pitted terrain (Fig. XVII-3a) and cratered terrain (Fig. XVII-3b), and the visible superposition relationships suggest an erosional unconformity (Ref. XVII-1). It is also apparent that the boundary between the layered deposits and the underlying terrains does not represent the maximum areal extent of deposition, but merely a
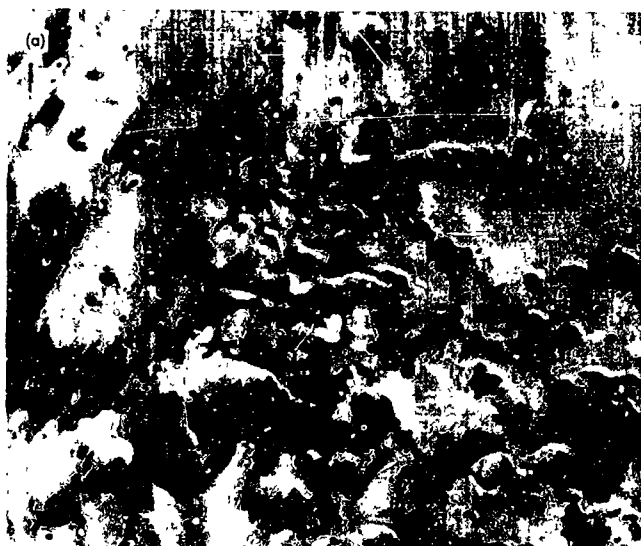
Fig. XVII-5. Escarpments on the surface of layered terrain which are large-scale features typical of laminated terrain. The escarpments shown at high resolution in Fig. XVII-2a can have quite varied planimetric form. (a) Those seen in the region of Thyles Mons (77°S, 155°W) and known informally as the "riffles" exhibit a sinuous form with extensive albedo variations. (MTVS 4179-6, DAS 06964758) (b) Beneath the residual south polar cap, circular forms are more in evidence. (MTVS 4173-8, DAS 06784788)

stage of erosional stripping. The processes of burial and the subsequent removal of materials have certainly modified the original landscape, and remnants of the mantling blanket may still remain. However, exhumed topographic features such as craters seem to preserve much of their original structure. This sets some limitations on the character of the deposits, the depositional process, and the mechanism of exhumation of the terrain. A more complete descriptive treatment of the layered deposits and their relationship to other terrains is in preparation.

B. Processes Involved in the Formation of the Layered Deposits

Some fundamental inferences about the nature of the layered deposits can be drawn from the characteristics already discussed. Their apparent uniqueness to the polar regions is interpreted to mean that the Martian atmosphere was involved in their formation. There seem to be three possibilities that could occur singly or in some combination. The layered deposits could consist almost entirely of condensed volatiles which may be mantled by only a thin veneer of silicate debris. Alternatively, the layered deposits could be predominantly nonvolatile materials which were at one time precipitated from the atmosphere in association with condensing volatiles. Finally, volatiles could be neither a component of the deposits nor an agent in their formation, in which case the formation of the deposits must be attributed to some unique meteorologic characteristic of the polar regions favoring eolian accumulation. The lack of modification of the landscape underlying the layered deposits also tends to support the idea of a deposit of loosely consolidated or volatile materials removed easily without destroying the original surface.

The nature of the layering places other constraints on the mode of formation of the deposits. The uniformity in thickness, conformance to regional slope, and the absence of complex splitting and joining of the layers argues that deposition occurred contemporaneously over a broad area, and hence directly from atmospheric suspension, in much the manner that snow, frost, or loess (deposits of windblown dust) is formed on Earth. An alternative possibility, that layers have accumulated by lateral accretion, is regarded as much less probable. Terrestrial sandstone formations which are laterally persistent and fairly uniform in thickness have formed from accreting dune sand. If the polar layered deposits formed in this manner, this requires sources of material outside the polar regions and winds spreading saltating debris inward toward the pole. Yet in Paper I, the observational

evidence presented suggests that material is being eroded by prevailing winds blowing away from the poles. Although the layers are not thought to be dune sand, this is not to say that saltation has not been operative in the layered terrain. On the contrary it is probably responsible for much of the post-depositional modification of these surfaces.

The existence of repetitive layers of similar thickness bears most directly on the depositional history. It signifies either a long-term uniform rate of supply of materials, with the deposition modulated by events equally spaced in time, or episodic depositional events of approximately equal volume, although not necessarily occurring at equal intervals. In addition, variations in response to erosion must have been introduced between the top and bottom of each layer, as erosion has been uneven and has produced terraced slopes.

It requires little imagination to realize that the layered deposits of Mars must record the history of the Martian surface environment in much the same way as the pages of Earth's history are defined by terrestrial sedimentary rocks. One of the most interesting questions is the time span represented by the Martian deposits. Fundamental to this question are their composition and the source from which they were derived. Of further interest are the mechanism of formation and the reason for their stability in the polar environment. All of these questions are necessarily interrelated and, in seeking answers to one question, it is possible to gain further insight into the others. The first to be explored in detail here is the available source of materials, which strongly constrains the age and composition of the layered deposits.

C. Source of Materials

The layered deposits cover 2.6×10^6 km² in both hemispheres. Estimates of the number of layers and the thickness of each layer, together with preliminary maps of the relief in this part of Mars (Ref. XVII-7), suggest an average depth of about 2 km. The lack of precision in this estimate should be obvious. Thus, the approximate total volume of layered deposits on Mars is found to be 5×10^6 km³. Expressed another way, this is the volume of materials that would cover the entire planet uniformly to a depth of 35 m.

Although the volume of deposits seems vast, we can place it in perspective by some terrestrial comparisons. It is only a small percentage of the total volume of sedimentary rocks on the surface of Earth; it is only one-fifth

of the volume of the Antarctic ice cap, and it is only a little larger than the Greenland ice cap (Ref. XVII-8). One approach in pursuing the composition and history of the layered deposits which might show whether they are closer to an ice cap or to sedimentary rocks in their characteristics, is to examine possible sources of materials.

Early explorations of Mars by Mariners 6 and 7 suggested that Mars was almost entirely crater-covered and that the planet had never outgassed. The discovery of extensive volcanic regions by Mariner 9 suggests that volatiles such as water and carbon dioxide have been released into the surface environment, but provide little indication of what quantities were produced. Whatever water was produced must have been partitioned between accumulation at the poles and adsorption on the Martian subsurface (Ref. XVII-9) or completely lost from the planet. Escape of hydrogen, presumably resulting from the photodissociation of water, has been observed (Ref. XVII-10), and a plausible explanation of an equivalent rate of loss of the oxygen produced has been proposed (Ref. XVII-11).

A more profitable line of inquiry is to search for sources of materials other than water and carbon dioxide. Although the layered deposits may contain these volatiles, they are clearly not totally composed of them. The albedos of the layered deposits exposed outside the remnant polar caps are too low for this to be the case. Temperatures in this region also seem to preclude the stability of carbon dioxide even if it were deeply buried and make the perennial cap a far more favorable location for permanent deposits of water. Other species of frozen volatiles seem unlikely components, as Mariner 9 spectral observations show no evidence for their occurrence. Thus, we suspect that nonvolatile materials and probably silicates may be a significant part of the layered deposits. If we were to demonstrate that water and carbon dioxide ices were absent or only represented a small part of their total value, silicates would almost certainly be the dominant component.

From what part of Mars could any silicate materials in the layered deposits be derived? It is possible that materials have been derived from extensive areas of the planet. McCauley (Ref. XVII-12; also see Section X of this Report) and Cutts (Paper I; also see Section XV) find evidence of erosional stripping of the surface in equatorial, mid-, and polar latitudes. Cutts and Smith (Ref. XVII-6; also see Section XI), however, recognize areas of eolian deposition on the extensive cratered terrains of Mars. In the canyonlands and other depressed terrains of the Tharsis ridge, the evidence for a source of eolian materials is not only persuasive, but estimates can be made of the volumes of material available. Although some of these features can be interpreted as structural features, graben, and fault blocks created by the stress patterns associated with the Nix Olympica volcanism, erosional processes have been active. Landslides are visible in many areas, and the Coprates canyon (Fig. XVII-6) has clearly expanded by scarp recession.

To explain these features, one not only needs a mechanism for removal of the material that has collapsed from the wall into the canyon floor, but also a site where the removed materials have accumulated. Disposing of materials from the canyonlands is problematical, especially in the case of entirely closed basins (Fig. XVII-6b). The preservation of the surface of mesas within the basins (Fig. XVII-6a) argues against subduction of materials. Transport across the surface by water or gravity slippage is impossible in many cases because of the unfavorable slopes. A plausible mechanism is wind and, if so, the materials derived from the canyons must now reside elsewhere on the surface of Mars.

The volume of the canyonlands (Fig. XVII-7) is calculated to be 3×10^6 km³. However, a significant fraction of this must have been induced tectonically, and the figure overestimates the quantity of eolian materials furnished. Another possibly important source is the periphery of the great shield volcano Nix Olympica. Surrounding this feature is a vast circular scarp (Fig. XVII-8a; see Ref XVII-13). Features indicative of scarp recession such as landslide tongues can be recognized at points around the periphery (Fig. XVII-8d). The surrounding plains, where they are not smooth, exhibit an intensely grooved appearance, which McCauley (Ref. XVII-12; see Section X of this Report) attributes to eolian erosion. In one location (Fig. XVII-8e) many ridges that attain about one-third of the height of the bounding escarpment (Fig. XVII-8d) have been recognized. The ridges are elongated in the same direction as the grooves that mark the surrounding plain. Most of them are sharply crested, but flat-topped, mesa-like features are visible near the right-hand margin of this picture. The association of these streamlined ridges with the grooved plains suggests that they are erosional remnants, and the flat-topped ridge may preserve the surface of the uneroded volcanic shields. If this is so, it gives an indication that the original Nix Olympica shield sloped gradually beyond the present peripheral scarp. With the assump-
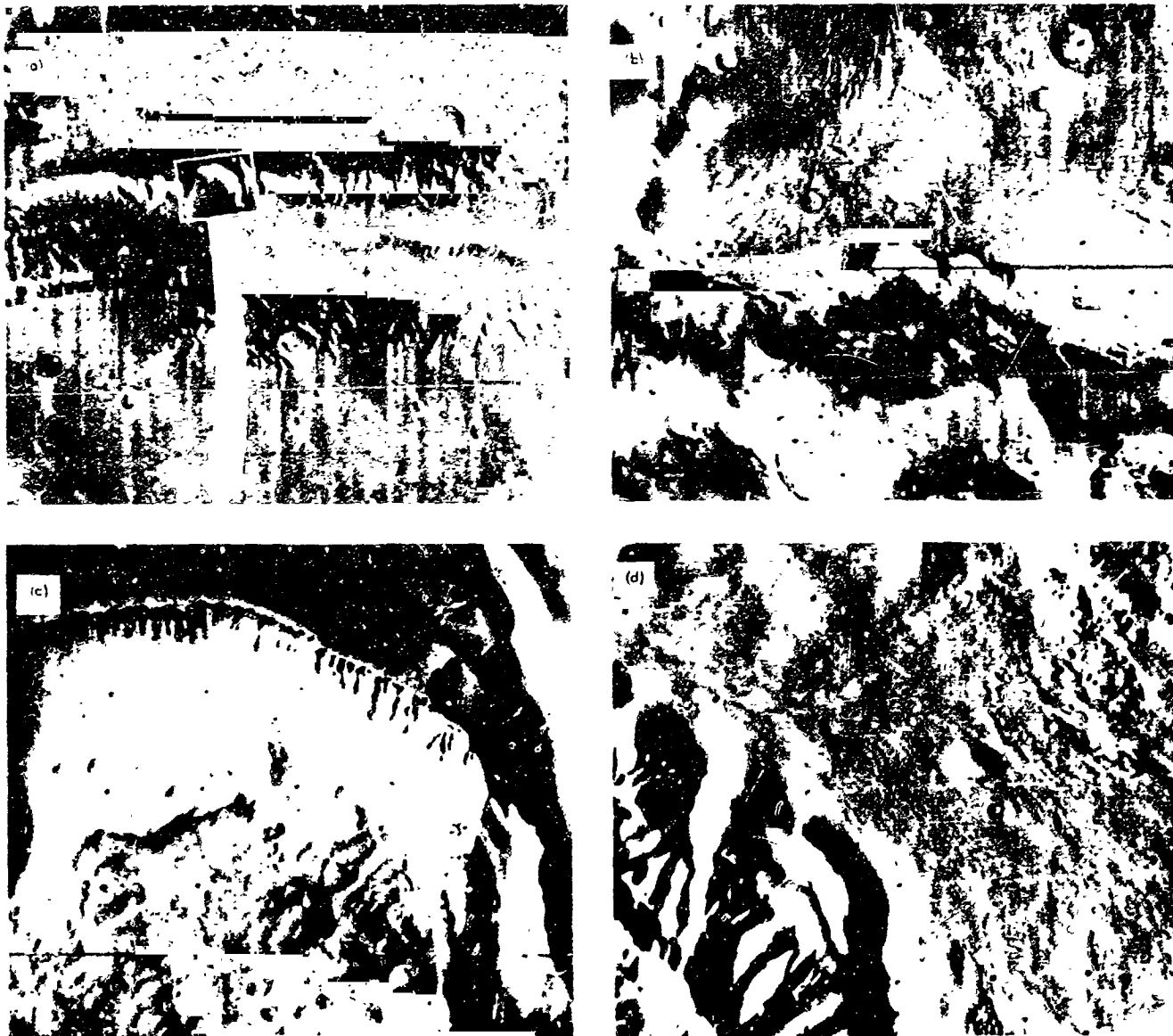
Fig. XVII-6. Features of troughed terrain (canyonlands) suggestive of wind deflation. The part of the major trough seen in (a) is 400 km long by almost 100 km wide. A portion of the crater wall viewed at higher resolution (c) reveals castellated cliffs with irregular debris at its foot. In other areas of the troughed floor (d), the surface is different and exhibits long sinuous features which roughly parallel the foot of the canyon wall. These may indicate layering in the wall, or they could be eolian erosional or depositional features. They differ from the slump surface in (d) and suggest that deflation of the canyons has played a part in their formation. The closed depression in (b) tends to support this idea (a) MTVS 4144-87, DAS 05851968. (b) MTVS 4193-54, DAS 07399108. (c) MTVS 4275-22, DAS 10204679. (d) MTVS 4295-36, DAS 12865578.
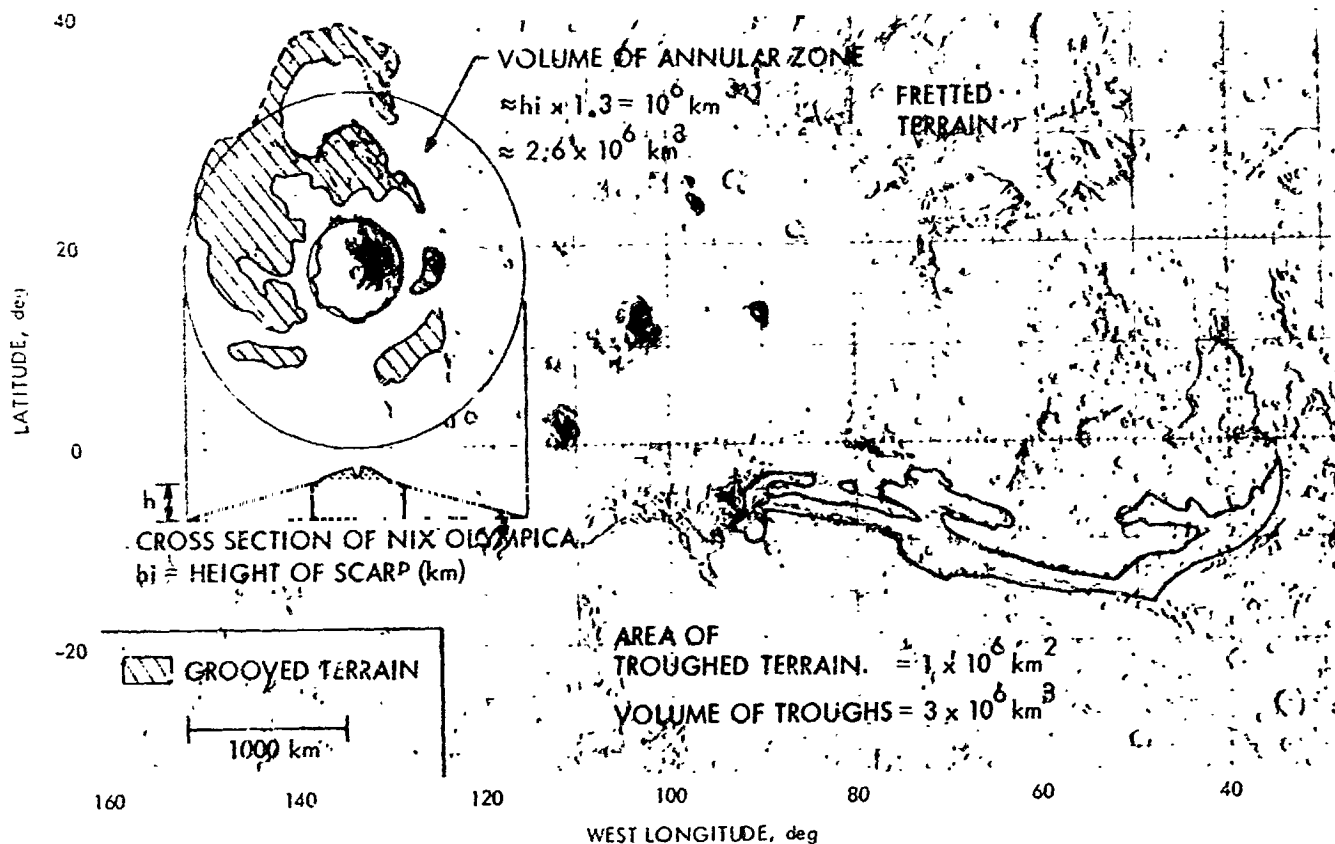
Fig. XVII-7. This map of the equatorial zone of Mars is used to identify areas from which materials may have been deflated and illustrates the way in which the volumes of these materials have been estimated. Several circular patterns suggestive of the roots of former shield structures appear in the grooved terrain, and the annular zone surrounding Nix Olympica is an oversimplification. The base map is derived from an airbrushed 1:25,000,000 scale map published by the U. S. Geological Survey.

tion of a constant slope and radial symmetry, one calculates that about $2.6 \times 10^{\circ}$ km· of material has been eroded from this feature.

Sharp (Ref. XVII-13; also see Section VI of this Report) has described another lowland surface, fretted terrain, which is adjacent to the Tharsis ridge, covers $4.75 \times 10^{\circ}$ km² and is margined by a 1-km escarpment. Ground-ice sapping is believed to have reduced the surface in this part of Mars to debris, but the export of perhaps $4.75 \times 10^{\circ}$ km² from the basins is attributed to fluvial or eolian action. Milton (Ref. XVII-14; also see Section III of this Report) contends that only fluvial action could account for scarp recession and redistribution of materials in this part of Mars.

Thus, the morphologies of the troughed terrains, grooved terrains surrounding Nix Olympica, and fretted terrains imply the removal of $10 \times 10^{\circ}$ km³ of material. Part of this represents a downward motion of material

induced by tectonic deformation. However, most of it must correspond to material which now resides elsewhere on the surface of Mars. Ash deposits from the volcanic regions and impact debris from the cratered terrains are additional sources of fine debris in the Martian environment, but the quantity of material supplied from these sources is difficult to estimate. However, there seem to be ample sources of silicate debris from the depressed terrains alone to account for the volume of materials in the layered deposits ($5 \times 10^{\circ}$ km³). Eolian action seems a likely mechanism of transport to the poles.

There are three modes of eolian transport that may be operative on Mars: atmospheric suspension, saltation, and traction. It has been stated above that deposition from atmospheric suspension can best explain the observed characteristics of the layered deposits. In order to have remained suspended for any adequate period of time, any silicate materials in the deposits must have been in the form of fine dust less than a few tens of micro-
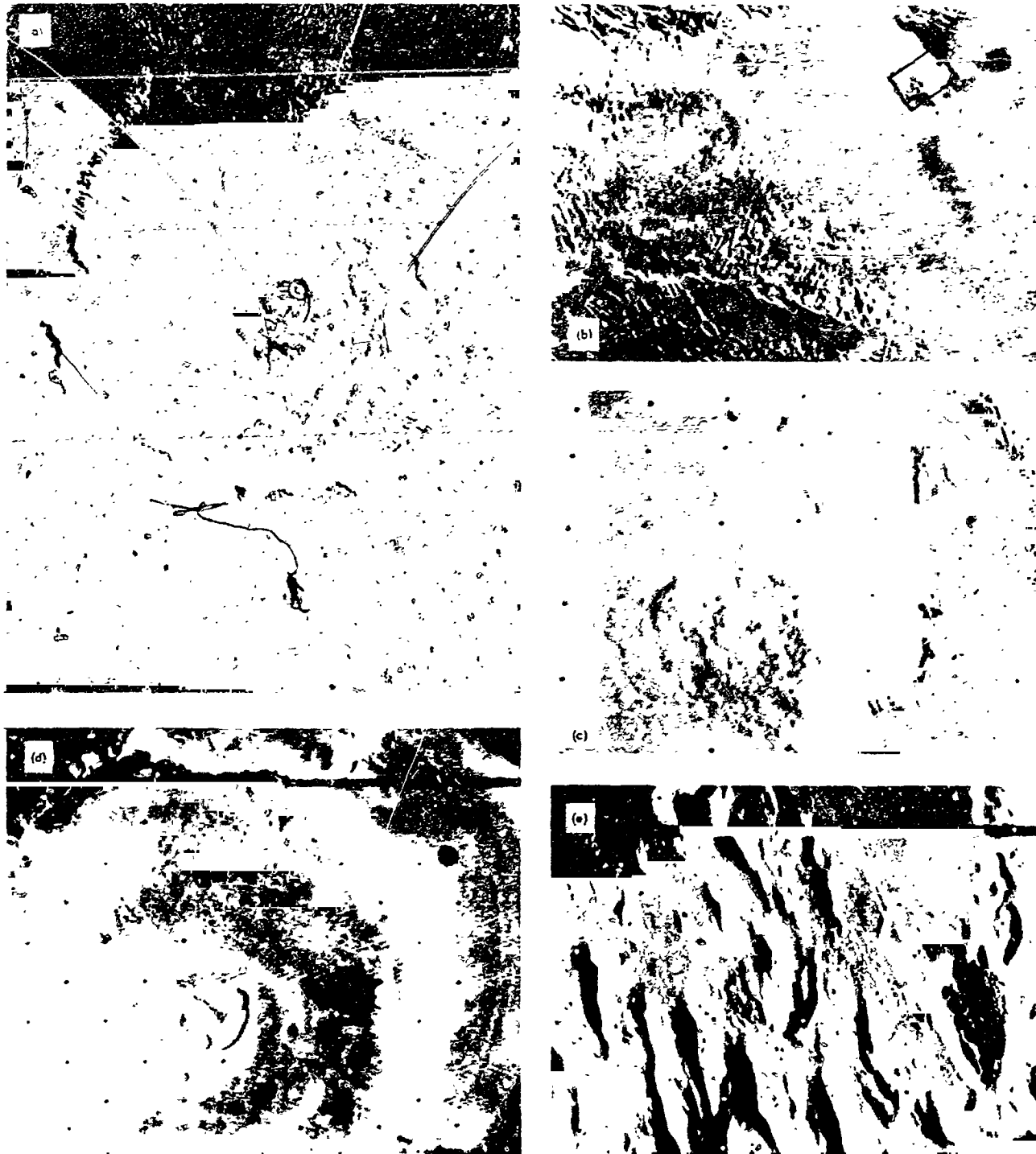
Fig. XVII-8. Features peripheral to the Nix Olympica shield suggesting massive removal of materials by wind erosion. The Nix Olympica volcanic shield (a) is about 500 km in diameter and bounded by a circular escarpment. Contiguous with the escarpment seen again in (b) (upper right) is a smooth plain and an area known as grooved terrain. The escarpment exhibits landsli tongues indicating scarp recession (c). High-resolution views of grooved terrain (e) reveal a striated plains surface and streamlined mesas which may be remnants of the original shield surface. Brightening around the base of the shield (d) suggests that clouds are forming which result from loss of water from the receding scarp. (a) IPL Roll 677, 240743. (b) IPL Roll 497, 191512. (c) MTVS 4288-90, DAS 11657070. (d) MTVS 4174-86, DAS 06823743. (e) MTVS 4174-74, DAS 06823393.

meters in diameter. Larger particles, although capable of surface saltation, could not have been deposited uniformly and contemporaneously over a broad area. One should question how so much dust could have been produced on Mars. Features such as the landslide tongue Fig XVII-5d show that the surface of Mars does disintegrate into pieces at least as small as the resolution of the television cameras. Possible mechanisms for this process are salt weathering Ref. XVII-15 or certain types of chemical weathering Ref. XVII-16. However, the further comminution into fine particles of dust is most readily attributed to eolian abrasion Ref. XVII-12; also see Section X of this Report. If the Nix Olympica volcanic province consists of deposits of tephra (volcanic ash interbedded with lavas, as frequently happens on Earth, then the rapid production of dust is much easier to understand. Not all material derived from the depressed terrains need have been converted to dust, however. Conceivably, deposits of larger particles transported from any of the postulated source areas by saltation and traction now lie in the equatorial and mid-latitudes of the planet.

The equatorial erosional features have other attributes that lend credibility to the idea that they are the source of materials for the polar deposits. They have all expanded by scarp recession, which appears to be a relatively uniform process making available a steady supply of materials. Scarp recession may not only supply silicates but, if Sharp (Ref. XVII-17; see Section V of this Report) is correct in inferring a large ice content for the depressed terrains, it also may supply volatiles. Some suggestion that volatiles are being lost from the surface of the recessional scarp appears in a *Mariner 9* picture of Nix Olympica, taken during north polar summer, showing clouds concentrated around it (Fig. XVII-8c).

Stages in the recession of escarpments of the depressed terrains also should correspond to particular layers in the polar deposits. In a general way, the youthfulness of both the surface of the layered deposits and the floors of the depressed terrains, as indicated by crater populations, is consistent with this theory.

D. Mechanism of Transport and Polar Deposition

The existence of layered deposits in the polar regions of Mars requires an original source of materials, and possible sources of silicate debris have been identified in the equatorial regions. Sources of carbon dioxide and water are more difficult to evaluate, but stability considerations suggest that these materials are at least less abundant in the layered deposits outside the perennial cap. We now turn from the question of supply of materials to the problem of mechanism of formation and attempt to estimate rates of accumulation of dust and water ice in the polar regions in terms of recent observations of these materials in the Martian atmosphere.

Preferential accumulation of dust deposits in the polar regions requires either preferential deposition or preferential stability of eolian materials in this part of the planet. Both effects are probably important, but the evidence for preferential deposition is evaluated first on the basis of a physical model of dust deposition. The objective is to find not only where and when deposition takes place, but also to estimate the rate at which materials accumulate. This permits estimates of the time period represented by each layer and the total age of the deposits. These estimates involve several assumptions in series and may therefore be grossly in error, but they serve to illustrate an approach to the history of the Martian surface which ultimately may be developed with much greater precision.

Of all the components of the Martian atmosphere including gases, condensates, and dust, only the transport of the major constituent carbon dioxide is well understood. Studies of the heat balance of the Martian polar caps (Ref. XVII-18) suggest that the fully developed annual northern polar cap contains 7×10^{-18} g of carbon dioxide and the southern cap 11×10^{18} g. These quantities represent a large fraction of the average mass of carbon dioxide in the Martian atmosphere (22×10^{-18} g), and so about half of the atmosphere is displaced into each growing cap during the winter season.

Variations in total atmospheric pressure between solstice and equinox result from differences in sublimation and condensation rates (Ref. XVII-19) and between the two equinoxes because of the different sizes of the cap The massive exchange of atmosphere between the po and the tremendous thermal contrast at the polar cap edge drastically perturb the atmospheric circulation from that expected for an atmosphere whose major constituents are not subject to condensation. It will also transport dust and whatever else is entrained in the atmosphere toward the growing polar cap.

1. Precipitation of Dust

The rate of precipitation of dust in the polar regions depends upon many factors such as the concentration of dust, the size range, and the atmospheric conditions. In

270

polar winter many factors are favorable for the precipitation of dust, and, if it is supplied to the polar regions in sufficient concentrations we should expect considerable deposition. The first mechanism of precipitation is gravity deposition, one which takes place all over the planet. Particles fall out of the atmosphere at a rate influenced by their size and density and by the viscosity and turbulence of the atmosphere. Under nonturbulent conditions, the Stokes–Cunningham equation describes the limiting velocity of fall of particles (Ref. XVII-20).

At the winter pole, the surface will be extremely cold, and thermal convective turbulence will be suppressed. Provided that the surface winds are low, boundary layer turbulence will also be low, and the fallout rate of dust particles will be accelerated. One expects this rate to be enhanced by the precipitation of volatiles on suspended dust particles increasing their mass. Theoretical analyses (Ref. XVII-21) show only a weak reverse cellular convection slowing the rate of precipitation of dust.

An important mode of precipitation, and one unique to the poles, is the flux of carbon dioxide into the growing cap, which embeds entrained dust in the cap. Cross (Ref. XVII-18) has calculated that, during polar winter, 0.432 g/cm² of carbon dioxide precipitates during each 24-hr period. This is equivalent to a column of atmosphere 250 m high flowing into the surface during each 24-hr period and corresponds to a velocity of $\frac{1}{3}$ cm/sec. For example, a 3-μm particle on Mars, of density 3 g/cm³, falling in a still atmosphere at the rate predicted by the Stokes–Cunningham relationship, will have the same velocity.

Given the mass concentration of dust, f, in the Martian atmosphere, one can calculate precisely the rate of deposition, M, of dust entrained with carbon dioxide that occurs during a 24-hr period of Martian winter.

$$M = 0.432f \text{ g/cm}^2$$

where f is the mass of suspended dust as a fraction of atmospheric mass. Estimates of particle fallout, in contrast, are imprecise. We have no accurate data on particle sizes or the extent to which turbulence modifies their fallout. If dust particles are a few micrometers in size, as suggested by Hanel et al. (Ref. XVII-22), and under nonturbulent conditions, the rate of deposition of dust by fallout should be approximately comparable to the precipitation of dust entrained with condensing carbon dioxide. In subsequent analyses, we make this

assumption and take the total rate of precipitation to be

$$M = 2 \cdot 0.432 = 0.9f \text{ g/cm}^2$$

At the summer pole where the cap is evaporating, frost evaporates at a rate on the order of 0.5 g/cm² per 24-hr period, creating a net upward flow of $\frac{1}{3}$ cm/sec. Not only are no particles entrained with carbon dioxide deposited, but particles with diameters smaller than 3 μm cannot fall to the surface at least for a large part of the day because of the upward flux of gas. A significant volume of the atmosphere in the vicinity of the cap is filled with freshly evaporated carbon dioxide, which is dust-free, displacing dust-filled air to higher latitudes. Winds may be low in this area (Ref. XVII-21) causing this region of low dust concentration to persist and perhaps explaining the clarity of the atmosphere above the south polar cap during the planet-wide dust storm of 1971. In summary, deposition of dust will occur preferentially over the entire area of the winter frost cap when it is still accumulating carbon dioxide. Deposition will be less over other parts of the planet and least at the summer polar cap where ablation of carbon dioxide is at a maximum.

As well as assessing where deposition takes place, we also can use the theory to estimate how rapidly dust accumulates. Of particular interest is the time required to accumulate a single layer and the entire mass of the layered deposits. In order to make these estimates, only the contribution of dust from global storms is considered. During a global storm the atmospheric concentration of dust exceeds that in the clear atmosphere by several orders of magnitude, so this simplification seems reasonable.

The most reliable information about the quantity of dust suspended during a global dust storm was obtained by *Mariner 9*. Chase et al. (Ref. XVII-23) estimate at least 10^{-3} g/cm² over the south polar region. However, for reasons discussed, dust deposition takes place at the winter pole; therefore, the concentration of dust at the south pole, diluted by freshly evaporated carbon dioxide, is likely to be much smaller than over the north pole where deposition actually occurs.

As a working hypothesis, we adopt a value of 40×10^{-4} g/cm² as the quantity of dust in suspension over the winter pole during a global dust storm and also a value of 16 g/cm² as the amount of carbon dioxide in a vertical column. It is assumed further that the dust storm lasts for 50 days; if a dust storm of this magnitude occurs

every Martian year, the annual deposit of dust, D, is given by

$$D = 50 \cdot 0.9f \text{ g/cm}^2$$
$$= 50 \cdot 0.9 \times 40 \times 10^{-3}/16$$
$$= 11 \times 10^{-3} \text{ g/cm}^2$$
$$= 5 \times 10^{-5} \text{ m}$$

(assuming density of deposit $= 2 \text{ g/cm}^3$)

Observational evidence of variability in dust storm intensity suggests that the rate of dust deposition varies from year to year. There is also evidence, discussed further below, that the average rate being estimated above varies over geologic time. In some preliminary calculations, however, the value 5×10^{-5} m/yr is adopted.

Alternation in deposition between the two polar regions is one significant effect we do allow for when estimating the time required to accumulate thick layers. Dust storms seem to occur close to perihelion, possibly because of the strong heating induced by close approach to the Sun. However, the equinoctial precession of 51,000 years, whose possible role in Martian climatology was first recognized by Leighton and Murray (Ref. XVII-19), causes the season at which the planet reaches perihelion to change gradually. In 25,500 years from now, one would anticipate that dust storms still occur at perihelion but, at that time, the south pole will be the winter pole and the repository of accumulating frost and dust.

As a consequence, taking 30 m as the thickness of an individual layer of the polar deposits, the time of accumulation, T, is given by

$$T = \frac{2 \times 30}{D} = 1.2 \times 10^6 \text{ Martian years}$$

$$= 2.2 \times 10^6 \text{ terrestrial years}$$

Formation of the entire deposit will have taken much longer. Although the average thickness of the layered deposits is estimated as 2 km, the maximum thickness and the maximum number of layers underlie the polar caps. Taking 6 km as the total thickness

$$T = \frac{2 \times 6 \times 10^3}{D} = 2.4 \times 10^8 \text{ Martian years}$$

$$\approx 500 \times 10^6 \text{ terrestrial years}$$

Implicit in this estimate is the concept of a single cycle of deposition. We also neglect any reduction in the thickness of the deposits underlying the remnant polar cap due to erosion. The calculations may not prove that the layered deposits are hundreds of millions of years old, but they indicate that this is at least a plausible estimate. Earlier reports that the layered deposits were extremely young and possibly millions of years old at most (Ref. XVII-1) were based erroneously on the age of the surface topography, which is clearly very youthful, and a speculative association of the actual layering with the 50,000-year equinoctial precession.

2. Relationship of Layering to Martian Planetary Dynamics

The regularity of the layering in the polar deposits and their great number suggest that there has been some temporal modification in the conditions of their formation. Such effects are familiar in Earth science. Annual laminae (varves) produced by deposition from seasonal glacial meltwater enables DeGeer (Ref. XVII-24) in Sweden to date accurately the end of the last ice age. However, as we have shown, the layers recognized on Mars by *Mariner 9* require not 1 year, but probably at least 1 million years to accumulate. Periodic variations in varve thickness have been studied by Anderson and Koopmans (Ref. XVII-25) and Anderson et al. (Ref. XVII-26). In the former case, a climatic modulation period near 90 years was suggested, and in the latter case, a 1000- to 3000-year period.

Variations in solar activity have been proposed as a possible explanation of such periodic effects. However, solar variations are largely speculative; periodic variations in planetary heating are also implied by well tested theories of planetary dynamics. Correlations with climate variations resulting from variations in the planetary motions are therefore likely to provide sounder insights into planetary histories.

Planetary movements of both Earth and Mars undergo th cyclic disturbances: periodic variations in the obliquity of the ecliptic, eccentricity of the orbit, and precession of the equinoxes. Variations in the heat received by Earth as a result of interaction of these three cycles were first recognized by M. Milankovitch and have been studied by several workers including Emiliani (Ref. XVII-27). They have attempted to relate the astronomical sequences of cool summers with the geologic sequence of Pleistocene glacial phases during the last 1 million years. These efforts have been only partially successful. However, the cyclic perturbations of Mars are

somewhat larger, and one's intuitive impression is that processes on that planet are likely to respond more obediently to the variations in planetary heating that accompany them.

Murray et al. (Ref. XVII-28) have already investigated insolation variations caused by the perturbations of Mars in connection with the characteristics of the layered deposits. However, their time scale and their basic assumptions about the processes involved appear to contradict those developed here. Two types of perturbation to the Martian orbit are discussed in Ref. XVII-28: 1) equinoctial precession with an effective period of 51,000 years, which has already been mentioned, and 2) changes in orbital ellipticity with a high-frequency component of 95,000 years superimposed on an envelope with a 2-million-year repetition. Murray et al. interpret the 30-m layering of the polar deposits in terms of some kind of control on volatiles exercised on the shorter time scale of 95,000 years, but assign no significant role to the 50,000-year period in the formation of laminated terrain. They interpret an escarpment as the series of 21 layers that formed in the 2-million-year interval. In these terms the laminated terrains are extraordinarily young with a range of perhaps 12 million years between oldest and youngest.

The analysis made by this author suggests that in 95,000 years, less than 2 m of dust would accumulate, which would be quite invisible to the *Mariner 9* cameras. However, 2 million years is just about the right amount of time for accumulating the 30-m thickness that is the finest layering recognized in the *Mariner 9* pictures. The layering may result from the modulation of dust storm activity induced by this ellipticity perturbation. Murray et al. (Ref. XVII-28) point out that these ellipticity variations cause periodic variations in both the average and the peak insolation experienced by the planet. As dust storms are strongly correlated with perihelion, one might expect the variations in perihelic insolation to modify the intensity of global dust storms, as suggested by G. A. Briggs (Ref. XVII-29). He speculates that, during a significant part of the 2-million-year cycle, the insolation at Mars is inadequate to allow generation of unstable global dust storms.

A depositional hiatus is one possible underlying reason why layers erode into terraces. It was stated above that terraces imply a variation in erosional response between the top and bottom of a layer. These variations could have been introduced during deposition because of temporal changes in the composition or particle sizes of material forming the layer. They could also have been created by post-depositional reworking of the upper surface of a layer, possibly by meteorite bombardment, but more likely by eolian activity.

3. Precipitation of Water Ice and Vapor

Although attention has been focused on the precipitation of dust at the poles, it is not the only material that is deposited there. Other suspended condensates and vapors that condense at or above the temperature of frozen carbon dioxide will also be precipitated. The most important of these is water. The problem of estimating its rate of accumulation is addressed in the subsequent paragraphs.

In an earlier assessment of the transport of water to the Martian polar caps, Leighton and Murray (Ref. XVII-19) attributed much of the migration to water vapor transport, on the basis of a random walk meridional transport. They estimated that 20 to 30×10^{-4} g/cm^2 of ice is deposited annually on the transient polar cap. While their mechanism is probably valid, it may underestimate the total deposition, for the flux of carbon dioxide into the growing polar caps will carry entrained water vapor and water ice just as it carries dust.

Water vapor concentrations in the equatorial regions have been estimated at 10 to 20×10^{-4} g/cm^2 column (Ref. XVII-22). As water vapor is transported from the equatorial region toward the winter pole, some deposition will occur on the surface at mid-latitudes, and this may involve adsorption on the Martian regolith (Ref. XVII-9). However, the existence of a cloud or "hood" that obscures the polar regions during the winter season and which is higher in temperature than the sublimation point of carbon dioxide seems to imply that water ice crystals, as well as residual amounts of water vapor, remain in the cold polar atmosphere.

Although it is evident that less than 1 μm of water vapor is present in the polar atmosphere (Ref. XVII-22), it seems plausible that much larger amounts of water exist adsorbed on large dust particles and nucleated as ice crystals on small ones. So low is the water concentration in the Martian atmosphere that the small (fractional micrometer) ice crystals will not exist in sufficient number to grow rapidly by accretion (Ref. XVII-20).

To estimate the annual flux of water into the growing cap, the total vertical abundance of ice and vapor in the vicinity of the growing cap is assumed to be 5 μm or

between one-fourth and one-half of the equatorial abundance. This allows for significant exchange with the surface in mid-latitudes (Ref. XVII-30). Atmospheric water is assumed to be uniformly mixed, and water adsorbed on dust is neglected. Gravitational fallout of fractional micrometer ice crystals is negligible.

Following the approximations of Cross (Ref. XVII-18) that the north pole is in darkness for 306 days and the south pole for 381 days, the accumulation of water at the poles is computed in a similar way to the entrainment of dust.

At the north pole (90°N)

$$\text{Mass of water} = 306 \times 0.432 \times \frac{5 \times 10^{?}}{16} \text{ g/cm}^2$$
$$= 40 \times 10^{-4} \text{ g/cm}^2$$

At the south pole (90°S)

$$\text{Mass of water} = 50 \times 10^{-4} \text{ g/cm}^2$$

The close agreement with values computed both by Leighton and Murray (Ref. XVII-19) and by Leovy (Ref. XVII-30), who also estimate 40×10^{-4} g/cm² per year for the inner cap using quite different methods, is probably fortuitous.

It was estimated earlier that 2.2×10^6 years are required to accumulate a 3?-m layer of dust if present rates of dust accumulation are applicable and if all the dust is retained after deposition. With the same assumptions, the amount of water (D) accumulated during the same period can be estimated (density of water ice = 0.9 g/cm³)

$$D = \frac{2.2 \times 10^4 \times 40 \times 10^{-4} \times 10^{?}}{1.84 \times 0.9} = 55 \text{ m}$$

The remarkable result of this analysis is that at least as much water ice as dust is currently being deposited in the Martian polar regions. There is potential for error in these estimates, and the concentration of both dust and water in the Martian atmosphere may have undergone considerable change during the time period of formation of the layered deposits. However, since it is at least plausible that both dust and ice are being deposited at comparable rates, under current conditions an assessment of the stability of both materials in the polar zone is warranted.

4. Stability of Dust and Water Ice in the Polar Regions

There are two principal environments affected by condensed materials in the polar region: the area of perennial frost and the peripheral zone of annual frost cover (Fig. XVII-1a). Although estimates of deposition rates have been performed only for the poles, codeposition of dust and water in both annual and perennial frost areas during the winter season is implicit in the analysis performed so far.

During the spring and summer season, carbon dioxide sublimes from both perennial and annual frost zones. The loss of carbon dioxide from the annual frost zone is followed by the sublimation of water ice, although some water ice may be retained in shaded areas. However, the perennial frost cap, which always has a high albedo and absorbs much less solar energy, should retain the annual deposit of water ice and should be the major repository of water ice on Mars.

Dust deposits are not susceptible to sublimation, but they are subject to erosion; glacial and wind erosion are both possible mechanisms. Fluvial action seems less likely because of the cold temperatures of the polar zone. If the existence of the layered deposits is to be accounted for in terms of dust deposition, then these processes could not have been effective during the period of formation of the layered deposits.

E. Implications of Morphology and Distribution of Layered Deposits

These ideas on dust and water deposition and retention can be translated into predictions of the distribution of the layered deposits which can be compared with the observations. One of the simplest models that can be devised is based on the assumption that the dust deposited in the area of annual frost is all retained, whereas the only permanent trapping of water takes place in the small area of perennial frost.

Dust deposition rates have been calculated only for the geometric pole. One's intuitive expectation about the areal distribution is that dust deposition would be quite uniform in a central polar area; it would drop gradually with radial distance from the pole and more abruptly near the maximum radial extent of the annual frost cover to a value that approached the planetary average. Many millions of years of steady accumulation would then result in vast, featureless, domed plateaus symmetrical about both poles and with small-scale topographic fea-

tures visible only near the borders where the pre-existing topography emerged from the thinning deposits. The flat terrain surface would be composed only of the newest deposits conformably overlying older ones; without a cross section incised into the surface, we would be entirely ignorant of any layering in the surface materials. Near the center of this plateau would be the small perennial polar cap beneath which the deposits would contain water ice and possible carbon dioxide in addition to dust.

Such a description is obviously far removed from the reality of laminated terrain. Instead of these vast, featureless, domed plateaus, we recognize subdued uplands dissected by curving and sinuous escarpments and channels (Fig. XVII-5) occupying only a small fraction of the area of annual frost cover. Contacts between the layered deposits and underlying units imply the stripping of the surface and not a gradual feathering out of the deposit. However, the existence of thick deposits extending as far from the pole as 72°S (Fig. XVII-2) do support the concept that deposition originally took place over a large part of the area of annual frost cover. There is, in summary, considerable evidence to suggest that there once were domed plateaus of layered deposits in the polar regions of Mars, but they now are extensively eroded and occupy only part of the region in which they originally formed.

There is a body of evidence to indicate that wind erosion, and not glacial or fluvial action, for example, has caused the stripping and dissection of the layered deposit. The pattern of albedo markings around the pole, grooving in the contiguous pitted terrain, and fluting on the interscarp surfaces of the layered terrain point to the existence of active wind erosion in the polar regions (Paper I; see Section XV of this Report). Intensification of winds near the edge of the receding polar cap is a possible explanation of the intense erosion in the circumpolar belt. What is surprising is that, if wind is so effective an erosional agent, why are there any layered deposits still in existence and how did they accumulate to a significant thickness initially.

One possible explanation is that dust deposits have been cemented and therefore protected by the ice of the perennial frost. There is some indication that the perennial frost does protect the surface. Erosional features such as flutes and grooves are not observed in the area of perennial ice, although considerable textural detail is visible. The layered deposits are also thicker under the permanent frost caps. The crucial difficulty with this idea stems from the observation that the layered deposits are in fact preserved for considerable distances outside the perennial frost caps.

Alterations of deposition and erosion close to the boundary of the present perennial caps could be accounted for by variations in the extent of perennial frost because of astronomical perturbations. However, the existence of a freshly eroded, laminated-terrain surface over 1000 km from the edge of the perennial cap (Fig. XVII-2) suggests some major secular change in the Martian environment.

F. Discussion

Possible objections to the model presented for the nature and origin of "laminated terrain" range from fundamental disputes about the processes involved to relatively minor questions about the details of sources, mechanisms, stability, and whether an episodic or continuous history was involved.

The principal objection in the first category, at the time of writing, centers on a basic question of interpretation of the photographic data. Murray and Malin (Ref. XVII-31) and Murray et al. (Ref. XVII-2) contend that the circumpolar cliffs and escarpments of laminated terrain are primary constructional forms and not erosional features. They attribute the accumulation of materials in this unusual manner to a process involving volatile condensation, modulated by periodic variations in average solar insolation. This is considered to lead to the formation of circular plates of frozen volatiles and dust concentric with the polar axis. Polar wandering is invoked to explain the fact that the "plate edges" (circular escarpments in this section) are not concentric with the present polar axis, and the "plate edges" are then interpreted as fossil latitudinal circles.

The polar wandering aspect of this hypothesis has difficulties that have been discussed elsewhere by Cutts (Paper I; see Section XV of this Report). The foremost objections are that many of the topographic features of laminated terrain are actually channels not scarps, and many are irregular or sinuous and therefore not concentric to any single point. It seems easier to explain these features by wind erosion, which is suggested by many independent and corroborative lines of evidence (Paper I; see Section XV of this Report) and which is less geometrically confining than the polar wandering hypothesis.

A difficulty with the ideas presented in this section is that a major secular change in climatic conditions is required to account for the erosion of layered deposits that is presently occurring outside the perennial cap, particularly near 72°S. One speculative possibility is that the perennial polar caps once had a very much greater area, preventing erosion of the area now being eroded. Murray suggests that polar wandering can account for the observed distribution of layered deposits without a major secular climatic change. He argues that if dust were retained only in the perennial caps and if the perennial caps were about the size they are now, but had wandered around the polar region, then this could also account for the observation. Detailed tracing of layered strata throughout the entire polar region may establish which of these two possible models is closer to reality.

The existence of dunes either on the layered terrain or in the materials apparently derived from them (Ref. XVII-6; also see Section XI of this Report) seems paradoxical if the layered deposits are formed from windblown dust. A basic characteristic of windblown dust is that it does not participate in saltation and presumably cannot form dunes. Possible explanations are that individual dust particles are consolidated either by compaction or meteorite impact. Less likely, as surface winds do not seem to favor it, is the transport of saltating particles from the surrounding cratered terrains.

Another problem concerns the material "missing" from the layered deposits. Material derived from the original featureless, domed plateau, which was inferred to have once existed in the polar regions, must now reside elsewhere on Mars unless multiple cycles of erosion and deposition have occurred. Evidence presented in Paper I (also see Section XV of this Report) indicates that wind erosion has transported material outward in a spiral path. Evidence for extensive mantling of terrains in the mid-latitudes has been presented by Soderblom et al. (Ref. XVII-32; also see Section IX of this Report). The layered deposits may well be the source of much of this material. Thus, Table XVII-1 presents a greatly oversimplified life cycle of the layered deposits of Mars according to the scheme favored by Smalley and Vita-Finzi (Ref. XVII-33).

While there is no evidence of the existence of water ice in the layered deposits that can be unequivocally demonstrated from the pictures, the calculated rates of deposition of water and stability considerations suggest rapid accumulation in the area of the residual cap. Many other anomalous layers associated with volcanic eruptions are probably to be found also and may be particularly rich

in volatiles. Growth of segregated bodies of ice from the vapor phase is also a possibility; the formation of liquid carbon dioxide at some depth within the layers, where the temperature and pressure of the triple point is reached (Ref. XVII-3; also see Section XVIII of this Report), cannot be excluded.

G. Conclusions

Layered deposits in the Martian polar regions are interpreted as accumulations of dust derived from atmospheric suspensions. Depressed and eroded terrains of the equatorial region are considered to be the principal sources of dust. A depositional model based on polar precipitation of dust predicts the formation of a vast, dome-shaped, featureless plateau underlain by layered deposits and occupying most of the area of annual frost cover. What is observed can be interpreted as a highly eroded remnant of this hypothetical plateau, and a major secular change in the erosional conditions in the polar regions is concluded. One speculative possibility is that the size of the perennial polar caps has decreased.

The rates of accumulation of dust and water ice in the polar regions have been estimated on the basis of atmospheric conditions in the present era. The analysis indicates an accumulation time of about 500×10^6 years for the layered deposits and the presence of significant quantities of water ice in the deposits beneath the perennial cap.

The layering is tentatively correlated with modulations of dust deposition induced by 2×10^6 year periodicities in the orbital ellipticity of Mars. Particularly in view of the secular changes that seem to have occurred on Mars, these age estimates should be treated with great reservation. However, earlier ideas that the layered deposits represented an extremely short span of Martian history, a few tens of millions of years, appear to be no longer valid.

The formation of terraced erosional surfaces corresponding to individual layers or groups of layers indicates variations in response to erosion. One possible explanation is that reworking of the surface by eolian action has occurred during intervals of non-deposition. Fluting and grooving of the terraced terrains are observed outside the perennial polar cap, and this erosion may account for the lack of small impact craters. Material eroded from the layered deposits appears to be partly redeposited in the mid-latitudes of Mars.

References

XVII-1. Murray, B. C., Soderblom, L. A., Cutts, J. A., Sharp, R. P., Milton, D. J., and Leighton, R. B., "A Geological Framework for the South Polar Region of Mars," *Icarus*, Vol. 17, p. 328, 1972.

XVII-2. Murray, B. C., and Malin, M. C., "Volatiles on Mars—Theory vs Observation" (submitted to *Science*).

XVII-3. Sagan, C., "Liquid Carbon Dioxide and the Martian Polar Laminae," *J. Geophys. Res.*, Vol. 78, 1973.

XVII-4. Soderblom, L. A., Malin, M. C., Murray, B. C., and Cutts, J. A., "Mariner 9 Observations of the Surface of Mars in the North Polar Region," *J. Geophys. Res.*, Vol. 78, 1973.

XVII-5. Cutts, J. A., "Wind Erosion in the Martian Polar Regions," *J. Geophys. Res.*, Vol. 78, 1973 (Paper 1).

XVII-6. Cutts, J. A., and Smith, R. S. U., "Eolian Deposits and Dunes on Mars," *J. Geophys. Res.*, Vol. 78, 1973.

XVII-7. Mariner 9 Television-Experiment Team, "The New Mariner 9 Map of Mars," *Sky and Telescope*, Vol. 44, p. 77, 1972.

XVII-8. Holmes, A., *Principles of Physical Geology*, 1288 pp., Thomas Nelson, Edinburgh, 1965.

XVII-9. Fanale, F., and Cannon, W. A., "Adsorption on the Martian Regolith," *Nature*, Vol. 230, p. 502, 1971.

XVII-10. Anderson, D. E., and Hord, C., "Mariner 6 and 7 Ultraviolet Spectrometer Experiment: Analysis of Lyman α Data," *J. Geophys. Res.*, Vol. 76, p. 6666, 1971.

XVII-11. McElroy, M. B., "Mars: An Evolving Atmosphere," *Science*, Vol. 175, p. 443, 1972.

XVII-12. McCauley, J. F., "Mariner 9 Evidence for Wind Erosion in the Equatorial and Mid-Latitude Regions of Mars," *J. Geophys. Res.*, Vol. 78, 1973.

XVII-13. McCauley, J. F., Carr, M. H., Cutts, J. A., Hartmann, W. K., Masursky, H., Milton, D. J., Sharp, R. P., and Wilhelms, D. E., "Preliminary Mariner 9 Report on the Geology of Mars," *Icarus*, Vol. 17, p. 289, 1972.

XVII-13. Sharp, R. P., "Mars: Fretted and Chaotic Terrains," *J. Geophys. Res.*, Vol. 78, 1973.

XVII-14. Milton, D. J., "Water and Processes of Degradation in the Martian Landscape," *J. Geophys. Res.*, Vol. 78, 1973.

XVII-15. Malin, M., "Salt Weathering on Mars" (in preparation).

XVII-16. Soderblom, L. A., and Wenner, D. B., "A Fossil Water Table on Mars" (in preparation).

XVII-17. Sharp, R. P., "Mars: Troughed Terrain," *J. Geophys. Res.*, Vol. 78, 1973.

XVII-18. Cross, C. A., "The Heat Balance of the Martian Polar Caps," *Icarus*, Vol. 15, p. 100, 1971.

XVII-19. Leighton, R. B., and Murray, B. C., "Behavior of Carbon Dioxide and Other Volatiles on Mars," *Science*, Vol. 153, p. 136, 1966.

References (contd)

XVII-20. Junge, C. E., Chagnon, C. W., and Manson, J. E., "Stratospheric Aerosols," *J. Meteorology*, Vol. 18, p. 81, 1961.

XVII-21. Leovy, C., and Mintz, Y., "Numerical Simulation of the Atmospheric Circulation and Climate of Mars," *J. Atmos. Sci.*, Vol. 26, p. 1167, 1969.

XVII-22. Hanel, R., Conrath, B., Hovis, W., Kunde, V., Lowman, P., Maguire, W., Pearl, J., Pirraglia, J., Prabhakara, C., Schlachman, B., Levin, G., Straat, P., and Burke, T., "Investigation of the Martian Environment by Infrared Spectroscopy on Mariner 9," *Icarus*, Vol. 17, p. 423, 1972.

XVII-23. Chase, S. C., Hatzenbeler, H., Kieffer, H. H., Miner, E., Münch, G., and Neugebauer, G., "Infrared Radiometry Experiment on Mariner 9," *Science*, Vol. 175, p. 308, 1972.

XVII-24. DeGeer, G., *Geochronologia Suecica Principles*, Text and Atlas, Almquist and Wiksells, Stockholm, 1945

XVII-25. Anderson, R. Y., and Koopmans L. H., "Harmonic Analysis of Varve Time Series," *J. Geophys. Res.*, Vol. 68, p. 877, 1963.

XVII-26. Anderson, R. Y., Dean, W. E., Kirkland, D. W., and Snider, H. I., "Permian Castile Varved Evaporite Sequence," "West Texas and New Mexico," *Geol. Soc. Am. Bull.*, Vol. 83, p. 59, 1972.

XVII-27. Emiliani, C., "Pleistocene Temperatures," *J. Geology*, Vol. 63, p. 538, 1955.

XVII-28. Murray, B. C., Ward, W. R., and Yeung, S. C., "Periodic Insolation Variations on Mars" (submitted to *Science*).

XVII-29. Briggs, G., "Periodic Variations in Martian Dust Storm Activity and the Layered Deposits of the Polar Region" (in preparation).

XVII-30. Leovy, C., "Exchange of Water Vapor Between the Atmosphere and Surface of Mars," *Icarus*, Vol. 18, p. 120, 1973.

XVII-31. Murray, B. C., and Malin, M., "Polar Wandering on Mars" (submitted to *Science*).

XVII-32. Soderblom, L. A., Kreidler, T. J., and Masursky, H., "The Latitudinal Distribution of a Debris Mantle on the Martian Surface," *J. Geophys. Res.*, Vol. 78, 1973.

XVII-33. Smalley, I. J., and Vita-Finzi, C., "The Formation of Fine Particles in Deserts and the Nature of Desert Loess," *J. Sedimentary Petrology*, Vol. 38, p. 766, 1968.

Acknowledgments

XVIII. Liquid Carbon Dioxide and the Martian Polar Laminae

Carl Sagan

Laboratory for Planetary Studies
Cornell University, Ithaca, New York 14850

One of the most important findings of the *Mariner 9* mission was the existence of a set of apparent stacked layers in both the north and south polar regions of Mars (Ref. XVIII-1). The individual layers have been called laminae and the zones in which they appear laminated terrain. The total thickness of the laminated terrain is approximately several kilometers, in agreement with a crude estimate of the thickness of the residual north and south polar caps of Mars made before the *Mariner 9* mission (Ref. XVIII-2). Because the Martian atmosphere is composed largely of CO_2 and because the frost point of CO_2 is known to be reached in both polar regions, it has been assumed that the volatiles in the bright laminae are in appreciable part condensed CO_2, although condensed H_2O, and a CO_2–H_2O clathrate are also possible. As long as the ratio of CO_2 to H_2O is large, the physical properties will be dominated by the CO_2.

Murray and Malin (Ref. XVIII-3) propose that the absence of discernible laminated terrain more than several kilometers deep in the polar regions can be attributed to Mars having had an atmosphere only in its rather recent history. Earlier, they propose, there was no atmosphere, and therefore no polar laminae could be layered down. These two views together imply that the age of the Martian atmosphere and the time scale since the differentiation of the planet is only ~ 10^5 years. However the shape of the crater frequency-diameter curve for the old cratered areas of Mars (Refs. XVIII-4 and XVIII-5), as well as the eroded appearance of large craters, seems to speak for atmospheric erosional events in the more distant Martian past. A high contemporary eolian erosion rate has been deduced for Mars (Ref. XVIII-6; also see Section XII of this Report).

I propose here an alternative view of the thickness of laminated terrain, which follows from the fact that the triple point of CO_2 is at $T_t = 217°K$ and $P_t = 5.1$ bars. At temperature/pressure pairs larger than these values, CO_2 will exist in the liquid state.

The existence of great volcanoes with summit calderas (Ref XVIII-7), as well as the high silicate content of the Martian surface dust (Ref. XVIII-8), leads directly to the view that Mars has been differentiated, and therefore that the content of radioactive U, Th, and K at the surface of Mars may be comparable to that at the surface of Earth. Accordingly, a temperature gradient caused by

radioactivity decay of some 10 to 40 K°/km, a value typical of Earth and the Moon, may also apply to Mars. This would then be the temperature gradient at the boundary of and beneath the polar laminae. Within the frost layers themselves, the content of radioactivity will be less, but the thermal diffusivity of water and CO_2 ice is comparable to that of dry dust. For a constant heat flux from below, the temperature gradient within the polar laminae should be no significantly different from that of their boundaries. Accordingly, T is reached at a depth of only a few kilometers within the polar laminae. The hydrostatic pressure load at such a depth is $\gg P_r$. Hence, depths of CO_2 frost more than several kilometers thick cannot exist on Mars. At the bottom of such a layer, the CO_2 liquefies and is laterally transported by the weight of the overlying solid layers that do not float in the liquid. The liquid, exposed to ambient Martian con-

ditions (assuming that the atmospheric pressure on Mars was never above 5.1 bars), vaporizes or freezes. Radioactivity melts about 1 cm CO_2/yr, giving a time constant $< 10^5$ years for establishing the equilibrium thickness of the full set of laminae plates. The total thickness of the Martian polar laminae stock (as well as the thickness of individual laminae) may therefore be a consequence of the phase diagram of CO_2 and not of the history of the Martian atmosphere.

Thus, it by no means follows from the structure of the Martian polar laminae that the atmosphere of Mars is a relatively recent arrival on the Martian scene. Even a dense atmosphere dating back to the origin of Mars is not excluded. This argument also can be read in reverse, the thickness of the laminae being an argument for a terrestrial value of the subsurface heat flux on Mars.

References

XVIII-1. Murray, B. C., Soderblom, L. A., Cutts, J. A., Sharp, R. P., Milton, D. J., and Leighton, R. B., "Geological Framework of the South Polar Region of Mars," *Icarus*, Vol. 17, p. 328, 1972.

XVIII-2. Sagan, C., "The Long Winter Model of Martian Biology: A Speculation," *Icarus*, Vol. 15, p. 511, 1971.

XVIII-3. Murray, B. C., and Malin, M. C., "Mars Atmosphere—A Late Arrival?" (in preparation).

XVIII-4. Chapman, C. R., Pollack, J. B., and Sagan, C., "An Analysis of the Mariner 4 Cratering Statistics," *Astron. J.*, Vol. 74, p. 1039, 1969.

XVIII-5. Hartmann, W. K., "Martian Cratering II: Asteroid Impact History," *Icarus*, Vol. 15, p. 396, 1971.

XVIII-6. Sagan, C., "Sandstorms and Eolian Erosion on Mars," *J. Geophys. Res.*, Vol. 78, 1973.

XVIII-7. Masursky, H., Batson, R. M., McCauley, J. F., Soderblom, L. A., Wildey, R. L., Carr, M. H., Milton, D. J., Wilhelms, D. E., Smith, B. A., Kirby, T. B., Robinson, J. C., Leovy, C. B., Briggs, G. A., Young, A. T., Duxbury, T. C., Acton, C. H., Jr., Murray, B. C., Cutts, J. A., Sharp, R.P., Smith, S. A., Leighton, R. B., Sagan, C., Veverka, J., Noland, M., Lederberg, J., Levinthal, E., Pollack, J. B., Moore, J. T., Jr., Hartmann, W. K., Shipley, E. N., de Vaucouleurs, G., and Davies, M. E., "Mariner 9 Television Reconnaissance of Mars and Its Satellites: Preliminary Results," *Science*, Vol. 175, p. 394, 1972.

References (contd)

XVIII-8. Hanel, R., Conrath, B., Hovis, W., Kunde, V., Lowman, P., Maguire, W., Pearl, J., Pirraglia, J., Prabhakara, C., Schlachman, B., Levin, G., Straat, P., and Burke, T., "Investigation of the Martian Environment by Infrared Spectroscopy on Mariner 9," *Icarus*, Vol. 17, p. 423, 1972.

Acknowledgments

XIX. Mars Atmosphere During the *Mariner 9* Extended Mission: Television Results

C. B. Leovy
University of Washington, Seattle, Washington 98195

G. A. Briggs
Jet Propulsion Laboratory/California Institute of Technology, Pasadena, California 91103

B. A. Smith
New Mexico State University, Las Cruces, New Mexico 98001

After the period of regular data-taking by *Mariner 9*, during which data from two revolutions each day were acquired and played back, data acquisition was limited to irregular intervals as shown in Table XIX-1. These data from the *Mariner 9* extended mission provide a record of seasonally varying processes from mid-spring to early summer in the northern hemisphere of Mars. In this section, we report on atmospheric phenomena observed by the television cameras during this period. Preliminary television results on the atmosphere from the regular data-taking period have been reported elsewhere (Ref. XIX-1). The map (Fig. XIX-1) shows locations on Mars of most of the subsequent figures.

A. Atmospheric Clarity

Surface features were viewed more clearly in pictures taken during this period than in any previous spacecraft pictures of the planet. Extensive cloudiness can be seen near the left side of Fig. XIX-2, but the exceptionally clear character of the cloud-free atmosphere is apparent

Table XIX-1. Extended mission data acquisitions

Revolution numbers (sequential from orbital insertion, Nov. 14, 1971)	1972 Earth date (GMT)	Equivalent Mars seasonal date	Areocentric longitude of the Sun, L_s
262[a]	March 23	March 25	4
416/417	June 8	May 1	40
422/423	June 14	May 4	43
430/431	June 18	May 6	44
436/437	June 21	May 7	46
444/445	June 25	May 9	48
450/451	June 28	May 10	49
458/459	July 2	May 12	51
478/479	July 12	May 15	54
528/529	August 6	May 27	65
533	August 9	May 29	67
667/668	October 16	June 28	96
675/676	October 21	June 30	98

[a]Last orbit of standard mission.
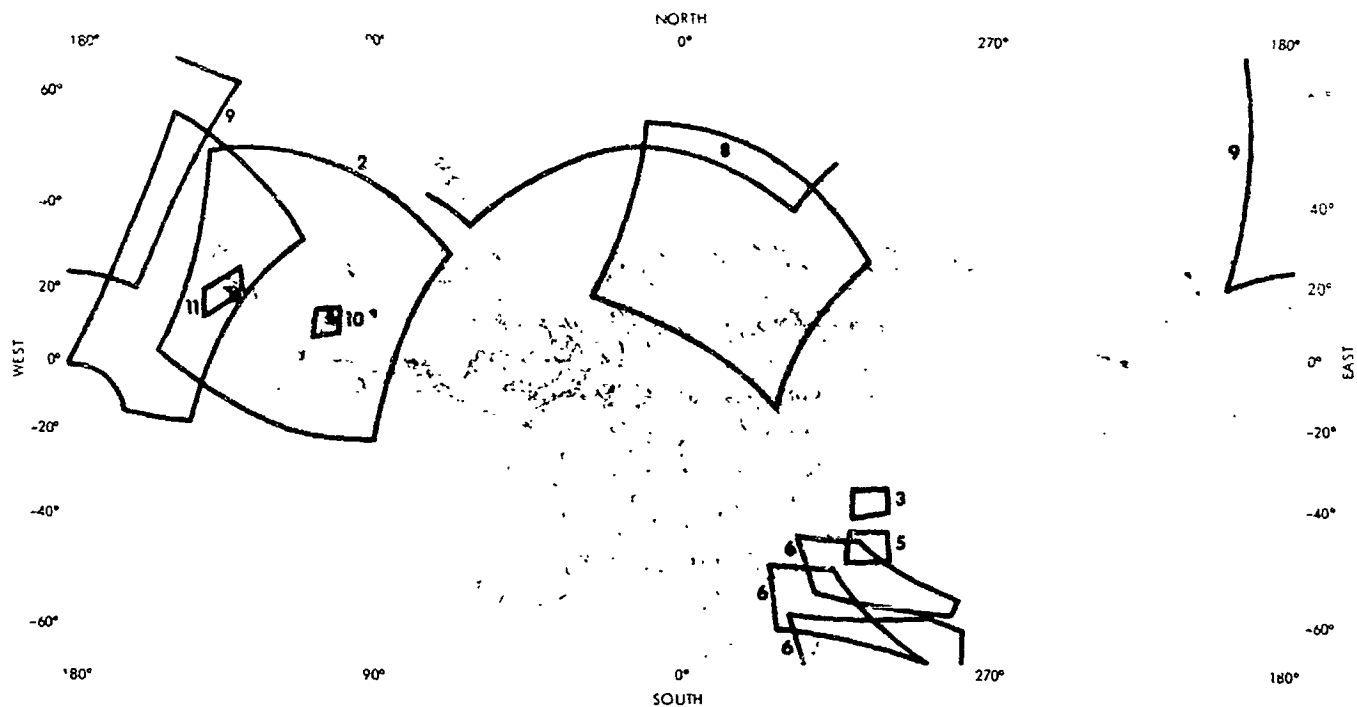
Fig. XIX-1. Map showing locations for the accompanying figures. The numbers refer to the figure numbers in this section.

near the limb in the lower-right part of the figure.[1] Here surface topographic detail, part of the extensive tropical canyon system near 10°S, 90°W, can be seen at emission angles as large as 88°. This clarity is typical of limb pictures taken during this period. Terminator frames show similar clarity; sharp detail can be seen up to the shadow line. By contrast, data taken during the earlier part of the *Mariner 9* mission (the standard mission) after the global dust storm had cleared (mid-February to mid-March 1972) showed a degradation in the clarity of surface features within 5° of the terminator. *Mariner 6* and 7 television pictures showed the same effect; surface details were best seen 8° or more from the terminator, and their visibility deteriorated at lower Sun angles (Ref. XIX-2). Although the lack of detail near the terminator may have been due in part to unexpectedly low sensitivity of the *Mariner 6* and 7 television cameras at low light levels, it is likely that atmospheric haze was responsible for most of the effect. This conclusion is supported by the gradual decrease in brightness across the limb, as shown by *Mariner 6* and 7 television data (Ref. XIX-3). With a few exceptions (noted below), the limb was more sharply defined during the *Mariner 9* extended

mission. Further evidence for general atmospheric haze was reported by the *Mariner 6* and 7 ultraviolet spectrometer (UVS) experimenters (Ref. XIX-4).

Visibility changes in the Hellas basin are of particular interest. Near the end of the standard mission, some topographic features had been seen on the floor of the basin in an area which had previously appeared to be quite smooth. The dust raised during the global dust storm was apparently slower settling over Hellas than elsewhere (Ref. XIX-1). Figure XIX-3 shows sharp detail on a part of the Hellas floor on which surface detail had not been seen before. The subtle topographic features can be seen quite close to the morning terminator (upper left).

On the basis of the visibility of features observed near the limb and terminator, we estimate the normal incidence optical depth throughout the extended mission period to be less than 0.04. Similar estimates for the earlier spacecraft data are compared in Table XIX-2. The *Mariner 4* estimate in Table XIX-2 also shows a small optical depth. It is taken from the analysis of Young (Ref. XIX-5), in which a substantial instrumental contribution to brightness had to be removed from the data. Although only a few data points are available, it is possible that the optical depth variations shown in Table XIX-2 represent a real seasonal variation in the normal

---

[1]For identification purposes, the *Mariner 9* pictures are identified in the frame captions by roll and frame number and DAS time. All pictures can be ordered from the National Space Science Data Center, Code 601, Greenbelt, Maryland 20771.
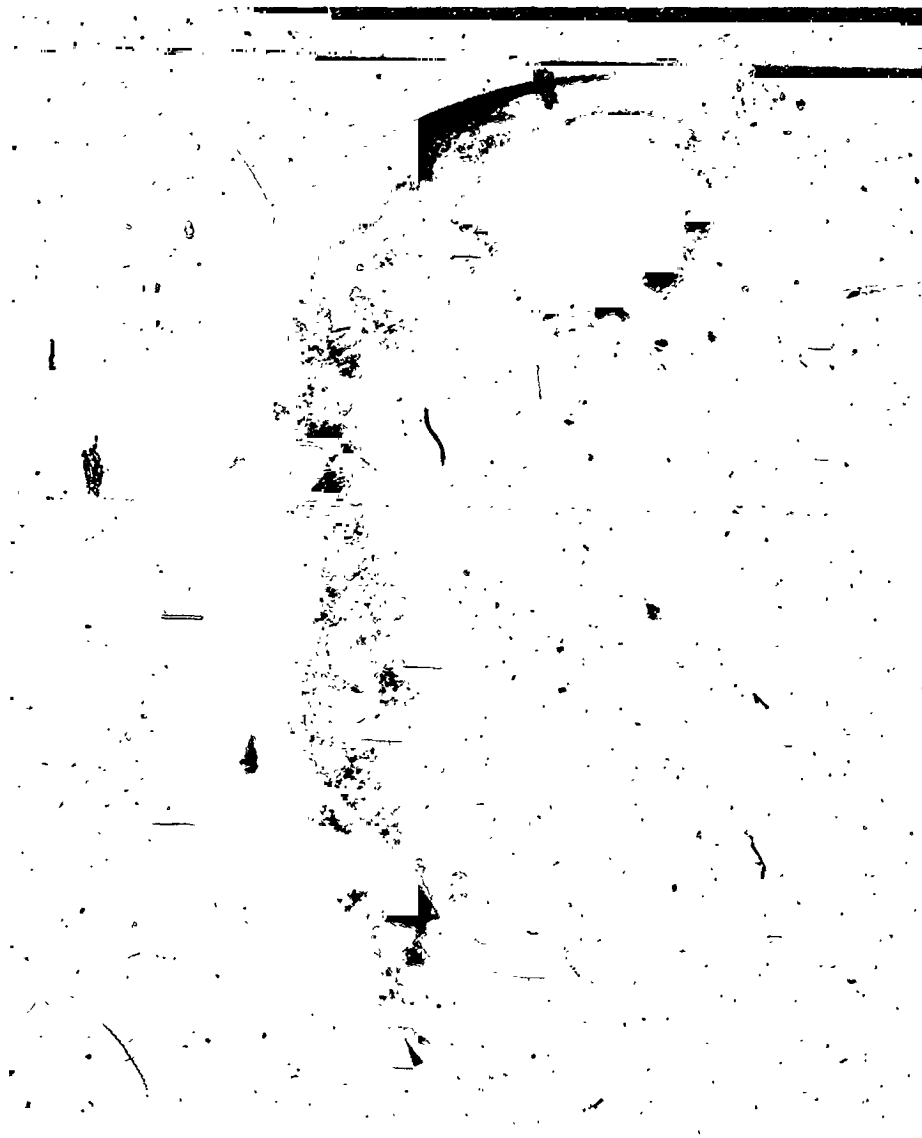
Fig. XIX-2. Global mosaic showing the Tharsis region on revolution 528. Note the clarity near the limb in the vicinity of Tithonius Lacus (bottom right) and the brightening on the west sides of the calderas (bottom and left). The marker indicates the location of the limb profile of Fig. XIX-4. Only the bottom picture of this mosaic is shown on Fig. XIX-1. (MTVS 4296-55, DAS 12994387; MTVS 4296-51, DAS 12994317; MTVS 4296-47, DAS 12994247)

optical depth, exclusive of the great dust storm events. Such a seasonal opacity variation could be explained by widespread suspended dust raised predominantly during the northern autumn and winter seasons. The latter is also the season of Mars' perihelion.

A few exceptions to the usually sharp limb profiles were observed. Figure XIX-4 shows a limb profile in which the upper boundary of a thin haze layer shows as a faint shelf in the brightness above the limb seen in Fig. XIX-2. This shelf also can be seen by careful inspection of the original television picture. The layer occurs near 20°S latitude during the afternoon, and its top is estimated to be 15 to 25 km above the surface. It may correspond to the upper limit of the active convection layer predicted by Gierasch and Goody (Ref. XIX-6). There was no indication of the very high (70-km) haze layer which was observed during the planet-wide dust storm (Ref. XIX-1).

Fig. XIX-3. Hellas basin near the morning terminator on revolution 430 (see Fig. XIX-1 for location). The morning terminator is just beyond the lower-left corner. This picture has been high-pass filtered in the vertical direction to reduce the large-scale variation in solar illumination. (MTVS 4289-7, DAS 11797001)
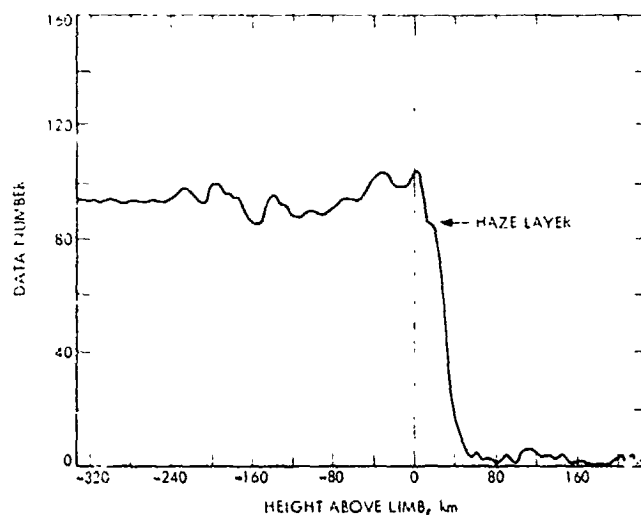
Fig. XIX-4. Limb profile on revolution 533 (see Figs. XIX-1 and XIX-2 for location). The arrow indicates the top of a thin haze layer.

Table XIX-2. Atmospheric normal incidence optical depth

Mission	Mars seasonal date	L_s	Estimated normal incidence optical depth
Mariners 6 and 7	October 14	200	0.10 (TV)
Mariners 6 and 7	October 14	200	0.06 (UVS; Ref. XIX-4)
Mariner 9 Standard mission (Post dust storm)	March 1–25	350 to 340	0.05 to 0.10
Mariner 9 Extended mission	April 24–July 1	30 to 100	< 0.04

B. Clouds in the Polar and Sub-Polar Regions

Figure XIX-5 shows extensive bright streaks over the southern part of Hellas near the morning terminator. The streaks are similar in form to some very faint streaks viewed in the same region early in the mission, also in the morning (revolution 136, Jan. 22, terrestrial date). In both cases surface features were partly or totally ob-

scured, and the streaks are therefore inferred to be clouds. The brightness of the clouds, especially near the terminator, suggests that they are composed of condensates rather than dust. In the lowest one or two scale heights, temperatures are above the CO_2 condensation temperature at this latitude and season (Ref. XIX-7; also see Section XXXVI of this Report), and therefore the most likely candidate for the cloud material is water ice. Hellas has been observed to brighten frequently at this season (Ref. XIX-5), and cloudiness of this type appears to be responsible for this recurrent seasonal brightening. Although the clouds are partially obscuring the surface, some surface features can be seen dimly through the clouds, suggesting that the optical depths are mostly ~ 1. There is a suggestion of wave clouds near the left edge of the picture. These may be due to the influence of the west rim of the basin if the flow is from the west.

Wave clouds formed by strong flow over topography were seen over the southern polar region south of 50 S (Fig. XIX-6). These were similar in appearance to the clouds seen in the north during the northern winter. In particular, the predominant wavelengths are comparable
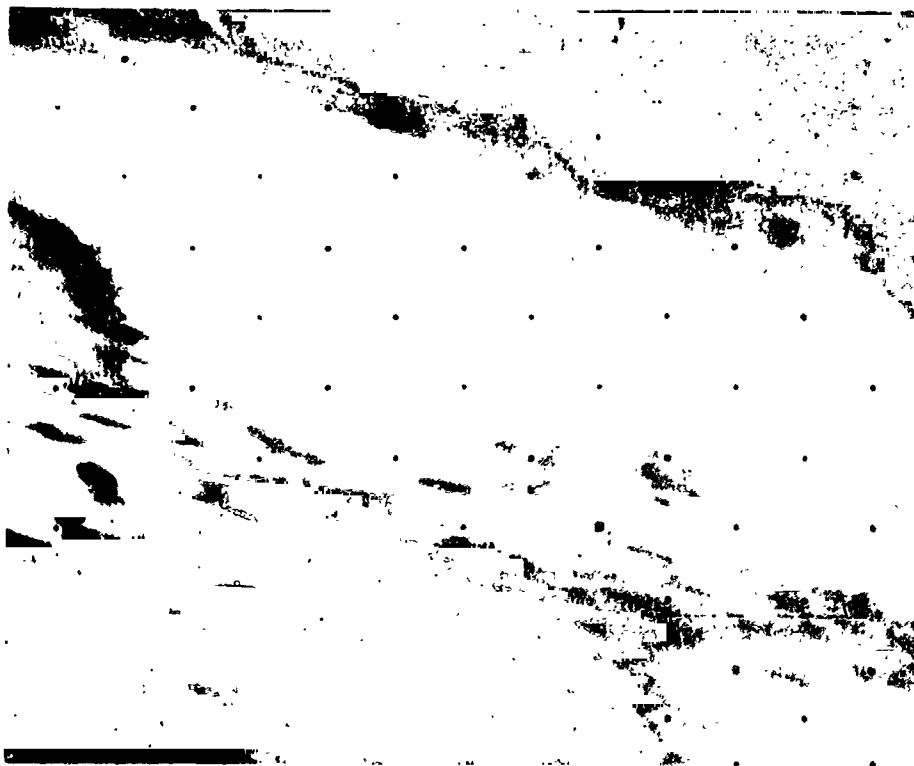
Fig. XIX-5. Clouds over Hellas basin near the morning terminator (see Fig. XIX-1 for location) on revolution 430. This picture has been high-pass filtered in the vertical direction to enhance details. (MTVS 4289-3, DAS 11796791)

Fig. XIX-6. Mosaic of frames showing clouds over the south polar region on revolution 459 (see Fig. XIX-1 for location). (MTVS 4294-71, DAS 12535245; MTVS 4294-75, DAS 12535175; MTVS 4294-79, DAS 12535105)

(30 to 40 km); the relationship between the waves and underlying topography shows that waves are formed in westerly winds in both cases, and wave clouds are restricted mainly to the latitude band between 30° and 40° from the pole in both the northern winter and southern winter. Closer to the pole, the wave-cloud field gives way to diffuse widespread haze. The surface can be seen faintly through the thin haze south of 60°S, and does not yet appear to be frost-covered in the illuminated portion of this region (May 11, Mars date), even though this region does become covered with CO_2 frost by the end of southern winter. A few bright patches near the terminator (bottom of Fig. XIX-6) may be localized patches of frost.

The receding north polar cap in general was seen clearly during this period, but close inspection of a number of pictures revealed faint clouds over the cap and just south of its edge. Figure XIX-7a is a wide-angle camera view of the cap in which, at this low resolution, the cap area appears to be cloud-free. A narrow-angle camera picture, taken a few minutes earlier over the cap,

Fig. XIX-7 (a) Wide-angle view of the north polar cap, on revolution 529, showing footprint locations of Figs. XIX-7ᵗ and XIX-7c. (MTVS 4296-102, DAS 13028127) (b) Narrow-angle view taken at about the same time as (a). Note the wave clouds to the west of the large crater. This picture has been subject to high-pass filtering in the vertical to enhance small-scale details. (MₜVS 4296-99, DAS 13027322) (c) Portion of wide-angle view near the cap edge on revolution 423. This picture has been subject to high-pass filtering in the horizontal. (MTVS 4288-116, DAS 11658890)

shows very subtle wave clouds to the west of a large crater (Fig. XIX-7b). These clouds appear to have formed in east-to-west flow over the crater. Another example of the appearance of subtle wave clouds is shown in Fig. XIX-7c. Here the wave-cloud pattern resembling fish scales appears to be formed in northeast-to-southwest flow off the polar cap edge. The apparent flow from northeast to southwest revealed by the clouds is consistent with the flow direction expected near the cap at this season: subliming CO_2 should generate a mass outflow which would be deflected toward the west by the coriolis force. The occurrence of clouds in the vicinity of the north polar cap during spring and summer contrasts with an absence of identifiable clouds over the south polar cap at a somewhat later summer season when the *Mariner 9* orbital observations began. This difference may be related to the greater abundance of water in the atmosphere at this season (Ref. XIX-9). The composition of the clouds seen in Fig. XIX-7 is unknown, however.

A remarkable atmospheric feature related to the cap can be seen in Fig. XIX-8. The long streaks near the terminator curving from north toward the west are coupled with a general haziness north of 45°N, which is very unusual in the extended mission pictures. This haziness is indicated by an albedo variation near 45°, by partial obscuration of the surface features north of that latitude, and by the irregular shape of the terminator in the same latitude belt. The streaks may be due to concentration of the outflow from the cap into a relatively narrow jet. If so, it is unlike anything known in Earth's atmosphere. This is the only time such a feature was observed by *Mariner 9*.

C. Localized Brightening Phenomena in the Tropics

Significant new observations were made of several of the localized brightenings in the Amazonis, Tharsis, and Nix Olympica regions; they have been recognized by planetary astronomers as recurrent white clouds (Ref. XIX-10). These phenomena will be treated in more detail in a later paper; here we discuss briefly the new observations. Attempts to photograph these brightenings early in the mission were severely hampered by the obscuring global dust storm and by unfavorable orbit geometry. Nevertheless, brightenings were observed over Nix Olympica and over the southernmost of the three major aligned calderas in Tharsis ("South Spot"). The pictures confirmed that these brightenings were diffuse clouds (Ref. XIX-1). In one case relatively distinct cloud elements casting distinct shadows were observed over the caldera floor of South Spot. The shadows indicated a cloud height of 5 to 10 km, too low for CO_2 condensation at this latitude, and the clouds were inferred to be water ice, as suggested by Smith and Smith (Ref. XIX-8).

The changing orbital geometry afforded an opportunity to obtain synoptic coverage of these features during the afternoon late in the extended mission. As Earth-based data had shown that these features begin to brighten in the early afternoon and continue through the afternoon, several sequences of pictures were planned to take advantage of this viewing opportunity. Analysis of the Earth-based data by S. A. Smith at New Mexico State University indicated that the northern-most aligned caldera ("North Spot") and Nix Olympica could be expected to be especially active during this season, and these two

Fig. XIX-8. Wide-angle mosaic showing streaks related to the north polar cap on revolution 478 (see Fig. XIX-1). Brightness data for this picture have been divided by a factor proportional to $\mu_0^{0.7}$, where μ_0 is the cosine of the solar incidence angle, in order to reduce the large-scale solar illumination variation. Portions of the scene near the lower left and over part of the polar cap show vidicon saturation caused by high illumination levels. (MTVS 4295-71, DAS 12874573; MTVS 4295-67, DAS 12874503)

features were selected for intensive coverage. Results amply justified this prediction.

The first afternoon view of Nix Olympica during the extended mission was obtained on revolution 479 from an altitude of 13,000 km (Fig. XIX-9). In this picture, the western side of the escarpment at the base of the mountain (arrow) can be seen near the terminator. Extending across this region toward the north and west for about 1000 km is an area of rather faint cloudiness. The circular banding of the outlying clouds and radial streakiness suggest that the cloud system is spreading outward from the volcano. Shadows of some of the cloud bands can be discerned, the clouds casting these shadows appear to be some 20 to 30 km above the surface which, in this region, is relatively low (surface pressure greater than 5 mb).

The extended mission also provided an opportunity to observe Nix Olympica in mid-morning. Figure XIX-10 is a wide-angle picture acquired on revolution 423 at a range of 2300 km with the caldera at about 9 a.m. local time. The marked brightening around the northern and eastern escarpments of the volcano's base may be due to atmospheric scattering, but if so, it is unexpected at this early time of day. Alternatively, the brightening may be the result of the photometric properties of the
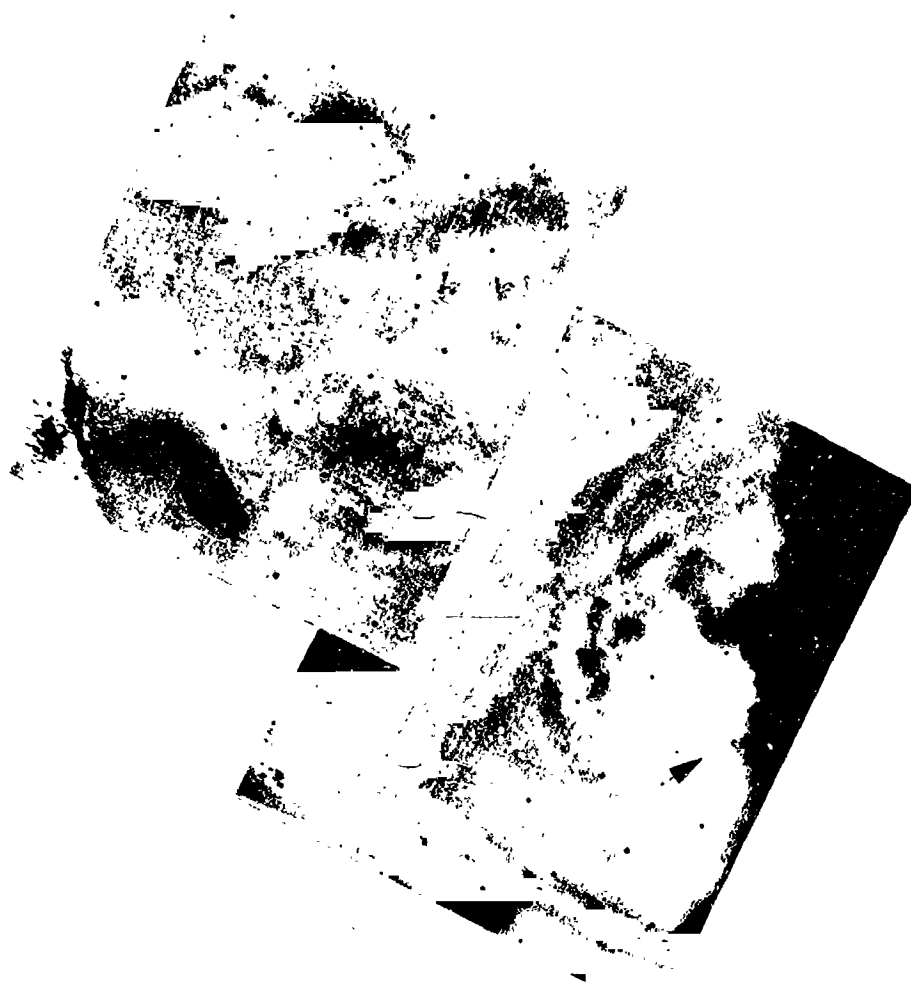
Fig. XIX-9. Wide-angle mosaic of the Amazonis region (see Fig. XIX-1), on revolution 479, showing the clouds over the west of Nix Olympica. The arrow marks the scarp at the base of the mountain. Data for this picture have been divided by $\mu_0^{0.8}$ to reduce the large-scale solar illumination variation. Parts of the scene near the left edge show vidicon saturation. (MTVS 4295-119, DAS 12909993)

Fig. XIX-10. Wide-angle view of Nix Olympica in mid-morning, on revolution 423, showing brightening around the scarp at the base of the volcano. (MTVS 4288-91, DAS 11657070)

material that makes up the cliff base, material which is probably much less consolidated than that making up the flanks of the mountain. The photometric angles at the picture center are: phase, 21.3°; incidence, 29.3°; and emission, 21.6°. Certainly not all the bright slopes are sunward facing (the shadows within the caldera are the best visual guide to the Sun's direction), but at the present an interpretation of the brightening as an atmospheric phenomenon is unconvincing. If, however, further analysis points in this direction, the atmospheric scatterers, presumably condensates, must be very low to conform so well to the surface topography.

Figure XIX-2 is the first synoptic view of the Amazonis–Tharsis region acquired on revolution 528. Distinct brightening appears near each of the three aligned calderas and Nix Olympica, with the strongest brightening on the west slopes of Nix Olympica and North Spot. Fainter brightening also appears over Arcadia, and over a part of the canyon system near Tithonius Lacus. The nature of the brightenings is unclear from Fig. XIX-2, but two narrow-angle pictures taken at this time are more revealing. Figure XIX-11 is a narrow-angle picture showing the west slopes of North Spot (local time is about 16:00).

The brightening is obscuring surface details, indicating that it is due to clouds or fog; it is also confined to the lower slopes of the volcano, and is strongly constrained by topography. Figure XIX-12 shows marked brightening around Nix Olympica (local time 14:00), particularly over the western slopes. Surface detail again is obscured by the clouds, which are strongly constrained by the topography and confined mainly to the lower slopes. In the case of Nix Olympica, however, several distinct clouds can be seen over the rim of the caldera extending in over the caldera floor. These clouds are better defined and more sharply bounded than the diffuse cloudiness on the outer slopes of Nix Olympica or North Spot. The scale of the individual elements of this cloud system is large; individual elements are 10 to 20 km in diameter. No definite shadows have been identified as yet in the narrow-angle pictures of Figs. XIX-11 or XIX-12.

The final pictures of the mission, taken on two sequences 5 days apart during mid-October, included additional pictures of the Tharsis and Nix Olympica regions. On each sequence, pictures were scheduled at intervals during the afternoon in order to study the diurnal behavior and to look for day-to-day changes. As these pic-
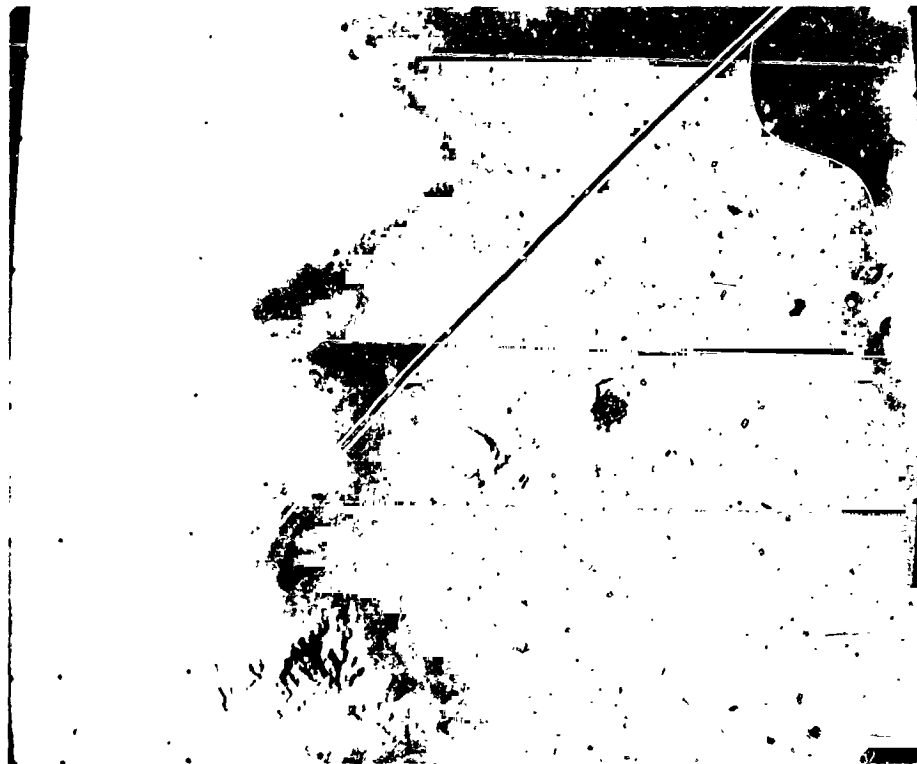
Fig. XIX-11. Narrow-angle view showing brightening west
of North Spot. (MTVS 4296-62, DAS 12995262)

tures were acquired only recently, they have as yet received only preliminary processing, and only two of the thirteen pictures acquired will be presented and discussed here.

Figure XIX-13a, taken on revolution 675, has Sun and viewing geometries similar to those of Fig. XIX-2. The local time is about 13:30 at Nix Olympica and about 15:30 at North Spot. The brightenings appear in almost precisely the same locations as on the earlier revolution, but are somewhat more intense around both Nix Olympica and North Spot on the later revolution. Smith and Smith (Ref. XIX-8) had shown from Earth-based data that increasing activity of these features was to be expected during the season. Two features appear in Fig. XIX-13 that were absent in Fig. XIX-2. A series of linear bright streaks northeast of North Spot trend northwest–southeast in a region in which there are no known topographic features, although the features appear to be topographically controlled. The brightening near the canyon system in Tithonius Lacus, which is more intense than that shown in Fig. XIX-2, includes some linear bright patches that probably correspond to part of the canyon (see Fig. XIX-13b). Again, there is strong topo-

graphic control of the major bright cloud systems. The identification of the clouds seen on this revolution as water ice has been confirmed by the infrared interferometer spectrometer data.

Figure XIX-14 is a narrow-angle view of North Spot taken at about the same time. The topographic control of the cloud system is apparent, but internal structure is also shown. The structure resembles convective cells of rather large scale (about 10 km) and some tendency for alignment of the cloud cells in an east–west direction.

The source of water for these recurrent clouds is unknown. Local degassing of water absorbed in the upper few centimeters of the surface material is one possibility (Ref. XIX-11). Water desorbed from this upper layer, which is subject to the diurnal thermal wave, might or might not be replenished in part by some upward flux of juvenile water from below. In either case, the volcanic surface material located in the cloud region may be a particularly good adsorber (Ref. XIX-11). Degassing models call for expulsion of water from the ground each day so that the seasonal and diurnal repetition of the phenomenon requires daily replenishment of small amounts of water (at

Fig. XIX-12. Narrow-angle view showing brightening west of Nix Olympica and clouds over the summit caldera. (MTVS 4296-58, DAS 12995122)

least 1 mg/cm³ or seasonal replenishment of larger amounts (at least 100 mg/cm³). Seasonal storage in a deep layer could provide the moisture needed for daily replenishment of the thin, diurnally heated layer from which daily moisture expulsion takes place, but the details of how seasonal replenishment could take place are not clear to us.

On the other hand, as Peale (Ref. XIX-12) has pointed out, local degassing may not be required to explain the phenomena. Orographic uplift coupled with active convection could be sufficient. The very high correlation between white cloud occurrence and elevation has been pointed out by Sagan et al. (Ref. XIX-13). The four calderas around which the brightenings occur are probably the highest locations on Mars; they were the most clearly visible features during the global dust storm (Ref. XIX-14), probably because they were higher than much of the dust. The region around Tithonius Lacus is not one of the highest on the planet, but it is high and has very steep canyon slopes, so that it too might be an especially favored region for orographic cloud formation. Blumsack et al. (Ref. XIX-15) have shown that strong upslope winds are to be expected during the afternoon over slopes that are either steep or very extensive. The fact that the

clouds form around the slopes, often around the lower slopes, of the volcanic mountains appears to argue against this hypothesis. The almost complete absence of cloud shadows, even in cases where shadows might have been seen for clouds that were no more than 2 or 3 km above the surface, also argues against a purely convective origin for the clouds. On the other hand, even the bases of the three aligned volcanic piles in Tharsis are very high (e.g., Ref. XIX-16); air arriving at the base of South Spot from surrounding lowlands will have undergone considerable lifting.

Radar profiles of accuracy comparable to that near South Spot are unfortunately not available for North Spot, but North Spot appears to be located on the same high ridge as South Spot. Nix Olympica has a lower base, but the clouds occur well up the slope of this very high mountain. (The morning brightening around the base of Nix Olympica, shown in Fig. XIX-10, may be a significant exception.) Contrary to the *Mariner 9* observations, orographic–convective clouds might be expected to surmount the highest nearby topographic features, but there is a powerful mechanism for checking their growth in height. Once formed, they will become very effective infrared radiators. A cloud containing only 1 mg/cm² of
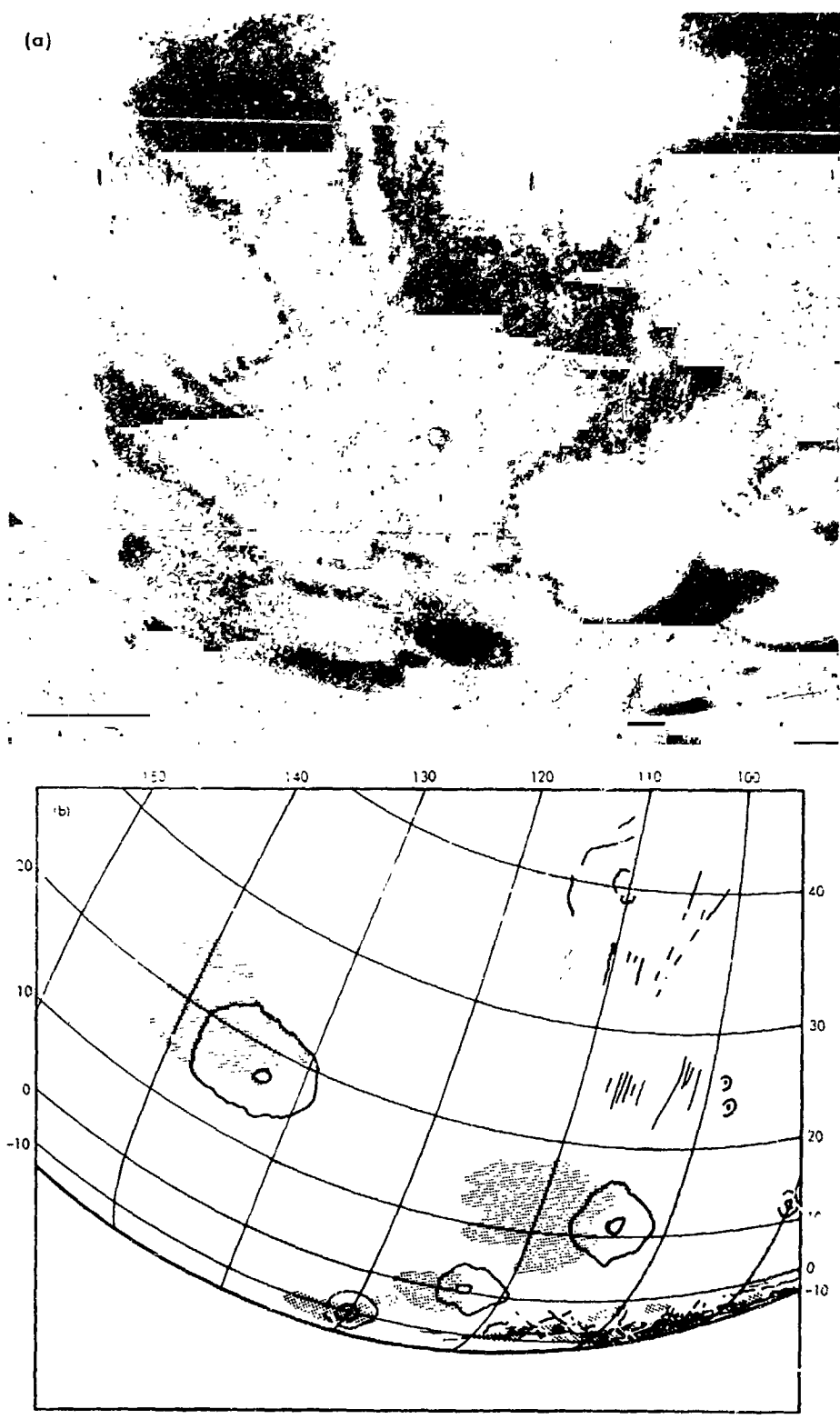
Fig. XIX-13. (a) Wide-angle view of the Tharsis and Nix Olympica regions showing brightenings on revolution 676. Note the brightenings near Tithonius Lacus (lower right). (MTVS 4298-82, DAS 13502983). (b) Orthographic projection key map for (a); brightenings are shown by shading.
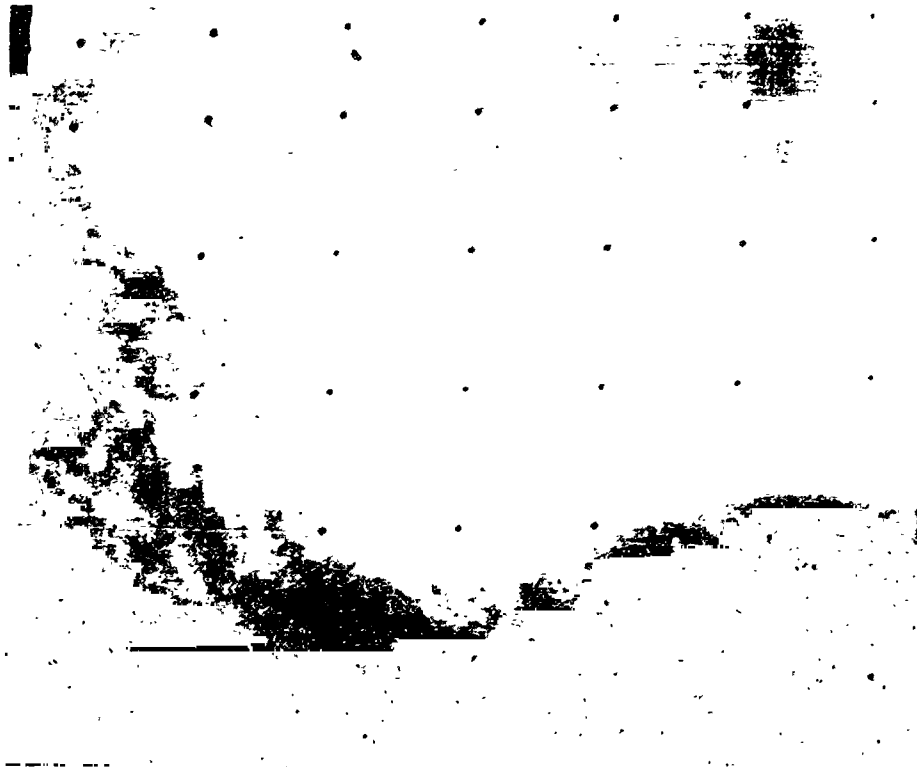
Fig. XIX-14. Narrow-angle view of North Spot, on revolution 675, showing convective structure in the brightening region. The caldera is in the lower-right corner. (MTVS 4298-78, DAS 13502983)

ice will have an emissivity of order unity in the thermal infrared (Ref. XIX-17). Because of the low-volume heat capacity of the Mars atmosphere, such an effective thermal radiator could easily stabilize both the lapse rate and vertical cloud growth. The orographic-convective cloud model can explain the cloud diurnal behavior: both forced uplift and thermal convection would be strongest during the afternoon. This model is also consistent with the seasonal cloud behavior. The clouds are observed to occur when the moisture content of the atmosphere as a whole is greatest. Possibly all three factors, orographic uplift, convection, and local degassing, may be needed to form the observed clouds.

D. Summary

The extended mission provided seasonal coverage data from northern spring to early summer. Among the most important atmospheric phenomena observed by the television cameras were:

(1) Remarkable atmospheric clarity at this season.

(2) A faint shelf of brightne   near 20 km in height, which may correspond to t e top of the convective layer.

(3) Condensate clouds over Hellas in the early morning.

(4) Wave clouds over the south polar region (50° to 60°S) indicating strong west to east winds.

(5) Faint wave clouds over the north polar cap, probably composed of water ice, and indicating northeast to southwest flow off the cap.

(6) Clouds over the major volcanos and Tithonius Lacus which show remarkable repeatability, strong topographic control, and, in some cases, evidence for convective structure.

Additional analysis of the synoptic sequences over the Tharsis, Amazonis, and Nix Olympica regions may clarify the cause of the cloud occurrences there.

References

XIX-1. Leovy, C. B., Briggs, G. A., Young, A. T., Smith, B.A., Pollack, J. B., Shipley, E. N., and Wildey, R. L., "The Martian Atmosphere: Mariner 9 Television Experiment Progress Report," *Icarus*, Vol. 17, p. 373, 1972.

XIX-2. Leighton, R. B., Horowitz, N. H., Murray, B. C., Sharp, R. P., Herriman, A. H., Young, A. T., Smith, B. A., Davies, M. E., and Leovy, C. B., "Mariner 6 and 7 Television Pictures: Preliminary Analysis," *Science*, Vol. 166, p. 49, 1969.

XIX-3. Leovy, C. B., Smith, B. A., Young, A. T., and Leighton, R. B., "Mariner Mars 1969: Atmospheric Results," *J. Geophys. Res.*, Vol. 76, p. 297, 1971.

XIX-4. Hord, C. W., "Mariner 6 and 7 Ultraviolet Spectrometer Experiment: Photometry and Topography of Mars," *Icarus*, Vol. 16, p. 253, 1972.

XIX-5. Young, A. T., "High Resolution Photometry of a Thin Planetary Atmosphere," *Icarus*, Vol. 11, p. 1, 1969.

XIX-6. Gierasch, P. J., and Goody, R. M., "A Study of the Thermal and Dynamical Structure of the Martian Lower Atmosphere," *Planet. Space Sci.*, Vol. 15, p. 615, 1968.

XIX-7. Kliore, A. J., Fjeldbo, G., Seidel, B. L., Sykes, M. J., and Woiceshyn, P. M., "S-Band Radio Occultation Measurements of the Atmosphere and Topography of Mars with Mariner 9: Extended Mission Coverage of Polar and Intermediate Latitudes," *J. Geophys. Res.*, Vol. 78, 1973.

XIX-8. Smith, S. A., and Smith, B. A., "Diurnal and Seasonal Behavior of Discrete White Clouds on Mars," *Icarus*, Vol. 16, p. 509, 1972.

XIX-9. Barker, E. S., Schorn, R. A., Woszcyk, A., Tull, R. G., and Little, S J., "Mars: Detection of Water Vapor During Southern Hemisphere Spring and Summer Season," *Science*, Vol. 170, p. 1308, 1970.

XIX-10. Slipher, E. C., *A Photographic History of Mars*, Sky Publishing Company, 1962.

XIX-11. Fanale, F. P., and Cannon, W. A., "Adsorption on the Martian Regolith," *Nature*, Vol. 230, p. 502, 1971.

XIX-12. Peale, S., "Water and the Martian W-Cloud," *Icarus*, Vol. 18, 1973.

XIX-13. Sagan, C., Veverka, J., and Gierasch, P., "Observational Consequences of Martian Wind Regimes," *Icarus*, Vol. 15, p. 253, 1971.

XIX-14. Masursky, H., Batson, R., McCauley, D., Soderblom, L., Wildey, R., Carr, M., Milton, D., Wilhelms, D., Smith, B., Kirby, T., Robinson, J., Leovy, C., Briggs, G., Young, A. T., Duxbury, T., Acton, C., Murray, B., Cutts, J., Sharp, R., Smith, S., Leighton, R., Sagan, C., Veverka, J., Noland, M., Lederberg, J., Levinthal, E., Pollack, J. Moore, J., Hartmann, W., Shipley, E., de Vaucouleurs, G., and Davies, M., "Mariner 9 Television Reconnaissance of Mars and Its Satellites: Preliminary Results," *Science*, Vol. 175, p. 294, 1972.

References (contd)

XIX-15. Blumsack, S., Gierasch, P., and Wessel, R., "An Analytical and Numerical Study of the Martian Planetary Boundary Layer Over Slopes," *J. Atmos. Sci.*, Vol. 30, 1973.

XIX-16. Pettengill, G. H., Rogers, A. E., and Shapiro, I. I., "Martian Craters and Scarps as Seen by Radar," *Science*, Vol. 174, p. 1321, 1971.

XIX-17. Leovy, C. B., "Mars' Ice Caps," *Science*, Vol. 154, p. 1178, 1966.

Acknowledgments

XX. Atmospheric and Surface Properties of Mars Obtained by Infrared Spectroscopy on *Mariner* 9

B. Conrath, R. Curran, R. Hanel, V. Kunde, W. Maguire,
J. Pearl, J. Pirraglia, and J. Welker
Goddard Space Flight Center, Greenbelt, Maryland 20771

T. Burke
Jet Propulsion Laboratory/California Institute of Technology, Pasadena, California 91103

The infrared spectroscopy experiment on *Mariner* 9 obtained data over much of Mars during the almost 1-year operational lifetime of the spacecraft. Thermal emission spectra have been recorded by the Michelson interferometer from 200 to 2000 cm^{-1} (50 to 5 μm) with a spectral resolution of 2.4 cm^{-1} in the apodized mode of data reduction. The spatial resolution corresponds to a circular area of 125-km diameter at periapsis and vertical viewing but changes with spacecraft–Mars distance. A noise-equivalent-radiance of 0.5×10^{-7} W cm^{-2} sterad^{-1}/cm^{-1} has been deduced from the repeatability of the calibration spectra taken periodically from deep space and from a built-in blackbody. The calibration spectra also indicated constancy of the responsivity of the instrument between prelaunch tests and end of mission.

The scientific objectives of the experiment include the interpretation of the thermal emission of Mars in terms of atmospheric temperatures, wind fields and dynamics, surface temperatures, surface pressure and topography, mineral composition, and minor atmospheric constituents including isotopic ratios, as well as a search for unexpected phenomena. The derived physical parameters also may be pertinent to biological investigations. The availability of a large and continuous portion of the spectrum permits flexibility in designing methods of interpretation and allows analysis of unforeseen phenomena. The latter was well demonstrated by the significance of information extracted from spectra obtained during the unexpectedly violent dust storm.

The scientific goals of the infrared spectroscopy experiment, as established in advance of the mission, have been discussed (Ref. XX-1); a description of the Fourier transform spectrometer used in this experiment has been given (Ref. XX-2); and first results and interpretation of the data up to May 1972 have been published (Refs. XX-3 and XX-4). This section contains a report on the analysis of the data carried out from June through October 1972. Because the data analysis is far from complete, this section is primarily a progress report on ongoing work.

A. Carbon Dioxide and Water Vapor Transmittances

Fundamental to the quantitative interpretation of planetary emission spectra is a precise knowledge of the transmittances of atmospheric gases present: in this case primarily carbon dioxide and water vapor.

In addition to providing the basis for analysis of atmospheric temperatures and surface pressure, the CO_2 transmittances also are required to estimate isotopic abundances of carbon and oxygen, and to allow identification of other gaseous constituents in the spectral range covered by the instrument. Refinement of the CO_2 transmittances as a function of wavenumber, temperature, and pressure has continued. In order to assess the validity of the theoretical transmittances and as a check on the internal consistency of the techniques used for the retrieval of surface pressure and atmospheric temperatures, a synthetic Martian spectrum has been calculated using a line-by-line integration technique (Ref. XX-5). Molecular absorption by CO_2 and H_2O is included in this theoretical model. The computed spectrum is based on a solution of the equation of radiative transfer and uses the surface pressure and temperature profile derived from portions of the same set of spectra for which the comparison is made. Because the operational computer program that derives surface pressure and atmospheric temperatures uses a parameterized form of the CO_2 transmittances, which is not as precise as the line-by-line integration technique, small differences between the computed and the experimental radiances are expected. Use of parameterized transmittances is dictated by the great expense in computer time required by the line-by-line integration method for processing individual spectra.

Observed spectra were chosen from revolution 174 near local noon and near the sub-solar latitude to maximize the thermal contrast, thereby enhancing the appearance of spectral features. Eighteen spectra were

averaged to reduce the random noise to approximately 1×10^{-7} W cm⁻ sterad⁻¹/cm⁻¹. While this noise-equivalent-radiance is approximately independent of wavenumber, the corresponding noise-equivalent-temperature varies from less than 0.7°K at 300 cm⁻¹ to less than 0.1°K at 800 cm⁻¹, to less than 0.6°K at 1600 cm⁻¹.

The 200 to 590 cm⁻¹ and the 500 to 800 cm⁻¹ regions, respectively, of the average measured brightness temperature are compared with theoretical spectra in Figs. XX-1 and XX-2. The theoretical spectra were computed using the surface pressure and vertical temperature profile retrieved from the radiances in the 668 to 750 cm⁻¹ region and a total water vapor content of 10 precipitable micrometers as determined from the H_2O lines in the 250 to 325 cm⁻¹ region. The H_2O line parameters were from Benedict and Kaplan in 1967; the CO_2 parameters were generated from band positions and band strengths obtained from Benedict in 1970 and from Drayson (Ref. XX-6). Numerous rotational absorption lines, due to atmospheric H_2O, are evident in the 200 to 500 cm⁻¹ region shown in Fig. XX-1. The comparison of the observed and the theoretical spectrum shows good spectral correspondence between the known H_2O lines, even for the weak lines in the region of 500 cm⁻¹. No unidentified or anomalous features are evident in this spectral interval.

Strong molecular absorption by atmospheric CO_2 appears between 500 and 800 cm⁻¹, as shown in Fig. XX-2. Several of the strongest CO_2 bands for the five most common isotopes are listed in order of descending band strength in Table XX-1. The band strengths for the iso-
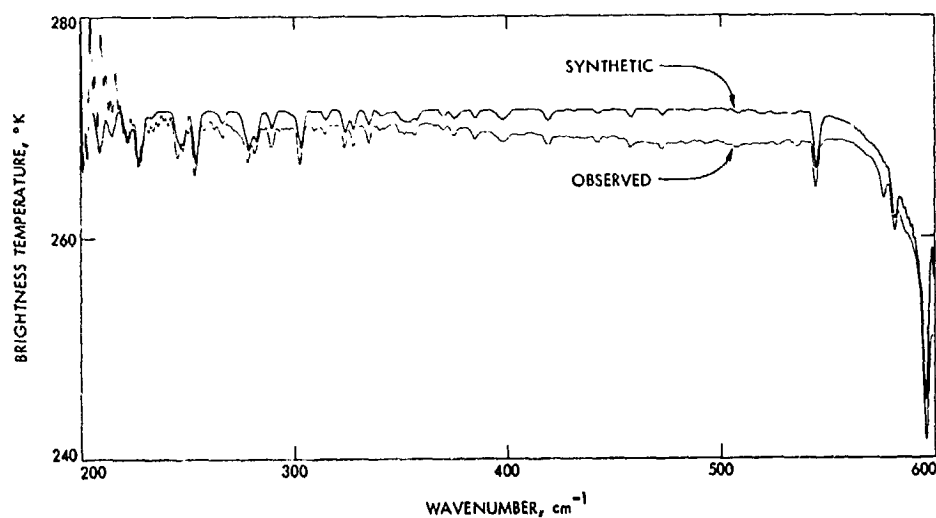
Fig. XX-1. Comparison of synthetic and observed spectra for revolution 174 (−30° latitude, 32° longitude, 14:00 local time) in the region of absorption by atmospheric water vapor. The synthetic spectrum contains 10 μm of precipitable water vapor.
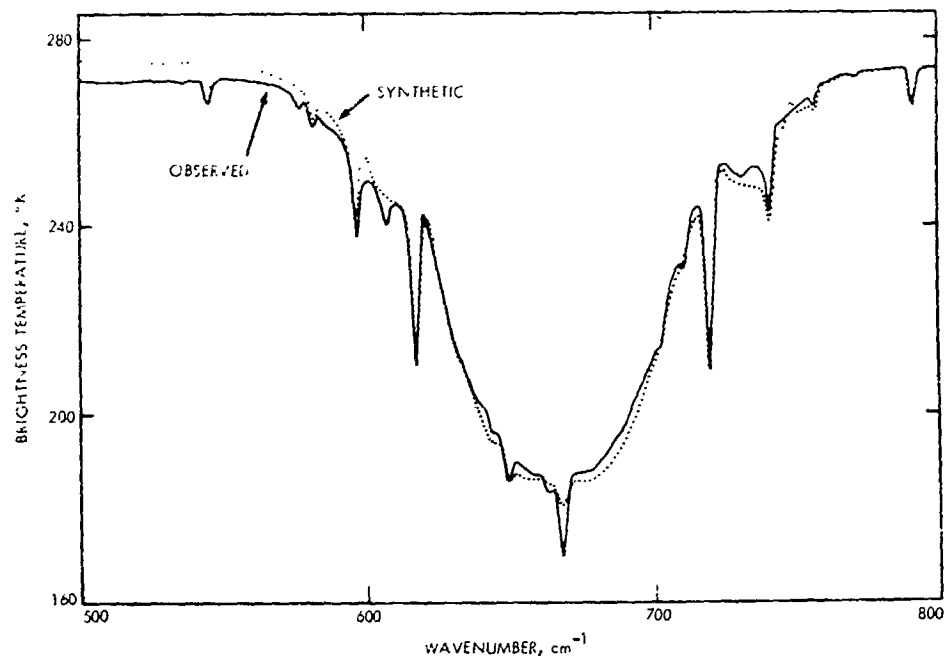
Fig. XX-2. Comparison of synthetic and observed spectra for revolution 17.4 (−30° latitude, 32° longitude, 14:00 local time) in the region of absorption by atmospheric carbon dioxide. Numerous Q-branch features of individual CO_2 bands, superimposed on the strong absorption by the CO_2 fundamental at 667 cm⁻¹, are evident in the observed spectrum.

Table XX-1. Lower and upper level quantum numbers (V_1, V_2, V_3, l) and corresponding band centers for selected isotopes of carbon dioxide

Lower level	Upper level	$O^{16}C^{12}O^{16}$	$O^{16}C^{13}O^{16}$	$O^{16}C^{12}O^{18}$	$O^{16}C^{12}O^{17}$	$O^{16}C^{13}O^{18}$
0000	0101	667.38	648.52	662.32	664.72	643.49
0101	0202	667.74	648.87	662.69	665.07	643.96
0101	1000	720.81	721.58	703.57	711.33	699.16
0101	0200	618.0.	617.31	597.17	607.63	601.79
0202	0303	668.13	649.29	663.11	665.48	644.48
0200	0301	647.08	630.72	642.12	644.35	624.53
1000	1101	688.65	667.07	683.36	685.95	663.33
1101	1202	683.82	663.24	678.73	681.17	659.03
0202	1101	741.71	739.78	724.24	732.21	718.53
0202	0301	597.37	599.16	576.60	586.91	582.36

topes have been determined from the corresponding $O^{16}C^{12}O^{16}$ band strength scaled in accordance with terrestrial isotopic abundances (Ref. XX-7). The very weak bands enclosed by the dashed line in the right-hand corner do not appear in the available laboratory CO_2 spectra, so their molecular parameters are not readily available. Consequently, these bands were not included in the present computations.

Some of the stronger CO_2 bands observed in the 667 cm⁻¹ region of the Martian spectra are given in Table XX-2. A search has been made for isotopes of carbon dioxide in the Martian infrared spectra, but the identification of bands belonging to other than the main isotope is hindered by their relative weakness. Nevertheless, the $O^{16}C^{13}O^{16}$ fundamental is observed at 648.52 cm⁻¹, the $O^{16}C^{13}O^{18}$ fundamental at 643.49 cm⁻¹, and the

Table XX-2. Lower and upper level quantum numbers (V, V, V, ℓ) for carbon dioxide identifications in the 15-μm band

Wavenumber, cm^{-1}	Lower level	Upper level	Isotope ($O^{16}C^{12}O^{16}$ unless otherwise listed)
544.25	1000	0301	
581.70	0303	0402	
597.34	0202	0301	
618.03	0101	0200	
643.49	0000	0101	
648.52	0000	0101	$O^{16}C^{12}O^{18}$
662.32	0000	0101	$O^{16}C^{13}O^{16}$
667.38	0000	0101	$O^{16}C^{12}O^{16}$
720.81	0101	1000	
741.74	0202	1101	
757.43	0303	1202	
770.36	0404	1303	
791.45	0200	1101	

$O^{16}C^{13}O^{16}$ fundamental at 662.32 cm^{-1}. The relative strengths of these observed bands are in general agreement with the corresponding theoretical bands, indicating the $C^{12}:C^{13}$ and $O^{16}:O^{18}$ ratios for Mars are close to the terrestrial values.

Beyond 800 cm^{-1}, the observed spectrum exhibits features caused by numerous weak CO_2 bands (800 to 2000 cm^{-1}), by silicate dust (900 to 1200 cm^{-1}), and by the 1595 cm^{-1} H_2O band (1400 to 1800 cm^{-1}). A comparison with a synthetic spectrum for this region is not made at this time because of uncertainties in some of the molecular parameters for the weak CO_2 bands and in the theoretical modeling of the silicate dust.

Two related problem areas are apparent from the comparison shown in Fig. XX-2. The first area is concerned with the presence of anomalous spectral features in the observed spectrum which do not appear in the theoretical CO_2 spectrum. The second problem area concerns inaccuracies in the retrieved surface pressure and temperature profiles which, in turn, lead to differences between the theoretical and observed spectrum in the 500 to 800 cm^{-1} region.

The anomalous spectral features include Q-branch type absorptions at 577, 607, 702, and 711 cm^{-1} and a more diffuse feature near 730 cm^{-1}. Because they are highly correlated in appearance with adjacent weak CO_2 bands which are known to be formed in the lower scale height of the atmosphere, the features are inferred to be

of atmospheric origin. Their behavior throughout the mission implies that they are produced by an absorber having a constant mixing ratio over the planetary disk. These characteristics strongly suggest that the disagreement is due either to an incomplete theoretical treatment of CO_2 or that CO_2 connected phenomena exist. Several additional weak bands of CO_2 are shown in Table XX-1 below and to the right of the dotted line. Because most of the anomalous features are nearly coincident with these weaker CO_2 bands which have not been included in the present computations, it would be premature to speculate on the origin of these features until the CO_2 spectrum can be completely specified. A revised set of CO_2 lines, including many weaker bands, is now in preparation.

The atmospheric molecular transmittances employed in the algorithms for determining surface pressures and atmospheric temperature profiles from the observed radiances in the 667 to 750 cm^{-1} region currently contain two main sources of error. One source is the theoretical CO_2 absorption parameters which are based mainly on laboratory data obtained at room temperature and terrestrial pressures. Further laboratory CO_2 data, not now available, should be recorded under Martian temperature, pressure and CO_2 path conditions in order to verify the theoretical CO_2 parameters for the Martian application. A second source of error in the transmittances is the unknown opacity of the anomalous spectral features. The features at 702 and 711 cm^{-1} are of particular concern, as these wavenumbers are close to spectral intervals that are employed in estimating temperature profiles and surface pressures.

B. Water Vapor Abundance and Distribution

During the mid-summer season in the southern hemisphere of Mars, the atmospheric water vapor abundance was approximately 10 to 20 precipitable micrometers over most of the planet except the northern polar area, where no water vapor could be detected (Ref. XX-4). Additional water vapor estimates based on subsequent data show a strong seasonal effect marked by the disappearance of water vapor over the south polar region and its appearance in the north polar area.

The total water vapor abundances again were determined from a comparison of synthesized and observed spectra, such as those shown in Fig. XX-1, assuming the vertical water vapor distribution was well mixed for the early periods, up to revolution 120, and decreased exponentially with a 5-km scale height thereafter.

The water vapor abundances are summarized in the lower three sections of Fig. XX-3 for the north polar cap, sub-solar point, and south polar cap regions with the upper section of the figure showing the classical polar cap regression curves. The cross-hatched areas and upper limit designations, representing the Earth-based water vapor determinations from the 1965 and 1969 oppositions, have been taken from Barker et al. (Ref. XX-8). The vertical extent of the cross-hatched areas includes the Earth-based measured latitudinal differences of water vapor. For convenience the Earth-based values are indicated in each of the summary sections. The average abundances for the 1971–1972 opposition by Tull and Barker are marked by the dashed lines and represent a measurement of the entire Martian disk. The early conclusions concerning the Martian water vapor were summarized in Ref. XX-4.

An upper limit to the amount of water vapor that can be observed is determined by the saturation level of the atmosphere, which in turn is strongly controlled by the atmospheric temperatures. Typical temperature profiles for the south and north polar cap regions are shown in Fig. XX-4 with the corresponding planetocentric longitude of the Sun, L_s.
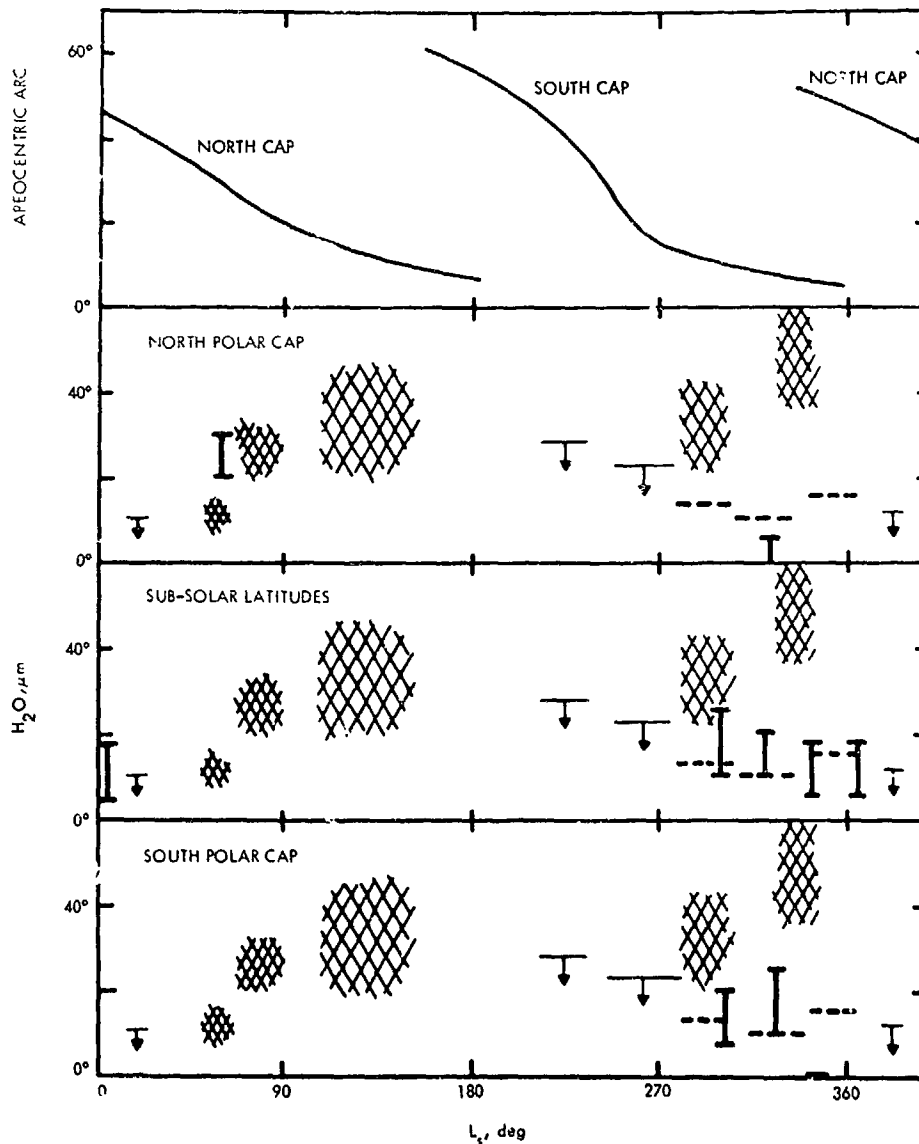
Fig. XX-3. Summary of latitudinal distribution of atmospheric water vapor with changing Martian season.
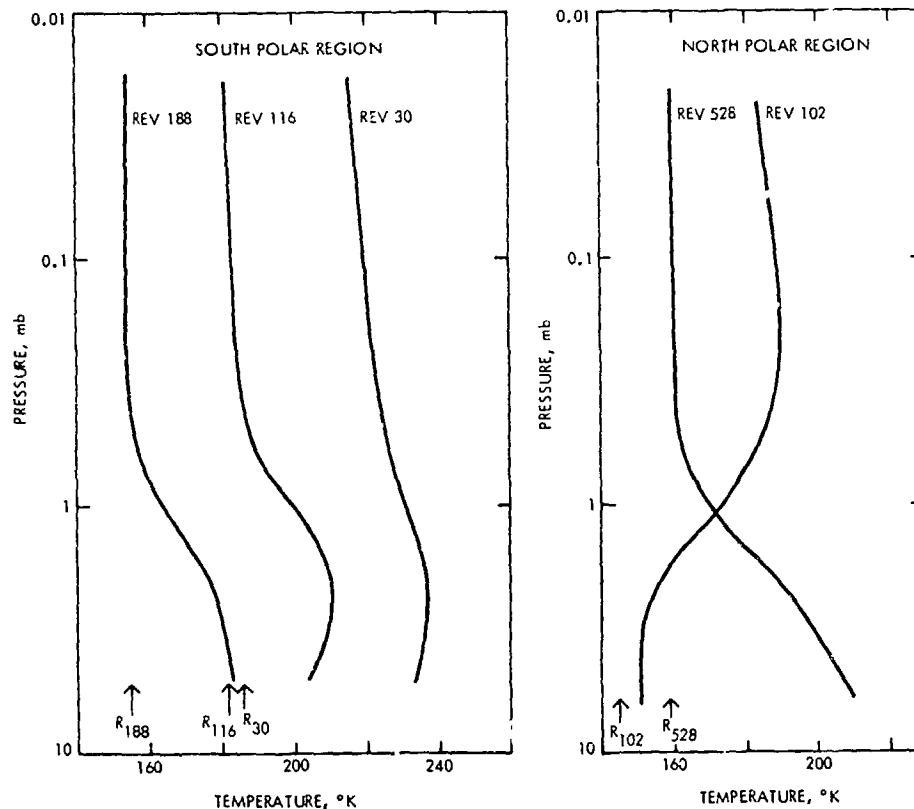
Fig. XX-4. Temperature profiles retrieved from the 667 cm⁻¹ CO₂ band summarized for the south polar cap region during southern summer and for the north polar cap region during northern winter and spring. The arrows near the bottom of the figure indicate the measured surface temperature from the 400 cm⁻¹ region of the spectrum.

The three profiles over the south polar cap region cover the last half of a southern summer. The surface pressure was assumed to be 5 mb. The decrease in atmospheric temperatures between revolutions 30 and 188 is a consequence of the decreasing solar illumination in the south polar region as the sub-solar point moves toward the equator with the passage of summer and of the dust settling after the storm.

The temperature profile for revolution 528, corresponding to late northern spring conditions, manifests the increasing solar illumination. The assumed surface pressure was 6 mb. A summary of surface pressure, surface temperature, and observed and saturation amounts of atmospheric water vapor are given in Table XX-3. The surface brightness temperatures given in the table were derived at 400 cm⁻¹. Because the instrument's field of

Table XX-3. Surface and water vapor parameters for polar regions

Earth date	Revolution	Region	Planetocentric longitude of the Sun, deg	Surface pressure, mb	Surface temperature, °K	Atmospheric water vapor at saturation, m	Observed water vapor amounts, μm
11/29/71	30	South polar cap	301	5	186	4200	10 to 20
1/11/72	116	South polar cap	326	5	181	99	15 to 25
2/16/72	188	South polar cap	346	5	155	0.7	Not detectable
1/4/72	102	North polar cap	322	6	145	8	Not detectable
8/3/72	528	North polar cap	60	6	156	30	30

view includes both frost-covered and clear areas over the polar caps (Ref. XX-3), these temperatures are not inconsistent with a CO₂ cap.

Through saturation limits alone, the observed behavior of the south polar cap temperature profiles constrains the late summer atmospheric water vapor content to small amounts. For example, the maximum water vapor content for revolution 188 must be less than 0.7 μm; in fact, water was no longer evident in the spectra of the south polar cap area. On revolution 528, approximately two-thirds through northern spring, the north polar cap area showed about 20 to 30 precipitable micrometers of water vapor, which is close to the saturation level at that time. The distribution of water vapor at mid-latitudes remains quite stable during the entire mission. On revolution 261, during northern spring over the sub-solar latitudes, the abundance was still 10 to 20 precipitable micrometers.

Further analysis of the water vapor is expected to refine the absolute determination of the abundance, determine a crude scale height, give a more complete representation of the latitudinal and seasonal distribution, and yield some insight into the water vapor sources and transport processes.

C. Surface Pressure and Topography

Surface pressures have been derived for more than 3500 points on the planet where spectra show a large thermal contrast between mean atmospheric temperatures and soil surface temperatures. Data points are generally spaced at intervals of 100 to 200 km along the instrument ground track; the separation between ground tracks is as much as 600 km. The spatial resolution element of each measurement varies from 125 to 200 km in diameter.

The data have been averaged over areas 5° on a side to provide a low-resolution pressure map of the half of the planet between latitudes of −60° and −25° (Fig. XX-5) The average surface pressure over the sampled area is 4.8 mb. The highest pressures observed (about 8 mb) occur in Hellas and in the Isidis Regio–Amenthes area. Other relatively high-pressure regions (about 6 mb) are Argyre I and portions of Chryse and Margaritifer Sinus. The Tharsis–Syria plateau is characterized by pressures less than 3.5 mb, with a pressure of 1.5 mb at the top of South Spot (−9°, 120°). Even at the low resolution of this figure, the great Coprates canyon complex is suggested between 35° and 95° longitude. Correlations with other large features, such as the large crater centered at (−52°, 82°) in southern Bosporos, are also evident.
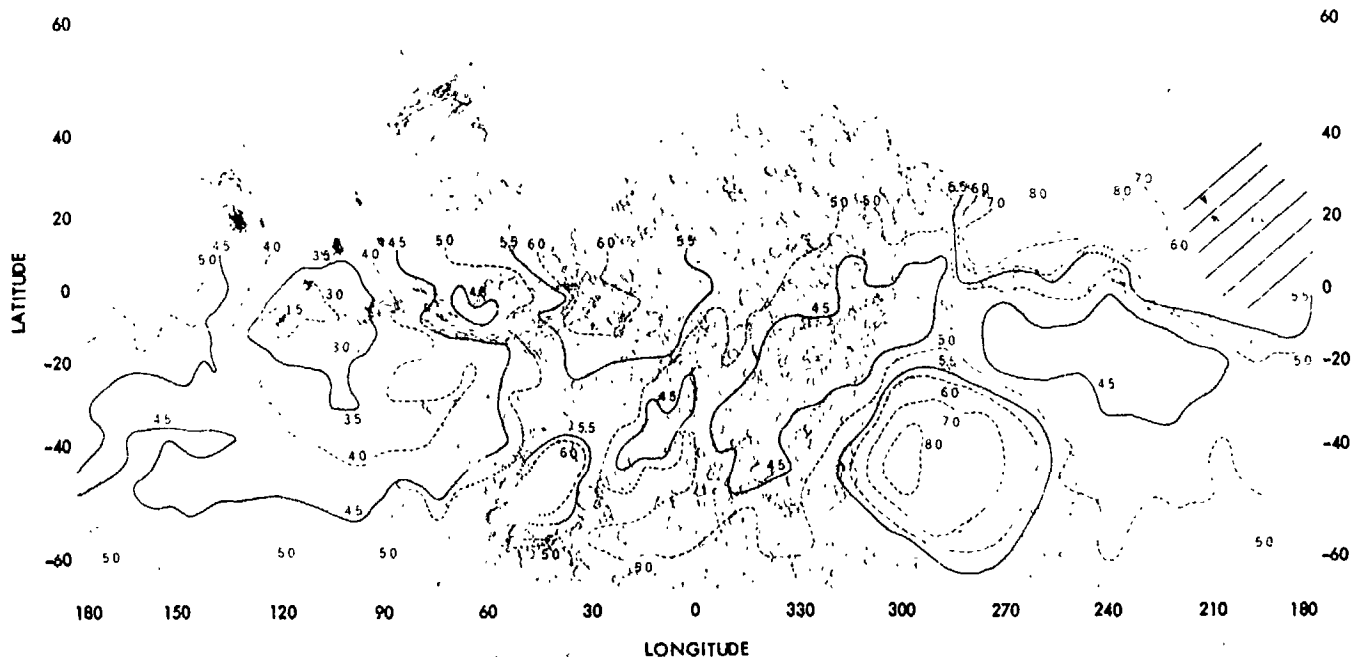
Fig. XX-5. Preliminary pressure map based on pressure averaged over areas 5° on a side. Pressure contours (in millibars) are shown overlaying the feature map produced from *Mariner 9* television pictures by the U. S. Geological Survey. Contours corresponding to integer pressure values are dashed, and those corresponding to half integer values are solid. Dotted portions of the contours are interpolated across data gaps. Accuracy of the pressure determinations is 10 to 15%.

Martian topography can be obtained from the surface pressure distribution by use of the barometric law. Topographic maps of Hellas and the Tharsis area, based on an atmospheric scale height of 10 km and a zero level at the 6.1-mb triple point pressure of water, have been published (Ref. XX-4). A similar investigation of the Coprates canyon (Fig. XX-6) suggests that the canyon does not slope uniformly down from the Tharsis ridge to Chryse, but that it has a local low area in the enlarged region between 70° and 75° longitude. Before this can be conclusively established, however, the fact that the instrument field of view includes contributions from the canyon rim must be considered. Nevertheless, at (−10.6°, 70.0°) the canyon bottom lies at least 5 km below the southern edge of the canyon rim.

Several systematic effects are being evaluated which will affect large-scale topographic mapping. The theoretical CO_2 transmittances from which atmospheric opacity and total CO_2 amounts are obtained are being finalized; changes to the preliminary map in Fig. XX-5 are ex-

pected to be 10 to 15%. Pressure variations caused by tidal motions in the atmosphere, to be discussed below, introduce a latitude-dependent effect of perhaps 10% in the area sampled and must be included. The 10-km scale height used in converting surface pressure to topographic altitudes must be refined by integrating down the actual atmospheric temperature profiles, which are also obtained from the IRIS data; an increase in the average scale height by about 10% will result. Irregularities in the Martian gravitational field (Ref. XX-9) will also contribute minor systematic effects, amounting to shifts of on the order of 1 km in the geopotential surface to which topographic altitudes are referred.

D. Atmospheric Circulation

Temperature profiles obtained from measurements in the 667 cm^{-1} CO_2 bands have been employed in the construction of semi-global temperature fields from which preliminary estimates of large-scale winds during the great dust storm of 1971–1972 were made (Ref. XX-4).
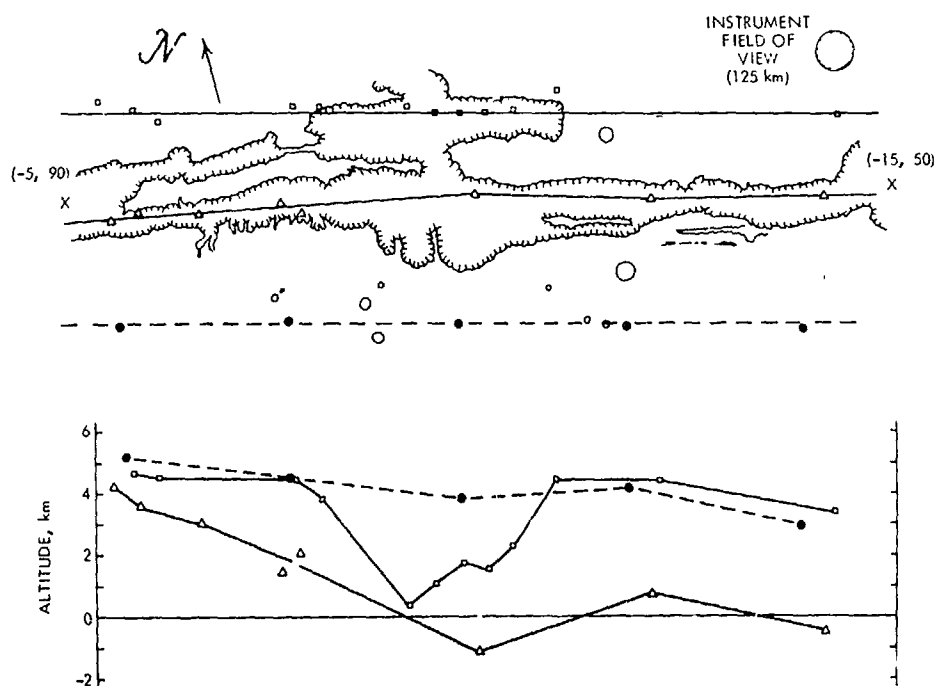
Fig. XX-6. Preliminary topography in Coprates canyon region. Upper portion of figure shows configuration of the canyon between longitudes 50° and 90°. Data points chosen from several data are indicated along three lines closely paralleling the main canyon structure. Lower part of figure shows topography along these lines as obtained from pressure data using a 10-km scale height and an altitude zero at 6.1 mb. The dashed line lies over the generally smooth terrain south of the canyon, and provides a measure of the overall slope of the region. The maximum apparent depth of 5 km is at about longitude 70°; correction for instrument's field of view must be made before this can be conclusively established as a local minimum in the canyon structure.

In that work, the surface pressure was assumed to be constant, surface friction and orographic effects were not included, and nonlinear terms in the hydrodynamic equations were neglected. The large diurnal fluctuations observed in the temperature fields imply the existence of strong tidal effects which can appreciably alter the near surface winds; consequently, the second step in a continuing analysis of the wind fields has been the incorporation of tidal theory into the calculations. Tidal theory treats the harmonically varying part of the planetary circulation, taking into account surface pressure fluctuations but neglecting nonlinear effects, surface friction, and topography.

As in the previous report, the observed temperature field was modeled using a spherical harmonic representation consisting of two meridional harmonics each for zonal wavenumbers zero and one. In this way, the temperature fields were extrapolated into those regions for which no direct measurements exist, primarily in the night hemisphere. The vertical temperature structure was included by using altitude-dependent coefficients for the harmonic terms. The resulting temperature model was used to evaluate the driving terms of the hydrodynamic equations. Unlike more conventional calculations which employ the heat input to the system as the driving agent, the present wind calculations do not make use of the energy equation directly; instead it can be used to calcu-

late the heat input required to be consistent with the derived motions and observed temperatures. Many approximations were made to render the hydrodynamic equations tractable, including linearization, the neglect of surface friction and orographic effects, and the assumption of a linear damping term with a 4-day time constant. With these approximations, the dynamic equations were reduced to an inhomogeneous tidal equation for the surface pressure. Solution of this equation yielded the surface pressure field which, along with the temperature field, was used in the momentum equations to calculate the tidal winds.

The calculated surface pressure field during the great dust storm is shown in Fig. XX-7. Diurnal tidal pressure fluctuations are found to be approximately 12% of the global average surface pressure. The maximum amplitude occurs at a latitude approximately half-way between the equator and the latitude of the maximum temperature fluctuation; in the absence of damping, the maximum pressure amplitudes would occur almost on the equator. The pressure minimum occurs in local time near the temperature maximum, but with a light lag caused by the damping.

Near-surface winds obtained from the calculations are shown in Fig. XX-8 and again in Fig. XX-9 as viewed from the poles. Comparison of these results with the earlier
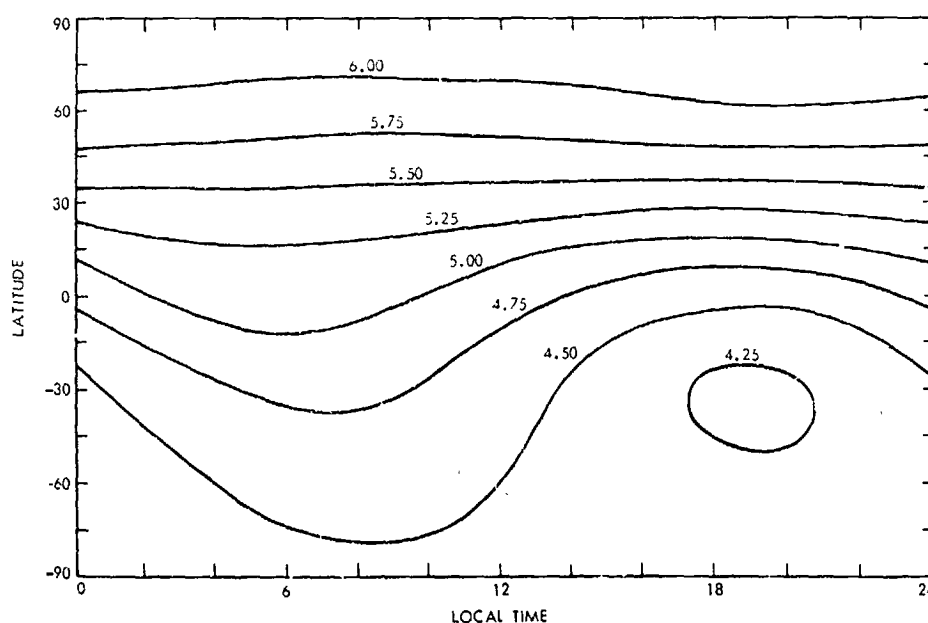
Fig. XX-7. Calculated tidal surface pressure contours. The surface pressures shown are the sum of the diurnal tidal pressures and a latitude-dependent seasonal pressure field. The pressure is expressed in millibars, and the average surface pressure is 4.8 mb. Topography and surface friction are not included.
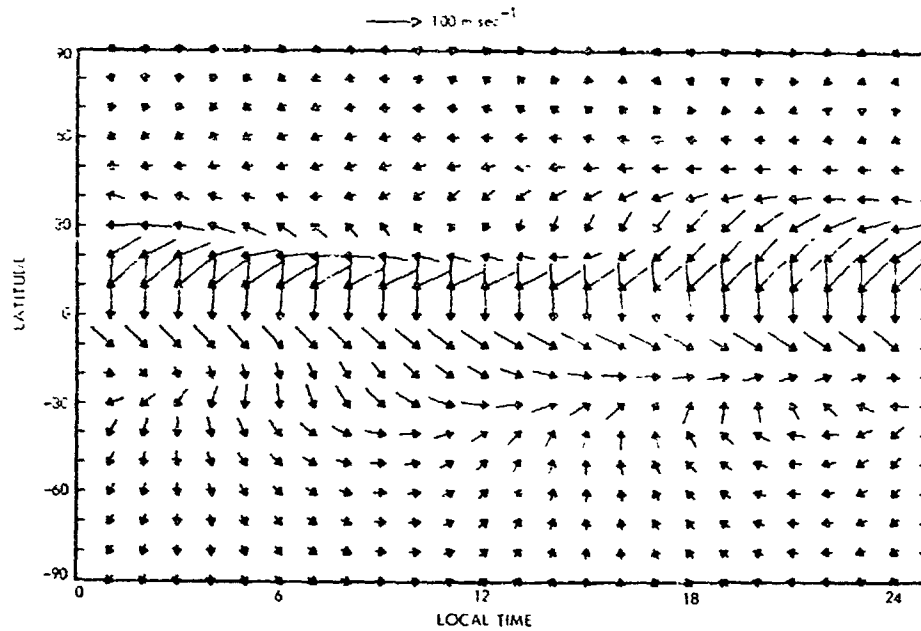
Fig. XX-8. Near-surface winds during the great dust storm. The wind field, just above the surface boundary layer, is generated from the measured temperature field and its associated surface pressure. The amplitude is indicated by the scaled vector.
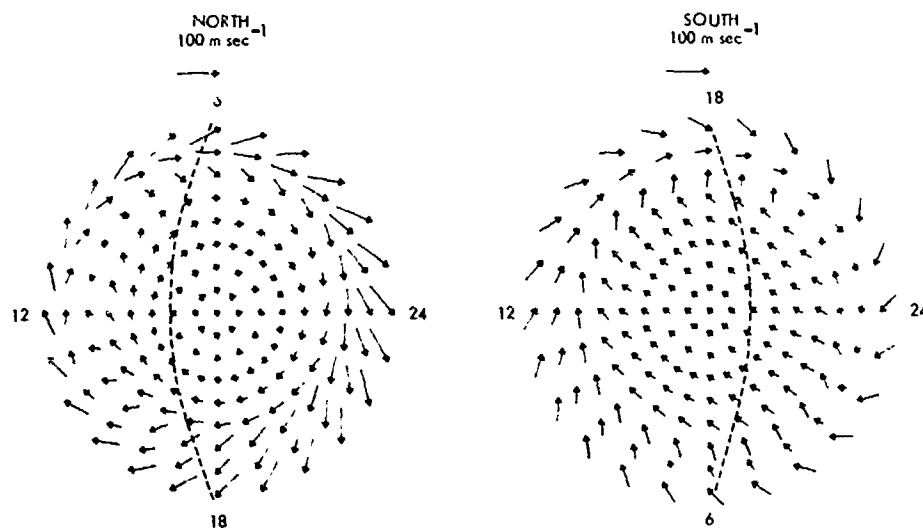
Fig. XX-9. Polar plots of the wind fields of Fig. XX-4 . Winds are shown from the poles to within 10° latitude of the equator. The magnitude of the wind velocity is indicated by the scaled vector. The dotted line indicates the positon of the terminator.

calculations indicates that inclusion of the surface pressure fluctuations almost reverses the near-surface wind direction. However, the high-altitude wind patterns remain essentially unaffected. Convergence and divergence of the horizontal winds generate vertical winds which cause a diurnal partial overturning of the atmosphere in addition to a seaso. al meridional circulation. The magnitudes of the winds sh , vn in Fig. XX-8 near the equator are highly uncertain because of a strong dependence on the amount of damping used and possibly also on nonlinear terms which have been neglected. Large-scale topography may significantly alter both the magnitude and direction of the winds at all latitudes. An effort is currently underway to include in the calculations topographic information derived from the surface pressure mapping results.

E. Atmospheric Dust

An estimate of the approximate silicon oxide content of the atmospheric dust cloud has been given (Ref. XX-4). To help define the properties of the cloud particles, a radiative transfer model is being constructed which allows the computation of the emission spectrum of a cloud, between 200 and 2000 cm^{-1}, given the complex refractive index of the cloud material, the particle size distribution, the number density as a function of height, and the atmospheric temperature profile.

In first tests of this model, the particles were assumed to be quartz spheres of various diameters. Agreement with the measured Martian spectra is not expected to be good because the dust is not pure SiO_2 (quartz) nor is it composed of spherical particles distributed over a narrow range of particle sizes. Some qualitative conclusions can be reached, however, even though the present computations are primarily a test of the method.

Quartz was chosen because its complex refractive index (Fig. XX-10) is well known (Ref. XX-10). The Mie theory was assumed to apply, and rectangular particle size distributions we· · chosen with mean radii at 0.1, 1, 2, 4, and 10 μm. In order to obtain smooth solutions, a width-to-mean-radius ratio of 0.1 was employed in all five cases. Using these distributions, the scattering and absorption cross sections were calculated in a manner similar to that of Peterson and Weinman (Ref. XX-11) for a birefringent material. The cross sections are shown in Fig. XX-11 for particle sizes of 0.1 μm and 10 μm. The dominant interaction changes from absorption to scattering as particle size is increased through this range.
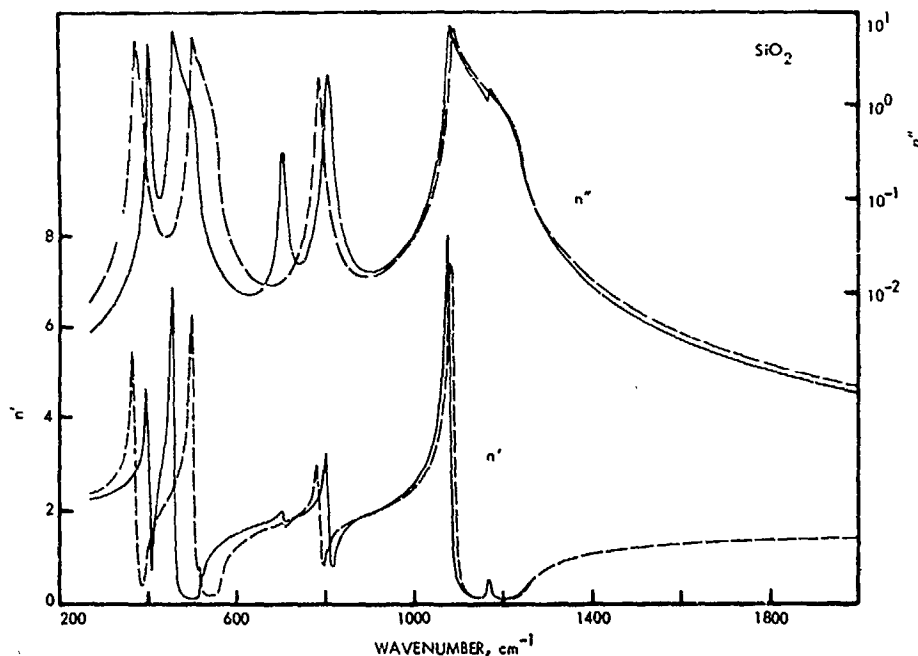
Fig. XX-10. Complex refractive indices of SiO_2 in the infrared. The real part of the refractive index is indicated by n' and the imaginary part by n''. Indices for the ordinary ray are represented by solid lines and the extraordinary ray by dashed lines.
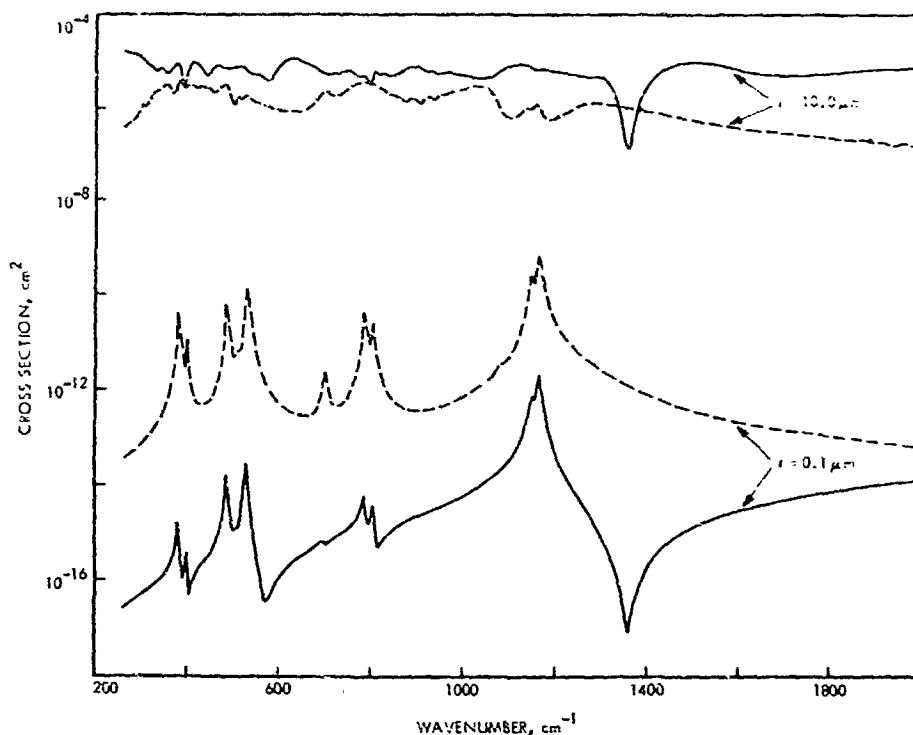
Fig. XX-11. Infrared cross sections for 0.1-μm and 10.0-μm-radius particles. The absorption cross sections are indicated by dashed lines and the scattering cross sections by solid lines.

Next, the wavenumber-dependent ratios of the total infrared optical depths to the visible optical depth (at 20,000 cm⁻¹) were evaluated. Results for three different particle sizes are shown in Fig. XX-12. It can be seen that the smaller particles tend to interact with the infrared radiation field less efficiently than the larger particles. A comparison of the optical depths for the smaller particles in Fig. XX-12 with the indices of refraction in Fig. XX-10 indicates that maxima in the optical depths correspond to regions of maximum absorption. As the particle size increases, the regions of low absorption in the total optical depth become filled in because of increased scattering; for a particle size of 10 μm, scattering dominates as shown in Fig. XX-11, and sharp spectral features are no longer prominent in the total optical depth.

Finally, the absorption and scattering cross sections were used as input to a numerical solution of the equation of radiative transfer for the dust-laden Martian atmosphere. The radiative transfer calculations were normalized to a visible optical depth of unity, so that the integrated number of particles in a vertical column decreases as the dimensions of the particles increase (Table XX-4). The numerical solution accounts for the absorption and multiple scattering of the radiation by

the dust in the atmosphere and the emission from both the lower bounding surface and the dust particles. Results of the radiative transfer calculations for five particle sizes are shown in Fig. XX-13. For these calculations, the surface was assumed to be at a temperature of 260 K, the atmospheric temperature distribution was that derived on revolution 20 at mid-latitudes (Ref. XX-4), and the particles were distributed exponentially with altitude assuming a scale height of 10 km. Many of the features observed in the optical depths of Fig. XX-12 are noticeable in Fig. XX-13, with the widths of the spectral features generally increasing with particle radius.

Table XX-4. Vertically integrated column number density, N, and mass density, m, as functions of particle radius, r, assuming unit visible optical depth

r, μm	N, cm⁻²	m, g cm⁻²
0.1	7.04×10^9	7.79×10^{-5}
1.0	1.21×10^7	1.34×10^{-4}
2.0	3.38×10^6	2.98×10^{-4}
4.0	8.85×10^5	6.26×10^{-4}
10.0	1.50×10^5	1.66×10^{-3}
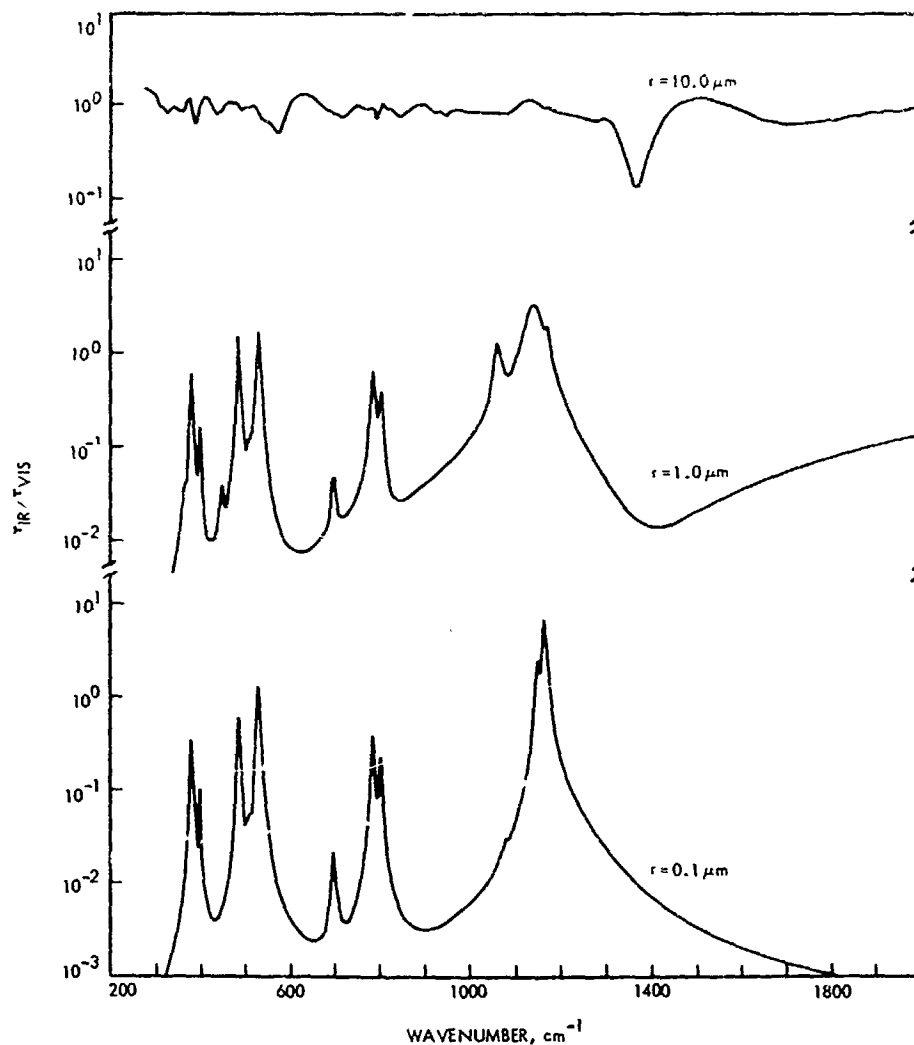
Fig. XX-12. Ratios of infrared to visible optical depths (τ_{IR}/τ_{VIS}) for 0.1-, 1.0-, and 10.0-μm-radius particles.

The most striking feature of these results is the strong dependence of the sharpness of the spectral features on particle size. A crude comparison of the sharpness of the features in the calculated brightness temperature spectra with those in the measured dust cloud spectra such as that shown in Fig. XX-14 appears to favor particles with radii between 1.0 and 10.0 μm.

Proceeding on the assumption that the dust in the Martian atmosphere is siliceous in nature, though not pure quartz, the radiative transfer modeling effort is being extended to include other minerals in the SiO_2 family. Effects due to broader particle size distributions are also being investigated. Present indications are that the correspondence between measured and calculated spectra will be improved by these efforts.

F. Summary

This section reports on recent progress in the interpretation of the thermal emission spectra of Mars. Improvements have been made in the CO_2 transmittances, which form the basis for the determination of the surface pressure and atmospheric temperature profiles, and which must be well understood before a final analysis of minor gaseous constituents and of the mineral composition of the dust and of the surface can be made. Analysis of the water vapor distribution has revealed strong seasonal effects in the polar regions. By late southern summer ($L_s = 346°$, revolution 188) the atmospheric water vapor content over the south polar cap had dropped below 0.7 μm of precipitable water, which is the saturation limit for the cold polar atmosphere. The wettest portion of the

planet encountered during the orbital mission appears to be in the north polar cap region where saturated water vapor abundances of 20 to 30 μm were observed during northern spring ($L_s = 60°$, revolution 528). Because the entire planet was not observed through a complete seasonal cycle and because of the interfering dust storm in the southern summer, it is not possible to infer from the observed behavior of the water vapor distribution an imbalance in water vapor content between the northern and southern hemispheres. However, continued analysis of the water vapor distribution as a function of Martian season will contribute much to the understanding of polar phenomena and to the general interaction of surface and atmosphere.

The analysis of the atmospheric pressure at the surface and of the topographic relief of Mars is proceeding from individual case studies to a global analysis. Even at low resolution, correlations between visual features and pressure variations are evident. Final analysis of pressures and topography await inclusion of improved CO_2 transmittances, corrections for diurnal pressure fluctuations, and corrections for distortions of the Martian geoid, as well as the use of a measured scale height instead of a constant value.

Inclusion of tidal theory in the analysis of atmospheric dynamics indicates that significant diurnal pressure fluctuations exist. During the dust storm, diurnal pressure
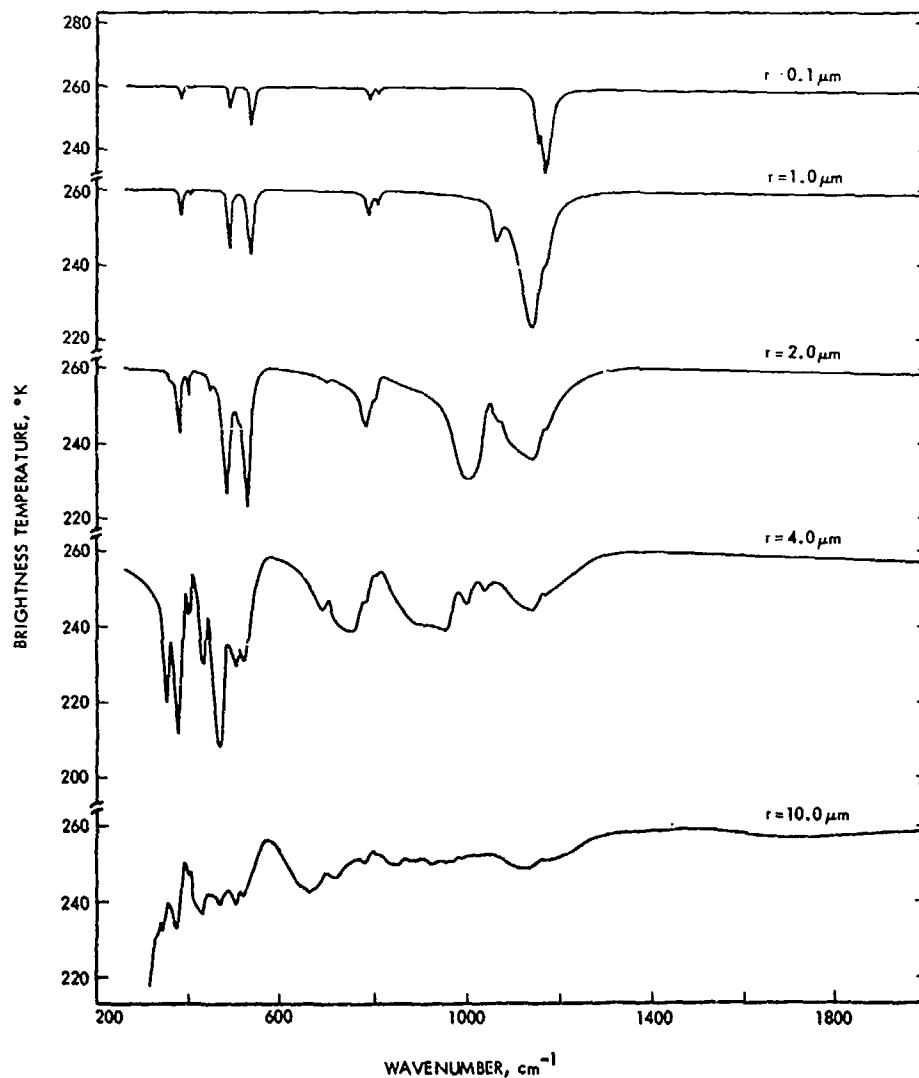
Fig. XX-13. Synthetic brightness temperature spectra calculated for indicated particle sizes. The radiative transfer calculations include only the scattering and absorption effects of the particles and neglect the effects of molecular absorption.
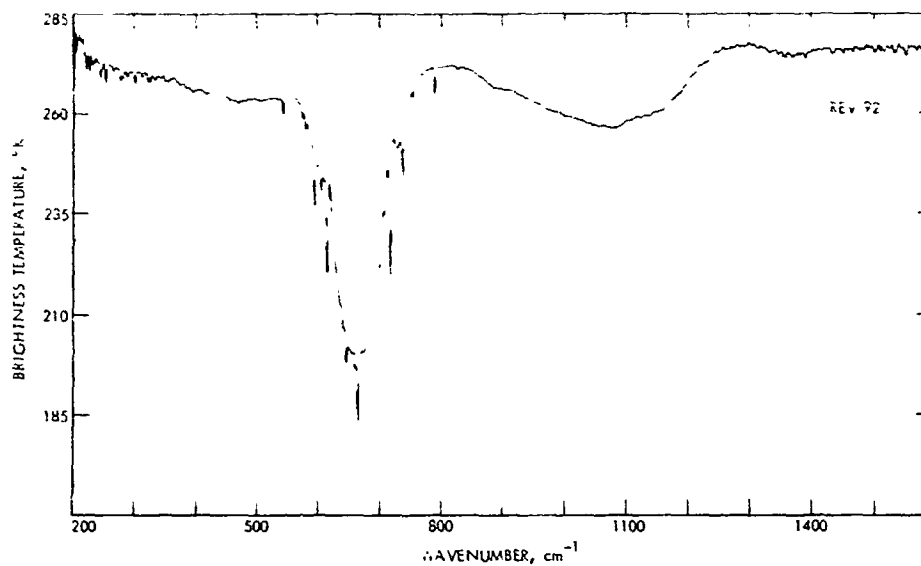
Fig. XX-14. Measured brightness temperature spectrum from revolution 92 showing diffuse spectral features caused by atmospheric dust.

fluctuations occurred with a maximum near 07:00 local time and −20° latitude and a minimum at 19:00 hours and the same latitude. The calculated wind field near the surface shows a strong latitudinal as well as diurnal dependence. The surface boundary layer and surface topography are two important aspects that remain to be included in the model.

Using Mie theory and radiative transfer calculations, synthetic spectra of clouds of quartz spheres of various radii have been evaluated. Qualitative comparison of the computed spectra with measured spectra suggests that particle radii were on the order of a few micrometers; if smaller particles dominated, rather sharp spectral features would be expected; substantially larger particles would have resulted in obscuration of the surface, even near the Christiansen frequency around 1300 cm . Although the present models do not yet realistically parameterize the particle composition, size, or shape, refinements of the models promise to be useful for more specific identification of the Martian mineral dust composition and particle sizes.

References

XX-1. Hanel, R. A., Conrath, B. J., Hovis, W. A., Kunde, V., Lowman, P. D., Prabhakara, C., and Schlachman, B., "The Infrared Spectroscopy Experiment for Mariner Mars 1971," *Icarus*, Vol. 12, p. 48, 1970.

XX-2. Hanel, R. A., Schlachman, B., Breihan, E., Bywaters, R., Chapman, F., Rhodes, M., Rodgers, D., and Vanous, D., "The Mariner 9 Michelson Interferometer," *Appl. Opt.*, Vol. 11, p. 2625, 1972.

XX-3. Hanel, R. A., Conrath, B. J., Hovis, W. A., Kunde, V. G., Lowman, P. D., Pearl, J. C., Prabhakara, C., and Schlachman, B., "Infrared Spectroscopy Experiment on the Mariner 9 Mission: Preliminary Results," *Science*, Vol. 175, p. 305, 1972.

References (contd)

XX-4. Hanel, R., Conrath, B., Hovis, W., Kunde, V., Lowman, P., Maguire, W., Pearl, J., Pirraglia, J., Prabhakara, C., Schlachman, B., Levin, G., Straat, P., and Burke, T., "Investigation of the Martian Environment by Infrared Spectroscopy on Mariner 9, *Icarus*, Vol. 17, p. 423, 1972.

XX-5. Kunde, V. G., "Theoretical Molecular Absorption of CO in Late-Type Atmospheres," *Ap. J.*, Vol. 153, p. 435, 1968.

XX-6. Drayson, S. R., "Atmospheric Radiative Transfer by Carbon Dioxide," *Proceedings of Conference on Atmospheric Radiation*, pp. 77-79, Colorado State University, Fort Collins, Colorado, 1972.

XX-7. *Handbook of Chemistry and Physics*, Chemical Rubber Publishing Co., 1971.

XX-8. Barker, E. S., Schorn, R. A., Woszczyk, A., Full, R. G., and Little, S. T., "Mars: Detection of Atmospheric Water Vapor During the Southern Hemisphere Spring and Summer Season," *Science*, Vol. 170, p. 1308, 1970.

XX-9. Lorell, J., Born, G. H., Christensen, E. J., Jordan, J. F., Laing, P. A., Martin, W. L., Sjogren, W. L., Shapiro, I. I., Reasenberg, R. D., and Slater, G. L., "Mariner 9 Celestial Mechanics Experiment: Gravity Field and Pole Direction of Mars," *Science*, Vol. 175, p. 317, 1972.

XX-10. Spitzer, W. G., and Keinman, D. A., "Infrared Lattice Bands of Quartz," *Phys. Rev.*, Vol. 121, p. 1324, 1961.

XX-11. Peterson, J. T., and Weinman, J. A., "Optical Properties of Quartz Dust Particles at Infrared Wavelengths," *J. Geophys. Res.*, Vol. 74, p. 6947, 1969.

Acknowledgments

XXI. Preliminary Report on Infrared Radiometric Measurements From *Mariner 9*

H. H. Kieffer
Department of Planetary and Space Science
University of California, Los Angeles, California 90024

S. C. Chase
Santa Barbara Research Center, Goleta, California 93017

E. Miner
Jet Propulsion Laboratory/California Institute of Technology, Pasadena, California 91103

G. Münch and G. Neugebauer
Division of Physics, Math and Astronomy
California Institute of Technology, Pasadena, California 91109

The infrared radiometer experiment carried on *Mariner 9* was intended to thermally map the surface of Mars at 10 and 20 μm with a spatial resolution unobtainable from the Earth, and to extend the coverage achieved by the radiometers aboard *Mariners 6* and *7*. In 1969, approximately 2% of the Martian surface was observed by the radiometers with a linear resolution of, at best, 50 km (Ref. XXI-1; hereafter called Paper I.) On the *Mariner 9* mission, more than 35% of the surface was observed with a spatial resolution of 100 km or less; many areas were observed with a resolution as good as 15 km.

From the *Mariner 6* and *7* observations, which covered a limited range of latitudes and local times, average thermal properties of the surface were deduced; a best fit to the bulk of the data was achieved with a bolometric albedo, A, around 0.3 and a thermal inertia, $I = (k\rho c)^{1/2}$,

of 0.006.[1] The thermal model using these values has been used as the basis for a preliminary comparison with the 1971 data; the model will be referred to as the *Mariner 69* thermal model.

Although the average thermal properties deduced in 1969 adequately represented most of the observed Martian thermal structure, some large areas, especially Hellas, were systematically different and required inertias as high as 0.010. There was a clear correlation of temperatures with the classical features on Mars. In addition, a few local thermal features appeared at the limit of the

---

[1] As in Paper I, the following units will be used throughout this work and usually omitted from the text: thermal conductivity k, cal cm^{-1} sec^{-1} °K^{-1}; specific heat c, cal g^{-1} °K^{-1}; density ρ g cm^{-3}; thermal inertia $I = (k\rho c)^{1/2}$, cal cm^{-2} sec$^{-1/2}$ °K^{-1}.

spatial resolution of the radiometer. In particular, one such feature was tentatively identified with a crater in Deucalionis Regio.

Earth-based infrared observations of Mars before the *Mariner 6* and *7* missions were reviewed in Paper I. Although several observational Earth-based programs have been carried out since that time relating to specific Martian problems, no global study of the thermal properties has been published.

A single-channel radiometer covering the wavelength range 5 to 40 μm was incorporated in the Soviet spacecraft *Mars 1* and *2*. Preliminary reports show apparent agreement between the Russian and *Mariner 9* data (Refs. XXI-2 and XXI-3).

In this section, a preliminary summary of some aspects of the radiometer measurements is presented. About 1.5×10^6 individual measurements of the surface temperature of Mars were obtained in each of the two radiometric channels. The data, as received, contain transmission bit errors that must be eliminated for computer processing. Furthermore, detailed analyses of instrumental properties necessary to delineate effects of the off-axis response of the radiometer have not been completed. As a result, the data treated in this section are limited to those which were taken sufficiently far from the Martian limb so that any corrections for the extended field response would be less than 10% in flux. In effect, this excludes observations with emission angles greater than 60°. Primarily, this limitation postpones detailed evaluation of the absolute value and phase dependence of emissivity; the north and south polar caps will also be reserved for future discussion. All temperatures presented will necessarily be brightness temperatures, T_{10} and T_{20}, at either 10 or 20 μm.

The discussion of the data is divided into three sections, each concerned with thermal features with different linear scales. The planet as a whole defines a natural upper scale. The classical features seen on the planetary surface define the large-scale structure. Finally, the instrumental resolution of 15 to 100 km defines the smallest meaningful scale. The division is clearly arbitrary, and only a minimal attempt at a rigorous consistency in following it has been made.

A. Instrumentation

The infrared radiometer flown on *Mariner 9* has been described by Chase (Ref. XXI-4), Chase et al. (Ref. XXI-5),

and reviewed in Paper I. The only essential modification from the instrument of the 1969 mission was in the reduction from 0.7° to 0.5° of the field of view of the 10-μm channel.

During the 1971 mission, data were taken every 1.2 sec when the instrument platform was nominally pointed at Mars. As observations ranged from periapsis to apoapsis, the linear scale of the area observed ranged from about 15 to about 1000 km. The radiometer was rigidly boresighted with the television cameras, and initial orbital elements were selected to maximize television contrast. As a result, the coverage on the planet was nonuniform with respect to local times. For example, near the end of the mission, the data obtained from latitudes of −30° to −40° were concentrated in a band of local times (with 0° at midnight) between 13 and 17ʰ; in contrast, equatorial data in the early parts of the mission were concentrated in the two bands 5 to 9ʰ and 15 to 18ʰ.

Rapid scans onto the bright limb of Mars show the existence of a significant extended field response of the radiometer. The instrument sensitivity falls off rapidly at the edges of the nominal fields of view to less than 10% at 0.5° and 0.6° from their centers for the 10- and 20-μm channels, respectively. However, the sensitivity decreases slowly and is less well known at larger angles. Approximately 10 and 40% of the total response comes from the area beyond 1.4° from the center for the 10- and 20-μm channels, respectively. The data discussed in this section have not been corrected for this effect. As stated, however, a first-order analysis has been used to exclude the small fraction of the data where the correction is estimated to be larger than 10% in flux. As the central field of view is well defined, the spatial resolution used in analysis of local features is little affected by the extended response. On the basis of pre-launch calibrations and comparisons with the internal reference calibrator, the brightness temperatures presented have an absolute accuracy of better than 5°K near 250°K; the resolution of both the 10- and 20-μm temperatures is better than 1°K. The internal calibration was very stable throughout the mission.

B. Planet-Wide Properties

1. Observations

The smoothed 10-μm brightness temperatures observed at three epochs in the mission are shown in Figs. XXI-1 through XXI-3. In presenting the general picture of the planetary temperatures, the data are considered as a

Fig. XXI-1. Observed and model temperatures. The following data are shown, averaged over bins of 5° latitude by ½ hour local time. (a) Observed 10-μm brightness temperatures, averaged over 30 revolutions centered around December 9, 1971. The subsolar latitude is −19°. (b) Observed 10-μm temperatures minus those computed using the Mariner 69 thermal model. (c) Temperatures for the model using parameters that best fit the observed data from latitudes −70° to +40°. (d) Observed 10-μm temperatures minus those obtained from the best-fit model.
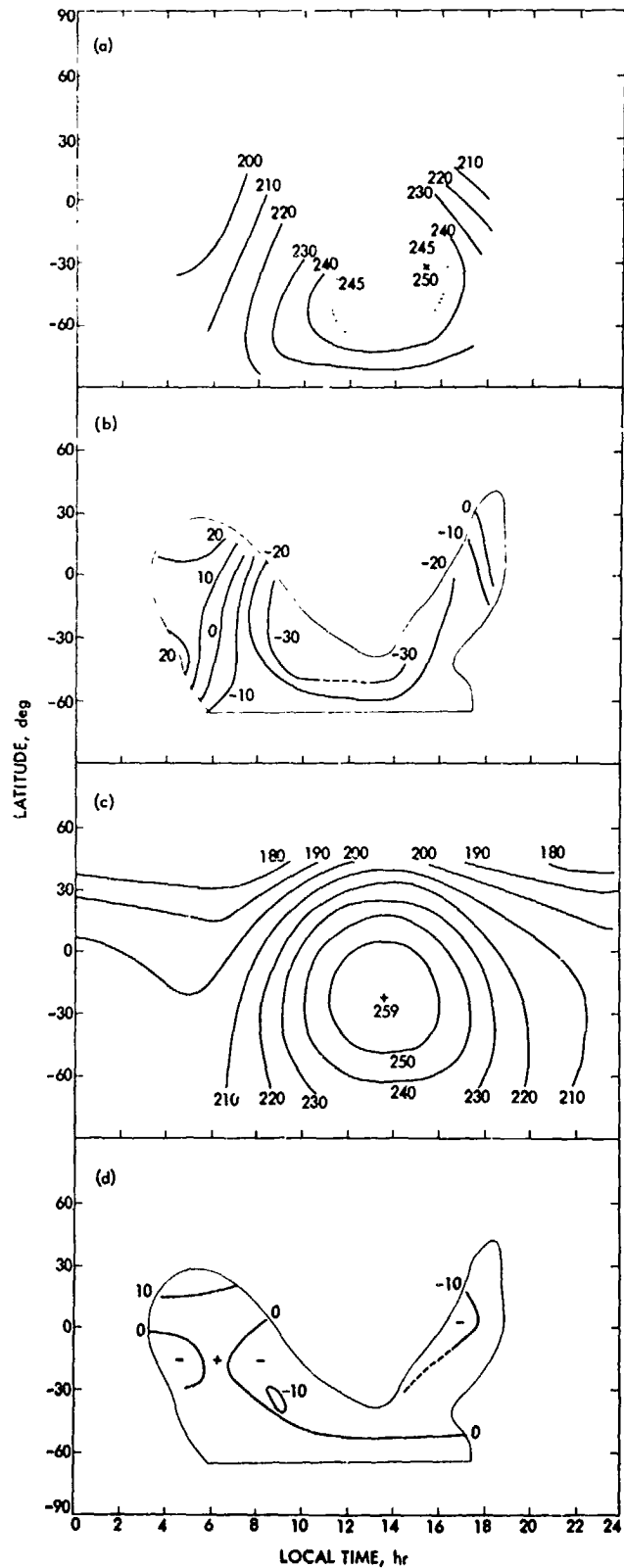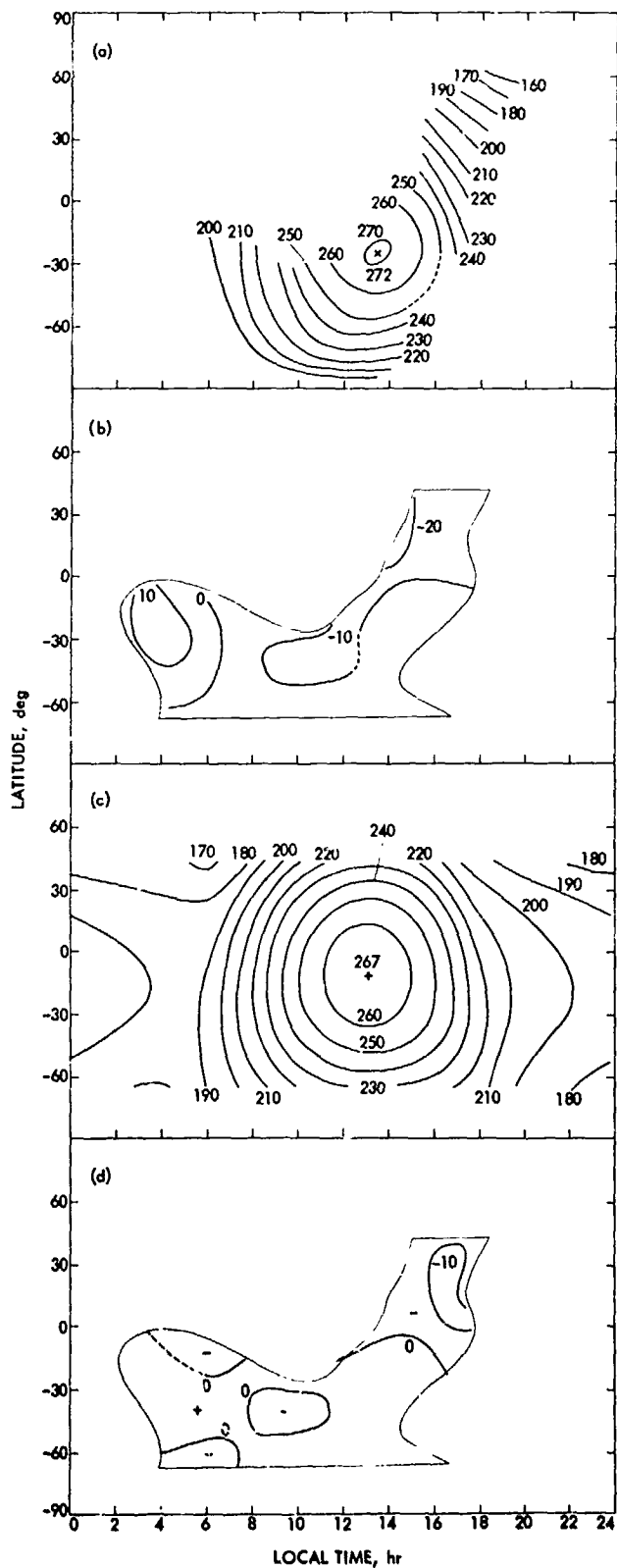
Fig. XXI-2. Same as Fig. XXI-1 for data centered on
January 18, 1972, with subsolar latitude of −13°.
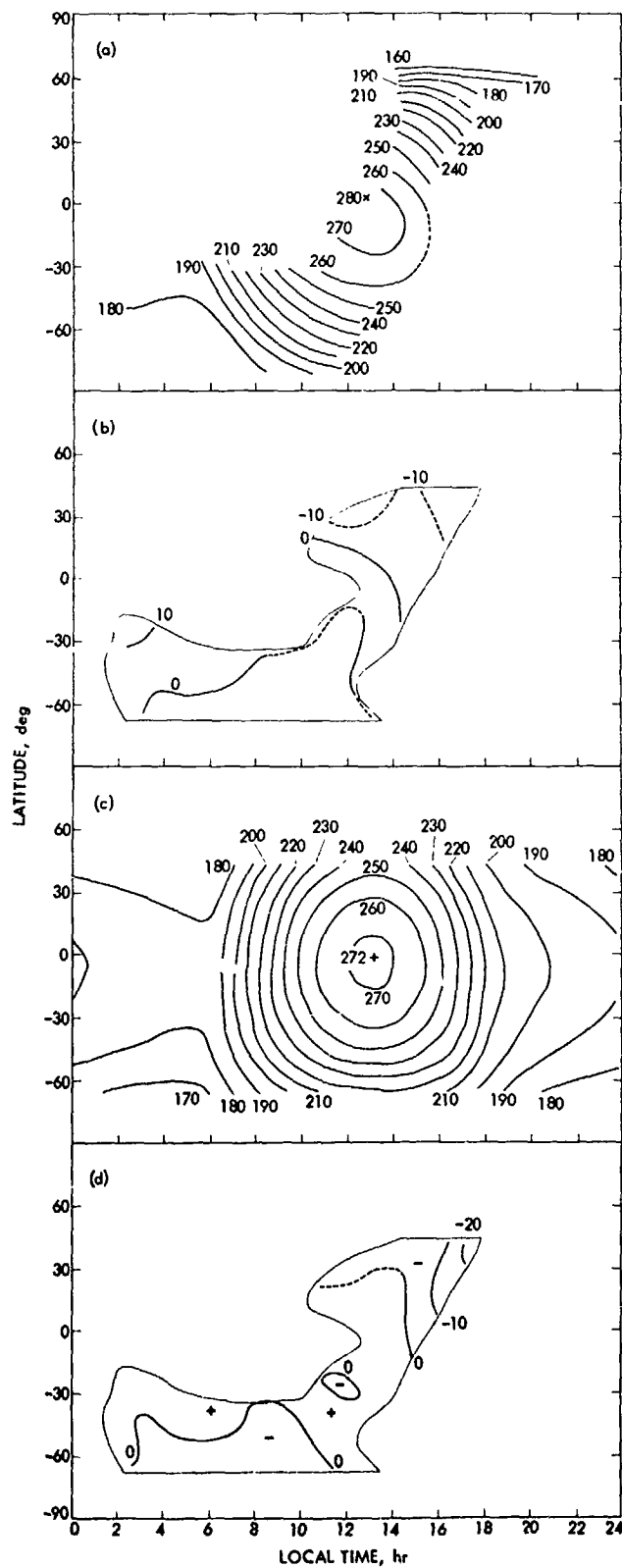
Fig. XXI-3. Same as Fig. XXI-1 for data centered on
February 17, 1972, with subsolar latitude of −6°.

function of only latitude and local time, and variations with longitude have been ignored.

At the beginning of the mission, temperature variations across the planet were small, and the maximum temperature occurred at latitudes well south of the subsolar latitude. Near latitude −40, the peak temperatures occurred almost 3 to 4 hr after noon. The temperature pattern differed radically from that predicted by calculations using the physical parameters derived from the Mariner 69 data. The planet looked smooth thermally, and it was evident that the temperature changes expected from the surface albedo variations were absent. The one exception, other than the southern polar cap, was the set of dark areas observed in the early television pictures and later identified as the volcanoes along the Tharsis ridge. These dark areas had temperatures clearly different from the surrounding areas and approaching those predicted by the Mariner 69 thermal model.

As the mission progressed, the temperature contrast across the planet increased, and the position of maximum temperature shifted toward the subsolar latitudes and to a time 1 hr after noon. The maximum temperature increased through the mission, although Mars moved farther from the Sun in its eccentric orbit. The highest observed temperature was 285°K.

2. Thermal Models

Analysis of the radiometer data, whether on the global or localized scales, has always been made with respect to a basic thermal model described in Paper I. Fundamentally, the model consists of a spherical, homogeneous, conductive solid, heated by insolation and radiating to space. The free parameters defining the model are the bolometric albedo (A) and the thermal inertia (I), hereafter frequently referred to as simply albedo and inertia. The effect of atmospheric radiation is included explicitly only by incorporating a constant atmospheric back radiation equal to 0.02 of the noon solar flux at that latitude.

The effects on the model surface temperatures of varying the albedo and inertia are shown in Fig. XXI-4. Increasing albedo decreases the temperatures at all times, the effect being largest near mid-day and diminishing steadily until dawn. Increasing inertia decreases the amplitude of the diurnal variation and increases the delay of peak temperatures after noon; it also increases the average temperature slightly. Most significantly, for representative ranges of albedo and inertia the derivatives of Fig. XXI-4 show that data obtained around local noon depend strongly on the bolometric albedo. In contrast,

the properties of the data taken just before sunrise, the so-called "predawn" data, depend almost exclusively on the assumed thermal inertia. The model diurnal variation for Martian albedos and inertias is largely a function of the assumed thermal inertia.

Within the ranges of $0.2 \leq A \leq 0.4$ and $0.005 \leq I \leq 0.010$, temperatures have been calculated using a linear expansion and the derivatives in Fig. XXI-4. This procedure has been verified to be accurate to within 2°K by comparison with a limited set of direct integrations.

A free parameter of the thermal model is the emissivity in the 10- to 20-μm region, which is incorporated as a boundary condition. In the model calculations made to analyze the Mariner 9 data, an emissivity ϵ of 1.0 was assumed, thus facilitating direct comparison with the observed brightness temperatures. In the 1969 model an emissivity of 0.9 was assumed, but the observed Mariner 9 brightness temperatures have nevertheless been compared directly with the model surface kinetic temperatures. Characteristically, the Mariner 69 model temperatures are too warm by $(1 - \epsilon)^{1/4} T \approx 0.02 T$; this small discrepancy does not significantly affect comparison between observations at different times or places.

Finally, the regular radiometer observations lasted from November 1971 through mid-March 1972. During that time, the Mars solar distance increased from 1.41 to 1.52 AU and the subsolar latitude changed from −23° to 0°. The peak temperature predicted by the thermal model with the Mariner 69 set of thermal parameters correspondingly decreased from 292° to 274°K.

3. Discussion

The observed 10-μm brightness temperatures T_{10}, for the latitude range −70 to +40° have been fit, in a least-squares sense, to the thermal model calculated for the appropriate season. All data obtained in a 42-sec period were averaged; then the averaged local time and latitude were used to sort T_{10} into bins of 5° latitude and ½ hour local time. Each bin was weighted by the square root of the number of observations at that location. Using a starting model temperature T_m and $\partial T_m/\partial A$ and $\partial T_m/\partial I$ as shown in Fig. XXI-4, a least-squares fit model temperature T_L was found. Because possible large data errors caused by bit errors in transmission could affect this fit, any points with $|T_{10} - T_L| > 15°$K were deleted in this preliminary analysis and a second fit made. A program is in progress to identify and correct or eliminate all data affected by significant bit errors.
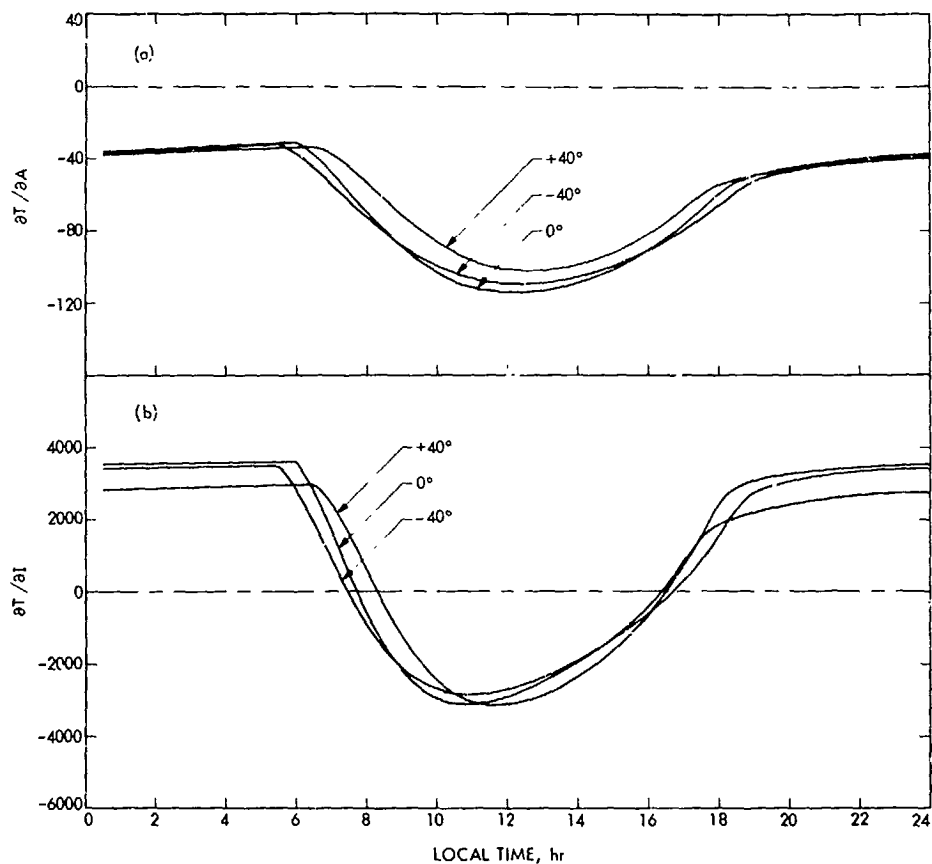
Fig. XXI-4. Dependence of the model temperatures on albedo (a) and inertia (b). Curves are shown for three latitudes on January 28, 1972. Notice that $\partial T/\partial A$ is always negative, with the maximum absolute value near noon, diminishing rapidly until sunset and then steadily at a lesser rate until dawn. In contrast, $\partial T/\partial I$ has a small positive average over the day, with large negative values near mid-day and nearly constant positive values at night. The magnitude of $\partial T/\partial I$ decreases as the length of day and night becomes unequal.

The results of the fit are included for three epochs of the mission in Figs. XXI-1 through XXI-3. It is obvious that, even late in the mission when effects of the dust storm had diminished, consistent departures from the best-fit models exist. The observed temperatures are generally low with respect to the best-fit models at latitudes from $-70°$ to $-40°$, and near 16 hr local time for all latitudes observed. This latter effect was particularly evident on revolutions 120 to 130 in January 1972, when a set of special observations was incorporated, during a gap in the television mapping sequence, to cover all the accessible range of local times at latitudes $+10$ to $+40°$. This rapid drop in temperature is not reproducible with the thermal model and may indicate an increased thermal coupling between the surface and the atmosphere in the late afternoon.

The time variations of albedo and inertia derived for the best planet-wide fit to the thermal model are shown

in Fig. XXI-5. The derived parameters early in the mission are not meant to be taken as physically meaningful, but rather as indications of the effect of the dust storm and its smooth progression with time. Also, the results for the early orbits are far from the region for which the model derivatives were evaluated and hence are not accurate. The oscillations in inertia observed during the earlier part of the mission apparently are due to statistically significant variations in the predawn temperatures. The inertia oscillations have a period of 40 revolutions, which corresponds to the beat period of the spacecraft periapsis point and the Martian longitude. The times of minimum inertia were obtained when many of the predawn observations were at longitudes near 110°, a region which is significantly colder than other longitudes before sunrise.

Toward the end of continuous coverage (March 15, 1972), the best-fit inertia approaches 0.007 ±0.001. The
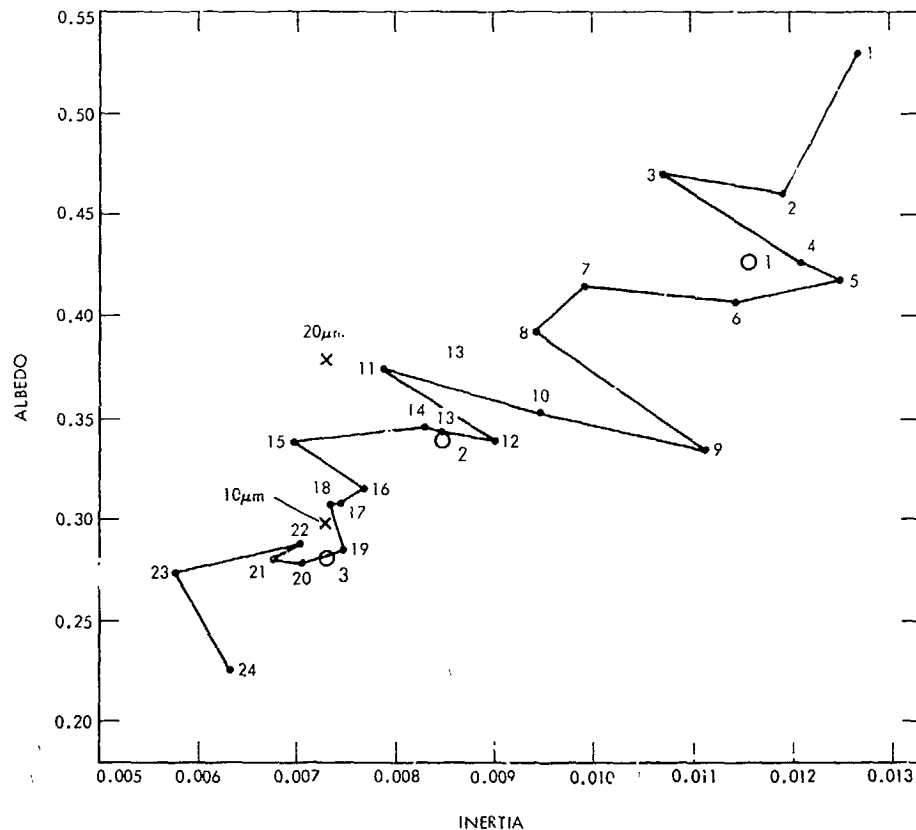
Fig. XXI-5. The variation through the mission of apparent albedo and inertia as derived from the best-fit models over groups of 10 revolutions. The large oscillations have a period of about 40 revolutions, corresponding to the time required for the radiometer swath to cover the planet once. The last two points are different from the converging trend of previous orbits and may be due to errors in the spacecraft–planet geometry. The numbers by the solid dots indicate sequential groups of 10 orbits. The three numbers in the open circles show the values of albedo and inertia derived from the data of Figs. XXI-1 through XXI-3. The crosses indicate the values derived using the *Mariner 6* and *7* data.

albedo was still decreasing steadily, but the asymptotic value must be within 0.25 ±0.05. The large variations in the last 20 revolutions may result from errors in the geometry source tapes. The values of albedo and inertia derived by fitting the 20-μm brightness temperature T_{20} are similar to those for the T_{10} fit, which is a corollary of the general agreement of T_{10} and T_{20} at equatorial and temperature latitudes. Significant differences between T_{10} and T_{20} were apparent only during early stages of the mission.

It should be interjected that the temperature pattern observed early in the mission can be accounted for by the addition of a single cloud layer to the normal thermal model (Refs. XXI-2 and XXI-6). Such a model for the dust-covered planet requires stipulation of at least four additional parameters that vary with latitude and time; this should be contrasted with the three time-independent

parameters which specify the nominal thermal model. Detailed study of the progression of the dust storm incorporating a dust layer has consequently been omitted from this report.

The best-fit parameters for the Mariner 69 data, rederived from the brightness temperatures using the same procedure employed with the 1971 observations, also are shown in Fig. XXI-5. The increased albedo for the Mariner 69 T_{20} model fit results from the average brightness temperatures at 20 μm being significantly colder than that at 10 μm for the Mariner 69 data; in Paper I this was taken to indicate an emissivity difference between 10 and 20 μm. This effect represents a clear difference of about 3° at 250°K between the 1969 and 1971 results. The discrepancy has not been resolved at the present time and may be either in the calibration or a vestigial effect of the dust storm.

C. Large-Scale Structure

Several large areas outlined in Fig. XXI-6 were selected to look for regional differences in the thermal properties of Mars. The boundaries were chosen to include areas of uniform visual reflectivity on the *Mariner 9* planning chart (Ref. XXI-7) and of uniform general surface morphology as shown on the preliminary Mars chart (Ref. XXI-8); polar regions were specifically excluded.

The three large regions near 0° longitude (1–3 in Table XXI-1) were selected to be representative of classic light and dark areas and to have similar apparent large-scale morphology, in this case fairly uniformly cratered terrain with few "volcanic" or "canyonland" features.

Several other regions were selected to cover a range of albedo, elevation, and surface types. Syrtis Major (5) and Mesogaea (4) are two lightly cratered areas with very different albedos. They are at the same latitude and hence have had nearly identical observational coverage. Hellas (8) is a large area of low elevation that has long been associated with white clouds (Refs. XXI-9 and XXI-10) and is the type example for "featureless terrain" (Ref. XXI-11). The Bosporos region (9) is at the same latitude and has a similar visual reflectivity as the south light area (3), but is less heavily cratered. Mare Cimmerium (7) is a moderately cratered, but quite dark, area.

One area, South Tharsis (6) was not chosen on the basis of the two maps mentioned above but because, early in the mission, it was noticed as having unusually low predawn temperatures. It is a high elevation area with low relief except for "South Spot" volcano and the western extreme of the "canyonlands."

In the analysis, the temperature data were divided according to local time into predawn, mid-day (10 to 16^h), and all other times. As discussed, predawn temperatures are primarily dependent on thermal inertia and mid-day temperatures are primarily dependent on bolometric albedo (Fig. XXI-4). To avoid the major effects of the dust storm, only observations from the last half of the mission were used. Because of the position of the orbit, essentially no predawn data are available from this portion of the mission for areas north of the equator. The differences from the Mariner 69 model are presented in Table XXI-1. It is obvious that the diurnal amplitude of the observed temperatures is generally less than predicted on the basis of the Mariner 69 data.

The residual temperatures of the three large, heavily cratered areas (1–3) are remarkably similar despite their striking differences in visual albedo. At mid-day, the two light areas were only 1° to 2°K cooler than the equatorial dark area. Likewise, the predawn temperature of the dark area (2) was only 2.5°K warmer than that of the south light area (3). The small differences in the amplitude of the diurnal temperature variation thus indicate that there is almost no connection between the classic visual reflectivity and thermal inertia for these areas. Similarly, the close agreement of the temperature residuals for pairs of areas that have similar surface morphology, but generally different visual reflectivities (e.g., areas 3 and 9, 7 and 10, and 11 and 12, listed in Table XXI-1), again points to a lack of correlation between the classic brightness and mid-day temperatures. In contrast, the areas of Syrtis Major (5) and Mesogaea (4) show approximately the expected correlation between classic brightness and temperature; the 12°K difference in the mid-day temperatures corresponds to a bolometric albedo difference of 0.1, while the visual albedo difference is about 0.15 (Ref. XXI-12). In general, the mid-day temperatures appear to have less dependence on visual reflectivity for cratered areas than for smooth areas. We have in progress a more general study of the relation of surface temperatures to the visual reflectivity as measured from the *Mariner 9* television pictures.

There is no a priori way of choosing areas that represent extremes in thermal inertia. Of the 13 areas selected, Hellas has been conspicuous throughout the mission for its small diurnal temperature variations. The amplitude of 68°K is 27°K less than predicted by the Mariner 69 model, and is the smallest amplitude observed for all these areas; it corresponds to an inertia of about 0.011. The diurnal amplitude of the south Tharsis region averages 7°K greater than the model, by far the largest observed, equivalent to an inertia of about 0.005.

The visual reflectivity of Mars shows a general dependence on latitude as shown in Fig. XXI-6. Thus, in addition to the selected areas of Table XXI-1, the whole planet between −60° and +40° was divided into 5° wide latitude bands; temperature residuals from the Mariner 69 model are shown in Fig. XXI-7. Surprisingly, the data show a more consistent pattern than do the areas selected only on the basis of visual reflectivity. There are bands with low mid-day temperatures from −60° to −30° and from +10° to +20° latitude. Although the variations are small, the trends are significant in view of the large number of observations incorporated in the data.

Fig. XXI-6. Outline of the areas listed in Table XXI-1. The areas are marked on the *Mariner 9* planning chart (Ref. XXI-7) showing the albedo variations expected shortly after southern midsummer.

1. Predawn Observations

In addition to selecting areas on the basis of predicted or observed physical properties, a large group of areas was studied on the basis of their being observed after midnight local time and before sunrise. For these areas, the surface temperatures depend almost exclusively on the thermal inertia, as the effects of albedo variations and slopes are then the smallest (see Figs. XXI-4 and XXI-8). The observed predawn 10-μm brightness temperatures are shown in Fig. XXI-9 as differences from the Mariner 69 model. Because of physical limits in viewing directions, there is little predawn coverage north of the equator and the northern limit moved south through the mission.

Many pronounced local and regional variations were observed in predawn temperatures. Early in the mission, these variations were partially masked by the dusty atmosphere. On the basis of Earth-based measurements, Morrison et al. (Ref. XXI-13) have suggested that lower visual reflectivity is correlated with higher thermal inertia. Although both lower albedo and higher thermal inertia increase predawn temperature, the temperatures measured from Mariner 9 do not consistently increase onto dark areas. While some examples of such a correlation can be found, e.g., between Mare Tyrrhenum and Ausonia (latitude = −30°, longitude = 250°), many counter examples exist, e.g., Thaumasis and Bosporos (−36°, 72°W); some of the highest contrast borders show little effect at all, e.g., Sinus Sabaeus and Deucalionis Regio (−10°, 340°W), and the borders of Hellas. The

Table XXI-1. Observed minus model 10-μm brightness temperatures of selected areas

Area	Pre-dawn	Mid-day	Other	Residual diurnal amplitude
1. North light area		−8.2	−19.9	
2. Equatorial dark area	7.4	−6.2	−5.4	−13.7
3. South light area	4.8	−7.3	−5.4	−12.1
4. Mesogaea		−13.4	−22.6	
5. Syrtis Major		−1.5		
6. South Tharsis	−7.2	−0.1	−3.7	7.1
7. Mare Cimmerium	3.0	−3.1		−6.1
8. Hellas	8.9	−18.2	−4.5	−27.1
9. Bosporos region	2.3	−7.9	−3.7	−10.2
10. Electris	6.1	−6.6	−7.2	−12.7
11. Sinus Meridiani		−3.6	−10.4	
12. Deucalionis Regio	3.0	−5.9		−8.9
13. Niliacus Lacus		−8.7	−8.9	

Fig. XXI-7. Average temperature differences, observed model, divided according to local time as a function of latitude from January through March 1972. The variation of the mid-day temperature average generally ʌs the albedo pattern depicted by Earth-based observers.
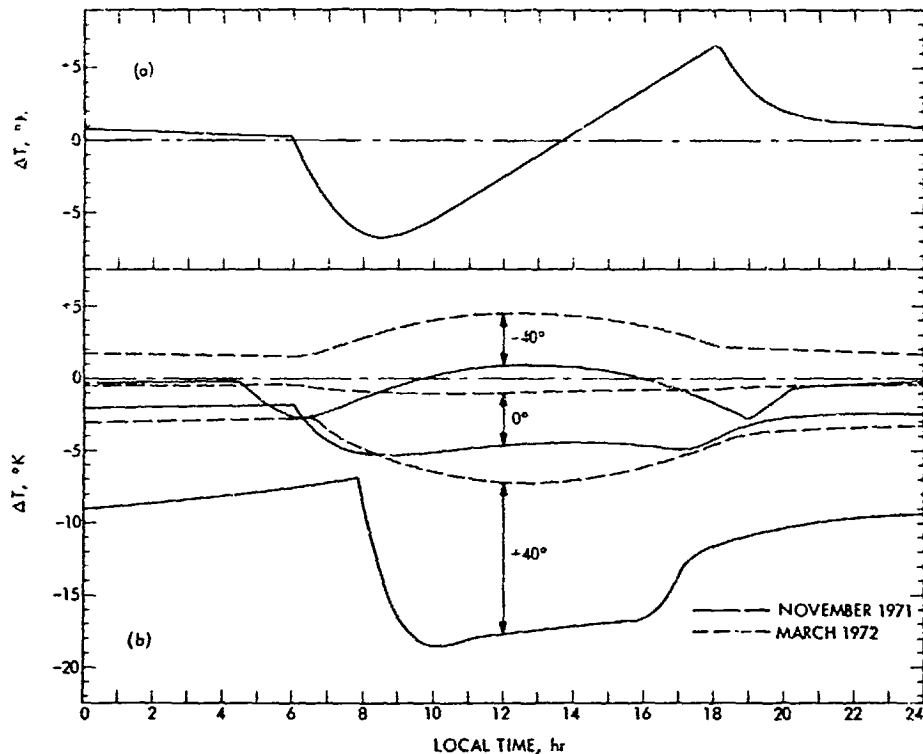
Fig. XXI-8. (a) The temperature change attributable to a 5° west-facing slope as a function of Mars local time. Variation of this function with latitude and season is small and has been omitted from the figure. (b) The temperature change attributable to a 5° north-facing slope as a function of Mars local time for three latitudes (0°, ±40°). Solid lines depict this dependence shortly after orbit insertion; dashed lines represent the situation near the end of the standard mission.

range of predawn temperatures observed is far greater than could be attributed to albedo variations, and implies major variations of the thermal inertia.

Using the preliminary Mars chart of Ref. XXI-8, no consistent relation has been discovered between the predawn temperatures and morphology. However, a cautionary note on the preliminary Mars chart states that positional inaccuracies as large as 60 km exist throughout the chart. Such a positional error is greater than the field of view for the radiometer during predawn observations. Some crater rims appear as local temperature increases (e.g., −57°, 20°W), though counter examples are common (−17°, 300°W). The parallel large canyons, but not the cross-patterned area at their western extreme (the "chandelier"), appear warmer than the surrounding areas before sunrise.

Many of the features seen in the predawn data are as small as the field of view of the radiometer, approxi-

mately 40 km at this part of the orbit. The large number of these features at the scale of the radiometer's resolution suggests that the real sources are in fact smaller and hotter than indicated by the apparent brightness temperature.

A few of the more pronounced local predawn temperatures that are high were also hand-plotted on the *Mariner 9* television pictures. The pictures were, of necessity, taken at other times; thus, small inconsistencies in relative location may exist. No general rule relating predawn temperatures to specific morphologies has become apparent. There are examples of local temperature increases corresponding to small, dark areas or to areas near the borders of rough geologic provinces, and examples where there is no apparent reflectivity or topographic feature at the location of the thermal contrast.

A major feature of the predawn observations is the large region of very low temperatures around Tharsis.

(a)

NORTH

WEST

SOUTH

NORTH

280° 270° 260° 250° 240° 230°

WEST

EAST

3°

40°

50°

60°

350° 340° 330° 320° 310° 300° 290° 280° 270° 260° 250° 240° 230° 220° 210° 200° 190° 180°

SOUTH

-30 20 10 0 10 20 30

RESIDUAL TEMPERATURE °K
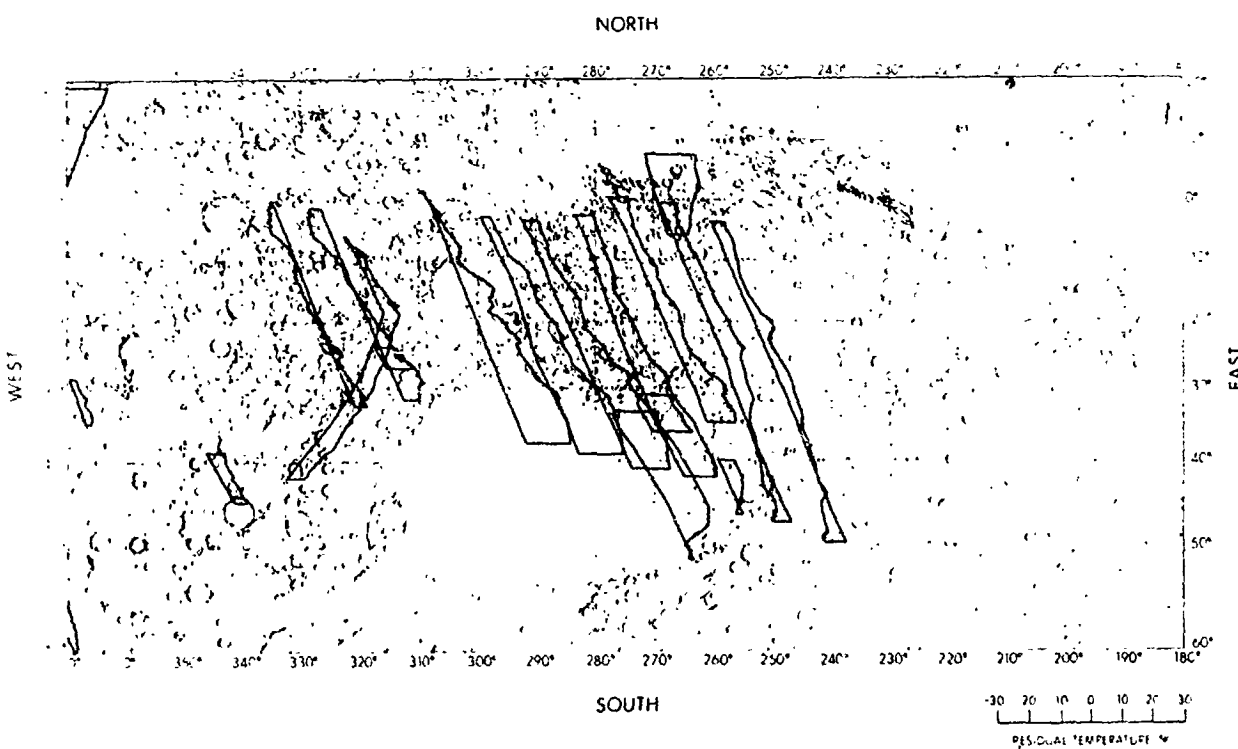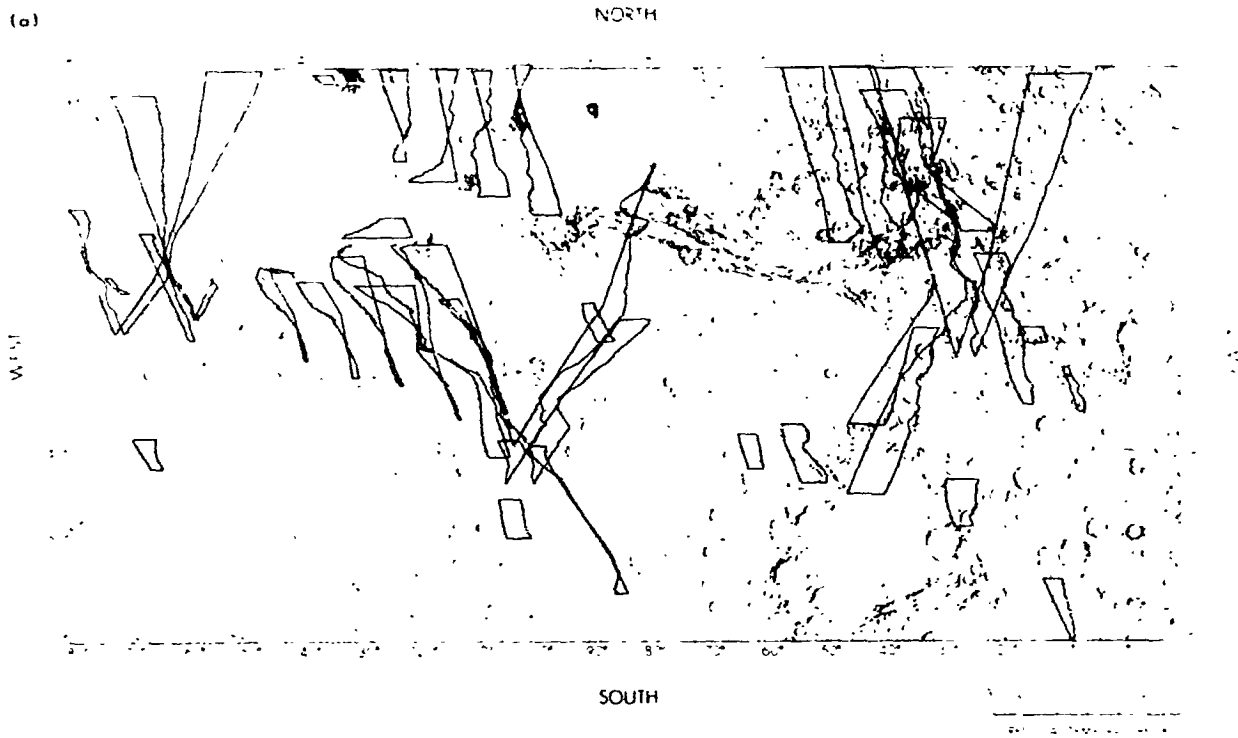
Fig. XXI-9. Predawn residual temperatures. The observed temperature minus the Mariner 69 model temperature is shown as an offset from the trace of the radiometer observation across the planet. Temperature increases to the right as indicated in the legend; no offset represents a +10° difference. (a) Data from December 14, 1971, to January 13, 1972. (b) Data from January 14 to February 12, 1972. (c) Data from January 13 to March 13, 1972.

(b)

Fig. XXI-9 (contd)

(c)

NORTH

SOUTH

NORTH

SOUTH
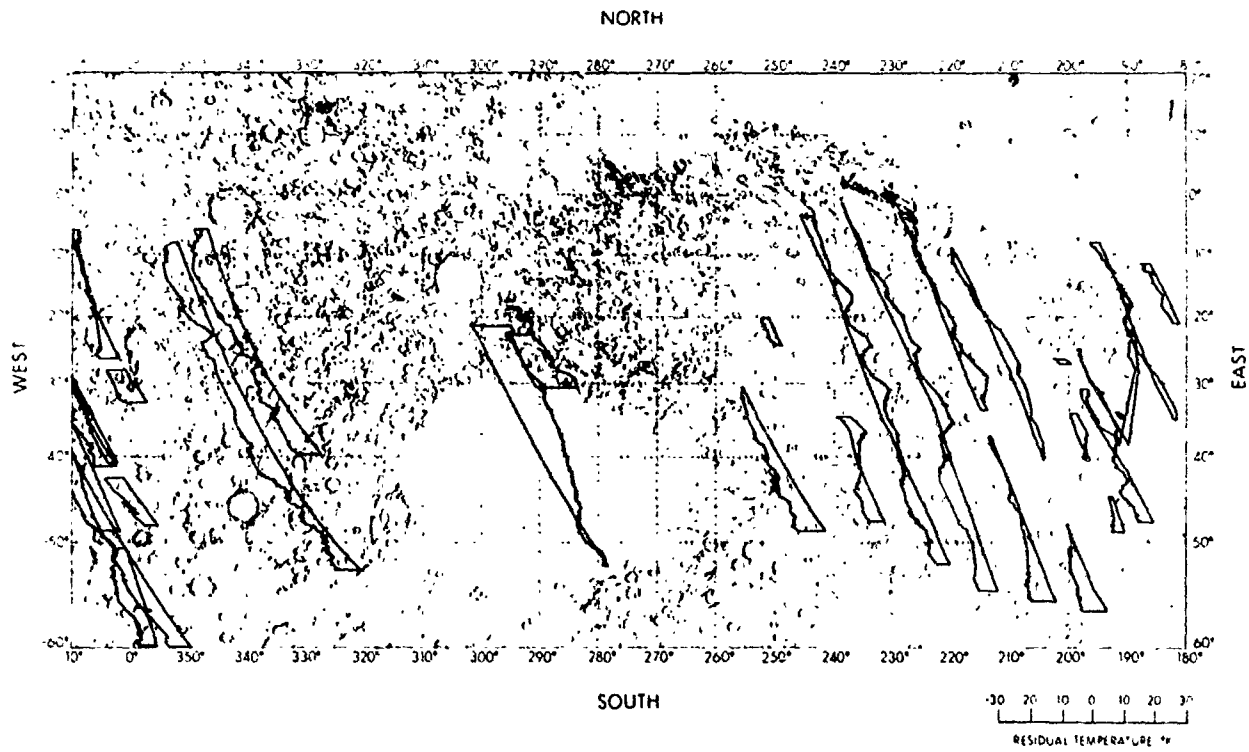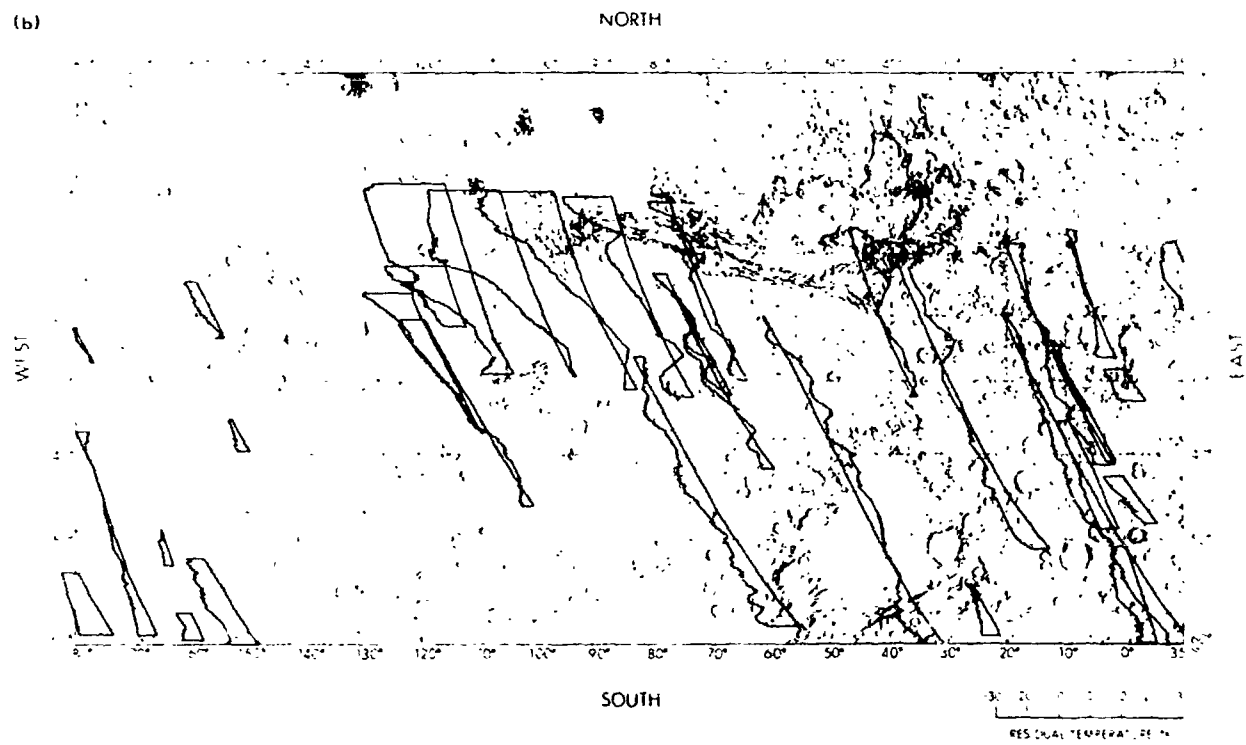
RESIDUAL TEMPERATURE, °K
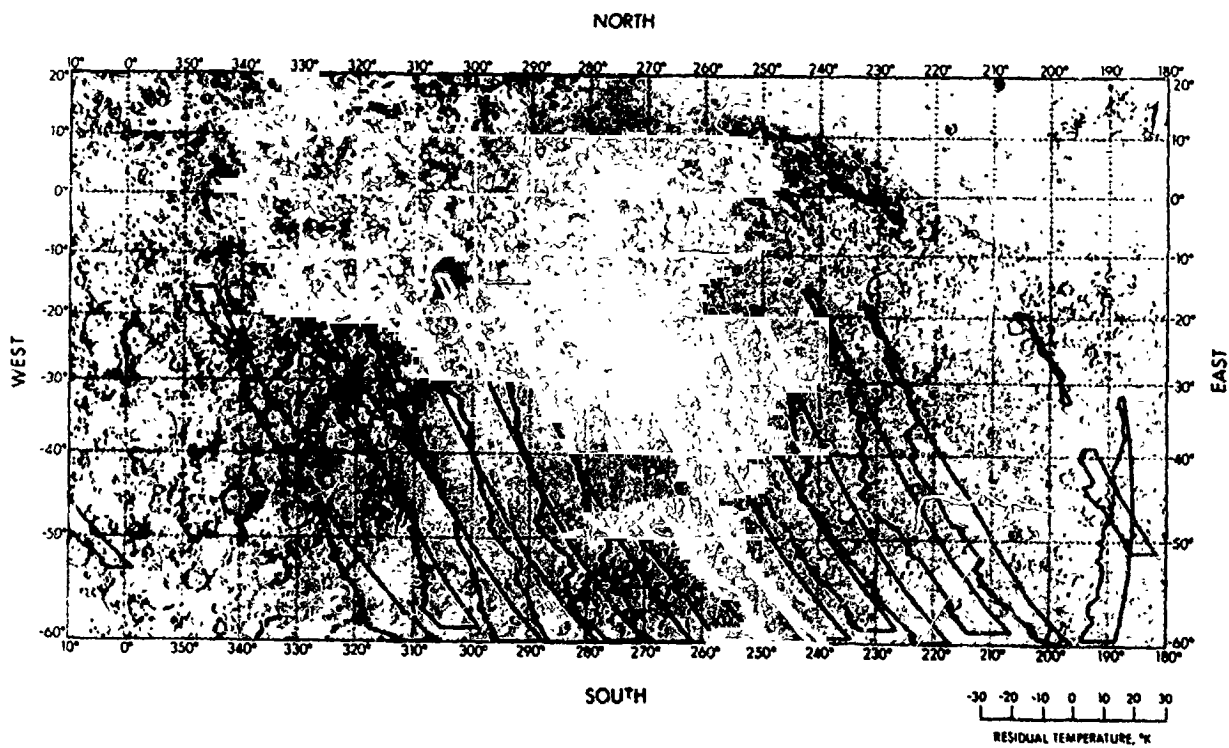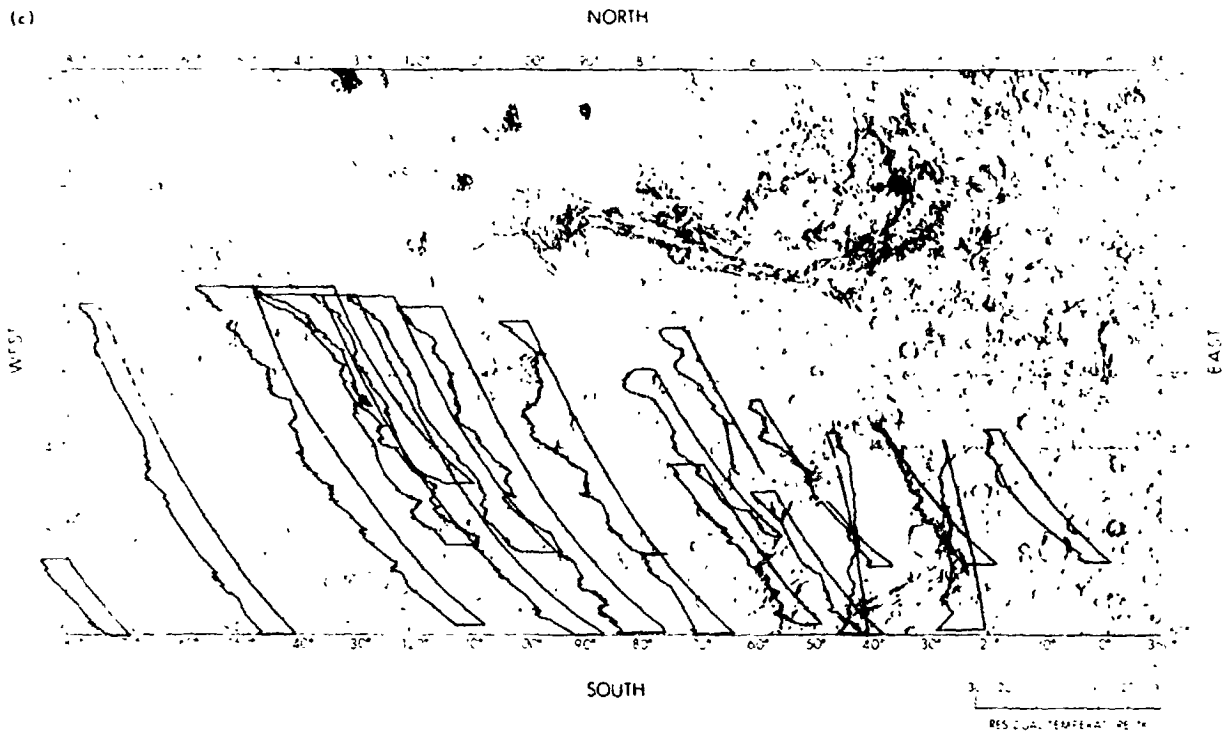
Fig. XXI-9 (contd)

As this part of Mars was known to be high, a general correlation between temperature residuals and altitude was sought. The predawn temperatures and elevation data were each averaged over 5° square areas from −30 to −30° latitude. Two sets of elevation data were used: (1) a topographic map based on data from all available sources, and (2) elevations derived from the 1971 Haystack radar observations. Using either set of elevation data, there is a general decrease of average predawn temperature with increasing height of about 1.5°K/km, although the data show wide variations. As thermal conductivity of granulated rock depends upon gas pressure when the mean free path of the gas molecules is comparable to the soil pore dimension, a decrease in thermal inertia with height is expected; the mean free path is about 10^{-3} cm at the mean surface pressure and temperature on Mars. Wechsler and Glaser (Ref. XXI-14) have compiled thermal conductivity measurements of granulated samples made over a range of pressures. For pressures between 1 and 10 mb, the thermal conductivity of a wide range of powdered materials increases approximately as the square root of the gas pressure, or the thermal inertia increases as the fourth-root of the pressure. For a height range of ±6 km around the mean surface level, corresponding to ±³⁄₄ of the Martian scale height, this corresponds to a ∓20% change in thermal inertia or a ∓4.2°K change in the predawn temperatures. Thus, decreasing gas pressure can account for an elevation dependence of about −0.7°K/km. This is about half that observed, and the remaining amount must be attributed to a decrease of average thermal inertia with increasing elevation.

Pettengill has used the 1971 Haystack radar observations to derive the dielectric constant and root mean square slopes of a band of the Martian surface overlapped by the predawn data. Although dielectric constant increases with density and the amount of solid rock (Ref. XXI-15), and might be expected to show a correlation with thermal inertia as has been observed for the Moon (Ref. XXI-16), no significant correlation was found between predawn temperatures and the data presented by Pettengill.

2. Implied Physical Properties

The predawn data are the most directly interpretable of the thermal data presented here. Figure XXI-10 shows the relation between the thermal inertia and the diurnal amplitude and predawn temperatures. The diurnal amplitude, where determined, is a somewhat better indicator

of thermal inertia than is predawn temperature, as it has a smaller dependence on albedo.

As discussed in Paper I, the main physical property determining thermal inertia for materials relevant to Mars is thermal conductivity, which is closely related to particle size. Wechsler and Glaser (Figs. 4, 8, and 11 of Ref. XXI-14) have compiled, at several gas pressures, thermal conductivity measurements of powdered rocks with particle diameters from 0.004 to 0.08 cm and have interpolated them across the pressure range relevant to Mars. Over this particle size range, the thermal conductivity varies approximately linearly with particle size. We are unaware of any thermal conductivity measurements at relevant pressures for geologic materials with mean particle diameters between 0.1 cm and several centimeters. Lacking measurements for centimeter-size particles, a smooth curve drawn through the available data for small particles and asymptotically approaching the conductivity of solid rocks at 100 cm has been adopted and is shown in Fig. XXI-11. This is an estimate of the thermal conductivity of uniformly sized lithic soils at 6 mb, but should serve as an indication of the surface properties required by the observed temperatures.

At the scale of classic features, the extremes of predawn residual temperatures and diurnal amplitudes listed in Table XXI-1 imply a range of inertia from 0.005 for south Tharsis to 0.012 for Hellas. Interpreted as regional variations of uniformly sized soil, the mean particle size ranges from 0.015 to 0.2 cm. The fact that these two areas also appear to represent the elevation extremes on Mars suggests a general dependence of temperature variations on height. A possible cause is the size sorting nature of eolian transport and the inability of the Martian atmosphere to carry larger material to high elevations. The derivation of surface physical properties within the Hellas basin is complicated by the apparent presence of an exceptionally persistent local dust storm. Examination of television pictures taken late in the mission indicate that the surface was obscured through most of the mission. The apparent thermal inertia would be significantly affected if the dust caused strong radiative coupling through more than the lower few hundred meters of the atmosphere.

At the limit of the radiometer's spatial resolution, the lowest residual predawn temperature found, −15°K in the Tharsis area, corresponds to an inertia of 0.0035 and a nominal particle size of 0.006 cm. There can not
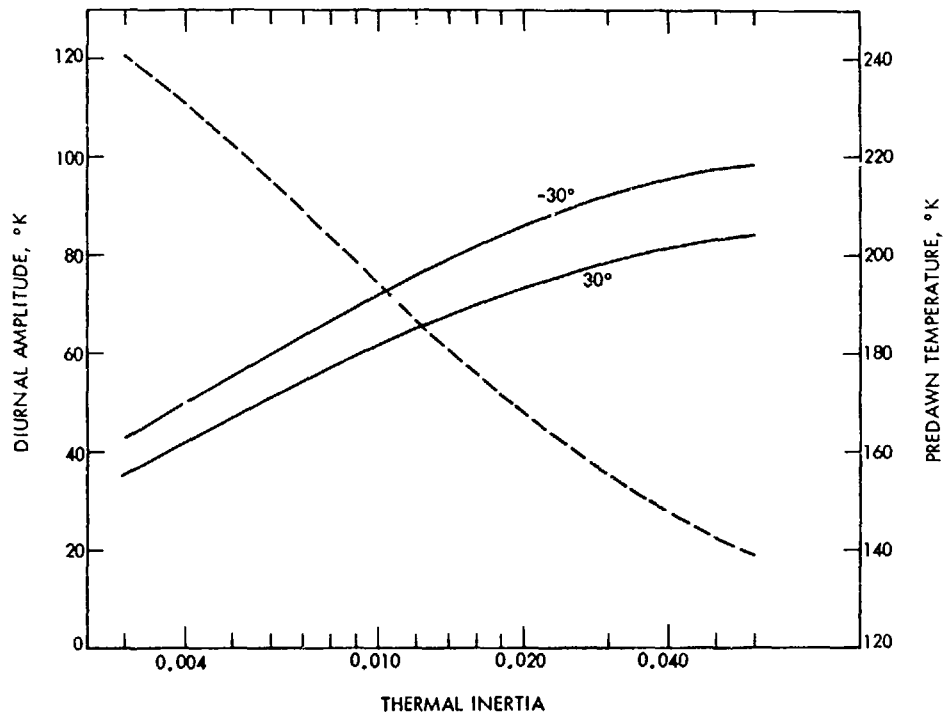
Fig. XXI-10. Diurnal temperature amplitude at −30° latitude (dashed line) and predawn temperatures at +30° and −30° latitude (solid curves) for a constant albedo of 0.3 during January 27, 1972. Although the absolute predawn temperature depends on latitude and Martian season, the shape of the curve, and hence residual temperature, is almost independent of season or latitude away from the polar regions.

be any appreciable fraction of material greater than 0.02 cm in diameter exposed on the surface of that area. The corrections for the lower gas pressure and conductive coupling to the atmosphere are of opposite sign, and a nominal net correction would result in approximately a 20% increase in these particle sizes. As the expected effect of the dust storm is to increase the apparent inertia, these estimates of minimum particle size are likely to fall within the actual range. Estimates of maximum particle size could be moved to unrealistic values by the effects of a dusty atmosphere; hence, only data from the last half of the mission are considered. In contrast to the apparent localization of the lowest inferred inertias around south Tharsis, high predawn residual temperatures of about +20°K were found at several locations. The highest predawn residual temperature found after January 15, 1972, was +23°K measured near the north edge of Hellas, outside the area of the local dust storm mentioned above, corresponding to an inertia of about 0.017 and a mean particle size of about 0.5 cm. It should be cautioned that the thermal model used thus far is physically naive. Of the various complications possible, the occurrence of nonuniformly sized material and thermal coupling with the atmosphere probably are dominant.

As an example of nonuniformly sized material, we consider the occurrence of large blocky material with a high inertia exposed on a surface whose inertia is small. This requires assignment of the inertias of both the homogeneous surface and the blocky material. As an example, if blocks 10 cm or larger and with an inertia 0.030 are exposed on a surface of 0.01-cm particles with an inertia 0.004, the observed temperatures listed in Table XXI-1 imply that the fraction of the surface covered by exposed blocks ranges from 5 to 35%. The small diurnal amplitude observed locally near Hellas would require 70% exposure of blocky material.

Conductive heat transfer between the atmosphere and the surface tends to decrease the diurnal temperature variation in comparison to that which would result if the atmospheric boundary layer were perfectly insulating. The inertia indicated by the daily temperature variation is therefore larger than should be attributed to the surface material alone. Based on calculations of Gierasch and Goody (Ref. XXI-17), Neugebauer et al. (Ref. XXI-1) estimated that this process increases the apparent inertia by about 10%, but there is a large uncertainty associated with this estimate because of our lack of knowledge of
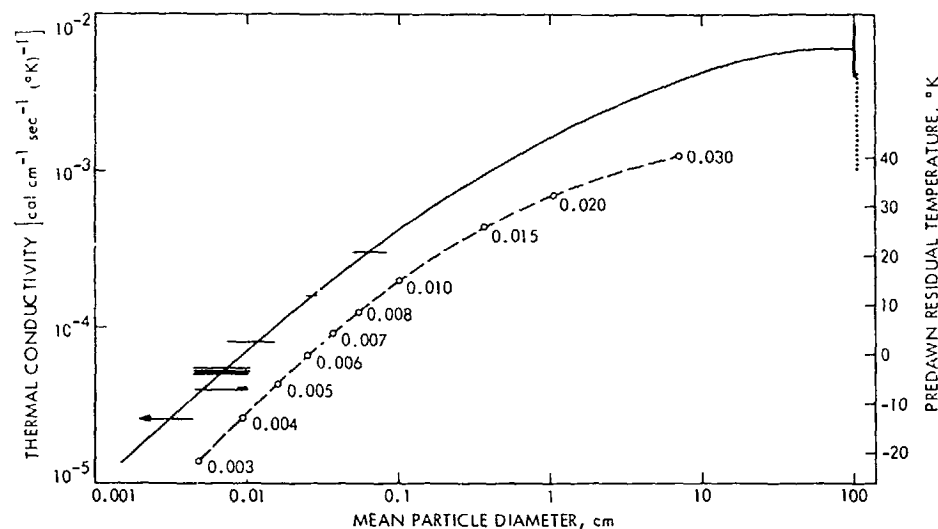
Fig. XXI-11. Nominal dependence of thermal conductivity and inertia on particle size. The data are taken from Wechsler and Glaser (Ref. XXI-14). The solid line is a smooth curve hand-plotted between the data for fine particulate samples and solid rocks. The horizontal lines represent reported size ranges. The vertical solid line is the range of conductivities for dense igneous rocks, while the vertical dotted line represents vesicular basalts. The dashed line represents the computed relation between the particle size and the predawn residual temperature (i.e., the observed minus Mariner 6S model temperature) as presented in Fig. XXI-9 The calculations assume a volume specific heat, ρc, of 0.24; calculations are for $-30°$ latitude on January 28, 1972, but are not a strong function of latitude, date, or time before sunrise.

the boundary layer conditions on Mars. During the dust storm, thermal coupling between the surface and atmosphere almost certainly increased over that estimated for clear conditions. Such effects have not been accounted for in this analysis; consequently, the derived inertia presented here must be somewhat larger than the actual values for the surface material.

D. Localized Thermal Features

The search for localized thermal features was one of the primary goals of the infrared radiometry experiment. A preliminary search has been made for local deviations from the mean thermal background which can be associated with features observed by the television cameras. The method of selecting the local anomalies has eliminated all areas larger than about 800 km (about 15 areocentric degrees) in extent. The search was systematically conducted for all revolutions between January 3, 1972, when the television mapping sequence started and it was first possible to easily identify surface features, and March 13, 1972, when the signal-to-noise ratio became significantly degraded. Data taken when the instrument platform was in motion have been omitted. Several hundred areas between latitudes $-60°$ and $+40°$

on the planet appear to be localized thermal features differing in temperature from their surroundings by 4°K or more. Of these, the 27 tabulated in Table XXI-2 show differences of at least 8°K; their locations and approximate extent also have been plotted on a television mosaic of the planet in Fig. XXI-12, where it can be seen that many of the areas may be associated with topographic features on the planet.

In Table XXI-2, an attempt has been made to delineate the probable cause of the temperature variations on the basis of their visual appearance. Thus, for example, the Martian canyonlands (areas 5, 8, 11, and 12), characterized by sharp topographic boundaries, may be areas of distinct thermal inertia. The large crater at $-13°$ latitude and 305° longitude may be another such area (area 24). One clear example of a thermal feature probably caused by an albedo variation is the dark area (area 21) near the southern boundary of Elysium at $+11.5°$ latitude and 216° longitude. This area also has been found by the radiometer onboard the Russian *Mars 2* spacecraft to be anomalously warm. In general an examination of the uncorrected television pictures shows a correlation between temperatures and visual albedo on a small scale.

Table XXI-2. Areas with local temperature deviations

Area	Longitude, deg	Latitude, deg	Local time, hr	Background temperature, K	ΔT	Date	Feature: probable cause
1.	7.4	+6.9	15.1	251	+8	Feb. 9, 1972	Dark area in cratered terrain: low albedo
2.	9.8	+1.5	14.9	254	+8	Feb. 9, 1972	Dark area in cratered terrain: low albedo
3.	19.7	−30.7	13.3	271	−8	Feb. 10, 1972	Crater floor: high inertia
4.	22.9	−19.2	13.0	271	−8	Feb. 29, 1972	Crater floor: high inertia
5.	46.9	−11.8	13.5	275	−8	Feb. 26, 1972	Plateau in canyonlands: high inertia
6.	51.2	−54.7	9.5	210	+10	March 2, 1972	SW edge of Argyre basin: cause undetermined
7.	56.2	−51.7	10.5	231	−8	Feb. 29, 1972	SW edge of Argyre basin: cause undetermined
8.	57.4	−14.0	13.4	275	−10	Feb. 25, 1972	Canyonlands: high inertia
9.	64.8	+23.0	16.9	204	+13	Jan. 14, 1972	Flow channel: cause undetermined
10.	78.8	−30.2	14.1	268	+8	Feb. 3, 1972	Dark area in cratered terrain: low albedo
11.	81.8	−7.4	13.8	276	−8	Feb. 22, 1972	South rim of canyonlands: high inertia
12.	85.2	−6.6	12.7	273	−10	March 12, 1972	South rim of canyonlands: high inertia
13.	108.6	−24.5	13.3	280	−9	Feb. 20, 1972	Indistinct feature: high albedo
14.	118.9	−11.2	17.7	216	+8	Nov. 14, 1971	South Spot volcano: dust storm effects (typical)
15.	125.3	−20.9	12.6	275	−8	March 8, 1972	Bland area: high albedo
16.	129.1	−20.7	14.7	276	−8	Jan. 28, 1972	Bland area: high albedo
17.	179.6	+36.0	15.4	233	+9	Feb. 28, 1972	Clearing in north polar hood or low albedo
18.	210.4	+30.9	15.4	236	+11	Feb. 25, 1972	Volcanic pile in Elysium: west-facing slope
19.	212.3	+25.0	15.1	251	−9	Feb. 25, 1972	Volcanic pile in Elysium: east-facing slope
20.	213.5	+24.2	15.2	236	+11	Jan. 19, 1972	Volcanic pile in Elysium: west-facing slope
21.	216.1	+11.5	16.3	225	+9	Jan. 17, 1972	Well defined dark spot: low albedo
22.	285.5	+38.2	16.1	218	+8	Feb. 16, 1972	Clearing in north polar hood or low albedo
23.	295.7	−33.5	14.5	252	−10	Jan. 30, 1972	North edge of Hellas basin: high inertia
24.	304.9	−13.2	13.8	277	−8	Feb. 17, 1972	Floor of large crater: high inertia
25.	316.3	−18.4	13.7	277	−8	Feb. 16, 1972	Two circular bright areas: high albedo
26.	334.0	−27.8	14.5	270	−12	Jan. 26, 1972	Crater floor: high inertia and high albedo
27.	358.8	−29.3	13.4	272	−9	Feb. 12, 1972	Crater floor: high inertia

Local temperature features also may be caused by topographic slopes. To first order, those thermal effects caused by topographic slopes may be approximated by assuming they correspond to an effective translation in latitude, longitude, or a combination of the two, as demonstrated in Fig. XXI-8. Although large slopes might be expected in the canyonlands area (areas 5, 8, 11, 12), their effect on temperature should be negligible at the times indicated for these anomalies. Slopes on the order of 10° would account for the thermal features observed in areas 19 and 20, on the flanks of a volcanic mountain in Elysium.

The inverse of the procedure in the preceding paragraph has been applied to a slope analysis of the volcanic mountain called South Spot. By chance, one radiometer scan passed in an approximate east–west direction directly over the central crater. Assuming that albedo and thermal

inertia are uniform across the volcano and that the floor of the central crater is locally flat, temperature differences from a uniform background may be interpreted as local slopes. Integration of these slopes along the path of the scan yields the profile shown in Fig. XXI-13. The results are in fair agreement with altitude profiles obtained by the ultraviolet spectrometer[2] and infrared interferometer spectrometer (Ref. XXI-18; also see Section XX of this Report).

Several cool areas observed by the radiometer during daylight hours have been identified in the television images as clouds (Ref. XXI-19; also see Section XIX of this Report). None of these apparent clouds caused temperature drops as large as 8°K. Inhomogeneities in extensive cloud cover may produce apparent warm areas; areas 17 and 22 near the southern edge of the north polar

[2]A. Lane, personal communication, 1972.
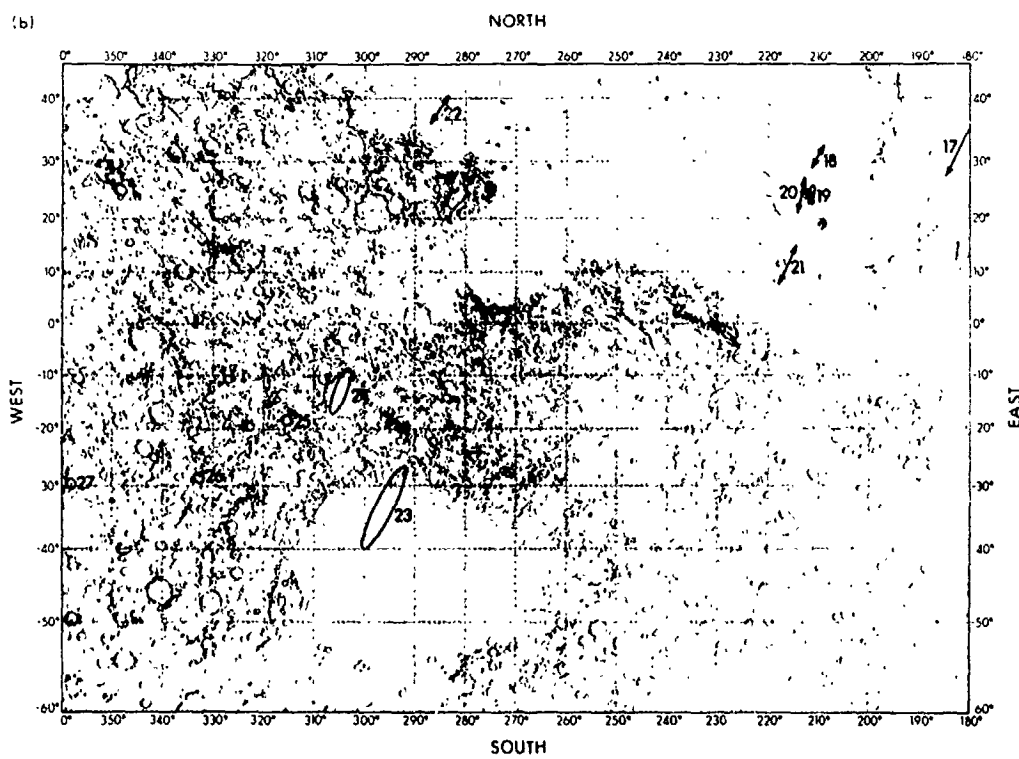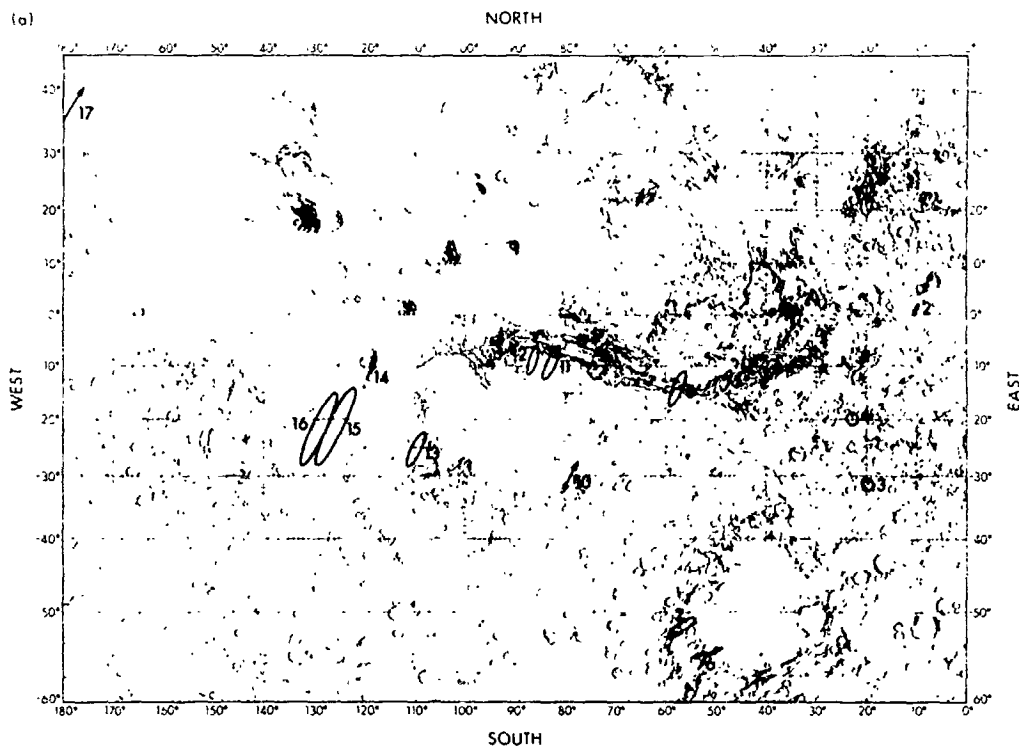
Fig. XXI-12. (a) Locations and approximate extent of the localized thermal features listed in Table
XXI-2. The 16 areas that are colder than their background are shown by ellipses, the 11 warmer areas
by double pointed arrows. Longitudes 0° to 180°. (b) Same as Fig. XXI-12a. Longitudes 180° to 360°.

MARS COORDINATES
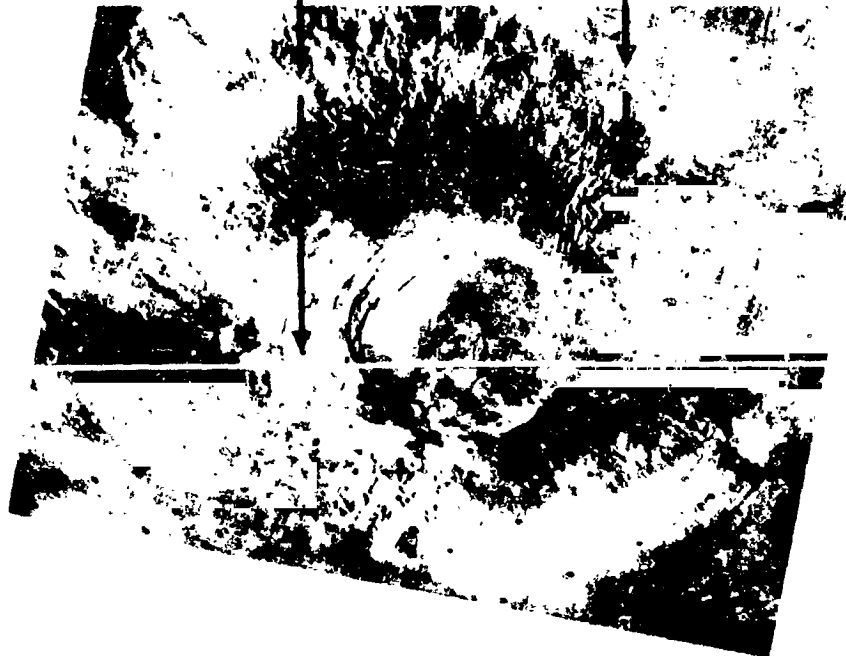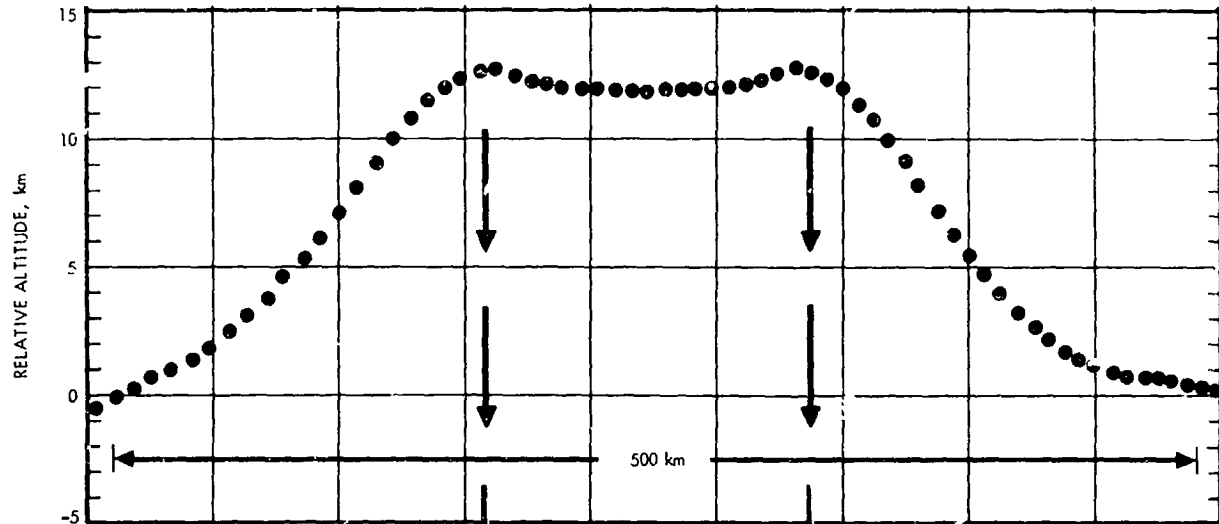
Fig. XXI-13. Altitude profile of South Spot (Nodus Gordii, −9.5°, 120°W). Vertical scale may be in error by as much as ±50% because of simplifying assumptions.

hood provide examples which are tentatively identified with holes in clouds.

Four cold anomalies (areas 3, 4, 26, 27) are associated with impact craters that appear in the much enhanced television images to have bright areas on their floors. From their appearance, one might be tempted to identify them as water frost deposits on the crater floors. As these observations were obtained during the warmest part of the day, however, it is unlikely that they represent frost deposits, and the temperature drop probably is due to the albedo or inertia variation. The albedo variation necessary to explain the observed temperature ($\Delta A \simeq 0.1$) is larger than the apparent reflectivity difference in the television images. Therefore, these areas may also have higher inertia than the Martian average.

One of the objectives of the infrared radiometer experiment was to search for possible sites of active volcanism. No areas of Mars as large as the projected radiometer field have been observed with brightness temperatures in excess of 300°K. If a hot spot is smaller than the projected area of the radiometer field, the observed brightness temperature will clearly be less than the actual temperature of the feature. A temperature devi-

ation of at least 2°K is required for certain recognition. In Fig. XXI-14, the detectability of features as a function of their linear size and inherent temperature is indicated for the 10-µm channel of the radiometer; the background is taken to be 250°K. The warm anomalies listed in Table XXI-2 would have to fall in the shaded area of Fig. XXI-14 to be attributed to internal heat. An upper limit to expected temperatures of an active lava lake is near 1500°K. No such hot spot greater than 0.5 km has been observed from distances of 2000 km or less. A lava lake would have to be at least 0.2 km in extent and be within the radiometer's field of view to be detected as a 3°K rise. Even if Mars had twice the volcanic activity of Earth, the probability of observing such a feature would be very small.

Several thermal features were observed at times of day when they could not readily be attributed to inertia variations, and no appropriate reflectivity or slope variations were evident. While these currently have no probable cause identified, they may be due to some unusual combination of surface properties and there is no other evidence to suggest that they are due to internal heat flow. Further investigation of these features is in progress.
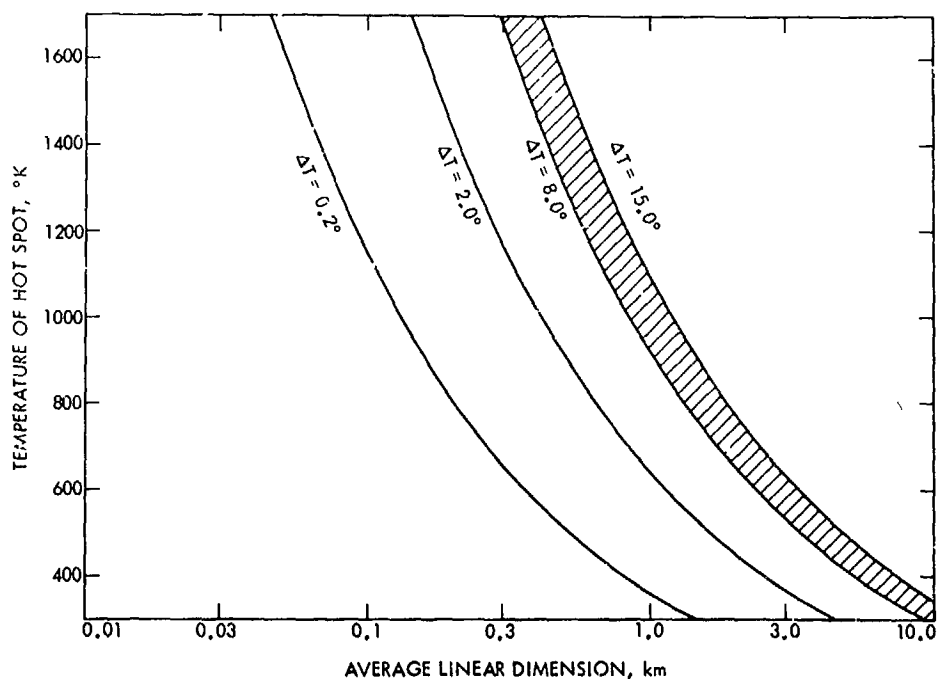
Fig. XXI-14. Detectability of a hot spot smaller in extent than the radiometer field of view as a function of its average linear dimension. The digitization limit is represented by the 0.2°K curve. The warm anomalies listed in Table XXI-2 would have to be found in the shaded area to be attributable to internal heat.

E. Summary

The results of the preliminary analysis of the *Mariner 9* radiometer data can be summarized as follows:

(1) Once the planet-wide dust storm had subsided, the cross thermal characteristics of Mars agreed qualitatively with those observed with a poorer spatial resolution in 1969. The ranges in inertia and albedo, $0.001 \lesssim I \lesssim 0.017$ and $0.2 \lesssim A \lesssim 0.4$, were comparable for both missions. Again, thermal features were visible at the limit of the spatial resolution.

(2) The dust storm changed the thermal picture of Mars radically. At the observed height of the storm, the average dayside temperatures of the planet were lower by about $20°K$ than without the dust storm.

(3) Over large-scale physiographic visual features, no univocal correlation between albedo and thermal inertia seems to exist. In the small scale, fluctuations in thermal inertia apparently unrelated to albedo changes appear in predawn data. Small-scale brightness variations visible in television pictures generally are associated with simultaneous temperature fluctuations of approximately the expected amplitude, but this is understood as a consequence of the stronger daytime dependence of temperature on albedo than on thermal inertia. In general, it appears as if albedo and thermal inertia are not dependent on only one and the same property of the Martian soil.

(4) At the limit of resolution of the radiometer, there are many areas that differ significantly from their surroundings. These differences, however, are plausibly explained in terms of modest variations in thermal inertia, bolometric albedo, and topographic slopes without having to invoke internal heat sources.

(5) The surface particle sizes derived from the observed thermal inertias vary between 0.006 cm and 0.5 cm, a range wider than previously estimated.

References

XXI-1. Neugebauer, G., Münch, G., Kieffer, H., Chase, S. C., and Miner, E., "Mariner 1969 Infrared Radiometer Results: Temperatures and Thermal Properties of the Martian Surface," *Ap. J.*, Vol. 76, p. 719, 1971 (Paper I).

XXI-2. Chase, S. C., Jr., Hatzenbeler, H., Kieffer, H. H., Miner, E., Münch, G., and Neugebauer, G., "Infrared Radiometry Experiment on Mariner 9," *Science*, Vol. 175, p. 308, 1972.

XXI-3. "Initial Results of Mars Probe Analyzed," *Pravda*, p. 3L, August 25, 1972.

XXI-4. Chase, S. C., "Infrared Radiometer for the 1969 Mariner Mission to Mars," *Applied Optics*, Vol. 8, p. 639, 1969.

XXI-5. Chase, S. C., Miner, E., Münch, G., and Neugebauer, G., "Infrared Radiometry Experiment for Mariner Mars 1971," *Icarus*, Vol. 12, p. 46, 1970.

XXI-6. Gierasch, P. J., and Goody, R. M., "The Effect of Dust on the Temperature of the Martian Atmosphere," *J. Atmos. Sci.*, Vol. 29, p. 400, 1971.

XXI-7. de Vaucouleurs, G., "A Mars Chart for the Mariner Flights," *Sky and Telescope*, Vol. 41, p. 283, 1971.

XXI-8. U. S. Geological Survey, Shaded Relief Map of Mars, Atlas of Mars, MM 25M IR 1:25,000,000 Cartographic Series, I-810, 1972.

XXI-9. Slipher, E. C., *A Photographic Study of the Brighter Planets*, p. 46, Northland Press, Flagstaff, Arizona, 196C.

XXI-10. Smith, S. A., and Smith, B. A., "Diurnal and Seasonal Behavior of Discrete White Clouds on Mars," *Icarus*, Vol. 16, p. 509, 1972.

XXI-11. Sharp, R. P., "The Surface of Mars: 2. Uncratered Terrains," *J. Geophys. Res.*, Vol. 76, p. 331, 1971.

XXI-12. de Vaucouleurs, G., "A Low-Resolution Photometric Map of Mars," *Icarus*, Vol. 7, p. 310, 1967.

XXI-13. Morrison, D., Sagan, C., and Pollack, J. B., "Martian Temperatures and Thermal Properties," *Icarus*, Vol. 11, p. 36, 1969.

XXI-14. Wechsler, A. E., and Glaser, P. E., "Pressure Effects on Postulated Lunar Materials," *Icarus*, Vol. 4, p. 355, 1965.

XXI-15. Campbell, M. J., and Ulrichs, J., "Electrical Properties of Rocks and Their Significance for Lunar Radar Observations," *J. Geophys Res.*, Vol. 74, p. 5867, 1969.

XXI-16. Zisk, S. H., Carr, M. H., Masursky, H., Shorthill, R. W., and Thompson, T. W., "Lunar Apennine-Hadley Region: Geological Implications of Earth-Based Radar and Infrared Measurements," *Science*, Vol. 173, p. 808, 1971.

XXI-17. Gierasch, P. J., and Goody, R. M., "A Study of the Thermal and Dynamical Structure of the Martian Lower Atmosphere," *Planetary Space Sci.*, Vol. 16, p. 615, 1968.

References (contd)

XXI-18. Conrath, B., Curran, R., Hanel, R., Kunde, V., Maguire, W., Pearl, J., Pirraglia, J., Welker, J., and Burke, T. "Atmospheric and Surface Properties of Mars Obtained by Infrared Spectroscopy on Mariner 9," *J. Geophys. Res.*, Vol. 78, 1973.

XXI-19. Leovy, C. B., Briggs, G. A., and Smith, B. A., "Mars Atmosphere During the Mariner 9 Extended Mission: Television Results," *J. Geophys. Res.*, Vol. 78, 1973.

Acknowledgments

XXII. *Mariner* 9 Ultraviolet Spectrometer Experiment: Afternoon Terminator Observations of Mars

J. M. Ajello and A. L. Lane
Jet Propulsion Laboratory/California Institute of Technology, Pasadena, California 91103

C. W. Hord, C. A. Barth, and A. I. Stewart
Laboratory for Atmospheric and Space Physics
University of Colorado, Boulder, Colorado 80302

During the *Mariner 9* mission, there were approximately 200 observations of the Martian evening twilight. In these observations, the motion of the *Mariner* spacecraft swept the field of view of the *Mariner 9* ultraviolet spectrometer across the terminator. During these terminator crossings, the ultraviolet spectrometer obtained a complete spectrum each 3 sec covering the wavelength interval from 1100 to 3400 Å at 15-Å resolution. For this initial analysis of ultraviolet spectrometer terminator data, the variation in intensity observed in a 100-Å wavelength band centered at 3050 Å is considered. Data points shown in subsequent figures are plotted each 9 sec, which is adequate to show the gross variations described here.

Some previous results from other phases of the *Mariner 9* ultraviolet experiment are described by Barth et al. (Refs. XXII-1 and XXII-2), Hord et al. (Refs. XXII-3 and XXII-4), Lane et al. (Ref. XXII-5), and Stewart et al. (Ref. XXII-6).

During the mission, the geographical point of the terminator crossing moved, in general, northward with the advance of spring in the north. At the same time, the lower atmosphere began to clear from the dusty conditions of the early mission.

The modeling and interpretation of twilight data have been described in detail in Ref. XXII-7. Determination of altitude distributions for absorbing and scattering constituents from Earth-based observations of the Earth's twilight have been carried out by a number of authors (e.g., Refs. XXII-8 and XXII-9). Terminator observations provide a measure of atmospheric properties down to an altitude where the incident extinction optical path to the scatterers, along the instrument's line of sight, becomes greater than one.

A. Terminator Model

The Mars terminator, as observed at 3050 Å, is quite dim compared with the intensities expected from a pure scattering, optically thick model, indicating that multiple scattering is not important. The lack of a multiple scattering correction may effect the interpretation for

large solar depressions angles, $\beta > 5°$. None of the interpretations given here depend critically upon data obtained at large solar depression angles. As the optical depths are not large, refraction effects are also neglected.

The geometry of observation is shown in Fig. XXII-1, where ϑ is the emission angle, θ_o is the solar incidence angle, β is the solar depression angle, R_p is equal to the radius of Mars, and ψ is equal to the supplement of the scattering angle. It is convenient to use the quantities $\mu = \cos\theta$ and $\mu_o = \cos\theta_o$, where $\beta = \mu_o$ for small β.

In this discussion, ultraviolet spectrometer twilight measurements will be interpreted in terms of two simple models. For the first model, the atmosphere is assumed to be homogeneous and to have a constant scale height. Under these conditions, three independent parameters that describe the atmosphere are the scale height, H; the total vertical extinction optical depth, τ; and the effective single scattering albedo, $\bar\omega$. The second model, in addition to the homogeneous lower atmosphere of the first model, has a pure scattering layer. The parameters necessary to specify the scattering layer are Z, the height of the bottom of the scattering layer above the level where total slant incident optical path is 1; h, the thickness of
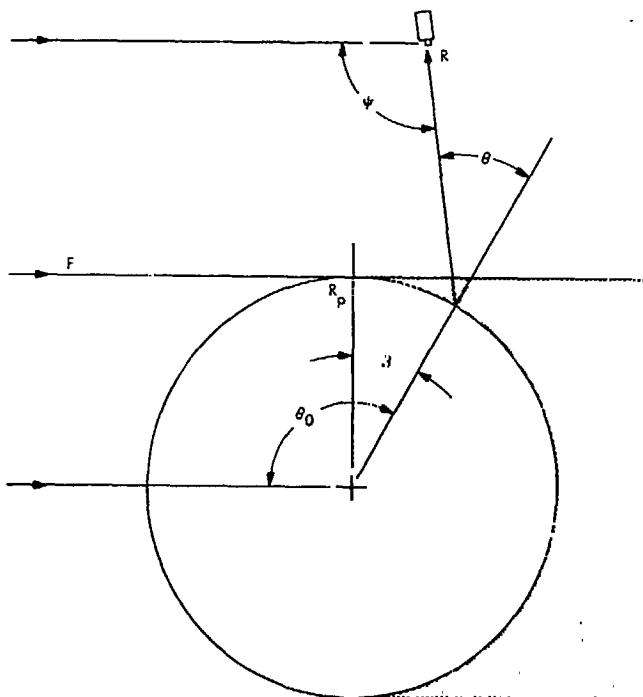
the layer in kilometers; and τ_L, the scattering optical thickness.

For the homogeneous model, the predicted reflectivity is

$$R = \frac{p(\psi)\bar\omega}{4\mu M} \exp(-x\mu_o/2)[1 - \exp(-\tau M)] \qquad (1)$$

where $p(\psi)$ is the phase function of the scatterers, M is an air mass factor, and $x = R_p/H$. The value of R from Equation (1) is to be compared with the measured reflectivity, which is intensity multiplied by π and divided by the solar flux. The air mass, correct to 0.1%, is given by

$$M = (\pi x/2)^{1/2}[1 - \mathrm{erf}(x\mu_o/2)^{1/2}] - (1/\mu)\exp(-x\mu_o/2) \qquad (2)$$

and is defined as the number of vertical optical depths traversed by a 3050-Å photon along a path tangent to the surface and singly scattered into the spectrometer's field of view. The error function is represented by erf. For a typical Mars scale height of 10 km, M varies from 23 for zero solar depression angle to 46 as the solar depression angle increases. When the maximum optical path τM becomes greater than 1, the predicted reflectivity is insensitive to extinction optical depth, τ, and, therefore, to the absolute altitude measured from the surface of Mars. In this case, the predicted reflectivity is completely specified by $\bar\omega_o$ and H. The dominant dependence of R is in the factor $\exp(-x\mu_o^2/2)$, which represents the decrease in intensity as the shadow height $(R_p\mu_o^2/2)$ increases with increasing solar depression angle.

Figure XXII-2 shows the homogeneous terminator model for different values of $\bar\omega_o$ and τ for an atmosphere having a 10-km scale height. For pure molecular scattering from a 5-mb CO_2 atmosphere, $\tau = 0.027$ at 3050 Å. The coincidence of these models as the solar depression angle increases is a consequence of all models having the same scale height. The slope of reflectivity as a function of the square of solar depression angle, $\beta^2 \approx \mu_o^2$, on a semilogarithmic scale is a measure of scale height.

The effect of adding an additional pure absorption component with a scale height, H_A, different from that of the homogeneous part is shown in Fig. XXII-3. Values of $\bar\omega_n$ are given at an extinction optical depth of 1 measured from the top of the atmosphere. This model, which corresponds to absorbing dust mixed in decreasing relative amount at higher altitudes, is not found to improve agreement materially with observation.
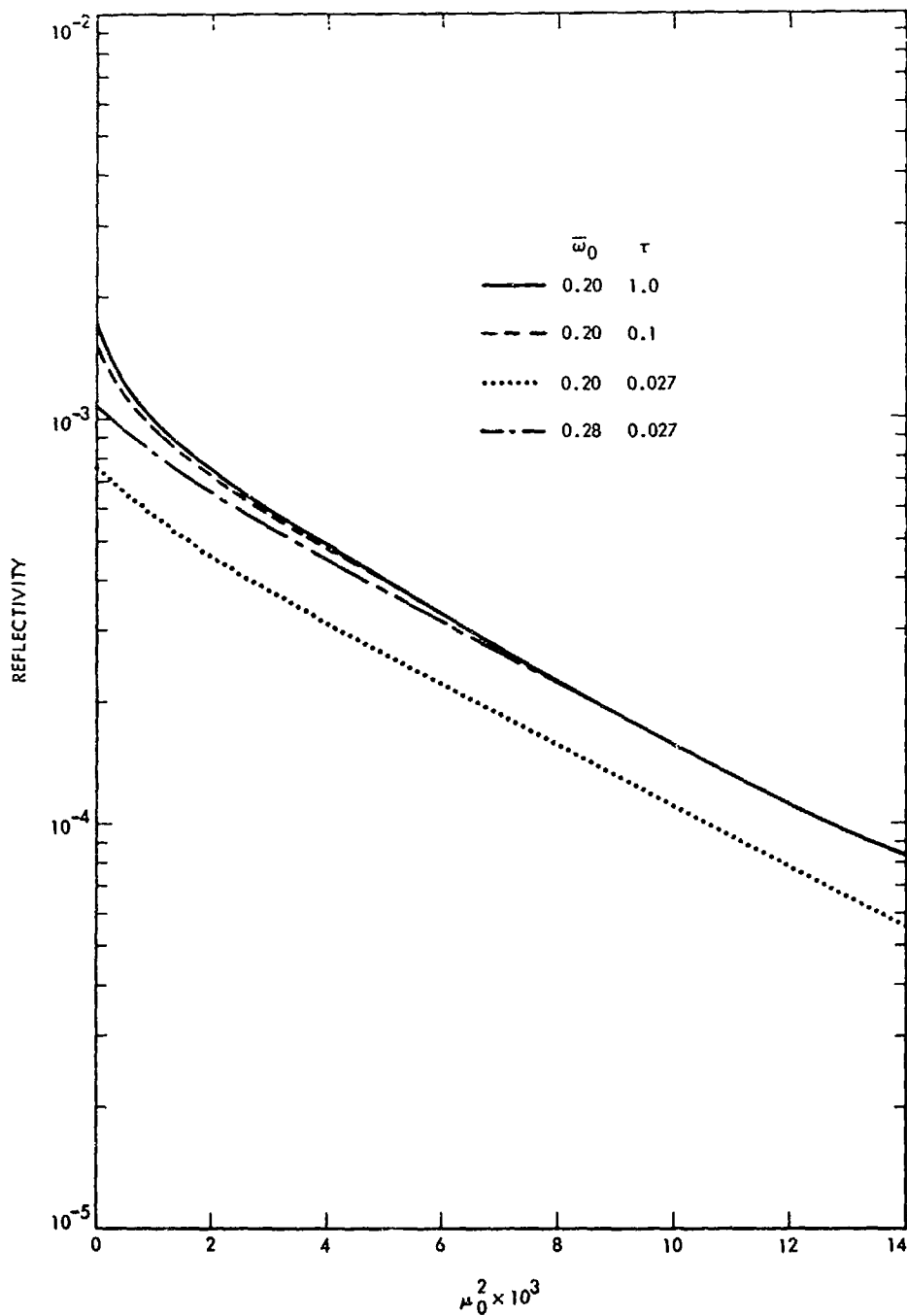
Fig. XXII-2. Model twilight reflectivity for a homogeneous atmosphere with $H = 10$ km, for different values of the single scattering albedo, $\bar{\omega}_0$, and vertical extinction optical thickness τ. The horizontal axis is μ_0^2, which is equal to the square of the solar depression angle. Multiplying the abscissa value of $\mu_0^2 \times 10^3$ by 1.7 gives the geometrical shadow height in kilometers. Vertical viewing is assumed, i.e., $\mu = 1$.
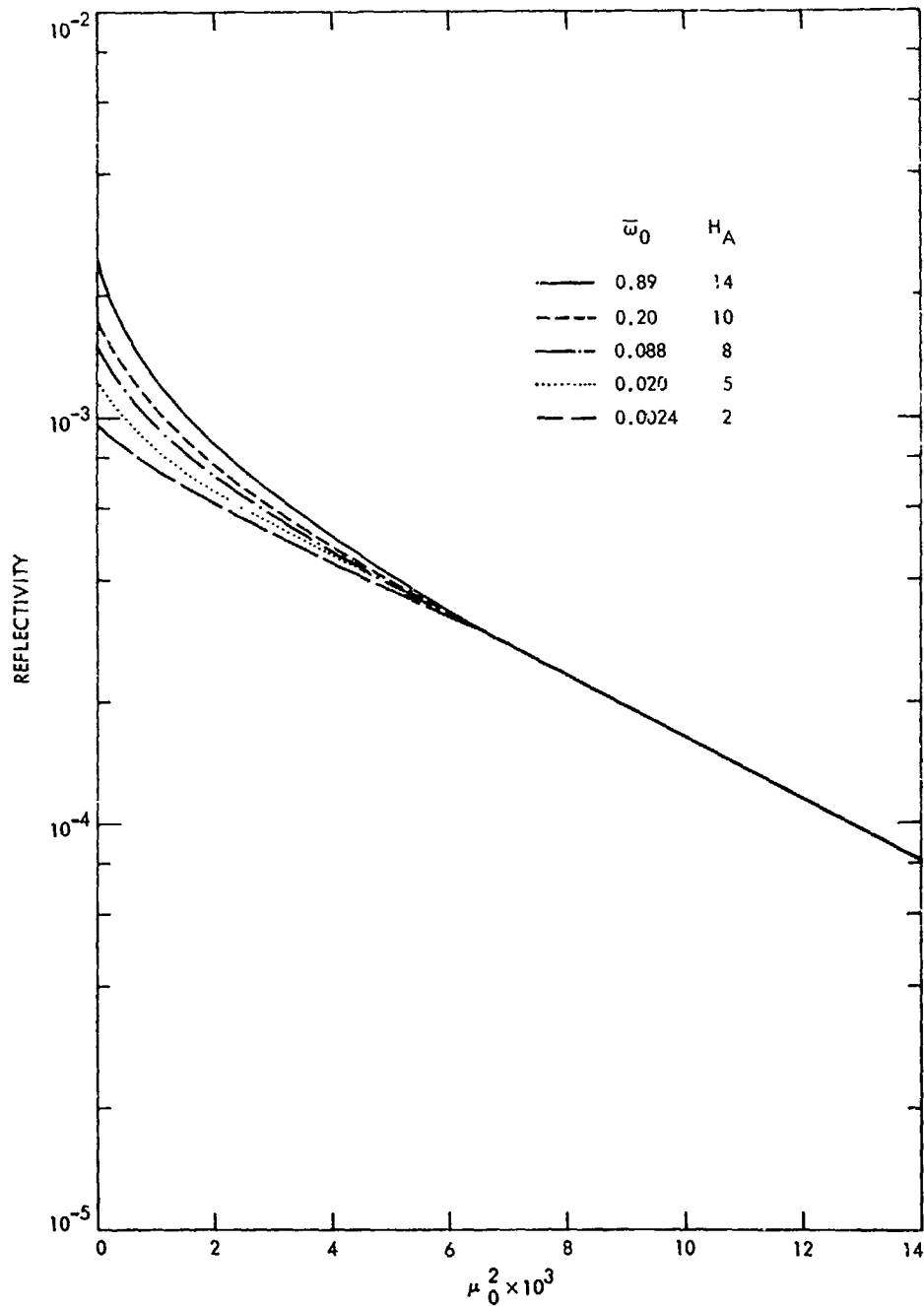
Fig. XXII-3. Model twilight reflectivity for a two-component atmosphere. The vertical optical depth is 1; the scale height is 10 km.

Twilight observations made in the mid-latitudes show a relatively slow decrease in reflectivity with solar depression angle. If these terminator crossings are interpreted in terms of a homogeneous model, the apparent scale heights are on the order of 20 or 30 km, which are physically unreasonable values. A scale height of 10 km corresponds to a terminator temperature of 190°K. In order to explain these large apparent scale heights with a spherically symmetric atmosphere, it is necessary for a high-altitude scattering layer to exist.

Figure XXII-4 shows model terminator reflectivities for several values of the homogeneous lower atmosphere parameters, τ and $\bar{\omega}_0$, and varying values of the scattering

τ	τ_L	$\bar{\omega}_0$	h	ALT	Z
1.0	0.005	0.1	3	60	22
1.0	0.010	0.2	5	60	22
1.0	0.005	0.1	5	60	22
1.0	0.005	0.1	5	90	52
0.027	0.005	0.1	5	50–80	50–80
1.0	0.005	0.2	5	75	37
1.0	0.005	0.1	5	80	42
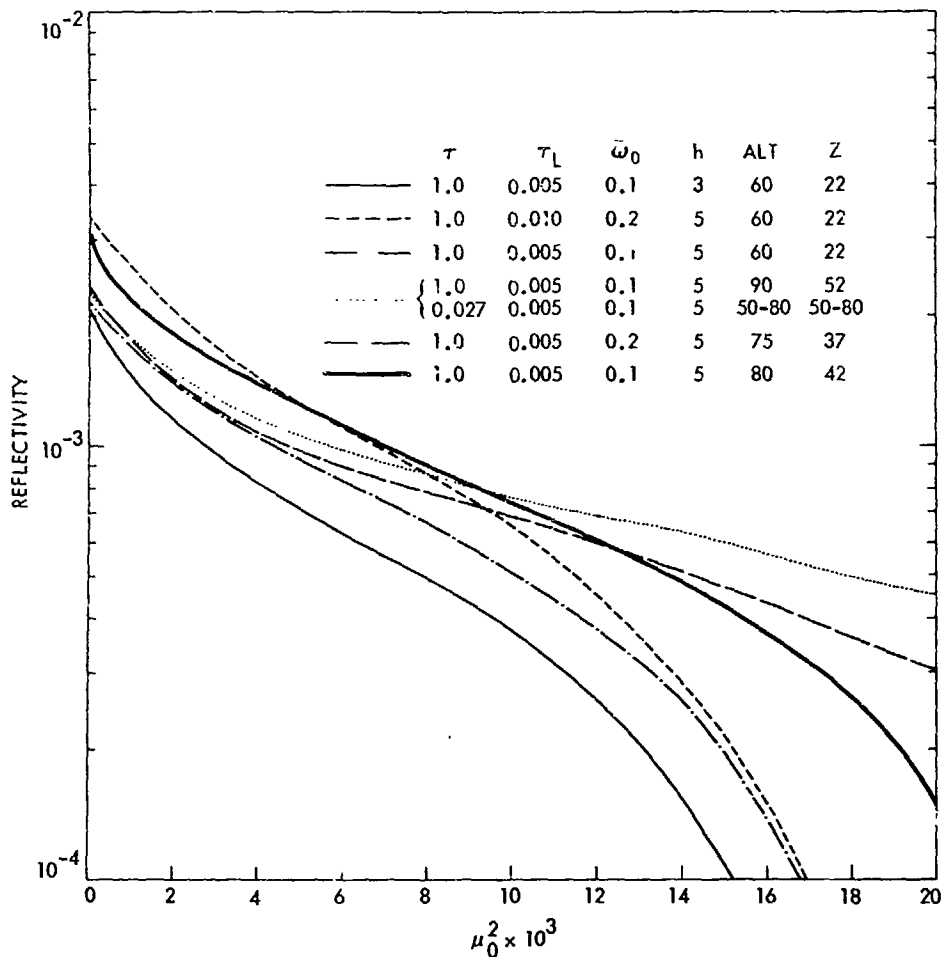
Fig. XXII-4. Model twilight reflectivity for a scattering layer above a homogeneous lower atmosphere. The altitude of the scattering layer above the surface of the planet is designated by ALT.

layer parameters, τ_L, h, and Z. A scale height of 10 km is assumed for all of the lower atmosphere models, and $p(\psi)$ is taken to be 1 for both the lower atmosphere and the scattering layer. For the scattering layer, $\bar{\omega}_0 = 1$.

The scattering layer model is of the right shape and magnitude to reproduce the terminator data, if $\tau_L \approx 0.005$. For $\tau_L > 0.02$, the apparent scale height of the predicted reflectivity is too small, i.e., the falloff of the predicted intensity with μ_0^2 is too steep. This is because most of the direct radiation is scattered out of the incident solar beam before reaching a large value of μ_0^2. On the other hand, if $\tau_L < 0.002$, the predicted signal from the layer is too small to reproduce the measured data. Values of the scattering layer optical thickness, τ_L, tend to be upper limits, as effects of multiple scattering and refraction both tend to increase the brightness beyond the termina-

tor and cause the apparent scale height to be larger than predicted by the simple model used here.

If the scattering layer is placed too low, $Z < 20$ km, then atmospheric extinction reduces the predicted intensity below the observations for large solar depression angles, i.e., large values of μ_0^2. Mariner 9 television pictures (Ref. XXII-10) of Mars obtained during the dust storm also place the scattering layer at about 20 km above slant optical depth one. Thus, the Mariner 9 ultraviolet spectrometer data of the terminator during the dust storm is consistent with these results with $Z = 20$ km, $\tau_L = 0.005$, $\tau = 1$, $h = 5$ km, and $\bar{\omega}_0 = 0.1$. The vanishing of the scattering layer over the north polar cap, which is shown in the Mariner 9 television pictures (Ref. XXII-11), is also evident in the ultraviolet spectrometer observations.

Since the tangent extinction optical path, τM, is greater than one, it is not possible to place the absolute altitude of the scattering layer on the basis of these data alone. A coordinated *Mariner 9* experiment using combined data from the radio occultation experiment (Ref. XXII-12), the television experiment (Ref XXII-10), and the ultraviolet spectrometer experiment place the altitude of the scattering layer at 70 km. The procedure was to use the altitude of maximum ionospheric electron density as an absolute altitude reference. This altitude was determined accurately by the radio occultation experiment and was also seen by the ultraviolet spectrometer as the region of maximum ionospheric ultraviolet emission. Since the ultraviolet spectrometer was boresighted with the *Mariner* television cameras, an absolute altitude could be assigned to the limb haze or scattering layer seen in a limb television picture. By fixing the scattering layer at an altitude of 70 km, a quantitative estimate of the extinction optical depth of the atmosphere can be made. The optical depths and revolution number are listed in Table XXII-1.

Table XXII-1. Vertical extinction optical depth of the Martian atmosphere as a function of revolution, assuming constant scattering layer altitude

Revolution	τ
34	2.0
60	1.5
72	0.5
120	0.2
150	0.1
166	0.1

B. Data

A summary of results for the period from November 13, 1971, to February 12, 1972, is given here. It is convenient to express the time of observation in terms of the spacecraft orbit or revolution number. *Mariner 9* orbited Mars twice each day, and the results reported here are from the even revolutions when nearly all of the twilight data were obtained. Data from revolution 2 were obtained on November 13, 1971, and data from revolution 182 on February 12, 1972. The latitudes and longitudes of the terminator observations as a function of revolution are indicated in Fig. XXII-5. Ninety percent of the afternoon terminator crossings have $\psi = 98° \pm 2°$, and μ is generally 0.85 ± 0.15.

At the terminator, the reflectivity is controlled by the effective single scattering albedo, $\tilde{\omega}_o$. During the dust storm, the slant optical path, τM, was much greater than unity and even in the later revolutions up to 216, $\tau M \gtrsim 1.5$. Under these conditions where τM is large and 3050-A radiation does not reach the surface, Equation (1) may be solved for the single scattering albedo, giving

$$\tilde{\omega}_o = \frac{4\mu MR}{p(\psi)} \qquad (3)$$

In Figs. XXII-6 and XXII-7, $\tilde{\omega}_o$ is plotted as a function of revolution and latitude assuming a Rayleigh phase function. The effective albedo increased slowly until about revolution 130, when the observations passed into the polar hood region and there was a large increase in signal. The change is associated with either a waning of the dust storm in time or/and a latitudinal effect indicating clearer air in the north. The effective albedo is physically meaningful only for a homogeneous atmosphere.

Figures XXII-8 through XXII-17 show detailed modeling of individual terminator crossings. The individual twilight observations subdivide into distinctive time periods on the basis of brightness at the terminator and apparent scale height.

Measurements made from November 15, 1971, to December 15, 1971, revolutions 6 to 64, are very similar in shape and intensity. These terminator crossings occurred during the height of the dust storm at latitudes of $-20°$ and $+10°$. The shape of the reflectivity curve as a function of μ_o^2 indicates the predominant part of the signal is due to scattering from an optically thin haze of scattering optical depth 0.005 at an altitude of 60 to 90 km above the surface. The effect of the dust storm is apparent for $\mu_o^2 > 0.01$ as the lower atmosphere begins to occult the scattering layer. The effect is diminution in the amount of solar flux reaching the scattering layer and a corresponding decrease in the reflected signal. This effect depends on the scale height of the absorbing species in the atmosphere and indicates dust was uniformly mixed with the molecular atmosphere, since the measured scale height is 9 ± 1 km. Assuming a homogeneous atmosphere, the effective single scattering albedo at the terminator is 0.2. About half of the reflectivity may be ascribed to the scattering layer. For large μ_o^2, $\mu_o^2 > 0.10$, all the signal may be attributed to the scattering layer.
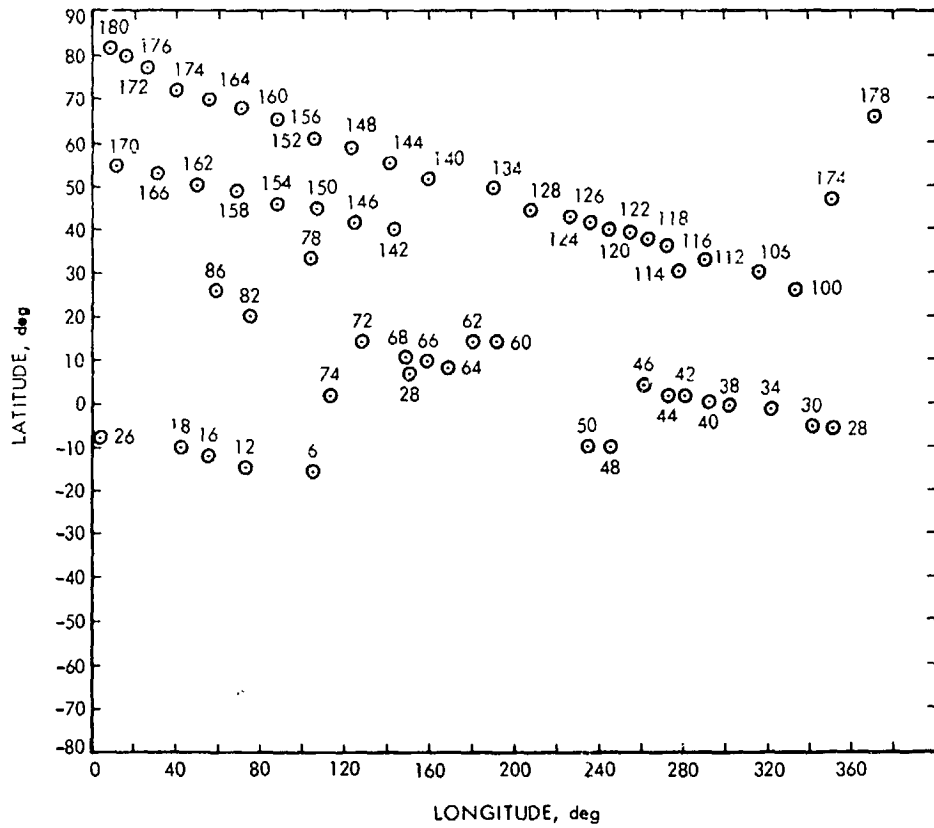
Fig. XXII-5. Latitudes and longitudes of afternoon terminator observations.
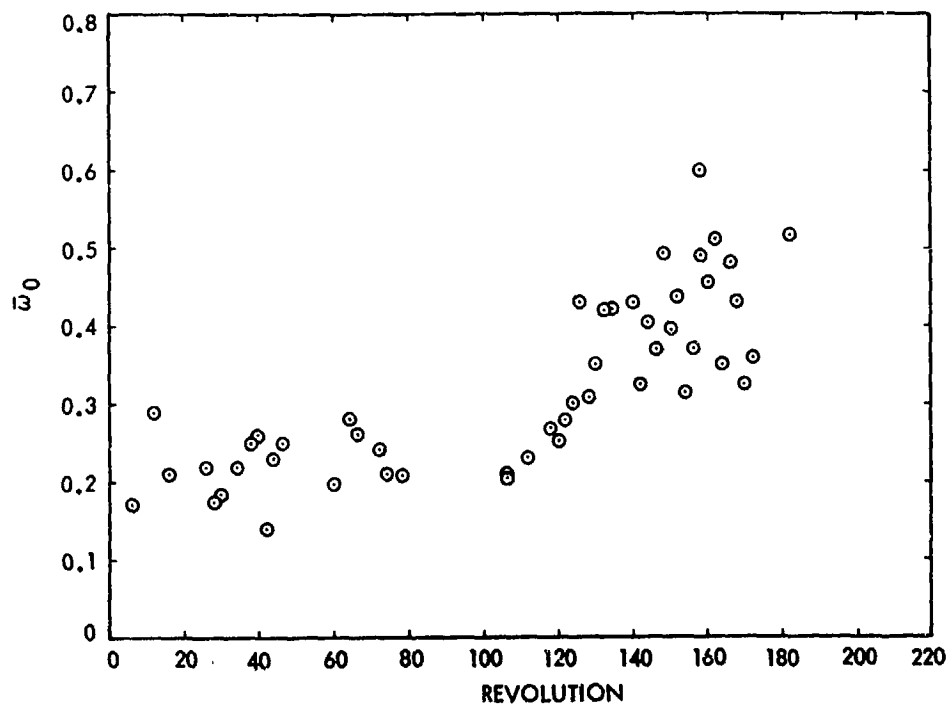
Fig. XXII-6. Effective single scattering albedo, $\bar{\omega}_0$, as a function of orbital revolution. Revolution 2 corresponds in time to November 13, 1971; revolution 182 corresponds to February 12, 1972.
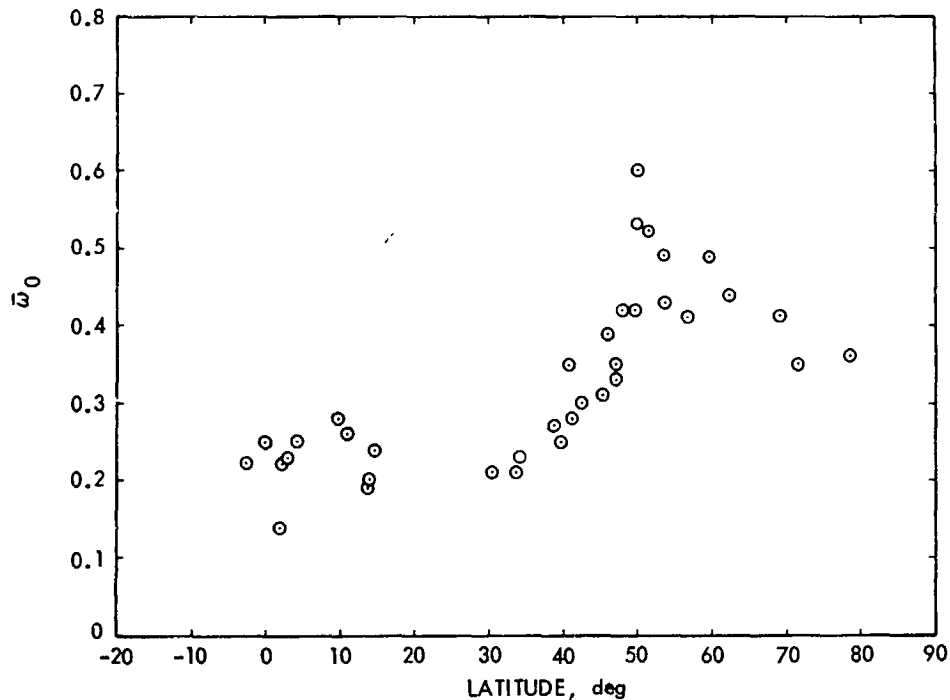
Fig. XXII-7. Effective single scattering albedo, $\bar{\omega}_0$, as a function of latitude.
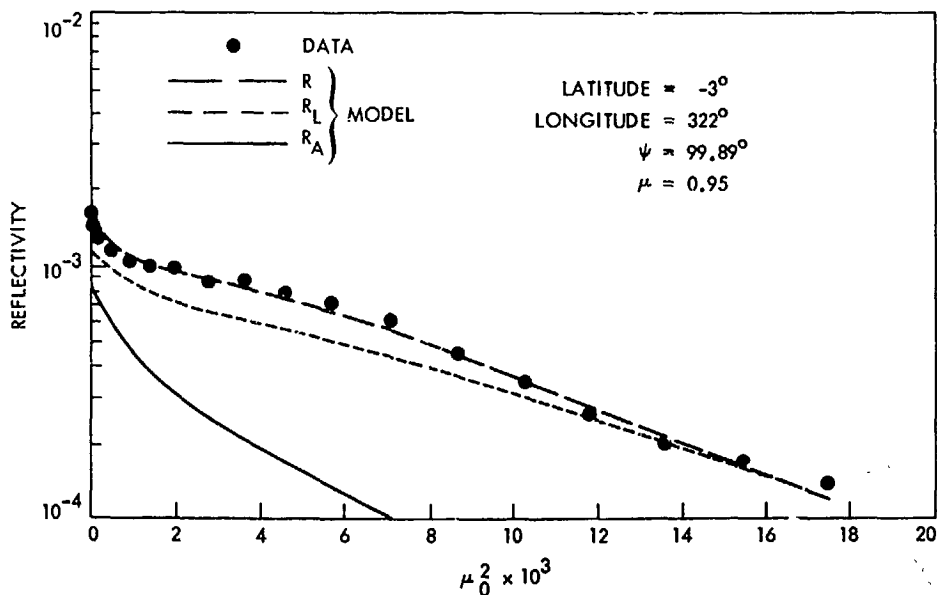
Fig. XXII-8. Terminator observation on revolution 34 with the following model: $\tau_L = 0.005$, $\bar{\omega}_0 = 0.08$, $h = 3.5$ km, $H = 9.5$ km, $Z = 20$ km. The lower atmosphere component is indicated by R_A; the scattering layer contribution is indicated by R_L. Combining these two components gives the composite model R. The effect of the lower atmosphere upon the scattering layer signal by absorption has been considered. Effectively, the illumination of the scattering layer at large solar depression angles is reduced by lower atmosphere absorption. The reduction in illumination of the lower atmosphere by the scattering layer is negligible. A reduction in the illumination of the scattering layer by its own absorption is sizable for small solar depression angles and has been considered.

346
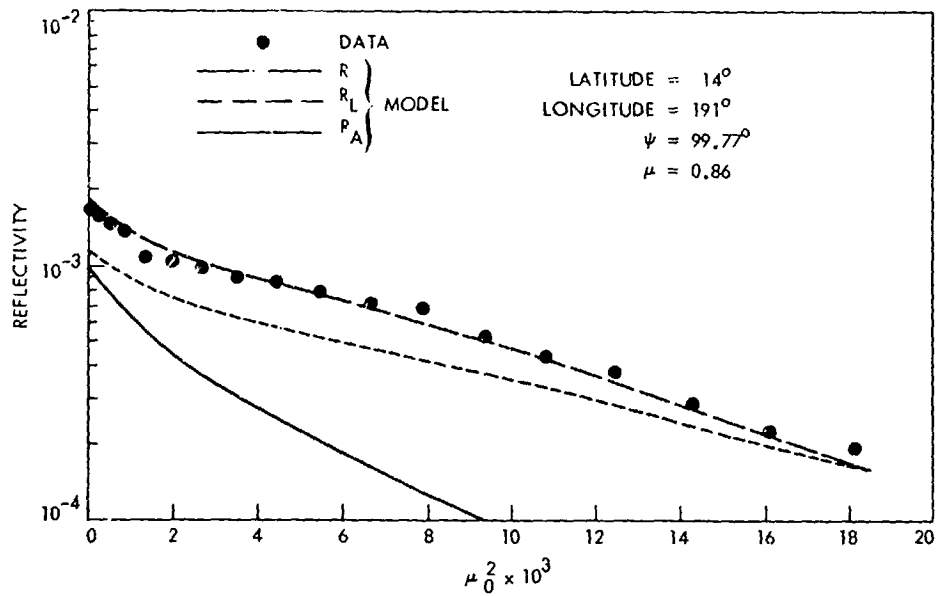
Fig. XXII-9. Terminator observation on revolution 60 with the following model:
$\tau_L = 0.005$, $\tilde{\omega}_0 = 0.08$, $h = 3$ km, $H = 10$ km, $Z = 25$ km.
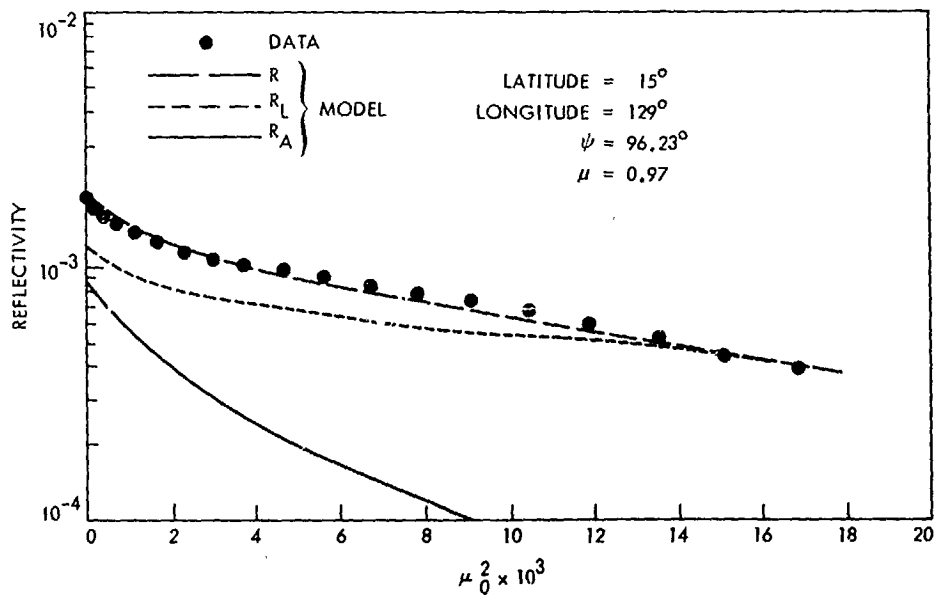
Fig. XXII-10. Terminator observation on revolution 72 with the following model:
$\tau_L = 0.005$, $\tilde{\omega}_0 = 0.08$, $h = 3$ km, $H = 10$ km, $Z = 39$ km.
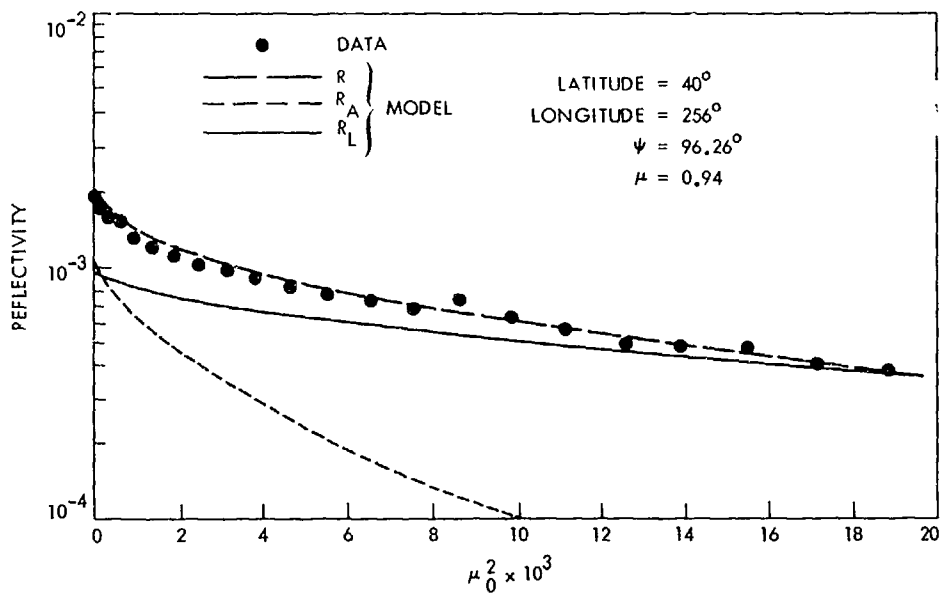
Fig. XXII-11. Terminator observation on revolution 120 with the following model: $\tau_L = 0.004$, $\bar{\omega}_0 = 0.09$, $h = 4$ km, $H = 10$ km, $Z = 48$ km.
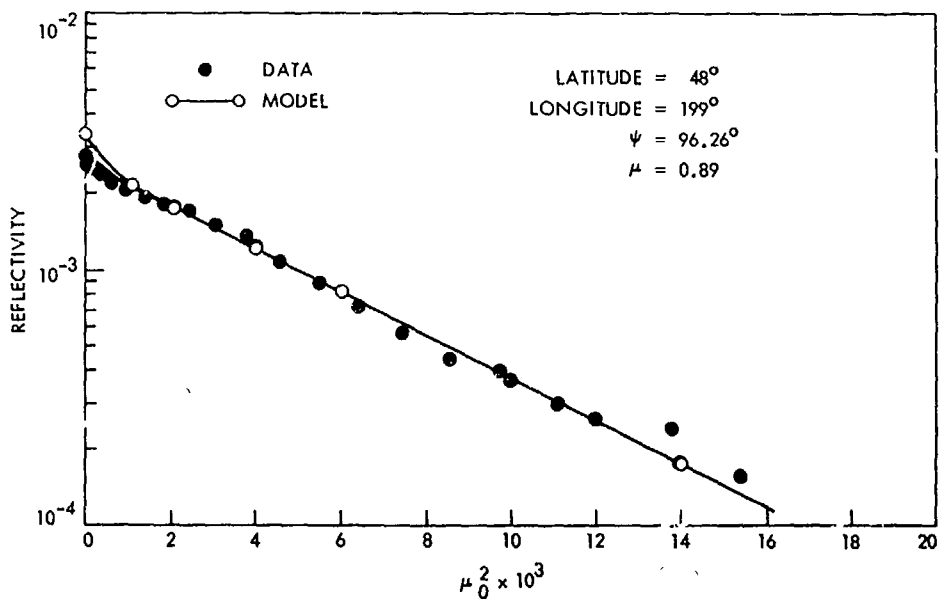
Fig. XXII-12. Terminator observation on revolution 132 with the following models: (I) $\tau = 0.027$, $\bar{\omega}_0 = 0.73$, $H = 9$ km; (II) $\tau \geq 0.1$, $\bar{\omega}_0 = 0.42$, $H = 10$ km. The two models nearly coincide except for $\mu_0^2 < 10^{-4}$.
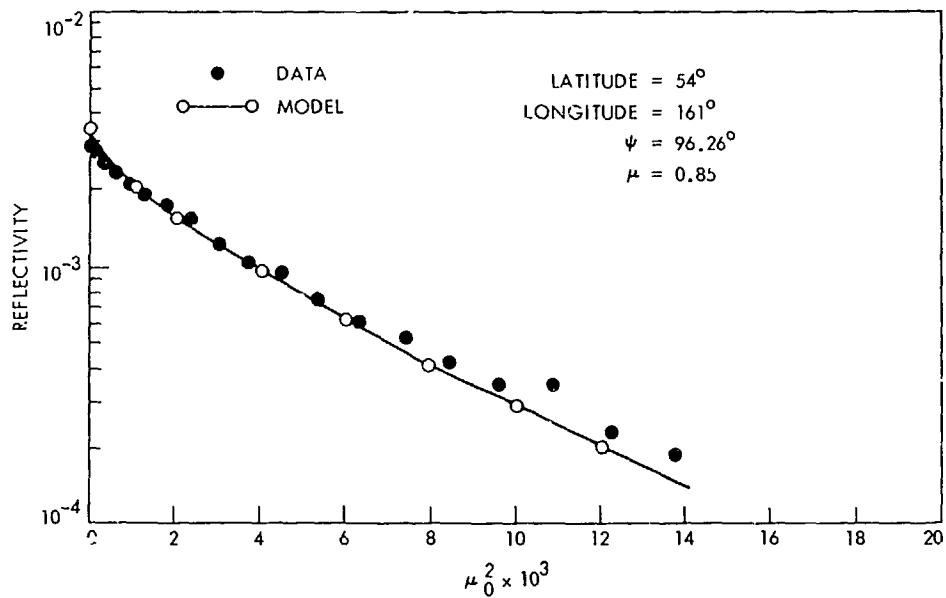
Fig. XXII-13. Terminator observation on revolution 140 with the following models: (I) $\tau = 0.027$, $\bar{\omega}_0 = 0.74$, $H = 8.5$ km; (II) $\tau \geq 0.1$, $\bar{\omega}_0 = 0.43$, $H = 9.0$ km. The two models nearly coincide.
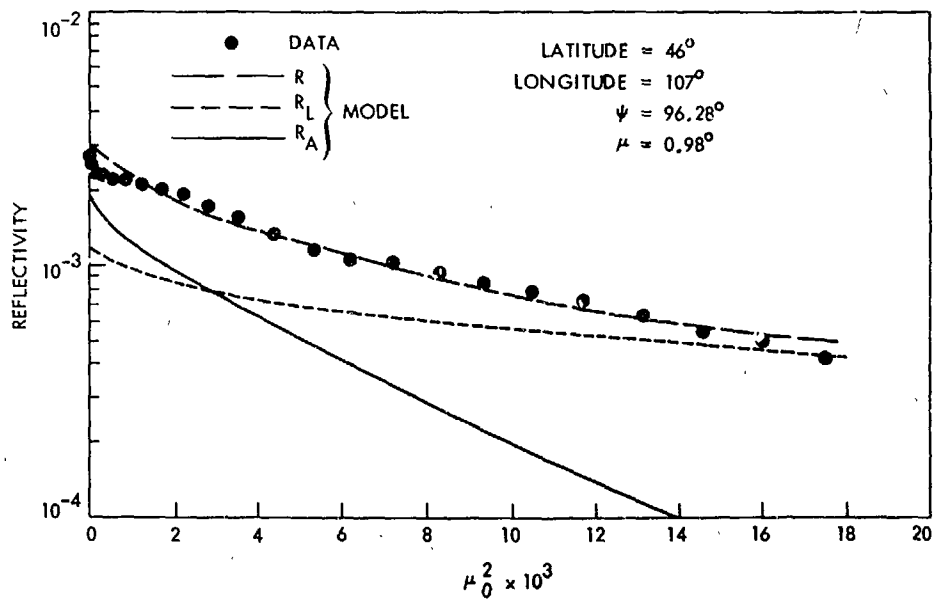
Fig. XXII-14. Terminator observation on revolution 150 with the following model: $\tau_L = 0.005$, $\bar{\omega}_0 = 0.2$, $h = 4.5$ km, $H = 10$ km, $Z = 55$ km.
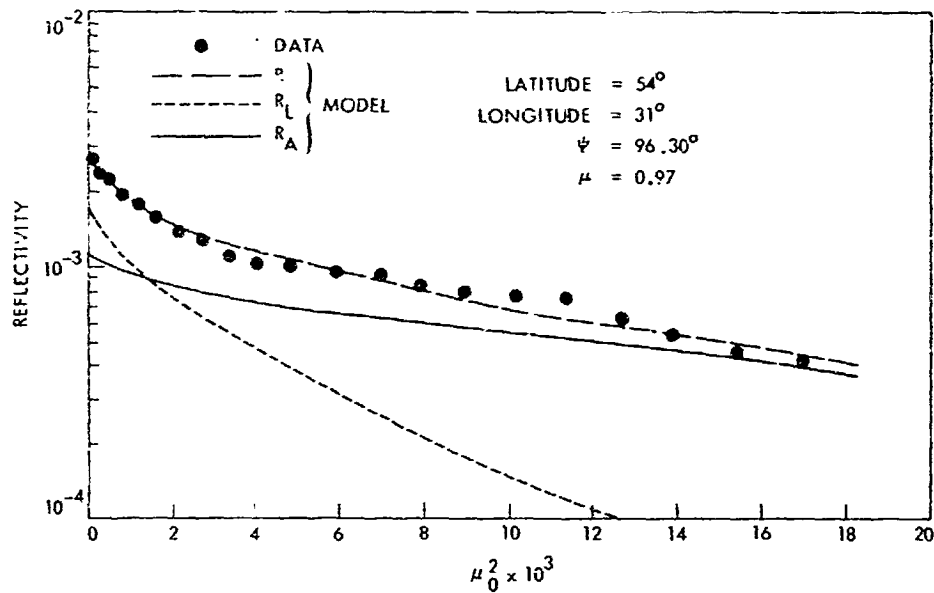
Fig. XXII-15. Terminator observation on revolution 166 with the following model:
$\tau_L = 0.005$, $\bar{\omega}_0 = 0.16$, $h = 4$ km, $H = 1$ km, $Z = 55$ km.
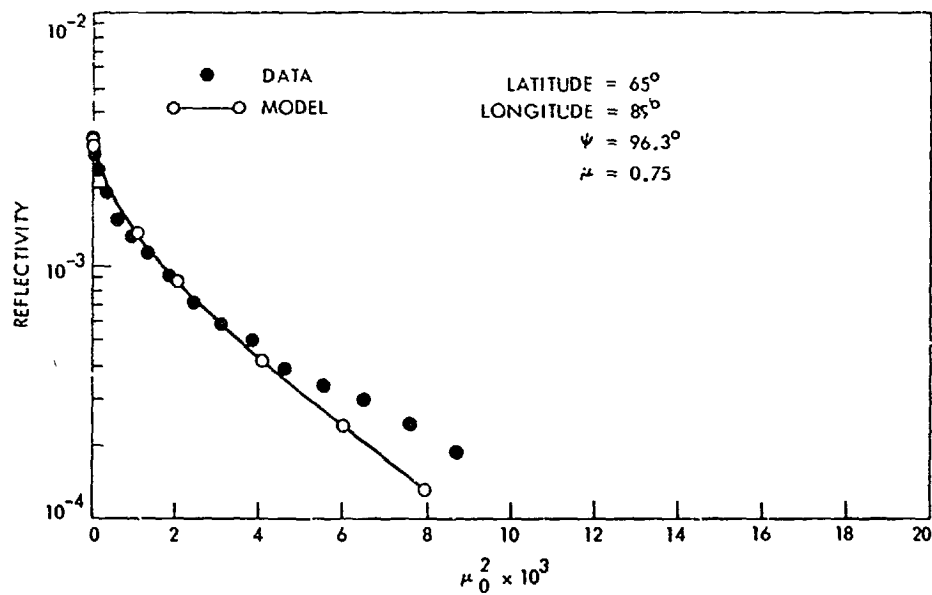
Fig. XXII-16. Terminator observation on revolution 156 with the following model:
$\tau \geq 0.1$, $\bar{\omega}_0 = 0.4$, $H = 6$ km.
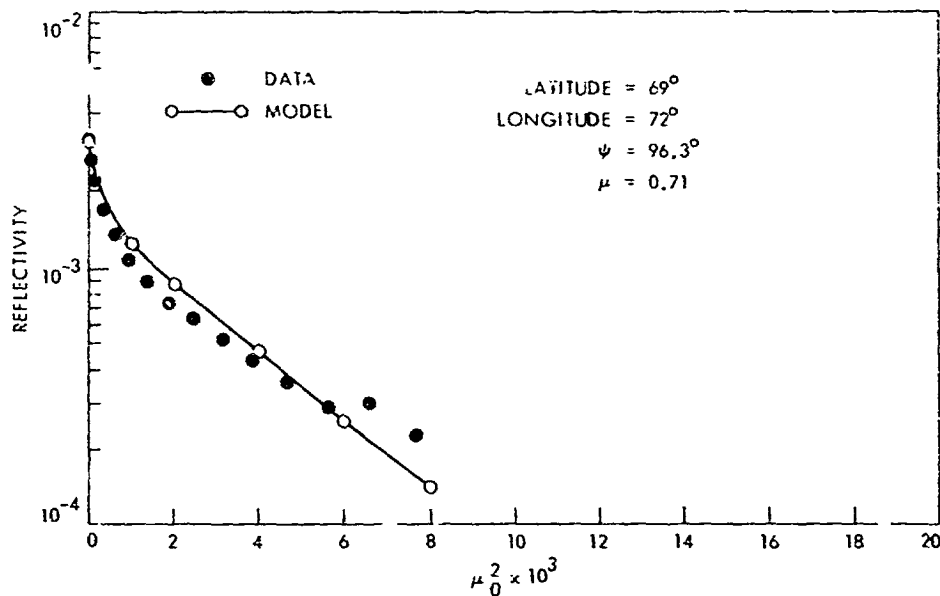
Fig. XXII-17. Terminator observation on revolution 160 with the following model:
$\tau \gtrsim 0.1$, $\bar{\omega}_o = 0.35$, $H = 6$ km.

Two typical terminator observations are shown in Figs. XXII-8 and XXII-9, which are revolutions 34 and 60, respectively. Revolution 34 data indicate a value of 0.08 for $\bar{\omega}$. The layer is about 20 km above the level where the slant optical depth is 1.

Data obtained for revolutions 66 to 126 covered the time period from December 16, 1971, to January 15, 1972. These terminator observations occur in the $10°N$ to $40°N$ region. For values of $\mu_o^2 > 0.01$, the apparent scale height is very large, $H \approx 20$ km. The interpretation of this result is that the dust storm is diminishing in intensity, and the total vertical absorption optical depth is decreasing. The absorption of the solar radiation by the lower atmosphere is minimal up to the largest depression angles observed by Mariner 9. Thus, the scattering from the layer is essentially independent of the homogeneous atmosphere. Two typical terminator observations during this period are during revolutions 72 and 120. They are shown in Figs. XII-10 and XXII-11. Note the apparent scale height of the signal for large μ^2 has increased from the previous period.

Data obtained for revolutions 128 to 146 covered the time period from January 16 to January 25, 1972. For these revolutions, the point of terminator crossing is at the edge of the north polar hood. This region serves as a transition zone. The dust storm is subsiding, and the intensity of the scattering from the layer is less. The edge

of the haze is in the $50° \pm5°$ region. For these revolutions, the point of terminator crossing was moving northward and the measured scale heights were 9 ± 1 km.

The albedo for single scattering has increased to a value of about 0.4. Plotted in Figs. XXII-12 and XXII-13 are data from revolutions 132 and 140. Two possible homogeneous atmosphere model fits to the data are presented. The shape of the terminator observation is independent of extinction optical depth for $\tau > 0.1$.

Data from revolutions 148 to 182 were obtained for the time period from January 2 to February 12, 1972. Figures XXII-14 and XXII-15, revolutions 150 and 166, respectively, were terminator observations south of $50°N$ and indicate the continued presence of a scattering layer. They also indicate a clearer atmosphere, as is denoted by the increasing value of $\bar{\omega}_o$. Figures XXII-16 and XXII-17 show two observations, taken north of the polar hood, of the twilight during this time period. Observations during this period can be modeled with a homogeneous atmosphere having a 6- to 8-km scale height, an albedo for single scattering in the limits of $0.3 < \bar{\omega}_o < 0.5$, and an extinction optical depth in the limits $0.05 < \tau < 0.15$. From the shape of the reflectivity-vs-μ_o^2 curve for the terminator observations northward of $55°N$, there is no indication of the presence of a scattering layer.

C. Summary

It is possible to model the ultraviolet terminator observations of *Mariner 9* either with a homogeneous atmosphere or with a scattering layer in addition to a homogeneous atmosphere. The characteristic shape of the twilight intensity variation is dependent on the latitude of observation. Observations north of 55°N require a homogeneous model. Twilight measurements south of 55°N indicate that a scattering layer may be a general Martian occurrence, at least in the evening. The day-to-day surveillance of the Martian terminator during the first 216 *Mariner 9* revolutions indicates haze formation in the evening, and its continued presence until early morning is a daily occurrence in mid-latitudes up to 50°N.

The formation of hazes, scattering layers, or condensate clouds in the Martian atmosphere is not a new concept. Some of these layers have been variously identified as the blue clouds or violet haze (Refs. XXII-13 through XXII-19). Detached haze layers at the terminator were observed by the *Mariner 9* television cameras (Ref. XXII-10).

Clouds of water crystals or carbon dioxide ice are the probable scatterers that explain the large apparent scale height in Martian twilight at 3050 A.

During the dust storm, the profiles of reflectivity as a function of μ^2 indicated a vertical extinction opacity of 1 to 2, a single scattering albedo of about 0.05, and a scale height of 9 ±1 km. By revolution 130, January 17, 1972, the atmosphere showed marked clearing either because of a waning of the dust storm or because of a clearer atmosphere at northern latitudes. By revolution 150, February 10, 1972, the albedo for single scattering had values between 0.3 and 0.5, indicating the continued presence of absorbing dust in the atmosphere. The vertical extinction optical depth at that time was 0.1 ±0.05, which is about three times the clear atmosphere value.

References

XXII-1. Barth, C. A., Stewart, A. I., Hord, C. W., and Lane, A. L., "Mariner 9 Ultraviolet Spectrometer Experiment: Mars Airglow and Variations in Lyman Alpha," *Icarus*, Vol. 17, p. 457, 1972.

XXII-2. Barth, C. A., Hord, C. W., Stewart, A. I., and Lane, A. L., "Mariner 9 Ultraviolet Spectrometer Experiment: Initial Results," *Science*, Vol. 175, p. 309, 1972.

XXII-3. Hord, C. W., Barth, C. A., and Pearce, J. B., "Ultraviolet Spectrometer Experiment for Mariner Mars 1971," *Icarus*, Vol. 12, p. 63, 1970.

XXII-4. Hord, C. W., Barth, C. A., Stewart, A. I., and Lane, A. L., "Mariner 9 Ultraviolet Spectrometer Experiment: Photometry and Topography of Mars" *Icarus*, Vol. 17, p. 443, 1972.

XXII-5. Lane, A. L., Barth, C. A., Hord, C. W., and Stewart, A. I., "Mariner 9 Ultraviolet Spectrometer Experiment: Observations of Ozone on Mars," *Icarus*, Vol. 18, p. 102, 1973.

XXII-6. Stewart, A. I., Barth, C. A., Hord, C. W., and Lane, A. L., "Mariner 9 Ultraviolet Spectrometer Experiment: Structure of Mars Upper Atmosphere," *Icarus*, Vol. 17, p. 469, 1972.

XXII-7. Rozenburg, G. V., *Twilight*, Plenum Press, New York, 1966.

XXII-8. Volz, F. E., and Goody, R. M., "The Intensity of the Twilight and Upper Atmospheric Dust," *J. Atmos. Sci.*, Vol. 19, p. 385, 1962.

References (contd)

XXII-9. Hunten, D. M., "A Study of Sodium in Twilight. I. Theory," *J. Atm. Terr. Phys.*, Vol. 5, p. 44, 1954.

XXII-10. Masursky, H., Batson, R., McCauley, J. F., Soderblom, L. A., Wildey, R. L., Carr, M. H., Milton, D. J., Wilhelms, D. E., Smith, B. A., Kirby, T. B., Robinson, J. C., Leovy, C. B., Briggs, G. A., Young, A. T., Duxbury, T. C., Acton, C. H., Murray, B. C., Cutts, J. A., Sharp, R. P., Smith, S. A., Leighton, R. B., Sagan, C., Veverka, J., Noland, M., Lederberg, J., Levinthal E., Pollack, J. B., Moore, J., Hart, ..., W., Shipley, E., de Vaucouleurs, G., and Davies, M., "Mariner 9 Television Reconnaissance of Mars and Its Satellites: Preliminary Results," *Science*, Vol. 175, p. 294, 1972.

XXII-11. Leovy, C. B., Briggs, G. A., Young, A. T., Smith, B. A., Pollack, J. B., Shipley, E. N., and Wildey, R. L., "The Martian Atmosphere: Mariner 9 Television Experiment Progress Report," *Icarus*, Vol. 17, p. 373, 1972.

XXII-12. Kliore, A. J., Cain, D. L., Fjeldbo, G., Seidel, B. L., Sykes, M. J., and Rasool, S. I., "Atmosphere and Topography of Mars From Mariner 9 Radio Occultation Measurements," *Icarus*, Vol. 17 p. 484, 1972.

XXII-13. Capen, C. F., *The Mars 1964–1965 Apparition*, Technical Report 32-990, Jet Propulsion Laboratory, Pasadena, Calif., 1966.

XXII-14. Dollfus, A., *Planets and Satellites, Vol. III of The Solar System*, edited by G. P. Kuiper and B. M. Middlehurst, University of Chicago Press, Chicago, Illinois, Chapters 9 and 15, 1961.

XXII-15. Gifford, F., "A Study of Martian Yellow Clouds That Display Movement," *Mon. Weather Rev.*, Vol. 92, p. 435, 1964.

XXII-16. Humason, M. L., "Photographs of the Planets with the 200-Inch Telescope," Chapter 16 in *Planets and Satellites, Vol. III of The Solar System*, edited by G. P. Kuiper and B. M. Middlehurst, University of Chicago Press, Chicago, Illinois, 1961.

XXII-17. Öpik, E. J., "The Atmosphere and Haze of Mars," *J. Geophys. Res.*, Vol. 65, p. 3057, 1960.

XXII-18. Pollack, J. B., and Sagan, C., *An Analysis of Martian Photometry and Polarimetry*, Smithsonian Inst. Astrophys. Obs., Spec. Rep. 258, Washington, D. C., 1967.

XXII-19. Slipher, E. C., "An Outstanding Atmospheric Phenomena of Mars," *Pub. Astron. Soc. Pacific*, Vol. 49, p. 137, 1937.

Acknowledgments

XXIII. *Mariner 9* Ultraviolet Spectrometer Experiment: Mars Atomic Oxygen 1304-Å Emission

D. J. Strickland, A. I. Stewart, C. A. Barth, and C. W. Hord

Department of Astro-Geophysics and Laboratory for Atmospheric and Space Physics
University of Colorado, Boulder, Colorado 80302

A. L. Lane

Jet Propulsion Laboratory/California Institute of Technology, Pasadena, California 91103

The *Mariner 9* OI 1304-Å data provide the opportunity to study temporal and geographical variations in the distribution of atomic oxygen O in the Martian thermosphere (Refs. XXIII-1 and XXIII-2). Previously deduced values of the O concentration can also be refined (Refs. XXIII-3 through XXIII-6). Atomic oxygen has been known to be a minor constituent in the Martian lower thermosphere since interpretation of the *Mariner 4* dual-frequency S-band occultation data (see, e.g., Refs. XXIII-7 and XXIII-8). This inference has inspired considerable research efforts aimed at explaining why the Martian thermosphere is largely undissociated (Refs. XXIII-9 and XXIII-10). At present there is no generally accepted theory to explain the stability of the CO_2-dominated atmosphere. Strong vertical mixing by small-scale turbulence or so-called eddy mixing has been invoked in most recent efforts. On the other hand, global transport of O from the dayside to the nightside has been suggested by Dickinson (Ref. XXIII-11; also see Ref. XXIII-12) as a mechanism for removing O and CO and maintaining relatively high CO_2 concentrations on the dayside for Venus and Mars. One key to the significance of global transport is the geographical distribution and local time variations in O. A goal of this work will be to provide information of this nature.

In this section, selected 1304-Å data are presented and analyzed for both the bright limb and disk of Mars. They were recorded in first order by the short wavelength (G) channel of the ultraviolet spectrometer. The data considered are from even-numbered orbits 6 through 98, between November 17 and December 31, 1971. More than 30 useful limb profiles are available for the time interval considered, and disk data are available for nearly all even passes.

Strickland et al. (Ref. XXIII-6; hereafter referred to as STS) concluded that resonance scattering of the solar 1304-Å flux is responsible for most of the 1304-Å intensity from Mars. The intensity is then a function primarily of: (1) the O density ([O]) specified at some reference altitude, (2) the thermospheric temperature profile, and (3) the solar 1304-Å fluxes at line center. The emergent 1304-Å flux is rather insensitive to the densities of O in the lower thermosphere and, hence, to the altitude of the turbopause. These parameters vary in their degree of importance to the intensity from limb to disk. Limb intensities contain useful information both in their shape and overall magnitude. The shape depends on (1) and (2), either of which can be determined from the shape alone if the other parameter is given. For a given value of [O]

and temperature profile, the magnitude of the intensity is directly proportional to (3), the solar 1304-Å fluxes. The disk intensity is much less sensitive to (1) and (2) and, similar to the limb intensity, is directly proportional to (3). It is, thus, less feasible to estimate either the absolute O concentration or temperature information from disk data, especially in the absence of precise knowledge of the solar 1304-Å fluxes. However, important information on relative variations in |O| can be obtained from disk data without precise information on (3), provided the solar fluxes are constant with time during the collection of data considered.

Before presenting the results of the *Mariner 9* 1304-Å data analysis, atmospheric modeling and sources of excitation considered in the theory are discussed. This is followed by an analysis of limb and disk data. The last part summarizes the results obtained from the first 100 passes. Geometrical parameters used are discussed in the Appendix to this section.

A. Model Atmospheres

Density profiles for O and CO_2 and their corresponding temperature profiles are given in Fig. XXIII-1, in which diffusive equilibrium is assumed at all altitudes. The temperature profiles are adapted from those calculated by Stewart (Ref. XXIII-13). At 135 km, the CO_2 column density is about 4×10^{16} cm⁻², appropriate for the F1
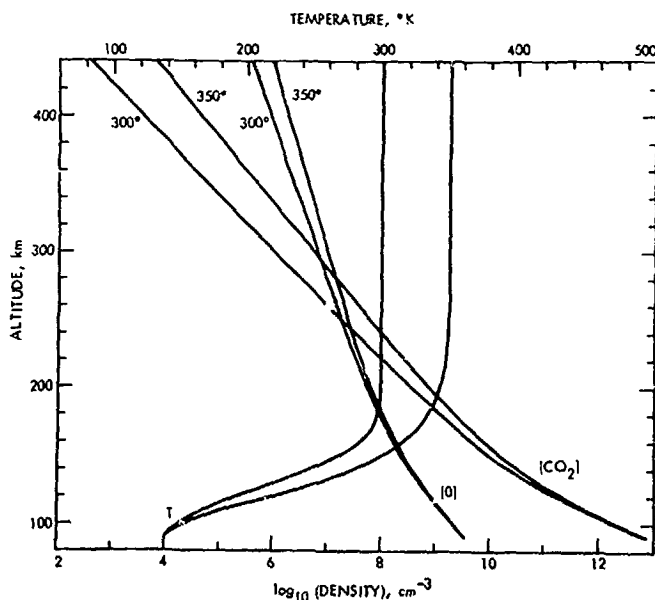
Fig. XXIII-1. Model atmospheres with exospheric temperatures of 300° and 350°K for Mars. The O density is about 1% in each model at the altitude (about 135 km) where the CO_2 column density is 4×10^{16} cm⁻².

ionospheric peak situated near this altitude. The O density for the models shown is about 1% of the total density at 135 km. The concentration of O will be referenced as a percentage at 135 km, the convention used by Thomas (Ref. XXIII-4). One calculation was performed in which the atomic oxygen assumed the scale height of CO_2 below a hypothetical turbopause at 150 km.

B. Theory

The assumptions made and techniques used to calculate the theoretical intensities are described by STS in their analysis of *Mariner 6* and *7* data. The geometrical information given in the Appendix is also used. Sources of excitation incorporated into the theory are: (1) the solar 1304-Å fluxes and (2) photoelectron impact on O (*e* on O). Relative strengths and widths of the solar lines are given by STS. The excitation rate for *e* on O is parameterized in terms of a *g*-value defined by

$$S_O^{ir}(z,\mu_o) = [O]_z \, g[N(z,\mu_o)]$$

where $S_O^{ir}(z,\mu_o)$ is the volume production rate (excitations-cm⁻³-sec⁻¹) at altitude z and at the solar zenith angle (SZA) given by its cosine, μ_o, and N is the total slant column density. The shape of g is given in STS and comes from unpublished theoretical work by A. I. Stewart. Two values of $g(N = 0)$ have been considered. One value, taken from STS, is 3.6×10^{-5} at 1 AU, and the other value is four times larger. The smaller value was derived by STS from Earth dayglow data and is consistent with the calculated *e* on O cross section of Rountree and Henry (Ref. XXIII-14). The larger value is consistent with the revised measured *e* on O cross section of Zipf and Stone (personal communication). The original cross section is given by Zipf and Stone in Ref. XXIII-15. As will become clear, the uncertainty in the true value of g does not seriously affect the conclusions drawn in this analysis. This is because our preferred values of the O density are such that *e* on O is not an important excitation mechanism. For details of the theory, the reader is referred to STS.

C. Limb Data and Analysis

Figure XXIII-2 shows 1304-Å limb data for selected passes. The altitude scale refers to the point of closest approach or tangent point for the line of sight. Each of the three profiles shown was obtained by averaging data for the given passes. Pertinent geometrical information is given in Table XXIII-1. Each data value used in the averaging was obtained by subtracting a constant noise
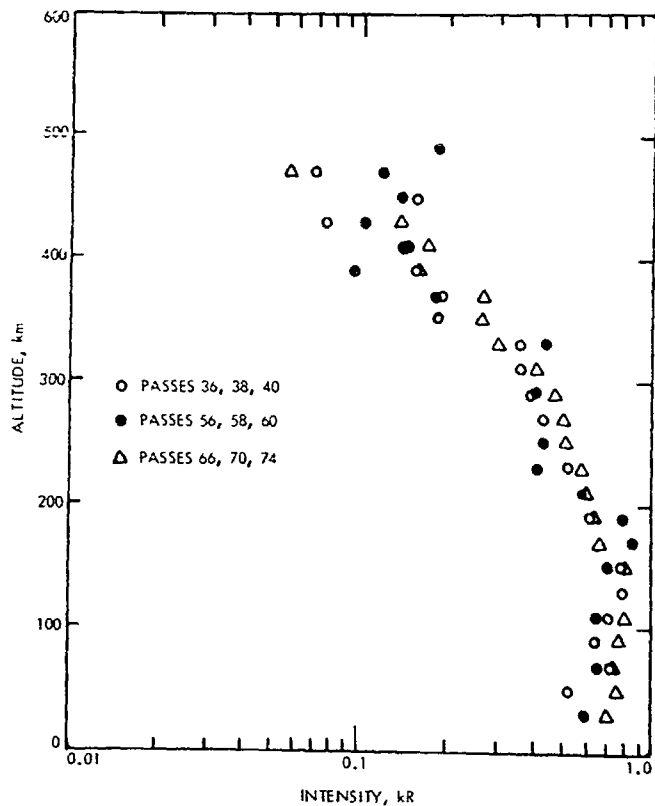
Fig. XXIII-2. *Mariner 9* limb data. Each set was obtained by averaging data for the passes indicated.

Table XXIII-1. Geometrical information associated with the limb data in Fig. XXIII-2

Passes	500 km		100 km		
	SZA	Local time	SZA	Local time	Latitude
36–40	36°	10:00 A.M.	34°	10:10 A.M.	−45°
56–60	36°	10:00 A.M.	34°	10:10 A.M.	−45°
66–74	31°	10:00 A.M.	16°	11:10 A.M.	− 5°

background and fitting a triangular function by a least-squares method to the 1304-Å feature for five successive spectra. The assumption of normal statistics is implied in this method of estimating the intensity, i.e., the assumption that, for a given incident intensity, the statistical distribution in the instrumental response is symmetric (and Gaussian) about its mean. Some statistical bias or asymmetry was, however, observed by STS in the *Mariner* 6 and 7 instruments at low signal levels. We make the reasonable assumption that a similar statistical bias exists in the *Mariner* 9 instrument, since all three are of the same type. This effect is discussed.

Figure XXIII-3 provides a comparison between the *Mariner* 7 and *Mariner* 9 limb data. The *Mariner* 7 profile was obtained by averaging the data from the two *Mariner* 7 limb crossings. Each data value was obtained by the same least-squares method described above, with one spectrum rather than five spectra considered. The estimates of the intensity from the same raw data by STS are based on a more detailed statistical treatment. The *Mariner* 9 profile was obtained by averaging the profiles in Fig. XXIII-2. The *Mariner* 9 data are 20 to 30% greater below 250 km. The calculations of STS show that an increase in the O density of more than an order of magnitude would be required to explain this. It is more likely that the increase arises from changes in the solar 1304-Å fluxes, or from differences in the calibration of the two instruments at 1304 Å. Part of the disagreement may also be statistical in origin.

A comparison of the overall shapes of the two sets of data suggests that the exospheric temperature at the time of the *Mariner* 9 observations was, if anything, less than the 350°K deduced from the *Mariner* 6 and 7 observations (Refs. XXIII-13 and XXIII-16). Lower temperatures
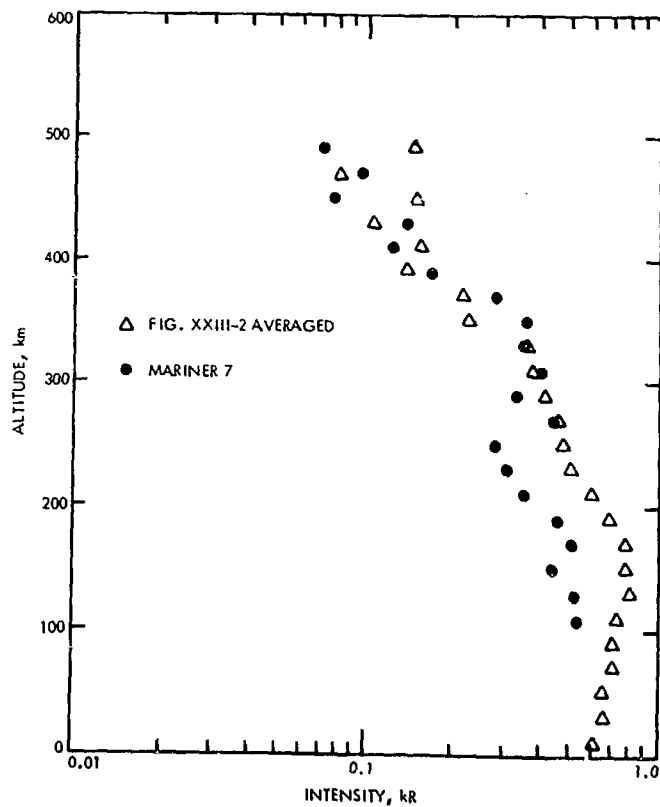
Fig. XXIII-3. *Mariner 7* and *9* limb data. *Mariner 7* data were obtained by averaging the data from both of its limb crossings. The *Mariner 9* data are the average of the data in Fig. XXIII-2.

averaging 325°K are also indicated by *Mariner 9* UVS measurements of the scale height of the CO Cameron bands (Ref. XXIII-17). Calculations presented here are for models with exospheric temperatures of 300°K and 350°K.

To interpret the limb data, theoretical intensities have been fitted to the data by a least-squares technique. The intensity is

$$4\pi I(T_x, p, h) = 4\pi I_{pe}(T_r, p, h) + c4\pi I_s(T_r, p, h)$$

where pe and s refer to the e on O and solar 1304-Å sources. The arguments are: T_r, the exospheric temperature assumed in the model atmosphere; p, the percent of O at 135 km in the model; and h, the altitude at the limb tangent point. The parameter c is the same one appearing in STS and scales the solar 1304-Å fluxes. It is determined by the fit and equals unity for the values observed by Hall and Hinteregger (Ref. XXIII-18). The magnitude of $4\pi I_{pe}$ is determined by the choice of $g_{pe}(X)$ and the arguments indicated. The magnitude of g is not varied in the fitting procedure and equals 3.6×10^{-8} at 1 AU except where otherwise noted. The quantity minimized is:

$$\sum_{nk} w_{nk} \{d_{nk} - 4\pi I_s(T_r, p)\}^2$$

The index n spans the number of passes considered, k specifies the altitude for pass n, and w_{nk} is the weighting factor and has been chosen to vary inversely with the measured intensity, d_{nk}. Values of d_{nk} near zero are removed to avoid unwanted weighting.

An example of a fit for 300°K to the data for passes 66, 70, and 74 is shown in Fig. XXIII-4. The p-value yielding this fit is 0.56%. An important feature of this figure is the difference exhibited below 200 km between the data and the multiple scattering solution. The discrepancy strongly suggests that we are observing a component of the 1304-Å intensity from dissociative excitation of CO_2. Such a source should produce a significant fraction of its photons beyond the Doppler core of the resonance line profile, and for that fraction, the resultant intensity will exhibit the characteristics of an optically thin emission. The expected profile for such an emission is included in Fig. XXIII-4. When this profile with a peak intensity of 0.2 kR is added to the multiple scattered solution, the fit is modified, as indicated by the broken line below 200 km and results in an excellent overall fit.
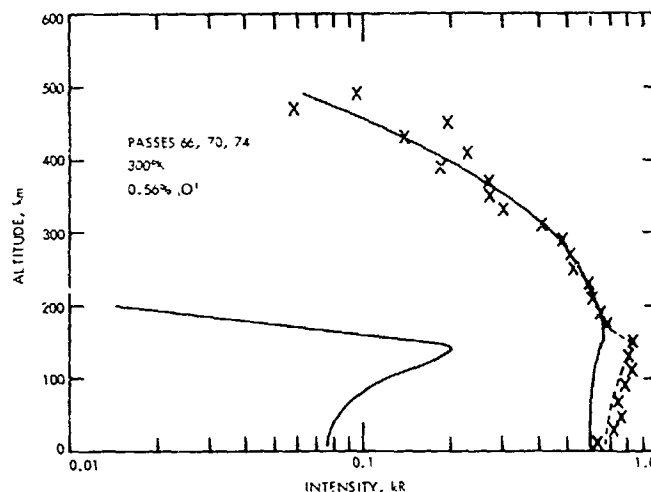
Fig. XXIII-4. Example of a best fit to the data between 200 and 500 km for passes 66, 70, and 74. The chosen exospheric temperature is 300°K. The lower profile has the shape of the limb intensity predicted for dissociative excitation of CO, assuming no multiple scattering. The dashed portion of the fit is obtained by adding the dissociative excitation component to the multiple scattered component.

The possibility of a measurable contribution by dissociative excitation to the 1304-Å limb intensity was considered by STS, but no firm conclusions were drawn due to insufficient data from *Mariners* 6 and 7. The available evidence on dissociative processes in CO_2 does not preclude a limb intensity of 200 R arising from these sources. Using the electron impact cross sections of Ajello (Ref. XXIII-19) and of Mumma et al. (Ref. XXIII-20), we calculate limb intensities in the optically thin case of up to 70 R from photoelectron impact:

$$CO_2(X^1\Sigma) + e \rightarrow CO + O(^3S).$$
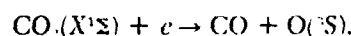
Transmission studies (Ref. XXIII-21) suggest that this intensity would be reduced 20 to 30% by resonance scattering. The limb intensity for the spin-forbidden photodissociative process,

$$CO_2(X^1\Sigma) + h\nu \rightarrow CO(X^1\Sigma) + O(^3S)$$
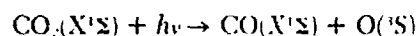
is negligible, based on the cross section measurements of Gentieu and Mentall (Ref. XXIII-22). No measurements are available for the spin-allowed process,

$$CO_2(X^1\Sigma) + h\nu \rightarrow CO(a^3\Pi) + O(^3S)$$
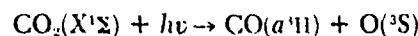
but it would produce ~100 R on the limb if the cross section were ~10^{-20} cm² in the range 150 to 350 Å.

Photons in this wavelength range should produce a broader line than the electron impact mechanism, reducing still farther the effects of resonance scattering.

Estimates of p and c for the data in Fig. XXIII-2 are shown in Fig. XXIII-5. The fitting procedure described above was used and, based on the results in Fig. XXIII-4,

data were not considered below 200 km. The lower part of the figure gives the root mean square (RMS) error (in kiloRayleighs) versus p for 300° and 350°K. This is

$$RMS = \sum_{nk} w_{nk}(d_{nk} - 4\pi I_{nk}^{\prime} - c4\pi I_{nk}^{\prime})^2 \bigg/ \sum_{nk} w_{nk}$$

The upper part of the figure gives the value of c at each p yielding the best fit. At 350°K, the best estimate of p is less than 0.2%. If the statistical bias in the response characteristics of the Mariner 9 instrument is similar to that of the Mariner 7 instrument, the least-squares estimate of p should be increased. The analysis by STS, which included the effects of this statistical bias, gave a p-value of between 0.5 and 1% for the Mariner 7 limb data. The least-squares treatment of the same data gives smaller p-values. The quantitative differences between the two methods are shown in Fig. XXIII-6. The two sets of closed contours are from STS, and the value assigned to each contour is the likelihood of the set (p, c) outside that contour. Each set of contours has the form of a ridge. The two additional lines in the figure are the tops of the ridges formed by similar sets of closed contours obtained by the least-squares method. The arrows indicate the RMS

Fig. XXIII-5. Results of least-squares fitting theoretical limb intensities to the three averaged data profiles in Fig. XXIII-2. The root mean square (RMS) error indicates the quality of fit and c is the least-squares parameter scaling the theoretical intensity $4\pi I_c$. The RMS error and c are plotted against p, the percent [O] at 135 km.
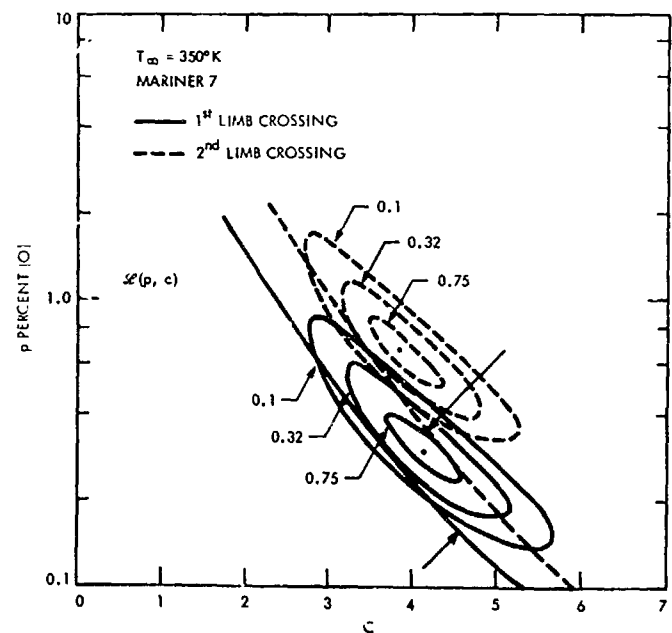
Fig. XXIII-6. Sets of contours for the likelihood function $\mathcal{L}$ from STS and lines denoting the tops of ridges for similar sets of contours obtained by least-squares methods. The arrows mark the points for which best least-squares fits are achieved and are to be compared with the dots specifying the maximum values of $\mathcal{L}$.

minimum. The displacement of the lines from the contours shows the degree to which the least-squares estimates of c are too large. Thus, if the statistical bias is similar for *Mariner* 9, the estimates of p in Fig. XXIII-5 should be increased perhaps as much as a factor of 2, and the c values decreased by as much as 20%. With this in mind, the best p values at 300°K from Fig. XXIII-5 become about 0.5 to 1%.

There is a sufficient quantity of *Mariner* 9 1304-Å limb data to study possible variations in the O distribution with time. As an initial effort in this study, RMS profiles have been obtained for 1304-Å limb data from several individual passes. The results are shown in Fig. XXIII-7. The exospheric temperature 300°K is assumed for all fits, and, as before, altitudes below 200 km are excluded. Data for 16 revolutions numbered between 26 and 78 are considered. For the given temperature, most passes yield estimates of near 0.5 to 1%, allowing for some statistical bias. There are, however, some p estimates significantly smaller and larger. Pass 78 yields a very small value, and passes 30 and 44 yield large values. The differences in the profiles between pass 78 and, for example, pass 30 are further illustrated by considering the data for their limb profiles in Fig. XXIII-8. At 500 km, the SZA's at the tangent point are 35° and 46° for passes 30 and 78, respectively. At 100 km, the SZA's are 34° and 33°. Geometrical effects are not responsible for the degree of difference observed. Either the noise characteristics of the instrument have altered, or significant differences existed in the O distributions on these passes. If the data indicate the true trend in the limb intensity, they lead to some interesting implications regarding time variations in loss processes for O. Variations in the exospheric temperature are not expected to be large enough to have much effect on the data. The topside plasma scale heights for passes 30 and 78 by Kliore et al. (Ref. XXIII-24) are not significantly different from other values between these passes. The scale heights, however, were recorded at different geographical locations than the ultraviolet data. We leave to a future analysis a more detailed study of the data in Fig. XXIII-8 and other such data showing peculiar characteristics.

Fig. XXIII-7. RMS profiles versus p, the percent [O] at 135 km, for an exospheric temperature of 300°K. The results for 16 passes are shown between passes 26 and 78. Data were considered between 200 and 500 km.
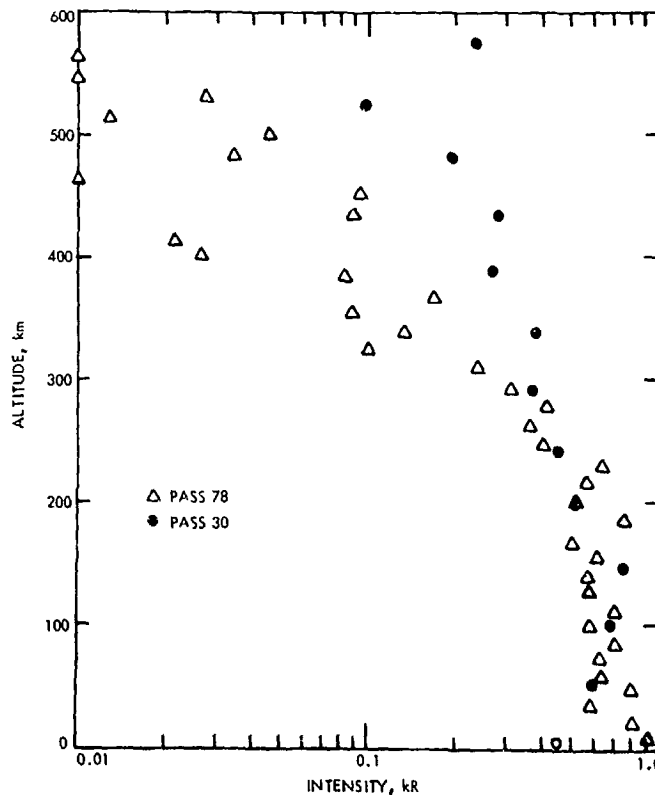
Fig. XXIII-8. Limb data from passes 30 and 78. These data show the largest variations observed between limb profiles in the first 100 passes.

The magnitude of the g-value has been held fixed for the RMS results presented in this section. For the assumed value, best fits to the data are obtained for $p \sim 0.5$ to 1%. The theoretical intensity at such p-values is dominated by resonantly scattered solar 1304-Å photons. If the g-value were increased by a factor of 4 (see previous part of this section), the RMS results below 1% do not change significantly. Above 1%, however, a second minimum occurs in the region of 5% with an RMS value comparable to the minimum value near 0.5%. Figure XXIII-9 shows a best fit for the region above 1% to the data from passes 66, 70, and 74 based on the larger g-value. The p-value is 5.6%, and the resulting c-value is 0.95, giving solar 1304-Å fluxes comparable to those measured by Hall and Hinteregger (Ref. XXIII-18). The dominant source under these conditions is excitation of O by photoelectrons. Without invoking the additional CO_2 dissociative excitation source, the overall fit between 0 and 500 km in Fig. XXIII-9 is superior to the fit in Fig. XXIII-4.

There are reasons for preferring the results in Fig. XXIII-9: the assumed g-value is consistent with Zipf and Stone's revised e on O cross section; the solar fluxes are consistent with the values measured by Hall and Hinteregger (Ref. XXIII-18); and an O concentration of 5% leads to less severe requirements on loss rates for O than does 0.5%. However, if the CO_2 dissociative source is included, the fit in Fig. XXIII-4 is substantially better than the fit in Fig. XXIII-9. Also, although the interpretation of the Mariner 9 data is ambiguous if the larger
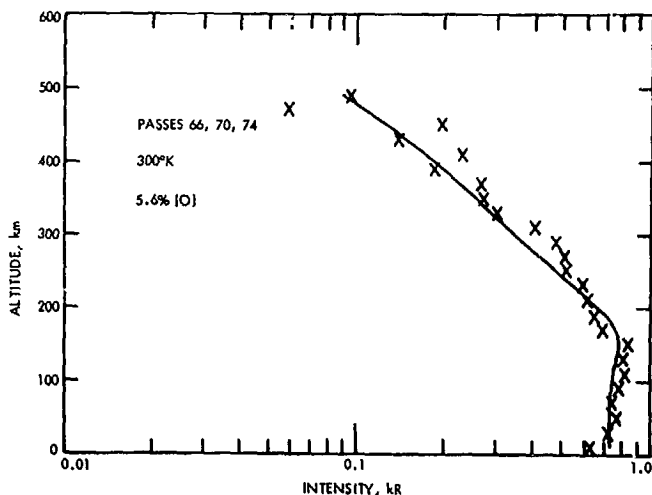
Fig. XXIII-9. Example of a fit to the data between 0 and 500 km for passes 66, 70, and 74 with the e on O g-value four times larger than assumed for the results in Fig. XXIII-4. The assumed exospheric temperature is 300°, and the fit was obtained for 5.6% [O].

g-value for e on O is in fact appropriate, there are good reasons for preferring the smaller value. These reasons derive from the analysis by STS of observations of the terrestrial 1304-Å airglow using a Mariner-type instrument.

Neither the above conclusions, nor those to follow, are significantly affected by possible departures of the O distribution from diffusive equilibrium. We have compared intensities for a 1% [O] distribution in diffusive equilibrium with one that is identical above 150 km, but that assumes the scale height of $[CO_2]$ below this altitude. The latter distribution would be appropriate for a 150-km turbopause level. Limb intensities are within 1% of each other above 250 km. Below this altitude, the maximum difference is $\sim 5\%$ for the solar 1304-Å component and about 15% for the smaller photoelectron component. These small changes illustrate the fact that in an optically thick medium, changes in the distribution of the resonance scatter near the lower boundary have a small effect on emergent intensities.

D. Disk Data and Analysis

A significant accomplishment of the ultraviolet spectrometer experiment is the ability to observe individual features against a bright disk background. Figure XXIII-10 shows examples of 1304-Å disk data together with the geometrical parameters describing the line of sight (see Appendix) and selected theoretical intensities. Each data value was obtained by fitting a triangular function to the sum of five successive spectra over the spectral range of the 1304-Å feature. (The same method was used on the data reported in the previous section.) The geometrical information applies to each of the selected passes, 30, 36, and 46 and to a similar 80 min for all alternate passes between 24 and 60 with the exceptions of 42, 48, and 50. The parameter μ_0 is the cosine of the SZA ϕ; μ is the cosine of α; and ψ is the cone angle (see Fig. XXIII-16). The theoretical intensity is based on an atmospheric model with an exospheric temperature of 300° and containing 1% [O]. The e on O g-value is 3.6×10^{-8} at 1 AU and the c-value is ~ 4 for the solar 1304-Å fluxes. The overall shape of the theoretical profile is not sensitive to the assumed model.

Figure XXIII-11 shows the variation in latitude and longitude corresponding to the data in Fig. XXIII-10 for pass 30. Except for a shift along the longitude axis, passes 36 and 46 have similar plots. The longitude at the subsolar point is indicated in the figure at about 70° longitude. The
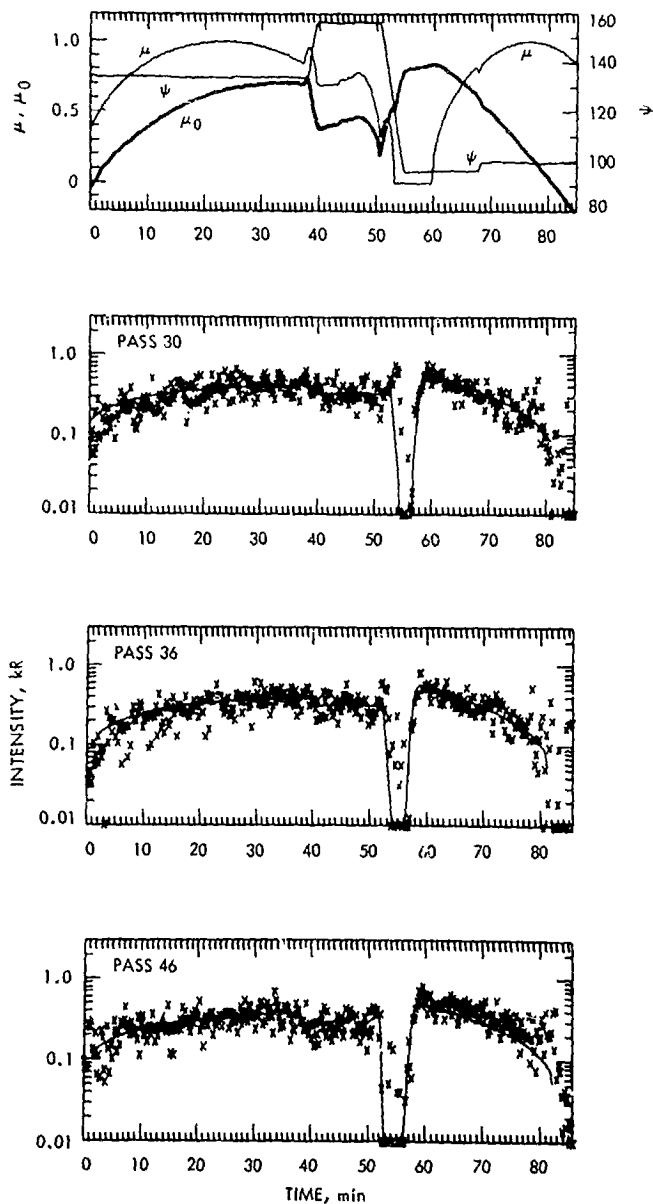
Fig. XXIII-10. Disk and limb data, theory and geometrical parameters vs time for passes 30, 36, and 46. The theoretical intensity is based on a model atmosphere having an exospheric temperature of 300° and 1% [O]. The parameter u_0 is the cosine of the SZA ϕ, μ is the cosine of α, and ψ is the cone angle (see Fig. XXIII-A-2).

Fig. XXIII-11. The variation in latitude and longitude for pass 30 corresponding to the data in Fig. XXIII-10. The subsolar point is indicated and occurs near latitude 20°S and longitude 70°. The morning side is to the left of the subsolar point.

tangentially through the atmosphere. Upon its return to the bright disk, its motion was sufficiently slow to obtain useful limb data between 55 and 60 min. Examples of limb data for the given viewing conditions were already presented in Fig. XXIII-2. The disk data past 65 min were obtained from the afternoon side and reach the background noise level just past 80 min, where the evening terminator is crossed.

A diurnal effect is exhibited in Fig. XXIII-10 based on a comparison between the data and theory. The O concentration or temperature or both increase with local time from the morning to the evening terminator. The theoretical intensities in the figure have been fitted to the mid-morning data. The afternoon data, then, tend to be above the theory, most noticeably for pass 46. To attribute the above differences to local time effects alone may be an oversimplification. Latitudinal effects, however, are not obvious from considerations of Fig. XXIII-11. The data near 80 min on passes 30 and 46 suggest the possibility of a local enhancement in the 1304-Å intensity near the evening terminator. Such an enhancement would occur either from an enhanced O concentration during these passes or because of an anomalous localized source of excitation. At 80 min, the theory passes through the data for pass 30 and is about a factor of 2 too small for pass 46.

morning side of the plot occurs at longitudes greater than this value. The information in Fig. XXIII-11 is helpful to determine the locations and local times corresponding to the data in Fig. XXIII-10. Initially, the instrument is viewing the morning terminator near the equator. The line of sight then moves south and remains on the morning side for most of the first 65 min. At one point, about 50 min, the line of sight moves from the disk and passes

A factor of 2 variation in disk data requires an even greater variation in the O concentration. The relationship between density and disk intensity is further discussed below.

The disk and limb of Mars have been viewed under a variety of observing conditions. Quite different from the data variations in Fig. XXIII-10 are those for pass 74 shown in Fig. XXIII-12. About 50 min, between the values of 30 and 80, were spent viewing the atmosphere tangentially. During this time, two useful limb profiles were obtained. The rate of descent of the line of sight on the first crossing (near 40 min) was slow enough to achieve one of the best limb profiles during the mission. This profile was included in Fig. XXIII-2, averaged together with profiles from passes 66 and 70 having similar viewing conditions. Morning disk data in Fig. XXIII-12 were observed between 0 and 30 min and afternoon disk data after 75 min. The morning data appear to vary more strongly than the theory. The dominant source of variation in the theory is the variation in μ_0. The pattern in the data may suggest geographical variations in [O].

It is possible to study geographical and time dependent effects in [O] and the latter type of effect in the solar 1304-Å fluxes with the quantity of data available as exemplified in Figs. XXIII-10 and XXIII-12. Initial results of such a study are shown in Fig. XXIII-13. In the lower part of the figure, the 10.7-cm solar flux is plotted as recorded on Earth. The circles in the upper panel represent the difference, expressed as a ratio, between the morning data and a fixed theoretical model. Those in the

middle panel represent the difference for the afternoon data. The solid line in both panels is the average of the morning and afternoon differences. The model used has an O concentration of 1^{c} at 135 km and an exospheric temperature of 350°K. The results in Fig. XXIII-13 are not sensitive to the choice of model.
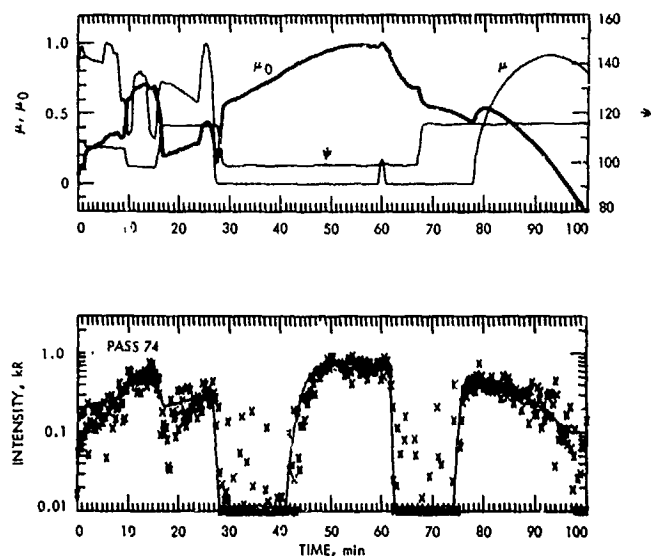
Fig. XXIII-12. Data, theory, and geometrical parameters for pass 74 similar to those in Fig. XXIII-10.
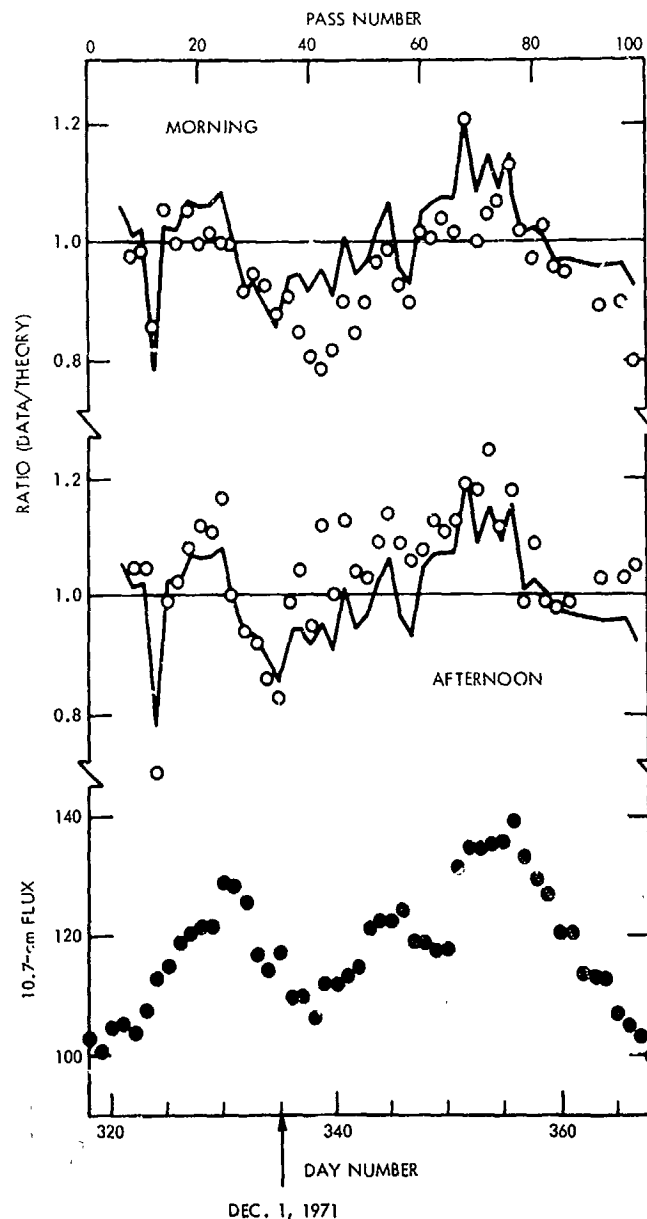
Fig. XXIII-13. The 10.7-cm solar flux as recorded o Earth and deviations in the disk data from theory based on a fixed model and fixed values of the excitation parameters. The solid curves are identical and were obtained by least-squares fitting the theory to both morning and afternoon disk data. The circles were obtained by fitting the theory to the morning and afternoon data separately.

If the solar 1304-Å fluxes were constant with time and the atmosphere did not vary with either time or location, no pattern should emerge for the types of plots shown in Fig. XXIII-13. There is, however, a clear pattern showing: (1) a correlation in the data with the 10.7-cm flux and (2) an enhancement in the afternoon data, already noted from Fig. XXIII-10. The first of these effects is most likely caused in large part by a variation in the solar 1304-Å fluxes with time. The solar III Lyman-α flux is known to vary with time and to correlate well with the 10.7-cm flux (Refs. XXIII-25 and XXIII-26). The relative variation required in the fluxes is comparable to the relative variation in the 10.7-cm flux. The supposed variation in the 1304-Å flux would be seen 3 days earlier on Mars than on Earth at the time the data in Fig. XXIII-13 were recorded because of the positions of the planets relative to the rotating Sun (Ref. XXIII-1). Since the 10.7-cm flux was recorded on Earth, a 3-day lag in the pattern of variation of this flux should be seen relative to the pattern exhibited by the mean ratio. There is an indication of such a lag.

If, on the other hand, the solar 1304-Å flux did not vary with time, nor did the exospheric temperature experience large temporal variations, then a factor of about 3 variation in the global concentration of O would be required to produce the observed pattern. The factor of 3 is based on results in Fig. XXIII-14, which show the predicted relationship between disk intensity and the O concentration for selected exospheric temperatures of 250° and 350°K. The mean density for an SZA of 49° is considered to illustrate the density dependence. The required variation in the O concentration seems less likely than the suggested variation in the solar 1304-Å flux, even though some variation must occur in the rate at which O is formed by photodissociation of CO_2.

Regarding the second effect noted above, the largest differences between morning and afternoon occur around pass 40. Fig. XXIII-14, together with the results in Fig. XXIII-13, suggests that as much as three times more O occurs on the average in the afternoon for selected passes. This value should be reduced a small amount since the atmosphere is probably warmer in the afternoon.

The scatter in the results has the appearance of noise (Fig. XXIII-13). The error bars are much smaller than this scatter since several thousand spectra are typically used to obtain a single point. This may imply that random, as well as systematic, variations are occurring in the mean O distribution, or it may merely reflect an imperfect
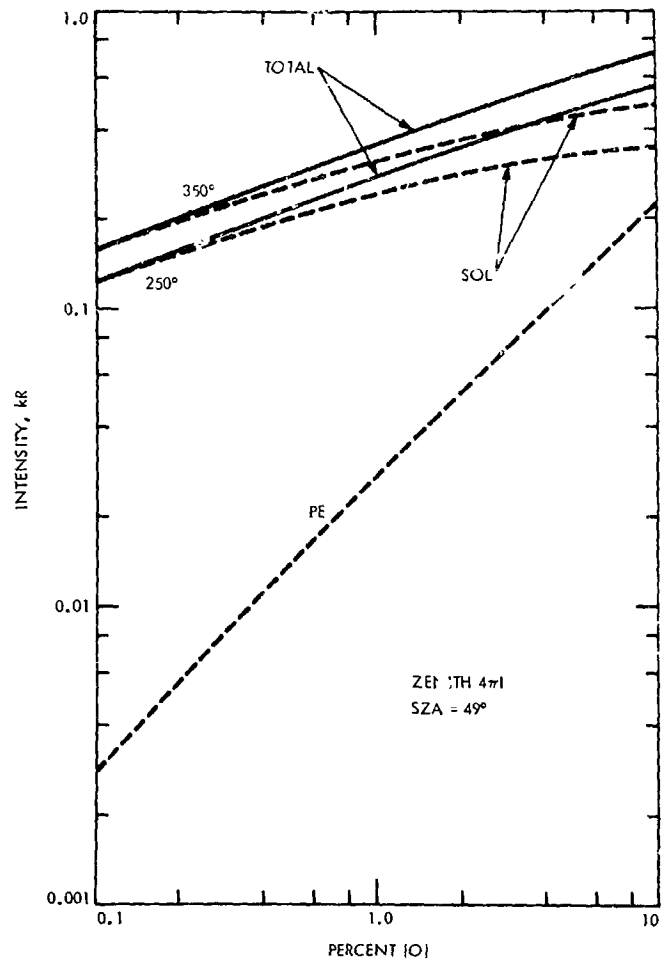
Fig. XXIII-14. Predicted variation of the 1304-Å disk intensity with p, the percent [O] at 135 km, and exospheric temperature. The zenith intensity for an SZA of 49° was chosen to show the variation.

correlation between the solar 1304-Å flux and the 10.7-cm flux.

E. Summary

Selected results have been presented for a considerable quantity of *Mariner 9* 1304-Å data for the first 100 revolutions from both the bright limb and disk of Mars. The limb data suggest that the exospheric temperature is less than it was in 1969 when *Mariners 6* and *7* encountered the planet. Similar |O| concentrations (0.5 to 1%) are derived for a temperature of about 300°K. Structure in the limb profiles below 200 km suggests the possibility that about 0.2 kR of the observed ~0.8 kR near 150 km is due to dissociative excitation of CO_2 (Fig. XXIII-4). The source is unimportant to the disk intensity. Some significant differences were observed in selected limb profiles (Fig. XXIII-7 and XXIII-8). If their source is not attributed

largely to instrumental effects, important variations with time occur in the [O] distribution. In view of the suggested variation with location in the previous section, a factor of 3 or more is not unexpected.

The analysis of the disk data shows: 1) a correlation between the disk intensities and 10.7-cm solar flux; and 2) an enhancement in the O density in the afternoon relative to the morning. The first of these effects is probably due largely to variations in the solar 1304-Å fluxes with time. Relative variations in the solar 1304-Å flux comparable to those observed in the 10.7-cm flux can account for the effect. Regarding the second point, enhancements by as much as a factor of 3 in the mean afternoon densities are indicated (Figs. XXIII-13 and XXIII-14). This much local time variation implies an effective residence lifetime for an O atom on the scale of 1 day or less. The removal mechanism is unlikely to be chemical (see, e.g., Ref. XXIII-16), but our present understanding of Martian dynamics does not enable us to distinguish between mechanisms involving vertical and horizontal transport.

Selected data suggest that local as well as random variations in [O] occur. A local enhancement in [O] near the evening terminator may be responsible for the structure in the data for pass 46 shown in Fig. XXIII-10. Random variations in [O] are suggested by the scatter shown in Fig. XXIII-13 which is considerably larger than the expected noise variation.

References

XXIII-1. Barth, C. A., Hord, C. W., Stewart, A. I., and Lane, A. L., "Mariner 9 Ultraviolet Spectrometer Experiment: Initial Results," *Science*, Vol. 175, p. 309, 1972.

XXIII-2. Barth, C. A., Stewart, A. I., Hord, C. W., and Lane, A. L., "Mariner 9 Ultraviolet Spectrometer Experiment: Mars Airglow Spectroscopy and Variations in Lyman Alpha," *Icarus*, Vol. 17, p. 457, 1972.

XXIII-3. Barth, C. A., Hord, C. W., Pearce, J. B., Kelly, K. K., Anderson, G. P., and Stewart, A. I., "Mariner 6 and 7 Ultraviolet Spectrometer Experiment: Upper Atmosphere Data," *J. Geophys. Res.*, Vol 76, p. 2213, 1971.

XXIII-4. Thomas, G. E., "Neutral Composition of the Upper Atmosphere of Mars as Determined From the Mariner UV Spectrometer Experiments," *J. Atmos. Sci.*, Vol. 28, p. 859, 1971.

XXIII-5. McElroy, M. B., and McConnell, J. C., "Dissociation of CO_2 in the Martian Atmosphere," *J. Atmos. Sci.*, Vol. 28, p. 880, 1971.

XXIII-6. Strickland, D. J., Thomas, G. E., and Sparks, P. R., "Mariner 6 and 7 Ultraviolet Spectrometer Experiment: Analysis of the O I 1304- and 1356-Å Emissions," *J. Geophys. Res.*, Vol. 77, p. 4052, 1972.

XXIII-7. Donahue, T. M., "Upper Atmosphere and Ionosphere of Mars," *Science*, Vol. 152, p. 763, 1966.

XXIII-8. McElroy, M. B., "The Upper Atmosphere of Mars," *Astrophys. J.*, Vol. 150, p. 1125, 1967.

XXIII-9. Shimizu, M., "The Recombination of CO and O in the Upper Atmospheres of Venus and Mars," *Icarus*, Vol. 9, p. 593, 1968.

XXIII-10. McElroy, M. B., and Hunten, D. M., "Photochemistry of CO_2 in the Atmosphere of Mars," *J. Geophys. Res.*, Vol. 75, p. 1188, 1970.

XXIII-11. Dickinson, R. W., "Circulation and Thermal Structure of the Venusian Thermosphere," J. Atmos. Sci., Vol. 28, p. 885, 1971.

XXIII-12. Dickinson, R. E., and Ridley, E. C., "Large-Scale Transport and the Composition of the Venusian Thermosphere, *J. Atmos. Sci.*, Vol. 29, p. 1577, 1972.

XXIII-13. Stewart, A. I., "Mariner 6 and 7 Ultraviolet Spectrometer Experiment: Implications of the CO_2^+, CO, and O Airglow," *J. Geophys. Res.*, Vol. 77, p. 54, 1972.

XXIII-14. Rountree, S. P., and Henry, R. J. W., "Electron-Impact Excitation Cross Sections for Atomic Oxygen: P — 3s S°," *Phys. Rev.*, Vol. A6, p. 2106, 1973

XXIII-15. Zipf, E. C., and Stone, E. J., "Photoelectron Excitation of Atomic Oxygen Resonance Radiation in the Terrestrial Airglow," *J. Geophys. Res.*, Vol. 76, p. 6865, 1971.

XXIII-16. Anderson, D. E., and Hord, C. W., "Mariner 6 and 7 Ultraviolet Spectrometer Experiment: Analysis of Hydrogen Lyman Alpha Data," *J. Geophys. Res.*, Vol. 75, p. 6666, 1971.

References (contd)

XXIII-17 Stewart, A. I., Barth, C. A., Hord, C. W., and Lane, A. L., "Mariner 9 Ultraviolet Spectrometer Experiment: Structure of Mars' Upper Atmosphere," *Icarus*, Vol. 17, p. 469, 1972.

XXIII-18. Hall, L. A. and Hinteregger, H. E., "Solar Radiation in the Extreme Ultraviolet and Its Variation With Solar Rotation," *J. Geophys. Res.*, Vol. 75 p. 695, 1970.

XXIII-19. Ajello, J. M., "Emission Cross Sections of CO by Electron Impact in the Interval 1260–4500 Å, II.," *J. Chem. Phys.*, Vol. 55, p. 3169, 1971.

XXIII-20. Mumma, M. J., Stone, E. J., Borst, W. L., and Zipf, E. O., Jr., "Dissociative Excitation of Vacuum Ultraviolet Emission Features by Electron Impact on Molecular Gases. III. CO_2," *J. Chem. Phys.*, Vol. 57, p. 68, 1971.

XXIII-21. Poland, H. M., and Lawrence, G. M., "Doppler Broadening of OI 1304 Å Multiplet in Dissociative Excitation of CO_2 and O_2," *J. Chem. Phys.*, Vol. 58, p. 1425, 1973.

XXIII-23. Gentieu, E. P., and Mentall, J. E., *Cross Sections for Production of the $CO(A^1\Pi - X^1\Sigma)$ Fourth Positive Band System and $O(^1S)$ by Photodissociation of CO_2*, NASA Report X-691-72-418, 1972.

XXIII-24. Kliore, A. J., Cain, D. L., Fjeldbo, G., Seidel, B. L., Sykes, M. J., and Rasool, S. I., "The Atmosphere of Mars From Mariner 9 Radio Occultation Measurements," *Icarus*, Vol. 17, p. 484, 1972.

XXIII-25. Blamont, J. E., and Vidal-Madjar, A., "Monitoring of the Lyman-Alpha Emission Line of the Sun During the Year 1969," *J. Geophys. Res.*, Vol. 76, p. 4311, 1971.

XXIII-26. Thomas, G. E., and Bohlin, R. C., "Lyman-Alpha Measurements of Neutral Hydrogen in the Outer Geocorona and in Interplanetary Space," *J. Geophys. Res.*, Vol. 77, p. 2752, 1972.

Acknowledgments

Appendix

Geometrical Parameters Used to Derive Theoretical Intensities

A. Non-Intersecting Path

Figure XXIII-A-1 shows a non-intersecting line of sight diagram and the parameters specifying altitude and the corresponding SZA along the path. The parameters R, ϕ, and ψ are given as part of the spacecraft attitude-orbit information. R is the radial distance to the tangent point, ϕ is the SZA at R, and ψ is the cone angle, i.e., the angle of direct scattering of solar photons into the instrument. A set of path lengths, P, is first specified by the chosen limits on altitude and by the integration scheme used for deriving theoretical intensities. We choose about 700 km as the upper limit on altitude and use a Gaussian scheme for performing the integration. The altitudes are derived from P, R, and R. The cosine of the SZA, given by μ_P, is

$$\mu_P = \frac{\hat{S} \cdot \bar{R}}{\bar{R}} = (R_\perp \cos \phi \pm P \cos \psi)/(R_\perp^2 + P^2)^{1/2}. \quad (1)$$

where $\hat{S}$ is a unit vector pointing to the Sun. The minus sign is used for points along the path to the far side of $\bar{R}_\perp$. With $\bar{P}$, its corresponding altitude, and μ_P, quantities such as density, optical depth along the line of sight, and volume emission rates may be specified.

B. Intersecting Path

Figure XXIII-A-2 shows an intersecting line of sight diagram and the parameters specifying altitude and the corresponding SZA along the path. For the intersecting case, the given parameters are α, the angle between the line of sight and the normal at the surface intersection point, ϕ, the SZA at the intersection point, and ψ, the cone angle. By extending the line of sight to the tangent point specified by $R_\perp$ the intersecting and non-intersecting geometries may be treated similarly. The angle, ϕ, however, is defined differently for the two cases. Here, it is the SZA at the intersection point; above it is the SZA at the tangent point. As above, a set of P values is first specified. The range is from $-[(R_o + 100)^2 - R_\perp^2]^{1/2}$ to $[(R_o + 700)^2 - R_\perp^2]^{1/2}$. The cosine of the SZA at $\bar{R}$ is

$$\mu_P = \frac{\hat{S} \cdot \bar{R}}{|\bar{R}|} = [\hat{S} \cdot \bar{R}_o + (P - R_o \cos \alpha)\hat{S} \cdot \hat{P}]/\bar{R}$$

$$(2)$$

$$= [R_o \cos \phi - (P - R_o \cos \alpha)\cos \psi]/(P^2 + R_\perp^2)^{1/2}.$$

Fig. XXIII-A-1. Non-intersecting line of sight diagram. The parameters ϕ, ψ, and $R_\perp$ describe the geometry along the line of sight used to calculate theoretical limb intensities. The unit vector $\hat{S}$ points to the Sun.
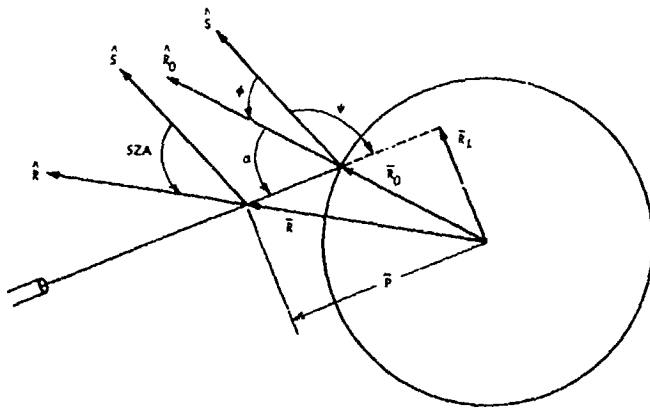
Fig. XXIII-A-2. Intersecting line of sight diagram. The parameters ϕ, ψ, α describe the geometry along the line of sight used to calculate theoretical disk intensities. The unit vector $\hat{S}$ points to the Sun.

XXIV. *Mariner* 9 Ultraviolet Spectrometer Experiment: Seasonal Variation of Ozone on Mars

Charles A. Barth, Charles W. Hord, and A. Ian Stewart
Department of Astrogeophysics and Laboratory for Atmospheric and Space Physics
University of Colorado, Boulder, Colorado 80302

Arthur L. Lane
Jet Propulsion Laboratory/California Institute of Technology, Pasadena, California 91103

Mary L. Dick and Gail P. Anderson
Laboratory for Atmospheric and Space Physics
University of Colorado, Boulder, Colorado 80302

Between November 14, 1971, and October 27, 1972, systematic observations of ozone on Mars were made with the *Mariner* 9 ultraviolet spectrometer. This time period covered almost half of a Martian year or two complete seasons in each hemisphere. Since *Mariner* 9 made observations in both hemispheres, summer and fall were observed in the south, winter and spring in the north. An important result is that ozone is present in the atmosphere in the polar regions (poleward of 45° latitude) and that the amount varies with the changing season. Within the detection limits of the ultraviolet spectrometer, no ozone was found in the equatorial region (equatorward of 45° latitude). A somewhat simplified description of the seasonal variation in the polar regions is as follows: Early in summer, there is no ozone in the atmosphere. In late summer and early fall, ozone begins to appear both over the polar cap and in association with the formation of the polar hood. In winter, the entire polar region from 45° latitude to the pole is covered by the polar hood. It is at

this time that the maximum amount of ozone is observed over the polar cap. As the season progresses, less and less ozone is present until, by the beginning of summer, ozone disappears from over the polar cap and the entire polar region.

Ozone is measured by the ultraviolet spectrometer by observing the Hartley absorption continuum between 2000 and 3000 Å in the ultraviolet light reflected from the planet. The ultraviolet solar radiation that is reflected from Mars arises from Rayleigh scattering, from scattering by large particles in the polar hood, and from reflection from the bright polar cap (Ref. XXIV-1). A great deal of information about the polar hood and polar cap of Mars has been acquired by several of the *Mariner* 9 instruments. In this report, the following operational model of these two Martian phenomena will be used. The polar hood is a fog or cloud bank of water ice crystals that covers most of the winter hemisphere

poleward of 45 . It begins to form in the fall and portions of it remain until the spring. The polar cap is primarily composed of frozen carbon dioxide and may also contain water ice.

The behavior of ozone in the polar region between 50°S and 75°S during the southern summer and fall is demonstrated in Fig. XXIV-1a. During most of the summer, no ozone was observed in this latitude region. Toward the end of summer, before the polar hood became visible, ozone began to appear in the atmosphere near 60°S. At the end of summer, the amount increased from the detection limit of 3 μm-atm to an amount greater than 10 μm-atm. (The amount of ozone is expressed in terms of micrometer-atmospheres, the thickness of the ozone column in micrometers when compressed to standard pressure and temperature on Earth; 1 μm-atm = 1 $\times$ 10^{-4} cm-atm = 2.69 $\times$ 10^{15} molecules per square centimeter. The amount of ozone in Earth's atmosphere is approximately 0.3 cm-atm.) During these summer measurements, the ultraviolet spectrometer was able to make continuous observations over a range of latitudes. The maximum amounts of ozone observed in the latitude range 50°S to 75°S are plotted in Fig. XXIV-1a. When Mariner 9 observations were made in the middle of the southern fall, the polar hood was visible and the amount of ozone was observed to have increased to more than 30 μm-atm. The final three measurements were made at specific targets in the southern hemisphere and, hence,

are not necessarily the maximum values in this latitude band.

The behavior of ozone in association with the northern polar hood is shown in Fig. XXIV-1b. On all occasions when observations were made north of 45°N during winter, ozone was measured and the polar hood was always visible. The data plotted in Fig. XXIV-1b are the maximum amounts of ozone observed in the latitude range 50°N to 75°N. The amount measured varied, ranging all the way from the detection limit of 3 μm-atm up to the largest value observed on Mars by Mariner 9, 57 μm-atm. In spring when measurements were made of specific targets in the north, there was less ozone than in the winter and the polar hood was not readily visible.

The behavior of ozone over the south polar cap in summer is shown in Fig. XXIV-2a. The Mariner 9 observations show that there was no ozone over the remnant of the cap throughout the summer. Near the end of the summer the amount of ozone increased above the detection limit, reaching a value of 6 μm-atm. Favorable viewing conditions were not attained during the fall in the south.

The behavior of ozone over the north polar cap during the winter and spring is shown in Fig. XXIV-2b. Toward the end of winter, when the polar hood cleared sufficiently to permit the cap to be seen by the Mariner 9 in-
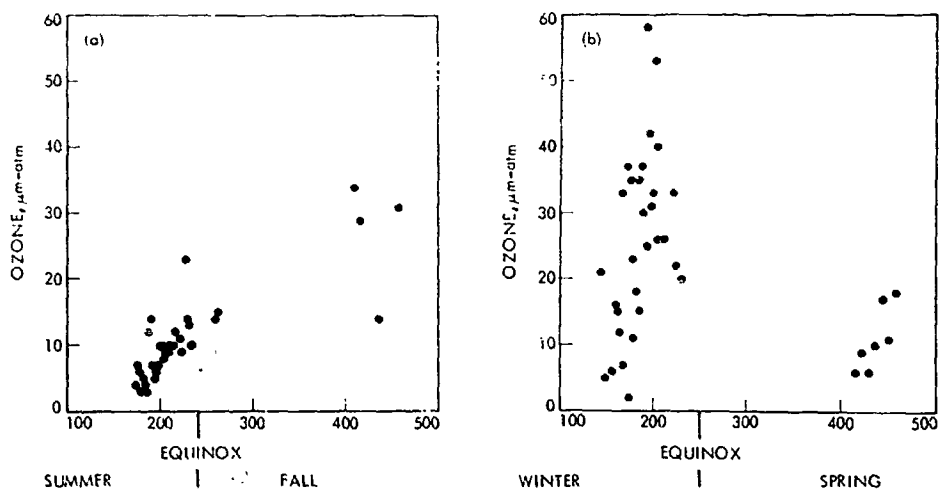
Fig. XXIV-1. (a) Amount of ozone observed in the south polar region during summer and fall. Numerical values along the abscissa correspond to the Mariner 9 orbital revolution numbers. The amount of ozone plotted corresponds to the maximum value found between 50°S and 70°S, except for the last three points. (b) Amount of ozone observed in the north polar region during winter and spring. The ordinate is the maximum amount of ozone found between 50°N and 75°N.
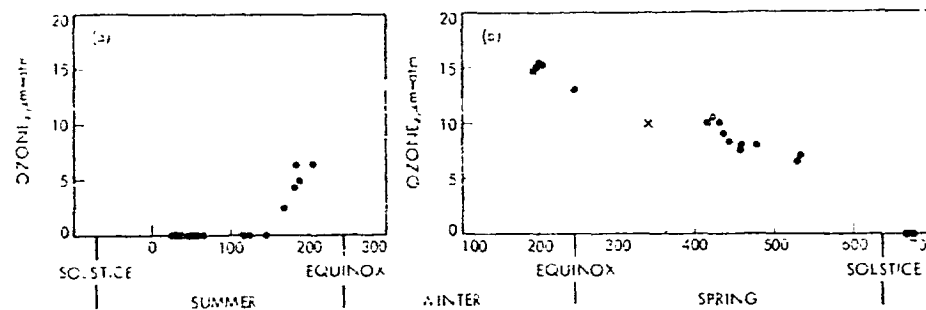
Fig. XXIV-2. (a) Amount of ozone observed over the south polar cap during summer. (b) Amount of ozone observed over the north polar cap during winter, spring, and beginning of summer. The cross refers to the *Mariner 7* measurement made over the south polar cap in 1969. The ordinates and abscissas are defined as in Fig. XXIV-1.

struments. the amount of ozone measured was 16 μm-atm. In the middle of spring the quantity of ozone above the polar cap was 10 μm-atm. and its magnitude decreased monotonically during the latter half of the northern spring. During the last two orbital operations of *Mariner 9* just after the northern summer solstice. observations of the north polar cap showed that the ozone had disappeared.

The amount of ozone measured in 1969 by the *Mariner 7* ultraviolet spectrometer over the south polar cap was 10 μm-atm (Ref. XXIV-1). The season on Mars at that time was southern spring. This value is plotted in Fig. XXIV-2b at the corresponding seasonal time for comparison with the *Mariner 9* data for the 1972 northern spring.

When ozone was observed in association with the polar hood in the fall and winter seasons, the ultraviolet spectrometer also detected increased reflectivity in the region from 3000 to 3500 A compared to the reflectivity of the clear atmosphere. This increased reflectivity presumably is produced by the ice crystals of the polar hood. We have suggested elsewhere that this correlation of the appearance of ozone with the appearance of the polar hood is experimental evidence for the suppression of ozone in the presence of water vapor (Ref. XXIV-2). Current theoretical treatments (Refs. XXIV-3 and XXIV-4) suggest

that not only water vapor, but also hydrogen peroxide (which is a byproduct of the photolysis of water vapor by sunlight in the presence of molecular oxygen) should have this effect. However, a full explanation of the present results will probably involve the effects of variations in atmospheric temperature and of the global transport of water vapor in addition to photochemical considerations.

Achieving an understanding of the presence and variation of ozone in the Martian atmosphere is important for our knowledge of current conditions on Mars and the state of evolution of its atmosphere. In addition, this understanding of ozone photochemistry in a planetary atmosphere is relevant to Earth's atmosphere. where questions arise as to the stability of Earth's ozone in the presence of added impurities. On Mars, the *Mariner* observations show a twenty-fold variation in the amount of ozone, depending on the presence or absence of another minor constituent, water vapor, in the atmosphere. In the evolution of Earth's primitive atmosphere, the formation of an ozone layer may have played an important role in the prebiotic chemistry that took place on the surface. The seasonal formation and disappearance of ozone in the contemporary Martian atmos here may be of consequence in any prebiotic chemistry that may be occurring there.

References

XXIV-1. Barth, C. A., and Hord, C. W., "Mariner Ultraviolet Spectrometer: Topography and Polar Cap." *Science*, Vol. 173, p. 197, 1971.

XXIV-2. Lane, A. L., Barth, C. A., Hord, C. W., and Stewart, A. I., "Mariner 9 Ultraviolet Spectrometer Experiment: Observations of Ozone on Mars." *Icarus*, Vol. 18, p. 102, 1973.

XXIV-3. Parkinson, T. D., and Hunten, D. M., "Spectroscopy and Aeronomy of O_2." *J. Atmos. Sci.*, Vol. 29, p. 1380, 1972.

XXIV-4. McElroy, M. B., and Donahue, T. M., "Stability of the Martian Atmosphere." *Science*, Vol. 177, p. 986, 1972.

Acknowledgments

XXV. *Mariner* 9 Television Observations of Phobos and Deimos II

J. B. Pollack
NASA Ames Research Center, Moffett Field, California 94035

J. Veverka, M. Noland, and C. Sagan
Laboratory for Planetary Studies
Cornell University, Ithaca, New York 14850

T. C. Duxbury, C. H. Acton, Jr., and G. H. Born
Jet Propulsion Laboratory/California Institute of Technology, Pasadena, California 91103

W. K. Hartmann
Science Applications, Inc., Tucson, Arizona 85704

B. A. Smith
Department of Astronomy
New Mexico State University, Las Cruces, New Mexico 88070

The first close-up pictures of the Martian satellites Phobos and Deimos obtained by *Mariner* 9 are discussed in two earlier reports (Refs. XXV-1 and XXV-2, henceforth Paper I). Both satellites were found to be irregular heavily cratered objects whose present shapes are largely determined by cratering, associated impact fragmentation, and spallation. They were found to be in synchronous rotation, to have nearly identical geometric albedos (about 0.05), and to possess crater densities close to saturation On the basis of their crater populations, the satellite surfaces were estimated to be at least several billion years old and most probably as old as the solar system. The mean radii of Phobos and Deimos were estimated to be 10.9 ±1.5 km and 5.7 ±0.5 km, respectively. The earlier reports also contain improved ephemerides.

This section extends the analysis of the *Mariner* 9 pictures of Phobos and Deimos and includes corrections to the orbits of the satellites, an estimate of their principal axes, additional confirmation of their synchronous rotation, a search for new satellites, photometric evidence for the presence of a regolith, and a discussion of their internal structure.

A. Orbits of Phobos and Deimos

Processing of the *Mariner* 9 television pictures has resulted in improved ephemerides of Phobos and Deimos. The details of the data reduction and the corrections to satellite ephemerides based upon the first 40 pictures are described in Paper I. Here, we report results based upon the reduction of about 20 additional pictures, including all narrow-angle pictures of Phobos and Deimos obtained by *Mariner* 9 before the extended mission. Typically, a satellite's orbital position could be determined to within 5 km from a single picture. A large fraction of this observational error was the result of uncertainties in the camera pointing direction. In a few cases much better determination could be made because of the presence of a star background on the picture.

As described in Paper I, a first-order general perturbation theory (Ref. XXV-3) was used to obtain the corrections to the ephemerides. This theory includes the perturbation from Mars' zonal harmonics J_2, J, J_4, but not those from Mars' tesseral harmonics or from those of the Sun. The satellite ephemeris model errors were less than 10 km over the processed 4-month data arc. The initial conditions for the first-order theory were obtained from Wilkins (Ref. XXV-4). The extension of Wilkins' work by Sinclair (Ref. XXV-5) was not available when the computer programs were developed for mission operations. Comparisons with Sinclair's ephemerides will be made in a later publication.

The most important corrections found were a 2.8° (about 600 km) advance in the mean longitude of Phobos and a 0.3° decrease in the inclination of its orbital plane relative to Earth's equatorial plane. The inclination correction results almost entirely from the difference in the orientation of Mars' spin axis given by Wilkins' analysis of Phobos and the best current value based on other *Mariner* data (Ref. XXV-6). The most important correction for Deimos is a 0.3° (about 150 km) decrease in its mean longitude. The orientation of the spin axis of Mars given by Wilkins' analysis of Deimos is close to the current value.

B. Shape and Rotation Period

In this section, we present estimates of the principal axes of Phobos and Deimos, discuss determinations of their rotation periods, and consider the conditions needed for synchronous rotation. A preliminary determination of the sizes, shapes, and orientations of Phobos and Deimos was achieved by assuming their surfaces to be triaxial ellipsoids. Assuming synchronous rotation, one axis of such an ellipsoid must be along the Mars–satellite vector, the second in the orbital plane, and the third normal to this plane. Librations, orbit eccentricity, and solar perturbations were neglected.

A computer-generated overlay was produced for each high-resolution satellite picture. The ellipsoid axes were adjusted so that the predicted limb outline in the overlay fit the satellite images. A sufficient range in viewing geometry was available to determine accurately all three axes for Phobos. Only the two smaller axes of Deimos could easily be determined because of the *Mariner* 9 orbit geometry. The spacecraft's orbit was inside that of Deimos, and only the side of Deimos facing Mars could be viewed at high resolution.

Figure XXV-1 shows the relative sizes and shapes of Phobos and Deimos. The three principal axes (radii) and the volumes and masses implied by them are given in Table XXV-1. Increased accuracy in the determination of the three principal axes will be obtained by using standard cartographic techniques for mapping surface features. Also, Viking Orbiter imaging data of the satellites will be of great value, particularly for determining the largest axis of Deimos. In both cases, the largest axis lies along the Mars–satellite vector, while the smallest one lies normal to the orbital plane. This is the most stable configuration for a satellite in synchronous rotation according to the Euler dynamical equations (see, e.g.,

PHOBOS   DEIMOS

a = LONGEST AXIS, TOWARD MARS
b = INTERMEDIATE AXIS, IN ORBIT PLANE
c = SHORTEST AXIS, NORMAL TO ORBIT PLANE
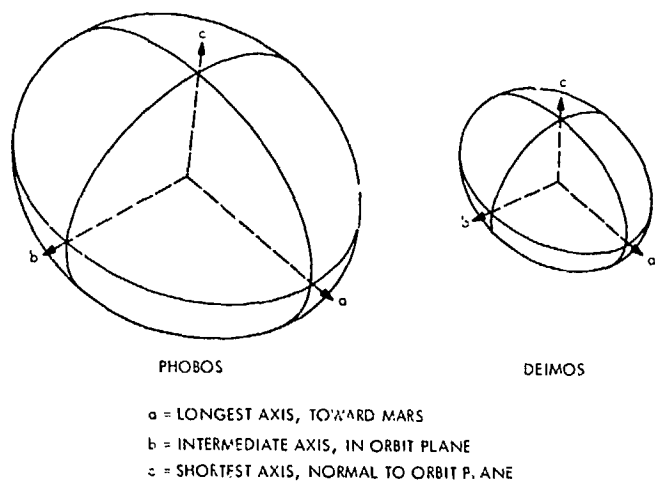
Fig. XXV-1. A comparison of the sizes and shapes of Phobos and Deimos. The longest axis, a, points toward Mars; the shortest one, c, lies normal to the orbital plane. The intermediate-sized axis, b, lies within the orbital plane and normal to the direction toward Mars.

374

Satellite	Largest axis, km	Inter-mediate axis, km	Smallest axis, km	Volume, km³	Mass,[b] 10¹⁸ g
Phobos	13.5 ± 1	10.7 ± 1	9.6 ± 1	5810	17.4
Deimos	7.5 ₋.₁⁺·³	6.0 ± 1	5.5 ± 1	1040	3.11

The axes are radii, *not* diameters
[b] A density of 3 g/cm³ has been assumed

Refs. XXV-7 and XXV-8). If the satellites had different orientations, they would experience large amplitude oscillations that would tend to align them in this most stable orientation.

By making use of the ellipsoidal overlays with latitude–longitude grids superimposed upon them, we have confirmed that the satellites are in synchronous rotation by checking that certain surface features always appear at approximately the predicted latitude–longitude points. Altogether, 40 pictures of Phobos and 5 of Deimos were used for this purpose. These pictures span a time of about 100 days. The worst case of disagreement between the predicted and observed position of a feature was 5°. From this and the time span of observation, we can estimate that the periods of Phobos and Deimos are equal to the synchronous value to about 1 part in 10⁴ and 1 part in 3×10^5, respectively.

What conditions must be met in order for the satellites to have synchronous rotation periods? Initially they will have another period, but will evolve to their final spin state through frictional dissipation of tides raised on them by Mars. However, this final spin state need not be the synchronous value, but could be some simple fraction of the synchronous period as is illustrated by the case of Mercury. According to Goldreich (Ref. XXV-9), the condition that the final spin state be synchronous is given by the following inequality between the moments of inertia and the orbital eccentricity, e:

$$[3(B - A)/C]^{1/2} \geq 9.5\pi e^2/2 \tag{1}$$

where C is the moment of inertia about the spin axis, and B and A are the larger and smaller moments in the equatorial plane, respectively. If we assume that the satellites are homogeneous, the moment of inertia C is related to the principal axes in the equatorial plane a and b by

$$C \approx (a^2 + b^2) \tag{2}$$

Similar expressions hold for A and B. By making use of the values of the principal axes given in Table XXV-1 and the known orbital eccentricities (Ref. XXV-4), we find that the term on the left side of Equation (1) is on the order of unity for both satellites, while the right side is on the order of 10⁻³ for Phobos and even smaller for Deimos. Thus, the final spin state for both satellites is expected to be synchronous.

A second condition must be met for synchronous rotation: the time scale for tidal evolution must be sufficiently small. In particular, it must be less than the age of the solar system. In Paper 1, we quoted Burns' estimate that this last inequality is met. However, this estimate was based on a particular model of the internal structure of the satellites. In a later section we discussed other time scales based on the two structural models described below.

C. Search for New Satellites

A search for new satellites was made on the 19 pictures of Phobos and Deimos acquired before orbit insertion. These were long-exposure (6-sec), narrow-angle pictures obtained at large distances from Mars. All but one were targeted for Deimos, starting at 66 hr before Mars orbit insertion (MOI − 66 hr) and continuing to MOI − 9 hr. Figure XXV-2 shows the television camera field of view for each picture. The television "footprints" are based on the range of the spacecraft from Mars and are drawn to scale with the satellite orbits.

Images of Deimos or Phobos and those of stars as faint as visual magnitude +9 (signal to noise ≈ 1.7) were detected on individual pictures by computer algorithms. These same algorithms were used to scan the central 95% of each picture for additional satellites. None was found. All signals detected other than those arising from the known satellites or stars have been identified as bit errors, vidicon blemishes, or noise. These spurious signals could readily be distinguished from signals due to a point or near-point source, as would be produced by a small satellite at the ranges of observation. For example, vidicon blemishes occur in the same location on the vidicon on several pictures. An image of a star, Phobos, or Deimos is characterized by an elliptical shape with the intensity declining from the center toward the edge.

Upper limits on the diameter of unknown satellites may be obtained from the vidicon point source detection threshold of +9 visual magnitude and the range of the spacecraft from Mars. For this purpose, we assume that
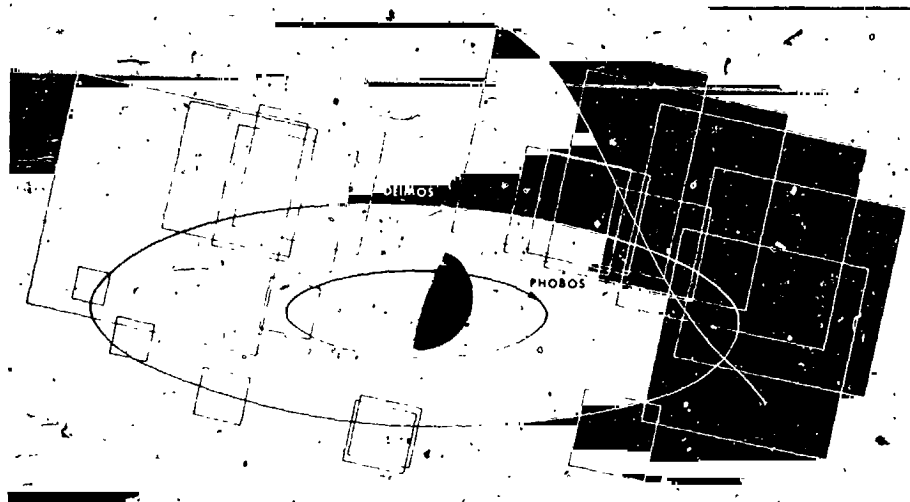
Fig. XXV-2. Footprints of the pre-orbital pictures of the satellites. Mars and the orbits of Phobos and Deimos are drawn as seen from the spacecraft. These pictures were searched for the presence of new satellites.

any new satellite would have the same albedo as Phobos, and make use of the observed diameter of Phobos (Paper I) and of Kuiper's (Ref. XXV-10) Earth-based observation of the visual magnitude of Phobos near opposition, corrected to the phase angle of observation (~60°) on the basis of *Mariner* data discussed in another part of this section. The upper limit on the diameter ranges from 1.6 to 0.25 km for the first and last pre-orbital pictures, respectively. If the albedo of an unknown satellite were higher than that of Phobos or Deimos (it is not likely to be lower), these values would be reduced.

These limits may be compared with an upper limit of 1.6 km set by Kuiper (Ref. XXV-11) from Earth-based photographs of the region outside the orbit of Phobos. Our observations supplement Kuiper's results by providing smaller limits on our last pictures. However, our pictures cover only a fraction of the possible time-space domain of an unknown satellite. The exact fraction covered depends upon how similar the period of an unknown satellite is to that of Deimos, as all but one of our pictures were centered on Deimos. For example, an unknown satellite with a period close to that of Deimos, but on the opposite side of Mars, would not have been detected.

In the subsequent part of this section dealing with the structure of Phobos and Deimos, the possibility is raised that these satellites originated from the breakup of a larger body. In that con..., the search for smaller satellites of Mars assumes special importance. It is hoped that pre-orbital pictures will be obtained on future Mars missions.

D. Satellite Pictures

Besides supplementing the morphologic information discussed in earlier papers (Ref. XXV-1; Paper I), high-resolution, narrow-angle pictures of the satellites provide valuable information about the surface texture and internal structure of Phobos and Deimos.

The satellite pictures used in this report were processed either at the Image Processing Laboratory of the Jet Propulsion Laboratory or at the Stanford University Artificial Intelligence Laboratory. The geometry is always such that the Sun-satellite-spacecraft plane (the plane of vision) is horizontal, the sun is always to the left and the terminator on the right. In Fig. XXV-4, north is toward the top of the picture.

The sub-spacecraft latitude and longitude given in the figure captions refer to a coordinate system with origin at the center of the satellite and with an X-axis in the orbital plane and pointing toward the center of Mars. The X-axis intersects the satellite surface at the equator at 0° longitude; east–west and north–south conventions are the same as those for Mars.

The picture of Phobos displayed in Fig. XXV-3 shows a long, linear feature partly in shadow, running the length of the satellite. The topography of this feat
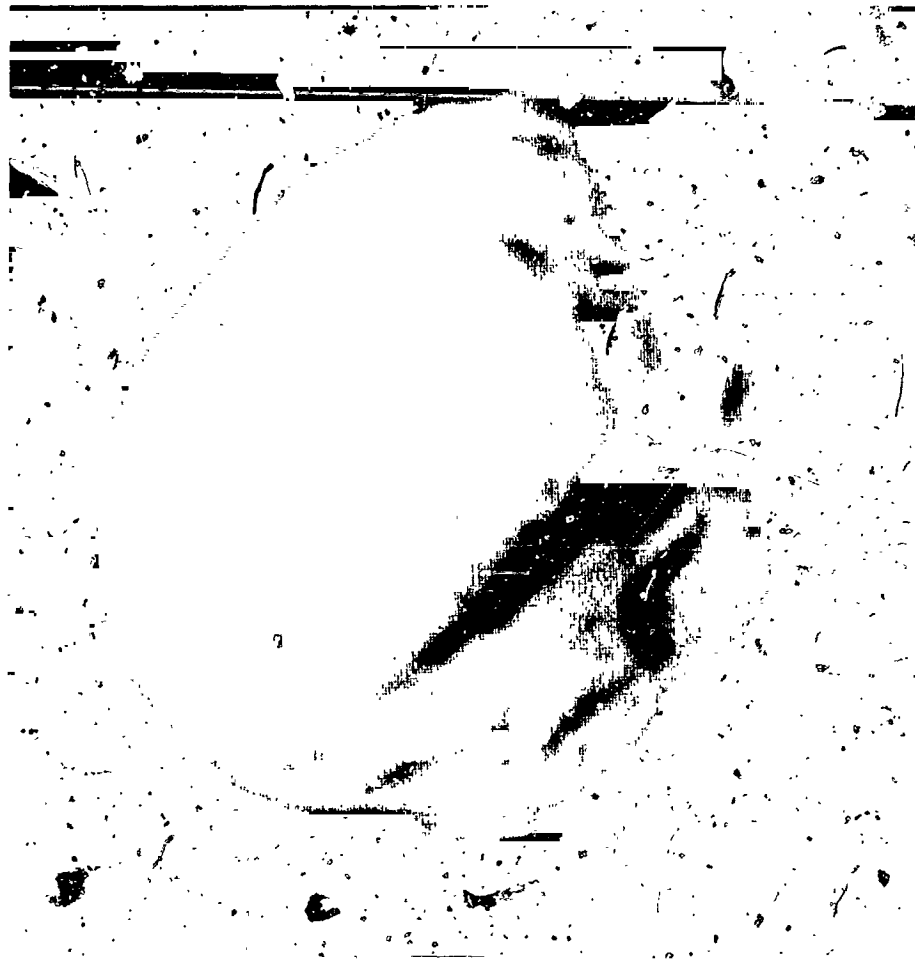
Fig. XXV-3. Computer-processed picture of Phobos taken during revolution 129; phase angle = 19°, range = 12,650 km, predicted sub-spacecraft point = 28°S, 19°W. The illuminated area is approximately 22 km high and 20 km wide. (JPL Roll 1114, 174232,

may be inferred by considering the variations of brightness along a line running perpendicular to the shadow. Because there is no bright edge running parallel to the shadow, this feature is not due to the presence of a local variation in surface altitude, but to a large-scale change in altitude from one side to the other. The genetic origin of this feature was discussed in Paper I and is dealt with extensively in a subsequent part of this section. The large, well defined crater near the terminator is about 5 km across. For convenience, in this section we will refer to it as Crater A. (This is not meant as an attempt at a permanent nomenclature system for the satellite craters, an attempt better dealt with elsewhere.) An even larger crater-like depression about 8 km across occupies the lower left of Fig. XXV-3, but is difficult to discern in this high-Sun view (phase angle = 19°). It is clearly visible near the top of Fig. XXV-4b.

Figure XXV-4a is an example of a minimum-range, high-resolution view of Phobos, in which craters as small as 0.3 km are visible. Crater A, with its well defined, scalloped rim, is visible close to the terminator in Figs. XXV-4a and XXV-4b. The 8-km crater-like depression appears at the top of Fig. XXV-4b, and its edge constitutes the sharp, concave segment of the upper limb in Fig. XXV-4a. Note that this feature does not have a prominent rim, and looks more like a chip knocked off Phobos than like a true crater. This suggests that, in the case of Phobos, the limiting size for clearly recognizable craters with well defined rims lies between 5 and 8 km (or about one-quarter to one-third of the satellite diameter).

Figure XXV-4 shows that craters of all degrees of sharpness occur on Phobos. There is also a wide range
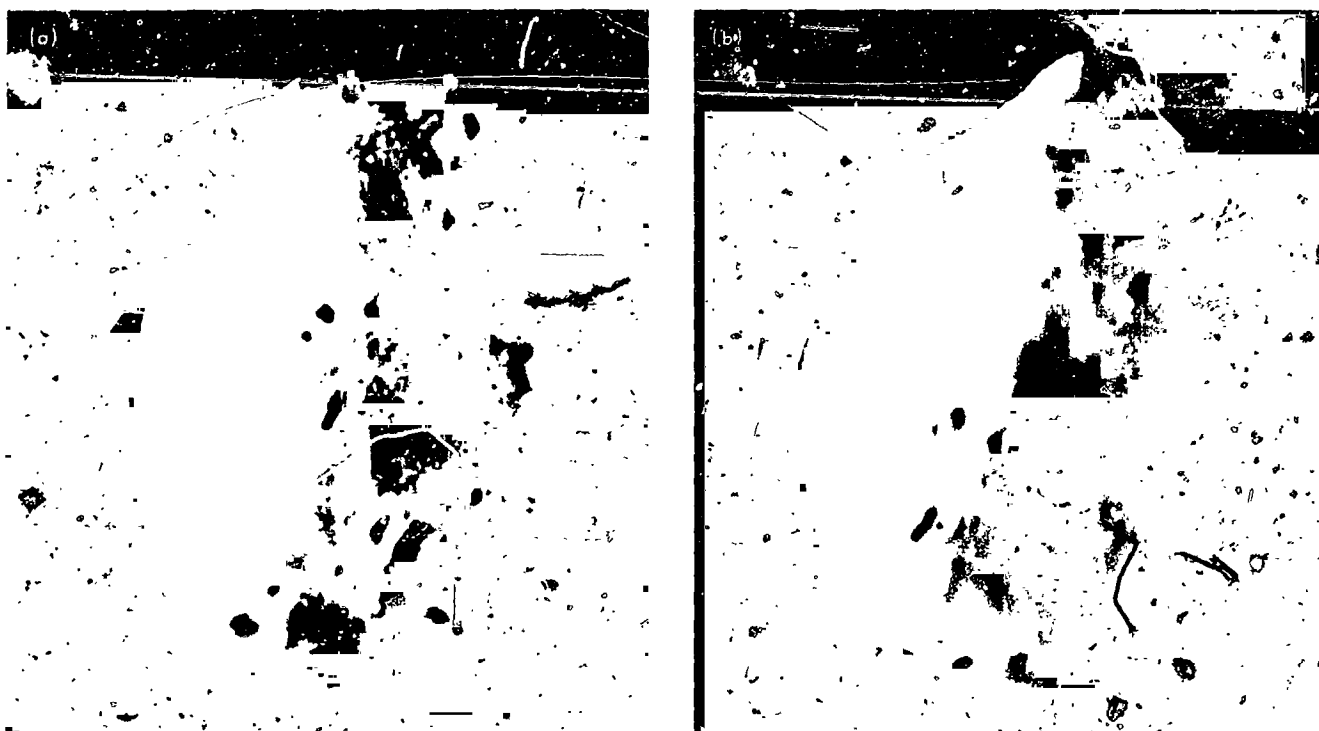
Fig. XXV-4. Computer-processed pictures of Phobos. (a) Revolution 34, phase angle = 59°, range = 5720 km, predicted sub-spacecraft point = 70°S, 161°W. The illuminated area is approximately 23 km high and 15 km wide. (IPL Roll 820, 002025) (b) Revolution 80, phase angle = 83°, sub-spacecraft point = 65°S, 356°W. The illuminated area is approximately 23 km high and 13 km wide. (IPL Roll 937, 103305)

of crater shapes, ranging from an elongated double crater (near the center of Fig. XXV-4a, for example), to perfectly circular craters, such as the 2.5-km crater (Crater B) near the lower-left limb in Fig. XXV-4a.

Figure XXV-5 provides an example of the extensive coverage of Phobos obtained during the Mariner 9 mission. Maps of the surface of this satellite are now in preparation using picture sequences such as those shown in the figure. Note that Craters A and B are visible in all three views. In Fig. XXV-5a, Crater A is on the limb at top, while Crater B is close to the mid-point of the terminator. In Fig. XXV-5c, Crater A is close to the mid-point of the terminator, while Crater B is against the lower limb close to the terminator. The apparent positions of the craters in Fig. XXV-5b are intermediate between those in Figs. XXV-5a and XXV-5c. Note that, in all views, Crater B appears to have a well defined, sharp, raised rim.

Somewhat below the 5-km crater and beginning close to the prominent small crater near the terminator in Fig. XXV-5a is an apparent linear array of four small craters, also visible in other pictures. Such a crater "chain" is unlikely to have formed by successive random impacts. Can it be a surface expression of internal fracturing caused by the formation of a nearby large crater?

Mariner 9 coverage of Deimos was more limited. Three versions of a high-resolution, low-Sun (phase angle 65°) view of Deimos are shown in Fig. XXV-6. Craters of all stages of freshness are present; the smallest visible crater is about 0.3 km across. The subdued crater, close to the terminator in the middle of the picture, is about 2 km across. The smaller 1-km crater just below the 2-km crater has been shown to have a raised rim (Ref. XXV-1). We showed in Paper I that the crater density on Phobos and Deimos was close to the saturation limit. The presence of subdued craters such as this 2-km crater on Deimos, as well as similar craters on Phobos, provides independent confirmation of this inference. Presumably subdued craters are relatively old and are heavily eroded by newer craters that form within or near them.

The array of bright markings near the limb, especially prominent in Figs. XXV-6b and XXV-6c, constitute one of the most striking features in Fig. XXV-6. By contrast,
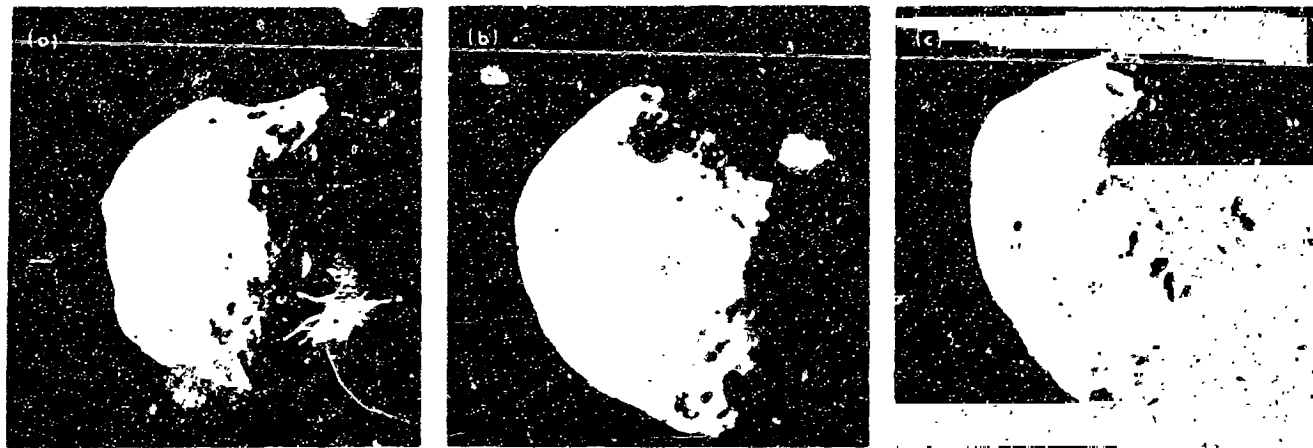
Fig. XXV-5. Computer-processed pictures of Phobos. (a) Revolution 43, phase angle = 66°, range = 7390 km, predicted sub-spacecraft point = 18°S, 152°W. The illuminated area is approximately 18 km high and 14 km wide. (IPL Roll 831, 224914) (b) Revolution 73, phase angle = 57°, range = 6460 km, predicted sub-spacecraft point = 42°S, 135°W. Illuminated area is approximately 20 km by 19 km. (IPL Roll 983, 101203) (c) Revolution 87, phase angle = 42°, range = 7110 km, predicted sub-spacecraft point = 58°S, 77°W. Illuminated area is approximately 24 km by 20 km. (IPL Roll 1009, 093920)
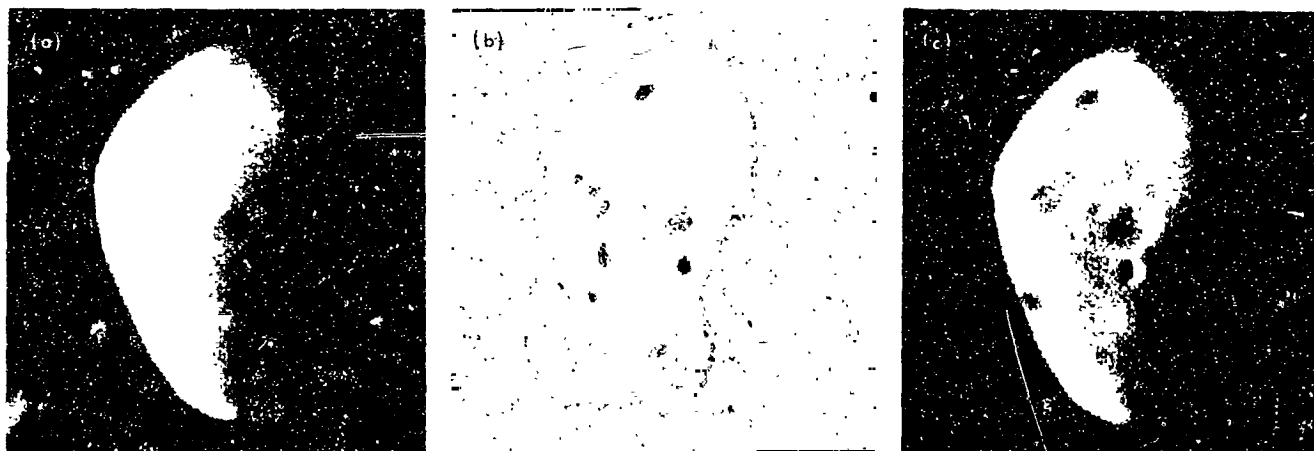
Fig. XXV-6. Three versions of picture of Deimos taken during revolution 149; phase angle = 65°, range = 5465 km, predicted sub-spacecraft point = 28°N, 355°W. The illuminated area is approximately 12 km high and 7 km wide. (Stanford AIL Product: STN 0156, 020501) (a) Contrast stretched. (b) High-pass filtered (11x11) to bring out topographic detail; contrast stretched. (c) High-pass filtered (21x21); contrast stretched.

the surface of Phobos appears to be photometrically homogeneous, with no evident albedo variations. In the next part of this section, we present evidence for the existence of a regolith on both satellites. In a subsequent part, we will indicate how such a regolith may originate. The bright markings on Deimos may be the result of a recent impact which has caused a temporary variation in the regolith thickness, perhaps even locally exposing the underlying surface.

Unfortunately, it is difficult to obtain morphologic evidence for the existence of a regolith, on the Moon,

this is done by noting the change in crater shape as the depth of the crater becomes comparable to the depth of the regolith. Because of the small range of crater sizes resolvable in the *Mariner 9* satellite pictures, it is impossible to carry out this procedure in the case of Phobos and Deimos.

E. Satellite Photometry

The photometric properties of Phobos and Deimos contain information about the nature of the satellites' surfaces. To fully determine the photometric functions

of the satellite surfaces, an accurate knowledge of their shapes is needed to find the angles of incidence and scattering at a given point on the surface. For photometric purposes, one cannot assume that Phobos and Deimos are spherical. Further refinement of the shape information given earlier ultimately will supply the needed information.

An approximate photometric function may be obtained, without knowing the exact shapes, from the brightness at the limb as a function of phase angle. For dark, texturally complex surfaces, such as those of the Moon or the asteroids, a good approximation to the photometric function is (Ref. XXV-12):

$$B(i, \epsilon, \alpha) \simeq C \left(\frac{\cos i}{\cos i + \cos \epsilon} \right) f(\alpha) \qquad (3)$$

for the apparent brightness at a given point. Here C is a constant; i and ϵ are the angles of incidence and scattering, respectively; and α is the phase angle. The equation is only approximate, as f in fact depends on i and ϵ as well as on α; however, for the type of surface considered here, the individual dependence on i and ϵ is small.

From Equation (3), we may write:

$$\frac{B(\text{limb}, \alpha)}{B(\text{limb}, 20°)} = \frac{f(\alpha)}{f(20°)} = F(\alpha) \qquad (4)$$

and $F(\alpha)$ may be regarded as an approximate photometric function for the surface because, in conjunction with Equation (3), it describes the scattering properties of the surface.

When B, i, ϵ, and α are all easily measurable, as in the case of lunar and laboratory observations, $F(\alpha)$ is easily determined from Equation (3). In the case of Phobos and Deimos, i and ϵ are usually uncertain as the shape of the satellites is not yet fully determined. But $\epsilon = 0°$ at the limb, so that $F(\alpha)$ can be found from Equation (4) if the brightness at the limb can be found. We have assumed that, as for the Moon, the maximum brightness at any phase angle occurs at the limb and have estimated these values from the digital photometric data corresponding to the narrow-angle pictures of the satellites. By considering the dispersion in the limb brightness values measured at various points along the limb, we have found a range in $F(\alpha)$ from each satellite picture. These are plotted against phase angle in Fig. XXV-7. We suspect that most of the dispersion is due to significant slope variations close to the limb, but effects of variations in surface albedo cannot be excluded.

In plotting the individual measurements for the two satellites in Fig. XXV-7, care was taken to normalize the points in a consistent manner. For each satellite, we have fitted a cubic polynomial in phase angle to the brightness values and used the value of the resulting function at a phase angle of 20° to normalize individual measurements. Comparing this normalizing factor for the two satellites, we find that the ratio of the reflectance of Deimos to that of Phobos is approximately 1.05 ± 0.05. Hence, to a very good approximation, the satellites are equally dark. This is in agreement with an independent argument given in Paper I, where the same conclusion was drawn on the basis of a combination of the *Mariner 9* size measurements and Earth-based magnitude determinations.

Also shown in Fig. XXV-7 are various comparison curves. The salient point of an $F(\alpha)$ plot is the degree of concavity. A very concave curve has a low value of $F(\alpha)$ near $\alpha = 90°$, and rises sharply as α approaches 20°. This indicates a strongly backscattering surface such as that of the Moon. Strong backscattering requires complex surface texture, and a dark surface material so that multiple scattering is negligible. Surfaces made of brighter materials or those that have less intricate textures show less backscattering and have less concave (that is, less peaked) $F(\alpha)$ curves (cf. Fig. XXV-7). For planetary surfaces, large-scale surface roughness can have an important effect on $F(\alpha)$ (Ref. XXV-12). For a given material, $F(\alpha)$ becomes more concave as large-scale surface roughness increases. This is the main reason why the lunar curve (6) in Fig. XXV-7 is more concave than the *Apollo 12* lunar dust curve (5).

Figure XXV-7 shows that the surface of Deimos is as backscattering as is that of the Moon, and that the surface of Phobos may be even more backscattering. Whether or not Phobos and Deimos really have slightly different photometric functions will have to await a more thorough analysis when the shapes of the two satellites are more accurately determined.

The photometric properties of the lunar surface are usually attributed to the fact that it consists of a texturally complex regolith, made of very dark material. By analogy from Fig. XXV-7, we infer that Phobos and Deimos may have surfaces of a similar nature. A regolith deep enough to cover the surface (at least a few millimeters) would explain adequately the photometric data. But these observations cannot be said to prove the existence of a regolith in the usual sense of an aggregate of loose, individual particles. A dark, very complex surface with
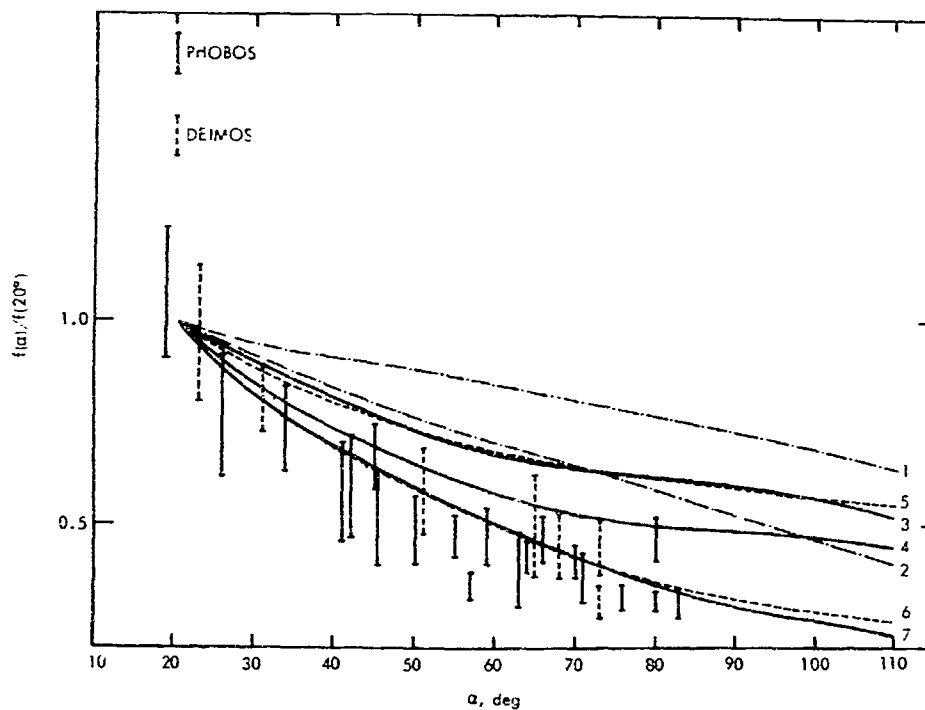
Fig. XXV-7. Approximate photometric function of Phobos and Deimos. The function $F(\alpha)$ (see text) has been normalized to unity at phase angle $\alpha \sim 20°$. The following curves are shown for comparison: (1) Bruderheim ordinary chondrite 74- to 150-μm particles (normal reflectance = 0.22), (2) chunks of the same meteorite coated with particles <37 μm (normal reflectance = 0.24) from Egan et al. (Ref. XXV-25), (3) limonite, coarse chunks (normal reflectance = 0.14), (4) limonite 37- to 88-μm powder (normal reflectance = 0.17) from Egan (Ref. XXV-26), (5) Apollo 12 lunar dust sample (normal reflectance = 0.12) from O'Leary and Briggs (Ref. XXV-27), (6) average curve for lunar regions based on Hapke (Ref. XXV-28) and Shorthill et al. (Ref. XXV-29) (mean normal reflectance $\approx$ 0.10), and (7) furnace slag (normal reflectance = 0.09) from Halajian (Ref. XXV-30).

F. Development of a Regolith

Analysis of the photometric television data described in the previous paragraphs provides possible evidence for the existence of a regolith on both satellites. Observations of Phobos made by the infrared radiometer (Ref. XXV-13) during and immediately after a Phobos eclipse provide strong, independent evidence for a regolith on Phobos. The Earth-based polarimetric observations of Deimos by Zellner (Ref. XXV-14) provide equally persuasive independent evidence for a regolith on Deimos. The presence of regoliths on bodies this small may be surprising at first; on the Moon, the fine-grained dust originates from repeated fragmentation of the surface material by meteoroid impact. Almost all material fragmented and ejected

many cavities, in which all particles are jointed together, such as furnace slag (cf. curve 7 in Fig. XXV-7) would do just as well.

by an impact is retained by the comparatively large lunar gravitational field. However, almost all ejecta arising from an impact on Deimos or Phobos will escape from these bodies; but as described below, it is the subsequent history of this material that may lead to the formation of a regolith.

First we estimate the mean depth to which craters have excavated the surface of Phobos and Deimos. The excavated material is highly fragmented and serves as the source of the regolith, as it does on the Moon. According to Paper I, observed crater densities on both satellites are close to the saturation limit—the limit reached when new craters are forming as fast as old ones are obliterated. The observed differential number of craters $n(D)\,dD$ per square kilometer of area that have diameters within dD of D kilometers is given by (Paper I):

$$n(D)\,dD = 2 \times 10^{-1}D^{-3}\,dD \tag{5}$$

The fraction of area F covered by craters whose diameter lies between a lower bound D_l and an upper bound D_u can be written as:

$$F = \int_{D_l}^{D_u} \frac{n-D}{4} \, dD = \frac{\pi}{4} \cdot 2 \times 10^{-3} \ln\left(\frac{D_u}{D_l}\right) \quad (6)$$

In Equation (6), we have neglected crater overlap. By setting F equal to 0.5 and D_u equal to the largest-sized crater on Phobos (8 km), we find that D_l is 0.33 km. This value of D_l means that 50% of the surface is covered by craters whose size exceeds D_l. Thus, the depth of a crater of size D_l provides an estimate of the mean depth to which the observed craters have excavated material on Phobos. Taking the average depth of a crater as one-sixth of the crater's diameter (Ref. XXV-15), we find that this depth is about 50 m for Phobos. The depth values are about a factor of 2 smaller for Deimos. In making the above estimate, we have neglected the "shielding" effect of ejecta produced by early craters on the formation of later craters.

The above mean depth is really a lower bound on the depth of excavation produced by craters on Phobos, as some of the earlier craters probably have been obliterated. To obtain an upper bound, we consider the depth excavated by the largest crater, about 1 km. If, over the past history of Phobos, there were many craters produced with an 8-km *diameter*, still bigger impacts, big enough to destroy Phobos, would be expected. We therefore conclude that the mean depth of excavation is much less than 1 km. Combining this with the lower bound of 50 m given above, we estimate a mean depth of excavation of several hundred meters for Phobos. The corresponding depth for Deimos is smaller by about a factor of 2.

This above calculation indicates that a large volume of material on the two satellites has been excavated and fragmented by impacts. Now we consider the fate of the excavated material produced, following the discussion of Soter (Ref. XXV-16, henceforth Paper II). A very large fraction of the material will have a sufficient velocity to escape from the weak gravitational fields of the satellites (the escape velocity is about 12 m/sec for Phobos and about 6 m/sec for Deimos), but insufficient velocity to escape from the neighborhood of Mars. Most of this material will go into orbit about Mars rather than escape from the region around Mars or impact the planet. The very smallest particles (less than 5 μm) are subject to large periodic perturbation of the eccentricities of their orbits by radiation pressure and will be lost. However, the remainder of the material reimpacts the satellites in a rather short time (about 100 years for Phobos and 10,000 years

for Deimos and suffers a loss of energy. After one or several such impacts, its velocity falls below the escape velocity, and it will be temporarily recaptured. The tertiary material produced by the impact of the secondary material does not contribute significantly to the dust around the satellites. The reasons for this are twofold. The secondary particles have much less kinetic energy than the primary impacting particles. As a result, the secondaries excavate a mass comparable to themselves, not much larger. This excavated tertiary material will have a much smaller ejection velocity than the secondary material originally had, so that the tertiary material will not escape, or if it does, it will be recaptured much more quickly than the secondary material.

The net result of all such processes (see Paper II for details) is that a significant fraction of the material ejected by impacts is recaptured and serves to form a regolith. According to Paper II, the steady-state solution for the amount of mass in orbit at a given time is only about 10^{-5} and 10^{-3} of the total mass excavated on Deimos and Phobos, respectively. The material close to the surface probably has been recycled many times, and hence should consist of finer, more heavily fragmented material than material located at greater depths in the fragmental layer.

G. Structure of Phobos and Deimos

Two very different extreme models of the structure of the satellites are possible. The satellites may be aggregates of small dust grains, chiefly held together by gravity; they also may be composed of well consolidated rock, in which case the structural strength of the rock dominates the gravitational binding forces. Radically different evolutionary histories are implicit in the two models. In this section, we use available evidence to try to choose between the two possibilities.

In Paper I, we have argued that the energy needed to produce the largest crater on Phobos might suffice to destroy the entire satellite, if it were gravitationally bound. This argument, based on a commonly used scaling law, may not necessarily be applicable. For the dust grain model, the energy that goes into doing work against the hydrostatic pressure resulting from the formation of a cavity controls the size of the crater (gravity scaling); for the rock model, the energy that goes into fragmenting the material controls the size of the crater (strength scaling). The constants of proportionality and the value of the exponent in the relationship between crater diameter and impact energy are different in the two cases.

In searching for empirical data relevant to the two situations, we have found it difficult to obtain a conclusive result, especially since we must extrapolate the results to a different gravity environment and to materials with uncertain properties.

Nevertheless, other arguments can be used to indicate that Phobos and Deimos probably are composed of well consolidated material. First we consider morphological evidence. In Paper I, it was pointed out that the existence of craters with raised rims could be explained by either model. However, the presence of the long step-like linear edge which runs the length of Phobos (Fig. XXV-3) is quite conclusive. It was suggested in Paper I that this feature resulted from fragmentation and spalling accompanying an unusually severe meteoroid impact. Such features have been observed in laboratory studies when the energy of impact is less than the energy needed to disintegrate the target, but is within an order of magnitude of this critical energy (Ref. XXV-17). These laboratory studies have involved well consolidated material, and it is difficult to see how the long step-like edge could have resulted if Phobos were simply an aggregate of small dust grains. Formation of fracture zones, as observed in the laboratory experiments, results from the dissipation of the shock energy in a narrow band circumventing the surface of a circular region antipodal to the impact point. This is possible only in a crystalline material.

In the part of this section describing the *Mariner 9* pictures, the presence of a linear array of small craters was noted (Fig. XXV-5a). If, as we suggested, this crater array is the surface manifestation of a fracture zone generated by a large nearby impact, this again points to a solid Phobos. Such an explanation would be inconsistent with a sand-grain model.

As a second line of argument, we consider the effect of the largest meteoroid likely to hit the satellites within the age of the solar system. Could such an event break up the satellite? From considerations of the number of large, Mars-crossing asteroids and impact theory, Soter (Paper II) has estimated the size of the largest asteroid likely to hit Phobos and Deimos over the last $4\frac{1}{2}$ billion years. The answer depends on the exponent s describing the cumulative number of Mars-crossing asteroids, as he has to extrapolate from the largest such asteroids that can be observed to the size of interest. The energy of impact is the kinetic energy of the asteroid, E_i:

$$E_i = \frac{2\pi}{3}\rho_a R_a^3 V_a^2 \tag{7}$$

where ρ, R, and V are the density, radius, and velocity of the asteroid, respectively. We will assume that ρ and V are 3 g/cm and 10 km/sec, respectively (Papers I and II). For the range of values for s considered to be plausible by Soter (1.6 to 2.4), R varies from 35 to 290 m for Phobos. Inserting these values into Equation (7), we find that:

$$3.4 \times 10^{-} \text{ erg} \leq E_i \leq 1.5 \times 10^{-} \text{ erg} \tag{8}$$

The lower energy limit corresponds to the lowest value of s.

In his calculations, Soter makes a modest correction for the fact that some Mars-crossing asteroids are being lost with time, so that the time-averaged population is larger than the present value. This correction is based upon the estimate made by Öpik (Ref. XXV-18) of the mean lifetime of present Mars-crossing asteroids. There are two reasons to believe that this value should be significantly lowered. First, in a more exact calculation, Anders (Ref. XXV-19) has found that the mean lifetime is smaller by about a factor of 3 than assumed by Öpik. Second, the lifetime of the present population is not a representative value; and, undoubtedly, there were many more short-lived meteoroids present in the early history of the solar system (Ref. XXV-20). As a result, the above values of E_i are probably too low.

Next we compare the above impact energy with the binding energy of a satellite for each of the two models. In the gravity-dominated model, for a homogeneous sphere, the binding energy is simply the gravitational potential energy, E_G:

$$E_G = \frac{3}{5}\frac{GM^2}{R} = \frac{3G}{5}\left(\frac{4\pi}{3}\right)^2 \rho^2 R^5 \tag{9}$$

where G, M, R, and ρ are the gravitational constant, the mass, radius, and density of the satellite, respectively. For this model, we assume that ρ is 1.6 g/cm and use the observed radius of Phobos (Table XXV-1). This value of ρ is typical of the mean density of an aggregate of sand grains but, because of porosity, is lower than the density of an individual grain. We find that:

$$E_G = 1.6 \times 10^{21} \text{ erg} \tag{10}$$

Thus, for most of the range of possible values of s, the impact energy of the largest asteroid likely to have hit Phobos exceeds its binding energy. Therefore, this model appears to be ruled out, unless s is very close to the lowest value plausible. Even in that case, the model is prob-

ably untenable in view of the arguments given that the values of E, in Equation (8) may be too low by a significant factor.

For the strength-dominated model, the binding energy may be written as (Paper I):

$$E_s = \frac{4\pi R^3}{3} S \qquad (11)$$

Equation (11) can be derived by considering the work needed to create a cavity equal to the size of the satellite against the force per unit area represented by the strength.

Plausible values for S are 10^7 to 10^9 dynes/cm² (Paper I). These values imply that, for Phobos

$$4.2 \times 10^{20} \text{ erg} \leq E_s \leq 4.2 \times 10^{22} \text{ erg} \qquad (12)$$

Thus, for this model, it is highly likely that Phobos would not be disintegrated by the local meteoroid population. Completely analogous numbers and conclusions follow for Deimos.

The above arguments indicate that Phobos and Deimos are probably composed of well consolidated material. It is difficult to see how such a degree of consolidation could have resulted from the accretion of an object as small as Phobos or Deimos. Suppose that the energy of formation is comparable to the present gravitational binding energy. Then a comparison of Equations (10) and (12) indicates that the gravitational energy available is much too small to allow the formation of well consolidated material. It could be argued that the kinetic energy of the accreting grains could be much larger than the gravitational energy. However, under such circumstances, particle impacts would eject more mass than they would add to the forming satellite. This suggests that Phobos and Deimos were originally part of one or two much larger objects, for which $E_G \gg E_s$, and that they originated by fragmentation from these larger bodies (or body). It also is possible that other sources of energy, such as short-lived radioactive materials (Ref. XXV-21) and the early solar wind (Ref. XXV-22), were available to melt the original satellite material.

H. Time Scale to Achieve Synchronous Rotation

Considering Phobos and Deimos to be well consolidated bodies, we can now return to the question of how long it will take for tidal forces to lock the satellites into synchronous rotation.

According to Goldreich and Soter (Ref. XXV-23), the time T required to despin a satellite through the frictional dissipation of tides raised on it by its parent planet is given by:

$$T = \frac{64 - \Omega_i \quad \Omega_f \quad \rho \, r^6}{135 G M^2} \qquad 13$$

where Ω_i, Ω_f, ρ, r, G, and M are the initial angular spin rate, final angular spin rate, satellite density, distance between the satellite and planet, gravitational constant, and planetary mass, respectively. All these factors are either well known or can adequately be guessed. The principal uncertainty is the factor Q', which incorporates the details of tidal dissipation. It is related to the effective tidal dissipation factor Q, by Goldreich and Soter (Ref. XXV-23):

$$Q' = Q (1 - 38\pi a^4 \mu/3G m^2) \qquad (14)$$

where a, μ, and m are the satellite's radius, rigidity, and mass, respectively. In the above equations, the satellite has been assumed to be spherical. This is an adequate approximation for our purposes as rather large uncertainties enter into the calculation (below).

To evaluate Equation (13), we use the inference that the Martian satellites consist of well consolidated material. Accordingly, we assume ρ, is 3 g/cm³, μ is 3×10^{11} dynes/cm², a value typical of uncompressed solid rock (Ref. XXV-23), and Q, is between 10 and 500, the range of values inferred by Goldreich and Soter for the terrestrial planets and satellites. For this choice of parameters, the second term in Equation (14) is many orders of magnitude larger than the first. If we assume that the initial period of the satellites was 6 hr, a value typical of asteroids and presumably other small bodies, and make use of the size information given in Table XXV-1, we find for T_D, the time scale for despinning Deimos:

$$2.7 \times 10^6 \text{ years} \leq T_D \leq 1.3 \times 10^8 \text{ years} \qquad (15)$$

The corresponding time scales for Phobos are about 100 times shorter, principally because of the closer distance of Phobos to Mars. Had we performed the same calculation for the gravity-dominated model, we would have found a much smaller value of T because of the smaller value of μ. The numbers given in Equation (15) should be treated with caution as the real value of μ is uncertain. However, if the above value of μ is incorrect, it is in the sense of being an overestimate, in which case T should be smaller.

The above values of T are significantly less than the age of the solar system. Therefore, the satellites should be in synchronous rotation at the present time unless they were captured by Mars in the very recent past ($< T$) or if they were recently struck by a large meteoroid. Let us consider the latter possibility in detail. If a meteoroid strikes the satellite tangentially (resulting in a maximum torque) from considerations of conservation of angular momentum, the change in spin rate, $\Delta\Omega$, is given by:

$$\frac{\Delta\Omega}{\Omega_s} = \frac{m_a}{m}\frac{v}{a a \Omega_s} \qquad (16)$$

where m_a, v, and a are the meteoroid's mass, meteoroid's velocity, and a factor on the order of $\frac{1}{2}$, respectively. Note that, if the excavated material is ejected symmetrically about the local normal, it will impart no net torque.

Let us evaluate Equation (16) for the largest meteoroid likely to strike Deimos. According to Paper II, the radius of this object ranges between 16 and 160 m, depending on the value of the population index s. Using the same numbers to characterize a meteoroid as in the regolith discussion, we find that $\Delta\Omega/\Omega$ is about $\frac{1}{2}$ for the 160-m object. We see from Equation (13) that the time scale required to restore Deimos to synchronous rotation would be about $\frac{1}{4} T_D$. Noting that $T \sim \Delta\Omega \sim r_a$, where r_a is the meteoroid's radius, we see that the time scale required to restore synchronous rotation falls sharply as the size of the impacting object is reduced. Similar figures hold for Phobos. The above time scales can be used to set lower bounds on the time since a satellite was last hit by a meteoroid of a given size. These times are much shorter than the mean time between collisions by impacting objects of a given size. For example, with the 160-m meteoroid, the mean time interval between successive collisions is 4.5 billion years.

I. Conclusions and Prospectus

The principal *Mariner 9* findings concerning Phobos and Deimos will now be summarized, and suggestions made for satellite studies on future space missions to Mars, such as Viking. Our knowledge of the orbits of Phobos and Deimos has been improved as a result of the *Mariner 9* imagery of the satellites. Additional analysis of the pictures, which span a time period of about 1 year, should result in a more accurate determination of the secular acceleration of Phobos than is possible from Earth-based measurements. An accurate value of this parameter is of interest for two reasons:

(1) A positive determination of the secular acceleration will lead to an estimate of the dissipation function Q' for Mars and thereby provide some information about the interior of the planet.

(2) It will permit meaningful studies of the orbital evolution of the satellites; this may help to clarify various hypotheses regarding their origin.

The *Mariner 9* pictures have resulted in the direct determination of the sizes and shapes of the satellites. By combining these sizes with Earth-based brightness measurements (Ref. XXV-10), we have inferred that both satellites have very low geometric albedos (about 0.05). Using a very low-resolution *Mariner 7* picture of Phobos projected against Mars, Smith (Ref. XXV-24) obtained values of the shape and albedo of Phobos in good agreement with our results. Such low albedo suggests that the satellites consist either of carbonaceous chondrite or basaltic material. Color information currently being analyzed may help distinguish between these two possibilities. The fact that Phobos and Deimos have almost identical albedos may suggest a common composition.

Several pieces of evidence imply that the satellites possess a regolith. Its genesis may be understood in terms of impact events excavating material, which escapes from the satellite, goes into orbit about Mars, and is eventually recaptured. Material near the surface is probably recycled many times.

Both satellites appear to be in synchronous rotation. This is consistent with the final spin state expected from tidal evolution. The time scale for tidal evolution is short compared with the age of the solar system, and the time between collisions with meteoroids that can significantly alter the rotation period.

Several arguments were advanced to indicate that Phobos and Deimos are made of well consolidated material and once may have been parts of much larger objects. As the bombardment rates probably were much higher in the early history of the solar system, the fragmentation of large bodies may have been much more common at that time than it is now.

Finally, let us consider the potential of future spacecraft photography of Phobos and Deimos, for example from the Viking Orbiters. First, this would provide a baseline of about 5 years for orbital studies, which would mean a gain by about a factor of 5 in the accuracy with which secular acceleration could be measured. There are

still some areas of Phobos and many on Deimos, which have not been photographed at high resolution. In the case of Phobos, such photography could lead to a complete three-dimensional reconstruction of the satellite, a task which is presently underway with the limited data presently available. In addition, pictures at closer range could be obtained from a low inclination orbit. Higher-resolution pictures of Phobos would have many advantages, including the possibility of estimating the depth of the regolith from crater morphology. Pre-orbital pictures could extend the search for unknown satellites—a search which is especially important since the two large satellites may have resulted from the breakup of a larger body or bodies. Much has been learned, but much remains to be learned. It would be a pity if future missions did not provide a continuation of this work.

References

XXV-1. Masursky, H., Batson, R. M., McCauley, J. F., Soderblom, L. A., Wildey, R. L., Carr, M. H., Milton, D. J., Wilhelms, D. E., Smith, B. A., Kirby, T. B., Robinson, J. C., Leovy, C. B., Briggs, G. A., Young, A. T., Duxbury, T. C., Acton, C. H., Jr., Murray, B. C., Cutts, J. A., Sharp, R. P., Smith, S., Leighton, R. B., Sagan, C., Veverka, J., Noland, M., Lederberg, J., Levinthal, E., Pollack, J. B., Moore, J. T., Jr., Hartmann, W. K., Shipley, E. N., de Vancouleurs G., and Davies, M. E., "Mariner 9 Television Reconnaissance of Mars and Its Satellites: Preliminary Results," *Science*, Vol. 175, p. 294, 1972.

XXV-2. Pollack, J. B., Veverka, J., Noland, M., Sagan, C., Hartmann, W. K., Duxbury, T. C., Born, G. H., Milton, D. J., and Smith, B. A., "Mariner 9 Television Observations of Phobos and Deimos," *Icarus*, Vol. 17, p. 394, 1972 (Paper I).

XXV-3. Aksnes, K., "On the Use of the Hill Variables in Artificial Satellite Theory: Brouwer's Theory," *Astronaut. and Astrophys.*, Vol. 17, p. 70, 1972.

XXV-4. Wilkins, G. A., in *Mantles of the Earth and Terrestrial Planets*, edited by Runcorn, John Wiley, London, 1967.

XXV-5. Sinclair, A. T., "The Motions of the Satellites of Mars," *Mon. Not. Roy. Astron. Soc.*, Vol. 155, p. 249, 1972.

XXV-6. Lorell, J., Born, G. H., Christensen, E. J., Jordan, J. F., Laing, P. A., Martin, W. L., Sjogren, W. L., Shapiro, I. I., Reasenberg, R. D., and Slater, G. L., "Mariner 9 Celestial Mechanics Experiment: Gravity Field and Pole Direction of Mars," *Science*, Vol. 175, p. 320, 1972.

XXV-7. Koziel, K., "Differences in the Moon's Moments of Inertia," *Proc. Roy. Soc. Am.*, Vol. 296, p. 248, 1967.

XXV-8. Burns, J., "The Dynamical Characteristics of Phobos and Deimos," *Reviews of Geophys. and Space Phys.*, Vol. 10, p. 463, 1972.

XXV-9. Goldreich, P., "Final Spin States of Planets and Satellites," *Astron. J.*, Vol. 71, p. 1, 1966.

References (contd)

XXV-10. Kuiper, G. P., quoted by Harris in Chapter 8 of *Planets and Satellites*, edited by G. P. Kuiper and B. M. Middlehurst, University of Chicago Press, Chicago, p. 289, 1961.

XXV-11. Kuiper, G. P. "Limits of Completeness," in *Planets and Satellites*, edited by G. P. Kuiper and B. M. Middlehurst, University of Chicago Press, Chicago, pp 551–552, 1961.

XXV-12. Veverka, J., "The Physical Meaning of Phase Coefficients" in *Physical Studies of Minor Planets*, SP-267, National Aeronautics and Space Administration, Washington, D. C., 1971.

XXV-13. Gatley, I., Kieffer, H., Miner, E., and Neugebauer G., *Ap. J.* (in press).

XXV-14. Zellner, B., "Minor Planets and Related Objects, VIII, Deimos," *Astron. J.*, Vol. 77, p. 183, 1972.

XXV-15. Moore, H. J., Pike, R. J., and Ulrich, G. E., *Lunar Terrain and Transverse Data for Lunar Roving Vehicle Design Study*, U.S. Geological Survey Report, 1969.

XXV-16. Soter, S., *The Dust Belts of Mars*, Center for Radiophysics and Space Research, Report 462, Cornell University, Ithaca, New York (Paper II).

XXV-17. Gault, D. E., and Wedekind, J. A., "The Destruction of Tektites by Micrometeoroid Impact," *J. Geophys. Res.*, Vol. 74, p. 6780, 1969.

XXV-18. Öpik, E. J., "The Stray Bodies in the Solar System," Part 1, *Advan. Astron. Astrophys.*, Vol. 2, p. 219, 1963.

XXV-19. Anders, E., "Origin, Age, and Composition of Meteorites," *Space Sci. Rev.*, Vol. 3, p. 583, 1964.

XXV-20. Hartmann, W. K., "Lunar Cratering Chronology," *Icarus*, Vol. 13, p. 299, 1970.

XXV-21. Fish, R. A., Goles, G. C., and Anders, E., "The Record in Meteorites III. On the Development of Meteorites in Asteroidal Bodies," *Astrophys. J.*, Vol. 132, p. 243, 1960.

XXV-22. Sonnett, C. P., Colburn, D. S., and Schwartz, K., "Electrical Heating of Meteorite Parent Bodies and Planets by Dynamo Induction From a Pre-main Sequence T. Tauri Solar Wind," *Nature*, Vol. 219, p. 924, 1968.

XXV-23. Goldreich, P., and Soter, S., "Q in the Solar System," *Icarus*, Vol. 5, p. 375, 1966.

XXV-24. Smith, B. A., "Phobos: Preliminary Results From Mariner 7," *Science*, Vol. 168, p. 828, 1970.

XXV-25. Egan, W., Veverka, J., Noland, M., and Hilgeman, T., "Photometric and Polarimetric Properties of the Bruderheim Meteorite," *Icarus* (in press).

XXV-26. Egan, W., "Polarimetric and Photometric Simulation of the Martian Surface," *Icarus*, Vol. 10, p. 223, 1969.

References (contd)

XXV-27. O'Leary, B. T., and Briggs, F., "Optical Properties of the Apollo 11 Lunar Samples," *J. Geophys Res.*, Vol. 75, p. 6532, 1970.

XXV-28. Hapke, B., "Lunar Surface Properties Inferred From Optical Properties," *Science*, Vol. 159, p. 76, 1968.

XXV-29. Shorthill, R. W., Saari, J. M., and Baird, F. E., *Photometric Properties of Selected Lunar Areas*, NASA Report CR-1429, 1969.

XXV-30. Halajian, J. D., *Photometric Measurements of Simulated Lunar Surfaces*, Grumman Research Dept. Rept. RE-219, 1965.

Acknowledgments

XXVI. The *Mariner* 9 Celestial Mechanics Experiment: A Status Report

Jack Lorell

Jet Propulsion Laboratory/California Institute of Technology, Pasadena, California 91103

Irwin I. Shapiro

Department of Earth and Planetary Sciences
Massachusetts Institute of Technology, Cambridge, Massachusetts 02139

A. Gravity Field and Related Constants

There are two main objectives in the Mars gravity-field analysis. The first is to generate a picture of the gravity field which can be used in conjunction with other types of data to elucidate the interior, surface structure, and history of Mars. The second is to aid the orbit determination aspect of the relativity experiment, as discussed in the next part of this section.

It has been found that the Martian gravity field is rougher (i.e., the harmonic expansion coefficients are larger) than had been expected by about an order of magnitude. Thus, to represent the field to a given accuracy, it is necessary to include a larger number of terms in the spherical harmonic expansion than had been planned. As a result, in the analysis, one is called upon to simultaneously estimate upward of 50 parameters. Because of this large number, and because of the large correlations exhibited by these parameters in the estimator, the models of the Mars gravity potential are very sensitive to inadequacies in the mathematical model of the Doppler shift of the spacecraft's radio signal. Among the known error sources are the unmodeled spacecraft gas leaks, uncertainty in the direct solar radiation pressure, effects of Mars radiation (reflected and infrared), unmodeled effects of the propagation medium, uncertainties in the tracking station locations, and, perhaps most important, the unmodeled (high-degree harmonics) portion of the gravity field.

A multipronged attack has been made in an effort to extract from the data a Mars gravity model of reasonable fidelity. Various spherical harmonic models have been made ranging through degree and order 10, and often including several zonal harmonics beyond the basic size of the model.

In addition to the spherical harmonic analysis, a parallel effort using a surface mass representation is being pursued with some success. This technique involves the differentiation of Doppler residuals for acceleration contours, similar to the technique used to detect lunar mascons. Preliminary conclusions from the surface-mass studies include the following:

(1) There is one very large gravity high covering the region of Nix Olympica and the three peaks to the

east 110° longitude. This correlates well with earlier gravity results using the classical spherical harmonic approach, and with the large topographic high from radar analysis. The anomaly is 17 times greater than any on Earth and implies either that Mars must have a crust much thicker than that of Earth to support such loading or that surface materials must be stronger or that the anomaly had its origin in fairly recent geologic history.

2) There are no large negative gravity anomalies comparable to the positive

3) The large 3000-km canyon seems to originate in a gravity high and end in a gravity low. This would be consistent with any hypothesis for fluid flow in the channel.

4) No mascon was detected in the Hellas basin although a feature of this size, if it existed, should be within resolution of the data.

The emerging picture of the Martian gravity field can be characterized as follows (Ref. XXVI-1):

The gravity field of Mars is considerably rougher than the fields of either Earth or the Moon. The largest positive gravity anomaly uncovered is in the Tharsis region, which is also topographically high and geologically unusual. The best determined coefficients of the harmonic expansion of the gravitational potential are:

$$J_2 = (1.96 \pm 0.01) \times 10^{-3}$$
$$C_{22} = (5.1 \pm 0.2) \times 10^{-5}$$

and

$$S_{22} = (3.1 \pm 0.2) \times 10^{-5}$$

The other coefficients have not been well determined on an individual basis, but the ensemble yields a useful model for the gravity field for all longitudes in the vicinity of 23°S latitude, which corresponds to the periapsis position for the orbiter. However, the post-fit residuals show systematic trends, especially near periapsis where the residuals often reach the order of 1 Hz.

In regard to the other Martian quantities of interest to which the *Mariner 9* data are sensitive, we find (Ref. XXVI-1):

The value obtained for the ratio of the Sun's mass to that of Mars (3 098 720 ±70 M_s^{-1}) is in good agreement with previous determinations from *Mariner* flyby trajectories. The direction found for the rotational pole of Mars referred to the mean equinox and equator of 1950.0 is characterized by $\alpha = 317.3 \pm 0.2$, $\delta = 52.7 \pm 0.2$. This result is in excellent agreement with Sinclair's (Ref. XXVI-2) recently determined from Earth-based observations of Mars satellites but differs by about 0.5 from the previously accepted value. Other important physical constants that have either been refined or confirmed by inference from the harmonic coefficients derived from the *Mariner 9* data include 1) dynamical flattening $f = 5.24 \pm 0.02 \times 10^{-3}$, 2) the maximum principal moment of inertia $C = 0.373 \pm 0.006 M_M R^2$, and 3) the period of precession of Mars' pole $P = (1.73 \pm 0.03) \times 10^5$ years, corresponding to a rate of precession of 7.4 sec of arc per year. (The subscript M denotes Mars.)

B. Test of General Relativity

In terms of the Eddington–Robertson parameter γ, general relativity ($\gamma = 1.0$) predicts an Earth–Mars round-trip time delay in excess of that of classical physics which is proportional to $(1 + \gamma)/2$. At Mars superior conjunction, this relativistic delay is nearly 200 μsec. For the Brans-Dicke scalar-tensor theory, with Dicke's estimate of the free parameter characterizing the scalar admixture $(1 + \gamma)/2 = 0.94$ and the relativistic delay is 6% less than that predicted by Einstein's theory. A main object of the relativity experiment is to distinguish between the two theories by estimating γ.

For the relativity experiment, the ranging data (i.e. round-trip signal travel times) are the primary data in that they provide information most directly related to $(1 + \gamma)/2$. As the processing of the ranging data requires a good knowledge of the spacecraft orbit with respect to Mars, it is also essential to have Doppler data over the orbits of interest. Differenced range versus integrated Doppler (DRVID) is a derived data type used to calibrate both the range and Doppler for charged-particle effects. These DRVID data are also being used to study the dynamics of the solar corona and the interplanetary medium (Ref. XXVI-3; also see Section XXXV of this Report).

The range and Doppler data are being analyzed using two different methods for the relativity experiment. One uses a least-squares differential correction processor to determine the values of the relativity parameter γ, the solar corona parameters B and ϵ, together with

spacecraft and planetary ephemeris parameters that best model the data. The other method uses an intermediate stage of data processing in which Doppler data are used in short arcs of one or a few days, together with the associated ranging points to determine Earth-Mars distance. Thus with each spacecraft range measurement there is associated a normal point which is essentially the Earth-Mars distance determined from that range point and the observed spacecraft orbit. Once the normal points are obtained, the relativity parameters are determined by a differential correction processor in which the relativity, solar corona, and planetary ephemeris parameters are estimated, but the gravity field coefficients and spacecraft orbit parameters are no longer involved.

A model of the mean effect of the solar corona on the observable is included in the analysis. However, because the corona exhibits large unmodeled fluctuations about

the mean which degrade the accuracy, the data taken nearest superior conjunction are downweighted.

An essential part of the relativity analysis is the determination and use of precise planetary ephemerides. This involves the correlation of all available optical, radar, and spacecraft data that have been accumulated in past years.

Because of the large number of small unresolved problems, it is too early to give a meaningful estimate of $1 + \gamma/2$. However, some members of the celestial mechanics team are guardedly optimistic that the final uncertainty will be in the neighborhood of 0.01, which would represent a several-fold improvement over the present accuracy in the determination of this quantity, and would serve to distinguish reliably between the predictions from general relativity and those from the Brans–Dicke theory.

References

XXVI-1. Lorell, J., Born, G. H., Christensen, E. J., Esposito, P. B., Jordan, J. F., Laing, P. A., Sjogren, W. L., Wong, S. K., Reasenberg, R. D., Shapiro, I. I., and Slater, G. L. "Gravity Fields of Mars from Mariner 9 Tracking Data," *Icarus*, Vol. 18, p. 304, 1973.

XXVI-2. Sinclair, A. T., "The Motions of the Satellites of Mars," *Mon. Not. Roy. Astron. Soc.*, Vol. 155, p. 259, 1972.

XXVI-3. Callahan, P. S., "Plasma Column Changes at Small Solar Elongations," *J. Geophys. Res.*, Vol. 78, 1973.

Acknowledgments

XXVII. Mars Gravity Field Via the
Short Data Arcs

W. L. Sjogren, J. Lorell, S. J. Reinbo. J, and R. N. Wimberly
Jet Propulsion Laboratory/California Institute of Technology, Pasadena, California 91103

The classical approach of obtaining planetary gravity fields uses long arcs of satellite tracking data and estimates the coefficients for a spherical harmonic expansion (Refs. XXVII-1 through XXVII-3). However, the analysis presented utilizes the high-frequency variations in relatively short arcs of data: each arc is analyzed independently, and results for each are plotted on a composite. Although these results are more qualitative than quantitative, they can be scaled to give some quantitative values. The analysis technique is essentially the same as that used on lunar orbit data to study the mascons and other lunar gravity anomalies (Refs. XXVII-4 through XXVII-6). The detail that is so evident in the lunar data cannot be obtained with the Mars data because of the high spacecraft altitudes (i.e., 10 to 30 km for the Moon, 1650 to 5000 km for Mars). However, there are definite regions that do correlate with broad topography and allow geophysical interpretation.

There is also another short-arc analysis scheme. Data reduction using this method has just begun, and it appears that these results will be more realistic than the map reported in this article. It yields a surface mass distribution via point masses. Some preliminary values are reported here.

A. Data

The data were derived from spacecraft velocity observations (Doppler) taken 1 hr before periapsis to 1 hr after periapsis. The sampling rate was one observation per minute (i.e., 120 points for each independent arc), having a one-sigma noise level of 1 mm/sec. The special spacecraft orbital geometry required for this experiment was not available until May and June 1972, when the orbital plane was almost parallel with the Earth–Mars line, and the Earth–Mars periapsis angle was near minimum (Fig. XXVII-1). This geometry allowed the Doppler observations to measure almost directly the vertical component of gravity. Figure XXVII-2 shows the gravitational forces acting on the spacecraft for a surface mass anomaly. If one places the Earth near the top of Fig. XXVII-2 and in the plane of the paper, one clearly sees that the vertical accelerations are almost directly measured by the Doppler observables (at least for features near the Earth–Mars line).
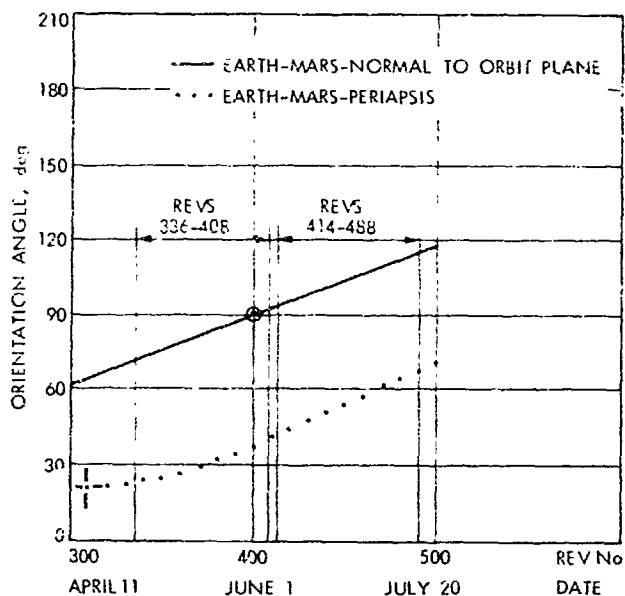
Fig. XXVII-1. Orbit geometry.

Fig. XXVII-2. Gravity force from a surface mass anomaly.

Two independent data blocks were acquired, each covering a period of 37 days. During this interval, however, not all tracking data were obtained because of antenna commitments to other projects. Since only the 64-m antenna at Goldstone can lock on to the weak signal from the spacecraft at a distance of 2.4 AU, data could be acquired only every other revolution. Only 21 tracks out of a possible 37 tracks (57%) in the first block, and 26 out of 37 (70%) in the second block actually were

acquired. The distribution of orbital ground tracks over the Martian surface for which data were obtained is shown in Figs. XXVII-3 and XXVII-4. Each curved arc of unreadable numbers represents the data from an orbital track.

B. Reduction and Results

Each orbit of data (the 2 hr of data near periapsis) was analyzed as an independent set. An orbit determination program with all known dynamical and physical phenomena was used in the calculation of the Doppler measurements. For the Mars gravity field, only the cen-
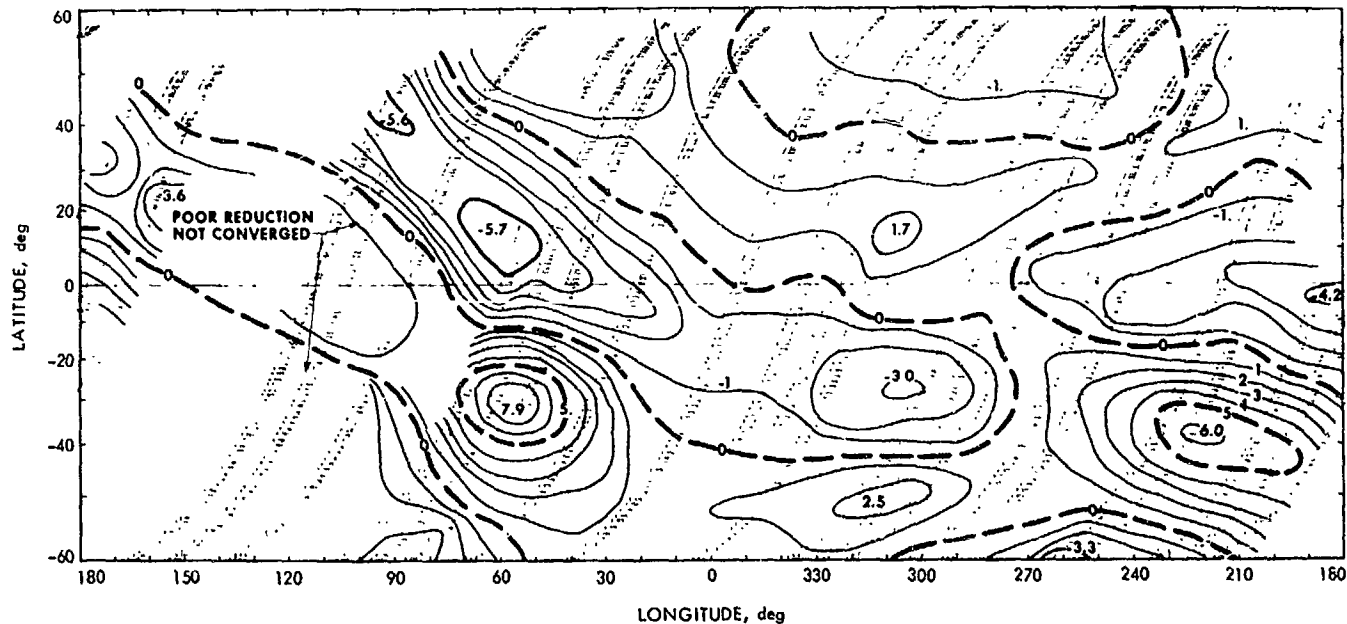
Fig. XXVII-3. Accelerations for orbital tracks during revolutions 336 to 408.
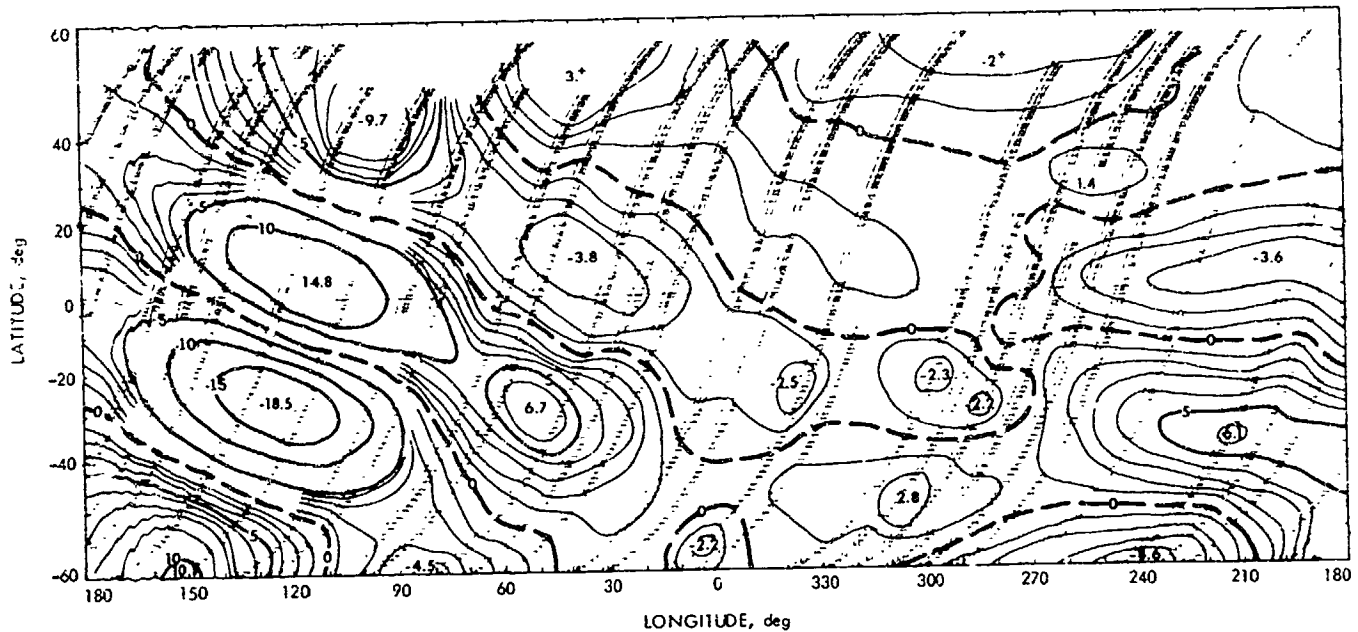
Fig. XXVII-4. Accelerations for orbital tracks during revolutions 414 to 488.

tral term and the J_2 oblateness term were included. ($J_2 = 0.197 \times 10^{-2}$; $GM = 42828.439$ km³/sec².) Then an iterative least-squares solution was obtained for the best spacecraft position and velocity at epoch. The Doppler residuals remaining after the solution were attributed to Martian gravity-field variations over and above the J_2 term (Fig. XXVII-5). The residuals were next fit with patched cubic splines having second derivatives continuous at the patch points. These were analytically differentiated, providing line-of-sight accelerations. A typical portion (30 min of an orbit of data) is shown in Fig. XXVII-6. Acceleration results from each orbit as well as the appropriate spacecraft positions were stored on magnetic tapes. When all orbits had been thoroughly ex-

amined (i.e., blunder points removed and proper spline fits obtained), all accelerations from a block of orbits were plotted on a Mercator projection sheet that could overlay a map of Mars. This intermediate printout is shown in Figs. XXVII-3 and XXVII-4. The most sensitive region was periapsis (24°S latitude), where the altitude was 1650 km. At 55°N the altitude was 5000 km, and at 60°S the altitude was 2300 km. No correction was made to the accelerations to normalize them to a uniform sur-
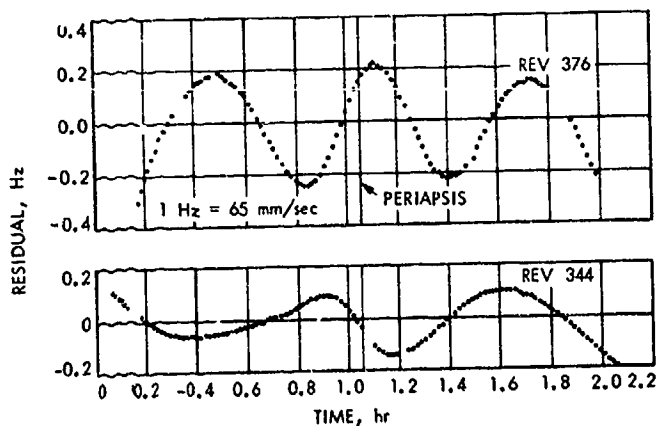
Fig. XXVII-5. Typical Doppler residuals.
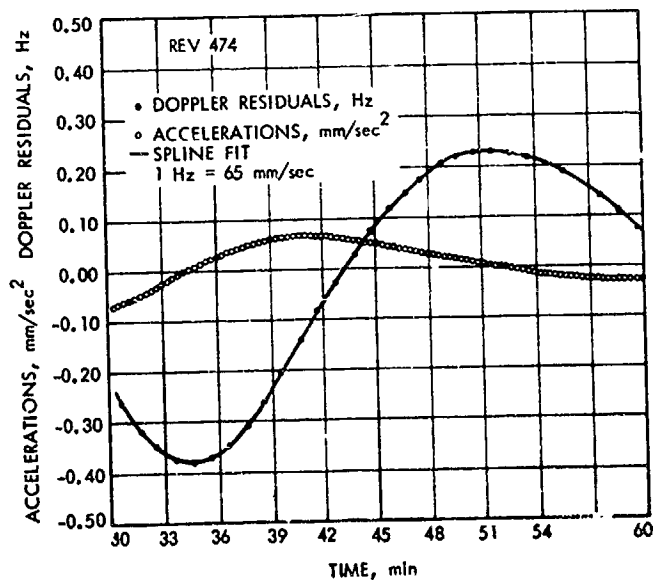
Fig. XXVII-6. Typical spline fit for acceleration data.

face height. The acceleration sheet was then contoured, and the contours in milligals were superimposed on a Martian map (Fig. XXVII-7). Although the coverage from the first block is not as complete as the second, the acceleration maps (Figs. XXVII-3 and XXVII-4) are similar, thus showing consistency of the data and the reduction technique.

Another contour map of the second block of data (revolutions 414 to 488) was generated using a third-degree potential model[1] as the basic reference. The second- and third-degree terms used in this model are the best determined coefficients so far obtained in the harmonic analysis of the *Mariner* 9 tracking data. When Figs. XXVII-7 and XXVII-8 are compared, striking differences can be seen. The third-order model has reduced the Tharsis anomaly as expected; however, is doing so, it has introduced variations in the region $180°$ in longitude from the Tharsis area, which previously was smoother using the J_2 reference. Therefore, since spurious variations from the third-degree model developed, it seems that, for more realistic interpretation of results, the J_2 reference (Fig. XXVII-7) should be adopted.

To give some guidelines on the interpretation and conclusion to be made from these results, a study was made using simulated data, which were then processed in precisely the same manner as the real data reduction. The primary observations from the study were that:

(1) Only 30% of the perturbing force is detected.

(2) A large negative acceleration is introduced near periapsis in the case where only one positive anomaly is placed beyond periapsis (i.e., $30°$ farther along track).

(3) The maximum positive acceleration locations are near the location of the perturbing masses.

Another study, which at present has only a few limited results but may provide a good estimate of a surface mass distribution in the near future, can now provide some additional confidence in the results shown in Fig. XXVII-7. The approach of the study is to estimate dynamically surface mass points directly beneath the spacecraft track as well as spacecraft state parameters using the same data arcs previously described. The residuals approach the random noise of 1 mm/sec, and the mass values reflect a surface distribution. Results from only five different data arc reductions are available so far, and these are displayed in Table XXVII-1. Lines 1 through 4 show that consistency in the mass values is clearly evident when orbit arcs are overlapping. Again, consistency is good even with a $10°$ separation between

---

[1] $J_2 = 0.0019644$, $C_{22} = -0.5508 \times 10^{-3}$, $S_{22} = 0.3142 \times 10^{-3}$, $C_{31} = 0.0478 \times 10^{-3}$, $S_{31} = 0.2662 \times 10^{-3}$, $C_{33} = 0.0496 \times 10^{-3}$, $S_{33} = 0.0355 \times 10^{-3}$. These values are based on results of the gravity analysis, and differ only slightly from those reported by Lorell et al. (Ref. XXVII-7).
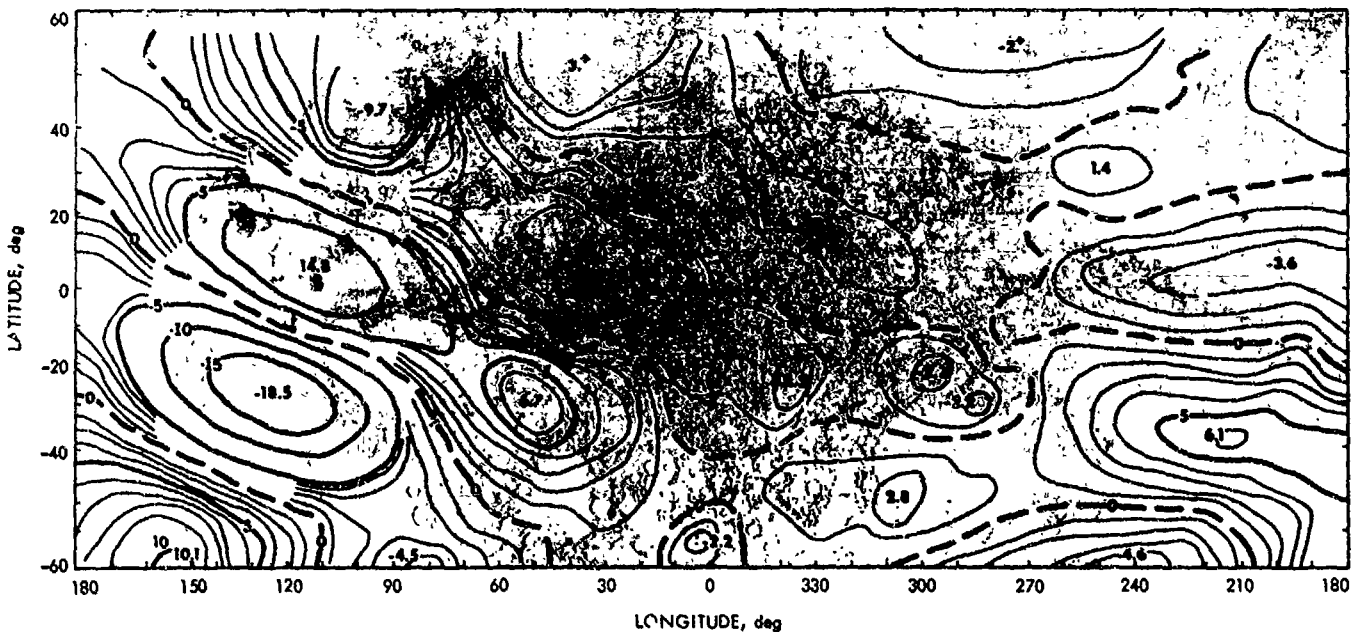
Fig. XXVII-7. Contours of acceleration data from revolutions 414 to 488 using a J_2 base (units: milligals; unnormalized for spacecraft altitude).
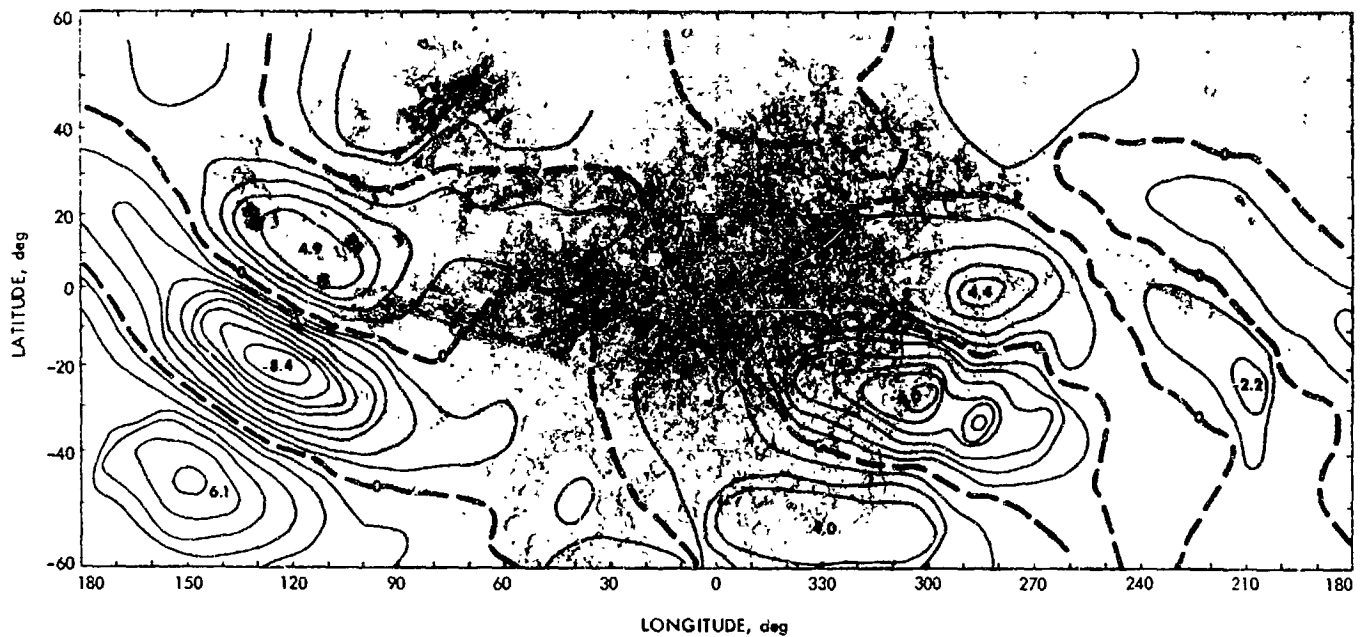
Fig. XXVII-8. Contours of acceleration data from revolutions 414 to 488 using a third-order base (units: milligals; unnormalized for spacecraft altitude).

Table XXVII-1. Surface mass[a] estimates

Line	Latitude, deg	Longitude, deg	Mass value[b] (first revolution)		Mass value[b] (second revolution)		Formal standard deviation	Remarks
1	−42	12	Rev 336	− 4.8	Rev 414	− 5.5	0.6	Central region,
2	−15	− 2		− 4.5		− 4.0	0.7	overlapping
3	23	−17		− 2.0		− 0.9	1.1	revolutions 336
4	43	−29		12.7		13.0	0.9	and 414
5	−40	130	Rev 388	14.0	Rev 468	7.1	0.9	Tharsis region,
6[c]	−10	120		76.0		76.8	1.1	orbits 39 days apart,
7[d]	12	105		95.4		87.9	1.0	orbits do not overlap,
8	40	90		73.9		67.1	2.4	10° separation, revolutions 388 and 468
9[e]	−42	−69	Rev 432	−11.6		—	0.6	
10	−25	−80		− 7.3		—	0.5	Hellas region, one
11	− 3	−86		− 8.4		—	0.5	orbit, revolution 432
12	17	−93		−10.6		—	0.7	

[a]All masses are point masses 100 km. below surface.

[b]Mass values are surface mass point estimates divided by total Martian mass × 10⁶.

[c]South Spot.

[d]North Spot.

[e]Hellas.

orbit tracks (lines 7 and 8). If one uses the 0.95×10^{-4} GM (line 7) and calculates an acceleration at the spacecraft altitude, the result is 65 milligals. Applying the fact that only 30% of the total perturbing force is detected in the Fig. XXVII-7 solution, the comparable value is 20 milligals. This seems to be within reasonable agreement with the 14.8 milligals shown on Fig. XXVII-7. However, the large negative regions (Fig. XXVII-7) north and south of the Tharsis anomaly are completely inconsistent with the surface mass estimate. These negatives must be considered erroneous and attributed to the least-squares smoothing process in analogy with the previously mentioned simulated data cases.

Another comparison of the Tharsis region can be obtained from Fig. XXVII-9 (Fig. 1 of Ref. XXVII-1), which shows the equivalent surface mass distribution obtained from harmonic analysis. The calculation of the amount of mass in the 2-km-high cone (25000-km-radius cone) centered at 120° longitude yields a value of 1.2×10^{-4} GM. This is in good agreement with Table XXVII-1 (lines 6 and 7, revolution 388).

We believe that the orientation of the Tharsis positive high to include the Nix Olympica area is real. The correlation with the large 300-km-long canyon running from

the gravity high to the gravity low at longitude 35° appears to be realistic also.

Continuing eastward, the gravity field seems to be relatively smooth with a high developing near 210° longitude. There are no surface mass estimates to compare for this high; however, there is one reduction west of it over the Hellas basin. As shown in Table XXVII-1 (lines 9 through 12), all masses are negative; therefore, it does not reveal Hellas as a mascon as one might suspect from lunar studies. The large positive anomaly at 240° longitude in Fig. XXVII-9 is not detected. This may be unreal in the spherical harmonic case, for the data sensitivity (i.e., high altitudes and occulted region) is low in this region, and to enable the good Tharsis fit an erroneous bulge may have been introduced.

Comparison with an Earth gravity field can be seen using Figs. XXVII-7 and XXVII-10 (Ref. XXVII-8). Remember that the Mars field shown in this figure is a factor of 3.3 too small and that it lies between 1650- and 5000-km altitudes. The falloff with altitude is not quite the inverse square, but that rule is close enough. For example, the largest Mars anomaly is about 50 milligals at 2200 km, whereas Earth's largest anomaly would be about 3 milligals. Mars definitely has a much larger gravity variation than Earth.
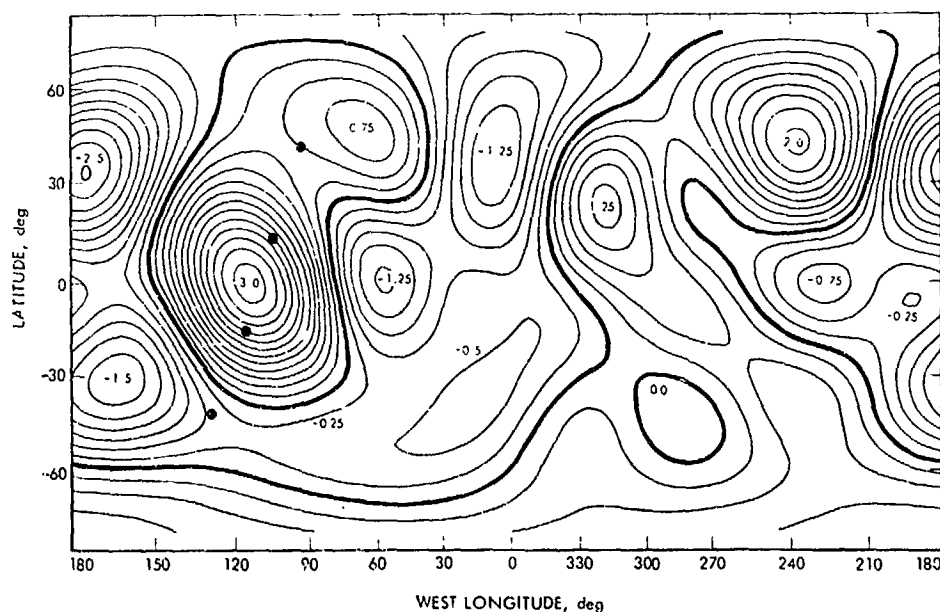
Fig. XXVII-9. Contours of equivalent surface height deduced from a sixth-degree spherical harmonic model for a Mars gravity field. (Contour interval is 250 m; units: kilometers.) Contours represent the deviations from sphericity of a uniformly dense body with the external potential given by the sixth-degree solution with the effect of J_2 omitted (Ref. XXVII-1).
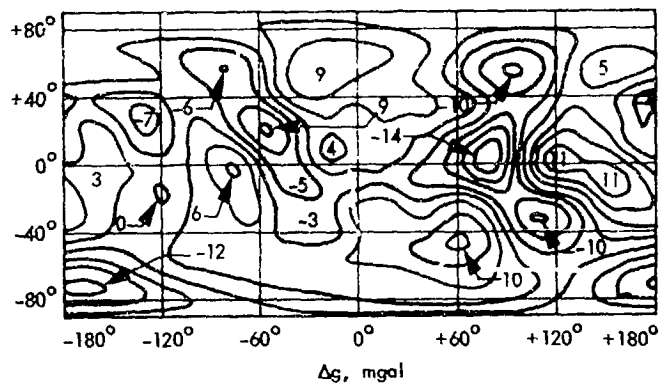
Δg AT 1000-km ELEVATION
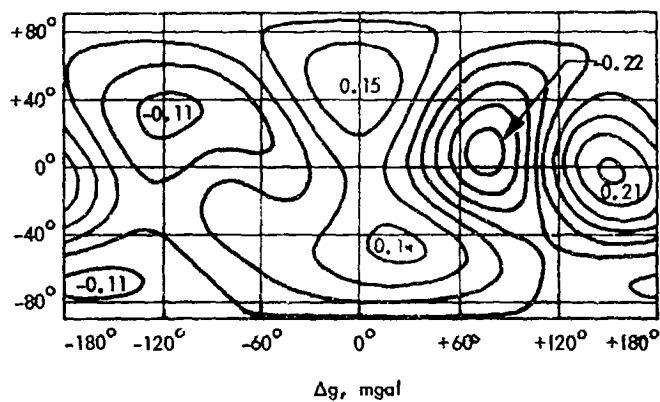
Δg AT 10,000-km ELEVATION

Fig. XXVII-10. Contours of acceleration at 1000-km elevation (top) and 10,000-km elevation (bottom) for Earth's gravity field (units: milligals; referenced to International Ellipsoid; see Ref. XXVII-8).

C. Summary

The final results of this reduction (Fig. XXVII-7) must be interpreted cautiously. The accelerations are qualita-tive at best because the positive amplitudes are a factor of 3.3 low, and the large negative anomalies are errone-ous. The resolution of features is on the order of 2000 km. The primary definitive statements that can be inferred are:

(1) There is one large gravity high covering the region of Nix Olympica and the three peaks to the east (~110° longitude). This is almost perfectly cor-related with the large radar peak results (Refs. XXVII-9 and XXVII-10) and the previous gravity results (Ref. XXVII-1). It has an amplitude of 50 milligals (above J_2 effect) at 2200-km altitude and implies a surface mass anomaly of approximately 1.0×10^{-4} GM_z or 6.4×10^{22} g. This anomaly is 17 times greater than any on Earth and implies that Mars must have a crust much thicker than that of Earth to support this load, or that surface materials must be much stronger, or that the anomaly has its origin in fairly recent geologic history.

(2) There are no large negative gravity anomalies com-parable to the positive.

(3) The large 3000-km canyon seems to originate in a gravity high and end in a gravity low. This would be consistent with any hypothesis for fluid flow in the channel.

(4) No mascon was detected in the Hellas basin although one its size, if it existed, should be within resolution of these data. The surface mass estimate yielded a negative anomaly of -0.12×10^{-4} GM_z or -7.7×10^{21} g.

(5) A more realistic gravity map should be forthcoming from our current work on the estimation of a grid of surface mass points.

References

XXVII-1. Lorell. J.. Born, G. H., Christensen. E. J., Jordan. J. F., Laing, P. A., Sjogren. W. L., Shapiro, I. I., Reasenberg. R. D., and Slater, G. L., "Mariner 9 Celestial Mechanics Experiment: Gravity Field and Pole Direction of Mars." *Science*, Vol. 175, p. 317, 1972.

XXVII-2. Michael. W. J.. Jr.. and Blackshear. W. T., "Recent P sults on the Mass, Gravitational Field and Moments of Inertia of the Moon," *The Moon*, Vol. 3, p. 388, 1972.

XXVII-3. Liu. A. S. and Laing. P.A., "Lunar Gravity Analysis From Long-Term Effects," *Science*, Vol. 172, p. 1017, 1971.

XXVII-4. Muller, P. M.. and W. L. Sjogren, "Mascons: Lunar Mass Concentrations," *Science*, Vol. 161, p. 680, 1968.

XXVII-5. Sjogren, W. L.. Gottlieb, P., Muller, P. M., and Wollenhaupt, W. R., "Lunar Gravity Via Apollo 14 Doppler Radio Tracking," *Science*, Vol. 175, p. 165, 1972.

XXVII-6. Sjogren, W. L., Gottlieb, P. Muller, P. M.. and Wollenhaupt, W. R., "S-Band Transponder Experiment, in *Apollo 15 Preliminary Science Report*, SP-289, p. 201, National Aeronautics and Space Administration, Washington, D.C., 1972.

XXVII-7. Lorell. J., Born, G.H., Christensen. E. J., Esposito, P. B., Jordan, J. F., Laing, P. A., Sjogren, W. L., Wong, S. K., Reasenberg, R. D., Shapiro, I. I., and Slater, G. L., "Gravity Field of Mars from Mariner 9 Tracking Data," *Icarus*, Vol. 18, No. 2, 1973.

XXVII-8. Strange, W. E., "Comparison with Surface Gravity," in *Geodetic Parameters for a 1966 Smithsonian Institution Standard Earth*, Vol. 3, edited by C. A. Lundquistand, G. Veis, Smithsonian Astrophysical Observatory Report 200, 1966.

XXVII-9. Pettengill, H., Rogers, A. E. E., and Shapiro, I. I., "Martian Craters and a Scarp as Seen by Radar," *Science*, Vol. 174, p. 1321, 1971.

XXVII-10. Downs, G. A., Goldstein. R. M., Green, R. R., and Morris, G. A., "Mars Radar Observations: A Preliminary Report," *Science*, Vol. 174, p. 1324, 1971.

Acknowledgments

XXVIII. Mars Gravity Derived From Long-Period Motion of *Mariner 9*

A. J. Ferrari and E. J. Christensen

Jet Propulsion Laboratory/California Institute of Technology, Pasadena, California 91103

The long-period motion of *Mariner 9* was perturbed by the non-central properties of the Martian mass distribution and by the disturbing effects of the Sun, solar radiation, and other planets. As expressions for both *n*-body and solar radiation perturbations are well known (Refs. XXVIII-1 and XXVIII-2), the long-period variations in the orbital elements can be adjusted to remove these effects. The resulting orbital element variations can, therefore, be ascribed to anomalous Martian gravity features.

The spherical harmonic coefficients in the gravity field of Mars are determined using a two-stage filtering process. In the first stage, a weighted least-squares orbit determination processor is applied to *Mariner 9* Doppler tracking data to estimate Kepler elements and rates. In the second stage, the Kepler element rates are used as input to another weighted least-squares processor that estimates gravity coefficients using the Lagrange perturbation equations. The novelty in this method is the fitting of element rates rather than the elements themselves. This procedure hopefully decouples the results from the effects of internal spacecraft dynamics such as venting, or at least makes them less sensitive.

This section presents the theory and equations that constitute the method. Some preliminary results are given which demonstrate the effectiveness of the method in determining gravity coefficients.

A. Mathematical Theory

The time dependence induced in each of the Kepler elements by perturbing effects is given by the Lagrange perturbation equations (Ref. XXVIII-3)

$$\frac{d\bar{k}}{dt} = \sum_{l,m} \sum_{p} \sum_{q} F(a, e, i) \left[C_{lm} \cos \psi_{lmpq} + S_{lm} \sin \psi_{lmpq} \right] + \dot{\bar{k}}_{\odot} + \dot{\bar{k}}_{\mathcal{U}} + \dot{\bar{k}}_{sR} \tag{1}$$

where $\bar{k}$ is the six-vector of orbital elements $(a, e, i, \Omega, \omega, M)$, $\bar{k}_{\odot}$, $\bar{k}_{\mathcal{U}}$, and $\bar{k}_{sR}$ are the solar gravity, Jupiter, and solar radiation pressure perturbations and

$$\psi_{lmpq} = (l - 2p)\,\omega + (l - 2p + q)\,M + m\,(\Omega - \theta) \tag{2}$$

where l and m are the degree and order of the spherical harmonic coefficients in the Mars gravity field, p and q are dummy indices, and θ is the sidereal time. Using first-order perturbation theory, solutions to these equations can be approximated. If only the variations generated from Mars non-central gravity are considered, the solution is a function of ψ_{lmpq}, and the harmonics in Equation (1) will generate almost periodic orbital element rates with the characteristics as given in Table XXVIII-1. Because the orbital period of *Mariner 9* and the rotation

Table XXVIII-1. Harmonic perturbations

Term	Type	Period
$(\ell - 2p + q)\,\dot{M}$	Short period	12 hr or less
$m\,(\dot{\Omega} - \dot{\theta})$	Medium period	24 hr or less
$(\ell - 2p)\,\dot{\omega}$	Long period	Years
$m = 0$ $(\ell - 2p) = 0$ $(\ell - 2p + q) = 0$	Secular	Constant rate

period of Mars are almost commensurable (1:2), a resonance condition exists for some of the short-period perturbations. The commensurability of rotation periods is defined by the relation

$$\frac{\dot{M}}{2} \approx -(\dot{\Omega} - \dot{\theta}) \qquad (3)$$

Mariner 9 was almost at the critical inclination (value of inclination at which the C_{20} secular rate of $\dot{\omega}$ is zero); hence, the rate of the argument of perifocus is small relative to $\dot{\Omega}$ and $\dot{M}$. Using the commensurability condition given by Equation (3) and $\dot{\omega} = 0$, the following relationship is obtained:

$$\dot{\psi} = \left[(\ell - 2p + q) - \frac{m}{2} \right] \dot{M} \qquad (4)$$

For resonance, $\dot{\psi} \approx 0$; hence:

$$(\ell - 2p + q) = \frac{m}{2} \qquad (5)$$

Any even-ordered harmonic in the gravity field generates terms that fulfill this relationship, and thus creates a resonance perturbation in the orbital elements (Ref. XXVIII-3). For the orbital configuration of *Mariner 9*, the dominant resonance perturbations have a period of about 19.5 days.

The long-period motion of *Mariner 9* is found by taking the average of the perturbations over the orbital period. All perturbation terms with a period of 12 hr or less average to zero. The resulting motion is characterized by secular and long-period variations generated by zonal harmonics, resonance variations from all even-degree tesserals, interacting medium-period/short-period variations from all odd-ordered tesserals, and long-period n-body perturbations.

B. First-Stage Filter

In this stage, batches of Doppler data are processed to determine the long-term time history of the *Mariner 9* orbital elements. The orbit determination strategy used was to perform a series of one-revolution fits using data beginning about 4 hr before apoapsis and continuing to 4 hr after apoapsis. The solution vector in all cases was the six-vector of orbital elements referenced to time of apoapsis. Analysis has shown that the osculating orbital elements at apoapsis are very near the average elements. Each solution produces an estimated state vector at apoapsis and an associated covariance matrix.

The trajectory model used in this filter includes the perturbation effects of C_{20} and those of the Sun, Jupiter, and solar radiation pressure.

$$\bar{k}(t) = \bar{k}(t_a) + \delta\bar{k}_{C_{20}} + \delta\bar{k}_{\odot} + \delta\bar{k}_{2\!\!1} + \delta\bar{k}_{sr} \qquad (6)$$

In this equation $\bar{k}(t_a)$ is the state vector at apoapsis; $\delta\bar{k}_{C_{20}}$, $\delta\bar{k}_{\odot}$, $\delta\bar{k}_{2\!\!1}$, $\delta\bar{k}_{sr}$ are the explicit expressions for the perturbation effects of C_{20}, the Sun, Jupiter, and solar radiation. The orbit determination process is repeated for each available revolution of data. The Kepler element rates are found by algebraically using three sets of apoapsis estimates.

For the purpose of preliminary investigation, inflight orbit determinations and predictions were used to generate pseudo element rates for *Mariner 9*. A history of the Kepler elements of the orbit (relative to Mars true equator of date), obtained from the *Mariner 9* Navigation Team, was used to describe the long-period variations in the orbit (see Figs. XXVIII-1 and XXVIII-2; Ref. XXVIII-4). These orbital element variations are obtained by sampling short-arc (one to six revolutions) orbit determination solutions once per satellite revolution at periapsis and apoapsis. Only the apoapsis history was used, as periapsis results were noisier because of the interaction between short- and long-period effects. The Kepler elements used span *Mariner* revolutions 5 through 502 (about 250 days). The semimajor axis and anomalistic period variations are referenced to an epoch value at apoapsis 5. In order to show periodic variations on this scale, the remaining elements are referenced to two different epochs: one at apoapsis 5 and one at apoapsis 95. (Reference values are given in Table XXVII-2.)

An average error in the estimate for these orbital elements is:

$$\delta a = 0.3 \text{ km}$$

$$\left.\begin{array}{l} \delta e \; - \; 10^{-} \\ \delta i \; -- \; 0.001 \\ \delta \Omega \; = \; 0.001 \\ \delta \omega \; = \; 0.001 \\ \delta M \; = \; 5 \times 10^{-6} \end{array}\right\} \text{radians}$$

As can be seen from the figures, the orientation angles i, Ω, ω possess discontinuities between adjacent solutions. These irregularities are a manifestation of observability
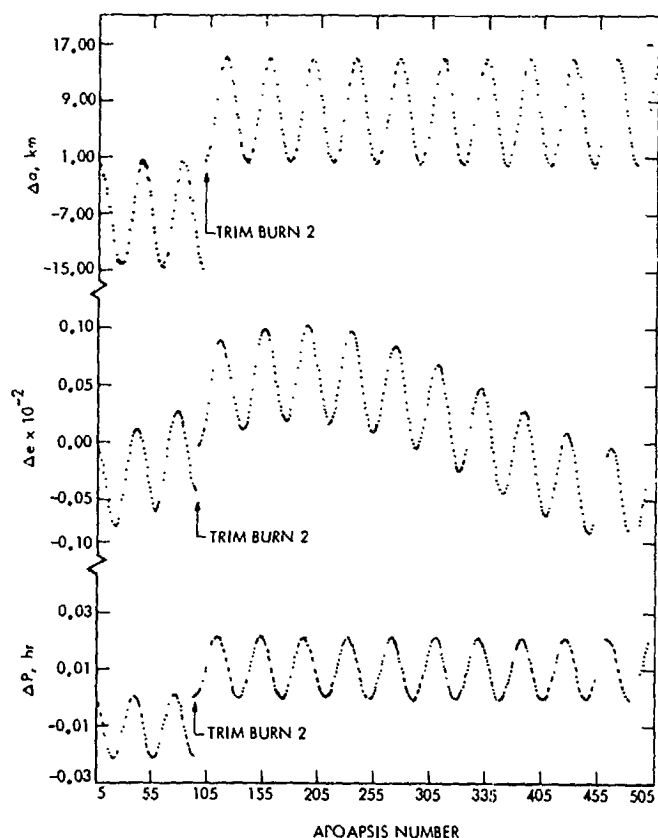
Fig. XXVIII-1. In-plane orbital elements.

Table XXVIII-2. Reference values

Apoapsis 5	Apoapsis 95
$a = 12636.91$ km	$e = 0.6009897$
$P = 11.98028$ hr	$i = 64°3845$
$e = 0.621734$	$\Omega = 34°1737$
$i = 64°7257$	$\omega = -25°9870$
$\Omega = 42°679$	
$\omega = -24°3022$	
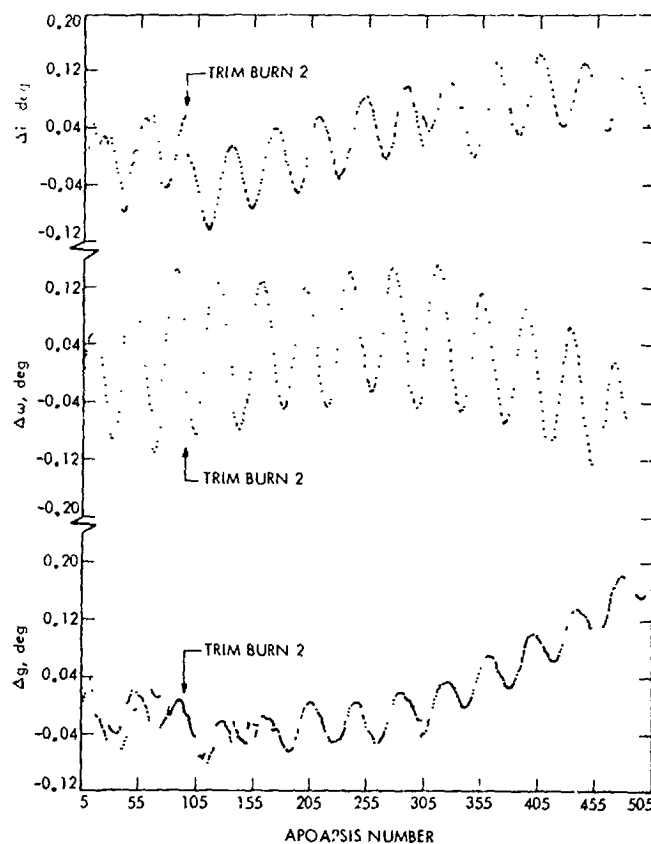
Fig. XXVIII-2. Orientation angles relative to Mars true equator.

problems associated with node in the plane of the sky determination.

Pseudo rates were generated by using *Mariner 9* apoapsis history as the average value orbital elements. The psuedo rates were formed as:

$$\dot{\bar{k}}(A_{N+2}) = \frac{\bar{k}(A_{N+1}) - \bar{k}(A_N)}{4P} \tag{7}$$

where $\bar{k}(A_N)$ is the value of the orbital element state at apoapsis N, and P is the anomalistic period. These calculated element rates contain n-body and solar pressure effects which must be removed so that remaining Kepler element rates $\dot{\bar{k}}_{\dagger}$ are ascribed to the non-central part of Mars gravity. The corrected orbital element rates are found as:

$$\dot{\bar{k}}_g = \dot{\bar{k}} - \dot{\bar{k}}_\odot - \dot{\bar{k}}_\gamma - \dot{\bar{k}}_{sp} \tag{8}$$

The pseudo long-term variations obtained for *Mariner 9* orbital elements are shown in Fig. XXVIII-3. These element rates have been edited to remove points derived across the trim maneuver, and others of obvious irregular
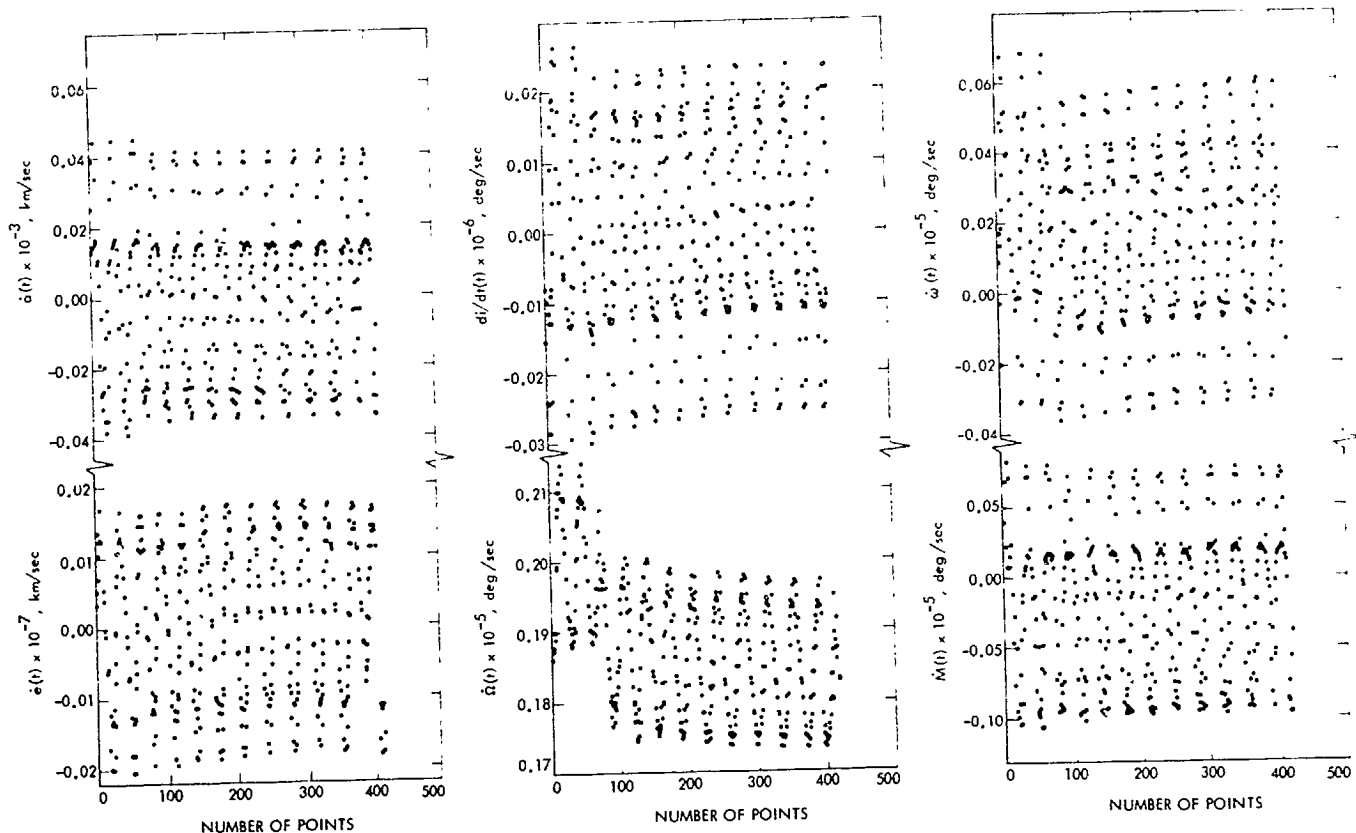
Fig. XXVIII-3. Orbital element rate variations.

character. An examination of these variations reveals two distinct periodic effects. Analysis has shown that the apparent presence of two periodic variations is caused by short- and medium-period interactions arising from the odd-ordered tesserals in the Mars gravity.

The orbital element rates are simultaneously processed to obtain gravity coefficients. Because the input to the second-stage filter consists of six different quantities, a weighting matrix is required to define the relative accuracies of each of the rates. The weighting matrix for the orbital element rates, W, is a (6×6) matrix having the following form (Ref. XXVIII-5):

$$W^{-1} = \begin{bmatrix} \sigma_a^2 & \tau_{12} & \tau_{13} & \cdots & \tau_{16} \\ \tau_{21} & \sigma_e^2 & \tau_{23} & \cdots & \tau_{26} \\ \cdot & & & & \cdot \\ \cdot & & & & \cdot \\ \cdot & & & & \cdot \\ \tau_{61} & \tau_{62} & \tau_{63} & \cdots & \sigma_M^2 \end{bmatrix} \quad (9)$$

where $\sigma_{\dot{k}}^2$ is the error variance among the rates and τ_{ij} is the covariance. Approximate weighting matrices for the element rates were obtained by transforming orbital element covariance matrices into rate matrices as follows.

$$W^{-1} = \text{cov } \dot{\bar{k}}(A_{N+2}) \approx \frac{1}{16p^2} \left[\text{cov } \bar{k}(A_{N+1}) + \text{cov } \bar{k}(A_N) \right] \quad (10)$$

In calculating this weighting matrix, cross-product terms were assumed to be zero.

C. Second-Stage Filter

The gravity field determination is performed in a second weighted least-squares filter that uses as input the Kepler element rates, the estimated Kepler elements, and a weighting matrix, and outputs a set of spherical harmonic coefficients (see Fig. XXVIII-4). The perturbation equations for Mars gravity are of the form:

$$\dot{\bar{k}}_d = \bar{f}(\bar{k}, \bar{p}, t) \quad (11)$$

$$\hspace{6cm} (14)$$

where m ... ... dons for the second
... ...

$$\hspace{2cm} (15)$$

... Projected ...

... ...

$C \quad 0.1963 \times 10 \qquad \sigma \quad 0.12 \quad 10$

$C_{..} \quad -0.5180 \times 10^{-4} \qquad \sigma \quad 0.13 \times 10$

$S_{..} \quad 0.3560 \times 10 \qquad \sigma = 0.135 \times 10$

The values of these coefficients are in good agreement with results obtained using the direct method (Ref. XXVIII-9).

Solutions obtained thus far result in unrealistically large magnitudes for the estimated higher-degree zone harmonics. Analysis has shown that the partial derivatives

(sensitivity) of these zonal terms are of the form:

$$\frac{\dot{k}}{C_i} \quad \bar{f}(a,e,i) \begin{Bmatrix} \cos i \quad 2\omega \\ \\ \sin i \quad 2\omega \end{Bmatrix} \quad (16)$$

Under normal orbital conditions (noncritical inclination orbits), for the case of one satellite, the variation induced in these partial derivatives arises almost entirely from the perifocus motion. However, for *Mariner 9* the total variation in the argument of perifocus over 250 days is only $\Delta\omega \approx 2.5$. Consequently, all of these partial derivatives are nearly constant. Under this condition the separation of long-term zonal effects becomes difficult. Potential solutions are being investigated in the areas of improved data weighting schemes and inversion methods for numerically ill-conditioned matrices.

References

XXVIII-1. Lorell, J., and Liu, A., *Method of Averages Expansion for Artificial Satellite Application*, Technical Report 32-1513, Jet Propulsion Laboratory, Pasadena, Calif., 1971.

XXVIII-2. Kozai, Y., *Effects of Solar Radiation Pressure on the Motion of an Artificial Satellite*, Smithsonian Institution Special Report No. 56, 1961.

XXVIII-3. Kaula, W. M., *Theory of Satellite Geodesy*, Blaisdell Publishing Co., Waltham, Mass., 1966.

XXVIII-4. Born, G. H., Christensen, E. J., Ferrari, A. J., Jordan, J. F., and Reinbold, S. J., *The Determination of the Satellite Orbit of Mariner 9*, paper presented at AIAA/AAS Astrodynamics Conference, Palo Alto, Calif., 1972.

XXVIII-5. Battin, R. H., *Astronautical Guidance*, McGraw-Hill, New York, 1964.

XXVIII-6. Kozai, Y., "New Determination of Zonal Harmonic Coefficients in the Earth's Gravitational Potential," *Pub. Astron. Soc. Japan*, Vol. 16, 1964.

XXVIII-7. Lorell, J., "Lunar Orbiter Gravity Analysis," *The Moon*, Vol. 1, p. 190, 1970.

XXVIII-8. Ferrari, A. J., "An Empirical Derived Lunar Gravity Field," *The Moon*, Vol. 3, p. 390, 1972.

XXVIII-9. Lorell, J., Born, G., Christensen, E., Esposito, P., Jordan, J., Laing, P., Sjorgren, W., Wong, S., Reasenberg, R., Shapiro, I., and Slater, G., "Gravity Field of Mars From Mariner 9 Tracking Data," *Icarus*, Vol. 18, No. 2, 1973.

XXIX. Data Acquisition and Editing for the Celestial Mechanics Experiment

W. L. Martin, A. I. Zygielbaum, and J. W. Layland

Jet Propulsion Laboratory/California Institute of Technology, Pasadena, California 91103

R. Reasenberg

Massachusetts Institute of Technology, Cambridge, Massachusetts 02139

A. Doppler Subsystem

Figure XXIX-1 is a simplified block diagram of the radio tracking subsystem, in which the critical elements are the frequency standard and its distribution subsystem, as they ultimately limit the accuracy of both range and Doppler measurements. A rubidium vapor standard with a stability of a few parts in 10^{12} serves as the primary reference. After frequency multiplication to S-band and additional amplification, the carrier is transmitted to the spacecraft where a phase-locked receiver–transmitter system filters the signal, introduces a slight frequency shift, and retransmits it to the ground. Doppler is measured by comparing the received frequency with that currently being transmitted. The voltage output from the Doppler extractor, V_e (Ref. XXIX-1) is described by:

$$V_e = \cos\left[\frac{2\pi bf}{4}\int_{t_0}^{t}\left(\frac{2v}{c} + \frac{v^2}{c^2} + \alpha\right)dt\right] \quad (1)$$

where

b = transponder frequency multiplication ratio (240:221)

f = transmitted S-band carrier frequency

v = spacecraft topocentric range rate

c = velocity of light in a vacuum

α = columnar time rate of change of charged-particle density

$$\alpha = \frac{B}{cf^2}\left(\dot{I}_{up} + \frac{1}{b^2}\dot{I}_{dn}\right) \quad (2)$$

where

B = 40.31 weber/m^2

$\dot{I}_{up}$ = uplink columnar time rate of change of charged-particle density

$\dot{I}_{dn}$ = downlink columnar time rate of change of charged-particle density

Thus, the topocentric range rate is measured by a frequency shift on the RF carrier produced by the Doppler effect. Mechanization of the Doppler extractor requires that the sample be taken over some non-zero time interval. This amounts to measuring the range change occurring while the sample is being taken. Doppler data are collected as a cumulative cycle count and treated solely as a change in phase delay, as any attempt to convert these data to a change in range (meters) must necessarily involve assumptions regarding the propagation of radio waves.

B. Ranging Subsystem

Range (group delay) is obtained by counting cycles of the rubidium frequency standard which occur between the transmission and reception of an encoded signal. Range in this context is a measurement of elapsed time rather than distance, and, as with Doppler, attempts at conversion to the latter form must involve assumptions regarding the velocity of radio signals.

The sequential (Mu) ranging system measures the time required for an encoded signal to traverse the distance from ground station to spacecraft and to return. The machine is connected to and receives its instructions from a computer located at the tracking station. A direct teletype data link with the Jet Propulsion Laboratory allows real-time monitoring of the ranging data.

Operation is as follows: A squarewave range code, coherent with the transmitted carrier, is generated by applying a harmonic of the rubidium frequency standard to a binary counter. Each of 18 counter outputs is individually selectable for modulating the transmitter. The period t_n of the nth squarewave range code component is given by:

$$t_n = \frac{64 \times 2^n}{3f_s} \qquad (3)$$

where f_s is the synthesizer frequency, obtained from the frequency distribution system (Fig. XXIX-1).

The carrier, phase-modulated by the range code, is transmitted to the spacecraft where the radio subsystem demodulates the code. Thereafter, this signal is modulated on the new carrier frequency for return to the ground station. Upon arrival, the information present in the second IF (10 MHz) of the ground receiver is of the form (see Refs. XXIX-2 and XXIX-3):

$$V_r = \cos[\omega_i t + \phi'_m \cos(\gamma + \theta_0)] \qquad (4)$$

where

$V_r = $ voltage output from receiver's 10-MHz IF

$\omega_i = 2\pi \times 10_7$ (receiver IF carrier frequency)

$\phi'_m = $ spacecraft's modulation index

$\cos(\ ) = $ squarewave approximation of $\cos(\ )$;

$\qquad + 1$ if $\cos(\ ) > 0$; -1 if $\cos(\ ) < 0$

$\theta_0 = $ phase shift in modulation caused by spacecraft's range

$\gamma = $ perturbation of range code caused by spacecraft's velocity and charged-particle activity in medium

$$\gamma = \omega_m \int_{t_0}^{t} \left[\left(1 + \frac{v}{c} \right)^2 - \alpha \right] dt \qquad (5)$$

where $\omega_m = 2\pi f_m$, and f_m is the modulation frequency.
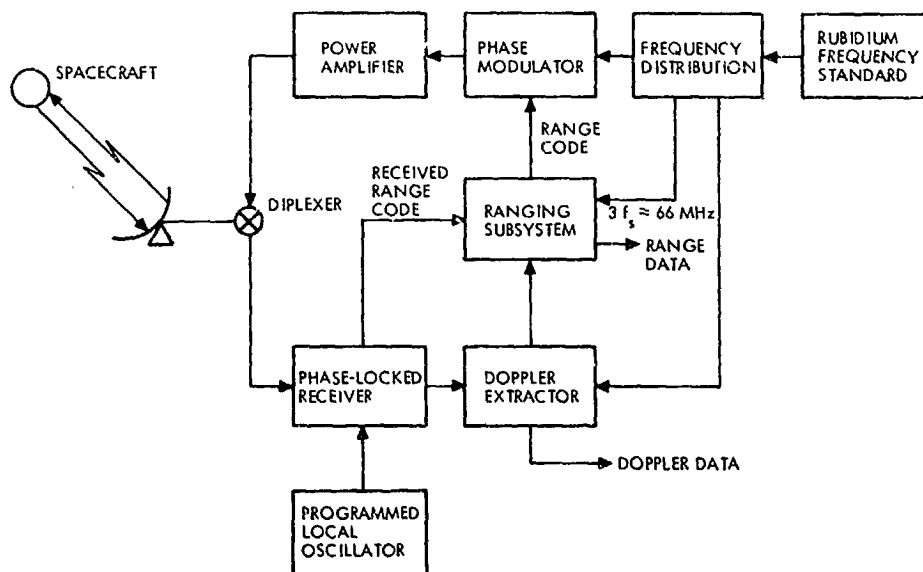
Fig. XXIX-1. Simplified radio tracking subsystem block diagram.

The comparison of Equations (1), (4), and (5) illustrates the effect of phase and group propagation velocities upon the respective signals. This difference forms the basis of the differenced range versus integrated Doppler (DRVID) measurements and provides a measure of the columnar time rate of change of the charged-particle density.

Range is measured by comparing the phase of the returning code with a locally generated model. A range acquisition comprises the measurement of a complete set of codes. Correlation detection is used to obtain a quantitative measure of the phase shift caused by the round-trip flight time. Ranging code component 1, whose period is approximately 2 μsec. determines the range measurement's precision, while the lower-frequency components serve to resolve ambiguities associated with the frequent repetition of the higher-frequency codes. An a priori estimate of range limits the required code length, or repetition period, to a value sufficient to resolve the error in that estimate (Ref. XXIX-2).

Measurement precision is dependent upon both system calibration and signal conditions. Before launch, the time delay in the spacecraft's radio is carefully calibrated over a variety of signal and temperature conditions. Daily ground equipment calibration, when used together with adjustments to compensate for the delay caused by the spacecraft's electronics, ensures that the errors contributed by these sources do not exceed a few meters (Ref. XXIX-3).

An additional error in the range measurement is introduced by the additive noise. As the ranging signal-to-noise ratio becomes poorer, the integration, or averaging time, must be increased to maintain a constant level of uncertainty. Figure XXIX-2 shows the predicted two-way range error for several integration times and signal conditions. During the *Mariner 9* mission, the received ranging power varied from about −185 dBm to a minimum of −205 dBm. Integration times were selected to keep the range uncertainty less than 100 nsec (15 m) and preferably less than 30 nsec (5 m).

C. Special Adaptive Ranging Program

The ranging system is controlled and operated by a medium-scale digital computer, the Xerox Data Systems 920. The range calculations and all interface functions are accomplished by appropriate software. The original system software used during the *Mariner 6* and 7 missions was oriented toward hardware checkout rather than mission support. This program was capable of only a single ten-component acquisition with an indefinite number of redeterminations of the highest-frequency code phase. If the acquisition failed, a new acquisition could be initiated only by stopping and restarting the program, thereby losing data for one round-trip light time. A mission-oriented software system dubbed "Super Mu" was designed specifically to support the *Mariner 9* relativity experiment.

The fundamental distinction between Super Mu and previous programs is the ability to "pipe-line" data acquisitions. Because of the long round-trip light time, several complete acquisition sequences can be strung in the Goldstone–spacecraft–Goldstone ray path. Each time the program initiates a transmit sequence, it sets a time flag for one round-trip light time later in the program's scheduler. At this time, the acquisition receive sequence is started. The program is capable of pipelining up to 50 acquisitions. This feature is especially important during superior conjunction when, because of weak signals and high system noise temperatures, the probability of a successful acquisition is small.

Four major operator supplied parameters ($T1$, $T2$, CR, and CT) determine the operating characteristic of Super Mu. $T1$ is the integration time for phase determination of the first, the highest-frequency, component. All other components are integrated for time $T2$. $T1$ thus estab-
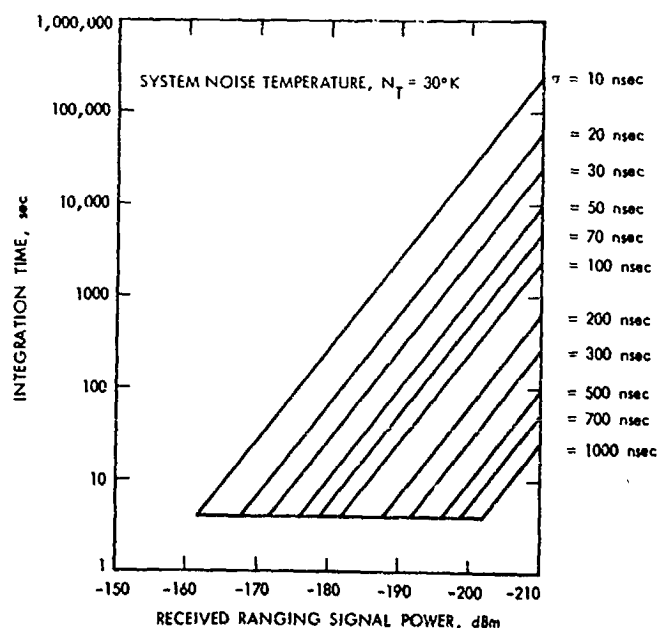
Fig. XXIX-2. Predicted two-way range error.

lishes a bound on the measurement precision (Fig. XXIX-2), while $T2$ establishes the probability of a successful acquisition. The range ambiguity is determined by the number of code components to be transmitted CT. The number of code components to be received plus the number of phase redeterminations of the first component is CR.

Super Mu operates continually, starting a new acquisition as soon as the previous one is completed. Operating parameters can be changed without affecting any current or imminent acquisition receive sequences. The operator can also force a new acquisition without losing any data already in the pipeline. The ability to make dynamic changes in the program enhanced the ranging experiments by allowing the experimenter to modify operating parameters to fit operating conditions in real time.

Range data computed by Super Mu was sent automatically to the experimenters by way of teletype. Figure XXIX-3 is a typical acquisition printout. Each acquisition is preceded by a header giving the spacecraft, date, and operating parameters. The time that the receive and transmit coders are synchronized is $T0$. This is the time at which the spacecraft's range is measured, by fixing the relationship between the returning range code and its locally generated model. Each succeeding line represents the data associated with the receipt of a component. The range number is the range in microseconds modulo the period of the indicated component. DRVID is not measured during the first CT components, in this case 1 to 8. After CT components are received, all succeeding components are the redeterminations of the highest-frequency components phase. If there were no charged-particle effects, the range number would not change. In the present

example, components 10 and 11 differ by approximately 22 nsec because of DRVID.

D. Programmed Local Oscillator

Because of the great disparity between the up- and down-link transmitting powers (400 kW vs 20 W), the ground receiver was operating near threshold for much of the Mariner 9 mission. Scintillations caused by solar corona activity at small Sun–Earth–probe angles prevented the receiver from properly locking to the spacecraft's signal. The result was a complete loss of data approximately 1 week before superior conjunction when spacecraft accelerations caused the received frequency to change from that to which the receiver had been tuned. A spectral broadening experiment, being conducted concurrently with Mariner 9, employed a programmed local oscillator (PLO). Arrangements were made to connect this device to the receiver supplying range and Doppler data. Using a computed ephemeris to keep the receiver tuned to the correct frequency at all times, the PLO eliminated virtually all loop stress in the phase-locked receiver. Thus, when the coronal activity decreased sufficiently to allow signal penetration, the receiver could easily acquire and hold the down-link carrier long enough to adequately measure range and Doppler. During the critical superior conjunction period, several good data points were obtained because of this additional equipment.

E. High-Power Transmitter

As superior conjunction approached, the radio signal, already weakened by distance (2.5 AU) was further degraded by a high system noise temperature, N_T, of several hundred degrees Kelvin caused by imperfections (side lobes) in the pattern of the 64-m (210-ft) antenna. To compensate for the poor ranging signal-to-noise ratio, the new high-power transmitter was pushed to its full output of 400 kW. The twentyfold improvement in ranging power resulted in a concomitant increase in the number of acquisitions during a tracking pass. Typical acquisition counts of 10/day rose to as many as 60 for the equivalent period and resulted in a correspondingly greater probability of obtaining successful range measurements.

F. Real-Time Operations

Members of the celestial mechanics team participated in real-time mission operations during the critical period

Fig. XXIX-3. Typical acquisition "Super Mu" printout.
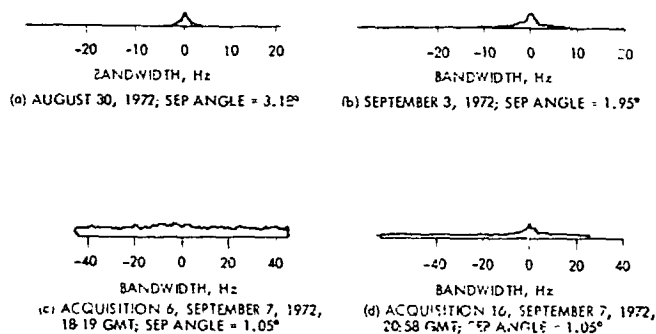
Fig. XXIX-4. Spectral spreading of RF carrier.

of August and September. A special communications line was provided which connected the ranging advisor's desk in the Space Flight Operations Facility with the station operating personnel at Goldstone. The purpose of this link was to allow virtually instantaneous modification of the tracking parameters based upon information obtained from a variety of sources.

One such source was the previously mentioned spectral broadening experiment. As the plasma's activity in the ray path increased because of a decreasing Sun–Earth–probe angle, the spectral width of the spacecraft's carrier was increased from a fraction of a Hertz to several tens of Hertz. Figure XXIX-4 indicates the extent of this broadening at various times throughout the superior conjunction period. To prevent hunting, an effort was made to adjust the receiver's loop bandwidth to a value commensurate with the spectral width. Additionally, changes in the ranging integration times and number of code components were made to take advantage of present signal conditions.

Received ranging power, as measured by the ranging equipment, also provided an indication of the amount of distortion introduced by the medium. As the received ranging power fell, integration times could be adjusted to compensate, or the number of code components could be reduced to complete the range measurements more quickly.

G. System Analysis

During the *Mariner 9* mission, four operational constraints were placed on the ranging system:

(1) Enough independent acquisitions were to be obtained in order that errors could be detected by intercomparison. This is equivalent to using a single

acquisition with longer averaging times and stationary, Gaussian, and trend-free data noise.

(2) Near the time of superior conjunction, a sufficient number of independent acquisitions was necessary to permit the range data to be used for spacecraft orbit determination.

(3) The range estimate had to be precise, on the order of 0.1 μsec.

(4) The range had to be determined unambiguously (i.e., the length of the longest code must substantially exceed the a priori range uncertainty).

The amount of time allotted to spacecraft ranging was limited by the availability of the ground equipment. Given that a trade had to be made among precision, number of acquisitions, and ambiguity the most efficient utilization of available time was considered in two separate temporal regions: (1) far from superior conjunction (more than 60 days), and (2) near superior conjunction (within 10 days).

In the first region, the ranging signal power was always greater than −200 dBm; thus, the averaging time needed to achieve a precision of 0.1 μsec was under 5 min (see Fig. XXIX-2). In the usual operation, 10 range components were used yielding an ambiguity of 150 km. This exceeds the a priori uncertainty in range by a factor of not less than 50. With the averaging time for components 2 through 10 normally 2 min, the probability of an ambiguity error at −200 dBm ranging power was approximately 1 in 50 for each acquisition. The total averaging time for component 1 (five estimations at 3-min averaging time each) was 15 min so that an acquisition required 33 min.

In the second region, the solar corona had a severe degrading effect on the signal. The Doppler receiver was unable to consistently hold lock, which set an upper bound on the averaging time for component 1, and placed a greater part of the burden of spacecraft orbit determination on the range data.

Near the time of superior conjunction, the system was run in two modes differing in the choice of the period of the highest-frequency code. In one, the usual 2-μsec code was used; in the other, component 3, an 8-μsec code was used. In both, the longest component was number 6, which gave an ambiguity of 10 km; the averaging times were typically 5 and 3 min, respectively, for the shortest component and each of the other components. The

highest-frequency component was estimated twice, once at the beginning and once at the end of each acquisition.

In data analysis thus far performed, only the first estimate of the highest-frequency component has been used. Because Doppler counter slippage appears as an additive error, the second estimate has been temporarily rejected. Eventually, each estimation of the highest-frequency component will be treated as a separate observation. The time tags will be moved from the start of the acquisition to the midpoint of the component averaging interval, and the range corrected by the observed Doppler, integrated to the new time.

H. Data Editing

One of the most difficult tasks facing the celestial mechanics team was the ex post facto screening to select usable points. Typically, 20 to 40 range acquisitions were made during a pass, several of which contained errors caused by the plasma activity and poor signal-to-noise ratios. To avoid any chance of biasing the experiment, it was decided to use only those range measurements that could be certified as good beyond any reasonable doubts. Developing an acceptance criteria to meet these rather stringent requirements was no small task. Eventually, several tests were combined to grade each point, with the provision that a single failure would necessitate rejection.

Perhaps the most important test was the likelihood plots, which provided a quanitative measure of the data quality. As previously described, the ranging system measures the phase shift introduced into a sequence of square-waves by their round-trip time of flight to the spacecraft. In doing so, the received signal is correlated against two phase shifts of a local reference coder which is a replica of the transmitted code at 0° and 90°. Correlation functions for the two phases appear in Fig. XXIX-5. For the first, or highest-frequency, squarewave signal, the phase of the arriving code is estimated directly from these two measurements. A delay is then introduced into the local reference coder until its 0° signal corresponds in phase to the code being received from the spacecraft. Thereafter, the phase of the second received range code component must be either 0° or 180° with respect to the local coder. Subsequent operation shifts the 0° local reference code to align it with that being received from the spacecraft. Shifting decisions are made using the 0° reference only; if an error is made, the next lower-frequency square-wave will be at 90° or 270° rather than 0° or 180°. This corresponds to the zero point in the correlation function
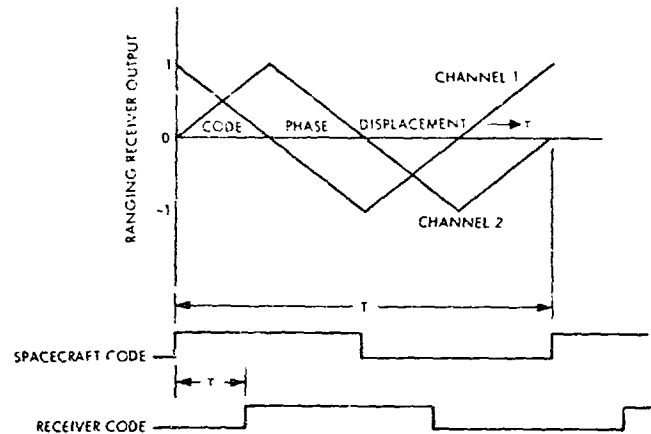
Fig. XXIX-5. Ranging receiver output characteristics.

(Fig. XXIX-5) for the 0° code, with the result that the system will be integrating essentially pure noise.

Using both the 0° and 90° reference codes together, the received code's phase can be estimated, and the erroneous decisions on the preceding component can possibly be corrected. Moreover, the correlation between the received code and any phase shift of the reference codes also can be computed. The noise disturbing these estimates is almost exclusively additive White Gaussian noise. It is well known in communications theory that the correlation between such a noisy signal and some (unit energy) local reference is proportional to the log of the probability that the received signal is equivalent to that local reference (Refs. XXIX-4 and XXIX-5).

The received code in the ranging system is a square-wave at some unknown phase. The correlation function for possible phases of this received squarewave can be constructed, using correlation measurements obtained with the 0° and 90° reference codes. Periodicity of the individual correlation functions, together with the harmonic relationships existing between the range code components, allows construction of a single composite correlation or likelihood function for the complete set of codes.

The compound full-acquisition range signal likelihood function has been plotted for a number of acquisitions near superior conjunction (Fig. XXIX-6). The zero delay point (left edge) on these curves corresponds to the phase estimated for the first component, while the maximum delay point (right edge) corresponds again to that zero delay point displaced by the period of the lowest frequency code.

(a) ACQUISITION 5,
SEPTEMBER 18, 1972, 16:07 GMT

(b) ACQUISITION 13,
SEPTEMBER 18, 1972, 17:23 GMT

(c) ACQUISITION 6,
SEPTEMBER 7, 1972, 18:19 GMT

(d) ACQUISITION 16,
SEPTEMBER 7, 1972, 20:58 GMT
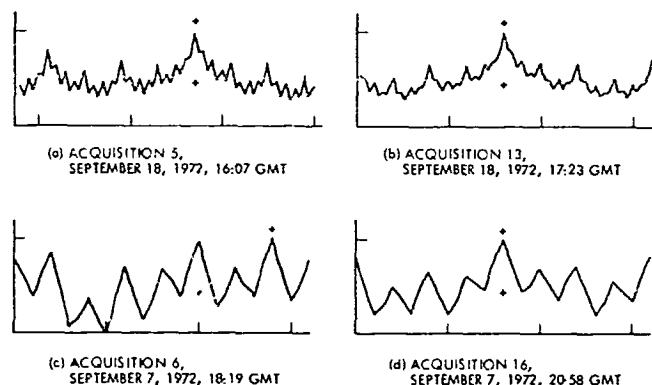
Fig. XXIX-6. Typical ranging likelihood plots.

As previously noted, the peak corresponds to the overall most probable point, and is indicated by a "+" *above* each figure. Range computed by the ranging machine is indicated by a "+" *below* each figure. If the channel is assumed to be disturbed only by additive White Gaussian noise, then the relative height of these peaks is proportional (scaled by received signal-to-noise ratio) to the log of the posteriori probability that each of these is the correct range. Near superior conjunction, the range measurement is also disturbed by significant amounts of solar plasma, which affects both signal strength and delay and makes it very difficult to assign numerical confidence values to the range measurement. We know only that the measurement is no better than it would be if the channel were in fact disturbed only by additive White Gaussian noise.

Figures XXIX-6a and XXIX-6b show typical composite likelihood functions for data obtained 1½ weeks after superior conjunction. Note the single peak and agreement in phase of the two "+" marks, indicating that there was only one clear choice and that the ranging equipment agreed with this selection. Contrast the preceding with a similar acquisition on the day of superior conjunction (Fig. XXIX-6c) where there are several equally probable phases of the range code. Note also that the ranging machine and likelihood plots predict different ranges, as indicated by the separation in the "+" marks. The result is strong indication that significant plasma interference existed during this measurement, and resulted in a lack of confidence in the measurement's correctness.

Finally, a second range acquisition, also made on the day of superior conjunction (Fig. XXIX-6d), shows a textbook example of a good measurement. The single peak

and agreement between results from the ranging machine and likelihood raises a strong presumption that the measurement is correct. Moreover, upon examining signal spectrograms for the corresponding time of day, it was found that the disturbance caused by the medium was substantially less than at other times during that day (Fig. XXIX-4c and XXIX-4d). Further indications that this was a good ranging acquisition were obtained by observing the relatively low system noise temperature and absence of receiver out-of-lock indications occurring during the same period.

The final test in the acceptance criteria is a comparison of the orbit residuals from two or more data points meeting all preceding requirements. Uncertainties in the coronal model make the absolute fit less important than the consistency between points.

Table XXIX-1 provides a summary indicating the number of acceptable data points obtained during the critical period near superior conjunction. Note that, with the exception of 2 days where there were equipment problems, data were obtained throughout the period.

Table XXIX-1. Quantity and distribution of two-way range measurements during superior conjunction

Pre-superior conjunction		Post-superior conjunction	
Pass date, 1972	Range data	Pass date, 1972	Range data
8/17	22	9/7	Several
8/18	15	9/8	Several
8/20	14	9/9	Several
8/21	14	9/10	Several
8/23	20	9/11	13
8/24	12	9/12	15
8/25	19	9/13	9
8/26	10	9/14	16
8/27	11	9/16	22
8/28	11	9/17	21
8/30	16	9/18	58
8/31	Several	9/20	45
9/2	15	9/21	22
9/3	—	9/22	30
9/4	Several	9/23	30
9/5	—	9/24	23
9/6	Several	9/25	24

References

XXIX-1. MacDoran, P. F., and Martin, W. L., "DRVID Charged Particle Measurements With a Binary Coded Sequential Acquisition Ranging System," Space Programs Summary 37-63, Vol. II, p. 34, Jet Propulsion Laboratory, Pasadena, Calif., 1970.

XXIX-2. Martin, W. L., "A Binary Coded Sequential Acquisition Ranging System," Space Programs Summary 32-57, Vol. II, p. 72, Jet Propulsion Laboratory, Pasadena, Calif., 1969.

XXIX-3. Martin, W. L., "Performance of the Binary Coded Sequential Acquisition Ranging System of DSS-14," Space Programs Summary 37-62, Vol. II, p. 55, Jet Propulsion Laboratory, Pasadena, Calif., 1970.

XXIX-4. Woodward, B. A., *Probability and Information Theory, With Applications to Radar*, Pergammon Press, New York, 1953.

XXIX-5. Timor, U., "Sequential Ranging With the Viterbi Algorithm," *The Deep Space Network Progress Report for January and February 1971*, Technical Report 32-1526, Vol. II, p. 75, Jet Propulsion Laboratory, Pasadena, Calif., 1971.

XXX. Determination of Normal Points for the Relativity Test of the Celestial Mechanics Experiment

J. F. Jordan, R. K. Hylkema, and S. J. Reinbold

Jet Propulsion Laboratory/California Institute of Technology, Pasadena, California 91103

A. Definition of Normal Points

The relativity test is based on *Mariner 9* tracking data acquired by the Deep Space Network. These data consist of two types of measurements: (1) two-way frequency difference (Doppler) measurements that are proportional to the tracking station–spacecraft range rate, and (2) signal round-trip time-delay measurements that are proportional to the station–spacecraft range. Ideally, the total combined data set of range and range rate measurements could be processed simultaneously via regression analysis to estimate the parameters affecting both the radio signal and the motion of the spacecraft, Mars, and Earth. However, analysis of the *Mariner 9* tracking data has led to the conclusion that Mars is gravitationally rough, with second-order tesseral harmonics four to five times larger than expected before flight (Ref. XXX-1). Specification of a gravity model with a finite number of parameters accurate enough to integrate the probe motion over hundreds of revolutions has not yet been accomplished, although the effort to produce an adequate model by direct estimation is continuing. The computer expense of such regression analyses is also a limiting factor.

A data compression scheme has been employed to alleviate the accuracy and cost difficulties of the direct approach. The compression scheme consists of: (1) using the Doppler data to solve for the spacecraft orbit and to relate the spacecraft position to the center of mass of Mars, and (2) combining this result with the station–spacecraft range measurements to obtain measurements of the Earth–Mars distance. These Earth–Mars pseudo range measurements, called normal points, contain all of the information in the individual time-delay measurements and the local Doppler data that is pertinent to a detailed knowledge of the Earth–Mars motion. The Earth–Mars angular information content of the Doppler is weak because of uncertainties in the locations of the tracking stations on Earth, and thus has been neglected here.

B. Data

During *Mariner's* year in orbit, more than 300,000 two-way Doppler measurements, taken at 1-min count times, have been recorded. In the first 280 revolutions, two-way Doppler tracking data were obtained in an almost continuous fashion by DSS 12 and DSS 14 at Goldstone, California; DSS 41 at Woomera, Australia; and DSS 62 at Madrid, Spain. As the Earth–Mars distance gradually increased since orbital insertion, the signal-to-noise ratio of the spacecraft communications link decreased. In

late March, increased data noise rendered the 26-m (85-ft) antennas ineffectual. Consequently, since revolution 280, only the 64-m (210-ft) antenna at Goldstone was used for tracking the spacecraft. Figure XXX-1 illustrates the evolution of the accuracy of the Doppler data by showing the RMS of the Doppler residuals plotted against time through October 1972. Individual RMS values have been obtained from short orbit fits to the data. Also included on the figure is the magnitude of the Earth–Mars distance, showing its increase from about 1.2×10^8 km at insertion to about 5×10^8 km after 600 revolutions. Note that, as the Earth–Mars distance approached 3×10^8 km, the noise observed at the 26-m antenna increased markedly, while that for the 64-m antenna increased only slightly.

The quality of the Doppler data during the month around superior conjunction was degraded sharply because of the effects of the rapidly varying quantities of charged particles along the signal path caused by the solar corona. The RMS of the Doppler noise did reach a maximum of 1 Hz on the day of conjunction, when the

Sun–Earth–Mars angle was 1.04° and the signal path passed within 4 solar radii of the Sun.

Two-way time-delay measurements, which are proportional to station–spacecraft range, were obtained using the Mu ranging machine at Goldstone throughout the Mariner 9 mission. Range measurements were acquired several times per week from November 1971 until August 1972, at which time the frequency of independent range measurements was increased to several measurements per Goldstone pass. More than 1300 individual range measurements were acquired during the satellite phase of Mariner 9, most of which were obtained in the 8 weeks bracketing superior conjunction. These ranging measurements, which are normally precise to a few meters, were perturbed by charged particles in the transmission media. Charged particles retard the signal and thus contribute to a larger time delay than that which is predicted from the true coordinate range. As the signal path for Mariner 9 neared the Sun, the amplitude of the steady-state charged-particle content and the amplitude of the stochastic variations along the signal path increased. However, the effect of the steady-state content can be
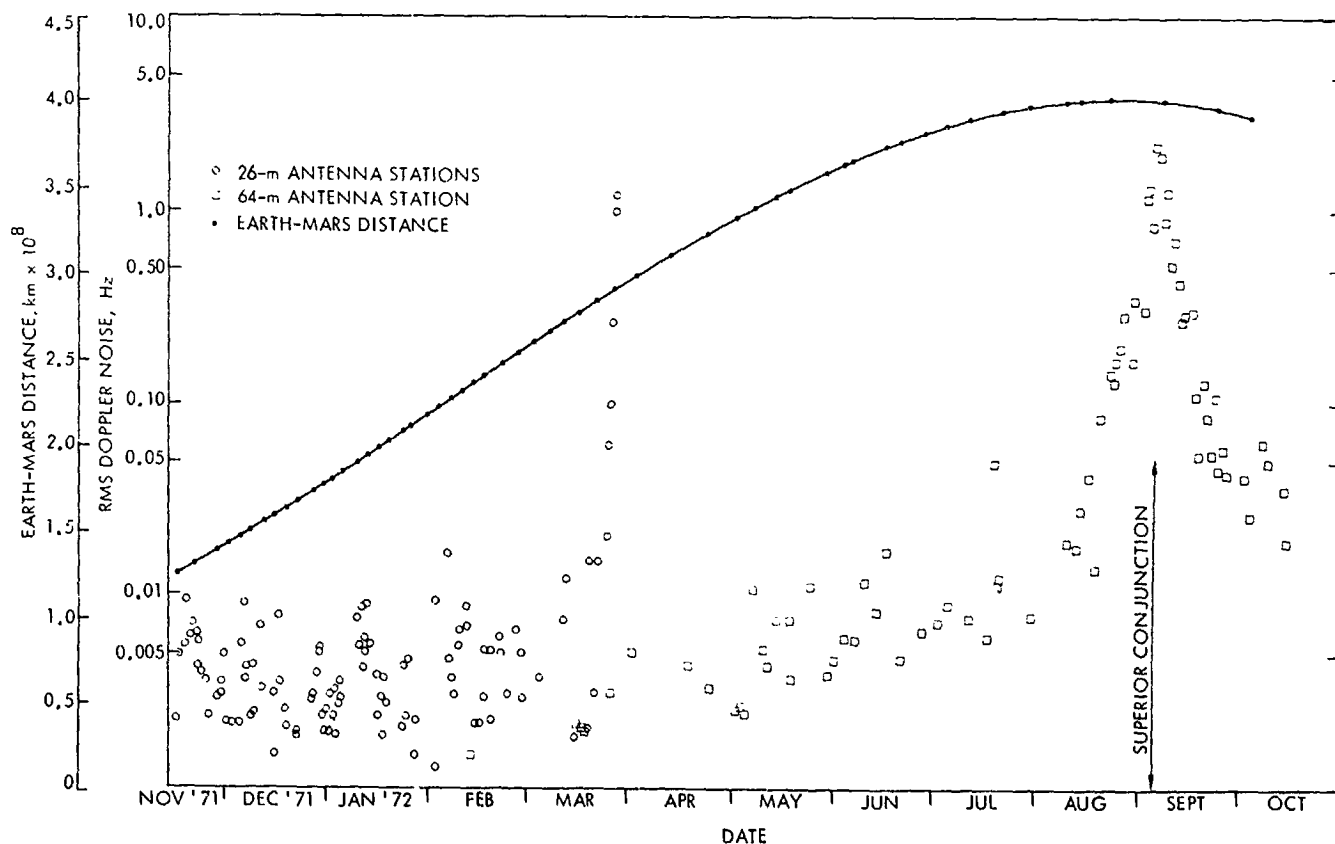
Fig. XXX-1. Time history of RMS Doppler noise and Earth–Mars distance.

modeled (Ref. XXX-2) and so caused few problems. At closest proximity to the Sun on September 7, 1972, the average electron content of the signal path through the solar corona was at its maximum and caused a time delay of about 20 μsec (out of a total round-trip light time of about 45 min). As 1 μsec of time delay corresponds to about 150 m one-way range to the spacecraft, the maximum corona effect was about 3000 m in range.

On the other hand, the stochastic variations in the corona induced a range uncertainty that is difficult, if not impossible, to model. On a scale of 1 day, the effect can be several microseconds. With an effect of this magnitude, we were obliged to evaluate the impact on the normal point calibrations, which we did with the help of the differenced range vs integrated Doppler (DRVID) measurements.

The DRVID technique, discussed previously by MacDoran and Martin (Ref. XXX-3), was used to calibrate charged-particle activity in the signal path for small Sun–Earth–probe angles and to provide corrections for the computation of normal points. Raw DRVID data provide a time history of the observed range difference from the initial range observation in a continuous pass minus the integrated range rate from the Doppler data. The data measure twice the round-trip range change during a pass because of the charged particles, but do not indicate the total group delay.

DRVID data were obtained by two modes of operation. Because of its mechanization, Mu ranging machine outputs DRVID data automatically during any single range acquisition. However, the data also can be constructed externally from counted Doppler and individual range acquisitions. DRVID data spanning entire passes were generated, using primarily the second mode, for the periods August 10 to 25 and September 16 to October 12. Data nearer conjunction could not be obtained because of poor Doppler quality. Data farther from conjunction are now being processed. The data were least-squares fit with a polynomial of the lowest order which reasonably represents its structure. The coefficients of this polynomial were used to adjust the Doppler and range data in the spacecraft orbit fitting software.

Figures XXX-2a, XXX-2b, and XXX-2c show the DRVID data for passes beginning August 20, 23, and 25, respectively. Curves that show the least-squares fit polynomial are superimposed on the actual data. On the days
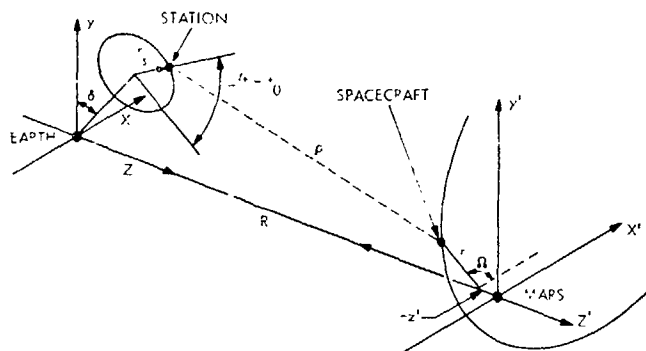
Fig. XXX-2. Differenced range versus integrated Doppler time histories. (a) August 20. Order fit 8. (b) August 23. Order fit 3. (c) August 25. Order fit 3.

shown, the variation in observed range caused by charged particles in a single pass was as high as 300 m, with a maximum slope of 75 m/hr.

C. Computation of Normal Points

A normal point, or Earth–Mars range measurement, is computed on the basis of station–spacecraft time-delay measurements. The station–spacecraft coordinate range (see Fig. XXX-3) is related to the Earth–Mars coordinate vector $\vec{R}$ by the exact expression

$$\rho = |\vec{R} + \vec{R}_{s/c} - \vec{R}_s|$$ (1)

where the vector $\vec{R}_{s/c}$ is the planet-centered coordinate vector of the spacecraft, which is determined from Doppler tracking. The quantity $\vec{R}_s$ is the accurately known Earth-centered coordinate vector of the station. Equation (1) can be written in the following approximate form, accurate to 0.1 m for the *Mariner 9* geometry,

$$\rho = R + z' - h_z + \frac{1}{2R}\left[(r\sin\Omega - h_y)^2 + (r\cos\Omega - h_x)^2\right]$$ (2)

where z', r, and Ω are cylindrical coordinates defining the position of the spacecraft relative to Mars at the time of range observation, and where h_x, h_y, and h_z are components of the station in the Earth-centered Cartesian coordinate system defined in Fig. XXX-3, and are given by the expressions

$$h_x = r_s \sin \omega t$$

$$h_y = h \cos \delta - r_s \sin \delta \cos \omega t$$

$$h_z = h \cos \delta + r_s \sin \delta \cos \omega t$$
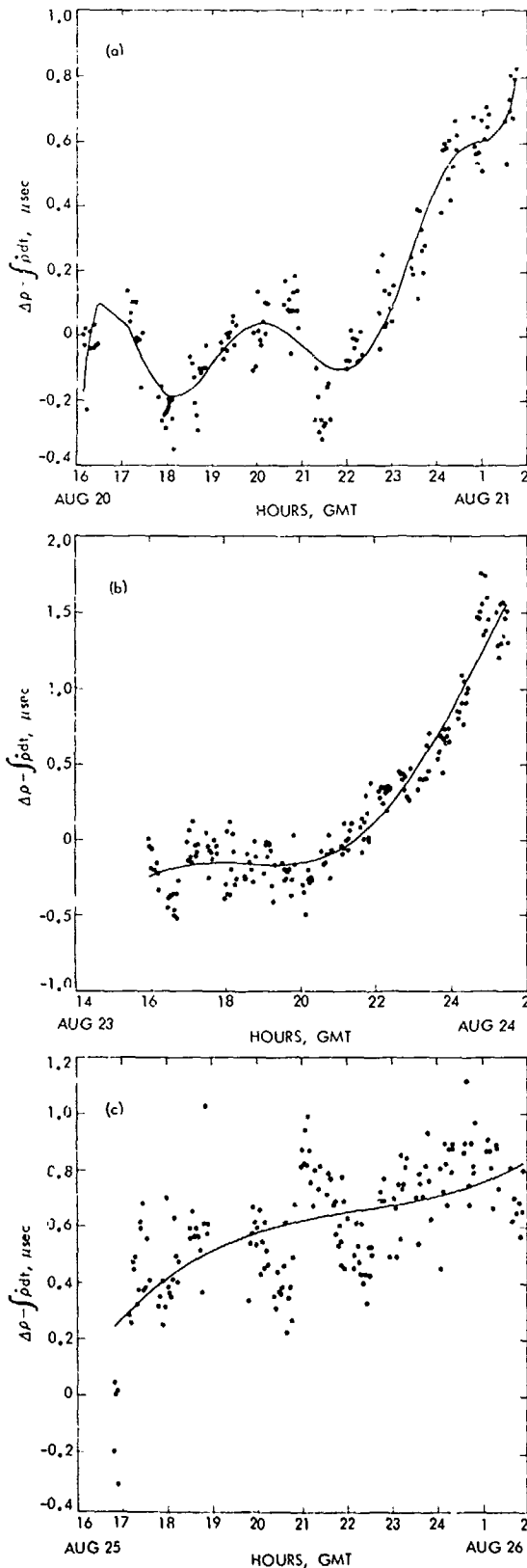
Fig. XXX-3. Earth–station–spacecraft–Mars configuration.

where

h = distance from station to Earth equator along Earth spin axis

δ = geocentric declination of Mars

ω = angular rate of Earth

t = time from station meridian passage of Mars

r_s = station distance from the spin axis

Equation (2) can be solved directly for the Earth–Mars distance R from a measured value of the station–spacecraft coordinate time delay, using the expression

$$c\Delta t = \rho + (1 + \gamma)m \ln \left[\frac{r_o - r_1 - \rho}{r_o - r_1 - \rho} \right] \qquad (3)$$
$$m = \mu_\cdot/c^2$$

where r_o, and r_1 are coordinate distances representing, respectively, the Sun–observer distance and the Sun–spacecraft distance, to convert to range ρ.

In practice an initial value of R is chosen from the currently used planetary ephemeris, and the difference between the measured and predicted values of ρ is then related to a differential correction in R. The correction is then added to the initial value, yielding a pseudo-measured value of R at the time of the spacecraft ranging. Equation (3) is again used to convert R into a relativistically consistent pseudo-observable in terms of coordinate time, $c\Delta t$. It should be noted that γ is set to unity in this computation, but that the charged-particle delay is included in the measured value of $c\Delta t$.

D. Normal Point Accuracy

The error in the determined value of R can be related to the error in the range measurement $\Delta\rho$, the error in the station locations $(\Delta h_x, \Delta h_y, \Delta h_z)$, and the error in the Doppler-determined spacecraft position relative to Mars $(\Delta z', \Delta r, r\Delta\Omega)$ by the following approximate expression, which is accurate to 0.1 m,

$$\Delta R = \Delta\rho + \Delta h_z - \Delta z'$$
$$- \frac{1}{R_o}\left[(r - h_x \cos\Omega - h_y \sin\Omega)\,\Delta r \right.$$
$$\left. + (h_x \sin\Omega - h_y \cos\Omega)\,r\Delta\Omega \right] \qquad (4)$$

As the distance of the station from Earth's spin axis and the station longitude are known to less than 10 m

from analysis of data acquired during planetary encounters on past *Mariner* missions, the error in the distance of the station from the Earth's equator is the only term that contributes more than 10 m to Δh_z. Hence, Δh can be expressed as $\Delta h \sin \delta$, plus terms that contribute less than 10-m errors.

The remaining errors in Equation (4) are due to the uncertainty in the Doppler-determined spacecraft position relative to Mars. The coefficients of the errors of the spacecraft position in the Earth's plane of sky, Δr and $r\Delta\Omega$, are on the order of 10^{-1}; thus, Equation (4) can be written in the form

$$\Delta R = \Delta\rho - \Delta h \sin\delta - \Delta z' - (10^{-1})\Delta r - (10^{-1})r\Delta\Omega$$
$$- (<10m \text{ terms}) \qquad (5)$$

The accuracies to which z', r, and Ω can be estimated for *Mariner* 9 have been discussed by Reynolds et al. (Ref. XXX-4); Zielenbach and Jordan (Ref. XXX-5); and Jordan et al. (Ref. XXX-6). The effect of uncertainties in z', r, and Ω on the accuracy of the computed normal points was given by Jordan et al. in Ref. XXX-7. A summary of this information is given in Table XXX-1, which lists the 1-sigma uncertainties of the components of position, r, $r\Omega$, and z', along with their respective contribution to the error in R.

Pre-flight values, actual pre-gravity sensing results from revolutions 1 through 4, and post-gravity sensing results from the three-station and single-station tracking configurations are shown in the table, along with the maximum uncertainties caused by the stochastic solar corona near superior conjunction. Contributions from $r\Delta\Omega$ and Δr are negligible throughout the mission, leaving the

contributions from $\Delta z'$ the only spacecraft position error of importance. Equation (5) can then be expressed in the form

$$\Delta R = \Delta\rho + \Delta h \sin\delta - \Delta z' - (<10m \text{ terms}) \qquad (6)$$

where neither the contribution from measurement error $\Delta\rho$ or spacecraft position error $\Delta z'$ are highly correlated in time. The station location error Δh is a constant.

E. Normal Point Residuals

The local orbit of *Mariner* 9 and hence values of r, Ω, and z' have been estimated from the Doppler data for each revolution in which range measurements have been acquired. These orbit estimates have been used to predict values of ρ. Observed residuals in the observed ρ have been related to values of R, and hence $c\Delta t$, at the times of the range measurements.

Residuals of the normal points over the almost 1 yr of *Mariner* 9 are given in Fig. XXX-4, where the elements of the orbits of both Earth and Mars have been fit with the normal points obtained before July 31. The dashed line indicates the apparent drift in the extrapolated ephemeris. The sampled RMS of the normal points is 0.1 μsec in the three-station configuration region and 0.3 μsec in the one-station region before July 31. The effect of the charged particles caused by the solar corona is observed in 8 weeks surrounding superior conjunction. The apparent two-way time delay increases to a value near 20 μsec. In addition, daily variations of several microseconds can be observed; these variations appear to be almost as large as the steady-state delay itself. The insert in Fig. XXX-4 shows, on a larger scale, the normal point residuals before and after DRVID corrections for the time

Table XXX-1. One-sigma uncertainties in the Doppler-determined *Mariner 9* position when ranging is taken

Pre-flight		Actual pre-gravity sensing, revolutions 1 to 4	Post-gravity sensing, revolutions 4 to 280 (three stations)	Post-gravity sensing, revolutions 280 to 650 (one station)	Post-gravity sensing (conjunction region)
$r\Delta\Omega$	30 km	120 km	5 km	10 km	<30 km
Δr	100 m	400 m	20 m	60 m	<150 m
$\Delta'z$	50 m	200 m	20 m	60 m	<150 m
Error contributions to the Earth–Mars measurement					
$r\Delta\Omega$	3 m	12 m	0.5 m	1 m	<3 m
Δr	0.01 m	0.04 m	0.002 m	0.006 m	<0.015 m
$\Delta'z$	50 m	200 m	20 m	60 m	<150 m
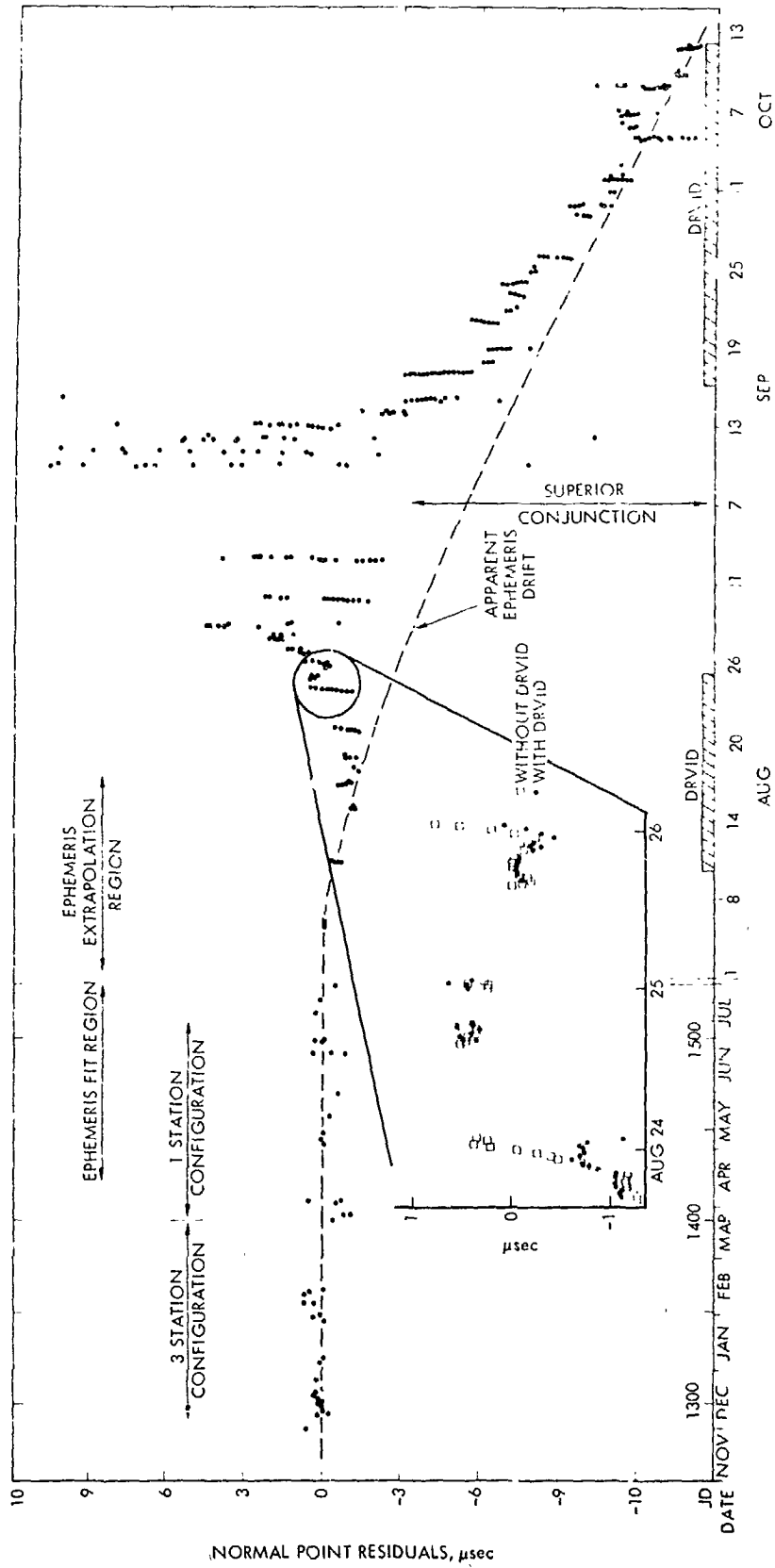
Fig. XXX-4. Normal point residuals referenced to a fit to data through July 31. Insert shows DRVID improvement for August 23 through August 26.

period from August 23 to August 26. Drifts of almost 2 μsec in the residuals are observed on August 24 and 26 if DRVID corrections are not applied, but the total residual spread of a single pass is limited to 0.5 μsec by the application of DRVID corrections.

DRVID corrections are currently being generated for all passes of data in which the variations in charged-particle content are large enough to significantly influence the accuracy of the Doppler-determined spacecraft orbit. In addition, the prospect of using range data to determine the spacecraft orbit is being investigated. A normal point can be computed from an estimated range bias value, if the spacecraft orbit is determined from range data only. This mode of computation has possible applications for normal point generation in the region within a few days of superior conjunction, as the Doppler data are severely corrupted in that region. In summary, it is hoped that continued refinement of the normal point generation methods will yield a complete data set, the points of which are accurate to a 1-sigma value less than 0.5 μsec.

References

XXX-1. Lorell, J., Born G. H., Christensen, E. J., Jordan, J. F., Laing, P. A., Martin, W. L., Sjogren, W. L., Shapiro, I. I. Reasenberg, R. D., and Slater, G. L., "Mariner 9 Celestial Mechanics Experiment: Gravity Field and Pole Direction of Mars," *Science*, Vol. 175, p. 317, 1972.

XXX-2. Muhleman, D. O., Anderson, J. D., Esposito, P. B., and Martin, W. L., "Radio Propagation Measurements of the Solar Corona and Gravitational Field: Applications to Mariners 6 and 7," in *Proceedings of the Conference on Experimental Tests of Gravitation Theories*, Technical Memorandum 33-499, Jet Propulsion Laboratory, Pasadena, Calif., 1971.

XXX-3. MacDoran, P. F., and Martin W. L., "DRVID Charged-Particle Measurements With a Binary Coded Sequential Acquisition Ranging System," Space Programs Summary 37-57, Vol. II, p. 72, Jet Propulsion Laboratory, Pasadena, Calif. 1969.

XXX-4. Reynolds, G. W., Russell, R. K., and Jordan, J. F., *Earth Based Orbit Determination for a Mars Orbiting Spacecraft*, paper presented at the AIAA Ninth Aerospace Sciences Meeting, New York, 1971.

XXX-5. Zielenbach, J. W., and Jordan, J. F., *Orbit Determination Strategy and Results for the Mariner Mars 1971 Missions*, paper presented at the AAS/AIAA Astrodynamics Specialists Conference, Fort Lauderdale, Fla., 1971.

XXX-6. Jordan, J. F., Melbourne, W. G., and Anderson, J. D., *Testing Relativistic Gravity Theories Using Radio Tracking Data From Planetary Orbiting Spacecraft*, paper No. a13 presented at the XV Plenary Meeting of COSPAR, Madrid, Spain, 1972.

XXX-7. Jordan, J. F., Born, G. H., Christensen, E. J., and Reinbold, S. J., *Preliminary Results of the Satellite Orbit Determination of Mariner Mars 1971*, paper presented at the ION National Space Meeting, Orlando, Fla. 1972.

XXXI. Determination of the Relativistic Time Delay From the *Mariner* 9 Superior Conjunction Data: A Status Report

P. B. Esposito and S. J. Reinbold

Jet Propulsion Laboratory/California Institute of Technology, Pasadena, California 91103

The purpose of the analyses performed is to investigate the *Mariner* 9 superior conjunction range and Doppler data in order to determine the values for the relativity and solar corona time-delay parameters. This approach differs from, but is complementary to, the long are "normal point" approach described by Anderson and Lau (see Section XXXII of this Report). The two methods of analysis differ insofar as: (1) This analysis investigates a much shorter arc of data; at present, data within the interval from August 17 to September 26, 1972, are being analyzed. (2) This procedure deals directly with the *Mariner* 9 Doppler and range data; therefore, it avoids the intermediate step involved in constructing "pseudo-data." It is complemente.y to the reduction of the normal-point data because it relies upon the generation of an Earth–Mars ephemeris, which is determined from the analysis of "normal points" as well as past optical and radar data.

The effect of the solar gravitational field on the propagation of radio signals has been investigated theoretically by Shapiro (see Ref. XXXI-1) and Muhleman and Reichley (Ref. XXXI-2); a series of related papers (Refs. XXXI-3 through XXXI-5) discussed the measurement and interpretation of the general relativity time delay. The results of passive (i.e., a planet is used to reflect radar pulses) as

well as active (i.e., a spacecraft is used in the reception and retransmission of a radio signal) time-delay experiments conducted at MIT and JPL have been published by Shapiro et al. (see Refs. XXXI-6 and XXXI-7) and Anderson et al. (see Refs. XXXI-8 and XXXI-9), respectively. An overall review of the progress and planning of time-delay experiments and other relativity experiments was made by Thorne and Will (Ref. XXXI-10), Schiff (Ref. XXXI-11), and D·.vies (Ref. XXXI-12).

The parameterized, two-way, relativistic time-delay expression in isotropic coordinates is

$$\Delta t = \frac{2m}{c}(1 + \gamma)\ln\left(\frac{r_0 + r_1 + \rho}{r_n + r_1 - \rho}\right) \qquad (1)$$

where ρ, r_n, and r_1, respectively, represent the tracking station–spacecraft, Sun–tracking station, and Sun–spacecraft coordinate distances. Equation (1) was derived by Holdridge (Ref. XXXI-13) and Tausner (Ref. XXXI-14); the historical development of the parameterization of the space–time metric can be found in the works of Eddington (Ref. XXXI-15) and Robertson (Ref. XXXI-16). In Equation (1), m represents the "gravitational radius" of the

Sun (i.e., product of the universal gravitational constant and the mass of the Sun divided by the speed of light squared), which has an approximate magnitude of 1.5 km; c is the speed of light in a vacuum; and γ is a dimensionless relativity parameter that has a nominal (Einstein) value of unity. By determining the numerical value of γ, along with other parameters pertinent to the analyses, directly from the data, one obtains a measure of the relativistic time delay.

A. Characteristics of the *Mariner 9* Superior Conjunction

Some of the characteristics of the *Mariner 9* superior conjunction compared with those of *Mariner 6* are presented in Table XXXI-1. Although geometric parameters are basically similar, the essential difference is that *Mariner 6* was in an elliptical orbit about the Sun, and *Mariner 9* is an artificial satellite of Mars.

The nominal ($\gamma = 1$) relativistic time delay for a 2-month interval centered on superior conjunction is presented in Fig. XXXI-1, which is plotted as a function of calendar date with the corresponding Sun–Earth–Mars angles. At 1 month outside superior conjunction, the delay is approximately 106 μsec compared with a maximum delay of 195 μsec. During this interval, the spacecraft is within 10° of the Sun and reaches a minimum of 1.04° at conjunction. The shaded boxes at the top of the figure represent quality measurements of the round-trip time of flight of an S-band radio signal between the tracking station and spacecraft (i.e., two-way range) obtained on that particular day, thus serving as a guide to the distribution of the range data.

There is a time delay caused by the charged particles in the signal path, which are most concentrated in the solar corona. The steady-state, solar corona electron density is modeled as

$$N_e \, (\text{cm}^{-3}) = \frac{A}{r^6} + \frac{B}{r^{2-\epsilon}} \qquad (2)$$

with nominal values and standard deviations for the constants A, B, and ϵ given as $(1.30 \pm 0.9) \times 10^8$, $(1.15 \pm 0.7) \times 10^6$, and 0.3 ± 0.3, respectively. These values were developed from an analysis of classical, solar eclipse, photometric observations and are discussed in detail by Muhleman et al. in Ref. XXXI-17. The quantity r is the distance from the center of the Sun to the ray path in units of the solar radius. Based upon this nominal model, the time delay attributed to the refraction of the S-band radio signal, within 1 month of superior conjunction, is shown in Fig. XXXI-2. In this plot, the contribution of the interplanetary (represented by the B term) as well as the outer solar corona electrons (represented by the A term) to the total time delay are shown separately and combined. One month outside superior conjunction, the time delay is 1 μsec, compared with a maximum total effect of 26 μsec at conjunction. Note that the A term in the model contributed a delay of 0.1 μsec or greater only when the spacecraft was within 1 week of superior conjunction or within 2.5° of the Sun.

Figure XXXI-3 is a plot of the normalized relativistic and solar corona time delays and was generated by

Table XXXI-1. *Mariner 6 and 9 superior conjunction characteristics*

Characteristic	Mariner 6	Mariner 9
Superior conjunction	April 29, 1970, 17^h	September 7, 1972
Earth–spacecraft distance, km	402.25 × 10^6	400 × 10^6
Round-trip travel time, min	44.72	44.4
Sun–Earth–spacecraft angle, deg	0.95	1.04
Closest approach of signal to solar surface ($R_\odot$)	2.58	2.9
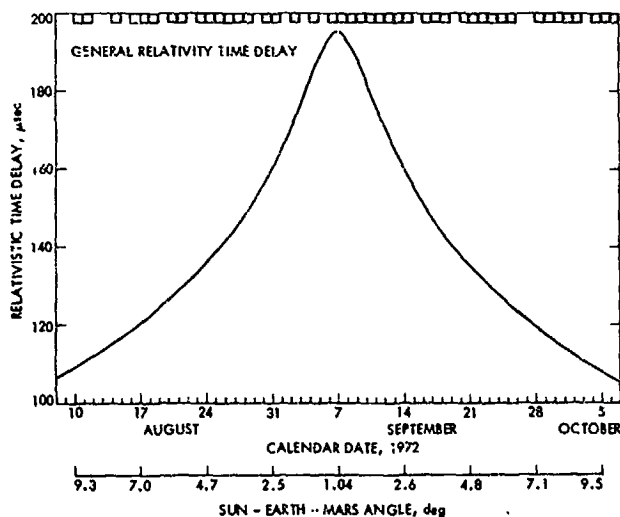
Fig. XXXI-1. Magnitude of relativistic time delay as a function of calendar date and Sun—Earth—Mars angle.
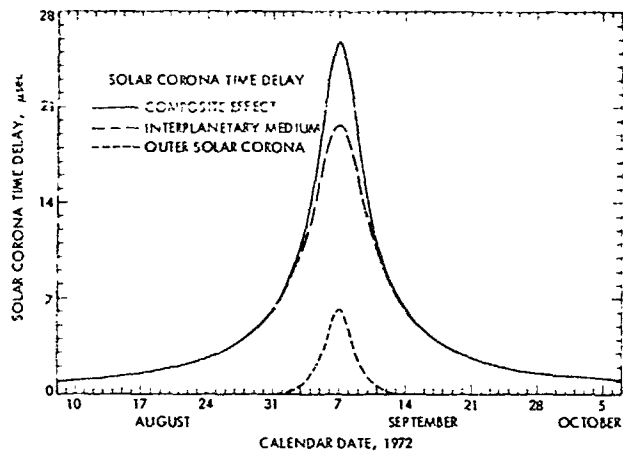
Fig. XXXI-2. Nominal solar corona time delay separated into its two basic components and then combined.

Fig. XXXI-3. The nominal relativity and corona time delays have been normalized and plotted together in order to contrast their different structures.

dividing the time delay on a particular day by the maximum delay (at superior conjunction). The structure of these two curves shows that, at half amplitude, the width of the relativity delay is greater than 2 months, compared with approximately 7 days for the solar corona delay. Thus, the relativity delay gradually climbs to a maximum, whereas the solar corona delay rises sharply within 1 week of conjunction. Based upon this dissimilar structure, we hope to uncouple the relativistic and solar corona time delays in the orbit determination and refinement.

B. Orbit Determination and Data Analysis

1. Modeling the Mariner 9 Orbit

With August 17, 1972, as the initial epoch, Mariner 9 superior conjunction data covering 6 weeks were analyzed. Because the spacecraft's motion is gravitationally dominated by Mars, the current best estimates of the direction of the spin axis of Mars and its gravitational harmonics were used in the numerical integration of the spacecraft's equations of motion. The Martian gravity field used in this work consisted of a tenth-degree and tenth-order model in the potential function expansion, which is given by

$$V = \frac{\mu}{r}\left\{1 - \sum_{n=2}^{\infty}\left(\frac{R}{r}\right)^n\left[J_nP_n(\sin\phi) + \sum_{m=1}^{n}(C_{nm}\cos m\lambda + S_{nm}\sin m\lambda)P_{nm}(\sin\phi)\right]\right\} \quad (3)$$

A description of the analysis leading to the determination of these coefficients as well as some preliminary results are given by Lorell et al. (Ref. XXXI-18), Born et al. (Ref. XXXI-19), and Ferrari and Christensen (see Section XXVIII of this Report).

During this interval, the spacecraft did not pass through Mars' shadow nor did it undergo an occultation as viewed from Earth. The solar radiation pressure was computed by a three-dimensional model with components along the pitch, yaw, and roll axes of the spacecraft. Each component of the force can be estimated and its uncertainty considered in an error analysis. During this time period, only DSS 14 was collecting data. The coordinates defining the station's location are known to within 5 m in longitude and distance from Earth's spin axis and 15 m in distance perpendicular to Earth's equatorial plane (Ref. XXXI-20). At present, these uncertainties are being used to estimate the influence of station location errors on the estimated parameters.

The ephemerides used to specify the motion of the Moon and planets, especially the Earth–Moon system and Mars, is referred to as DE 82. This development ephemeris is the result of the analysis of past optical and radar data that have been supplemented by 98 Mariner 9 normal points covering the interval from November 20, 1971, to July 30, 1972 (see Section XXXIV of this Report). In addition to providing an estimate of the initial state of each planet at some epoch, the planetary data analysis also yields a full covariance matrix for the Set III orbital elements (see Ref. XXXI-21) of each planet. This a priori information is important in the analysis of the Mariner 9

data because it conditions the solution for parameters that are pertinent to the analysis. Furthermore, the influence of parameters that are peripheral to the analysis, usually designated as "consider parameters," can be accounted for in the estimate of the standard deviations of parameters directly related to this experiment. Thus, with reasonable uncertainties in the Set III elements established, we can constrain solutions for particular subsets of elements to vary within these bounds. In this way, the direct analysis of the spacecraft data is guided by the results of the evaluation of a large quantity of past optical and planetary radar data.

Smaller influences on the orbiter's motion such as non-gravitational forces (i.e., attitude-control-induced perturbations, reflected radiation pressure, etc.) and the gravitational influence of the Martian moons are under investigation.

2. Data Analysis

The quantity and distribution of range data used in the analyses are given in Table XXXI-2. Data measurements

Table XXXI-2. Quantity and distribution of two-way range data used in analysis

Pre-conjunction		Post-conjunction	
Tracking pass date, 1972	Independent range measurements	Tracking pass date, 1972	Independent range measurements
8/17	22	9/7	—
8/18	15	9/8	3
8/20	14	9/9	4
8/21	14	9/10	6
8/23	20	9/11	13
8/24	12	9/12	15
8/25	19	9/13	9
8/26	10	9/14	16
8/27	11	9/16	22
8/28	11	9/17	21
8/30	16	9/18	58
8/31	5	9/20	45
9/2	9	9/21	21
9/3	—	9/22	28
9/4	—	9/23	29
9/5	—	9/24	22
9/6	—	9/25	24

made with a few days of superior conjunction have undergone stringent quality control tests (see Section XXIX of this Report). Although only the highest quality data have been used in the analyses, a small quantity of additional data (especially on September 4, 6, and 7) is available and will be used in future analyses. During most of these passes, a full pass of Doppler consisting of about 11 hours from DSS 14 rise to set also is available. However, during the interval from August 28 to September 10, 1972, the Doppler data are noisy, and the tracking coverage is not continuous, but rather intermittent; in general, these data have not been used in the analysis. This situation exists primarily because of the interference induced by the dynamic solar corona on the S-band frequency ≈ 2.2 GHz) Doppler and, to a lesser degree, on the range tracking systems. Approximately 500 range measurements and 5000 individual Doppler data points, varying in averaging times from 60 to 300 sec, have been analyzed.

The round-trip range measurements possess an inherent precision of at least 0.1 μsec for data collected outside of superior conjunction. However, in order to approximate the influence of the dynamic behavior of the solar corona in degrading the precision of the range data during the conjunction, these data have been weighted according to the relation

$$\sigma^2 = \sigma^2 \text{ (inherent data precision)}$$

$$+ \sigma^2 \text{ (dynamic corona influence)} \qquad (4)$$

such that σ (dynamic corona) $= Kp^{-3/2}$ with the data weight given by $W = \sigma^{-2}$. In the latter expression, K is a constant whose magnitude is dependent upon assumptions concerning the solar corona electron-density fluctuations and p represents the impact parameter of the ray path.[1] Assuming a value of $K = 33$ μsec, Fig. XXXI-4 shows the variation of the impact parameter for the *Mariner 9* (Mars) trajectory and the associated standard deviation deduced from Equation (4) for the two-way range measurements.

Currently, the analysis has been performed using a differential correction, weighted, least-squares algorithm. A simplified form of the parameter estimation equation is

$$\Delta x = \left(A^T W A + \widetilde{\Lambda}_x^{-1} \right)^{-1} A^T W \Delta z \qquad (5)$$

---

[1]Muhleman, D. O. (private communication). The weighting scheme was developed by Dr. Muhleman for the *Mariner 6* and 7 relativity test.
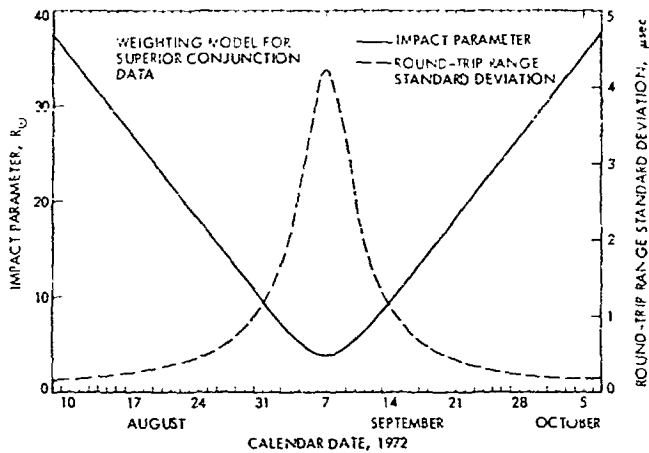
Fig. XXXI-4. Basic weighting model utilized in the analysis of the Mariner 9 range data.

with the estimated parameter covariance matrix given by

$$\Lambda_r = \left(A^T W A + \tilde{\Lambda}_r^{-1} \right)^{-1} \qquad (6)$$

The residuals (observed minus computed) for the range and Doppler data are represented by Δz, and Δx represents corrections to the estimated parameters. W is the weighting matrix, usually assumed to be diagonal, and $\tilde{\Lambda}_r$ is the a priori parameter covariance matrix. The A matrix contains the partial derivatives of data with respect to estimated parameters; thus, it relates variations in the data vector to variations in the estimated parameter vector. The basic parameters used in this analysis, either to be estimated directly or to be considered in an error analysis, include: (1) six elements of the initial state of the spacecraft; (2) twelve Set III orbital elements defining the orbital motion of the Earth–Moon barycenter and Mars; (3) three parameters, each relating to a solar radiation pressure and attitude-control perturbation model; (4) three parameters for the Earth-based tracking station; (5) relativity time-delay parameter and a three-parameter, steady-state, solar corona electron-density model; and (6) a variety of parameters used to probe the effect of possible biases in the data, errors in Mars' gravitational constant and harmonics, and uncertainties in the astronomical unit and Earth–Moon mass ratio.

In a typical analysis, the solve-for parameter subset includes the initial state of the spacecraft's orbit, three elements each referring to the orbital motion of Mars and the Earth–Moon barycenter, B, ϵ, and γ. Of the six planetary orbital elements, the data are most sensitive to the semi-major axis and eccentricity. A representative set

of range residuals deduced from such an analysis is shown in Fig. XXXI-5. These residuals are essentially confined within ±6 μsec with a few data points exhibiting larger residuals. Although these residuals seem large, they are reasonable at this stage of the analysis. Figures XXXI-6 and XXXI-7 reveal the structure of the residuals for the first four tracking passes. The first plot reveals a systematic pattern with the peak being reached as the spacecraft goes through periapsis. These systematic trends in the residuals are due to inaccuracies in some of the harmonic coefficients which describe the Mars gravity field. In the second plot in this figure, for which range data at periapsis do not exist, we have a significantly reduced residual trend and a more optimistic set of statistics. The statistics given in these two figures represent the mean residual, the mean squared residual, the RMS residual, and the square root of the variance. This type of residual pattern is repeated throughout the 6 weeks of data under analysis.

C. Status of Analysis

At this stage of the analysis, which is still preliminary, it is difficult to quote values for γ or the solar corona parameters A, B, and ϵ. However, the solutions do exhibit a trend and cluster about the Einstein value for γ. Rigorous error analyses are still in progress, and any attempt to quote realistic standard deviations for γ or other parameters would be inappropriate.

The major areas under investigation which have a potential for degrading the determination of the relativity time-delay parameter are as follows. First, the a priori gravitational coefficients that define the gravity field of Mars have yielded an accurate spacecraft ephemeris. However, the systematic pattern in the range (Figs. XXXI-6 and XXXI-7) and Doppler residuals are a direct indication that this model requires additional refinement. Work to achieve such a "fine tuning" is in progress. Second, the Mariner 9 data are particularly sensitive to the semi-major axis and eccentricity of Mars and the Earth–Moon barycenter. However, the data show little or no sensitivity, beyond the current knowledge, to the orientation of the planet's plane of motion. Additional analysis in this area is necessary before these conclusions can be converted into quantitative statements. Third, the relativity and solar corona time delays are exhibiting a tendency to correlate; however, the full impact of the correlation requires additional analysis. Indications are that the corona time delay is lower than the nominal delay shown in Fig. XXXI-2. During the Mariner 9 superior conjunction, measurements were made of the fluctuation
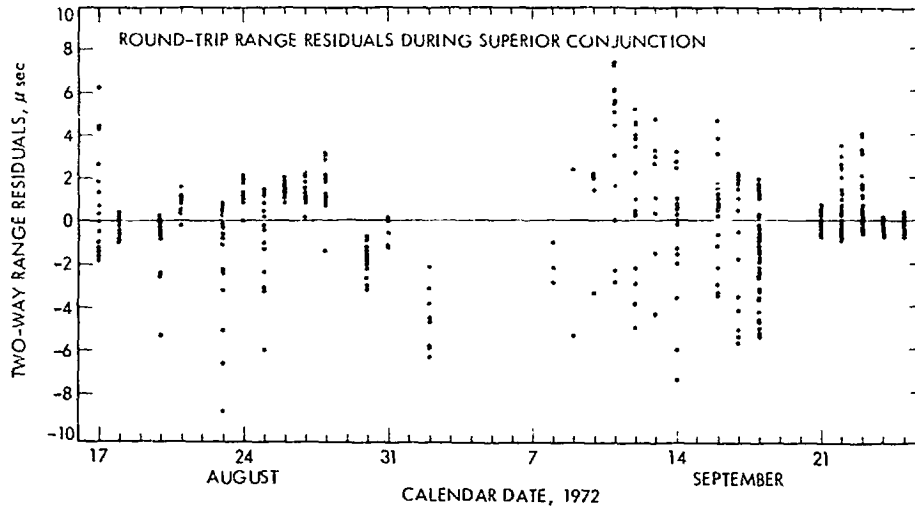
Fig. XXXI-5. Representative set of residuals deduced from the analysis of 6 weeks of superior conjunction data.

	8/17/72	8/18/72
FIRST MOMENT, μ sec	0.249	−0.268
SECOND MOMENT, μ sec^2	5.293	0.245
RMS, μ sec	2.301	0.495
STANDARD DEVIATION, μ sec	2.287	0.416
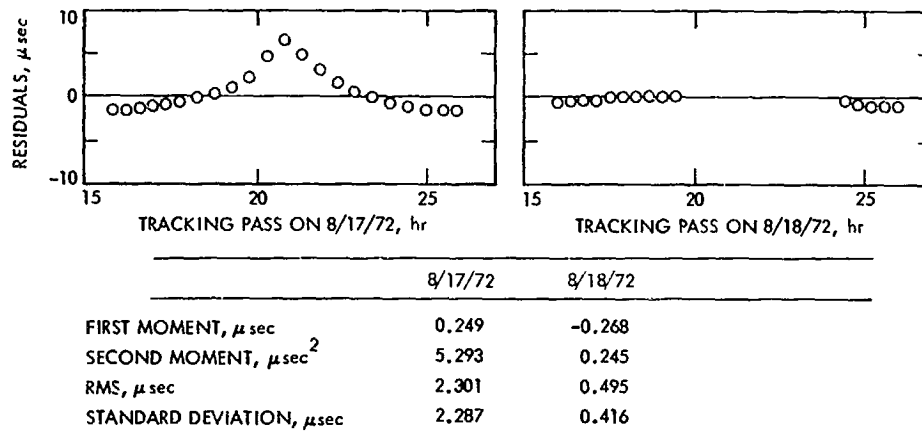
Fig. XXXI-6. Residuals and associated statistics for the first two tracking passes shown in Fig. XXXI-5.

	8/20/72	8/21/72
FIRST MOMENT, μ sec	−0.787	0.842
SECOND MOMENT, μ sec^2	2.857	0.918
RMS, μ sec	1.690	0.958
STANDARD DEVIATION, μ sec	1.496	0.457
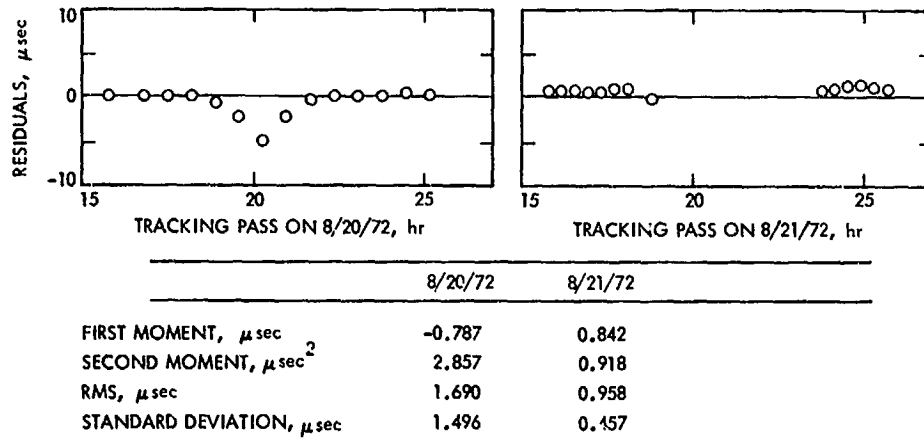
Fig. XXXI-7. Residuals and associated statistics for the third and fourth tracking passes shown in Fig. XXXI-5.

of the electron density along the spacecraft's line of sight; these measurements will be converted into calibrations to the Doppler and range data (see Section XXX of this Report). Although the work is still in progress, calibrations for the effect of the dynamic corona on the tracking data will be available and utilized in the orbit refinement. Finally, the full impact of nongravitational forces and uncertainties in basic constants, such as the astronomical unit, have yet to be fully explored.

Indications are that this method of analysis is yielding fruitful results and that it has the potential for refining the relativity time-delay parameter beyond its present knowledge.

References

XXXI-1. Shapiro, I. I., "Fourth Test of General Relativity," *Phys. Rev. Letters,* Vol. 13, p. 789. 1964.

XXXI-2. Muhleman, D. O., and Reichley, P., "Effects of General Relativity on Planetary Radar Distance Measurements," Space Programs Summary 37-29, Vol. IV, Jet Propulsion Laboratory, Pasadena, Calif., 1964.

XXXI-3. Shapiro, I. I., "Radar Determination of the Astronomical Unit," *Bulletin Astronomique.* Vol. 25, p. 177. 1965.

XXXI-4. Ross, D. K., and Schiff, L. I., "Analysis of the Proposed Planetary Radar Reflection Experiment," *Phys. Rev.,* Vol. 141, p. 1215, 1966.

XXXI-5. Shapiro, I. I., "Testing General Relativity with Radar," *Phys. Rev.* Vol. 141, p. 1219, 1966.

XXXI-6. Shapiro, I. I., Pettengill, C. H., Ash, M. E., Stone, M. L., Smith, W. B., Ingalls, R. P., and Brockelman, R. H., "Fourth Test of General Relativity: Preliminary Results," *Phys. Rev. Letters,* Vol. 20, p. 1265, 1968.

XXXI-7. Shapiro, I. I., Ash, M. E., Ingalls, R. P., Smith, W. B., Campbell, D. B., Dyce, R. B., Jurgens, R. F., and Pettengill, C. H., "Fourth Test of General Relativity: New Radar Result," *Phys. Rev. Letters, Vol. 26,* p. 1132, 1971.

XXXI-8. Anderson, J. D., Esposito, P. B., Martin, W. L., and Muhleman, D. O., "A Measurement of the General Relativistic Time Delay with Data From Mariners 6 and 7," *Proceedings of the Conference on Experimental Tests of Gravitation Theories,* Technical Memorandum 33-499, p. 111, Jet Propulsion Laboratory, Pasadena, Calif., 1971.

XXXI-9. Anderson, J. D., Esposito, P. B., Martin, W. L., and Muhleman, D. O., paper No. a.14, presented at XIV Plenary Meeting of CC JPAR, Seattle, Washington, June 17 to July 2, 1971, 1971.

XXXI-10. Thorne, K. S., and Will, C. M., "High-Precision Tests of General Relativity," *Comments on Astrophys. and Space Phys.,* Vol. 2, p. 35, 1970.

XXXI-11. Schiff, L. I., "Relativity Experiments in Space Vehicles," *Reviews of Geophys. and Space Phys.,* Vol. 9, p. 407, 1971.

References (contd)

XXXI-12. *Proceedings of the Conference of Experimental Tests of Gravitation Theories*. Technical Memorandum 33-499, Jet Propulsion Laboratory, Pasadena, Calif., 1971.

XXXI-13. Holdridge, D. B., "An Alternate Expression for Light Time Using General Relativity," Space Programs Summary 37-48, Vol. III, p. 2, Jet Propulsion Laboratory, Pasadena, Calif., 1967.

XXXI-14. Tausner, M. J., *General Relativity and Its Effect on Planetary Orbits and Interplanetary Observations*, Lincoln Lab. MIT Technical Report No. 425, 1966.

XXXI-15. Eddington, A. S., *The Mathematical Theory of Relativity*, Cambridge University Press, Cambridge, England, 1923.

XXXI-16. Robertson, H. P., in Space Age Astronomy, "Relativity and Cosmology," p. 228, Academic Press, New York 1962.

XXXI-17. Muhleman, D. O., Anderson, J. D., Esposito, P. B., and Martin, W. L., "Radio Propagation Measurements of the Solar Corona and Gravitational Field: Applications to Mariner 6 and 7," *Proceedings of the Conference on Experimental Tests of Gravitation Theories*, Technical Memorandum 33-499, p. 92, Jet Propulsion Laboratory, Pasadena, Calif., 1971.

XXXI-18. Lorell, J., Born, G., Christensen, E., Esposito, P., Jordan, J., Laing, P., Sjogren, W., Wong, S., Reasenberg, R., Shapiro, I., and Slater, G., "Gravity Field of Mars from Mariner 9 Tracking Data," *Icarus*, Vol. 18, No. 2, 1973.

XXXI-19. Born, G. H., Christensen, E. J., Ferrari, A. J., Jordan, J. F., and Reinbold, S. J., *The Determination of the Satellite Orbit of Mariner 9*, paper No. 72-928, presented at AIAA/AAS Astrodynamics Conference, Palo Alto, Calif., 1972.

XXXI-20. Mulhall, B. D., Chao, C. C., Mottinger, N. A., Muller, P. M., Ondrasik, V. J., Sjogren, W. L., Thuleen, K. L., and Trask, D. W., *Tracking System Analytic Calibration Activities for the Mariner Mars 1969 Mission*, Technical Report 32-1499, Jet Propulsion Laboratory, Pasadena, Calif., 1970.

XXXI-21. Brouwer, D., and Clemence, G. M., *Methods of Celestial Mechanics*, Chapter 9, Academic Press, New York, 1961.

Acknowledgment

XXXII. Determination of the Relativistic Time Delay for *Mariner 9*: A Status Report on the JPL Analysis of Normal Points

J. D. Anderson and E. K. Lau

Jet Propulsion Laboratory/California Institute of Technology, Pasadena, California 91103

A. Background

The objective of that part of the celestial mechanics experiment reported in this section is to perform a high-precision test of general relativity. Although the experiment does not concern the planet Mars, by using the tracking data from the *Mariner 9* orbiter a measurement of the relativistic time delay in the ranging signal to the orbiter was performed at superior conjunction. This delay, which amounts to a maximum of about 195 μsec at superior conjunction, was discovered theoretically by Shapiro in 1964 (Ref. XXXII-1), and calculations were carried out independently by Muhleman and Reichley (Ref. XXXII-2). In Refs. XXXII-3, and XXXII-4, Shapiro demonstrated the observational reality of the delay. Since its discovery, the effect has been measured to an accuracy of ±5% with passive radar to Mercury and Venus at superior conjunction (Ref. XXXII-5), and to an accuracy of ±4% with active ranging to the interplanetary spacecraft, *Mariners 6* and 7, at their superior conjunctions in the spring of 1970. Each of these experiments was affected by quite different, but very serious, limiting error sources, which are not a significant factor when ranging to an orbiter anchored to a planet, such as *Mariner 9*. The primary difficulty with the passive radar measurements to Mercury and Venus is that the ranging signal bounces off the front cap of the planet, and topographic variations make it difficult to determine the distance between Earth and the center of mass of the planet, at least to the same precision which can be achieved with a planetary orbiter or lander. However, the main difficulty with ranging to interplanetary spacecraft such as *Mariners 6* and 7 is that the orbits of these spacecraft are affected by nongravitational forces from solar radiation pressure and from the spacecraft's attitude control system. A high-precision measurement of the relativistic time delay to an interplanetary spacecraft is really only possible if that spacecraft can be made purely gravitational or drag free to an acceleration level of 10^{-10} m/sec^2 or more. However, in all of these experiments, the measurement of the relativistic time delay is performed with a radio signal that passes through the interplanetary medium. Consequently, a delay is introduced into the ranging signal by free electrons in the ray path. It is, therefore, necessary to separate the plasma delay from the relativistic delay before a significant test of relativity can be achieved. Because the plasma effects are dispersive and vary as the inverse square of the frequency of the transmitted signal, the effects of the interplanetary medium can be minimized

by ranging at two frequencies. The relativistic delay is independent of frequency. However, in all tests performed to date, including *Mariner 9*, the ranging signal has been transmitted at only one frequency, an S-band frequency of about 2200 MHz. In the future, beginning with the *Mariner* Venus/Mercury 1973 mission, United States' spacecraft will have the capability of being tracked at both S-band and X-band (~8500 MHz). Thus, the Viking mission to Mars may provide experimental relativity with both an anchored spacecraft and a dual-frequency radio system for the calibration of the interplanetary medium. In the meantime, *Mariner 9* and techniques developed in earlier experiments to minimize the error introduced by the interplanetary medium must suffice, in particular, the methods developed by D. O. Muhleman for the *Mariner 6* and 7 relativity test (Ref. XXXII-6).

An accurate method for the interplanetary plasma is difficult to formulate, but a reasonable model consists of an average steady-state component, which is strongly dependent on distance from the Sun, plus a variable stochastic component, which will introduce random delays into the ranging signal and which will cause a loss of coherence in the radio signal as it passes near the Sun. In addition, both range and Doppler data will become increasingly noisy as the spacecraft approaches superior conjunction. The exact nature of the increase in the Doppler noise for *Mariner 9* has been studied empirically (see Section XXX of this report). In the present analysis of the reduced range data (normal points), the stochastic effect of the solar corona is accounted for by downweighting each point by an amount that depends on the distance of the ray path from the Sun. This may be an oversimplification of the actual physics of the solar corona, but it is used here only as a means of downweighting data. The equation used to determine the standard deviation on a single range measurement was derived by Muhleman for *Mariners 6* and 7. This standard deviation is given by

$$\sigma^2 = \sigma_0^2 + \frac{(32.7 \ \mu sec)^2}{p^3} \tag{1}$$

where σ_0 is the instrumental error in the measurement of range, and p is the distance of the ray path from the Sun in solar radii. The constant 32.7 μsec was determined from *Mariner 6* and 7 range residuals and represents a random fluctuation of about 80% in the interplanetary plasma.

The average steady-state component of the plasma delay is obtained by assuming an electron density N_e,

which is a function of distance r from the Sun, and which is given by

$$N_e = \frac{A}{r} + \frac{B}{r^{2.6}} \tag{2}$$

where r is given in units of solar radii, and the constants A, B, and ϵ are parameters that can be estimated from the ranging data. By performing an exhaustive study of the literature of solar eclipse investigations before the *Mariner 6* and 7 test, Muhleman was able to obtain a priori estimates of the parameters A, B, and ϵ as well as values for their standard deviations.

$$A = (1.3 \pm 0.9) \times 10^6 \ \text{electrons/cm}^3$$

$$B = (1.15 \pm 0.7) \times 10^6 \ \text{electrons/cm}^3$$

$$\epsilon = 0.3 \pm 0.3$$

These values have been adopted as a priori estimates of the steady-state corona for *Mariner 9*. In addition, errors in B and ϵ are assumed to be almost perfectly correlated in the a priori covariance matrix to constrain the standard deviation on the number of electrons at Earth's distance (215 solar radii). As a result, the assumed steady-state electron density at Earth is 5 ± 5 electrons/cm^3.

The time delay through the steady-state plasma model given by Eq. (2) can be obtained by integrating along the ray path for each range observation (Ref. XXXII-6). In a similar way, the relativistic time delay can be derived. Perhaps the simplest expression for this delay has been obtained in isotropic coordinates by Holdridge (Ref. XXXII-7) and by Tausner (Ref. XXXII-8). The total one-way light time between the observer and the subject is given in this form by

$$c\Delta t = \rho + (1 + \gamma)m \ln\left(\frac{r_0 + r_1 + \rho}{r_0 + r_1 - \rho}\right) \tag{3}$$

where ρ, r_0 and r_1 are coordinate distances representing, respectively, the observer–spacecraft distance, the Sun–observer distance, and the Sun–spacecraft distance. The parameter m is equal to one-half the gravitational radius of the Sun and is equal to

$$m = \frac{GM_\odot}{c^2} = 1.4766 \ \text{km} \tag{4}$$

To compute the actual round trip of the ranging signal, it is necessary to solve light-time equations for the times of transmission and reception of the signal and to compute the coordinates at the appropriate times.

The second term in the light-time equation (Eq. 3) represents the relativistic time delay. It is parameterized in terms of the relativity parameter γ which can be determined by the method of least squares from the Mariner 9 data. Actually, γ is one of two important parameters (β, γ) in a generalized space–time metric first introduced by Eddington in 1923 (Ref. XXXII-9). It includes post-Newtonian terms and is given in isotropic coordinates by

$$ds^2 = \left[1 - 2\frac{m}{r} + 2\beta\left(\frac{m}{r}\right)^2\right]c^2\,dt^2$$

$$- \left[1 + 2\gamma\frac{m}{r}\right](dx^2 + dy^2 + dz^2) \qquad (5)$$

It has been shown by Will (Ref. XXXII-10) that if any metric theory of gravity possesses integral conservation laws for energy, momentum, angular momentum, and center-of-mass motions, then the Eddington metric (Eq. 5) is sufficient to describe these metric theories of gravity in their post Newtonian or weak-field limits, a limit which is certainly applicable to solar system tests of relativity.

In Einstein's general relativity theory, both β and γ are unity. An experimental determination of β or γ differing significantly from the Einstein values would require that an alternative theory of gravity be adopted. At this time, no reliable experiment indicates values of β or γ that are significantly different from unity; in fact, no significant measurement of β has yet been achieved. The superior conjunction time-delay and light-deflection experiments are sensitive to a parameter $\gamma^* = 1/2\,(1 + \gamma)$ which, as can be seen from Eq. (3), determines the amount of the time delay. The 4% test of general relativity achieved by the tracking of Mariners 6 and 7 implies an accuracy of $\pm 8\%$ in γ. This is not sufficiently accurate to exclude a value of γ that differs significantly from the Einstein value. For example, based on a measurement of the solar oblateness (Refs. XXXII-11 through XXXII-13) and on the accurate determination of the precession of the perihelion of Mercury (Ref. XXXII-14), it can be concluded that γ should be equal to 0.86, although the deflection and time-delay experiments indicate that a value this small is unlikely. Therefore, the goal of the Mariner 9 data analysis, which represents the first analysis for an anchored spacecraft, is to obtain a value for γ which will be significantly more accurate than previous determinations, whether by means of the measurement of the deflection of radiation from radio sources, or by the measurement of the time delay

in radio signals to the planets and Mariners 6 and 7. This goal has not yet been achieved, but some of the progress made to date is reported here, and the methods of the data analysis are explained.

The last data from Mariner 9 were obtained approximately 2 weeks before the writing of this report, and the analysis of the relativity data, which is being performed jointly by experimenters at JPL and at MIT, has just begun. In fact, the experience gained to date has convinced all experimenters that the data analysis is quite complicated and that it is not possible to predict at this time with any certainty what the accuracy of the result will be or when it will be obtained. It is anticipated that several months will be required to obtain a significant result. Yet, despite the difficulty of the analysis, the experimenters remain optimistic about the importance of the Mariner 9 determination of γ. Also, although a value of β will not be obtained from approximately 1 year of ranging data, nevertheless Mariner 9 will be important to an ultimate determination of this parameter, when it is possible to combine the data now available with future passive radar ranging to the planets and with future data from Mariner Venus/Mercury 1973, Helios, and Viking.

B. Method of Data Analysis

To perform a relativity test at superior conjunction to an accuracy of about 1% with ranging data from Mariner 9, the relative position of the Earth and Mars must be known to an accuracy on the order of a few tens of meters. Even with all of the past radar and optical data, it is not possible to achieve these accuracies. The last radar data to Mars were taken in October 1971, and thus any Earth–Mars orbits which are determined solely from the past radar and optical data must be extrapolated into the region of the Mariner 9 mission. Extrapolated orbits are notoriously unreliable, and for this reason the Mariner 9 relativity test depends heavily on the accurate determination of the relative Earth–Mars orbit from the data taken over the entire period from injection into orbit on November 14, 1971 (GMT), until the last ranging pass on October 27, 1972.

Ideally, the analysis of the tracking data for the relativity experiment could be accomplished by placing all of the range and Doppler data into a gigantic least-squares estimation program and then by determining simultaneously all of the parameters that define the models for the orbit of the spacecraft, the orbit of Mars, the orbit of Earth, the gravity fields of Mars, the relativity

parameters β and γ, the steady-state solar corona parameters A, B, and ϵ, and so on. In practice, this is clearly impossible. Not only would the computational time and storage capabilities of the computer be exceeded, but also the nongravitational forces acting on the spacecraft would prevent the determination of its orbit over such a long period of time. It would be necessary to resort to methods of sequential estimation with respect to the spacecraft orbit, which in itself would place greater demands on storage capabilities and computer time. Therefore, it is essential to find a method for reducing the tracking data to a tractable set of compressed data, which will still contain all of the relativity information of the raw data.

The procedure which has been chosen to accomplish a reduction of the *Mariner* 9 tracking data makes use of Doppler data over relatively short arcs of about one to nine orbital revolutions to determine the orbit of the spacecraft about Mars. Next, with the knowledge of the Mars-centered orbit, it is possible to use the range data to the spacecraft to determine the distance between the center of Earth and the center of Mars for each short interval of tracking data. These reduced range measurements between the centers of the two planets make up the basic data for the relativity test. The details of the generation of these reduced data, called normal points, are discussed in Section XXX of this Report. The raw data used to generate the normal points are described in Section XXIX. The performance of the relativity experiment up to and including the generation of the normal points has been a joint effort between the experimenters at JPL and MIT. By mutual agreement, the subsequent analysis, which involves making least-squares fits to the normal points and solving for the relativity parameters along with other orbital and coronal parameters, will be performed independently by the MIT and JPL teams. The experimenters will reach a mutual agreement on the final results of the experiment. The analysis of the normal points at JPL is being performed using a set of computer programs called the Solar System Data Processing System (SSDPS; Ref. XXXII-15). At MIT, the analysis is being performed with a similar, but completely independent, system called the Planetary Ephemeris Program (PEP). Because the final results from both JPL and MIT will depend directly on the validity of the normal points, the experimenters at both institutions are taking an active part in the generation of the points. Also, as a check on the solutions obtained from the normal points, P. B. Esposito (see Section XXXI of this Report) is fitting both the raw range and Doppler data over a 6-week arc centered about superior conjunction.

The first set of normal points was generated and a least-squares fit was obtained by differentially correcting the orbital elements of Earth and Mars. The fit was surprisingly good with an RMS residual of about 0.12 μsec (18 m). The interval of time from the first to last normal point extended from November 20, 1971, to February 14, 1972. Sometime later, a second set of normal points was generated, which extended this arc to July 30, 1972. With a little over 8 months of normal points now available, new ephemerides for the inner planets were generated by combining the *Mariner* 9 data with all of the past radar and optical data that had been included in previous JPL ephemerides. This work is discussed in Section XXXIV of this Report. As a result of the work, a new ephemeris was produced which contains both the JPL radar data from the 1971 Mars opposition and 8 months of *Mariner* 9 normal points. This new ephemeris, which was called Development Ephemeris 82 (DE 82), was used to evaluate later tracking data; it was able to predict range data to an accuracy of a few microseconds.

During August, September, and October, new normal points were generated on a schedule of about once per week, and they were fit with new corrections to the orbits of the inner planets. These fits were useful in the editing and evaluation of the validity of the normal points. However, in all solutions performed during this period, it was never possible to obtain a significant solution for the relativity parameter γ. The solutions were quite sensitive to changes in the data weighting scheme, the parameter set used in the solution, and the number of normal points used in the fit. It became clear that the analyses of the normal points and the determination of a definitive value of γ from the *Mariner* 9 data would be difficult, and that it would require a considerable amount of time to understand a new and unfamiliar experiment which was presenting many unforeseen problems. It was evident that, before the experiment was over, it would be necessary to perform one or more refinements of the normal points and to experiment with a number of methods of fitting those points. The correct procedure for combining the normal points with the past optical and radar data would have to be determined, and new gravity and topographical models for Mars would have to be obtained.

The procedure that has been followed to date for processing the *Mariner* 9 normal points within the SSDPS is first to input the normal points on punched cards into a program which writes a magnetic tape containing the equations of condition for the least-squares process. Data residuals are formed by directly differencing the

input normal point and a predicted normal point based upon a standard ephemeris. Because the equations of condition for all past radar and optical data at JPL are referred to Development Ephemeris 69 (DE 69), the standard ephemeris for the reduction of the normal points is also DE 69 for consistency. This ephemeris is accurate enough that linear corrections to the elements of the planets are sufficient to determine the least-squares fit to all radar, optical, and spacecraft data. All that is involved in computing the predicted value of the normal point, which is simply the instantaneous distance between the center of Earth and the center of Mars, is to read the DE 69 ephemeris tape at the time associated with the normal point and to find the Earth–Mars distance at that time. To this basic coordinate distance, the relativistic time delay given by Eq. (3) is added, as well as a correction for the coronal delay, which is obtained by integrating along the ray path through a plasma with an electron density given by Eq. (2). The normal point represents the round-trip light time, $c\Delta t$ between the center of Earth and the center of Mars; hence, the residual placed on the tape containing the equations of condition is parameterized according to the following symbolic representation:

$$(O - C) \sim \Delta t \text{ (normal point)}$$

$$- \frac{2}{c} \rho \text{ (ephemeris parameters, } \gamma)$$

$$\Delta_R (\gamma) - \Delta_c (A, B, \epsilon) \qquad (6)$$

The range ρ is the coordinate distance between Earth and Mars. The correction Δ_R is the relativity delay and to the first order in meters is a function of γ only. The correction Δ_c represents the delay through the interplanetary medium and is a function of the coronal parameters A, B, and ϵ. The coordinate range ρ is also a function of the relativity parameter γ, for the reason that the range is determined by the relativistic orbital dynamics of Earth and Mars. Consistency between the orbital dynamics and the propagation delay in this experiment is ensured by performing all calculations in isotropic coordinates. For example, DE 69 is based on a numerical integration of the relativistic orbital equations in isotropic coordinates with the parameter γ set equal to the Einstein value of unity. The residuals before the fit in all of the solutions performed to date are based on the Einstein theory ($\gamma = 1$) and on the a priori corona model discussed in Section XXXII-A. The differential correction process finds new values for all of the parameters so that the residuals after the fit are minimized in a least-squares

sense. If the total set of all parameters is given by x and if the partial derivatives of the normal points with respect to the whole set of parameters are collected into a matrix Φ, and, further, if the weights associated with the normal points are collected into a diagonal weighting matrix W, then the least-squares differential correction formula is

$$(\Phi^T W \Phi) \Delta x = \Phi^T W \Delta z \qquad (7)$$

where Δz represents the set of all residuals before the fit and Δx represents the corrections to be applied to the nominal parameters to best fit the data. The residuals after the fit $\Delta z'$ can be obtained from the linear relationship

$$\Delta z' = \Delta z - \Phi \Delta x \qquad (8)$$

In addition to the residuals and their associated weights, which are computed by Eq. (1), the partial derivatives are evaluated by subprograms within the SSDPS and are placed on magnetic tape. The partial derivatives with respect to the relativity parameter γ involve both a dynamical variation through the coordinate range ρ in Eq. (6) as well as an explicit derivative in the propagation term Δ_c. The partial derivatives with respect to the corona parameters A, B, and ϵ are evaluated by means of a subroutine, constructed by Esposito and Hamata, which computes both the correction Δ_c and the partial derivatives of the correction with respect to the three coronal parameters. This routine allows for the possibility of an asymmetric corona with different values of the three parameters in the pre-conjunction and post-conjunction phases of the mission. However, to this time, the data analysis has assumed a symmetric corona, and this appears adequate for the *Mariner 9* data analysis (see Section XXXII-G).

The next step in the formation of a best-fit solution to the normal points is to use the tape containing the partial derivatives Φ, the diagonal elements of the weighting matrix W, and the residuals Δz and then to form the normal equations of Eq. (7). The matrices $\Phi^T W \Phi$ and $\Phi^T W \Delta z$ are output on punched cards. The advantage of having this information on cards is that it is now possible to combine the normal equations from the spacecraft data. Thus, solutions are easily obtainable for varying sets of data and for any subset of parameters among the total set included in the normal equations. The normal equations for various data sets are combined according to the linear relations

$$[\Sigma(\Phi^T W \Phi)] \Delta x = \Sigma(\Phi^T W \Delta z) \qquad (9)$$

The linear equation (9) is solved by means of routines discussed in Ref. XXXII-16 by Lawson and Hanson. Residuals after the fit for any solution Δx can be obtained by returning to the data tape containing the equations of condition and by applying Eq. (5). These residuals after the fit can be plotted automatically by computer routines.

In essence, this is the procedure that is being followed in the analysis of the *Mariner 9* normal points. Computational details and the many options available to the user of the SSDPS have been omitted from this discussion. Many details pertaining to the analysis of the interplanetary medium can be found in Ref. XXXII-6. The equations necessary to incorporate general relativity into the spacecraft tracking problem can be found in Refs. XXXII-6 and XXXII-17. The logical structure of the SSDPS and a description of its subroutines are given in Ref. XXXII-18.

C. Preliminary Set of Normal Points From *Mariner 9*

A preliminary set of normal points is available now over an interval of time extending from November 17, 1971, to October 11, 1972. A discussion of the generation of these points is given in Section XXX of this Report, and their accuracy is evaluated. A normal point is defined as the instantaneous round-trip light time between the center of Earth and the center of Mars at a given time of observation. The actual relativistic time delay and the coronal time delay are included in the normal point. There are often two or more normal points for a single time of observation. When this occurs, it means that more than one determination of the spacecraft orbit was used to determine the normal point. Usually one point will be generated from an orbit determined over one revolution of the spacecraft, whereas another point will be determined from a longer arc, from about three to nine revolutions. No attempt has been made at this point in the analysis to distinguish between the normal points from a short arc and those from a long arc. The systematic drifts in the normal points over a single pass, whether caused by variations in the interplanetary plasma density or by errors in the orbit determination of the spacecraft, are of greater concern with respect to this preliminary set of points.

As a starting point for the *Mariner 9* data analysis, it was decided to compute residuals in the normal points to DE 80 rather than the nominal ephemeris DE 69 because DE 80 contains the 1971 Mars opposition data, and the residuals in the normal points are smaller than those based on DE 69. To compute these residuals to DE 80, it was necessary to apply corrections to the parameters of DE 69 which are given in Ref. XXXII-19. The corrections to the parameters of DE 69, which produce DE 80, are listed in Table XXXII-1. In all, there are 32 parameters which have been differentially corrected. These include six orbital elements for each of the four inner planets, bias corrections to the right ascension and declination measurements of Mercury and Venus to account for phase effects, the radii of Mercury, Venus, and Mars, and the astronomical unit. The value of the astronomical unit in DE 69 is 149,597,893.0 km. The values of β and γ are both unity, and the quadrupole moment in the Sun's gravity field is assumed to be 0. The radii of the planets and their inverse mass ratios are given in Table XXXII-2. All planetary masses except for Mercury are based on spacecraft flybys and are of relatively high accuracy with respect to determinations that can be performed with radar and optical data alone. The mass of Earth is determined from near-Earth data on *Ranger* and *Mariner* missions, and the mass of the Earth–Moon system is of comparable accuracy because of accurate determinations of the lunar inequality from interplanetary spacecraft and radar observations.

The computation of coronal delays for each normal point, as well as the partial derivatives of the data with respect to the coronal parameters, requires a knowledge of the transmitted frequency through the interplanetary medium. Although this frequency was a variable and was changed from pass to pass, the total difference between the smallest frequency transmitted and the largest was less than one part in 10^4 of the transmitted frequency; and, for purposes of coronal delay, calculations can be neglected. A good average transmitted frequency that can be attached to all of the normal points is a value of 2.1144×10^9 Hz. The frequency transmitted from the spacecraft back to the ground station is not the same as the transmitted frequency. In the spacecraft, the frequency received from the ground is multiplied by a factor of 240/221. The difference in the frequency on the up-leg of the transmission and the down-leg is taken into account in the coronal subroutine used to compute corrections and partial derivatives. The normal points up to the Julian Ephemeris Date (JED) 2441325.5 were constructed with ranging data taken from DSS 12 of the Deep Space Network. After that date, the ranging equipment was moved to DSS 14, and all subsequent normal points were generated with ranging data from that station.

Table XXXII-1. DE 69 corrections for radar and optical data

Parameter[a]	DE 80	Past	Δ past − DE 80	σ (past)	Δ/σ (past)
$\Delta l_o - \Delta r$ for Mercury	−0.193	−0.049	0.144	0.101	1.43
Δ_p for Mercury	0.123	−0.158	−0.281	0.180	−1.56
Δ_l for Mercury	−0.101	0.131	0.232	0.157	1.48
$e \Delta r$ for Mercury	−0.034	−0.036	−0.002	0.047	−0.04
$\Delta a/a$ for Mercury	0	−0.040	−0.040	0.040	−1.00
Δe for Mercury	0.004	0.036	0.032	0.026	1.23
Bias in right ascension for Mercury	0.007	−0.009	−0.016	3.38	−0
Bias in declination for Mercury	0.185	0.241	0.056	3.66	0.02
Radius of Mercury, km	1.982	0.329	−1.653	7.46	−0.22
$\Delta l_o \div \Delta r$ for Venus	−0.204	−0.071	0.133	0.092	1.45
Δ_p for Venus	−0.009	0.071	0.080	0.093	0.86
Δ_q for Venus	−0.177	0.034	0.211	0.095	2.22
$e \Delta r$ for Venus	−0.002	−0.026	−0.024	0.023	−1.04
$\Delta a/a$ for Venus	0	−0.033	−0.033	0.029	−1.14
Δe for Venus	0.001	0.014	0.013	0.013	1.00
Bias in right ascension for Venus	−0.746	−0.430	0.316	0.191	1.65
Bias in declination for Venus	−0.085	0.086	0.171	0.177	0.97
Radius of Venus, km	1.900	−0.901	−2.801	6.97	−0.40
$\Delta l_o - \Delta r$ for Earth–Moon barycenter	−0.213	−0.086	0.127	0.086	1.48
Δ_p for Earth–Moon barycenter	0.081	0.082	0.001	0.081	0.01
Δ_q for Earth–Moon barycenter	0.139	0.073	−0.066	0.090	−0.73
$e \Delta r$ for Earth–Moon barycenter	−0.003	0.006	0.009	0.011	0.82
$\Delta a/a$ for Earth–Moon barycenter	0	−0.024	−0.024	0.022	−1.09
Δe for Earth–Moon barycenter	0.002	0.023	0.021	0.020	1.05
$\Delta l_o + \Delta r$ for Mars	−0.210	0.088	0.122	0.089	1.37
Δp for Mars	−0.014	−0.120	−0.106	0.146	−0.73
Δ_q for Mars	0.038	−0.027	−0.065	0.145	−0.45
$e \Delta r$ for Mars	−0.013	−0.006	0.007	0.013	0.54
$\Delta a/a$ for Mars	0.001	−0.017	−0.018	0.019	−0.95
Δe for Mars	0.008	0.023	0.015	0.021	0.71
Radius of Mars, km	19.28	33.98	14.70	25.36	0.58
Mass of Mercury (inverse mass units)		42887		141600	0.30
Mass of Venus (inverse mass units)		6.60		440	0.02
Mass of Earth–Moon barycenter (inverse mass units)		33.97		281	0.12
Mass of Mars (inverse mass units)	—[b]	−912		22942	−0.04
Mass of Jupiter (inverse mass units)	—[b]	0.27		0.67	0.40
Mass of Saturn (inverse mass units)	—[b]	−25.7		74	−0.35
Mass of Uranus (inverse mass units)	—[b]	−1723		4585	−0.38
Mass of Neptune (inverse mass units)	—[b]	−5698		27588	−0.21
Mass of Pluto (inverse mass units)	—[b]	−1.80 D6		491 D6	−0
Astronomical unit, km	1.788	−0.495	−1.293	7.253	−0.18
Beta (dimensionless)	—[b]	4.47		3.54	1.26
Gamma (dimensionless)	—[b]	0.890		1.48	0.60
J_2 of the Sun (dimensionless)	—[b]	29.5 D − 5		25.96 D − 5	1.14

[a]Units are arc seconds unless specified.

[b]Parameter is not included in the DE 80 solution.

Table XXXII-2   Standard DE 69 values

Parameter	Standard DE 69 value, km
Radius of Mercury	2441
Radius of Venus	6053
Radius of Mars	3376
Inverse mass of Mercury	5,983,000
Inverse mass of Venus	408,522
Inverse mass of Earth–Moon barycenter	325,900.1
Inverse mass of Mars	3,098,700
Inverse mass of Jupiter	1047.3908
Inverse mass of Saturn	3499
Inverse mass of Uranus	22,930
Inverse mass of Neptune	19,260
Inverse mass of Pluto	1,812,00

A plot of all residual points before the fit, referred to DE 80, is shown in Fig. XXXII-1. The striking systematic error evidenced in these residuals is caused primarily by an error in the eccentricity of Mars in DE 80.

As shown in the plot, a rough curve fit to the normal point residuals shown in Fig. XXXII-1 will produce some very small residuals after the fit, and these residuals can be used to eliminate the few normal points whose errors are very much larger than the RMS residual after the fit. All of these blunder points have been removed from the given data set, and, consequently, a preliminary editing of the data has been accomplished.

D. Radar and Optical Data

Considerable information on the orbits of the inner planets, including Earth and Mars, is available from past radar and optical data. The relativity test could be strengthened by combining the normal point data discussed previously with the set of data that went into the construction of DE 80. With this in mind, normal equations produced by Keesey et al. for the development ephemerides (see Section XXXIV of this Report) were obtained on punched cards. However, it was decided, at least for the preliminary analysis, to downweight the past radar and optical data for two reasons: (1) A measurement of the time delay requires an accurate orbit of Mars with respect to Earth. Only the *Mariner 9* data provide additional information on Mars in this region. Therefore, it was decided to perhaps over-emphasize the importance of the normal points in the determination of the Earth–Mars orbit. (2) The radar bounce data to the inner planets are systematically in error because of topo-
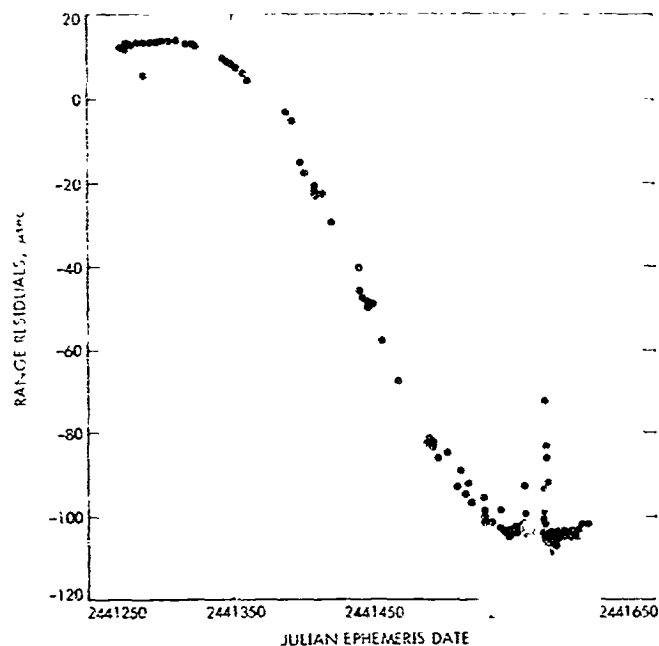
Fig. XXXII-1.   Range residuals of all *Mariner 9* normal points using DE 80.

graphic variations on these planets. Because of errors, it was decided that the radar data would be used only to condition the least-squares solution for the orbit of the inner planets; the orbits of Earth and Mars would not necessarily be constrained to fit the radar data.

The procedure adopted to account for systematic errors from topographic variations in the radar data was to downweight each set of normal equations by an amount consistent with the RMS residual on the data associated with a particular set of normal equations. At least in the first stages of the data analysis, a most conservative weighting of the radar and optical data was adopted. The RMS residual on each set of radar data used as the limiting error on that set and each observation was weighted by multiplying the square-root of the total number of points in the data set by the RMS residual. Each RMS value was determined from plots of all radar residuals from DE 82. Similarly, for the 28,237 meridian circle observations, which were compressed into six sets of normal equations, a value of 0.058 arc sec was somewhat arbitrarily selected as the limiting error, and the square root of the total number of optical observations for each set of normal equations was multiplied by this limiting error.

A summary of the weighting scheme is shown in Table XXXII-3. The last two columns of the table are included for comparison purposes only. They give the amount by

Table XXXII-3. Past data

Normal equation	Observatory	Planet observed	Number of observations	Unweighted RMS residual, μsec	Weighting σ for each point, μsec	Weighting factor	Weighting factor, (DE 80), deg
			Past radar data				
1	Arecibo	Mercury	119	70	770	77	1
2	Haystack	Mercury	88	15	141	12	1
3	Haystack	Venus	63	10	80	11	1
4	Millstone	Venus	101	100	1000	5	1
5	JPL (=13 monostatic)	Venus	285	30	507	25	1
6	Arecibo	Mars	30	182	990	5	1
7	Haystack	Mars	118	50	550	14	20
8	JPL (=13 monostatic; =13 and 14 bistatic)	Mars	242	20	310	160	20
9	JPL (=13 and 14 bistatic; =14 monostatic)	Mars	761	25	685	655	20

Normal equation	Observation type	Number of observations	Weighting factor	Weighting factor (DE 80)
		Past optical data[a]		
10	Declination	7222	8.5	1
11	Right ascension	7386	8.6	1
12	Declination	6384	8.0	1
13	Right ascension	6766	8.2	1
14	Declination	230	1.5	1
15	Right ascension	249	1.6	1

[a]Meridian circle observations of Mercury, Venus, Mars, and the Sun from the United States Naval Observatory. Each point has an a priori σ of 0.1 arc sec.

which each set of normal equations was downweighted from its a priori value for both the conservative weighting scheme described here and for the weighting scheme that was used to produce DE 80. The most significant difference between these two weighting schemes is a factor of about 34 in the weighting of the 1971 Mars opposition data.

The use of the RMS residual as the limiting error on a set of data and the corresponding weights given in Table XXXII-3 are generally conservative. In the future, when the topographic variations have been removed from the data, the present weighting scheme should then be abandoned in favor of a more optimistic one. However, in the current analysis, all of the normal equations listed separately in Table XXXII-3 have been combined into a single set of normal equations by applying the weights

given in column 7 of the table and by summing according to Eq. (9). In this way a single set of normal equations has been produced which represents all past radar and optical data that have been included in the JPL development ephemerides. This by no means represents all of the existing radar data. The experimenters at MIT have processed considerably more data, including some very important superior conjunction data which resulted in the 5% test of relativity reported in Ref. XXXII-6. These data from the Arecibo and Haystack Observatories are now available to the experimenters at JPL and are being reduced. Although this is a very important effort in the overall area of experimental relativity, it is not directly related to the *Mariner* 9 relativity test. From the viewpoint of this test alone, the use of a set of normal equations which incorporates only the past [?] data is justified. Again, the normal equations for the

past data are intended only as a means of conditioning the *Mariner 9* solution. However, it is possible to place more importance on the past data by uniformly upweighting the single set of normal equations for the past data when they are combined with the *Mariner 9* normal equations. By this technique, the relative weighting of the 15 individual sets of normal equations for the past data is unchanged. If in the future it is decided, for example, that the 1971 radar opposition data should be made more important, then it will be necessary to reprocess all 15 sets of normal equations with a smaller standard deviation on the 1971 opposition set

As a means of investigating the effect of the new weighting scheme on the least-squares estimate of the parameters of the inner planets, the set of normal equations for the past radar and optical data were first solved without the introduction of any *Mariner 9* data. The result is shown in the third column of Table XXXII-1 beside the solution for DE 80. The difference between the two solutions, which used exactly the same set of data but differed in the application of weights, is also shown in Table XXXII-1. The standard deviations are tabulated and obtained from the square root of the diagonal elements of the inverse normal matrix $\Phi^T W \Phi$ from the solution with the conservative weighting. This solution is labeled "past" in Table XXXII-1. The ratio of the differences in the two solutions and the standard deviations are tabulated in column 6 of Table XXXII-1. Outside of a few minor corrections to the orientation elements p and q of the inner planets, the only really significant difference between DE 80 and the solution with a more conservative weighting is that the mean longitudes of all the inner planets have been shifted by about 0.13 arc sec. However, this is not important because without the optical data it would be impossible to define an absolute reference direction in space for the planetary orbits. The radar data can determine accurately the relative positions of the planets, but it contains no information on their absolute positions with respect to the fixed stars. The optical data tie the solar system to an inertial reference or star catalog (FK4) upon which the optical observations are based. A change in the relative weighting of the six sets of normal equations for the optical data can easily produce changes in the definition of the absolute reference direction for the planetary orbits.

The solution to the past data and the estimate of the error or standard deviation on each parameter are acceptable. The corrections to the masses of all the planets are insignificant with respect to their standard errors, although it should be pointed out that all of these masses

are better determined by other data than by those used in this solution. However, the fact that all of the masses are essen... 'y consistent with DE 69, which uses a current set of planetary masses, indicates that the overall solution is valid. Also, the standard deviations, although somewhat large, seem reasonable. They indicate, for example, that the JPL radar and optical data set can determine the astronomical unit to about ± 7 km. This is about a factor of 2 larger than the error estimate from previous determinations of the astronomical constants, where a realistic standard deviation was determined by performing many solutions and by observing the range of variations in the constants (Ref. XXXII-18). Of course, a solution such as that presented here, which includes a number of parameters that can not be determined well from the data, will predict some unrealistically large errors in parameters that should be determinable. The most striking example of this is in the radius of Mars, which is uncertain by ± 25 km. However, a removal of the mass of Mars from the solution reduces this uncertainty to about ± 6 km, a value which is much more consistent with the assumed limiting error of 25 μsec (3.75 km) in the normal set (Eq. 9). The important consideration with respect to the solution given in Table XXXII-1 is that it represents a meaningful set of normal equations for all of the past JPL ephemeris data.

Experimentation with the set of normal equations for the past data support the conclusion drawn from Table XXXII-1 that there is no relativity information in the past data. This is consistent with findings by Shapiro (Ref. XXXII-14) with respect to β and J_2 and is not inconsistent with the fact that he has reported a 5% determination of the constant $1/2\ (1+\gamma)$; some very important superior conjunction data are included in the MIT reduction which are not included here. The lack of information on γ in the JPL past data means that the use of the normal equations for these data will not bias the relativity solution when the *Mariner 9* normal points are added. The solution for γ from the past data of 0.890 ± 1.48 shows that the *Mariner 9* data can be used to determine practically any value of γ that will fit the normal points. However, the orbits of Earth and Mars are constrained by the past data by a conservative, but fairly realistic, amount.

E. Edited Normal Points

A plot of residuals to DE 80 for all normal points is shown in Fig. XXXII-1. The scale of this plot makes it impossible to evaluate short period variations in the normal points over a single pass of range data. To

investigate these short period variations, several fits to the normal points have been used to generate residuals over every pass where more than three normal points are available. There are passes before superior conjunction when the residuals decrease with time, and periods after superior conjunction when they increase, just the opposite of the behavior predicted by the steady-state model. Some of these systematic variations in the normal points are undoubtedly caused by plasma fluctuations, but others in regions far from superior conjunction must be caused by errors in the spacecraft orbit determination. Every attempt is being made at the present time to eliminate systematic errors from the normal points (see Section XXX of this Report). However, until this is accomplished, some alternative must be found to using all of the normal points in the least-squares fit. Otherwise, very little progress will be made in the analysis of the normal points for relativity purposes. Probably the best approach is to eliminate the rapid variations by arbitrarily selecting from each pass of normal points one point to represent the entire pass. As a result of this type of selection procedure, the total edited set of 1194 normal points has been reduced by a second editing or selection to only 94 points. These points are listed in Table XXXII-4. The first column gives the Julian Ephemeris Date for the normal points; the second column gives the normal points themselves; the third column gives the assumed weight on the normal points, as computed from the Muhleman weighting model of Eq. (1). The assumed instrumental error σ_u for all normal points before the date of the loss of the overseas tracking stations is 0.1 μsec; after that date it is assumed equal to 0.3 μsec. These figures are probably too small at this stage, but a factor of 3:1 is about right for the relative weighting. The entire set of normal points can be downweighted uniformly to account for a large absolute error, if desired.

Equations of condition have been formed for the 94 normal points given in Table XXXII-4, and a set of normal equations has been generated based on the weights given in that table. The parameters are the same as those used to construct the normal equations for the past radar and optical data (see Table XXXII-1). These normal equations can now be used to obtain solutions for the relativity parameter γ.

F. Solutions for Constants and Relativity Parameters

Three representative solutions are shown for subsets of the parameters included in the normal equations for the past data and the Mariner 9 normal points. Because all of the solutions to date were obtained for the purpose of gaining an understanding of the problems with the analysis of the Mariner 9 normal points, the emphasis of the analysis described here is on a comparison of fits to three data sets. The first set contains the past radar and optical data alone; the second contains the past data and the 94 Mariner 9 normal points of Table XXXII-4; the third contains the normal points and all past data, with the exception of the radar measurements to Mars. Solutions to the first set indicate what can be achieved with the past JPL data set alone. This set does not include the available Haystack data from April 1971 to February 1972. Fits to the second set include opposition data from radar ranging and spacecraft ranging, and fits to the third set can be used to check the consistency of the Goldstone Mars radar data and the Mariner 9 normal points. A fit to the third set of data generates an Earth–Mars ephemeris based on the normal points alone, and the validity of this ephemeris can be tested by computing residuals on the radar data not in the fit. This provides a strong test because the fit to the normal points, which extend from November 20, 1971, to October 27, 1972, must be extrapolated backward in time over a 6-year period to compute residuals on all Mars radar data.

The three solutions given in Table XXXII-5 show good consistency in the values of all constants except for the relativity parameter γ. The determination of the mass of Mercury is of particular interest because it appears that the Mariner 9 normal points contain information about it. Although the solutions can not be taken too seriously at this preliminary stage of the analysis, the computed standard deviation of about ±2500 (0.4%) on the inverse mass ratio is significant, if valid. Its validity will be checked by comparing it with similar solutions from the MIT group. However, the uncertainty in the mass of Jupiter is relatively larger and is not significant. Discussions of the current uncertainty in the masses of all principal planets have been given by Kovalevsky (Ref. XXXII-20) and by Ash et al. (Ref. XXXII-2).

The solutions for the corona parameters (B, ϵ) are reasonable, although the convergence to the least-squares estimates is nonlinear. Three iterations on values of the corona parameters, taken above, were required before the corrections to B and ϵ were small enough ($\sim 0.1\ \sigma$) to conclude that a converged solution had been obtained. The a priori values of all other parameters, except B and ϵ, were well within the linear region of convergence.

Table XXXII-4. Edited set of *Mariner 9* normal points selected on the basis of one point per tracking pass

Julian date of observation	Normal point	Standard deviation for weight	Julian date of observation	Normal point	Standard deviation for weight
.244127568405093 + 007	.852421861025504 − 009	.100	.244140255280093 + 007	.193521736504456 ± 010	.300
.244127668057870 − 007	.860004179896432 ÷ 009	.100	.244140954793981 − 007	.199178552916768 ÷ 010	.300
.244127752432870 − 007	.866449284264243 − 009	.100	.244141023821759 ÷ 007	.199729458026805 − 010	.300
.244127870142361 − 007	.875478540810764 ÷ 009	.100	.244142048335648 ÷ 007	.207737767380891 − 010	.300
.244127972224537 − 007	.883344402-797408 − 009	.100	.244144150627315 ÷ 007	.222989983503683 − 010	.301
.244128166668981 − 007	.898413571207307 ÷ 009	.100	.244144356460648 ÷ 007	.224389955004365 − 010	.301
.244128365974537 ÷ 007	.913975759018295 ÷ 009	.100	.244144663127315 ÷ 007	.226442721527644 010	.301
.244128442363425 − 007	.919970854900273 − 009	.100	.244145650696759 ÷ 007	.232764093531037 ÷ 010	.301
.244128664932870 − 007	.937533649479015 ÷ 009	.100	.244146848474536 − 007	.239802202183434 − 010	.301
.244128741668981 + 007	.943621629076560 ÷ 009	.100	.244149046043981 − 007	.250800761921585 − 010	.302
.244128864238426 · 007	.953380744391295 ÷ 009	.100	.244149358613426 − 007	.252147654761528 ÷ 010	.302
.244128964238426 − 007	.961374643002958 ÷ 009	.100	.244149722293980 − 007	.253645674797492 ÷ 010	.303
.244129040974537 − 007	.967528202522920 ÷ 009	.100	.244151118682870 ÷ 007	.258686015690602 ÷ 010	.305
.244129163196759 − 007	.977363936863365 − 009	.100	.244151616668981 ÷ 007	.260195981240918 ÷ 010	.307
.244129343057869 − 007	.991914784656633 − 009	.100	.244152021877314 + 007	.261310978586218 ÷ 010	.309
.244129445835648 ÷ 007	.100027002182909 ÷ 010	.100	.244152943682870 ÷ 007	.263470278882264 ÷ 010	.316
.244129563196759 ÷ 007	.100984618561542 ÷ 010	.100	.244153028335647 ÷ 007	.263642228825379 ÷ 010	.317
.244129863474537 ÷ 007	.103451454409520 ÷ 010	.100	.244153442918981 − 007	.264418833909284 − 010	.323
.244129960766204 − 007	.104255704855730 + 010	.100	.244154036043981 ÷ 007	.265335828110288 ÷ 010	.340
.244130060766204 − 007	.105084791367076 + 010	.100	.244154438474537 + 007	.265825683708937 + 010	.362
.244130161043981 ÷ 007	.105918610195486 ÷ 010	.100	.244154627085648 ÷ 007	.266018512503223 ÷ 010	.377
.244130248960648 ÷ 007	.106651593740970 ÷ 010	.100	.244154734585647 + 007	.266117974644905 + 010	.388
.244130360071759 ÷ 007	.107580482423178 ÷ 010	.100	.244154829238425 ÷ 007	.266199295516850 ÷ 010	.399
.244130650349537 ÷ 007	.110019825134447 ÷ 010	.100	.244155040210647 + 007	.266359558355130 ÷ 010	.431
.244130759377315 ÷ 007	.110940481662067 ÷ 010	.100	.244155125210647 + 007	.266415967927587 ÷ 010	.448
.244131247224537 ÷ 007	.115086914002985 + 010	.100	.244155339168981 + 007	.266537307560370 + 010	.504
.244131867363426 + 007	.120416048360822 ÷ 010	.100	.244155428196759 + 007	.266579110399086 + 010	.535
.244132249307869 ÷ 007	.123729120034695 ÷ 010	.100	.244155532780091 + 007	.266621704431884 + 010	.579
.244132447224537 + 007	.125454600865049 + 010	.100	.244155624863426 + 007	.266653379376001 + 010	.627
.244132547224537 + 007	.126328541825055 + 010	.100	.244155727085648 + 007	.266682136703699 ÷ 010	.693
.244134470141204 + 007	.143315784413338 + 010	.100	.244155843821759 + 007	.266706704361319 + 010	.789
.244134672224537 + 007	.145111129934851 + 010	.100	.244157228057870 + 007	.266307731852884 + 010	1.929
.244135072918981 + 007	.148673119321758 + 010	.100	.244157345141203 + 007	.266214829231797 + 010	1.506
.244135470141204 + 007	.152205324740234 + 010	.100	.244157433821759 + 007	.266138361881723 + 010	1.273
.244136172918981 + 007	.158447031040027 ÷ 010	.100	.244157538752314 + 007	.266041116528737 + 010	1.066
.244134770488426 + 007	.145984422593102 + 010	.300	.244157734863425 + 007	.265839812087827 + 010	.809
.244134872224537 + 007	.146888749499433 + 010	.300	.244157824030092 + 007	.265739906459510 + 010	.728
.244135372918981 + 007	.151340849005016 + 010	.300	.244157935766203 + 007	.265607366745929 + 010	.648
.244139951530093 + 007	.191024643361692 + 010	.300			

Table XXXII-5. Solutions

Parameters	1 Radar and optical	2 Radar, optical, and Mariner 9	3 Radar (Mercury, Venus), optical, and Mariner 9
Astronomical unit	149597893.0 ± 5.6	149597891.8 ± 0.9	149597891.6 ± 2.1
Radius of Mercury	2440.8 ± 5.6	2440.7 ± 2.6	2439.2 ± 2.7
Radius of Venus	6050.7 ± 3.3	6051.4 ± 1.4	6050.6 ± 1.4
Radius of Mars	3394.6 ± 6.6	3389.0 ± 2.0	—[a]
Inverse mass of Mercury	6022406.5 ± 77572.2	5983544.7 ± 2244.2	5984530.0 ± 2569.6
Inverse mass of Jupiter	—[a]	1047.51 ± 0.10	—[a]
B corona	—[a]	$0.325 \times 10^{6} \pm 0.205 \times 10^{6}$	$0.237 \times 10^{6} \pm 0.628 \times 10^{6}$
ϵ corona	—[a]	-0.004 ± 0.089	-0.089 ± 0.270
β	5.2 ± 3.2	—[a]	2.4 ± 2.0
J_2 (Sun)	$24.5 \times 10^{-5} \pm 24.9 \times 10^{-5}$	—[a]	$15.0 \times 10^{-5} \pm 22.9 \times 10^{-5}$
γ	2.0 ± 1.3	1.12 ± 0.05	1.02 ± 0.04

[a]Nominal values of Table XXXII-2 were used.

It is tempting to look at the solutions for γ in Table XXXII-5 and to conclude that a unity value is indicated. Solution 3 yields a value of 1.02 ± 0.04. However, at this stage of the data analysis, a strong objective reason for preferring Solution 3 over Solution 2, which indicates $\gamma = 1.12 \pm 0.05$, can not be found. The inconsistency between the values of γ in Solutions 2 and 3 is viewed as an indication that something is wrong with the fits to the data, or that either the spacecraft or radar data, or both, contain systematic errors. Residuals for the 94 normal points are shown in Fig. XXXII-2 for Solution 3.

G. Steady-State Plasma Model

The least-squares solutions of Section XXXII-F contain the interplanetary plasma parameters B and ϵ. Here, a preliminary evaluation of the physical significance of one of the solutions for these parameters (Solution 2) is attempted. It is important to remember that B and ϵ were assumed to be almost perfectly correlated so that the electron density at the distance of Earth from the Sun would be constrained to 5 ± 5 electrons/cm³. Also, no attempt has been made to estimate the parameter A from the normal points, because all of the data used in the fit were taken sufficiently far from the Sun that there is no real information on the parameter A in the least-squares normal equations. In fact, because of the almost perfect correlation between B and ϵ, the solutions in Section XXXII-F for the corona
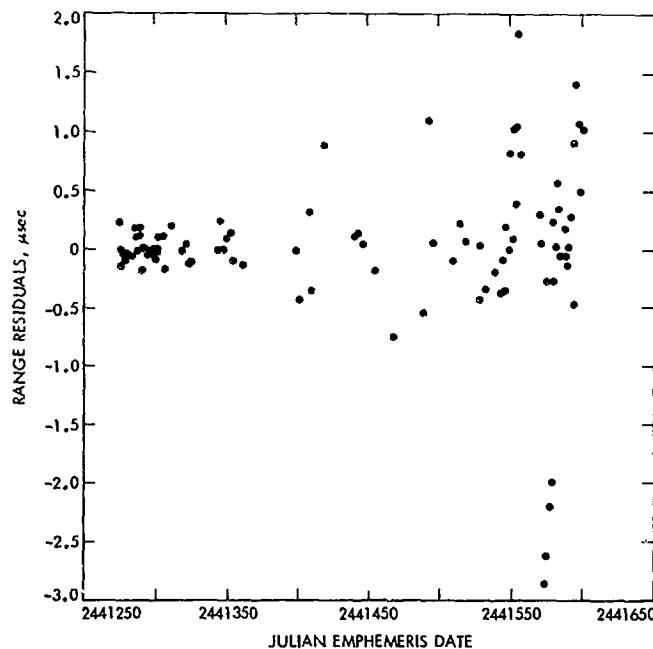
Fig. XXXII-2. Solution 3 range residuals for edited set of Mariner 9 normal points.

parameters are essentially determining only one parameter for the plasma model. It would be possible, for example, to fix the value of ϵ at its a priori value and solve for only the parameter B. Although a very reasonable fit to the normal points could be achieved this way, the constraint on the number of electrons at the Earth's distance would almost surely be violated. There-

fore, for purposes of evaluating the steady-state plasma density at the time of the *Mariner* 9 superior conjunction, it is far superior to solve for both parameters B and ϵ. The fixing of the parameter A at its a priori value in effect places an additional constraint on the plasma model. The electron density in a region very near the limb of the Sun is determined almost completely by the A term in the corona model. Thus, the interplanetary electron density is constrained to a value of $1.3 \times 10^{-}$ electrons/cm^{3} at the limb of the Sun and to 5 electrons/cm^{3} at the distance of Earth. In effect, the plasma model used in the *Mariner* 9 data analysis is fixed at two end points, but it contains one degree of freedom, which can be used to best fit the normal points in the region of interplanetary space probed by the *Mariner* 9 ranging signal.

As a first step in the determination of a plasma model for the *Mariner* 9 superior conjunction, an attempt was made to evaluate the real coronal time delay for each normal point in the region of superior conjunction. This evaluation was accomplished by constructing a new set of equations of condition for the normal points, but unlike those for the solutions of Section XXXII-F, the corona correction (Δ_c in Eq. 6) was set equal to zero when computing residuals before the fit. Normal equations were formed in the usual manner, and a least-squares fit to the uncorrected residuals was obtained. The relativity parameter γ and the corona parameters B and ϵ were not included in the solution. Thus, a value of unity was assumed for γ, and the best orbits of Earth and Mars, consistent with the Einstein theory, were used to fit the normal points and to obtain residuals after the fit. Because no plasma corrections were applied to the computed data, these residuals after the fit should reflect the real plasma delay, if the normal points are valid. This is true because the orbital elements of Earth and Mars can not be adjusted to absorb a significant portion of the coronal time d ' , at superior conjunction.

A plot of the residuals after the fit is shown in Fig. XXXII-3. A time delay at superior conjunction is clearly evident and, assuming that Einstein's general relativity theory is correct, the delay is caused solely by the passage of the S-band signal through the solar corona. The curve appears fairly symmetrical. This fact is more obvious if a plot of the log of the residuals on both sides of conjunction is constructed as a function of the log of the distance p of closest approach of the ray path to the Sun. Such a plot is shown in Fig. XXXII-4, where both the post-conjunction residuals and pre-conjunction residuals have been plotted. The pre-conjunction and post-conjunction residuals are completely consistent, and, for all
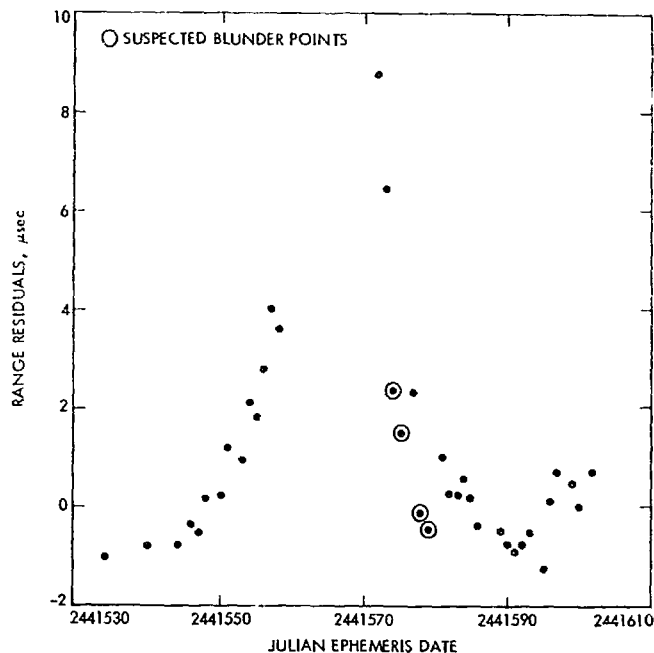
Fig. XXXII-3. Solar coronal delay in *Mariner* 9 normal points.
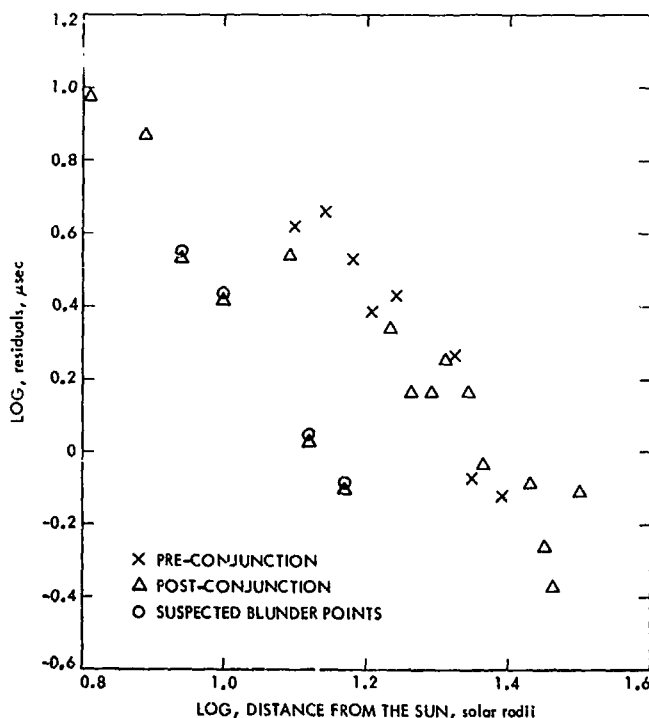
Fig. XXXII-4. Plot of the log of the residuals of the edited set of *Mariner* 9 normal points around superior conjunction as a function of the log of the closest approach of the ray path to the Sun.

444

practical purposes, they indicate that a symmetrical corona model is adequate for the *Mariner* 9 analysis. The four exceptional residuals probably reveal blunder points that should be removed from the data set. However, because the magnitudes of the actual residuals are small with respect to the standard deviation used in the weighting scheme (see Table XXXII-4), a removal of these four points is difficult to justify.

The best values of the corona parameters A, B, and ϵ from the *Mariner* 9 data at the present time are given by the a priori value of A and the values of B and ϵ from Solution 2. These values are

$$A = (1.30 \pm 0.9) \times 10^{\star} \text{ electrons/cm}^{3}$$

$$B = (0.325 \pm 0.205) \times 10^{6} \text{ electrons/cm}^{3}$$

$$\epsilon = -0.004 \pm 0.089$$

The electron density that results from this *Mariner* 9 model is plotted in Fig. XXXII-5, along with the density profiles from the superior conjunctions of *Mariners* 6 and 7 (Ref. XXXII-15). It can be seen that the corona model determined from all three spacecraft is similar, although the *Mariner* 9 conjunction is separated by about 28 months from the conjunctions of the two earlier *Mariners*. All three corona models fall significantly below the a priori model, which is also plotted in Fig. XXXII-5.

As pointed out by Muhleman (Ref. XXXII-6), the integrated electron density is a more fundamental quantity for the evaluation of the model of the solar corona. It is directly proportional to the measured time delay, and it can be computed by integrating the electron density given by Eq. (2) along a radial direction from the Sun between a point at distance r_0 to a point at the Earth's distance. A plot of this integrated density as a function of the heliocentric distance r_0 is shown in Fig. XXXII-6. Three representative points from a profile determined by eclipse observation (Ref. XXXII-22) are also shown on this plot for comparison purposes. Also shown is a direct measurement by the dual-frequency technique of the integrated density between the Earth and *Mariner* 4, when it was near Venus (Ref. XXXII-23), and a dual-frequency radar measurement to the surface of Venus (Ref. XXXII-24). The *Mariner* 9 curve is in excellent agreement with the eclipse observations. These observations are affected by the integrated plasma relatively near the Sun, and this is the region where the plasma model must fit the *Mariner* 9 data as well. The values of the directly determined integrated densities between Earth and Venus indicate that the spacecraft
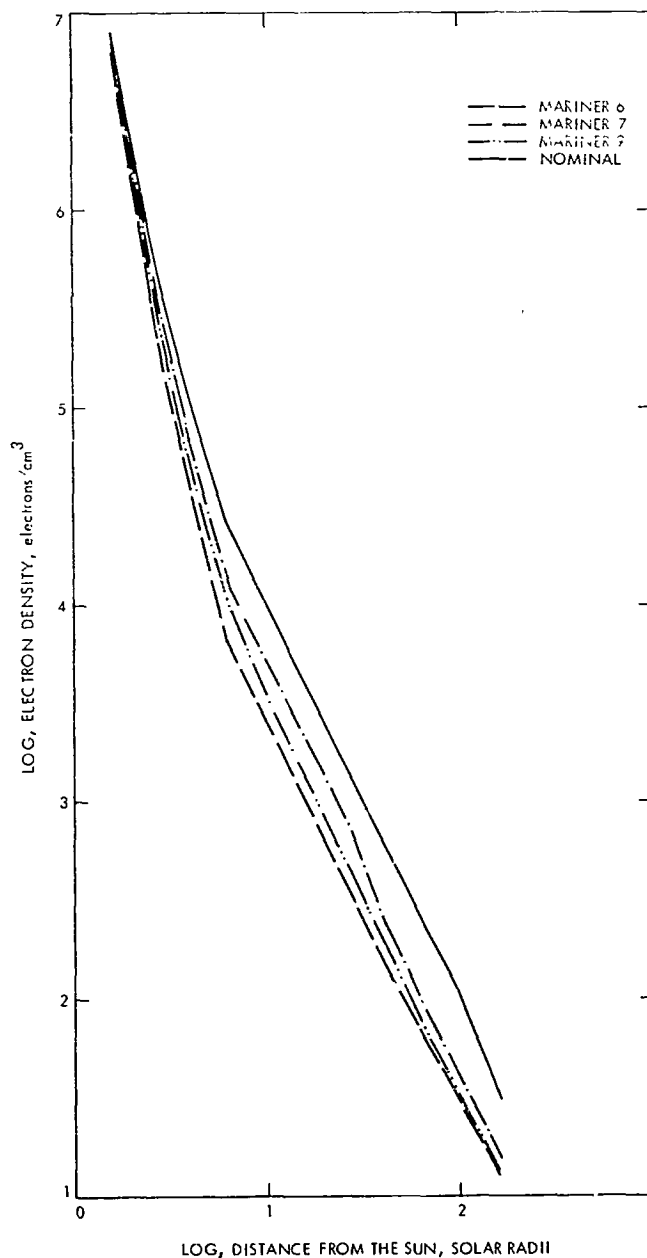
Fig. XXXII-5. Electron density curves from *Mariner* 9 compared with those from *Mariner* 6, *Mariner* 7, and the standard corona model.

plasma models do not decrease rapidly enough in a region beyond 0.7 AU. However, because the total plasma delay (~ 0.03 μsec) for an integrated electron density of 10^{14} electrons/cm^2 is less than the instrumental error in the ranging system (~ 0.1 μsec), a deficiency in the model at distances far from the Sun is unimportant to the analysis of the *Mariner* 9 data.
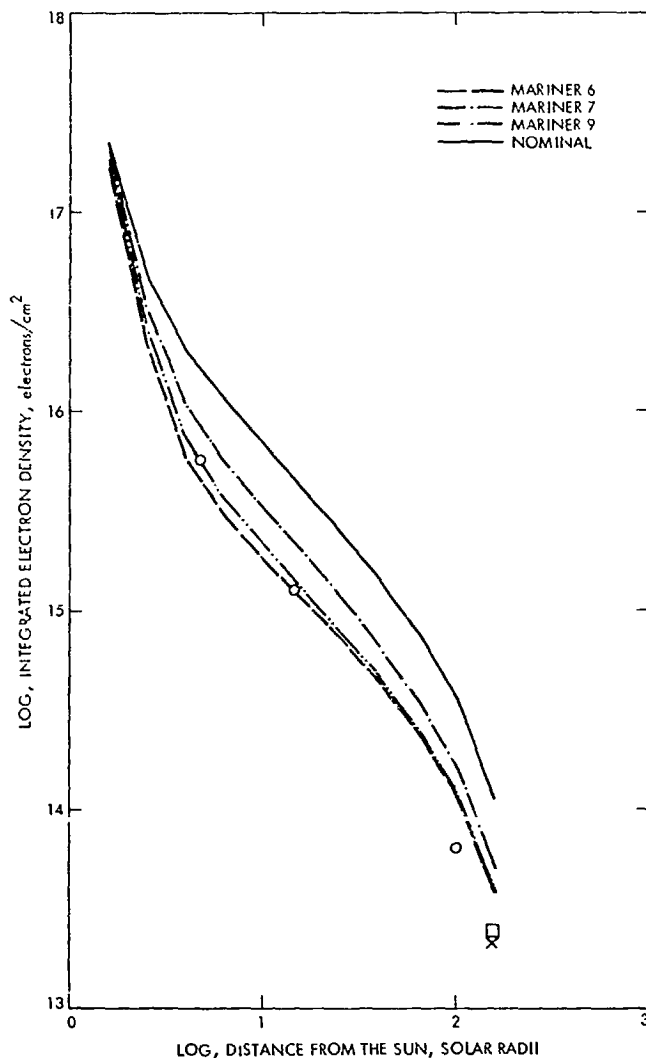
Fig. XXXII-6. Integrated electron density curves from Mariner 9 compared with those from Mariner 6, Mariner 7, and the standard corona model. Three profile points (O) of Blackwell are plotted. The x represents a Mariner 4 two-frequency measurement near Venus, and the ▢ represents a two-frequency radar measurement to Venus (Refs. XXXII-22, through XXXII-24).

H. Closure Analysis

In all solutions that combine the normal points from *Mariner* 9 with past radar data, it is important to check for consistency between the two data sets. The normal points provide tracking to the center of Mars, while the radar signals, which are reflected from various locations on the surface, will be at a different distance or radius from the center of the planet; and noise will be introduced into the radar residuals, even if the orbits of the Earth and Mars are accurately known. This type of noise is called "topographic noise" to distinguish it from other error sources such as the instrumental equipment

or the ephemerides. Also, topographic noise is distinguishable from other noise sources because it is something that does not exist in the spacecraft data. In principle, it could also be eliminated from the radar data, if all measurements were made to exactly the same spot on the planet, although this would severely limit the size of the data set. In the 1971 Mars opposition data, there are a few radar measurements which are significantly separated in time and which are referred to approximately the same location on the planet. By using these pairs of points (closure points), it is possible to greatly reduce the topographic noise on the points. It should then be possible to examine the residuals in the closure points and to attribute any systematic effects in the residuals to errors in the ephemerides. With respect to the *Mariner* 9 relativity experiment, the analysis of closure points should provide an excellent method for evaluating the accuracy of the Earth–Mars orbits and for determining the consistency of the fits to the normal points and the radar data, when both data types are included in the solutions.

Some experimentation with a closure analysis has been performed as a part of the relativity test. This experimentation is in a preliminary state and is reported here primarily for purposes of completeness. Plans are to develop the method more fully in the future and to apply it to all solutions that combine spacecraft and radar data. The experimentation to date will be described by means of examples.

A listing of 13 pairs of closure points from the 1971 opposition is given in Table XXXII-6. Absolute locations of the points may be doubtful because of errors in the ephemerides. Locations of individual points can differ by 12 km, depending on whether they are computed with DE 80 or DE 82, but relative positions of closure points differ by less than 1 km. Also included in Table XXXII-6 are residuals from the three solutions of this report. The difference between the residuals for each closure point is divided by the interval of time between the two radar measurements, and this result is also tabulated as a range-rate error in microseconds/day. The first solution of the table is that of Section XXXII-D to the past radar and optical data. The second is Solution 2 in which both the Mars radar and the normal points are in the fit; the third is Solution 3 in which the Mars radar is left out of the fit. This last tabulation is particularly interesting because it indicates how well the ephemeris produced by the *Mariner* 9 normal points can predict the Mars radar data not in the fit. The solution reported here (Solution 3) does this, but some other

reasonable fits to the normal points fail the closure test by as much as 120 μsec. At the present time, study continues to determine why some solutions lack closure, whereas others achieve it easily. About all that can be done until the reasons are found is to reject solutions that fail closure and tentatively accept those that pass.

To interpret the lack of closure in the three solutions of Table XXXII-6, the difference in the closure residuals divided by the time interval is assumed equal to the range-rate error in the ephemeris at a time midway between the two times of observation. The result is plotted for the three solutions in Figs. XXXII-7 through

XXXII-9. The error appears small in all three cases (0.1 μsec/day ≈ 0.17 mm/sec), although the range-rate residuals are nearer to zero in the two solutions when the *Mariner 9* data are used than in the solution with radar and optical data alone.

To study the ephemeris error in Solution 3 in more detail, a quadratic fit to the range-rate errors of Fig. XXXII-9 has been performed. The fit satisfies the criterion of weighted least squares, wherein the standard deviations for the weights have been computed by dividing an arbitrary proportion of the geographic separation of the points by the time interval between them. Thus,

Table XXXII-6. Closure points, radar residuals, and ephemeris error in range rate for three solutions

Time of observation, JED	Latitude, deg	Longitude, deg	Residual Solution 1 (past data), μsec	Range-rate μsec/day	Residual Solution 2, μsec	Range-rate error, μsec/day	Residual Solution 3, μsec	Range-rate error, μsec/day
2441122.89584	−17.885	286.871	15.17	0.020	−40.68	0.067	−124.66	−0.087
2441235.74793	−18.034	287.071	17.44		−33.17		−134.42	
2441129.01946	−17.797	274.251	4.14	0.050	−49.00	0.073	−136.52	−0.055
2441235.71112	−18.028	274.170	9.4		−41.18		−142.43	
2441129.03196	−17.796	278.635	9.01	0.055	−44.13	0.079	−131.64	−0.050
2441235.72432	−18.030	278.795	14.90		−35.71		−136.96	
2441129.07015	−17.795	292.029	14.18	0.048	−38.93	0.071	−126.47	−0.057
2441235.76182	−18.036	291.940	19.28		−31.3		−132.58	
2441155.94654	−16.127	2.144	15.81	0.169	−26.77	0.031	−126.45	0.039
2441221.58751	−15.965	2.387	26.89		−24.74		−123.89	
2441155.98404	−16.124	15.278	21.61	0.160	−20.96	0.022	−120.66	0.030
2441221.62362	−15.970	15.050	32.12		−19.51		−118.67	
2441173.83196	−14.554	161.872	11.78	0.205	−29.53	−0.055	−131.64	0.039
2441207.67362	−14.467	161.845	18.71		−31.38		−130.31	
2441170.85765	−14.789	197.439	18.61	0.159	−22.42	−0.082	−124.49	−0.001
2441210.85348	−14.744	197.457	24.98		−25.70		−124.51	
2441173.95696	−14.545	205.766	0.94	0.213	−40.38	−0.047	−142.49	0.047
2441207.79932	−14.477	205.946	8.15		−41.97		−140.89	
2441173.76946	−14.559	139.925	−2.43	0.198	−43.73	−0.055	−145.84	0.034
2441210.68959	−14.729	139.962	4.89		−45.76		−144.58	
2441173.77918	−14.558	143.339	3.01	0.209	−38.29	−0.044	−140.40	0.045
2441210.69932	−14.730	143.372	10.73		−39.93		−138.74	
2441176.87709	−14.338	151.184	5.72	0.261	−36.04	−0.009	−138.07	0.092
2441207.64307	−14.464	151.125	13.76		−36.33		−135.25	
2441176.94932	−14.333	176.545	−0.42	0.308	−42.18	0.	−144.21	0.138
2441207.71598	−14.470	176.708	9.06		−41.04		−139.97	
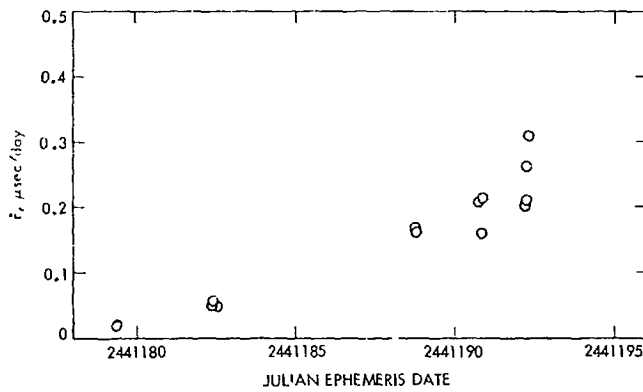
Fig. XXXII-7. Range-rate error in the Earth–Mars ephemeris as deduced from a closure analysis on Mars radar residuals from a fit to past radar and optical data only.
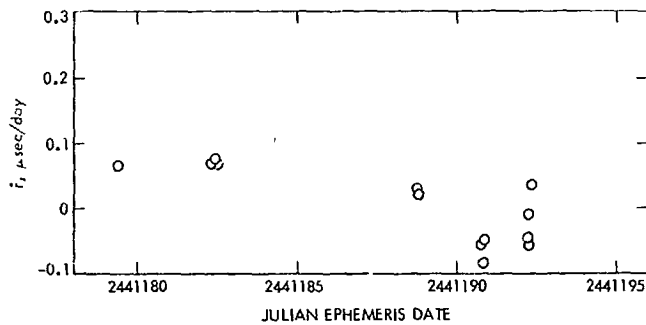
Fig. XXXII-8. Range-rate error in the Earth–Mars ephemeris as deduced from a closure analysis on Mars radar residuals from a fit to both Mariner 9 and past radar and optical data.
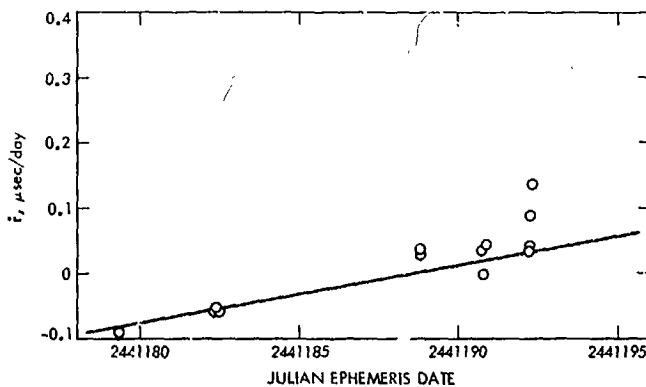
Fig. XXXII-9. Range-rate error in the Earth–Mars ephemeris as deduced from a closure analysis on Mars radar residuals from a fit to Mariner 9 and past data, but with the Mars radar data left out of the fit. A quadratic fit to the error points is shown.

points which are close together on the surface of Mars and which are separated by a large time interval receive the highest weights in determining the range-rate error in the ephemeris.

The fit to the range-rate errors of Solution 3 is shown in Fig. XXXII-9, and the corresponding polynomial for the range-rate error $\delta \dot{r}$ in the ephemeris is given by

$$\delta \dot{r} \ (\mu\text{sec/day}) = -1.4379 + (6.169 \times 10^{-3})\,\tau$$
$$+ (7.710 \times 10^{-6})\,\tau^2 \tag{10}$$

where $\tau = \text{JED} - 2441000.0$. This error curve can be integrated and an expression for the error in the distance to Mars can be obtained. The result is

$$\delta r \ (\mu\text{sec}) = \delta r_0 - 1.4379\,\tau + (3.084 \times 10^{-3})\,\tau^2$$
$$+ (2.570 \times 10^{-6})\,\tau^3 \tag{11}$$

Now, if any residual from Solution 3 for the 1971 opposition data is subtracted from this polynomial for δr, the result, except for the unknown constant δr_0, should represent a determination of the distance from the center of Mars to the subradar point on its surface. Thus, by using closure points to find the range-rate error in the Earth–Mars ephemeris produced by Solution 3, it is possible, over the region of the 1971 opposition data, to remove this ephemeris error from the radar residuals and to interpret the resulting corrected residuals in terms of topographic heights above a reference sphere. Such heights for all radar observations that comprise the 13 closure points are shown in Table XXXII-7. The first column gives the time of observation, the second the uncorrected residual from Solution 3, and the third gives the difference between the polynomial of Eq. (14) and the residual for each point. The constant in Equation (14) has arbitrarily been set equal to 4.870 μsec so that the mean of all the resulting heights for the 26 observations of the closure points is equal to zero. The heights are given in meters, where a unit conversion of 1 μsec = 149.9 m has been applied to the difference of the polynomial and the residual.

If it were possible to remove the ephemeris error completely from the radar residuals, if the two subradar points of each closure point were exactly coincident, and, if the errors in the radar range measurements were zero, then the heights for the two subradar points would agree exactly. The failure of an exact agreement in Table XXXII-7 indicates that one or more of these conditions is not being satisfied. It is known that the

448

Table XXXII-7. Residuals for closure points referred to a reference sphere with ephemeris range-rate error removed

Time of observation, JED	Residual Solution 3, μsec	Height, m	Δh, m
2441122.89584	−124.66	627	184
2441235.74793	−134.42	811	
2441129.01946	−136.52	1910	100
2441235.71112	−142.43	2010	
2441129.03196	−131.64	1178	12
2441235.72432	−136.96	1190	
2441129.07015	−126.47	400	137
2441235.76182	−132.58	537	
2441155.94654	−126.45	−1222	−343
2441221.58751	−123.89	−1565	
2441155.98404	−120.66	−2091	−255
2441221.62382	−118.67	−2346	
2441173.83196	−131.64	−1009	−97
2441207.67362	−130.31	−1106	
2441170.95765	−124.10	−2016	132
2441210.85348	−124.51	−1884	
2441173.95696	−142.49	615	−132
2441207.79932	−140.89	483	
2441173.76940	−145.84	1121	−3
2441210.68959	−144.58	1118	
2441173.77918	−140.40	306	−63
2441210.69932	−138.74	243	
2441176.87709	−138.07	−99	−268
2441207.64307	−135.25	−367	
2441176.94932	−144.21	820	−477
2441207.71598	−139.97	343	

two subradar points are separated on the average by about 12 km, which in itself could explain the disagreements tabulated in column 4 of Table XXXII-7. Average slopes in terrain of about 1.7% would be sufficient to explain these disagreements. However, if they are caused by errors in measurement, then the standard deviation in a single radar observation can be found by dividing the estimate of the standard deviation on the values of Δh by $2^{1/2}$. The mean of the values of Δh is −82.5 m,

and an estimate of the standard deviation is 205 m. Thus, the error in a radar range measurement needed to produce the discrepancies of Table XXXII-7 is ±145 m, or ±0.97 μsec. Actually, precision of a radar measurement is closer to 0.1 μsec; the error of ±145 m is probably caused by the topography.

Whatever the source of the error in the closure analysis, an accurate set of heights can be obtained by averaging each pair of values for the two subradar points. The 13 results are given in Table XXXII-8, wherein the latitudes and longitudes are average values for the two subradar points of each pair. An estimate of the accuracy of these heights can be obtained by dividing the estimate of the standard deviation in the values of Δh by two. Thus, the heights should be accurate to ±103 m. However, it is important to note that these heights represent distances above a reference sphere of unknown radius. The accuracy of the absolute distance to points on the surface of Mars is limited by an uncertainty in the mean radius of the planet. This limit is at least an order of magnitude larger than the error in the relative heights.

Table XXXII-8. Average latitude, longitude, and height above a reference sphere for 13 closure points. (Latitude and longitude are accurate to ±0.2°. Standard longitude error in heights is ±103 m.)

Latitude, deg	Longitude, deg	Height, m
−17.960	286.971	719
−17.913	274.211	1960
−17.913	278.715	1184
−17.916	291.985	469
−16.046	2.266	−1394
−16.047	15.164	−2219
−14.511	161.859	−1058
−14.767	197.448	−1950
−14.511	205.856	549
−14.644	139.944	1120
−14.644	143.356	275
−14.401	151.155	−233
−14.402	176.627	582

References

XXXII-1. Shapiro, I. I., "Fourth Test of General Relativity," *Phys. Rev. Lett.*, Vol. 13, p. 789, 1964.

XXXII-2. Muhleman, D. O., and Reichley, P., "Effects of General Relativity on Planetary Radar Distance Measurements," Space Programs Summary 37-29, Vol. IV, p. 239, Jet Propulsion Laboratory, Pasadena, Calif., 1964.

XXXII-3. Shapiro, I. I., "Radar Determination of the Astronomical Unit," *Bulletin Astronimique*, Vol. 25, p. 177, 1965.

XXXII-4. Shapiro, I. I., "Testing General Relativity With Radar," *Phys Rev. Lett.*, Vol. 141, p. 1219, 1966.

XXXII-5. Shapiro, I. I., Ash, M. E., Ingalls, R. P., Smith, W. B., Campbell, D. B., Dyce, R. B., Jurgens, R. T., and Pettengill, G. H., "Fourth Test of General Relativity: New Radar Results," *Phys. Rev. Lett.*, Vol. 26, p. 1132, 1971.

XXXII-6. Anderson, J. D., Esposito, P. B., Martin, W. L., and Muhleman, D. O., in *Proceedings of the Conference on Experimental Tests of Gravitational Theories*, Technical Memorandum 33-499, Jet Propulsion Laboratory, Pasadena, Calif., 1971.

XXXII-7. Holdridge, D., "An Alternate Expression for Light Time Using General Relativity," Space Programs Summary 37-48, Vol. III, Jet Propulsion Laboratory, Pasadena, Calif., 1967.

XXXII-8. Tausner, M. J., *General Relativity and its Effect on Planetary Orbits and Interplanetary Observations*, Lincoln Laboratory Technical Report 425, Massachusetts Institute of Technology, Cambridge, Mass., 1966.

XXXII-9. Eddington, A. S., *The Mathematical Theory of Relativity*, Harvard University, Cambridge, Mass., 1923.

XXXII-10. Will, C. M., *The Theoretical Tools of Experimental Gravitation*, Lectures presented at Course 56 of the International School of Physics "Enrico Fermi," Italy, July 17 to July 28, 1972.

XXXII-11. Dicke, R. H., and Goldenberg, H. M., "Solar Oblateness and General Relativity," *Phys. Rev. Lett.*, Vol. 18, p 313, 1967.

XXXII-12. Dicke, R. H., "Internal Rotation of the Sun," *Ann Rev. Astron. and Astrophys.*, Vol. 8, p. 297, 1970.

XXXII-13. Dicke, R. H., "The Solar Oblateness and the Gravitational Quadrupole Moment," *Astrophys. J.*, Vol. 159, p. 1, 1970.

XXXII-14. Shapiro, I. I., Pettengill, G. H., Ash, M. E., Ingalls, R. P., and Campbell, D. B., "Mercury's Perihelion Advance: Determination by Radar," *Phys. Rev. Lett.*, Vol. 28, p. 1594, 1972.

XXXII-15. Anderson, J. D., Esposito, P. B., Martin, W., and Muhleman, D. O., *Measurement of General Relativistic Time Delay With Mariners 6 and 7*, paper No. a.14, presented at XIVth Plenary Meeting of COSPAR, June 17 to July 2, 1971.

References (contd)

XXXII-16. Hanson, R. J., and Lawson, C. L., "Extension and Applications of the Householder Algorithm for Solving Linear Least Squares Problems," *Math. Comp.*, Vol. 23, p. 787, 1969.

XXXII-17. Moyer, T. D., *Mathematical Formulation of the Double-Precision Orbit Determination Program (DPODP)*, Technical Report 32-1527, Jet Propulsion Laboratory, Pasadena, Calif., 1971.

XXXII-18. Lieske, J. H., Melbourne, W. G., O'Handley, D. A., Holdridge, D. B., Johnson, D. E., and Sinclair, W. S., "Simultaneous Solution for the Masses of the Principal Planets from Analysis of Optical, Radar, and Radio Tracking Data," *Celestial Mechanics*, Vol. 4, p. 223, 1971.

XXXII-19. O'Handley, D. A., Holdridge, D. B., Melbourne, W. G., and Mulholland, J. D., *JPL Ephemeris Number 69*, Technical Report 32-1465, Jet Propulsion Laboratory, Pasadena, Calif., 1969.

XXXII-20. Kovalesky, J., Détermination des Masses des Planetes," *Celestial Mechanics*, Vol. 4, p. 213, 1971.

XXXII-21. Ash, M. E., Shapiro, I. I., and Smith, W. B., "The System of Planetary Masses," *Science*, Vol. 174, p. 4009, 1971.

XXXII-22. Blackwell, D. E., and Petford, A. D., "Observation of the 1963 July 20 Solar Eclipse," *Mon. Not. Roy. Astron. Soc.*, Vol. 131, p. 383, 1966.

XXXII-23. Fjeldbo, G., and Eshleman, V. R., "Atmosphere of Venus as Studied With the Mariner 5 Dual Radio-Frequency Occultation Experiment," *Radio Sci.*, Vol. 4, p. 879, 1969.

XXXII-24. Campbell, D. B., and Muhleman, D. O., "Measurements of the Electron Content of the Interplanetary Medium Between Earth and Venus," *J. Geophys. Res.*, Vol. 74, p. 1138, 1969.

Acknowledgments

XXXIII. Time-Delay Test of General Relativity and Earth–Mars Ephemeris Improvement From Analysis of *Mariner 9* Tracking Data: A Status Report

Irwin I. Shapiro and Robert D. Reasenberg
Department of Earth and Planetary Sciences
Massachusetts Institute of Technology, Cambridge, Massachusetts 02139

Mariner 9 has offered the opportunity to perform the most stringent test of the fundamental theory of gravity in over 100 years.[1] With the ranging system (see Section XXIX of this Report) capable of a 0.1-μsec precision in the measurement of round-trip time delays between the tracking station and the spacecraft, it appeared that the predicted increase near superior conjunction of about 200 μsec in these delays,[2] attributable directly to the Sun's gravity field, could be observed with an uncertainty of no more than about 1%. At this level of accuracy, the test performed by *Mariner 9* could provide conclusive discrimination between the predictions of Einstein's purely tensor theory of gravity and those of the scalar-tensor Brans–Dicke theory when the fraction of scalar-field admixture in the latter is set in accord with the Princeton solar oblateness experiment: For the time-delay test, the

predicted excess "delays" of the Brans–Dicke theory are about 6% less than for general relativity. The distinction between the two theories is of far-reaching importance for the correct understanding of numerous astrophysical phenomena, ranging from the origin of the universe to the evolution of Earth. The prime goal of our efforts, therefore, has been directed toward the achievement of this discrimination.

Secondary goals include the improvement of the ephemerides of Earth and Mars. This improvement is important for several reasons:

(1) Because of the differences between the secular effects on planetary orbits caused by relativity and those caused by the second harmonic of the Sun's gravity field, we will eventually be able to separate the contributions and, hence, to test stringently the relativistic predictions of planetary motion and to determine an accurate value for the second harmonic, or equatorial bulge, of the solar gravity field.

---

[1] We refer here only to "non-null" experiments.

[2] This "fourth test" experiment was first proposed by I. I. Shapiro (Ref. XXXIII-1). Independent calculations, based on Shapiro's personal communication of this proposal, were conducted by D. O. Muhleman and P. Reichley (Ref. XXXIII-2).

(2) Spacecraft navigation problems will be eased substantially through more precise location of the DSN tracking stations with respect to the planetary system; such improved precision does, of course, depend on comparable improvement in the ephemerides.

(3) Correct interpretation of the Mars radar ranging data in terms of topography with respect to the center of mass of Mars will be ensured by the development of accurate orbits of Earth and Mars from the *Mariner 9* data.

Our progress toward these goals is described in the subsequent paragraphs.

A. Data Set and Sensitivity Tests

All of our analyses to date of the *Mariner 9* data have been based on the so-called pseudo time-delay observables ("normal points") provided to us by the JPL co-investigators of the celestial mechanics experiment (see Section XXX of this Report). Each such observable represents the round-trip time, at a given UTC epoch, of a hypothetical light signal transmitted from the center of the (assumed transparent) Earth, reflected from the center of mass of the (assumed transparent) Mars, and received again at Earth's center of mass. Both Earth and Mars are assumed to remain at the positions they occupy at the coordinate-time epoch corresponding to the given UTC epoch, for the duration of the round-trip travel of the light signal. The pseudo observables, derived from each independent acquisition of the ranging signal from orbit insertion on November 13, 1971 (UT) to October 11, 1972, fall naturally into three groups. The first, comprising data obtained during the first 2 months following orbit insertion, were obtained on a fairly regular basis at least several times weekly, with one or at most two separate acquisitions each day. Because Mars was at a distance of only about 1 AU during this period, the signal-to-noise ratios were large and the resultant delays of high precision (see Section XXIX of this Report). The second group, spanning the period from late January to late June 1972, contains few delays, most of which are of lower quality. The final group contains the July through October 1972 data. These points are well distributed in time, except for occasional gaps of 1 week to 10 days. The data from the first group were obtained at DSS 12 and the remainder at DSS 14. On some passes near superior conjunction as many as 25 separate acquisitions were obtained. Although each such acquisition yields an independent measurement of round-

trip group delay to the spacecraft, the individual members of the set do *not* yield independent values of the Earth–Mars pseudo observable. The reason is simple: The uncertainties in the latter quantities are due primarily to those in the determination of the spacecraft orbit and hence are highly correlated. Examples are given below.

We have not yet received any Doppler data from tracking periods after early June 1972. Consequently, we have not been able to check directly to determine the sensitivity of the pseudo observables obtained near superior conjunction to uncertainties in the gravity field of Mars, to variations in the coronal plasma, to noise and "drop-outs" in the Doppler data, etc. We did do some limited sensitivity studies, however, for pseudo observables from early in the mission for which we had Doppler data. Specifically, we took the Doppler data from about 8.5 hr UT on November 16, 1971, to about 20.8 hr on November 23, 1971 (15 revolutions) and, using an eighth-degree, eighth-order preliminary gravity model, generated in part from simultaneous analysis of two separated spans of 19 days of Doppler data each, we solved for the initial conditions of the spacecraft's orbit with respect to Mars. Based on this solution, we calculated, for a set of points uniformly spaced in time, the round-trip time equivalent of the projection of the spacecraft's position vector (with respect to the center of mass of Mars) along the Earth–Mars line. We then repeated the entire procedure using only a three-revolution arc of Doppler data, extending from about 8.5 hr UT on November 19, to about 20.8 hr UT on November 20. In this manner we were able to test the sensitivity of an Earth–Mars delay measurement, inferred from *Mariner 9* ranging data, to the orbit determined from "nested" spans of Doppler data. Several iterations of the linearized weighted-least-squares estimation algorithm, including a re-integration of the variational equations (partial derivatives), were carried out to ensure convergence. A sample of the differences in the inferred round-trip delays from the two spans are shown in Fig. XXXIII-1 for approximately two of the "common" orbital revolutions. The differences vary most rapidly near periapsis and reach values as high as 1 μsec, about an order of magnitude larger than the inherent precision of the ranging system. The average difference is seen to be about 0.5 μsec. Thus, at least for conditions of high signal-to-noise ratio, with minimal propagation-medium effects, the main limitation on the accuracy of the inference of Earth–Mars time delays appears to be set by the uncertainty in the determination of the spacecraft's orbit about Mars. The proper apportionment of this uncertainty among the vari-
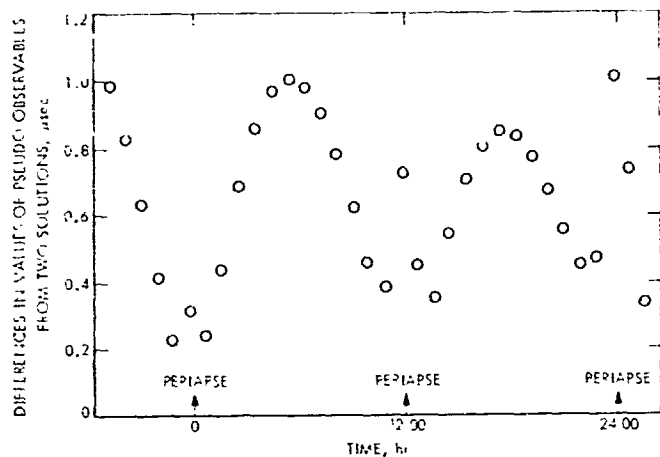
Fig. XXXIII-1. Comparison of reduction of spacecraft ranging data from November 1971 to equivalent Earth–Mars time delays from three- and fifteen-revolution state-vector solutions.

Table XXXIII-1. Summary of *Mariner 9* and radar data

Type	Target	Number of observations	Interval covered
Mariner 9 pseudo delays	Mars	1143	November 17, 1971, to October 11, 1972
Radar time delays and Doppler shifts[a]	Mercury	762	1966 to 1972
	Venus	1073	1966 to 1972
	Mars	2668	1967 to 1972

[a]These data were obtained partly at the Haystack Observatory and partly at the Arecibo Observatory.

ous contributing factors (gravity field, non-gravitational forces, etc.) is by no means clear, but is under intense study. Unless such apportionment is well understood, it will not be possible to place reliable error bounds on the results of the analyses of the inferred Earth–Mars delays.

In addition to the *Mariner 9* pseudo observables, we also have the time-delay measurements obtained from radar ranging observations of Mars. Use of these radar data is indispensable to the proper analysis of the *Mariner 9* data. The arc over which the latter data extend is too short compared with Mars' orbital period to allow an adequate separation of the direct relativistic contribution to the delay from the Earth–Mars orbital contribution. The optical observations accumulated over the past 2 centuries provide the basis both for the outer-planet orbits, necessary to compute the perturbations on the orbits of Earth and Mars,[3] and for the motion of Earth about its center of mass, primarily precession, nutation, polar motion, and Earth-rotation variations. But, as for their direct use in the determination of, for example, the astronomical unit and the orbits of Earth and Mars, the optical observations are completely outclassed by the radar measurements.

The set of *Mariner 9* pseudo observables and the set of radar data used in our analyses are described in Table XXXIII-1. It is important to note that the *number* of observations is not a reliable indicator of usefulness

in orbit determination. The *distribution* of the observations over the relative orbital positions of the planets involved is far more important. For example, the number of separate Mars radar observations looks impressive, but in reality they are very closely bunched in time: On the average, each day's observations yield about 80 delay values and the days of observation are all clustered around Martian oppositions. By contrast, the radar observations of Mercury and Venus, useful for the determination of Earth's orbit, are spread much more uniformly over the relative orbital configurations with no gaps longer than 1 or 2 months for the past 6 years. For observations of these planets, it was sufficient to have only one or two delay values for a given day because of the much slower rotation and the more muted topographic variations on these planets than on Mars. One more point should be made. Although the rapid spin of Mars is helpful in the separation of topographic from orbital effects on the delay data, the high ($\simeq 24°$) inclination of Mars' equator to its orbital plane, and our present inability to obtain useful data throughout a synodic period, make the time scale for obtaining widely separated "closure" points (i.e., observations of the same topographic location from different relative orbital positions) for all latitudes approach a decade in extent. Mercury and Venus are more cooperative in this respect.

B. Data Analysis

The data analysis was divided into two stages. In the first, only the *Mariner 9* pseudo observables were used directly in order to investigate the suspected presence of various systematic errors. Those parameters of the

---

[3]For this purpose, as well as others, the orbits of the inner planets are better determined from past radar observations of these bodies.

overall dynamical system to which the *Mariner 9* data were relatively less sensitive were fixed in accord with the results from previous analyses of the radar data. In the second stage of the analysis, combined radar and *Mariner 9* data sets were employed.

If our theoretical models were sufficiently well developed so that the resultant errors were truly unbiased, independent gaussian random variables, the processing of the data to extract their scientific content would be very straightforward in principle, if arduous in practice. But the dynamical system involved is immensely complicated and it is not possible at present to develop adequate theoretical models. Thus, our model for the Mars gravity field introduces, in effect, poorly specified correlated non-gaussian noise. In our analysis we attempt to set accurate bounds on the effects of these model deficiencies on the estimates of the physical parameters of interest. It is a nontrivial task. In fact even the approach to take is not obvious. In the following discussions we adopted what has become the conventional technique in such matters; it might be dubbed "cut and try." Through careful comparison of myriad computer solutions, in which relative data weights are varied, different subsets of parameters are estimated, different parameterized models for imperfectly known physical effects are used, etc., we try to ferret out the sources, and approximate magnitude and effect, of the systematic errors. Even when one is attempting to estimate a parameter associated with a periodic effect on the observables, the task is more subtle than might at first appear; with a necessarily finite data span that is not greatly in excess of all relevant periodicities affecting the data, results can be obtained for which the formal standard errors, based on postfit residuals, seriously underestimate the true uncertainty. Previous studies (unpublished) showed that, for example, the topography on Venus, if ignored, can cause a change in the least-squares estimate of the Earth–Moon mass ratio of about 10 times its formal uncertainty, despite the wide disparity (a factor of 6) between the Moon's orbital period and Venus' spin period as viewed from Earth. Armchair philosophy aside, we proceed to a description of the results.

1. *Mariner 9* Pseudo Observables

Treating all *Mariner 9* pseudo-delay observables equally and omitting none, we solved for corrections to the most relevant of the orbital parameters of Earth and Mars: the semi-major axis, eccentricity, argument of perihelion, and initial mean anomaly of the latter; and the semi-major axis and eccentricity of the former. The

direct relativistic effect of solar gravity on travel time, Δt, was assumed to obey:[1]

$$\Delta t = \frac{2r_s}{c}(1 + \gamma) \ln \left(\frac{r_e + r_m + R}{r_e + r_m - R} \right) \qquad (1)$$

where $r_s \equiv GM_\odot/c^2 \simeq 1.5$ km is the gravitational radius of the Sun, c the speed of light, r_e the heliocentric distance of Earth, r_m the heliocentric distance of Mars, and R the Earth–Mars distance; γ, the Eddington–Robertson parameter from the generalized Schwarzschild metric (Refs. XXXIII-5 and XXXIII-6), was assumed to be unity, the value given by general relativity. The solar corona was represented by an electron-density function that decreased inversely with the square of the distance from the Sun's center. The electron density was normalized to a value of 7 electrons cm^{-3} at the distance of Earth's orbit. This model is, of course, a gross oversimplification of the corona, which is well known to be highly variable with time. Thus, pulsar measurements (Refs. XXXIII-7 and XXXIII-8) of the electron density integrated along the line of sight through the corona show very large variations from day to day and from year to year. Radio interferometric observations of quasars near solar occultation (Ref. XXXIII-9) and the *Mariner 9* DRVID data (Ref. XXXIII-10; see Section XXXV of this Report) also show substantial variability on almost all time scales.

Representative samples of the postfit residuals from each of the three groups of pseudo-delay observables, discussed in Section XXXIII-A, for the above-described solution are shown in Fig. XXXIII-2. Systematic errors are evident in each group. It is tempting to weed out the "discordant" values from the first two groups. But unless inspection of the details of the ranging observation or of the reduction to a pseudo-delay observable discloses unusual errors, such a weeding process could lead to self-consistent, but erroneous results.

In the third group, several different characteristics stand out. For most days not too close to superior conjunction, in which multiple acquisitions were made, one sees a clear systematic trend to the residuals. As the spread for some passes reaches as high as 10 μsec, almost two orders of magnitude larger than the random error associated with a delay measurement from a typical acquisition, it is obvious that these separate acquisitions, after conversion to pseudo observables, can not be con-

---

[1]This convenient form for the delay was first derived by M. J. Tausner (Ref. XXXIII-3), and independently by D. Holdridge (Ref. XXXIII-4).

Fig. XXXIII-2. Samples of postfit residuals for *Mariner 9* pseudo observables ("normal points") from solution for orbital-element corrections; see text for discussion. The error bars associated with the observables were chosen somewhat arbitrarily.

sidered as independent measurements. The causes for the systematic trends are probably due in part to the indirect effects of the plasma on the spacecraft orbit determination from the Doppler data (see Sections XXX and XXXI of this Report). Careful study is required to evaluate this possibility.

On several days, for example July 30, the same spacecraft ranging data were reduced to pseudo observables in two different ways each involving a different span of Doppler tracking data (see Section XXX of this Report). The resulting postfit residuals in Fig. XXXIII-2 split into two distinct groups, separated by about 3 μsec. This difference is even greater than was obtained from our earlier experiment with "nested" data sets illustrated in Fig. XXXIII-1.

The Group 3 pseudo observables obtained within about 1 week of superior conjunction exhibit chaotic variations in their residuals, some values reaching as high as 40 μsec. Many of these points may well be suffering from ambiguity problems. Nonetheless, it is doubtful that this portion of the data will ever be of use in the relativity test in view of the large and difficult-to-model variable coronal influences.

In summary, Fig. XXXIII-2 shows that, with the present values for the pseudo-delay observables, it will certainly not be possible to estimate $(1 - \gamma)/2$ with an uncertainty reliably at the 1% level or below. To achieve our accuracy goal, the reductions from spacecraft Doppler and ranging data to pseudo observables must first be improved.

Although we did not have the data necessary to attempt to improve the determination of the pseudo observables for the time period near superior conjunction, as mentioned in Section XXXIII-A, we nonetheless felt it worthwhile to analyze the present pseudo observables to determine the level of accuracy at which we could estimate γ [or $(1 - \gamma)/2$]. For this purpose, we selected several different subsets of the data with which to perform numerical experiments to get an indication, albeit perhaps misleading, for the range of possible values of γ "consistent" with the data. We must emphasize again that the pseudo observables obtained from independent acquisitions on a given day have highly correlated errors, as the latter are dominated by the errors in the determination of the spacecraft orbit. In fact, even the errors from pseudo observables obtained on separate days are likely to be correlated if the same

gravity model was used to determine the spacecraft orbit, and especially if only a single orbit was determined from the Doppler data that spanned those days. Thus, the assumption, made in our data processing programs, that the observables have independent, gaussianly distributed errors is clearly erroneous. To compensate partially for this poor assumption, without modification of the measurement noise moment matrix, we chose for most of the numerical experiments only a single pseudo observable from each set of data obtained on a given pass i.e., rise-to-set of *Mariner 9* as viewed from Goldstone. Because the residuals from the independent acquisitions on a given pass showed systematic structure, as mentioned, that varied from pass to pass (see Fig. XXXIII-2), and because the residuals never encompassed a full orbit, it is clear that any choice of a "representative" observable from the independent acquisitions from a given pass still will not lead to a set of observables with unbiased, gaussianly distributed errors. To test the sensitivity (within limits) to these unfortunate consequences of any choice, we made several different ones. In particular, we chose an observable for each pass based on its residual being: (1) the average, (2) the maximum, and (3) the minimum. Because the number of independent acquisitions per pass is usually no more than one or two before late June, the above selections were mainly applicable to data obtained from July onward. The resultant data sets formed the basis for our numerical experiments. We could, of course, have produced deliberately more exaggerated variations, especially in the estimate of γ, had we selected our points so that, for example, the residuals increased from minima to maxima before superior conjunction and decreased from maxima to minima thereafter. But, as we show below, the results depend so sensitively on the choices already outlined as to imply the necessity for the redetermination of the pseudo observables in order to improve on the value of γ determined from other experiments.

Partial results from a small sample of our computer experiments are presented in Table XXXIII-2. Each such experiment is sufficiently complicated as to make impractical the presentation of a complete description. The first solution shown involved all of the pseudo-delay observables with assumed errors as follows: 0.5 μsec for each acquisition made in the intervals November 17, 1971, to August 31, 1972, and September 16 to October 11, 1972; 4 μsec for each in the interval September 1 to September 12, 1972; and 1 μsec for each in the interval September 13 to September 15, 1972. The remaining four solutions involved only one acquisition from each pass,

Table XXXIII-2. Variations in solutions for γ from *Mariner 9* data

Solution	$(1+\gamma)/2$[a]	Number of parameters[b]	Number of observations[b]	RMS of postfit residuals[b]
1	0.987 ± 0.007	8	1143	$\sim 2\ \mu\text{sec}$
2	1.10 ± 0.02	8	102	1.3
3	1.02 ± 0.02	8	102	1.2
4	1.08 ± 0.02	8	102	1.5
5	1.04 ± 0.02	8	102	1.2

[a]The one-standard-deviation formal errors are based on the weighted RMS values of the postfit residuals being set to unity.

[b]Further details on the parameters, observations, and relative weights are given in the text.

equally weighted, with data from August 31 through September 13 omitted. The data used in these four solutions were chosen from four sets: the first set contained the delay with the maximum residual from each pass before August 31, the second the maximum for each pass after September 13, the third the minimum from each pass before August 31, and the fourth the minimum from each pass after September 13. Solution 2 involved the first and second sets, Solution 3 the third and fourth, Solution 4 the first and fourth, and Solution 5 the third and second; all the pseudo observables were given equal weight in the solutions. In addition to the six orbital elements mentioned above, the eight parameters estimated included $(1+\gamma)/2$ and the Earth–Moon mass ratio. The coronal parameter was estimated in other computer experiments and found to be highly correlated (correlation coefficient -0.98) with $(1+\gamma)/2$; inclusion of results from such experiments in Table XXXIII-2 would only widen the spread in the values for $(1+\gamma)/2$. Examination of the postfit residuals discloses systematic trends, as expected. The solutions obtained using a single "average" value for the pseudo observable from each pass, with various parameters being estimated, also exhibit systematic trends in the postfit residuals and yield a spread of values for $(1+\gamma)/2$ several-fold larger than the individual formal standard deviations.

We conclude tentatively that: (1) Without a priori constraints, the coronal effects are not easily separated from the direct relativistic effects on delay. (2) Almost all of the parameters exhibit variations from solution to solution that are large compared with the formal standard errors. Even the estimates of the Earth–Moon mass ratio, which is only weakly coupled to the other

parameters, show variations up to ten-fold larger than the formal standard errors. These results simply serve to emphasize the sensitivity of the relativity test to the systematic errors affecting the pseudo observables.

2. Combination of *Mariner 9* and Radar Data

A combination of the *Mariner 9* pseudo observables with the radar measurements of time delays between the Earth and the inner planets allows more diagnostic tests to be made. A sample of some of the results obtained from this combination is given in Table XXXIII-3. The *Mariner 9* data were chosen from the sets composed of a single acquisition per pass, as described above, and each observable was assumed to have a 1-μsec standard error, unless otherwise noted. The radar time-delay data, described briefly in Table XXXIII-1, were downweighted in each solution such that the minimum error in Earth–Mars delay was set at 10 μsec, with the corresponding minimum for Earth–Venus and Earth–Mercury delays being 3 μsec. The actual measurement uncertainties were as low as several tenths of a microsecond in many cases, but these values were not used in an attempt to mute the effects of the high-frequency components of the topography variations. The low-frequency components were modeled with a two-dimensional Fourier series. The number of topography parameters estimated in the solutions presented in Table XXXIII-3 was 202, broken down into 122 for Mars and 40 each for Mercury and Venus. The other 38 parameters were made up of the orbital initial conditions for each inner planet, their masses, the astronomical unit, the relativity parameter, and various bias parameters. Other solutions, not shown, included the plasma parameter; these seemed to indicate that a single plasma parameter was insufficient to encompass properly all of the data.

Let us now discuss those aspects of the solutions which are presented in Table XXXIII-3. The values obtained for $(1+\gamma)/2$ seem to depend strongly on the relative weight given to the *Mariner 9* pseudo observables and on the inclusion or omission of the topography parameters. The mass of Mercury is seen to be relatively unaffected by the variations represented in Table XXXIII-3, except that the *Mariner 9* data, when allowed to dominate via the introduction of unrealistically low assumed errors as in Solution 8, cause an enormous change compared with the formal error. Examination of all of the formal errors shows, for example, that the *Mariner 9* data, when "properly weighted," have essentially no effect on the estimate of the mass of Mercury; the change in the formal standard error is only in the third

Table XXXIII-3. Variations in solutions for γ and other parameters from combination of *Mariner 9* and radar data

Solution	$(1+\gamma)/2$	Inverse mass of Mercury $(M_\odot^{-1})$	Inverse mass of Venus $(M_\odot^{-1})$	Inverse mass of Earth plus Moon $(M_\odot^{-1})$	Inverse mass of Mars $(M_\odot^{-1})$	Earth–Moon mass ratio[b]	Astronomical unit[b]	Radius of Mars, km	Number of parameters	Number of observations	Comments
6	1.011 ±0.006	6,024,300 ±1,200	408,493 ±5	328,915 ±4	3,098,200 ±100	81.3009 ±2	499.0047814 ±4	3394.7 ±0.2	240	4625	*Mariner 9* and radar data "properly" weighted
7	0.970 ±0.006	6,023,700 ±1,200	408,494 ±5	328,909 ±4	3,098,100 ±100	81.3007 ±2	499.0047828 ±4	3394.9 ±0.2	240	4625	Same as 6, except *Mariner 9* data set changed from that in 2 to that in 3 (see Table XXXIII-2)
8	1.1570 ±0.0002	6,148,100 ±1,600	409,031 ±2	328,958 ±5	3,106,700 ±100	81.30189 ±1	499.0047510 ±4	3468.0 ±0.2	240	4625	Same as 6, except *Mariner 9* data errors multiplied by 0.01 (i.e., *Mariner 9* data dominate solution)
9	0.96 ±0.02	6,021,300 ±1,200	408,521 ±6	328,885 ±4	3,098,600 ±100	81.3015 ±3	499.0047840 ±5	3394.1 ±0.3	240	4625	Same as 6, except *Mariner 9* data errors multiplied by 100 (i.e., radar data dominate solution)
10	0.98 ±0.02	6,022,700 ±900	408,519 ±5	328,897 ±4	3,098,600 ±100	81.3014 ±3	499.0047822 ±5	3393.2 ±0.3	240	4523	Same as 9, except *Mariner 9* data omitted altogether
11	1.10 ±0.01	6,019,400 ±1,200	408,612 ±5	328,859 ±4	3,099,300 ±100	81.2995 ±3	499.0047720 ±4	3390.2 ±0.2	36	4625	Same as 6, except topography unmodeled
12	1.12 ±0.03	6,019,300 ±1,200	408,612 ±6	328,857 ±5	3,098,400 ±100	81.2990 ±4	499.0047778 ±6	3390.6 ±0.3	36	4625	Same as 11, except *Mariner 9* data errors multiplied by 100 (i.e., radar data dominate solution)

[a] The one-standard-deviation formal errors are based on the weighted RMS values of the postfit residuals being set to unity, except for Solution 8 where the standard errors are determined by the data weights (see text).

[b] Error refers to formal uncertainty in last digit.

[c] Further details on the parameters, observations, and relative weights are given in the text.

significant figure.[3] Estimates of the masses of Venus, Earth plus Moon, and Mars, were made to check reliability as these parameters are better determined from other data (Refs. XXXIII-11 and XXXIII-12). In particular, "accepted" values for the inverse masses of these three bodies are $M_\odot^{-1} = 408{,}522$; $M_{\oplus+\mathbb{C}}^{-1} = 328{,}900.1$, and $M^{-1} = 3{,}098{,}700$. Again, we find remarkable agreement between these values and the corresponding ones in which the *Mariner* data do not dominate and in which the topography is modeled. The effects of the latter are seen by comparison of Solution 6 with 11 and Solution 9 with 12.

The estimate of the astronomical unit is also not strongly affected by the *Mariner 9* data, but when these data dominate, as in Solution 8, the estimate of the astronomical unit is changed by about 30 μsec to a value quite inconsistent with the radar data.

The mean equatorial radius of Mars follows the same pattern: the "radar alone" value of 3394 km (see Ref. XXXIII-13) is supported except when either *Mariner 9* data dominate or the topography is unmodeled, the latter being less serious. Other checks on the mean radius and topography of Mars are possible through comparison of the radar and *Mariner 9* occultation data. These comparisons are still under study, but seem to indicate a systematic difference of a few kilometers, with the radar data yielding smaller results. Limited self-consistency checks on the topography are possible through the existence of so-called "closure points"—observations made with respect to the same region of the Martian surface, but from a different orbital configuration. The Mars radar data obtained at Haystack from April 1971 to February 1972 included, by design, a number of series of such closure points; for most regions closure was obtained to within 1 μsec (Ref. XXXIII-14).

The orbit of Mars can definitely be improved by inclusion of the *Mariner 9* data. The improvement in Earth's orbit is less marked. In Table XXXIII-4 we present the orbital elements of both planets as determined in Solution 6. Comparison of the postfit residuals of the pseudo observables for the various solutions shows that:

(1) For Solution 6, there are no systematic trends larger than a few microseconds.

Table XXXIII-4. Osculating orbital elements for Earth and Mars

Element	Earth[a]	Mars[a]
Epoch, Julian Ephemeris Date	2,440,000.5 (May 1968)	2,440,000.5 (May 1968)
Semi-major axis, AU	0.999 982 764 7	1.523 604 541 4
Eccentricity	0.016 752 712 5	0.093 457 814
Argument of perihelion, deg	102.033 94	332.101 06
Inclination, deg	23.443 357 8[b]	24.693 034
Longitude of ascending node, deg	0.000 665 9[b]	3.346 602
Initial mean anomaly, deg	139.365 807	89.899 737

[a]In almost all cases the uncertainty should be confined to the last two digits listed.

[b]Fixed on basis of previous solutions involving optical and radar data.

---

(2) For Solution 9, radar data dominant (*Mariner* data downweighted), the pseudo-observable residuals reach a peak of several tens of microseconds.

(3) For Solution 12, radar data dominant, topography unmodeled, the pseudo-observable residuals reach nearly 100 μsec, further demonstrating the necessity to include a model of topography in the analysis of planetary radar data.

From the above solutions, and others not shown, we can summarize our findings as follows:

(1) The radar data are essential for an accurate determination of γ; the *Mariner 9* data can not be used alone because they span too short an arc of the relative orbits of Earth and Mars.

(2) Only improvements in the orbit of Mars and small improvements in the orbit of Earth result from inclusion of the *Mariner 9* data because of the present presence of the large systematic errors in the pseudo observables.

(3) The *Mariner 9* data will add little to the determination of the astronomical unit and the masses of the inner planets.

(4) Proper account of the topography of the inner planets must be taken to ensure reliable results from the radar data.

C. Conclusions

Because of the large systematic errors that at present accompany the conversion of the spacecraft ranging data to equivalent Earth–Mars time delays, the corresponding determination of γ does not now allow the predictions of general relativity to be distinguished from those of the Brans–Dicke scalar-tensor theory with the fraction s of scalar field admixture being 0.06. The uncertainty in the determination of $(1 + \gamma)/2$ at the present stage of the Mariner 9 data analysis is at about the 10% level, almost comparable to the results from previous experiments (Refs. XXXIII-15 and XXXIII-16). The prospects for improvement are substantial, but the required effort is large. The tracking data must be reanalyzed by a number of different techniques to produce: (1) an adequate model of the gravity field and of the nongravitational forces; (2) accurate estimates of the spacecraft's orbit with respect to Mars for each period during which ranging data are available; and (3) appropriate models of the solar corona and the topography of the inner planets so that the Mariner 9 pseudo observables and the planetary radar measurements of delay and Doppler can be combined to yield a much improved estimate of γ.

The ephemeris of Mars suffers from the same problem: Only with the elimination of a major fraction of the systematic errors affecting the Mariner 9 pseudo observables will a truly substantial improvement be possible in the determination of the orbit.

References

XXXIII-1. Shapiro, I. I.. "Fourth Test of General Relativity," *Phys. Rev. Lett.,* Vol. 13, p. 789, 1964.

XXXIII-2. Muhleman, D. O., and Reichley, P., "Effects of General Relativity on Planetary Radar Distance Measurements," Space Programs Summary 37-29, Vol. IV, p. 239, Jet Propulsion Laboratory, Pasadena, Calif., 1964.

XXXIII-3. Tausner, M. J., *General Relativity and Its Effect on Planetary Orbits and Interplanetary Observations,* Lincoln Laboratory Technical Report 425, Massachusetts Institute of Technology, Cambridge, Mass., 1966.

XXXIII-4. Holdridge, D., "An Alternate Expression for Light Time Using General Relativity. Space Programs Summary 37-48, Vol. III, p. 2, Jet Propulsion Laboratory, Pasadena, Calif., 1967.

XXXIII-5. Eddington, A. S., *The Mathematical Theory of Relativity,* p. 105, Cambridge University Press, New York, 1957.

XXXIII-6. Robertson, H. P., in *Space Age Astronomy,* p. 228, eds. A. J. Deutsch and W. E. Klemperer, Gordon and Breach, New York, 1964.

XXXIII-7. Counselman, C.C. III, and Rankin, J. M., "Density of the Solar Corona From Occultations of NP 0532," *Ap. J.,* Vol. 175, p. 843, 1972.

XXXIII-8. Counselman, C. C. III, and Rankin, J. M., *Ap. J.* (in press).

References (contd)

XXXIII-9. Knight, C. A., Robertson, D. S., Shapiro, I. I., Whitney, A. R., Rogers, A. E. E., Clark, T. A., Marandino, G. E., and Goldstein, R. M., "Observations With the Haystack–Goldstone Interferometer of Phase Scintillations Due to the Solar Corona," Bull. Am. Astron. Soc., Vol. 3, p. 447, 1971.

XXXIII-10. Callahan, P. S. "Plasma Column Changes at Small Solar Elongations," J. Geophys. Res., Vol. 78, 1973.

XXXIII-11. Anderson, J. D., and Efron, L., "The Mass and Dynamical Oblateness of Venus," Bull. Am. Astron. Soc., Vol. 1, p. 231, 1969.

XXXIII-12. Null, G. W., "A Solution for the Mass and Dynamical Oblateness of Mars Using Mariner 4 Doppler Data," Bull. Am. Astron. Soc., Vol. 1, p. 356, 1969.

XXXIII-13. Pettengill, G. H., Rogers, A. E. E., and Shapiro, I. I., "Martian Craters and a Scarp as Seen by Radar," Science, Vol. 174, p. 1321, 1971.

XXXIII-14. Pettengill, G. H., Shapiro, I. I., and Rogers, A. E. E., "Topography and Radar Scattering Properties of Mars," Icarus, Vol. 18, p. 22, 1973.

XXXIII-15. Shapiro, I. I., Ash, M. E., Ingalls, R. P., Smith, W. B., Campbell, D. B., Dyce, R. B., Jurgens, R. T., and Pettengill, G. H., "Fourth Test of General Relativity: New Radar Result," Phys. Rev. Lett., Vol. 26, p. 1132, 1971.

XXXIII-16. Anderson, J. D., Esposito, P. B., Martin, W. L., and Muhleman, D. O., in Proceedings of the Conference on Experimental Tests of Gravitational Theories, Technical Memorandum 33-499, Jet Propulsion Laboratory, Pasadena, Calif. 1971.

Acknowledgement

Note Added In Proof

This section represents the state of the analysis of the *Mariner 9* data as of the late fall 1972. In February 1973 it was discovered that the pseudo observables. or normal points, that we had been analyzing were not, in fact, the normal points obtained by Jordan et al. (see Section XXX of this Report). Through a series of unfortunate misunderstandings, the values we thought represented the normal points actually represented the differences between twice the normal-point values and the computed values ("$2 O - C$" instead of "O"), where the computed values were based on a contemporary Earth–Mars ephemeris in use at JPL. Thus, the low-frequency components of the time variation of the "normal points" that we used were contaminated primarily by errors in the JPL ephemeris, whereas the high-frequency components were affected mainly by the real normal points, leading, for example, to a factor-of-two exaggeration in the amplitude of the variations in the residuals for a single pass (see Fig. XXXIII-2).

Any results based on the normal points that we used are clearly of no scientific value. Why did we therefore not withdraw our report in its entirety? There are two reasons: (1) The results presented that depend primarily on the radar data are still valid. (2) The results that depend importantly on the "wrong" *Mariner 9* data provide a valuable lesson for some sceptics who have been known to fear that all manner of systematic errors could be absorbed virtually without a trace in the estimation of the large number of parameters involved in solar-system dynamics. Despite the inclusion of a host of parameters to be estimated and the performance of a wide range of numerical experiments, the systematic trends in the "normal-point" residuals never disappeared and the inconsistency between the radar and "normal-point" data remained clearly in evidence.

XXXIV. Effect of *Mariner* 9 Normal Points on Planetary Ephemerides

M. S. W. Keesey, J. H. Lieske, and E. M. Standish

Jet Propulsion Laboratory/California Institute of Technology, Pasadena, California 91103

A. Observational Data

To assess the influence of the spacecraft data on the planetary positions, a set of ephemerides designated as Development Ephemeris 82 (DE 82) has been created. The differences between DE 82 and a previous set of ephemerides, designated as DE 80, are due to the *Mariner* 9 normal points. The meridian circle observations which have been used in DE 80 and DE 82 consist of transit measurements of Mercury, Venus, Mars, and the Sun over a 60-year time span beginning in 1911. These observations have been obtained by the Six and Nine Inch Transit Circles of the U. S. Naval Observatory. The total number of observations contained in the optical data set is over 28,000 for the 60 year time span. The radar time delay data have been provided by several sources, including the Arecibo Observatory, the MIT Haystack and Millstone facilities, and the JPL Goldstone facilities (Ref. XXXIV-1). A summary of the time-delay measurements used in both DE 80 and DE 82 is presented in Table XXXIV-1. It should be noted that some of the data are of questionable value, in particular the 1964 observations of Venus by the JPL Goldstone facilities. Also, although there is a sizable number of Goldstone observations of Venus, they were obtained within short time periods so that the data arcs are rather short. In addition, since the Mars data were obtained during periods of opposition sizable data arcs for this planet are lacking entirely.

Table XXXIV-1. Radar range measurements used in DE 80 and DE 82

Observed body	Source	Number of time-delay range measurements	Year
Mercury	Arecibo	119	1964-1966
	Haystack	88	1966-1968
	Total	207	
Venus	Haystack	63	1966-1968
	Millstone	101	1964-1967
	Goldstone	285	1964-1967
	Total	449	
Mars	Arecibo	30	1965
	Haystack	118	1967
	Goldstone	242	1969
	Goldstone	761	1971
	Total	1151	

B. Addition of Spacecraft Data to the Observation Data Set

The spacecraft data utilized in the generation of DE 82 were composed of two groups: the first group consisted of 63 edited "norm" points" (Ref. XXXIV-2) which extended from November 20, 1971, to February 14, 1972; a second group of less precise data was composed of 35 points and extended from March 23, 1972, to July 30, 1972.

Before the second group became available, an interim ephemeris was generated that utilized the first group of spacecraft data (with standard deviation of 0.1 μsec) in addition to the radar and optical data presented above. Range residuals were computed for the *Mariner 9* data using this temporary ephemeris. These residuals, which were all less than 0.5 μsec for the first group, are shown in Fig. XXXIV-1.

However, when the second group of spacecraft data became available, it was found that residuals between those data and the interim ephemeris drifted to more than 40 μsec, as indicated in Fig. XXXIV-2. It was concluded that the original spacecraft data are too short and that the second group of data should be included in the generation of the ephemeris. A second ephemeris was thus generated (DE 82), with the second group of
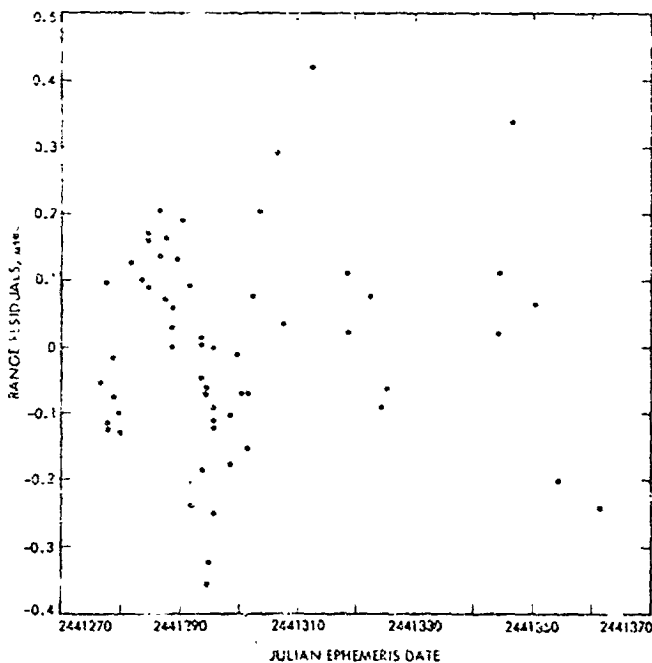
Fig. XXXIV-1. Range residuals of first group (Nov. 20, 1971, to Feb. 14, 1972) of *Mariner 9* normal points using an interim ephemeris.
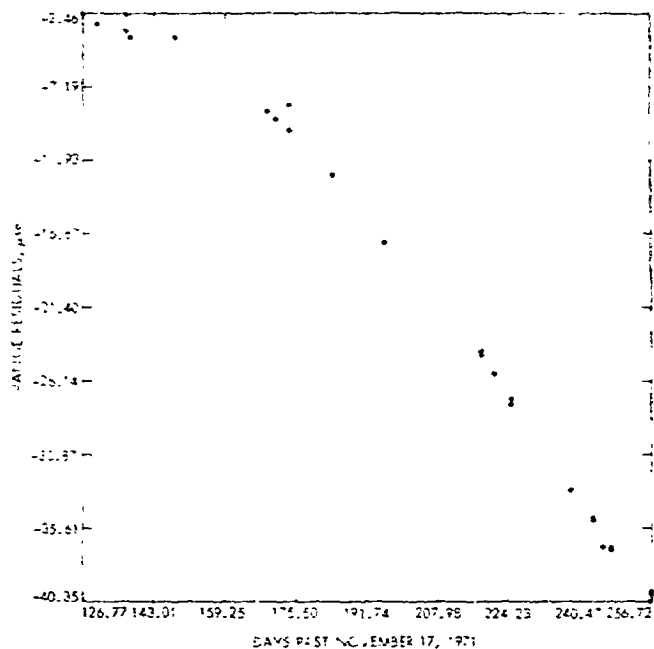
Fig. XXXIV-2. Range residuals of second group (March 23 to July 30, 1972) of *Mariner 9* normal points using an interim ephemeris.

normal points also included in the data set. As the 26-m antennas were rendered ineffectual by the increasing Earth–Mars distance after late March 1972 (see Section XXX of this Report), the standard deviations of the second group of spacecraft data were downweighted to 1 μsec.

Residuals for both sets of normal points were then recomputed using DE 82. As indicated in Figs. XXXIV-3 and XXXIV-4, the residuals for the second group were reduced to less than 2 μsec in absolute magnitude and the first set to less than 0.4 μsec; the RMS value for the combined sets was 0.3 μsec.

The incorporation of 6 months of spacecraft data into the observation data set seemed to be not only an improvement over the interim ephemeris, but also over DE 80 (insofar as spacecraft data are concerned), as indicated by Fig. XXXIV-5. This figure, which contains not only the 98 points used in the generation of DE 82, but also the additional normal points that were acquired through conjunction, indicates quite clearly the presence of a periodic effect in DE 80 or in the spacecraft data. To determine the source of this effect, the Earth–Mars range has been algebraically formulated as a function of the orbital elements utilizing computer manipulation programs (Ref. XXXIV-2). The resulting periodicities in the range formulation have been evaluated in an attempt to
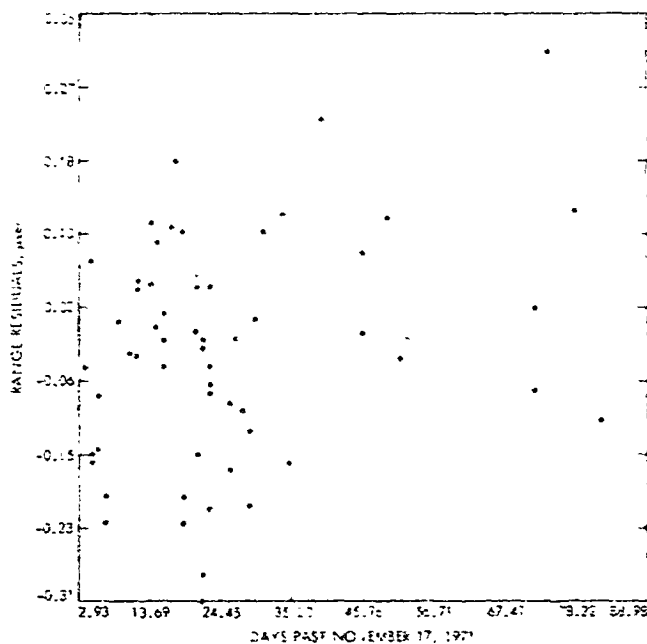
Fig. XXXIV-3. Range residuals of first group (Nov. 20, 1971, to Feb. 14, 1972) of *Mariner 9* normal points using DE 82.
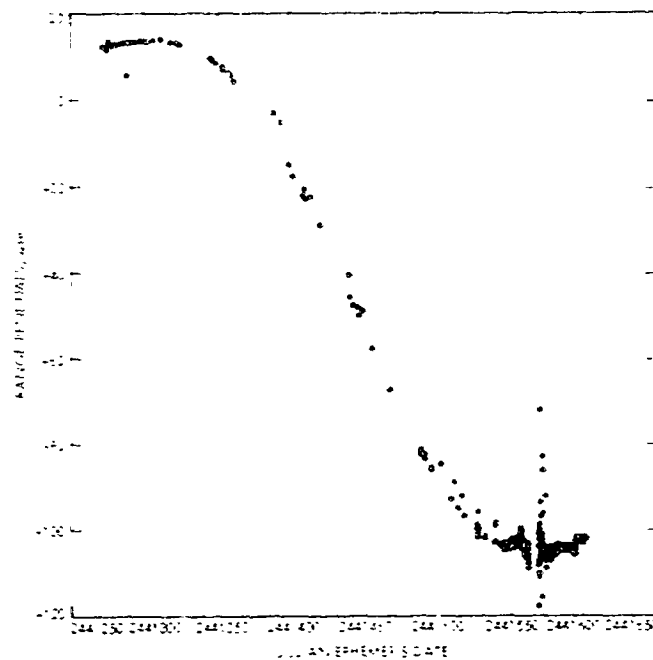
Fig. XXXIV-5. Range residuals of all *Mariner 9* normal points using DE 80.
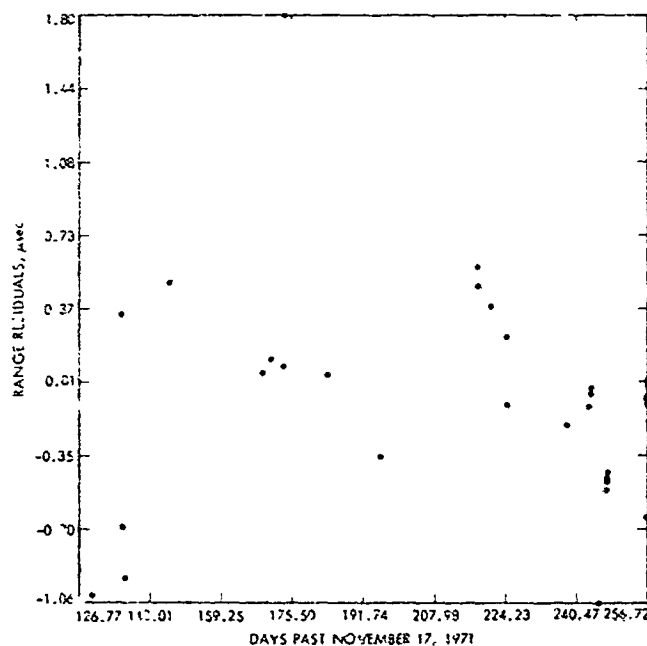
Fig. XXXIV-4. Range residuals of second group (March 23 to July 30, 1972) of *Mariner 9* normal points using DE 82.

determine which orbital parameters yield a period compatible with the residuals of Fig. XXXIV-5. At the present time, it appears that such a period (ca 500 to 560 days) is impossible to obtain from orbital element errors if

the curve depicted in Fig. XXXIV-5 is a pure sine or cosine function. An investigation is currently underway to determine the physical origins of the periodic residual (viz. the influence of a variation in Jupiter's mass on the ephemeris or effects caused by topographical variations on Mars).

C. DE 82 Fit to Early Radar Range Data

Although the fit of DE 82 to the spacecraft data was good, the fit for the early Mars radar bounce data was inadequate. The range residuals for the Mars data presented in Table XXXIV-1, which have been computed using DE 80, are plotted in Figs. XXXIV-6a through XXXIV-9a; the corresponding residuals computed with DE 82 are found in Figs. XXXIV-6b through XXXIV-9b. As the only difference between DE 80 and DE 82 was the addition of the spacecraft data to the observation data set, a comparison of the figures demonstrates the effect on the ephemeris of utilizing the spacecraft data.

Comparison of Figs. XXXIV-6a and XXXIV-6b indicates a 50-μsec increase in the range residuals for the 1965 Arecibo data when the spacecraft data are added to the data set. However, the new values are still less than the standard deviations of the data, which are as high as 300 μsec.
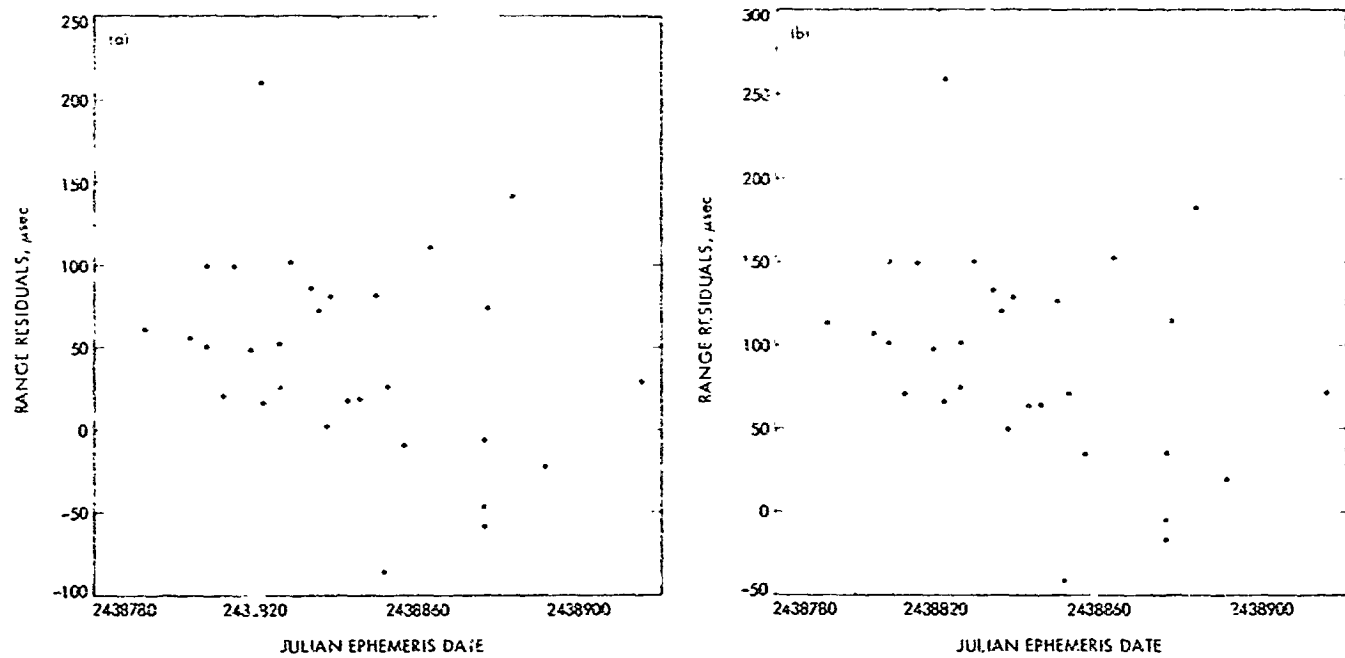
Fig. XXXIV-6. Range residuals for 1965 Arecibo observations of Mars. (a) Using DE 80. (b) Using DE 82.
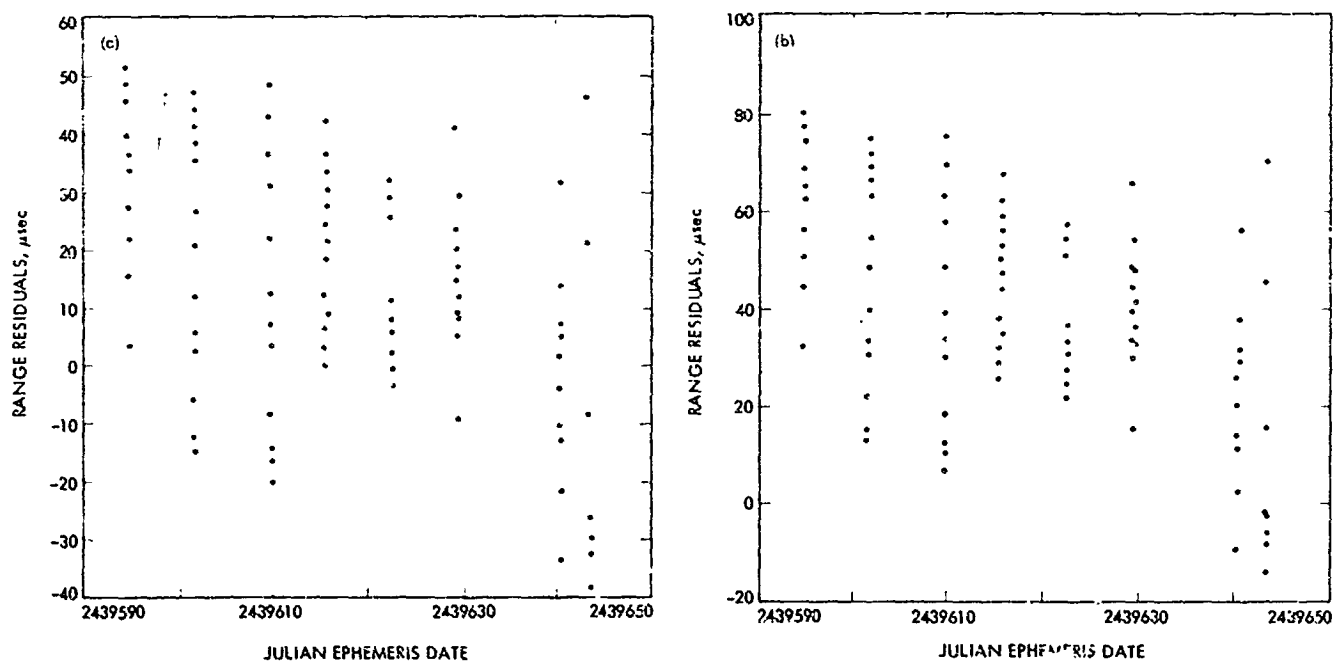
Fig. XXXIV-7. Range residuals for 1967 Haystack observations of Mars. (a) Using DE 80. (b) Using DE 82.
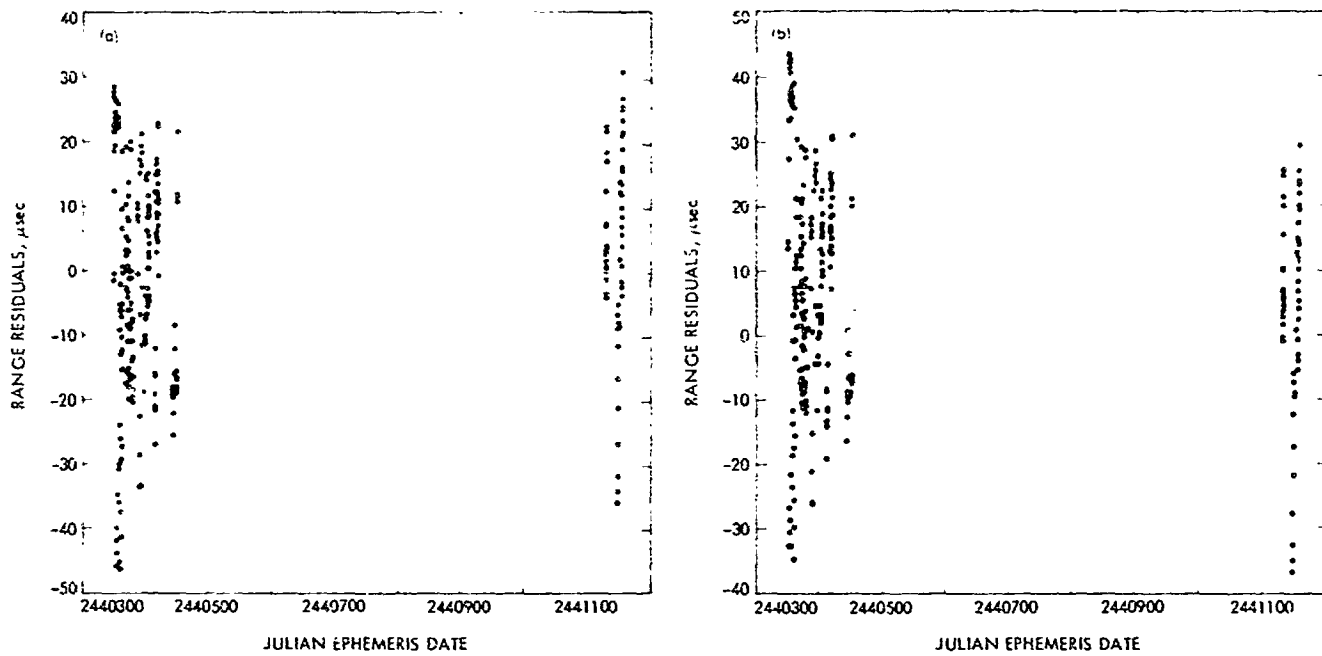
Fig. XXXIV-8. Range residuals for JPL bistatic observations of Mars. (a) Using DE 80. (b) Using DE 82.
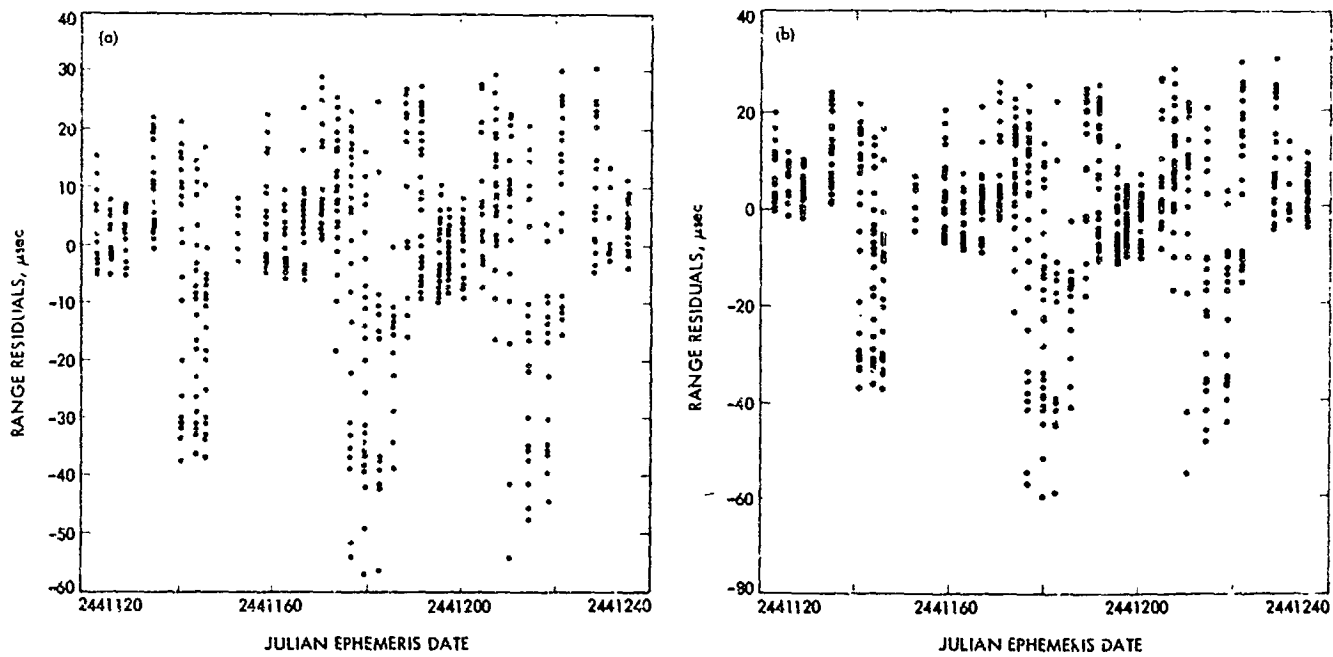
Fig. XXXiV-S. Range residuals for JPL monostatic (DSS 14) observations of Mars. (a) Using DE 80. (b) Using DE 82.

The range residuals of the 1967 Haystack data, however, are increased by 25 μsec (as indicated by Figs. XXXIV-7a and XXXIV-7b) such that the new residuals do exceed the standard deviations of the data; most of these are less than 20 μsec. The same is true of the residuals produced with the 1969 JPL bistatic data (cf. Figs. XXXIV-8a and XXXIV-8b), with the increment to the residuals being 10 μsec and the standard deviation of the data 2 μsec for most of the observations. Only the range residuals produced by the 1971 JPL bistatic data (as also indicated by Figs. XXXIV-8a and XXXIV-8b) and the 1971 JPL DSS 14 monostatic data (cf. Figs. XXXIV-9a and XXXIV-9b) remain essentially constant using DE 80 or DE 82.

Introduction of spacecraft data into the observation data set thus produces increased range residuals for Mars radar-bounce data that are progressively larger for each opposition as one goes back in time. This implies that the spacecraft data are producing a secular or, most probably, a long period effect in the ephemeris of Mars. The reason for this is unknown, but the problem is presently under study, as indicated above.

It is possible to account for at least part of this secular-type trend by fitting the surface of Mars with a general ellipsoid. The most important effect in this respect would be a displacement of the center of figure from the center of mass in a southerly direction along the pole of Mars. This would introduce an apparent error in the radar range of $z_0 \sin \beta$, where z_0 is the displacement and β is the Martian latitude of the radar sub-Earth point. The geometry is shown in Fig. XXXIV-10. Since β decreases
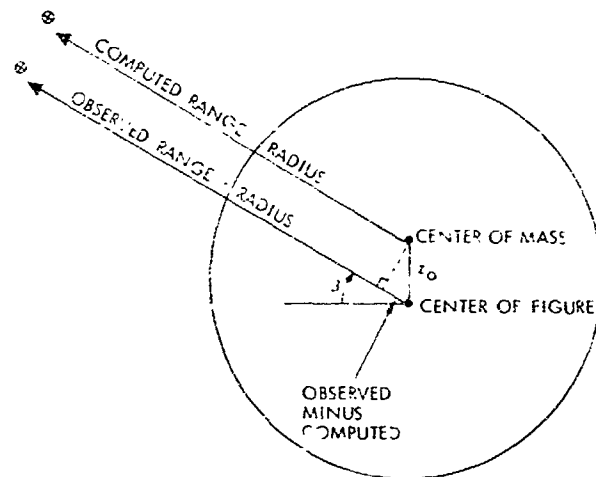
Fig. XXXIV-10. The effect of an offset center of figure on an observed radar range.

from 1967 to 1971, a secular-type trend would be the result over this interval of time.

Preliminary ellipsoidal fits to the surface of Mars have been made; these fits show a southerly displacement of the center of figure with a magnitude of a few kilometers. What is striking, moreover, is that a similar fit using the *Mariner 9* occultation data agrees well with the fits from the radar data. From the occultation data, a similar 3-km offset was found in the polar direction (Ref. XXXIV-3).

In addition to the ephemeris of Mars, the *Mariner 9* spacecraft data have also affected the geocentric ephemeris of Venus, producing changes up to 5 km in range.

References

XXXIV-1. O'Handley, D. A., and Lieske, J. H., *Ephemeris of Mars for Mariner 9 Based on Radar Range and Optical Data*, paper presented at the American Astronomical Society Meeting, National Astronomy and Ionosphere Center, San Juan, Puerto Rico, 1971.

XXXIV-2. Broucke, R. A., and Garthwaite, K., "A Programming System for Analytical Expansions on a Computer," *Celestial Mechanics*, Vol. 1, p. 270, 1969.

XXXIV-3. Standish, E. M., Jr., "The Figure of Mars and Its Effect on Radar-Ranging," *J. of Astronomy and Astrophysics* (a European Journal; in press).

XXXV. Plasma Column Changes at Small Solar Elongations

P. S. Callahan

Jet Propulsion Laboratory/California Institute of Technology, Pasadena, California 91103

The differenced range versus integrated Doppler (DRVID) technique, discussed by MacDoren and Martin in Ref. XXXV-1 and by Muhleman and Johnston in Ref. XXXV-2, was used to study charged-particle changes in the ray path between Earth and *Mariner* 9. Similar work using *Mariners* 6 and 7 has been discussed by Callahan et al. (see Ref. XXXV-3).

For studying plasma activity near the Sun, DRVID data were obtained from August 10 to October 24, 1972, surrounding the *Mariner* 9 superior conjunction on September 7. The range of Sun–Earth–probe (SEP) angles is 3° to 16° or about 11 to 62 $R_\odot$ at the ray path's closest approach. For SEP angles less than 3°, Doppler phase lock could not be maintained, and no data were acquired. The data consist of records obtained during each tracking pass (about 10 hr) of the charged-particle-induced range change. No corrections have been made for Earth's ionosphere as it is always less than the data noise.

Data from August 10 to September 25 have been scanned. The range change during a record is highly variable from day to day, with values rather uniformly spread between 30 and 330 m (round trip) or 1.8 to 20 $\times 10^{15}$ electrons m^{-2}. The maximum rate of change is $\lesssim$ 150 m hr^{-1} (2.5 $\times 10^{13}$ electrons m^{-2} sec^{-1}); typical rates are 15 to 30 m hr^{-1}.

If the records are viewed in terms of range change or range change rate, the day-to-day fluctuations in these quantities mask the changes expected due to the varying solar elongation. Thus, while the steady-state total electron content varies by a factor of 4 (assuming an r^{-2} law), the columnar content changes show no systematic variations.

Two types of structure are observed. First, there are "slopes" that last many hours with the rates given above. The rate is fairly constant, and there is essentially no small-scale structure visible in the data. Second, there are "humps" or "clouds" in which the range moves up and down by 20 to 60 m on a time scale of 2 to 4 hr. In this case, the rate of change dominates the data noise. If the time scale is multiplied by the solar wind velocity, we find a scale size of about 3 $\times 10^6$ km. If we suppose that all of the columnar content change occurs in a localized region near the ray path's closest approach to the Sun, we find local density changes on the order of 100% of the mean (which is assumed to vary as r^{-2}).

The types of structure observed and their amplitudes are being studied with autocorrelation and power spectrum techniques as a function of SEP angle and other variables. From the entire data set, it should be possible to place limits on the heliocentric variation of charged-particle fluctuations and to characterize their wavenumber spectrum.

References

XXXV-1. MacDoran. P. F., and Martin, W. L., "DRVID Charged Particle Measurement With a Binary Coded Sequential Acquisition Ranging System," Space Programs Summary 37-62, Vol. II, p. 34, Jet Propulsion Laboratory, Pasadena, Calif., 1970.

XXXV-2. Muhleman, D. O., and Johnston, I. D., "Radio Propagation in the Solar Gravitational Field," *Phys. Rev. Let.*, Vol. 17, p. 455, 1966.

XXXV-3. Callahan, P. S., MacDoran, P. F., and Zygielbaum, A. I., *Near Sun Observations of the Solar Wind*, paper presented at COSPAR meeting, Seattle, Washington, 1971; published in *Space Research XII*, Akademie-Verlag, Berlin, 1972.

XXXVI. S-Band Radio Occultation Measurements of the Atmosphere and Topography of Mars With *Mariner 9*: Extended Mission Coverage of Polar and Intermediate Latitudes

A. J. Kliore, G. Fjeldbo, B. L. Seidel, M. J. Sykes, and P. M. Woiceshyn

Jet Propulsion Laboratory/California Institute of Technology, Pasadena, California 91103

Mariner 9 was inserted into orbit about Mars on November 14, 1971 (UT). At the time of arrival, the orbital geometry relative to Earth was such that the spacecraft was occulted from view of Earth by Mars once each revolution, beginning several minutes after peri-apsis. At that time, *Mariner's* high-gain antenna was directed toward Earth, and each occultation could be observed by using the 26-m antennas at the tracking stations in Australia and Spain for the Goldstone nadir occultations and the 64-m antenna station at Goldstone, California (DSS 14) for the Goldstone zenith occultations. These occultations continued for the first 40 days of the mission, providing 160 separate measurements, the results of which have been described in previous publications (Refs. XXXVI-1 and XXXVI-2).

Beginning on May 7, 1972, another set of Earth occultations began, and continued for 49 days until June 25, 1972. At this time, the spacecraft's high-gain antenna was not pointed at Earth, and the spacecraft was at a distance of from 338 million to 378 million kilometers. Because of this, the received signal level at the 26-m antenna was below threshold; therefore, observations could be made only with the 64-m antenna at DSS 14. Consequently, only the occultations that occurred during the even-numbered revolutions from 352 to 450 could be observed. In addition, 9 tracking days were not available because of conflicts with other functions of Goldstone DSS 14. Thus, about 40 observation days were available during this period (called extended mission I) resulting in 80 separate occultation measurements. In contrast to the measurements made during the standard mission, which ranged in latitude from about $-40°$ to $+20°$ for the entries, with the exit measurements clustering about the latitude of $+65°$, these extended mission I measurements were remarkable, because the latitude coverage ranged from about $+86$ to $-80°$. Thus, for the first time, occultation measurements of the north and south polar regions of Mars were provided. The locations of these occultation measurements, as well as those of the standard mission measurements, are shown on the maps of Figs. XXXVI-1 and XXXVI-2. The maps that form the background for these figures were prepared by the U. S. Geological Survey from the mapping sequence pictures taken by *Mariner 9*. The locations are identified with the orbital revolution number and the type of measurement; the

Fig. XXXVI-1. Locations of all occultation points between the latitudes of +65° and -65°. The latitudes were computed under the assumption of a spherical planet of radius 3387 km. The background map was supplied by the U.S. Geological Survey and is based on Mariner 9 television pictures.

• STANDARD MISSION (0 - 79)
■ EXTENDED MISSION 1 (352 - 450)
▲ EXTENDED MISSION 2 (638 - 696)

N ENTER
X EXIT

N ENTRIES
X EXITS

● STANDARD MISSION (0 79)
■ EXTENDED MISSION 1 (352 450)
▲ EXTENDED MISSION 2 (638 696)

SOUTH POLAR REGION
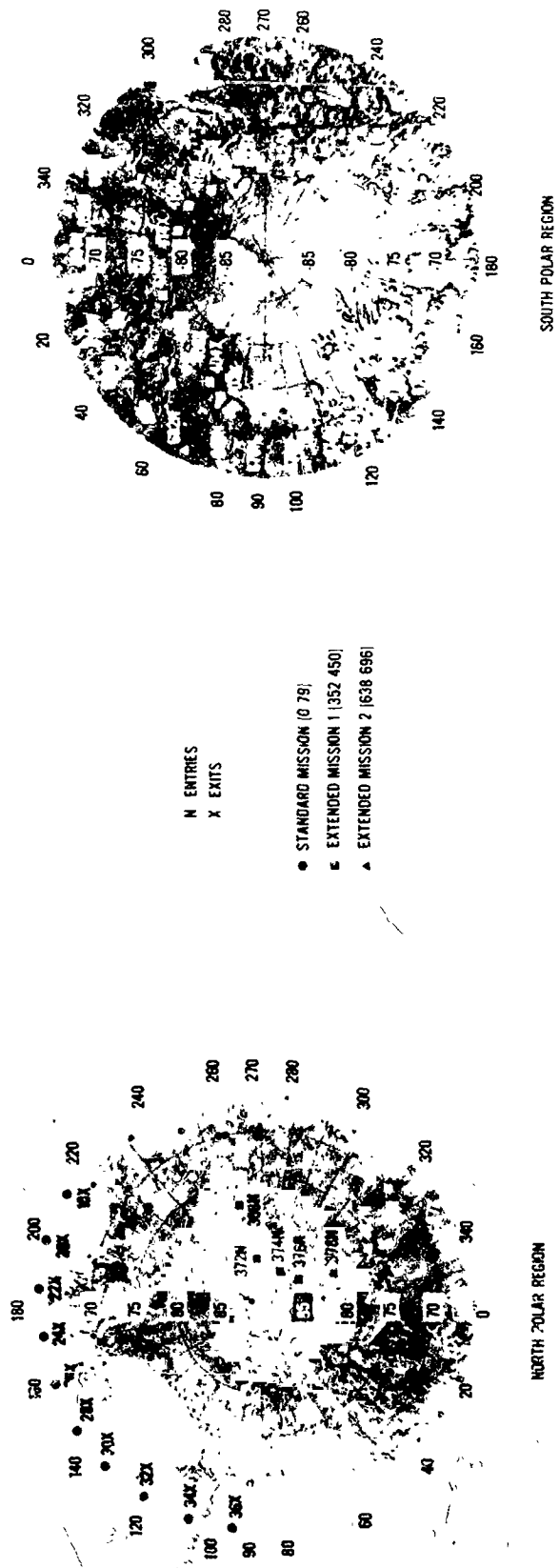
NORTH POLAR REGION

Fig. XXXVI-2. Location of occultation points in the polar regions.

letter N identifies the entry or immersion measurement, and the letter X identifies the exit or emersion. The standard mission measurements correspond to revolutions 0 to 79, and extended mission I, the subject of this section, corresponds to revolutions 352 to 450. The locations of the occultation measurements that correspond to a third set of occultations, beginning with revolution 638 and identified as extended mission II, also are shown on the map. However, data resulting from the extended mission II measurements have not yet been analyzed, and the results will be described at a future date.

In order to better evaluate the results, it is necessary to understand the conditions that existed on the surface of Mars at the points of measurement. The time of year corresponding with these measurements was northern hemisphere spring, with a sub-solar latitude ranging from 10.5° to 18.2°. The latitude, solar elevation angle, and Mars local time are shown for each entry measurement in Fig. XXXVI-3. These measurements began in darkness at mid-northern latitudes at local times corresponding to about 04:00. The latitudes of the measurements moved rapidly north with each successive revolution, and the solar illumination angle had risen above zero beginning with revolution 362. As the latitude of measurement approached the north pole, the solar elevation angle increased; the Martian local time changed rapidly until, by about revolution 390, it stabilized at about 17:00. For the remainder of the entry measurements, the latitudes became more southerly; the solar illumination, after reaching a maximum of about 17°, began to decrease as points of measurement reached the southern hemisphere. The corresponding quantities describing the exit measurements are shown in Fig. XXXVI-4. Here it is immediately evident that most of these measurements were

made at nighttime in the southern hemisphere, with the corresponding Martian time of day ranging from about 05:00 at the beginning to about 17:00 at the end; only the last two measurements occurred with the Sun above the horizon, while the latitude of measurement covered the entire southern hemisphere to about −80°. All latitudes used in this section have been computed by the JPL POGASIS program under the assumption of a spherical figure for Mars with a radius of 3389 km. Because the true radius of Mars at the equator and the poles is substantially different from this figure, the true areographic latitudes of the occultation points will differ somewhat from the values given here.

The methods of acquisition, processing, and analysis of the data have been described in a previous paper on *Mariner 9* occultation results (Ref. XXXVI-2), and they will not be discussed here. However, certain aspects of the extended mission I data render them sufficiently different from the standard mission data to warrant some discussion. Because of the much lower level of the received signal (approximately −165 dBm as compared to about −138 dBm to −145 dBm for the standard mission), the acquisition of the signal by the phase-locked loop receivers upon exit of the spacecraft from occultation was much more difficult, and for most exits the signal was not reacquired until several seconds after it reappeared. For this reason, it was necessary to use data obtained from the open-loop receivers to derive results from all exit measurements. The entry measurements were taken in the two-way mode in which the spacecraft transponder received a signal from the tracking station and coherently retransmitted it, thus effectively imparting to the received signal the stability of the frequency standard at the station. The exit data were taken in the one-way mode;
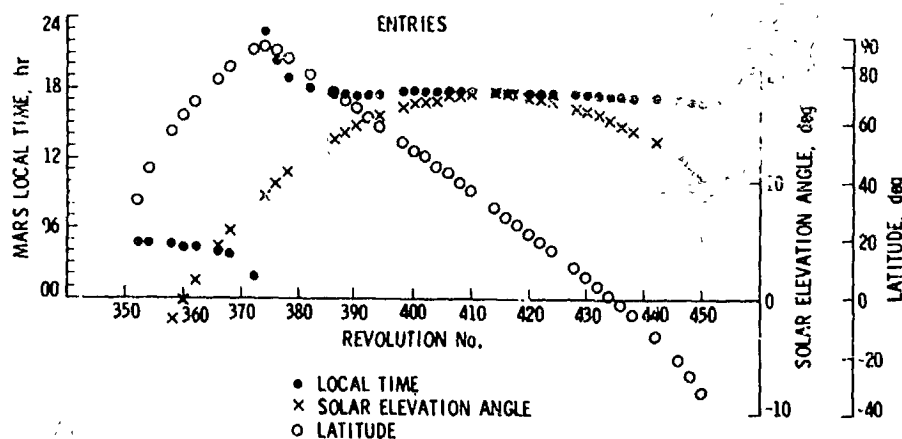
Fig. XXXVI-3. Latitudes, Mars local times, and solar illumination angles for entry measurements.
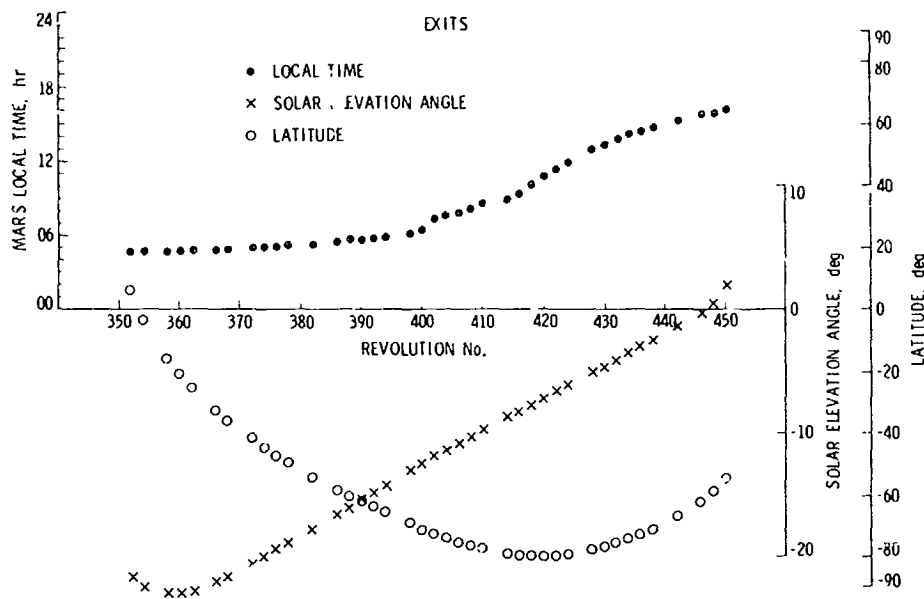
Fig. XXXVI-4. Latitudes, Mars local times, and solar illumination angles for exit measurements.

thus, their quality depended upon the stability of the crystal auxiliary oscillator onboard the spacecraft. During the standard mission, the quality of the one-way data was, in most cases, sufficient to derive such parameters as the surface pressure and temperature from the exit measurements, but not sufficiently good to allow computations of electron density in the ionosphere.

It appears that, between the time of the standard mission exit measurements and the measurements described here, the stability of the auxiliary oscillator had deteriorated, with the result that only a few of the exit measurements provide reliable temperature and pressure profiles. The measurements that were judged unreliable because of spurious low-frequency fluctuations in the observed Doppler residuals are marked with an asterisk in Table XXXVI-1. It is difficult to assign a quantitative measure to the uncertainty in the temperature and pressure derived from these measurements, but these results should be accepted with caution, and should not be used in applications requiring better than about 10% accuracy. The radii derived from these measurements are, however, quite acceptable.

The Mars–Earth geometry at the time of these measurements was such that the distance between the Earth and the spacecraft was relatively large, and the round-trip propagation time of the signal ranged from 37.6 to 42.0 min. This, in turn, produced a distance at Mars between the signal path up to the spacecraft and the path

down to Earth of as much as about 5 km for two-way measurements. The data were interpreted as resulting from an average effect between the uplink and downlink, with the surface radii determined from the distance of the downlink path from the center of Mars at the time of signal loss. The average refractivity profile was then extrapolated or interpolated to conform to that radius of the final measurement.

The accuracy of the radius measurements depends primarily on the precision of the timing of the occultation event as observed at Earth and on the precision of the knowledge of the spacecraft's orbit as represented by the uncertainty in its time of periapsis. During the standard mission, the accuracy of timing was on the order of 0.1 sec (Ref. XXXVI-3), and the uncertainty in the time of closest approach for each orbit was also of the same magnitude. Hence, with the vertical velocity of the radio beam to Mars of about 2.5 km/sec, the formal uncertainty in the standard mission radius measurements was about 330 m. Because of the much lower signal-to-noise ratio experienced during extended mission I, the timing of the occultation event, which was obtained by inspection of the spectrum of the received signal, could be obtained only with an uncertainty of about 0.7 sec because the spectra had to be averaged for that length of time to observe clearly the presence or absence of a signal. Concurrently, because of reduced tracking coverage during the extended mission, the accuracy of the orbit determinations also was reduced, resulting in uncertainties of

Table XXXVI-1. Summary of results (May to June 1972)

Revolution	Latitude, deg	Longitude, deg	Location	Radius, km	Surface pressure, mb	Surface temperature, °K	Solar zenith angle, deg	Peak electron density, el/cm³ × 10⁵	Peak radius, km	Radius at 6.1-mb pressure, km
352N	33.9	323.3	Arabia	3391.3	5.6	199	98.9	0.17	3547.5	3390.36
352X	6.7	329.0	Arabia	—[b]	—[b]	—[b]	111.5	—	—	—[b]
354N[a]	44.2	312.5	Protonius	3386.8	2.5	150	96.1	—	—	3380.13
354X	− 2.3	321.9	Aeria	3400.1	6.4	171	112.4	—	—	3400.54
358N	57.1	293.1	Umbra	3381.7	8.5	189	91.8	0.28	3550.1	3384.92
358X	−15.7	305.5	Iapygia	3398.5	5.3	163	112.8	—	—	3397.78
360N	62.2	284.0	North polar region	3379.1	7.2	191	90.1	0.47	3526.5	3380.68
360X[a]	−20.5	296.6	Iapygia	3394.1	3.1	143	112.8	—	——	3390.04
362N	66.8	275.3	North polar region	3378.1	7.3	198	86.5	0.45	3521.5	3379.88
362X[a]	−24.9	287.5	Mare Hadriacum	3392.1	2.2	141	112.6	—	—	3388.73
366N	75.0	260.5	North polar region	3377.2	6.5	187	85.6	0.49	3514.7	3377.81
366X[a]	−32.3	268.7	Mare Hadriacum	3390.0	9.0	209	111.9	—	—	3394.24
368N	78.7	255.7	North polar region	3375.9	6.5	182	84.3	0.60	3524.7	3376.53
368X[a]	−35.6	259.0	Ausonia	3391.6	4.0	175	111.5	——	—	3387 93
372X	−41.7	239.3	Ausonia	3388.5	4.0	160	110.5	—	—	3385.12
374N[a]	86.0	296.5	North polar region	3376.6	5.7	178	81.1	0.75	3512.7	3375.97
374X	−44.4	229.3	Eridania	—[b]	—[b]	—[b]	109.9	—	—	—
376N	84.7	326.6	North polar region	3376.8	6.0	181	80.1	0.78	3509.8	3376.64
376X	−47.0	219.3	Eridania	3388.6	6.6	200	109.4	—	—	3388.50
378N	82.1	335.5	North polar region	3378.1	5.2	186	79.2	0.91	3515.6	3376.62
378X	−49.4	209.3	Eridania	388.7	3.3	152	108.8	——	—	3383.23
382N	76.4	330.5	North polar region	3380.6	4.3	181	77.7	0.98	3516.1	3377.52
382X	−54.0	189.1	Mare Chronium	3386.7	4.2	161	107.7	—	—	3383.71
386N	70.5	317.5	North polar region	3379.7	5.5	186	76.3	0.99	3518.3	3378.72
386X	−58.2	168.8	Mare Chronium	3386 3	4.9	173	106.5	—	—	3384.35
388N	67.7	310.1	North polar region	3378.8	6.2	187	75.8	0.92	3513.4	3378.92
388X	−60.1	158.4	Palinuri Fretum	3385.6	5.2	170	106.0	——	—	3384.23

[a]Noisy data.

[b]Bad or missing data.

Table XXXVI-1 (contd)

Revolution	Latitude, deg	Longitude, deg	Location	Radius, km	Surface pressure, mb	Surface temperature, °K	Solar zenith angle, deg	Peak electron density, el/cm³ × 10⁵	Peak radius, km	Radius at 6.1-mb pressure, km
390N	64.8	302.3	North polar region	3379.5	7.0	210	75.2	0.99	3515.2	3380.73
390X	−62.0	147.9	Palinuri Fretum	3382.4	5.0	153	105.4	—	—	3381.13
392N	61.9	294.3	North polar region	3360.2	6.7	209	74.7	1.10	3514.2	3381.26
392X	−63.8	137.1	Thyle 1	3384.0	5.4	183	104.8	—	—	3382.87
394N[a]	59.1	287.1	Copais Palus	3380.5	6.6	209	74.3	1.00	3518.5	3381.28
394X	−65.6	126.0	South polar region	3383.4	4.2	186	104.2	—	—	3379.97
398N	53.5	269.1	Casius	3382.0	7.8	233	73.7	1.00	3514.0	3384.70
398X	−68.9	102.8	South polar region	—[b]	—[b]	—[b]	103.0	—	—	—
400N	51.2	260.2	Casius	3384.4	6.7	220	73.4	1.06	3514.0	3384.40
400X	−71.0	89.8	South polar region	3382.0	5.9	165	102.4	—	—	3381.74
402N	48.4	251.4	Utopia	3382.9	7.8	225	73.2	1.04	3522.1	3385.70
402X	−72.5	76.9	South polar region	3381.3	5.3	150	101.8	—	—	3380.23
404N	45.2	242.7	Aetheria	3384.1	6.8	202	72.9	1.20	3517.7	3385.20
404X	−73.5	64.3	South polar region	3380.3	4.5	154	101.4	—	—	3377.23
406N	42.4	233.7	Cebrenia	3385.7	6.8	218	72.7	1.01	3520.4	3386.79
406X	−74.3	50.3	South polar region	3380.9	8.1	197	100.8	—	—	3383.71
408N	39.5	224.8	Cebrenia	3386.5	6.5	216	72.6	1.10	3514.2	3387.10
408X[a]	−76.1	35.6	South polar region	3381.5	4.1	145	100.3	—	—	3379.51
410N	36.6	215.9	Cebrenia	3386.5	6.4	205	72.5	1.16	3520.1	3386.89
410X[a]	−77.1	20.2	South polar region	3380.9	7.7	205	99.7	—	—	3383.37
414N	30.9	198.2	Phlegra	3392.0	4.6	206	72.5	1.10	3522.2	3389.19
414X[a]	−78.8	346.6	South polar region	3383.9	3.7	146	98.7	—	—	3379.80
416N	27.8	189.5	Phlegra	3390.4	5.7	217	72.5	1.02	3518.1	3389.77
416X	−79.3	329.5	South polar region	3379.4	4.2	157	98.2	—	—	3376.60
418N[a]	24.9	180.9	Phlegra	3388.5	9.8	235	72.6	—[b]	—[b]	3394.14
418X[a]	−79.6	311.0	South polar region	3379.8	6.2	157	97.7	—	—	3379.93

[a]Noisy data.
[b]Bad or missing data.

Table XXXVI-1 (contd)

Revolution	Latitude, deg	Longitude, deg	Location	Radius, km	Surface pressure, mb	Surface temperature, °K	Solar zenith angle, deg	Peak electron density, el/cm³ × 10⁵	Peak radius, km	Radius at 6.1-mb pressure, km
420N	22.0	172.4	Amazenis	3390.4	6.7	230	72.7	1.06	3524.8	3391.47
420X	−79.7	292.3	South polar region	3379.9	4.9	155	97.2	—	—	3378.24
422N	19.1	164.0	Amazonis	3391.1	6.5	218	72.9	1.06	3522.7	3391.78
422X[a]	−79.6	273.3	South polar region	3380.1	3.8	145	96.6	—	—	3376.79
424N	16.1	155.6	Amazonis	3391.0	7.3	233	73.1	0.92	3522.6	3393.10
424X[a]	−79.2	255 1	South polar region	3380.0	4.0	148	96.1	—	—	3377.05
428N[a]	10.1	139.2	Nix Olympica	3394.0	3.8	212	73.7	—[b]	—[b]	—[b]
428X	−77.7	221.0	South polar region	3381.4	4.5	176	95.1	—	—	3378.84
430N	7.1	131.0	Pavonis Lacus	3398.4	4.6	223	74.0	1.09	3529.1	3395.43
430X[a]	−76.6	204.7	South polar region	3381.9	8.1	205	94.6	—	—	3384.71
432N	4.0	122.8	Pavonis Lacus	3403.5	3.1	210	74.3	0.99	3528.1	3396.88
432X[a]	−75.4	189.6	South polar region	3380.6	3.5	143	94.1	—	—	3377.27
434N	0.8	114.5	Pavonis Lacus	3417.1	1.0	209	74.7	0.89	3534.2	3397.94
434X	−74.0	175.1	South polar region	3383.8	7.0	149	93.5	—	—	3384.86
436N	− 2.4	106.2	Tharsis	3403.3	3.4	204	75.2	1.04	3524.2	3396.64
436X	−72.4	160.7	South polar region	—[b]	—[b]	—[b]	93.0	—	—	—
438N	− 5.8	97.9	Noctis Lacus	3407.1	2.0	185	75.6	1.02	3525.9	3397.24
438X[a]	−70.8	147.0	South polar region	3381.9	3.5	144	92.5	—	—	3377.84
442N	−13.1	81.4	Sinai	3401.3	3.1	211	76.7	0.90	3528.3	3394.73
442X[a]	−66.9	120.1	South polar region	3382.5	2.6	151	91.4	—	—	3374.29
446N	−21.4	65.4	Sinai	3390.0	3.4	201	78.0	0.93	3529.9	3394.60
446X	−62.0	93.5	Dia	—[b]	—[b]	—[b]	90.2	—	—	—
448N	−26.4	57.9	Mare Erythraeum	3398.2	3.8	214	78.7	0.73	3532.6	3393.18
448X	−58.7	80.0	Mare Australe	3384.2	5.3	148	89.6	—	—	3383.08
450N[a]	−32.6	51.2	Ogygis Regio	3392.4	3.3	166	79.5	0.50	3533.2	3387.64
450X	−54.3	65.9	Mare Australe	—[b]	—[b]	—[b]	88.9	—	—	—

[a]Noisy data.
[b]Bad or missing data.

up to 0.6 sec in time of closest approach. However, the maximum radial velocity of the radio beam was only 1.2 km/sec. Thus, with a total random timing uncertainty of about 0.9 sec in locating the occultation radius, the resulting maximum radius uncertainty is about 1.1 km.

Of the possible measurements, one entry measurement was lost because of operational difficulties, and six exit measurements were lost as a result of bad or missing data. Two of the entry measurements were made in the one-way mode (revolutions 418 and 218), which considerably reduced the value of the measurements. Thus, 73 successful measurements were obtained. Although these measurements cover almost all latitudes on Mars, the most significant measurements are those relating to the north pole; those measurements are discussed first.

The results of the standard mission (Ref. XXXVI-2) showed that the region at about 65°, where most of the exit measurements were taken, was low compared with the equatorial region, exhibiting high surface pressures and radii below 3380 km. Because no measurements at higher latitudes were obtained, one of two conclusions was suggested regarding the nature of the Martian north pole. If one were to assume that the systematically lower terrain at 65° was indicative of the general shape of the planet, then the polar radius would have to be about 3372 km, and the surface pressure would have to be about 12 mb. Alternatively, it was suggested that the

low elevation of the region around 65° could be a phenomenon peculiar to that latitude, and the conditions at the north pole could be different. It is now apparent that the latter conclusion is correct. The nine entry measurements obtained at latitudes above 65° indicate surface atmospheric pressures ranging from about 4.4 to 7.4 mb, with the average at about 5.7 mb (Fig. XXXVI-5). It is apparent in Table XXXVI-1 that the radii of these measurements average to about 3377.8 km. Thus, it appears that the radius of Mars changes by only about 2 km from a latitude of 65° to the north pole. When the altitudes corresponding to each point were computed relative to the 6.1-mb level, based on the surface pressure and the average scale height for the first 10 km, the results for the north polar measurements (Fig. XXXVI-6) show that the north polar area is about average in elevation, with most of the measurements indicating altitudes somewhat above the 6.1 mb reference. The temperature profiles derived from the north polar measurements are shown in Fig. XXXVI-7 with their locations on a north polar map. These temperature profiles, all taken at low solar elevation angles, do not show appreciable differences in temperature gradients, with the surface atmospheric temperatures varying with solar illumination angle and ranging from about 178°K to about 191°K, all substantially above the freezing point of carbon dioxide. As several of these measurements were taken directly over the north polar cap, these temperatures are indicative of the possibility that the remnant north polar cap may be at least partially composed of water ice.

REV No	362	364	366	368	370	372	374	376	378	380	382	384	386	388
LAT	66.8		75.0	78.7			86.0	84.7	92.1		76.4		70.5	67.7
LON	275.3		260.5	255.7			296.5	326.6	335.5		330.5		317.5	310.1
MLT, hr	4.36		4.01	3.67			22.90	20.19	18.92		17.99		17.65	17.54
GMT DATE (1972)	5/12		5/14	5/15			5/18	5/19	5/20		5/22		5/24	5/25

M.L.T. • MARS LOCAL TIME
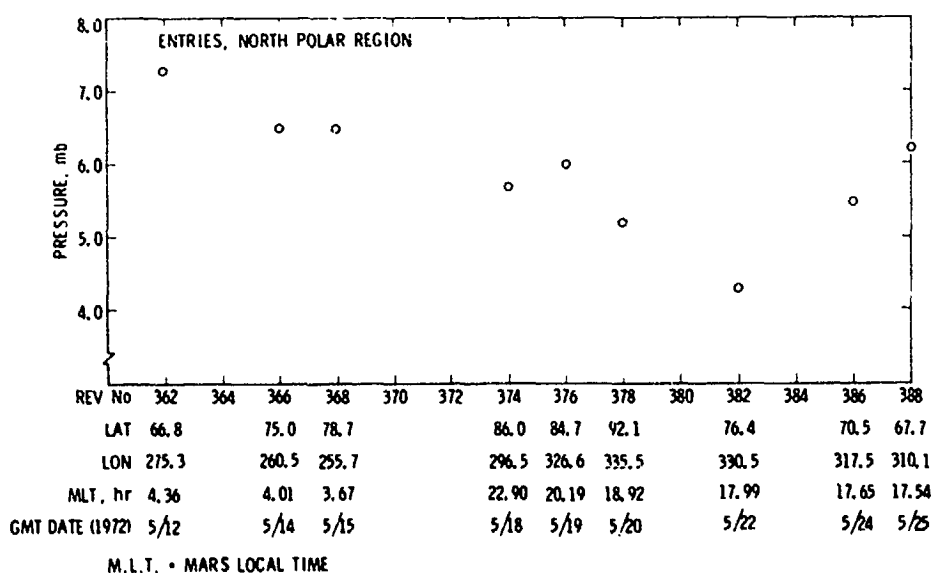
Fig. XXXVI-5. Surface atmospheric pressures for entry measurements in the north polar region.
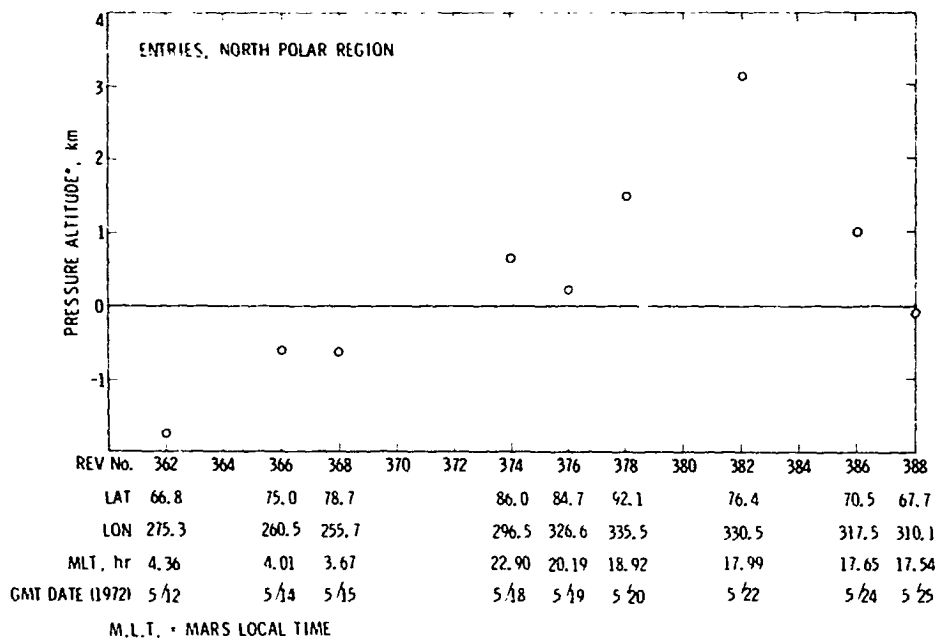
Fig. XXXVI-6. Pressure altitudes of measurements in the north polar region. Zero is equal to 6.1 mb.

The surface atmospheric pressures, as well as the corresponding pressure altitudes for the intermediate latitude (±65°) entry measurements, together with a map showing their locations, are shown in Fig XXXVI-8. Several points are worth noting. First, it is apparent that virtually all locations in the northern hemisphere in the Aetheria, Phlegra, and Amazonis regions exhibit pressure altitudes of from 1 to 3 km below the 6.1-mb level. These measurements are located on the right-hand side of the map. However, as the measurement locations cross into the Tharsis area, the elevations rise dramatically with a concomitant drop in the surface pressure. Measurements 432 and 436, apparently lying on the Tharsis plateau, indicate a pressure altitude of about 6.7 km. Measurement 438 taken in the "chandelier" region of the Coprates canyon indicates a pressure altitude of about 10 km with a surface pressure of 2 mb.

By coincidence, measurement 434 fell very near the top of the volcanic feature known as Middle Spot (Pavonis Lacus; Ref. XXXVI-4). The geometry of this occultation is shown in Fig. XXXVI-9. The location of the occultation tangency point for a spherical planet is represented by the large dot; the dashed line indicates the direction of the radio beam projected on the surface. It is apparent that, while the point of tangency does not fall in the caldera, the beam actually traverses an area close to the caldera and practically bisects the entire volcanic shield.

Thus, it is certain that the beam was actually interrupted by the highest feature along the beam track, which is likely to be the summit area. The radius that was measured is 3417.1 km. If one assumes that the radii corresponding to measurements 432 and 436 are indicative of the elevation of the surrounding terrain, a height of from 13.6 to 13.8 km is obtained for the volcanic construct of Middle Spot. Alternatively, on the basis of pressure altitudes, the height of Middle Spot is deduced to be about 12.5 km. This is in excellent agreement with the results of an ultraviolet spectrometer pressure mapping scan across Middle Spot which indicated a height of 12 to 13 km above the surrounding terrain and showed that the highest spot occurs not at the rim of the caldera, but considerably to one side of it. The pressure at the top of Middle Spot was found to be almost exactly 1 mb.

Some samples of temperature profiles obtained from the intermediate latitude entry measurements are shown in Figs. XXXVI-10 through XXXVI-12. Figure XXXVI-10 shows profiles for revolutions 352 to 360 and for revolution 390, with intervening profiles shown in Fig. XXXVI-7. The temperature profiles for revolutions 352 and 354, the initial near-grazing occultations, are noisy, and their isothermal nature may be due as much to asymmetry effects upon the inversion process as to the fact that the atmosphere is still in nighttime at this point. It should
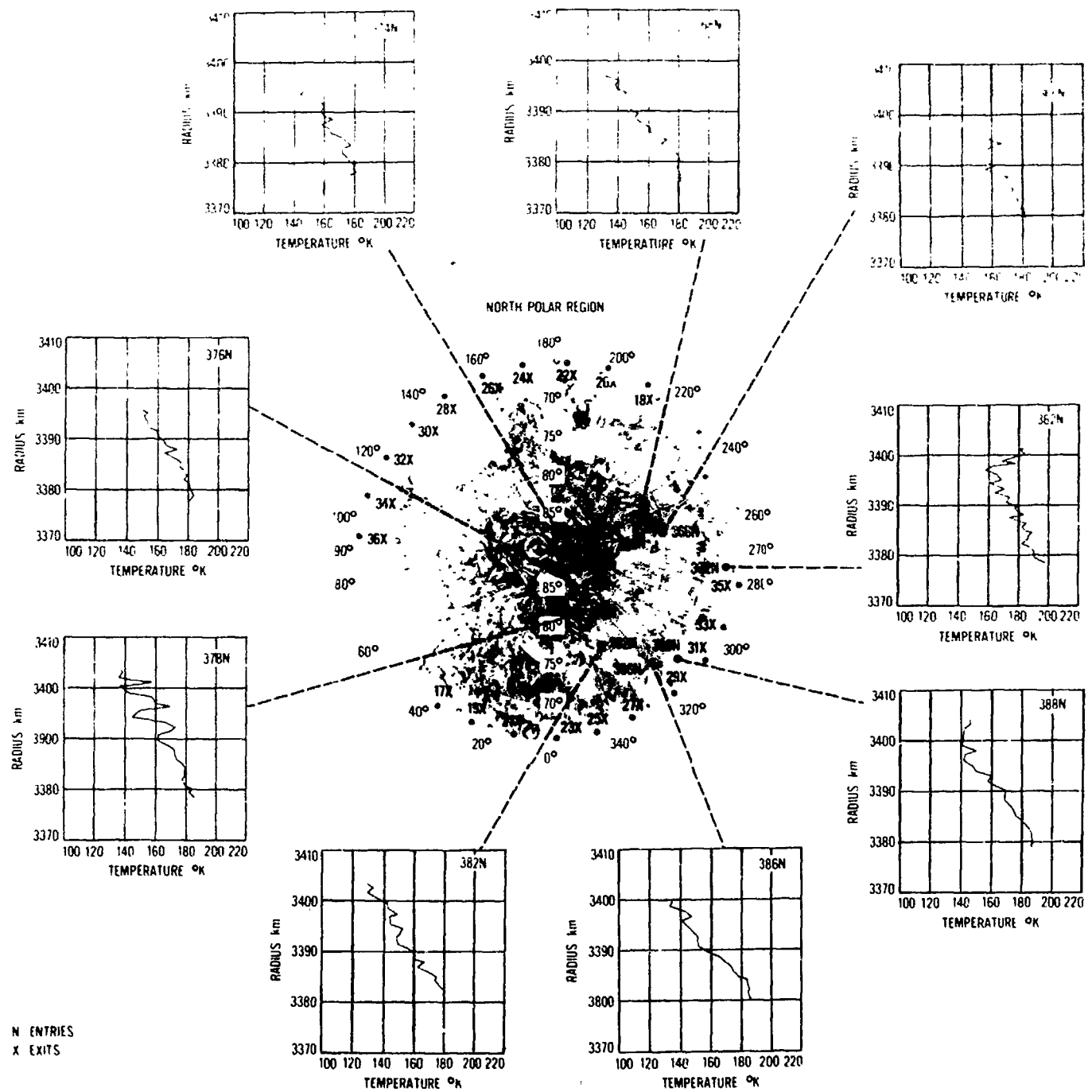
Fig. XXXVI-7. Temperature profiles measured in the north polar region.

N ENTRIES
X EXITS
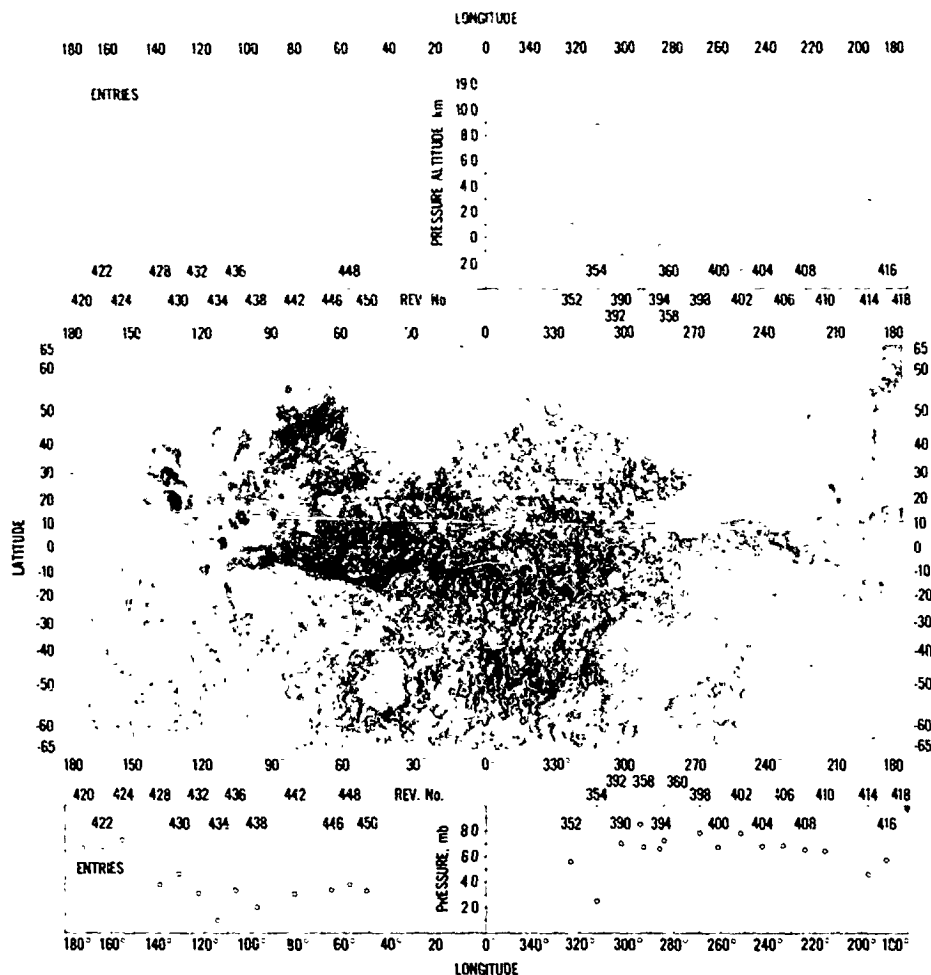
Fig. XXXVI-8. Surface atmospheric pressures and pressure altitudes for intermediate latitude entry measurements.

be mentioned that, for the grazing occultations, five-point averaging of the Doppler residual data was necessary to obtain meaningful results. Three-point averaging was used for data of revolution 358 and one-sample/sec data with no averaging were used for all revolutions from 360 to 446; averaging again was used for revolutions 448 and 450, the concluding near-grazing occultations. The profiles for revolutions 360 and 390 are similar in nature, as expected for similar latitudes and times of day. Figure XXXVI-12 shows some profiles for the high elevation measurements in the Tharsis area. The profile for revolution 428 shows the effect of the instability of one-way data upon a temperature profile. It must be concluded that the slow fluctuations in oscillator frequency completely mask any pertinent temperature profile information. A temperature profile for revolution 434 (Middle Spot) is noisy, as expected for data above the 1-mb level. Finally, the profile for the measurement taken at revolu-

tion 436 in the "chandelier" area shows an unexpected inversion near the surface.

Average temperature gradients in the troposphere for all entry measurements are shown in Fig. XXXVI-13. The gradients range from 0 to about $-3.8°K/km$ with no apparent correlation with latitude, Mars local time, or solar elevation angle. These values for the gradient are only slightly higher than those observed during the later portions of the standard mission when the atmosphere was still somewhat dusty, and they are all substantially below the theoretical adiabatic lapse rate of about $5°K/km$. Although all of these measurements were made at low solar elevation angles, this condition should not have had a large effect upon the temperature gradient, if the lower atmosphere is in radiative-convective equilibrium (Ref. XXXVI-5). It appears that, even in a clear Martian atmosphere, the temperature gradients are significantly
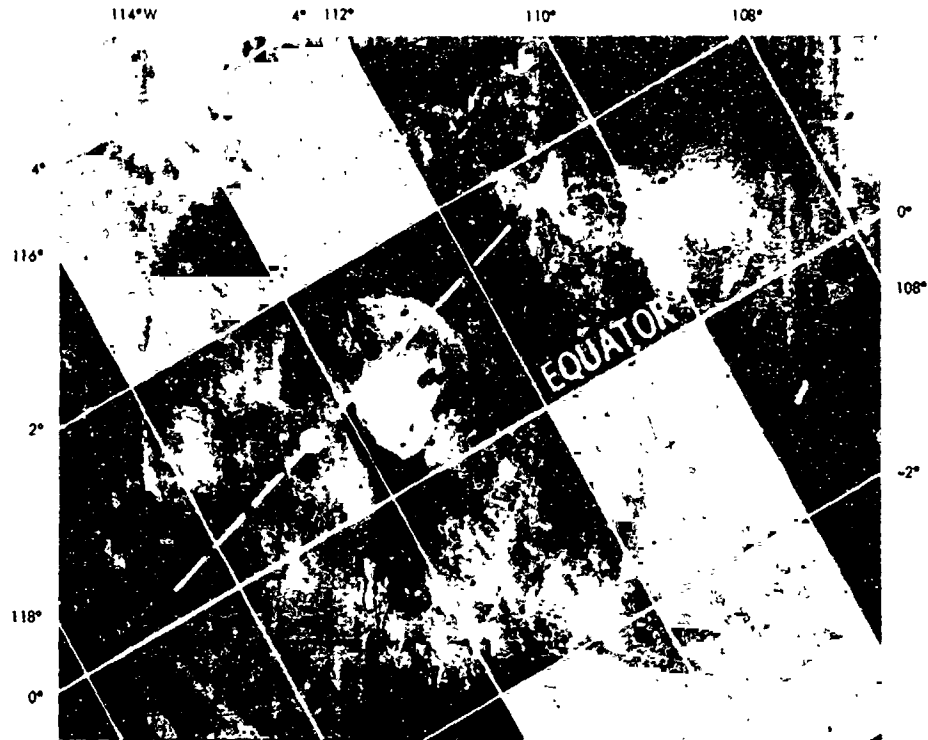
Fig. XXXVI-9. Geometry of the occultation on Middle Spot (Pavonis Lacus). The picture was provided by the *Mariner 9* Television Team.
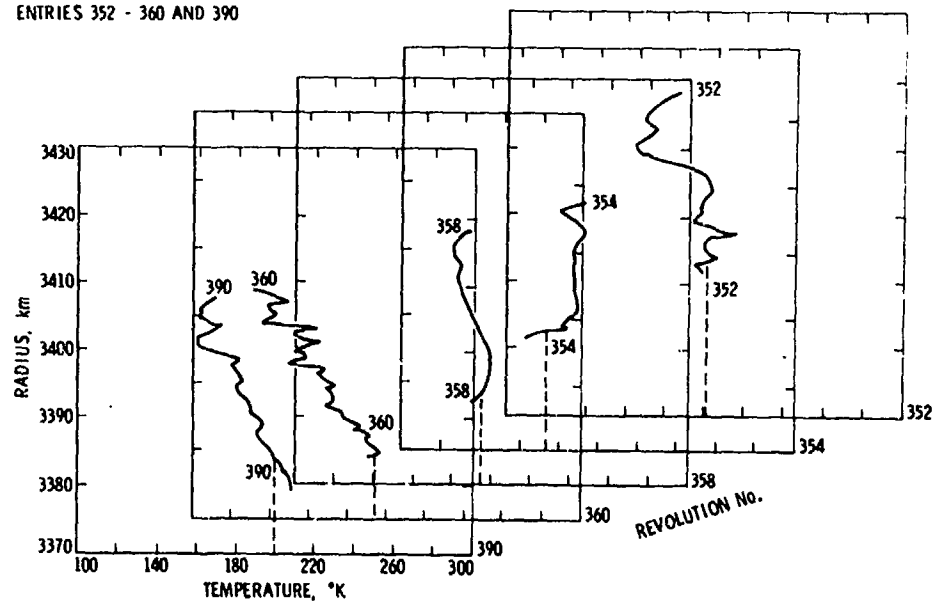
Fig. XXXVI-10. Temperature profiles for entry measurements of revolutions 352 to 360, and 390.

ENTRIES 404 - 414
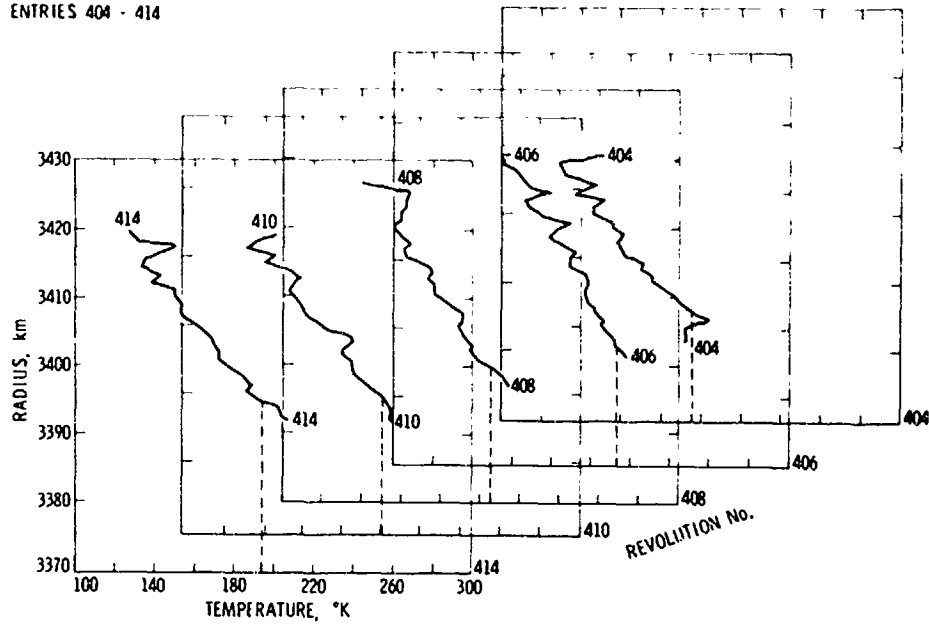
Fig. XXXVI-11. Temperature profiles for entry measurements of revolutions 404 to 414.

ENTRIES 428 - 436
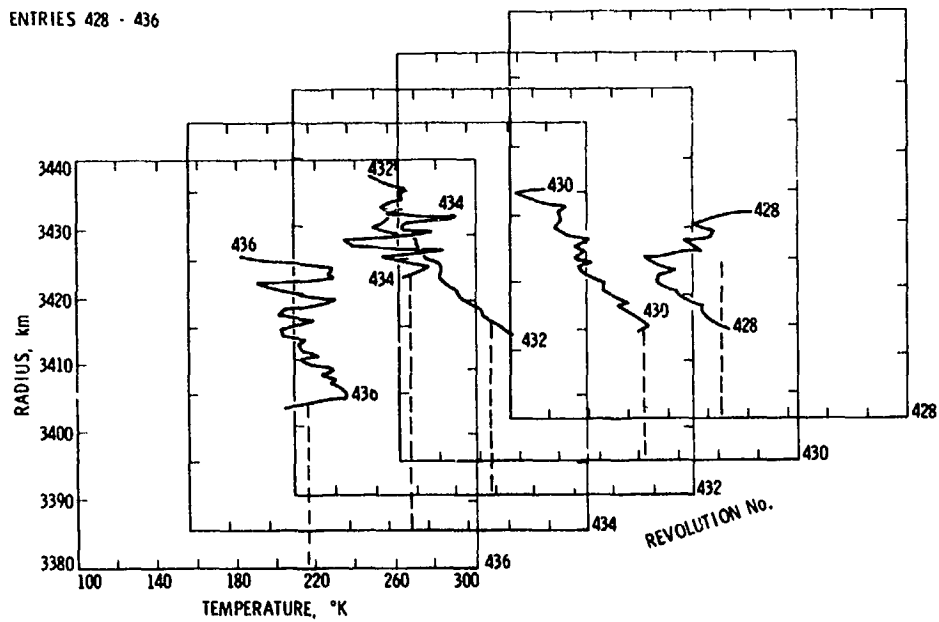
Fig. XXXVI-12. Temperature profiles for entry measurements of revolutions 428 to 436.
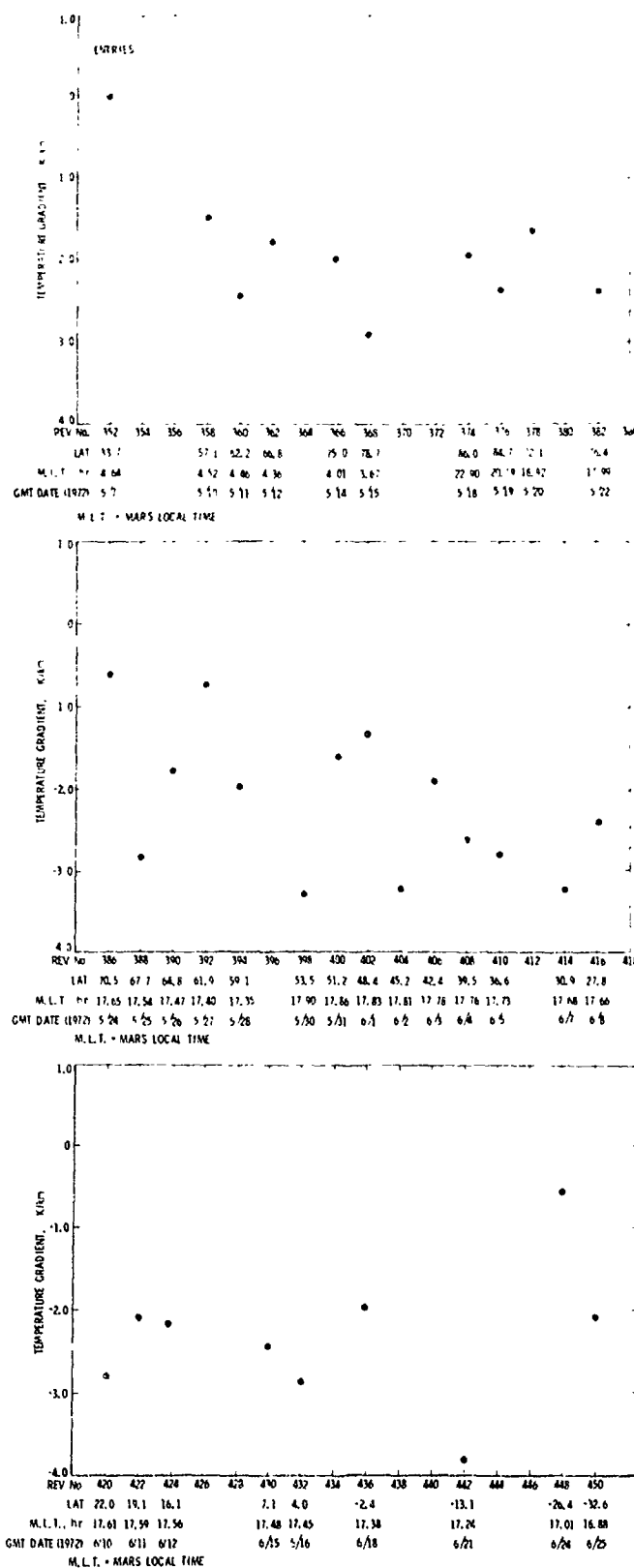
Fig. XXXVI-13. Temperature gradients in the lower atmosphere.

sub-adiabatic. In fact, the average gradient of about −2.3°K/km for these measurements is in good agreement with gradients deduced for a radiative-dynamical model of the lower atmosphere of Mars discussed by Stone in Ref. XXXVI-6.

The surface atmospheric pressures and pressure altitudes, together with a map giving the locations of the measurements on the planet's surface, are shown in Fig. XXXVI-14 for the intermediate latitude exit measurements. Temperature profiles representative of the exit measurements are shown in Figs. XXXVI-15 and XXXVI-16. Although five-point smoothing of the Doppler residual data was used during processing of almost all of these exit data, the temperature profiles of Figs. XXXVI-15 and XXXVI-16 show large fluctuations. These are most probably due to the random fluctuations in the frequency of the auxiliary oscillator.

It is evident from Fig. XXXVI-2 that 25 of the exit measurements occurred in the south polar area. Although the relatively poor quality of the exit data somewhat reduces the reliability of the temperature and pressure measurements, the measured radii are reliable. It can be seen in Table XXXVI-1 that radii in the south polar area average about 3381.2 km, or about 3.4 km higher than a corresponding reading in the north polar area. This is verified by the measured surface pressures (Fig. XXXVI-17) that cluster around 4 to 5 mb with only a few high values around 6 to 8 mb. The corresponding pressure altitudes referred to the 6.1-mb level are shown in Fig. XXXVI-18, which indicates an altitude of between 2 and 4 km for most of the measurements in the south polar region. Although the temperature profiles are not highly reliable, those shown in Fig. XXXVI-16, corresponding to a sample of the south polar region, indicate temperatures in the lower atmosphere consistent with the condensation of carbon dioxide, which is expected for nighttime in the winter at the south pole.

The surface atmospheric temperatures for all entry measurements and the more reliable exit measurements are plotted as a function of latitude in Fig. XXXVI-19. The entry temperatures, measured for the most part in the daytime, show the expected variation in temperature with latitude, with a maximum near the sub-solar latitude. The wide scatter of points probably is due to variations in topography, albedo, and other local effects. The exit temperatures, measured mostly during nighttime, show a wider scatter. However, the measurements taken near the south pole show temperatures in the vicinity of the condensation temperature of carbon dioxide.
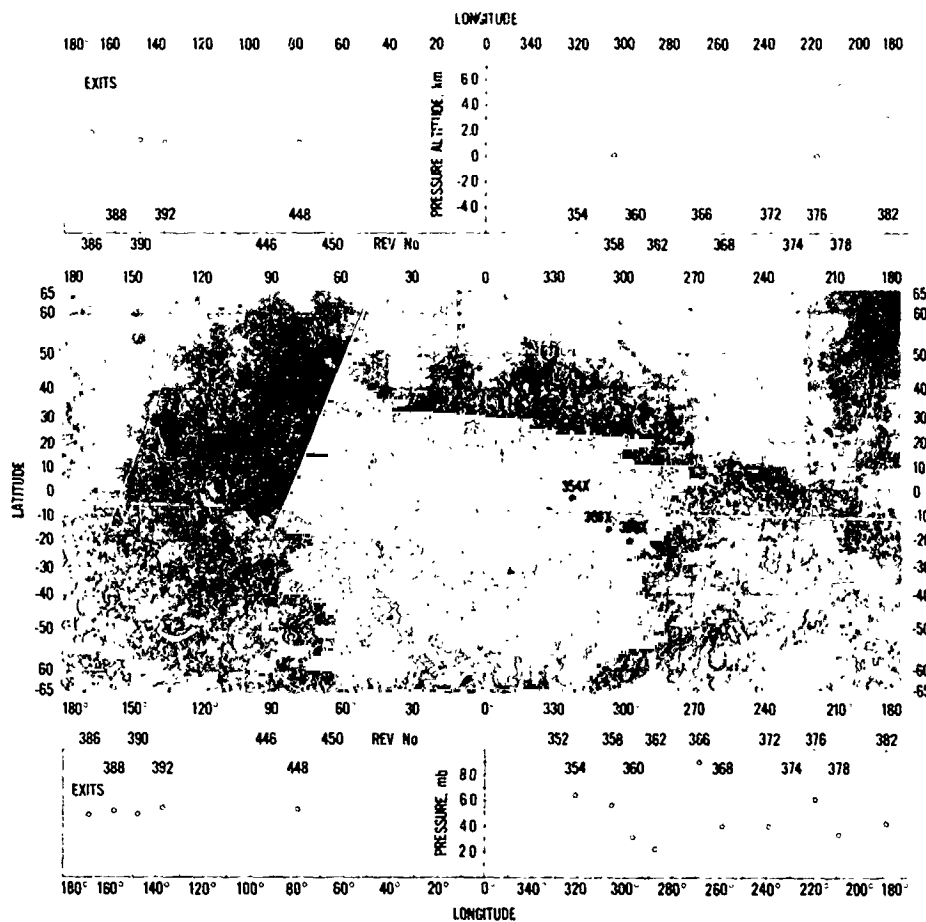
Fig. XXXVI-14. Surface atmospheric pressure and pressure altitude for intermediate latitude exit measurements.

In addition to providing information on the lower atmosphere pressures and temperatures, as well as measurements of the planet's radius, the entry measurements also provided information on the spatial electron density distribution in the upper atmosphere of Mars. As in the lower atmosphere, the horizontal refractivity changes were averaged in the process of computing the vertical refractivity profile. The effect of the horizontal gradients on the estimate of the local electron density is small compared to the errors produced by noise in the Doppler residual data.

Figures XXXVI-20 through XXXVI-22 summarize the observed properties of the Martian ionosphere. The first of these figures shows the top-side plasma scale height versus the revolution number. During the first revolutions, the measurements yielded scale height values approximately equal to 39 km. However, the spread of the scale height values is seen to increase with time. This

effect is believed to be due, at least in part, to decreasing signal-to-noise ratio and deterioration of the spacecraft's radio transponder. It should be noted here that the plasma scale height is more sensitive to radio phase instabilities than any other of the parameters deduced from the occultation measurements.

Figure XXXVI-21 shows the observed peak electron density versus solar zenith angle. The measurements covering the 47° to 57° range were made during the standard mission, and the data for angles greater than 72° were obtained during extended mission I. Also shown in Fig. XXXVI-21 is the expected dependence of the peak electron density on the solar zenith angle for an F_1-model ionosphere with a top-side scale height of 39 km. The model calculations assume an effective recombination rate coefficient that is independent of altitude and a constant EUV flux output from the Sun. As shown

EXITS, 372, 376, 378, 382, 386
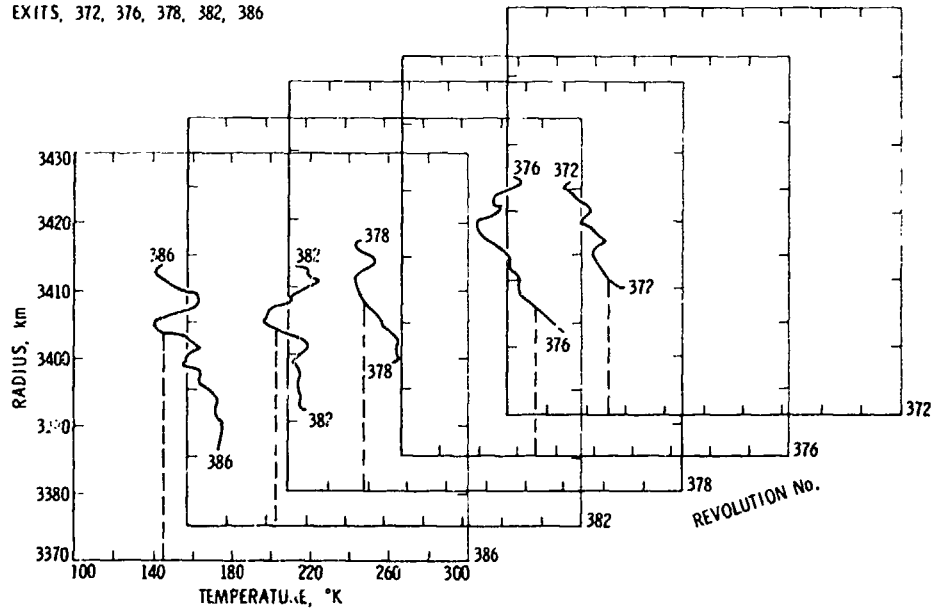
Fig. XXXVI-15. Temperature profiles for exit measurements taken during revolutions
372, 376, 378, 382, and 386.

EXITS, 416 - 424
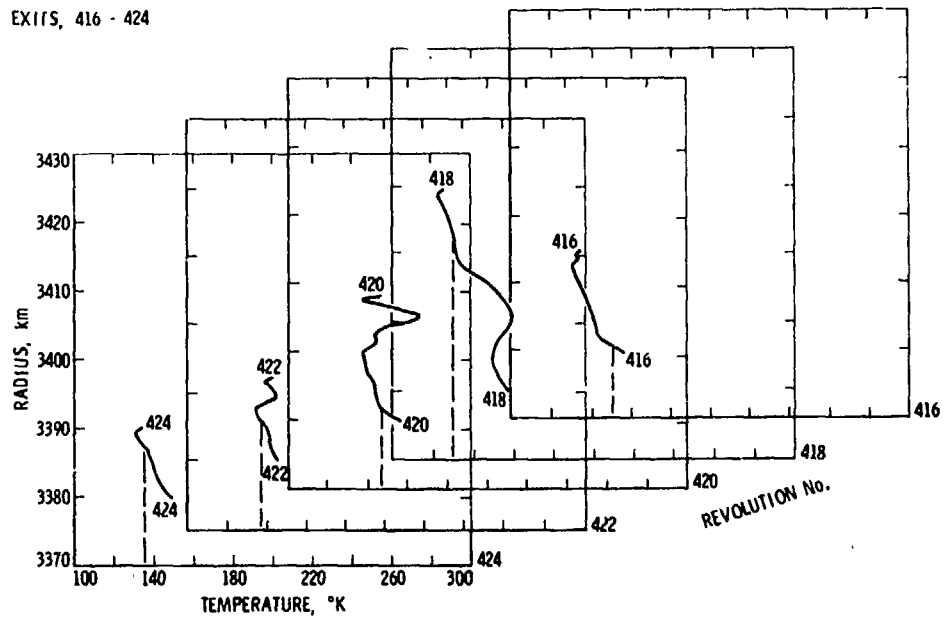
Fig. XXXVI-16. Temperature profiles for exit measurements taken during
revolutions 416 to 424.
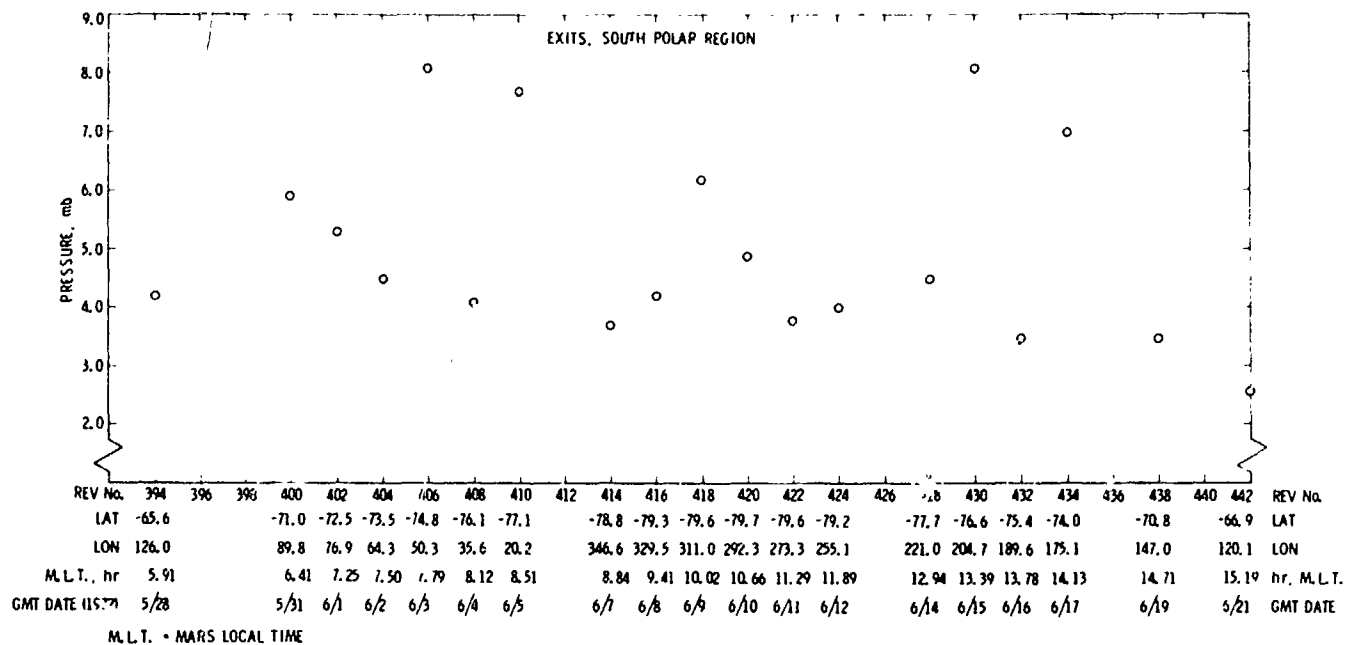
Fig. XXXVI-17. Surface atmospheric pressures for exit measurements in the south polar region.
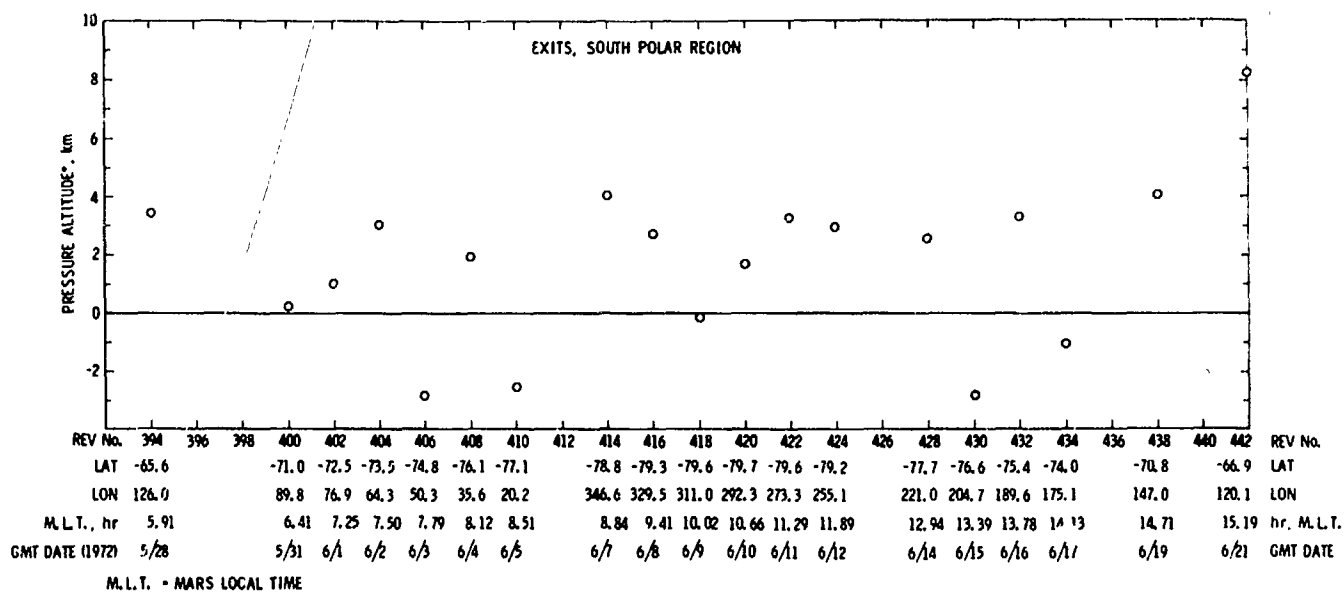
Fig. XXXVI-18. Pressure altitudes for exit measurements in the south polar region.
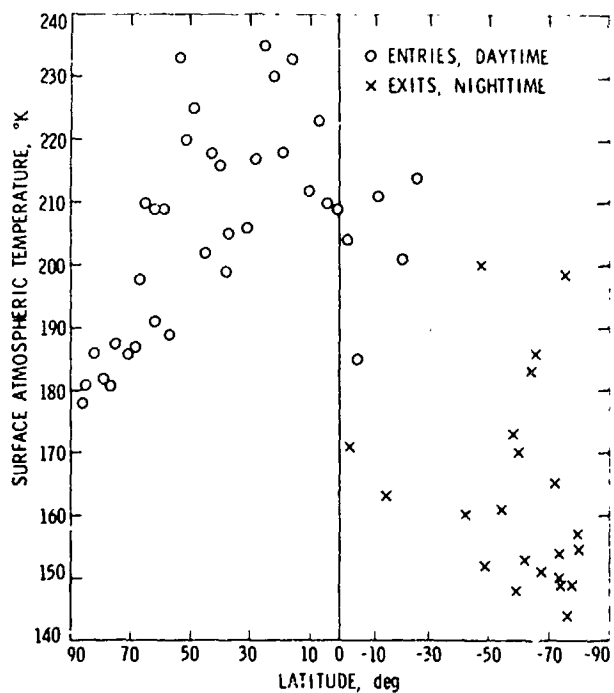
Fig. XXXVI-19. Surface atmospheric temperatures as a function of latitude.
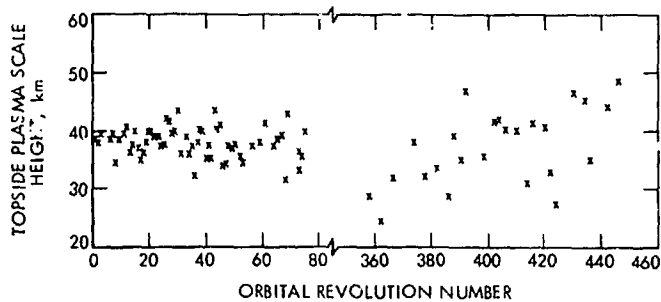
Fig. XXXVI-20. Topside plasma scale height from all data from Mariner 9 occultation measurements.

Fig. XXXVI-21. Peak electron density in the ionosphere as a function of solar zenith angle.
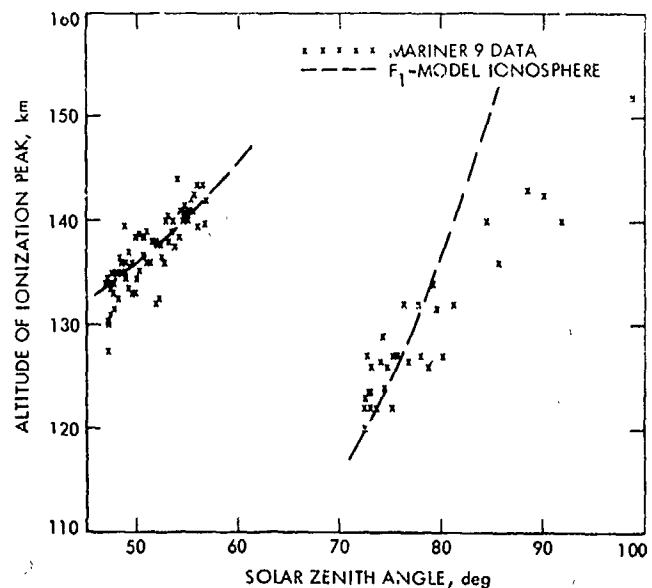
Fig. XXXVI-22. Altitude of the ionization peak as a function of solar zenith angle.

earlier, the measurements do not correlate well with day-to-day changes in 2800-MHz solar flux (Ref. XXXVI-2). The discontinuity in the dashed curve of Fig. XXXVI-21 between the two angular intervals covered by the measurements is due to an increase in the Mars–Sun range during the period from December 1971 to May 1972.

The observed changes in the altitude of the ionization peak are shown in Fig. XXXVI-22, again as a function of the solar zenith angle. The altitude was measured in each case relative to the 3-mb pressure level. The discontinuity in the altitude between 57° and 72° may have

been caused by a cooling of the atmosphere in the time interval between the two sets of measurements. A reduction on the order of 25 to 30% in the average atmospheric temperature below the ionization peak would be required to explain the entire altitude change. The model calculation indicated by the dashed curve of Fig. XXXVI-22 assumes atmospheric cooling to be the cause of the discontinuity. However, other possible effects such as a

decreasing effective recombination rate coefficient with altitude also may have contributed to the observed altitude reduction.

One of the most important aspects of the extended mission 1 measurements is the coverage of the north and south polar regions, which is of great value in defining the shape of the planet. The detailed discussion of the shape is the subject of a companion paper (Ref. XXXVI-7; also see Section XXXVII of this Report). However, certain conclusions are immediately evident upon examination of Figs. XXXVI-23 and XXXVI-24. Figure XXXVI-23 shows the pressure altitudes for each measurement made during the standard mission and extended mission 1 plotted versus latitude. The points are widely scattered, primarily because of the effects of topography. However, it is immediately obvious that the elevations in the southern hemisphere are much higher than those in the northern hemisphere. The altitudes in the northern hemisphere cluster primarily around 1 km at low and moderate latitudes, dropping to about −3 km at about 60° to 65° and returning to about zero altitude at the north pole. In the southern hemisphere, however, most measurements indicate altitudes of about 3 to 4 km in the low and moderate latitudes and about 2 to 3 km in the polar regions. In fact, with the exception of three measurements near the south pole, the only measurements indicating large negative elevations in the southern
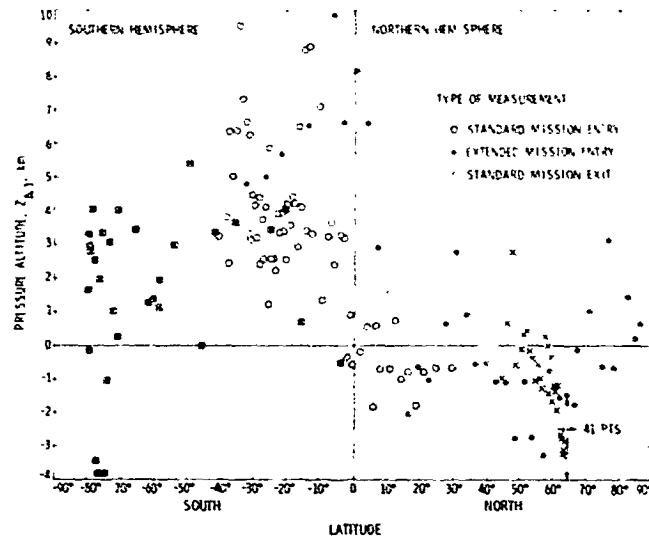
Fig. XXXVI-23. Pressure altitudes of all *Mariner 9* occultation measurements as a function of latitude.

hemisphere are those in Hellas (not shown in Fig. XXXVI-23). The same conclusion is evident from Fig. XXXVI-24, which shows the height of each measurement relative to the surface of a triaxial ellipsoid. The ellipsoid, computed from all radius data taken during both the standard and extended missions (Ref. XXXVI-7; also see Section XXXVII of this Report), has an equatorial major
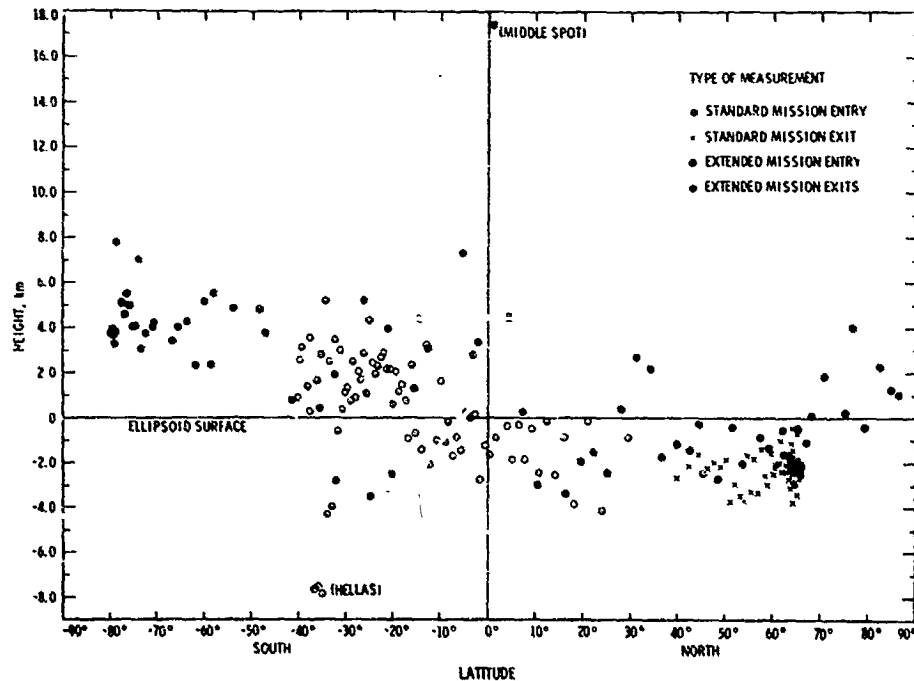
Fig. XXXVI-24. Heights relative to a triaxial ellipsoid model as a function of latitude.

axis of 3400.12 km, a minor axis of 3394.19 km, a polar radius of 3375.45 km, and a longitude of the major axis of 99.7°. Again, the north/south asymmetry is striking, with the only low-lying points in the southern hemisphere again being those in Hellas. It is thus evident that Mars, in addition to being asymmetrical equatorially, is also significantly asymmetrical in the north and south directions, with almost the entire southern hemisphere lying 3 to 4 km higher than the northern hemisphere. This is almost certainly t' result of internal activity within Mars, and it will undoubtedly be the subject of further study.

Another important conclusion suggested by the results of the set of occultation measurements described here is that temperature gradients in the clear atmosphere of Mars are only about one-half of the adiabatic gradients of 5°K/km, suggesting that dynamical processes are important.

This section represents a preliminary analysis of data taken during extended mission I. Additional analysis and interpretation of these data and results, as well as those taken during the standard mission and extended mission II, will be the subjects of future publications.

References

XXXVI-1. Kliore, A. J., Cain, D. L., Fjeldbo, G., Seidel, B. L., and Rasool, S. I., "Mariner 9 S-Band Martian Occultation Experiment: Initial Results on the Topography and Atmosphere of Mars," *Science*, Vol. 175, p. 313, 1972.

XXXVI-2. Kliore, A. J., Cain, D. L., Fjeldbo, G., Seidel B. L., Sykes, M. J., and Rasool, S. I., "The Atmosphere of Mars From Mariner 9 Radio Occultation Measurements," *Icarus*, Vol. 17, p. 484, 1972.

XXXVI-3. Cain, D. L., Kliore, A. J., Seidel, B. L., and Sykes, M. J., "The Shape of Mars From the Mariner 9 Occultations," *Icarus*, Vol. 17, p. 517, 1972.

XXXVI-4. Masursky, H., Batson, R. M., McCauley, J. F., Soderblom, L. A., Wildey, R. L., Carr, M. H., Milton, D. J., Wilhelms, D. E., Smith, B. A., Kirby, T. B., Robinson, T. C., Leovy, C. B., Briggs, G. A., Young, A.T., Duxbury, T. C., Acton, C. H., Jr., Murray, B. C., Cutts, J. A., Sharp, R. P., Smith, S., Leighton, R. B., Sagan, C., Veverka, J., Noland, M., Lederberg, J., Levinthal, E., Pollack, J. B., Moore, J. T., Jr., Hartmann, W. K., de Vaucouleurs, G., and Davies, M. E., "Mariner 9 Reconnaissance of Mars and Its Satellites: Preliminary Results," *Science*, Vol. 175, p. 331, 1972.

XXXVI-5. Gierasch, P., and Goody, R., "The Study of the Thermal and Dynamical Structure of the Martian Lower Atmosphere," *Planet. Space Sci.*, Vol. 10, p. 615, 1968.

References (contd)

XXXVI-6. Stone, P. H., "A Simplified Radiative-Dynamical Model for the Static Stability of Rotating Atmospheres," *J. Atmos. Sci.*, Vol. 29, p. 405, 1972.

XXXVI-7. Cain, D. L., Kliore, A. J., Seidel, B. L., Sykes, M. J., and Woiceshyn, P. M., "An Approximation to the Mean Surface of Mars and Mars Atmosphere Using Mariner 9 Occultations," *J. Geophys. Res.*, Vol. 78, 1973.

Acknowledgments

XXXVII. Approximations to the Mean Surface of Mars and Mars Atmosphere Using *Mariner* 9 Occultations

D. L. Cain, A. J. Kliore. B. L. Seidel, M. J. Sykes, and P. M. Woiceshyn

Jet Propulsion Laboratory/California Institute of Technology, Pasadena, California 91103

When the *Mariner* 9 spacecraft passed behind Mars in its orbiting phase, the radio beam (2300-MHz communication link) was cut off by some physical feature. These occultations occurred during the months of November and December 1971 and again in April and May 1972.[1] The fairly good global spread of these data (see Ref. XXXVII-1; also see Section XXXVI of this Report) was used herein to estimate the shape of the Martian globe, as definable by mathematical shapes (ellipsoidal and spherical harmonic).

The refraction profiles allowed the estimation of pressure near the occultation point; these, corrected back to an arbitrary fixed value of pressure, chosen to be 6.1 mb, were used as radii to (hopefully) an isobaric surface. Both sets of radii are given by Kliore et al. in Ref. XXXVII-1 (also see Section XXXVI of this Report). Also, detailed information about methods used were previously described by Kliore et al. (Ref. XXXVII-2) and by Cain et al. (Ref. XXXVII-3).

[1]Another set of occultations occurred later; however, these are still being reduced and are not considered here.

A. Surface Approximations

The latitude and longitude of the surface grazing point previously reported were recomputed to correspond to an updated pole direction estimate. obtained from a combination of Earth and *Mariner* observations.[2] The new figures for $X^2/A^2 + Y^2/B^2 + Z^2/C^2 = 1$, where Z = spin and X-axis pointing θ degrees west of the prime meridian, are:

$$A = 3400.12 \ (3400.8) \ \text{km}$$

$$B = 3394.19 \ (3394.7)$$

$$C = 3375.45 \ (3372.5)$$

$$\theta = 99.57° \ \text{longitude} \ (103.6)$$

[2]The right ascension δ, declination α, at any time T, Julian Centuries past January 1, 1950 (1950.0 Mean Earth Equator and Equinox System) were given by $\alpha = 317.32 - 0.1011T$, $\delta = 52.68 - 0.057T$, degrees. The rotation rate used was $350°.891962/\text{day}$ and the meridian was $148°.7668$ east of the Mars vernal equinox at the same epoch.

Parentheses indicate previous figures from Cain et al. (Ref. XXXVII-3). Thus, the inclusion of an increased number of southerly points has decreased the flattening result from $f = 0.00743$ to $f = 0.0064$. The root mean square of the differences between the data and this figure was ᵤ km.

To obtain a better approximation, a more complex model was used, of the form

$$r = R \sum_{n=1}^{N} \sum_{m=1}^{n} P_{nm}(\sin \phi) \, (C_{nm} \cos m\lambda - S_{nm} \sin m\lambda)$$

where

$R =$ a constant (arbitrarily taken as 3393.4 km)

$P_{nm} =$ associated Legendre function, e.g.,
$P_{2,1}(Z) = 3Z (1 - Z^2)^{1/2}$

$C_{nm}, S_{nm} =$ coefficients adjusted to least-squares fit the data

$\phi, \lambda =$ latitude, longitude (°W)

The results are given in Tables XXXVII-1 through XXXVII-4 for $N = 2, 3, 4,$ and 5. The C_{10} and C_{11}, S_{11} terms are equivalent to a figure displacement from the mass center. For a second-order approximation, the best fit is displayed southward from the mass center by 2.85 km. There is also an equatorial displacement of about 1.7 km in the direction of about 100°W. The other models are similar with better fits for higher order as shown in Table XXXVII-5. The resulting mean equatorial and polar equatorial and polar radii for $N = 2$ (similar for other N's) are 3400.66 and 3379.66, giving a flattening value of 0.00607.

Table XXXVII-1. Second-order harmonic coefficients and their standard deviations

Identification	Coefficient	Sigma
C(0,0)	.999004	0.000023
C(1,0)	−0.000836	0.000034
C(1,1)	−0.000091	0.000042
C(2,0)	−0.004049	0.000045
C(2,1)	0.000156	0.000029
C(2,2)	−0.000236	0.000016
S(1,1)	0.000509	0.000042
S(2,1)	0.000236	0.000029
S(2,2)	−0.000123	0.000016

Table XXXVII-2. Third-order harmonic coefficients and their standard deviations

Identification	Coefficient	Sigma
C(0,0)	0.999060	0.000026
C(1,0)	−0.000837	0.000040
C(1,1)	−0.000101	0.000042
C(2,0)	−0.004115	0.000049
C(2,1)	0.000083	0.000032
C(2,2)	−0.000280	0.000018
C(3,0)	−0.000118	0.000061
C(3,1)	−0.000030	0.000025
C(3,2)	−0.000057	0.000009
C(3,3)	0.000022	0.000003
S(1,1)	0.000532	0.000045
S(2,1)	−0.000141	0.000031
S(2,2)	−0.000154	0.000017
S(3,1)	−0.000081	0.000024
S(3,2)	−0.000048	0.000008
S(3,3)	−0.000037	0.000004

Table XXXVII-3. Fourth-order harmonic coefficients and their standard deviations

Identification	Coefficient	Sigma
C(0,0)	0.999046	0.000028
C(1,0)	−0.000827	0.000040
C(1,1)	−0.000061	0.000048
C(2,0)	−0.004235	0.000053
C(2,1)	0.000093	0.000033
C(2,2)	−0.000294	0.000018
C(3,0)	−0.000009	0.000063
C(3,1)	−0.000061	0.000027
C(3,2)	−0.000068	0.000010
C(3,3)	0.000015	0.000004
C(4,0)	0.000493	0.000076
C(4,1)	0.000036	0.000021
C(4,2)	0.000037	0.000006
C(4,3)	−0.000004	0.000002
C(4,4)	0.0000005	0.000006
S(1,1)	0.000364	0.000065
S(2,1)	−0.000248	0.000039
S(2,2)	−0.000177	0.000018
S(3,1)	−0.000030	0.000025
S(3,2)	−0.000062	0.000009
S(3,3)	−0.000033	0.000004
S(4,1)	0.000027	0.000027
S(4,2)	0.000028	0.000005
S(4,3)	−0.0000011	0.000002
S(4,4)	0.000002	0.0000006

Table XXXVII-4. Fifth-order harmonic coefficients and their standard deviations		
Identification	Coefficient	Sigma
$C(0,0)$	0.999224	0.000043
$C(1,0)$	−0.000784	0.000046
$C(1,1)$	0.0000003	0.000053
$C(2,0)$	−0.004303	0.000059
$C(2,1)$	0.000016	0.000036
$C(2,2)$	−0.000389	0.000028
$C(3,0)$	−0.000375	0.000092
$C(3,1)$	−0.000115	0.000035
$C(3,2)$	−0.000116	0.000012
$C(3,3)$	0.000009	0.000005
$C(4,0)$	0.000357	0.000085
$C(4,1)$	0.000015	0.000025
$C(4,2)$	0.000040	0.000007
$C(4,3)$	−0.000002	0.000002
$C(4,4)$	0.000001	0.0000007
$C(5,0)$	0.000571	0.000119
$C(5,1)$	0.000128	0.000023
$C'(5,2)$	0.000011	0.000006
$C(5,3)$	0.000002	0.0000009
$C(5,4)$	0.0000001	0.0000002
$C(5,5)$	−0.0000003	0.00000007
$S(1,1)$	0.000188	0.000089
$S(2,1)$	−0.000258	0.000054
$S(2,2)$	−0.000286	0.000026
$S(3,1)$	−0.000027	0.000027
$S(3,2)$	−0.000092	0.000011
$S(3,3)$	−0.000030	0.000005
$S(4,1)$	0.000082	0.000035
$S(4,2)$	0.000029	0.000006
$S(4,3)$	0.000001	0.000002
$S(4,4)$	0.000005	0.0000007
$S(5,1)$	−0.000050	0.000024
$S(5,2)$	0.0000077	0.000005
$S(5,3)$	−0.0000009	0.0000009
$S(5,4)$	0.000002	0.00000025
$S(5,5)$	−0.0000001	0.00000007

Table XXXVII-5. Details of harmonic fit

N	RMS fit, km	Number of coefficients
2	2.22	9
3	1.93	16
4	1.73	25
5	1.52	36

B. Atmosphere Approximations

The mass center to 6.1-mb pressure distances first were fit to an ellipsoid. In the same notation

$$A = 3394.67 \ (3396.06) \text{ km}$$
$$B = 3393.21 \ (3395.22)$$
$$C = 3376.78 \ (3377.42)$$
$$= 108.5° \text{ longitude } (108.5)$$

There is a decrease in the flattening with the new points. Using the average equatorial radius to compute flattening, we get 0.00506, compared to that predicted by the external gravity field (0.005238; see Ref. XXXVII-4) and assuming hystrostatic equilibrium and uniform atmosphere. The root mean square of the residuals to this fit was 1.63 km.

As before, a small group of radii contributed heavily to the least sum of squares of the residuals; twelve had fit errors greater than 3 km. The largest misfit had a residual of 6.5 km. What part of these residuals represents experimental error and what part actual deviation of the isobaric surface from a simple ellipsoid remain to be determined.

Higher-order models, the same as above, were tried out on the 6.1-mb pressure radii, but resulted in no better fit. The fit did not improve because of the inability (even when $N = 5$) to fit the worst point, which was the entry occultation, May 8, 1972, identified as "354N" in Ref. XXXVII-1 (also see Section XXXVI of this Report) and indicated as "noisy data." Nearby points in this second series also fit poorly, and so the ellipsoidal shape should be considered as good an approximation as is justified at this time. When a good geoidal shape is made available from orbiter tracking, it will be compared to our pressure radii for purposes of finding whether, or how much, the 6.1-mb pressure surface varies from the geoid.

References

XXXVII-1. Kliore, A. J., Fjeldbo, G., Seidel, B. L., Sykes, M. J., and Woiceshyn, P. M., "S-Band Radio Occultation Measurements of the Atmosphere and Topography of Mars with Mariner 9: Extended Mission Coverage of Polar and Intermediate Latitudes," *J. Geophys. Res.*, Vol. 78, 1973.

XXXVII-2. Kliore, A. J., Cain, D. L., Fjeldbo, G., Seidel, B. L., Sykes, M. J., and Rasool, S. I., "The Atmosphere of Mars From Mariner 9 Radio Occultation Measurements," *Icarus*, Vol. 17, p. 484, 1972.

XXXVII-3. Cain, D. L., Kliore, A. J., Seidel, B. L., and Sykes, M. J., "The Shape of Mars From the Mariner 9 Occultations," *Icarus*, Vol. 17, p. 517, 1972.

XXXVII-4. Sinclair, A. T., "The Motions of the Satellites of Mars," *Mon. Not. Roy. Astron. Soc.*, Vol. 155, p. 249, 1972.

XXXVIII. Verification of Performance of the *Mariner 9* Television Cameras

T. E. Thorpe

Jet Propulsion Laboratory/California Institute of Technology, Pasadena, California 91103

Having successfully completed its landmark mission, the *Mariner 9* spacecraft transmitted to Earth the last of more than 7300 pictures on October 17, 1972. These observations will yield a quantitative, as well as a qualitative, description of the planet Mars, providing the reliability of camera performance is assessed. As with its predecessors (*Mariners 6* and 7), the *Mariner 9* television can as received extensive preflight calibration. These da', perm't removal of the instrument signature from the telemetry by correcting nonlinearities measured months earlier. Significant geometric and photometric distortions may consequently be corrected once the applicability of preflight measurements to flight conditions has been verified. The extended operational lifetime of this spacecraft has emphasized the need for frequent health checks and the difficulties in obtaining relevant photography. It is evident that future deep space exploration must incorporate scheduled verification sequences to utilize calibration values.

The *Mariner 9* television experiment has been described previously (see Ref. XXXVIII-1). The cameras, similar to those used on *Mariners 6* and 7 (Ref. XXXVIII-2), consist of two slow-scan vidicons with identical picture formats and electronics (see Table XXXVIII-1). Two sets of optics of differing focal lengths (10:1) were used to photograph Mars from orbital altitudes of 1200 to 5000 km twice each day (60 frames). After 4 months of operations in orbit (November 14, 1971, to March 20, 1972 GMT), photography was curtailed because of passage of the spacecraft through the Martian umbra (April to May 1972) and solar conjunction (August to September 1972). During the months of June, July, and October, however, several hundred additional pictures were obtained to complement the standard mission. Table XXXVIII-2 summarizes camera operation.

The *Mariner* preflight television calibration effort consisted primarily of 14 camera performance tests: five at room temperature ("bench"), and nine environmental, producing a total of more than 7000 pictures (Ref. XXXVIII-3). These data are categorized in Table XXXVIII-3 with various planning, operation, and decalibration uses.

Inflight verification began with playback of calibration pictures tape recorded before launch on September 29, 1972. The significant verification events that followed

Table XXXVIII-1. Optical parameters

Parameters	Wide-angle camera	Narrow-angle camera
Focal length, mm	52.267	500.636
f/number	4.0	2.35
T/number	4.46	3.55
Field of view, deg	13.47 × 10.45	1.41 × 1.09
Target size, mm	9.6 × 12.5	9.6 × 12.5
Number of scan lines	700	700
Number of samples/line	832	832
Readout time, sec	42	42
Shutter speeds, sec	0.003 to 6.144	0.003 to 6.144
Filters (Effective wavelength[a])		
Filter position (Fp)	2 4 6 8	
Medium bandpass	0.610, 0.545, 0.477, 0.414	—
Filter position (Fp)	1 3 5 7	
Broad bandpass	0.560 0.565 0.565 0.565	0.588
Wide-angle camera polarization filter angle with vertical (line) axis	Fp 3 = 0° Fp 5 = 60° Fp 7 = 120°	

[a]Solar spectral irradiance.

Table XXXVIII-2. Standard mission performance data for launch through March 31, 1972

Total pictures taken (through revolution 262)									10,364
Filter position	1	2	3	4	5	6	7	8	
Pictures received from wide angle camera	11	1,158	24	109	1,588	95	18	359	3,486
Pictures received from narrow-angle camera									3,362
Total pictures received									6,848
Shutter operations (included false shutters)									13,186
Filter-wheel operations									1,400
Television subsystem on time, hr									3,533
Beam on time, hr									651

consisted of four types of photography. Scan calibrations (scan calibrations I and II) were special picture-taking sequences designed to determine the accuracy with which the *Mariner 9* science instruments could be directed toward specific targets (Ref. XXXVIII-4). Photography of star fields provided this information and, in addition to permitting an evaluation of camera pointing accuracy,

also gave an early assessment of focus, system noise interference, and residual image. Saturn calibration followed shortly thereafter, and produced images of Saturn at several shutter speeds and locations within the field of view. These data indicated the camera's ability to produce a response proportional to illuminance, regardless of signal strength. This "light transfer" characteristic evaluation (analog of the film H and D curve) was especially valuable because the data source was independent of the future Mars photography. Mars calibrations (Mars calibrations I and II) were similar sequences directed toward Mars, while the planet still appeared small in size. These data were intended to complete the comparison link between *Mariner* Saturn and Mars orbital photography and Earth-based observations of both planets. Finally, during orbital operations, several instances of repeated photography of isolated regions on Mars gave additional information concerning light transfer and spectral and modulation transfer camera properties. These sequences are summarized in Table XXXVIII-4.

Although these sequences provided a total of 270 frames, verification of performance was limited by the following considerations:

(1) Almost 70% of this picture subset was taken before orbit insertion. When the Martian dust storm had

Table XXXVIII-3. Calibration measurements and uses

Calibration	Preflight planning use	Mission operations use	Post-flight decalibration use
Light transfer	Exposure	Exposure radiance	
Shading	Exposure	Mosaic	Radiance over field of view
Spectral response	Sequence planning	Filter-wheel analysis	Spectral photometry
Stray light	Satellite photography planning	Pre-orbital science satellite pictures	Radiance
Residual image	—	Picture sequencing, false shutter recording	Radiance
Reseau pattern	Geodesy, cartography	Pointing accuracy	Geometric distortion
Focal plane scale	Cartography	POGASIS[a] footprints	—
Modulation transfer function	Resolution	Light-level dependency for narrow-angle camera	Enhancement
Point spread function	Star photography	Detection threshold	—
Shutter response	—	—	Radiance
Alignment	POGASIS[a]	Non-TV instrument offsets	—
Noise power spectra	Nine-bit encoding	Coherent noise identification	—
Aging	Star calibration turn-ons	Weekly extended mission turn-ons	—

[a]POGASIS is a navigational forecast computer program.

Table XXXVIII-4. Calibration verification sequences

Sequence	Date	Description	Number of pictures
AFETR playback	9/29/71	Telemetry test	30
Scan calibration I	10/1/71	Narrow-angle camera calibration	31
		Pointing accuracy	
		Point source imagery	
		Noise analysis, geometry	
		Residual image	
Scan calibration II	10/8/71	Narrow-angle camera calibration	32
		Pointing accuracy	
		Point source imagery	
		Residual image	
Saturn calibration	,/4/71	Light transfer, residual image shading	31
Mars calibration I	11/9/71	Narrow-angle camera: shading light transfer	33
Mars calibration II	11/10/71	Wide-angle camera: shading light transfer, filter positions 2, 8	30
Revolution 6	11/16/72	Wide-angle camera: filter position 2, light transfer	8
Revolution 7	11/17/71	Wide-angle camera: filter positions 1, 2, 3, 7, 8, light transfer	21
		Narrow-angle camera: point source	10
Revolution 72	12/20/71	Narrow-angle camera: point source	18
Revolution 76	12/22/71	Wide-angle camera: filter position 2, light transfer	8
Revolution 225	3/5/72	Narrow-angle camera: light transfer	14
		Wide-angle camera: light transfer	3

cleared sufficiently to permit mapping of the planet, the priority of observing topography prevented additional verification sequences. Consequently, little information exists to describe quantitatively camera operation as a function of mission date or camera usage in flight.

(2) The number of pictures taken does not reflect the extent of the data available to verify a given calibration parameter; i.e., all pre-insertion data produced images which represent a very small fraction of the field of view, and hence significant spatial extrapolation is necessary over the vidicon format.

(3) Many of the calibration parameters require large numbers of frames per image location; e.g., a single light-transfer verification at five points within the field of view (using four light levels) necessitates 20 pictures per camera and filter position.

Hence, only limited operational modes under optimal conditions could be checked.

A. Geometric Distortions

The ability of a television camera to reproduce image locations with the same geometric relationship as exists in object space is of vital importance to Martian cartography. Geometric distortions were measurable in both *Mariner* cameras by locating a reference pattern on flight photographs and comparing its appearance with calibration pictures. Star images also provided geometric consistency checks at selected locations within the field of view. No apparent change from the preflight calibration of geometric behavior was observed in flight data for either camera to a measurable accuracy of 1 pixel (picture element).

1. Reseau Measurement

To provide geometric reference, a pattern of reseau marks was deposited on the photoconducting surface of each vidicon. This array of 111 points (wide-angle camera) and 63 points (narrow-angle camera) was measured to a position accuracy of 10^{-3} mm, and hence revealed any nonlinearities in the electronic readout scan. Distortion correction requires recognition of these points in flight data by automated computer programs. Successful "decalibration" verified their consistent appearance throughout the mission.

A raster shift, occurring as a consequence of leaving Earth's magnetic field, was observed by comparing reseau

positions with preflight calibration at equivalent light levels. The displacement measured in television lines and pixels is given in Table XXXVIII-5. Figures XXXVIII-1 and XXXVIII-2 display the change in reseau pattern exhibited by these flight data.

During the ground calibrations of *Mariners 6, 7,* and *9,* these reseau positions also were found to be dependent upon exposure. A shift of about 3 pixels to higher line values occurred during the transition from threshold to saturation light levels, and probably was due to a residual charge on the vidicon target bending the read beam. Inflight photography revealed a similar displacement. Figures XXXVIII-3 and XXXVIII-4 show wide- and narrow-angle-camera reseau displacements (magnified

Table XXXVIII-5. Inflight change in raster position (displacements measured in television lines and picture elements)

Displacement	Wide-angle camera	Narrow-angle camera
Vertical (lines)	$+2.44 \pm 0.01$	-0.26 ± 0.01
Horizontal (pixels)	-3.61 ± 0.01	2178 ± 0.01
Clockwise rotation, mrad	0.58 ± 0.1	3.6 ± 0.1
Scale (enlargement), %	-0.14	<0.1
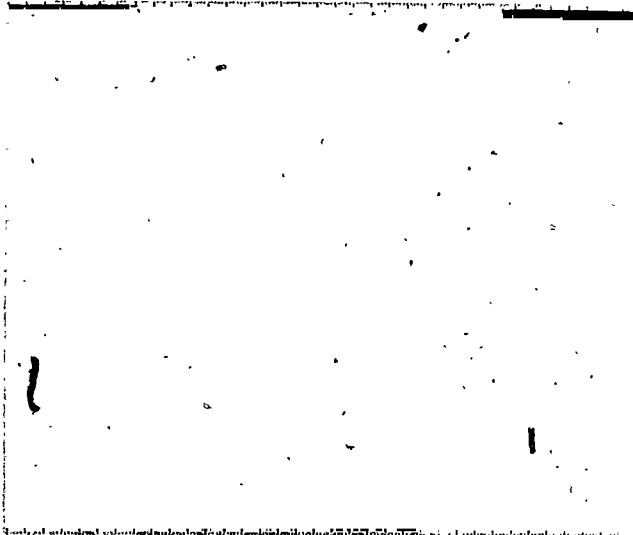
Fig. XXXVIII-1. Wide-angle-camera raster shift. More distinct marks are reseau locations measured during preflight bench calibrations. Less distinct marks are reseau locations of a typical flight picture.

10.×) at four signal levels (data numbers 30, 100, 280, 380), as observed on revolutions 2. 76, 200, and 225.

As a result, it has been possible to remove all remaining geometric distortions in the process of decalibration to an accuracy of 1 pixel.
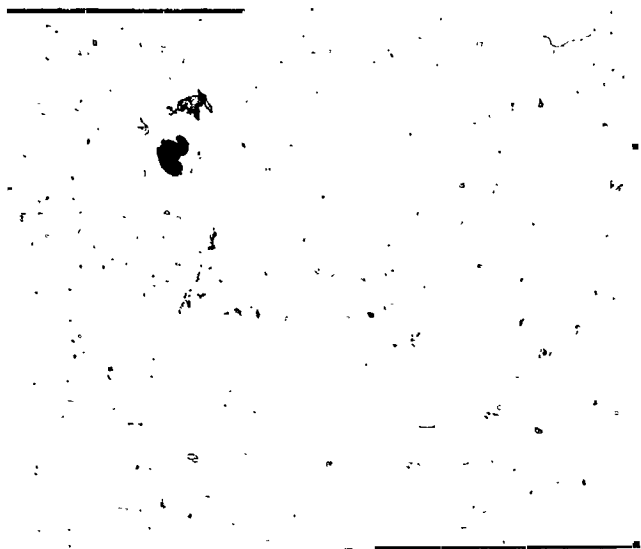
Fig. XXXVIII-2. Narrow-angle-camera raster shift. More distinct marks are reseau locations of a typical inflight picture. Less distinct marks are locations measured during preflight bench calibrations.
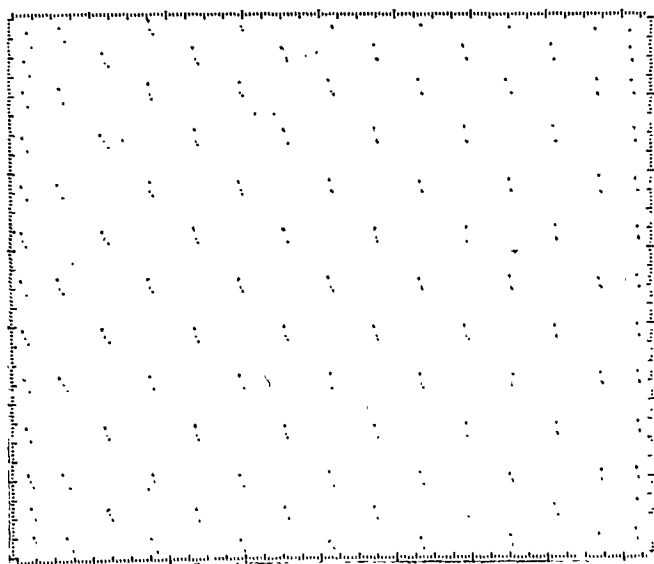
Fig. XXXVIII-3. Reseau locations vs light level for the wide-angle camera. Displacements are exaggerated 10×.
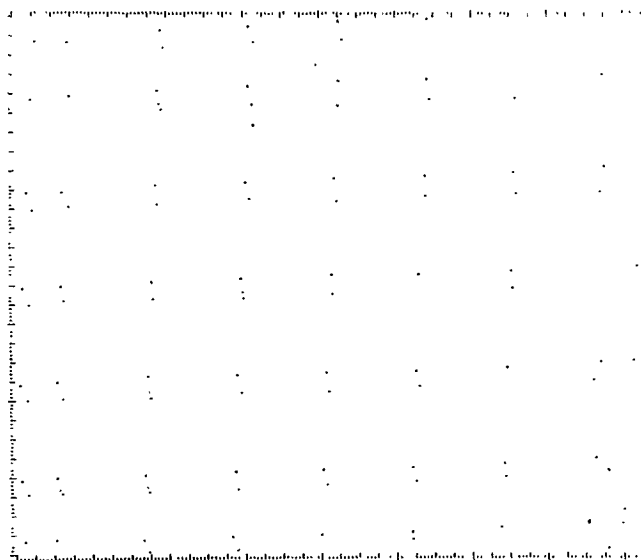
Fig. XXXVIII-4. Reseau locations vs light level for the narrow-angle camera. Displacements are exaggerated 10×.

2. Star Field Verification

The star field photography provided by scan calibrations I and II was also useful in revealing geometric distortions. Star images provide the inverse appearance to a reseau pattern and may be used for low light-level measurement. Unfortu..itely, because of partial image erasure by adjacent readout scanning and convolution effects within the read beam, even faint stars appear asymmetrical and several pixels in size (Ref. XXXVIII-5). A minimum dispersion of 1 pixel exists in the measurement of the separation of the centers of any two star images, and no residual distortion was consequently evident.

An additional geometric distortion is produced by deflection of read beam electrons in the presence of a large target change discontinuity. This phenomenon was especially noticeable for star images well above saturation (+4.0 magnitude), until extended image characteristics became evident (+1.0 magnitude). The asymmetrical appearance of typical star profiles imaged by the narrow-angle camera (Fig. XXXVIII-5) suggests the following vertical bias:

$$Displacement\,(Lines) = (B/B_{saturation})^{1/5}$$

where B = image brightness. As a consequence, residual star images on subsequent pictures were displaced from the original picture location.
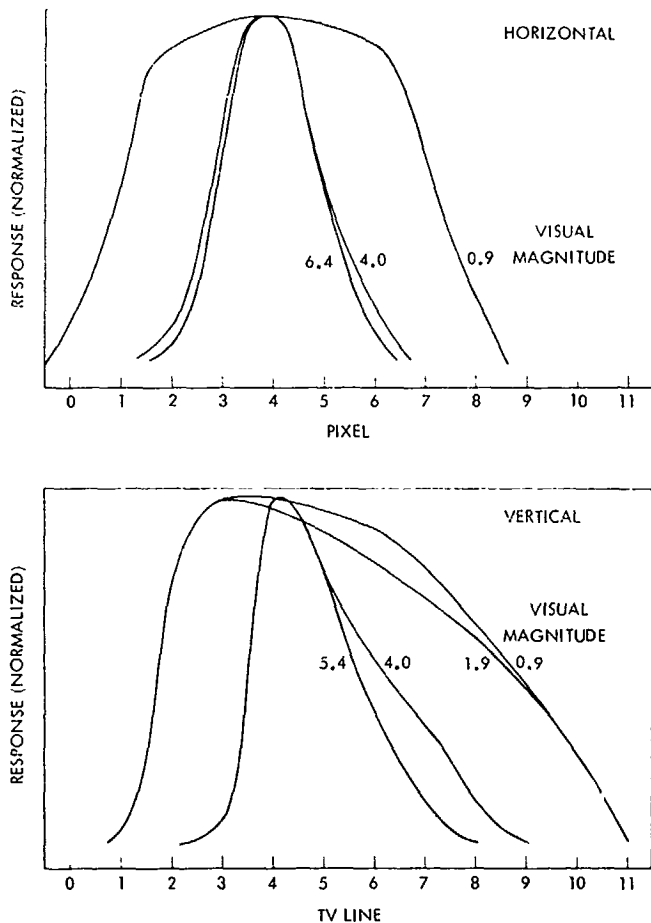
Fig. XXXVIII-5. Wide-angle camera star image profiles.

The establishment of accurate locations within the camera field of view permits the determination of orbit–surface geometry required to rephotograph selected targets. Before entering the Mars gravitational field and following the initial star photography to verify spacecraft trajectory, pointing accuracy was as follows (Ref. XXXVIII-4):

RMS pointing control: 0.486° cone; 0.376° cross cone.

RMS pointing knowledge: 0.153° cone; 0.096 cross cone.

Once in orbit, however, surface feature photography was subject to a combination of effects caused by orbit residuals, Mars rotational period uncertainty, timing constraints, platform stepping increments, and limit cycle. After 6 months of orbital photography, pointing control was about ±0.8° RMS.

B. Photometric Performance

Photometric performance may be described with respect to both consistency with preflight calibration and the accuracy in representing a realistic luminance environment. The ability of the television subsystem to produce a consistent signal output as a function of light level or position within the field of view is defined as the relative light-transfer response. Inflight performance agreement with preflight measurement, therefore, indicates the degree of similarity in transfer curve shape across the field of view or the expectation that a given signal output bears the same relation to input luminance, as measured in preflight tests. Absolute photometry refers to the accuracy with which this signal can be interpreted as source radiance information. Such performance implies frame-to-frame fidelity, knowledge of spectral sensitivity, and a predictable signal-flux efficiency.

1. Relative Light-Transfer Response

Mariner 9 television inflight response appears consistent to within 25% of preflight measurement for the wide-angle camera and to within 15% for the narrow-angle camera over the dynamic range of each system.

Five areas across the field of view of each camera were analyzed (center and four corners) using several photographic sequences. Successive overlapping pictures taken far from periapsis were used to place a feature of constant luminance geometry at these positions. For example, pictures taken in succession on revolutions 119 through 125 show a given surface feature moving diagonally from left to right across the field of view, and on revolutions 250 through 262 from right to left, with little change in viewing geometry. Mars calibration II also provided a constant scene with which to check preflight light-transfer calibration at several light levels.

Figure XXXVIII-6 displays the current best estimate of inflight wide-angle camera response through filter position 2 ($\lambda = 0.610$ μm) and narrow-angle camera (center of field of view). Because of the loss of filter wheel control on revolution 118, a similar set of measurements was made for all filter positions and revealed a lockup in position 5 (polarizing 60°). The lack of temperature calibration for this filter, however, has resulted in decalibration using "bench" data (Fig. XXXVIII-7). It may be seen that the effect of equivalent environmental temperature on a similar filter gives better agreement with observations and suggests that decalibration without temperature data for this filter yields luminosities 29%
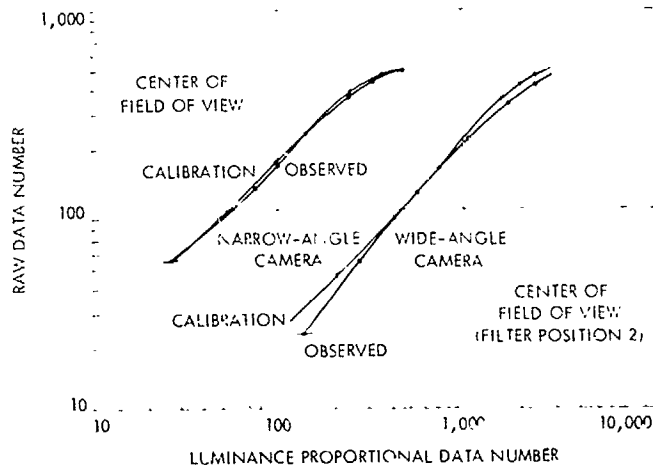
Fig. XXXVIII-6. Light-transfer response of wide-and-narrow-angle cameras.
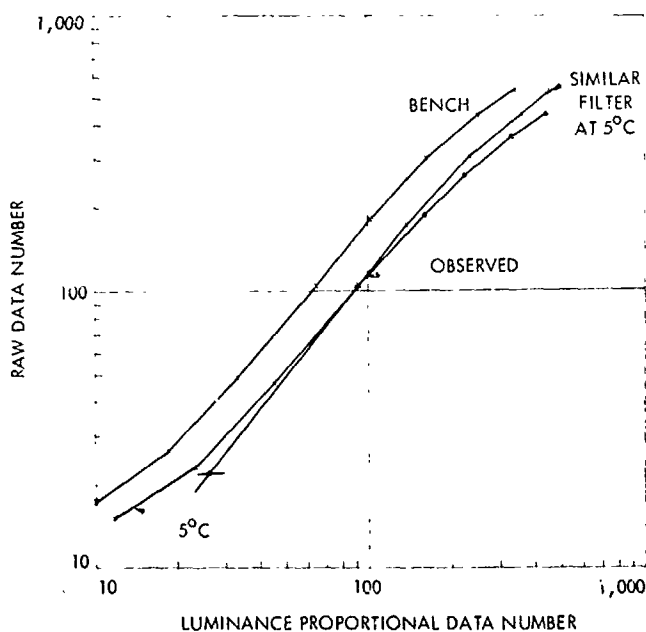
Fig. XXXVIII-7. Light-transfer response of wide-angle camera, filter position 5.

too low. At intermediate signal levels, the response near the corners of pictures taken by this camera has also changed (shading). Generally speaking, the right side of the vidicon appears somewhat less sensitive than the left side. This "wedge-shaped" response may be a nonuniform target charge buildup as a consequence of the typical photographic mode, which always placed the right side of the picture closest to the Martian terminator.

Confirmation of relative photometric performance is provided independently by analysis of a dust speck shadow. Use of preflight light-transfer calibration to convert wide-angle camera data to intensity proportional numbers results in a shadow contrast variation from 4 to 3%. The ratio of apparent contrast to true contrast is a derivative of the function relating the signal to a linear photometric scale. As the apparent contrast is a minimum near mid-scale, the calibration light-transfer curve should be shifted to a greater data number (DN) at high and low raw DN levels.

Star sequences also gave an indication of the camera's consistent light-transfer response performance with light level for point sources (Ref. XXXVIII-5). Figure XXXVIII-8 shows, however, that image motion (December 20 data revealed 3 pixels of smear) and the read beam interaction with small charge distributions produce a large data dispersion, making applicability to Mars data uncertain.

2. Absolute Photometry

The relation of decalibrated signal to luminosity, in addition to being of value to science interpretation, provides verification of exposure times, frame-to-frame photometric consistency, and filter factors.

Absolute photometry requires precise knowledge of all transmitting and responding elements as a function of radiance, wavelength, and temperature. The convolution of many small error sources, e.g., calibration source radiance vs lifetime may produce uncertainties as large as the in situ spacecraft health.
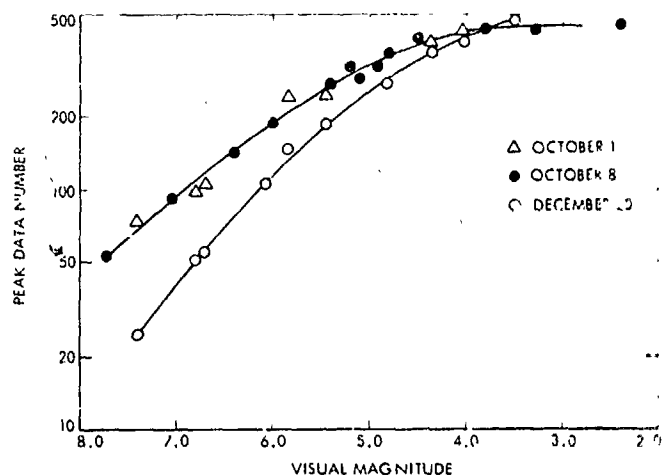
Fig. XXXVIII-8. Maximum amplitude response (6.144 sec) of narrow-angle camera.

Both frame-to-frame signal consistency and repeatability over the three star-photography sequences suggest small operational variance at exposures of 6.144 sec. The data scatter indicates a photon efficiency $[(S/N)^2_{at}/(S/N)^2_n]$ of 4×10^{-4} at mid-scale (fifth magnitude). At the 5%-of-saturation level (7 DN above dark current), limiting magnitudes correspond to $+4.0$ (wide angle) and $+8.6$ (narrow angle).

Although Saturn presents an image larger than stars on narrow-angle pictures, its ring system adds an unknown contribution to the integrated response. Using the average of the two largest image DN yields decalibrated DN/ft-L conversion factor of 1.772 (versus 1.859 predicted). Similar values to $\pm 10\%$ RMS are obtained over the range of 96- to 768-msec shutter speed. However, larger discrepancies may exist at speeds more typical of Mars photography (6 to 24 msec).

Verification of absolute performance using Mars itself implies knowledge of the planet radiance at a specific viewing geometry. This requirement was difficult to satisfy because of the added brightness contributed by the dust storm to what is, at best, a poorly known photometric function. Correcting all the above photometric nonlinearities in the *Mariner* data yields luminosity measurements to within $\pm 11\%$ RMS of the predicted Mars' brightness following revolution 100 at phase angles observable from Earth.

These three measurements suggest consistent camera performance in spite of calibration source differences. Using data presented in this document, *Mariner* 9 photometric measurements of Mars have achieved 15% (1σ) accuracy under limited conditions. These include: optimization of signal strength (200 to 275 DN); location within ± 200 pixels of camera line of sight; use of standard shutter speeds; and nominal operational temperatures (wide-angle camera, 7.2°C; narrow-angle, 10°C).

3. Spectral Response

The relative response differences through each of the medium bandpass filters (filter positions 2, 4, 6 and 8) of the wide-angle camera have been compared with prediction based on telescopic spectral observations of Mars (Ref. XXXVIII-6). A survey of wide-angle orbital pictures through revolution 130 was made to select samples with viewing parameters constant to within a few degrees. The decalibrated data numbers were divided by the camera response to the spectral luminance of a calibration 13-cm (5-in.) light source and normalized to filter position 2 (orange filter) photography. Evaluation of the response using filter positions 3, 5, and 7 (polarizing filters) was less extensive because of lack of inflight photography and sparse calibration data. Only a few polarizing pictures have been taken at viewing geometries comparable to spectral photography. (Table XXXVIII-6 summarizes these results.) Nevertheless, with the excep-

Table XXXVIII-6. Spectral response using similar viewing geometry

Example: Revolution 95									
Picture	Filter	Phase angle, deg	Incidence angle, deg	View angle, deg	Range, km	Shutter speed, msec	Average histogram video	Mode histogram video	Reduced DN average
12	6	63.4	34.8	27.9	3050	48	304	260	132
14	8	63.4	34.5	28.7	2950	48	160	130	140
16	2	63.3	33.9	30.1	2850	48	308	260	165
18	4	63.3	33.4	32.3	2750	48	258	210	85

Response			
Effective wavelength, μm	Filter position/ filter position 2	Observed DN/DN (Fp 2)	Subsystem measurements, DN/DN (Fp 2)
0.545	4	0.82 ± 0.02	0.83
0.477	6	0.92 ± 0.02	0.93
0.414	8	0.45 ± 0.02	0.55
0.565	5	1.28 ± 0.03	1.26
0.565	3	1.35 ± 0.02	1.32
0.565	7	1.275 ± 0.02	1.25

tion of filter position 8, the preflight camera spectral response has been verified to within the observable accuracy (see Table XXXVIII-6). Filter position 8 (violet filter) produced a long-term change in response in the vacuum environment. This observation has been duplicated in calibration tests and appears to be a change in filter transmission at the shortest wavelengths.

4. Shutter Speed

A change in shutter speed will produce an apparent difference in camera sensitivity. Using flight data, it is difficult to differentiate this occurrence from a possible change in vidicon sensitivity. Sequences that involve photography of the same scene under comparable lighting conditions at two or more shutter speeds create two widely different signal levels. Hence, a change in the predicted signal ratio of images photographed at 6 and 12 msec may, in fact, be a consequence of vidicon light-transfer changes.

If a consistent difference is present at all shutter speeds (e.g., ~12 msec), however, the change is most evident at the shorter exposure. Comparison then may be made between a scene photographed at 6 and 12 msec and subsequently rephotographed at lower luminosity such that a 12- and 24-msec picture pair produces the same signal levels. Any change will be a consequence of shutter variation, provided that camera parameters and surface reflectance have remained constant during the interval. A consistent ratio was obtained with either shutter speed combination to ±12%. Previous life testing of the shutter type being used on *Mariner 9* has shown that the expected number of shutter actuations would be more than 150,000 with 50% reliability. Through testing and flight operations, *Mariner 9* television shutter actuations were approximately 42,000 per camera, with 100% reliability.

5. Veiling Glare and Stray Light

Veiling glare in the presence of strong illumination was apparent in several pre-orbital narrow-angle pictures and in early limb pictures (wide angle). However, because optical scattering amounts to only a few percent, images of the limb of Mars at several times saturation intensity were required to produce a measurable loss of contrast with background space.

Narrow-angle-camera veiling glare was measured on a picture selected from pre-orbital photography of the Martian satellites. Figures XXXVIII-9 and XXXVIII-10 show an image of the Martian terminator at 10× satura-
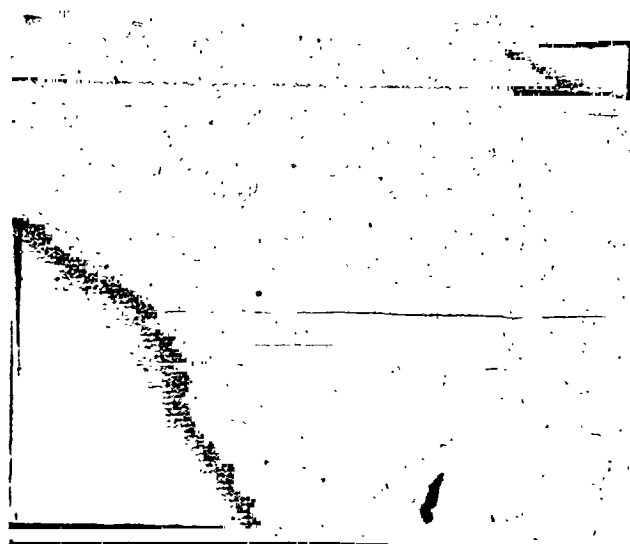
Fig. XXXVIII-9. Veiling glare picture of Mars and Phobos taken by the narrow-angle camera.
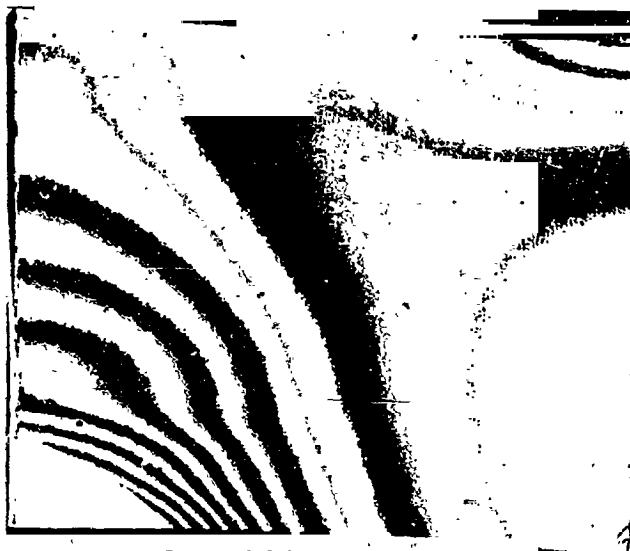
Fig. XXXVIII-10. Narrow-angle veiling glare pictures with brightness contours (16-DN intervals).

tion with adjacent brightness contours at 16-DN intervals. The calculated intensity indicated a maximum glare of 3.0% clearly discernible from atmospheric reflectance.

6. Blooming

Overexposure produces some charge spreading on the inner target surface of most television cameras. Such transfer is minimized in vidicons, however, owing to the high surface resistivity (10^{16} ohm-cm). Preflight camera
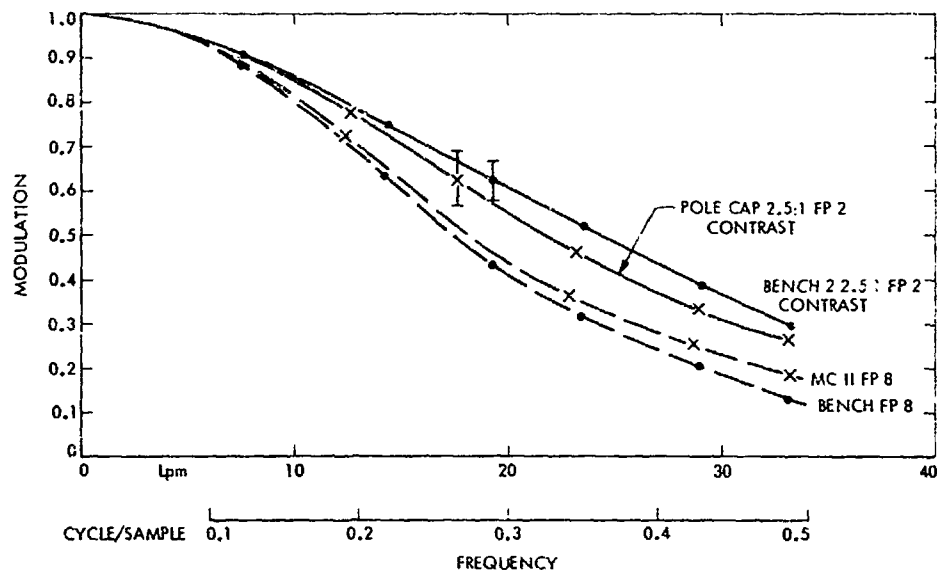
Fig. XXXVIII-11. Modulation-transfer function of wide-angle camera.

measurements indicated that a point source image will increase in size proportional to the one-quarter power of the brightness-to-saturation brightness ratio (Ref. XXXVIII-5). Inflight pictures taken with the narrow-angle camera of both stars (0 to 45× saturation) and Deimos (32× saturation) confirm this prediction.

7. Modulation-Transfer Function

The modulation transfer of each camera was evaluated using Fourier transforms of edge tracings across moderate-and-high-contrast features (wide-angle camera) and point source images (narrow-angle camera).

Response of the wide-angle camera was measured initially with pre-orbital limb profiles on pictures taken at distances such that a 30-km atmosphere would subtend an angle of less than 0.1 pixel. These data were combined with polar-cap-edge traces to yield contrasts more typical of calibration targets. Figure XXXVIII-11 indicates good agreement with bench calibration in both filter positions 2 and 8.

The modulation-transfer function of the narrow-angle camera at intermediate light levels also appears consistent with prediction (Fig. XXXVIII-12). Above mid-scale signal to noise, a loss of image modulation rapidly occurs. This light-level dependency was first observed in bench testing and is apparent in both mapping pictures and star photography. Both sets of measurements indicate, to the accuracy of available data, that no change in either optical or electronic focus has occurred through 14 months of mission operations.
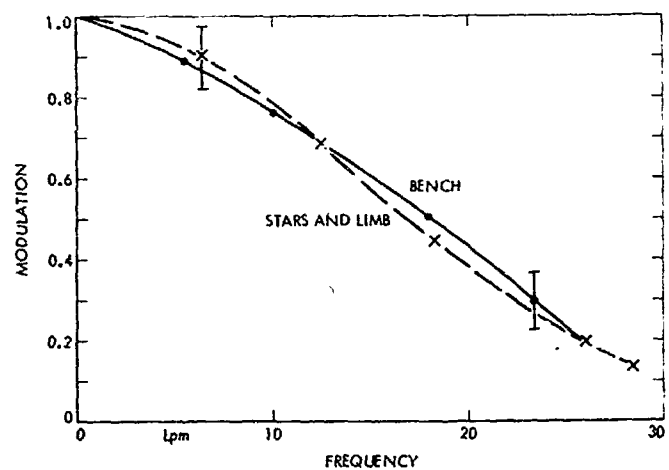
Fig. XXXVIII-12. Modulation-transfer function of narrow-angle camera.

C. Electronic Performance

1. Dark Current

The vidicons were closely monitored during the mission; small variations in dark current, observed through the use of the average video telemetry, have been noted along with the cathode current telemetry data. Visual inspection of typical picture DN listings showing black space reveals a background DN level of 14 (wide angle) and 17 (narrow angle). However, the dark currents decreased some by the end of the mission (wide-angle camera = 27.1%; narrow-angle camera = 31.1%).

2. Noise

Computed power spectra show no significant deviations from preflight camera performance during the standard mission. Wide- and narrow-angle camera spectra in Figs. XXXVIII-13 and XXXVIII-14 show no new coherent noise components when compared with preflight calibration. Random noise indicated by power spectra and black space photography (variations within the dark current) was 0.6 DN RMS (wide-angle camera) and 1.2 DN RMS (narrow-angle camera). Typical contrast-enhanced flight pictures reveal coherent noise (vertical bars) with amplitude 2 DN RMS. This source is a consequence of a beat between the carrier frequency (28.8 kHz) with a harmonic of the spacecraft power frequency (2.4 kHz). Occasionally, an interference at approximately 3-sec intervals is noticeable during the television readout (0.05 cycles/sample; 5- to 30-DN amplitude). This noise is produced by mechanical vibrations of the ultraviolet spectrometer (UVS) mirror, is transmitted to the television subsystem through the scan platform, and results in microphonic noise occurring in the vidicon during periods of UVS observation. This interference was the only new noise component detected following launch.

3. Cathode Current

Cathode currents of the wide- and narrow-angle camera vidicons exhibited a slow, but steady, decline (18 namp/day) through most of the mission. The total decrease in both vidicon cathode currents was 21.5% for the wide-angle camera and 25.4% for the narrow-angle camera (erase current value). This decrease was not detrimental to the image quality because of the 400% over-beaming that was provided in the subsystem to minimize the effects of decreases in cathode emission.

The continuing decrease in cathode emission could have determined the lifetime of the cameras. However, at the observed rate of decrease, operation was possible for an additional 1.9 years beyond the extended mission.

D. Conclusions

Based on limited data, the *Mariner* 9 performance appears consistent throughout its mission. Several corrections have been provided by inflight verification sequences. A change in photometric response, which will
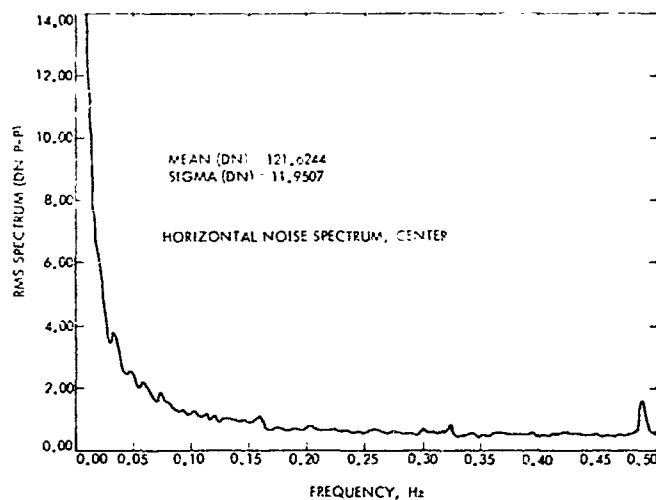
Fig. XXXVIII-13. Noise power spectra of wide-angle camera.
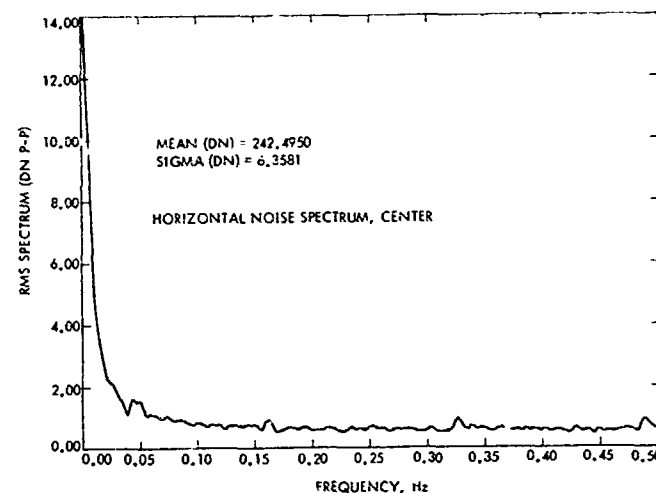
Fig. XXXVIII-14. Noise power spectra of narrow-angle camera.

impair precise photometric analysis, has been observed. Hence, only qualified photometric measurement appears feasible under limited conditions. Conversely, certain geometric and electronic parameters appear both measurable and congruent with preflight prediction. The role of inflight verification has been emphasized by these data to assess the in situ camera health and to promote efficient data analysis and interpretation. Future missions of extended duration should consequently devote a significant fraction of mission photography to verify critical imaging parameters.

References

XXXVIII-1. Masursky, H., Batson, R., Borgeson, W., Carr, M., McCauley, J., Milton, D., Wildey, R., Wilhelms, D., Murray, B., Horowitz, N., Leighton, R., Sharp, R., Thompson, W., Briggs, G., Chandeysson, P., Shipley, E., Sagan, C., Pollack, J. Lederberg, J., Levinthal, E., Hartmann, W., McCord, T., Smith, B., Davies, M., de Vaucouleurs. G., and Leovy, C., "Television Experiment for Mariner Mars 1971," *Icarus*, Vol. 12, p. 10, 1970.

XXXVIII-2. Danielson, G. E., and Montgomery, D. R., "Calibration of the Mariner Mars 1969 Television Cameras," *J. Geophys. Res.*, Vol. 76, p. 418, 1971.

XXXVIII-3. Snyder, L. M., *Mariner 9 TV Subsystem Calibration Report*, Internal Document 610-202, Jet Propulsion Laboratory, Pasadena, Calif., 1971.

XXXVIII-4. Havens, W. F., *Scan Pointing Calibration for the Mariner Mars 1971 Spacecraft*, Technical Memorandum 33-556, Jet Propulsion Laboratory, Pasadena, Calif., 1972.

XXXVIII-5. Thorpe, T. E., "Mariner 9 Star Photography," *Appl. Opt.*, Vol. 12, p. 359, 1973.

XXXVIII-6. McCord, T. B., and Westphal, J. A., "Mars: Narrow Band Photometry, From 0.3 to 2.5 Microns, of Surface Regions During the 1969 Apparition." *Astrophys. J.*, Vol. 168, August 1971.

Acknowledgments

XXXIX. Martian Surface Coordinates

Merton E. Davies
The Rand Corporation, Santa Monica, California 90401

David W. G. Arthur
U.S. Geological Survey, Flagstaff, Arizona 86001

Astronomers have long studied the surface markings of Mars and have used them to establish coordinate systems of the planet's surface. A comprehensive effort to combine the results of all of the telescopic observations into a single network of positions has recently been completed by de Vaucouleurs (Refs. XXXIX-1 and XXXIX-2). In contrast to the classical nets that were based on albedo markings, the *Mariner 6* and 7 flyby missions offered the first opportunity to establish a control net based on surface topography. This work was reported by Davies and Berg (Ref. XXXIX-3) and Davies (Ref. XXXIX-4). Only 21 of the near-encounter pictures of Mars were in the resolution regime best suited for the identification and measurement of control points. These few pictures covered a very small area, so low-resolution, far-encounter pictures were used to build the control net over most of the Martian surface.

The resolution of the pictures from the *Mariner 9* mission determines the distribution of the control points, as well as the gaps in the planet-wide control net. Work on this net began early in 1972 and the net has continued to expand since that time. Progress was first reported in August 1972 (Ref. XXXIX-5) and was updated in November 1972.

The *Mariner 9* orbit had a period of about 11.97 hr, an inclination of 65°, and a periapsis altitude of 1387 km, which was raised to 1650 km during a trim maneuver on December 30, 1971. Periapsis occurred at a latitude of about 23° south and varied slightly during the life of the mission. Thus, high-resolution pictures (the mapping sequences) were taken from a distance of less than 2000 km from about 65° south to 15° north and from about 3500 km in the south polar region to about 5000 km in the north polar region. Highest priority was assigned to the mapping sequences that were designed to obtain full coverage of the planet using the 50-mm focal-length camera. The characteristics of this camera and the footprint size as a function of distance are given in Table XXXIX-1. Although this is the *Mariner 9* wide-angle camera, its 11° × 14° field would normally be considered narrow-angle. In order to obtain coverage and keep the total number of pictures within reason, it was planned to use pictures taken from distances greater than 3500 km in the computation of the primary control net. In practice, this was not always possible. The secondary control net computations use mapping pictures exclusively.

The *Mariner 9* mission plan called for far-encounter pictures to be taken of the northern hemisphere before

Table XXXIX-1. *Mariner 9* wide-angle television camera

Sensor: slow scan vidicon

Optics: Zeiss Planar, 52.267-mm focal length, f/2 stopped down to f/4

Format: 9.6 mm × 12.5 mm, 700 × 832 pixels
Field of view: 11° × 14°

Normal distance to plane surface, km	Pixel size, km	Footprint, km
2000	0.56	380 × 500
3000	0.84	580 × 750
4000	1.1	770 × 1000
5000	1.4	960 × 1250
6000	1.7	1150 × 1500

insertion into orbit. Pictures of the southern hemisphere were to be taken along the morning terminator early in the orbital mission in order to establish a quick preliminary control net. The dust storm that enveloped Mars at the time *Mariner 9* arrived in mid-November 1971 caused a complete change in the plan. By January 1972, the dust had sufficiently settled to proceed with taking the geodesy sequence series of morning terminator pictures. Since November, however, the terminator had moved relative to the spacecraft's orbit, so it was necessary to take the sequence farther south in the orbit than was originally planned. The consequence is that these pictures are usable from about 70° to about 25° south latitude. The longitude coverage is good except for two gaps at about 90° and 270° due to the loss of data during a snowstorm at the Goldstone antenna.

Because many pictures of the south polar region were taken to monitor changes to the cap, the coverage there is good. The band from 25° south latitude to the equator contains pictures from the mapping sequence only. The sequences in this band, designed for full planetary coverage at maximum resolution, were taken near periapsis along the evening terminator. There is too little overlap between frames in these mapping sequences and the area covered per frame is too small for triangulation, thus requiring many frames for full coverage and resulting in gaps in the control net. For control purposes, special pictures were taken of the band from the equator to 20° north. North of 20° north, mapping pictures are used for control because the spacecraft was far from periapsis when they were taken.

During the next few years, many new charts and maps of Mars will be made, including large-scale maps that portray relatively small regions of the Martian surface containing few or no control points from the planet-wide

net. A secondary control net, consistent with the primary net, but with control points more closely spaced, will then have to be established in the area of interest. Although secondary control has not been required yet, the method of photogrammetric reduction has been prepared and tested.

After discussing the photogrammetric equations and the computational method used to establish the planetwide control net and the secondary net, the camera stations and the assumed physical properties of Mars are considered. Subsequent paragraphs contain a description of the control points, their measurements, and a discussion of how distortions are removed. Finally, results of the computations are given, with tables of coordinates for the control points.

A. Reduction Methods

1. The Primary Control Net

Determination of the positions of reference points in the primary network on the surface of Mars is essentially an exercise in multiphotograph stereophotogrammetry, but with important inputs from classical astronomy and the electronic sciences. Following selenodetic practice, the reference points are usually small, well defined craters that are easily bisected and that show relatively small phase effects.

Measurements of the control points are discussed later in this section. The pixel counts are reduced to millimeters, corrected for optical and electronic distortions, and the origin translated to the principal point, thus deriving the observed coordinates x_o, y_o. The focal length of the lens is f.

Stereophotogrammetry is peculiar in that the camera (spacecraft) positions come from the tracking data and are not determined in any way from the photogrammetry. The spacecraft positions could be adjusted for consistency using the photogrammetric data; however, since the camera has a narrow cone angle, the solutions for the spacecraft position as well as orientation would be highly correlated. Thus, it was necessary to hold one fixed, and because the a priori position data appear much better than the angular data, the values provided by the Jet Propulsion Laboratory (JPL) Science Data Team were used without change.

The geometric visualization of the computations is that the rigid perspective cones derived from the (x_o, y_o, f) arrays for each picture are rotated about fixed vertices

and oriented so that each set of corresponding rays meet as nearly as possible in one point. Corresponding rays are those derived from the same Martian surface point. The photogrammetric operation thus produces a scaled model of Mars in the form of an aggregate (X_i, Y_i, Z_i) of coordinated points.

The method of analysis may appear awkward in some ways; however, the coordinate systems are compatible with those used at JPL, permitting easy exchange of data. Also, the method is completely general, permitting a convenient solution for the spin axis of Mars as well as control point coordinates and camera orientation angles.

The computations involve four distinct three-dimensional coordinate systems XYZ, $X'Y'Z'$, $X''Y''Z''$, and $\xi\eta\zeta$. All the XYZ systems are Mars centered, but the first of these, XYZ, rotates solidly with Mars and is valid for fixed Martian surface coordinates. For this system we can write

$$X = R \cos \phi \cos (360° - \lambda)*$$ (1)

$$Y = R \cos \phi \sin (360° - \lambda)$$ (2)

$$Z = R \sin \phi$$ (3)

where R is the length of the areocentric radius to the surface point in kilometers, ϕ is the latitude of this radius (its inclination to the Mars equatorial plane), and λ is the west areocentric longitude measured from the positive X-axis.

The nonrotating or inertial system $X'Y'Z'$ is such that the X'-axis is directed through the ascending node of the Mars mean equator on the mean ecliptic of 1950.0. The Y'-axis is on the Mars equator.

The inertial system $X''Y''Z''$ has its X''-axis in the plane of the Earth mean equator of 1950.0 through the vernal equinox. The Y''-axis is on the Earth mean equator.

The system $\xi\eta\zeta$ uses the coordinate axes of the camera but applied to Mars surface points. The origin is the spacecraft.

If V is the hour angle of the mean equinox measured from the prime meridian, then the coordinates of a surface

---

*$(360° - \lambda)$ is used instead of λ in order that the coordinate system be right-handed.

point in the $X'Y'Z'$ system are

$$\begin{bmatrix} X' \\ Y' \\ Z' \end{bmatrix} = W \begin{bmatrix} X \\ Y \\ Z \end{bmatrix}$$ (4)

where

$$W = \begin{bmatrix} \cos V & -\sin V & 0 \\ \sin V & \cos V & 0 \\ 0 & 0 & 1 \end{bmatrix}$$ (5)

Now let M be the 3×3 orthogonal matrix representing the rotation from the Mars-centered inertial system $X'Y'Z'$ oriented on the Mars equator to the second Mars-centered inertial system $X''Y''Z''$ oriented on the 1950.0 Earth equator. Then

$$\begin{bmatrix} X'' \\ Y'' \\ Z'' \end{bmatrix} = M \begin{bmatrix} X' \\ Y' \\ Z' \end{bmatrix} = MW \begin{bmatrix} X \\ Y \\ Z \end{bmatrix}$$ (6)

As the spacecraft positions are S_x, S_y, S_z in the $X''Y''Z''$ system, the coordinates of the surface point with the spacecraft as origin are

$$\begin{bmatrix} X'' \\ Y'' \\ Z'' \end{bmatrix} - \begin{bmatrix} S_x \\ S_y \\ S_z \end{bmatrix}$$

and if the 3×3 orthogonal matrix C represents the rotation from the $X''Y''Z''$ system to the photographic system, then we have

$$\begin{bmatrix} \xi \\ \eta \\ \zeta \end{bmatrix} = C \begin{bmatrix} X'' \\ Y'' \\ Z'' \end{bmatrix} - C \begin{bmatrix} S_x \\ S_y \\ S_z \end{bmatrix}$$

$$= CMW \begin{bmatrix} R \cos \phi \cos (360° - \lambda) \\ R \cos \phi \sin (360° - \lambda) \\ R \sin \phi \end{bmatrix} - C \begin{bmatrix} S_x \\ S_y \\ S_z \end{bmatrix}$$ (7)

where (ξ, η, ζ) are the coordinates of the surface point in the photographic system with the spacecraft as origin. Now,

$$\frac{x}{f} = \frac{\xi}{\zeta}, \quad \frac{y}{f} = \frac{\eta}{\zeta}$$

where f is the calibrated principal distance. Thus

$$x_c = \frac{\xi f}{\zeta}, \quad y_c = \frac{\eta f}{\zeta}$$ (8)

The subscript c emphasizes that x_c and y_c, derived in this way from assumed R, ϕ, λ, are *computed* values as distinct from the observed values x_o, y_o.

Whereas the computation of x and y from R, ϕ, λ is direct, the reverse computation, which is what interests us, involves the solution of transcendental equations. The solution given in this section is the usual method of iteration in which discrepancies are computed rigorously using Equations (7) and (8). These are then used in the solution of approximate linear equations to compute the first-order corrections to the unknown parameters. For a point i imaged on picture j, the linear observation equations are

$$\sum_i \frac{\partial x_{ij}}{\partial P_i} \cdot \Delta P_i + \sum_k \frac{\partial x_{ij}}{\partial P_{jk}} \cdot \Delta P_{jk} = (x_o - x_c)_{ij} \qquad (9)$$

$$\sum_i \frac{\partial y_{ij}}{\partial P_i} \cdot \Delta P_i + \sum_k \frac{\partial y_{ij}}{\partial P_{jk}} \cdot \Delta P_{jk} = (y_o - y_c)_{ij} \qquad (10)$$

in which the P_i are the parameters defining the position of i, and the P_{jk} are the parameters ($k = 1, 2, 3$) defining the orthogonal matrix C_j. The subscripts o and c indicate observed and computed values, and the subscript ij indicates point i on picture j.

The matrix C is derived from the tracking data plus the telemetered clock and cone angles. However, it does not always have a precision commensurate with the other data and hence, in general, is merely used as a starting value in the iterations.

The photogrammetric method is general and, in principle, can be used to solve for almost any of the parameters. As the *Mariner* television pictures are poor for photogrammetric use and as they were frequently taken at non-optimum times for this purpose, it is desirable to minimize the number of variables in the solution. Thus, the camera stations (S_x, S_y, S_z) are taken from the Supplementary Experiment Data Record (SEDR), which is published by the Science Data Team at JPL. The accuracy of these coordinates of the spacecraft position is expected to be about 3 km in each direction. In all computations, the three angles that define the camera orientation matrix C are treated as variables and are part of the solution. The latitude and longitude of the control points are always variables; however, the vector radius R has usually been derived from the radio occultation experiment (Ref. XXXIX-6). The only exception is in the region of Nix Olympica where there was a deliberate effort to determine the altitude of the mountain photogrammetrically.

Because of the narrow cone angle of the camera, there usually are not adequate parallactic angles between successive exposures to obtain planetary radii measurements from the photogrammetric solution. Thus, they were principally derived from the radio occultation radii measurements.

The radius of each control point is the sum of the radius of the reference spheroid at the point's latitude and longitude and the elevation above the reference spheroid linearly interpolated from Table XXXIX-2. The elevations in Table XXXIX-2 are interpolated from the elevations at the occultation points given by Kliore et al. in Ref. XXXIX-6. In this table the elevation is assumed to be zero at the north pole and south of 65° south latitude, as there are no measurements reported south of 40° south.

Thus, each picture contributes three unknowns—the parameters of C; each point contributes two unknowns—ϕ and λ; and each observed image contributes two equations. Generally, three iterations are sufficient to attain stationary state in the solution.

The least-squares solution, which minimizes discrepancies in the picture plane, is general and does not distinguish between observations, unknown parameters, and a priori knowns. All become unknowns with appropriate weights. This gives the program considerable flexibility in regard to holding values fixed or permitting them to vary.

One of the principal problems is the size of the equation set to be solved. Because it is not feasible to attempt the simultaneous solution for the coordinates of all vertices of the primary triangulation, we have had to work in blocks Adjustments between blocks have been performed using common points and holding one block fixed in each adjustment. The procedure is far from perfect, but unfortunately the optimum procedure does not lie in the realm of practical economics.

2. The Secondary Control Net

The Mars secondary control net (triangulation), like its terrestrial counterparts, is intended to fill the interstices of the primary net with a much denser network of controls. Again, like its terrestrial parallels, the Mars secondary net is accomplished with simpler means, and its reductions are much less expensive than those of the primary net.

Table XXXIX-2. Surface elevations (in kilometers) above reference spheroid at 10° intervals (areocentric); derived from occultation experiment radii

West Longitude

Latitude	170	160	150	140	130	120	110	100	90	80	70	60	50	40	30	20	10	0
90	0.0	0.0	0.0	0.0	0.0	0.0	0.0	0.0	0.0	0.0	0.0	0.0	0.0	0.0	0.0	0.0	0.0	0.0
80	-1.01	-1.07	-0.86	-0.74	-0.69	-0.06	-0.51	-0.54	-0.53	-0.78	-0.87	-1.07	-1.19	-1.12	-1.16	-1.07	-0.89	-0.89
70	-2.02	-2.13	-1.71	-1.47	-1.39	-0.12	-1.03	-1.08	-1.05	-1.55	-1.74	-2.15	-2.38	-2.23	-2.32	-2.15	-1.78	-1.78
60	-2.39	-1.91	-1.51	-1.37	-0.92	-1.18	-0.91	-0.91	-1.07	-0.92	-1.32	-2.04	-2.82	-2.95	-3.03	-2.83	-2.36	-2.05
50	-2.09	-1.75	-1.61	-1.47	-0.12	0.26	0.38	0.23	0.19	0.58	-0.51	-0.92	-1.63	-2.12	-2.37	-2.47	-1.83	-1.59
40	-1.77	-1.81	-1.70	-1.59	0.68	1.77	1.83	1.68	1.62	1.76	0.34	-0.27	-0.67	-1.53	-1.79	-1.47	-1.31	-1.15
30	-1.72	-1.92	-0.14	0.32	1.43	3.29	3.29	3.14	2.88	2.94	1.19	0.39	0.29	-0.94	-1.44	-0.87	-1.11	-0.69
20	-1.73	-1.96	0.43	1.14	3.61	4.22	4.69	4.16	4.19	3.32	2.82	1.99	0.56	-0.38	-0.68	-0.36	-1.01	-0.23
10	-0.74	-0.53	0.24	1.97	4.45	5.32	6.14	5.61	5.44	4.25	3.65	2.70	1.56	1.07	-0.09	-0.15	-0.38	-0.23
0	0.68	0.38	1.54	3.27	5.29	6.42	7.60	7.06	6.70	5.18	4.48	3.41	2.56	1.97	0.85	0.44	0.25	1.05
-10	1.59	1.71	2.67	4.38	5.28	7.52	9.05	8.51	7.94	6.07	4.68	4.27	3.35	2.24	1.19	1.07	0.99	1.82
-20	3.30	3.04	3.79	4.56	6.60	8.48	8.78	9.06	8.24	6.17	5.61	4.24	3.28	2.42	1.76	1.50	1.80	2.58
-30	3.21	2.99	4.38	4.13	6.63	6.66	7.54	9.37	8.46	6.67	6.60	4.89	3.30	2.79	1.98	2.55	2.60	2.55
-40	2.29	2.14	2.11	5.14	4.12	5.92	6.41	5.64	6.76	5.21	4.35	3.52	2.36	1.99	1.42	1.82	2.05	1.82
-50	1.37	1.48	1.27	3.08	2.47	3.55	3.85	3.39	4.05	3.13	2.61	2.11	1.41	1.19	1.09	1.09	1.47	1.09
-60	0.46	0.49	0.42	1.03	0.82	1.19	1.20	1.13	1.35	1.04	0.87	0.70	0.47	0.40	0.28	0.36	0.29	0.36
-70	0.0	0.0	0.0	0.0	0.0	0.0	0.0	0.0	0.0	0.0	0.0	0.0	0.0	0.0	0.0	0.0	0.0	0.0
-80	0.0	0.0	0.0	0.0	0.0	0.0	0.0	0.0	0.0	0.0	0.0	0.0	0.0	0.0	0.0	0.0	0.0	0.0
-90	0.0	0.0	0.0	0.0	0.0	0.0	0.0	0.0	0.0	0.0	0.0	0.0	0.0	0.0	0.0	0.0	0.0	0.0

West Longitude

Latitude	350	340	330	320	310	300	290	280	270	260	250	240	230	220	210	200	190	180
90	0.0	0.0	0.0	0.0	0.0	0.0	0.0	0.0	0.0	0.0	0.0	0.0	0.0	0.0	0.0	0.0	0.0	0.0
80	-0.94	-0.84	-0.69	-0.79	-0.71	-0.31	-0.26	-0.51	-0.64	-0.65	-0.58	-0.70	-0.84	-1.03	-1.34	-1.03	-0.96	-0.97
70	-1.88	-1.67	-1.38	-1.58	-1.42	-0.62	-0.52	-1.21	-1.48	-1.30	-1.16	-1.41	-1.72	-2.07	-2.68	-2.06	-1.92	-1.95
60	-0.57	-1.74	-0.92	-1.36	-1.46	-1.34	-1.50	-1.50	-1.52	-1.55	-1.72	-1.86	-1.54	-1.84	-2.00	-2.14	-2.20	-2.15
50	-0.24	-1.11	-0.30	-0.58	-0.64	-0.76	-0.73	-0.98	-0.74	-1.09	-1.44	-1.59	-1.96	-1.80	-1.46	-1.77	-1.46	-1.65
43	-0.75	-1.11	-0.38	-0.04	0.19	0.06	0.11	-0.15	0.17	0.09	-0.58	-0.77	-0.94	-1.46	-1.16	-1.55	-1.46	-1.44
30	-0.12	0.78	1.18	0.65	0.48	0.89	0.94	0.68	1.65	1.33	0.32	0.21	0.45	1.12	-0.07	-1.27	-1.59	-1.43
20	0.51	1.36	1.98	1.66	1.20	1.78	1.61	2.51	1.73	2.17	1.18	0.76	0.04	0.81	-0.72	-1.07	-1.42	-1.40
10	1.27	2.46	2.60	2.49	1.92	2.59	2.44	3.31	2.71	3.00	2.04	1.74	0.37	0.46	-0.75	-0.88	-1.24	-1.36
0	2.12	2.94	3.17	2.72	2.71	3.41	3.26	4.10	3.69	3.84	2.90	2.71	2.26	0.12	0.05	-0.32	-0.32	-0.12
-10	3.00	3.43	4.08	3.72	3.27	4.22	4.09	4.90	4.57	4.53	2.44	3.36	4.04	1.50	1.50	1.97	1.98	1.14
-20	3.91	4.33	4.58	3.98	3.79	2.55	2.10	2.95	2.96	4.03	3.69	3.67	4.19	2.58	2.70	3.14	3.19	2.57
-30	3.15	3.46	3.51	4.22	0.03	-1.28	-1.47	-0.09	1.03	2.39	3.58	3.96	2.99	3.75	2.32	3.82	3.25	1.84
-40	2.25	2.47	2.51	3.62	-0.96	-3.38	-3.03	-1.17	0.20	1.53	2.65	2.83	1.79	2.68	2.73	2.32	2.32	1.84
-50	1.35	1.48	1.50	2.17	-0.57	-2.03	-1.82	-0.70	0.12	0.92	1.59	1.70	0.60	1.61	1.39	1.64	1.39	1.10
-60	0.45	0.49	0.50	0.72	-0.19	-0.68	-0.61	-0.23	0.04	0.31	0.53	0.57	0.60	0.54	0.46	0.55	0.46	0.37
-70	0.0	0.0	0.0	0.0	0.0	0.0	0.0	0.0	0.0	0.0	0.0	0.0	0.0	0.0	0.0	0.0	0.0	0.0
-80	0.0	0.0	0.0	0.0	0.0	0.0	0.0	0.0	0.0	0.0	0.0	0.0	0.0	0.0	0.0	0.0	0.0	0.0
-90	0.0	0.0	0.0	0.0	0.0	0.0	0.0	0.0	0.0	0.0	0.0	0.0	0.0	0.0	0.0	0.0	0.0	0.0

The primary network involves three unknowns per picture and two unknowns for each point fixed. In contrast, the secondary net determination involves four unknowns[1] per photograph, but no additional unknowns for points. In addition, because of its subsidiary and dependent nature, reduction and adjustment of the secondary net can be split into blocks, thus bringing the computation problem down to a manageable size.

The standard block size has been set up as 40 pictures (160 unknowns). Each USGS 1:5,0' 0,000 Mars chart will contain four or more blocks.

The materials used in the primary and secondary triangulations are substantially different. Whereas uncorrected pictures, frequently small-scale, were used in the primary work, with pixel counts to establish positions in the images, the secondary net is based on the use of rectified pictures, which are measured in ordinary two-coordinate comparators. The rectified pictures are the result of extensive processing at the Image Processing Laboratory (IPL) of the Jet Propulsion Laboratory. The method of producing the rectified pictures has been reported by Gillespie and Soha in Ref. XXXIX-7, and the programs and the parameters used in the *Mariner 9* mission have been discussed by Rofer.[2] The pictures are enhanced, corrected for electronic distortion, mathematically transformed into map fragments according to definite map projection formulas, and finally stored in this form on magnetic tapes. They are then converted into actual negatives with the Optronics Photowrite of the Center of Astrogeology, U. S. Geological Survey, Flagstaff, Arizona.

Although the Optronics equipment reproduces precisely what is on the tape, our measuring routines are intended to control errors arising from these imperfections that must occur in practice. Six marginal marks with known pixel counts in x and y are always included in the measures. Thus, all measurements can always be converted into pixel counts with fair precision.

As our measurements are on rectified pictures that are regarded as map fragments, it should be clear that the secondary triangulation is performed in the map plane. This practice is not at all unusual in the major geodetic establishments. The theory of the adjustment is very simple. Each mosaic element, regarded as a map fragment, is shifted, rotated, and dilated in such a manner

that the discrepancies in x and y at the tie points are minimized. These points are generally very small craters, but we have also used angles in shadows and ridges. Even with these angles it is frequently impossible to find common points between adjacent pictures, so that the fixation routes become somewhat dendritic. An adjustment such as the above can be represented by the general transformation of rectangular coordinates in two dimensions.

$$X = px - qy + a$$

$$Y = py + qx + b$$

where (x, y) is a position on the mosaic element and (X, Y) the corresponding map position. The above become the observation equations for control points. For a tie point i on pictures j, k, the observation equations are

$$p_j x_{ij} - q_j y_{ij} + a_j - p_k x_{ik} + q_k y_{ij} - a_k = 0$$

$$p_j y_{ij} + q_j x_{ij} + b_j - p_k y_{ik} - q_k x_{ik} - b_k = 0$$

The normals are formed and solved by the usual methods. Residuals are computed in order to monitor quality. As already noted, the programs for the USGS IBM 360/65 computer can handle 40 pictures in one adjustment. The 1:5,000,000 scale chart may contain at least twice this number of pictures, so subsidiary adjustments will generally be necessary to adjust the blocks to consistency. Figure XXXIX-1 is a sample layout of the secondary net for one of these charts.

Because most of the tie points are small and possibly elusive as to identity, the measures and reductions also carry one distinct and well defined crater for each picture, placed as nearly as possible at the center of the picture. These are the secondary controls. At this point it would be dangerous to predict their quality, but their absolute precision should not be appreciably inferior to those of the primary points, and their relative precision, the local positional consistency, should be better.

B. *Mariner 9* Control Net Parameters

A specific set of constants defining the areographic coordinate systems has been adopted by the *Mariner 9* Geodesy/Cartography Group of the Television Team, and these values are used for all *Mariner 9* cartographic products. This coordinate system, its derivation, and its rationale are discussed by de Vaucouleurs et al. in Ref.

---

[1]These unknowns are the coefficients of the general two-dimensional transformation of rectangular coordinates.

[2]Unpublished data, 1972.
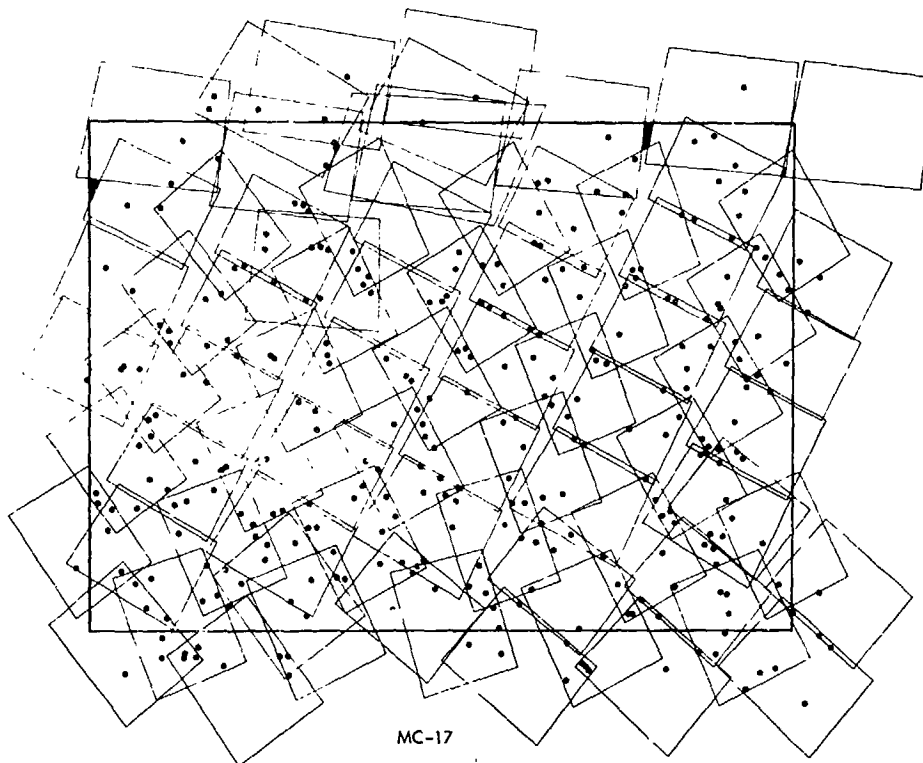
Fig. XXXIX-1. Sample layout of secondary control net for one Mars chart.

XXXIX-8, and in Section XXXX of this Report, and the spin axis, prime meridian, and reference spheroid for the maps are defined. These are used in the control net computations and provide the surface feature coordinates to the cartographers in a usable form.

Using the notation of Sturms (Ref. XXXIX-9), with T as the time in Julian centuries from the epoch 1950, January 1.0, E.T. (Julian Date 2433282.5), the right ascension and declination of the Martian pole are:

$$\alpha_{50} = 317°32 - 0.1011T$$

$$\delta_{50} = 52°68 - 0.0570T$$

The matrix M, which relates the Mars-equatorial coordinate system to the 1950.0 Earth-equatorial coordinate system on January 1.0, 1971 (*Mariner 9*), thus has the numerical value

$$M = \begin{bmatrix} -0.09879443 & 0.88973139 & 0.44566546 \\ -0.90538578 & 0.10547699 & -0.41127994 \\ -0.41293612 & -0.44413134 & 0.79512962 \end{bmatrix}$$

The prime meridian is now defined as passing through the center of the crater, provisionally designated Airy-0, that lies in the large crater provisionally called Airy. Airy-0 is seen on the narrow-angle frame number 533-3 (MTVS 4296-118, DAS 13165361; the frame number refers to the third frame taken on revolution 533). The control net position, particularly the position of Airy-0, must now be used to adjust the added constant in the angle V which is measured from the Mars vernal equinox to the Mars prime meridian along the equator. Thus, the adjusted value of V is

$$V = 148°68 + 350°891962 \quad (\text{JD} - 2433282.5)$$

The computations are performed entirely in terms of areocentric coordinates, that is, in terms of the latitude ϕ, the longitude λ, and the length R of the radius from the center of Mars through the point. All *Mariner 9* map products will use areographic coordinates in which the latitude ϕ' of a point is defined as the angle between the equatorial plane and the normal to the reference spheroid at the point. These planetographic coordinates are appropriate when the local vertical is used as a reference direc-

tion, such as on the surface of Earth, and they will therefore be relevant to the operation of landers and rovers on Mars. The adopted reference spheroid has an equatorial radius a of 3393.4 km and a polar radius c of 3375.8 km.[3] If a point lies on the spheroid, the areocentric and areographic latitudes are related by

$$\tan \phi = \left(\frac{c}{a}\right)^2 \tan \phi'$$

C. The Control Points

The control points are chosen on the basis of several criteria. The point must be uniquely related to a topographic feature, and often it is defined as the center of a small crater. It must be a point on the solid surface; care must be taken to avoid using points that are associated with clouds or ice, as they might be difficult to find in the future. Each point must be found on at least two pictures and, if possible, more. Each picture in the net must contain more than two points. Thus, the points must be close together when the picture covers a small area, and the craters can then be small because the resolution is good. On the other hand, a large number of frames must be used to cover a specific area. Thus, the planet-wide density of control points reflects the surface coverage of individual frames; this effect is seen in Fig. XXXIX-2, which shows the locations of all points of the primary net. In the future, effort will be made to reduce the size of the gaps by adding more points and pictures to the net.

To use the control net, it is necessary to identify the control point on the pictures and then refer to its coordinates in the tables given in the next part of this section. As the preliminary net is derived from several hundred frames, it is not practical to publish all of them with the points identified. However, most of the points have been located on a series of 1:5,000,000 uncontrolled photomosaics compiled by the U. S. Geological Survey and are seen in Figs. XXXIX-3 through XXXIX-31. The number of points not identified on these maps are given in Table XXXIX-3.

---

[3]These values of a and c were used in the reduction of the *Mariner* 6 and 7 pictures (Ref. XXXIX-4); at a meeting of the Geodesy/ Cartography Group on March 28, 1972, it was decided that the same values should be used in the reduction of the *Mariner* 9 pictures after discussions of the new data available regarding the shape of the planet (Ref. XXXIX-8; also see Section XXXX of this Report).

Table XXXIX-3. Control points not located on the USGS mosaics

0	761	1394	1598
27	762	1395	1599
187	766	1402	1600
192	813	1403	1602
196	863	1405	1605
197	865	1408	1608
234	891	1424	1611
236	938	1425	1612
243	946	1455	1614
246	948	1461	1616
271	949	1462	1617
276	950	1469	1618
279	951	1470	1619
306	954	1471	1620
316	957	1472	1621
335	959	1473	1622
338	963	1490	1623
358	977	1508	1624
368	1025	1514	1634
401	1026	1532	1635
403	1028	1533	1636
433	1039	1534	1640
476	1040	1535	1641
479	1053	1536	1646
481	1200	1537	1648
484	1240	1539	1649
485	1244	1545	1651
486	1268	1565	1652
494	1278	1569	1653
496	1285	1571	1654
498	1289	1573	1655
595	1291	1574	1678
615	1300	1577	
645	1308	1578	
654	1328	1580	
699	1329	1581	
701	1330	1582	
703	1340	1583	
704	1346	1586	
706	1356	1587	
708	1357	1591	
758	1383	1595	
757	1387	1596	
760	1392	1597	
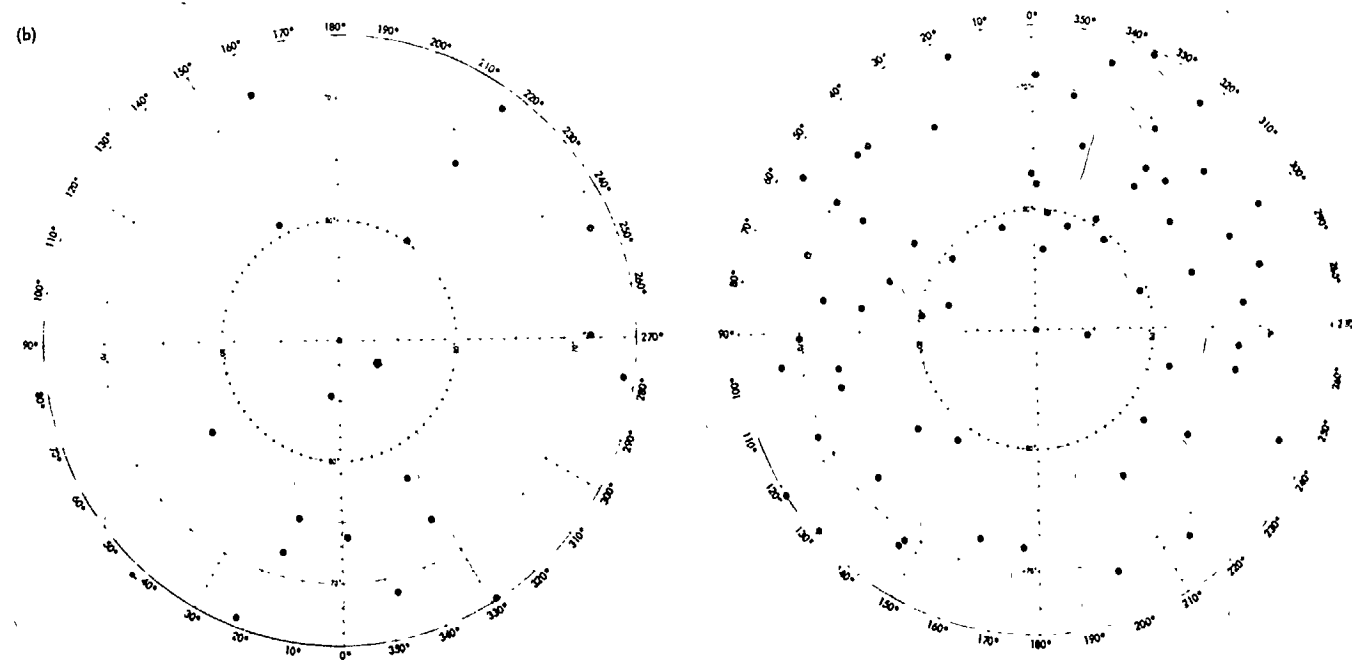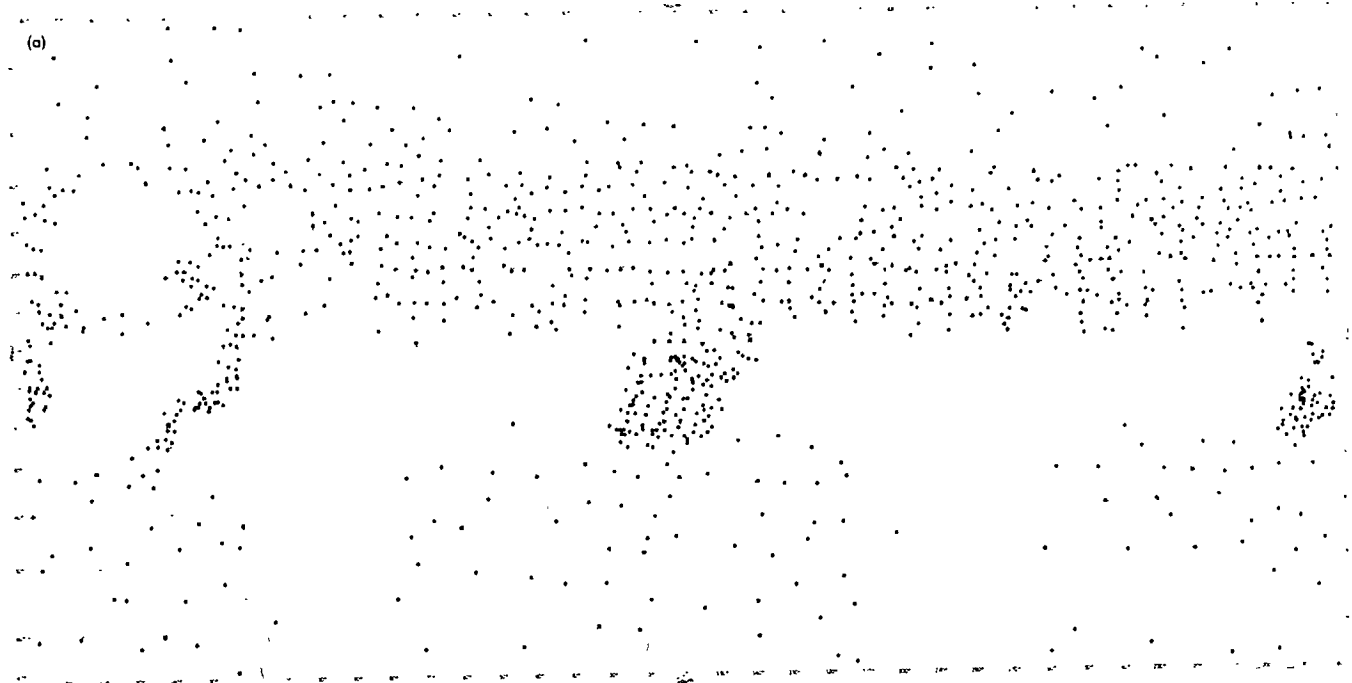
Fig. XXXIX-2. Points of the primary control net plotted on a chart of the central latitudes (Mercator projection) and charts of each pole (stereographic projection).

Fig. XXXIX-3. Control points identified on USGS MC-1 are north of 65°N.

For the primary net, the measurements of the points are made by counting pixels (picture elements) on pictures that have had no geometric processing. IPL produces special versions of the frames for this purpose; they are high-pass filtered and stretched, and a special counting grid is incorporated to help in pixel counting. The IPL uses a computer program to locate, in pixel coordinates, the 195 reseau points on each picture. During calibration before launch, the locations of the reseau points on the vidicon tube were carefully measured using an optical comparator, and the optical and geometric distortions relative to the reseau points were measured using special targets in the collimator. The data were used by Kreznar in 1972 (unpublished data) to prepare a program to remove the distortions when the reseau point locations were known. This program was used to transform the control point measurements in pixel coordinates into image coordinates (in millimeters), with the origin at the principal point of the optics. The pixel coordinates of each point on each frame are measured three or four times by two or three different persons. Any measurement differing from the median measurement by more than two pixels is rejected (as a gross error) and the pixel coordinates $(\overline{X}, \overline{Y})$ are the mean of the remaining measurements. Each individual measurement is estimated to the one-tenth pixel; the standard error of the mean is usually between 0.2 and 0.5 pixel (0.003 to 0.007 mm). This program, which transforms pixel coordinates $(\overline{X}, \overline{Y})$ into image coordinates (x_o, y_o), is essentially the same as the one used by the IPL to produce their geometrically corrected pictures.

Measurements for the secondary triangulation are made differently. A positive or negative of the picture is measured directly on a Mann two-coordinate monocomparator. The picture is then produced at the U. S.
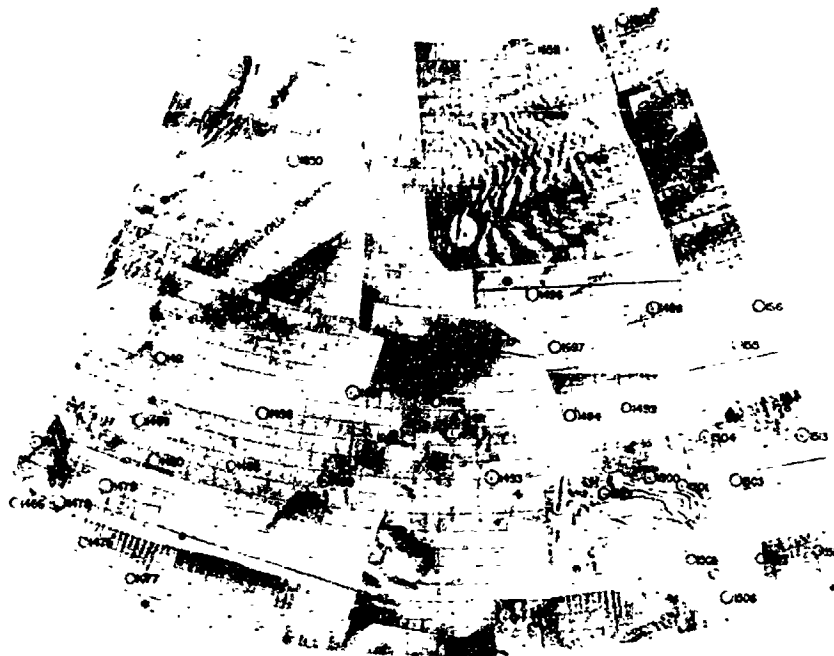
Fig. XXXIX-4. Control points identified on USGS MC-2 are bounded by latitudes 30°N, 65°N, and longitudes 120°, 180°.

Geological Survey, Flagstaff, Arizona, on an Optronics Photowrite machine from a magnetic tape supplied by IPL. These pictures are produced at USGS rather than at IPL/JPL because all the IPL video film converters use cathode-ray tubes, which introduce their own geometric distortions. This is the reason that the measurements for the primary net are made by pixel counting instead of measuring film with a comparator.

The crater Airy-0, which now defines the prime meridian, is identified on the narrow-angle picture mentioned above, but it is too small to be seen on wide-angle pictures. The primary control net is composed entirely of wide-angle pictures in order to maximize surface coverage, so it is necessary to determine the coordinates of Airy-0 on a wide-angle picture that also contains other points of the net. Wide-angle frame 533-1 (MTVS 4296-111, DAS 13165256) was taken at about the same time as 533-3, so that the viewing and lighting geometry of the low-resolution and high-resolution frames are similar. Alan Gillespie of IPL and Gordon Hoover of the California Institute of Technology independently transferred the point (Airy-0) from the narrow-angle frame to

the wide-angle frame and determined the pixel coordinates. This is more difficult than would appear at first because the narrow-angle frames are rotated 60° relative to the wide-angle frames, and there is a great deal of scale distortion in the uncorrected frames (because the horizontal and vertical pixel sizes are not the same on the vidicon camera, but are the same on the IPL video-film-converter versions of the pictures).

Gillespie transferred the position of Airy-0 from frame 533-3 to 533-1 using the IPL machine-matching program, as well as by eye, through interpolation between points common to both frames. Hoover transferred the point by eye to this frame and also to other frames containing this region. These measurements are summarized in Table XXXIX-4. It is felt that the machine-matching program gives the best results, so those measurements on 533-1 are used to define the prime meridian for the control net. The difference in longitude between this measurement and other measurements on 533-1 and other frames are given in Table XXXIX-4; the standard error of transfer was about 0°014 longitude.

Table XXXIX-4. Transfer of the location of Airy-J to low-resolution frames

Frame number	DAS	Source	Method of point transfer	Pixel coordinates		Longitude difference, deg[a]
				X	Y	
533-1	13165256	Gillespie	Machine	396.36	474.22	0
533-1	13165256	Gillespie	Eye	396.83	474.43	0.005
533-1	13165256	Hoover	Eye	396.9	474.8	0.006
137-30	06499678	Hoover	Eye	561.0	314.4	0.029
139-15	06571008	Hoover	Eye	563.5	138.8	0.009
180-17	08045768	Hoover	Eye	52.3	528.5	0.003

[a] $\sigma = 0.014$.
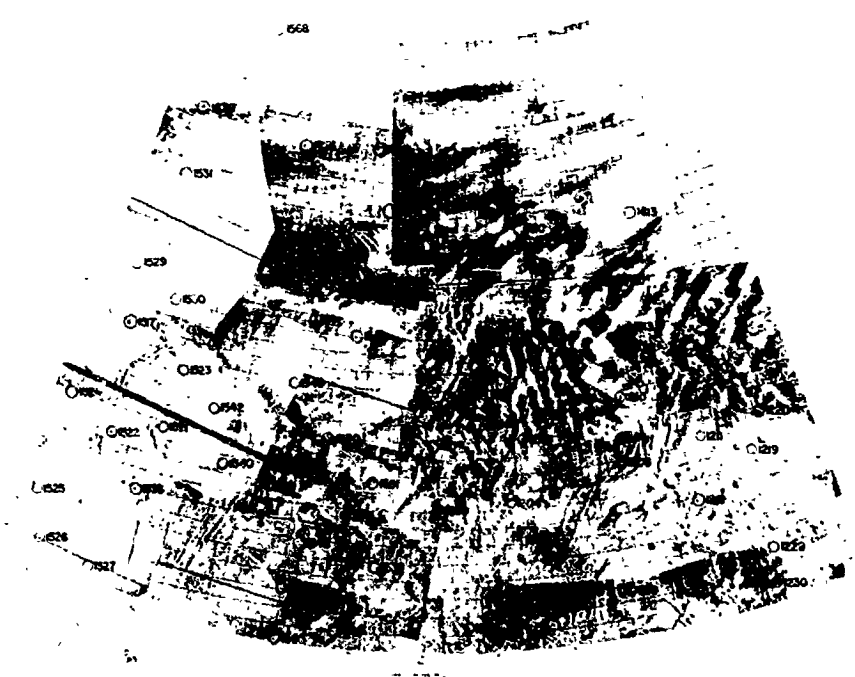
Fig. XXXIX-5. Control points identified on USGS MC-3 are bounded by latitudes 30°N, 65°N, and longitudes 60°, 120°.

D. The Computations

The effort on the primary net has been to add points and pictures to cover the entire surface of the planet. At this time, the net contains 1205 points on 598 frames and is planet-wide; however, some large gaps still exist. Future work will be aimed at reducing the gaps.

Work on the secondary net is about to start, and there are no specific results to report at this time. This triangulation is particularly important to fill gaps in the primary net and to increase the density of control points in particular regions used in the preparation of a large-scale map.

The number of points and frames now in the primary net is so large that the control computations have been divided into five overlapping blocks. The coordinates of the points in each block are computed as independent adjustments; however, in the overlap regions a few points are held at positions determined by the adjustment of the neighboring block. The block solution is iterative

Fig. XXXIX-6. Control points identified on USGS MC-4 are bounded by latitudes
30°N, 65°N, and longitudes 0°, 60°.
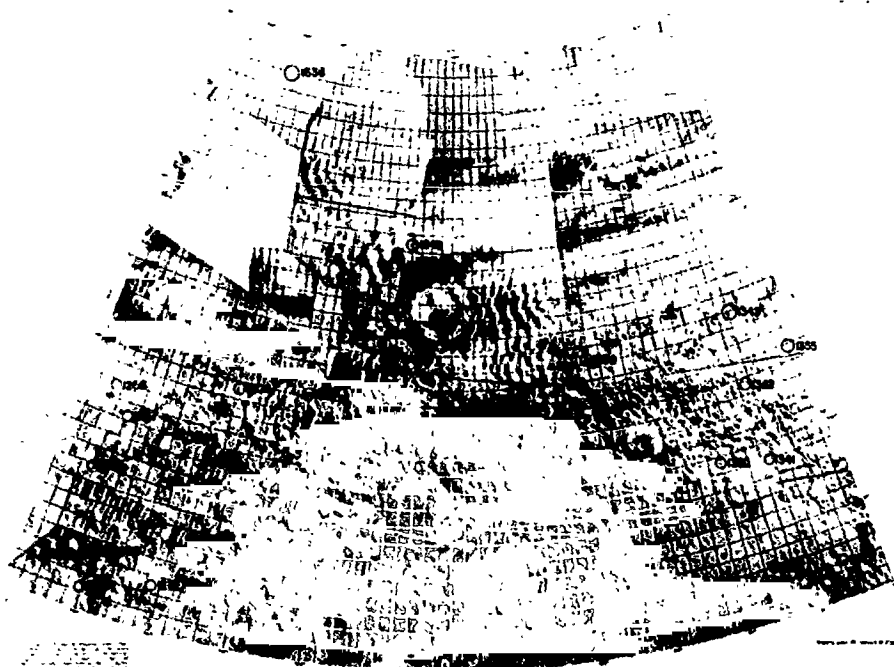
Fig. XXXIX-7. Control points identified on USGS MC-5 are bounded by latitudes
30°N, 65°N, and longitudes 300°, 0°.

Fig. XXXIX-8. Control points identified on USGS MC-6 are bounded by latitudes 30°N, 65°N, and longitudes 240°, 300°.

Fig. XXXIX-9. Control points identified on USGS MC-7 are bounded by latitudes 30°N, 65°N, and longitudes 180°, 240°.
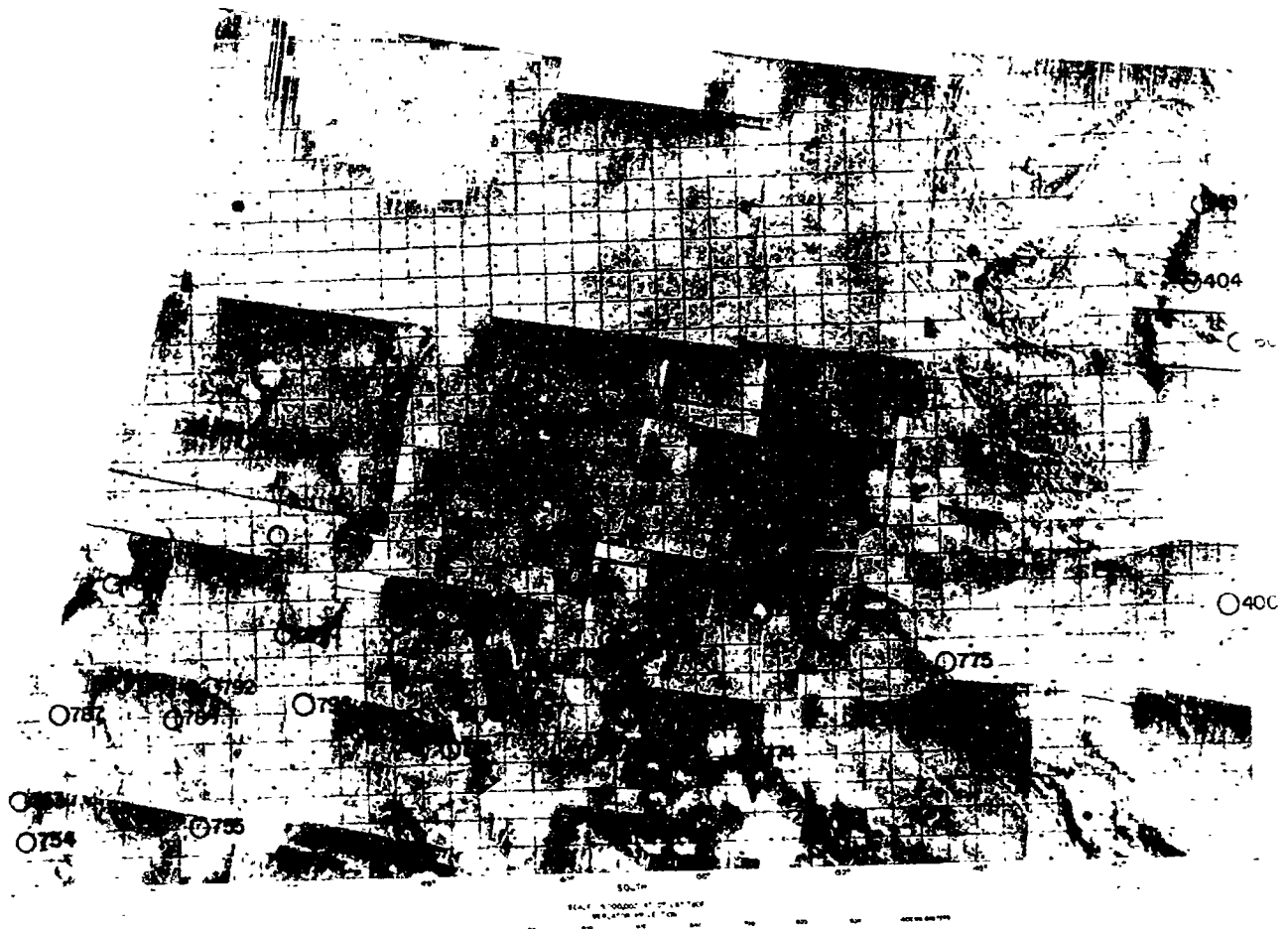
Fig. XXXIX-10. Control points identified on USGS MC-8 are bounded by latitudes 0°, 30°N, and longitudes 135°, 180°.

and the computations are continued until all of the point coordinates in the overlapping regions do not change. Usually two or three adjustments of each block are required for the solution. A summary of these results is given in Table XXXIX-5. The areographic coordinates of the points are given in Table XXXIX-6.

It is always difficult to estimate the accuracy of coordinates because frequently unknown systematic errors are more important than the standard errors that come from the computations. At this stage of the work, the random horizontal error is thought to be about 10 km. To this must be added a regional error that is a function of position; near Airy-0 this type of error is very small, whereas at the antipode of Airy-0 it may be as large as 20 km. This error will also be high, perhaps 15 km to 20 km, for those coordinates whose points lie on the periphery of the gaps in photographic coverage.

Table XXXIX-5. Summary of primary control net computations

Block	Number of points	Number of frames	Number of equations	Number of unknowns	Standard error, σ, mm
North polar	674	141	1652	971	0.0176
0° north	335	140	1657	1090	0.0301
180° north	363	140	1753	1146	0.0144
0° south	231	142	1584	888	0.0157
180° south	238	154	1514	938	0.0226
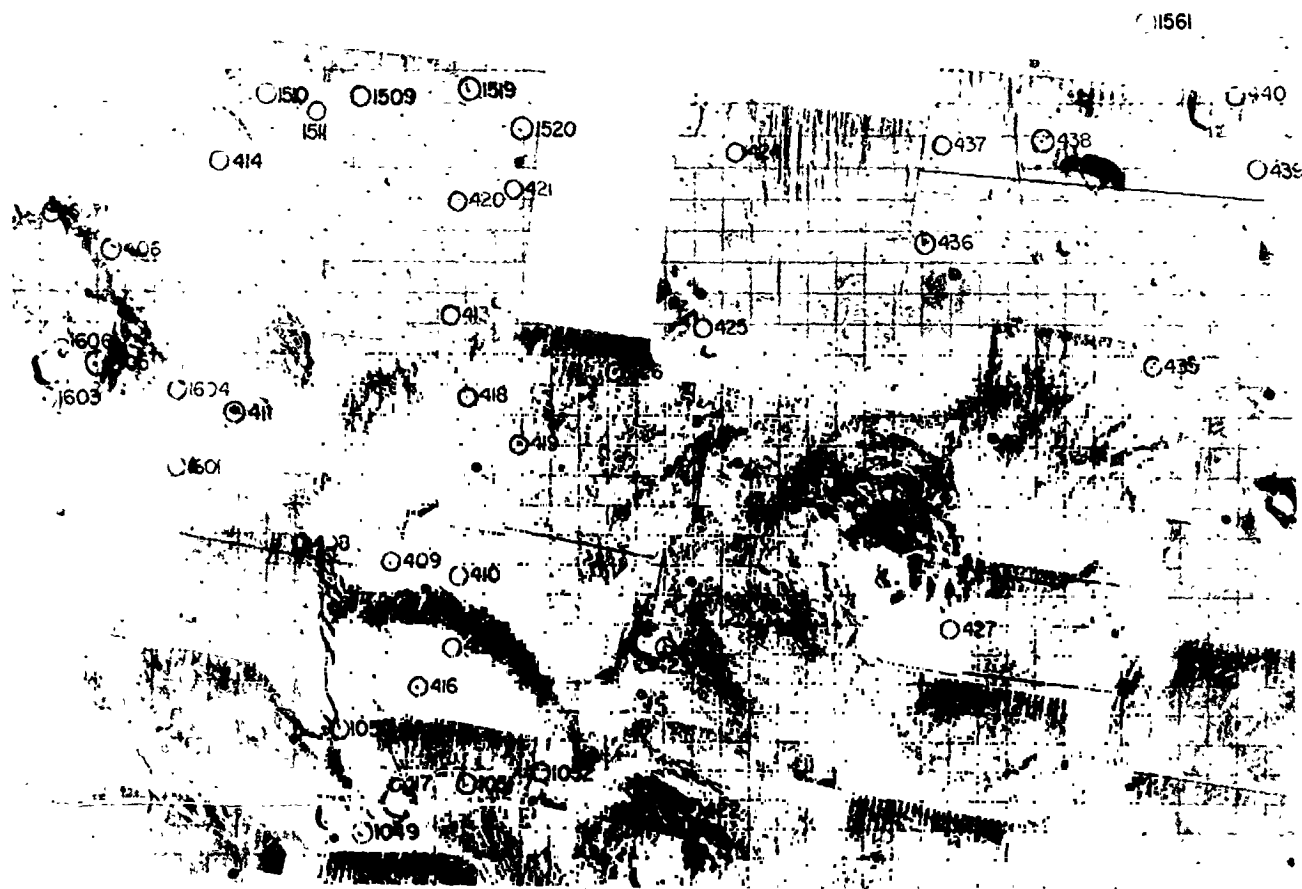
Fig. XXXIX-11. Control points identified on USGS MC-9 are bounded by latitudes 0°, 30°N, and longitudes 90°, 135°.

Fig. XXXIX-12. Control points identified on USGS MC-10 are bounded by latitudes 0°, 30°N, and longitudes 45°, 90°.
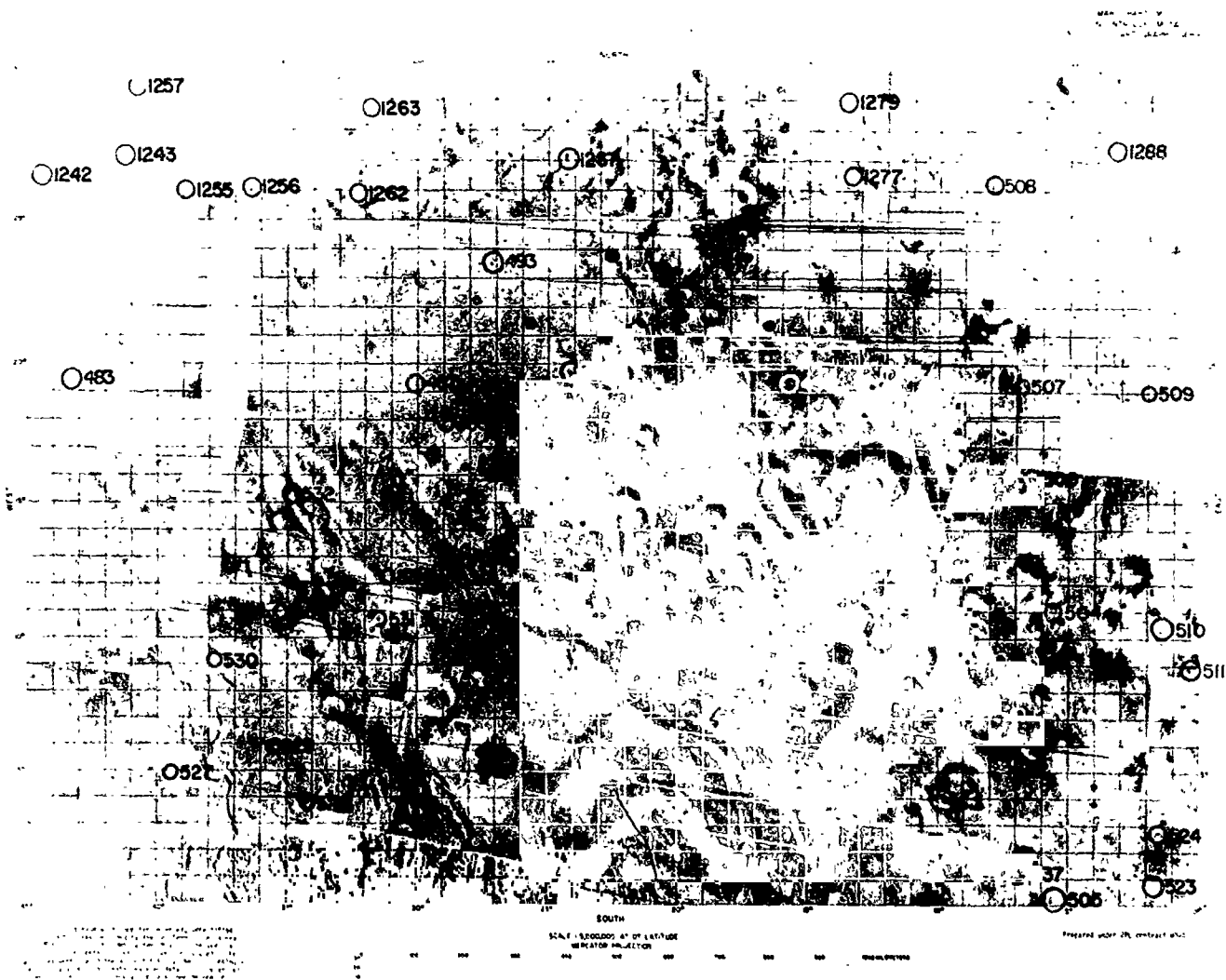
Fig. XXXIX-13. Control points identified on USGS MC-11 are bounded by latitudes 0°, 30°N, and longitudes 0°, 45°.
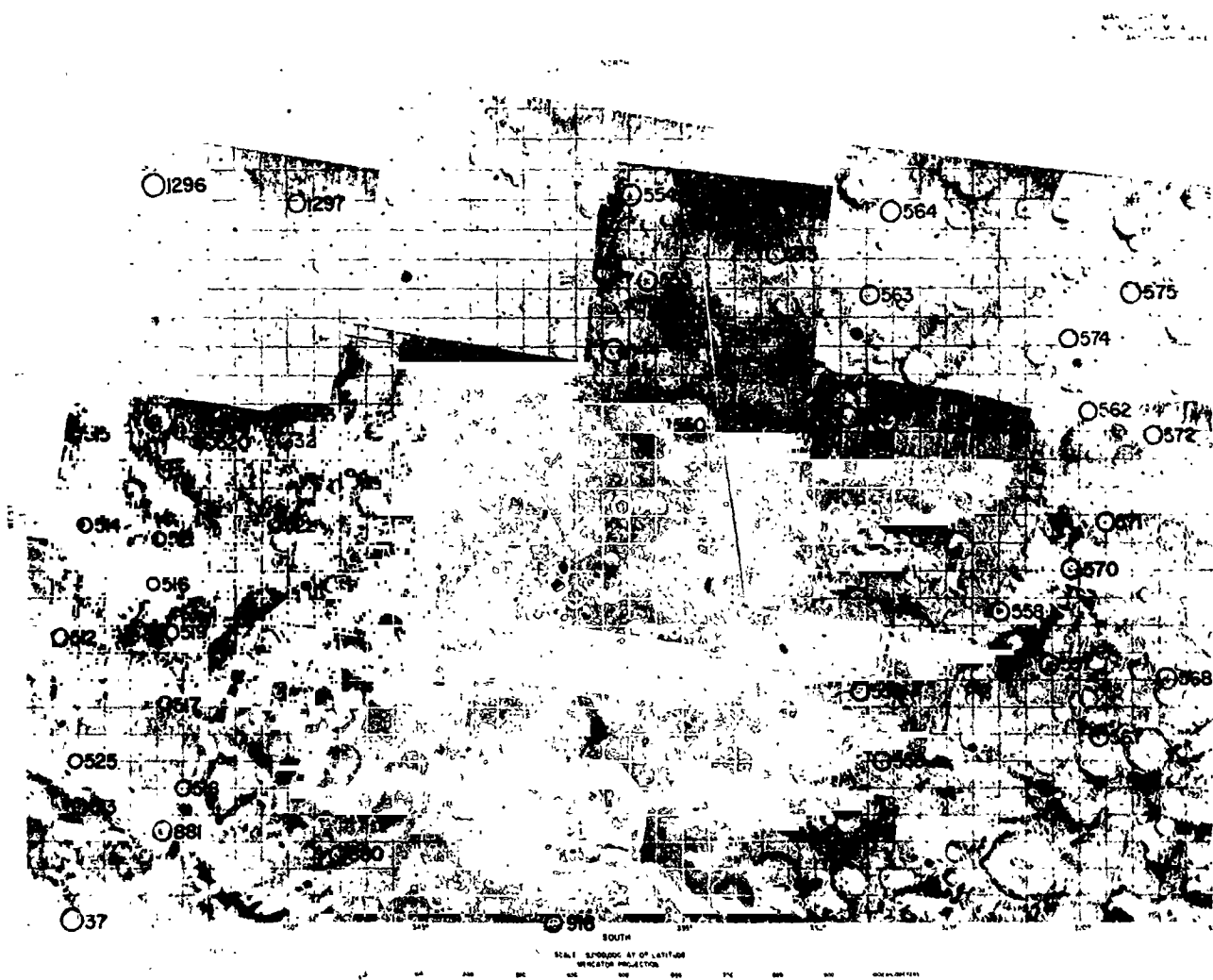
Fig. XXXIX-14. Control points identified on USGS MC-12 are bounded by latitudes 0°, 30°N, and longitudes 315°, 0°.
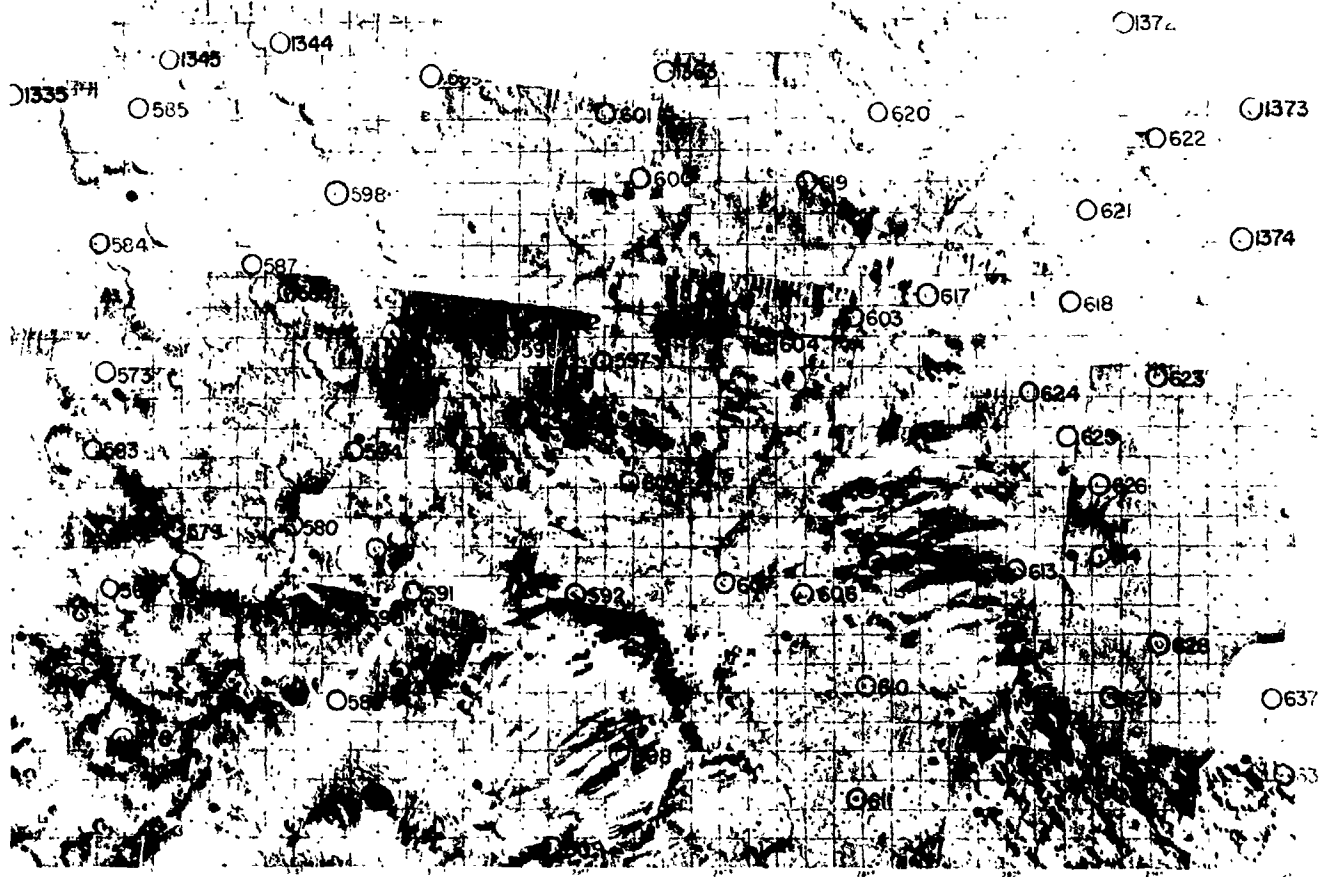
Fig. XXXIX-15. Control points identified on USGS MC-13 are bounded by latitudes 0°, 30°N, and longitudes 270°, 315°.
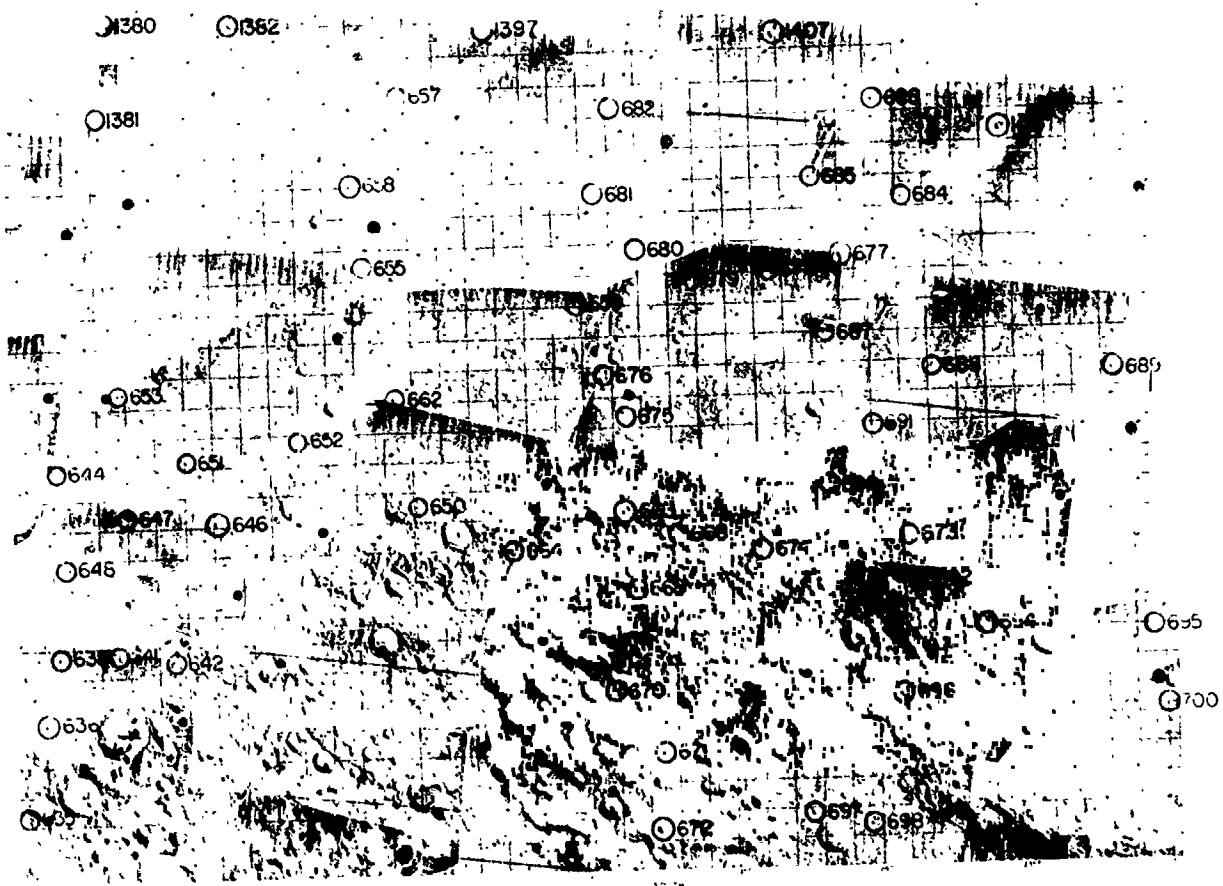
Fig. XXXIX-16. Control points identified on USGS MC-14 are bounded by latitudes 0°, 30°N, and longitudes 225°, 270°.
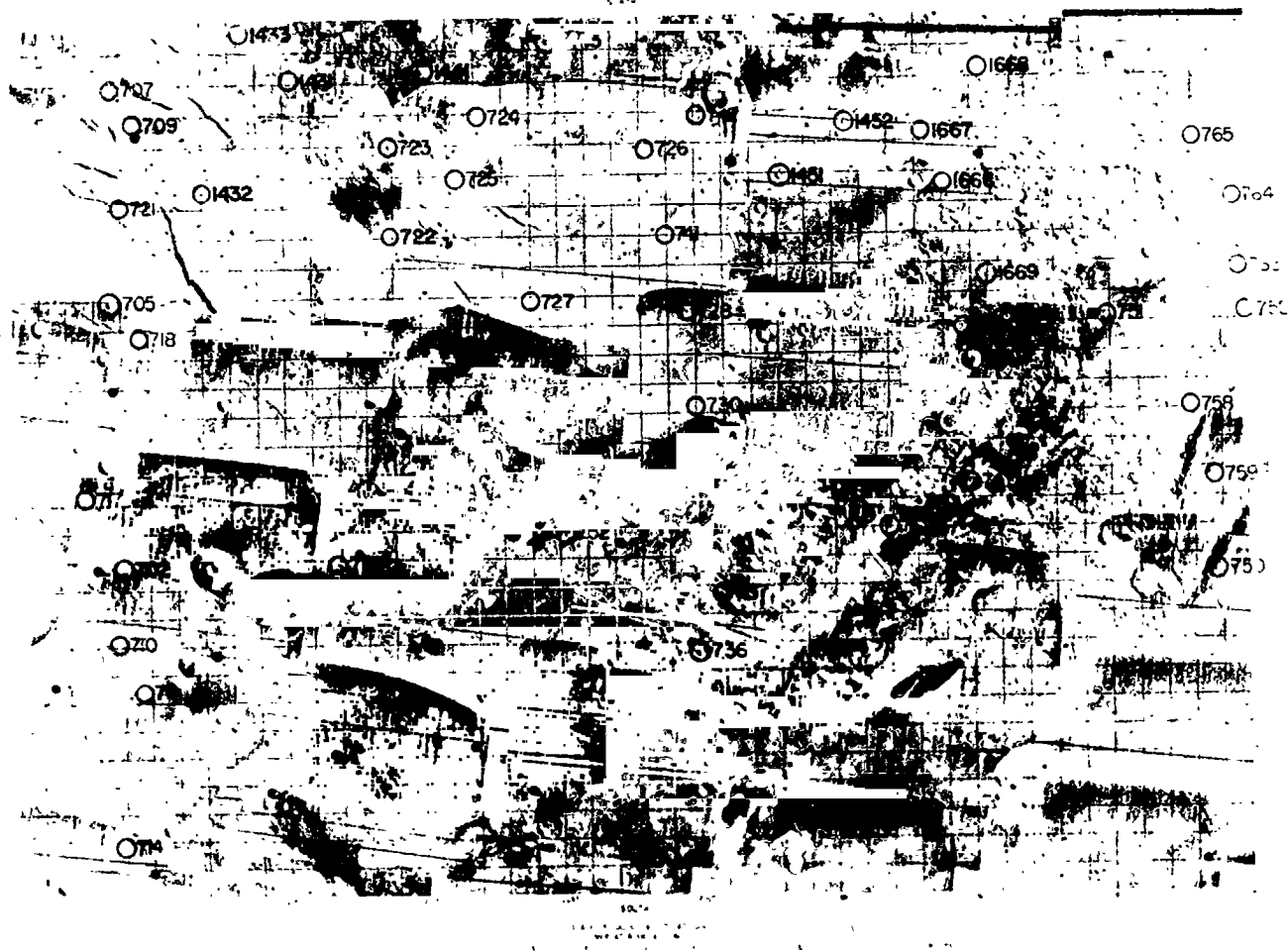
Fig. XXXIX-17. Control points identified on USGS MC-15 are bounded by latitudes 0°, 30°N, and longitudes 180°, 225°.

Fig. XXXIX-18. Control points identified on USGS MC-16 are bounded by latitudes 0°, 30°S, and longitudes 90°, 135°.

Fig. XXXIX-19. Control points identified on USGS MC-17 are bounded by latitudes 0°, 30°S, and longitudes 135°, 180°.

Fig. XXXIX-20. Control points identified on USGS MC-18 are bounded by latitudes 0°, 30°S, and longitudes 45°, 90°.
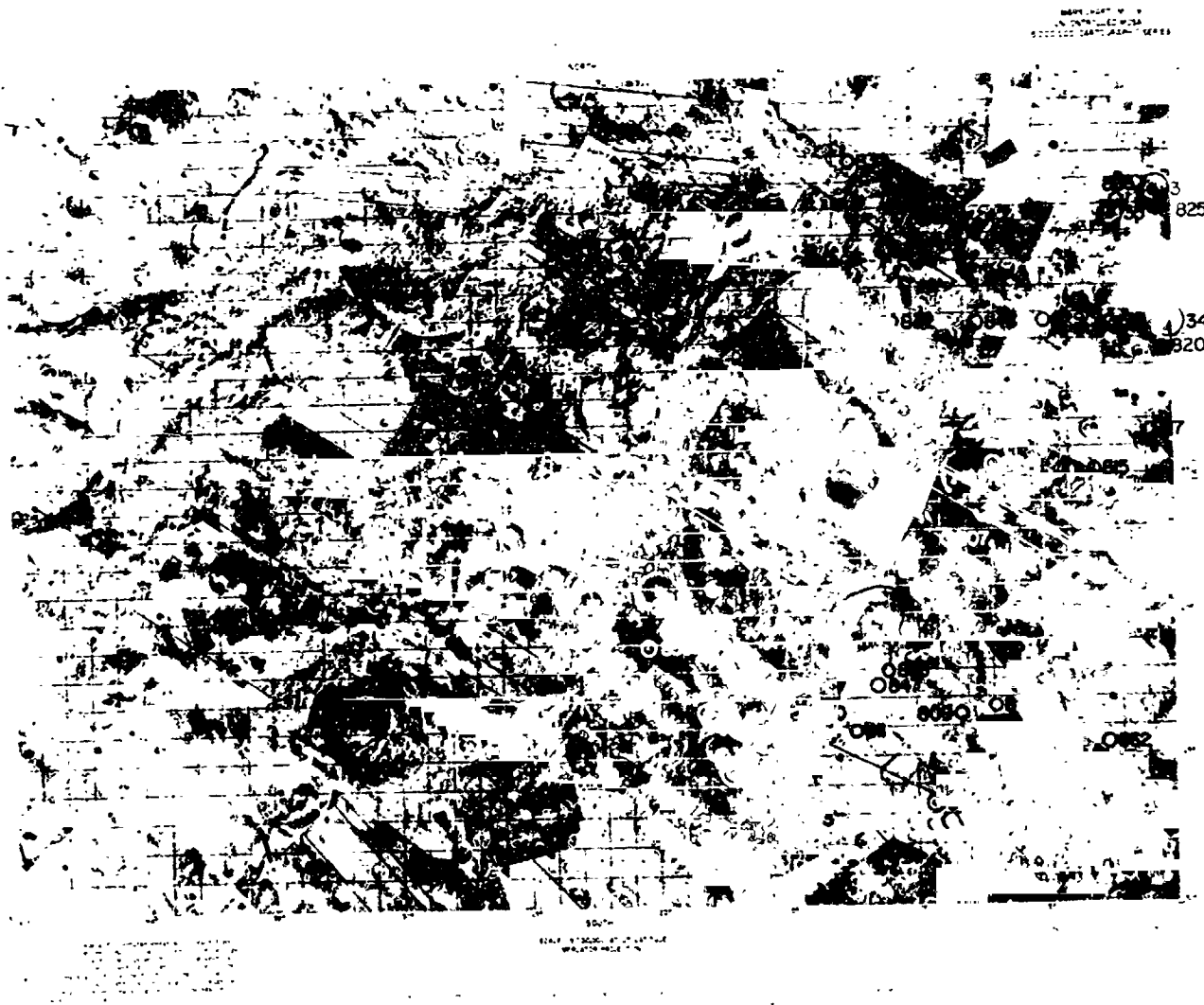
Fig. XXXIX-21. Control points identified on USGS MC-19 are bounded by latitudes 0°, 30°S, and longitudes 0°, 45°.

Fig. XXXIX-22. Control points identified on USGS MC-20 are bounded by latitudes 0°, 30°S, and longitudes 315°, 0°.
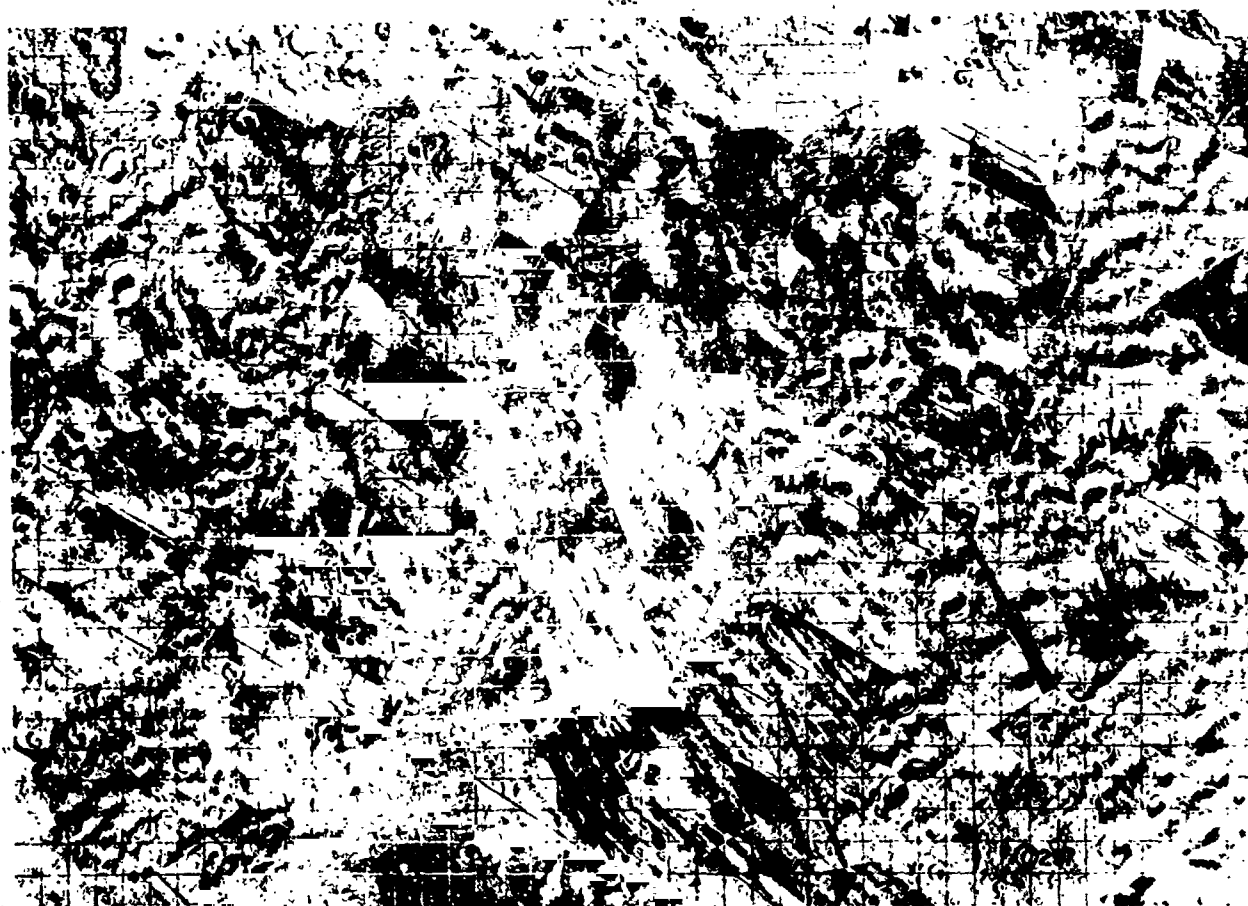
Fig. XXXIX-23. Control points identified on USGS MC-22 are bounded by latitudes 0°, 30°S, and longitudes 225°, 270°.

Fig. XXXIX-24. Control points identified on USGS MC-23 are bounded by latitudes 0°, 30°S, and longitudes 180°, 225°.

Fig. XXXIX-25. Control points identified on USGS MC-24 are bounded by latitudes 30°S, 65°S, and longitudes 120°, 180°.
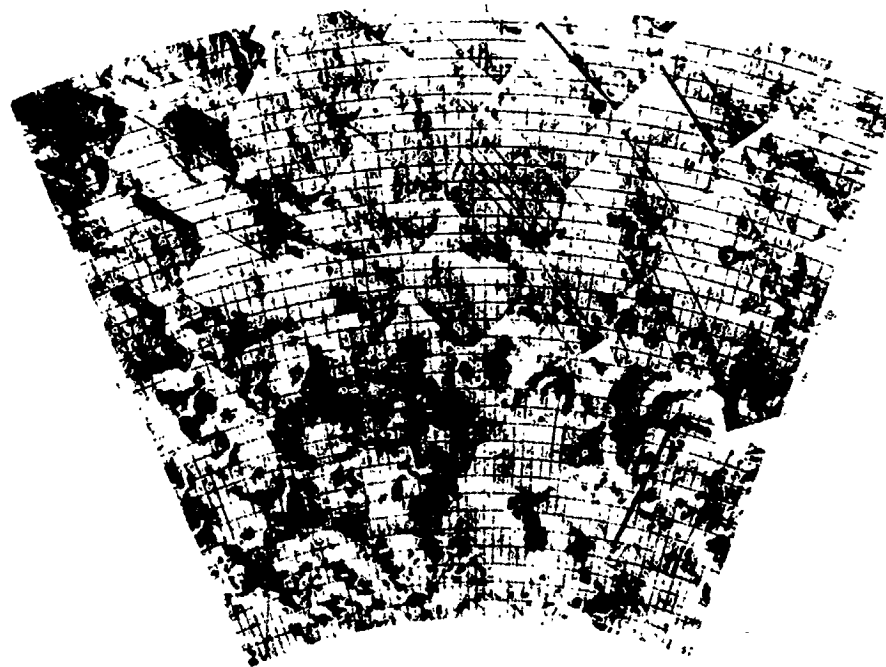
Fig. XXXIX-26. Control points identified on USGS MC-25 are bounded by latitudes 30°S, 65°S, and longitudes 60°, 120°.
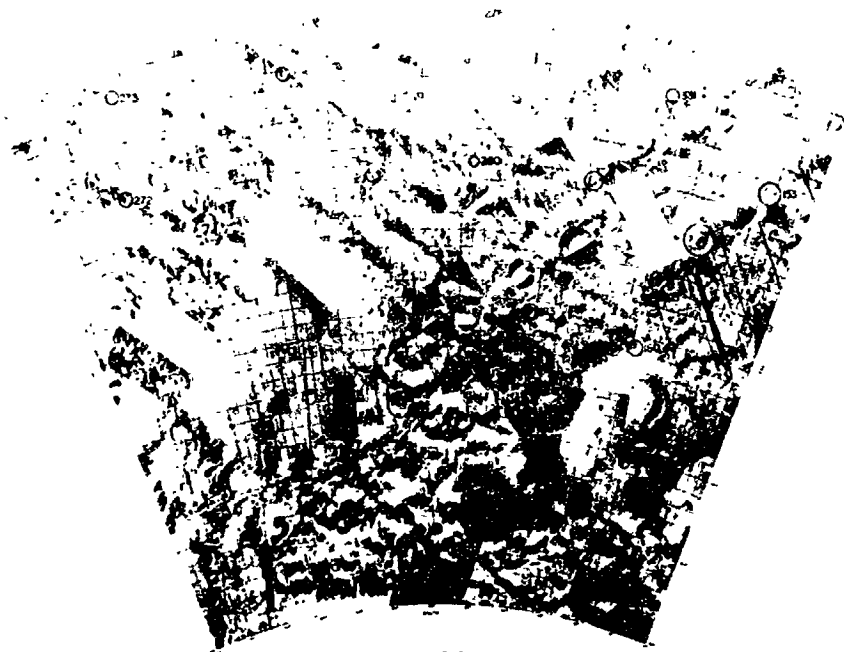
Fig. XXXIX-27. Control points identified on USGS MC-26 are bounded by latitudes 30°S, 65°S, and longitudes 0°, 60°.
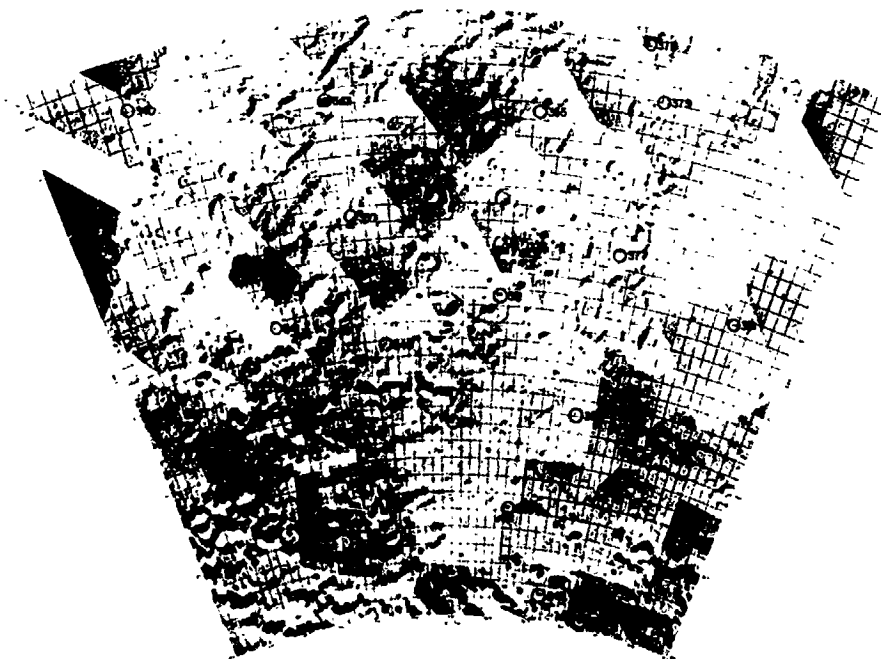
Fig. XXXIX-28. Control points identified on USGS MC-27 are bounded by latitudes 30°S, 65°S, and longitudes 300°, 0°.
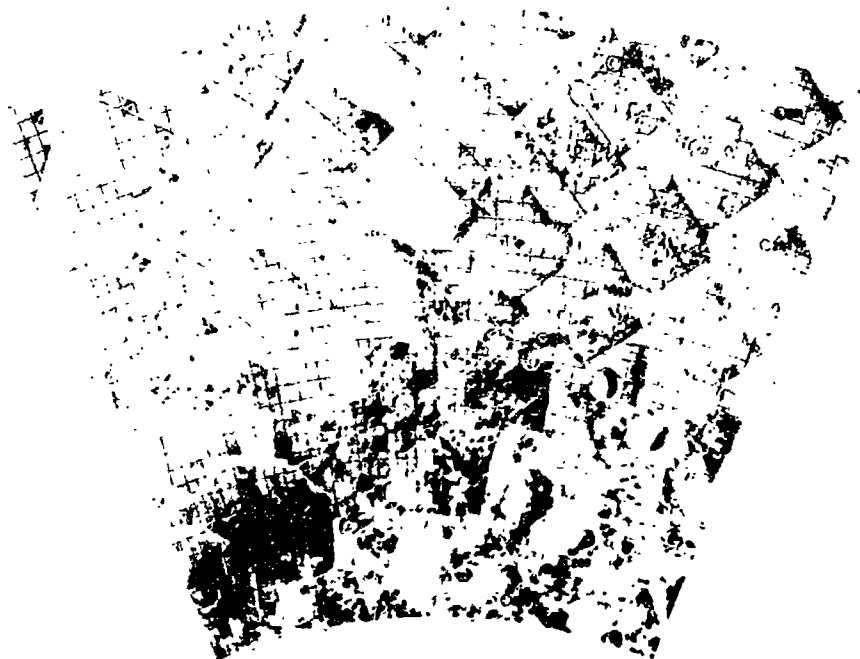
Fig. XXXIX-29. Control points identified on USGS MC-28 are bounded by latitudes 30°S, 65°S, and longitudes 240°, 300°.
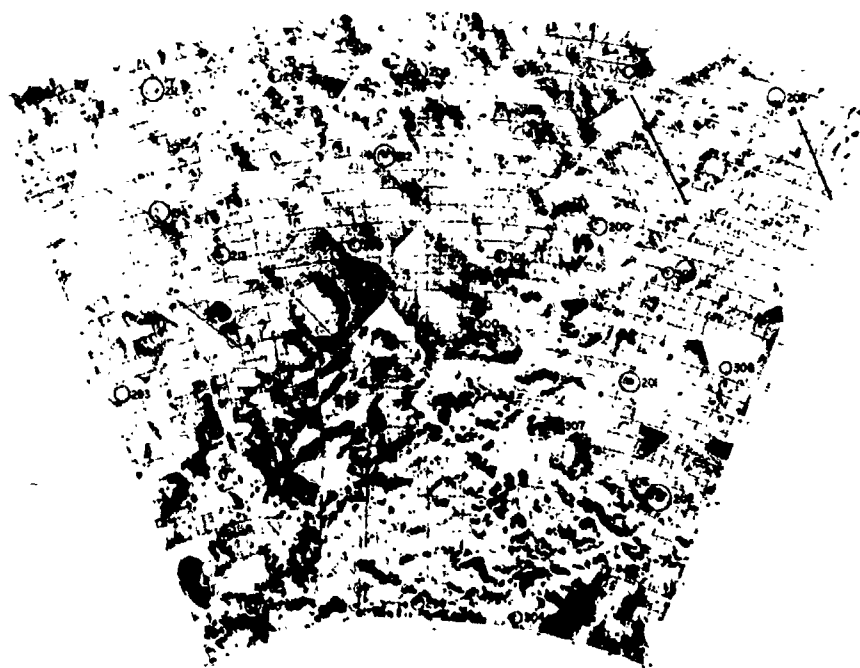
Fig. XXXIX-30. Control points identified on USGS MC-29 are bounded by latitudes 30°S, 65°S, and longitudes 180°, 240°.
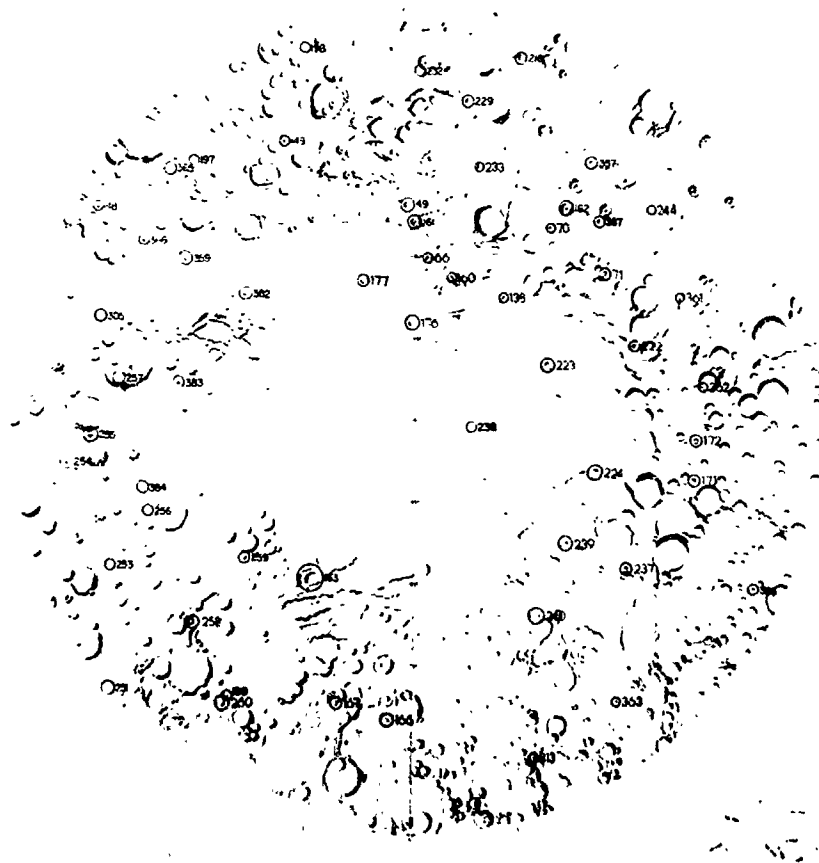
Fig. XXXIX-31. Control points identified on USGS MC-30 are south of 65°S.

Table XXXIX-6. Areographic coordinates of the control points

Point	Latitude (ϕ'°)	W.Longitude (λ°)	Elevation (km)
0	-5.11	0.0	1.44
26	-15.75	3.67	2.24
27	-14.47	2.39	2.15
28	-20.36	4.31	2.57
31	-5.88	358.86	1.60
33	-4.03	356.37	1.76
34	-8.65	0.36	1.70
35	-4.71	2.64	1.40
37	0.72	358.51	1.13
38	-3.81	0.99	1.34
49	-77.08	0.77	-0.00
66	-80.27	353.43	-0.01
70	-75.69	323.93	-0.01
71	-75.38	307.37	-0.01
138	-79.72	329.76	-0.01
147	-69.64	42.70	0.02
148	-66.97	56.87	0.21
149	-71.18	26.49	-0.00
150	-41.81	7.26	1.46
153	-37.72	2.93	1.87
160	-81.07	340.63	0.00
161	-78.08	358.88	0.0
162	-74.02	323.90	-0.01
163	-78.71	143.16	-0.01
166	-72.22	176.11	-0.01
167	-72.18	163.71	-0.01
171	-72.67	257.97	-0.01
172	-72.79	264.49	-0.01
176	-83.29	353.15	-0.00
177	-81.24	19.37	-0.00
180	-48.95	10.48	0.96
181	-39.71	16.31	1.72
182	-53.74	32.39	0.71
183	-48.05	20.05	1.24
187	-33.34	75.36	6.09
190	-42.33	67.97	3.85
191	-43.81	60.22	3.05
192	-51.97	56.88	1.69
193	-50.28	72.70	2.76
194	-45.37	74.11	3.76
196	-80.94	48.59	-0.00
197	-82.29	73.46	-0.00
198	-67.02	17.23	0.11
199	-69.58	146.07	0.03

Table XXXIX-6 (contd)

Point	Latitude (ϕ'°)	W.Longitude (λ°)	Elevation (km)
200	-42.11	195.91	2.39
201	-50.06	190.91	1.45
202	-55.64	185.05	0.82
203	-50.40	175.49	1.22
204	-40.35	177.79	1.93
205	-26.61	138.30	3.13
206	-32.53	186.13	2.82
207	-33.73	202.67	3.27
208	-34.07	210.03	2.89
209	-27.11	217.08	3.30
210	-27.86	207.90	3.19
211	-33.14	227.42	3.72
212	-38.79	212.35	2.54
213	-43.26	225.57	2.50
214	-39.87	229.55	3.01
215	-23.19	237.42	3.80
216	-67.44	342.87	0.12
222	-75.94	289.37	-0.00
223	-80.63	289.58	0.00
224	-78.52	253.94	0.00
229	-70.65	349.64	-0.01
232	-69.20	359.43	0.02
233	-74.29	344.49	-0.01
234	-68.89	297.87	-0.09
236	-80.54	320.51	-0.00
237	-74.39	235.08	-0.01
238	-85.57	263.76	0.00
239	-78.12	230.46	-0.00
240	-75.94	210.70	-0.00
242	-63.98	317.44	0.31
243	-67.00	322.71	0.20
244	-70.82	311.43	-0.00
245	-64.83	312.24	0.00
246	-70.39	284.88	0.00
248	-62.14	148.47	0.40
249	-55.34	152.16	0.86
250	-60.57	142.09	0.84
251	-65.51	131.11	0.37
252	-65.08	121.90	0.54
253	-69.78	114.81	0.04
254	-68.48	97.43	0.19
255	-70.26	92.16	-0.00
256	-72.95	105.58	-0.00
257	-72.05	82.02	-0.00

Table XXXIX-6 (contd)

Point	Latitude (ϕ'°)	W. Longitude (λ°)	Elevation (km)
258	-72.13	131.76	-0.01
259	-77.19	128.37	0.00
261	-58.69	111.38	1.65
262	-53.26	125.01	2.33
263	-46.84	120.85	4.15
264	-42.66	119.74	5.27
266	-36.67	128.33	5.11
268	-55.61	78.12	1.98
269	-62.75	70.89	0.66
270	-62.46	44.08	0.33
271	-30.73	65.38	5.74
272	-38.13	52.91	2.94
273	-32.31	51.67	3.37
274	-20.32	45.75	2.90
275	-33.31	39.65	2.53
276	-42.81	34.41	1.50
277	-52.73	41.36	1.02
278	-30.44	25.87	2.19
279	-32.36	18.56	2.33
280	-39.01	25.65	1.66
281	-53.79	20.95	0.81
282	-60.04	23.45	0.34
283	-46.08	9.53	1.12
284	-63.92	259.28	0.19
285	-63.01	231.27	0.38
286	-48.94	260.04	0.95
289	-61.34	252.56	0.41
291	-32.88	245.36	3.43
292	-32.68	256.67	2.49
293	-49.30	237.75	1.81
294	-40.12	243.33	2.75
295	-49.23	218.97	1.69
296	-64.08	209.82	0.27
297	-27.82	233.13	4.03
298	-33.74	219.31	3.34
299	-43.78	215.13	2.15
300	-46.34	205.93	1.67
301	-44.48	203.40	2.14
303	-43.68	189.73	2.02
304	-64.03	196.90	0.32
305	-69.98	71.81	0.02
306	-77.03	71.44	-0.01
307	-53.28	197.01	1.26
309	-47.52	183.08	1.44

Table XXXIX-6 (contd)

Point	Latitude $(\phi'°)$	W. Longitude $(\lambda°)$	Elevation (km)
310	-32.69	195.65	3.34
312	-61.03	177.02	0.36
313	-69.13	198.49	0.05
314	-32.48	175.85	2.64
315	-47.83	172.58	1.52
316	-33.23	165.79	2.87
317	-60.62	165.12	0.42
318	-46.73	162.03	1.64
319	-37.16	161.22	2.44
320	-42.32	131.99	3.99
321	-61.89	132.97	0.70
322	-34.12	151.54	3.32
323	-49.43	152.50	1.35
324	-55.25	155.92	0.87
325	-34.82	144.50	3.95
326	-31.36	159.91	2.91
327	-43.01	145.03	3.08
328	-55.61	136.45	1.36
329	-47.15	137.63	3.57
331	-33.97	11.66	1.91
334	-46.02	126.54	3.55
335	-34.04	0.18	2.24
336	-46.01	1.34	1.35
337	-56.18	8.53	0.54
338	-60.39	11.92	0.29
339	-26.18	2.08	2.45
340	-33.15	352.74	2.71
341	-47.92	345.71	1.61
342	-57.78	354.06	0.61
343	-35.06	339.04	2.98
344	-25.56	344.05	3.70
345	-23.40	352.57	3.36
346	-49.57	335.46	1.55
347	-61.52	338.90	0.42
348	-35.35	331.60	2.98
349	-24.71	332.96	4.03
350	-42.04	337.85	2.29
351	-46.67	325.05	2.26
352	-56.73	339.58	0.83
353	-59.24	322.57	0.78
354	-27.26	324.03	4.00
355	-35.76	322.79	3.61
356	-67.80	245.24	0.06
357	-70.73	327.75	-0.01

Table XXXIX-6 (contd)

Point	Latitude (φ'°)	W. Longitude (λ°)	Elevation (km)
358	-65.51	335.34	0.22
359	-73.04	57.44	-0.00
361	-72.04	294.36	-0.00
362	-72.37	276.17	0.01
363	-68.87	216.78	0.06
364	-54.36	328.97	1.12
365	-69.26	45.52	0.04
356	-70.37	57.05	0.00
367	-73.53	316.94	-0.00
368	-80.29	82.19	-0.01
375	-57.42	312.80	0.11
376	-43.79	323.68	2.73
377	-43.55	315.32	1.33
378	-31.11	316.26	2.63
379	-34.14	314.57	1.53
380	-55.25	316.79	1.06
381	-45.77	304.84	-1.70
382	-77.47	54.58	0.00
383	-75.22	82.84	0.00
384	-73.07	100.01	-0.00
400	9.9	136.89	3.04
401	10.86	135.33	12.81
403	19.25	140.87	1.24
404	20.70	137.25	6.24
405	18.67	131.83	24.52
406	22.14	131.55	5.07
407	23.18	136.70	6.36
408	12.03	124.81	4.76
409	11.54	121.70	5.01
410	11.05	119.28	5.27
411	16.32	127.45	4.14
413	19.82	119.79	4.34
414	24.65	128.09	2.92
415	6.61	119.53	5.58
416	7.25	120.70	5.62
417	3.91	121.44	5.89
418	17.07	119.15	4.68
419	15.53	117.42	4.96
420	23.60	119.39	3.99
421	23.89	117.40	4.02
422	3.26	111.23	7.07
423	8.16	112.82	6.24
424	24.91	109.86	4.10
425	19.12	111.09	4.86

Table XXXIX-6 (contd)

Point	Latitude (ϕ'°)	W. Longitude (λ°)	Elevation (km)
426	17.78	114.15	4.87
427	9.41	102.20	5.89
430	8.81	112.16	6.21
433	11.37	97.46	5.44
435	18.26	95.18	4.48
436	22.14	103.28	4.18
437	25.35	102.51	3.79
438	25.58	98.85	3.66
439	24.53	91.59	3.67
440	26.74	92.13	3.41
442	28.51	87.78	3.10
443	24.55	89.78	3.65
444	22.11	89.32	3.95
445	21.57	80.97	3.37
446	13.10	83.30	4.38
447	13.67	79.84	3.95
449	4.34	82.62	5.19
450	16.73	82.27	3.91
451	20.23	77.21	3.20
452	28.44	79.49	2.98
453	25.41	81.06	3.19
454	11.47	76.92	3.97
455	1.07	72.04	4.54
456	7.63	72.97	4.04
457	11.70	72.44	3.67
458	11.30	69.07	3.47
459	20.03	71.92	2.95
460	18.05	72.60	3.14
461	19.45	68.45	2.76
462	26.91	71.17	1.93
463	23.24	72.23	2.53
464	20.68	64.20	2.27
465	25.21	63.67	1.50
466	16.67	64.30	2.62
467	11.26	64.44	3.04
468	6.69	64.22	3.37
470	12.72	60.72	2.58
471	20.70	58.56	1.72
472	13.18	54.05	1.76
473	10.06	55.41	2.19
475	11.43	50.75	1.52
476	16.44	54.40	1.52
477	20.04	56.25	1.47
478	23.00	55.96	1.12

Table XXXIX-6 (contd)

Point	Latitude (ϕ'°)	W. Longitude (λ°)	Elevation (km)
479	20.32	47.18	0.45
480	24.78	47.11	0.20
481	19.35	45.30	0.42
483	19.53	42.07	0.24
484	10.58	40.10	0.99
485	7.46	46.02	1.60
486	2.43	46.31	2.11
487	19.59	29.84	-0.63
488	10.79	34.90	0.49
489	12.01	25.42	-0.01
490	8.40	25.36	0.22
491	17.33	24.95	-0.35
492	19.87	24.05	-0.48
493	23.69	26.85	-0.83
494	26.91	25.80	-0.99
495	19.56	15.77	-0.34
496	25.30	17.51	-0.65
497	19.79	12.11	-0.36
498	19.19	20.01	-0.32
500	11.29	17.28	0.11
501	4.91	16.35	0.48
502	11.19	12.13	0.15
503	10.30	16.12	0.18
504	11.00	6.67	0.18
505	0.44	6.88	0.98
506	15.93	7.23	-0.10
507	19.11	7.48	-0.29
508	26.02	7.67	-0.69
509	16.48	2.67	-0.19
510	10.21	2.72	0.23
511	8.46	1.54	0.36
512	11.15	358.82	0.29
513	5.11	358.08	0.83
514	15.51	357.84	0.16
515	18.78	358.21	-0.04
516	13.48	355.31	0.51
517	8.94	355.11	0.82
518	5.91	354.41	1.14
519	11.53	354.72	0.69
520	18.39	353.25	0.38
521	15.06	355.12	0.43
522	15.48	350.86	0.78
523	0.35	2.74	1.01
524	2.27	2.54	0.86

Table XXXIX-6 (contd)

Point	Latitude (ϕ'°)	W. Longitude (λ°)	Elevation (km)
525	6.80	358.24	0.67
527	4.92	38.88	1.40
528	4.04	33.66	0.94
529	6.10	35.00	0.90
530	9.01	37.27	0.88
531	10.48	31.38	0.20
532	15.40	34.73	0.09
533	18.23	29.06	-0.51
534	12.57	30.98	-0.01
535	9.74	346.36	1.72
536	9.42	345.66	1.83
537	14.41	344.97	1.46
538	12.87	338.95	2.18
539	14.61	346.14	1.33
540	10.59	348.15	1.44
542	16.69	347.07	0.88
543	20.73	345.55	0.85
544	22.15	338.19	1.34
545	11.37	336.92	2.39
546	5.37	338.88	2.70
547	10.94	331.94	2.52
548	11.25	329.77	2.53
549	16.02	337.32	1.92
550	19.62	336.53	1.62
551	19.04	333.00	1.98
552	19.47	329.16	2..
553	24.51	336.80	1.
554	27.35	337.42	1.01
555	6.91	328.13	2.74
556	9.40	328.86	2.62
557	10.43	321.61	2.48
558	12.15	323.56	2.38
560	16.10	329.66	2.23
561	19.23	324.70	1.89
562	19.80	320.56	1.72
563	23.64	328.45	1.65
564	26.42	327.62	1.38
567	7.84	319.76	2.53
568	10.28	317.47	2.33
569	10.44	311.74	2.00
570	13.99	321.03	2.20
571	15.72	319.84	2.03
572	18.77	318.24	1.70
573	17.68	312.15	1.49

Table XXXIX-6 (contd)

Point	Latitude (ϕ'°)	W. Longitude (λ°)	Elevation (km)
574	22.32	321.10	1.49
575	23.90	318.73	1.25
577	7.37	312.34	2.21
578	5.25	311.40	2.35
579	12.45	309.70	1.77
580	12.42	305.74	2.02
581	11.55	302.62	2.30
582	12.42	311.99	1.87
583	15.17	312.35	1.68
584	21.90	312.43	1.18
585	26.23	310.84	0.79
586	20.17	305.97	1.43
587	21.38	307.07	1.27
588	19.67	301.33	1.74
589	6.52	303.94	2.60
590	9.28	303.28	2.43
591	10.12	301.44	2.49
592	10.06	295.75	2.53
593	9.11	294.34	2.59
594	15.13	303.49	1.96
595	18.73	303.15	1.70
596	18.27	298.05	1.91
597	18.12	294.83	1.86
598	23.57	304.07	1.26
599	26.87	300.62	1.16
600	23.92	293.39	1.39
601	25.82	294.51	1.25
602	19.11	296.40	1.81
603	19.30	286.13	2.02
604	18.59	289.18	1.81
605	13.94	293.93	2.19
606	10.02	287.60	2.65
607	10.75	290.68	2.39
608	4.73	294.21	2.94
609	1.49	296.48	3.24
610	6.96	285.51	3.08
611	3.07	285.73	3.37
612	11.37	285.37	2.74
613	11.14	290.72	3.16
614	11.26	277.22	3.05
615	17.29	286.38	2.17
616	13.82	285.65	2.51
617	20.08	283.42	2.20
618	19.78	278.63	2.44

Table XXXIX-6 (contd)

Point	Latitude (ϕ'°)	W. Longitude (λ°)	Elevation (km)
619	23.51	287.54	1.51
620	25.72	284.90	1.37
621	22.67	277.86	1.99
622	24.93	275.42	1.66
623	17.34	275.12	2.38
624	17.00	280.08	2.75
625	15.43	278.87	2.82
626	13.60	277.19	2.85
628	8.22	275.17	3.19
629	6.47	276.79	3.43
631	6.23	279.59	3.59
632	18.38	350.88	0.57
633	19.30	350.15	0.56
634	3.82	270.51	3.35
635	2.78	269.91	3.42
636	5.96	269.10	3.13
637	6.39	270.73	3.12
638	8.11	268.56	2.94
641	8.14	266.66	2.99
642	7.87	264.82	3.06
643	17.04	268.41	2.09
644	14.34	268.78	2.34
645	13.29	268.72	2.44
646	12.35	263.38	2.70
647	12.61	266.06	2.59
648	11.18	267.92	2.66
650	13.08	256.35	2.38
651	14.69	264.35	2.46
652	15.16	260.60	2.56
653	16.94	266.51	2.19
654	20.29	258.90	2.04
655	21.27	258.10	1.90
657	26.63	256.58	1.27
658	23.85	258.36	1.68
659	19.35	250.66	1.30
662	16.62	257.02	2.15
663	12.56	249.18	1.79
664	11.65	253.23	2.21
668	12.64	247.62	1.73
669	9.91	248.71	2.00
670	6.51	249.50	2.32
671	4.45	248.06	2.46
672	1.81	248.27	2.70
673	11.52	239.08	1.48

Table XXXIX-6 (contd)

Point	Latitude ($\phi'°$)	W. Longitude ($\lambda°$)	Elevation (km)
674	11.28	244.64	1.76
675	15.81	248.90	1.50
676	17.20	249.58	1.40
677	20.49	241.17	0.77
678	20.19	243.71	0.90
679	20.08	246.34	1.02
680	21.82	248.78	0.97
681	23.61	250.06	0.87
682	26.13	249.38	0.63
684	22.75	238.92	0.44
685	23.33	242.07	0.54
686	25.70	239.76	0.22
687	18.07	242.00	1.03
688	17.17	238.12	0.37
689	17.11	231.86	0.28
690	13.18	241.76	1.49
691	15.35	240.26	1.23
692	10.01	236.94	1.61
693	9.08	241.02	1.86
694	8.56	236.92	1.44
695	8.51	231.53	0.67
696	6.27	239.71	2.07
697	2.11	242.63	2.55
698	1.74	240.75	2.55
699	9.85	230.98	0.53
700	5.89	231.26	0.75
701	12.32	229.70	0.26
702	12.33	221.09	-0.44
703	21.79	227.42	-0.29
704	21.23	224.77	-0.47
705	21.61	221.96	-0.69
706	29.88	229.41	-0.47
707	23.30	221.81	-0.92
708	29.13	228.25	-0.52
709	27.25	221.08	-0.94
710	9.67	221.39	-0.32
711	7.91	220.53	-0.33
714	2.14	221.32	-0.07
715	11.84	215.41	-0.63
716	12.02	213.31	-0.69
717	14.75	222.40	-0.41
718	20.35	220.58	-0.76
720	20.00	213.05	-0.86
721	24.73	221.63	-0.82

Table XXXIX-6 (contd)

Point	Latitude (ϕ'°)	W. Longitude (λ°)	Elevation (km)
722	23.67	211.53	-0.88
723	26.78	211.77	-0.89
724	27.53	208.27	-0.91
725	25.52	209.06	-0.83
726	26.56	202.31	-1.08
727	21.71	206.37	-0.95
728	20.79	200.78	-1.02
729	19.12	206.47	-0.91
730	17.38	200.16	-0.97
731	13.77	208.10	-0.80
732	13.14	205.27	-0.83
733	13.99	202.31	-0.87
734	13.19	201.28	-0.88
735	4.51	199.63	-0.34
736	9.03	200.21	-0.72
737	11.16	199.46	-0.87
738	13.64	198.59	-0.94
739	13.51	193.04	-1.13
740	12.28	190.83	-1.19
741	23.69	201.68	-1.05
742	27.52	200.49	-1.14
743	20.72	197.12	-1.12
744	20.79	195.01	-1.20
745	20.62	190.50	-1.34
746	17.44	190.98	-1.27
747	15.43	190.29	-1.26
750	11.82	181.40	-1.36
751	20.89	185.44	-1.35
752	20.93	181.01	-1.41
753	3.38	178.40	-0.20
754	1.99	178.19	0.01
755	2.73	172.41	0.21
756	13.58	177.97	-1.32
757	13.33	175.83	-1.26
758	17.88	182.77	-1.32
759	15.11	181.51	-1.31
760	20.64	178.51	-1.38
761	20.74	176.98	-1.43
762	19.98	174.74	-1.57
763	22.51	181.13	-1.35
764	24.78	181.20	-1.35
765	26.70	182.51	-1.37
766	28.04	180.42	-1.44
769	12.82	169.42	-0.98

Table XXXIX-6 (contd)

Point	Latitude (ϕ'°)	W. Longitude (λ°)	Elevation (km)
771	5.47	163.42	-0.11
772	6.67	163.08	-0.24
773	10.09	152.57	0.07
774	4.98	152.81	0.64
775	7.69	145.45	1.39
785	7.63	174.88	-0.62
786	6.46	173.22	-0.40
787	6.51	177.11	-0.58
788	11.03	175.32	-1.09
791	9.47	169.30	-0.62
792	7.57	171.78	-0.47
793	16.02	170.53	-1.30
796	6.87	168.43	-0.26
797	8.94	157.60	-0.22
798	11.89	170.26	0.09
800	-26.32	9.19	2.27
801	-26.90	7.60	2.29
802	-24.36	5.98	2.43
803	-27.04	14.72	2.21
804	-23.96	14.97	2.13
806	-18.50	4.55	2.45
807	-17.05	8.30	2.35
808	-23.96	7.71	2.42
809	-23.06	7.45	2.46
810	-22.96	4.33	2.50
811	-21.25	5.54	2.55
812	-22.66	6.17	2.49
813	-19.10	1.23	2.49
814	-17.64	3.49	2.39
815	-13.97	3.11	2.10
817	-12.45	1.06	1.99
818	-14.99	358.73	2.32
819	-8.64	2.44	1.70
820	-9.62	0.57	1.78
822	-10.65	356.06	2.30
823	-7.61	358.32	1.80
824	-14.26	6.71	2.13
825	-4.60	0.52	1.40
826	-4.20	2.41	1.36
827	-5.35	358.71	1.60
828	-3.72	358.26	1.51
829	-8.58	4.97	1.69
830	-10.67	11.58	1.71
831	-10.39	10.20	1.80

Table XXXIX-6 (contd)

Point	Latitude ($\phi'°$)	W. Longitude ($\lambda°$)	Elevation (km)
832	-8.92	10.47	1.66
833	-6.88	13.95	1.29
834	-5.05	9.45	1.39
835	-4.28	9.40	1.35
836	-3.22	12.19	1.20
837	1.40	8.21	0.89
839	-12.46	14.81	1.58
840	-16.75	13.34	1.98
841	-16.26	12.42	2.03
842	-14.10	11.75	1.94
843	-15.30	13.36	1.88
844	-18.90	9.24	2.50
845	-13.14	9.96	2.03
846	-8.83	7.30	1.70
847	-22.41	10.54	2.42
848	-18.66	12.07	2.24
849	-18.28	14.43	1.97
850	-23.11	13.91	2.17
851	-17.76	15.08	1.77
852	-22.63	16.42	2.00
853	-22.36	15.28	2.07
854	-20.35	14.52	2.09
856	-21.74	10.28	2.47
857	-23.56	16.12	2.06
858	-22.64	17.44	1.92
859	-21.42	19.60	1.65
861	-25.49	16.83	2.13
862	-24.17	2.73	2.50
863	-22.07	0.23	2.56
864	-21.52	355.78	3.06
865	-20.33	359.84	2.57
866	-17.61	358.86	2.50
867	-14.93	357.97	2.41
868	-16.70	353.81	3.08
869	-12.60	356.03	2.47
870	-11.91	351.71	2.93
871	-11.14	353.80	2.62
872	-9.71	356.39	2.19
873	-5.13	355.32	1.95
874	-9.01	354.63	2.35
875	-5.84	353.08	2.26
876	-6.39	352.13	2.42
877	-1.95	350.11	2.27
878	-2.31	352.17	2.08

Point	Latitude (ϕ'°)	W. Longitude (λ°)	Elevation (km)
879	-0.53	353.51	1.78
880	3.37	348.53	1.96
881	4.09	354.69	1.27
882	-26.00	358.09	2.71
883	-24.09	358.91	2.65
884	-23.20	356.45	2.93
885	-24.95	358.05	2.73
887	-20.27	353.09	3.46
888	-24.48	354.33	3.11
890	-18.55	355.26	3.05
891	-17.86	353.14	3.27
892	-19.26	351.88	3.55
893	-13.97	352.71	2.98
895	-15.16	349.05	3.48
896	-8.74	350.94	2.75
897	-9.99	352.55	2.66
898	-10.40	346.94	3.15
899	-9.21	348.58	2.98
900	-5.87	349.91	2.62
901	-8.50	347.46	2.98
902	-9.18	344.92	3.14
903	-8.33	343.82	3.15
904	-7.54	345.45	3.01
905	-4.51	340.87	3.09
906	-3.69	342.71	2.95
907	-2.55	344.00	2.76
908	-17.21	351.23	3.45
909	-17.75	348.44	3.74
910	-21.95	351.09	3.60
911	-23.85	11.93	2.29
912	-4.13	348.82	2.55
913	2.75	345.33	2.31
914	1.68	344.54	2.46
915	2.24	340.70	2.76
916	0.87	340.30	2.86
917	6.41	342.67	2.35
918	5.26	339.96	2.69
919	5.21	337.72	2.73
920	-24.56	195.70	3.35
921	-25.30	188.66	3.16
922	-28.62	190.66	3.29
923	-22.64	194.05	3.24
924	-2.70	178.67	0.46
925	-2.33	177.80	0.48

Table XXXIX-6 (contd)

Point	Latitude (ϕ'°)	W. Longitude (λ°)	Elevation (km)
926	-3.76	175.30	0.79
927	-7.22	175.06	1.21
928	-5.38	175.55	0.95
929	-9.59	178.31	1.19
930	-10.32	178.34	1.28
931	-10.90	176.26	1.53
932	-9.52	175.94	1.39
933	-10.90	174.25	1.70
934	-9.54	173.45	1.60
935	-11.40	172.77	1.89
936	-14.63	173.92	2.23
937	-15.42	174.38	2.30
938	-11.87	180.08	1.44
939	-12.72	178.20	1.62
940	-13.87	177.27	1.86
941	-14.44	178.01	1.88
942	-15.46	178.27	2.00
946	-15.87	183.61	2.25
947	-16.85	180.85	2.19
948	-17.71	176.81	2.28
949	-15.43	184.88	2.41
950	-17.51	185.68	2.61
951	-18.84	184.15	2.68
952	-19.22	186.27	2.86
954	-20.33	185.76	2.96
955	-21.57	183.31	2.80
956	-17.30	188.29	2.76
957	-22.04	184.28	2.87
958	-22.90	186.08	2.99
959	-22.31	187.74	3.09
960	-24.18	187.47	3.07
961	-24.13	188.68	3.15
962	-21.88	190.41	3.20
963	-18.14	180.18	2.33
964	-19.85	180.49	2.59
965	-19.51	181.73	2.62
966	-21.24	180.31	2.61
969	-22.57	190.55	3.20
970	-24.47	190.96	3.24
971	-23.87	194.09	3.29
972	-25.91	193.19	3.33
973	-17.85	189.05	2.87
974	-18.43	188.36	2.90
975	-19.69	189.22	3.11

Table XXXIX-6 (contd)

Point	Latitude (φ'°)	W. Longitude (λ°)	Elevation (km)
976	−19.41	191.38	3.08
977	−12.81	186.94	2.10
978	−14.12	186.69	2.25
979	−14.26	138.49	2.40
980	−15.22	187.60	2.46
981	−15.90	189.42	2.66
982	−16.83	188.38	2.71
988	−19.74	194.55	3.11
989	−21.40	191.82	3.20
991	−15.96	191.33	2.68
992	−16.79	189.47	2.78
993	−11.88	188.48	2.11
994	−7.82	184.97	1.21
995	−2.95	186.49	0.38
996	−3.02	185.52	0.39
997	−7.46	184.34	1.11
1000	−5.31	185.45	0.79
1001	−4.76	133.37	0.67
1002	−6.41	183.39	0.92
1003	−5.35	179.70	0.67
1004	−24.04	139.44	4.36
1005	−25.20	145.86	4.16
1006	−25.09	143.23	4.22
1007	−23.57	143.09	4.23
1008	−21.10	140.33	4.44
1009	−20.85	138.44	4.70
1010	−23.19	140.81	4.33
1011	−25.72	140.52	4.25
1012	−18.64	138.66	4.70
1013	−19.78	140.37	4.45
1014	−15.92	141.27	4.31
1015	−16.77	137.86	4.83
1016	−15.65	136.83	5.05
1017	−13.58	136.48	5.10
1018	−13.18	137.76	4.87
1019	−14.66	133.00	5.73
1020	−14.23	131.82	5.95
1021	−13.42	129.95	6.30
1022	−10.87	131.73	5.91
1023	−10.30	132.20	5.81
1024	−12.23	130.61	6.15
1025	−30.70	143.11	4.19
1026	−31.97	147.55	4.03
1027	−27.84	150.44	4.11

Table XXXIX-6 (contd)

Point	Latitude (ϕ'°)	W. Longitude (λ°)	Elevation (km)
1028	-14.48	129.26	6.43
1029	-15.36	129.36	6.43
1030	-13.47	127.51	6.66
1031	-14.27	125.40	7.02
1032	-13.18	126.57	6.78
1033	-10.81	128.19	6.47
1034	-10.57	126.85	6.65
1035	-10.00	122.96	7.11
1036	-8.52	125.99	6.62
1037	-7.39	123.86	6.77
1038	-8.07	123.83	6.84
1039	-17.73	177.95	2.34
1040	-19.38	177.28	2.63
1041	-9.83	121.36	7.32
1042	-6.75	121.50	7.00
1043	-6.95	120.07	7.19
1044	-4.93	121.73	6.79
1045	-4.23	123.45	6.51
1046	-2.90	126.26	6.04
1047	1.06	120.90	6.26
1048	-2.32	120.39	6.67
1049	2.18	122.66	5.95
1050	5.76	123.40	5.53
1051	3.94	119.11	6.14
1052	4.42	116.56	6.34
1053	1.39	124.66	5.81
1054	-15.46	132.98	5.75
1056	-14.74	131.83	5.96
1200	32.89	89.14	2.54
1201	32.16	96.14	2.82
1202	32.46	86.92	2.61
1203	34.05	81.76	2.48
1204	38.90	83.81	1.87
1205	39.67	80.20	1.83
1206	40.35	75.62	1.22
1207	42.19	89.47	1.46
1208	42.19	82.59	1.57
1209	44.10	78.73	1.25
1210	43.69	74.82	0.78
1211	40.84	69.58	0.33
1212	49.08	68.77	-0.39
1213	47.49	73.48	0.22
1215	27.20	76.66	2.41
1216	33.31	76.25	1.98

Table XXXIX-6 (contd)

Point	Latitude (±1°)	W. Longitude (1°)	Elevation (km)
1217	32.77	72.61	1.43
1218	37.46	70.64	0.69
1219	39.47	65.17	0.20
1220	41.46	64.64	-0.05
1221	44.56	64.04	-0.31
1222	45.57	69.87	-0.05
1223	44.24	53.15	-0.90
1224	40.55	56.87	-0.43
1225	37.64	56.36	-0.21
1226	39.30	41.99	-1.33
1227	41.55	50.92	-0.76
1228	39.17	45.51	-0.91
1229	33.98	66.34	0.61
1230	32.15	67.06	0.81
1231	25.98	67.84	1.71
1232	27.00	55.94	0.69
1233	28.00	57.63	0.66
1234	28.86	59.45	0.60
1235	25.28	53.93	0.72
1236	32.33	56.59	0.20
1237	34.52	56.59	0.03
1238	34.27	52.16	-0.05
1239	33.40	50.48	-0.00
1240	32.35	48.58	-0.07
1241	27.38	50.26	0.38
1242	26.32	43.25	-0.24
1243	27.07	40.16	-0.60
1244	30.07	51.17	0.31
1245	33.92	46.32	-0.46
1246	33.23	43.65	-0.70
1247	34.29	42.98	-0.85
1248	32.47	41.05	-0.94
1249	32.02	36.93	-1.09
1250	36.33	43.00	-0.91
1251	41.94	42.18	-1.49
1252	38.52	35.03	-1.61
1253	40.90	34.54	-1.74
1254	37.40	39.59	-1.41
1255	25.94	37.77	-0.64
1256	26.12	35.29	-0.80
1257	29.39	39.83	-0.85
1258	33.75	30.38	-1.55
1259	34.01	34.25	-1.40
1260	41.12	24.57	-1.70

Table XXXIX-6 (contd)

Point	Latitude (ϕ'°)	W. Longitude $(\lambda^\mp)$	Elevation (km)
1261	39.22	25.24	-1.61
1262	28.02	31.88	-1.01
1263	28.64	31.28	-1.26
1264	33.21	21.22	-1.12
1265	34.35	25.70	-1.40
12__	37.83	30.40	-1.71
1257	28.66	24.14	-0.89
1268	30.21	21.92	-0.99
1269	33.07	17.17	-1.06
1270	34.17	11.82	-1.13
1271	38.15	21.24	-1.40
1272	38.84	18.49	-1.37
1273	43.60	9.10	-1.40
1274	42.61	15.11	-1.56
1275	41.66	10.57	-1.38
1276	39.26	11.76	-1.30
1277	28.48	13.00	-0.75
1278	30.28	14.89	-0.95
1279	28.99	13.21	-0.90
1280	34.09	6.94	-1.05
1281	32.61	2.67	-0.88
1282	36.75	8.66	-1.16
1283	39.96	3.20	-1.17
1284	38.47	356.73	-0.90
1285	42.01	0.45	-1.24
1286	43.20	356.81	-1.05
1287	41.76	355.24	-0.94
1288	26.76	2.87	-0.61
1289	26.14	358.00	-0.38
1290	31.09	5.98	-0.92
1291	34.16	0.23	-0.88
1292	32.83	357.69	-0.70
1293	34.16	353.91	-0.57
1294	41.59	350.45	-0.69
1295	40.90	348.44	-0.57
1296	26.94	355.44	-0.27
1297	26.56	349.91	0.11
1298	31.91	354.98	-0.50
1299	33.12	350.12	-0.31
1300	30.11	355.39	-0.42
1301	31.94	345.26	0.20
1302	36.16	352.61	-0.60
1303	40.40	343.72	-0.11
1304	38.82	338.63	0.37

Table XXXIX-6 (contd)

Point	Latitude (φ'°)	W.Longitude (λ°)	Elevation (km)
1305	38.90	346.66	-0.31
1306	45.03	347.46	-0.46
1307	45..3	341.72	-0.44
1308	29.25	346.92	0.21
1309	32.90	340.80	0.55
1310	36.54	343.38	0.14
1311	40.86	334.43	0.31
1312	46.02	334.69	-0.21
1313	25.37	332.09	1.46
1314	31.31	337.64	0.81
1315	34.05	337.95	0.64
1316	32.51	333.39	0.88
1317	33.77	329.42	0.88
1318	35.27	332.58	0.75
1319	38.48	331.39	0.54
1320	41.57	327.64	0.24
1321	39.70	321.12	0.11
1322	48.85	330.63	-0.20
1323	40.65	324.47	0.18
1327	32.44	324.88	0.76
1328	33.16	317.35	0.47
1329	34.29	322.89	0.64
1330	38.06	323.51	0.40
1331	39.88	315.79	0.10
1332	40.30	310.02	0.21
1333	47.50	319.22	-0.39
1334	45.02	320.30	-0.24
1335	26.60	315.09	0.89
1339	33.93	308.22	0.41
1340	37.47	311.21	0.28
1341	39.74	306.46	0.19
1342	44.12	306.68	-0.15
1343	48.36	306.27	-0.51
1344	28.10	305.75	0.82
1345	27.67	309.66	0.68
1346	30.75	309.23	0.50
1347	33.05	303.63	0.57
1348	33.39	298.94	0.64
1351	41.97	298.98	-0.06
1352	40.04	297.66	0.12
1353	39.11	292.77	0.21
1354	44.71	295.85	-0.26
1355	45.42	302.47	-0.30
1356	29.07	300.75	0.96

Table XXXIX-6 (contd)

Point	Latitude (ϕ'°)	W.Longitude (λ°)	Elevation (km)
1357	30.75	296.49	0.85
1358	33.98	292.80	0.62
1359	33.15	288.43	0.66
1360	38.15	295.77	0.28
1361	35.43	292.40	0.52
1362	41.46	294.60	0.01
1363	27.07	292.35	1.16
1364	41.56	287.23	-0.05
1365	39.55	289.24	0.17
1367	36.58	288.41	0.39
1368	34.58	284.47	0.44
1369	38.26	284.31	0.13
1371	40.31	273.00	0.42
1372	28.11	276.51	1.26
1373	25.77	272.22	-0.11
1374	21.93	272.64	-0.06
1375	33.87	275.91	0.76
1376	33.50	278.92	0.50
1377	32.58	273.36	1.11
1378	41.81	272.25	0.35
1379	36.95	278.36	0.25
1380	28.88	266.78	1.60
1381	25.96	265.99	1.69
1382	28.76	262.28	1.50
1383	29.76	271.04	1.56
1384	33.38	266.60	1.21
1385	34.10	262.07	0.90
1386	37.14	268.04	0.85
1387	36.86	264.27	0.64
1388	40.58	261.42	-0.07
1389	39.69	254.63	-0.41
1390	36.74	260.81	0.11
1391	38.52	256.11	-0.18
1392	30.11	263.78	1.46
1393	32.80	257.38	0.73
1394	33.00	252.65	0.23
1395	36.26	260.43	0.46
1397	25.55	253.49	0.79
1399	32.60	248.76	0.06
1400	32.85	243.68	-0.20
1401	34.43	250.44	-0.04
1402	36.57	252.28	-0.15
1403	35.71	249.38	-0.35
1404	39.31	243.83	-0.65

Table XXXIX-6 (contd)

Point	Latitude (ϕ'°)	W.Longitude (λ°)	Elevation (km)
1405	42.84	246.10	-0.38
1406	40.44	230.37	-0.83
1407	26.16	243.36	0.15
1408	29.83	243.52	0.30
1409	34.37	236.77	-0.47
1410	33.21	233.16	-0.52
1411	35.62	238.40	-0.62
1412	38.61	236.81	-0.76
1413	41.76	233.28	-1.06
1414	40.15	227.87	-1.09
1415	24.71	235.57	0.08
1418	34.23	230.68	-0.62
1419	34.33	226.31	-0.86
1420	32.47	223.79	-0.94
1421	38.20	226.78	-1.05
1422	41.53	223.92	-1.38
1423	40.85	218.56	-1.46
1424	30.24	226.66	-0.67
1425	26.33	226.48	-0.53
1426	33.67	221.08	-1.22
1427	32.09	216.41	-1.07
1428	36.60	221.96	-1.26
1429	41.47	209.25	-1.29
1431	28.76	215.29	-0.97
1432	25.24	218.28	-0.94
1433	29.84	217.03	-1.03
1434	33.63	210.06	-0.94
1435	32.77	205.26	-1.08
1436	34.46	215.74	-1.13
1437	36.43	210.24	-1.11
1438	39.11	204.75	-1.27
1439	41.34	199.88	-1.65
1440	44.50	207.00	-1.45
1441	29.06	210.45	-0.86
1442	32.44	208.58	-0.95
1443	29.86	205.87	-0.99
1444	31.98	202.13	-1.18
1445	33.82	196.44	-1.37
1446	33.71	202.69	-1.21
1447	36.98	204.67	-1.22
1448	37.86	201.07	-1.38
1449	41.25	196.44	-1.51
1450	39.59	194.01	-1.47
1451	25.55	197.21	-1.21

Table XXXIX-6 (contd)

Point	Latitude (ϕ'°)	W.Longitude (λ°)	Elevation (km)
1452	27.17	194.91	-1.31
1454	34.34	193.01	-1.42
1455	34.64	188.12	-1.44
1456	36.35	193.82	-1.45
1457	40.74	190.63	-1.45
1458	38.48	187.50	-1.46
1459	38.74	182.23	-1.44
1460	47.26	190.71	-1.66
1461	49.44	193.51	-1.72
1462	51.40	169.44	-1.79
1465	34.84	184.48	-1.40
1466	34.18	179.09	-1.37
1467	37.50	179.52	-1.45
1468	40.60	172.75	-1.59
1469	47.42	180.58	-1.60
1470	45.12	180.24	-1.54
1471	27.17	176.76	-1.44
1472	26.83	174.36	-1.51
1473	27.91	178.59	-1.38
1476	33.63	174.03	-1.53
1477	32.74	170.48	-1.63
1478	34.98	176.50	-1.45
1479	36.70	173.83	-1.64
1480	38.77	170.96	-1.74
1481	44.25	172.64	-1.80
1482	39.59	165.40	-1.81
1486	42.78	163.94	-1.84
1487	44.83	157.08	-1.62
1489	39.66	158.53	-1.68
1490	49.65	151.72	-1.61
1491	44.14	147.81	-1.17
1492	45.06	149.70	-1.16
1493	40.78	145.44	-1.14
1494	43.88	138.75	-1.33
1496	50.83	140.36	-1.52
1497	47.85	138.94	-1.38
1498	48.87	129.56	-0.01
1499	43.72	134.23	-0.45
1500	39.51	132.99	0.06
1501	38.71	130.83	0.60
1502	39.10	136.40	-0.62
1503	38.24	127.05	1.18
1504	40.99	128.36	0.77
1505	34.71	131.29	0.98

Table XXXIX-6 (contd)

Point	Latitude (φ'°)	W.Longitude (λ°)	Elevation (km)
1506	32.21	129.53	1.45
1507	33.79	126.71	1.75
1508	28.70	125.77	2.55
1509	26.96	122.74	3.26
1510	27.04	126.25	2.77
1511	26.49	124.37	3.11
1512	33.26	123.02	2.41
1513	39.55	121.35	1.70
1514	42.68	119.97	1.41
1515	45.41	123.65	0.72
1516	47.03	120.99	0.70
1517	46.21	115.13	0.95
1519	27.07	118.79	3.68
1520	25.77	116.98	3.83
1521	41.14	110.35	1.67
1522	40.07	113.97	1.82
1523	44.41	109.93	1.18
1524	41.43	117.76	1.60
1525	35.91	117.84	2.53
1526	33.38	116.57	3.09
1527	32.64	112.90	3.16
1529	49.45	116.20	0.46
1530	48.17	112.08	0.70
1531	55.05	114.78	-0.30
1532	28.58	116.03	3.67
1533	30.00	113.75	3.50
1534	26.49	109.24	3.90
1535	25.60	104.79	3.84
1536	32.91	107.86	3.01
1537	32.60	104.43	2.95
1538	37.51	111.12	2.20
1539	35.22	108.70	2.81
1540	39.93	105.43	1.85
1541	39.37	101.64	1.85
1542	42.79	106.90	1.46
1543	45.01	100.83	1.06
1544	48.36	96.13	0.61
1545	27.70	106.12	3.63
1546	31.37	99.75	2.97
1547	33.81	99.78	2.62
1548	36.38	98.95	2.24
1549	37.52	102.84	2.13
1550	42.40	97.76	1.43
1551	40.14	94.12	1.73

Table XXXIX-6 (contd)

Point	Latitude (ϕ'°)	W.Longitude (λ°)	Elevation (km)
1552	38.21	95.84	1.94
1553	44.49	91.01	1.18
1554	54.27	97.24	-0.16
1555	51.92	90.92	0.22
1556	58.69	102.97	-0.68
1557	58.77	94.70	-0.74
1558	35.59	93.58	2.26
1559	38.86	89.10	1.61
1561	28.97	94.98	3.16
1562	43.27	85.11	1.40
1564	51.87	125.59	-0.14
1565	66.41	278.19	-1.28
1566	55.18	93.24	-0.26
1568	64.53	109.29	-0.95
1569	54.85	88.15	-0.15
1570	59.11	115.38	-0.88
1571	52.41	297.19	-0.83
1573	58.83	289.51	-1.30
1574	62.09	289.20	-1.30
1577	45.07	278.84	-0.32
1578	43.20	244.44	-0.93
1579	49.21	241.31	-1.51
1580	41.48	236.00	-0.97
1581	55.27	227.01	-1.80
1582	50.64	225.67	-1.91
1583	59.63	222.11	-1.82
1584	66.61	216.34	-2.28
1586	58.71	214.02	-2.34
1587	53.74	195.93	-1.98
1588	48.93	199.55	-1.80
1591	60.27	207.25	-2.67
1592	79.83	215.38	-1.17
1593	72.21	214.48	-2.15
1594	60.58	230.91	-1.60
1595	55.01	256.17	-1.40
1596	48.77	271.03	0.01
1597	51.88	267.35	-0.50
1598	69.23	270.36	-1.26
1599	50.34	77.03	0.35
1600	11.58	133.75	11.80
1601	14.28	129.47	9.55
1602	15.23	130.85	12.57
1603	17.49	133.52	27.05
1604	17.42	129.33	11.86

Table XXXIX-6 (contd)

Point	Latitude ($\varphi^{'\circ}$)	W.Longitude (λ°)	Elevation (km)
1605	14.35	131.49	11.42
1606	19.06	133.10	25.07
1607	23.23	133.50	4.29
1608	20.67	135.44	6.03
1609	18.75	135.79	9.06
1610	53.96	81.20	0.08
1611	50.08	61.27	-0.83
1612	51.95	64.53	-0.86
1613	53.60	70.97	-0.62
1614	49.43	43.77	-1.90
1615	60.68	58.02	-2.15
1616	54.46	39.00	-2.53
1617	49.78	34.72	-2.26
1618	53.94	31.64	-2.63
1619	47.43	28.00	-2.26
1620	50.93	18.40	-2.46
1621	48.07	13.65	-1.98
1622	43.65	23.87	-1.94
1623	62.59	23.67	-2.78
1624	50.20	8.31	-1.85
1625	65.82	21.57	-2.51
1627	76.89	55.11	-1.49
1628	85.03	7.78	-0.43
1629	74.73	13.62	-1.50
1630	72.02	15.64	-1.83
1631	73.74	358.35	-1.49
1632	77.04	334.32	-1.00
1633	73.28	333.42	-1.25
1634	68.77	347.69	-1.74
1635	43.25	5.32	-1.44
1636	50.03	356.91	-1.24
1638	62.27	353.69	-1.34
1639	65.25	329.04	-1.23
1640	61.39	336.11	-1.48
1641	56.56	337.64	-1.36
1642	54.41	333.71	-0.89
1643	49.49	339.20	-1.02
1644	49.59	334.95	-0.68
1645	54.15	188.86	-2.00
1646	54.53	183.15	-1.96
1648	55.00	169.51	-2.27
1649	52.83	160.92	-1.88
1650	57.11	159.09	-1.88
1651	61.06	170.60	-2.40

Table XXXIX-6 (contd)

Point	Latitude (φ'°)	W.Longitude (λ°)	Elevation (km)
1652	72.19	306.51	-1.02
1653	60.49	303.50	-1.37
1654	70.17	295.29	-0.56
1655	62.17	318.83	-1.44
1656	68.54	160.89	-2.14
1657	79.01	153.17	-1.02
1658	64.67	139.17	-1.42
1659	60.75	138.32	-1.32
1660	64.88	126.38	-0.97
1661	57.87	134.37	-1.04
1662	53.69	244.57	-1.52
1663	67.21	246.72	-1.39
1666	25.23	191.55	-1.39
1667	26.82	192.22	-1.39
1668	28.62	190.09	-1.49
1669	22.17	190.23	-1.38
1678	73.30	308.32	-0.74

References

XXXIX-1. de Vaucouleurs, G., "Charting the Martian Surface," *Sky and Tele-scope*, Vol. 30, p. 196, 1965.

XXXIX-2. de Vaucouleurs, G., *Research Directed Toward Development of a Homogeneous Martian Coordinate Syst.*, Final Report, AFCRL-69-0507, Air Force Cambridge Research Laboratories, 1969.

XXXIX-3. Davies, M. E., and Berg, R. M., *A Preliminary Control Net of Mars*, The Rand Corporation, RM-6381-JPL, November 1970; *J. Geophys. Res.*, Vol. 76, p. 373, 1971.

XXXIX-4. Davies, M. E., *Coordinates of Features on the Mariner 6 and 7 Pictures of Mars*, The Rand Corporation, R-896-NASA, October 1971; *Icarus*, Vol. 17, p. 116, 1972.

XXXIX-5. Davies, M. E., *Mariner 9 Control Net of Mars: August 1972*, The Rand Corporation, R-1122-JPL, October 1972.

XXXIX-6. Kliore, A. J, Cain, D. L., Fjeldbo, G., Seidel, B. L., Sykes, M. J., and Rasool, S. I., "The Atmosphere of Mars from Mariner 9 Radio Occultation Measurements," *Icarus*, Vol. 17, p. 484, 1972.

XXXIX-7. Gillespie, A. R., and Soha, J. M., "An Orthographic Photomap of the South Pole of Mars From Mariner 7," *Icarus*, Vol. 16, p. 522, 1972.

XXXIX-8. de Vaucouleurs, G., Davies, M. E., and Sturms, F. M., Jr., "Mariner 9 Areographic Coordinate System," *J. Geophys. Res.*, Vol. 78, 1973.

XXXIX-9. Sturms, F. M., Jr., *Polynomial Expressions for Planetary Equators and Orbit Elements With Respect to the Mean 1950.0 Coordinate System*, Technical Report 32-1508, Jet Propulsion Laboratory, Pasadena, Calif., 1971.

Acknowledgments

PRECEDING PAGE BLANK NOT FILMED

XXXX. *Mariner* 9 Areographic Coordinate System

Gerard de Vaucouleurs
Department of Astronomy
The University of Texas, Austin, Texas 78712
and
Lunar and Planetary Laboratory
University of Arizona, Tucson, Arizona 85721

Merton E. Davies
The Rand Corporation, Santa Monica, California 90401

Francis M. Sturms, Jr.
Jet Propulsion Laboratory/California Institute of Technology, Pasadena, California 91103

The television experiment of the *Mariner* 9 Mars orbiter has provided several thousand pictures of the planet with a resolution limit some 2 orders of magnitude smaller than the best Earth-based telescopic photographs. The large-scale (1:5,000,000) maps of the planet that are being prepared by the cartographic teams of the U.S. Geological Survey, Astrogeology Branch, in Flagstaff (topography) and of the University of Texas, Astronomy Department, in Austin (albedo), require a commensurate improvement in the definition of the areographic coordinate system used to locate features on the surface of Mars. It is the purpose of this section to explain and justify the redefinition of the Mars-centered system that has been developed by the Geodesy/Cartography Group of the *Mariner* 9 Television Team and adopted for future cartographic products. Early map products (distributed before November 1, 1972) were generally consistent with the current American Ephemeris system. We will also establish, insofar as is possible, the relations between this new "*Mariner* 9 cartographic system" (hereafter designated as the M9 system) and the traditional astronomical system embodied in the physical ephemeris of Mars as published in the current (British) Nautical Almanac and the American Ephemeris (hereafter designated as the NA3 system).

The fundamentals of the physical ephemeris of Mars have been presented by de Vaucouleurs in Ref. XXXX-1; the expressions adopted at the Jet Propulsion Laboratory for the planetary equators and orbits have been reported by Sturms in Ref. XXXX-2. Briefly, the areographic coordinates ϕ, latitude, and λ, west longitude, of a point P on Mars may be computed from the following input elements:

(1) Apparent coordinates (X, Y) of P at the instant t of observation with respect to the center O of the disk, the Y axis being the projection of the spin axis of the planet on a plane normal to the direction defined by the center of Mars and the observer, or in the case of the spacecraft the coordinates in

an "image plane" normal to the direction of the observation.

(2) Direction of the spin axis usually specified by the equatorial coordinates α_0, δ_0, of the north (celestial) pole of Mars for a fixed equinox.

(3) Direction of the observer with respect to the center of Mars in an inertial coordinate system (or equivalent celestial coordinates).

(4) Direction of the prime meridian on Mars at time t, usually specified by the longitude $\omega(t)$ of the central meridian with respect to the origin of areographic longitudes.

(5) Shape of the reference spheroid, usually defined by the ellipticity (flattening) $f = (a - c)/a$ of an ellipsoid of revolution whose polar axis c coincides with the spin axis.

We will re-examine each of these elements in the light of new information.

A. Apparent Coordinates

Consider first the case of telescopic observations; i.e., the orthographic projection of a spherical planet of radius R observed from a great distance (Fig. XXXX-1). We neglect here the effect of ellipticity discussed later. Let λ and ϕ be the planetocentric longitude and latitude of a point P of the surface, D the planetocentric latitude of the Earth, ω the longitude of the central meridian and
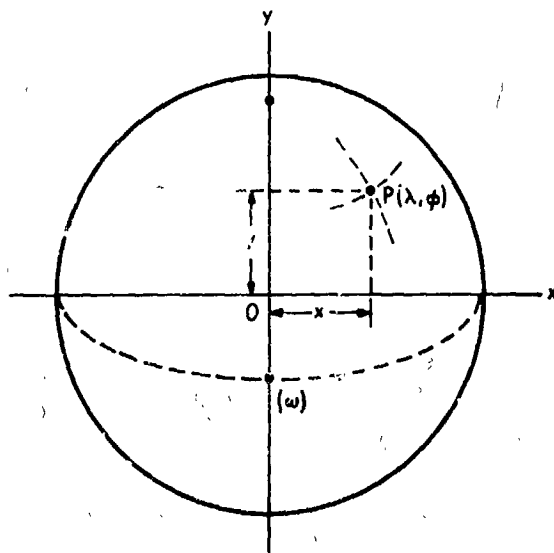

Fig. XXXX-1. Mars apparent coordinates for telescopic observations.

OX, OY the rectangular axes defined by the center of the disk O and the projection OY of the rotation axis. The rectangular coordinates of P are

$$X/R = \cos \phi \sin (\lambda - \omega)$$
$$Y/R = \sin \phi \cos D - \cos \phi \sin D \cos (\lambda - \omega)$$

(1)

X is positive with $\lambda - \omega$ in the astronomical system of areographic longitudes increasing westward on the planet, i.e., $O\vec{X} > 0$ toward the morning terminator in the case of Mars. (Longitudes reckoned in this traditional left-handed system, reaffirmed by Commission 16 of the IAU at its Brighton meeting in 1970, are more specifically labeled "west longitudes" in *Mariner 9* documents to avoid confusion with the east longitudes, increasing in the direction of rotation, used in some *Mariner 6* and *7* documents.)

Reference is made to earlier publications (Refs. XXXX-3 through XXXX-5) for a description of methods of measurement and reduction of areographic coordinates from Earth-based telescopic observations (visual or photographic). In general, the true precision of individual measurements (as derived from external errors) is lower than the original observers quoted, on the order of 3 to 4 degrees areocentric (mean error) for drawings, 2 to 3 degrees for photographs. Mean coordinates of secularly stable surface markings (albedo stations), based on all available telescopic data of the past 80 to 90 years and reduced to a homogeneous system, have nominal mean errors on the order of $0°.5$ to $1°$, depending on the number and quality of the observations and the character of the station (Ref. XXXX-5). Overall, the net formed by the ensemble of the best stations (about 100) may be said to represent the longitude system to within a few tenths of a degree (about 10 to 20 km on Mars). This, in turn, limits to a few milliseconds the precision with which the rotation period of Mars may be derived from the past century of observations; more generally, the relative precision is $\sigma_p/P \cong 10^{-2}/\Delta T$ if ΔT is the time base in centuries.

Consider next the case of spacecraft observations in which a picture of a small fraction of the planet is televised from an orbiter at close range (approx 10^3 to 10^4 km). At the Jet Propulsion Laboratory, the trajectory of the spacecraft is computed in a Mars-centered right-hand inertial coordinate system in which the axes are defined by mean Earth equator and the equinox of 1950.0 (Julian Ephemeris Date 2433282.4233577; Ref. XXXX-2). Conventional areocentric coordinates R, ϕ, λ (radius in kilometers, latitude, west longitude) are used to define the

position of a point on the surface of Mars. These *body-fixed* Mars-equatorial coordinates can be converted to the *celestial* Mars-equatorial system by use of the orthogonal matrix,[1] W, which is a simple rotation through the angle defined by the Mars prime meridian (the fixed system) and the Mars vernal equinox. In both systems, the third axis is in the direction of the planet's spin axis. The orthogonal matrix,[1] M, is used to rotate coordinates from the *celestial* Mars-equatorial system into the mean equinox and Earth equator of 1950.0 system. All of these coordinate systems have their origin at the center of Mars.

The television camera coordinate system has its origin at the principal point of the optics, with axes in the direction of the optical axis and the image plane pattern of reseau marks. If S_x, S_y, S_z are the Mars-centered rectangular coordinates of the spacecraft referred to the mean equinox and Earth equator of 1950.0, the camera coordinates (ξ, η, ζ) of a point P on Mars having areocentric coordinates (R, ϕ, λ) are given by

$$\begin{bmatrix} \xi \\ \eta \\ \zeta \end{bmatrix} = CMW \begin{bmatrix} R\cos\phi\cos(360° - \lambda) \\ R\cos\phi\sin(360° - \lambda) \\ R\sin\phi \end{bmatrix} - C \begin{bmatrix} S_x \\ S_y \\ S_z \end{bmatrix} \quad (2)$$

The matrix C rotates the axes from the 1950 Earth-equatorial system to the camera image-plane coordinate system. Further details can be found in Ref. XXXX-6. The coordinates (x_c, y_c) of this point P in the focal plane of the camera are:

$$x_c = \frac{\xi}{\zeta} f, \quad y_c = \frac{\eta}{\zeta} f \quad (3)$$

where f is the focal length of the lens. The subscript c indicates computed values of x, y on the assumption that M, W, R, S_x, S_y, S_z are known.

B. Spin Axis

The axis of rotation of Mars in current use in the American Ephemeris is defined by the celestial coordinates of its north pole referred to a fixed equinox, viz.

$$\alpha_0 = 316°.55, \delta_0 = 52°.85 \quad \text{(Equinox 1905.0)}$$

being the average of determinations from the poles of satellite orbits (Ref. XXXX-7) and from the paths of

selected surface markings (Ref. XXXX-5). Details of the discussion of these and other determinations were given by de Vaucouleurs in Ref. XXXX-1. This mean value, recommended by IAU Commission 4 in 1964 and Commission 16 in 1967 (IAU Transactions Vol. XIIB, p. 105, 1966, and Vol. XIIIB, p. 94, 1968), has been adopted by the American Ephemeris Office for the physical ephemeris of Mars since 1968. A revised ephemeris for the years 1877 to 1967 was also computed in the same system at the U. S. Naval Observatory (Ref. XXXX-9). This change in the pole from the previously adopted values (317°.5, −54°.5) introduced the current (NA3) system. All other constants remained the same as those used between 1960 and 1967 (NA2 system). The constants used in the physical ephemeris of Mars between 1869 and 1967 were tabulated by de Vaucouleurs (Ref. XXXX-1).

New determinations of the spin axis of Mars made by several methods during the *Mariner 9* flight and a new solution from all telescopic observations of the natural satellites from 1877 to 1969 have recently appeared. The excellent agreement illustrated by Table XXXX-1 gives confidence that the mean values

$$\alpha_0 = 317°.32, \delta_0 = +52°.68 \quad \text{(Equinox 1950.0)}$$

adopted on March 28, 1972, at a meeting of the *Mariner 9* Geodesy/Cartography Group are probably correct within a few minutes of arc. The individual determinations in Table XXXX-1 have estimated uncertainties of 0°.05 to 0°.1 and agree with one another within 0°.08 in α and 0°.15 in δ.

The shift of the pole location in celestial coordinates from that adopted in the NA3 system is $\Delta\alpha\cos\delta = +0°.29$ and $\Delta\delta = -0°.32$. The corresponding change in the inclination I of the planet's equator to the plane of its orbit is from 24°.94 to 25°.20 (1950).

1. Remarks on Precession Corrections

The combination of the Earth and Mars polar motions leads in the first-order (i.e., linear) approximation to total variations (per year) of approximately $+0°.00675$ in α_0, and $+0°.00346$ in δ_0 for the NA3 pole (Ref. XXXX-1, p. 239). Slightly incorrect values ($+0°.006533$ and $+0°.003542$, respectively) were used in the American Ephemeris volumes of 1968 to 1970 and in the revised ephemeris for 1877 to 1967 (Ref. XXXX-3). Fortunately, the cumulative errors are too small ($<0°.02$ per century) to be of consequence for the reduction of past Earth-based observations. The correctly recomputed rates ($+0°.006750$ and $+0°.003479$, respectively) have been

---

[1] Defined in Ref. XXXX-2 as functions of basic constants, $W \equiv V^T$, $M \equiv A^T$.

Table XXXX-1. Equatorial coordinates of Mars pole for 1950.0[a]

Method	α	δ	Ref.
Sixth-degree harmonic model radio pole, four revolutions tracking data	317.32 ($\pm$0.2)	52.63 ($\pm$0.2)	XXXX-14
Eighth-degree, radio pole, 38 revolutions tracking data	317.29 ($\pm$0.15)	52.78 ($\pm$0.15)	XXXX-14
Landmark tracking in south polar area; revolutions 1-38	317.32 ($\pm$0.2)	52.71 ($\pm$0.1)	XXXX-14
Star Deimos TV observations	317.37 ($\pm$0.2)	52.77 ($\pm$0.2)	XXXX-15
Control net of surface topographic features (133 stations south of –30°; revolutions 97–152)	317.37 ($\pm$0.15)	52.67 ($\pm$0.1)	—[b]
Phobos and Deimos (3107 telescopic observations 1877–1969)	317.31 ($\pm$0.65)	52.65 $\pm$0.3	XXXX-16
Recommended values	317.32	52.68	

[a]Referenced to mean equator and equinox of 1950.0. Error estimates are in parentheses.

[b]Davies, M. E., personal communication, 1972.

incorporated in the American Ephemeris beginning with the 1971 volume. Over long periods of time, the linear expansions of the precession corrections are increasingly inaccurate and, furthermore, the Earth lunisolar precession rates are more precisely known than the smaller Mars solar precession rate. To avoid the small, but unnecessary, errors due to linear approximations of the Earth's precession, the following procedure, illustrated in Fig. XXXX-2, was adopted. The NA3 pole at 1905.0 was brought forward to 1950.0 with the correct linear precession rates, to establish a new reference. Thereafter, values of the pole coordinates are computed in the 1950.0 system, using only the rates from the Mars' precession (Ref. XXXX-2):

$$\alpha_o(1950.0) = 316.8538 - 0.0996T$$

$$\delta_o(1950.0) = 53.0966 - 0.0566T$$

where T is measured in Julian Centuries from JD 2433285.5. Conversion of values from the above expressions to equator-of-date coordinates using precise Earth precession differ from the linear NA3 expressions by 0°.00013 in α and 0°.00044 in δ for dates during the Mariner 9 mission. Nonlinearity in the Mars' precession rates (T^2 terms) are negligible, amounting to less than 10^{-5} degrees in 50 years. These constants were adopted in the orbit geometry computer program used at the Jet Propulsion Laboratory during the Mariner 9 mission and are reflected by the preliminary Mariner 9 cartography.

Similarly, the revised pole adopted for the post-mission Mariner 9 mapping is at:

$$\alpha_o(1950.0) = 317°.32 - 0°.1011T$$

$$\delta_o(1950.0) = +52°.68 - 0°.0570T$$

where the Mars precession rates (per Julian Century) have been revised accordingly. Additional parameters resulting from the new pole are:

(1) Inclination of the Mars equator to the Mars orbit

$$i = 25°.19969 + 0.01219T + 0.00006T^2$$

(2) Angle along the Mars equator from the 1950.0 Earth equator to the Mars autumnal equinox[2]

$$\Delta_{50} = 42°.93538 - 0.09040T - 0.00010T^2$$

(3) Angle from the Mars vernal equinox to the Mars prime meridian (computed with the current NA definition of Mars longitudes)

$$V = 148°.766801 + 350°.891962 \, (JD - 2433282.5)$$

C. Direction of Observing Station

For an Earth-based observer the direction of observation is fixed with a high degree of precision by the relative orbital positions of Mars and Earth at the time of observation, with allowance for light-travel time from Mars to Earth. This information is derived from the basic

[2]Δ_{50} is equivalent to Δ in Sec. 11G of the Explanatory Supplement to the American Ephemeris, except that it is measured from 1950.0 Earth equator rather than the equator of date. Also $\Delta \equiv \pi - \theta$ in Ref. XXXX-1.
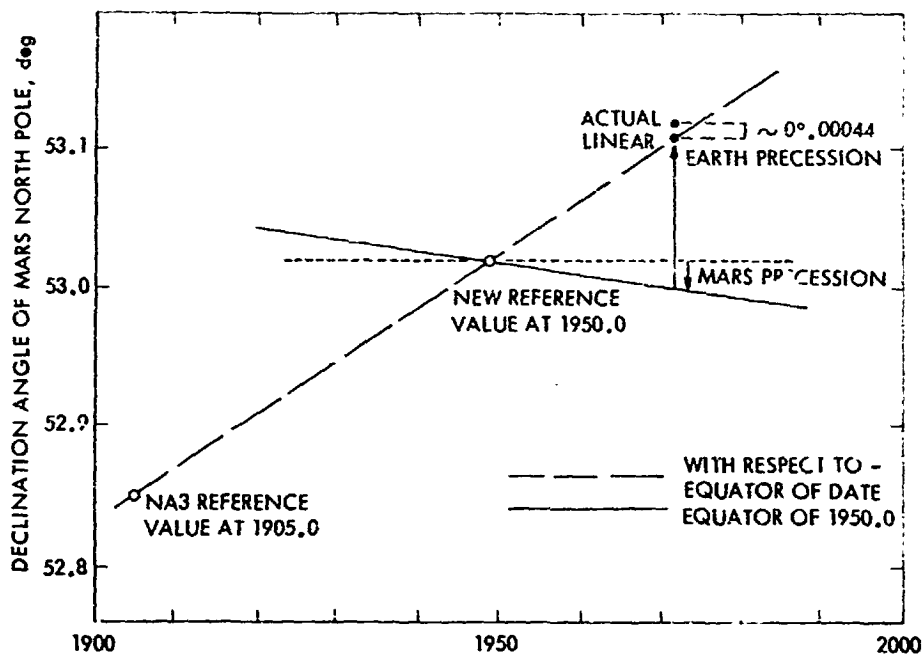
Fig. XXXX-2. Method for deriving new pole expressions.

theories of planetary motions through available tables of rectangular heliocentric coordinates of the planets in an inertial frame of reference (see explanatory supplement to the American Ephemeris, pp. 16, 17) and is eventually expressed in the orbital ephemeris by the geocentric apparent celestial coordinates of the center of mass of the planet at a given instant of ephemeris time. The remaining errors in tables of planetary motions ($<1''$), in the negligible errors ($<0°.01$) in the derived areographic current (extrapolated) value of $ET - UT (<1 s)$ and the usual neglect of the parallactic correction introduce coordinates of the center of the disk. At this point of the surface of Mars, the Earth is at the zenith at the instant of reflection.

In the case of a planetary orbiter, the corresponding concept is the sub-spacecraft point, the point where the straight line from the center M of Mars to the spacecraft crosses the surface of the planet. The precision with which this point is defined for *Mariner 9* depends on the location of the spacecraft on its elliptical orbit (whether near periapsis or near apoapsis) and on the precision of the orbital radio tracking. Navigation data suggest that in general the orbit periapsis may be located to within ±5 km (along the orbit), and the time of passage of the spacecraft at periapsis may be determined to within ±1 sec. The location of the spacecraft itself on the orbit is defined to some ±3 km (in each of the three coordinates) and about ±0.1 sec. The corresponding errors of

the sub-spacecraft point are on the order of ±0°.05 near periapsis (about 1200 km above the surface) and correspondingly smaller values at greater areocentric distances.

The direction of observation does not usually coincide with the sub-spacecraft point, but is defined by the cone and clock angles of the scan platform on which the television cameras and other instruments are mounted. Because of deadband limitations and other factors, the direction of the scan platform or, more specifically, of the optical axis of the cameras is not known a priori to better than ±0°.25—a large angle compared with the $11° \times 14°$ and $1° \times 1°.4$ fields of view of the wide- and narrow-angle cameras. This initial uncertainty is greatly reduced, however, by using information contained in the pictures, as is done in computing the control net.

The control net is formed by selecting a few topographic features, perhaps two to ten, on each frame, which can be located on two or preferably more frames. The most common feature chosen is a crater, and the control point is defined as the center of the crater. The positions of these points on the frames are measured in "pixel" (picture elements) units. The pixel measurements are corrected for optical and electronic distortions and transformed into coordinates in millimeters referred to the focal plane of the camera. Corrections and the lens focal length are derived from preflight calibration of the television camera (Ref. XXXX-10).

With a large set of points and measurements, we can solve for many unknown parameters by standard photogrammetric procedures. The *Mariner 9* computations are designed to solve for the latitude and longitude of the control points and the camera pointing angles when the frames were taken. The radii at the control points are derived from those measured by the occultation experiment, and the spacecraft's positions when the pictures were taken are furnished by the JPL Navigation Team.

The procedure for solving for the unknowns is an iterative one in which corrections to approximate values of the parameters are found. Measured coordinates (x_o, y_o) exist for each point on each picture, and coordinates (x_c, y_c) can be computed for each point on each picture using Equations (2) and (3) and starting with approximate values of the unknown parameters (P_k). Then the observation equations can be written

$$x_{o.ij} - x_{c.ij} = \sum_{k=1}^{n} \frac{\partial x_{c.ij}}{\partial P_k} \Delta P_k \qquad (4)$$

$$y_{o.ij} - y_{c.ij} = \sum_{k=1}^{n} \frac{\partial y_{c.ij}}{\partial P_k} \Delta P_k \qquad (5)$$

where the subscripts i index the points on the picture j [e.g., $(x_o, y_o)_{ij}$ are measured coordinates of the i-th point on the j-th picture]. The differential corrections, ΔP_k, can be found by solving the normal equations corresponding to these observation equations by standard least-squares procedures. If the starting values of the variable parameters are fairly good, the iteration converges rapidly. This method of establishing a control net for Mars was first used with *Mariner 6* and *7* pictures (Ref. XXXX-6) and later with *Mariner 9* pictures (Refs. XXXX-11 and XXXX-12; also see Section XXXIX of this Report).

The random errors associated with the solution of the control net computation are rather small, perhaps 5 to 10 km in horizontal position and perhaps 0°.01 to 0°.02 in determining the direction of the camera's optical axis. The systematic errors are most difficult to estimate; however, they might increase the horizontal position error to 10 or 15 km, or 0°.2.

D. Prime Meridian and Rotation Period

The prime meridian (0° longitude) was initially defined by Schiaparelli in 1877 as passing through the center of Sinus Meridiani (Dawes Forked Bay on many maps of

1864–1877) following the lead of Beer and Mädler who first used this spot, marked *a* on their 1837 map, as an origin. For some years after 1877, the physical ephemeris of Mars, computed by Marth until 1896, and by Crommelin after 1898, attempted to maintain this definition through successive changes of the input constants of the ephemeris (for details see Table I in Ref. XXXX-1). However, after 1896 and especially after 1909 when the (British) Nautical Almanac and the American Ephemeris began publishing the physical ephemeris of Mars, the original definition was virtually abandoned and the main concern was the continuity of the ephemeris.

This is the correct approach because there is an inherent conflict between the two possible methods of definition: either the zero meridian is defined *ne varietur* by a specific, fixed surface feature (the equivalent of Greenwich Observatory Meridian on Earth), or the zero is defined by an auxiliary angle fixing the direction of the prime meridian at some initial epoch and its direction at any later time is carried forward from a knowledge of elapsed ephemeris time and an assumed value of the angular rotation velocity of Mars. In the latter case, if the rotation period adopted in the ephemeris is in error by ΔP, the areographic longitude λ of a surface feature will appear to drift slowly with time; that is, $\lambda = \lambda_0 + B(t - t_0)$ and the drift rate B is related to the error ΔP through

$$\Delta P = -6.91B$$

where ΔP is expressed in milliseconds and B in areocentric degrees per century. An error of 0.007 sec in P will cause a drift of 1° per century in the longitudes. Clearly it is not possible, except by fortunate accident, to maintain over long periods of time the coincidence between longitudes measured from a fixed surface feature and longitudes measured by elapsed time. The frequent changes in the constants of the Mars ephemeris between 1869 and 1909 illustrate the point (Table I in Ref. XXXX-1).

The ephemeris makers wisely decided in 1909 that it was more important to maintain the continuity of the ephemeris and that, henceforth, the zero point of the areographic longitude system would be defined by the condition that on January 15, 1909, at noon, Greenwich Mean Time, that is, on January 15.5 Universal Time or Julian Day JD 2418322.0, the longitude of the central meridian of Mars, observed from Earth, was $\omega_0 = 344°.41$. This definition has remained in effect unchanged to the present time throughout the vicissitudes of several sub-

sequent changes in the other basic constants of the Mars ephemeris (for details see Ref. XXXX-1). The net result of this definition and of these changes is that the current longitude of the center of Sinus Meridiani, and of the south point of the dividing feature called Fastigium Aryn, is about 357° in the NA3 system, but it would have been closer to 358° in 1909 and in the NA1 system in use between 1909 and 1959. The difference arises mainly through the change in the ephemeris rotation period adopted since 1960 (see below). In either case, the longitude of Sinus Meridiani is definitely different from the 0° value intended by the nineteenth century observers and t is incorrect to show it centered at 0° as it still is on too many Mars charts, and, regrettably, on the de Mottoni map of 1958 published in IAU Transactions, Vol. X.

The *sidereal* rotation period of Mars adopted in the ephemeris between 1909 and 1959 was $P_1 = 24^h37^m22^s.6542$ of mean solar time which corresponds to an angular velocity $R_1 = 350°.89202$ per mean solar day. These same values had been in use since 1896 in the Marth and Crommelin ephemerides. The pole coordinates were changed in 1909, however, and as stated in the Nautical Almanac for 1909, "As the adoption of a new position for Mars' North Pole involved a discontinuity in that ephemeris, the longitude at the beginning of the ephemeris has been made as if the former value had been continued" (Appendix, p. 48). Note that the *sidereal* period is referred to the vernal equinox of Mars which precesses about 7 arc sec/yr; hence the true rotation period of Mars with respect to inertial axes is 0.0012 sec longer than the sidereal period. The difference is smaller than the uncertainty in current estimates of that period, but the distinction will become significant in the future.

A new determination of the rotation period by Ashbrook (Ref. XXXX-13) from meridian transit observations, $P_2 = 24^h37^m22^s.6689 \pm 0^s.0026$ (m. e.) of Ephemeris Time and corresponding to an angular velocity $R_2 = 350°.891962$ per 24 hr of Ephemeris Time was adopted by the American Ephemeris and used in the physical ephemeris since 1960. The change $\Delta P = P_2 - P_1 = +0.015$ sec introduced a cumulative difference $\Delta\omega_0 = -0°.0212t - 1909.04)$ in the longitude of the prime meridian amounting to about 1° at the beginning of 1960.

As noted previously, when revised coordinates for the pole were introduced in 1968 no change was made in P_2, and a revised physical ephemeris going back to 1887 was recomputed in this new NA3 system so that all areographic coordinate data could be reduced to a uniform homogeneous system (Refs. XXXX-1, XXXX-3, and XXXX-5).

Specifically the longitude of the central meridian is given in this system by

$$\omega = (V - 180°) - (A_E - 180°) - 2.026612 D_y$$

where D_y is the Earth–Mars distance in astronomical units, and

$$V + 180° = (V_o + 180°) + 350°.891962 (JD - 2418322.0)$$

with $V_o = 149°.475$, for the areocentric hour angle of the equinox (Ref. XXXX-9).

A consistent expression was used in the orbit geometry computer program during the *Mariner 9* standard mission. Toward the end of the mission, however, new determinations of the pole and of the rotation rate became available. The pole coordinates have been discussed in earlier paragraphs.

Corrections to the ephemeris rotation period have been recently derived from:

(1) All series of visual and photographic areographic coordinate measurements from 1877 to 1958 reduced to the current NA3 system in the Harvard-Texas Mars Map Project (Refs. XXXX-3 through XXXX-5).

(2) All meridian transit observations from 1877 to 1971 reduced to the same system.

(3) A comparison of coordinates of about 80 albedo stations measured on *Mariner 6* and 7 pictures with their standard coordinates for epoch 1909 as derived in (1).

All three approaches are in good agreement to give a drift rate coefficient $B \cong -2°.0$ per century and indicating that the current ephemeris rotation period P_2 is too long by about 14 msec, that is a corrected sidereal rotation period $P_3 = 24^h37^m22^s.655$ with an uncertainty of a few milliseconds. Note that P_3 agrees exactly with the value P_0 derived by Wislicenus in 1886 from telescopic observations between 1659 and 1881, and it is very nearly (within 0.001 sec) equal to the value P_1 in ephemeris use between 1909 and 1959. We may, therefore, conclude that $P_3 = P_0$ is the best available estimate of the mean rotation period of Mars in the past 3 centuries and that no further improvement is likely to appear for quite some time.

We may also presume that this revised value of P, together with the new determination of the pole of Mars, will eventually be incorporated in the physical ephemeris (NA4 system).

Nevertheless, even with these improvements the inherent characteristics of a system of areographic longitudes based on elapsed time and rotation rate would remain, leading to further revisions and changes in the system. The *Mariner 9* Geodesy/Cartography Group proposes that the prime meridian of Mars be redefined by a fixed topographic feature, namely the center of a small, nearly circular crater, and more precisely the center of the circle best fitting the horizontal projection of the ridge line of the crater walls.

A suitable crater was selected at a special meeting of the Geodesy/Cartography Group on August 14, 1972, by H. Masursky and two of the authors (G. de Vaucouleurs, M. Davies), on a high-resolution narrow-angle picture of the Sinus Meridiani area specially taken for this purpose by *Mariner 9* on August 6, 1972. Criteria for the selection of the crater whose center would define the 0-degree meridian were:

(1) The new longitudes would not differ greatly from current *Mariner 9* longitudes.

(2) The diameter of the crater should be small, of the order of 1 km.

(3) It should be geometrically related to a large crater which would be easily recognized on low-resolution pictures.

The crater chosen is seen on narrow-angle picture camera frame, DAS 13165361 (MTVS 4296-118, -119, -120). It is about ½ km in diameter and lies within a large distinctive crater which has a secondary crater breaking its southern rim. This large crater is easily seen on *Mariner 6* wide-angle frames 6N11 and 6N13 and *Mariner 9* wide-angle pictures MTVS 4164-90, DAS 06499678; MTVS 4166-45, DAS 06571008; MTVS 4212-51, DAS 08045768; and MTVS 4296-111, DAS 13165256. It is proposed that the large crater be named Airy[3] and the small 0° Meridian crater be named Airy-0 (Fig. XXXX-3). The larger crater "Airy" is visible near longitude 359°.8, −4°.9 on the USGS preliminary topographic Mars chart. The precision with which the center of this crater is defined on present

[3]Sir George Biddell Airy was the Astronomer Royal (Director of Greenwich Observatory) from 1835 to 1881 and installed the transit instrument which was used to define the 0° meridian on Earth (adopted in 1884).

Mariner 9 pictures is about 0.05 km or 0°.001 areocentric. In the future, when higher-resolution pictures become available, this point could be located to a higher degree of precision, if required, by refinements in the definition of the geometric center. We believe that the choice of this crater center fixes the prime meridian of Mars with a potential precision of 0.01 km or better, which should suffice to serve the needs of astronomy and of the space program in the foreseeable future.

The areographic coordinate system used in *Mariner 9* mapping products (control net, topographic and albedo charts) is based on this new definition of the prime meridian. It is recommended that the same coordinate system be used to locate the results of other *Mariner 9* experiments.

As mentioned previously, the angle from the Mars vernal equinox to the Mars prime meridian in the current NA definition of longitudes is

$$V = 148°.766801 + 350°.891962 \, (JD - 2433282.5)$$

Computation of the control net during November 1972 (Ref. XXXX-12; also see Section XXXIX of this Report) using the crater (Airy-0) definition of the prime meridian gives the angle with the vernal equinox as

$$V = 148°.68 + 350°.891962 \, (JD - 2433282.5)$$

Correcting for the improved rotation period, the hour angle becomes

$$V = 148°.24 + 350°.892017 \, (JD - 2433282.5)$$

Improved values of the constant term in this expression will come from later control net computations.

E. Reference Spheroid

If the surface of a planet is an oblate spheroid of semi-axes a, c with $a > c$, the *planetocentric* latitude ϕ, defined by the radius CP (Fig. XXXX-4), and the *planetographic* latitude ϕ'', defined by the normal to the spheroid PN, are related through

$$\tan \phi = \left(\frac{c}{a}\right)^2 \tan \phi'' = (1 - f)^2 \tan \phi''$$

The difference $\phi'' - \phi$ is zero at the equator and the poles; it is maximum for $\phi \simeq 45°$, where $\phi'' - \phi \simeq f$.
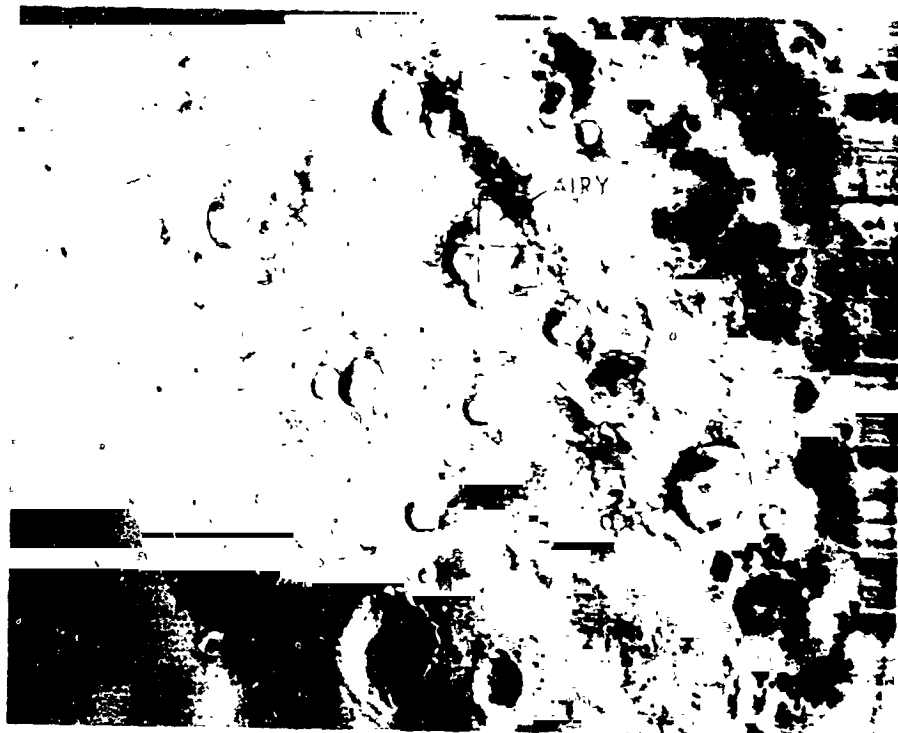
Fig. XXXX-3. The prime meridian passes through the center of the small crater Airy-0 shown in the high-resolution picture. Airy-0 lies within the large crater Airy which is shown above in a low-resolution picture. (Top) MTVS 4296-111, DAS 13165256. (Bottom) MTVS 4296-118, DAS 13165361.
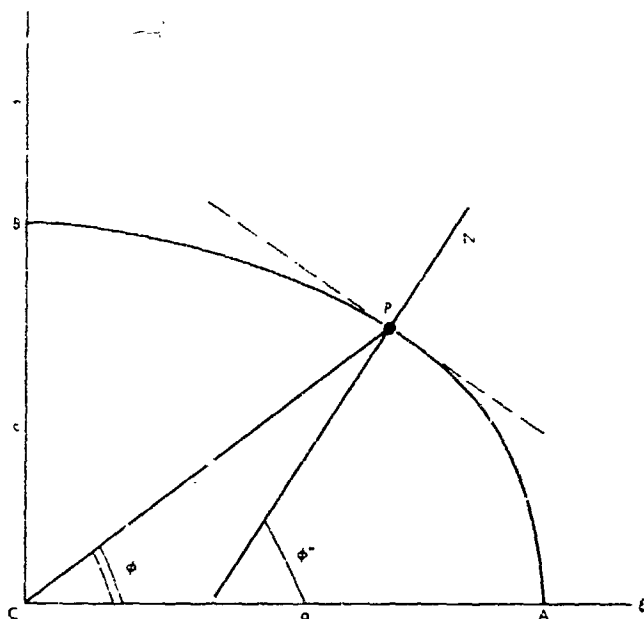
Fig. XXXX-4. Planetocentric latitude ϕ and planetographic latitude ϕ'' on the reference spheroid.

In the case of Mars the correct value of f applicable to the surface was long in doubt, either the dynamical value $f_d = 0.0052$ or the optical value $f_o = 0.0105$ (Ref. XXXX-1). The maximum difference between areographic and areocentric latitudes (near $\phi \simeq \phi'' \simeq 45°$) is $\phi'' - \phi \simeq f \simeq 0.6$ for f_o and 0.3 for f_d (note that $1°$ of latitude corresponds to about 60 km at the surface of Mars). *Mariner 9* data confirmed both f_o and f_d. The higher optical value reflects the accumulation of mountains and high plateaus in the equatorial regions as indicated by the radio occultation experiment; the lower dynamical value refers to the average internal density distribution as derived from the orbital motions of the natural and artificial satellites.

After extensive discussions of the new evidence on the shape of the planet (occultations, radar, equipotential and isobaric surfaces) and considering the needs of various mapping applications, the Geodesy/Cartography Group decided at its meetings of July 15, 1971, and March 28, 1972 to recommend the following sets of constants:

(1) For *surface mapping* (topography and albedo areographic coordinates should be projected along the normal on to the spheroid having a circular equator of radius ($a = b = R_e$)

$$R_e = 3393.4 \text{ km}$$

and a semi-polar axis ($c = R_p$)

$$R_p = 3375.8 \text{ km}$$

corresponding to the dynamical ellipticity $1/192$. *Areographic* latitudes (ϕ'') should be used (not areocentric) to conform with usage on terrestrial maps and to better serve the needs of future Mars landers for which the local vertical will be a natural reference direction.

(2) *Elevations* of stations in the control net will be initially measured with respect to the reference spheroid until a satisfactory planet-wide reference surface (the equivalent of the geoid, possibly a triaxial ellipsoid) is defined from a combination of sources (ultraviolet and infrared photometry, radio occultations, Earth-based radar, etc.).

Preliminary *Mariner 9* map products were based on computed areocentric coordinates at the point where the optic path intercepts a *spherical* reference figure for Mars. The intercept point on a reference ellipsoid would in general have slightly different values of radius, latitude, and longitude. For near-vertical viewing used for mapping, these differences are on the order of $0.1°$ in latitude and longitude, which is negligible compared to the uncertainties of the initial uncontrolled mosaics and maps.

As explained above, the final *Mariner 9* map products will be based on a control net that is independent of the initial computed coordinates based on a spherical planet.

References

XXXX-1. de Vaucouleurs, G., *The Physical Ephemeris of Mars*, The Rand Corporation, RM-3999-NASA, Jaunary 1964, and *Icarus*, Vol. 3, p. 236, 1964.

XXXX-2. Sturms, F. M., Jr., *Polynomial Expressions for Planetary Equators and Orbit Elements with Respect to the Mean 1950.0 Coordinate System*, Technical Report 32-1508, Jet Propulsion Laboratory, Pasadena, California, 1971.

XXXX-3. de Vaucouleurs, G., "Precision Mapping of Mars," in *La Physique des Planetes*, Mem. Soc. R. Sci. Liege, 5° Serie, Tome VII, Liege, p. 369, 1963.

XXXX-4 de Vaucouleurs, G., "Charting the Martian Surface," *Sky and Telescope*, Vol. 30, p. 196, 1965.

XXXX-5. de Vaucouleurs, G., *Research Directed Toward Development of a Homogeneous Martian Coordinate System*, Final Report Contract No. F19628-67-C-0416, Air Force Cambridge Research Laboratories, Office of Aerospace Research, USAF, Bedford, Mass., No. AFCRL-58-0507, 221 pp., 1969.

XXXX-6. Davies, M. E., *Coordinates of Features on the Mariner 6 and 7 Pictures of Mars*, The Rand Corporation, R-896-NASA, October 1971, and *Icarus*, Vol. 17, p. 116, 1972.

XXXX-7. Burton, H. E., "Elements of the Orbits of Satellites of Mars," *Astron. J.*, Vol. 39, p. 155, 1929.

XXXX-8. Camichel, H., "Détermination Photographique du Pôle de Mars, de son Diamètre et des Coordonnées Areographiques," *Bulletin Astronomique*, Vol. 18, p. 83, 1954; Vol. 20, p. 131, 1956.

XXXX-9. Meiller, V., *Physical Ephemeris of Mars 1877–1967*, U. S. Naval Observatory Circular No. 98, 1964.

XXXX-10. Snyder, L. M., *Mariner 9 TV Subsystem Calibration Report*, Internal Document 610-62, Jet Propulsion Laboratory, Pasadena, California, 1971.

XXXX-11. Davies, M. E., *Mariner 9 Control Net of Mars: August 1972*, The Rand Corporation, R-1122-JPL, October 1972.

XXXX-12. Davies, M. E., and Arthur, D. W. G., "Martian Surface Coordinates," *J. Geophys. Res.*, Vol. 78, 1973.

XXXX-13. Ashbrook, J., "A New Determination of the Rotation Period of Mars," *Astron. J.*, Vol. 58, p. 145, 1953.

XXXX-14. Born, G. H., Christensen, E. J., Mohan S. N., Jordan, J. F., and Duxbury, T. C., *Determination of the Mars Spin Axis Direction From Mariner 9*, paper presented at meeting of the AAS, Planetary Sciences Division, Hawaii, March 20–24, 1972.

XXXX-15. Born, G. H., and Duxbury, T. C., *Determination of the Orbits of Phobos and Deimos from Mariner 9*, paper presented at meeting of the AAS, Planetary Sciences Division, March 20–24, 1972.

XXXX-16. Sinclair, A. T., "The Motions of the Satellites of Mars," *Monthly Notices Royal Astron. Soc.*, Vol. 155, p. 249, 1972.

PRECEDING PAGE BLANK NOT FILMED

XXXXI. Photogrammetric Evaluation of
Mariner 9 Photography[1]

S. S. C. Wu, F. J. Shafer, G. M. Nakata, and Raymond Jordan
U.S. Geological Survey, Flagstaff, Arizona 86001

K. R. Blasius
Division of Planetary and Geological Sciences
California Institute of Technology, Pasadena, California 91109

This section discusses some attempts to produce, with an AP/C analytical plotter, stereo models using *Mariner 9* pictures. The first attempt using geometrically uncorrected mission test video system (MTVS) imagery failed; the second, using corrected reduced data record (RDR) pictures also failed, probably because they were reconstructed through a vidicon display which introduces additional distortion. By using images obtained from RDR tape data through the Optronics Photowrite device, models were successfully obtained.

By using a histogram of grey levels of each picture, the contrast can be adjusted by computer before the picture is reconstructed. This allows a selection of different contrasts to permit more detail for the purpose of photogrammetric measurements. However, as the spacing between consecutive picture elements from which the pictures are constructed is 50 μm, resolution is equivalent to only 20 lines per millimeter. Even though distortions still exist in the picture, the geometry of the pictures

reconstructed through the Optronics Photowrite device is a significant improvement over those reconstructed using a vidicon display.

For a preliminary scientific evaluation of the photogrammetric application and geologic study of pictures from the *Mariner 9* mission, three models were set up in the AP/C analytical plotter at the Center of Astrogeology in Flagstaff, Arizona. Two models were from the wide-angle camera (medium resolution), with a 52.267-mm focal length; and one from the narrow-angle camera (high resolution), with a 500.636-mm focal length.

Because the *Mariner 9* mission was not specifically planned for making three-dimensional photogrammetric measurements, in most cases models could be constructed only by combining pictures that were taken from camera stations in different orbits. As a consequence, the pictures of the stereo model have different flight heights, different appearance of the same surface area caused by shadowing effects from different Sun angles, and very unusual model geometry. Setting up these models called for spe-

cial unconventional photogrammetric procedures that were developed using the latest mission support data.

The first models selected were of prominent features on the Martian surface which would be of obvious geologic interest. Contour maps were compiled from three models: two wide-angle camera models that cover Nix Olympica and South Spot, and one model of the narrow-angle camera photography covering the canyonland area of the Martian surface.

High-altitude characteristics of the photography and limitations of the plotter geometry made it impossible to apply corrections for curvature to models of the wide-angle photography. Therefore, contour maps of Nix Olympica and South Spot do not represent their true relief. However, curvature correction was applied to profiles of these areas by an off-line PDP-11 computer. The true ground relief of these prominent features can be determined from these profiles. Because these pictures were taken from such a high altitude, displacements due to ground relief are so insignificant that the pictures can be rectified through perspective projection to correlate with contour maps compiled from the unrectified pictures.

A. Preliminary Photogrammetric Evaluation

Because photography from the *Mariner* 9 mission is quite unconventional and because there are no ground control data, the usual photogrammetric methods and procedures cannot be applied in setting up models. Instead, special techniques and procedures have been developed using the mission support data. These developments, as well as the results for the preliminary photogrammetric evaluations, are described in the following paragraphs.

B. Procedures for Setting up Models on the AP/C Plotter

Most models of the *Mariner* 9 photography can be formed only by pictures taken from different orbits (as shown in Fig. XXXXI-1). If C_1 and C_2 are the two camera stations of the convergent photography and N_1 and N_2 are their nadir points, respectively, it is easier to obtain a model when the principal line N_1P_1, which contains the principal point and the nadir point of the left picture (P_1), is set along the X-axis of the plotter and when the model zero coordinates are set at the principal point. It is advantageous to prepare initial orientation parameters in which both BY and ω of the left picture (P_1) are zero.
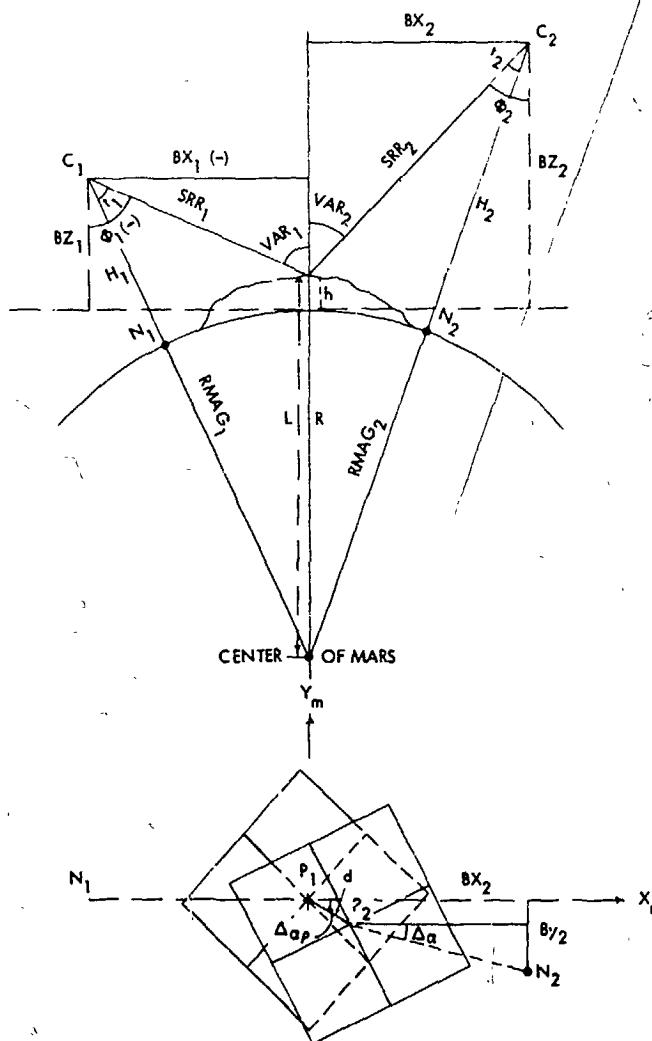

Fig. XXXXI-1. Geometric configuration for setting up models on the AP/C analytical plotter.

The longitudinal Φ of P_1 is simply equal to VAR_1, which is VAR-5 in the supplementary experiment data record (SEDR) of P_1 (the angle between the local vertical and the direction of the spacecraft). Other parameters of P_1 can be determined as:

$$BX_1 = (SRR\text{-}Q)(\sin VAR_1) \qquad (1)$$

$$BZ_1 = (SRR\text{-}Q)(\cos VAR_1) + h \qquad (2)$$

where SRR-Q in the SEDR data is the slant range from the camera station to the principal point.

The determination of the initial parameters of the right picture (P_2) is almost the same as P_1, as the principal line of P_2 is coincident with the principal line of P_1. However, this is usually not the case, as is shown in the lower part

of Fig. XXXXI-1. The procedure used in determining the initial parameters of P_2, in this case, is to use the given longitudes and latitudes of the principal point and the nadir point of each picture. From these, it is possible to find the azimuth of N_1P_1, P_1P_2, and P_2N_2. Then $\Delta\alpha\rho$ and $\Delta\alpha$, which are the differences between N_1P_1 and P_1P_2, and N_1P_1 and P_2N_2, respectively, can be determined. Then:

$$BX_2 = [(SRR\text{-}Q)\,(\sin VAR_2)]\cos\Delta\alpha + d\cos\Delta\alpha\rho \quad (3)$$

$$BY_2 = [(SRR\text{-}Q)\,(\sin VAR_2)]\sin\Delta\alpha + d\sin\Delta\alpha\rho \quad (4)$$

$$BZ_2 = (SRR\text{-}Q)\,(\cos VAR_2) + h \quad (5)$$

$$\phi_2 = \arctan (BX_2/BZ_2) \quad (6)$$

$$\omega_2 = \arctan (BY_2/BZ_2) \quad (7)$$

where $SRR\text{-}Q$ in the SEDR data is the slant range from camera station 2 to the principal point of P_2, and VAR_2 is the local zenith at the principal point of P_2 as is explained for P_1; d is the distance between the two principal points which can be determined from given coordinates of each point.

Parameters for each picture should be reduced to the model scale which can be taken as the photo scale at the principal point of P_1, and determined approximately as:

$$S_p = \frac{f_1(1 - \tan t_1/2 \sin t_1)}{H_1 - h_1} \quad (8)$$

where

$$H_1 = RMAG1 - R \quad (9)$$

$RMAG$ in the SEDR data is the slant range from the spacecraft to the center of Mars; t_1 is the tilt angle (QST in the SEDR data); and R is the radius of Mars at the nadir point of P_1. This is determined as:

$$R = A\,(1 - F\sin^2\phi) \quad (10)$$

where

A = the semi-major axis of Mars = 3393.4 km

F = 0.0052, the flattening of Mars

ϕ = latitude at the nadir point.

h_1 = elevation at the principal point of P_1, which can be ignored when comparing with H_1

Once all initial parameters are prepared, the AP/C plotter is used for the relative orientation.

It should be mentioned that, as there are no ground control points for an absolute orientation, the model is scaled by the given coordinates of the two principal points or other reseau marks. Leveling of the model is usually done arbitrarily by using the initial parameters of P_1 as a guide.

C. Results

The pictures used for the stereo model processing on the AP/C are reconstructed from the Optronics Photowrite at approximately $3.8\times$ magnification. Information for the pictures is listed in Table XXXXI-1.

The base-to-height ratios of the convergent photography from the wide-angle camera are generally larger than 0.5. This gives a stronger geometric configuration for the model from which better heighting measurements can be obtained. Therefore, the repeatability of elevation readings from the model is better than expected.

As listed in Table XXXXI-1, the standard errors of elevation measurements are obtained by making three

Table XXXXI-1. Photography and stereo model data

Camera		Wide-angle		Narrow-angle
Model		Nix Olympica[a]	South spot[b]	Canyonland[c]
Slant range to the center of Mars, km		5582 6356	5252 5116	5123 5321
Tilt angle, deg		7.06 12.91	15.89 3.00	2.08 18.40
Base-to-height ratio		0.89	0.53	0.37
Standard error of elevation (km) measurements	Range	0.021 to 0.064	0.025 to 0.127	0.029 to 0.061
	Average	0.043 (6)	0.078 (5)	0.043 (5)
Model scale		1:10,800,000	1:9,300,000	1:920,000

[a]Pictures used for this stereo pair are MTVS 4133-93, DAS 05492378 and MTVS 4174-93, DAS 0682x)18.

[b]Pictures used for this stereo pair are MTVS 4224-51, DAS 08441904 and MTVS 4182-45, DAS 07038748.

[c]Pictures used for this stereo pair are MTVS 4191-42, DAS 07326763 and MTVS 4273-11, DAS 10132929.

readings at each point without moving in the X and Y directions. These measurements are obtained for five or six such points in each model, as indicated in parentheses.

Figure XXXXI-2 is a contour map of Nix Olympica which was compiled at an original scale of 1:1,000,000 with a contour interval of 2 km; Fig. XXXXI-3 is the contour map of South Spot at an original scale of 1:1,000,000 with a contour interval of 1 km. As both models have scales smaller than 1:1,000,000, curvature correction was not possible on the AP/C plotter because of program limitations. Therefore, the true relief of these two features is expressed in profiles taken approximately along north–south and east–west directions. Elevations indicated in the parentheses are curvature-corrected; numbers preceding the parentheses are uncorrected. Because

the curvature corrections of the horizontal distances are insignificant, as shown by Equation (11), only elevation corrections were made, according to Equation (12):

$$C_H = D^2/6R^2 \tag{11}$$

$$C_t = D^2/2R \tag{12}$$

where D is the horizontal distance from the principal point and R is the radius of Mars.

Therefore, from the attached profiles we find that Nix Olympica, at latitude 19.0°N and longitude 134.2°, has a relief of about 23 km. South Spot, located at latitude −8.4°S and longitude 121.6°, has a relief of at least 7 km.
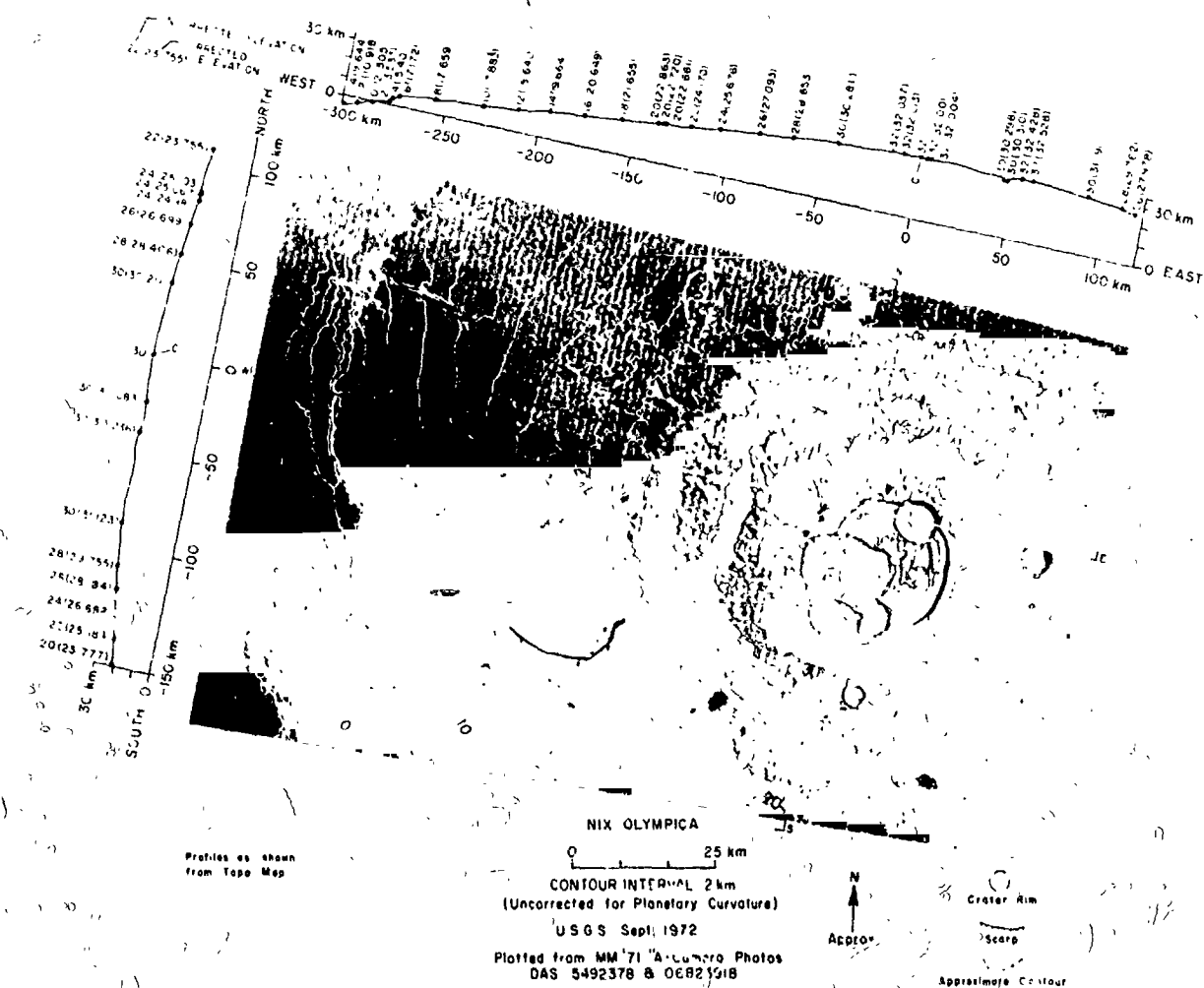

Fig. XXXXI-2. Photo map (curvature corrected) of Nix Olympica (original scale, 1:1,000,000) constructed from wide-angle pictures MTVS 4133-93, DAS 05492378 and MTVS 4174-93, DAS 06823918. Photo base was rectified picture MTVS 4133-93, DAS 05492378.
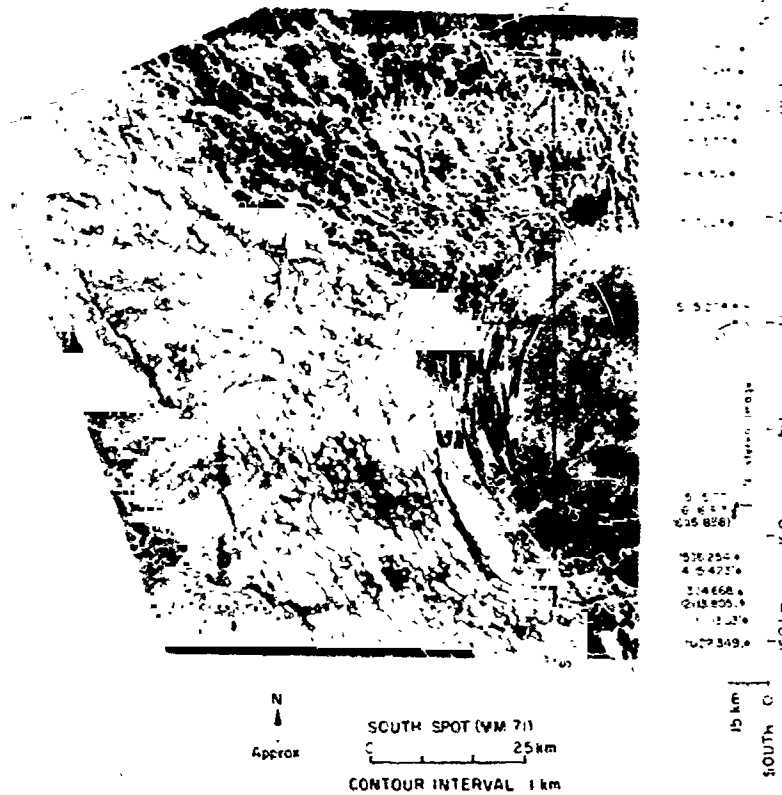
Fig. XXXXI-3. Photo map (curvature uncorrected) and profiles (curvature corrected) of South Spot (original scale, 1:1,000,000) constructed from wide-angle pictures MTVS 4224-51, DAS 08441904 and MTVS 4182-45, DAS 07038748. Photo base was rectified picture MTVS 4182-48, DAS 07038748.

Figure XXXXI-4 is a contour map of a small part of the Martian canyonland area. The original map was compiled at a scale of 1:100,000 with a primary contour interval of 400 m and with 200-m supplemental contours. As it is possible to correct curvature for scales larger than 1:1,000,000, this contour map expresses the true relief of this 4.5-km region. The area is located at latitude −7.3°S and longitude 87.0°.

Figures XXXXI-2 through XXXXI-4 show contour lines superimposed on pictures rectified in two stages with a Bausch & Lomb rectifier. Because of the high tilts, a two-stage rectification was necessary.

It should be noted that the datum for each contour map is arbitrarily set because of the lack of ground control data.

D. Conclusions

The main conclusion reached from this photogrammetric evaluation is that *Mariner 9* RDR data can be processed through an Optronics Photowrite system, which introduces a minimum amount of distortion. Imagery from both the wide- and narrow-angle cameras can be used to obtain topographic information by photogrammetric methods. Because of unconventional geometric conditions, however, the imagery can be processed only by applying special techniques and procedures and using advanced analytical plotters such as the AP/C, AS-11-A and AS-11-B.

The elevation reading repeatability of a specific image point in the model has produced unpredictable results (see Table XXXXI-1). The measurements may not repre-

sent accurately the heighting capability of the photography because of the pixel-by-pixel composition of the imaged terrain. However, it is our opinion that, with further improvement in the picture such as adjustment of the image contrast by computer methods and a favorable Sun angle on flat terrain, a contour interval of 500 m from the wide-angle and 100 m from the narrow-angle camera may be feasible. If this can be accomplished, *Mariner 9* photography will provide significant photogrammetric measurements for the Viking lander.

FHEL V∩ARY TOPO MAP AAS COMPILED
CH AM.C PLOTTER FLAGSTAFF,ARIZONA
.S∩G PHOTOS 07376763 10132929
B CAMERA CURVATURE CORRECTED

MARS "CANYONLANDS"

0 ————————— 6 km

CONTOUR INTERVAL 400 meters

— — — SUPPLEMENTAL CONTOUR (200 M)
C CRATER RIM
X SPOT ELEVATION

Fig. XXXXI-4. Photo map of canyonland (original scale, 1:100,000) constructed from narrow-angle pictures MTVS 4191-42, DAS 07326763 and MTVS 4273-11, DAS 10132929. Photo base was rectified picture MTVS 4191-42, DAS 07326763.

XXXXII. A Study of Martian Topography by Analytic Photogrammetry[1]

Karl R. Blasius

Division of Planetary and Geological Sciences
California Institute of Technology, Pasadena, California 91109

When the television experiment for the Mariner Mars 1971 Project was planned, the stereometric potential of the television cameras was ignored in favor of scientific objectives that required only single pictures or multiple coverage without a requirement of different viewing perspectives (Ref. XXXXII-1).

However, as the mission developed, with one spacecraft instead of two and with a severe dust storm obscuring surface features, a re-evaluation was required, and much day-to-day improvisation was necessary. As a result, early in the mission we obtained significant multiple photographic coverage of the few surface features that were relatively clear of intervening dust. In the equatorial regions of Mars, four of these features proved to be great volcanic shields with local relief on the order of tens of kilometers. This discovery, coupled with the availability of many overlapping pictures, made photogrammetry from *Mariner 9* pictures an exciting possibility.

While the mission was still in the planning stage, it was realized that the potential for photogrammetry might exceed original expectations, so an analytic routine was prepared to test the quality of any potential stereo pairs for determining relative relief of point features seen in two pictures taken from sufficiently different camera stations (see Appendix). This technique now has yielded several stereo models of surface features of great geologic interest and has demonstrated the potential of the *Mariner 9* pictures for construction of contoured topographic maps through the use of stereo plotters. This latter work is in progress and its first results are now being published (Ref. XXXXII-2; also see Section XXXXI of this Report). This section discusses the photogrammetric potential of *Mariner 9* data and the analytically determined topography of certain Martian landforms.

A. Precision of Relief Measurements

The photographic phenomenon which allows height measurement from photography is termed "relief displace-
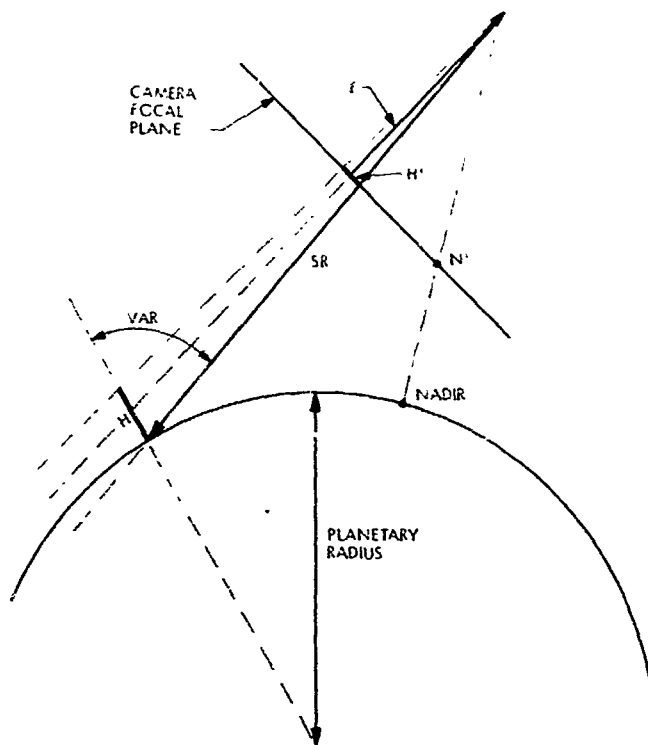

Fig. XXXXII-1. Basic elements of the geometry of an oblique planetary-scale picture in the principal plane (the plane containing the nadir and the camera axis).

ment." Referring to Fig. XXXXII-1, in which an object, "H," of height H imaged by a camera of focal length f is represented, we see that the image of the top of "H" is formed at a point farther from the nadir image, N', than is the image at the foot of "H." The distance, H', between these two image points is the relief displacement of the top of "H" due to its elevation. If "H" is imaged within a small angle of the camera axis[2], these quantities are approximately related by the equation:

$$H = \frac{H'}{\sin(VAR)} \frac{SR}{f} \qquad (1)$$

where SR is the slant range of the camera from the feature, and VAR is the viewing angle at the feature measured from the local vertical. If we take partial derivatives of Equation (1), we obtain an equation for small changes, ΔH, in any relief determination in terms of small changes in the other quantities:

$$\Delta H = C_0 \Delta H' + C_1 \Delta f + C_2 \Delta SR + C_3 \Delta VAR \qquad (2)$$

---

[2]This is a very good approximation for the *Mariner* cameras, whose angular fields are only $1°1$ by $1°4$ and $11°$ by $14°$.

where

$$C_0 \equiv \frac{SR}{f \cdot \sin(VAR)}$$

$$C_1 \equiv \frac{-H'}{\sin(VAR)} \frac{SR}{f^2}$$

$$C_2 \equiv \frac{H'}{\sin(VAR)} \frac{1}{f}$$

$$C_3 \equiv \frac{-H' \cdot \cos(VAR)}{\sin^2(VAR)} \frac{SR}{f} \qquad (3)$$

The quantities whose variations are shown in Equation (2) to contribute to ΔH fall into two distinct categories according to their effect on a stereo model. Many determinations of H' go into the construction of a single stereo model, so random errors in the measurement process may appear as inconsistencies in the derived topography (see Appendix). Errors in f, SR, or VAR, on the other hand, create an overall model scaling error. We shall find that predicted random errors in H' account well for the inconsistencies observed in the stereo models and should dominate the effects of errors in f, SR, and VAR in wide-angle *Mariner* 9 photography.

For a sample error analysis, consider the simple case where one picture of a pair was taken from an oblique perspective (the case of Fig. XXXXII-1), and the other was taken from a vertical perspective ($VAR = 0$). In Table XXXXII-1, typical values of the parameters of Equation (1) are given for the members of such a *Mariner* 9 picture pair. The uncertainties in some of the quantities on the right-hand side of Equation (1) can be estimated from work performed by Jet Propulsion Laboratory (JPL) scientists. Preflight calibration data (Ref. XXXXII-2) gives one-sigma uncertainties in the focal lengths as listed in Table XXXXII-1.

In creating a self-consistent stereo model (see Appendix) the slant range, SR, may have to be changed from the nominal value for one of the pictures, so the unchanged SR of the other picture sets the scale for the model. The basic quantities involved in calculating SR are the radius of the planet R, the range to the planet's center $RMAG$, and the tilt angle of the camera axis away from the direction to the planet's center. For the small tilt angles of our examples (less than 20° for the oblique pictures) the probable error in SR, ΔSR, is due to ΔR, and $\Delta RMAG$. Both preflight and postflight analyses agree that there is a 5-km (1-σ) uncertainty in calculated values of $RMAG$ at periapsis. This error scales approximately as a constant

**Table XXXXII-1. Typical values of photogrammetric parameters associated with
Mariner 9 pictures of the Martian surface**

Camera	SR, km	$f(\pm 1\sigma)$, mm	VAR, deg	H, km	H' derived using Equation (1), mm
Wide angle	2×10^3	52.267 ± 0.006	30	5	6.25×10^{-2}
Narrow angle	2×10^3	500.636 ± 0.036	30	5	6.25×10^{-1}

percentage of *RMAG*. For the largest values of *RMAG* that affect our models, we find $\underline{\Delta}RMAG = 8$ km.

Estimating Mars' radius at any location is a very subjective matter, as preliminary and scattered data must be combined from several sources such as *Mariner 9* occultation and spectrometer experiments and Earth-based radar data. Based on such an informal procedure, we estimate a probable error of 5 km in the assumed values of Mars' radius. Combined with the value of $\underline{\Delta}RMAG$ given above, we find $\underline{\Delta}SR \simeq 10$ km.

A JPL study of the precision of the spacecraft pointing angles from the positions of ground features in repeated photography concluded that they were generally accurate to better than 0.1°. This translates into a $\underline{\Delta}VAR$ of about 0.1° for each photo of our sample stereo model, since they were not taken from extreme altitudes or extremely oblique perspectives. The total $\underline{\Delta}VAR$ for a model, assuming the errors are uncorrelated, is then approximately 0.15°.

The uncertainty in H' is related to the accuracy with which the distance between point features can be determined in the camera focal plane. Two factors are involved here: the spatial resolution of the cameras and the geometric fidelity of the processed pictures. There is no single figure for spatial resolution, as this characteristic is a function of the contrast of the target scene. A discussion of this problem in connection with photography from spacecraft is contained in a recent paper (Ref. XXXXII-1). For this error analysis, I use a spatial resolution of 0.027 mm corresponding to a high-contrast target such as a steep-walled crater illuminated by a Sun low in the sky. The point features to be located are the centers of such resolved features. This is easily done to an accuracy of 0.007 mm. (The point features chosen to construct the stereo models presented later in this section closely approximate this ideal.) The derivation of one elevation requires the location of four image points, the same pair of features in two pictures. H' is then derived from the difference in the image distances between that pair of features.

The geometric fidelity of the pictures is a complicated problem that involves the preflight measurement of electronic and optical distortions created by the cameras and their removal from returned pictures. A detailed discussion of this procedure is now in preparation (Ref. XXXXII-3). In part of the calibration routine, a square grid of lines was used. Accurate determinations of the coordinates of about 400 intersections on that grid can be compared with their coordinates on a geometrically corrected image of the grid. (It is believed that there are several uncalibrated sources of systematic, but small, errors in the image coordinates.) For both *Mariner 9* cameras, the RMS separation of the actual intersection positions from their images is less than 0.004 mm. If we assume that this figure can be applied to the *Mariner 9* pictures generally, we can estimate the probable error for a single point feature position determination, $\underline{\Delta}P'$, by combining the effects of picture resolution and geometric distortion:

$$\underline{\Delta}P' \approx [(0.007)^2 + (0.004)^2]^{1/2} = 0.008 \text{ mm} \qquad (4)$$

Picture resolution is the dominant source of error here. The uncertainty in H', due to four such determinations, is estimated as:

$$\underline{\Delta}H' \approx [4(\underline{\Delta}P')^2]^{1/2} = 0.016 \text{ mm} \qquad (5)$$

Using the foregoing estimates of the parameters in Equation (1) and their probable errors, the terms of the right-hand side of Equation (2) may be evaluated to check their relative importance. Table XXXXII-2 lists their calculated values. It is clear that the first term is by far the most important for wide-angle photography; errors due to $\underline{\Delta}H'$, primarily due to photo resolution, should dominate over the three sources of error in overall model scale. Elevation differences in this model would have to be stated with "±1300 m" independent of their magnitude.

For the narrow-angle photography, $\underline{\Delta}VAR$ should result in an uncertainty in elevation differences of about 4.5% (225 m in 5000 m) in addition to "±130 m" due to $\underline{\Delta}H'$.

Table XXXXII-2. Calculated values from evaluation of terms of right-hand side of Equation (2)

Camera	Coefficient	Probable error	Contribution to probable error in $H = 5000$ m
Wide angle	$C_0 = 8 \times 10^7$	$\underline{\Delta}H' \approx 0.016$ mm	$C_0\underline{\Delta}H' = 1280$ m
	$C_1 = 10^5$	$\Delta f(1\sigma) = 0.006$ mm	$C_1\underline{\Delta}f = 0.6$ m
	$C_2 = 2.5 \times 10^{-3}$	$\Delta SR \approx 10$ km	$C_2\underline{\Delta}SR = 25$ m
	$C_3 = 8.6 \times 10^3$ m	$\Delta VAR \approx 0.°15$	$C_3\underline{\Delta}VAR = 225$ m
Narrow angle	$C_0 = 8 \times 10^6$	$\underline{\Delta}H' \approx 0.016$ mm	$C_0\underline{\Delta}H' = 128$ m
	$C_1 = 10^4$	$\Delta f(1\sigma) = 0.036$ mm	$C_1\underline{\Delta}f = 0.36$ m
	$C_2 = 2.5 \times 10^{-3}$	$\Delta SR \approx 10$ km	$C_2\underline{\Delta}SR = 25$ m
	$C_3 = 8.6 \times 10^3$ m	$\Delta VAR \approx 0.°15$	$C_3\underline{\Delta}VAR = 225$ m

A shortened form of Equation (2), including only the term due to $\underline{\Delta}H'$, can be used to predict the scatter of relief determinations, $\underline{\Delta}H$, in our stereo models:

$$\underline{\Delta}H \approx \frac{SR}{f \cdot \sin(VAR)} 1.6 \times 10^{-5} \text{ meters} \quad (6)$$

A slight elaboration of the meaning of Equation (6) must be added. $\underline{\Delta}H$ calculated by Equation (6) applies to a stereo picture pair consisting of one picture taken from a vertical perspective and a second from an oblique perspective. If, instead, we have the more general case of two oblique pictures with the camera stations lying in a vertical plane at the target on opposite sides of the target,
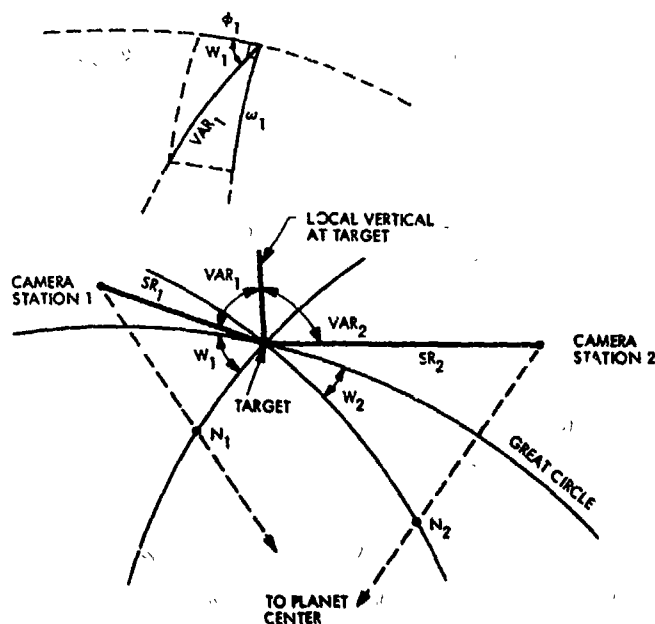

Fig. XXXXII-2. Geometry of two camera stations from which a stereo pair of oblique pictures may be taken. The breakdown of the viewing angle, VAR_1, into perpendicular components is illustrated. Only ϕ_1 contributes to relief determinations.

the cumulative relief displacement in the two pictures (subscripts 1 and 2) is:

$$H'_T \equiv H'_1 + H'_2 \quad (7)$$

where, from Equation (1):

$$H'_1 \equiv H \cdot \sin(VAR_1) \cdot \frac{f_1}{SR_1}$$

$$H'_2 \equiv H \cdot \sin(VAR_2) \cdot \frac{f_2}{SR_2} \quad (8)$$

Thus, H and $\underline{\Delta}H$ are given by more general forms of Equations (1) and (6):

$$H = \frac{H'_T}{\left[\frac{f_1}{SR_1} \cdot \sin(VAR_1) + \frac{f_2}{SR_2} \cdot \sin(VAR_2)\right]} \quad (9)$$

$$\underline{\Delta}H = \frac{1.6 \times 10^{-5}}{\left[\frac{f_1}{SR_1} \cdot \sin(VAR_1) + \frac{f_2}{SR_2} \cdot \sin(VAR_2)\right]} \text{ meters} \quad (10)$$

In the most general case, the camera stations of a stereo pair do not lie in a plane intersecting the ground target vertically. Then only the components of VAR_1 and VAR_2 in a vertical plane at the target contribute to relief determinations. In Fig. XXXXII-2, we represent the ground target, the camera stations, and the ground trace, labeled "GREAT CIRCLE," of a vertical plane through the target. We now find the components of VAR_1 and VAR_2 in this plane. This is most easily done using a well known identity for right spherical triangles. In Fig. XXXXII-2 the two perpendicular components of VAR_1 are designated ϕ_1 (in our vertical plane) and ω_1 (opposite angle W_1). ϕ_1 is given by:

$$\tan(\phi_1) = \tan(VAR_1) \cos(W_1) \quad (11a)$$

similarly:

$$\tan(\phi_2) = \tan(VAR_2) \cos(W_2) \quad (11b)$$

By using Equations (1), (6), (11a), and (11b), we obtain generalized forms of (1) and (6):

$$H = \frac{H'_T}{\left[\frac{f_1}{SR_1} \cdot \sin(\phi_1) + \frac{f_2}{SR_2} \cdot \sin(\phi_2) \right]}$$ (12)

$$\underline{\Delta}H = \frac{1.6 \times 10^{-5}}{\left[\frac{f_1}{SR_1} \cdot \sin(\phi_1) + \frac{f_2}{SR_2} \cdot \sin(\phi_2) \right]} \text{ meters}$$ (13)

Table XXXXII-3 lists predicted errors in H for stereo models presented in the next part of this section. These were calculated using Equation (13).

B. Stereo Models

The topography of a number of interesting Martian landforms has been derived using our analytic technique of photogrammetry (see Appendix). This report has two purposes: the validation of the technique and a demonstration of the quality of the data for a more thorough analysis. We confine ourselves here to a minimum of geologic interpretation. Such interpretation and speculation is the continuing work of this author and many others both inside and outside the Mariner Mars 1971 Project.

The essentials of our first two stereo models, designated Model I and Model II, are displayed pictorially in Fig. XXXXII-3, a photomosaic of a large volcanic cone with a central crater. This feature has been named "Middle Spot," a reference to its two similar neighbors to the northeast and southwest and its dark dot-like appearance on low-resolution pictures of Mars taken early in the Mariner 9 mission. Centers of circles in Fig. XXXXII-3

mark point features whose elevations have been determined analytically. Using four pictures, we have been able to establish two independent stereo models of Middle Spot. Elevations in kilometers are given in parentheses next to the circles as (I, II), derived from Model I and Model II, respectively. One point has been chosen arbitrarily as zero elevation for both models. The photo identification numbers and other information concerning the models are given in Table XXXXII-3. The column labeled "Observed general error in model elevations" contains a figure that is half the largest spread of values for the relief between two points. The sample in a model was always too small to calculate a meaningful formal error such as a standard deviation, so this estimate was adopted. Note that, for most models, this figure is within a factor of 2 of the predicted error. $\underline{\Delta}H$.

A validation of the analytic technique is the essential agreement of independent stereo models except for a general tilt of one model relative to the other. This is demonstrated to be the case for Models I and II by the profiles in Fig. XXXXII-4. The 15-13 section of each profile is approximately perpendicular to the remainder, so we are able to estimate the two components of the relative tilt of the models. From the general error for model elevations given in Table XXXXII-3, we have calculated the slope differences and uncertainties along the profile. These are listed in Table XXXXII-4. We observe that Model II disagrees with Model I only by a relative tilt of about 1°2 to the west around the 13-5 axis and 1°2 to the north about the 13-15 axis.

Let us now turn our attention to other profiles of Middle Spot in Fig. XXXXII-5. The low slopes on the flanks of the cone and the total relief of about 10 km point to the

Table XXXXII-3. Stereo models of Martian topography presented in this section

Model	Photomap Figure	Feature	Approximate location		Photo DAS time	Camera focal length, mm	Observed general error in model elevations, m	ΔH Predicted error calculated from Equation (13), m
I	XXXXII-3	Middle Spot	0°5N	113°W	3858340	500.64		
					8585894	52.267	200	300
II	XXXXII-3	Middle Spot	0°5N	113°W	4402135	52.267		
					7111128	52.267	400	700
III	XXXXII-6	Residual south polar cap	86°3S	356°W	6029803	500.64		
					8331829	500.64	300	120
IV	XXXXII-6	Residual south polar cap	86°8S	5°W	5741963	500.64		
					7791983	500.64	300	130
V	XXXXII-7	Nix Olympica	18°N	133°W	5492378	52.267		
					6823918	52.267	1000	1350
VI	XXXXII-8	Intra-trough ridge	7°3S	87°1W	10132929	500.64		
					7326763	500.64	90	130

Fig. XXXXII-3. A mosaic of the Martian volcanic shield "Middle Spot." The pictures have been rectified to a vertical perspective. Point elevations (in kilometers) in parentheses have been determined by analytic photogrammetry from Models I and II (I, II). (MTVS 4184-54, DAS 07111128; MTVS 4184-60, DAS 07111198)

basaltic shield volcano as the closest terrestrial analog. A group of basaltic shields, the island of Hawaii stands approximately 10 km above the sea floor, and unmodified slopes range from 2° to 12° (Ref. XXXXII-4). The central crater of Middle Spot, approximately 47 km across, is, however, much larger than those associated with early shield volcanoes. For example, the summit caldera of Mauna Loa measures only 2.4 × 4.8 km.

A second pair of overlapping stereo models, on the residual south polar cap, is presented in Fig. XXXXII-6. Figure XXXXII-4 contains profiles common to these two models. Again we can account for the differences in the profiles with a simple tilt of one model relative to the other. The axis of the tilt appears to run through points 36 and 1.

The residual south polar cap is an area of surface frost observed to persist through the southern hemisphere summer in 1971–1972. The dark strips of defrosted terrain running through the cap suggest that the underlying materials are the same as those of a very widespread polar geologic unit now designated "laminated terrain" (Ref. XXXXII-5). The name is derived from the narrow
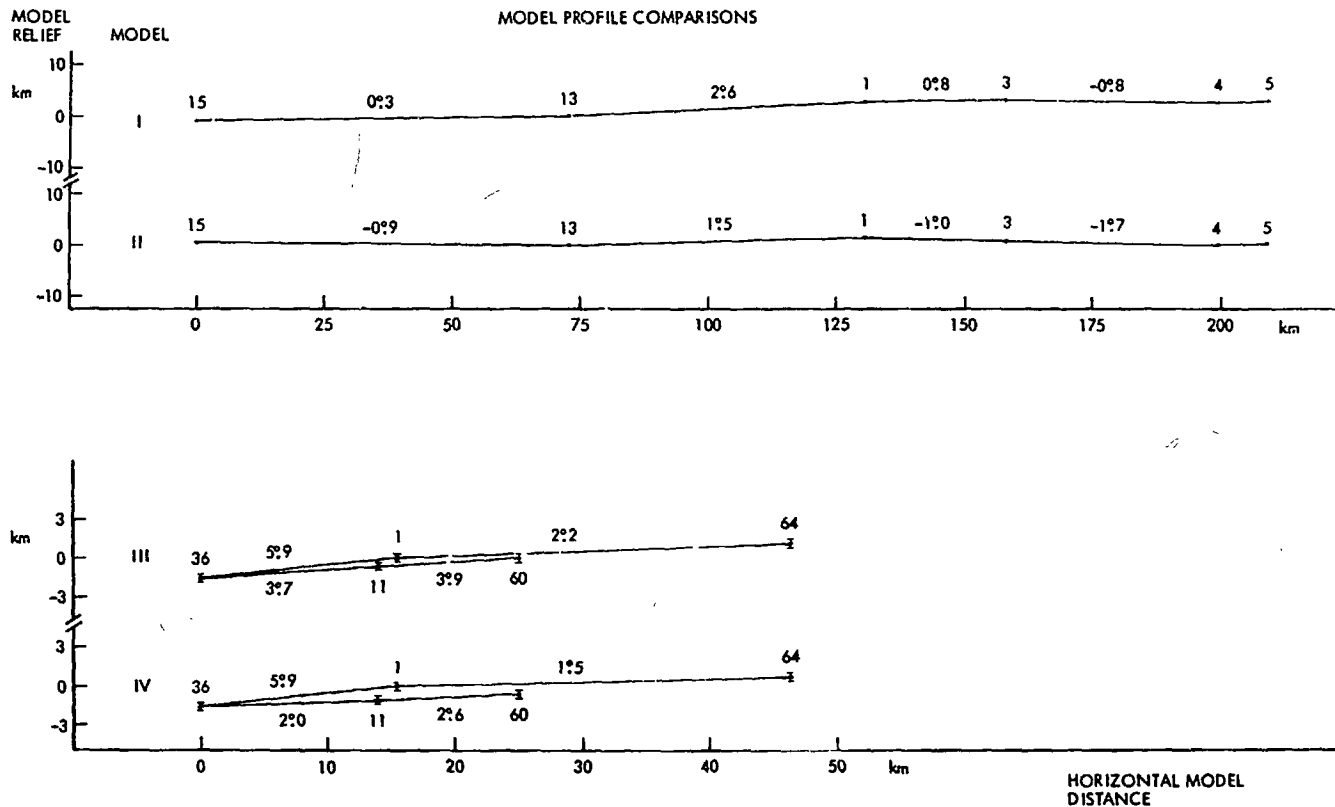
Fig. XXXXII-4. Vertical profiles for comparison of independent stereo models on Middle Spot (Models I and II) and the residual south polar cap (Models III and IV).

Table XXXXII-4. Systematic differences in topography between Models I and II

Profile section	Slope		Slope difference = relative tilt of models
	Model I	Model II	
13–15	$0°3 \pm 0°2$	$-0°9 \pm 0°3$	$1°2 \pm 0°4$
13–1	$2°6 \pm 0°2$	$1°5 \pm 0°3$	$1°1 \pm 0°4$
1–3	$0°8 \pm 0°4$	$-1°0 \pm 0°8$	$1°8 \pm 0°9$
3–4	$-0°8 \pm 0°3$	$-1°7 \pm 0°5$	$0°9 \pm 0°6$

parallel bands which seem to follow the contours of the topography. On pictures of the region of Fig. XXXXII-6, which have been specially processed to bring out detail in the dark areas, it is possible to see eight bands in the wide defrosted strip to the east and three bands on the narrow strip in the southwest. If these bands represent stratified geologic units, it becomes important to estimate the total relief across a defrosted strip to place some constraints on the depositional process. We will attempt this for the narrow defrosted strip using the profiles for Model IV in Fig. XXXXII-5.

Because surfaces of equal elevation in our topographic model differ from such surfaces on Mars only by a small tilt, we can estimate the relief across the dark strips only if we systematically untilt straight profiles through at least three points. For example, profile 65–69–92 is shown in Fig. XXXXII-5. Points 65 and 69 lie on one side of the strip and point 92 lies on the other. We assume that points 65 and 69 lie in the same horizontal surface and then project that surface on to point 92, which is calculated to lie 175 m below that reference level. This assumption of very low relief in the continuously frosted area is justified by systemic changes in slope observed on profiles crossing both defrosted strips. Relief across the narrow strip has been calculated for four profiles (see Table XXXXII-5). The stereo model indicates a slope downward toward the southwest with relief on the order of 200 m.
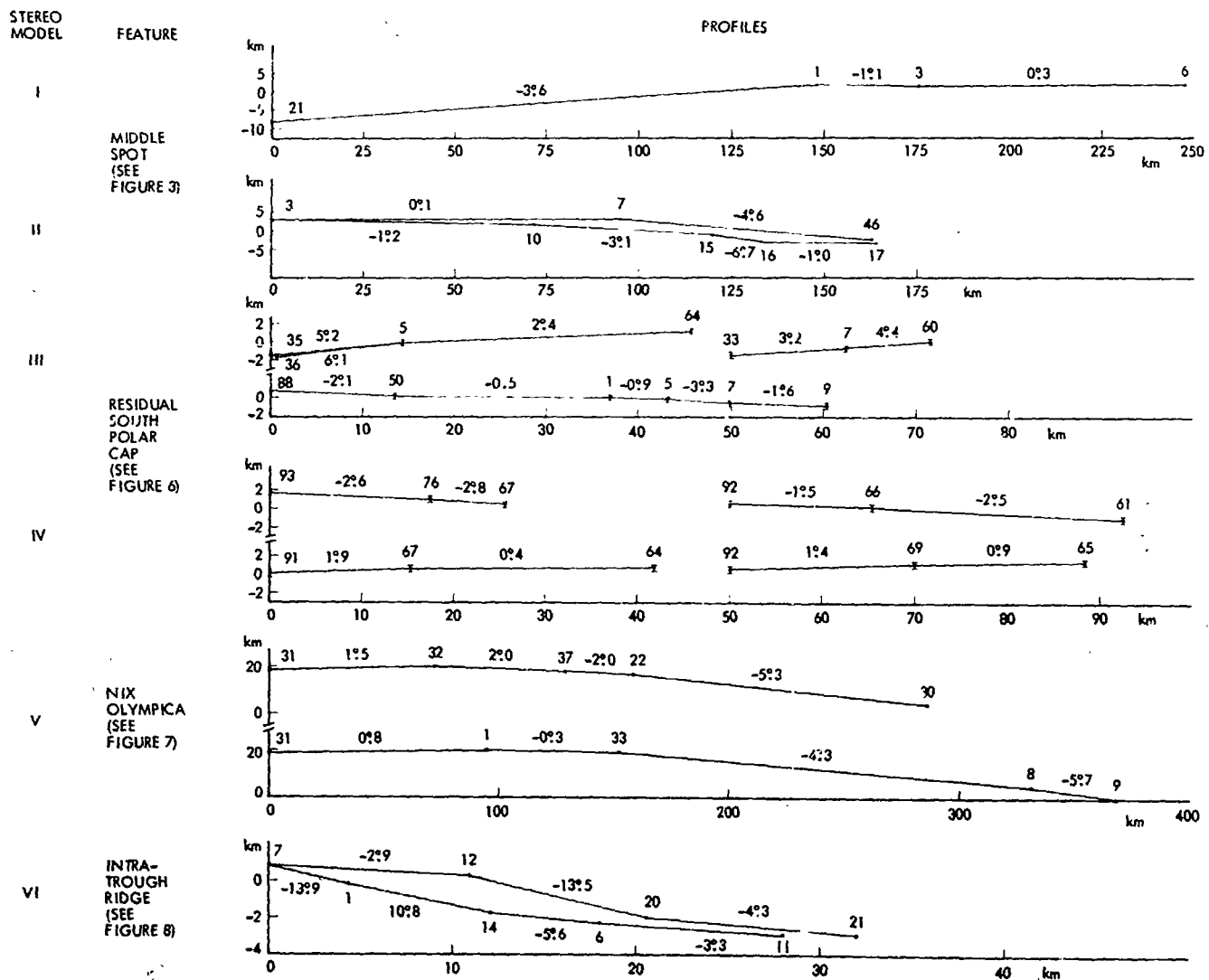
Fig. XXXXII-5. Vertical profiles of Martian surface features from six stereo models.

Table XXXXII-5. Estimating relief across a defrosted strip within the residual south polar cap

Profile	Points held level	Derived relief across defrosted strip, m
61–66–92	61, 66	270
67–76–93	67 76	54
65–69–92	65, 69	175
64–67–91	64, 67	400

Before passing on to another Martian feature, we note the anomalous relationship of the general model error to the calculated ΔH for the south polar cap models. The observed error is approximately twice the predicted error. This discrepancy may be attributed to the nature of the features used in these models. Instead of fixed point fea-

ture such as crater centers, which were commonly used elsewhere on Mars, we have used dark spots of defrosted ground and albedo markings within the frost. Such features have the unfortunate property of changing size and shape significantly with time, tending to increase $\Delta H'$.

Model V shown in Fig. XXXXII-7 is another Martian volcano, Nix Olympica. The slopes shown in the profiles of Fig. XXXXII-5 are similar in angle to those of Middle Spot, but the base of the cone is larger, so the total relief from the top of the basal scarp (point 9) to the rim of the complex caldera is about 20 km, twice that of any similar feature on Earth.

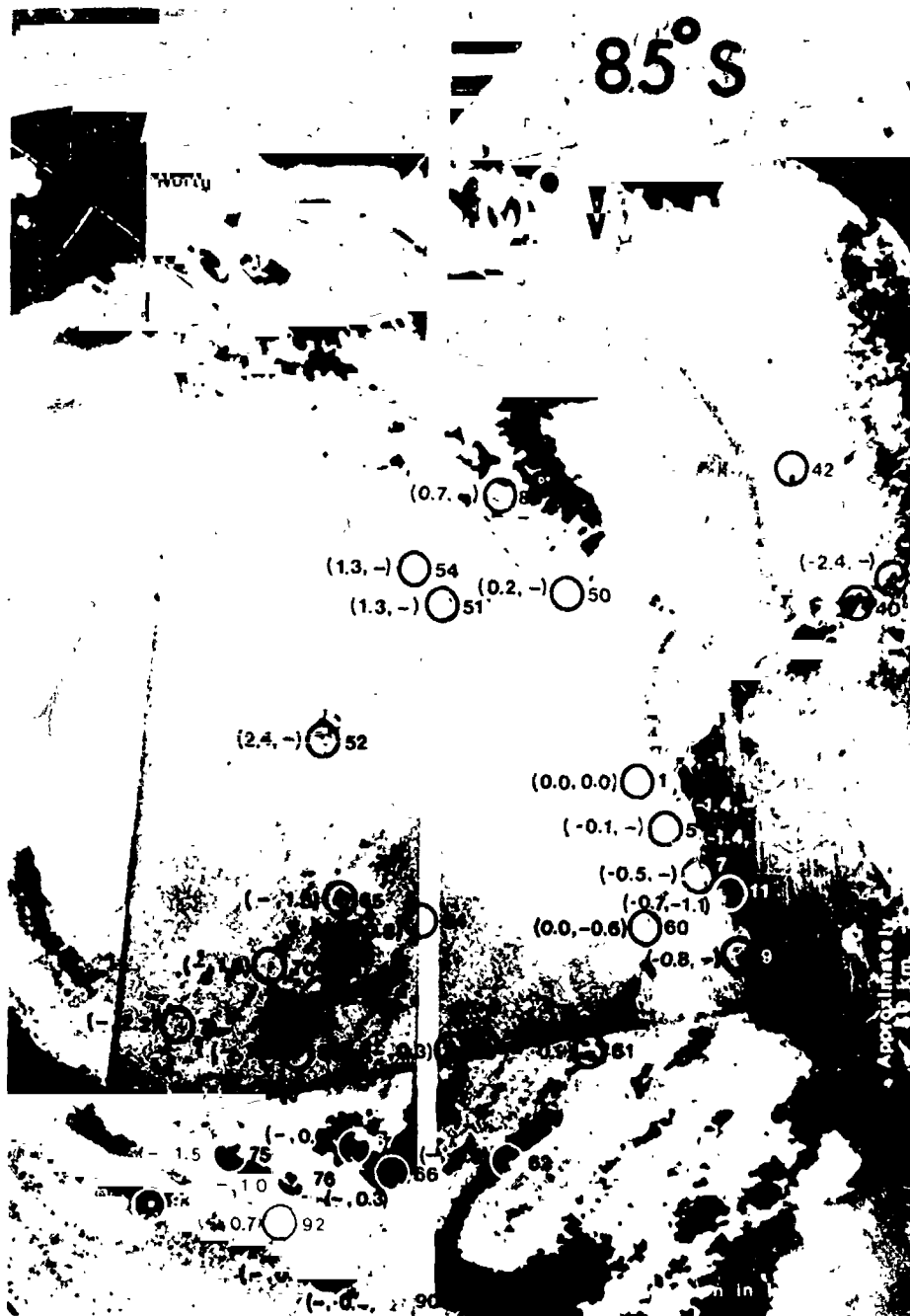Model VI shown in Fig. XXXXII-8 represents the limits of precision attainable from *Mariner* 9 data. A pair of

Fig. XXXXII-6. A mosaic of pictures of the residual south polar cap rectified to a polar stereo-graphic projection. Point elevations (in kilometers) in parenthᵉ ses have been determined by analytic photogrammetry from Models III and IV (III, IV). (MTVS 4149-21, DAS 06029803; MTVS 4221-06, DAS 08331829; MTVS 4140-27, DAS 05741963; MTVS 4205-102, DAS 07791983)

high-resolution pictures taken near periapsis were used in its construction. The area is part of the Coprates canyon or trough system which stretches 4800 km across Mars between the equator and 20°S. The plateau shown sits inside a trough over 200 km wide. The craters on its upper surface resemble those outside the canyon and suggest that this was once part of a continuous stretch of cratered terrain which has been partially destroyed by the canyon-forming process. The local relief, about 3.5 km, represents material removed to create the trough. The slopes, up to
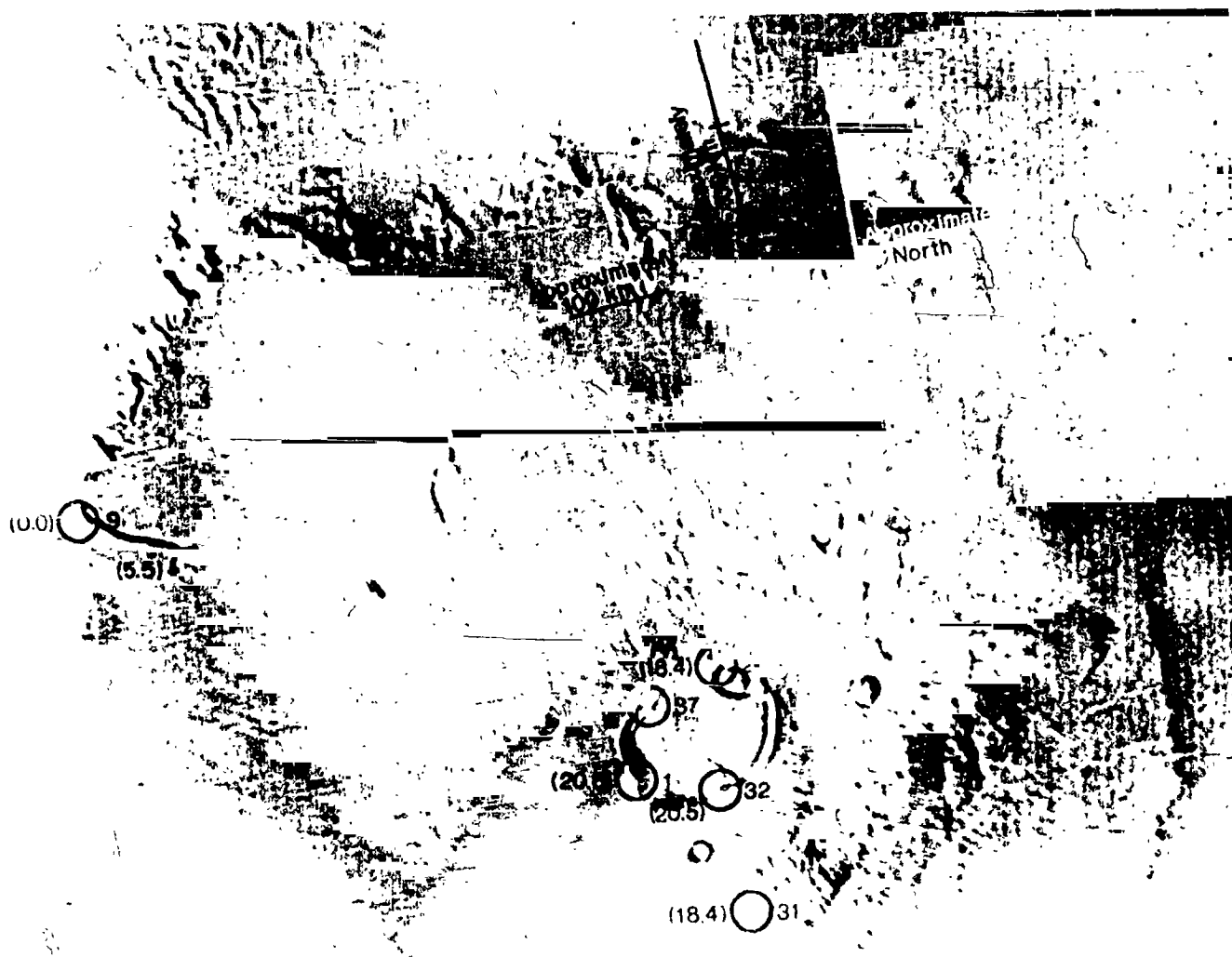
Fig. XXXXII-7. A slightly oblique view of part of the volcanic shield Nix Olympica. Point elevations (in kilometers) in parentheses have been determined by analytic photogrammetry. (MTVS 4174-93, DAS 06823918)

at least 13°9, are distinctly steeper than those seen on the flanks of the volcanoes, but are not particularly steep by Earth standards.

While demonstrating a useful technique and testing the quality of topographic data from *Mariner 9* pictures, this section has made only a small contribution to data reduction. We must now start the task of sorting out the stereo coverage on interesting features and determining which photogrammetric techniques to apply. Such work will certainly take years, and the larger task of geologic interpretation will proceed for decades.
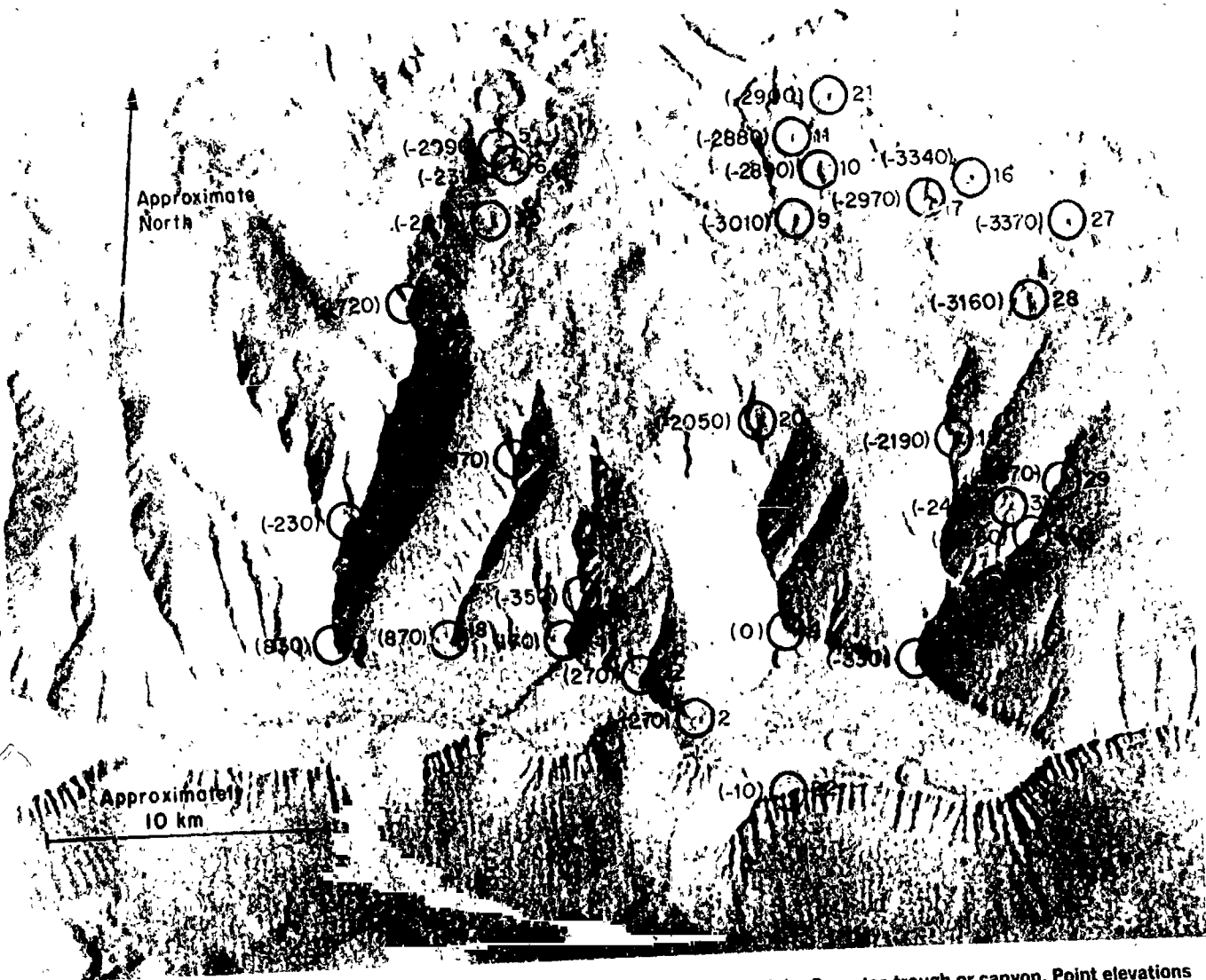
Fig. XXXXII-8. A nearly vertical view of a flat-topped ridge rising from the bottom of the Coprates trough or canyon. Point elevations (in meters) in parentheses have been determined by analytic photogrammetry. (MTVS 4191-42, DAS 07326763)

603

References

XXXXII-1. Masursky, H., Batson. R., Borgeson, W., Carr, M., McCauley. J, Milton, D., Wildey, R., Wilhelms, D., Murray, B.. Horowitz. N., Leighton, R., Sharp, R., Thompson. W., Briggs. G., Chandeysson. P.. Shipley. E.. Sagan. C., Pollack, J., Lederberg, J.. Levinthal. E.. Hartmann, W.. McCord. T.. Smith, B., Davies, M., de Vaucouleurs, G.. and Leovy, C., "Television Experiment for Mariner Mars 1971," *Icarus*, Vol. 12, p. 10, 1970.

XXXXII-2. Snyder, L. M., *Mariner 9 TV Subsystem Calibration Report*, Internal Document 610-202, Jet Propulsion Laboratory, Pasadena, Calif., 1971.

XXXX'I-3. Kreznar, J., *User and Programmer guide to the MM'71 Geometric Calibration and Decalibration Programs* (in preparation).

XXXXII-4. Macdonald, G. A., *Volcanoes*, Prentice-Hall, New Jersey, 510 pp.,1972.

XXXXII-5. Murray, B. C., Soderblom, L. A., Cutts, J. A., Sharp, R. P., Milton, D. J.. and Leighton, R. B., "Geological Framework of the South Polar Region of Mars," *Icarus*, Vol. 17, p. 328, 1972.

Acknowledgments

Appendix

A. Scheme for Describing the Geometry of Oblique Pictures

Figure XXXXII-A-1[3] contains all quantities that are important for the determination of relief between point features seen in an oblique picture. For this report, I shall merely present the relations derived from this diagram and defer an outline of their derivation to another place. The relief shown in Fig. XXXXII-A-1 is the vertical distance H which is related to other quantities in the diagram by the basic relation:

$$H = \frac{H' \cdot SR}{x} \frac{\cos(SUBR)}{\sin(VAR)} \qquad (A\text{-}1)$$

where the quantities are defined:

H = vertical relief to be determined

H' = relief displacement of the crest of H from its foot, i.e., the length of the image of H in the focal plane

SR = slant range from the camera to the feature H

x = distance from the optic center of the lens to the image of h in the focal plane

$SUBR$ = angle between a line, perpendicular to the direction of H' and passing through the optic center of the lens, and the optic path to feature H

VAR = emission angle at the surface at feature H

The quantities SR, x, $SUBR$, VAR from which H is calculated are all derived from a more fundamental set of quantities describing the position and orientation of the camera when photographing H. There is a great deal of flexibility in the choice of this set but, as an example, we shall use the following:

R = radius of the planet at feature H

$RMAG$ = range from the spacecraft to the center of the planet

TA = tilt angle, the angle between the camera axis and the direction to the center of the planet

f = focal length of the camera

---

[3]Partially based on Imhof, R. K., and Doolittle, R. C., p. 913, in "Mapping From Oblique Photographs," *Manual of Photogrammetry*, 1966.

L, K = coordinates of the image of feature H in the focal plane

The quantities in Equation (A-1) are related to the above by:

$$x = (K^2 + L^2 + f^2)^{1/2} \qquad (A\text{-}2)$$

$$\left.\begin{array}{l} SUBR = \tan^{-1}\left[(SI - SIA)/x\right] \\[6pt] SI = \{K^2 + [f \cdot \tan(TA) + L]^2\}^{1/2} \\[6pt] SIA = f \cdot \tan(TA)\,[1 - (K/SI)^2]^{1/2} \end{array}\right\} \qquad (A\text{-}3)$$

$$\left.\begin{array}{l} VAR = \sin^{-1}\left[(RMAG/R) \cdot \sin(NAA)\right] \\[6pt] NAA = SUBR + SUA \\[6pt] SUA = \tan^{-1}(SIA/x) \end{array}\right\} \qquad (A\text{-}4)$$

$$SR = R \cdot \sin(VAR - NAA)/\sin(NAA) \qquad (A\text{-}5)$$
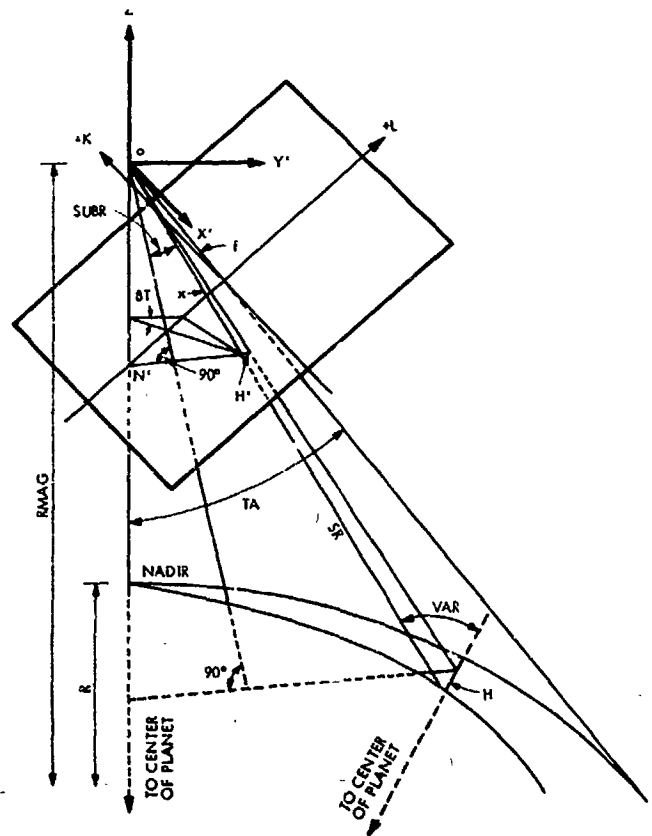
Fig. XXXXII-A-1. The geometry of relief, H, imaged in a planetary-scale oblique picture.

The relationships among the quantities of Equations (A-3), (A-4), and (A-5) are exhibited in Figs. XXXXII-A-2 and XXXXII-A-3.

B. Determination of Relief of Surface Features

Because real geologic features do not consist of upright posts or vertical scarps that would be imaged as H is in Fig. XXXXII-A-1, we must somehow infer a relief displacement H' for a feature, for example a hilltop, which is the image of the relief of the hilltop above some point at its base. This is possible if we have a second picture of the same feature taken from a different perspective. Figure XXXXII-A-4 consists of schematic diagrams of two

such pictures of a hypothetical feature. A and B represent point features at the crest and foot of a hill, respectively, imaged in two separate pictures. We wish to derive the vertical relief along traverse AB. This is imaged as H'_1 in picture A and H'_2 in picture B, but the point C defining the length of H'_1 and H'_2 is not imaged in the pictures as it is below the ground surface vertically beneath point A at the elevation of point B. The location of point C in a picture is inferred from two facts:

(1) It is located on a line joining A and the nadir point N'. An axiom of photogrammetry, which is obvious from Fig. XXXXII-A-1, is that relief displacement is radially outward from the nadir point.

(2) The ground distance $\overline{BC}$ derived from the image lengths $\overline{BC'_1}$ and $\overline{BC'_2}$ in the pictures must be the same.
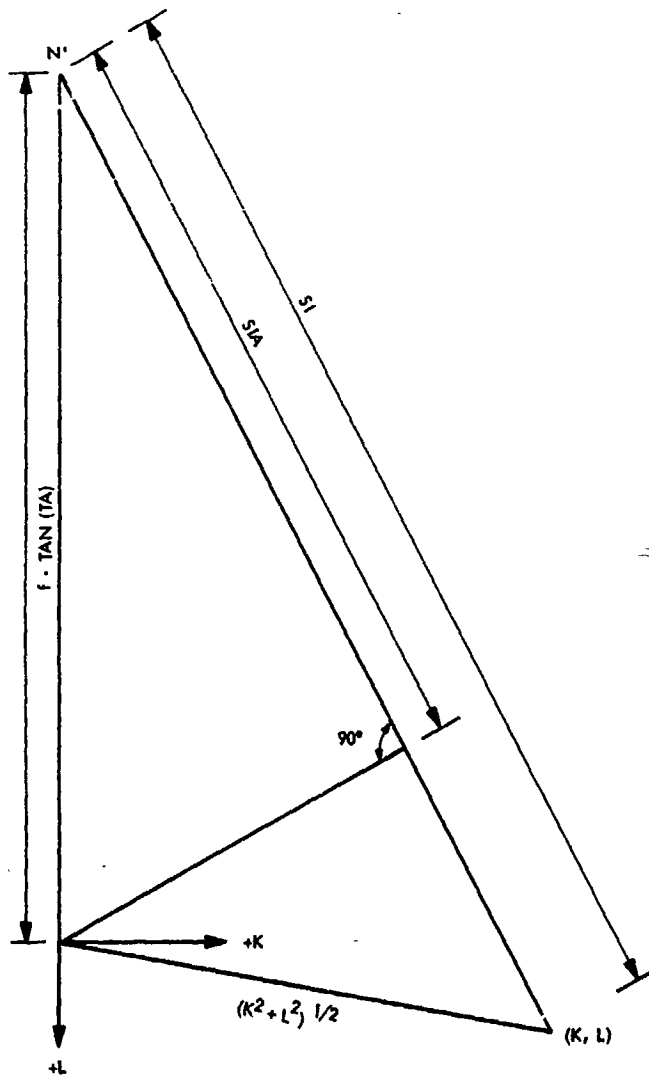

Fig. XXXXII-A-2. The geometry of some quantities in the focal plane of an oblique picture. Some relations are given by Equations (A-3) and (A-4).
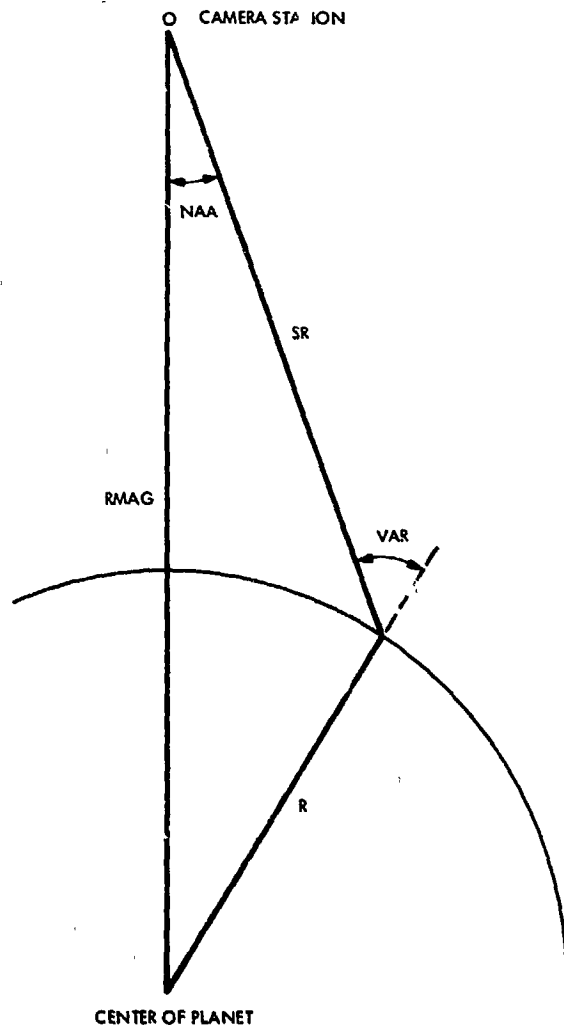

Fig. XXXXII-A-3. The geometry of some quantities in the principal plane (the plane containing the camera axis and the nadir) of an oblique picture (see Equation A-5).

The problem now is to find a pair of distances in the focal plane, H_1' and H_2', which represent the same value of H according to Equation (A-1) and give identical horizontal ground distances from the consequent image lengths $\overline{BC_1'}$ and $\overline{BC_2'}$. Because of the nonlinear nature of Equations (A-1) to (A-5), I have adopted an iteration procedure. Briefly it is:

(1) Pick an H_1' and calculate H from (A-1).

(2) Calculate H_2' from (A-1).

(3) Calculate the ground distance $\overline{BC}$ for each photo from $\overline{BC_1'}$ and $\overline{BC_2'}$.

(4) Use the value of $(\overline{BC_1} - \overline{BC_2})$ to correct H_1'.

All that remains to implement the above procedure is to outline a technique for the derivation of the horizontal ground distance, $\overline{BC}$, from its image (step 3) as above. One scheme is to find the difference of vectors from the spacecraft to B and C. The coordinate system of these vectors, centered at O, is shown in Fig. XXXXII-A-1. If we label the vectors to B and C as $\tilde{B}$ and $\tilde{C}$, respectively, then their components can be derived from Fig. XXXXII-A-1 as:

$$B_X = SR_B \cdot \sin(NAA_B) \cdot \sin(BT_B)$$

$$NA_B \simeq L + f \cdot \tan(TA)$$

$$BT_B = \tan^{-1}\{-K_B/[NA_B \cdot \cos(TA)]\}$$

$$\quad\quad (A-6)$$

$$B_Y = SR_B \cdot \sin(NAA_B) \cdot \cos(BT_B)$$

$$B_Z = SR_B \cdot \cos(NAA_B)$$

The components of $\tilde{C}$ are similarly derived with the appropriate "C" subscript on parameters. The cord distance from B to C is just $/\tilde{B} - \tilde{C}/$. This deviates from the exact distance $\overline{BC}$, following the curvature of the planet, by less than 1 part in 10^3 for $\overline{BC} \lesssim 350$ km on Mars. This is adequate for our work on generally small features.

C. Consistency Arguments to Improve Input Parameters

If the values of the basic input parameters describing the geometry of a picture — $RMAG$, TA, and the orientation angle of the K-L coordinate system, θ in Fig. XXXXII-A-4, are sufficiently imprecise, the elevations derived from point features may be contradictory. Let us designate as $H(a, b)$ the derived elevation of point "a"
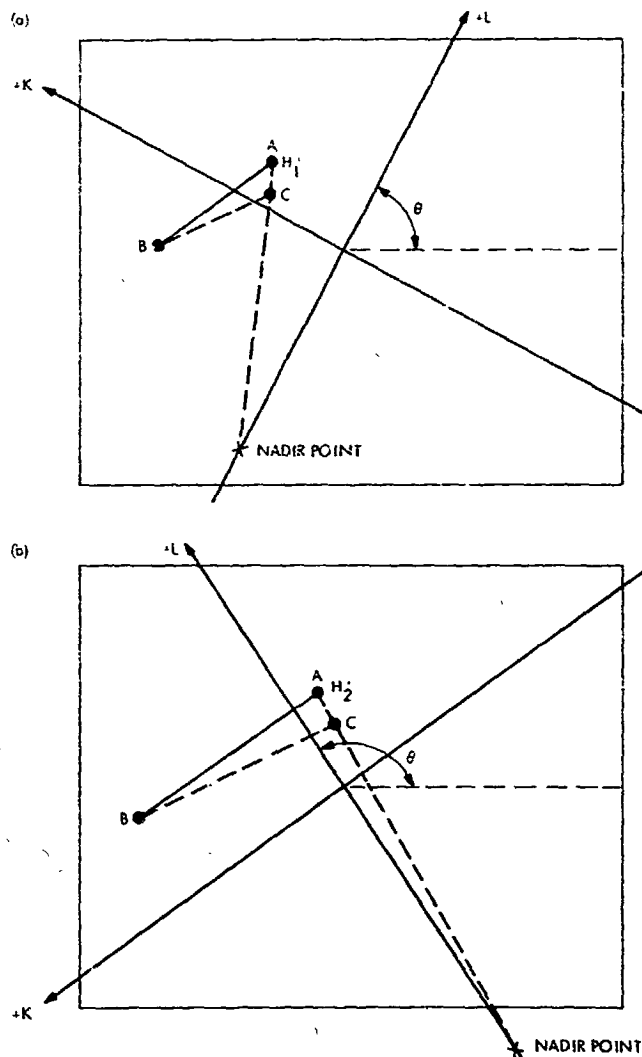

Fig. XXXXII-A-4. Schematic diagrams of a topographic feature observed in two oblique pictures.

above point "b". The contradictions we find are of the form:

$$H(1,2) - H(1,3) \neq H(4,2) - H(4,3) \quad\quad (A-7)$$

Given a sufficient number of point features in the stereo overlap region of a pair of pictures, we can devise any number of conditions such as:

$$H(1,2) - H(1,3) = H(4,2) - H(4,3) \quad\quad (A-8)$$

to control an iteration scheme to improve the values of any or all of $RMAG$, TA, and θ. The procedure is to hold these quantities constant for one of the pictures and let them vary for the other until conditions such as Equa-

tion (A-8) are satisfied to the desired accuracy. This procedure is commonly termed a relative orientation. It was required to establish Models III, IV, and V presented in the main body of this section. Changes required in θ and TA were less than $0°5$ in all cases, and only one model required adjustment in the nominal value of $RMAG$. Because the parameters of one picture were held constant, the resulting three-dimensional model of topography may have an overall tilt relative to the local horizontal reflecting errors in TA and θ for that picture.

Caution must be exercised in the performance of a relative orientation with extremely narrow-angle photography, such as that from the *Mariner 9* narrow-angle camera. D. W. G. Arthur (personal communication) pointed out that in the extreme case, imaginary orthographic pictures, the angle between the camera stations measured from the ground target is indeterminate. The magnitude of this angle controls the scale of the stereo model so it should be held constant while performing a relative orientation. This constraint has been maintained in the construction of models in this section which were derived from narrow-angle photography.

Arthur has shown that the above restriction can be avoided if a minimum of three pictures of a feature can be employed. This author has not pursued this possibility because of the extreme rarity of such triple coverage by the *Mariner 9* narrow-angle camera.

XXXXIII. Cartographic Products From the Mariner 9 Mission[1]

R. M. Batson
U.S. Geological Survey, Flagstaff, Arizona 86001

Simultaneous acquisition of geodetic, cartographic, geologic, and other scientific data on Mars from *Mariner 9* required extensive modification of conventional methods of mapping. Traditionally, topographic mapping precedes geologic mapping, and control net computation precedes topographic mapping. During the *Mariner 9* mission, however, it was necessary to perform preliminary evaluation of all data simultaneously in order to optimize future data-gathering sequences. The mission lasted almost 1 year; during this time data-gathering priorities were continuously modified as a result of acquisition of new information about the planet. In assigning priorities, constant consideration was given to the ever-present danger that one or more of the on-board sensors could fail at any time. Subsequent to mission operations, reporting schedules and support requirements for the 1975 Viking Project required continuation of these rather unorthodox mapping procedures. The final result has been the generation of an inordinately large number of interim cartographic products enroute to a final cartographic atlas of Mars. This section discusses the production of the interim products, and defines the final ones although, at the time of this writing, final products have not yet been produced.

A. Map Formats

1. Systematic Mapping

The selection of the scales at which Mars would be mapped, the projections to be used, and the way the planet would be divided into quadrangles was based on the resolution of *Mariner 9* pictures and upon the resources available over the lifetime of the Mariner Mars 1971 Project and of other sources of funding.

In planning the cartography, it was stipulated that the scale of quadrangles used in the systematic mapping be large enough that any feature appearing on the *Mariner 9* pictures that could be classified geologically could also be annotated legibly at map scale. Mission plans called for a spacecraft orbital altitude such that 70% of the planet would be viewed with approximate average geometric resolution of 1 km per television line. A rule of thumb developed by geologists engaged in planetary mapping suggests that a feature must subtend approximately eight resolution elements to be classified geologically (Ref. XXXXIII-1). The minimum size geologic annotation acceptable for clarity was assumed to be 1 mm. In the smallest scale map acceptable as a geologic base, therefore, 1 mm would represent 8 km, and the map scale would

be 1:8,000,000. The nearest scale in common use larger than 1:8,000,000 is 1:5,000,000. It was therefore decided that 1:5,000,000 would be the smallest scale at which systematic quadrangle mapping of Mars would be made.

The surface area of Mars is approximately 145,000,000 square kilometers, or 5.8 square meters at 1:5,000,000. If all quadrangles are approximately 0.5×0.5 m, at least twenty-three 1:5,000,000-scale quadrangles would be required to map Mars. If a scale of 1:1,000,000 were used, at least 580 quadrangles would be required. On this basis, the choice of the 1:5,000,000 scale was the inevitable optimum.

2. Special Maps

Although the 1:5,000,000 scale is accepted by the *Mariner 9* experimenters as the basic scale for the systematic mapping of Mars, special purpose maps will be made at other scales. All Mars maps will be published at one of four scales, differing by factors of 4 or 5. The use of a limited set of map scales facilitates comparison of similar geologic features. For example, comparison of two kinds of volcanoes is simplified if both are mapped at the same scale, rather than if one is shown at 1:5,000,000 and the other at 1:1,000,000.

A prime requirement for any reconnaissance mapping program is a small-scale map of the entire project. Such a map was compiled at 1:25,000,000 from Earth-based observations by de Vaucouleurs and Roth (Ref. XXXXIII-2) before the *Mariner 9* mission. A shaded relief map at the same scale has been published by the U.S. Geological Survey (Ref. XXXXIII-3); it was compiled from preliminary data and is intended as a pictorial representation of the planet. It does not incorporate the geodetic information derived from *Mariner 9* data, so that discrepancies in relative placement of features are present, as well as variation in interpretation of their prominence because of incomplete electronic processing of the source materials at the time the map was made. A final version of this map will be produced at the end of the systematic mapping program, and will incorporate all known and usable geodetic, topographic, morphologic, and albedo information.

Large-scale maps are required for special scientific study and for study of Viking landing sites. Although the resolution of *Mariner 9* wide-angle pictures does not, in general, justify their enlargement to scales larger than 1:5,000,000, extra map area is required for legible portrayal of complex geologic relationships. Pictures taken by the narrow-angle camera have ten times the resolution of the pictures from the wide-angle camera, and some

areas of the planet have sufficient contiguous narrow-angle coverage that wide-angle pictures are required only for horizontal control. The two map scales planned for special maps are 1:1,000,000 and 1:250,000.

3. Map Projections

Four conformal map projections are used in the mapping of Mars. In conformal projection from an ellipsoid to a plane, scale distortion in longitude is the same as that in latitude at any point, implying that small features retain their correct shape, even though systematic scale variation is present in the maps. A more complete discussion of map projections is given in Ref. XXXXIII-4. The mathematics of the projections are given in Ref. XXXXIII-5. Table XXXXIII-1 shows the kind of map in which each projection is used. The formulas, as modified from Thomas and Adams, used to construct the projections are given in the Appendix. In accordance with recommendations by the *Mariner 9* Geodesy Cartography Group, areographic, rather than areocentric, coordinates are used for all maps.

The quadrangle layout scheme for the 1:5,000,000 systematic mapping is similar to that devised for the Moon by the U.S. Air Force Aeronautical Chart and Information Center (ACIC), and was designed to meet the following criteria:

(1) Number of quadrangles must be kept to a minimum.

(2) Quadrangles should be as close to the same shapes and physical sizes as possible.

(3) Quadrangles should join on their east and west boundaries, rather than on north and south, thus providing a continuous strip map of the equatorial zone to simplify preparation of a 1:25,000,000 planet-wide map and to support the Viking mission whose area of interest is the equatorial zone.

The layout shown in Fig. XXXXIII-1 meets these criteria. The quadrangles in this scheme extend across more degrees of longitude than of latitude, which suggests the use of projections with classical orientations, rather than transverse orientations to minimize internal scale variations. Such projections meet the third criterion, because they can be joined together on their east and west boundaries. Accordingly, polar stereographic projections have been selected for the polar regions for latitudes higher than 65° north or south. Lambert conformal projections 60° wide were selected for the north and south latitude bands between 30° and 65°. Mercator projections, each with dimensions of 45° in longitude by 30° in latitude, are used in the equatorial zone. The quadrangle layout,

Table XXXXIII-1. Mars mapping projections

Map scale series	Format	Projection	Standard parallels	Remarks
1:25,000,000	65°N to 65°S 0° to 360°W	Mercator	0°	$K_{60} = 1.99219$ $K_{eq} = 1.00000$ (i.e., scale at equator is 1:25,000,000; scale at 60°N and 60°S is 1:12,549,000)
	90°N to 55°N 0° to 360°W 55° to 90°S 0° to 360°W	Polar stereographic		$K_{60} = 1.99219$ (chosen to match scale of Mercator projection at 60°N and 60°S latitude; scale at 60°N or 60°S is 1:12,549,000)
1:5,000,000	Two bands of eight quads each between 30°N and 30°S. Each quad, 30° latitude by 45° longitude	Mercator	0°	$K_{eq} = 1.0000$ $K_{30} = 1.1532$ (i.e., scale at equator is 1:5,000,000; scale at 30°N or 30°S is 1:4,335,761)
1:5,000,000	Two bands of six quads each, 65°N to 30°N, and 30°S to 65°S. Each quad, 35° latitude by 60° longitude	Lambert conformal	59.17°N 35.83°N 35.83°S 59.17°S	$K_{30} = 1.1532$ $K_{65} = 1.1611$ (i.e., scale at 30°N or 30°S is 1:4,335,761; scale at 65°N and 65°S is 1:4,280,822; chosen to match scale of 1:5,000,000 Mercator series at 30°N and 30°S)
1:5,000,000	90°N to 65°N 0° to 360°W 65°S to 90°S 0° to 360°W	Polar stereographic		$K_{65} = 1.1611$ (i.e., scale at 65°N or 65°S is 1:4,280,822 chosen to match scales of 1:5,000,000 series of Lambert conformal projections at 65°N and 65°S)
1:1,000,000	Specially selected areas. Quadrangles cover approx 600 to 800 km by 600 to 800 km	Polar stereographic from 90°N to 65°N and from 65°S to 90°S Transverse Mercator from 65°N to 65°S		$K = 1.00000$ at central parallel (i.e., scale at central parallel = 1:1,000,000) $K = 1.00000$ at central meridian
1:250,000	Specially selected areas. Quadrangles cover approx 200 × 200 km	Same as 1:1,000,000 above		$K = 1.00000$ at central meridian

with correct relative sizes and shapes, is shown in Fig. XXXXIII-1. The areas covered by the quadrangles are shown in Fig. XXXXIII-2. Special interest maps at 1:1,000,000 and 1:250,000 are compiled- on transverse Mercator projections rather than those selected for the 1:5,000,000 maps. This decision was made because:

(1) There is no requirement for compatibility between projections on special maps and those on the 1:5,000,000 maps.

(2) The areas to be mapped at the larger scales are scattered randomly over the planet, and some lie on latitude boundaries between the 1:5,000,000 quadrangles.

(3) Transverse Mercator projections can be drawn of areas anywhere on the planet with minimal scale variation. Throughout a 1:1,000,000 map, therefore, 1 mm will correspond very nearly to 1 km.

4. Quadrangle Nomenclature

The quadrangle names shown in Figs. XXXXIII-1 and XXXXIII-2 were adopted by the Geodesy/Cartography Group of the *Mariner* 9 Television Team. Since these quadrangles will define and coincide with named provinces on Mars that will be part of a new system of Martian surface feature nomenclature, the names are subject to approval by the Nomenclature Committee of the International Astronomical Union (IAU) at its meeting in August
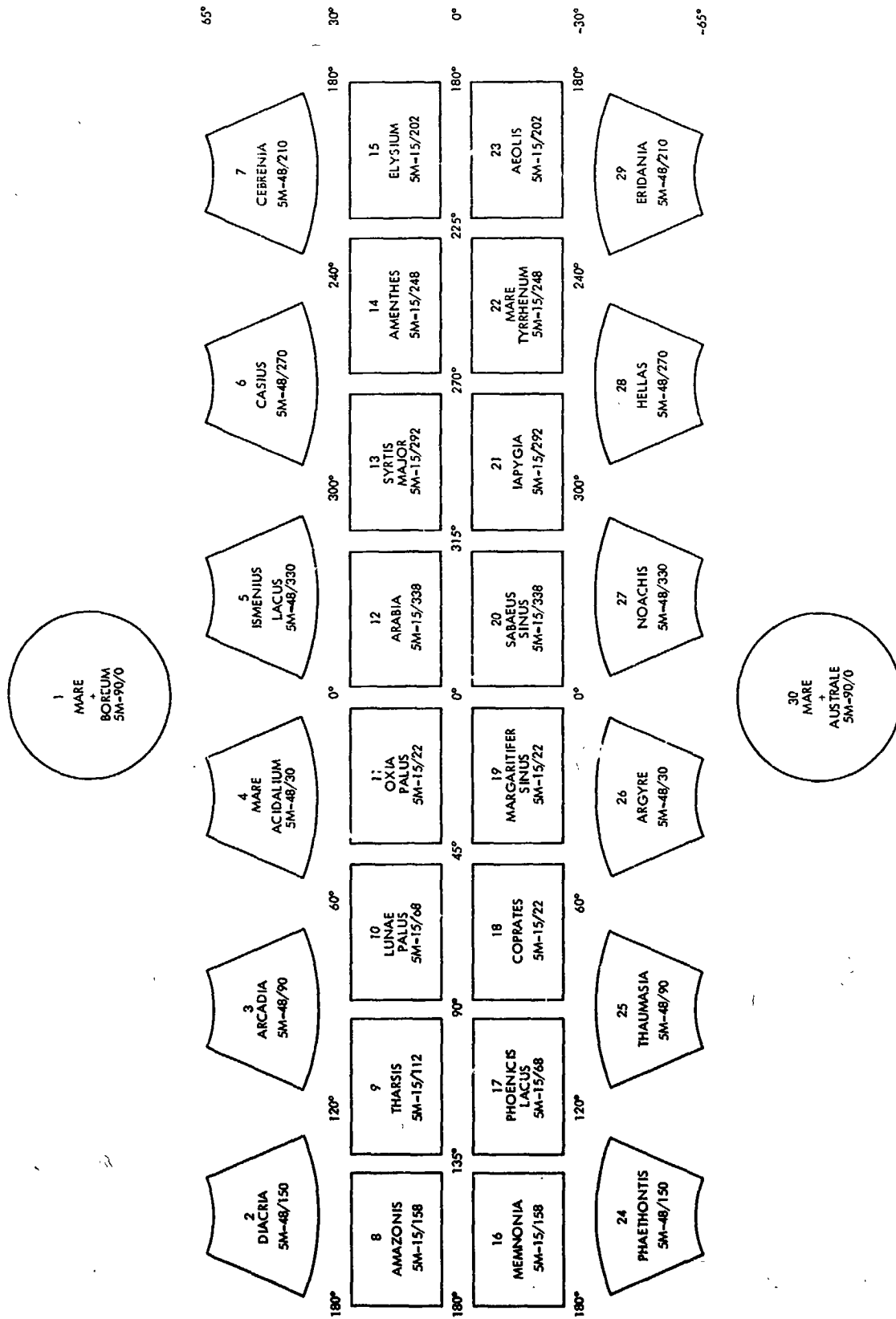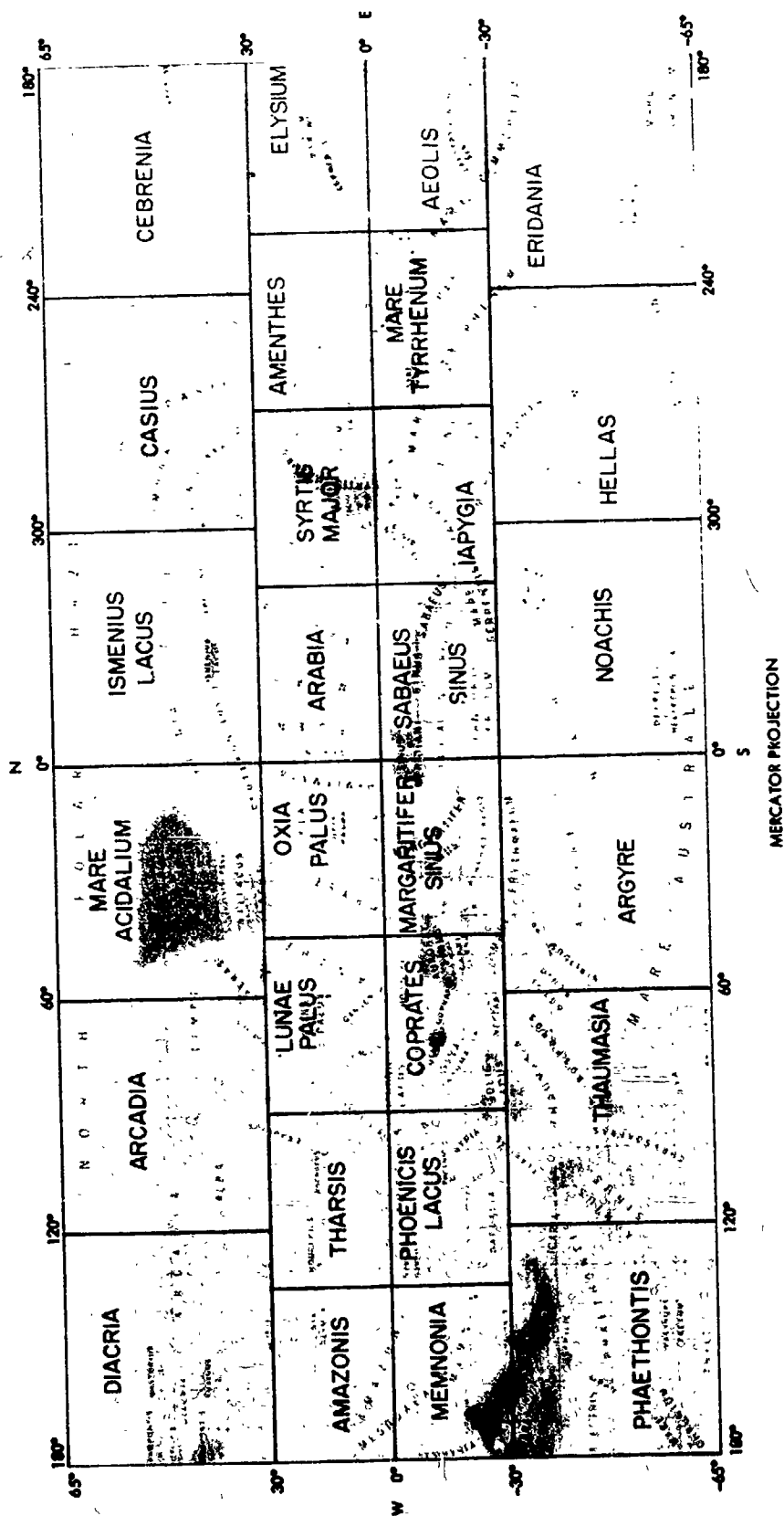
Fig. XXXXIII-1. Quadrangle layout for 1:5,000,000 mapping of Mars, showing provisional quadrangle names and alphanumeric nomenclature. A working set of numbers from 1 to 30 was used during the Mariner 9 mission, and is also shown in the quadrangle layout.

Fig. XXXIII-2. Areas on Mars covered by the 1:5,000,000 quadrangles, exclusive of the polar regions. Base map by de Vaucouleurs and Roth (Ref. XXXIII-2).

1973. Some quadrangles will be published before IAU approval of the names is official, however, and may therefore carry unapproved titles.

An abbreviated alphanumeric quadrangle nomenclature scheme is useful for filing and locating maps. An initial working set of arbitrary numbers from 1 to 30 was assigned to the 1:5,000,000 quadrangles, as shown in Fig. XXXXIII-1. Arbitrary systems of this kind become cumbersome and less useful as the number of maps increases. Another system, requiring minimum reference to a glossary of codes, was therefore devised for the Mars maps. It was purposely designed to be compatible with future mapping programs of planets other than Earth and the Moon. The number of maps of these two bodies is large and varied, and no single system exists for them.

The alphanumeric quadrangle designator code for Mars maps has four parts:

(1) *An alphanumeric prefix identifying the planet.* If the system is applied to other bodies in the solar system, the planet Mercury would be designated "Hermes" (H). Venus maps would be prefixed "V". Minor planets would be designated by lowercase letters. For example, if a map of Ceres is ever compiled, its prefix would be "c". Designations of maps of satellites would have two-letter prefixes, in which the first initial is that of the primary body, and the second that of the satellite. The designation of a map of Phobos would thus be prefixed "MP."

(2) *The scale of the map.* This is the denominator of the representative fraction in alphanumeric notation based on the International System of Units. For example, a 1:5,000,000 map is designated "5M" and a 1:250,000 map is designated "250k."

(3) *The location of the area mapped.* In some terrestrial map designations, the latitude and longitude of a map corner point is used. Users of Mars maps frequently know the coordinates of features in which they are interested, so Mars maps are being designated by their center coordinates (to the nearest degree only). Planet-wide maps not in quadrangle format will have this designation replaced by a simple numeric code.

(4) *The kind of map (i.e., controlled or uncontrolled mosaic, shaded relief, etc.).* An abbreviation or code consisting of three letters or less is invented at the time a particular type of map is compiled. No attempt has yet been made to define more than a few of the Mars map types that will eventually be published.

By the system outlined, a 1:5,000,000 shaded relief map of Mars with latitude boundaries of 0° and 30°S and longitude boundaries of 45° and 90°W is designated M 5M-15 68R. Designations of all quadrangles are shown in Fig. XXXXIII-1.

5. Feature Nomenclature

It will be apparent to anyone familiar with *Mariner* pictures of Mars that an entirely new set of names must be devised for Mars, because the classical names used by astronomers (see Ref. XXXXIII-6) since Schiaparelli refer only to vague light and dark markings visible telescopically from Earth. These markings are large and diffuse, and very few of them appear related in any way to the complex topographic features that will dominate future maps of Mars. The derivation of an entirely new set of designations that will almost certainly number in the thousands is an extremely complex matter that is the responsibility of Commission 16 of the IAU. A more thorough discussion of the problem and proposed solutions are being considered by the Mars Nomenclature Working Group headed by G. de Vaucouleurs; proposals will be submitted to Commission 16 of the IAU in its 1973 meeting in Sydney, Australia. It seems that at least one generation of the Mars maps will be without names.

6. Map Controls

Initial versions of the maps must be controlled solely by *Mariner 9* telemetered orientation and spacecraft tracking data, because the data for deriving map controls were gathered at the same time as were the map data, and reporting schedules require simultaneous processing. The result is that the first cartographic products from the *Mariner 9* mission are controlled by camera orientation and position data which were based on obsolete astronomical definitions of the spin axis and system of longitudes. Products compiled after September 1972 are controlled by a preliminary network of horizontal control points derived by Davies (Ref. XXXXIII-7). These points are related to a newly defined spin axis and Mars first meridian (Ref. XXXXIII-8; also see Section XXXX of this Report). This net will be refined and augmented, and as the new controls become available, subsequent maps will be compiled to them. The results will be that some earlier maps will eventually be reissued with graticules shifted to agree with the final control net. Some recompilation of early products will undoubtedly be necessary where simple translation does not produce satisfactory issues. The reference spheroid for the areographic coordinate system has an equatorial radius of 3393.4 km and a flatten-

ing of 1 192, corresponding to values obtained by Earth-based observation.

Data from non-television sensors have been used to measure topographic spot elevations on the Martian surface. These sensors include:

(1) Infrared radiometer (IRR : G. Neugebauer, California Institute of Technology, Principal Investigator (Ref. XXXXIII-9; also see Section XXI of this Report).

(2) Infrared interferometer spectrometer (IRIS): R. Hanel, Goddard Space Flight Center, Principal Investigator (Ref. XXXXIII-10; also see Section XX of this Report).

(3) Ultraviolet spectrometer (UVS): C. Barth, University of Colorado, Principal Investigator (Ref. XXXXIII-11).

(4) S-band occultation: A. Kliore, Jet Propulsion Laboratory, Principal Investigator (Ref. XXXXIII-12; also see Section XXXVI of this Report).

(5) Goldstone and Haystack dish antennas, used to measure topography in the equatorial region by radar (Refs. XXXXIII-13 through XXXXIII-17).

(6) Celestial mechanics experiment, which utilizes spacecraft tracking data to aid in the development of a reference geoid: J. Lorell, Jet Propulsion Laboratory, and I. Shapiro, Massachusetts Institute of Technology, Principal Investigators (Ref. XXXXIII-18; also see Section XXVI of this Report).

Data from the above experiments, when correlated with television images, can be used to compile very generalized topographic contour lines over very large areas of the planet. Many convergent stereoscopic picture pairs were obtained of specific features, which, in some cases can be used to help establish the relationship between data from the various non-television sensors, in addition to compiling detailed large-scale maps of the features themselves (Ref. XXXXIII-19; also see Section XXXXI of this Report).

Vertical elevations must be related to an equilibrium surface, so that slopes with respect to local gravity vectors can be derived from the contour lines. For example, if a map indicates the presence of a channel that might conceivably have been formed by fluid erosion, it would be important to know the gradient and direction of such flow. None of the sensors mentioned above measured topographic relief with respect to such a datum. For example, the ultraviolet spectrometer measured surface

atmospheric pressure, which varies as a function of temperature and other factors. The S-band occultation experiment, on the other hand, measured geometric radii of the planet. The relationship between these data sets and a reference geoid is not obvious, and must be resolved before meaningful contour lines can be drawn.

B. Map Data Processing

1. Computer Processing

As the digital picture data were received on Earth, they were processed for mapping purposes according to the sequence shown in Fig. XXXXIII-3. First, they were processed by the mission test computer (MTC) for reconstitution into a video image for display on television monitors in the Space Flight Operations Facility (SFOF) and for recording on 70-mm film by the mission test video system (MTVS). This image was first displayed in its raw form. Then, the signal was processed to correct approximately for known camera shading characteristics; its contrast was enhanced, and this "shading corrected" image was displayed and recorded. Finally, the high-frequency part of the signal was amplified, and this "high-pass filtered" version was displayed and recorded. Vertical and horizontal high-pass filters were used on pictures taken during all but the first part of the mission. Thus, each picture was displayed and photographically recorded four times in near-real time.

Tape recordings of each picture have been reprocessed to remove electronically induced geometric distortions, to correct for photometric distortions, and to enhance contrast. These reduced data record (RDR) versions were photographically reproduced by the Jet Propulsion Laboratory for distribution to the *Mariner* 9 experimenters and to the National Space Science Data Center (NSSDC). The digital tape recordings of this version were further processed to the central picture projections of the images to transform standard map projections for cartographic purposes.

2. Real-Time Mosaics

As the pictures were received, it was necessary to arrange them in some comprehensible array for display and evaluation. Compilation of the necessary mosaics is complicated by the ellipticity of orbit of *Mariner* 9 and the consequent scale variations of the pictures in each pass. Mosaic control graticules were therefore designed with appropriate scale variations with latitude to accommodate the pictures.
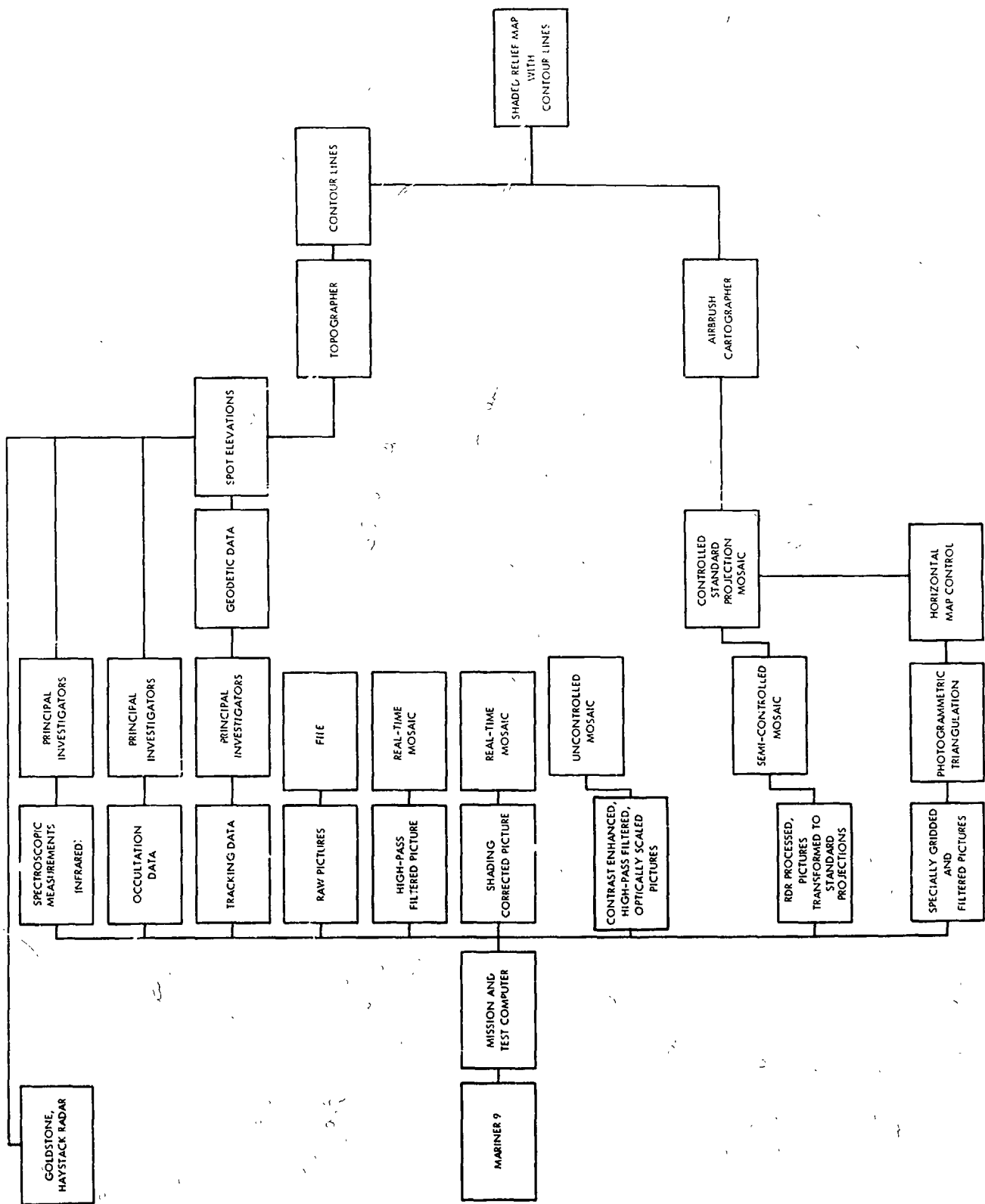
Fig. XXXXIII-3. Mariner 9 map data flow.

Fig. XXXXIII-4. Partial real-time mosaic of *Mariner* 9 high-pass filtered pictures of the Phoenicis Lacus quadrangle. Gores between strips of pictures in the eastern half of the mosaic were filled on subsequent revolutions.

The mosaics were made by placing the pictures on the graticules of meridians and parallels using the latitudes and longitudes of the corners by tracking and orientation data. A transparent copy of the graticule was placed over the completed mosaic (Fig. XXXX111-4). Separate mosaics were compiled with shading corrected pictures, and with high-pass filtered pictures. In the latter, high-frequency topographic detail and small light and dark markings are enhanced, whereas broad topographic and albedo variations are suppressed. In the shading-corrected pictures, broader albedo variations are dominant.

Mosaics prepared in this way fulfilled the functions for which they were designed. They provided a rough view of coverage; they showed approximate latitudes and longitudes of features; and they showed gaps in coverage. The mosaics are rather crude, however, because of scale dif-

ferences in the zones of overlap between pictures, because scale varies solely with latitude only in the case of a polar orbit, and because some pictures were obliques rather than verticals.

3. Uncontrolled Mosaics

When preliminary analytical picture processing was complete, but before the production of RDR and transformed pictures, a second generation of mosaics was made (Ref. XXXXIII-20). A set of templates was made for each picture in each 1:5,000,000 quadrangle, showing the projection of that picture at map scale. The untransformed pictures were then fitted to the templates as closely as possible by optical enlargement. Although these pictures, especially those taken with more than a few degrees of camera tilt, could not be made to fit their footprints precisely, the set of mosaics compiled with them proved
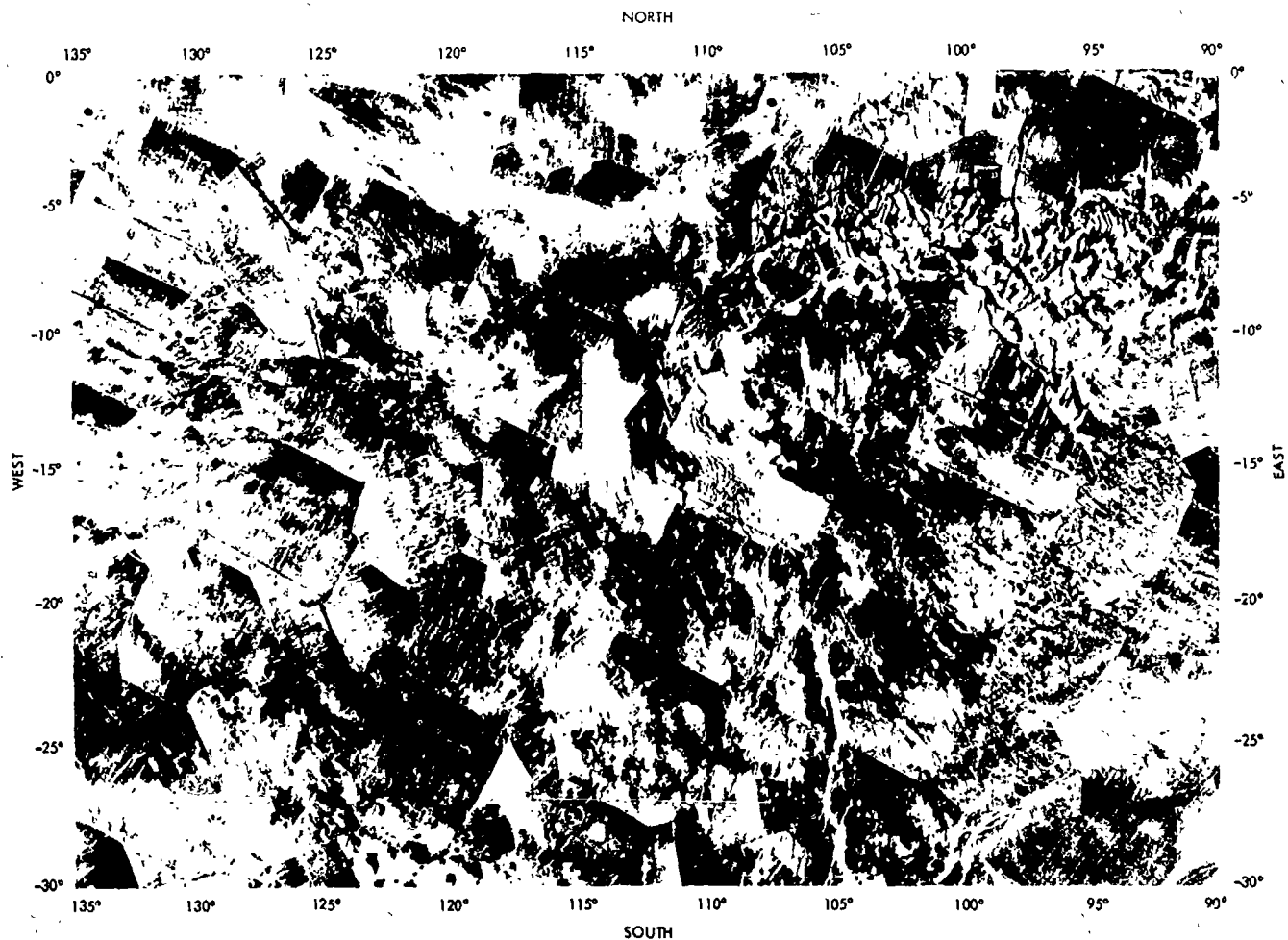
Fig. XXXXIII-5. Uncontrolled mosaic of *Mariner 9* optically scaled, high-pass filtered pictures of the Phoenicis Lacus quadrangle.

to be a great improvement over the real-time mosaics (Fig. XXXXIII-5). Discrepancies in placement of images in overlapping frames were as large as 12 mm at 1:5,000,000, or 60 km on the planet. Even though such mosaics are rather poor in a cartographic sense, they are sufficiently accurate and coherent to serve as bases for preliminary geologic mapping.

Because of large camera tilts over the south polar region, this method could not be used with pictures taken of that area. A preliminary shaded relief map was therefore prepared (Ref. XXXXIII-21). Transparent latitude/longitude overlays were placed over the untransformed MTC/MTVS pictures, and were transferred manually to a polar stereographic projection. After this crude sketch was completed and discrepancies between pictures adjusted, the features were drawn and enhanced with the airbrush. The map was completed approximately 2 weeks

after the pictures were received, attesting to the utility of the airbrush method as a tool for making useful preliminary sketches and drawings, as well as final maps.

4. Semi-Controlled Mosaics

When transformed RDR pictures became available, a third generation of mosaics was made by methods similar to those utilized in compiling the uncontrolled mosaics. It was not necessary to make templates to scale the pictures because scale factors computed during the transformation could be used for precise scaling. The tracking and orientation data were again used as control in making the mosaic. The graticule, on which the most recent available control points were plotted, was fitted to the completed mosaic by superimposing, as well as possible, the control points over their images in the mosaic. Image-position discrepancies were reduced tenfold in this set of mosaics, and the refined processing resulted in pictures of
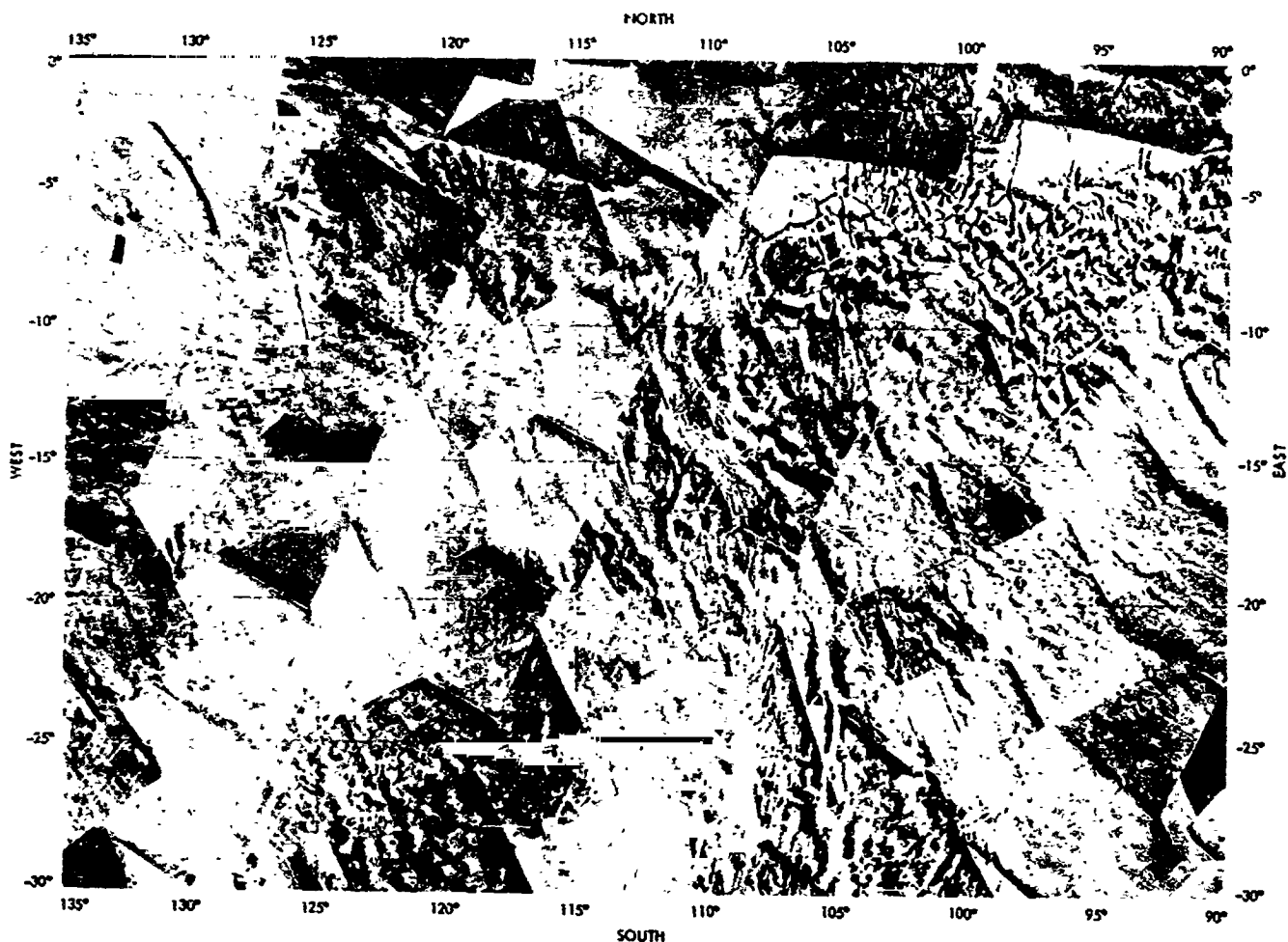
Fig. XXXXIII-6. Semi-controlled mosaic of *Mariner 9* RDR pictures, transformed to a Mercator projection, of the Phoenicis Lacus quadrangle.

more uniform tone. The distracting edge effects present in the uncontrolled mosaics (Fig. XXXXIII-6) also were ameliorated.

C. Final Map Preparation

The cartographic products described were designed primarily to aid in cataloging picture data and to provide a basis for preliminary scientific reporting. As the pressure of mission operations has subsided, it has been possible to begin preparation of an atlas of pictures and maps with lasting scientific utility. This will require a fourth generation of mosaics and a final merging of topographic data from non-imaging experiments.

1. Controlled Mosaics

A final set of mosaics will be made, controlled by the primary geodetic control net and by a secondary net of horizontal controls derived by a mutual fitting of the

pictures in a manner which minimizes discrepancies to be used in the mosaic (Ref. XXXXIII-22; also see Section XXXIX of this Report). This set of mosaics utilizes photographic prints from the same negatives as those used to prepare the semi-controlled mosaics. These controlled mosaics provide the basis of the final published maps.

2. Shaded Relief Maps

A map that is a useful base for portrayal of scientific information has several properties. It has uniform ground resolution and illumination throughout so that apparent topographic variations are real and not induced. The map contains all available topographic information that can be presented within the constraints imposed by image resolution and map scale. Map details are portrayed so as not to interfere with overlays of scientific information. On the basis of previous experience with lunar maps and with our

own efforts to make maps from *Mariner 6* and 7 pictures, the airbrush shaded relief method was tentatively selected as the best way to make the final Mars maps. This technique has been used successfully by the U.S. Air Force ACIC to make lunar maps at a variety of scales using *Apollo, Lunar Orbiter*, and Earth-based telescopic observation and photography. These maps can be prepared quickly by skilled cartographers, and can incorporate the full range of detail that never appears in single pictures of an area. The topographic portrayal is made to emphasize only the high-frequency information, thus avoiding broad tonal changes that distort colors in geologic overprints. Significant albedo variations are mapped separately from the topography so that they need not appear in composite topographic and geologic maps. Extensive interpretation or over-interpretation on the part of the airbrush cartographer is avoided, lest the final drawing become an "artist's rendition" rather than a map. To ensure that the cartographer has included and accurately portrayed all significant structural detail visible in the pictures, the final product will be critically reviewed by geologists who will use it as a base for geologic mapping.

The shaded relief will be supported by contours, or more accurately by form lines, based on the vertical controls mentioned. These rather general curves will be modified locally to be in accord with the shaded relief renderings.

References

XXXXIII-1. Masursky, H., Batson, R., Borgeson, W., Carr, M., McCauley, J., Milton, D., Wildey, R., Wilhelms, D., Murray, B., Horowitz, N., Leighton, R., Sharp, R., Thompson, W., Briggs, G., Chandeysson, P., Shipley, E., Sagan, C., Pollack, J., Lederberg, J., Levinthal, E., Hartmann, W., McCord, T., Smith, B., Davies, M., de Vaucouleurs, G., and Leovy, C., "Television Experiment for Mariner Mars 1971," *Icarus*, Vol. 12, p. 10, 1970.

XXXXIII-2. de Vaucouleurs, G., and Roth, J., *Mariner Mars 1971 Mars Planning Chart*, 1971.

XXXXIII-3. U. S. Geological Survey, Shaded Relief Map of Mars, MM 25M 1R, 1972.

XXXXIII-4. Clark, D., *Plane and Geodetic Surveying for Engineers*, Vol. 2, fifth ed , pp. 594–604 (revised and enlarged by J. Glendenning), Constable and Co. Ltd., London, 1963.

XXXXIII-5. Thomas, P. D., *Conformal Projections in Geodesy and Cartography*, U. S. Dept. Commerce, Coast and Geodetic Survey, Special Publication No. 251, U. S. Government Printing Office (Fifth printing, 1968), Washington, D. C., 1952.

XXXXIII-6. MacDonald, T. L., "The Origins of Martian Nomenclature," *Icarus*, Vol. 15, p. 233, 1971.

XXXXIII-7. Davies, M. E., *Mariner 9 Control Net of Mars: August 1972*, Rand R 1122-JPL, 1972.

XXXXIII-8. de Vaucouleurs, G., Davies, M. E., and Sturms, F. M., "The Mariner 9 Areographic Coordinate System," *J. Geophys. Res.*, Vol. 78, 1973.

References (contd)

XXXXIII-9. Kieffer, H. H., Chase, S. C., Miner, E., Münch, G., and Neugebauer, G., "Preliminary Report on Infrared Radiometric Measurements From the Mariner 9 Spacecraft," *J. Geophys. Res.*, Vol. 78, 1973.

XXXXIII-10. Conrath, B., Curran, R., Hanel, R., Kunde, V., McGuire, W., Pearl, J., Pirraglia, J., Welker, J., and Burke, T., "Atmospheric and Surface Properties of Mars Obtained by Infrared Spectroscopy on Mariner 9," *J. Geophys. Res.*, Vol. 78, 1973.

XXXXIII-11. Hord, C. W., Barth, C. A., and Pearce, J. B., "Ultraviolet Spectroscopy Experiment for Mariner Mars 1971," *Icarus*, Vol. 13, p. 63, 1970.

XXXXIII-12. Kliore, A. J., Fjeldbo, G., Seidel, B. L., Sykes, M. J., and Woiceshyn, P. M., "S-Band Radio Occultation Measurements of the Atmosphere and Topography of Mars With Mariner 9: Extended Mission Coverage of Polar and Intermediate Latitudes," *J. Geophys. Res.*, Vol. 78, 1973.

XXXXIII-13. Pettengill, G. H., Counselman, C. C., Rainville, L. P., and Shapiro, I. I., "Radar Measurements of Martian Topography," *Astron, J.*, Vol. 74, p. 461, 1969.

XXXXIII-14. Rogers, A. E. E., Ash, M. E., Counselman, C. C., Shapiro, I. I., and Pettengill, G. H., "Radar Measurements of the Surface Topography and Roughness of Mars," *Radio Science*, Vol. 5, p. 465, 1970.

XXXXIII-15. Goldstein, R. M., Melbourne, W. G., Morris, G. A., Downs, G. S., and O'Handley, D. A., "Preliminary Radar Results of Mars," *Radio Science*, Vol. 5, p. 475, 1970.

XXXXIII-16. Pettengill, G. H., Rogers, A. E. E., and Shapiro, I. I., "Martian Craters and a Scarp as Seen by Radar," *Science*, Vol. 174, p. 1321, 1971.

XXXXIII-17. Downs, G. S., Goldstein, R. M., Green, R. R., and Morris, G. A., "Mars Radar Observations: a Preliminary Report," *Science*, Vol. 174, p. 1324, 1971.

XXXXIII-18. Lorell, J., and Shapiro, I., "The Mariner 9 Celestial Mechanics Experiment: A Status Report," *J. Geophys. Res.*, Vol. 78, 1973.

XXXXIII-19. Wu, S. S. C., Shafer, F. J., Nakata, G. M., Jordan, R., and Blasius, K. R., "Photogrammetric Evaluation of Mariner 9 Photography, *J. Geophys. Res.*, Vol. 78, 1973.

XXXXIII-20. U. S. Geological Survey, Open File, Uncontrolled Mosaics of Mars, 1972.

XXXXIII-21. U. S. Geological Survey, Open File, Preliminary Shaded Relief Map of South Pole of Mars, 1972.

XXXXIII-22. Davies, M. E., and Arthur, D. W. G., "Martian Surface Coordinates," *J. Geophys. Res.*, Vol. 78, 1973.

Acknowledgments

Appendix
Projection Equations

λ = longitude

Φ = latitude

s = scale

r = adopted radius = 3393.4 km

ϵ = adopted eccentricity = 0.101929

Φ_1, Φ_2 = standard parallels for Lambert conformal projection = 35.83°, 59.17°

$t = \tan(45° + \Phi/2)[(1 - \epsilon \sin \Phi/2)/(1 + \epsilon \sin \Phi/2)]^{\epsilon/2}$

Mercator Projection

$$x = sr\lambda \tag{1}$$

$$y = sr \ln t \tag{2}$$

Scale factor for Mercator projection:

$$k_m = \sec \Phi (1 - \epsilon^2 \sin^2 \Phi)^{1/2} \tag{3}$$

Lambert Conformal Projection

$$x = sa_1 k_1 \cos l\lambda \tag{4}$$

$$y = sa_1 k_1 \sin l\lambda \tag{5}$$

Scale factor for Lambert conformal projection:

$$k_l = a_1 l (1 - \epsilon^2 \sin^2 \Phi)^{1/2}/r \cos \Phi \tag{6}$$

where

$n_1 = r/(1 - \epsilon^2 \sin^2 \Phi_1)^{1/2}$

$n_2 = r/(1 - \epsilon^2 \sin^2 \Phi_2)^{1/2}$

$t_1 = \tan(45° + \Phi_1/2)[(1 - \epsilon \sin \Phi_1)/(1 + \epsilon \sin \Phi_1)]^{\epsilon/2}$

$t_2 = \tan(45° + \Phi_2/2)[(1 - \epsilon \sin \Phi_2)/(1 + \epsilon \sin \Phi_2)]^{\epsilon/2}$

$l = \log[(n_1 \cos \Phi_1)/(n_2 \cos \Phi_2)]/\log(t_2/t_1)$

$a_1 = n_1 t_1^l \cos \Phi_1/lt^l$

$k_1 = 1.125895 = k_m/k_l$ for k_m and k_l at ±30° latitude

Polar Stereographic Projection

$$x = sa_2 k_2 \cos \lambda \tag{7}$$

$$y = sa_2 k_2 \sin \lambda \tag{8}$$

Scale factor for polar stereographic projection:

$$k_p = 2a_2 (1 - \epsilon^2 \sin^2 \Phi)^{1/2}/r \cos \Phi \tag{9}$$

where

$a_2 = [r/t(1 - \epsilon^2)^{1/2}][(1 - \epsilon)/(1 + \epsilon)]^{\epsilon/2}$

$k_2 = 2.213446 = k_1 k_l/k_p$ for k_l and k_p at ±65° latitude

Transverse Mercator Projection

$$
\begin{aligned}
x = s\{&n\lambda \cos \Phi + (n\lambda^3 \cos^3 \Phi/6) \\
&\times [1 - \tan^2 \Phi + \eta^2 + (\lambda^2 \cos^2 \Phi/20) \\
&\times (5 + 14\eta^2 + \tan^4 \Phi - 58\eta^2 \tan^2 \Phi - 18 \tan^2 \Phi)]\}
\end{aligned}
\tag{10}
$$

$$
\begin{aligned}
y = s\{&[s_1 + (n\lambda^2 \cos^2 \Phi \tan \Phi/2)] + (n\lambda^4 \cos^4 \Phi \tan \Phi/24) \\
&\times [5 - \tan^2 \Phi + 9\eta^2 + 4\eta^4 + (\lambda^2 \cos^2 \Phi/30) \\
&\times (61 + 270\eta^2 + \tan^4 \Phi - 330\eta^2 \tan^2 \Phi - 58 \tan^2 \Phi)]\}
\end{aligned}
\tag{11}
$$

Scale factor for transverse Mercator projection:

$$
\begin{aligned}
K = 1 + &\lambda^2 \cos^2 \Phi/2[1 + \eta^2 + (\lambda^2 \cos^2 \Phi/12) \\
&\times (5 + 14\eta^2 - 4 \tan^2 \Phi - 28\eta^2 \tan^2 \Phi)]
\end{aligned}
\tag{12}
$$

where

$\mu = [1 - (1 - \epsilon^2)^{1/4}]/[1 + (1 - \epsilon^2)^{1/4}]$

$b = 1.5\mu(0.75\mu^2/2 - 1)$

$c = (15/4)(\mu^2/2)(1 - \mu^2/2)$

$d = -35\mu^3/12$

$e = 315\mu^4/64$

$\eta^2 = \epsilon^2 \cos^2 \Phi/(1 - \epsilon^2)$

$\omega = \Phi + \sin 2\Phi[b + \cos 2\Phi(c + 0.5e - e \sin^2 2\Phi) + 0.75d - d \sin^2 2\Phi]$

$s_1 = r\omega\{1 - \mu + [(\mu^3 - \mu^2)/4][-5 + 9\mu^2/16(25\mu^2 - 9)]\}$

$n = r/(1 - \epsilon^2 \sin^2 \Phi)^{1/2}$

XXXXIV. Preliminary Albedo Map of the South Polar Region

Gerard de Vaucouleurs, James Roth, and Claire Mulholland
Department of Astronomy
University of Texas, Austin, Texas 78712

The accompanying preliminary albedo map of the south polar region in stereographic projection was prepared mainly from the Jet Propulsion Laboratory's mission test video system (MTVS) prints before rectified and gridded prints were received, but some adjustments were made to conform with a semi-controlled photomosaic prepared by the U.S. Geological Survey in Flagstaff. Wherever possible, use also was made of the crater coordinates derived by M. Davies at The Rand Corporation.

Two versions of the map are presented: one with a coordinate grid overlay (Fig. XXXXIV-1) and one without it (Fig. XXXXIV-2). The grid overlay was prepared at Flagstaff under the direction of S. Wu. The precision of the coordinates is generally within $1°$ in latitude ϕ and the corresponding arc ($1°$ sec ϕ) in longitude. The maps show both the albedo markings and, with subdued contrast, the craters and topographic features that are necessary to locate the former. The map covers the range of latitudes from $-65°$ to the south pole, corresponding to Mars Chart Nr. 30 in the scheme adopted by the *Mariner 9*

Team for the proposed combined photometric and topographic 1:5,000,000 Mars Atlas. The original art work is on the corresponding scale. The latitude circles are at $1°$ spacing; the longitude meridians are traced at every $5°$ up to $-85°$ and every $10°$ between $-85°$ and $-89°$.

Excluding the ice cap, the average visual ($\lambda \simeq 0.56\ \mu m$) albedo of the south polar regions estimated from Earth-based telescopic data is about 0.10; the depicted albedo markings are estimated to range from about 0.03 to 0.04 for the darkest spots to 0.10 to 0.12 for the lightest areas. (Photometrically corrected versions of the *Mariner 9* pictures were not available.)

The south polar ice cap remnant covers a roughly elliptical area measuring about 7×5 areocentric degrees, in good agreement with telescopic data for the late summer of the southern hemisphere. Notwithstanding occasional statements to the contrary in the literature, this south polar remnant never vanishes completely, except for understandable telescopic limitations (Refs. XXXXIV-1,
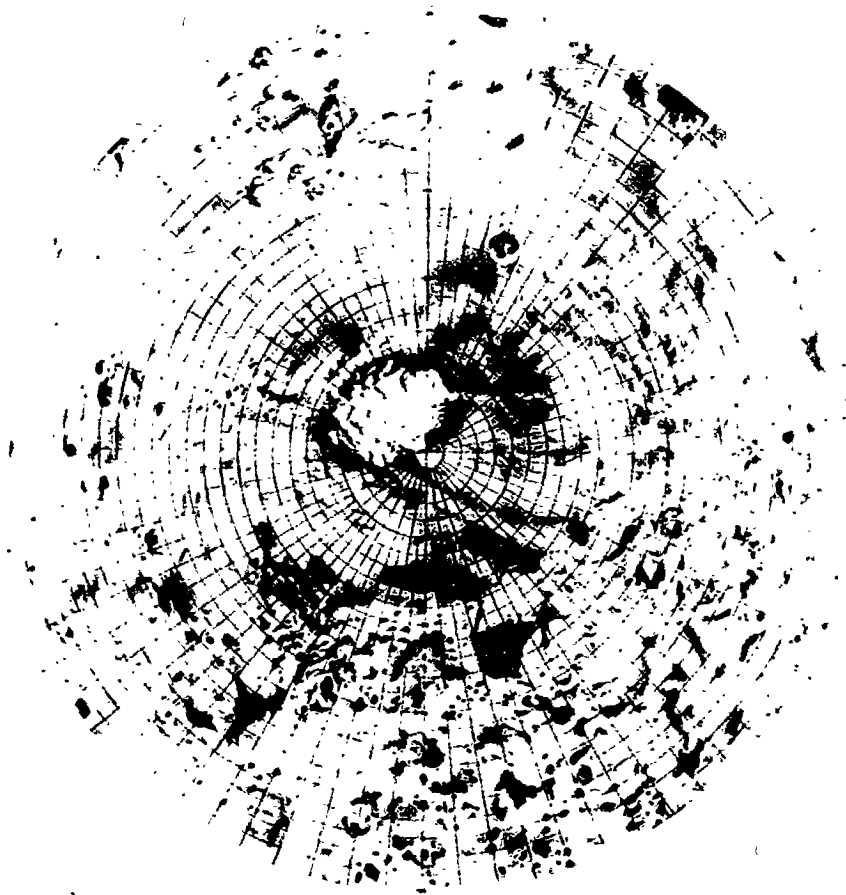
Fig. XXXXIV-1. Preliminary albedo charts of the south polar region of Mars from *Mariner 9* data in polar stereographic projection with coordinate grid overlay. Note that contrast is exaggerated by photographic reproduction.

pp. 205, 212; Ref. XXXXIV-2, p. 36; Ref. XXXXIV-3, p. 22; and Ref. XXXXIV-4, p. 27). The same remark holds for the north polar cap (Ref. XXXXIV-5, pp. 313, 317). The final phase of the rapid shrinkage of the south polar cap was recorded by *Mariner 9* in the first month of orbital operation; no further significant reduction was observed. The rapid decay of the large and obviously thin, peripheral surface deposit during early summer contrasts with the insignificant reduction of the residual cap after mid-summer. This behavior suggests a two-component model for the polar caps: a "hard core" of water ice (perhaps relatively thick) near the pole and a thin overlying and widespread seasonal deposit of dry ice. The infrared spectral reflectivity data might provide a check for such a model.

The *Mariner 9* data are significantly at variance with older telescopic data on the location of the centroid of the residual ice cap. Whereas the best telescopic observa-

tions of the past century were in good agreement to locate this point near longitude 23°, latitude −85° (Ref. XXXXIV-6, Circ. No. 3), the new map shows it near longitude 45°, latitude −87°, a displacement of 2.5 aerocentric degrees.

The difference is in part due to the change in the adopted direction of the spin axis (Ref. XXXXIV-7; also see Section XXXX of this Report), but most of it must probably be ascribed to the difficulty of deriving, from Earth-based observations, precise coordinates near the poles.

A comparison of the albedo distribution with the topography is assisted by reference to telescopic observations of the large-scale albedo markings seen in the polar regions at different phases of the seasonal evolution of the south polar cap. Figure XXXXIV-3 shows the appearance of the south cap in the early spring of the southern
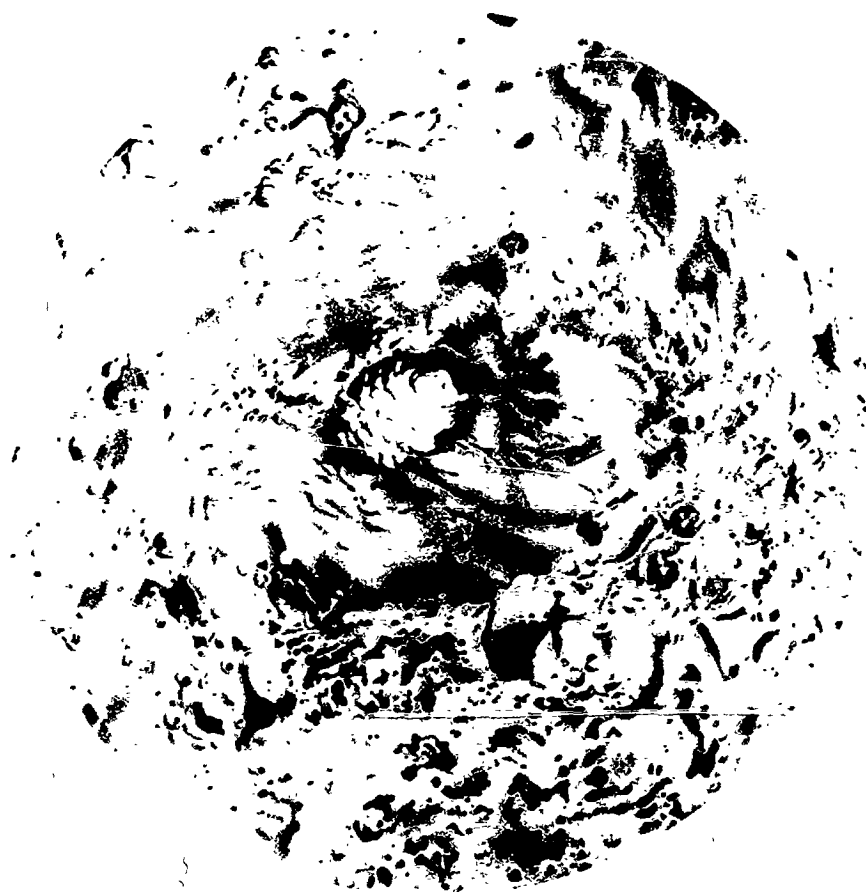
Fig. XXXXIV-2. Same as Fig. XXXXIV-1 without overlay.

hemisphere from observations made in June–July 1971 near $L_s = 220°$ with the 76-cm reflector of the USGS Observatory near Flagstaff and the 155-cm reflector of the Catalina Observatory of the University of Arizona near Tucson (Ref. XXXXIV-7; see Section XXXX of this Report). Figure XXXXIV-4, based on earlier data at corresponding oppositions (1911, 1926, 1941, 1958), shows the expected appearance of the polar remnant and surface markings near $L_s = 320°$ corresponding to a nominal date of January 1, 1972, approximately matching that of the Mariner map in Fig. XXXXIV-1. Note that Figs. XXXXIV-3 and XXXXIV-4 show a slightly larger area ($\phi < -60°$) than Figs. XXXXIV-1 and XXXXIV-2 ($\phi < -65°$). Figure XXXXIV-3 shows the familiar bright promontories near the edge of the seasonal cap, namely, Mons Argenteus near longitude 30°, Thyle I near 160°, Thyle II near 240°, and Novus Mons near 320°. Novus Mons contracts to Novissima Thyle (the "Mountains of Mitchel") at a later phase of the seasonal evolution of the cap. Note that the polar cap remnant, designated as

Hypernotius Mons, visible near the pole in Fig. XXXXIV-4 is not seen as a brighter or distinct entity in the early spring view of Fig. XXXXIV-3 when large dark areas known as Depressio Magna (near 270°) and Depressio Parva (near 180°) are prominent. The latter apparently vanishes without trace when the icy deposit evaporates later in the spring, but the north boundary of Depressio Magna seems to correspond closely with a long, curved rim visible on the Mariner chart between longitude 260°, latitude −75° and longitude 320°, latitude −80°. The USGS topographic map indicates that the drop is on the south side so that "Depressio" turns out to be an appropriate designation for the albedo marking.

Very little else in the topography of the polar regions seems to correlate closely with the albedo markings of the telescopic views. This is consistent with the results of radar observations at lower latitudes which first brought out this remarkable lack of general correlation between

Fig. XXXXIV-3. South polar cap of Mars with large-scale albedo features near $L_x = 220°$ from telescopic observations.

Fig. XXXXIV-4. South polar regions of Mars with large-scale albedo features near $L_x = 320°$ from telescopic observations. Compare with Fig. XXXXIV-2.

albedo and elevation. (This does not preclude close correlations in localized areas such as the Coprates canyon.) It must be kept in mind, nevertheless, that the MTVS pictures were processed to emphasize small-scale topographic details, and thereby eliminated completely any albedo differences on a scale larger than the averaging length. (Photometrically corrected versions may later force some revisions of these tentative conclusions.)

The most remarkable of the small-scale albedo features are the numerous small, dark patches eccentrically located

on the floors of many craters. Some larger craters have several such spots, but most small craters have just one, and there is a tendency for the spots to be offset from the crater centers in the same general azimuth for all craters in a given area. This property is not limited to the polar region, and it has been noticed in other areas of the planet. It is suggestive of windblown dust accumulating preferentially in specific areas relative to the surrounding topography. The bright and dark "comet tails" associated with some crater fields in other parts of the planet are probably a related phenomenon.

References

XXXXIV-1. Flammarion, C., *La Planete Mars*, Vol. 2. Gauthier-Villars, Paris, 1909.

XXXXIV-2. Antoniadi, E. M., *La Planete Mars*, Vol. 1, Hermann, Paris, 1920.

XXXXIV-3. de Vaucouleurs, G., *The Planet Mars*, Faber and Faber, London, 1951.

XXXXIV-4. de Vaucouleurs, G., *Physics of the Planet Mars*, Faber and Faber, London, 1954.

XXXXIV-5. de Vaucouleurs, G., *Planetary Atmospheres*, IAU Symposium No. 40, p. 130, 1971.

XXXXIV-6. de Vaucouleurs, G., Mars News, 1917, *Bull. Nrs. 1, 2, 3*, circulated to *Mariner* 9 TV Team; see abstracts in *Sky and Telescope*, Vol. 42, pp. 134, 263; Vol. 43, p. 20, 1971.

XXXXIV-7. de Vancouleurs, G., Davies, M. E., and Sturms, F. M., Jr., "Mariner 9 Areographic Coordinate System," *J. Geophys. Res.*, Vol. 78, 1973.

Appendix
Extended Mission Operations Summary

M. E. Goble

Jet Propulsion Laboratory/California Institute of Technology, Pasadena, California 91103

At the start of *Mariner 9* orbital operations on November 14, 1971 (GMT), the standard mission was scheduled to last for 90 days and to end on February 11, 1972; however, because of the unexpected dust storm conditions at the planet, the standard mission was continued until the beginning of the first solar occultations occurring on April 2. The extended mission covered the period from April 2 until the end of spacecraft life on October 27, 1972. Extended mission events are shown in Table A-1.

The objectives of the extended mission were to:

(1) Preserve the spacecraft as long as it could obtain meaningful scientific data.

(2) Gather unique data around superior conjunction on September 7, when Earth and Mars were on opposite sides of the Sun.

(3) Receive high–latitude data to complete global mapping.

(4) Supplement data with additional occultations that could be observed.

(5) Continue the celestial mechanics experiment.

(6) Obtain continuing variable-features coverage and observe specified Viking landing sites.

Manpower was appreciably reduced during the extended mission because personnel were released to other projects to curtail costs. Further, only the 64-m antenna at DSS 14 (Goldstone, Calif.) could receive data from the spacecraft. With an increasing distance from Earth and other constraints, as described below, it became more difficult and time-consuming to send commands and receive data from the spacecraft.

Although it was known that the Mission Operations System (MOS) staffing would be reduced substantially, it was assumed that the operations would be simplified enough that the objectives could be met with less effort than before. This assumption was not correct. The extended mission was in many ways as challenging as the standard mission because of the complexity of opera-

Table A-1. *Mariner 9* extended mission events

Event	Date 1972 (GMT)
Complete standard mission mapping	Feb. 29
Start Sun occultations (first period)	April 2
Start Earth occultations (second period)	May 6
Final Sun occultation (first period)	June 5
Playback of first extended mission tape load	June 9
Final Earth occultation (second period)	June 26
Solar superior conjunction	September 7
Start Earth occultations (third period)	September 27
Start Sun occultations (second period)	October 4
Final high-gain antenna maneuver playback	October 17
Last usable data from *Mariner 9*	October 27 (17:41)
End of mission (end of track)	October 27 (23:41)

tions, reduced manpower, and unavailability of stations. Although the objectives were met, near the conclusion of the extended mission, all systems, ground stations, and the spacecraft were being used beyond their design margin, thus making operations extremely difficult.

From April 2 through June 5, the spacecraft flew into the shadow of Mars briefly during each revolution, undergoing solar occultation. An automatic sequence was designed for the spacecraft to operate under central computer and sequencer (CC&S) control during these periods. Although an occultation occurred each revolution, only the zenith revolutions were visible when DSS 14 was tracking; therefore, the sequence was designed to be independent of ground command. Because the Sun could not be used for attitude reference during occultation, the spacecraft was placed in an all-inertial mode during occultation periods. The duration of the solar occultations varied from a few minutes to approximately 1.5 hr at the maximum, with the longest occultation occurring

on April 23. During these times, electrical power normally provided by the solar panels was not available, requiring shutdown of the on-board science instruments for the entire period. Only engineering subsystems and heaters were on as required, and only the S-band occultation and celestial mechanics experiments were able to acquire data.

It was known at the time the trajectory was designed that *Mariner 9* would at times enter the shadow of Mars and experience solar occultations. However, the Project considered survival of the spacecraft beyond solar occultations as a secondary objective because of cost factors and anticipated technical difficulties. Nevertheless, the knowledge gained from other missions in which solar occultations occurred was used whenever possible; operational personnel, informed of the importance of having the spacecraft survive solar conjunction, carefully analyzed all data to assess spacecraft performance.

During the 66 days of solar occultations, certain spacecraft elements, for example the attitude-control gas jets, dropped below approved temperature limits. The solar panels frequently reached extreme temperatures for which they had not been tested. Twice each day they were subjected to thermal shock on entering the shadow and then exiting into the bright sunlight. Although operations proceeded normally, it should be noted that the readable lower limit of the solar-panel temperature transducer was $-124°C$; yet, by extrapolation, it appeared that the panels were experiencing temperatures of $-157°C$.

During the week of April 12, tests of the 400-kW transmitter were performed at the 64-m antenna site because the transmitter would be required during the critical period centered around superior conjunction. Many problems were encountered during these initial attempts to use the transmitter. As a result, the 20-kW transmitter was used while a "tiger team" identified and solved the problems with the 400-kW transmitter. When *Apollo 16* was launched, *Mariner 9* was not tracked for 4 days because of the priority of the *Apollo* mission.

As the distance increased between the spacecraft and Earth, the threshold of 33⅓ engineering bps was reached on April 15. After that date, unless the spacecraft performed a high-gain-antenna maneuver, the data rate available would be 8⅓ bps.

On April 19, it became difficult to maintain receiver lock at periapsis because of the high Doppler rate caused by the geometry of the spacecraft in relation to the planet Mars and its aspect angle with Earth. A third-order filter was installed in the S-band receiver at DSS 14 to help remedy a receiver out-of-lock condition. The filter eliminated out-of-lock occurrences during periapsis, and valuable data were obtained for celestial mechanics and other experiments. The only problem encountered with the third-order filter was the difficulty in locking the receiver, but this problem was eliminated as experience was gained in operating the equipment.

After observing *Mariner 9* during occultations for about 3 weeks, it was determined that gas consumption was greater than expected because of the automatic acquisition each time the spacecraft came out of occultation and acquired the Sun. As the gas supply was critical to the lifetime of the spacecraft, it was important to minimize the effects of this problem. By sending a DC-32 ground command once per revolution, the spacecraft was placed in an inertial mode. This mode required one-fourth the amount of gas and did not require the spacecraft to perform an automatic acquisition.

The best tracking data for use in the study of the gravitational anomalies of Mars were obtained during a 5-week period starting approximately on April 23. These data were available as the geometry presented the spacecraft in an "edge-on" orbit, as viewed from Earth at periapsis.

Earth occultations, ranging from about 44 to 90 min in duration each revolution, resumed on May 6 and continued until June 26. Fortunately, despite the limited command time between the start of track and the start of Earth occultation, it was still possible to transmit the DC-32 commands.

On May 11, the gas leaks, which had occurred previously in the roll jet, were increasing noticeably and jeopardizing the remainder of the mission. The CC&S was, therefore, programmed to clear the jets by appropriate command at specified intervals. These commands were used instead of the previous procedure of sending ground commands to turn the gyros on and off because the spacecraft was tracked only periodically by DSS 14.

Later, because orbit geometry, as viewed from Earth, was changing, the DC-32 commands were not transmitted because DSS 14 could not view the spacecraft when required. To avert this problem, the Project decided to send the commands "in the blind." The procedure of sweeping the uplink and sending commands

from a 26-m station was initiated by DSS 62 on May 17. At each occurrence, the commands were sent six times for a reserve and to allow telemetry verification when the spacecraft was tracked by DSS 14.

From May 20 to May 24, the *Pioneer* Project was conducting a unique experiment which prohibited the normal tracking of *Mariner 9*. DSS 14 would track *Mariner 9* for a short period of time before the spacecraft entered Earth occultation, while DSS 62 maintained the two-way uplink. This interval allowed valuable occultation data to be received and, in addition, permitted a limited amount of telemetry to be acquired to assess spacecraft performance.

From the start of the standard mission, the exciter drive continued to decline slowly with a reduced signal received at Earth. Analysis indicated that, if the redundant exciter was switched in, an increased signal strength should be observed. On May 30, the exciter in the radio frequency subsystem was switched from position 2 to position 1, and an approximate 1.3-dB increase was observed by the ground station. The 1.3-dB increase permitted 8 kbps to be received when the high-gain-antenna maneuvers were initiated. These maneuvers were required to permit reception of high-rate science data at Earth.

On June 1 and 2, CC&S updates were loaded for anticipated science and engineering tests. On June 4, the Canopus tracker was turned on for the first time since the start of Sun occultation, and Canopus was acquired. On June 5, the last of the solar occultations for this period was observed. An engineering maneuver was conducted to point the high-gain antenna at Earth to receive data. The science instruments were then turned on and evaluated. In addition, a solar-array test was conducted and revealed that the science instruments were working well. The television cameras were calibrated, and some meaningful data were obtained by the ultraviolet spectrometer and infrared radiometer. A maneuver was performed to roll the spacecraft to Arcturus, because the acquisition of this star was required for planned science sequences. Further analysis showed that interference from Deimos was expected. To circumvent this situation, the CC&S was programmed to prevent the interference. However, Phobos also entered the tracker's field of view, causing loss of lock on Arcturus, and a roll search for Canopus occurred. About 0.018 kg (40 mlb) of attitude-control gas was expended in this search.

After the engineering tests, the next phase of the *Mariner 9* operations was started. The objectives of this phase were: (1) to complete the mapping of the region 40°N latitude to the north pole, an area previously obscured by the north polar hood, and (2) to examine the topography of the 20 to 30 proposed Viking landing sites.

On June 8, data were again recorded, and 31 pictures were received at Earth on June 9. The extended mission playback profile is shown in Table A-2. This playback was conducted both at 4 kbps and 8 kbps. At 4 kbps, good spectral instrument data were obtained, which were not possible at 8 kbps because of the signal-to-noise ratio. The pictures indicated that the obscuring north polar hood had diminished sufficiently for the television cameras to photograph the north polar terrain.

During this period, continuing Earth occultations reduced the available playback time by about 1.5 hr. To obtain as much playback time as possible, the initial commands to start the high-gain-antenna maneuver, transmitted from DSS 62, were timed so that the spacecraft's high-gain-antenna beam would be directed toward Earth at the time of DSS 14 acquisition of the spacecraft. By this technique, the maximum available time was obtained for playback of science data.

Analysis of the spacecraft data indicated that the proposed mission plan for this phase, which called for two high-gain-antenna maneuvers per week for 9 weeks, was in jeopardy because the attitude-control gas was being consumed at an excessive rate. Thus, the spacecraft might not be able to perform the high-priority superior conjunction test of relativity for the celestial mechanics experiment. Although it appeared that two gas bottles were preferred to ensure that the spacecraft control would be symmetrical about its axis during the relativity test, the celestial mechanics experimenters determined that one bottle would be sufficient.

Based on this conclusion two maneuvers per week were allowed in June, one maneuver on July 10, and one maneuver on August 7. This strategy was designed so that some attitude-control gas would still remain for superior conjunction and, hopefully, so that four maneuvers could be completed after superior conjunction to observe long-term changes in Martian surface features.

The high-gain-antenna maneuver performed on July 10 was unique in that science data were acquired on three revolutions instead of two. This scheme permitted the experimenters to select targets which could not otherwise

Table A-2. Picture playback profile of extended mission

Acquisition		High-gain antenna maneuver		Number of pictures anticipated	Number of pictures actually received	Reference star
Date 1972 (GMT)	Revolution	Date 1972 (GMT)	Revolution			
June 8 and 9	416 and 417	June 9	418	30	31	Arcturus
June 11 and 12	422 and 423	June 12	424	30	31	Arcturus
June 15 and 16	430 and 431	June 16	432	30	31	Arcturus
June 18 and 19	436 and 437	June 19	438	30	30	Arcturus
June 22 and 23	444 and 445	June 23	446	30	30	Arcturus
June 25 and 26	450 and 451	June 26	452	30	30	Arcturus
June 29 and 30	458 and 459	June 30	460	30	30	Arcturus
July 7, 9 and 10	473, 478, and 479	July 10	480	30	30	Canopus[a]
August 3 and 6	528, 529, and 533	August 7	536	30	30	Canopus[b]
October 11 and 12	667 and 668	October 13	670	30	29	Vega
October 15 and 16	675 and 676	October 17	678	30	27	Vega
				Total 330	Total 329	

[a]Data taken on three revolutions: July 6 nadir and July 9 and 10 zenith/nadir.

[b]Zenith/nadir revolutions on August 3 and 4; nadir revolution on August 6.

be obtained. Following the playback, the spacecraft was commanded into the roll-drift mode, which had been used during the Sun-occultation period. During the roll-drift mode, the Canopus sensor remained on, although not in a control loop. This mode allowed all stars that came within the field of view to be identified, and thus the roll rate of the spacecraft could be determined.

The CC&S load for the August 7 playback was the most complicated to date and illustrated the operational difficulties experienced. The CC&S load was designed to program the spacecraft data recording sequence covering three revolutions (the third separated by three intervening revolutions), and to guard against possible interference by stray light from Phobos and Mars. Because the capacity of the on-board computer was exceeded, the load was divided between 2 days. While performing this load, a time-critical operation was accomplished by sending a command at the correct time to acquire Canopus just as the star appeared in the tracker field of view, thereby saving gas because the spacecraft did not have to operate in a roll-search mode.

The Project relinquished support from DSS 14 from July 23 through July 30 so maintenance could be per-

formed to prevent permanent damage to the hydrostatic bearings. The required maintenance was performed ahead of schedule, and tracking was resumed on July 30.

Starting on August 16 and continuing until October 19, the Project dedicated its entire effort to gathering ranging and Doppler data for the prime objective of the relativity portion of the celestial mechanics experiment. The critical period for the relativity test was the 7 days before and after superior conjunction. At that time, the 400-kW transmitter was considered the prime transmitter and was used until the end of the celestial mechanics experiment. The transmitter was operated on alternate passes at 200 kW and 400 kW to determine which was the most reliable mode of operation. It was decided that 400 kW could be utilized most effectively during the critical superior conjunction period. In addition, a special voice net was established temporarily for the duration of the experiment. This net (called "ranging advisers") allowed the ranging adviser to discuss technical problems and questions directly with the personnel at DSS 14, and the net was monitored by personnel in the SFOF.

It was known that the ability to receive engineering data would degrade and eventually disappear from ap-

proximately 10 days before until 10 days after superior conjunction. This condition was caused by the increasing signal-to-noise temperature of the receivers at DSS 14 as the spacecraft traveled directly opposite to the Earth on the other side of the Sun. The normal receiver temperature at DSS 14 is approximately 30°K; with the solar effect caused by the spacecraft and the Sun, as seen from Earth, having the same celestial longitude, the temperature reached approximately 600°K, thereby preventing telemetry data reception.

The spacecraft was programmed so that no additional spacecraft cyclic events (2A events), which would turn the ranging channel off, would be issued after August 28; and the last usable engineering data before superior conjunction were obtained on August 30. The greatest distance between Earth and Mars for Mariner 9 was reached on August 31, when the two planets were separated by about 399,817,000 km (248,435,000 mi). On that day, the round-trip light time to and from the spacecraft was 44 min, 26 sec. The first usable engineering telemetry after superior conjunction was received at the SFOF on September 14, 1972. Telemetry readings of the gas bottles showed that one bottle was reading zero and the other was reading 8 DN. However, the limit cycle appeared normal, which indicated that even though the low bottle read zero, some gas remained in both bottles.

On August 28, at DSS 14, one of the two 750-kW diesel generators used to power the 400-kW transmitter, when on auxiliary power, experienced a major failure. The 750-kW generator was returned to Los Angeles for repair, and was operating again by September 4. The major effect of losing the generator was that the station transmitter could have operated only at about 175 kW instead of the desired 400 kW while on auxiliary power.

The ranging data were analyzed by the ranging advisers, and as the spectrum became worse, the receivers were observed to be out of lock more often. To retain receiver lock, thereby gathering the required ranging data for the relativity test, a programmed local oscillator (PLO), which automatically adjusted the receiver in a preprogrammed manner, was installed in receiver 2 at DSS 14 on September 3. The PLO worked well and retained receiver lock on the signal most of the time. Superior conjunction occurred at 4:00 a.m. September 7, 1972. Mars, with the spacecraft in orbit about it, passed within approximately 1° of the Sun as viewed from Earth.

In addition to the inclusion of a third-order filter and the PLO in the receiver, other modifications continually were made in the Mu-ranging program. The modifications

were incorporated as needed and usually were operative on the next day. Spacecraft command was resumed as required on September 20. The quality of the data continued to improve and was acceptable by the end of September.

A series of engineering tests was conducted from September 28 through October 17. These tests dealt primarily with the radio frequency subsystem and the flight command subsystem, but tests were also performed on the solar array and the pyrotechnics subsystem. A special Phobos long-exposure picture was obtained to assess the camera's capability to perform the optical navigation required in the Mariner Jupiter/Saturn mission.

On October 4, Mariner 9 experienced its second series of solar occultations. However, during this phase the spacecraft continued to gather science data. To conserve gas, the spacecraft had been operating in a roll-drift, rate-controlled mode since August 7. On October 11, the spacecraft locked onto the star Vega to provide better viewing of Mars. Twenty-nine pictures were received on October 13. They were of excellent quality and showed a clear north pole. Some spectral instrument data were also obtained. This was the first science data returned from the instruments since August 7.

At the onset of the solar occultation phase, DC-32 commands were initiated from DSS 14 and DSS 41 to conserve gas, as in the previous solar occultation sequence. Another high-gain-antenna maneuver was performed, with 27 pictures and spectral data received on October 17.

The spacecraft was permitted to go into the roll-drift mode after playback on October 17, as the next science sequence would be obtained using the star Canopus. In preparation for the science data-tracking sequence on October 25, an attempt was made to acquire Canopus. It had been predicted that the acquisition of Canopus would be difficult because of stray light problems from Mars and its satellites. The acquisition of Canopus was started at the beginning of track and required most of the day. Many problems were encountered because of the uncertainty regarding which object had been acquired. In addition, the spacecraft logic was in an undesirable state and caused the consumption of about 0.009 kg of gas. After Canopus was acquired, an analysis indicated that the Canopus tracker was in a degraded state, which caused the initial acquisition difficulty. Acquisition was accomplished by stepping the Canopus tracker from brightness gate 1 to brightness gate 2.

Near the conclusion of end of track on October 25, there was a critically low gas supply in the spacecraft. Therefore, for the first time, the *Mariner 9* downlink was turned off by ground command. This precautionary procedure was taken so that, if the spacecraft had a malfunction and could not be commanded, the *Mariner 9* radio signal would not interfere with future programs. Early on October 26, *Mariner 9* responded to a command to turn the radio signal back on. The plans were revised so only two recorder tracks of science data would be played back, instead of four tracks, to conserve gas. The spacecraft radio was again commanded off in preparation for the high-gain-antenna maneuver on October 27.

Early on October 27, commands were again sent to turn the *Mariner 9* transmitter on; the spacecraft responded. Telemetry analysis showed that the spacecraft was extremely low on gas, and the limit cycle was not normal. The one remaining gas bottle was below regulation pressure. A meeting was held to determine whether or not the high-gain-antenna maneuver should be attempted. There were, at this time, 15 pictures on the tape. The decision was to proceed with the maneuver. The spacecraft performed a zero roll turn as programmed. When it was time to exercise the yaw turn, the spacecraft took approximately 2 min to gain near-normal speed for

the turn. However, during the activity, the gas was exhausted, and the turn could not be stopped. The spacecraft continued to yaw as the low-gain antenna approached the predicted null, and the last data from the *Mariner 9* spacecraft were received at 17:41:10 GMT. Procedures were initiated immediately to turn the spacecraft off. The spacecraft then entered Earth occultation, which prevented further attempts to enter commands.

After the spacecraft exited occultation, it was observed that the spacecraft signal was being momentarily locked every 51 min, which was in close agreement with the tumble rate prediction of attitude-control personnel. With that knowledge, a timed uplink sweep was performed to acquire the spacecraft and to obtain a command lock while the low-gain antenna was pointed toward Earth. A series of commands was sent to turn the transmitter off; the last command was sent at 22:10:00 GMT. The last signal from *Mariner 9* was received at 22:31:00 GMT.

The end of mission operations, and the end of a very successful *Mariner 9* mission, was declared at 23:41:00 GMT on October 27, 1972, at the end of track by DSS 14. *Mariner 9* operated for a total of 515 days, 19 hr, and 18 min with a total inflight time of 12,379 hr and 18 min.